NIST SPECIAL PUBLICATION 801

Laser Induced Damage in Optical Materials: 1989

BOULDER DAMAGE SYMPOSIUM

SPIE Volume 1438

STP 1117

NIST SPECIAL PUBLICATION 801

Laser Induced Damage in Optical Materials: 1989

Proceedings of the Boulder Damage Symposium, November 1-3. 1989

Sponsored by

National Institute of Standards and Technology
American Society for Testing and Materials
International Society for Optical Engineering
Defense Advanced Research Project Agency
Department of Energy

October 1990

Edited by

Harold E. Bennett
Naval Weapons Center
China Lake, California 93555

Lloyd L. Chase
Lawrence Livermore National Laboratory
Livermore, California 94550

Arthur H. Guenther
Los Alamos National Laboratory
Los Alamos, New Mexico 87545

Brian E. Newnam
Los Alamos National Laboratory
Los Alamos, New Mexico 87545

M.J. Soileau
University of Central Florida
Orlando, Florida 32816

U.S. Deprtment of Commerce
Robert A. Mosbacher, Secretary

National Institute of Standards and Technology
John W. Lyons, Director

National Institute of Standards and Technology
Special Publication 801, 670 pages (Oct. 1990)
CODEN: NBSAV

U.S. GOVERNMENT PRINTING OFFICE
WASHINGTON: 1990

For sale by the Superintendent of Documents, U.S. Government Printing Office, Washington, DC 20402-9325

FOREWORD

The Proceedings contain the papers presented at the Twenty-First Symposium on Optical Materials for High-Power Lasers held at the National Institute of Standards and Technology in Boulder, Colorado, on November 1-3, 1989. The Symposium was sponsored jointly by the National Institute of Standards and Technology, the American Society for Testing Materials, the International Society for Optical Engineering, the Defense Advanced Research Project Agency, and the Department of Energy. The Symposium was attended by approximately 200 scientists from the United States, Canada, the United Kingdom, Japan, France, and the Federal Republic of Germany. It was divided into sessions devoted to the following topics: Materials and Measurements, Mirrors and Surfaces, Thin Films, and, finally, Fundamental Mechanisms. The Symposium Co-Chairmen were Harold E. Bennett of the Naval Weapons Center, Arthur H. Guenther of the Los Alamos National Laboratory, Lloyd L. Chase of the Lawrence Livermore National Laboratory, Brian E. Newnam of the Los Alamos National Laboratory, and M. J. Soileau of the University of Central Florida. They also served as editors of the proceedings.

The editors assume full responsibility for the summary, conclusions, and recommendations contained in the report, and for the summaries of discussion found at the end of each paper. The manuscripts of the papers presented at the Symposium have been prepared by the designated authors, and questions pertaining to their content should be addressed to those authors. The interested reader is referred to the bibliography at the end of the summary article for general references to the literature of laser damage studies. The Twenty-Second Annual Symposium on this topic will be held in Boulder, Colorado, October 24-26, 1990. A concerted effort will be made to ensure closer liaison between the practitioners of high-peak power and high-average power.

The principal topics to be considered as contributed papers in 1990 do not differ drastically from those enumerated above. We expect to hear more about improved scaling relations as a function of pulse duration, area, and wavelength, and to see a continuing transfer of information from research activities to industrial practice. New sources at shorter wavelengths continue to be developed, and a corresponding shift in emphasis to short wavelength and repetitively pulsed damage problems is anticipated. Fabrication and test procedures will continue to be developed, particularly in the diamond-turned optics and thin-film areas. It has been our intention to pause and reflect on progress over the past twenty years to the Symposium on Optical Materials for High Power Lasers. It will be our pleasure to present the last (Thin Film, the Second Decade) in a comprehensive array of tutorial lectures by distinguished workers in the field of laser induced damage in optical materials.

The purpose of these symposia is to exchange information about optical materials for high-power lasers. The editors will welcome comments and criticism from all interested readers relevant to this purpose.

H. E. Bennett, A. H. Guenther, L. L. Chase,
B. E. Newnam, and M. J. Soileau,
Co-Chairmen

DISCLAIMER

Certain papers contributed to this publication have been prepared by non-NIST authors. These papers have not been reviewed or edited by NIST; therefore, the National Institute of Standards and Technology accepts no responsibility for their accuracy, nor for their comments or recommendations.

Certain commercial equipment, instruments, and materials are identified in this publication in order to explain the experimental procedure adequately. Such identification in no way implies approval, recommendation, or endorsement by the National Institute of Standards and Technology, nor does it imply that the equipment, instruments, or materials identified are necessarily the best available for the purpose.

CONTENTS

Page

FOREWORD iii
H.E. Bennett, A.H. Guenther, L.L. Chase, B.E. Newnam, and M.J. Soileau

DISCLAIMER iv

SYMPOSIUM WELCOME xii
M.J. Soileau

SEARCH FOR TECHNOLOGY TRANSFER IN HIGH POWER OPTICS xvi
C. Martin Stickley

SUMMARY OF MEETING 1
H.E. Bennett, L.L. Chase, A.H. Guenther, B.E. Newnam, and M.J. Soileau
1. Introduction 1
2. Overview 3
3. Acknowledgments 5
4. References 6

1989 INDEX - BOULDER DAMAGE SYMPOSIUM

MATERIALS AND MEASUREMENTS

Set of Standard Definitions for Laser Damage in Parameters and Procedures 9
J.W. Arenberg

Optical Characterization of Transparent Materials Using Ellipsometry 10
S.F. Nee and H.E. Bennett

Microindentation as a Technique For Assessing Subsurface Damage In Optics 25
R.S. Polvani and C. Evans

Automated Damage Testing Facility for Excimer Laser Optics.....39
K. Mann and H. Gerhardt

Expanded Damage Test Facilities at LLNL.....47
A.J. Morgan, F. Rainer, F.P. DeMarco, R.P. Gonzales,
M.R. Kozlowski, and M.C. Staggs

Laser Damage Database at 1064 nm.....58
F. Rainer, R.P. Gonzales, and A.J. Morgan

Damage Measurements on Optical Materials for Use in High-Peak-Power Lasers.....74
F. Rainer, R.M. Brusasco, J.H. Campbell, F.P. DeMarco,
R.P. Gonzales, M.R. Kozlowski, F.P. Milanovich,
A.J. Morgan, M.S. Scrivener, M.C. Staggs, I.M. Thomas,
S.P. Velsko, and C.R. Wolfe

Laser Induced Damage to Thallium Arsenic Selenide(TAS).....84
A.A. Said, M. Sheik-Bahae, M.J. Soileau, E.W. Van Stryland
N.B. Singh, and T. Henningsen

Laser Induced Damage in Schott's OG-550 Optical Absorption Glass.....88
T. Whittaker, R. Goedert, and D. Templeton

Effects of Laser Damage Processes on Microwave Propagation.....96
R.S. Eng, M.D. Abouzahra, N.W. Harris, D.R. Cohn, and P.P. Woskov

Laser Induced Damage to Silicon Photosensor Arrays.....115
Chen-Zhi Zhang, Thierry Benchetrit, Steve E. Watkins,
Rodger M. Walser, and Michael F. Becker

Sensitive n_2 Measurements Using A Single Beam.....126
M. Sheik-Bahae, A.A. Said, T.H. Wei, D.J. Hagen,
E.W. Van Stryland, and M.J. Soileau

Optical Breakdown in Particle Suspension.....136
Kamjou Mansour, M.J. Soileau and E.W. Van Stryland

Annealing of Induced Damage in Flouride Glass Components.....151
Osama H. El-Bayoumi, M.J. Suscavage, and L.P. De Rochemont

The Effect of Laser Annealing on Laser Induced Damage Threshold.....164
N.C. Kerr and D.C. Emmony

Shockwave Detection, An Efficient Way to Determine Multiple-Pulse Damage Thresholds.....180
S. Petzoldt, A.P. Elg, J. Reif, and E. Matthias

Application of the Ronchi Ruling Beam Profiling Method to Axially Symmetric Laser Beams.....187
Robert M. O'Connell and Cheng-Hao Chen

Prediction of Laser Induced Damage by Comparison of Laser Fluence Profile to Damage Spot Radius.....200
R. Goedert, T. Whittaker, and D. Templeton

IR Laser Beam Profiling Using Quenched Fluorescence.....214
N.C. Kerr, S.E. Clark and D.C. Emmony

Laser-Induced Failure in Biased Silicon Avalanche Photodiodes.....220
Steve E. Watkins, Chen-Zhi Zhang, Rodger M. Walser, and Michael F. Becker

SURFACES AND MIRRORS

The Effect of Subsurface Defects on "Incipient" (Below Threshold) Laser Damage Nucleation In Fused Silica Optical Flats.....230
T.J. Magee, C.S. Leung, F.D. Orazio, J.D. Boyer, B.R. Mauro, and V.E. Sanders

Quantitative Analysis of Surface Trace Metal Contamination on Substrates and Films by TXRF.....239
R. S. Hockett

An Error Analysis of the Wyko TOPO Noncontact Surface Profiler.....254
Van A. Hodgkin

Ultra-Precision Grinding of LHG-8 Laser Glass and Laser Damage Thresholds.....255
Y. Namba, K. Yoshida, H. Yoshida, and S. Nakai

Low Scatter Surfaces on Silicon Carbide.....256
Roger A. Paquin and Matthew B. Magida

Physical Limits on Ultra-High Albedo Diffuse Reflectors.....263
Perry Miles

Optical Damage on SiO_2 Cavity Mirrors Produced by High-Power VUV Laser Irradiation.....267
Y. Takigawa, K. Kurosawa, M. Okuda, W. Sasaki,
K. Yoshida, E. Fujiwara, Y. Kato, and Y. Inoue

Damage Assessment and Possible Damage Mechanisms to 1-Meter Diameter
Nova Turning Mirrors.....278
G. Edwards, J. Campbell, R. Wolfe, E. Lindsey

Thermal Transport Studies of Optical Coatings, Interfaces and Surfaces
by Thermal Diffusion Wave Interferometry.....291
Randall T. Swimm and Gary Wiemokly

Thin Films

Investigation of Thin Films Using Total Internal Reflection Microscopy.....299
F.L. Williams, C.K. Carniglia, B.J. Pond, and W.K. Stowell

Scattering Characterization of Materials in Thin Film Form.....309
C. Amra

Optical Properties and Laser Damage Measurements of Inorganic Polymer Films.....324
Gregory J. Exarhos and Kevin M. Crosby

Interfacial Stability in Optical Coatings.....335
K.L. Lewis, A.M. Pitt, A.G. Cullis, K. Welford, and I.T. Muirhead

Surface Analytical Methods for the Assessment of Damage in Optical Thin Films.....350
James R. Hoenigman

Laser Conditioning of Optical Thin Films.....360
C.R. Wolfe, M.R. Kozlowski, J.H. Campbell, F. Rainer,
A. J. Morgan, and R. P. Gonzales

Large Area Laser Conditioning of Dielectric Thin Film Mirrors.....376
M.R. Kozlowski, C.R. Wolfe, M.C. Staggs, and J.H. Campbell

Population Distribution of Conditioned Damage Thresholds on AR Coated BK-7 Glass
With Varing Laser Spot Size.....393
D.W. Mordaunt and J.W. Arenberg

Damage Threshold Measurements of Reflective and Transmissive Optics at 130 nm.....403
C.H. Muller, III and C.E. Hamilton

Laser Induced Damage Thresholds of Dielectric Coatings at 193 nm and Correlations to
Optical Constants and Process Parameters.....404
J. Kolbe, H. Müller, H. Schink, H. Welling, and J. Ebert

Angular Dependence of Thin-Film Dielectric Coating Damage Thresholds Revisited.....417
J. D. Boyer, S. R. Foltyn, B. R. Mauro, and V. E. Sanders

Pulse-width Dependence of Optical Coating Damage at 1052 nm.....425
K. Yoshida, S. Ikunishi, H. Yoshida, Y. Kato, and S. Nakai

Damage Resistant Optical Coatings Prepared Using High Temperature, Plasma
Chemical-Vapor Deposition.....426
J.H. Campbell, J.L. Emmett, R.M. Brusasco, F. Rainer, R.Th. Kersten,
V. Paquet, and H.W. Etzkorn

A High Temperature, Plasma-Assisted Chemical Vapor Deposition System.....443
R.M. Brusasco, J.A. Britten, C.B. Thorsness, M.S. Scrivener,
W.G. Unites, J.H. Campbell, and W.L. Johnson

The Evolution of Molecular Beam Deposition (MBD) from Laboratory to Production Usage.....455
C.C.H. Hale, I.T. Muirhead, S.P. Fisher, G.J.H. Mathew

Investigation and Modelling of Laser Damage Properties of Fabry-Perot Filters.....471
A. McInnes, C.M. MacDonald, D.R. Gibson and A.D. Wilson

High Damage Threshold AlO.OH-SiO_2 HR Coatings Prepared by the Sol-Gel Process.....484
Ian M. Thomas

1-on-1 and n-on-1 Laser Strength of Binder Aided ZrO_2 and ZrO_2-SiO_2 Reflective Sol-Gel Coatings.....490
H.G. Floch and J.J. Priotton

Structural Modification of D_2O/H_2O-Dosed CaF_2 Optical Thin Films.....509
J.B. Franck

FUNDAMENTAL MECHANISMS

Non-Avalanche Dielectric Breakdown in Wide-Band-Gap Insulators at DC and Optical Frequencies.....528
P. Braunlich, S.C. Jones, X.A. Shen, R.T. Casper, E. Cartier, D.J. DiMaria, M.V. Fischetti, and P. Kelly

UV Seeding of IR Laser Induced Damage.....541
N.C. Kerr, S.E. Clark and D.C. Emmony

Measurements of uv Induced Absorption in Dielectric Coatings.....551
M.H. Bakshi, M. Cecere, D.A.G. Deacon, and A.M. Fauchet

The Response of Multilayer Dielectric Coatings to Low Fluence Ultraviolet Light Exposure.....561
V.E. Sanders, J.W. Early, and W. Leamon

Radiation Damage in Single Crystal CsI (Tl) and Polycrystal CsI.....568
O. Barnouin, A. Procoli, H. Chung, and G.H. Miley

Effects of Thermal Conductivity and Index of Refraction Variation on the Inclusion Dominated Model of Laser-Induced Damage.....576
M.Z. Fuka, J.K. McIver, and A.H. Guenther

Theoretical Determination of the Nonlinear Optical Properties of Inorganic Polymers.....584
Steven M. Risser and Kim F. Ferris

Relation Between n_2 and Two-Photon Absorption.....591
M. Sheik-Bahae, D.J. Hagan, E.W. Van Stryland, T.H. Wei
A.A. Said, E. Canto, and A. Miller

Photoconductivity of ZnS and ZnSe.....598
B.E. Mason and C.D. Marrs

Formation of a Pregiven Reflecting Surface Topography by Elastic Deformation of the Mirror Substrate. New Concept of Adaptive Optical System.....606
V.V. Apollonov, S.A. Chetkin, E.A. Ivanova, A.M. Prokhorov, G.V. Vdovin

Application of Ultrasonic Capillary Effect in Elements of Power Optics Cooled by Means of a Heat Pipe.....618
V.V. Apollonov, S.A. Chetkin, V.N. Kharchenko, V.N. Motorin,
and A.M. Prokhorov

Appendix I. List of Attendees.....631

WELCOME FOR 21st BOULDER DAMAGE SYMPOSIUM

M. J. Soileau
Professor of Electrical Engineering and Physics
Director, Center for Research in Electro-Optics and Lasers
University of Central Florida
Orlando, Florida

It is my pleasure and duty to call this year's meeting to order. I was abroad when the final program was put together by my co-chairs and did not learn of this honor until a couple of weeks ago. I had no time to prepare until this weekend, so this will be a bit rough and without the benefit of elegantly prepared slides.

I don't mean to take a stab at my co-chairs, but I must admit that as I began my preparation I couldn't remember a single thing about previous opening remarks by my esteemed colleagues! Did I miss something? Surely these distinguished leaders of national laboratories must have said something profound and prophetic! So I spent part of the day Saturday reviewing the past utterances which have launched this meeting.

It is true that the memory is the second thing to go, because as I read the opening remarks for the past 20 meetings, I found many, profound statements--a few of which are listed below:

This is a quote from the next speaker from 1972:

"It is a pleasure to be here this afternoon."
Martin Stickley, 1972.

"Whatever turns you off." (Alex's definition of damage)
Alex Glass, 1974

"A name which invokes images of people cracking rocks."
Alex Glass, 1976. (In response to Martin Stickley's call for a more positive sounding name for the conference.)

"Our onion unfortunately, exists in Hilbert Space." (Alex borrowing from an ancient philosopher's description that learning is like peeling an onion--each layer exposes another.)

"Who cares?" (Alex on why study damage?)
Alex Glass, 1976.

"It is my annual hope that each year's symposium will be the last." (Alex the failed prophet.)
Alex Glass, 1978.

"The key...is terawatts per megabuck.
Alex Glass, 1978.

"Power Optics." (A supplier of megabucks at the time in comparing laser optics to electronics.)
Harry Winsor, 1978.

"Aside from a gain medium, lasers require mirrors." (Insightful words from the great visionary.)
Harry Winsor, 1978.

"Progress has been made, but I am confident that in 10 years we will celebrate the 20th and Art and Alex will still be running it!" "...we owe a debt to these 2 young men." (Note the term young.)
Martin Stickley, 1978.

To this point I've spared you the profound utterance of my current co-chairs such as:

"Welcome to the Tenth Anniversary Damage Symposium." (Art Guenther gave this greeting at the 11th meeting.)
Art Guenther, 1979.

Then there were profound things said regarding the international participation.

"...countries represented include the British Isles, Canada, England, France, Japan, Scotland, and West Germany:"
Brian Newnam, 1980.

"International contributors...have come a long way..."
Hal Bennett, 1985.

It should be clear to all how difficult it is for me since these guys have used up all the good stuff! Further review of these openings presented me with a good outline for my remarks. I will follow the trail blazed by my predecessors:

Outline

1. Welcome participants.

2. Acknowledge sponsorship of NIST, ASTM, and others.

3. Count the papers for this year's meeting and comment on the statistical distribution.

4. Observe that thin films are a major problem.

5. Profound and prophetic statement about the future of the meeting.

I do welcome you to the 20th Anniversary Boulder Damage Symposium. Those of you who are still asleep or partially hung over, may be confused by the fact that last year was our 20th Anniversary celebration. The resolution of this dilemma is the fact that last year was the 20th meeting and this is

the 20th Anniversary (but the 21st meeting). One might say that this meeting is old enough to drink - but you will also note that there is no wine and cheese this year. This situation has resulted from rulings by NIST accountants. In fact, the accountants have made it difficult for us to conduct business as usual, so you can expect further changes next year.

We do want to thank NIST and the ASTM for their continued sponsorship and all the helpful folks at Boulder who make the meeting run smoothly.

There are about 70 papers this year with contributions from 6 countries, in addition to the U.S. The talks from abroad constitute 27% of the papers, about the same percentage as from Livermore and Los Alamos. About an equal number of papers come from U.S. aerospace companies (15%) and U.S. universities (16%). About 9% are from DoD labs and the remaining 8% from various other sources.

Our next speaker (Martin Stickley) has suggested on a number of occasions that the name of the conference be changed to something more positive. I want to finish this presentation by noting that there are many positive things being done with phenomena studied by participants in these meetings. Here is a list of a few:

<u>"Spin Offs" of LID Phenomena</u>

1. Laser marking, cutting and drilling of materials.

2. Laser medicine
   a. laser scalpel
   b. laser-induced breakdown for eye treatments and plaque removal.

3. Laser disc storage - the first application of LID to consumer products.

4. Photorefractive information storage, processing, and phase conjugation interconnects.

5. Nonlinear refraction and nonlinear absorption for limiters, switches, and optoelectronic computing.

6. Electro-absorptive switches using UHV manufactured quantum well devices (SEED's).

So I issue a challenge to us all to keep the name Damage Symposium, but continue to seek positive applications of the phenomena we study. A wise professor once told me that phenomena are neither good or bad--they exist and it's up to us to find ways to make good things using phenomena given by nature.

Before I left Orlando, I looked into by crystal ball for a glimpse of future laser damage or optical materials problems--here is my short list:

<u>Future Topics for Optical Materials Research</u>

1. Thin films for all applications. Two talks viewing 20 years of thin film work.

2. New laser host and nonlinear optical materials for compact, efficient, tunable and solid state lasers for many old and many new applications.

3. X-ray optics for lasers (remember Harry Winsor said that lasers have mirrors...), and optics for x-ray microscopy and x-ray lithography.

4. Materials for x-ray lithography.

I'm sure that these and other topics will keep optical materials people busy for some time--the only question is where will the funding come from? DoD funding will surely decline as peace is breaking out all over. DOE funding usually finds its way to the national labs--but not much finds its way out. DARPA, under Martin Stickley's leadership, provided much of the spark that lead to modern day materials and much of the research reported at this conference. Materials research tends to be too long-term for present day funding. We need to all do our part in ensuring continued research support for the foundation of the technology food chain--materials research.

Since we don't have an official wine and cheese gathering, I hereby propose that we forgo small gatherings of old friends for dinner, etc. and meet instead at the Dark Horse for an informal, pay as you go, social hour.

Manuscript received
2-14-90

SEARCH FOR TECHNOLOGY TRANSFER IN HIGH POWER OPTICS

C. Martin Stickley

BDM International, Inc.
1300 N. 17th St., Suite 950
Arlington, VA 22209

In the late 60's and through the 70's, DARPA supported a broad program to develop optics for use with high power cw CO_2 lasers and new laser and nonlinear optical materials. This paper summarizes those efforts and asks anyone who knows in what defense systems these have been used to contact the author.

In the late 1960's and through the 1970's, the Materials Sciences Office (now the Defense Sciences Office) of the Defense Advanced Research Projects Agency (DARPA) funded a broad program to develop optics for high power continuous development of approaches to fabricate large area windows with high transparency (absorption of 10^{-5} per cm), optical surface preparation techniques which leave very little residual absorption, and techniques for depositing antireflection as well as reflecting coatings for transparent windows and mirrors. Some development of new laser and nonlinear optical materials was also funded. Approximately $22.9 M dollars were spent between 1967 and 1978.

The Defense Sciences Office is now searching for examples of where optical parts fabricated using these techniques and the laser and NLO materials have been used in defense systems. While defense uses are of primary importance, NASA and industrial uses are also of interest.

Technologies which may have had the best chance of being utilized include, for windows: casting of fluorides, reactive atmosphere processing of halides, forging of halides, and CdTe growth, distortion and damage studies; for surfaces and coatings: polymers and surface preparation of halides, fluorides, and selenides; for lasers: erbuim glass, and holmium and erbium in YLF; for mirrors: beryllium optics; and for laser damage: platinum removal and surface preparation of Owens-Illinois glass, and bulk and surface damage of ruby.

The tables which follow summarize the activities which were supported in each major area. Included are the specific technology developed (e.g. fluoride fusion casting), the contractor, the amount of funding provided, and at the time period where the work was done.

If the reader knows of areas where any of these technologies may have been used in defense systems (as well as for NASA and the commercial sector), please contact the author.

LASER WINDOW MATERIALS

Fluorides

● Fluoride Fusion Casting	Raytheon	166K	76–77
● Scaling of Fluoride Casting	Raytheon	790K	74–76

Halides

● Halide Superalloys for High Power Windows	Raytheon	191K	72–73
● Halide OH Removal	Hughes Res. Labs	174K	72
● Reactive Atmosphere Processing	Hughes Res. Labs	215K	76–78
● RAP of KBR	Hughes Res. Labs	244K	74–76
● Extrusion and Cross-Rolling	Honeywell	1 95K	72–73
● Forging of Alkali Halides	Honeywell	1483K	73–78
● Radiation Hardening	Oklahoma	113K	72–74
● Press Forging Halides	NRL	521K	72–75
● RAP of KBR - Characterization	NRL	80K	76

BDM INTERNATIONAL, INC.

LASER WINDOW MATERIALS

II–VI Materials

● II–VI Distortion and Damage	USC	1336K	72–77
● CVD of Cadmium Telluride	Raytheon	192K	73–75
● CVD of CdTe and GaP	Raytheon	196K	75–77
● Characterization of II–VI Materials	MIT	308K	73–76

Chalcogenides

● Oxygen–Free Chalcogenides	Catholic University	283K	72–74
● Structure–Dependent Absorption	Texas Instruments	72K	73–74

Other

● Covalent Carbon Window Materials	UCLA	114K	75–76
● Copper–Leaded CERVIT	Owens Illinois	27K	76

LASER WINDOW MATERIALS

Measurement Techniques

● Spectroscopy of Halides	Cornell	209K	75–76
● Emissivity Facility	Block Eng.	250K	73–75
● Multiple Wavelength Calorimetry	Alabama	58K	74–76
● Chemical Laser Window Absorption	Raytheon	60K	74–75
● CO_2 Laser Window Evaluation	AVCO	279K	75–76
● Proof Testing	MIT	168K	75–76
● Mechanical Properties	MIT	320K	72–75

Theory

● Theory of Coatings and UV Materials	Xonics	1342K	72–78

BDM INTERNATIONAL, INC.

LASER COATINGS AND SURFACES

● Polymer Protective Coatings	UC Berkeley	169K	75–77
● Polymer Protective Coatings	Rockwell	149K	73–74
● Surface and Coating Technology	Hughes Res. Lab	1076K	73–76
● Window Polishing and Characterization	NWC	1696K	72–77
● Passive Characterization/HF Coatings	NWC	1042K	76–77
● Coating Stress Measurements	Perkin Elmer	200K	76–77
● Coating Growth and Stress	AFCRL	255K	73–75
● Transparent Abrasives	Raytheon	207K	73–75

LASER MATERIALS

● Erbium Glass	American Optical	191K	69–71
● Holmium in YLF	Sanders Associates	203K	71–73
● Near Visible Laser Materials	Sanders Associates	270K	72–75
● Ceramics for Lasers	Union Carbide	193K	1977
● Wide Linewidth Materials	Texas Instruments	225K	72–73

MIRRORS AND SURFACES

● Beryllium for Optics	Perkin Elmer	1434K	Prior to 69
● Ion Beam Optical Figuring	Kollsman	146K	Prior to 69

BDM INTERNATIONAL, INC.

NONLINEAR OPTICAL MATERIALS

● Cinnabar	Tyco	190K	70–71
● Chalcopyrite	Stanford	279K	70–74
● High Damage Threshold Materials	Isomet	98K	1973
● Chalcogenides	Westinghouse	230K	72–75
● IR Laser Components	Westinghouse	201K	Before 1969
● IR Quantum Counter	Purdue		

DAMAGE TO LASER MATERIALS

Glass

● Laser Glass Damage	Owens Illinois	616K	69–71
● Glass Surface Treatment	Owens Illinois	291K	72–73

Ruby

● Bulk and Surface Damage	Hughes Res. Labs	400K	69–71

Measurement Techniques

● Laser Measurements	NBS	2369K	Prior to 69
● Laser Damage Measurements	NBS	161K	72–73

Mirrors

● RF Sputtered Metal Mirrors	Battelle NW	450K	72–73

Research

● Miscellaneous Topics	Harvard, NWC, USC, AFCRL, Raytheon, Bendix	749K	71–76

LASER WINDOW MATERIALS

Fluorides

● Fluoride Fusion Casting	Raytheon	166K	76–77
● Scaling of Fluoride Casting	Raytheon	790K	74–76

Halides

● Halide Superalloys for High Power Windows	Raytheon	191K	72–73
● Halide OH Removal	Hughes Res. Labs	174K	72
● Reactive Atmosphere Processing	Hughes Res. Labs	215K	76–78
● RAP of KBR	Hughes Res. Labs	244K	74–76
● Extrusion and Cross-Rolling	Honeywell	1 95K	72–73
● Forging of Alkali Halides	Honeywell	1483K	73–78
● Radiation Hardening	Oklahoma	113K	72–74
● Press Forging Halides	NRL	521K	72–75
● RAP of KBR – Characterization	NRL	80K	76

BDM INTERNATIONAL, INC.

LASER WINDOW MATERIALS

II–VI Materials

● II–VI Distortion and Damage	USC	1336K	72–77
● CVD of Cadmium Telluride	Raytheon	192K	73–75
● CVD of CdTe and GaP	Raytheon	196K	75–77
● Characterization of II–VI Materials	MIT	308K	73–76

Chalcogenides

● Oxygen–Free Chalcogenides	Catholic University	283K	72–74
● Structure–Dependent Absorption	Texas Instruments	72K	73–74

Other

● Covalent Carbon Window Materials	UCLA	114K	75–76
● Copper–Leaded CERVIT	Owens Illinois	27K	76

LASER WINDOW MATERIALS

Measurement Techniques

● Spectroscopy of Halides	Cornell	209K	75–76
● Emissivity Facility	Block Eng.	250K	73–75
● Multiple Wavelength Calorimetry	Alabama	58K	74–76
● Chemical Laser Window Absorption	Raytheon	60K	74–75
● CO_2 Laser Window Evaluation	AVCO	279K	75–76
● Proof Testing	MIT	168K	75–76
● Mechanical Properties	MIT	320K	72–75

Theory

● Theory of Coatings and UV Materials	Xonics	1342K	72–78

BDM INTERNATIONAL, INC.

LASER COATINGS AND SURFACES

● Polymer Protective Coatings	UC Berkeley	169K	75–77
● Polymer Protective Coatings	Rockwell	149K	73–74
● Surface and Coating Technology	Hughes Res. Lab	1076K	73–76
● Window Polishing and Characterization	NWC	1696K	72–77
● Passive Characterization/HF Coatings	NWC	1042K	76–77
● Coating Stress Measurements	Perkin Elmer	200K	76–77
● Coating Growth and Stress	AFCRL	255K	73–75
● Transparent Abrasives	Raytheon	207K	73–75

LASER MATERIALS

● Erbium Glass	American Optical	191K	69–71
● Holmium in YLF	Sanders Associates	203K	71–73
● Near Visible Laser Materials	Sanders Associates	270K	72–75
● Ceramics for Lasers	Union Carbide	193K	1977
● Wide Linewidth Materials	Texas Instruments	225K	72–73

MIRRORS AND SURFACES

● Beryllium for Optics	Perkin Elmer	1434K	Prior to 69
● Ion Beam Optical Figuring	Kollsman	146K	Prior to 69

BDM INTERNATIONAL, INC.

NONLINEAR OPTICAL MATERIALS

● Cinnabar	Tyco	190K	70–71
● Chalcopyrite	Stanford	279K	70–74
● High Damage Threshold Materials	Isomet	98K	1973
● Chalcogenides	Westinghouse	230K	72–75
● IR Laser Components	Westinghouse	201K	Before 1969
● IR Quantum Counter	Purdue		

DAMAGE TO LASER MATERIALS

Glass

● Laser Glass Damage	Owens Illinois	616K	69–71
● Glass Surface Treatment	Owens Illinois	291K	72–73

Ruby

● Bulk and Surface Damage	Hughes Res. Labs	400K	69–71

Measurement Techniques

● Laser Measurements	NBS	2369K	Prior to 69
● Laser Damage Measurements	NBS	161K	72–73

Mirrors

● RF Sputtered Metal Mirrors	Battelle NW	450K	72–73

Research

● Miscellaneous Topics	Harvard, NWC, USC, AFCRL, Raytheon, Bendix	749K	71–76

Laser Induced Damage in Optical Materials

Twenty-First ASTM Symposium
November 1-3, 1989

The Twenty-First Annual Symposium on Optical Materials for High-Power Lasers (Boulder Damage Symposium) was held at the National Institute of Standards and Technology in Boulder, Colorado, November 1-3, 1989. The Symposium was sponsored jointly by the National Institute of Standards and Technology, the American Society for Testing and Materials, the International Society for Optical Engineering, the Defense Advanced Research Project Agency, and the Department of Energy. Approximately 200 scientists, including representatives of the United Kingdom, France, Japan, Canada, and the Federal Republic of Germany, attended the Symposium. The Symposium was divided into sessions concerning Materials and Measurements, Mirrors and Surfaces, Thin Films, and, finally, Fundamental Mechanisms. As in previous years, the emphasis of the papers presented at the Symposium was directed toward new frontiers and new developments. Particular emphasis was given to materials for high power apparatus. The wavelength range of the prime interest was from 10.6 μm to the uv region. Highlights included surface characterization, thin film substrate boundaries, and advances in fundamental laser-matter threshold interactions and mechanisms. The scaling of damage thresholds with pulse duration, focal area, and wavelength was discussed in detail. Harold E. Bennett of the Naval Weapons Center, Arthur H. Guenther of the Los Alamos National Laboratory, Lloyd L. Chase of the Lawrence Livermore National Laboratory, Brian E. Newnam of the Los Alamos National Laboratory, and M.J. Soileau of the University of Central Florida were co-chairmen of the Symposium. The Twenty-Second Annual Symposium is scheduled for October 24-26, 1990, at the National Institute of Standards and Technology, Boulder, Colorado.

Key words: laser damage; laser interaction; optical components; optical fabrication; optical materials and properties; thin film coatings.

1. Introduction

The Twenty-First Annual Symposium on Optical Materials for High-Power Lasers (Boulder Damage Symposium) was held, as in previous years, at the National Institute of Standards and Technology in Boulder, Colorado, November 1-3, 1989. The Symposium was held under the auspices of the ASTM with the joint sponsorship of NIST, and the Department of Energy. Approximately 200 scientists, including representatives of the United Kingdom, France, Japan,

Canada, and the Federal Republic of Germany, attended the symposium. The Symposium was divided into sessions concerning Materials and Measurements, Mirrors and Surfaces, Thin Films, and, finally, Fundamental Mechanisms. In all, approximately 70 technical presentations were made. Harold E. Bennett of the Naval Weapons Center, Arthur H. Guenther, and Brian E. Newnam of the Los Alamos National Laboratory, Lloyd L. Chase of the Lawrence Livermore National Laboratory, and M. J. Soileau of the University of Central Florida were co-chairmen of the Symposium. Aaron A. Sanders of the National Institute of Standards and Technology acts as conference Coordinator.

The purpose of these symposia is to exchange information about optical materials for high power lasers. The authors welcome comments and criticism from all interested readers relevant to this purpose and particularly relative to our plans for the Twenty-second Annual Symposium, scheduled for October 24-26, 1990, at the National Institute of Standards and Technology, Boulder, Colorado.

2. Overview

The following comments by the Symposium co-chairmen represent their impression of significant advances that were discussed immediately after the close of the meeting. This is not meant to be a thorough review of the conference, but only a brief glimpse of some of the highlights.

The largest single group of papers in the Fundamental Mechanisms session dealt with the effects of high photon energies on laser-induced damage (LID) at lower photon energies. As one example, short-wavelength harmonic radiation generated within free-electron lasers can potentially reduce the LID at the fundamental lasing wavelength. Another case involved the effect of ultraviolet radiation on the damage resistance at 10.6 μm. Yet another paper dealt with the use of photoconductivity as a diagnostic to identify defects within the bandgap and to monitor the onset of LID.

One area covered at this meeting for the first time was the nonlinear properties of inorganic polymers as well as those of organic polymers. In addition, a theoretical paper described the contribution of conjugated electronic systems to the nonlinear polarizability of such materials which have potential use as photoelectronic devices.

Always of interest to theoreticians are the possible relationships of apparently different classes of materials properties. This year, one group studied the relationship between the nonlinear refractive index and two-photon absorption coefficient using a model that assumed that a Kramers-Kronig relationship exists between the two.

One paper provoked a great deal of discussion and controversy, and suggested that avalanche breakdown is not a fundamental mechanism even for intrinsically pure materials, as generally accepted. Data which they believed supported their claim that damage occurs first by multiphoton absorption followed by nonlinear free-carrier absorption and heating that then leads to damage were presented. To account for earlier observation by other experimenters, it was asserted that avalanche processes do take place after breakdown is initiated. Nevertheless, indications of avalanche before breakdown were ascribed to extrinsic processes and/or impure materials. These conclusion challenge the laser damage community to propose a set of independent experiments that can confirm or discount their proposed model.

Concerning surfaces and mirrors, perhaps one of the most encouraging developments, after many years of continuous effort, was the progress reported for the polishing of silicon carbide. SiC and Be are among the most attractive mirror materials now being considered for use in space missions. One study reported on two different techniques for producing SiC mirrors which could be finished to varying degrees of surface polish and which were stable. The most attractive technique was physical-vapor deposition finishing of SiC by ion-beam sputtering very smooth coatings with a low level of stress. The rms surface roughness on these elements was less than 0.5 nm(5 Å), and stable with time.

Another exciting development was that ultra-precise grinding of glass surfaces with diamond had attained 0.5 nm(5 Å) roughness, which is remarkable. A number of papers concentrated on mirrors for the vacuum ultraviolet, a new thrust this year. There was some concentration on production problems of working with a system with 1 m diameter mirrors subjected to very high laser fluences. Systematic errors in surface topography using noncontact interferometers were discussed. We also heard a novel suggestion for laser protection of surfaces by developing small spherical particles that would diffusely reflect incoming laser beans. The particles must have absorption levels of $\sim 10^{-5}$ to 10^{-6} cm^{-1}. If this becomes possible, then mirrors with very high reflectance of 99.999% or better could result.

In the area of thin film coatings, degradation by ultraviolet and vacuum-ultraviolet wavelengths was emphasized. One parametric study concerned degradation to ZrO_2 films caused by 25-eV synchrotron radiation. Surprisingly, after a short period, the initial damage apparently healed, possibly by the material evolving to a different crystal structure. Another paper described the much higher resistance of HfO_2 films to color-center formation caused by a 248-nm KrF laser when the usual 3% ZrO_2 impurity content was reduced to a few tenths of a percent. We also heard a report on much higher damage thresholds being attained for multilayer reflectors prepared by the sol-gel process as a result of altering the coating process to decrease the concentration of absorbing impurities.

3. Acknowledgments

The editors acknowledge the invaluable assistance of Aaron A. Sanders and the other involved staff members of the National Institute of Standards and Technology in Boulder, Colorado, for their interest, support, and untiring efforts in the professional operation of the symposium. Particular thanks to Susie Rivera of NIST for her lead in the preparation and publication of the proceedings, as well as Margalene Hartman of NIST. Thanks, also, to Pat Whited of the Air Force Weapons Laboratory and Delma Oberbeck of NIST for conference coordination.

4. References

[1] Glass, A.J.; Guenther, A.H., eds. Damage in Laser Glass, ASTM Spec. Tech. Pub. 469, ASTM, Philadelphia. PA; 1969.

[2] Glass, A.J.; Guenther, A.H., eds. Damage in Laser Materials, Nat. Bur. Stand. (U.S.) Spec. Publ. 341; 1970.

[3] Bloembergen, N. Fundamentals of Damage in Laser Glass, National Materials Advisory Board Publ. NMAB-271, National Academy of Sciences; 1970.

[4] Glass, A.J.; Guenther, A.H., eds. Damage in Laser Materials: 1971, Nat. Bur. Stand. (U.S.) Spec. Publ. 356; 1971.

[5] Bloembergen, N. High Power Infrared Laser Windows. National Materials Advisory Board Publ. NMAB-356; 1971.

[6] Glass, A.J.; Guenther, A.H., eds. Laser Induced Damage in Optical Materials: 1972, Nat. Bur. Stand. (U.S.) Spec. Publ. 372; 1972.

[7] Glass, A.J.; Guenther, A.H., eds. Laser Induced Damage in Optical Materials: 1973, Nat. Bur. Stand. (U.S.) Spec. Publ. 387; 1973.

[8] Glass, A.J.; Guenther, A. H. Laser Induced Damage in Optical Materials: A Conference Report. Appl. Opt. 13 (1): 74-88; 1974.

[9] Glass, A.J.; Guenther, A.H., eds. Laser Induced Damage in Optical Materials: 1974, Nat. Bur. Stand. (U.S.) Spec. Publ. 414; 1974.

[10] Glass, A.J.; Guenther, A.H. Laser Induced Damage in Optical Materials: 6th ASTM Symposium. Appl. Opt. 14 (3): 698-715; 1975.

[11] Glass, A.J.; Guenther, A.H., eds. Laser Induced Damage in Optical Materials: 1975, Nat. Bur. Stand. (U.S.) Spec. Publ. 435; 1975.

[12] Glass, A.J.; Guenther, A.H. Laser Induced Damage in Optical Materials: 7th ASTM Symposium. Appl. Opt. 15 (6): 1510-1529; 1976.

[13] Glass, A.J.; Guenther, A.H., eds. Laser Induced Damage in Optical Materials: 1976. Nat. Bur. Stand. (U.S.) Spec. Publ. 462; 1976.

[14] Glass, A.J.; Guenther, A.H. Laser Induced Damage in Optical Materials: 8th ASTM Symposium, Appl. Opt. 16 (5): 1214-1231; 1977.

[15] Glass, A.J.; Guenther, A.H., eds. Laser Induced Damage in Optical materials: 1977, Nat. Bur. Stand. (U.S.) Spec. Publ. 509; 1977.

[16] Glass, A.J.; Guenther, A.H. Laser Induced Damage in Optical Materials: 9th ASTM Symposium, Appl. Opt. 17 (15): 2386-2411; 1978.

[17] Glass, A.J.; Guenther, A.H. Laser Induced Damage in Optical Materials: 1978, Nat. Bur. Stand. (U.S.) Spec. Publ. 541; 1978.

[18] Glass, A.J.; Guenther, A.H., eds. Laser Induced Damage in Optical Materials: 10th ASTM Symposium, Appl. Opt. 18 (13): 2212-2229; 1979.

[19] Bennett, H.E.; Glass, A.J.; Guenther, A.H.; Newnam, B.E. Laser Induced Damage in Optical Materials: 1979, Nat. Bur. Stand. (U.S.) Spec. Publ. 568; 1979.

[20] Bennett, H.E.; Glass, A.J.; Guenther, A.H.; Newnam, B.E. Laser Induced Damage in Optical Materials: 11th ASTM Symposium, Appl. Opt. 19 (14): 23375-2397; 1980.

[21] Bennett, H.E.; Glass. A.J.; Guenther, A.H.; Newnam, B.E. Laser Induced Damage in Optical Materials: 1980, Nat. Bur. Stand. (U.S.) Spec. Publ. 620; 1981.

[22] Bennett, H.E.; Glass, A.J.; Guenther, A.H.; Newnam, B.E. Laser Induced Damage in Optical Materials: 12th ASTM Symposium, Appl. Opt. 20 (17): 3003-3019; 1981.

[23] Bennett, H.E.; Guenther, A.H.; Milam, D.; Newnam, B.E. Laser Induced Damage in Optical Materials: 1981, Nat. Bur. Stand. (U.S.) Spec. Publ. 638; 1983.

[24] Bennett, H.E.; Guenther, A.H.; Milam, D.; Newnam, B.E. Laser Induced Damage in Optical Materials: 13th ASTM Symposium, Appl. Opt. 22 (20): 3276-3296; 1983.

[25] Bennett, H.E.; Guenther, A.H.; Milam, D.; Newnam, B.E. Laser Induced Damage in Optical Materials: 1982, Nat. Bur. Stand. (U.S.) Spec. Publ. 669; 1984.

[26] Bennett, H.E.; Guenther, A.H.; Milam, D.; Newnam, B.E. Laser Induced Damage in Optical Materials: 14th ASTM Symposium, Appl. Opt. 23 (21): 3782-3795; 1984.

[27] Bennett, H.E.; Guenther, A.H.; Milam, D.; Newnam, B.E. Laser Induced Damage in Optical Materials: 1983, Nat. Bur. Stand. (U.S.) Spec. Publ. 688; 1985.

[28] Bennett, H.E.; Guenther, A.H.; Milam, D.; Newnam, B.E. Laser Induced Damage in Optical Materials: 15th ASTM Symposium, Appl. Opt. 25 (2): 258-275; 1986.

[29] Bennett, H.E.; Guenther, A.H.; Milam, D.; Newnam, B.E. Laser Induced Damage in Optical Materials: 1984, Nat. Bur. Stand. (U.S.) Spec. Publ. 272; 1986.

[30] Bennett, H.E.; Guenther, A.H.; Milam, D.; Newnam, B.E. Laser Induced Damage in Optical Materials: 16th ASTM Symposium, Appl. Opt. 26 (5): 813-827; 1987.

[31] Bennett, H.E.; Guenther, A.H.; Milam, D.; Newnam, B.E. Laser Induced Damage in Optical Materials: 1985, Nat. Bur. Stand. (U.S.) Spec. Publ. 746; 1987.

[32] Bennett, H.E.; Guenther, A.H.; Milam, D.; Newnam, B.E. Laser Induced Damage in Optical Materials: 1986, Nat. Inst. Stand. and Tech. (U.S.) Spec. Publ. 752; 1987.

[33] Bennett, H.E.; Guenther, A.H.; Milam, D.; Newnam, B.E.; Soileau, M.J.; Laser Induced Damage in Optical Materials: 1987, NIST (U.S.) Spec. Publ. 756; 1988.

[34] Bennett, H.E.; Guenther, A.H.; Newnam, B.E.; Soileau, M.J.; Laser Induced Damage in Optical Materials: 1988, NIST (U.S.) Spec. Publ. 775; 1989.

MANUSCRIPT NOT RECEIVED

A Set of Standard Definitions for Laser Damage Parameters and Procedures

J.W. Arenberg

Advanced Technology Department
TRW Space and Technology Group
One Space Park Drive O1/1210
Redondo Beach, CA 90278

ABSTRACT

It is an essential aspect of science, technology and commerce to be able to communicate in a common language of units, procedure and phenomenology. Presently, there exist no such standards for the field of damage testing, leading to the present problems in scientific communication, comparison of test results and commercial activities. A necessary precursor to the standardization and proper cataloging of laser damage test data is a common nomenclature. There are many cases where parameters, phenomenology and test results are denoted by identical names. Moreover, there are cases where a single idea is known by multiple labels. This lack of standardization in the definitions and nomenclature leads to difficult, tedious and frequently unfruitful literature searches. This paper is intended to be the first step in the standardization of the field of laser induced damage by reviewing the literature and assigning in one review paper, a set of exclusive definitions or labels to the various definitions of damage, threshold determination, spot size and pulse width. In making these assignments, a vehicle is provided for the necessary seminal discussions leading to eventual adoption of accepted standards of procedure and definition for laser damage testing.

Manuscript received
1-17-90

Optical Characterization of Transparent Materials Using Ellipsometry

S. F. Nee and H. E. Bennett

Physics Division, Research Department
Naval Weapons Center, China Lake, CA 93555-6001

Refractive indices of transparent materials can be measured with high accuracy on small laboratory samples using null ellipsometry. Measurement precision in both n and k obtained ellipsometrically is ±0.0004 for semi-transparent samples. Systematic errors in ellipsometric characterization of optical constants for transparent materials can result from back-surface reflection as well as from front-surface scattering caused by surface roughness. An analysis of the contribution of these errors and the methods of eliminating them are discussed. We conclude that careful ellipsometric characterization can give indices of refraction to three decimal places in the infrared for materials with low k.

Key words: ellipsometry; error analysis; extinction coefficients; optical measurements; polarizations; reflectometry; refractive indices; roughness effects; transparent materials.

1. Introduction

The index of refraction of a transparent material can be determined with high accuracy by making the material into a prism and determining the minimum angle of deviation [1]. For general characterization of newly developed materials, the minimum deviation method is not convenient, since a relatively large homogeneous sample is required. Often large pieces of developmental materials are not available. Other techniques for measuring the index of refraction n and the extinction coefficient k for glasses in the low k region are ellipsometry and the Kramer-Kronig (KK) analysis of reflectance data augmented by absorption measurements [2,3]. The KK technique is usually of lower accuracy for n than the minimum deviation method, and the k values determined from the reflection data are not reliable in the low k region. Additional absorption measurements using calorimetry or other techniques are required. However, if data are available, consistent index values can be determined over an extended wavelength range using a KK analysis. Ellipsometric measurements can be made on small developmental samples of material and can achieve accuracies approaching those obtainable using minimum deviation techniques, as will be shown. Often ellipsometric measurements are not that accurate because of systematic errors resulting from instrumentation or sample configuration. An analysis of some of these sources of error will be given. Most ellipsometric measurements have been made in the visible region of the spectrum. In the infrared region, contamination problems of the surface involving monatomic layers are less severe than in the visible region, so it is an even more attractive region in which to work. An attempt to characterize transparent materials by ellipsometry in the infrared region was described in a previous paper [4]. In that paper, the n and k for a smooth quartz sample were measured, and the change in ψ and Δ due to surface roughness as well as that due to a small difference in n and in k were

numerically computed. With these data, we could predict the maximum roughness allowed for reliable measurement and the accuracies of n and k obtainable by ellipsometry. Effects of roughness and texture were also investigated for semitransparent materials [5-7]. This paper presents a systematic analysis for the errors in ellipsometric characterization and discusses methods to eliminate errors. Comparison of the measured results with theoretical predictions and the Handbook results shows that reflection ellipsometry can offer accurate measurements of optical constants in the infrared region to three decimal places in both n and k.

2. Basic Analysis for Reflection Ellipsometry

Ellipsometry measures the relative change of amplitude and phase between p- and s-waves after light is output from a sample. For reflection ellipsometry, the ellipsometric parameters, ψ and Δ, are defined through the complex ratio ρ as

$$\rho = \frac{r_p}{r_s} = \tan\psi \, e^{i\Delta} \quad , \tag{1}$$

where r_p and r_s are the coefficients of reflection at a given incident angle θ for light initially polarized in the p- and s-directions, respectively. If the complex refractive index (n,k) of a sample is known, r_p and r_s can be computed from Fresnel equations; hence, ψ and Δ for a single interface system are only functions of n, k, and θ. Inversely, n and k can be solved from the measured ψ and Δ through Fresnel equations. Multiple angle measurements provide more data sets to increase the precision. The ideal conditions for measuring a perfect two-phase system are: (1) no back-surface reflection contributes to the measured front-surface reflection beam; (2) the front surface is smooth enough so that the scattering from surface roughness is negligible; (3) the sample is pure enough so that no observable volume scattering results from voids and impurities; (4) the surfaces are clean enough to prevent confusing contributions caused by surface contaminants. Condition (4) is particularly hard to satisfy in the visible region, where submonatomic layers can contribute to the ellipsometric change. Conditions (1)-(4) cannot always be satisfied. Thus, the effects of different imperfect conditions on the ellipsometric measurement results will be analyzed.

Let the coefficients of reflection for an idealized system be r_{po} and r_{so}, those for a real system be r_p and r_s, and the small deviations of these coefficients for a real system from the ideal condition be r_p' and r_s'. The relations among these variables are

$$r_p = r_{po} + r_p' \qquad \text{and} \qquad r_s = r_{so} + r_s' \, . \tag{2}$$

The ρ for a real system given by eq (1) can be expressed as

$$\rho = \rho_o \left(\frac{1 + r_p'/r_{po}}{1 + r_s'/r_{so}} \right) \approx \rho_o \left(\frac{r_p'}{r_{po}} - \frac{r_s'}{r_{so}} \right) \quad , \tag{3}$$

where ρ_o is the complex ratio for the ideal condition. The deviations in ψ and Δ caused by the deviation $D\rho$ (= $\rho - \rho_o$) are

$$D\psi = \frac{1}{2} \sin 2\psi \ \mathrm{Re}(D\rho/\rho_o) \tag{4}$$

$$D\Delta = \mathrm{Im}(D\rho/\rho_o). \tag{5}$$

It is obvious from eq (3) that the relative deviation in ρ is

$$\frac{D\rho}{\rho_o} \approx \frac{r_p'}{r_{po}} - \frac{r_s'}{r_{so}} \ . \tag{6}$$

Notice that r_{po} is small near the Brewster angle and the above deviation will be large. It is better to avoid the Brewster region when determining optical constants. Based on the above principle, the effects on the optical characterization due to small absorption, roughness, scattering, and other imperfect conditions are analyzed in the following sections.

3. Effect of Instrumental Errors on Measurement of n and k

The complex index n+ik is used in the Fresnel equations to compute r_p and r_s of absorbing materials. For semitransparent materials (k « 1), k can be treated as a small perturbation on the system with k = 0. In this case, r_{po} and r_{so} can be defined as the reflection coefficients for a nonabsorbing medium with index n. Expansions of the Fresnel equations for complex r_p and r_s to the first order of perturbation k give

$$r_s \approx r_{so}\left(1 + i\frac{2nk\cos\theta}{(n^2-1)\sqrt{n^2-\sin^2\theta}}\right), \tag{7}$$

$$r_p \approx r_{po}\left(1 - i\frac{2n^3k\cos\theta}{(n^2-1)(n^2\cos^2\theta-\sin^2\theta)\sqrt{n^2-\sin^2\theta}}\right), \tag{8}$$

where θ is the angle of incidence. The relative deviation of ρ obtained from eqs (6)-(8) is

$$\frac{D\rho}{\rho_o} \approx \frac{-i2nk\cos\theta}{(n^2-1)\sqrt{n^2-\sin^2\theta}}\left(1 + \frac{n^2}{n^2\cos^2\theta-\sin^2\theta}\right). \tag{9}$$

By eqs (4), (5), and (9), we see that the first-order effect of k changes only the value of Δ but not ψ. Thus, data of ψ determine n and data of Δ determine k for transparent materials. The Brewster angle θ_B is a singularity in eqs (8) and (9). $D\Delta$ increases as θ approaches θ_B. Certainly, eqs (8) and (9) do not hold at $\theta = \theta_B$. $D\Delta$ approaches 0 as θ

approaches 90°. Figure 1 shows the exact computed $D\Delta$ for the difference in Δ between the real system with nonvanishing k and the ideal system with k = 0. Behaviors implied by eq (9) agree with those exhibited by the exact curves of $D\Delta$.

In ellipsometry, errors in ψ and Δ are limited by the signal intensity and the angle precisions of the analyzer and polarizer. To determine k, θ is chosen such that it gives large enough $D\Delta$ as well as large enough signal. Signal is very small near θ_B. The regions about 10° away from either 90° or θ_B are good choices of the angle θ. The error in k can be estimated from

$$\delta k \approx \delta\Delta \frac{(n^2-1)\cos\theta\,(n^2-\tan^2\theta)\sqrt{n^2-\sin^2\theta}}{2n^3(\cos^2\theta+\cos^2\theta')}\ , \tag{10}$$

where $\delta\Delta$ is the instrumental precision in Δ and θ' is the refraction angle. $\delta\Delta$ depends on the precision of the polarizer as well as the signal intensity. It is obvious that δk is large for grazing incidence and for large n. For n = 1.9, θ = 45°, and $\delta\Delta$ = 0.04°, δk is estimated to be about 3.2×10^{-4}. Equation (10) gives the limit of ellipsometry on the determination of k. In general, ellipsometric characterization for k is good only for $k \geq 0.001$.

To determine n only, data of ψ alone are enough if $k \approx 0$. Data of ψ can be obtained either by ellipsometry or by reflectance measurements of both s- and p-polarizations. Following the same procedure of deriving δk, the error δn for ellipsometry can be obtained as

$$\delta n \approx \delta k \frac{2\,\delta\psi}{\sin 2\psi\,\delta\Delta}\ , \tag{11}$$

$$\approx \delta\psi \frac{(n^2-1)\cos\theta\,(n^2-\tan^2\theta)\sqrt{n^2-\sin^2\theta}}{n^3\sin 2\psi\,(\cos^2\theta+\cos^2\theta')}\ . \tag{12}$$

Equation (12) works also for data of ψ from reflectometry. For our ellipsometer, $\delta\psi$ = 0.01° and $\delta\Delta$ = 0.04° for ψ > 10°; then $0.5\,\delta k < \delta n < 1.5\,\delta k$ for normal operation conditions. Thus, errors in n and k due to the instrumental errors of an ellipsometer are about the same. Figure 2 shows the deviation of ψ for a system with a deviation of δn relative to a system with an index n. The inverse relation of eq (12) is the approximation of these curves for small δn. For a given $\delta\psi$, δn is smaller for θ nearer to θ_B than farther from θ_B. It is obvious from the figure that data for $\theta > \theta_B$ will give better accuracy than data for $\theta < \theta_B$.

The uncertainties $\delta\psi$ in reflectometry are subjected to the signal noise as well as the alignment of the field direction of the p- and s-polarizations. The errors from the reflectance measurements are much larger and more unpredictable than the

ellipsometric errors. Even though the errors are large, measurements at multiple angles of measurements can improve both accuracy and precision. Notice that the factor of $(n^2 - \tan^2\theta)$ in eq (12) changes sign at the opposite sides of θ_B; thus, by taking about an equal number of measurements at both sides, the accuracy can be dramatically improved.

4. Sources of Systematic Error

Possible sources of error may arise from surface roughness effects or from the detection of unwanted radiation from (1) back-surface reflection and scattering, (2) volume scattering from impurities and voids, or (3) scattering from surface contaminants. From eq (2), we see that detection of any radiation other than the smooth front-surface reflection will contribute to errors in ellipsometry. Scattered light is usually not randomly distributed; if it were, it could be considered as random noise. For a random noise source, the real and imaginary parts of $D\rho/\rho_o$ by eq (6) are about equal, and $D\psi \approx \sin 2\psi\ D\Delta/2$ by eqs (4) and (5). The corresponding errors of δn and δk will be about the same by eq (11). Significant scattered light may result in δn and δk of the order of 10^{-3}. This error is serious in the characterization of k, but it is still in the third decimal place for n. For $k < 0.001$, other methods such as calorimetry can give much higher accuracy in k than can ellipsometry. Absorption coefficients as low as 10^{-4}/cm, which at a wavelength of 4 μm corresponds to $k \approx 6 \times 10^{-9}$, have been measured calorimetrically.

The roughness effect on ellipsometry is a result of the polarization effect of the rough layer [5, 8-11]. The rough layer can be treated as having an effective thickness d, which is about $2\sqrt{2}$ times the rms roughness [5], and an effective complex index, which can be derived from effective medium theory [8-11]. For smooth surfaces with $d/\lambda << 1$, the expansion of ρ to the first order of d/λ is [12,13]

$$\rho \approx \rho_o \left[1 + \frac{i4\pi d}{\lambda} F(\theta,\varepsilon_b,\varepsilon_s) \right] , \tag{13}$$

where

$$F(\theta,\varepsilon_b,\varepsilon_s) = \frac{n_a \cos\theta\, \varepsilon_b (\varepsilon_b - \varepsilon_s)(\varepsilon_s - \varepsilon_a)}{\varepsilon_s(\varepsilon_b - \varepsilon_a)(\varepsilon_b \cot^2\theta - \varepsilon_a)} . \tag{14}$$

Here ρ_o is the correspondent ρ for the two-phase system with pure bulk; ε_a, ε_s, and ε_b are the complex dielectric constants for the ambient, surface layer, and bulk material, respectively, and n_a is the index of refraction for the ambient. The imaginary parts of both ε_b and ε_s are very small for transparent materials, since they are directly proportional to k. Thus, Re(F) » Im(F) by eq (14) and $D\Delta$ » $D\psi$ by eqs (4), (5), and (13). The major effect of roughness on ellipsometry for transparent material is the change of Δ from the ideal condition. The roughness effect might confuse the determination of k but not n. However, $D\Delta(\theta)$ caused by $k \neq 0$ is quite different from $D\Delta(\theta)$ caused by the roughness effect. A three-phase model should be used to reduce the ellipsometric data when the roughness effect is not negligible.

Figure 3 shows $D\psi$ for a rough sample of quartz at a wavelength λ of 5 μm relative to an ideal sample for 0.1 nm < d < 10 μm. Errors in ψ are negligible for roughnesses below

10 nm. The extinction coefficients for transparent materials are usually much smaller than $k \approx 0.004$ used in figure 3, so that the $D\psi$ are much smaller than the one shown in figure 3. Thus, the determination of n is immune from the roughness effect, since the roughnesses of transparent samples are usually below 2 nm. Figure 4 shows $D\Delta(\theta)$ for a rough sample of quartz at $\lambda = 5$ μm relative to the ideal condition for d being (A) 0.707 nm, (B) 2.828 nm, and (C) 14.14 nm. For case (B) where the rms roughness is about 1 nm, $D\Delta$ is larger than the noise level of the instrument. Thus, roughness effect is not negligible for determining k for roughness larger than 1 nm.

5. Experimental

The null ellipsometer [14] used to measure the ellipsometric parameters can also be used to measure the reflectances of both p- and s-waves. The apparatus and methods of data reduction for ellipsometry are described in detail in previous papers [4,5]. For reflectometry, data of reflectances of both p- and s-waves are converted to ψ first, and then the existing computer programs were used to reduce the data. Some previous data [4] are used for comparison purposes. These data are for a quartz sample with parallel front and back surfaces. The quartz sample has a 1-cm thickness, a 3.86-cm diameter, and a very rough back surface. New samples with small wedge angles between smooth front and back surfaces have been tried; data of only one such sample are reported here. The ellipsometric parameters for a fluoride glass sample were measured at $\lambda = 3.8$ μm at multiple incident angles using the null method. The fluoride glass sample is thin and smooth on both sides with a 0.3° wedge angle and a 2.54-cm diameter. The vacuum chuck holder was used for this sample. The back-surface reflection was completely blocked out for all incident angles of measurements.

Elimination or suppression of the unwanted radiation detected by the ellipsometer is essential for accurate characterization measurements. Volume scatterings from impurities and voids are characteristics of the sample itself; nothing can be done optically except to make a purer sample. Scattering from contaminants can be avoided by carefully cleaning the front surface. The roughness effect can be avoided by making the front surface roughness smaller than 1 nm. Back-surface reflection and scattering may give severe errors in ellipsometric characterization of transparent materials. If the back-surface reflection beam can be guided away, then the back-surface scattering can be reduced by making the back surface also very smooth. Methods to eliminate back-surface reflection are outlined below.

To prevent the back-surface reflection, a thick sample will provide large displacement between the reflection beams from front and back surfaces. The separation δ between the two parallel reflection beams is

$$\delta = \frac{t \sin 2\theta}{\sqrt{n^2 - \sin^2\theta}} \quad , \tag{15}$$

where t is the thickness of the sample. Figure 5 shows the separation $\delta(\theta)/t$ for different indices of refraction. Samples with lower n have larger displacement. The separation is large for angles between 30 and 70° and small for large θ. Conventional sample holders, whose frames might block part of the reflected light for large angles of incidence, fit nicely for thick samples. These holders allow the transmitted beam to go away, so that the back-surface scattering is minimized. The quartz sample was mounted

on this kind of holder. For the 1-cm-thick quartz sample, δ is larger than 6 mm for n ≈ 1.4. The two beams can be separated easily by rectangular 3-mm-wide apertures.

Thick and large samples of the correct size for the sample holder are usually not available for measurements. When a sample is thin, the back-surface reflection cannot be separated from the front-surface beam. A wedge angle of about 0.5° between the front and back surfaces can successfully separate the front-surface reflection from the back-surface reflection. If a vacuum chuck holds the sample in the sample holder, the spurious back-surface reflection beam from the holder plate can sometimes have a higher intensity than the front-surface reflection beam. The vacuum chuck holder has the convenience of holding a sample of any size and shape and making measurements for large incident angles; however, a wedge sample is necessary when using the vacuum chuck holder. Even though the back-surface reflection beam can be separated, the back-surface scattering can still be severe if the holder plate or the sample back surface is rough. A smooth back surface is better than a rough back surface for a wedge sample. A wedge angle larger than 1° in our setup can efficiently prevent the detection of near-angle scattering from the holder surface. Large angles of incidence also can reduce the back-surface scattering appreciably. A smooth holding plate will be ideal for the vacuum chuck holder.

The reflection angle θ'' for the back-surface reflection beam for a wedge sample with wedge angle α is

$$\theta'' = \sin^{-1}\left(\sin\theta\cos 2\alpha + \sin 2\alpha\sqrt{n^2 - \sin^2\theta}\right) \quad \text{for} \; \theta < \theta_c \;, \tag{16}$$

where

$$\theta_c = \sin^{-1}\left(\cos 2\alpha - \sin 2\alpha\sqrt{n^2 - 1}\right) \;. \tag{17}$$

At $\theta = \theta_c$, θ'' is 90°. For $\theta > \theta_c$, total internal reflection occurs for the back-surface reflection beam. For n = 2 and α = 2.5°, θ_c = 57.7°. θ_c is smaller for larger n and α. For very small α, the deflection angle $\delta\theta = \theta'' - \theta$ can be approximated as

$$\delta\theta \approx 2\alpha \sec\theta \sqrt{n^2 - \sin^2\theta} \;. \tag{18}$$

Figure 6 shows the exact $\delta\theta(\theta)$ obtained from eq (16) for α = 1° and different n. The deflection is larger for larger n and for larger θ. Thus, if the sample has a high index of refraction, a wedge sample is more effective for beam separation than a thick sample. For large angles of incidence, the reflection intensity is high and the measurements are much faster than for low-incident angles.

6. Results

Figures 7 and 8 show data of ψ at multiple incident angles for a quartz sample measured at λ = 3.846 and 5.0 μm, correspondingly. About the same number of measurements were taken at both sides of θ_B. Data obtained from null ellipsometry are indicated by crosses; reflectometry data are indicated by octagons. The solid lines are

the computed ψ using the Handbook values [3] of (n,k) as (1.395, 4.96 x 10^{-5}) at 3.846 μm and (1.342, 0.00398) at λ = 5.0 μm. It is obvious that the crosses fall directly on the theoretical curves and most of the octagons are above the solid curves.

To see how well the data fit to the theoretical curves, figure 9 plots the deviations $\delta\psi$ of the data with respect to their best-fit theoretical curves for both ellipsometric and reflectance measurements at λ = 3.846 μm. The best-fit values of n and k for the ellipsometric data give a minimum rms deviation of both ψ and Δ. The best-fit value of n for the reflectance data gives a minimum rms deviation of ψ. The least-square-fit method of reducing the ellipsometric data was described in detail in previous work [4,5]. Results of the best-fit values for different sets of data and their rms deviations are listed in table 1. The rms deviation σ_ψ for reflectometry is much larger than σ_ψ for ellipsometry. Instrumental errors occurring in reflectometry are higher than those in ellipsometry. However, reflectance measurement is quick, while precise ellipsometric measurement using the null method is slow.

Table 1. Ellipsometric results of optical constants obtained by direct average of n and k for different θ and by the least-square-fit method. Abbreviation E represents ellipsometry, and R represents reflectometry. The Handbook values at the corresponding wavelengths are also quoted.

Wavelength (μm)	3.846	3.846	5.00	5.00
method	E	R	E	R
By direct average:				
n	1.3965	1.3958	1.3407	1.337
σ_n	$\pm 5.6 \times 10^{-4}$	± 0.017	$\pm 5.5 \times 10^{-4}$	± 0.016
k	2.1×10^{-4}		0.00396	
σ_k	$\pm 6.6 \times 10^{-4}$		$\pm 4 \times 10^{-4}$	
By least-square-fit:				
n	1.3965	1.3917	1.3408	1.337
k	2.3×10^{-4}		0.00379	
σ_ψ (deg)	0.0143	0.373	0.015	0.502
σ_Δ (deg)	0.049		0.063	
N	8	14	10	14
Handbook values:				
n	1.395		1.342	
k	4.96×10^{-5}		3.98×10^{-3}	

To see more clearly the deviations for ellipsometric measurements, figure 10 plots the deviations $\delta\psi$ of the measured data with respect to their best-fit theoretical curves for both wavelengths. The deviations are randomly distributed about the base and are close to the instrumental error. Thus, the uncertainty in the measurement is at the level of the instrumental noise in this case. From table 1, the rms deviation σ_ψ is about 0.015°. This number gives an rms deviation of n of σ_n = 2.1 x 10^{-4}, as calculated from eq (12) for n = 1.3965 for the data set of λ = 3.846 μm. The standard deviation σ_n

computed from individual n values using the Fresnel equations is 5.6 x 10^{-4}, as listed in table 1. Thus, the n reduced from the least-square-fit program gives better accuracy than the n averaged from individual n values obtained using Fresnel equations.

Figure 11 shows the refractive indices computed directly from the ellipsometric and reflectance data for λ = 3.846 μm using the Fresnel equations. The reference line is set at the Handbook value [3] of n at the corresponding wavelength. By comparing figures 9 and 11 for λ = 3.846 μm, we see that the deviations of n from the reference line for reflectometry switches sides for $\theta > \theta_B$. If the same mechanism causes large $\delta\psi$ values with the same sign, then δn for $\theta > \theta_B$ has the opposite sign against δn for $\theta < \theta_B$. As these values of n are averaged, the systematic errors are mostly cancelled out. Thus, by taking about the same number of measurements on both sides of θ_B, the reflectance measurements can give a rough estimate of n for a transparent material. The n computed from the more precise ellipsometric data stays at about the same value, and the standard deviation is much smaller than the reflectance data.

Table 2 shows the ellipsometric data and the computed optical constants for a wedge sample of fluoride glass. A vaccum chuck sample holder is used for this sample. The values of Δ shown are at the level of the instrumental errors. Thus, the back-surface reflection and scattering from the sample holder plate have been eliminated using a wedge sample. Since Δ is at the noise level, the value of k is expected to be of the order of or smaller than 10^{-4}. The deviations of n and k in table 2 are at about the same level as those shown in table 1. The use of wedge samples for measuring at high angles of incidence is much faster than measuring near Brewster angle, since the signal is much more intense.

Table 2. Ellipsometric data and the computed optical constants for a wedge fluoride glass sample at multiple angles of incidence and at 3.8-μm wavelength. n and k are computed directly from ψ and Δ using Fresnel equations.

θ (deg)	ψ (deg)	Δ (deg)	n	k (0.0001)
65.0	15.72	-0.01	1.4174	0.894
67.5	19.25	0.0	1.4181	0.0
70.0	22.64	0.0	1.4181	0.0
72.5	25.87	-0.02	1.4179	3.437
75.0	28.93	-0.02	1.4182	4.225
77.5	31.85	0.0	1.4183	0.0
	Average		1.4180	1.426
	Standard deviation		3.225×10^{-4}	1.911
Least-squares fit to Fresnel equations:				
Best-fit value:			1.4177	0.995
rms error:	0.010°	0.011°		

7. Conclusions

For semitransparent materials, characterization of n depends only on ψ, and characterization of k depends only on Δ. The reflectance measurements with about the same number of measurements at both sides of Brewster angle can also be used to characterize n only. However, ellipsometry gives much higher accuracy and precision than reflectometry. The errors δn and δk for ellipsometry are derived and proved to be at the level of $\pm 5 \times 10^{-4}$ for normal operation. The estimated values agree with the observed uncertainty in the experimental results. The roughness effect affects mostly Δ but not ψ, so that characterization of n is more or less immune to surface roughness. A random noise source gives about the same magnitude of error in both n and k; these errors seriously affect the percentage accuracy of k but not of n. Samples with thicknesses larger than 1 cm or with wedge angles larger than 0.5° can largely reduce the back-surface reflection and scattering. We conclude that, if care is taken, ellipsometric measurements can give accurate as well as precise values of refractive indices to the third decimal place for transparent materials in the infrared region of the spectrum. The success of ellipsometric characterization of optical constants, roughness, and texture for semitransparent materials has set a solid ground for further investigations of subsurface damage, coatings, and other problems of optical materials using ellipsometry.

8. References

[1] Malitson, I. H. "Interspecimen comparison of the refractive index of fused silica," J. Opt. Soc. Am. 55; 1205; 1965.

[2] Philipp, H. R. "The infrared optical properties of SiO_2 and SiO_2 layers on silicon," J. Appl. Phys. 50; 1053; 1979.

[3] Palik, E. D., ed. Handbook of optical constants of solids. New York; Academic Press; 1985. Pp. 749-763.

[4] Nee, S. F.; Bennett, H. E. "Ellipsometric characterization of optical constants for transparent materials," Proc. SPIE 970; 62-69; 1988.

[5] Nee, Soe-Mie F. "Ellipsometric analysis for surface roughness and texture," Appl. Opt. 27 (14); 2819-2831; 1988.

[6] Nee, S. F.; Bennett, H. E. "Nondestructive evaluation of surface roughness in the 0.01- to 1.0-m range using infrared ellipsometry," Proc. SPIE 675; 260-269; 1986.

[7] Nee, S. F.; Bennett, H. E. "Quantitative characterization of rough SiO_2 surfaces by infrared ellipsometry," Proc. SPIE 818; 34-45; 1987.

[8] Fenstermaker, C. F.; McCrackin, F. L. "Errors arising from surface roughness in ellipsometric measurement of the refractive index of a surface," Surf. Sci. 16; 85-96; 1969.

[9] Aspnes, D. E.; Theeten, J. B.; Hottier, F. "Investigation of effective medium models of microscopic surface roughness by spectroscopic ellipsometry," Phys. Rev. B20; 3292; 1979.

[10] Aspnes, D. E. "Optical properties of thin films," Thin Solid Films 89; 249; 1982.

[11] Marton, J. P.; Chang, E. C. "Surface roughness interpretation of ellipsometer measurements using the Maxwell-Garnett theory," J. Appl. Phys. 45; 5008; 1974.

[12] Aspnes, D. E. "The accurate determination of optical properties by ellipsometry", in Handbook of optical constants of solids, Palik, E. D., ed. New York; Academic Press; 1985. Pp. 89-112.

[13] Aspnes, D. E. "Spectroscopic ellipsometry of solids", in Optical properties of solids: new developments, Seraphin, B. O., ed. Amsterdam; North-Holland; 1976.

[14] Leonard, T. A.; Loomis, J.; Haarding, K. G.; Scott, M. "Design and construction of three infrared ellipsometers for thin film research," Opt. Eng. 21(6); 971-975; 1982; also, UDRI-TR-84-128.

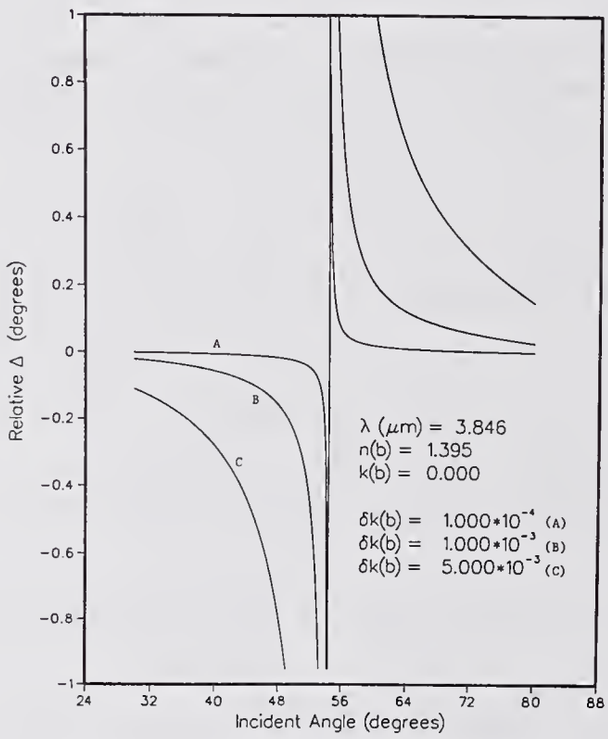

Figure 1. Difference function $D\Delta(\theta)$ for δk = (A) 0.0001, (B) 0.001, and (C) 0.005; all are evaluated at n = 1.395 and k = 0. The deviations in Δ are not negligible for δk = 0.001 for angles about ±3° away from the Brewster.

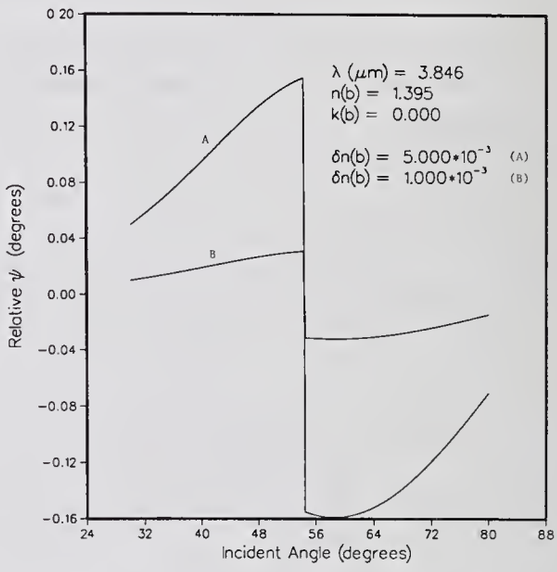

Figure 2. Difference function $D\psi(\theta)$ for δn = (A) 0.005 and (B) = 0.001; both are evaluated at n = 1.395 and k = 0. The deviations in ψ for θ from 40 to 70° for curve B are about 0.02 to 0.03°. Since the instrumen- tal error of ψ is 0.01°, the precision in n is expected to be better than 0.001.

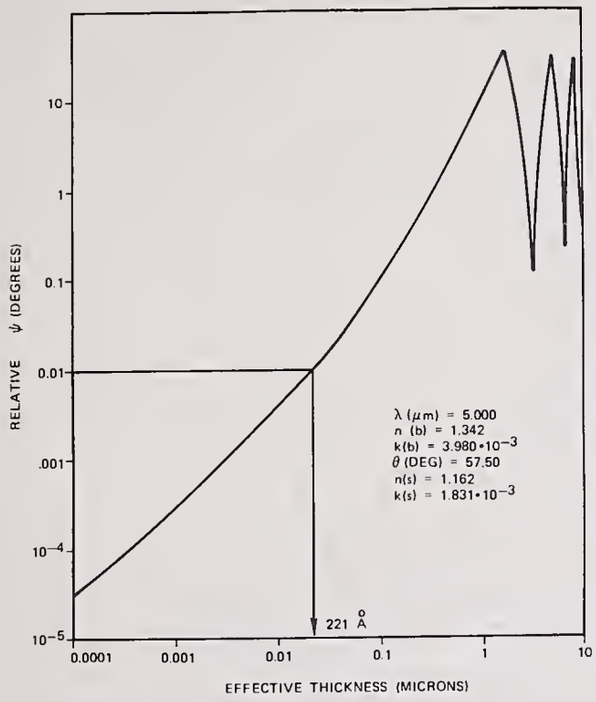

Figure 3. The relative change of ψ due to roughness with effective thickness of the rough surface ranging from 0.1 to 10^4 nm. Errors in ψ induced by roughness below 10 nm rms are less than 0.01°.

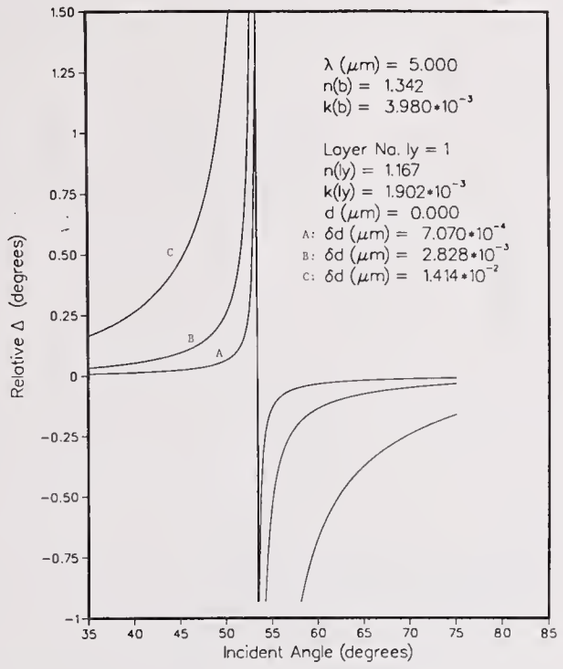

Figure 4. Difference function DΔ(θ) for quartz samples at 5-μm wavelength for effective thickness deviations of (A) 0.707, (B) 2.828, and (C) 14.14 nm, equivalent to rms roughnesses of (A) 0.25, (B) 1, and (C) 5 nm. The deviations in Δ for a 1-nm rms roughness are about at the noise level of the measurements.

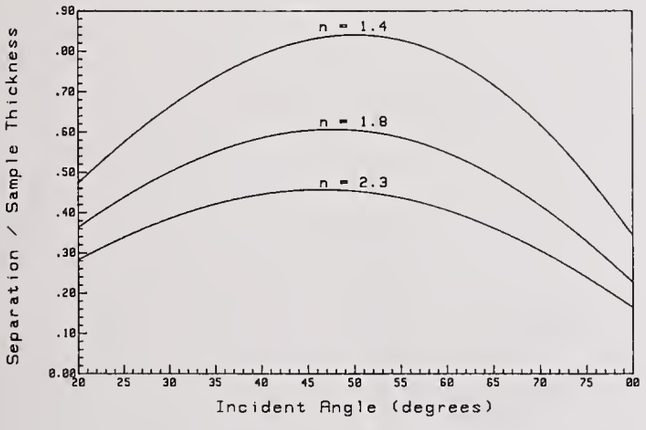

Figure 5. Separation δ(θ) between the parallel reflection beams from front and back surfaces per unit thickness of the sample for different refractive indices n. The separation is smaller for larger n.

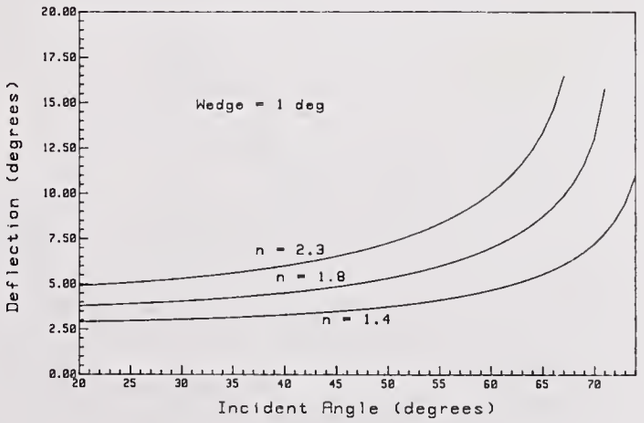

Figure 6. Deflection angle δθ(θ) between the reflection beams from front and back surfaces for 1° wedge angle and different n. The deflection is larger for larger n.

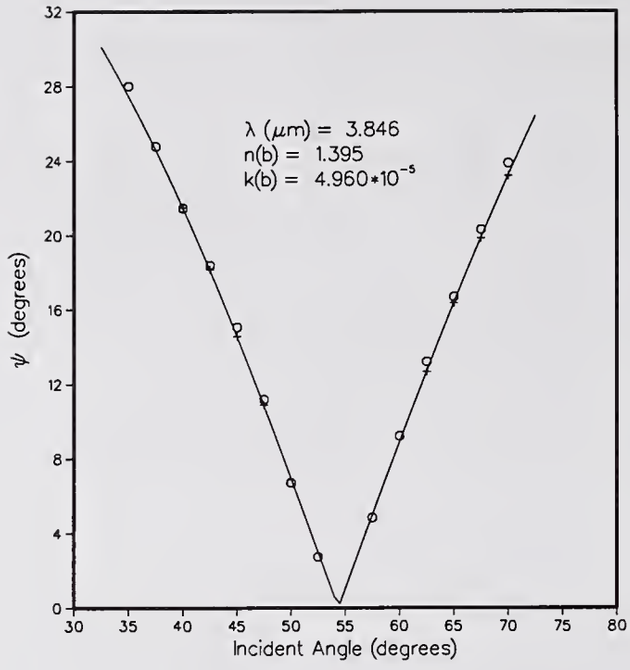

Figure 7. $\psi(\theta)$ for quartz at 3.846-μm wavelength. The solid curve is computed from the Fresnel equations for Handbook values of n = 1.395 and k = 4.96 x 10^{-5}. The experimental ellipsometry data of ψ are indicated by crosses, and reflectometry data are indicated by octagons.

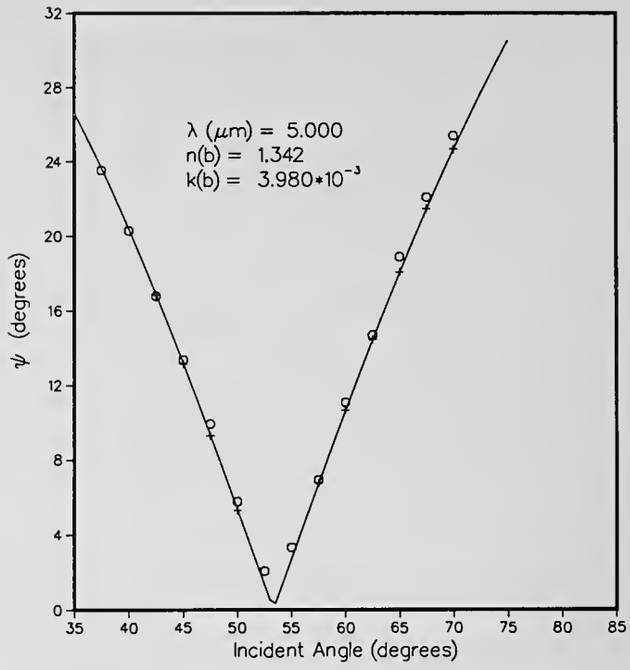

Figure 8. $\psi(\theta)$ for quartz at 5 μm wavelength. The solid curve is computed from the Fresnel equations for n = 1.342 and k = 0.00398. The experimental ellipsometry data of ψ are indicated by crosses, and reflectometry data are indicated by octagons.

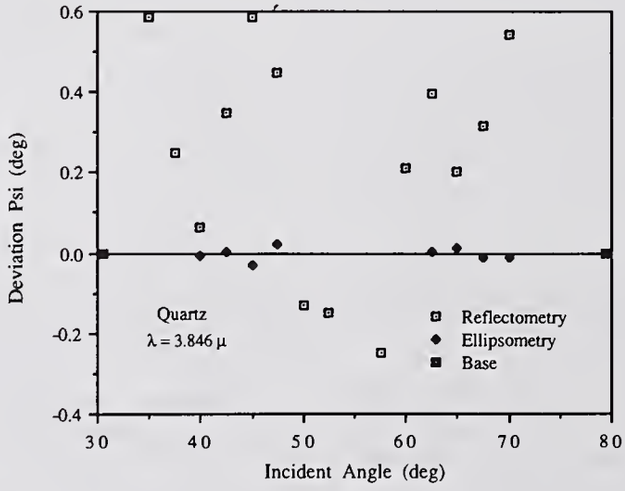

Figure 9. Deviations $\delta\psi$ of the experimental data of figure 7 with respect to their best-fit theoretical curves at λ = 3.846 μm for both ellipsometric and reflectance measurements. The best-fit values of n and k are listed in table 1.

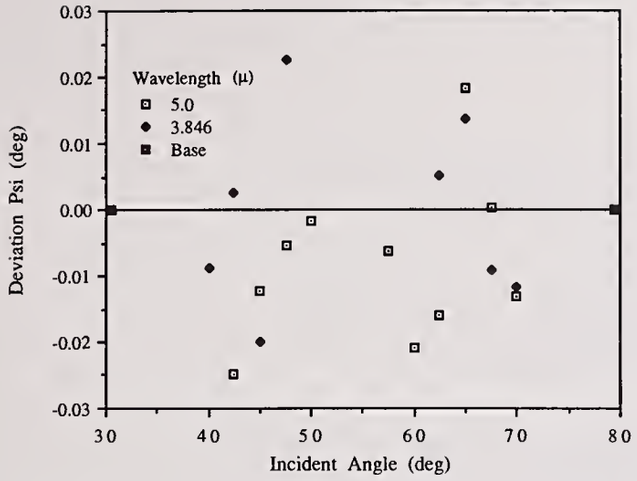

Figure 10. Deviations $\delta\psi$ of the ellipsometric data with respect to their best-fit theoretical curves for both wavelengths for the quartz sample. The systematic errors have been reduced to the level of the random instrumental errors.

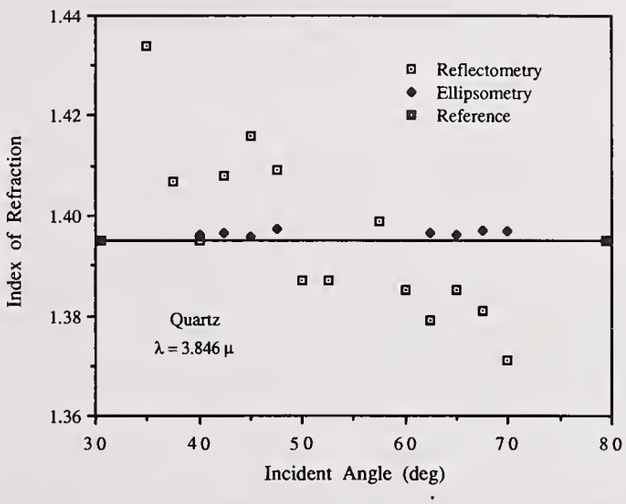

Figure 11. Refractive indices computed directly from data of figure 7 by ellipsometry and reflectometry for λ = 3.846 μm using the Fresnel equations. The reference line is set at the Handbook [3] value of n = 1.395.

COMMENTS

Question: These experiments were done in air?

Answer: Yes.

Question: Did you look at the time dependence of damage as measured by observing the pulse wave form?

Answer: No, not in this particular set of experiments. We've done that somewhere else but no not here. I would suggest that that's a very important thing to look at, for example, it would bear on the great controversy about avalanche and non-avalanche processes. If you are near a threshold then you should damage at the peak of pulse. If you have multiphoton effects dominating, damage should occur at the end of the pulse. We are working on developing such a system. The problem is that we are down on the nanosecond oscilloscope range and it is difficult. That is one of the areas that we plan to concentrate on.

Question: Wouldn't it be nice to put a piece of salt in there and observe the charging. You can have in one case a semiconductor that is totally absorbed in the UV, in the other glass, which is totally absorbed in the CO_2 region. It would be nice to have something in there which is mostly transparent to both of those regions.

Answer: Good idea.

Manuscript received
12-29-89

Microindentation as a Technique For Assessing Subsurface Damage In Optics

R. S. Polvani and C. Evans

National Institute of Standards and Technology
Precision Engineering Division
Gaithersburg, Md 20899

ABSTRACT: Efforts to optimize precision machining emphasize form and surface finish as the primary objectives. Minimizing subsurface damage is no less important for high power optics. This paper reports our usage of instrumented microindentation for subsurface damage assessments. Our instrument is an example of a new class of diagnostic tool. All apply controllable loadings to an indenter and continuously measure the load and resulting penetration. The utility of microindentation depends on appropriate interpretations of load-depth curves. The technique provides insight into the physical nature of the subsurface and is a means to obtain a variety of engineering properties from the subsurface region. We use it to profile flow stress and elastic modulus with depth, and to gauge creep and anelastic behaviors. Instrumented microindentation promises rapid and sensitive property assessments. We will use a range of examples to show this potential is realizable.

KEYWORDS: glasses; metals; microhardness; mechanical properties; microindentation; precision machining; semiconductors; single point diamond turning; subsurface damage; and Young's modulus

INTRODUCTION

Increasingly, optics are components combining precision machined surfaces and minimum levels of subsurface damage. Optical birefringence, X-ray diffraction (XRD), metallography, penetrant dyes, eddy current and many other techniques are available to assess damage. However, a need remains for better means of testing. The existing techniques have limitations: they may apply to one class of material, be time consuming and destructive, and too expensive to perform routinely. For example, XRD residual stress measurements can be made in metals but not glass optics, and X-ray topography is limited to single crystals, or very coarse grained material. Metallography can be used with all materials, but requires destroying the object. This paper will indicate a range of applications where subsurface damage is a critical factor, and describe a varied usage of microindentation testing. Our need is to determine the nature, extent and intensity of subsurface damage. The technique promises rapid, sensitive subsurface property measurements. We will try to show this promise is realizable with a range of examples.

A useful, but too simple model relates the damage to total depth of the layer of modified material, and the degree of modification. Degree is the difference between surface values and a representative for the sample's interior or bulk. A saturated, homogenous or monolithic layer is unlikely. A transition region made up of several discrete and possibly different layers is more likely. With depth below the surface, a property gradient would appear in our results, and that is exactly what we see.

The physical form of the damage depends on the type of material. In brittle materials-ceramics, glasses or semiconductors - damage is a combination of residual stresses and structural faults. These can be crazing, incipient crack sites, cracks or voids. Even in well polished glass optics, the faults can penetrate deep and cause a measurable depression of the local modulus. In ductile materials, the near surface is more likely to be work hardened. Figure 1 offers a schematic view of the surface and interior grain structure. Surface grains are more twinned, and smaller. They may be strongly aligned along a crystal direction, and have a high aspect ratio. Mechanically, a worked subsurface would have a higher yield strength. Lastly, the energy input from cutting can lead to the grains recrystallizing and higher concentrations of oxides. Both effects are seen in copper.

POTENTIAL APPLICATIONS: Modern single point diamond turning of metal infrared optics is a relatively mature technology [1]. The near surface damage levels, caused in fabricating thermal imaging systems or scanner mirrors, is considered functionally unimportant. That premise is questionable. Subsurface damage does affect the long term dimensional stability. It may also cause veiling glare in transmissive IR systems. For high power laser systems subsurface damage has immediate and striking effects. Wood surveyed materials defects which lower the laser damage threshold [2]. He included voids, pits, dislocations, residual stresses, low angle grain boundaries, and second phase inclusions. Further, Hurt provides graphic evidence of the severity of conditions immediately below the surface in diamond turned copper [3]. In some cases, the grains recrystallize either during or very soon after the part is fabricated. Hurt and his China Lake colleagues also found relationships between subsurface damage, optical scatter, reflectance and the laser damage threshold [4-6].

Damage thresholds in high power transmissive laser systems are also limited by subsurface damage. For assessments of glass optics, Brown and his colleagues pioneered taper polishing techniques [7,8]. They emphasize use of numerical damage indices. Two indices are "eighty (80) percent of the cracks shorter than" and basing damage penetration on a ratio with the deepest crack detected. Both can guide fabricators or process development, but taper polishing is slow, labor intensive, and destructive.

The IC industry also needs low damage transmission optics. Optical step and repeat systems are keeping pace with decreasing IC feature sizes by moving to ever shorter wavelengths. Visible wavelengths are being supplanted by the UV band. New steppers will require large numerical aperture aberration free lens systems, which will be made up of aspheric elements. Near UV optical systems will need significantly better surface finishs and subsurface damage levels, than systems operating in the visible. Stepper lens fabricators are likely to harness an emerging technique, ductile regime grinding, for rapid production of aspheric elements. The need is for aspherics with minimal damage and made without post polishing. GCA Corporation* has already developed an excimer laser based stepper system.

Excimer laser systems are of interest for a range of material removal processes [10].

Ablative processing offers high precision material removal without the heat affected zone of conventional laser processes. Different materials show different fluence thresholds for ablation, allowing differential processing. An example is polymer films on metal substrates. Laser crystals and semiconductors are still more applications sharing a need for undamaged surfaces.

For all, process optimization could be speeded if techniques for rapid damage assessment were available. Instrumented microindentation is a useful and versatile diagnostic tool. To demonstrate the capabilities, we will start by describing our experimental approach and then use a range of examples.

EXPERIMENTAL

Our test strategy emphasizes: complementing indentation assessments with other diagnostic methods, drawing conclusions from comparative property measurements, and placing little emphasis on the immediate surface. Other methods are used to complement rather than simply verify the microindentation testing. XRD and X-ray topography are used to gauge the residual stress levels in metals and ceramics. Metallography is used extensively to image cracking and grain morphology. Profilometry, differential interference contrast (DIC) and scanning electron microscopy (SEM) are used to characterize surface finish and form. Our evaluations try to reflect a consensus from several viewpoints. The general operating mode is to use the microindenter as a comparator. By making comparisons, reproducible results become the necessary and sufficient condition. Further, comparisons mask the large differences inherent in real materials.

Although the opportunities and need are fewer, we make and use absolute measurements. Moduli measurements are an example of absolute values. Measurements made within 0.025 micrometer of the surface, critically reflect: displacement resolution, surface condition, and an exact knowledge of the indenter geometry. A thin gold plate on steel substrate is a model system we use to estimate the error in the property measurements. The question is how large an error is acceptable? Characterizing layers less than 0.025 micrometers is not a current goal. Rather, it is to provide and use comparative measurements to aid precision machining research and process development.

INSTRUMENT: Several instrumented microindentation instruments are reported in the literature [10-13]. They were developed, in general, for use within a laboratory to

---

* Specific commerical items are identified only to provide a complete description and does not imply an endorsement.

meet a specific purpose. Ours started with a need to measure the effects of strain rate on the dynamic indentation fracture properties of glass. Some current capabilities of our instrument are largely refined carry overs from this start. Both its capabilities and limitations have shaped our test strategy. The Nanoindenter* was an IBM* laboratory development which is now a commercial product [13]. The unit developed at NIST, National Institute of Standards and Technology, is a flexible micromechanical properties test apparatus.

The instrument, method, and the analytical procedures used to obtain properties has been described in detail elsewhere [14-15]. The four functional subassemblies are computer, electromagnetic driver, main test frame, and electronic instrumentation. See figure 2. Originally, tests were fully computer controlled. An HP-85* generated the indenter loading, controlled the different electrical subassemblies, and processed the data. Now a Compaq Model 386/20e* is used, but with a role limited to data acquisition and processing. The electromagnetic driver is rated for loads to 10 Newtons. The main frame is a modified commercial stamping press. A translation stage with X-Y drives positions the specimen. Specimens may be attached to the translation stage with silicone grease, wax or cellulose adhesive, but adhesive is preferred. Specific sample features may be tracked or avoided with the use of a targeting microscope.

The instrument uses a load waveform which is a modification of the hardness tester loading. See figure 3a. The essentially square loading waveform was retained, so results would be compareable to hardness numbers. Modifications are using haver sine sections for up and down loadings, and holding a 10 percent post impression load. Haver sines segments minimize impact effects and the working bandwidth of the instrumentation. The Lyco hardness tester*, a cam driven machine, also uses sinusoidal up and down load segments. Our instrument uses the minor loading to prevent depth recovery. We do this to have comparability between our results and hardness numbers.

An indent is a three dimensional object. This instrument measures the impression size using the depth. Hardness numbers reflect entirely the projected surface dimensions of a recovered impression. In metals, recovery primarily reduces the impression depth. Recovery has little to no effect on surface dimensions. Using an unrecovered depth in the calculation, we gain comparability. For dynamic regime testing, a sinusoidal impulse is used. The impulse reduces the upper limit of the instrumentation bandwidth to the test frequency or reciprocal loading time. The driver signal is the amplified output from a Wavetek Model 75* arbitrary function generator. The waveform duration - up load to post dwell - is a test factor. Loadings of milliseconds to several hours are used. Unless specified, a 0.4 second duration was used. Two ways are used to measure load. At low loading rates, the current through the electromagnetic drive coil is used. At dynamic rates, a piezoelectric load cell is used. A full four arm bridge of eddycurrent transducers is used to measure displacement. Bridge resolution is better than 0.02 micrometers.

Instrumentation design avoids test frame and indenter compliance errors. The load and displacement measurements are made between the back of the indenter and sample surface. Both the placement and type of transducer reflect this design feature. A properly brazed indenter tip eliminates indenter compliance. This can be shown with three arguments. Apply Hooke's Law to the indenter, and compare the relative compressions of the diamond tip and shank. Second, use the Hertz Equation to calculate penetration of a ball indenter into an elastic sample, and compare the calculation with an experiment. With our instrument we obtain agreement. Third, our modulus measurements are within 15 percent of handbook values.

METHOD: A full range of indenter geometries are used. Vickers microindenters are used for investigations of glass and ceramic properties. For metals and where workable with glasses and ceramics, ball indenters are preferred because:

1. The test volume has a high surface area to penetration depth ratio.

2. Large, easily measured loads give small penetration depths. This is important for dynamic measurements where quartz cells are used.

3. Analytical and finite element solutions for ball indentations are available. We perform our routine calibrations using the Hertz Equation.

Ball size is an effective control variable. For elastic measurements, the hardest and largest ball diameter is used. For fracture threshold measurements, small balls are used. For plastic indentations, the size depends on three factors: need for an impression free test surface, relative hardness of the test material, and inhomogeneity of the sample. The lower limit to diameters is the difficulty of properly shaping diamond, and the upper limit is the 10 Newton driver capacity. Large diameter balls give better averaging. Size can minimize the contribution of crystal orientation or surface features to

the scatter. For example, to assess the effect of diamond turning an indent should include several tool marks. Despite the poor surface finish, a 400 micrometer diamond indenter is frequently used with ceramics materials. We are developing 25 and 100 micrometer chemically polished diamond indenters. These will be used to determine the fracture threshold for several optical glasses. The results presented here were obtained using an 1600 micrometer diameter silicon carbide ball. For a 1 micrometer depth, the sampled surface areas is 5,023 micrometers^2 or 80 micrometer in diameter.

Results are, typically, averages of twelve (12) repeat runs, each load-depth curve has 2048 data pairs. The number of repeats is not fixed. As many as sixty four (64) repeats have been necessary to evaluate the bulk or baseline property of a hot pressed ceramic. A 95 percent confidence limit is the criteria used to decide the number of replications. For diamond turned, metallographic sections or optically polished surfaces, run to run variation is low, so averaging over twelve runs is sufficient. Because the instrument is computer interfaced, high numbers of replications are practical.

To speed processing by the HP-85* and conserve storage, the full 2047 data array was not used. For plastic indentations, we tested the practice, and found no loss. Within the accuracy of Lotus/123*, results from either full or reduced data arrays coincided. With the Compaq 386/20e*, the full 2048 array is used. We plan to convert to a 8,192 data array. Attempts to measure individual fracture events in glass need the enhanced resolution.

PROPERTIES: Results are graphically presented in four ways: load and depth versus time, load-depth, flow pressure-depth and delta curves. Data are initially reported with a load and depth versus time curve, see figures 3a. In two steps, load and depth are cross plotted to obtain more sensitive results. First, a load-depth curve is obtained, see 3b. Second, after using the expressions described below, the data are transformed into a flow pressure-depth curve, see figure 4. Load-depth curves reflect the overall mechanical state. Flow pressure-depth curves summarize a local probing of the surface material. The Delta curve compares a reference to a set of surface values. Because it is a relative measurement, the curve scales to the differences. By masking out the absolute value, the Delta curve permits magnified displays. The reference for the Delta curves is a fifth order polynomial model of the indentation behavior. To obtain this model, the sample interior is exposed by metallographic or chemical polishing. A pattern of indentations is made using the same conditions that will be used to probe the test surface. The polynomial is obtained using linear regression.

Figure 3b gives load-depth curves for synthetic sapphire, diamond turned copper, and polymethylmethacrylate (PMMA). Sapphire behaves as a perfectly elastic material. The high value of the modulus, 390 GPa, causes a shallow depth, and dictates high slopes for the up load and down load segments. The elastic signature of alumina is the lack of a residual depth, or full closure over the loading cycle. PMMA is the other extreme of deformation behavior; it is a viscoelastic material exhibiting elastic, plastic, creep and anelastic behavior. The low Young's modulus of 1.35 GPa, causes large penetration depths and low slopes for the up and down load segments. The viscous or creep part of the deformation is shown by the continuing penetration at constant load, see the depth time curve in figure 3a. The plasticity is given by the closure failure of the cycle. Numerically, it is the difference between the actual final depth, and depth projection of the initial tangent to the down load curve. Diamond turned OFHC copper exhibits intermediate micromechanical behavior. Copper has a 120 GPa modulus.

Because the initial recovery on down loading is entirely elastic, load-depth curves are used to determine moduli [16]. Anelastic recovery also occurs, but later in the down loading. By regression, a straight line is fitted, but only to the initial portion of the segment. For a Vickers indenter and Poisson's ratio equal to 0.33, the modulus is given by the expression:

$$E = 0.163(dP/dh)(1/d_m)$$

The tangent to the down load curve is dP/dh, and typically coincides over the upper half. The maximum plastic penetration depth is d_m. Its value is intercept of the down load tangent line and the depth axis of the load-depth curve. The modulus has the units GPa when the load is given in Newtons and the depth in micrometers. We have developed an expression for the modulus from ball indentations [15]. In addition to the overall value, the modulus can be profiled against the penetration depth. A series of load-depth curves are obtained using different peak loadings.

Hardness number is based on the residual impression size. Flow pressure, the instantaneous indentation resistance, is related to the penetration depth, d, applied load, P and type of indenter by the relations:

$$\sigma = 0.0001253DP/d \quad \text{Ball}$$

$\sigma = 37.84P/d^2$ Vickers

$\sigma = 15.81P/d^2$ Knoop

D is the diameter of a ball indenter in micrometers. The units are Newtons for load, and micrometers for depth.

Flow pressure combines the elastic, plastic, creep and anelastic deformation components, but test strategy can separate the components. Time, shape and direction of loading are the important factors. By loading very quickly, creep can be neglected. By using identical waveforms for the up and down loadings, the plastic component can be decanted.

Flow pressure-depth profiles show the variation of the mechanical properties in near surface regions. It is a subtle alternative to the load-displacement curve. The underlying assumption is that the near surface region is not monolithic, but rather a multilayered or varying structure. If the measurements assess the state of a material, flow pressure should have two properties. It should be a function of depth, and independent of load. Stated differently, properties measured from indentations at different peak loads should lie on a single master flow pressure-depth curve, and they do. Figure 4 shows superimposed flow pressure-depth curves for polished fused silica. Measurements were made at peak loads of 0.25, 0.5, 1 and 4N. The three low loadings are a subset of the peak loading.

RESULTS and DISCUSSION

By example, we will show microindentation is an effective diagnostic tool and useful with all three material classes. Real time measurements, and freedom from a residual impresion are two clear, but still largely unexplored, advantages. Surface compliance is one example of a real time measurement. We find we can use these values to gauge the extent of cracking in brittle surfaces.

BRITTLE MATERIALS: Taylor and Syn, and Blake and Scattergood have shown that thickness determines the extent of subsurface damage in precision machined semiconductor materials, and so effective chip thickness is a critical factor [17,18]. Figure 5a show the effect of light and deep cuts into GaAs. Optical inspection and profilometry showed no significant difference between the two. The indentation behaviors are different. The light cut is a less compliant more fractured surface. The slopes of the up and down load segments are steeper, and there is less creep. Figure 6a reports the mechanical effects of sawing rather than chemically polishing the surface.

Consider the sensitivity to processing in a second semiconductor. Figure 6b shows load-depth curves for etched, diamond turned, and as sawn germanium wafers. Taper sections were made, and examined with optical and electron microscopy. Using optical microscopy, no visible differences were found. Immediately below the diamond turned surface, the scanning electron micrographs indicated a higher defect density. The mechanical differences in the germanium were quantified with moduli measurements. See table 1.

Table 1 Summary of moduli (GPa) of [100] axis single crystal germanium.

Applied load (N)	1	4
Etched	135	126
Diamond Turned	117	112
Sawed	61	55
Handbook	126	126

Both GaAs and germanium indicate a potential capability. Differences unseen by profilometry or optical inspection are detectable with microindentation.

METALS: The observation, that more damage occurs from finishing rather than roughing cuts, can be explained using the Ikawa and Shimida model. It relates extent of plastic work in ductile materials to the cutting conditons [19,20]. Ignoring factors such as friction and strain rate, the depth of damage can be equated to tool sharpness by:

$$\varphi = R_i \exp(\alpha - 0.5)$$

The ratio of flow pressure to tensile yield stress is α. R_i is the tool edge sharpness or radius, and φ is the radius of the plastic work front about a common center. Consider a new tool making very small depths of cut. The character of subsurface damage will reflect a change in feed rate. We found inverting the idea to be a way of evaluating tool wear. Using slow feed rates, 6061 T6 aluminum and OFHC copper samples were rough and finish diamond turned. We expected the flow pressure-depth profiles would indicate the sharpness. Figure 7a shows the affect of wear on a 0.625 mm nose radius tool. Using identically machined witness samples, surface conditions are reported for the tool as delivered and after machining a batch of nine 62.5 mm diameter OFHC copper mirrors. Figure 7b shows profiles for a 2.4 mm nose radius tool for the as delivered, and after cutting 50 miles and 150 miles of 6061 aluminum.

Both tools continued to produce perfectly acceptable surfaces. The tools appeared free of edge nicks or other types of catastrophic

damage. To inspect the 0.625 mm nose radius tool, we used Talystep traces across plunge cuts. The tool edge recession was less than 25 nanometers. Diamond tool break-in, and perhaps, wear is benign until the edge starts chipping. Here wear occurs as a small negative rake land forming between the clearance and rake surfaces [21, 22]. A negative rake land would cause increased subsurface damage. Negative rake would also increase the feed rate sensitivity. Figure 8 shows the effect of changing surface speed on subsurface damage of diamond turned 6061 aluminum. No effect was found in simultaneous tests with OFHC copper. This can be explained by the higher strain rate sensitivity of the aluminum. Yield strength increases, and ductility decreases with increasing rate.

GLASS OPTICS: The utility and sensitivity of microindentation to the damage levels typical of commercial optics were tested. Three aspects were considered. First, the effect of loading rate on the strength of soda lime glass was found. The results are reported in figure 9. Because glasses are viscoelastic materials, their flow properties are strongly rate sensitive. A modest increase in the loading rate causes a noticeable increase in the deformation resistance of the glass. This sensitivity of glass has implications for the fabrication of optics.

Second, the sensitivity of microindentation to the surface condition was probed. For this, our test piece was an optical flat. The type of glass is unknown. Figure 10 shows load-depth curves for the flat as-delivered, after swab etching in 25% hydrofluoric acid, and after submersion for 1 hour in the acid. Photomicrography revealed swab etching removes surface defects. Indentation showed swab etching caused a more compliant surface. After a 1 hour immersion, the visible defects increased. Microindentation gave a less compliant surface. The result is fully consistent with the finding of Dabbs and Lawn [23]. Who found brief acid exposures of subcritical flaws causes a sharp reduction in the crack initiation load. Initially, the acid enlarges the cracks. Long term immersion leads to large but blunt tipped cracks, and the observed strengthening.

Third, experiments are underway to evaluate the rate of removal of subsurface damage during the polishing of fused silica. Figure 11 shows flow pressure-depth profiles for as-ground and polishing times of 2, 8, and 14 hours. Using DIC at 500 magnification, we found a higher density of visible scratches in the 2 h sample, but after 2 hours, there was no visible difference among the samples. Talystep measurements revealed no systematic differences among the polishing times.

CONCLUSIONS

Microindentation is a quick convenient means of measuring the properties of the near surface of precision machined components. However, further comparisons with other methods of assessing subsurface damage are still required.

Instrumented microindentation shows both ductile and brittle materials are sensitive to the effects of cutting parameters. Experiments with glass show strain rate effects and chemical effects. Acid etching can cause both weakening or strengthening.

Tool wear and feed rate affect the intensity of sub-surface damage from single point diamond turning. A similar effect for depth of cut may exist. Surface speed effects in diamond turning of 6061 Aluminum have been demonstrated.

ACKNOWLEDGEMENTS

The authors are grateful to many colleagues at the National Institute for Standards and Technology for helpful comments and suggestions. In particular thanks are due to C. Brady (metallurgical preparations), C. Giaque (surface profilometry), and M. Postek (scanning electron microscopy). Germanium samples were supplied by T. Dow of North Carolina State University. F. Garcia at Los Alamos National Laboratory machined the aluminum samples on which Fig 7 is based. Fused silica samples were supplied by L. Lund of GCA Tropel Corporation.

REFERENCES

[1] Evans C. "Precision Engineering: An Evolutionary Perspective", M.Sc. Thesis, Cranfield Institute of Technology, March 1987.

[2] Wood R.M. "Laser damage in optical materials" Adam Hilger, 1987.

[3] Hurt H.H. "A Metallurgical Investigation of the Diamond Turned Optical Surface" PhD Thesis, University of Southern California, 1984.

[4] Hurt H.H. "Defects induced in optical surfaces by the diamond turning process" in Proc SPIE Vol 525, Measurement and Effects of Surface Defects and Quality of Polish, 1985.

[5] Decker D.L. "Tailoring of optical properties of diamond machined optical surfaces" Proc SPIE Vol 433 pp 96-103.

[6] Hurt H.H. and Franck J.B. "The effects of defects on laser damage performance

of metal mirror surfaces" 16th Annual Symposium on Optical Materials for High Power Lasers, Boulder, CO, 15-17 Oct 1984.

[7] Brown N.J., Fuchs B.A., Hed P.P. and Stowers I.F. "The Response of Isotropic Materials to Abrasive Processes" in Proc ASPE Spring Conference on Sub-Surface Damage in Glass, Tucson, AZ, April 1989, pp 66-87.

[8] Hed P.P., Edwards D.F., Davis J.B. "Subsurface Damage in Optical Materials: Origin, Measurement and Removal", in Proc ASPE Spring Conference on Sub-Surface Damage in Glass, Tucson, AZ, April 1989, pp 66-87.

[9] Znotins T.A. et al "Excimer lasers an emerging technology in materials processing", Laser Focus/Electro-optics, May 1987, pp 54-70.

[10] Bhushan B., Williams V.S. and Shack R.V. "In-Situ Nanoindentation Hardness Apparatus for Mechanical Characterization of Extremely Thin Films" Journal of Tribology, July 1988, Vol. 110, pp 563-571.

[11] Yanagisawa M. and Motomura Y. "An Ultramicro Indentation Hardness Tester and Its Application to Thin Films" Lubrication Engineering Jan. 1987, pp 52-56.

[12] Berdikov V.F., Pushkarev O.I. and Nazarenho V. A. "Microhardness Tester With Automatic Recording of Indentation or Scratching Diagram", translated from Zavodskaya, Vol. 46, No. 5, May 1980, pp 459-462.

[13] Pethica J.B., Hutchings R. and Oliver W.C."Hardness measurements at penetration depths as small as 20 nm" Phil Mag A, 1983, Vol 48 No. 4, pp 593-606.

[14] Polvani, R.S., Ruff A.W. Jr., and Whitenton E.P. "A Dynamic Microindentation Apparatus for Materials Characterization", Journal of Testing and Evaluation JTEVA, Vol 16, No. 1, Jan. 1988, pp 12-16.

[15] Polvani R.S. and Evans C.J. "Microindentation Assessment of Near Surface Material Properties and Subsurface Damage", Proceedings of the International Congress for Ultraprecision Technology, May 1988, Aachen, FRG. Springer-Verlag, New York, NY.

[16] Loubet J.L., Georges J.M. and Meille G., "Vickers Indentation Curves of Elastoplastic Materials" Microindentation Techniques in Materials Science and Engineering, ASTM 889, P.J. Blau and B.R. Lawn Eds. American Society for Testing and Materials 1986 pp 72-89.

[17] Taylor J., Syn C.K. and Donaldson R.R. "Observations of the brittle-to-ductile cutting mode transition during diamond turning tests of single crystal silicon" 2nd Annual Meeting of the American Society for Precision Engineering, Columbus, OH, Nov 1987

[18] Blake P.N. and Scattergood R. "Single point diamond turning of silicon and germanium" 2nd Annual Meeting of the American Society for Precision Engineering, Columbus, OH, Nov 1987

[19] Evans C., Polvani R., Postek M., and Rhorer R. "Some observations on tool sharpness and sub-surface damage in single point diamond turning" SPIE Vol 802 'In-process optical metrology for precision machining' (1987) pp 52-66.

[20] Ikawa N. and Shimida S. "Cutting tool for ultraprecision machining" Proceedings of the 3rd International Conference on Production Engineering, Kyoto, July 1977

[21] Donaldson R.R., Taylor J. and Syn C. "Diamond tool wear versus cutting distance on electroless nickel mirrors: SPIE Vol 676, "Ultraprecision machining and automated fabrication of optics", San Diego, August 1986

[22] Hurt H.H. and Showman G. "Wear of a pre-selected diamond tool" SPIE Vol 676, "Ultraprecision machining and automated fabrication of optics", San Diego, August 1986.

[23] Dabbs T.P. and Lawn B.R. "Acid enhanced crack initiation in glass" Journal of the American Ceramic Society, Vol 65, No 3, March 1982.

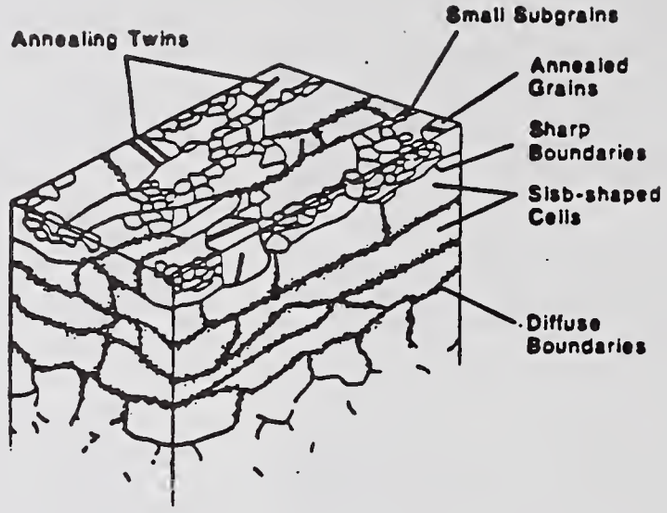

Figure 1. A simple model for the microstructure in a subsurface damaged metal.

OPERATING CAPABILITIES

Applied Load ... 10^{-3} to 5 N

Duration ... 10^{-3} to $>10^{+4}$ s

Depth Resolution .. <0.03 μm

Load Resolution .. <0.0003 N

Temperature ... 0 to 100 °C

Indenters ... Vickers, Knoop and Microball

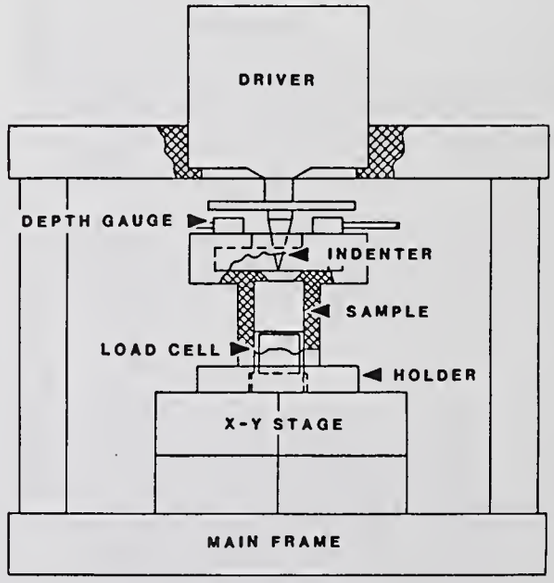

Figure 2. A schematic diagram of the main frame showing the placement of the instrumentation and sample.

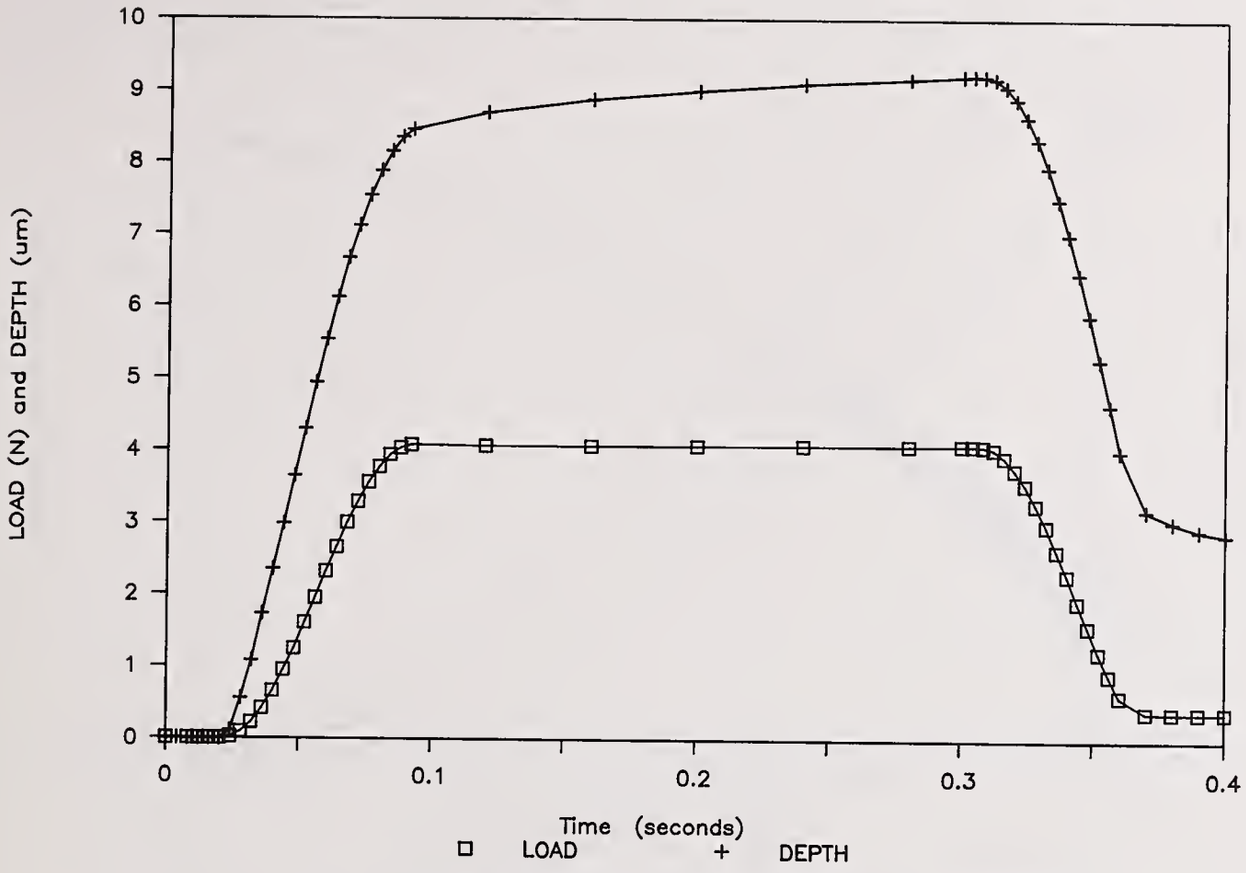

Figure 3a. Load and depth versus time curves for polymethylmethacrylate (PMMA).

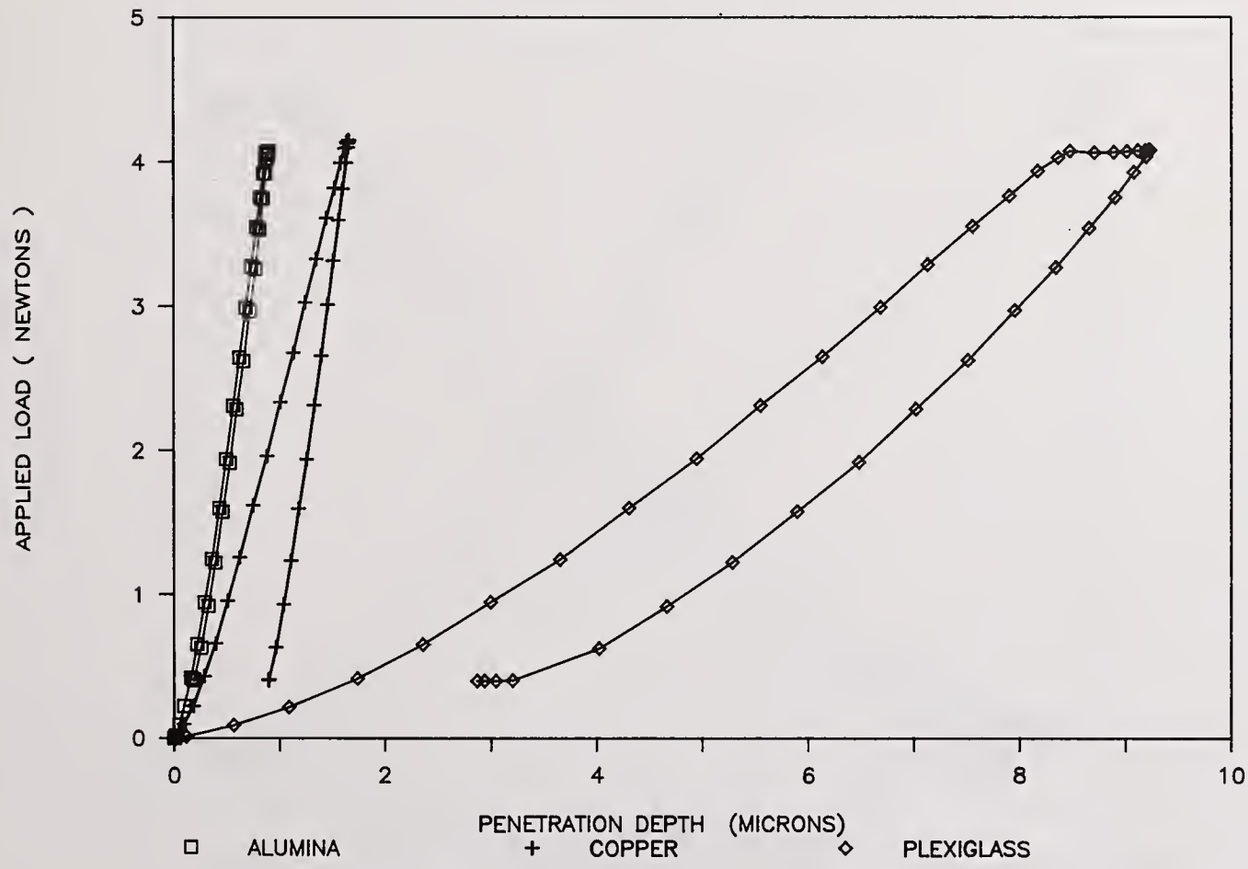

Figure 3b. Load-depth curves for synthetic sapphire, PPMA and OFHC copper.

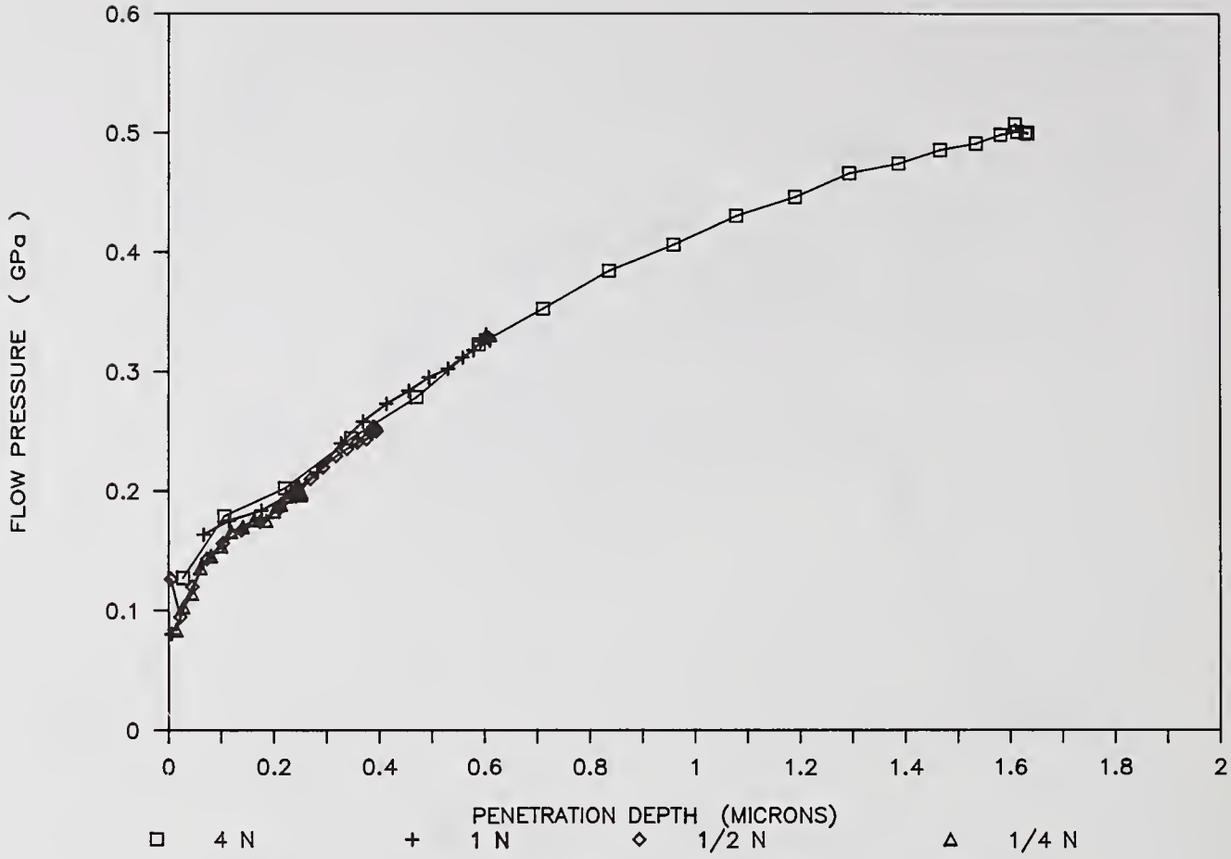

Figure 4. Flow pressure-depth curves at different peak loads for polished fused silica.

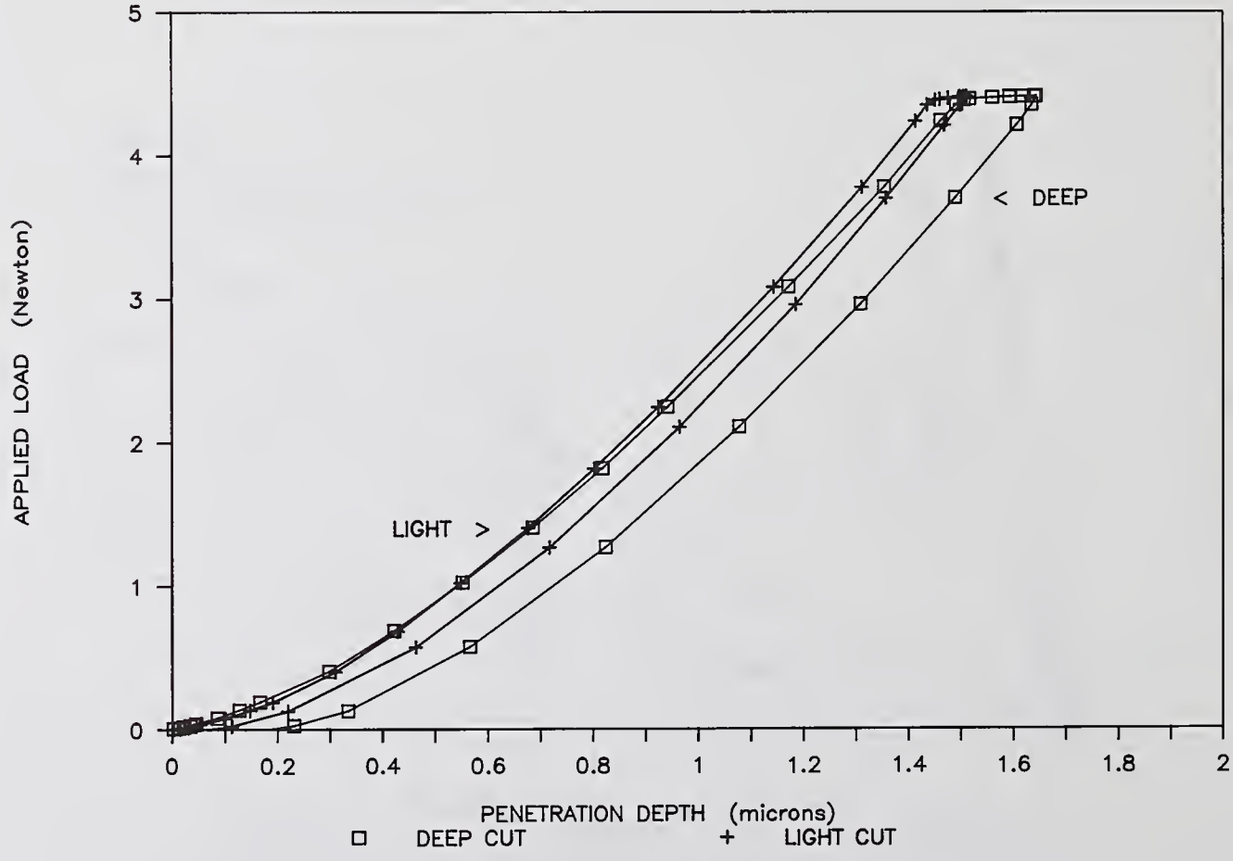

Figure 5. Load-depth curves for light and deep depths of cut in gallium arsenide.

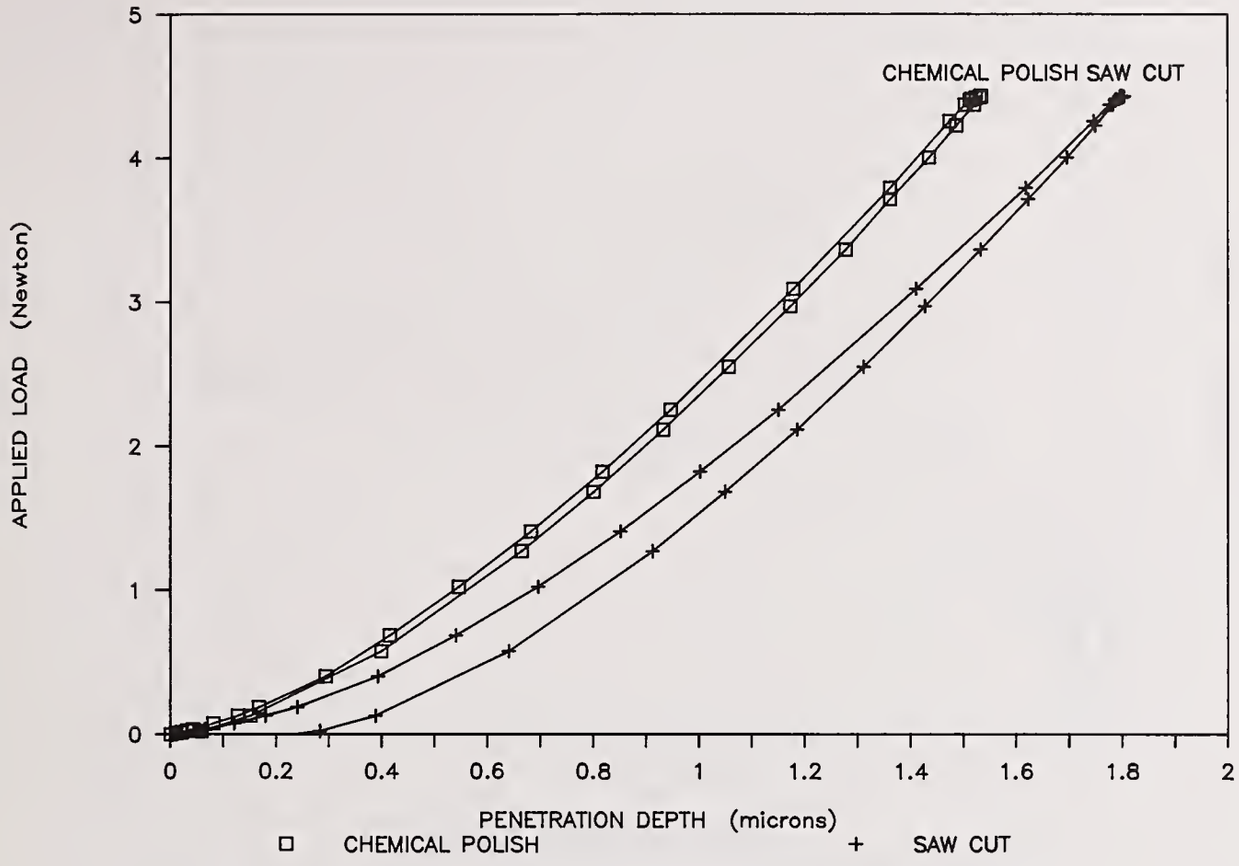

Figure 6a. Flow pressure-depth curves for gallium arsenide prepared by chemical polishing and saw cutting.

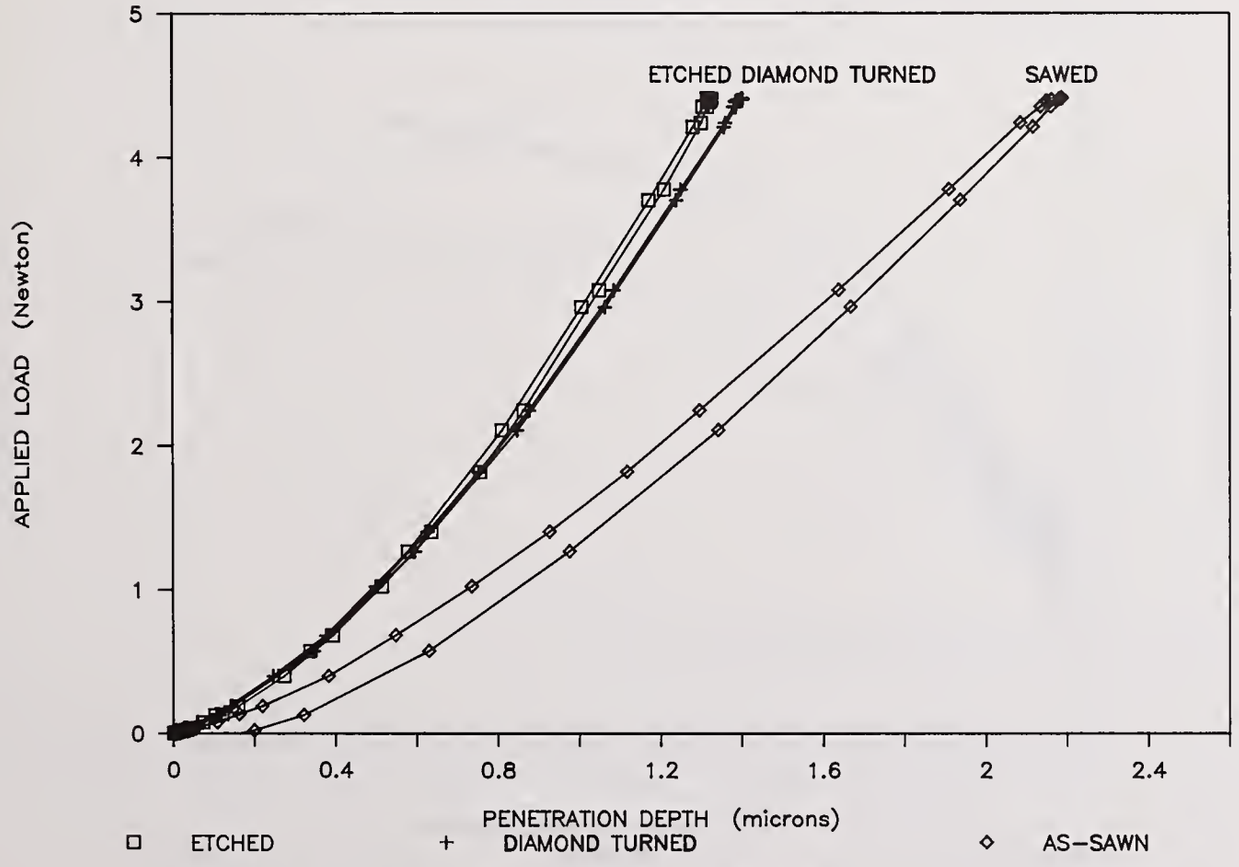

Figure 6b. Load-depth curves for germanium surfaces prepared with different processes.

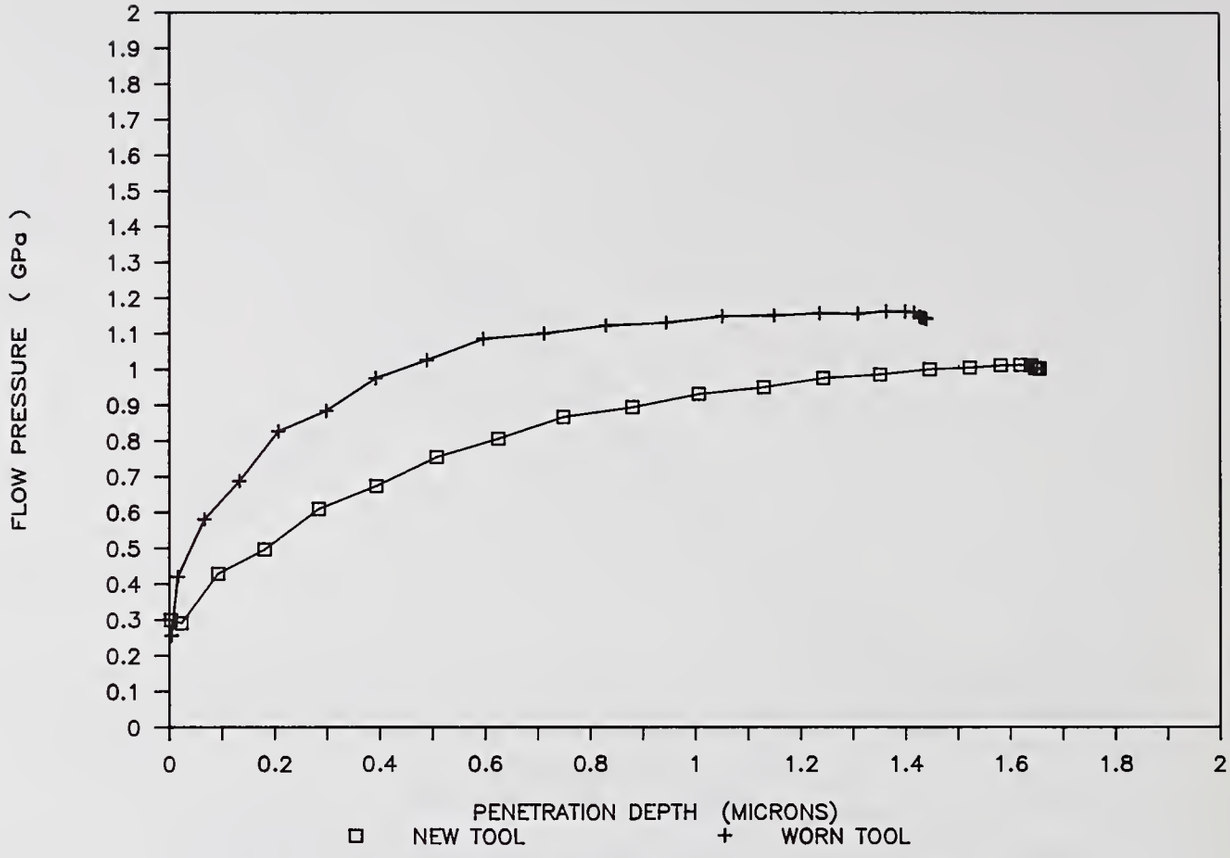

Figure 7a. Tool wear effects in the surfaces of diamond turned copper after machining one, and then eight more pieces.

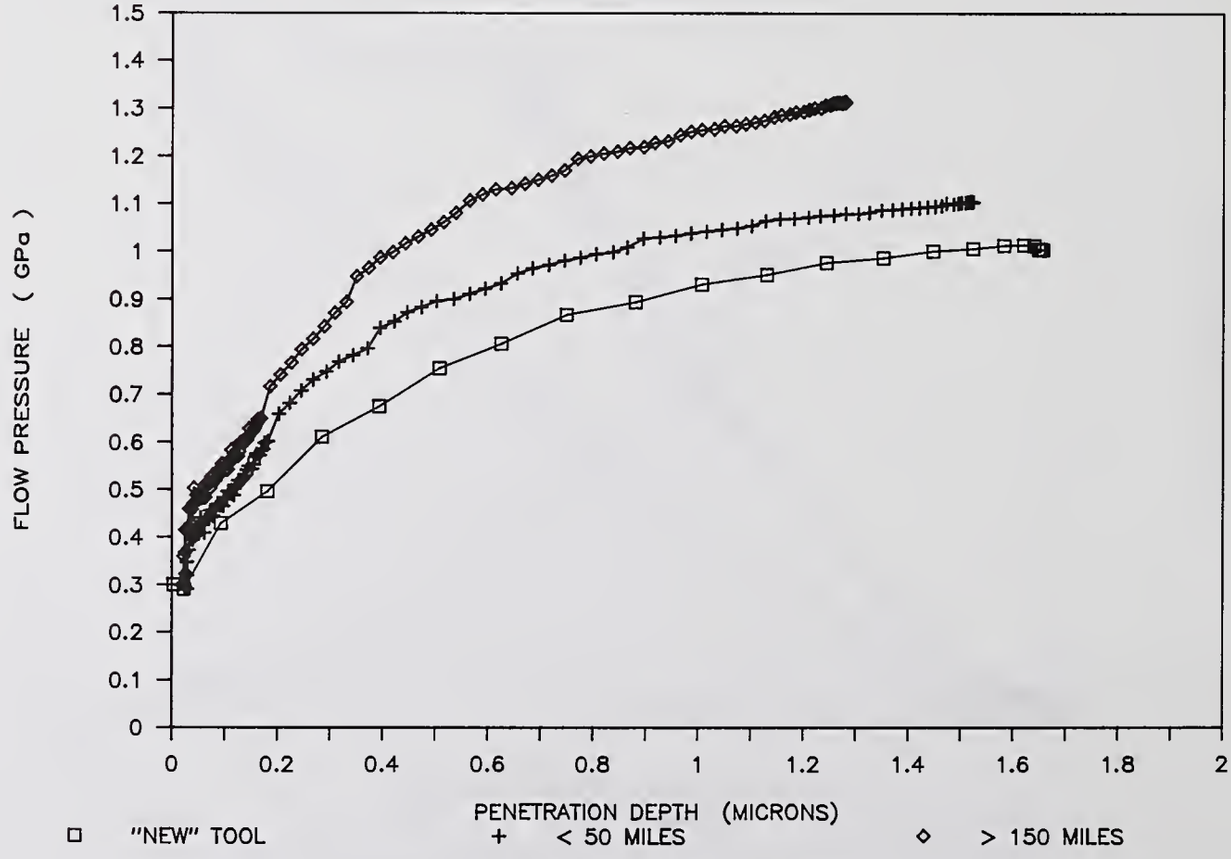

Figure 7b. Tool wear in diamond turned copper witness blanks after cutting 6061 aluminum for the indicated distances.

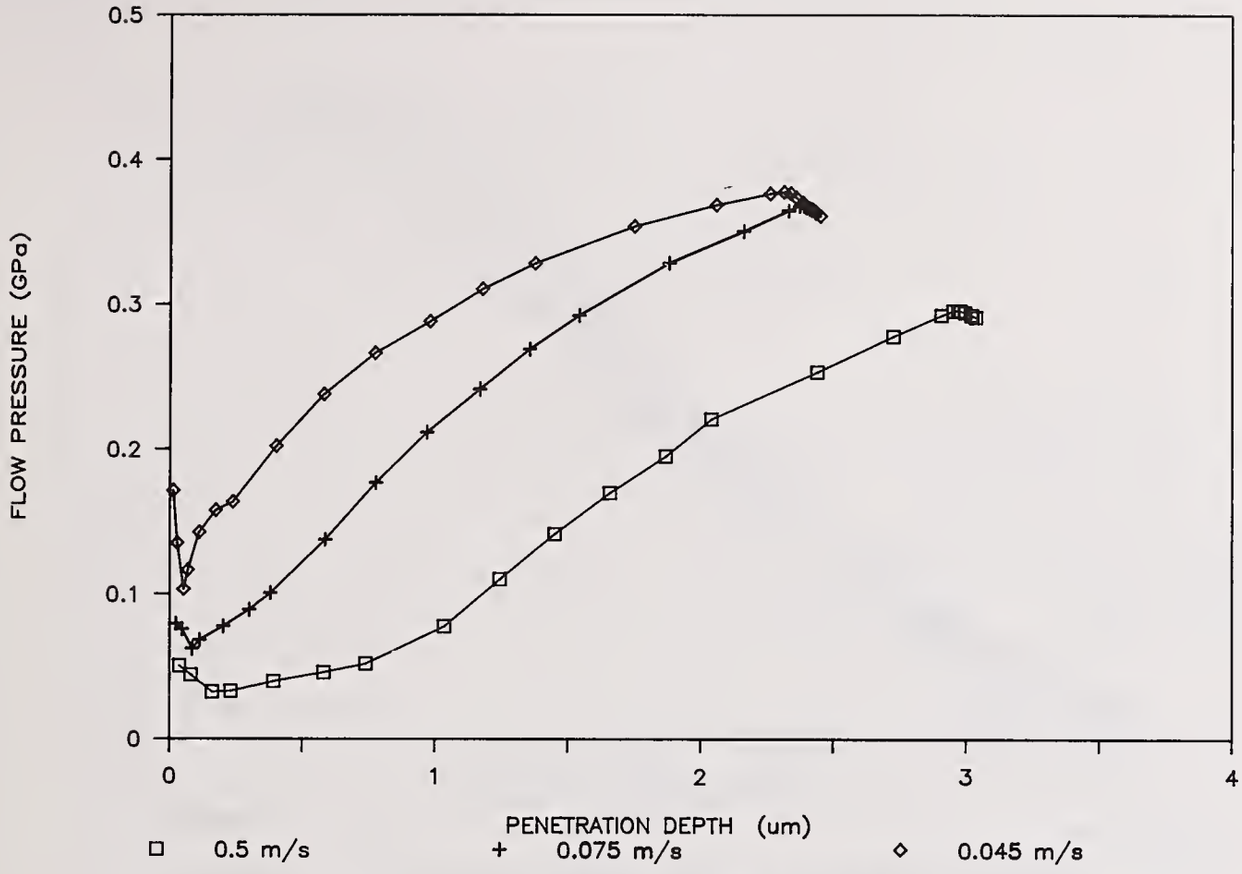

Figure 8. Effect of cutting rate on the surface condition of 6061 T6 aluminum samples.

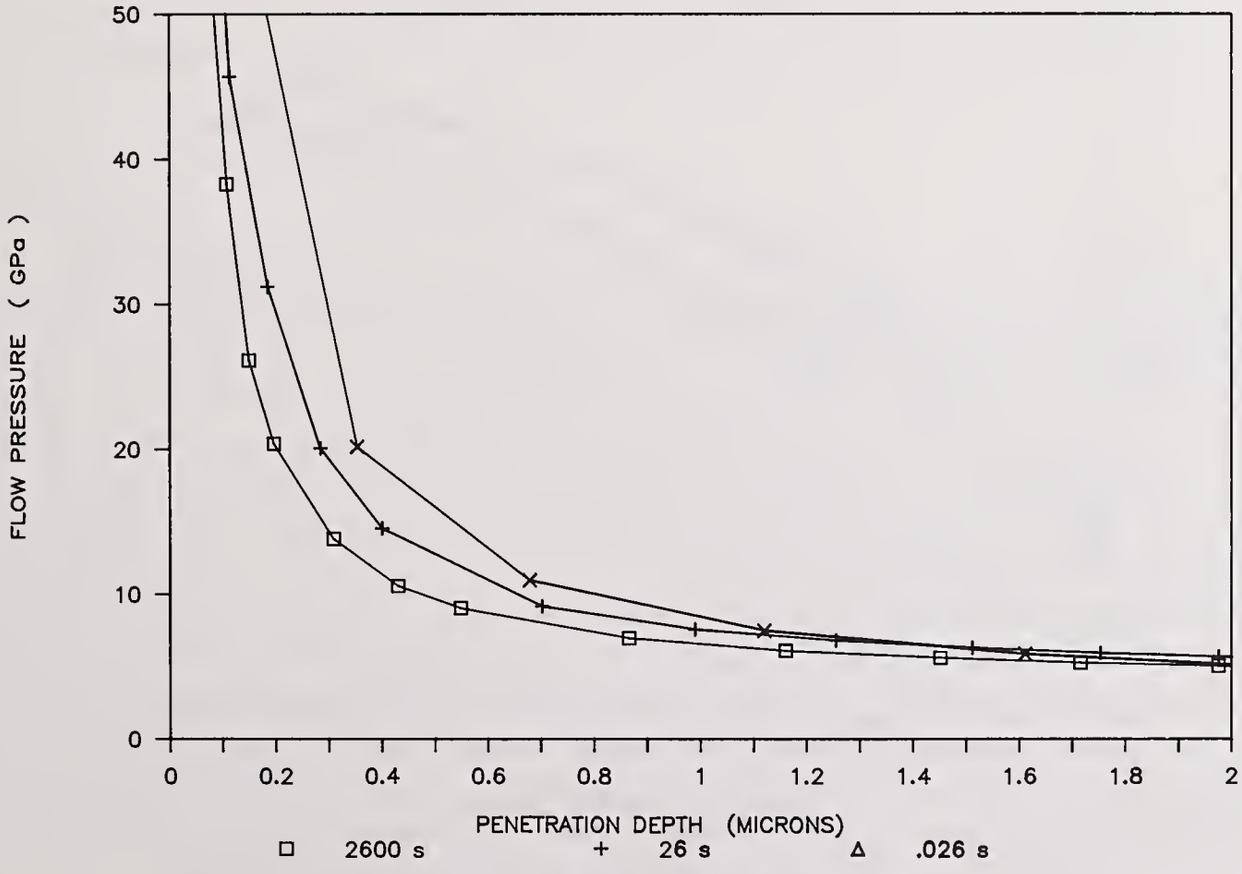

Figure 9. Effect of the loading rate on the strength of glass. The testing was performed on samples under water.

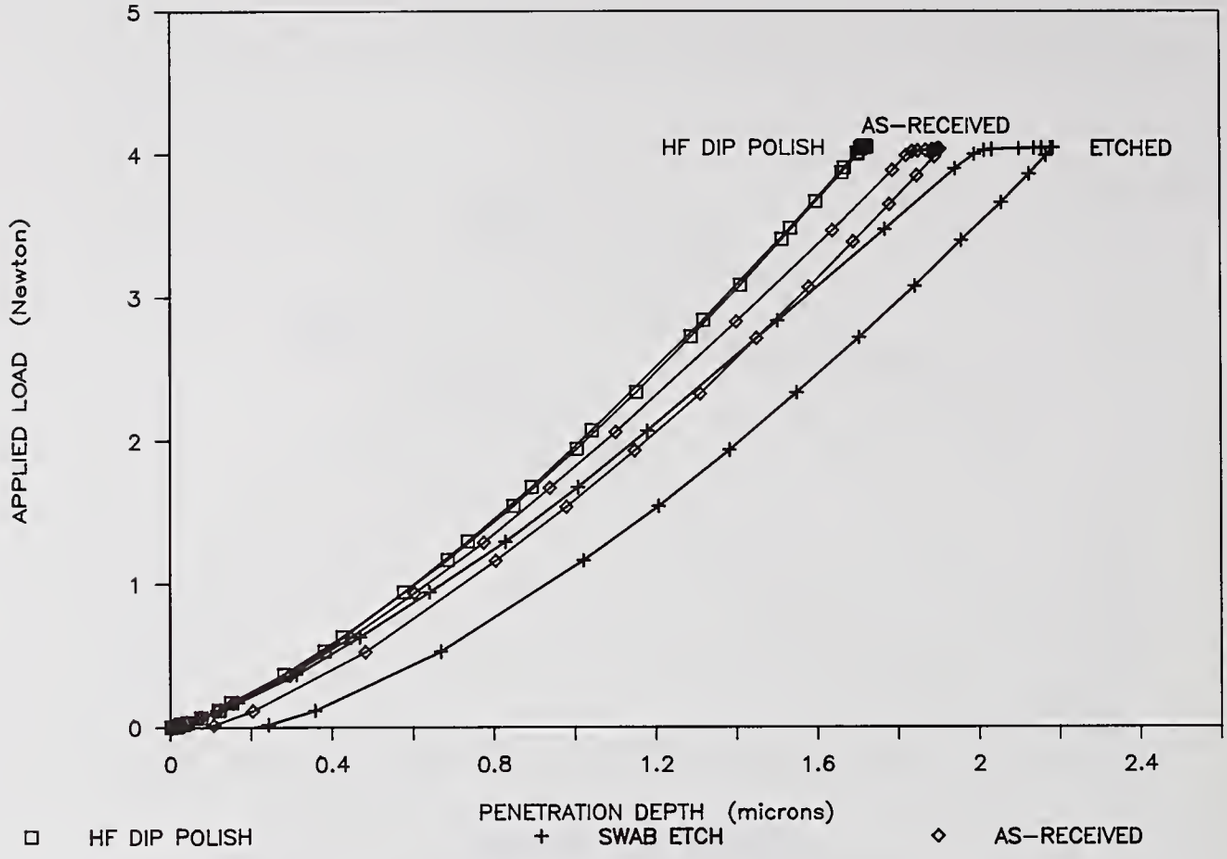

Figure 10. Effects of surface conditioning on the load-depth curves for an optical flat.

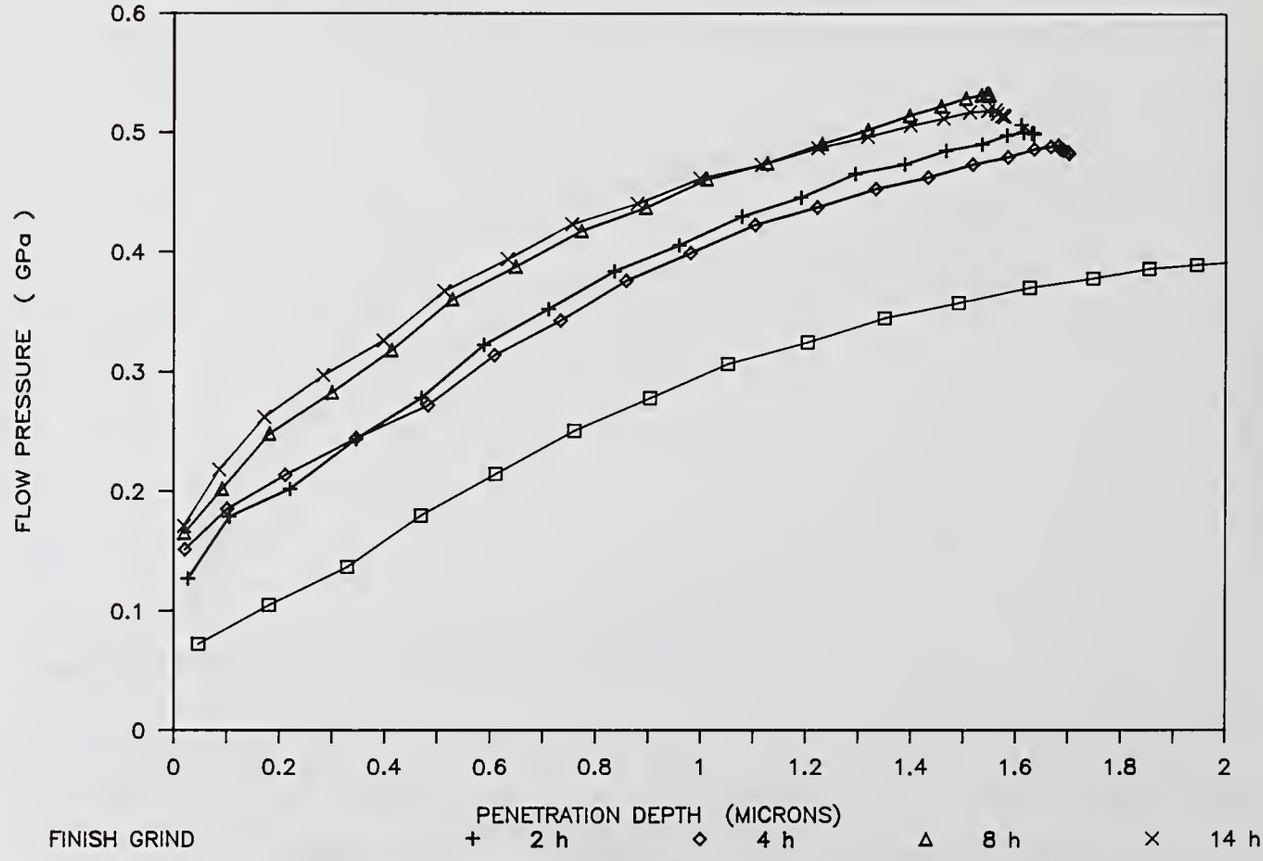

Figure 11. Effect of polishing time on the flow pressure-depth curves for fused silica.

Manuscript received
2-1-90

AUTOMATED DAMAGE TESTING FACILITY FOR EXCIMER LASER OPTICS

K. Mann and H. Gerhardt
Laser-Laboratorium Göttingen
3400 Göttingen, FRG

A set-up for automated measurement of damage thresholds on UV optical components is presented, being part of the EUREKA program "High Power Excimer Lasers". It includes on-line monitoring of probe beam parameters as well as sample condition, using digital image processing techniques for both laser beam profiling and high sensitivity damage detection. The latter is performed with a video microscopy system by pixel-to-pixel comparison of the video frames taken before and after the test laser pulse.
Along with a description of the experimental details for routine automated data acquisition, results of damage threshold measurements on bare UV substrates at 248 nm are presented, showing a clear correlation with the amount of absorbed radiation at this wavelength. On dielectric coatings strong evidence for impurity dominated defect generation is found.

Key words: UV laser damage, damage testing, threshold determination, spatial beam profiling, video microscopy, image processing, fluoride crystals, dielectric coatings

1. Introduction

Since laser induced damage of optical components has become a severe problem for the development of high power lasers during the last years, great efforts are made to improve the quality of the employed optics. This requires, however, the use of controlled damage testing experiments, which not only allow the accurate determination of damage thresholds, but can also give insight into the fundamental damaging processes [1].
The threshold determination requires the repetitive execution of a sequence of various measurements and computations, in order to characterize test laser pulse and sample condition. Hence, an automation of this procedure is advantageous, since it not only minimizes the possible sources of error but also provides a rapid and unbiased assessment of a sample.
At the Laser-Laboratorium Göttingen such an automated damage testing facility has been installed for routine measurements on UV optical components. The basic outline of this fully automated arrangement is described in this paper, together with the results of damage threshold measurements on various fluoride crystals and high reflection dielectric coatings at 248 nm. In addition, a procedure for a functional damage test on HR coatings is presented.

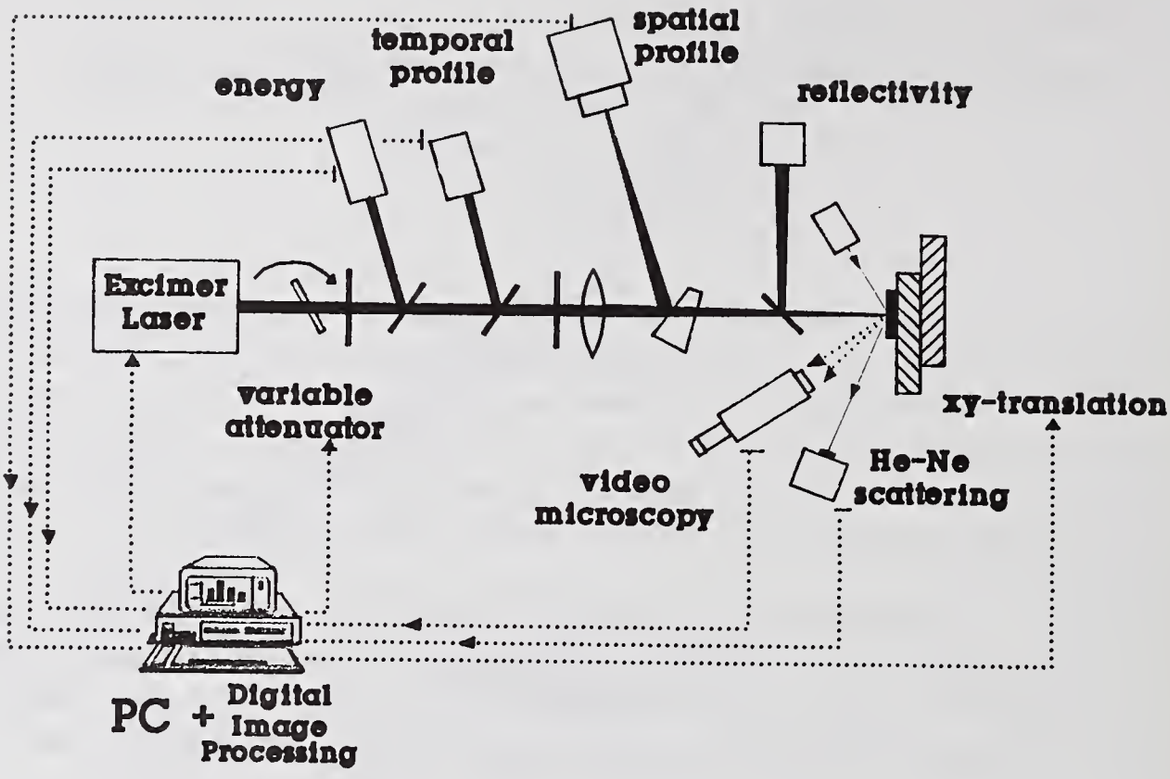

Fig. 1: Experimental arrangement

2. Experimental

2.1 Probe beam characterization

In Fig. 1 the experimental set-up used for damage threshold determination is shown schematically, including a sketch of the computer controlled data acquisition system.

An essential part of any damage testing experiment using pulsed laser radiation is the continuous variation of the laser fluence on the sample, followed by an inspection whether or not the respective pulse has caused damage. In our set-up the fluence can be varied by means of a dielectric filter with angle-dependent transmission. By rotating this attenuator with the help of a computer controlled stepper motor the output energy of the employed excimer laser (EMG 202 MSC ILC, Lambda Physik) and hence the energy density on the sample can be varied over almost two orders of magnitude. The necessary fluence values for controlled damage are obtained by focussing the beam onto the sample with a spherical lens.

As indicated in Fig. 1, three diagnostic beams are derived for characterization of the test laser pulse, i.e. measurement of

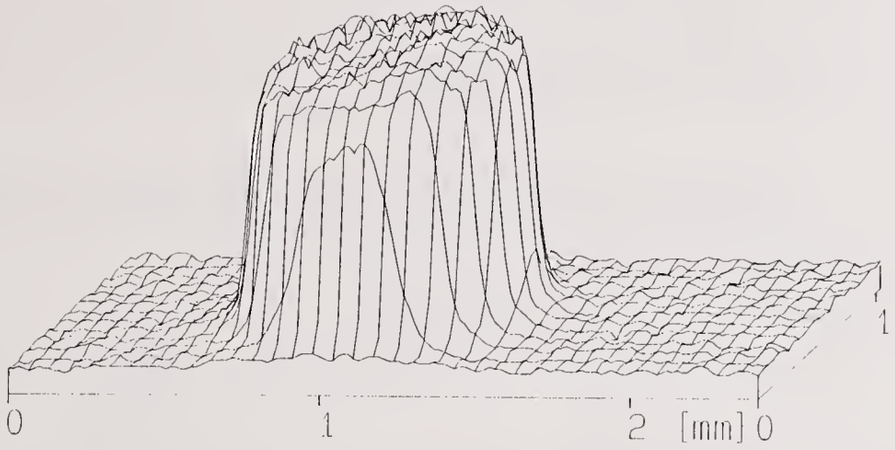

Fig. 2: 3D intensity profile of a typical test laser pulse at 248 nm

- pulse energy with a pyroelectric detector
- temporal waveform with a vacuum photodiode
- spatial profile

for each irradiating laser pulse. The spatial intensity distribution in a plane equivalent to the sample surface is measured with an UV laser beam profiling system, consisting of a special UV sensitive video camera and a PC-based digital image processing board (frame grabber). Details of this system are described elsewhere [2]. Fig.2 shows a 3D plot of the pulse profile at 248 nm as monitored with the camera. The relatively steep edges are obtained by imaging a circular aperture onto the camera plane (and hence the target surface), yielding a rather flat-topped distribution without occurence of "hot spots". During the measurements the intensity profile of each pulse is processed in order to calculate the correct fluence on the sample, taking into account pulse-to-pulse fluctuations of the beam.

2.2 Damage recognition

In previous examinations it has been demonstrated, that from the various techniques applied for damage detection the microscopic methods are the most sensitive ones [3]. Hence, in addition to high magnification Nomarski microscopy (off-line) and He-Ne scattering (which is used for comparison) in our set-up a video microscopy system is employed for standard on-line damage detection (cf. Fig. 1): By means of a CCD camera connected to a stereo microscope the sample surface can be viewed in real time, i.e. during the damaging pulse, on a video monitor.

Since it has been shown that a further enhancement of the detection sensitivity is possible by appropriate methods of digital image processing [4], our video frame grabber is used also for digitization and analysis of the microscopic image. This is accomplished by storage of the images before and after the damaging pulse is applied, followed by a pixel-to-pixel comparison and pseudo colour processing of these two data sets. In this way even faintest laser induced changes on the sample are easily detectable.

2.3 Measurement sequence for threshold determination

Damage thresholds are defined as the average of the lowest damaging and the highest non-damaging fluence. The actual values are determined under computer control by the use of a complex measuring program. The various steps of this automated measuring cycle are listed below:

1. Positioning the sample by a motor driven x-y-translation stage interfaced to the PC, using cursor keys; simultaneously the site to be tested is viewed on the video monitor by means of the video microscope
2. Storing the microscopic image in frame memory
3. Adjusting the attenuator transmission (i.e. pulse energy) with a PC triggered stepper motor
4. Triggering the excimer laser from the PC
5. Measurement of pulse energy, temporal waveform and spatial intensity profile of the excimer pulse; data transfer to the PC by A/D conversion and IEEE interface
6. Computation of the laser fluence and power density
7. Comparison of the actual microscopic image with the previous image; colouring of altered pixels
8. Decision damage/no damage
9. Storage of all data

The sequence 1.-9. is then repeated for a new sample position and varied pulse energy, until the damage threshold has been determined by an iteration procedure.

3. Results

3.1 Fluoride crystals

Since the UV transmission of many fluoride crystals is high, they are commonly used as optical components for excimer lasers, e.g. as resonator windows. For this reason a set of 6 commercial UV grade fluoride crystals has been tested at 248 nm (τ = 25 ns), together with two chloride crystals and a quartz substrate for comparison. The measurements were performed in the single pulse ("1 on 1") mode.

In Fig. 3 the results for rear, bulk as well as front surface damage are compiled, showing that in most cases damage starts on the rear surface. This known effect can be explained by the higher intensity on this surface due to constructive interference [5]. The highest damage thresholds are observed for CaF_2 as well as MgF_2 crystals (F_D = 16-17 J/cm^2), being in good agreement with results of Rainer and Hildum (CaF_2: F_D = 13 J/cm^2; MgF_2: F_D = 19 J/cm^2 [5]) and Scott (MgF_2: F_D= 17.4 J/cm^2 [6]) for the same wavelength and similar pulse duration. On the other hand, Scott has measured for CaF_2 a threshold of only 3.3 J/cm^2. Since for a second CaF_2 crystal from another vendor we have also obtained a much lower value (6.8 J/cm^2), this deviation is conceivable, indicating a large scatter in quality for the various samples.

The discrepancy in the CaF_2 results was the motivation for a further investigation: Since the absorption of laser radiation is a preliminary condition for the subsequent damaging process,

Fig. 3: Rear, bulk and front surface damage thresholds measured for various substrates at 248 nm

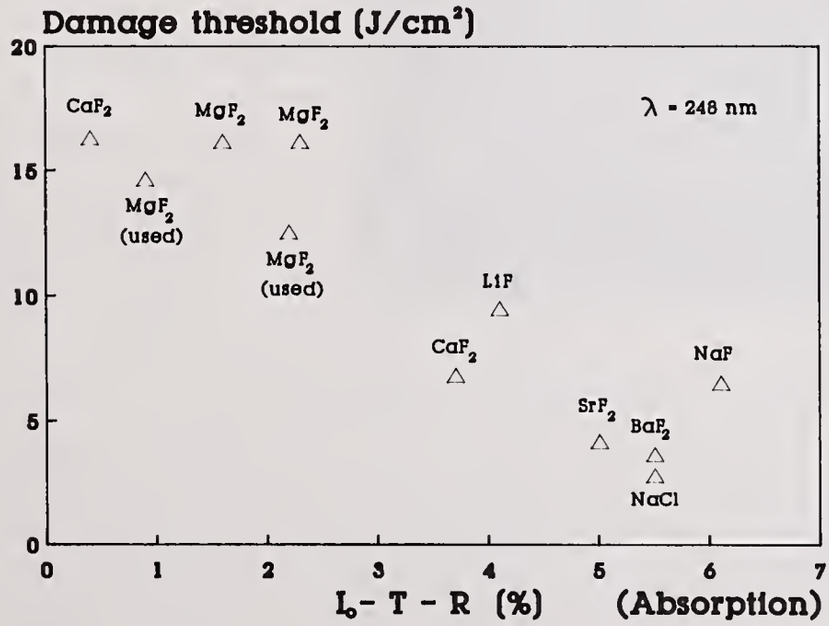

Fig. 4: Overall damage thresholds of Fig. 3, as a function of absorbed radiation (cf. text)

the dependence between damage threshold F_D and absorption A has been examined. Fig. 4 shows the overall damage threshold of the various fluoride crystals as a function of A, as determined indirectly by subtracting the transmission T (measured at 248 nm with an UV-Spectrometer) and the reflectivity R (calculated from Fresnels formula for given index of refraction) from 100 % (= I_O). Obviously, a clear correlation between damage and absorption is obtained, although in this crude model e.g. scattering losses are neglected. In particular, the lower damage threshold of one of the CaF_2 crystals coincides well with a much higher portion of absorbed radiation, possibly due to a higher amount of impurities.

before

after

Fig. 5: Micrographs of high reflection laser mirror before and after irradiation with 50 pulses of 1.5 J/cm² at 248 nm

Another interesting result is also compiled in Fig. 4, i.e. the thresholds of 4 different MgF_2 crystals. Whereas two new crystals show very similar values ($\approx$ 16 J/cm^2), for two other samples, which had been used already as resonator windows in a KrF laser, considerably smaller thresholds are obtained, demonstrating the adverse influence of the fluorine environment.

3.2 HR coatings

Single pulse damage thresholds have also been measured for variuos HR coatings at 248 nm and 193 nm. The actual values are considerably smaller than for the employed bare Suprasil substrates (i.e. 1-5 J/cm^2 at 248 nm, $<$ 2 J/cm^2 at 193 nm [7]), in good agreement with results of other authors [4,5].

In any case, damage is dominated by impurities in the dielectric coating, as can be readily seen from a comparison of the video microscopic images. This is illustrated in Fig. 5, showing micrographs of the same site of a HR coating before and after irradiation with 50 pulses of 1.5 J/cm^2 (λ = 248 nm). Clearly, damage starts at defect or impurity sites, which are visible already before testing. They absorb enough energy from the radiation field, that in their vicinity the coating is disrupted (inclusion heating model [4,8]). However, although there is no doubt about the cause of damage in this case, a complete identification (including elemental analysis) of the damaging (and non-damaging) inclusions is not yet possible. Further work in this direction is in progress.

4. Functional testing of HR coatings

In a few cases of HR dielectric coatings it has been observed that laser induced changes on the sample, as seen by video microscopy, do not necessarily correlate with functional failure of the component. Hence an alternative technique is applied for damage recognition, which is of somewhat more practical importance for the performance of high reflecting optics, i.e. measurement of the change in reflectivity of the sample on the laser irradiated site.

This is performed in the following way (cf. insert of Fig. 6): With the help of a beam splitter the UV radiation reflected from the sample at normal incidence is measured with a pyroelectric detector. For any laser pulse this signal is related to the corresponding incident energy, yielding a relative measure for the reflectivity R of the sample. The measurement is performed at a fluence small compared to the damage threshold, once before and once after the damaging pulse is applied. Thus the loss in reflectivity ΔR on the tested site can be determined. By proper evaluation of the pyroelectric signals with the help of a digital storage oscilloscope as well as averaging over many pulses a sensitivity $<$ 0.2 % is achievable.

Fig. 6 shows an example of this technique for a commercial HR coating at 248 nm with an initial reflectivity $>$ 99 %. Above the damage threshold F_D, as measured by video microscopy, the reflectivity drops drastically with increasing fluence, since increasing portions of the HR coating are ablated. Obviously, this functional test can be performed in a similar way for the transmitted signal, e.g. in case of substrates or AR coatings.

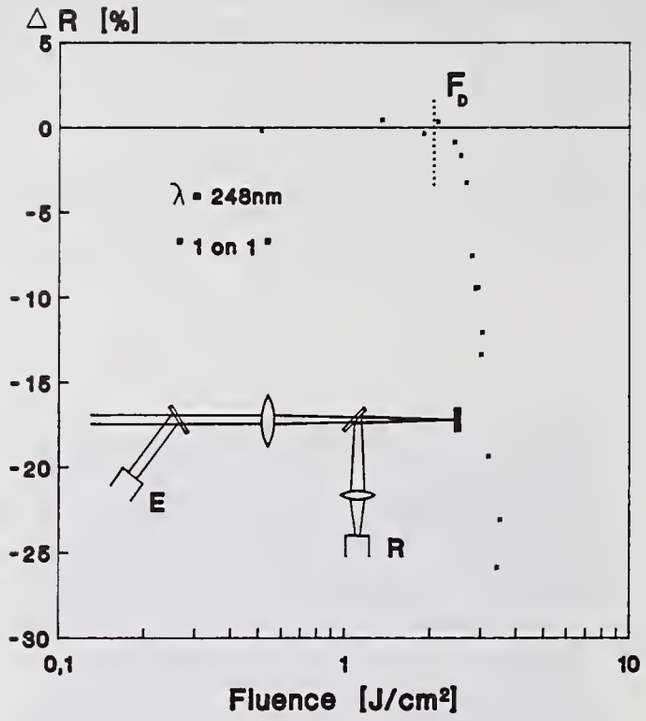

Fig. 6: Loss in reflectivity of HR coating on laser irradiated site

5. Conclusion

An automated damage testing facility for UV optics has been presented, which makes use of digital image processing techniques for both laser beam profiling and damage detection. Damage thresholds measured at 248 nm for various fluoride crystals show a strong dependence from the amount of absorbed radiation determined at this wavelength. In addition, by measuring the loss in reflectivity on the laser-irradiated site, a functional damage test for HR optics has been proposed.

References

[1] see e.g. "Laser Induced Damage in Optical Materials : 1987", NIST Spec. Publ. 756 (1987)
[2] K. Mann, H. Gerhardt in: "Laser und Optoelektronik" 4 (1989)
[3] K. Mann, H. Gerhardt in: "Laser Induced Damage in Optical Materials : 1988", to be published
[4] S.E. Clark, D.C. Emmony, ibid.
[5] F. Rainer, E.A. Hildum in: "Excimer Lasers and Optics", SPIE Vol. 710 (1986)
[6] M.L. Scott, in: "Laser Induced Damage in Optical Materials: 1983", NBS Spec. Publ. 688 (1983)
[7] J. Kolbe, H. Müller, H. Schink, H. Welling, J. Ebert in "Laser Induced Damage in Optical Materials: 1989", to be published
[8] T.W. Walker, A.H. Guenther, P.E. Nielsen: IEEE Journ. Quantum Electr. QE-17, 2053 (1981)

Manuscript Received
5-4-90

Expanded Damage Test Facilities at LLNL*

A. J. Morgan, F. Rainer, F. P. De Marco, R. P. Gonzales, M. R. Kozlowski, and M. C. Staggs
Lawrence Livermore National Laboratory
P.O. Box 5508, L-490
Livermore, CA 94550

We are completing a thorough expansion of the laser-induced damage-test capabilities at LLNL which allow us to conduct tests under a variety of parameter conditions. We have nine different laser systems which cover the following parameter space:

Laser	Wavelength (nm)	Max. PRF (Hz)	Duration (ns)	Peak Fluence (J/cm^2)
Reptile 1	1064	30	10	65
" 2/4	532, 266	10	10	40, 25
" 3	355	10	10	40
Chameleon 3	1064, 532, 355, 266	10	3	> 50
" 10	1064, 532, 355, 266	10	10	> 50
Raster Blaster	1064	17.8	8	60
Variable Pulse Laser (VPL)	1064	Single shot	1-100	> 70
Kilroy	1064	6000	65	10
Felix	350, 248	100	20	30

We describe details of the physical configurations of the individual systems, laser and sample diagnostics, and general testing procedures and capabilities. Damage test results are presented in a companion paper at this conference — "Laser Damage Database at 1064 nm".

Key words: damage; excimer lasers; frequency conversion; laser-induced damage; YAG lasers.

1. Introduction

Over the course of the last fifteen years, the Lawrence Livermore National Laboratory (LLNL) has established at least 12 different laser systems with the specific function of conducting studies in laser-induced damage to optical materials. Results from all of these facilities have been reported at the Boulder Damage Symposium for many years. These systems have included:

- Various Nd:glass or Nd:YAG systems operating at 1064 nm and possibly at one or more of the second, third and fourth harmonics of the fundamental wavelength;
- Excimer lasers operated at 351 or 248 nm;
- Copper vapor system operated at 500-650 nm (Laser Isotope Separation Laser Demonstration Facility).

* Work performed under the auspices of the U. S. Department of Energy by Lawrence Livermore National Laboratory under Contract No. W-7405-ENG-48.

In addition we have also conducted damage experiments on LLNL's 120-kJ Nova laser (1 to 3 ns at 1053 and 351 nm) and supported the establishment of laser-damage test facilities at Optical Coating Laboratory, Inc. (OCLI), Spectra-Physics, Inc., and Montana Laser Optics, Inc.

The facilities at LLNL have come and gone as funding and programmatic requirements have changed. We describe in this paper the facilities that we have utilized or constructed at LLNL in the past year. Specific test results from these lasers are described in several companion papers at these proceedings.

2. Laser diagnostics

Although each system incorporates slightly different laser diagnostics we have in general standardized our techniques for most of the facilities. In order to fully characterize the interaction of laser beams with optical materials we need to measure or know the conditions of the following laser parameters at the sample plane: wavelength, pulse-repetition frequency (PRF), pulse-irradiation sequence, polarization, angle of incidence, pulse energy, spatial beam profile, peak fluence, pulse duration, and temporal pulse shape. In figure 1 we show a generalized schematic of a typical damage-test facility with all of the possible laser and sample diagnostic components. Not all components are necessarily used in each facility. We shall describe the components in the sequence in which the laser pulse propagates from the laser to the test sample. We shall also inject some of the general philosophies that we have adopted in designing damage-test facilities in recent years.

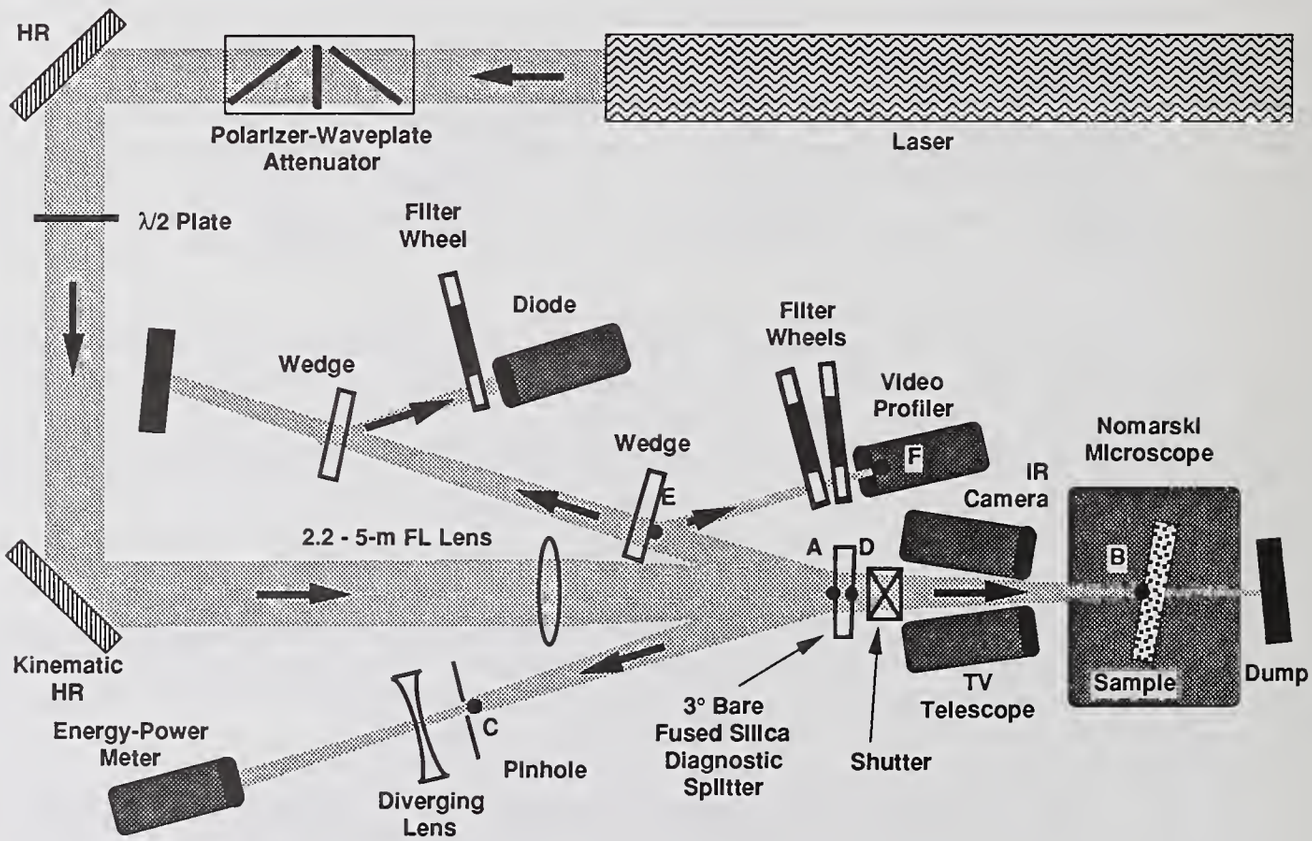

Figure 1. A typical layout of a laser damage test facility. Not all components are included in each system. The optical distances AB, AC and ADEF must all be equal in order to diagnose the laser parameters at the equivalent plane of the test sample.

2.1 Wavelength and PRF

The wavelength and PRF used for a particular experiment are usually determined by the laser system supplying the irradiating pulses. For the YAG lasers the wavelengths include the fundamental and possible second, third and fourth harmonics as determined by the frequency conversion crystals we utilize; for the

excimer lasers the gas mixture, KrF or XeF, determines which wavelength is obtained. In the case of frequency conversion we typically employ several multi-harmonic turning mirrors to not only steer the beam and physically decouple it from the laser but also to discriminate against the propagation of any unwanted harmonics. We usually maintain separate beam lines for the different wavelength beam paths until the final mirror position which directs the beam to the focusing lens, diagnostics and sample. At this final mirror position we mount the appropriate wavelength mirror on a kinematic mount so that we can change wavelengths with a minimum of realignment. The PRF is usually determined by the maximum operating rep-rate of the laser. This can range from single shots in the case of VPL, to 10 to 30 Hz for most of our lasers, up to 6000 Hz or more in the case of Kilroy. For most of the rep-rated lasers we can also operate at lower-than-maximum PRF, or with just single shots, by controlling either the rate at which the Q-switch Pockels' cell is triggered or by simply dialing in a rep-rate. This PRF is confirmed by the pulse duration diode at low oscilloscope sweep speeds.

2.2 Pulse irradiation sequence

The sequence of irradiating pulses, as well as the PRF, may affect the results of laser damage. Prior to the development of high power rep-rated lasers we conducted all of our tests with single shots. When done on a previously unirradiated site such tests were termed as 1-on-1 (alternately 1:1 or one shot per one site). Repeated irradiations in this single shot mode on the same site were termed N-on-1 (N:1). Typically each shot was done with successively higher fluences which contributed to higher bulk damage thresholds of frequency conversion crystals. [1] Variations of this improvement in damage thresholds have been called annealing, pre-conditioning, laser-conditioning, or simply conditioning. [2, 3 and related references therein]. In the single-shot mode this was a long, painstaking procedure which was improved upon with the use of rep-rated lasers. In a PRF mode we further distinguish our tests by the designation S-on-1 (S:1) if we irradiate a given site with many shots at the same fluence or by R-on-1 (R:1) if we ramp the fluence up from near zero to some designated maximum limit in a smooth step-wise fashion. The latter is another means of conditioning the sample in a matter of seconds rather than hours. Two other means of conditioning the sample are to scan the sample in one dimension or raster it in two dimensions through a rep-rated beam. The conditioning is then done by the wings of a typically gaussian-shaped beam wherein the sample is moved through successively higher fluence portions of the beam with each successive shot.

2.3 Polarization and energy control

The laser energy, and hence the laser fluence on the sample, can be controlled by a variety of techniques such as: (1) changing the number or pumping levels of the laser amplifiers, (2) adding absorbing or reflecting attenuators to the output beam, (3) changing the spot size on the sample, or (4) using polarizers and waveplates to discard some fraction of the beam. Each technique has some drawbacks in application or can change other parameters as well as fluence (pulse duration or shape change, spot size or shape change, loss of too much energy, uniformity of fluence increments, realignment of the irradiating or diagnostic beams, etc.). If our beam quality is good enough we usually employ the polarizer-waveplate technique. The polarized output of the laser is put through a halfwave plate designed for that specific wavelength. Rotation of the plate about the beam axis by a controlled amount rotates the polarization by twice the angle so that the following polarizer then discards some fraction of the beam energy and transmits a linearly polarized beam (typically P-polarization) of the remainder. This may be followed by another halfwave plate which can rotate the output beam to any desired linear polarization (e.g. to test sample polarizers for damage with either P- or S-polarized beams). This technique is easy to employ, provides continuously variable attenuation, and in the case of the above mentioned R:1 irradiation, provides a smooth way to ramp and condition a sample site. The technique has some disadvantages, however. If the laser is unpolarized then one must first use another polarizer which immediately throws away half the usable energy. Near maximum extinction and for poorly collimated beams the beam profile usually degrades into a multi-lobed beam which may prove difficult to analyze for peak fluence. If we do in fact wish to work with very low fluences we may use an 80% normal reflector in our beam line to discard most of the energy and thus operate the waveplate-polarizer pair in a lower extinction mode. Alternatively we may move our focusing lens closer to the sample to increase the spot size and lower the fluence on the sample. We mount our lens holders on rails or adjacent to guide bars which allow us to move the lens along the beam axis at will for changing spot sizes without major system realignments. The lens can also be

moved away from the sample to raise the fluence to higher levels but with the caveat in mind that small spot sizes (< 0.6 mm $1/e^2$) can lead to inaccurate fluence measurements (intrinsic damage of defect-free materials rather than actual macroscopic damage in larger areas). The polarization dependence of damage may also be subject to the incident angle of the laser beam to the sample surface. Typically we mount our samples at 10° incidence to avoid reflecting the beam back into the laser. This usually also provides sufficient offset so that, for a transmissive sample, the reflection from the rear surface will not overlap with the incident beam on the front surface. Such possible overlap can in fact produce pronounced interference effects and higher fluences on the front surface. Our sample stage has a graded rotation platform so that we can set the incident angle at any desired position from normal incidence to near grazing incidence. Thus, samples such as 45°-incident mirrors or Brewster-angle optics can be tested at their specified angles. The laser fluence, however, is always specified as that normal to the beam direction.

2.4 Energy or average power measurement

After our focusing lens we split off a portion of the laser beam with a bare polished, 3°-wedge-angle, fused silica splitter to diagnose the beam. The splitter is usually 1/3 to 1/2 the distance from the lens to the sample. This keeps the splitter in a low enough fluence range so that it does not get damaged and yet it still allows sufficient room to accommodate the diagnostic hardware. As shown in figure 1, we set up the experiment so that the optical distance from the front surface of the splitter (A) to the sample plane (B) is exactly equal to the optical distance from (A) to the calorimeter pinhole (C) and also from (A) to the profiler camera (F). Note that in the latter case the optical distance in question follows the path from (A) to the rear surface of the diagnostic splitter (D) to a second splitter (E) to the camera plane (F). This assures that the calorimeter pinhole and camera planes are in fact the equivalent planes of the sample. Whenever possible we orient the two diagnostic beams so that they reflect at equal angles on either side of the incident beam from the lens. This allows for maximum clearance around the lens and also keeps the angles of the diagnostic reflections near-normal incidence. Near-normal incidence reduces the effects due to polarization and simplifies calculations for the various harmonics. Knowing the index of refraction of the diagnostic splitter at the desired wavelength, we calculate the ratio of the energy transmitted to the sample at (B) and the energy at the calorimeter pinhole (C). We specifically utilize a pinhole at this equivalent plane in order to truncate our nominally gaussian spatial beam profile near the wings of the profile. We employ several pinholes of graded sizes in a stainless steel plate which can be translated to assure that the pinhole size does in fact satisfy this criterion. By measuring only the energy that is transmitted through the known-size pinhole (referred to as apertured calorimetry) we assure ourselves that our peak fluence calculation will not be greatly affected by ambiguities between true video signals and noise in the wings of the spatial profile as recorded by the video beam profiler (see below). The calorimeter may be used either as a single shot calorimeter or as an average power meter in the case of PRF irradiations. We utilize both in-house designed calorimeters and commercial power-energy meters. The commercial units employ a black absorbing surface which is relatively independent of wavelength so that it may be used for all the harmonics of a particular laser system. We use a lens before the calorimeter (taking into account reflection and absorption losses) in order to expand the beam to a size which will not damage the absorbing surface and yet assure that no portion of the beam is clipped by the calorimeter aperture.

2.5 Spatial beam profile

The second diagnostic beam is directed to the beam profile diagnostic. In the past we utilized a variety of techniques developed at LLNL in order to characterize the exact nature of the spatial profile at the sample equivalent plane. These included both exposed film and electronic array beam profilers. [4- 7] Currently we utilize commercially available beam profilers which provide not only accurate profile data but an assurance of uniformity between our laser systems. We have found that these commercial units do in fact agree with our prior beam profile techniques. The diagnostic beam is directed to the camera via a second bare fused silica wedge in order to further lower the beam intensity. We then use neutral density (ND) and/or band-pass filters to lower the intensity to a level high enough to provide sufficient light to the camera without saturating it. We use two types of filters to attenuate the beam over a wide range of intensities. The first consists of absorbing glass filters mounted in a filter wheel so that we can dial in the appropriate filter without handling it. These filters were fabricated in neutral-density increments of 0.125 from ND 1 to 1.875 for a fine adjust filter wheel and increments of 0.5 from ND 1 to 3.5 for a course adjust

filter wheel. The two wheels together provide a wide ND range in small increments. We avoid rear surface reflections from the filters by using filters no smaller than ND 1 and take care to avoid interference between other filter faces. The second type of filter consists of two opposed, linearly-graded, metallic, reflective plates each ranging from ND 1 to 4 and with rear surface AR coatings. By opposing the direction of the plates the net attenuation is uniform across the full width of the beam. The beam profiler captures an image of the beam cross section and then uses the apertured-calorimeter data to calculate the beam profile and peak fluence in units of J/cm^2. Although the profiler sees and displays the entire beam cross section, it uses only the information from the camera pixels that fall within the defined pinhole size. The calculation does not depend on knowledge of the transmission of the filters in front of the camera. As long as the filters are not changed the calibration remains fixed. We, however, recalibrate the system with the first shot in each sequence of irradiations.

2.6 Temporal profile

Finally, we measure the temporal beam profile of the laser pulse with a fast photo-diode. Unlike the spatial information, the pulse duration is not dependent on which plane it is measured in. Therefore it may be picked off from one of several different locations. Unless otherwise noted our temporal beam profiles are nominally gaussian in shape although with our multi-mode lasers we may in fact have modulation within that envelope. We have found that our measurements of damage thresholds agree between different laser systems independent of modulation for a given pulse duration.

3. Test sample diagnostics

We define damage to a site to be any detectable change in the optical sample after irradiation as compared to that site before irradiation. We utilize a variety of techniques to determine such a change without prejudging whether the change in the sample has rendered it unusable as an optical component in a laser system. Often damage may indeed be very subtle and have minimal impact on the sample's usefulness. Usually we try to measure absolute damage thresholds and characterize the damage morphology both at the threshold level and at fluences above that level. We distinguish damage that may occur on the front or rear surfaces of the sample as well as in the bulk material. In some cases damage in one of these regions may in fact preclude making an absolute determination of damage in another.

3.1 Nomarski microscopy

Our primary tool in assessing damage is Nomarski microscopy. We have designed and built a sample stage which allows the sample to be mounted at the appropriate angle of incidence for irradiation by the laser and then be translated directly into the field of view of the Nomarski microscope. The microscope is typically housed in a clean hood with filtered laminar air flow to keep the sample clean and expel any emitted debris from ablated coating or substrate materials. We take Polaroid photographs of the site both before and after irradiation and compare them for any changes. We may also make visual notes of the appearance of the sample in the microscope since there is some loss of resolution in the photographs. Typically, we utilize a magnification of 100x since this provides a photograph which essentially covers the entire irradiated region of a 1-mm diameter laser beam. We can detect changes but not necessarily resolve artifacts down to a few μm in size. We also have the capability of examining the sample under 50x, 200x, 500x and 1000x magnification. Much of our work entails looking at damage to the front surface of the sample. However, in some circumstances we may extend the Nomarski microscopy to look at bulk damage or rear surface damage through the front surface with some loss in resolution. Usually this involves a visual observation rather than site-to-site photography. At 100x magnification we have a depth of field of about 10 mm. We usually limit any assessment of bulk or rear surface damage to samples with no greater than this thickness. Our irradiating beam is gradually focused to a position 100 - 500 mm after the sample, typically using a 2- to 5-m focal length lens. We feel that self focusing and uncertainties in the beam fluence inside the sample much beyond 10 mm preclude making an accurate assessment of the damaging fluences. Rear surface damage may also be noted by looking at the irradiated sites by turning the sample around after completion of the test. Only more obvious damage can be detected this way since we would have no pre-irradiation photographs to distinguish possible pre-irradiation artifacts from actual damage. Finally we also utilize the microscope in a non-Nomarski mode by illuminating the sample from on top or by

backlighting. Backlighting proves to be an effective tool to detect forward scattered light from small bulk defects.

3.2 Visual observations of damage

Visual observations are made of each site before and after irradiation using either a bright white light source or scatter from a He-Ne laser. Subtle changes in a sample which entail no amplitude changes in a surface can in fact be nearly invisible under Nomarski microscopy and yet show up as a general "fogging" to the naked eye under bright light illumination. We also make visual observations of the sample while wearing appropriate laser goggles while we are irradiating the sample. Light emission from the sample can be an indication of damage but it can also indicate the expulsion of volatile components from a porous surface without any physical change or damage to the surface itself. We note the emission of light but do not use it as a criterion for damage. An after-the-fact test often used to indicate possible changes in a sample is a "breath test". Water vapor condensation on the irradiation sites can produce pronounced differences in damaged versus undamaged regions that are visible under bright light illumination. The very act of fogging the sample with one's breath can, however, contaminate the sample for future tests.

3.3 Recorded real-time damage diagnostics

We utilize two other tools to a lesser degree to examine changes in a sample during irradiation and to record the results on video tape for replay. We observe scattered light from a bright light source or He-Ne laser with a short distance telescope and record this with a CCD camera. The resolution of the video image is less than that of the Nomarski microscope but it does provide the capability of observing the sample under magnification during irradiation. Similarly, we have observed the thermal loading of absorptive surfaces with an IR camera. This is particularly useful under high-PRF irradiations where a sample may not fail on the first few shots but may fail after prolonged irradiation and heating.

4. Laser facilities

4.1 Reptile

The Reptile facility was so named because of its PRF capabilities and has been our primary system for conducting laser damage studies since 1986. It was originally intended to provide insights into laser damage at PRF's up to 120 Hz. Most of our work prior to Reptile was conducted in a single shot mode. We constructed Reptile with four separate commercial YAG laser systems each of which ran multi-mode at 30 Hz with 16-ns pulses at 1064 nm. We multiplexed the four lasers together into one beam line using synchronized rotating wave plates to yield a beam at 120 Hz. [7] The system ran in this fashion for six months until we completed our first round of tests. We determined that except for obvious defect-dominated samples there was no difference in damage thresholds measured at 120 Hz as was obtainable with just one laser at 30 Hz or even even with single shots. Damage may have been more pronounced under the PRF-irradiation compared to single shot tests, but this stemmed from the number of shots rather than the PRF. Therefore, the facility was used primarily as a one-laser, 30-Hz facility.

We have recently upgraded Reptile to expand its capabilities at the other harmonics of YAG. This configuration is shown in figure 2. Two of the lasers each had an amplifier and Faraday rotator installed to yield higher energies for the purpose of providing more efficient frequency conversion. One laser has been successfully operated as a dedicated third harmonic (355 nm) laser capable of yielding fluences exceeding 45 J/cm^2 at the sample plane with a nominal test-spot size of 1-mm diameter. We have also begun tests with the other laser at the second harmonic (532 nm) with comparable peak fluence outputs. This laser is also designed to double the second harmonic pulses with a second KD*P crystal to provide us with a fourth harmonic (266 nm) testing capability. The laser has been modified to yield separate beam lines so that only one kinematically mounted green mirror needs to be moved in order to select the desired wavelength. In order to accomplish sufficient frequency conversion these new lasers are operated at a reduced maximum PRF of 10 Hz. All of the lasers have been modified to yield pulse durations of 10 ns at the first three harmonics so that we can conduct wavelength-dependent studies at the same pulse duration. Prior to this upgrade the Reptile facility was operated at 16 ns.

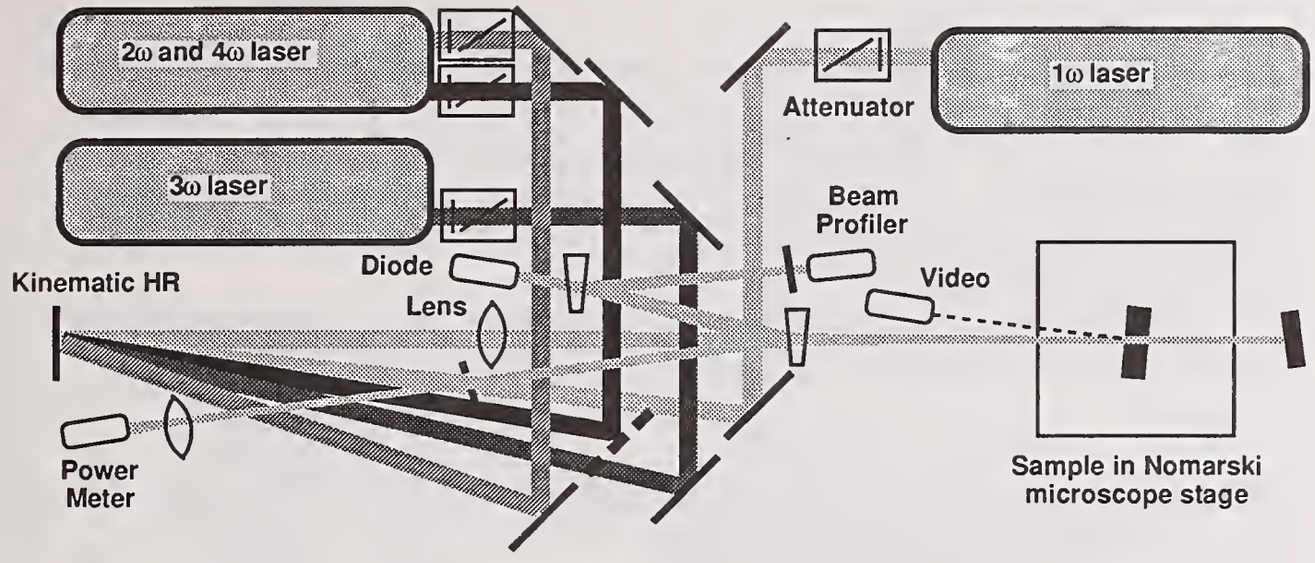

Figure 2. The Reptile damage-test facility utilizes three lasers to generate pulses at the first four harmonics of Nd:YAG (1064 nm, 532 nm, 355 nm and 266 nm). Most tests are conducted at 10 Hz with 10-ns pulses.

4.2 Chameleon

Chameleon was so named since it was one laser that could readily changes its color to any of the four first harmonics of Nd:YAG (1064 nm, 532 nm, 355 nm and 266 nm). Figure 3 shows the general layout of the facility. The system was designed to augment and improve upon the capabilities of the Reptile facility. The laser is a one-of-a-kind, system designed and built by Quantel International (Continuum) to yield nearly diffraction limited beams with nominally smooth temporal and spatial gaussian beam profiles. [8] The laser utilizes two separate oscillators to yield both short and long pulse durations. These are adjustable enough so that each harmonic can be tuned to yield nominally equal pulse durations both at 3 ns and 10 ns. This will allow us the added capability of conducting wavelength scaling and at least a minimal degree of pulse duration scaling. At 10 ns and 10 Hz the laser yields 1064-nm pulse energies > 2 J. We can conduct damage studies at all harmonics with fluences exceeding 50 J/cm² without having to resort to spot sizes below 1 mm. We have already begun damage tests with Chameleon at 1064 nm and are prepared to conduct tests at 532 nm and 355 nm as required.

4.3 Raster Blaster

The Raster Blaster laser was originally constructed as a prototype facility for the purpose of examining Nova laser glass for the presence of damage-causing platinum inclusions. [9] The system was then replicated so that laser-glass vendors could conduct these tests at their own facilities. The laser is a commercial Nd:YAG unit operating at 1064 nm with 8-ns pulses at a PRF of 17.8 Hz. The system name stemmed from its initial application when the large Nova glass disks were mounted in a large translation stage which was then rastered through the laser beam. The laser has subsequently been reconfigured as shown in figure 4. Its primary function is to be used as a resource facility for programmatic damage efforts without tying up our dedicated damage test facilities. To this end we have recently used the Raster Blaster in a concentrated study of the improvement in damage thresholds of optical coatings by "laser-conditioning". [2]

4.4 Variable Pulse Laser (VPL)

The Variable Pulse Laser was one of the original damage test facilities built at LLNL. In the course of 14 years we have used VPL to conduct 3200 damage tests. The system utilized a Nd:YAG oscillator and preamplifiers and Nd:glass amplifiers to produce very clean, high energy pulses at 1064 nm. The oscillator generated a nominal 100-ns pulse. The central portion of the pulse was then gated out with a spark-gap

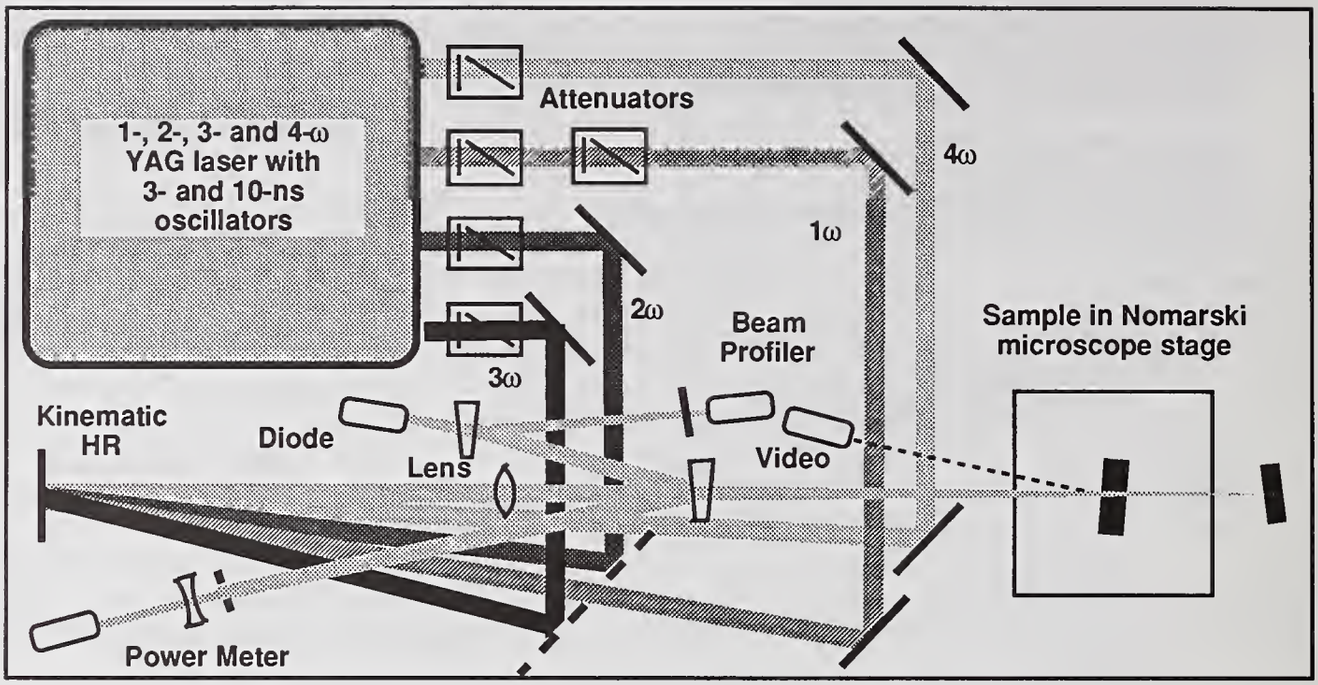

Figure 3. Chameleon employs one laser system with two oscillators to generate 3- and 10-ns pulses at the first four harmonics of Nd:YAG (1064 nm, 532 nm, 355 nm and 266 nm). The laser operates at 10 Hz and can generate peak fluences > 50 J/cm^2 with test-spot diameters > 1 mm at all four wavelengths.

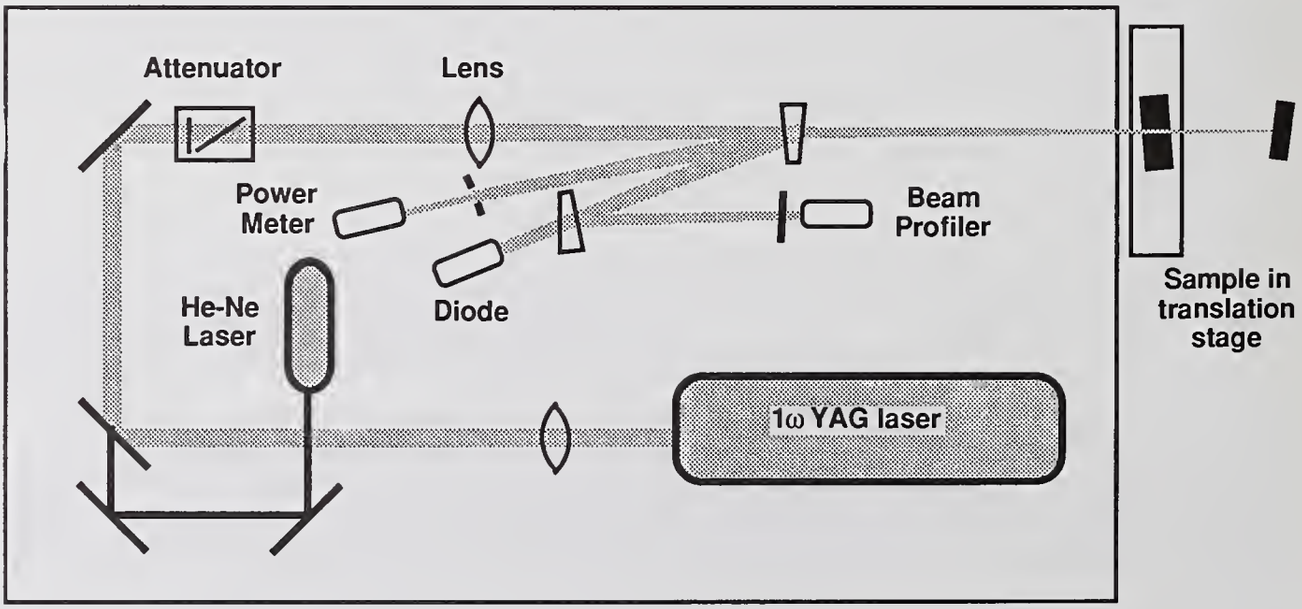

Figure 4. The Raster Blaster is a Nd:YAG laser facility which operates at 1064 nm with 8-ns pulses at 17.8 Hz. It is currently used to study laser conditioning of optical coatings.

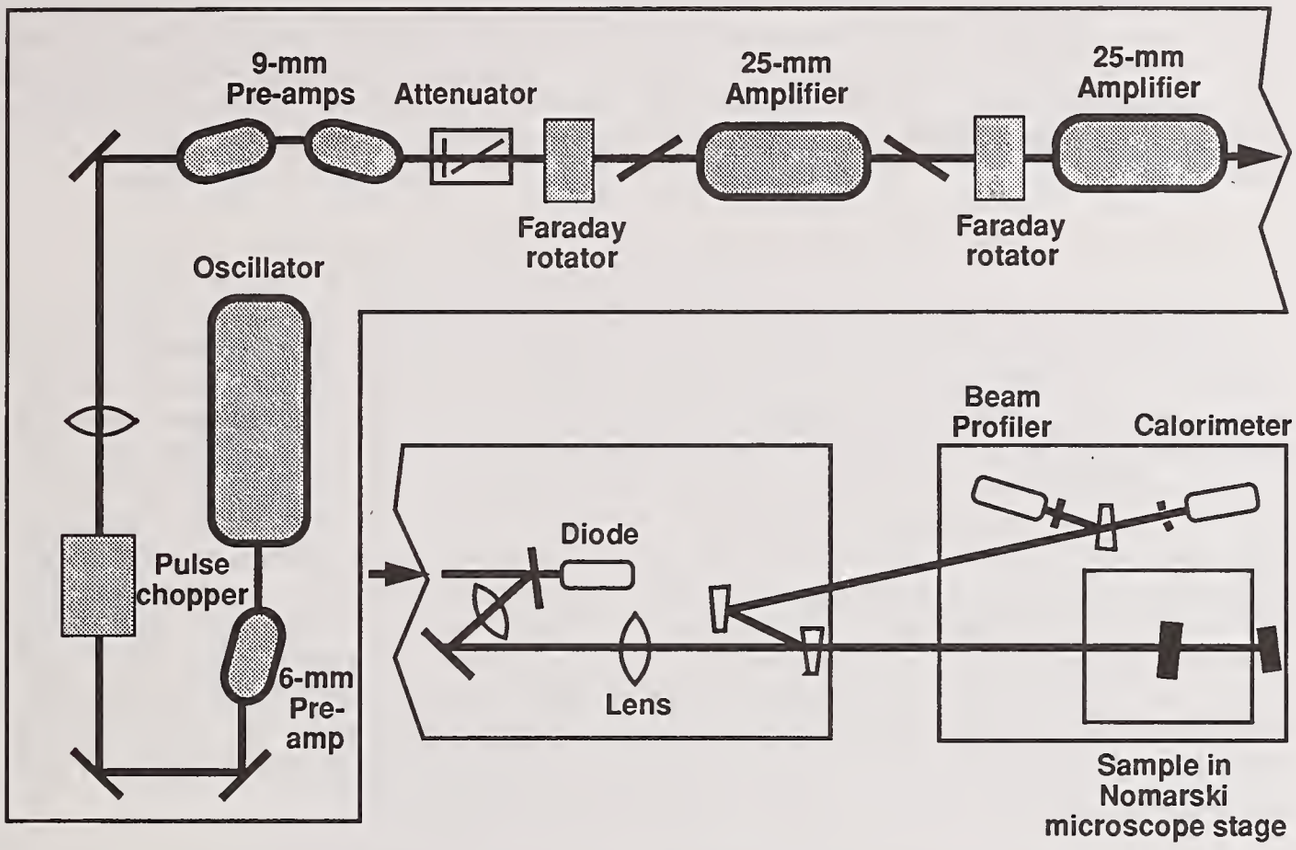

Figure 5. The Variable Pulse Laser (VPL) was a single shot Nd:YAG-glass laser system which was used for most of the earlier laser damage work conducted at LLNL. It could generate clean spatial profiles at pulse durations ranging from 1 to 100 ns. The facility was decommissioned at the end of 1989.

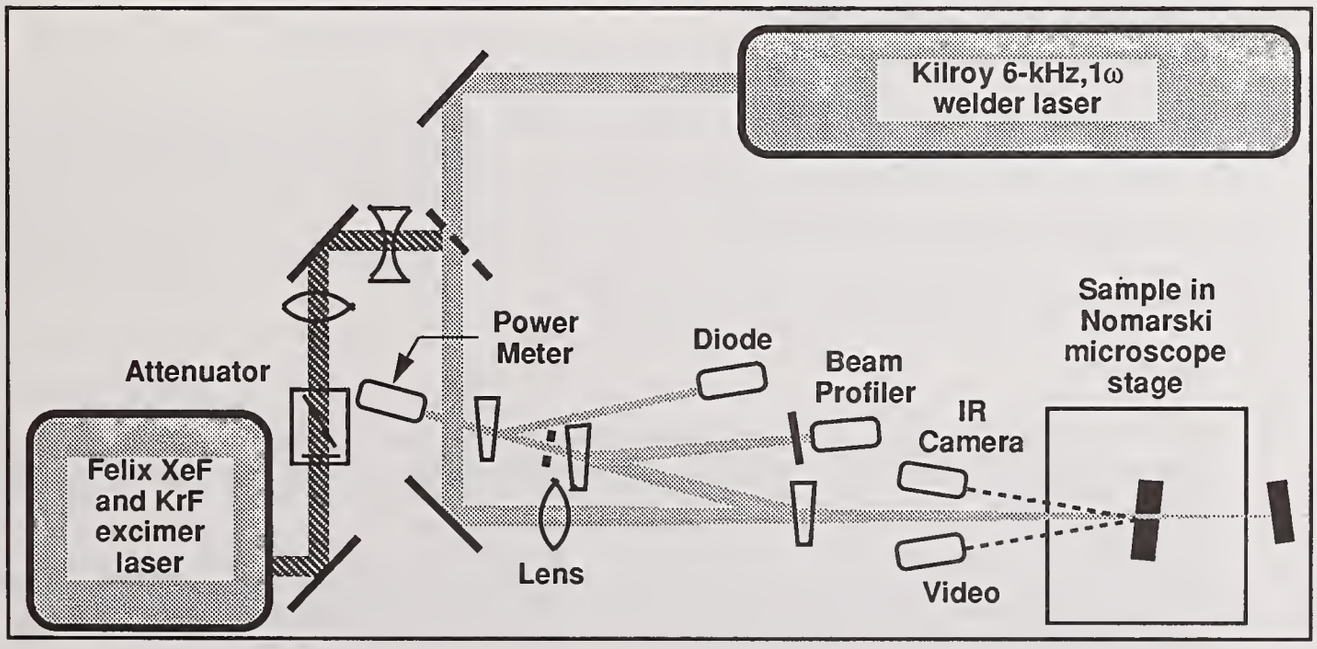

Figure 6. Kilroy is a Q-switched Nd:YAG laser used for high PRF damage and absorption measurements at 1064 nm. It can yield fluences up to 10 J/cm^2 with 65-ns pulses at 6 kHz. Felix is an excimer laser used for UV damage measurements at 351 or 248 nm. It can run at 100 Hz with 20-ns pulses.

driven Pockels' cell to yield pulses 1 to 50 ns in duration. Figure 5 shows the laser in its common configuration although we have at times also added a 50-mm amplifier for higher energies. Since the larger amplifiers were Nd:glass, we were restricted to operate at a rate of only one shot every 5 to 10 minutes to allow for sufficient cooling. Many of the components were more than 15 years old and required significant maintenance. The final damage tests on VPL were conducted in December 1989 and the facility was then decommissioned.

4.5 Kilroy

We constructed the Kilroy facility to extend the range of threshold data for 1064-nm pulses from a PRF of 120 Hz available from the Reptile faclity into the kilohertz regime. This high-PRF work was in support of LLNL's free electron laser (FEL) program. Rather than multiplexing many lasers together we opted to purchase a cw Nd:YAG welder laser with three heads. The laser cavity contains four acousto-optical Q-switches which can be synchronized to generate pulses at 500 Hz to 40 kHz. The pulse energy and pulse duration are a function of the rep-rate. We standardized on 6 kHz as being closest to meeting programmatic objectives. Figure 6 shows a schematic of the facility which is shared with the Felix excimer laser. Since Kilroy operates multi-mode we find it necessary to up-collimate the beam by a factor of ten in order to be able to ultimately focus it down to usable spot sizes ranging from 0.3 to 1 mm. We can achieve peak fluences up to 10 J/cm² with the smallest spot sizes. The pulse duration is highly modulated and at this PRF has an envelope width of 65 ns full-width half-maximum (FWHM). In order to measure peak fluences at the sample plane we need to gate out most of the pulses going to the beam profiler with a rotating aperture disk. The disk, beam profiler and laser are synchronized to sample 1% of the pulses at a rep-rate of 60 Hz. When operated as a cw laser Kilroy can be used as an effective tool in measuring absorption of optical components at 1064 nm.

4.6 Felix

The Felix laser is a successor to several excimer systems that we have utilized at LLNL to study laser damage phenomena in the UV regime. The laser can readily be switched from XeF to KrF operation which allow us to conduct damage tests at 351 and 248 nm respectively. We operate the laser at 100 Hz and can achieve peak fluences exceeding 30 J/cm2 with 20-ns pulses. The laser shares the facility with Kilroy and is shown schematically in figure 6.

5. Conclusions

We have nine separate lasers in five facilities at LLNL for conducting measurements of laser-induced damage to optical materials. These systems cover the spectrum from 1064 nm to 248 nm, at pulse durations ranging from 1 to 100 ns, and at PRF's ranging from single shots up to 6 kHz. The facilities support the efforts of the Inertial Confinement Fusion (ICF) and Advanced Application programs at LLNL for the purpose of continuing with our efforts to develop damage resistant optical materials for both existing facilities and those being designed for future use.

6. References

[1] Swain, J.E.; Stokowski, S.E.; Rainer, F.; Milam, D. Improving the bulk laser damage resistance of potassium dihydrogen phosphate crystals by pulsed laser irradiation. Appl. Phys. Lett. 40(4): 350-352; 1982 February 15.

[2] Kozlowski, M.R.; Staggs, M.C.; Wolfe, C.R.; Campbell, J.H. Large area laser preconditioning of dielectric thin film mirrors. Nat. Inst. Stand. & Tech. (U.S.) Spec. Publ.; (Laser Induced Damage in Optical Materials: 1989) - to be published.

[3] Wolfe, C.R.; Kozlowski, M.R.; Campbell, J.H.; Rainer, F.; Morgan, A.J.; Gonzales, R.P. Laser pre-conditioning of optical thin films. Nat. Inst. Stand. & Tech. (U.S.) Spec. Publ.; (Laser Induced Damage in Optical Materials: 1989) - to be published.

[4] Milam, D. Laser-induced damage at 1064 nm, 125 psec. Appl. Opt. 16(5): 1204-1213; 1977 May.

[5] Milam, D. Fluence in 1064-nm laser beams: its determination by photography with Polaroid film. Appl. Opt. 20(2): 169-171; 1981 January 15.

[6] Smith, W.L.; DeGroot, A.J.; Weber, M.J. Silicon vidicon system for measuring laser intensity profiles. Appl. Opt. 17(24): 3938-3944; 1978 December 15.

[7] Hildum, E. A.; Rainer, F.; Milam, D. A new average-power damage test facility at LLNL. Nat. Inst. Stand. & Tech. (U.S.) Spec. Publ. 756; 1987 October. 123 p.

[8] Forrest, G.T. Pulsed YAG emits four wavelengths. Laser Focus World: 27; 1990 January.

[9] Weinzapfel, C.L.; Greiner, G.J.; Walmer, C.D.; Hayden, J.S.; Komiya, K.; Kitayama, T. Large scale damage testing in a production environment. Nat. Inst. Stand. & Tech. (U.S.) Spec. Publ. 756; 1987 October. 112 p.

COMMENTS

Question: I appreciate what you are saying about mechanical properties that interface with chemical stability and the effects that they have on optical properties. What can you say about the thermal characteristics that cross those boundaries, particularly the thermal impedance and the heat flow.

Answer: One of the points that one must begin by talking about is that you've got to look at each particular layer separately. In fact using our MBE method we do get very enhanced lattice ordering. What you notice is that these layers are in fact crystalline. Therefore you are getting a true thermal conductivity in each of those particular layers. Now if we are getting reasonably good growth onto each layer, i.e., we have a good interface without to much dirt there, then we ought to be getting reasonably good thermal conductivity at that point also. We know at this point (and in fact a topic that I raised at Boulder about 2 years back), that we did in fact perform laser damage measurements on a complex digital structure of that type and compared it with what happened if we just mixed it and they were both equal. So it looks as though one does have the sort of basic thermal properties.

Question: Did you have an explanation of why the upper layers always separated in that one electron microgram from the lower layer?

Answer: It looks as though when you grow a II-VI compound on top of, in fact, anything, be it glass or be it anything else you've got, you've got S2 dimers which go down on to that particular interface. These have to move around to meet. Your S2 dimer then has to actually split up. That chemical process is different for that particular interface than it is where you have BaF_2 molecules as a whole going down. I think it is because of the basic difference in the way that the two species nucleate that's the cause of the separation.

Manuscript received
4-11-90

Laser Damage Database at 1064 nm*

F. Rainer, R. P. Gonzales, and A. J. Morgan
Lawrence Livermore National Laboratory
P.O. Box 5508, L-490
Livermore, CA 94550

In conjunction with our diversification of laser damage testing capabilities (see "Expanded Damage Test Facilities at LLNL" this conference), we have expanded upon a database of threshold measurements and parameter variations at 1064 nm. This includes all tests at low pulse-repetition frequencies (PRF) ranging from single shots to 120 Hz. These tests were conducted on the Reptile laser facility since 1987 and the Variable Pulse Laser (VPL) facility since 1988. Pulse durations ranged from 1 to 16 ns. The table below summarizes the test data scaled to 10-ns pulses.

Sample type	Number of tests	Damage thresholds (J/cm^2) scaled to 10 ns at 1064 nm		
		Min.	Average	Max.
AR coatings	164	0.8	19	> 56
HR coatings	283	0.7	18	56
Polarizers	47	0.8	8	41
Layers (1 or more, 1 material)	169	0.7	12	34
Metals (bare & enhanced)	49	0.4	6	40
Bare surfaces	226	1.6	26	61
Bulk material	175	0.8	21	61

Key words: anti-reflective (AR) coatings; bare substrates; bulk damage; damage; highly reflective (HR) coatings; laser-induced damage; metallic coatings; polarizers; reflectors; sol-gel coatings; thin films.

1. Introduction

For over fifteen years, the Lawrence Livermore National Laboratory (LLNL) has been actively involved in the development of damage-resistant optical coatings and materials and in the measurement of their laser-induced damage thresholds. In the course of that time we have conducted over 10,000 damage measurements, the results of which have been reported extensively at proceedings of the Boulder Damage Symposium as well as in technical journals. Typically, these reports have concentrated on a specific topic with data culled from a large database. In recent years more extensive publication of general databases have been made available in order to provide an overview of damage measurements covering a wide variety of materials, fabricated by numerous vendors, utilizing many different fabrication processes, and tested under countless different laser-parameter conditions. [1], [2]

* Work performed under the auspices of the U. S. Department of Energy by Lawrence Livermore National Laboratory under Contract No. W-7405-ENG-48.

This variety lends itself to the usefulness of a computer-based database but at the same time sets certain limitations to the user. In general there are often more caveats that must be appended to laser damage measurements than are practical within a tabular database. Hence, results of specific experiments are reported and elaborated on in journals and proceedings based on a compilation of data. The database will not of itself allow one to simply select the best optical component meeting a particular requirement without adherence to many of these hidden caveats. Moreover, the proprietary nature of much of the work by commercial vendors often prevents a total dissemination of the necessary information required in order to design or select a particular optical component.

2. Database parameters and conventions

Because of these limitations, the data we present here provide, to a first degree, only an index of measurements that have been conducted at LLNL during the past two or more years. The database is being enlarged on a daily basis as measurements are currently being conducted as well as relevant past measurements are added as time and program demands require. It must be strongly emphasized that these measurements do not necessarily represent the state-of-the-art nor necessarily a cross-section of what is achievable in terms of damage thresholds for a particular type of optical component. In virtually all cases, the data show a high preponderance of thresholds grouped near the lower end of the threshold range. Since the database does in fact list all measurements within a particular category, many of the research samples will naturally show poor performance. Not even the median thresholds should be construed as representing what one should expect within a particular category. Once we, or the vendors under contract to us, have developed a product that has achieved acceptably high damage thresholds we typically conduct sufficient tests to verify that the results are repeatable. Highlights of measurements taken at LLNL in support of high-peak-power lasers are presented in the companion paper at these proceedings. [3]

Comparing measurements taken under a variety of laser parameter conditions is difficult unless one takes into consideration the effects that the parameters and irradiation conditions may have on damage thresholds. The data presented here consist solely of recent measurements conducted at 1064 nm with pulse durations ranging from 1 to 16 ns. The data are always listed with the pulse durations used in the tests. Nearly all samples we have tested show a pulse-length scaling of between 0.2 and 0.5. In order to provide some capability of comparing these data we have also scaled the thresholds to 10-ns values by a value of 0.35 which is nominally the average temporal scaling factor according to the following relationship:

$$\text{Damage threshold} = k\,(\text{pulse duration})^{0.35}.$$

In table 1 we list the typical test-laser parameters which are based on laser capabilities and experimental requirements. Descriptions of the laser systems are presented in a companion paper at these proceedings. [4] Besides absolute damage threshold and laser parameters we also note the the type of irradiation and damage morphology at each site location as detailed in table 2.

Table 1. Laser parameters recorded with damage measurements

Pulse duration (ns)	1 - 65 depending on laser
Wavelength (nm)	1064, 532, 355, 351, 266, 248
PRF (Hz)	0 (single shot), 1, 6, 10, 15, 18, 30, 60, 100, 120, 6000
Polarization	Typically P; also S or mixed
Incident angle	0° to grazing; typically 10°, 45°, 57°
Spot diameter (1/e ^{2}) (mm)	0.3 - 3 depending on required fluence; typically about 1

An abbreviated sample of the computer database is shown in the appendix in table 3. Each test result is usually printed on one line of a large table in a reduced type format. To display this sample database in a readable fashion we have broken it up into four segments. In tables 4a and 4b we provide detailed information to the user about the variety of samples, techniques and vendors that have already been included in

Table 2. Sample irradiation conditions and observations

Site location	Front or incident surface Rear or exit surface Bulk material within the first 10 mm	
Irradiation per site	1-on-1	1 shot only
	N-on-1	N shots with increasing fluence, usually on a single shot basis
	S-on-1	S shots in PRF mode at the same fluence
	R-on-1	R shots in PRF mode ramped from near zero to the desired maximum fluence
	Scan	Sample moved through a PRF beam
Damage morphology	Description of damage at threshold at each applicable location (front, rear, bulk) Comparable morphology typically at fluences exceeding threshold to characterize damage growth	

the current database. We also supply information on how to interpret the data.

3. Overview of testing at 1064 nm

During the past two years we have have conducted over 1300 laser damage measurements, mostly at 1064 nm with 1- to 16-ns pulses at pulse repetition frequencies (PRF's) ranging from single shots up to 120.

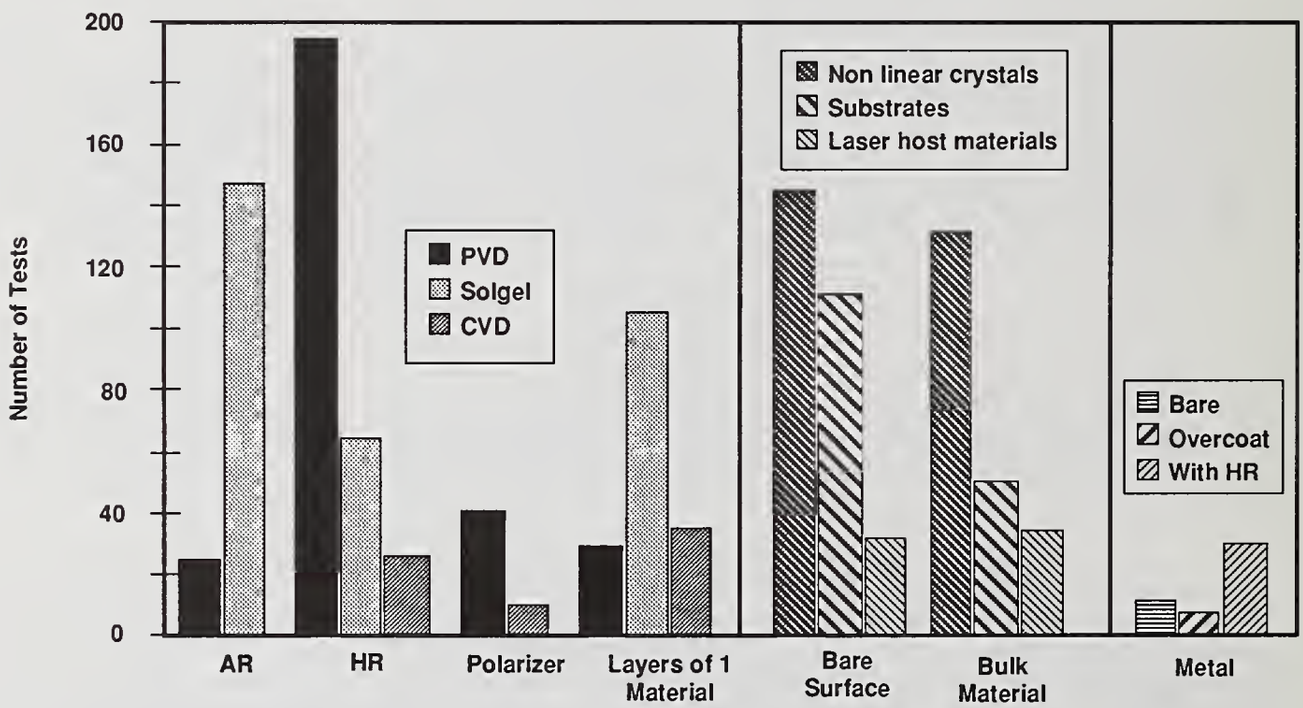

Figure 1. Two-year summary of laser damage tests at 1064 nm with 1- to 16-ns pulses.

An overview of these tests is shown in figure 1.

The major portion of our efforts have been concentrated on the development of high threshold sol-gel coatings (AR's, HR's and single layers), HR's fabricated by physical vapor deposition (PVD), and optically polished bare surfaces and bulk materials of non-linear crystals and substrate materials. We list below summaries of our tests conducted on seven broad categories of optical materials. For each category we show a general histogram of all laser damage tests conducted at 1064 nm with pulse durations scaled to 10 ns. Depending on the category type we also list applicable details such as substrate materials, coating

materials, process types, and vendors of coatings, bulk materials and surface processing. Since these tests cover such a wide variety of optical components, material combinations, processes and proprietary data, we do not itemize these details in most histograms. Related figures for each category show pertinent important highlights that are germane to the programmatic laser development efforts at LLNL.

4.1 Bare polished surfaces

We record bare surface damage thresholds of most substrate materials that we test for bulk damage as well as for samples which may have an AR coating on one surface but not the other. We observe rear surface damage if the results are not obscured by either front surface or bulk material damage. Typically well-polished bare surfaces have among the highest thresholds that we measure and are usually only exceeded by bulk damage to some materials. In figure 2 we show the aggregate test results of all bare surface measurements in recent years for over 20 different substrate types from over 20 different vendors. The vendor supplying the substrate was, however, not always the one who actually performed the surface processing. Most samples were lap polished but we also list the other surfacing techniques that we have investigated.

We have found that for several of the more commonly used substrate materials with refractive indices near 1.5, the optimized polishing techniques have yielded 1064-nm damage thresholds which scale relatively independent of the material types by a pulse-duration scaling factor of $\tau^{0.4}$. This is demonstrated in figure 3 for six materials (fused silica, BK-7, CVD glass, ULE glass, LG-750, and fluorophosphate glass) at seven different pulse durations ranging from 150 ps up to 40 ns. These measurements are average values of the best results obtained over a span of more than 12 years from at least six different laser systems.

4.2 Bulk materials

In figure 4 we summarize the measurements we have conducted on over twenty different types of bulk materials including non-linear crystals, laser host materials and substrates. Many of the entries at the higher fluence ranges actually represent lower limits of the thresholds. This was either because we ceased irradiation when massive damage occurred to the bare or coated surfaces or because we could not extract higher fluences from the laser. Our laser irradiation in the bulk material is conducted with a gently focusing beam using 2.5- to 5-m focal length lenses. We typically limit ourselves to a test volume over which the beam fluence changes $\leq 1\%$. We also find it useful to work within a depth of field which can be readily examined by Nomarski microscopy. Finally, within the constraints of the available laser fluence, we attempt to utilize as large a cross-section beam as possible. By this means we determine the threshold of a macroscopic volume of material with potential microscopic defects rather than the intrinsic threshold of a defect-free material. We irradiate with beams on the order of 1-mm diameter for a depth not exceeding 10 mm.

Of particular interest to us at LLNL is the improvement in damage thresholds of frequency conversion crystals to levels approaching those of substrate materials such as fused silica. We have pursued the development of a variety of high threshold materials such as deuterated and undeuterated potassium-dihydrogen phosphate (KDP) and ℓ-arginine phosphate (LAP). In 1981 we reported increases in bulk thresholds of KDP crystals by pre-irradiation of the material with a succession of sub-threshold laser shots. [5] This laser conditioning has been reported at these proceedings for several years both for non-linear crystals and optical coatings. Typical results of continued improvement are shown on the right half of figure 5.

4.3 High reflective (HR) coatings

Figure 6 summarizes the tests that we have conducted in recent years for a variety of HR coating techniques from 15 different vendors We list the assortment of materials used both for substrates and the coatings. All of the coatings consisted of muli-layer stacks of two or more materials. We list only the unique individual materials since the variety of material combinations is too numerous to elaborate upon. In this figure we combine the results of tests on single wavelength, multi-wavelength, and partially reflecting mirrors.

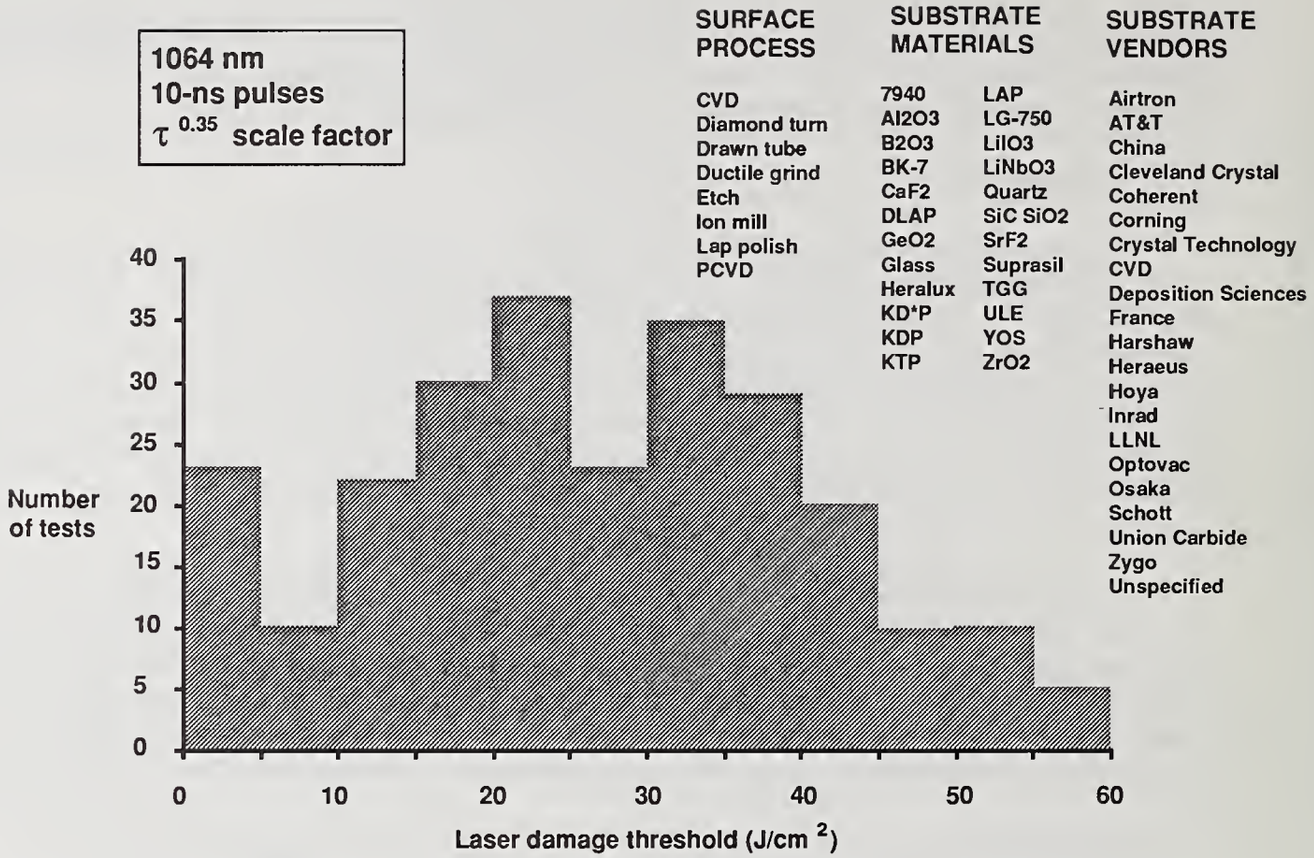

Figure 2. Summary of laser damage tests conducted on bare polished surfaces.

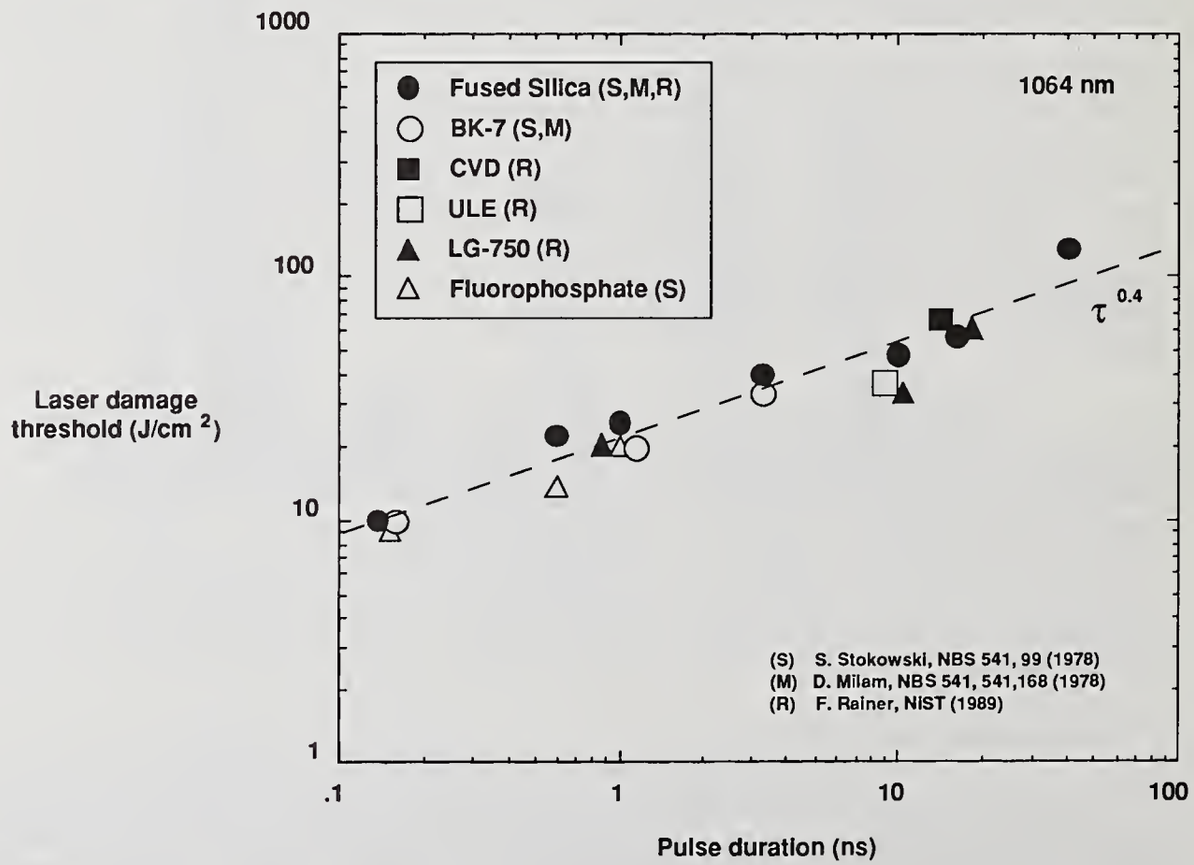

Figure 3. Damage thresholds of optimized polished surfaces scale as $\tau^{0.4}$ between 150 ps and 40 ns and are independent of glass type for a variety of common laser glasses having refractive indices near 1.5.

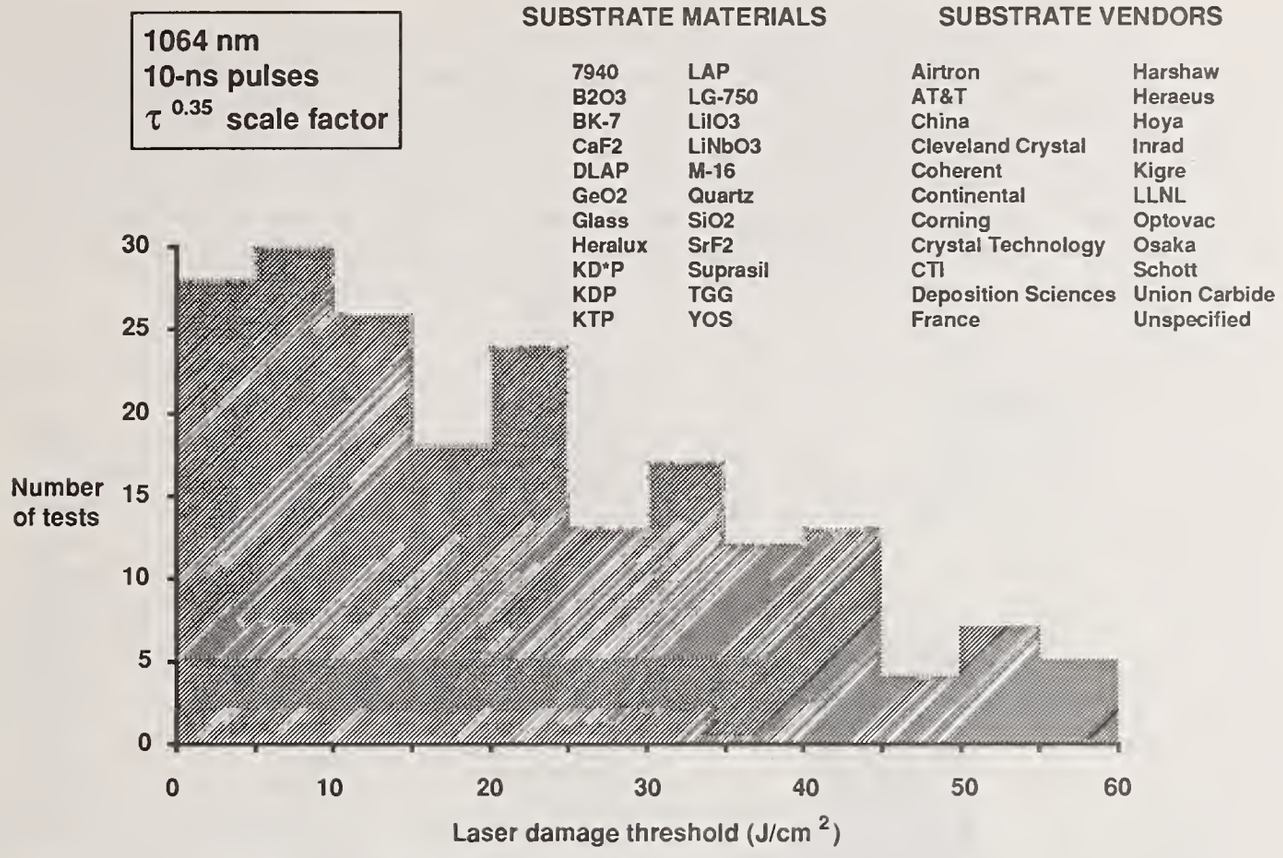

Figure 4. Summary of laser damage tests conducted on bulk materials.

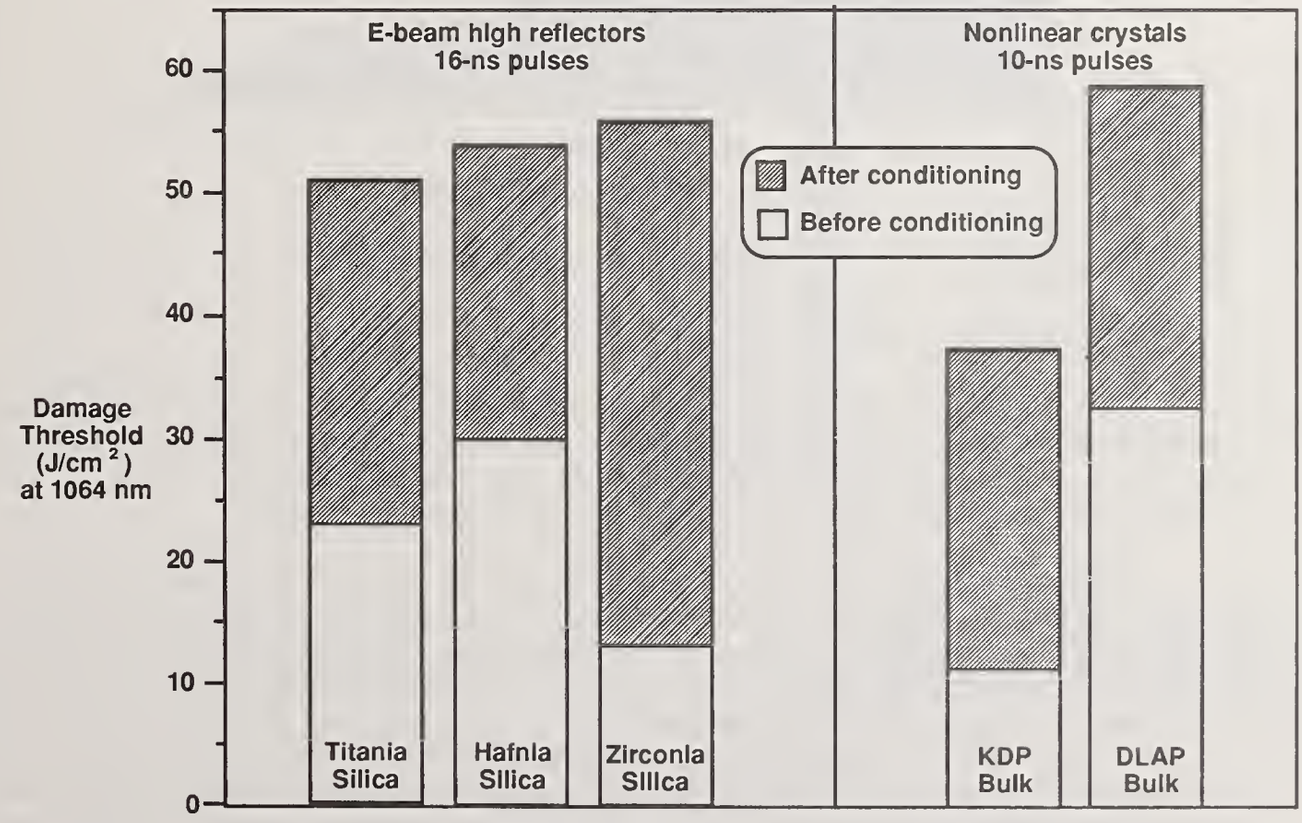

Figure 5. Pre-irradiation of PVD-fabricated HR coatings and non-linear crystals with sub-threshold laser pulses (conditioning) increases their damage thresholds above unconditioned thresholds.

We are investigating three major options for improved damage thresholds in HR coatings. These include laser-conditioned PVD coatings, sol-gel coatings, and plasma assisted chemical-vapor-deposition (PCVD) coatings. The latter two techniques and their results are reported upon in companion papers at this conference. [6], [7], [8] Examples of typical improvements in damage thresholds by laser conditioning to PVD HR coatings are shown on the left side of figure 5. Improvement usually has been found to range from 1.5 times to greater than 3 times unconditioned thresholds. We have found that the degree of improvement was often dependent upon the number and sequence of sub-threshold irradiation shots. Once conditioned the samples were found to retain their elevated thresholds permanently. [9], [10]

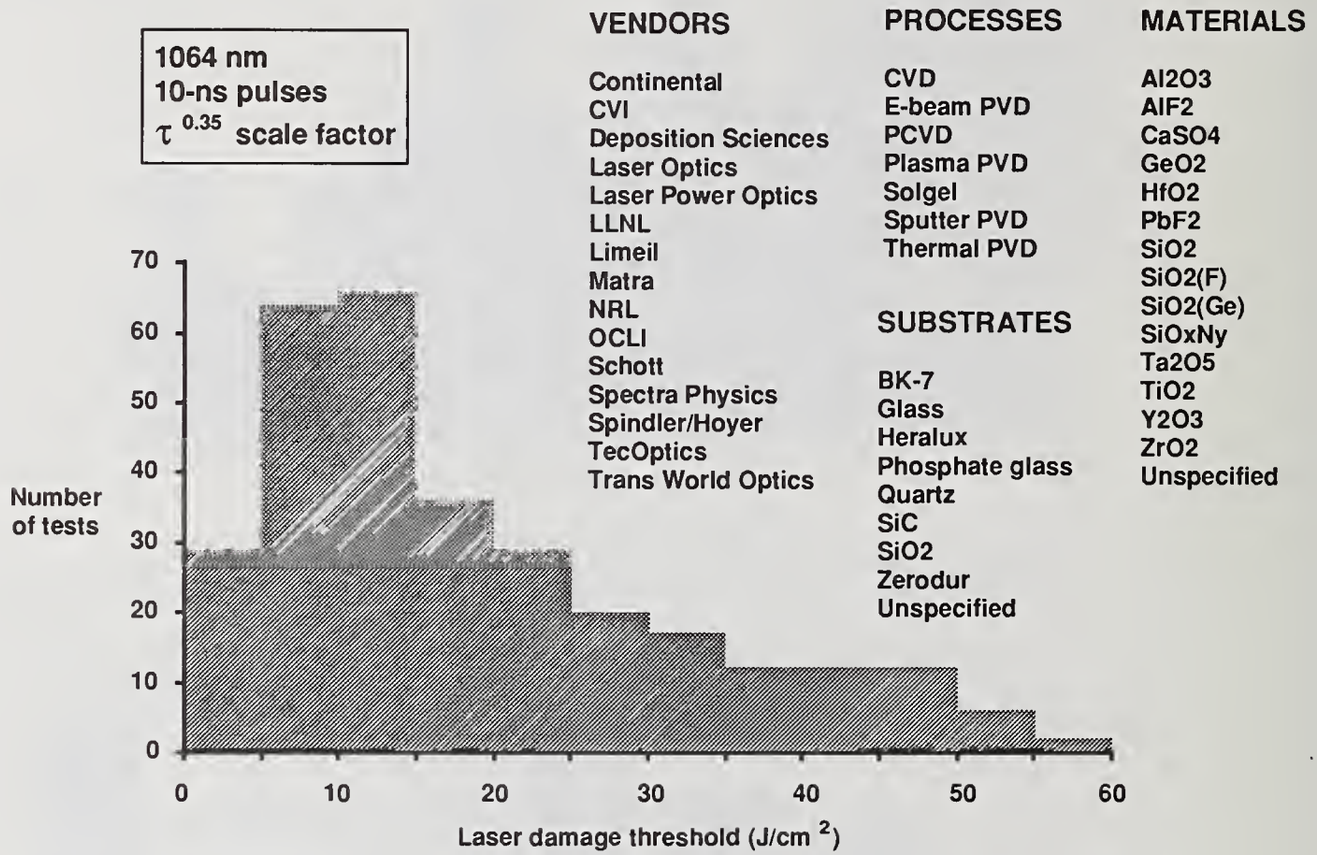

Figure 6. Summary of laser damage tests conducted on HR coatings.

4.4 Anti-reflective (AR) coatings

Figure 7 summarizes the extent of our recent AR coating testing. The bulk of this represented testing of research samples both for LLNL as well as outside vendors. Hence, many of the early results are concentrated at the lower threshold range. As with the case of the HR coatings we list both the variety of substrate and coating materials but do not elaborate on all of their combinations.

The major emphasis in this category has come from the development and implementation of the sol-gel process to produce damage-resistant AR coatings for fused silica substrates and lenses ranging up to 1-meter diameter and for large area arrays of KDP crystals for frequency conversion. Both of these applications have been extensively implemented on LLNL's Nova laser system. The extent of improvement in this technology in just the last few years is demonstrated in figure 8. The shaded portions of these histograms show all high threshold test results conducted in 1989 versus the best results (unshaded) obtained for the previous year. Blocks of tests with an arrow in them indicate that the sample thresholds were at least as great as the levels shown in the figure. Few tests were conducted at 355 nm since that testing capability had just been recently brought on line. Production of sol-gel AR coatings has become routine and reliable enough so that very little future testing of them is anticipated.

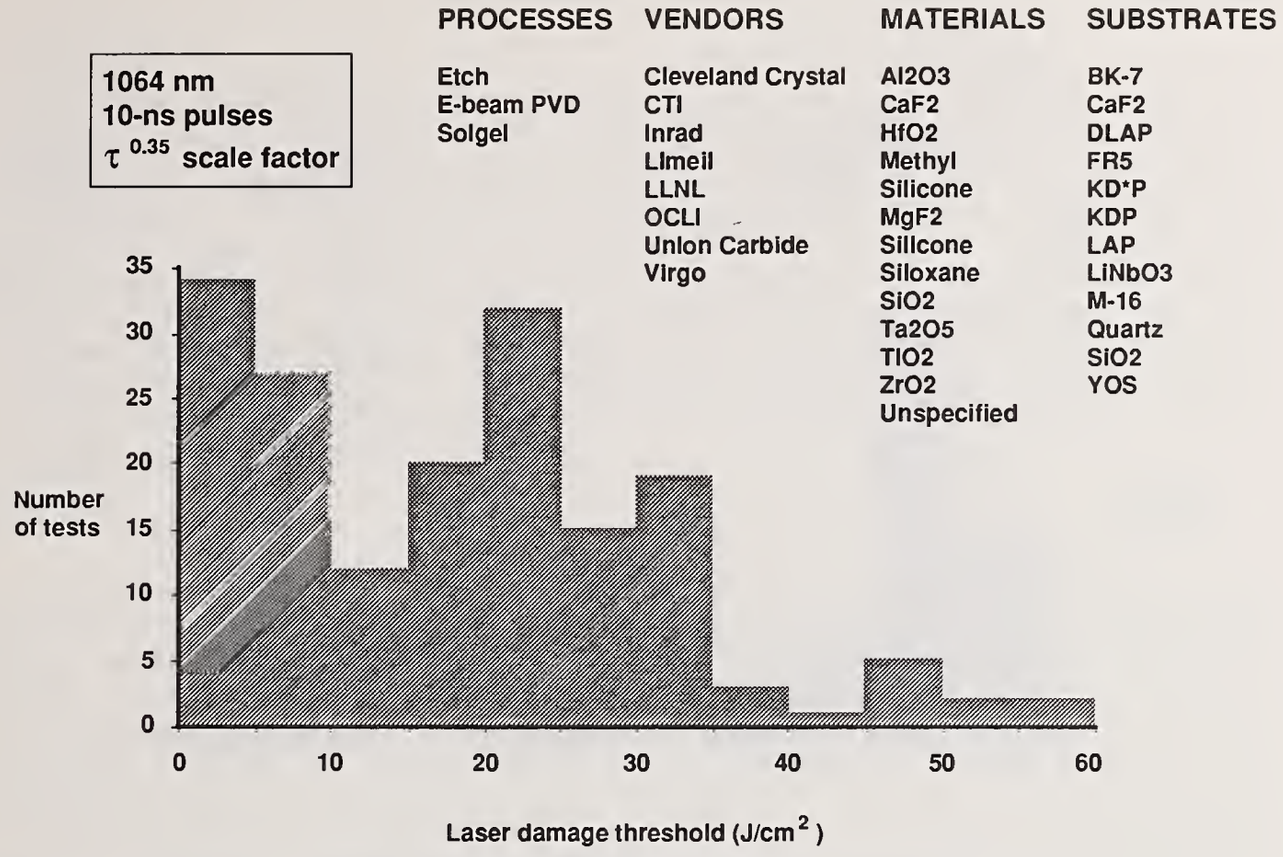

Figure 7. Summary of laser damage tests conducted on AR coatings.

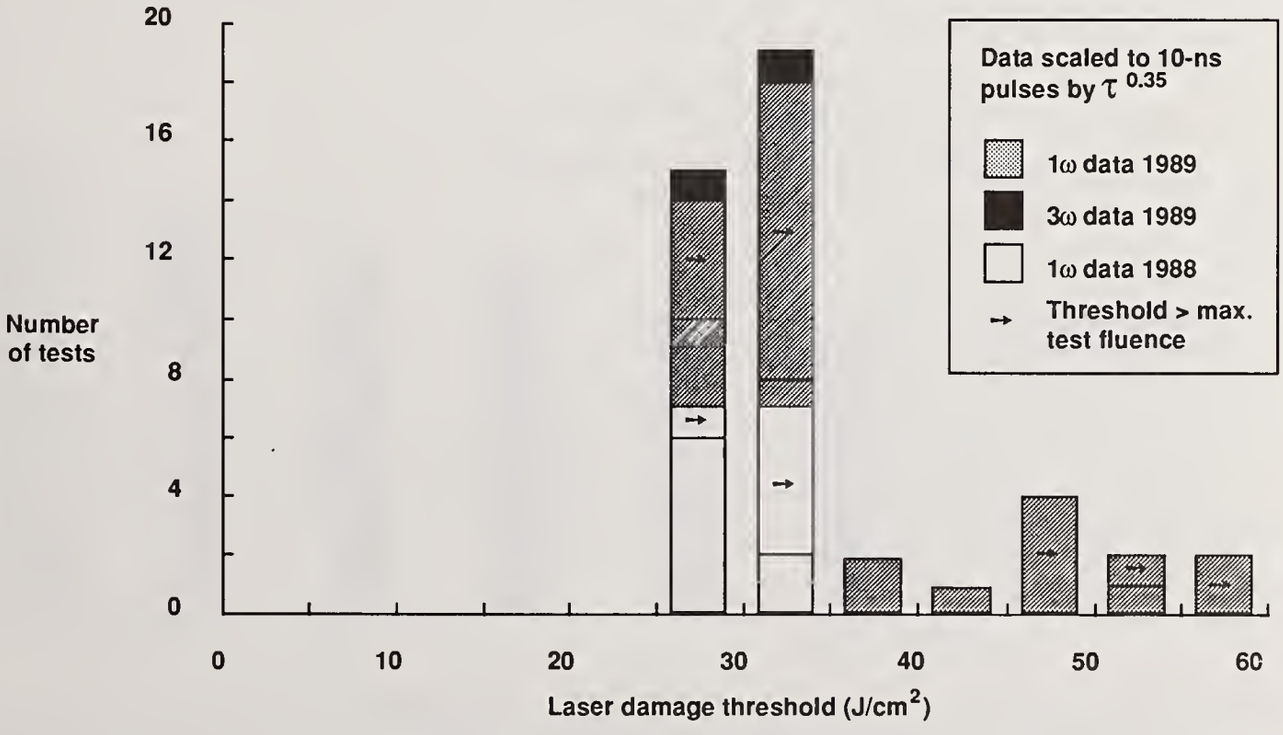

Figure 8. We have made significant improvements in laser damage thresholds of the best sol-gel AR coatings measured during the past year compared to those of the previous year.

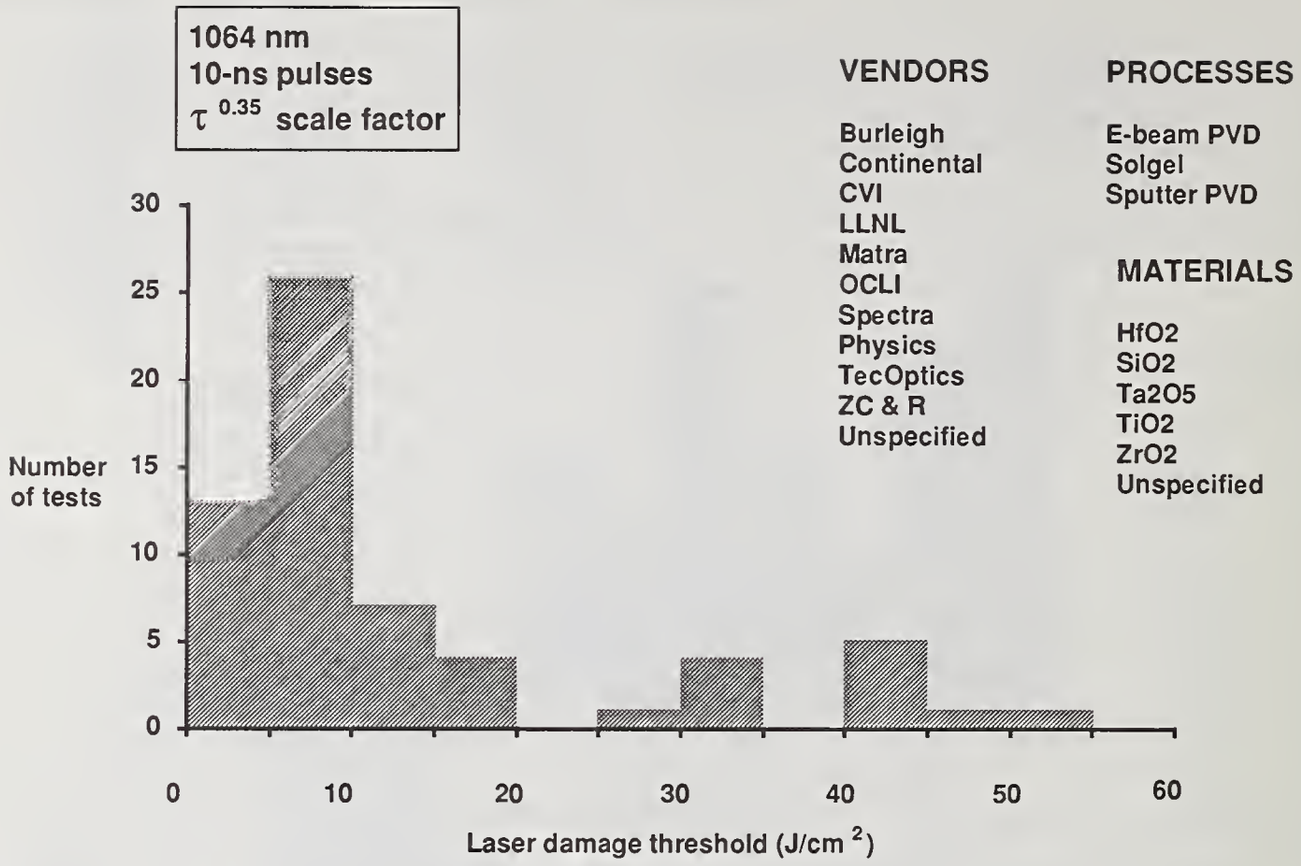

Figure 9. Summary of laser damage tests conducted on polarizers.

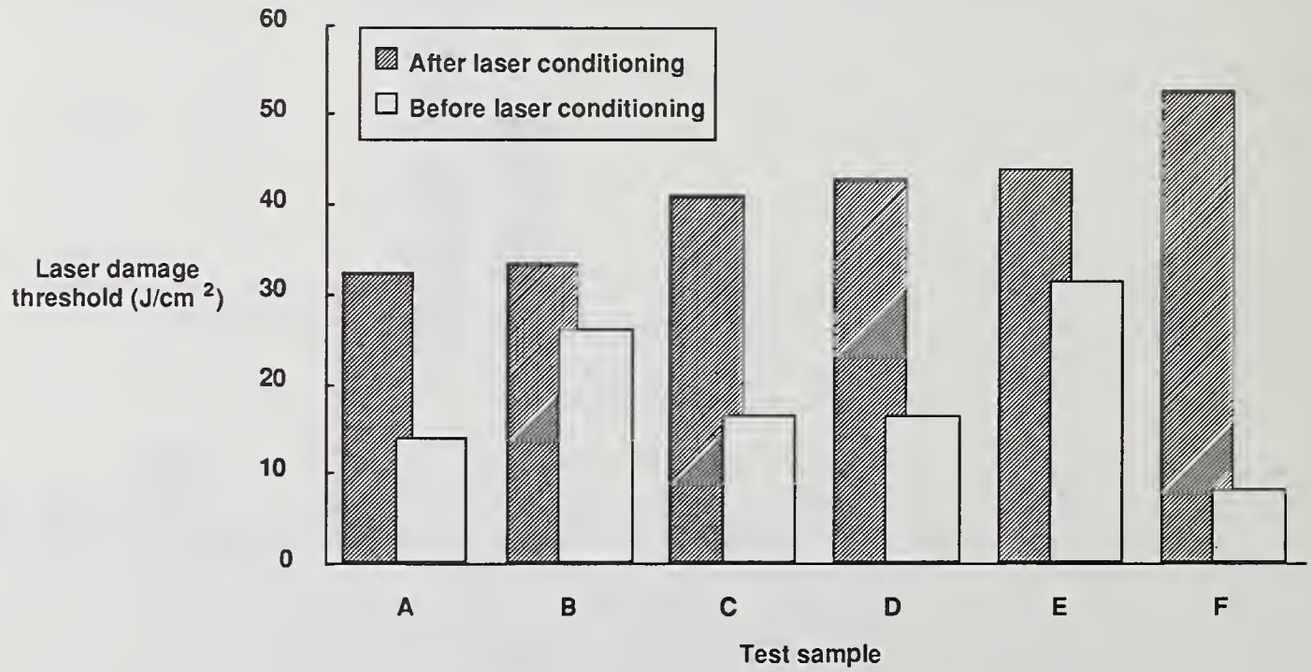

Figure10. Laser conditioning of commercial PVD-fabricated polarizers improves their damage thresholds by an average factor of two.

4.5 Polarizers

Multi-layer stack polarizers are typically fabricated with more complex coating designs using more layers than those used for comparable HR coatings. Unlike HR coatings, the coating-substrate interface of polarizers sees the full intensity of the transmitted laser beam. By their very nature, polarizers will also have greater angular sensitivity to each polarized component of the laser beam. These characteristics have usually combined to yield among the lowest thresholds for multi-layer coatings as is shown in figure 9. We have not conducted as many tests on polarizers in recent years as on AR and HR coatings but the distribution of thresholds at the lower fluence range of this figure is typical of polarizers. We have, however, recently also conducted conditioning tests on a variety of samples from several vendors. In figure 10 we show that, as with HR coatings, we can expect to find a significant improvement in thresholds by implementing laser-conditioning. From a limited database of conditioned polarizer tests we have observed average rises in thresholds of about a factor of two.

4.6 Single material coatings

Much of the research that we and many of our vendors have done in the development of multi-layer coatings began with testing of single layers or multiple layers of the same material by all of the standard deposition processes. In figure 11 we show the aggregate result of these tests on 25 different materials applied by PVD, CVD or sol-gel processes. These coatings were often half-wave thick layers at 1064 nm but not exclusively so. We list most of these materials specifically in figure 12 to illustrate the spread that one can expect in damage thresholds. One cannot specifically use these data in order to pick optimum material combinations for fabricating high-threshold multi-layer AR's, HR's or polarizers. This database represents a compilation of many research and development samples with a great variety of deposition parameters including process type, thickness, number of layers, cleanliness, substrate type, and deposition conditions.

4.7 Metal mirrors

Of all of the commonly used optical components in the laser industry, metal mirrors have consistently yielded the lowest damage thresholds. From a limited database we had reported thresholds no higher than 4 J/cm^2 for 16-ns pulses at 1064 nm. [1] The higher thresholds were usually obtained by enhancing the bare metal substrate or plated metal coating with a dielectric overcoat or a multi-layer dielectric HR stack. This produced a rise in threshold by a factor of two at best. A summary of those earlier tests and more recent tests shows a small database in figure 13. We have seen some minor improvement in bare metal thresholds but in general they still lie below 5 J/cm^2 at 1064 nm for 10-ns pulses. We attributed the failure of HR-overcoated metal mirrors to two factors. First of all, possible pinholes in the dielectric HR would allow energy to propagate through the HR stack to the metal itself. Secondly, defects on the metal could propagate corn growth on subsequent dielectric layers so that they do not behave as true HR's where the defects print through. With dielectric substrates any leaked energy through the HR stack would be dissipated by transmission through the substrate. A metal coating or substrate would, however, trap this leaked energy at this interface and cause catastrophic failure to the metal. Recent coatings that have been fabricated for us appear to have yielded superior dielectric HR stacks as is shown in figure 14. Although damage thresholds have improved for bare molybdenum substrates, print-through of defects from the substrates through the HR still caused thresholds to be low. However, when Mo coatings were plated on defect-free silicon or fused silica we found thresholds to equal those of the same HR's deposited on fused silica alone.

5. Conclusions

We have expanded upon our database of laser-damage tests at LLNL to include over 1300 tests conducted at 1064 nm in the last few years. This represents a small fraction of over 10,000 tests that we have conducted during the past 15 years. We have used a variety of laser systems to enable us to study the effects of spot size, pulse duration, PRF, polarization and incident angle. As time permits this database will be expanded to include relevant past data as well as all current testing. In addition, the database is currently being expanded to include tests at the second, third and fourth harmonic of 1064 nm.

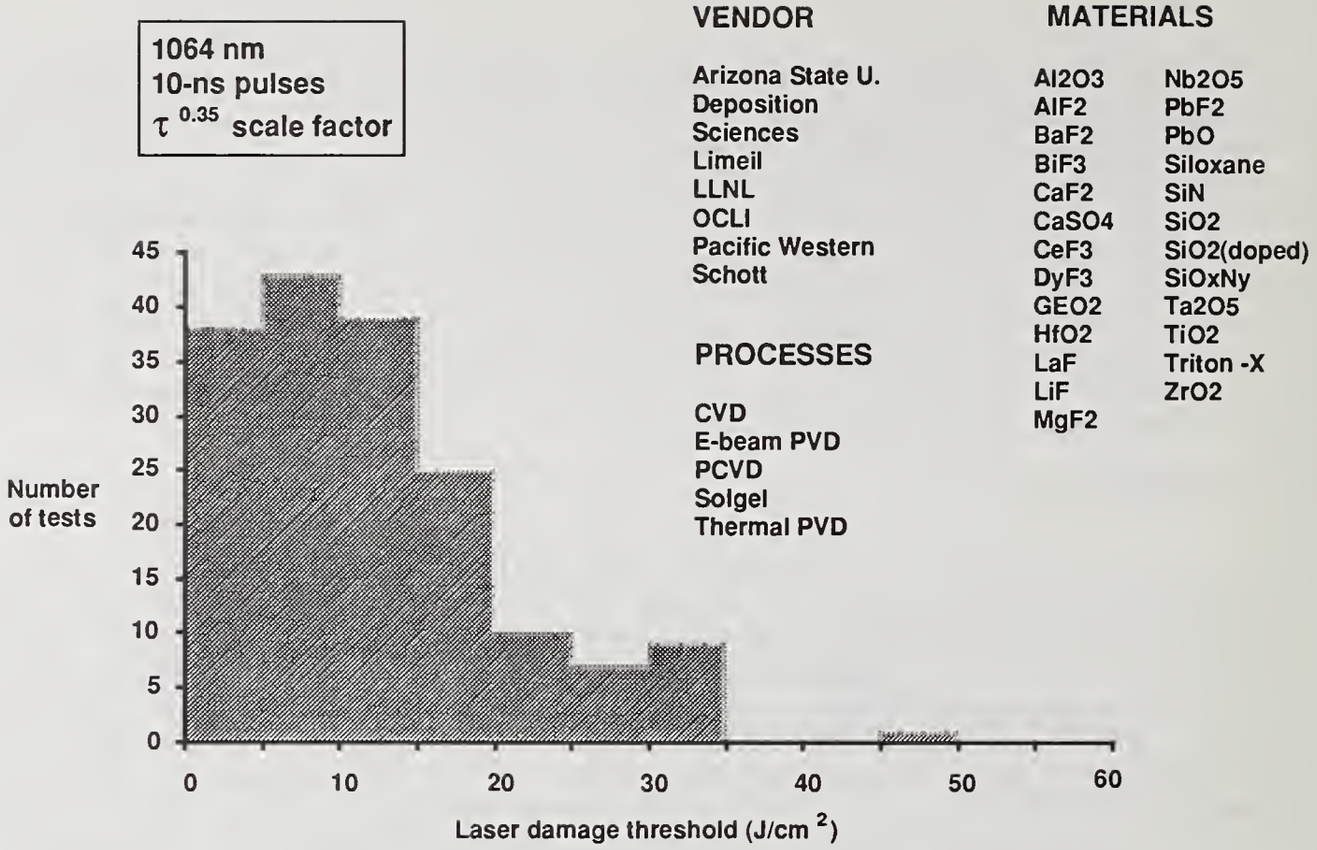

Figure 11. Summary of laser damage tests conducted on single or multiple layers of the same material.

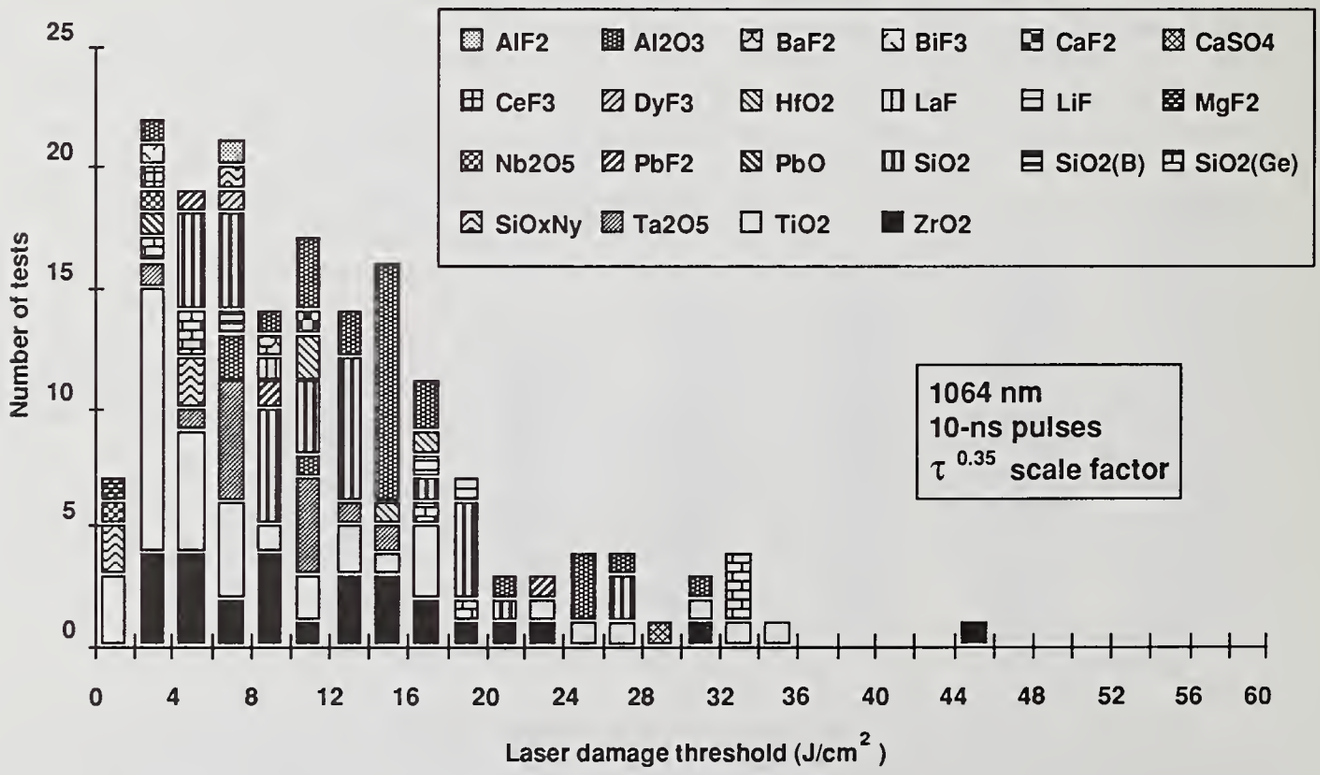

Figure12. Ranking of laser damage thresholds for a variety of single material coatings fabricated by PVD, CVD and sol-gel processes (except single-layer silica sol-gel AR's which are listed under the AR category).

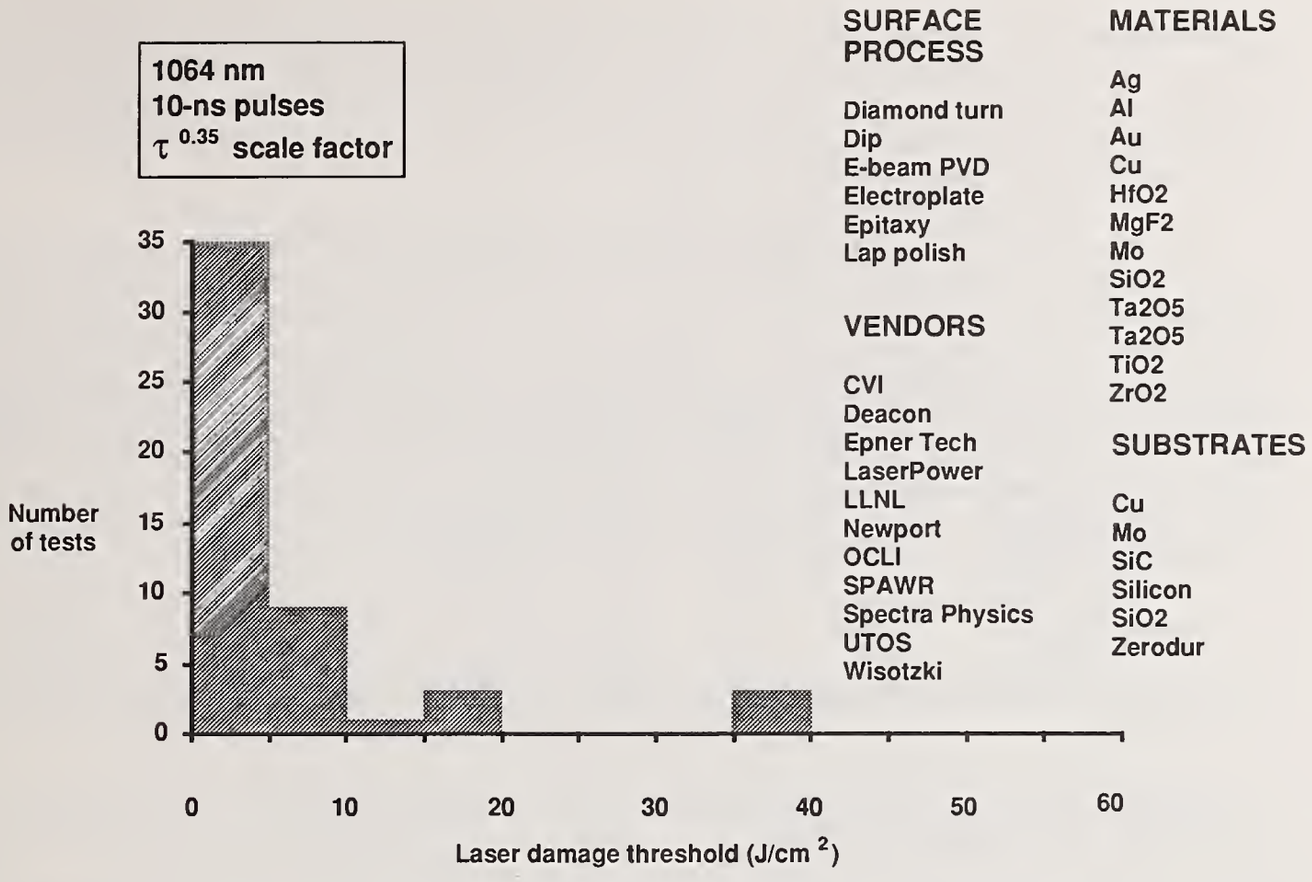

Figure 13. Summary of laser damage tests conducted on bare and enhanced metal mirrors.

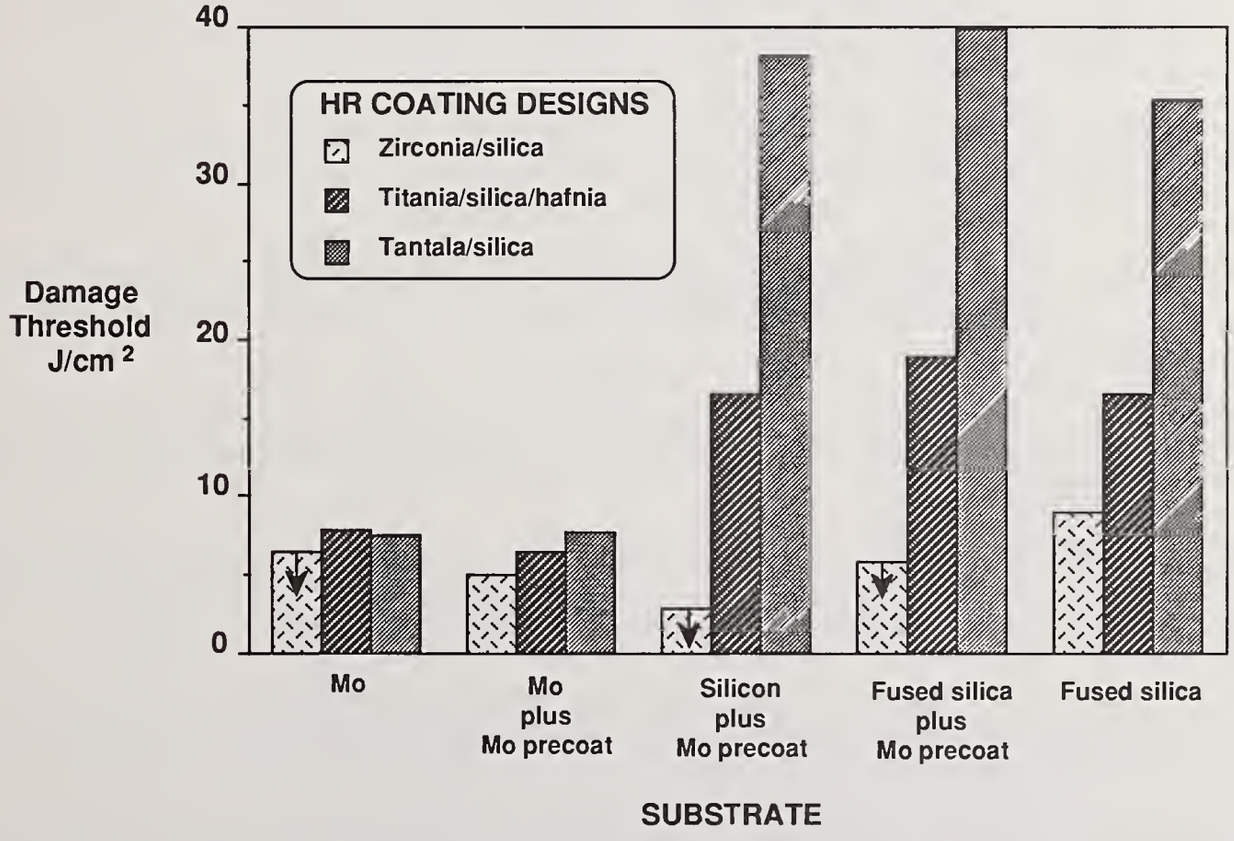

Figure14. Metal mirrors enhanced with pinhole-free dielectric HR stacks can have thresholds comparable to those of the stacks on dielectric substrates. The arrows indicate that the thresholds for those particular samples were less than the minimum test fluences shown.

We have broken our tests down into seven broad categories of optical samples including AR's, HR's, polarizers, single and multiple layers, metals, bare surfaces, and bulk material. We, or our vendors, have achieved 10-ns-normalized thresholds that reach or exceed 40 J/cm^2 in all of these categories . This has been accomplished by a variety of techniques worked on by LLNL and by our vendors including laser conditioning, sol-gel coatings and PCVD coatings.

The database provides us with an effective tool in being able to cull information from many test covering a large parameter space of sample fabrication and laser testing techniques. It is, to a first degree, an interactive computer tool rather than just a printed list of test data. To that extent it has a somewhat limited use when simply printed as a whole. The value of the database stems from our ability to be able to sort and search from a high volume of data. Unfortunately we are currently not at liberty to be able to publish a detailed database for general external use. To first order the database represents primarily research in optical component development by LLNL and its vendors. It does not guarantee to include all vendors and processes or even the best ones. At a later date we may be able to provide for distribution a cross-referenced database which approaches such a goal but which must of necessity be limited by proprietary information from our vendors.

6. References

[1] Rainer,F.; Hildum, E. A.; Milam, D. Database of average-power damage thresholds at 1064 nm. Nat. Inst. Stand. & Tech. (U.S.) Spec. Publ. 756; 1987 October. 410 p.

[2] Seitel, S.C. Laser damage test handbook and database of Nd:YAG laser optics. Bozeman, Montana: Montana Laser Optics, Inc.; 1988.

[3] Rainer, F.; Brusasco, R. M.; Campbell, J. H.; De Marco, F.P.; Gonzales, R.P.; Kozlowski, M.R.; Milanovich, F. P.; Morgan, A. J.; Scrivener, M. S.; Staggs, M. C.; Thomas, I. M.; Velsko, S. P.; Wolfe, C. R. Damage measurements on optical materials for use in high-peak-power lasers. Nat. Inst. Stand. & Tech. (U.S.) Spec. Publ.; (Laser Induced Damage in Optical Materials: 1989) - to be published.

[4] Morgan, A.J.; Rainer, F.; De Marco, F.P.; Gonzales, R.P.; Kozlowski, M.R.; Staggs, M.C. Expanded damage test facilities at LLNL. Nat. Inst. Stand. & Tech. (U.S.) Spec. Publ.; (Laser Induced Damage in Optical Materials: 1989) - to be published.

[5] Swain, J.E.; Stokowski, S.E.; Milam, D.; Rainer, F. Improving the bulk laser-damage resistance of KDP by baking and pulsed laser irradiation. Nat. Bur. Stand. (U.S.) Spec. Publ. 638; 1981 November. 119 p.

[6] Thomas, I.M. High damage threshold $Al_2O_3 \cdot H_3O\text{-}SiO_2$ HR coatings prepared by the sol-gel process. Nat. Inst. Stand. & Tech. (U.S.) Spec. Publ.; (Laser Induced Damage in Optical Materials: 1989) - to be published.

[7] Campbell, J.H; Emmett, J.L.; Brusasco, R.M.; Rainer, F. Deposition of damage resistant optical coatings using high temperature, plasma chemical-vapor-deposition. Nat. Inst. Stand. & Tech. (U.S.) Spec. Publ.; (Laser Induced Damage in Optical Materials: 1989) - to be published.

[8] Brusasco, R.M.; Britten, J.A.; Thorsness, C.B.; Scrivener, M.S.; Unites, W.G.; Campbell, J.H. A high-temperature, plasma-assisted chemical-vapor-deposition system. Nat. Inst. Stand. & Tech. (U.S.) Spec. Publ.; (Laser Induced Damage in Optical Materials: 1989) - to be published.

[9] Wolfe, C.R.; Kozlowski, M.R.; Campbell, J.H.; Rainer, F.; Morgan, A.J.; Gonzales, R.P. Laser pre-conditioning of optical thin films. Nat. Inst. Stand. & Tech. (U.S.) Spec. Publ.; (Laser Induced Damage in Optical Materials: 1989) - to be published.

[10] Kozlowski, M.R.; Staggs, M.C.; Wolfe, C.R.; Campbell, J.H. Large area laser preconditioning of

dielectric thin film mirrors. Nat. Inst. Stand. & Tech. (U.S.) Spec. Publ.; (Laser Induced Damage in Optical Materials: 1989) - to be published.

7. Appendix

Table 3. Sample of a computer-generated database table. The table has been broken into four parts to aid in presentation

1	2	3		4			
TEST #	& TEST Date	SAMPLE #	OTHER ID #	COATING (or Bare, or Bulk) Vendor	Type	Process	Materials
R 508 A	7/13/89	A279B	1-YOS-4#2	L-Thomas	AR 1	Solgel	AlO(OH)
R 508 B	7/13/89	A279B	1-YOS-4#2	L-Thomas	AR 1	Solgel	AlO(OH)
R 508 C	7/13/89	A279B	1-YOS-4#2	L-Thomas	BU LK	Solgel	AlO(OH)
R 508 D	7/13/89	A279B	1-YOS-4#2	L-Thomas	AR 1	Solgel	AlO(OH)
R 508 E	7/13/89	A279B	1-YOS-4#2	L-Thomas	AR 1	Solgel	AlO(OH)
R 508 F	7/13/89	A279B	1-YOS-4#2	L-Thomas	BU LK	Solgel	AlO(OH)

5					6					
SUBSTRATE Type	Source	Polish by	Process	LxW(or D)xT mm	LASER PARAMETERS nm	ns	Hz	pol	°	mm
YOS	Vendor	L-Prochnow	Lap	23dx7	1064	10	10	P	10	1.1
YOS	Vendor	L-Prochnow	Lap	23dx7	1064	10	10	P	10	1.1
YOS	Vendor	L-Prochnow	Lap	23dx7	1064	10	10	P	10	1.1
YOS	Vendor	L-Prochnow	Lap	23dx7	1064	10	10	P	10	1.1
YOS	Vendor	L-Prochnow	Lap	23dx7	1064	10	10	P	10	1.1
YOS	Vendor	L-Prochnow	Lap	23dx7	1064	10	10	P	10	1.1

7		8							9		10
THRESHOLD Loc	J/cm2	MORPH.(thresh />thresh) M	μ	#	M	μ	#	@	Shots/Site Meth.	#	REPORTS
F	38.2 ±5.7	M	999	1					S/1	30	LDG89-117
R >	20.9	M	999	1	M	999	1	34	S/1	600	LDG89-117
B	17.9 ±2.7	A	?	2	M	999	1	21	S/1	600	LDG89-117
F	43.1 ±6.5	A	5	1	N			47	R/1	600	LDG89-117
R >	47.1	N			N			47	R/1	600	LDG89-117
B	43.6 ±6.5	A	?	2	A	?	1	47	R/1	600	LDG89-117

11	12
SAMPLE DESCRIPTION & COMMENTS Before test ◊ After test	10-ns thresh
Nd3+:Y2SiO5 crystal ◊ Massive R&B dmg @ lower fluences	38.2
Nd3+:Y2SiO5 crystal ◊ Massive R&B dmg @ lower fluences	> 20.9
Nd3+:Y2SiO5 crystal ◊ Massive R&B dmg @ lower fluences	17.9
Nd3+:Y2SiO5 crystal ◊ Slight improve w/anneal	43.1
Nd3+:Y2SiO5 crystal ◊ No dmg	> 47.1
Nd3+:Y2SiO5 crystal ◊ Clean B areas survived above thresh	43.6

Table 4a. Explanation of database table entries

1 TEST numbers are prefixed by a LETTER which signifies the test laser or facility:

A — Air Force XeF Excimer	H — Chameleon	N — Nova
B — Raster Blaster	I — Isotope Separation	O — OCLI
C — Cyclops	K — Kilroy	R — Reptile
D — Comparative Damage	L — ILS	V — VPL
F — Felix XeF Excimer	M — Montana Laser	X — KrF Excimer

TEST NUMBERS follow chronologically for each laser.

LETTER SUFFIXES distinguish separate results obtained under the same test number such as location: front, rear surface, or bulk material; irradiation type: conditioned or unconditioned; etc.

2 DATE when test was begun — entries are in chronological order.

3 SAMPLE NUMBER (hopefully unique) assigned by us or the materials development group.

Any OTHER ID number that came with the sample (often not unique). Very long numbers may be partially hidden in print-outs but are extractable from the computer database.

4 Coating VENDOR; further numbers identify subtasks or runs from a particular vendor. If the "vendor" is an LLNL employee his name is preceeded by L-. For a bare surface, the vendor who polished or treated the surface is listed. For bulk material tests we list the front surface parameters in this section. The following surface vendors have been catalogued to date:

Airtron	Deacon	Laser Optics	PacificWestS.	Tinsley
Ariz.U.	Dep.Sci	Laser Power	Rochester	Trans World Optics
Burleigh	Epner Tech	Limeil	Schott	UnionCarbide
Cleveland	France	LLNL	Shandong	UTOS
Continental	Harshaw	Matra	SPAWR	UofNM
Corning	Hoya	NBS	Spectra Physics	Virgo
Crystal Tech	Inrad	Newport	Spindler/Hoyer	Wisotzki
CVD	Kodak	OCLI	TecOptics	ZC & R
CVI	Labsphere	Optovac	Thin Film Coat	Zygo

Optic TYPES are listed by the following general categories:

AR — antireflective coating — following numbers indicate for which harmonics the design applies: 1=1w (1064,1053 nm), 2=2w (532, 527 nm), 3=3w (355, 351 nm) 4=4w (266, 263, 248 nm)

BARE — bare surfaces which may have been polished, turned, extruded, etched, cleaved, etc., but without any applied coating.

BULK — bulk material as opposed to bare surface or coating.

HR — high reflector or partial reflector — following numbers indicate harmonics (see AR above).

LA — layer(s) of only one material — following numbers indicate number of such layers

MET — bare or deposited metal surface — following HR or OC indicates the metal is covered by a dielectric HR stack or a dielectric overcoat respectively.

MISC — miscellaneous such as liquid, powder,paint,cement.

POL — polarizer—following numbers indicate for which harmonics design applies (see AR above).

Coating PROCESSES cataloged to date are listed below. For bare surfaces some of these entries are the same as in the substrate section.

CVD	Epitaxy	PCVD	PVD-plasma	Solgel
Dip	Misc	Powder	PVD-sputter	
Electroplate	Paint	PVD-ebeam	PVD-thermal	

MATERIAL combinations have not all been catalogued consistently. In general, multiple layers are listed with a / between them. Dopants or mixtures are represented by { }. For cataloguing purposes a common material such as SiO2 is always listed last. UC = undercoat, OC = overcoat.

Ag	Cu	MgF2/Al	SiO2{l}/SiO2{h}	TiO2/Triton-x
Al/SiO2	DLAP	Mo	SiO2{N}	TiO2/HfO2/SiO2
Al/TiO2/SiO2	DyF3	Nb2O5	SiO2{N}/SiO2{N'}	TiO2/HfO2/SiO2/Mo
Al2O3	GeO2/P2O5/SiO2	Nd3:Y2SiO5	SiO2{P}	TiO2/Siloxane
Al2O3/AlF2	GeO2/SiO2	Opal	SiO2{Ti}	TiO2/SiO2
Al2O3/SiO2	Glass	PbF2	SiO2{Ti,F}/SiO2{F}	TiO2/SiO2/OC
Al2O3/TiO2/SiO2	Heralux WG	PbF2/AlF2	SiO2{silicone}	TiO2/SiO2/UC
AlF2	HfO2	PbF2/CaSO4	SiO2/silicone	TiO2/SiO2/HfO2
AlO(OH)	HfO2/SiO2	PbF2/SiO2	SiO2{siloxane}	TiO2/SiO2/ZrO2
AlO(OH){SiO2}	KD*P	PbO	Spectralon	ULE
AlO(OH)/SiO2	KDP	Phosphate	SrF2	ZrO2
AlO(OH)/TiO2/SiO2	KTP	Quartz	Ta2O5	ZrO2/MgF2/SiO2
Au	LAAC	Si3N4+d	Ta2O5/SiO2	ZrO2/SiO2
B2O3/SiO2	LaF	SiC	Ta2O5/SiO2/UC	ZrO2/SiO2/Mo
BaF2	LAP	Silicone	Ta2O5/SiO2/Mo	ZrO2/SiO2/HfO2
BaSO4	LG-750	SiN	TFF1	ZrO2/Y2O3
BiF3	Li-formate	SiO2	TGG	
BK-7	LiF	SiO2{B}	TiO2	
CaF2	LiIO3	SiO2{F}/SiO2	TiO2(anatase)	
CaSO4	LiNbO3	SiO2{Ge}	TiO2(rutile)	
CeF3	Methyl silicone	SiO2{Ge}/SiO2	TiO2/siloxane	
CH3OH	MgF2	SiO2{Ge}/SiO2{F}	TiO2/siloxane/Triton-x	

Table 4b. Explanation of database table entries

5 SUBSTRATE materials catalogued in the database to date are listed as follows:

7940	FR5	LAP	Phos.APG	TFF1
Al	GeO2{P}	LG-750	Quartz	TGG
Al2O3	GeO2/SiO2	Li-formate	SiC	TiO2
B2O3/SiO2	Glass	LiIO3	Silicon	ULE
BK-7	Heralux	LiNbO3	SiN	YOS
CaF2	Heralux WG	M-16	SiO2	Zerodur
Ceramic	KD*P	Mo	Spectralon	ZrO2
CH3OH	KDP	Nb2O5	SrF2	
Cu	KTP	None	Suprasil	
DLAP	LAAC	Opal	Suprasil F3	

SUBSTRATE AND POLISHING VENDORS OR SOURCES are listed as follows:

Airtron	CVI	Kodak	OCLI	UTOS
Applied Optics	Deposition Sciences	Labsphere	Optovac	Wisotzki
AT&T	France	Laser Power	Osaka	Zygo
China	Fujian	Limeil	Schott	
Cleveland	Harshaw	LLNL	Shandong	
Coherent	Heraeus	Matra	Spectra Physics	
Continental	Hoya	NBS	Spindler/Hoyer	
Corning	Inrad	Newport	Tinsley	
Crystal Technology	Kigre	NRL	Union Carbide	

POLISH or surface treatment PROCESSES used:

Beadblast	Drawn Tube	Fused	None	Super
Cleaved	Ductile	Ion mill	PACE	Unknown
Diam.T.	Etch	Lap	Replicate	

Substrate dimensions are in mm as length x width (or diameter if followed by d) x thickness.

6 Six laser parameters are specified:
WAVELENGTH in nm (1064, 1053, 532, 527, 355, 351, 266, 263, 248)
PULSE DURATION in ns (0.1 — 100).
Pulse repetition frequency (PRF) in Hz (0 — 8.6 k). All entries are in integers except high and low PRF values. Single shot is designated by 0.
POLARIZATION is given as P or S. Mixed or alternation polarization is listed as PS. Elaborations may follow in the comments section.
ANGLE OF INCIDENCE in degrees (0° — 85°) (fractions may be rounded off but stored in database).
SPOT DIAMETER (1/e^2) in mm.

7 Laser damage threshold LOCATIONS are:
F — at the front or incident surface of the sample
R — at the rear or exit surface of the sample. The entry is indented 1 space to aid in locating it.
B — within the bulk material of the sample (extensive surface damage may cause damage to propagate into the bulk material and vice versa). The entry is indented 2 spaces to aid in locating.
Thresholds are designated > or < if a full determination was not pursued because of lack of fluence, not of interest, severe damage elsewhere, or inability to measure.
THRESHOLDS and ERRORS are in J/cm2 to 0.1 J/cm2 but not necessarily accurate to that degree.
THRESHOLD COMMENTS may follow with R for retest, ? for doubtful measurement, etc.

8 Damage MORPHOLOGY comments are given in two sets of columns, the first at threshold, the second at a higher fluence (lower if no higher tests were taken) — listed under @ in J/cm2.
MORPHOLOGY under columns M is coded as:

A — artifact enhancement	M — massive damage	T — trail of bubbles or points
B — bulk damage	N — no damage	V — visual change (not seen by microscope)
C — crack or fracture	P — pinpoint damage	
D — delamination	R — coating removal	? — Not noted or unknown
F — foggy appearance	S — scald from plasma	

SIZE of largest damage at a site is given in μm in the μ columns (999 means ≥ 1 mm).
The NUMBER of observed damage phenomena is listed under #; note that many small damage points may be listed as 1 point when damage spreads to massive proportions (99 means ≥ 99).

9 IRRADIATION TYPE is coded as follows:
1/1 — ONE shot per site.
N/1 — NUMEROUS shots per site, 1 at a time with increasing fluences (conditioning or annealing).
S/1 — SEVERAL shots per site, each shot nominally at the SAME fluence with PRF irradiation.
R/1 — many shots per site, beginning near zero fluence and RAMPED up to highest stated fluence in PRF mode (conditioning).
scan — sample SCANNED along line through a PRF beam (conditioning by wings of beam).
rast — sample RASTERED in 2 dimensions through a PRF beam (conditioning by wings of beam).
The NUMBER OF SHOTS on the site which defined threshold is listed under #.

10 Identifying number of the REPORT in which the test results were written up. This is usually a Laser Damage Group Memo (LDG) (a + sign means more reports are listed but hidden in the print-out).

11 Abbreviated further details (sample description before the ◊, test results after). Abbreviations used for location and morphology apply. Coating stack described as [T/S]5 means 5 layer pairs of TiO2/SiO2. M F dmg @ 30 means massive front surface damage at 30 J/cm2.

12 If tests were conducted with other than 10-ns pulses, t, the threshold, T, is scaled to a 10-ns value by T=t^0.35. This is only a rough comparison aid. Scaling usually ranges between t^.2 and t^.5 if at all.

Manuscript Received
5-4-90

Damage Measurements on Optical Materials for Use in High-Peak-Power Lasers*

F. Rainer, R. M. Brusasco, J. H. Campbell, F. P. De Marco, R. P. Gonzales, M. R. Kozlowski, F. P. Milanovich, A. J. Morgan, M. S. Scrivener, M. C. Staggs, I. M. Thomas, S. P. Velsko, and C. R. Wolfe

Lawrence Livermore National Laboratory
P.O. Box 5508, L-490
Livermore, CA 94550

Recently, we have expanded our efforts to develop state-of-the-art optical components for use in large-scale, high-peak-power, solid state lasers. Laser-induced damage to many of these components sets critical constraints on construction costs and limits the peak powers attainable in current and proposed devices. Increasing the damage threshold whenever possible by improving materials fabrication technology is therefore the ultimate goal of our work. The optical components and technological developments we are investigating are:

Highly reflective mirrors	• Kilo-layer coatings fabricated by high-temperature, plasma chemical vapor deposition (PCVD)
	• Laser conditioned physical-vapor-deposition (PVD) coatings
	• Multi-layer sol-gel coatings
Anti-reflective coatings	• Single layer sol-gel coatings deposited on substrates and non-linear crystals
Non-linear crystals	• High purity KDP, LAP and related frequency conversion crystals
Substrates and laser hosts	• High threshold surface preparation techniques
	• High threshold bulk materials
Polarizers	• Advanced PVD multi-layer coatings

Our research has resulted in an extensive database of laser-damage measurements. We present summaries of these measurements with particular emphasis on those taken at 1064 nm and 355 nm.

Key words: antireflective (AR) coatings; bare substrates; bulk damage; conditioning; damage; frequency conversion crystals; highly reflective (HR) coatings; laser-induced damage; plasma chemical vapor deposition (PCVD); polarizers; reflectors; sol-gel coatings; thin films.

1. Introduction

The damage-test capabilities at the Lawrence Livermore National Laboratory (LLNL) support and work in conjunction with a wide variety of laser programs. We conduct and contract out to the commercial sector research and development efforts to produce optical components with high damage thresholds for use in both high-peak-power and high-average-power laser systems. The high-peak-power work is in support of LLNL's Inertial Confinement Fusion (ICF) program which involves (1) the existing Nova laser

* Work performed under the auspices of the U. S. Department of Energy by Lawrence Livermore National Laboratory under Contract No. W-7405-ENG-48.

system, (2) smaller ICF development laboratories, and (3) the Advanced Driver program for developing a successor to Nova. Much of this work has also overlapped with research conducted for the development of high-average-power laser systems including (1) the Medium Power Solid State Laser (MPSSL), (2) the free electron laser (FEL) program, and (3) the Laser Isotope Separation (LIS) program.

2. Laser damage-test capabilities

During the past year we have operated six dedicated damage-test facilities at LLNL, conducted full-aperture damage tests with the Nova laser, and also supported damage testing capabilities at several commercial locations. [1] Most of our lasers are single-shot or rep-rated Nd:YAG lasers operating at the fundamental wavelength, 1064 nm (1ω), or at one or more of its harmonics: 532 nm (2ω), 355 nm (3ω), and 266 nm (4ω). We also utilize excimer lasers for UV testing at 350 nm (XeF) and 248 nm (KrF). We operate with pulse durations ranging from 1 to 100 ns and at pulse-repetition frequencies (PRF) ranging from single shots up to 6000 Hz depending on the particular laser. Typically we conduct our tests with test-spot diameters of 1 to 2 mm, although we may resort to small spot measurements for very high fluences or also irradiate full-sized optics with one shot on LLNL's Nova laser. We conduct tests at a given site with one or more shots at a constant fluence or with successive shots at gradually increasing fluence (laser conditioning). This conditioning can raise damage thresholds of optical materials by factors of two to three. [2, 3]

3. Damage database

We have maintained and are expanding an extensive database of damage test results which cover 15 years of work at LLNL. [4, 5] In figure 1 we show a summary of these results for the past two years which represent 1300 tests conducted at 1064 nm with 1- to 16-ns pulses at PRF's ranging up to 120 Hz. The major portion of our efforts have concentrated on:

(1) antireflective (AR) coatings fabricated by the sol-gel process;
(2) highly reflective (HR) coatings fabricated by physical vapor deposition (PVD), plasma assisted chemical vapor deposition (PCVD), and the sol-gel process;
(3) polarizers fabricated by PVD;
(4) frequency conversion crystals; and
(5) laser host and substrate materials.

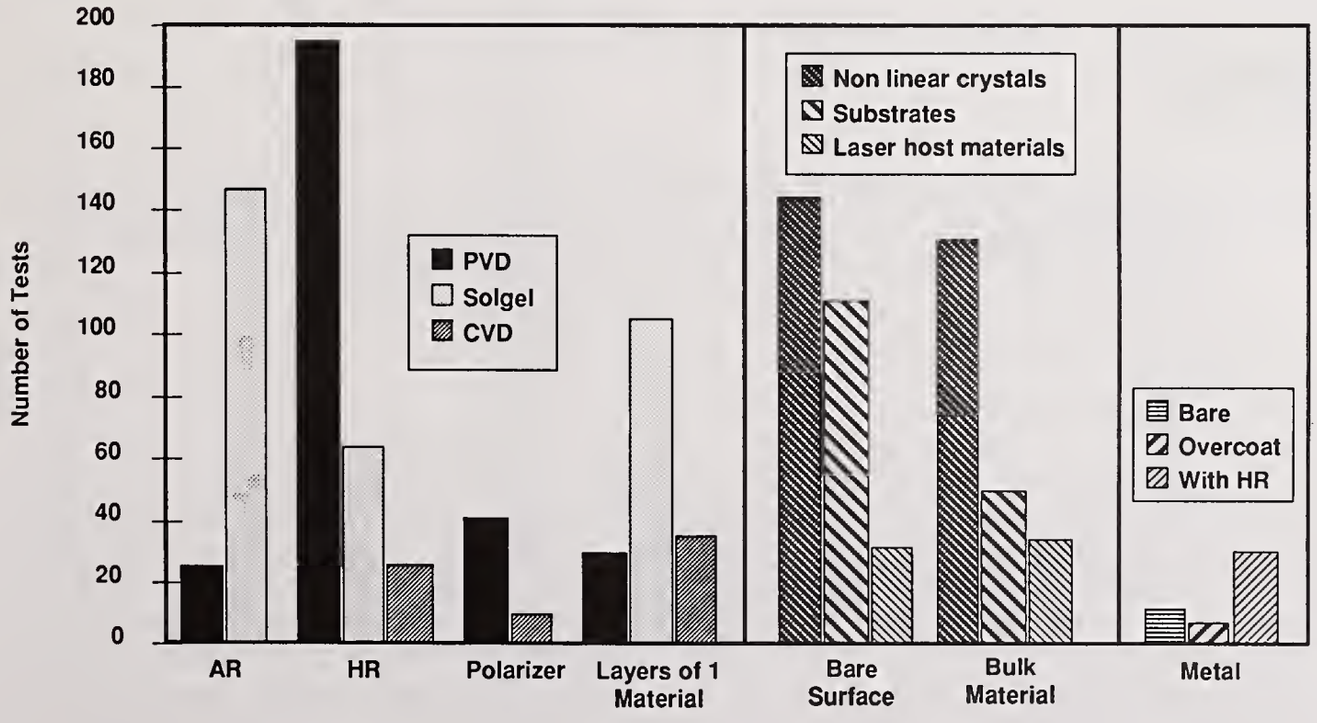

Figure 1. We have conducted over 1300 damage measurements in the past two years, most at 1064 nm with 1- to 16-ns pulses at PRF's ranging from single shots to 120 Hz.

During the past year we have re-established testing capabilities at the harmonics of Nd:YAG and are resuming testing of many of these same types of samples at these wavelengths also.

4. High-peak-power laser requirements

We show in figure 2 the schematic of a typical beam transport system for a proposed large-aperture, high-peak-power, solid state laser system for future ICF research. For 10-ns pulses the various components in such a beam line must be able to survive fluences of 35 J/cm^2 if they are subject to 1ω irradiation (laser glass, HR coatings, polarizers, frequency conversion crystals) and 25 J/cm^2 if they are subject to 3ω irradiation (frequency conversion crystals, focusing lenses, debris shields). We show in figures 3 and 4 an overview of the the current ranges of damage thresholds that we have achieved for these general categories at 1ω and 3ω respectively. These figures also provide information about specific materials, fabrication processes and irradiation conditions that allow us to achieve the desired design goals at each wavelength.

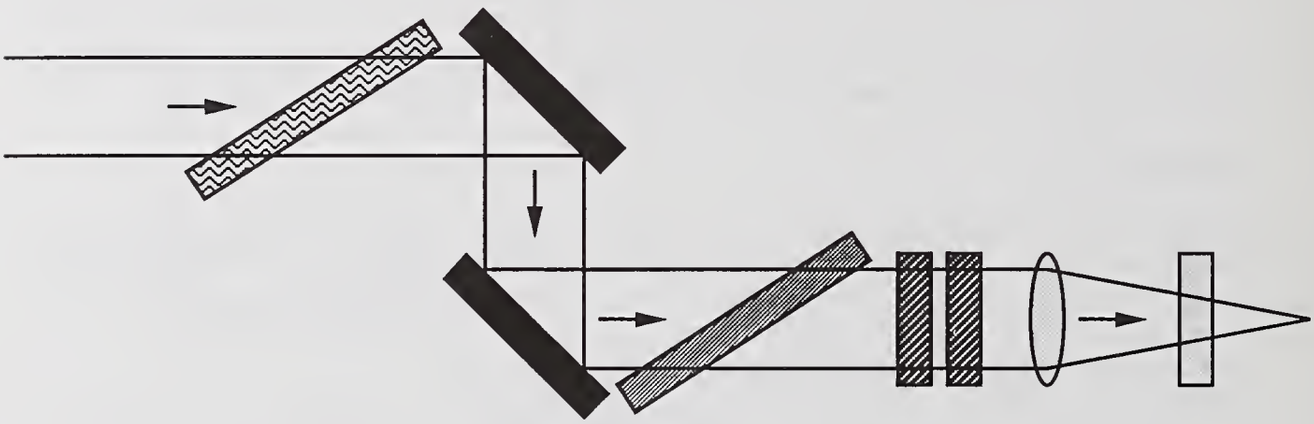

Component:	Laser glass	Mirror	Polarizer	Frequency Converter	Focus lens	Debris shield
Coating:	None	HR	Polarizer	AR	AR	AR
Frequency:	1ω	1ω	1ω	1, 2, 3ω	3ω	3ω
Damage threshold specification at 10 ns (J/cm^2):	35	35	35	35 - 1ω 25 - 3ω	25	~25

Figure 2. A schematic diagram of a typical beam line for a large-aperture laser system shows the representative components. We are designing a system with components which must survive fluences of 35 J/cm^2 at 1064 nm (1ω) and 25 J/cm^2 at 355 nm (3ω) for 10-ns pulses.

5. Specific threshold achievements

5.1 Highly reflective (HR) coatings

A significant portion of our efforts has concentrated on developing high damage threshold HR coatings by a variety of techniques (conditioned PVD coatings, kilo-layer PCVD coatings, and multi-layer sol-gel coatings). We have in fact achieved design goal thresholds with each technique as shown in figure 5. However, except for PVD coatings, much of our work is in the research stage and has not yet been scaled up to full-sized optics with dimensions ranging from 0.3 to 1 m. The damage thresholds of PVD HR coatings have gradually risen to levels at which they just barely meet our design goals. For several years numerous papers have reported on the improvement of laser damage thresholds of optical coatings by laser conditioning or "annealing" of the coatings. These past results have, however, reported only temporary improvement of damage thresholds to HR coatings. Recently we have found that HfO_2/SiO_2 HR coatings have yielded permanent threshold increases by factors of two to three to levels exceeding 50 J/cm^2 for

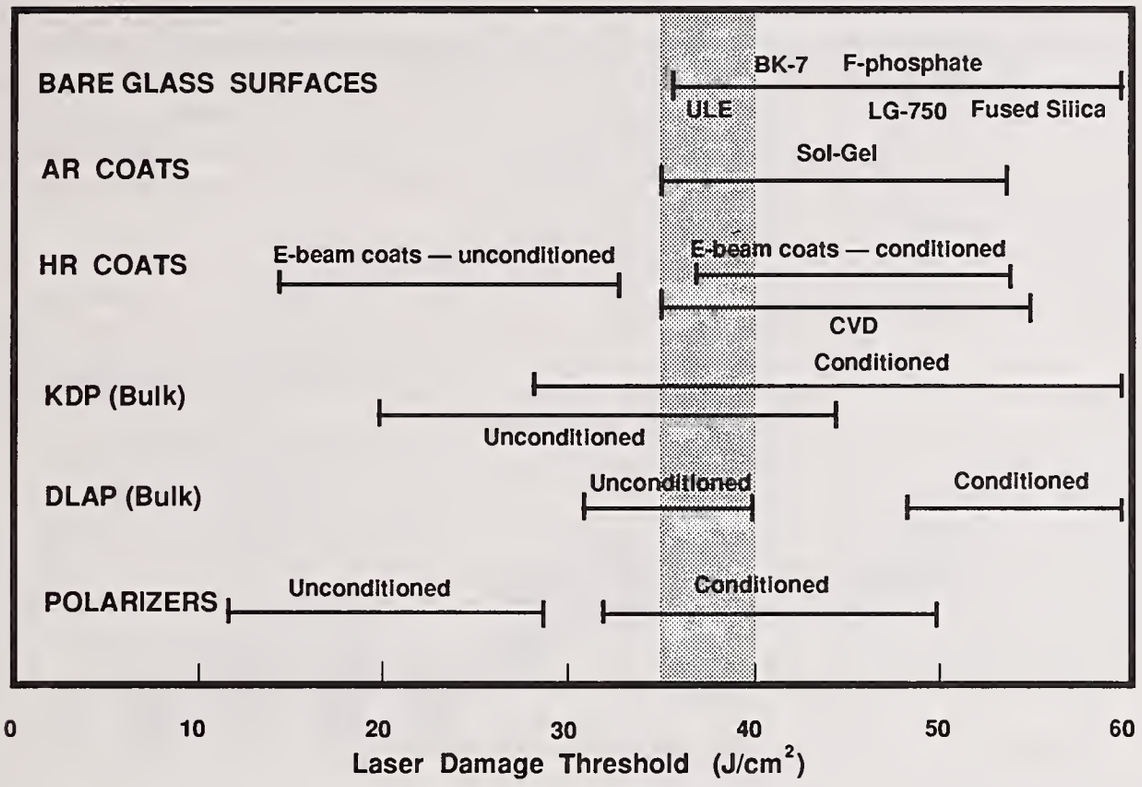

Figure 3. Our damage threshold goal for a large-aperture, high-peak-power, fusion laser system is 35 J/cm^2 at 1064 nm (1ω) for 10-ns pulses (grey vertical bar). The horizontal bars show our measured range of damage thresholds for various laser materials; laser "conditioning" of many of these materials places them near or above the threshold goal.

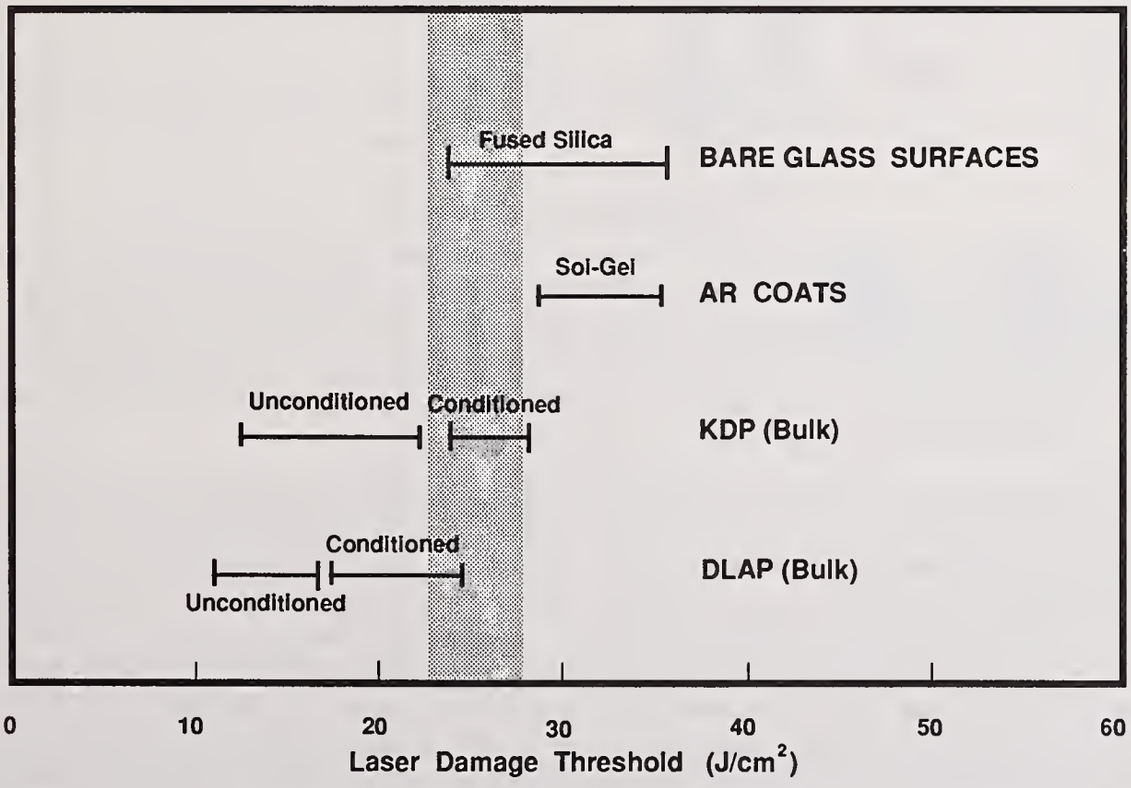

Figure 4. Our damage threshold goal for a large-aperture laser system is 25 J/cm^2 at 355 nm (3ω) for 10-ns pulses as indicated by the grey vertical bar. The horizontal bars show our measured range of damage thresholds for various laser materials at 355 nm with 10-ns pulses. As in figure 3, conditioning significantly (and permanently) improves the damage thresholds of some materials.

10-ns pulses and which in turn do not degrade with time. [3] Moreover we have shown that this improvement in threshold can be extended to full-sized optics. [2] The summaries shown in figure 5 show both the conditioned and unconditioned thresholds measured at 1064 nm for all of our highest threshold samples. A few tests were conducted with 1- or 16-ns pulse durations. We have determined that these coatings scale nominally as $\tau^{0.35}$ and have scaled the results accordingly to 10-ns values. [3] In some instances the damage thresholds were greater than the maximum fluence used for a particular test so that we only established a lower bound for these samples. These are indicated by arrows.

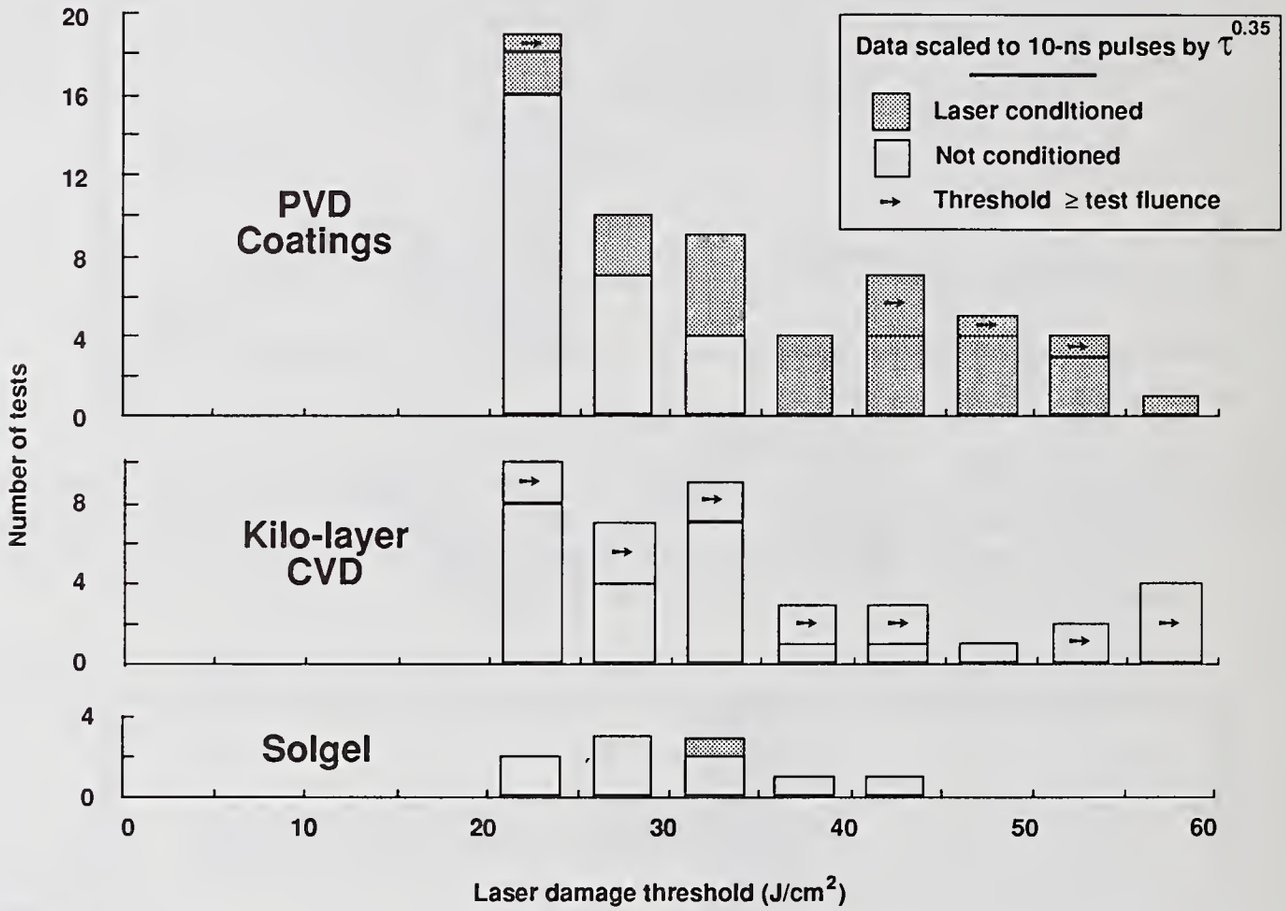

Figure 5. Over the past two years we have developed higher threshold HR coatings at 1064 nm by using the three coating methods given above. The CVD and solgel techniques are still in a research stage (i.e. small aperture); PVD coatings have been fabricated for full 1-m applications. The data show the number of coating samples tested that gave the damage thresholds shown on the abscissa. Most tests were conducted with 10-ns pulses but some 1- and 16-ns tests were scaled to 10-ns thresholds by $\tau^{0.35}$.

A promising technique we are investigating is the fabrication of PCVD HR coatings. [6] In this process alternate layers of slightly doped SiO_2 are deposited from the vapor phase plasma. The difference in index of refraction between alternating layers is relatively small requiring 1000 or more layers to produce an effective HR coating. Research samples produced by this process as well as a modified CVD process have yielded damage thresholds exceeding 60 J/cm^2 for 16-ns pulses at 1064 nm. We have plotted these data in figure 5 after scaling them to 10-ns thresholds. Most of the PCVD HR coatings were deposited on the inside of tubes nominally 1 cm in diameter. Threshold measurements were often limited by the poor optical quality of the drawn tubes rather than the actual HR coatings which are approaching thresholds close to that of fused silica substrates. We are presently completing the construction of a coating chamber which will allow us to fabricate PCVD HR coatings on flat fused silica substrates up to 6" in diameter. [7]

We have successfully employed the sol-gel process for producing single layer AR coatings for many years and have scaled their applicability up to optics exceeding 1 m in diameter. We have extended this

technology to produce multi-layer $AlO(OH)/SiO_2$ HR coatings on 2"-diameter substrates. In the near future we will apply this technology to 8"-diameter substrates. We have measured damage thresholds of these coatings that exceed 40 J/cm^2 for 16-ns pulses at 1064 nm. To conform with the other data in figure 5 we have scaled these results to 10-ns values.

5.2 Antireflective (AR) coatings

Virtually all of the work that we have engaged in recently in the development of AR coatings has revolved around the deposition of single layers of SiO_2 by the sol-gel process on fused silica, KDP, and other substrates. In figure 6 we show the results of tests conducted during the past two years at 1ω and 3ω. The tests represent a mixture of primarily 10- and 16-ns tests scaled to 10-ns values by $\tau^{0.35}$. Almost all samples we have tested in 1989 have comparable or higher damage thresholds than the best sol-gel AR coatings tested in the previous year. Moreover, in many of the recent tests we determined only lower bounds to the thresholds because we were either not able to achieve higher laser fluences for damage testing or because of massive damage to the blemished, uncoated rear surfaces of the substrates. It should be noted that most of the recent tests with thresholds < 35 J/cm^2 were for research coatings which do not in fact represent the state-of-the art of production technology. Routinely any sol-gel AR coating we fabricate at LLNL with known technology for high thresholds do in fact have thresholds exceeding 45 J/cm^2. Only a limited number of tests were conducted so far at 355 nm with all exceeding the design goal of 25 J/cm^2 for 10-ns pulses. We were unable to damage two of the samples at fluences exceeding 38 J/cm^2.

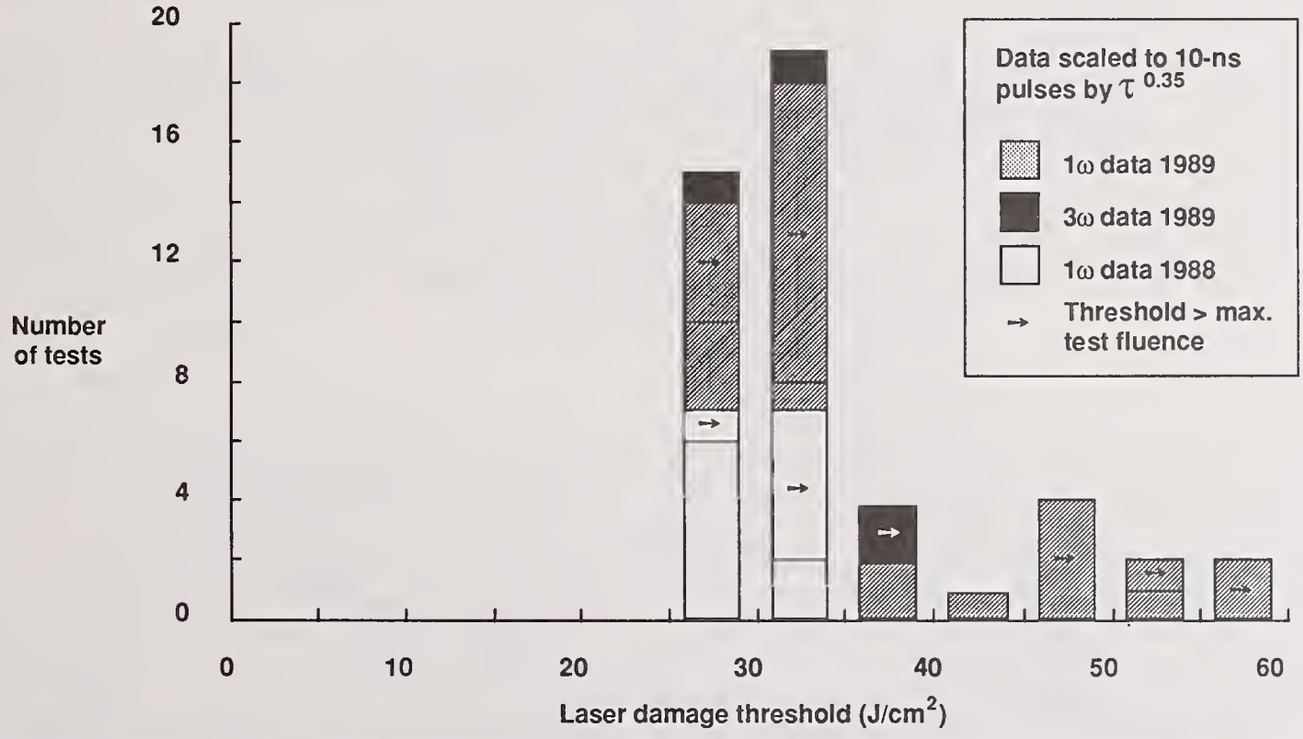

Figure 6. Damage thresholds of recent sol-gel AR coatings routinely exceed design goals for both 1064- and 355-nm tests. Earlier tests were conducted with 16-ns pulses which were scaled to 10-ns thresholds by $\tau^{0.35}$; more recent tests were conducted with 10-ns pulses.

5.3 Frequency conversion crystals

The conversion of laser beams from 1064 nm to shorter wavelengths is crucial for ICF applications. Frequency conversion crystals have always presented a significant problem from a damage standpoint in the construction of large-aperture laser systems. The crystals must first be grown to relatively large dimensions and yet be inclusion free to prevent bulk damage. The surfaces must then be figured and provided with AR coatings which are environmentally sound and yet keep losses and damage to a minimum. The latter problems have been routinely addressed with diamond turning and sol-gel AR coatings which can be

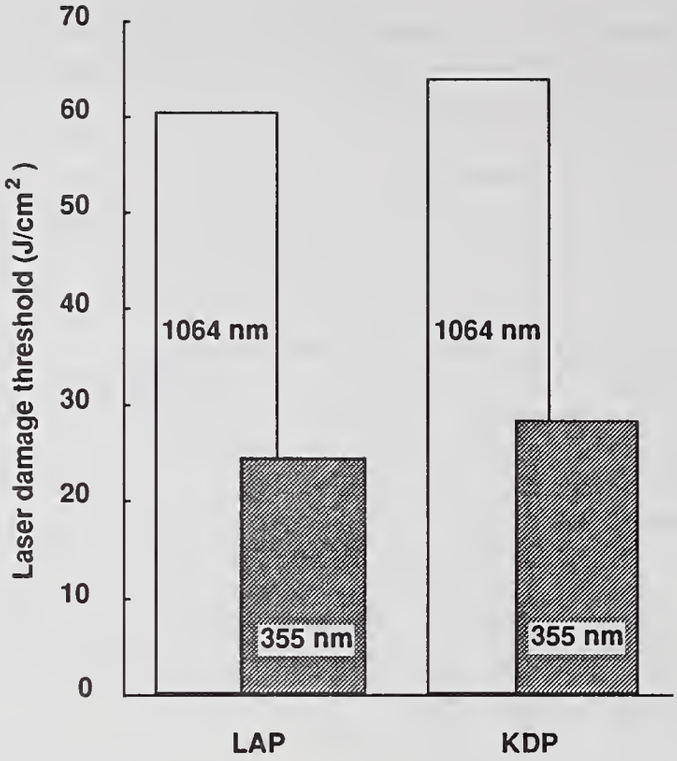

Figure 7. Both LAP and KDP crystals can be grown to yield bulk damage thresholds ≥ 60 J/cm² at 1064 nm with 10-ns pulses. The samples meet or exceed the design goal of 35 J/cm² at 1064 nm and 25 J/cm² at 355 nm.

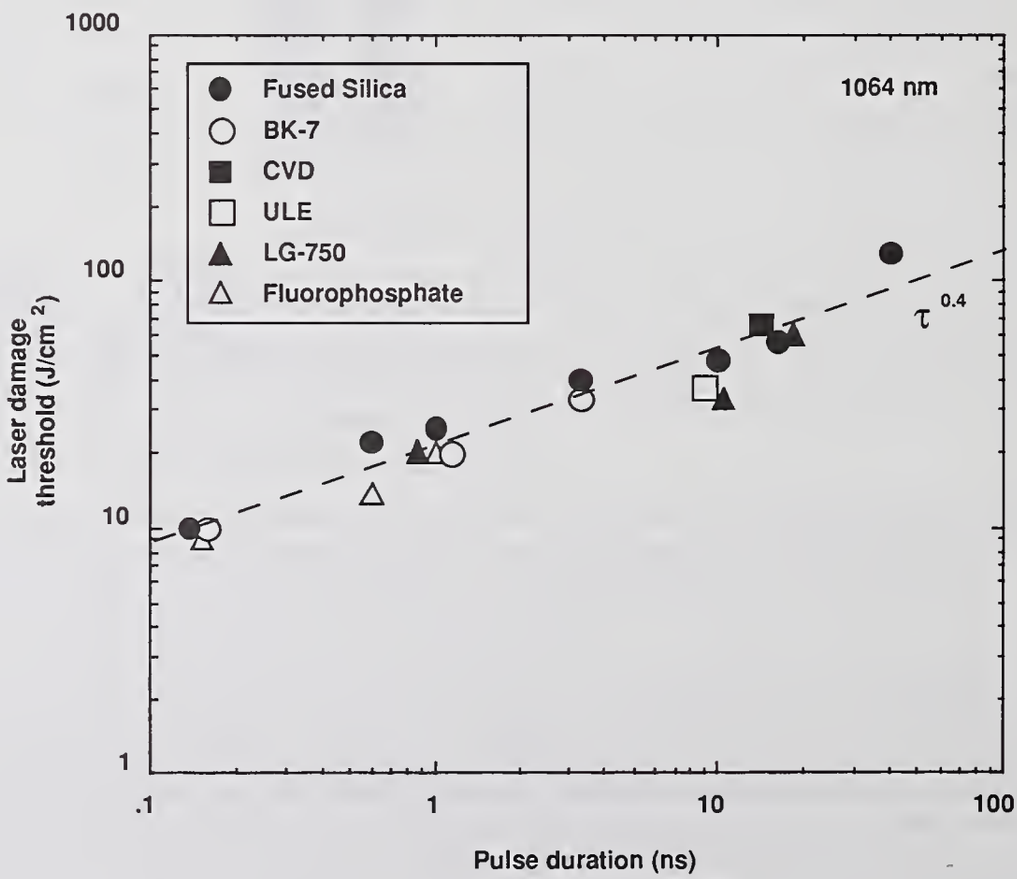

Figure 8. Average damage thresholds for many bare polished substrates with indices of refraction near 1.5 are independent of glass type and scale as $\tau^{0.4}$. The data are from references [4, 10, 11].

applied directly to the crystal surfaces at low temperatures. We have addressed the bulk damage issue by adhering to higher standards of cleanliness and the use of ultra-filtration of the constituent solutions used in growing conversion crystals. [8] We have conducted numerous damage tests on both deuterated and undeuterated versions of ℓ-arginine phosphate (LAP) and potassium dihydrogen phosphate (KDP). In figure 7 we show the results of damage tests on crystals which have been laser-conditioned using relatively large test-spot sizes (≥ 0.8 mm diameter). We have now standardized the technique to grow clean KDP crystals which have virtually no observable bulk inclusions and we are working on extending it to the growth of LAP. For both types of crystals we have measured 10-ns bulk damage thresholds exceeding 60 J/cm^2 at 1064 nm. At 355 nm these crystals meet or exceed the design goal of 25 J/cm^2 for 10–ns pulses.

5.4 Bulk materials and bare polished surfaces

Most elements in the typical beam line of a large-aperture laser systems have some type of optical coatings deposited on them (AR, HR or polarizer). Essentially the only exceptions are the actual laser glass disks, mounted at Brewster's angle, and occasional lenses, beam splitters or windows where reflections or losses are not critical or where fluences exceed those that coatings can tolerate. At LLNL bulk damage issues for laser glasses have have been addressed by an active campaign to reduce the inclusion of damage-causing platinum. [9] Other than frequency conversion crystals, the only other bulk materials typically included in the beam line are fused silica substrates or Faraday rotator materials. With the absence of inclusions, bulk damage to all these materials comfortably exceed 50 J/cm^2 and measurements often are indeterminate because of damage to surfaces at lower fluences. Recently we have conducted only isolated tests on bare surface samples. [4, 5] In figure 8 we show a compilation of the average thresholds for a variety of common substrate materials with nominal indices of refraction near 1.5. This shows that bare surface thresholds scale as $\tau^{0.4}$ and are independent of material type. Since these are average values, they are in fact relatively conservative because a wide variety of substrate types and polishing techniques are included. Many of our typical fused silica measurements are from rear surface tests conducted on bowl-feed polished (super-polished) substrates. These results are ancillary to the primary intent of measuring thresholds of good quality AR coatings which had been deposited on the front surfaces of these same substrates. Rear-surface damage to bare surfaces is usually easier to observe than front-surface damage and sets a conservative limit on the sample since the effective fluences at the rear are higher than at the front. [12]

5.5 Polarizers

Polarizers consisting of multi-layer stacks of dielectric materials are typically fabricated with more complex coating designs using more layers than those used for comparable HR coatings. Unlike with an HR coating, the coating-substrate interface of a polarizer sees the full intensity of the transmitted laser beam. By their very nature, polarizers will also have greater angular sensitivity to each polarized component of the laser beam. These characteristics have usually combined to yield among the lowest thresholds for multi-layer coatings. We have recently conducted conditioning tests on a variety of HfO_2/SiO_2 polarizers from several vendors. In figure 9 we show that, as with HR coatings, we can expect to find a significant improvement in thresholds by implementing laser-conditioning. From a limited database of conditioned polarizer tests we have observed an increase in threshold of about a factor of two to fluences > 40 J/cm^2.

6 Conclusions

We have constructed and utilized damage-test facilities at LLNL with which we have measured the damage thresholds for all crucial optical components necessary for the design of a multi-megajoule, high-peak-power, solid state laser system. Our results show that these materials can meet the damage specifications of 35 J/cm^2 at 1ω and 25 J/cm^2 at 3ω with 10-ns pulses. We have verified that the laser conditioning of multi-layer PVD HR's and polarizers can permanently raise 1064-nm damage thresholds above design goals and be scaled up to full-sized optics. Research-sized HR's can be fabricated by both PCVD and the sol-gel processes to exceed these goals and work is under way at LLNL to allow us to scale up this technology. Full-scale and research versions of sol-gel AR coatings on KDP crystals and fused silica substrates have reliably been operated and tested at fluences far in excess of design goals at both 1ω and 3ω.

Careful attention to clean growth conditions has yielded KDP crystals with bulk thresholds comparable to those of fused silica. Bare and sol-gel-AR coated surfaces of fused silica and KDP have comparable thresholds at their respective harmonics and also exceed the laser design goals at both harmonics.

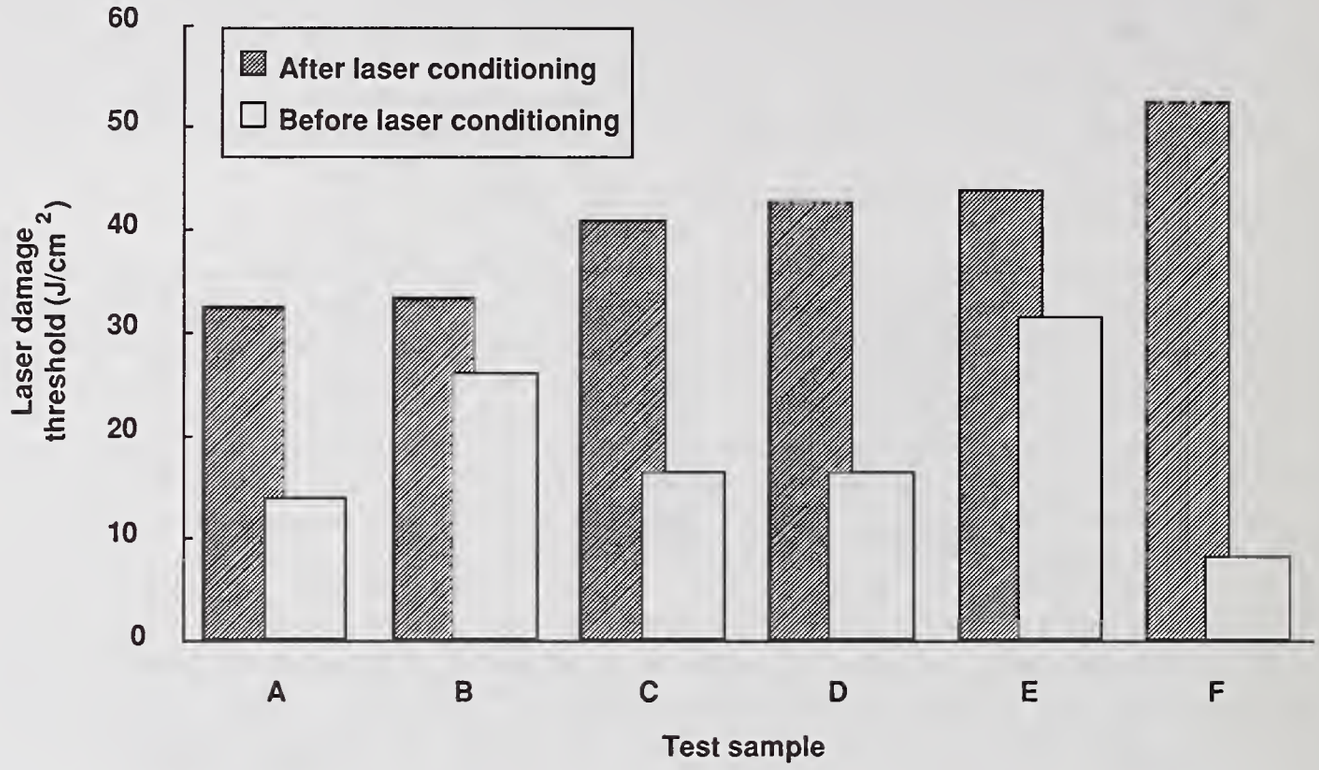

Figure 9. Laser conditioning of commercial PVD-fabricated polarizers improves their damage thresholds by an average factor of two to fluences > 40 J/cm^2 for 10-ns pulses at 1064 nm.

7. References

[1] Morgan, A.J.; Rainer, F.; De Marco, F.P.; Gonzales, R.P.; Kozlowski, M.R.; Staggs, M.C. Expanded damage test facilities at LLNL. Nat. Inst. Stand. & Tech. (U.S.) Spec. Publ.; (Laser Induced Damage in Optical Materials: 1989) - these proceedings.

[2] Kozlowski, M.R.; Staggs, M.C.; Wolfe, C.R.; Campbell, J.H. Large area laser preconditioning of dielectric thin film mirrors. Nat. Inst. Stand. & Tech. (U.S.) Spec. Publ.; (Laser Induced Damage in Optical Materials: 1989) - these proceedings.

[3] Wolfe, C.R.; Kozlowski, M.R.; Campbell, J.H.; Rainer, F.; Morgan, A.J.; Gonzales, R.P. Laser preconditioning of optical thin films. Nat. Inst. Stand. & Tech. (U.S.) Spec. Publ.; (Laser Induced Damage in Optical Materials: 1989) - these proceedings.

[4] Rainer, F.; Gonzales, R. P.; Morgan, A.J. Laser damage database at 1064 nm. Nat. Inst. Stand. & Tech. (U.S.) Spec. Publ.; (Laser Induced Damage in Optical Materials: 1989) -these proceedings.

[5] Rainer, F.; Hildum, E. A.; Milam, D. Database of average-power damage thresholds at 1064 nm. Nat. Inst. Stand. & Tech. (U.S.) Spec. Publ. 756; 1987 October. 410 p.

[6] Campbell, J.H.; Emmett, J.L.; Brusasco, R.M.; Rainer, F.; Gonzales, R. P.; Morgan, A.J.Kersten, R.T.; Paquet, V.; Etzkorn, H.-W. Damage resistant optical coatings prepared using high temperature plasma chemical-vapor-deposition. Nat. Inst. Stand. & Tech. (U.S.) Spec. Publ.; (Laser Induced Damage in Optical Materials: 1989) - these proceedings.

[7] Brusasco, R.M.; Britten, J.A.; Thorsness, C.B.; Scrivener, M.S.; Unites, W.G.; Campbell, J.H.; Johnson, W.L. A high-temperature, plasma-assisted chemical-vapor-deposition system. Nat. Inst. Stand. & Tech. (U.S.) Spec. Publ.; (Laser Induced Damage in Optical Materials: 1989) - these proceedings.

[8] Montgomery, K.E.; Milanovich, F.P. High-laser-damage threshold potassium dihydrogen phosphate. Submitted for publication J. Appl. Phys.

[9] Campbell. J.H.; Wallerstein, E.P.; Hayden, J.S.; Sapak, D.L.; Warrington, D.; Marker, A.J.; Toratani, H.; Meissner, H.; Nakajima, S.; Izumitani, T. Elimination of platinum inclusions in phosphate laser glasses. LLNL report UCRL 53932; 1989.

[10] Stokowski, S.E.; Milam, D.; Weber, M.J. Laser induced damage in fluoride glasses: a status report. Nat. Bur. Stand. (U.S.) Spec. Publ. 541; 1978 October. 99 p.

[11] Milam, D. 1064-nm laser damage thresholds of polished glass surfaces as a function of pulse duration and surface roughness. Nat. Bur. Stand. (U.S.) Spec. Publ. 541; 1978 October. 164 p.

[12] Crisp, M.D.; Boling, N.L.; Dubé, G. Importance of Fresnel reflections in laser surface damage of transparent dielectrics. Appl. Phys. Lett. 21(8): 364-366; 1972 October 15.

Manuscript received
3-8-90

Laser Induced Damage to Thallium Arsenic Selenide (TAS)

A. A. Said, M. Sheik-Bahae, M. J. Soileau, E. W. Van Stryland
Center for Research in Electro-Optics and Lasers (CREOL)
University of Central Florida
12424 Research Parkway, Orlando, FL 32826

and

N. B. Singh, T. Henningsen
Crystal and Device Research and Development Center
Westinghouse Electric Corp.
Pittsburgh, PA 15235

We present results of a study of the laser induced damage thresholds of Tl_3AsSe_3 at 10 μm using nanosecond and picosecond pulses. The damage threshold was found to be $\simeq$10 J/cm^2 with 130 ns (FWHM) and no damage was observed using 60 ps pulses.

Key words: damage threshold; CO_2 laser; nonlinear crystals; TAS; SHG.

Introduction:

Thalium Arsenic Selenide, Tl_3AsSe_3, or TAS is an important optical material for frequency conversion in the infrared region. It is an efficient material for harmonic generation and optical parametric oscillation. TAS posesses second order optical susceptibilities that are nearly three times larger than those of Ag_3AsS_2 (Proustite) and a transparency range from 1.26 to 18 μm.[1] This material has a low absorption coefficient of 8.2 m^{-1} which was determined by Barnes *et al*[2] by using a calorimetric technique.

In this paper, we present the results of a study of laser induced damage thresholds of two samples of Thallium Arsenic Selenide grown at Westinghouse.

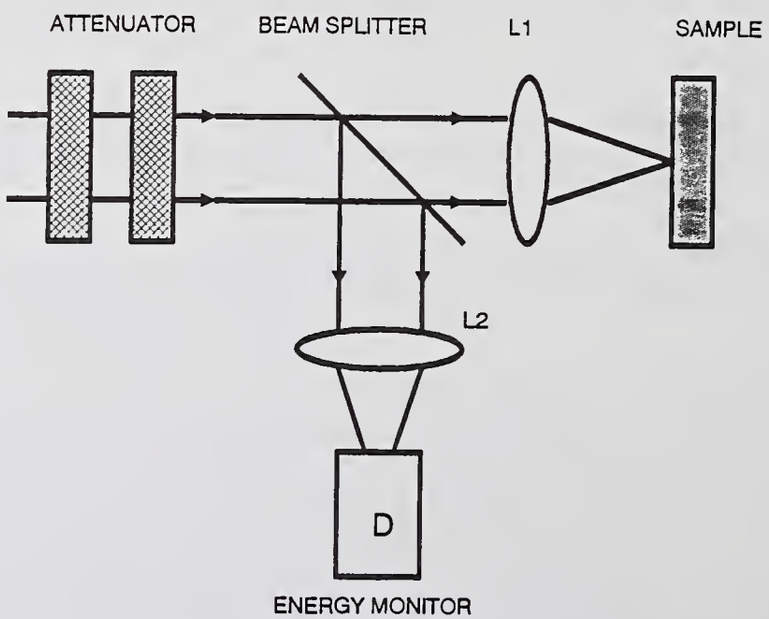

Fig.1. The experimental set-up. The 10.6 μm pulse was tightly focused on the front surface of the sample.

Experiment and Results:

Of the two samples one was doped with silver. It was cylindrical with a 2.5 cm diameter and 1.5 cm length. Only one surface was polished on which the damage measurements were taken. The other sample was undoped with a cone shape. The polished surface had a 2 cm diameter. The measurements were performed using linearly polarized, normally incident pulses from a TEA CO_2 laser system equipped with an optical free-induction decay system that can produce pulses from 30 ps to 300 ns. The laser beam was focused on the first surface of the sample by lens L_1 as depicted in Figure 1. The continuously variable attenuator consisted of two wire grid polarizers. Rotation of the first polarizer varied the input energy keeping the polarization at the sample constant. Detector D, which monitored the input energy, was calibrated using various Gentec energy detectors. The laser was operated in the TEM_{00} mode and single longitudinal mode with pulsewidths of 130 ns (FWHM) and 60 ps (FWHM). Figure 2 shows the temporal shape of the nanosecond pulse and the second order autocorrelation function of the picosecond pulse. This autocorrelation function was obtained using a pump-probe method in another TAS crystal to produce 5 μm light dependent on the temporal overlap of the pump and probe.

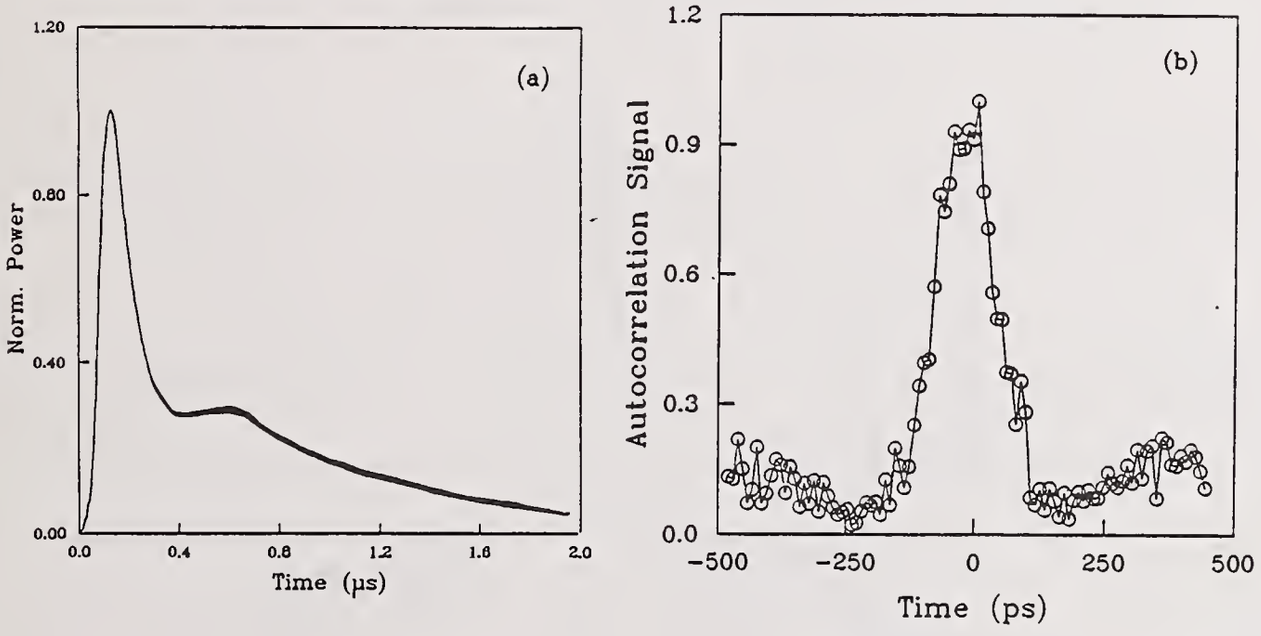

Fig.2. The temporal shape of the nanosecond (130 ns FWHM) 10.6 μm pulse (a) and autocorrelation scan of the OFID picosecond pulse (b). A pulsewidth of 60 ps (FWHM) was measured.

Pinhole size spatial beam scans were taken for each pulsewidth at the focal position of a 6.35 cm focal length lens L_1. These are shown in Figure 3 for nanosecond and picosecond pulses respectively. The beam spot size ω_0 measured was 57 μm (HWI/e^2M in the irradiance). This value agrees to witin 5% with the calculated ω_0 using the diffraction equation $\omega_0=\lambda f/\pi\omega$, where ω and ω_0 are the beam spot size before and after focusing respectively, λ is the wavelength and f is the focal length of the focusing lens. Each site was irradiated only once. The damage was visually detected through a long working distance microscope. With the nanosecond pulses, a damage threshold of 9.2 J/cm^2 (30 MW/cm^2) was measured for the doped sample when the beam waist was 57 μm and 11 J/cm^2 (37 MW/cm^2) with a calculated beam waist of 114 μm which was obtained by scaling the previously measured ω_0 to a 12.7 cm focal length lens. These thresholds do not show a significant difference. The damage thresholds for the undoped sample were 8.8 J/cm^2 (29 MW/cm^2) and 12 J/cm^2 (41 MW/cm^2) respectively. Figures 4 and 5 show the data from which the above damage thresholds were extracted. With 60 ps pulses, no damage was observed on either sample. The maximum fluence that could be reached was approximately 1.56 J/cm^2 (19 GW/cm^2). Note that this maximum irradiance is $\simeq$ 500 times higher than the nanosecond threshold. At this maximum fluence, one site of each sample was irradiated for 5 minutes at 2 pulses per second without any damage observed.

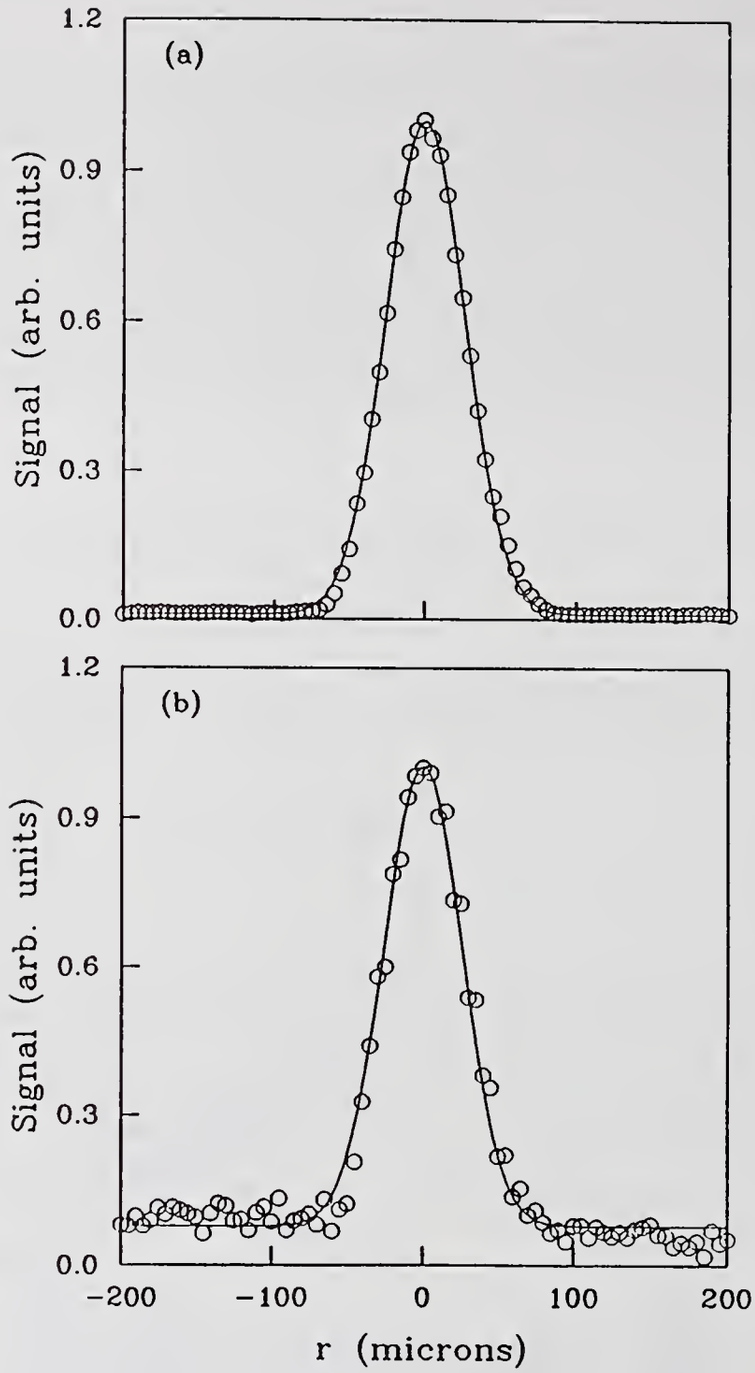

Fig.3. Beam scan of the nanosecond pulse.(a) A spot size of 57 μm (HW1/e^{2}M) in the irradiance was measured. Beam scan of the picosecond pulse.(b) The high background is due to the EMI noise arising from the 40 KV discharge of the laser amplifier.

Conclusion:

The damage threshold of TAS as obtained from the above measurements is deduced to be $\simeq$10 J/cm^2. This value is comparable to the damage thresholds of GaSe and $ZnGeP_2$ [3]. The damage threshold did not change upon doping TAS with silver. Moreover, changing the spot size by a factor of two did not make a significant change on the damage threshold value. While frequency doubling the 10.6 μm radiation an energy efficiency of 7% was obtained from a 3.8 cm long TAS crystal using 60 ps pulses with an input irradiance of 150 MW/cm^2 and a beam radius of .22 mm (1/e^{2}M in the irradiance).

References:

[1] J. D. Feichtner and G. W. Roland, Optical properties of a nonlinear optical material: Tl_3AsSe_3, Appl. Opt., vol. 11, 993-998, 1972.

[2] N. P. Barnes, Roger C. Eckhardt, D. J. Gettemy and L. B. Edgett, IEEE JQE, vol. QE-15, NO. 10, 1979.

[3] G. B. Abdullaev, K. R. Allakhverdiev, M. E. Karasev, V. I. Konov, L. A. Kulevskii, N. B. Mustafaev, P. P. Pashinin, A. M. Prokhorov, Yu. M. Starodumov and N. I. Chapleiv, Sov. J. Quantum Electron. 19 (4), 1989.

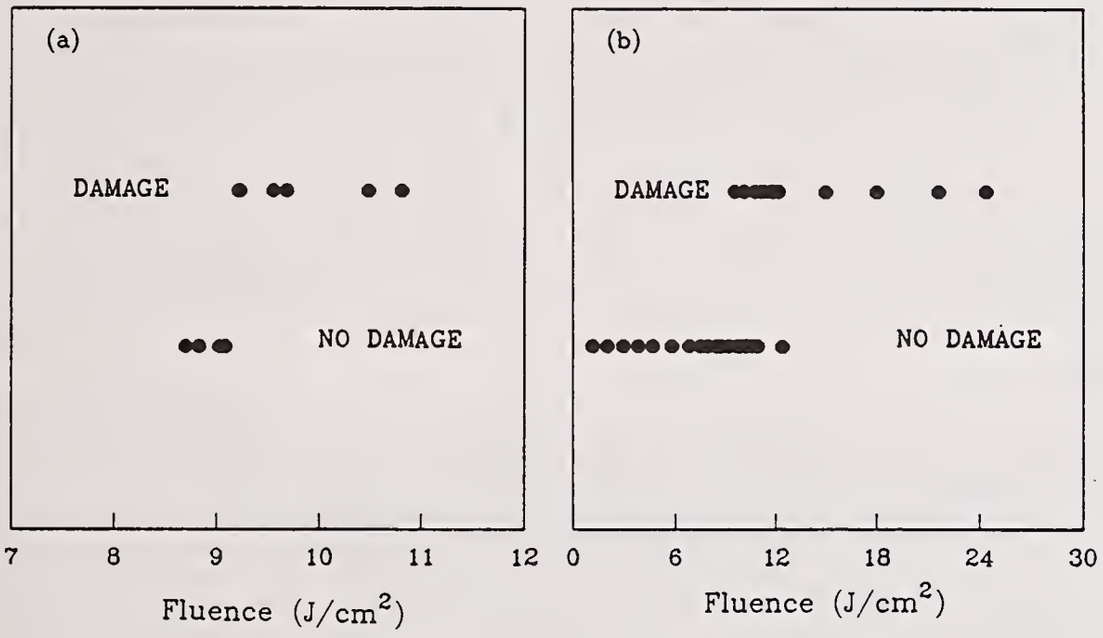

Fig.4. Damage data on doped sample using 130 ns (FWHM) pulses with 57 μm (a) and 114 μm (b) incident spot size at 10.6 μm.

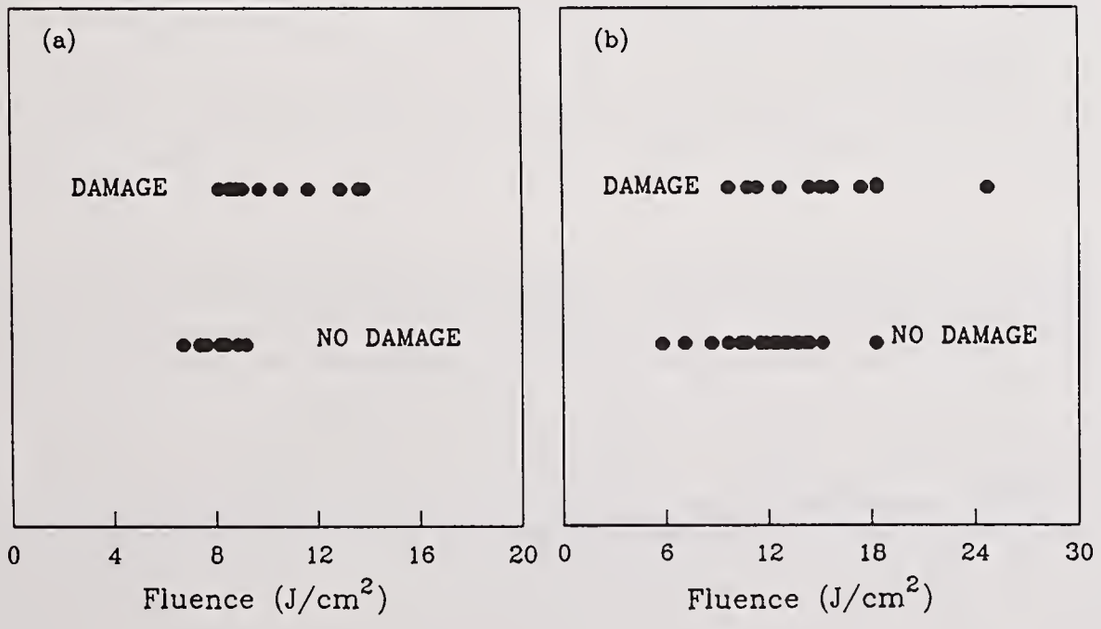

Fig.5. Damage data on undoped sample using 130 ns pulses with 57 μm (a) and 114 um (b) incident spot size at 10.6 μm.

Manuscript received
1-29-90

Laser Induced Damage in Schott's OG-550 Optical Absorption Glass

T. Whittaker, R. Goedert, and D. Templeton

U.S. Army Tank-Automotive Command
Attn: AMSTA-RSC
Warren, MI 48397-5000

Single and multiple shot laser induced damage threshold (LIDT) values were determined for Schott's OG-550 optical absorption glass using Q-switched 532 nm laser radiation. Bulk discoloration occurred for a single shot LIDT of 55 mJ/cm^2 while surface pitting resulted at a single shot LIDT of 5.6 J/cm^2. Multiple shot LIDTs were determined at 10, 5, and 2 Hz. For all three repetition rates, the multiple shot LIDTs decreased exponentially from the single shot LIDT, and level off at 35% of that value.

Key Words: laser induced damage threshold (LIDT); single shot (SS); multiple shot (MS); surface pitting; bulk discoloration.

1. Introduction

Today, lasers are used in the battlefield as rangefinders, target designators, and illuminators. These lasers have become so common in modern warfare that the eyes of soldiers are now endangered by accidental as well as intentional exposure.

Because of this relatively new and growing threat to the soldier's eye sight, the U.S. Army has initiated an Optical Improvement Program. The program's objective is to provide ocular protection from laser hazards for combat vehicle crewmen. An Optically Improved periscope incorporates a laser protection filter that is designed to protect the crewman's eyes from harmful laser radiation that may strike the periscope. Laser protection filters are classified into three types: Type I - Multilayer interference filter, Type II - Absorption filter, and Type III - Hybrid filter. In order to satisfactorily protect the crewman's eyes, each type of filter must withstand certain levels of laser radiation before damage occurs.

This paper presents the results of our preliminary investigation into the laser damage resistance of, OG-550 glass, an "off-the-shelf" optical absorption filter (Type II) produced by Schott. Both single and multiple shot laser induced damage thresholds (LIDTs) were measured.

2. Damage Determination

In this investigation, we define damage as any non-reversible change in a material's structure. This definition encompasses both surface damage and bulk damage.

2.1. Single Shot

For the single shot (SS) LIDT tests, we used two methods to determine if damage occurred: visual inspection and microscopic inspection. Visual inspection involved placing the orange OG-550 test sample on a white sheet of paper, illuminating it with white light, and inspecting the exposed sites for damage. Bright-field microscopic inspection was performed at 100x magnification.

2.2. Multiple Shot

For the multiple shot (MS) LIDT tests, we used a plasma spark to determine when surface damage occurred. When a plasma spark formed a flash of light was radiated away from the front surface of the test sample. A silicon energy detector was used to detect this emitted energy and to signify the pulse at which surface damage occurred.

3. Test Setups

3.1. Single Shot

Our SS LIDT test setup is shown in figure 1. In this experimental setup, the pulse of a linearly polarized, Q-switched Nd:YAG laser (532 nm wavelength, 8-10 nsec pulse duration, output energy up to 2 J, TEM_{00} mode, PRF 1-10 Hz), made by Quantel, was used to generate damage at the surface and in the bulk of the glass specimens. In order to cause surface damage, a positive, double-convex lens was placed in the optical path of the laser to focus the beam on to the sample (focal length of lens f = 17.5 cm, sample 3.2 cm away from focus). The lens was removed to produce bulk damage only. The test sample was placed on a stage that was vertically and horizontally adjustable (by increments of 10 um). The normal to the sample was rotated by 3 degrees relative to the axis of the beam to prevent laser light, reflected by the surface of the sample, from returning into the laser. Two BK-7 glass beamsplitters, a pyroelectric energy detector, and an energy meter were used to monitor the energy at the sample site through a calculated conversion factor. Two beam stops blocked the beamsplitters' second surface reflections. Variable attenuation was provided by different combinations of KG-3 and float glass filters. Last, an iris aperture was used to suppress multiple reflections from the attenuation filters.

3.2. Multiple Shot

Our MS LIDT test setup is also shown in figure 1. This setup is the same as the SS LIDT setup, with the addition of a silicon energy detector and another meter. In the setup, the silicon detector's energy meter counted the number of pulses that occurred after surface damage, and the pyroelectric detector's energy meter counted the total number of pulses incident on the test sample.

4. Spot Size Determination

During the LIDT tests, the energy and $1/e^2$ spot size of the beam, at the sample site, were determined so that the fluence could be calculated. For each pulse, the energy was found by measuring a fraction of the incident energy at the sample and adjusting this value by a conversion factor. The spot size (w) was determined by the slit method described below. The spot size was not measured for each pulse, but it was measured for each test.

A 120 um wide slit was placed on the test sample X, Y stage (where the test sample was normally located). A pyroelectric energy detector was also placed behind the slit and in the path of the laser beam. To avoid damaging the detector, several KG-3 filters were used to attenuate the beam. Starting from position zero, the slit was translated across the beam in 120 um increments. The average energy transmitted through the slit was recorded at each position after 100 shots had been fired.

Figure 2 shows the spatial energy distribution of a focused beam at the test sample. As the figure shows, the spatial energy distribution of the beam is approximately Gaussian in shape. To obtain the spot diameter (2w), the peak energy value is multiplied by $1/e^2$ (0.1353), the two positions corresponding to this new energy level are read from the graph, and the smaller position value is subtracted from the larger position value.

5. Test Procedures

5.1. Single Shot

Two SS LIDT tests were conducted. The first test used surface damage to define the damage threshold, while the second test used bulk damage. The procedures that were developed for these tests are described below.

For the first test, a 3.8 mm thick sample of OG-550 absorption glass was placed on the test sample X, Y stage, and 50 to 160 sites were illuminated once at each of a series of fluence levels ranging from 1 to 25 J/cm^2. The fluence level was recorded for each pulse and was varied by inserting different combinations of KG-3 and float glass filters into the optical path of the laser. For each sample, visual and microscopic inspection were conducted after all sites had been exposed. The SS LIDT was then determined by averaging the lowest laser fluence causing surface damage, $F_{min}(D)$, with the highest laser fluence producing no surface damage, $F_{max}(ND)$.

For the second test, a 3.8 mm thick sample of OG-550 glass was placed on the test sample X, Y stage and 40 to 50 sites were illuminated once at each of a series of fluence levels ranging from 20 to 200 mJ/cm^2. Once again, the fluence level was recorded for each pulse and was varied by inserting various combinations of KG-3 and float filters into the optical path of the laser. For each sample, visual inspection was performed after all sites had been exposed. In this case, the SS LIDT was determined by averaging the lowest laser fluence causing bulk damage with the highest laser fluence producing no bulk damage.

5.2. Multiple Shot

A 3.8 mm thick sample of OG-550 optical absorption glass was placed on the test sample X, Y stage and 51 sites were illuminated, with multiple shots until surface damage occurred, at each of a series of fluence levels ranging from 2 to 12 J/cm^2.

First of all, a fluence level slightly above the SS LIDT value was chosen by placing the proper combination of KG-3 and float glass filters into the optical path of the laser beam. This fluence level was determined, without exposing the test sample to laser radiation, by placing a beam stop in-between the lens and beamsplitter, firing 100 shots, and dividing the average energy at the sample site by the area of the beam. Next, the beam stop was removed and a laser pulse was repeatedly fired, at a PRF of 10 Hz, at the site until the silicon detector was triggered by the plasma spark. The fluence level, the number of shots that occurred after surface damage, and the total number of shots fired at the sample were then recorded. To obtain the number of pulses that were needed to cause damage, the number of pulses that occurred after the initial surface damage were subtracted from the total number of shots fired at the sample. Finally, each new site was exposed to a known lower fluence and the process was repeated.

This test was then repeated at a PRF of 5 Hz and 2 Hz. On each sample, 51 sites were exposed to multiple shots at each PRF.

6. Results

6.1. Damage Morphology

After exposing several sites to different fluence levels, two types of damage were observed: surface pitting and bulk discoloration. The first type of damage, surface pitting, occurred at a fairly high fluence. This type of surface damage occurred when the laser beam was was focused down to a small spot diameter and a little, crater-like pit (or pits) appeared on the front (entrance) surface of the OG-550 glass. When the pit was large enough it was easily seen with the naked eye. On the other hand, if the pit was very small a microscope had to be used to see it. We also noticed that for large pits a plasma spark would form. The second type of damage, bulk discoloration, occurred at a much lower fluence. This type of damage occurred when the laser beam was unfocused and a small, circular region slightly below the front surface of the OG-550 sample became discolored. This discolored region appeared black or grey and its diameter was about the same size as the incident spot diameter. This discolored region could be seen with the naked eye, but it could not be seen when viewed under a microscope. We also noticed that bulk discoloration always accompanied surface pitting.

6.2. Single shot

Table 1 gives a summary of the SS LIDT test's results. These results will be explained in the following paragraphs.

For the first SS LIDT test, six samples of OG-550 absorption glass were damaged at the surface. Two damage criteria were used to define the occurrence of surface pitting. Depending on the damage criterion used, the average SS LIDT values ranged from 5.6 J/cm^2 to 7.4 J/cm^2. Visual inspection, with the naked eye, provided the highest average SS LIDT, 7.4 J/cm^2. Using this criterion, the SS LIDTs were found to vary from 6.0 to 9.0 J/cm^2. Microscopic inspection, on the other hand, gave the lowest average SS LIDT with a value of 5.6 J/cm^2. In this case, the SS LIDTs ranged from 4.9 to 6.5 J/cm^2.

Because the microscopic SS LIDT did not vary much from sample to sample and because microscopic inspection provided the lowest average SS LIDT value it was determined to be the best (and most accurate) damage criterion. Visual inspection, on the other hand, was determined to be an acceptable alternative because it was a much quicker method that provided an average SS LIDT value that was close to the lower microscopic SS LIDT value.

Figure 3 shows the typical SS LIDT test results for a 3.8 mm sample of OG-550 glass using microscopic inspection as the surface damage criterion. As the figure shows, there is a range of fluence values where surface damage may or may not occur. This occurs because some of the sites are weaker than others due to scratches, pits, or absorbing inclusions in the glass [1]. This range, ΔF, is the difference between the maximum fluence producing no damage and the minimum fluence causing damage. For both criterions used, the average ΔF was approximately 3 J/cm^2.

After testing several samples, we observed that a plasma spark formed at fluences near and above the average visual SS LIDT. This flash of light formed at the front surface of the test sample whenever a pit was detected by visual inspection. At fluences well above the visual SS LIDT a plasma spark was easily seen. At fluences near the visual SS LIDT it was harder to see. This new observation would be used for the multiple shot LIDT tests.

For the second SS LIDT test, three samples of OG-550 absorption glass were damaged in the bulk of the material. Visual inspection, which was the only damage criterion used, provided an average SS LIDT value of 55 mJ/cm^2 and a range of SS LIDTs from 47 to 60 mJ/cm^2. Figure 4 shows the typical SS LIDT test results for bulk discoloration.

After inspecting the three samples for bulk discoloration, we noted that the discolored region was extremely hard to see within a rather large range of fluence levels above the SS LIDT value. Because the discoloration was so slight, there was no way to determine when bulk damage actually occurred when more than one shot was fired without removing and inspecting the test sample between shots. Thus, we concluded that multiple shot tests using bulk discoloration to define the damage threshold were impractical.

6.3. Multiple shot

Figure 5 shows the typical MS LIDT test results. The results show that damage occurred well below the visual SS LIDT level when multiple shots were fired at a site. The results also indicated that for each sample and for each PRF, the fluence level required for damage decreased exponentially with the number of pulses fired at a site from a maximum level to a minimum level. The maximum fluence level occurred after one shot, while the minimum level occurred after many shots. In each case, an equation was developed that simulated the results. The fluence level, in general, was represented mathematically by the equation:

$$F = (F_{max} - F_{min})\exp[(1-N)/a] + F_{min}$$

where F_{max} was the maximum fluence required for damage, F_{min} was the minimum fluence required for damage, N was the number of shots to damage, and "a" was a real constant. The actual fluence was determined by mathematically manipulating this equation and performing a linear regression on the data. For each PRF, the equation for the fluence, that best fit the data, took the form:

$$F = \exp(b - mN) + F_{min}$$

where N was the number of shots to damage, F_{min} was the minimum fluence required for damage, and b and m were constants that were determined by performing a linear regression on the function $\ln(F - F_{min})$. Table 2 shows the fluence equations found for each sample at each PRF.

Typically, the minimum fluence level required for damage increases with decreasing PRFs [1]. For OG-550 glass, this did not occur for the PRFs tested. As the PRF was increased, F_{min} increased some of the time but decreased others. In each case, the minimum fluence level changed by less than 0.6 J/cm^2. This variance was due to the fact that for the same number of shots there was usually a range of fluence values were damage occurred and was not due to the PRF effect.

For OG-550 absorption glass, the average minimum fluence level required to produce surface damage was 2.6 J/cm^2. After firing 25 or more shots the average fluence required to produce surface damage had dropped down to its minimum level. At this point, only a fluence value equal to 35% of the visual SS LIDT value (7.4 J/cm^2) was needed to generate surface damage. Even after 1000 shots, damage typically wouldn't occur at fluences below this value.

7. Summary

In conclusion, single shot LIDT tests and multiple shot LIDT tests were performed on 12 samples of OG-550 optical absorption glass filters. Over 1000 sites were exposed to laser pulses produced by a linearly polarized, Q-switched Nd:YAG laser operating at a wavelength of 532 nm. Two types of damage resulted and three damage criterion were used to define the occurrence of damage [2].

8. References

[1] Wood, R.M., Laser Damage in Optical Materials, IOP Publishing Limited, Accord, 1986, pp. 29-36.

[2] Whittaker, T.A., Laser Induced Damage in Optical Absorption Glass, Thesis, GMI Engineering & Management Institute, 1989.

TYPE OF DAMAGE: Surface Pitting

		SS LIDT (J/cm^2) DAMAGE CRITERION	
SAMPLE #	SPOT SIZE (um)	Visual	Micro
3	432	6.0	4.9
5	442	6.7	6.0
9	525	9.7	6.5
10	525	7.9	5.5
11	525	7.3	5.8
12	525	7.0	4.9
	AVERAGE	7.4	5.6

TYPE OF DAMAGE: Bulk Discoloration

		SS LIDT (mJ/cm^2) DAMAGE CRITERION	
SAMPLE #	SPOT SIZE (mm)	Visual	Micro
6	2.98	60	-----
7	2.98	57	-----
8	2.98	47	-----
	AVERAGE	55	-----

Table 1. SS LIDT Test Results

SAMPLE #	PRF	FLUENCE EQUATION
13	10	F = exp(2.12 - 0.23N) + 2.80
13	5	F = exp(2.00 - 0.23N) + 2.20
13	2	F = exp(2.17 - 0.27N) + 2.50
14	10	F = exp(2.20 - 0.18N) + 2.45
14	5	F = exp(2.17 - 0.23N) + 2.30
14	2	F = exp(2.07 - 0.23N) + 2.90
15	10	F = exp(1.71 - 0.15N) + 2.65
15	5	F = exp(1.92 - 0.23N) + 2.40
15	2	F = exp(1.80 - 0.23N) + 2.80

Table 2. MS LIDT Equations

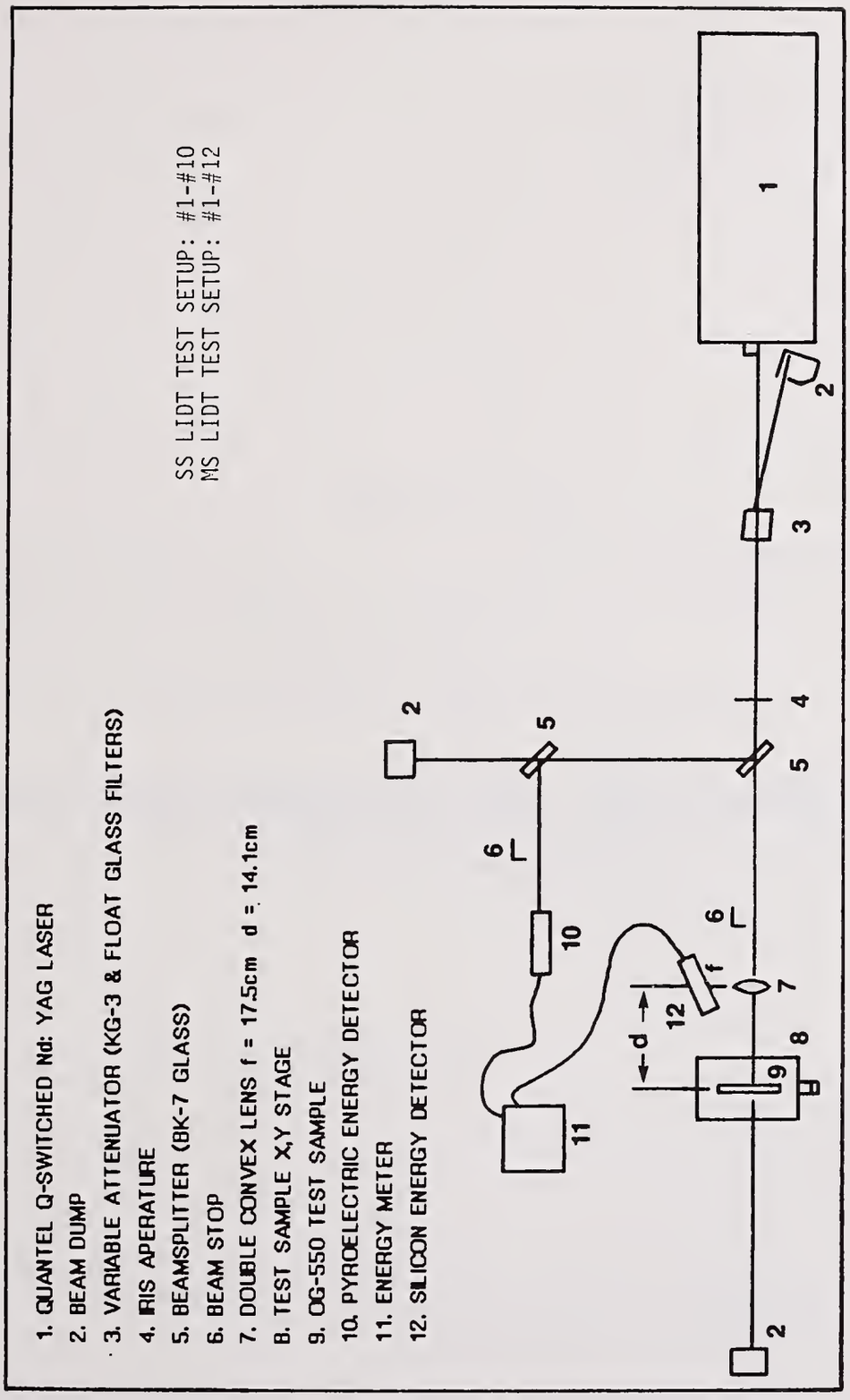

Figure 1. LIDT Test Setups

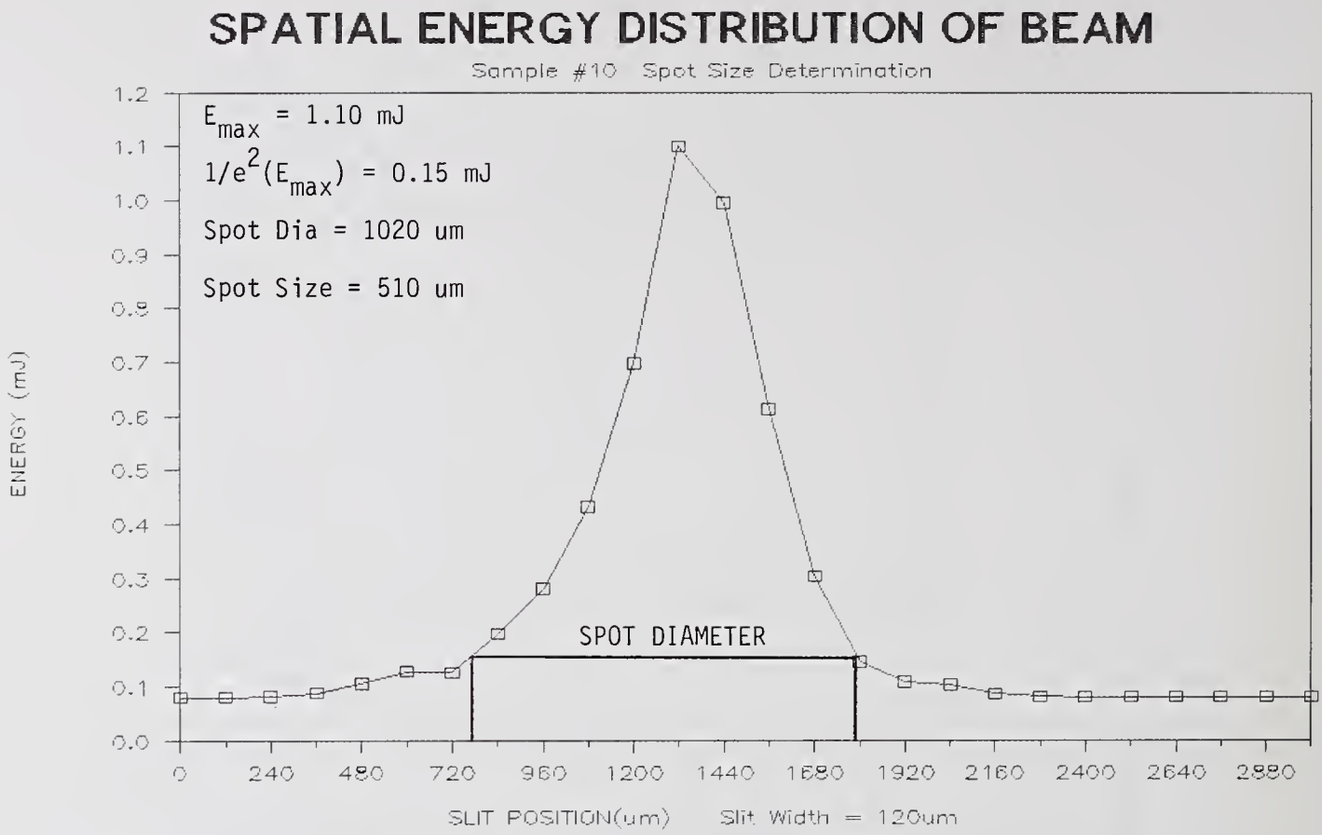

Figure 2. Spatial Energy Distribution of a Focused Beam

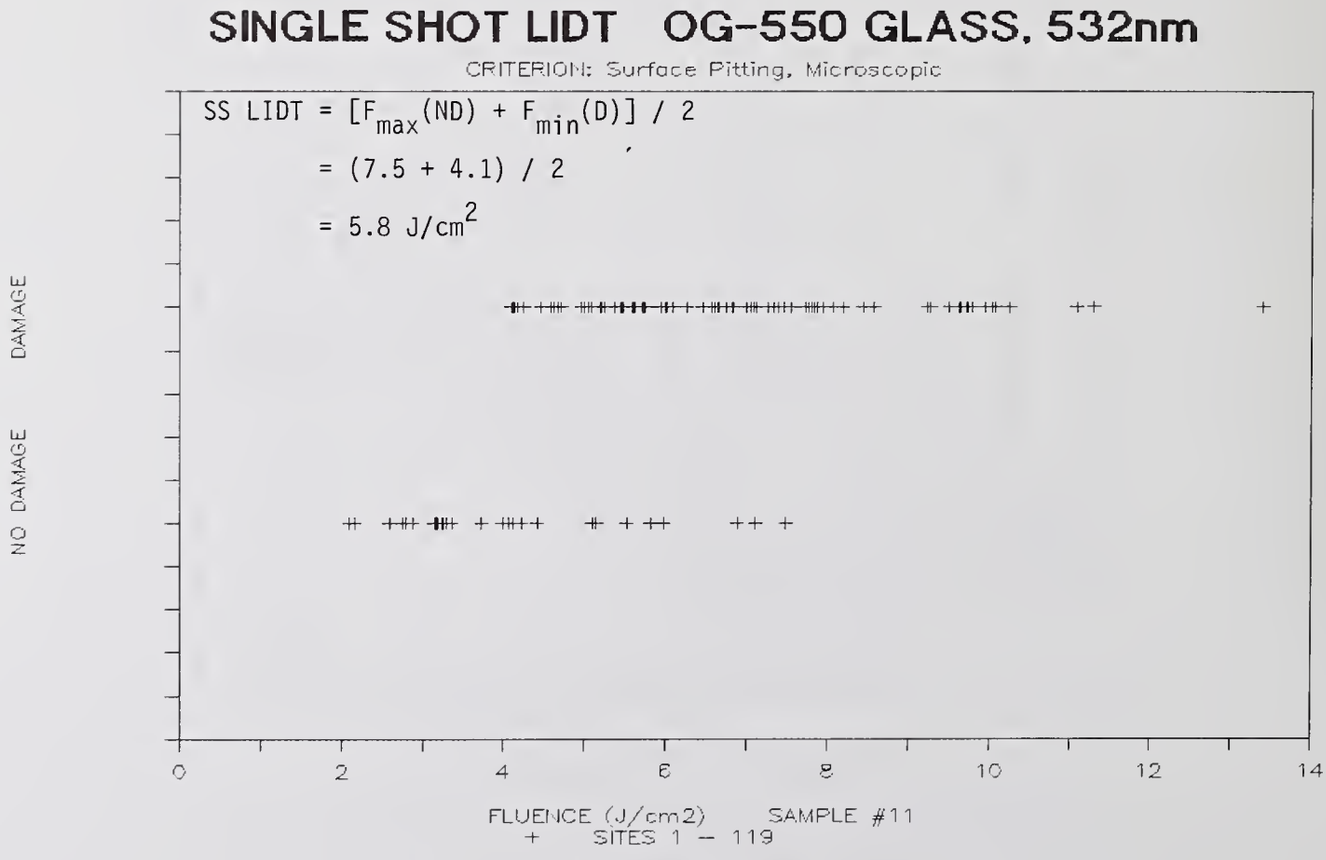

Figure 3. Typical OG-550 SS LIDT Test Results

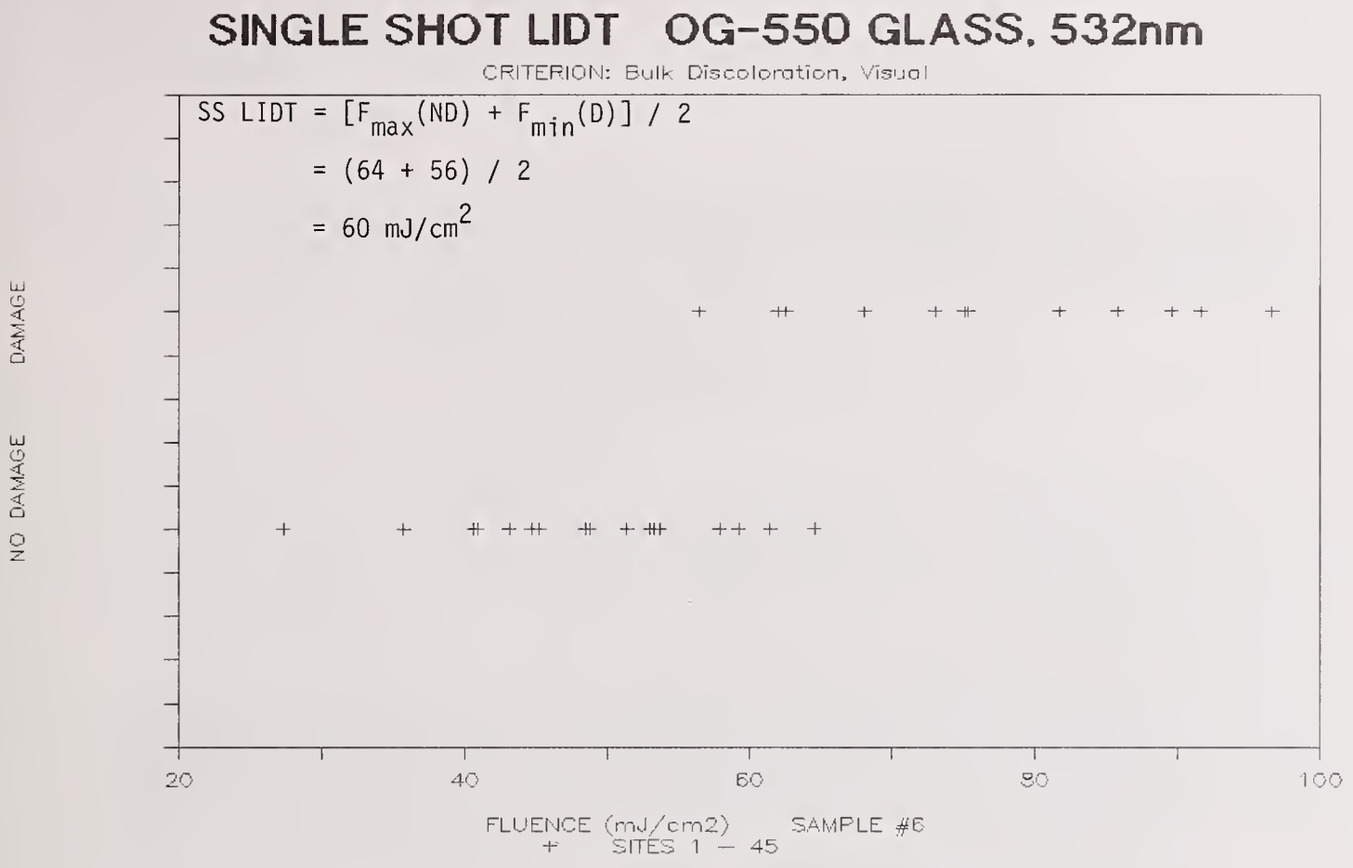

Figure 4. Typical OG-550 SS LIDT Test Results

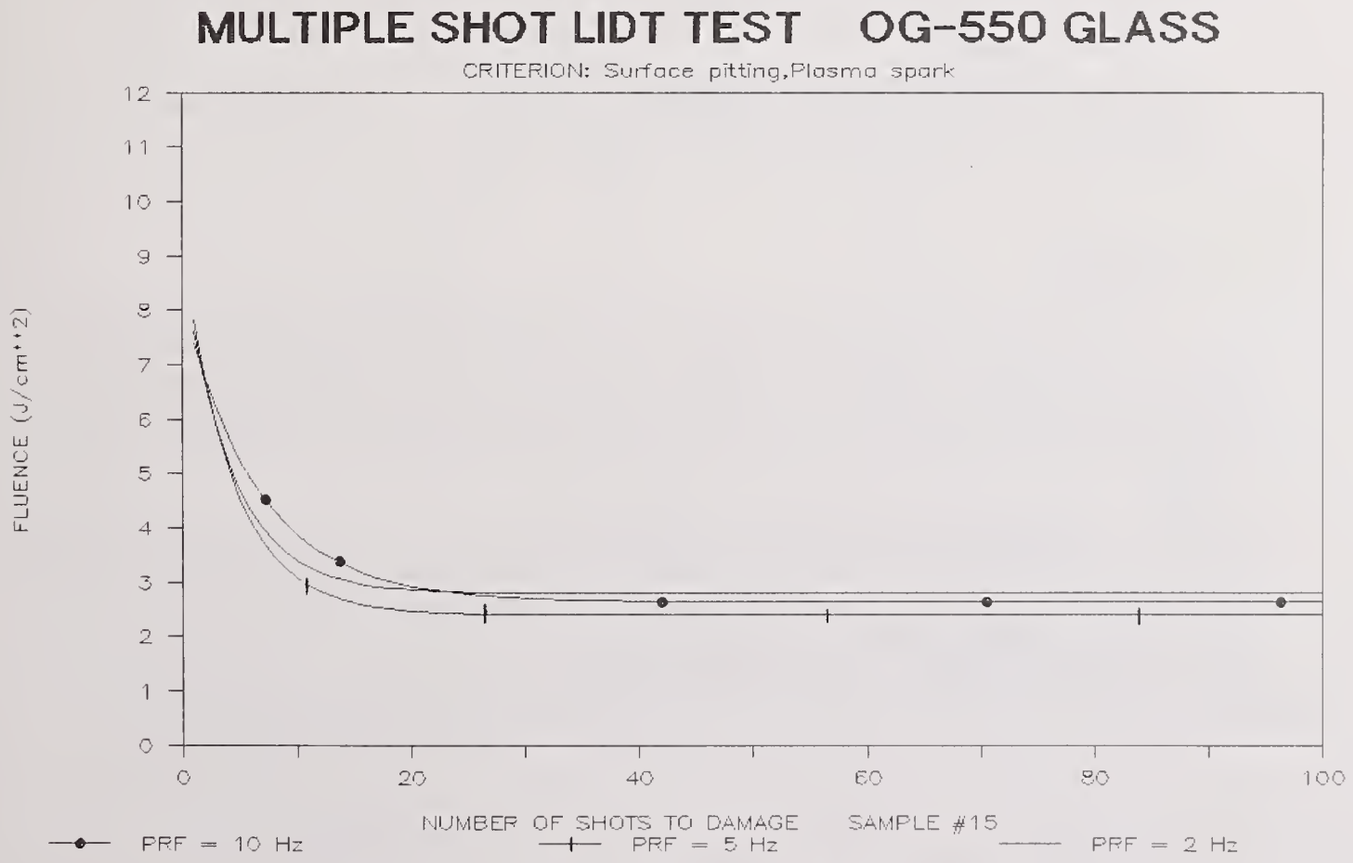

Figure 5. Typical OG-550 MS LIDT Test Results

Manuscript received
12-21-89

Effects of Laser Damage Processes on Microwave Propagation

R. S. Eng, M. D. Abouzahra, N. W. Harris
Massachusetts Institute of Technology
Lincoln Laboratory,
P. O. Box 73, Lexington, Massachusetts 02173

D. R. Cohn and P. P. Woskov
Massachusetts Institute of Technology
Plasma Fusion Laboratory
167 Albany Street, Cambridge MA 02139

Preliminary analysis has indicated that laser radiation may alter microwave propagation in transparent solids by both electron avalanche and thermally induced plasmas. These effects may occur at fluence levels below that at which visible damage occurs. Temperature rises well below the melting point may create sufficiently dense plasmas to affect propagation. The dependence of propagation effects upon plasma density and size has been modeled. Effects of varying the initial temperature have been studied. Irreversible changes in microwave absorption are also considered. Effects are analyzed for a CdTe microwave modulator for CO_2 laser radiation. Plasmas with densities $10^{15}-10^{16}$ cm^{-3} are generated at temperatures 500−700 °C in CdTe. At these densities, microwave propagation may be significantly affected. Microwave measurements of simulated plasmas have been carried out using metallic and resistive materials of different dimensions. Comparison is made with theoretical models. An experimental setup using a high energy pulsed CO_2 laser and a sensitive microwave reflectometer for measuring laser induced effects will be discussed.

Key Words: CO_2 laser induced damage, plasmas in solids, microwave transmission, temperature effects, cadmium telluride, pulsed laser heating.

1. Introduction

The propagation of microwaves in a semiconducting medium may be influenced by the heating of the medium by incident laser pulses. Depending on the laser fluence, the temperature of the medium can become significantly higher than the ambient temperature and optical damage can occur [1][2]. In microwave modulation of a high power CO_2 laser beam using an electro-optic (EO) modulator with semiconducting crystal such as CdTe, in addition to optical damage, [3][4], it is also necessary to consider the possibility that microwave propagation can be affected before the optical damage threshold is reached.

The pulse energy threshold for optical damage threshold is in general assumed to be that needed for melting. The melting point of CdTe is about 1100 °C. Because CdTe is a semiconducting material, free carrier generation by thermal excitation can be significant at temperatures well below the melting point. For example, at about 520 °C, the intrinsic free carrier (electron) density for CdTe is about 1.0×10^{15} cm^{-3}. It is thus possible to have a poorly conducting metallic sheet in crystal locations where there is high optical absorption that can result in damage (this absorption may be due to inclusions [5][6]). This medium can reflect as well as absorb microwave radiation.

In this paper we present theoretical analysis and experimental results concerning this possible interaction between an optical beam and a microwave signal. The experimental results include measurements of simulated media using sheets of different conductivities placed inside microwave waveguides. Our preliminary results have further increased the understanding of the damage processes and optical–microwave interactions in devices such as electro–optic modulators.

2. Electro–Optic Modulator Configuration

Figure 1 is a schematic diagram of an electro–optic modulator for microwave modulation of a CO_2 laser beam. A pulsed laser beam enters the microwave waveguide and impinges on the front face of the first of three 5.4 mm x 5.4 mm square CdTe crystals. After the optical beam passes through the modulator crystals, it then exits at the other end of the microwave guide. The microwave signal is led in through a bent square hollow waveguide; it is impedance matched to the dielectric–filled waveguide represented by the crystals which are gold–plated on all sides. Three or more crystals are needed to provide sufficient sideband conversion efficiency at moderate microwave drive levels. To minimize optical reflection losses, all crystal faces are anti–reflection coated. To generate a high sideband power, it is desirable to use a high level of optical fluence at the input to the modulator. The end faces of each crystal have been subjected to various optical fabrication processes and these are the places where high concentrations of impurity inclusions are likely to be present. High optical fluences coupled with strong absorption centers at these locations can cause the crystal temperature to rise significantly above the ambient temperature during the passage of an optical pulse.

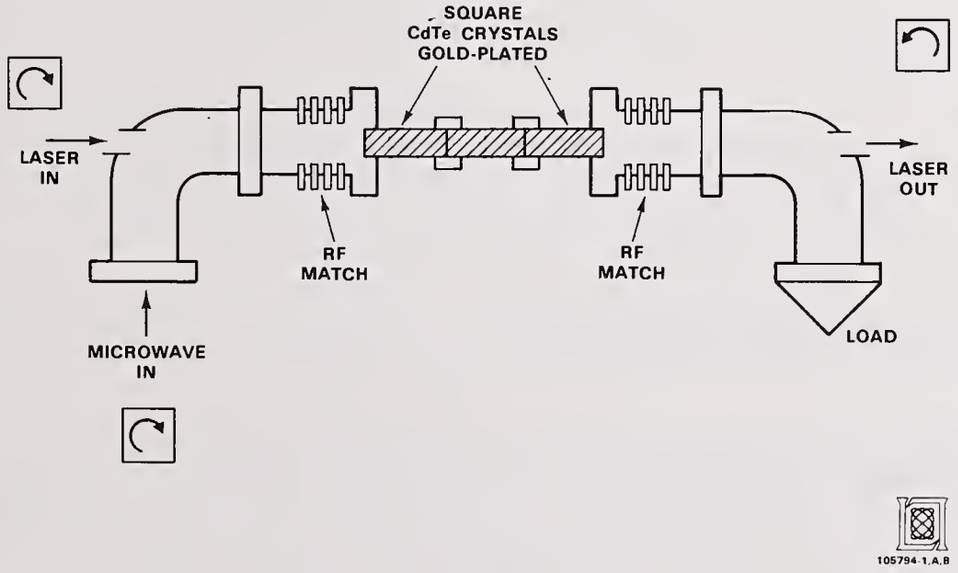

Figure 1. Schematic diagram of a CdTe single sideband electro–optic modulator

In the following paragraphs, an estimate of the temperature rise and the depth of heat penetration during the passage of the optical pulse will be made.

Consider a slab of semiconductor material with a thickness L which is heated by an impinging pulsed laser beam with a pulse width of τ and a power density of $J(r,t)$. The absorption coefficient is α. The energy absorbed over an area A(r) for a time t is given by

$$E_a(r,t) = J(r,t)A(r)(1 - e^{-\alpha(r)L}) \tag{1}$$

where both the power density and the absorption coefficient are functions of radial distance from the beam axis. For simplicity, however, the optical beam will be assumed to be uniform. Also, it is simpler to assume that the laser pulse is rectangular in shape. Finally, the absorption coefficient is in general a function of radial distance to account for any nonuniform distribution of absorption centers in the semiconductor medium. However, a detailed analysis of this general case is beyond the scope of this investigation; the objective here is to find some closed-form expressions that would yield a reasonable estimate of the effect of optical heating on microwave propagation characteristics. Therefore, it is assumed in the following analysis that the absorption coefficient is uniform over the laser beam cross section and is limited to a small axial distance L of a few μm. The assumption of absorption and resulting temperature increase over an area on the order of the laser beam cross section is consistent with one of the often observed patterns of damage [3][4].

Using the above assumption, eq (1) becomes:

$$E_a(t) = J_0 A(1 - e^{-\alpha_0 L})t \tag{2}$$

In laser pulse heating of a highly absorbing surface of a medium, the heat penetrates from the surface to a depth of penetration by thermal diffusion. The penetration depth is [7]:

$$s = \sqrt{2\kappa\tau} \tag{3}$$

where κ is the thermal diffusivity and τ is the laser pulse width. The thermal diffusivity of CdTe has been measured by Roussain and Le Bodo [8] for temperature from 100 K to 700 K. Table 1 lists the diffusivity of CdTe.

At room temperature, the diffusivity of CdTe is about 0.046 $cm^2 \cdot s^{-1}$ and the penetration depth for a 30 μs laser pulse is about 17 μm. This decreases to about 10 μm at about 700 K. Since the absorption is not confined to the surface and the charge carriers can transport the thermal energy away from the heated surface, an effective penetration depth of 30 μm appears to be a more suitable number to use for temperature rise calculations in the laser heated CdTe crystalline medium.

Having determined on the depth of thermal penetration, the next step is to obtain an estimate of the temperature rise of the heated semiconductor. The temperature rise is assumed to be governed by the heat capacity of the medium with [2]

$$\Delta T = \frac{E_a}{\rho c \Delta V} = \frac{E_a}{\rho c \pi w^2 \Delta \ell} \tag{4}$$

where

- E_a is the absorbed laser energy and it has been defined in eq (2);
- ρ is the density of CdTe;
- c is the specific heat (at constant volume);
- w is the beam spot radius;
- ΔV is the effective volume of heat penetration; and
- $\Delta \ell$ is the penetration depth.

Table 1. Thermal parameters of CdTe

T (K)	Diffusivity ($cm^2 \cdot s^{-1}$)	Conductivity ($J \cdot cm^{-1} \cdot K^{-1}$)	ρc ($J \cdot cm^{-3} \cdot K^{-1} \cdot s$)
100	0.240	0.310	1.20
150	0.160	0.184	1.23
200	0.110	0.127	1.25
250	0.074	0.095	1.28
300	0.046	0.075	1.63
350	0.033	0.064	1.94
400	0.025	0.056	2.25
450	0.022	0.050	2.26
500	0.020	0.045	2.27
550	0.018	0.041	2.28
600	0.016	0.038	2.30
650	0.015	0.035	2.31
700	0.014	0.032	2.32

The effective volume of heat penetration is the product of the laser beam cross section measured at the medium and the effective penetration depth. Using $D = k/(\rho c)$, where D is the thermal diffusivity and k is the thermal conductivity; the product of the density and the heat capacity ρc can be found. Table 1 also lists the calculated values of ρc from known values of thermal conductivity k [9] and thermal diffusivity D [8].

Using the following parameters, we obtain a temperature rise of about 500 $°C$:

- Incident energy=$E_0 = 2\ J$;
- Fraction of incident energy absorbed=0.15
- Beam spot size=$2w$=0.3 cm;
- Depth of penetration=30 x 10^{-4} cm;
- $\rho c = 2.3\ J \cdot cm^{-3} \cdot K^{-1}$

The 2 J incident energy is approximately the single shot damage threshold for CdTe for a 0.3 cm $1/e^2$ beam spot diameter extrapolated from damage test results using small $1/e^2$ beam diameters of approximately 0.1 cm [3][4].

The 0.15 fraction of energy absorbed may seem high when compared with known calorimetric measurement data using a cw laser beam. However, damage has occurred in pulsed laser testing on AR-coated CdTe surfaces and inside these surfaces [3][4]. The occurrence of damage implies that relatively high absorption has occurred by some mechanism, such as inclusions, and is roughly consistent with the 15% absorption discussed above.

2.1. Metallic Properties Induced by Laser Heating

Due to the energy absorbed, the temperature of the semiconductor rises. Associated with the temperature rise are the following changes:

1. Free carrier densities (electron and holes) increase in the conduction and valence bands, respectively;

2. The charge carrier drift mobility (≈Hall mobility) decreases due to higher collision rates at higher temperatures;

3. The change in the free carrier density alters the medium complex permittivity.

The complex permittivity is derived as follows [10]: The equation of motion for an electron in a semiconductor is:

$$m^* \frac{d^2x}{dt^2} + \frac{m^*}{\tau}\frac{dx}{dt} = -eE_x \tag{5}$$

where for simplicity we have limited the charge carrier motion to one dimension along the x direction, m^* is the effective mass, τ is the time between collisions, E_x is the electric field in the semiconductor medium, and e is the electronic charge.

Let the motion be a simple harmonic type with $x = X_0 e^{j\omega t}$ and $E_x = E_0 e^{j\omega t}$. The displacement $x(t)$ can be solved immediately and we obtain the amplitude X_0:

$$X_0 = \frac{eE_0}{m^*\omega(\omega - \frac{j}{\tau})} \tag{6}$$

The displacement X_0 of a charge e represents a dipole per unit volume and the overall volume effect is a polarization P which can be represented by:

$$P = -neX_0 = \frac{-ne^2E_0}{m*\omega(\omega - \frac{j}{\tau})} \tag{7}$$

where n is the free carrier density. By definition we have

$$P = \epsilon_0 \chi_f E \tag{8}$$

where ϵ_0 is the free space permittivity, χ_f is the susceptibility due to free charges (as opposed to bound charges); χ_f is then given by

$$\chi_f = \frac{ne^2}{\epsilon_0 m^*(-\omega^2 + j\frac{\omega}{\tau})} \tag{9}$$

The relative complex permittivity ϵ_r is related to the complex index n_r and the permittivity due to the lattice ϵ_L:

$$\epsilon_r = n_r^2 = \epsilon_L + \chi_f = \epsilon_L + \frac{ne^2}{\epsilon_0 m^*(-\omega^2 + j\frac{\omega}{\tau})} \tag{10}$$

Letting

$$\omega_p^2 = \frac{ne^2}{\epsilon_0 m^*} \tag{11}$$

$$\tau = \frac{1}{\nu} \tag{12}$$

where ω_p is the plasma frequency and ν is the collision frequency. The relative complex permittivity becomes

$$\epsilon_r = \epsilon' - j\epsilon'' = \epsilon_L - \frac{\omega_p^2}{\omega^2 + \nu^2} - j\frac{\nu}{\omega}\frac{\omega_p^2}{\omega^2 + \nu^2} \tag{13}$$

The real and imaginary parts of $n_r = \sqrt{\epsilon_r}$ are n and κ which are given below:

$$n_r = n - j\kappa = \sqrt{\frac{1}{2}A + \frac{1}{2}\sqrt{A^2 + B^2}} - j\sqrt{-\frac{1}{2}A + \frac{1}{2}\sqrt{A^2 + B^2}} \tag{14}$$

where

$$A = \epsilon_L - \frac{\omega_p^2}{\omega^2 + \nu^2} \tag{15}$$

$$B = \frac{\nu}{\omega} \frac{\omega_p^2}{\omega^2 + \nu^2} \tag{16}$$

From eq (13) it is seen that in order to find the relative permittivity, we must first determine the plasma frequency ω_p and the collision frequency ν, which depend on the free carrier density n and the time between collisions, τ, respectively.

First, in a CdTe crystal, the intrinsic carrier density for electrons, n_e, is given by [11]:

$$n_e = \sqrt{30} \times 10^{15} T^{\frac{3}{2}} e^{-0.99 \times 10^4 / T} \tag{17}$$

where T is in $^\circ K$ and n_e is in cm^{-3}. The carrier density is plotted in figure 2 as a function of medium temperature in °C. Next, for the time between collisions, τ, the general expression is:

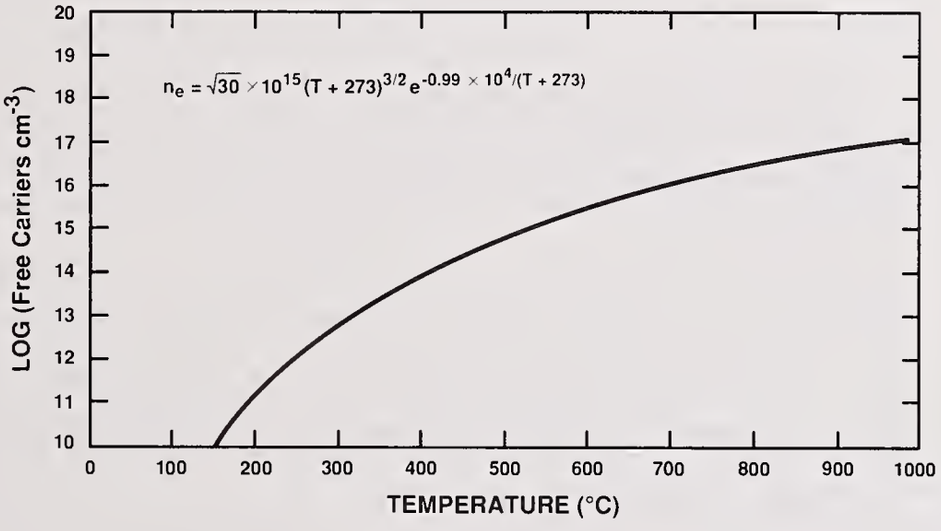

Figure 2. Carrier density as a function of CdTe medium temperature

$$\tau = \frac{\mu m^*}{e} \tag{18}$$

where μ is the drift mobility. Because there are two kinds of charge carriers, we must treat the electrons (subscript e) and holes (subscript h) separately and use separate effective masses m_e^* and m_h^* and mobilities μ_e and μ_h as follows:

$$\tau_e = \frac{\mu_e m_e^*}{e} \tag{19}$$

$$\tau_h = \frac{\mu_h m_h^*}{e} \tag{20}$$

Values of the electron and hole effective masses are $m_e^* = 0.1\ m_0$ and $m_h^* = 0.8\ m_0$, respectively, where m_0 is the electron rest mass. Measured values for the Hall mobilities were summarized in Ref. [12]. In the temperature range from room temperature to about 1200 K, the mobilities can be approximated by

$$\mu_e = 1402 - 1.66T + 0.0005T^2 \quad \mathrm{cm^2 \cdot V^{-1} \cdot s^{-1}} \tag{21}$$

$$\mu_h = 85(\frac{300}{T})^{1.4} \quad \mathrm{cm^2 \cdot V^{-1} \cdot s^{-1}} \tag{22}$$

In the above equations, we have assumed that the drift mobilities μ_e and μ_h for electrons and holes are equal to their respective Hall mobilities. The complete expression for the relative permittivity ϵ_r in eq (13) contains the individual contributions from electrons and holes as follows:

$$\frac{\omega_p^2}{\omega^2 + \nu^2} = \frac{ne^2}{\epsilon_0 m^*} \frac{\tau^2}{1 + \omega^2\tau^2} \Rightarrow \frac{n_e e^2 \tau_e^2}{m_e^* \epsilon_0 (1 + \omega^2 \tau_e^2)} + \frac{n_h e^2 \tau_h^2}{m_h^* \epsilon_0 (1 + \omega^2 \tau_h^2)} \tag{23}$$

$$\frac{\nu}{\omega} \frac{\omega_p^2}{\omega^2 + \nu^2} = \frac{ne^2}{\omega \epsilon_0 m^*} \frac{\tau}{1 + \omega^2\tau^2} \Rightarrow \frac{n_e e^2 \tau_e}{\omega m_e^* \epsilon_0 (1 + \omega^2 \tau_e^2)} + \frac{n_h e^2 \tau_h}{\omega m_h^* \epsilon_0 (1 + \omega^2 \tau_h^2)} \tag{24}$$

The intrinsic densities due to doping are small and have been neglected above.

Figures 3 and 4 show the real and imaginary parts of the refractive index n_r as functions of the plasma density n_e (or n_h) at 16 GHz and 5 GHz, respectively. It can be seen as the carrier density reaches 1×10^{15} $\mathrm{cm^{-3}}$, the semiconductor behaves like a metal with $n \approx \kappa$; that is, the effective conductivity becomes greater than the effective permittivity ($\omega\epsilon_0\epsilon'$) as shown below. From Maxwell's equations, assuming that there is no source of conductivity other than that from the thermally induced carriers as represented by eq (13)

$$\nabla \times \bar{\mathbf{H}} = \dot{\bar{\mathbf{D}}} \tag{25}$$

where $\bar{\mathbf{H}}$ and $\bar{\mathbf{D}}$ are the field quantities and $\dot{\bar{\mathbf{D}}}$ includes an effective conductivity term. $\dot{\bar{\mathbf{D}}}$ is given by

$$\dot{\bar{\mathbf{D}}} = j\omega\bar{\mathbf{D}} = j\omega\epsilon_r\epsilon_0\bar{\mathbf{E}} = j\omega\epsilon_0[\epsilon' - j\epsilon'']\bar{\mathbf{E}} = j\omega\epsilon_0\epsilon'\bar{\mathbf{E}} + \epsilon_0\omega\epsilon''\bar{\mathbf{E}} \tag{26}$$

and the term $\epsilon_0\omega\epsilon''\bar{\mathbf{E}}$ is equivalent to $\sigma_{eff}\bar{\mathbf{E}}$, where σ_{eff} is the effective conductivity.

As shown in eq (13),

$$\epsilon_r = \epsilon' - j\epsilon'' = \epsilon_L - \frac{\omega_p^2}{\omega^2 + \nu^2} - j\frac{\nu}{\omega}\frac{\omega_p^2}{\omega^2 + \nu^2}$$

The effective conductivity σ_{eff} is

$$\sigma_{eff} = \epsilon_0\omega\epsilon'' = \epsilon_0\nu\frac{\omega_p^2}{\omega^2 + \nu^2} \tag{27}$$

At microwave frequencies, for $\nu \gg \omega$

$$\sigma_{eff} = \epsilon_0\frac{\omega_p^2}{\nu} = n_e e\frac{e\tau}{m^*} = n_e e\mu \tag{28}$$

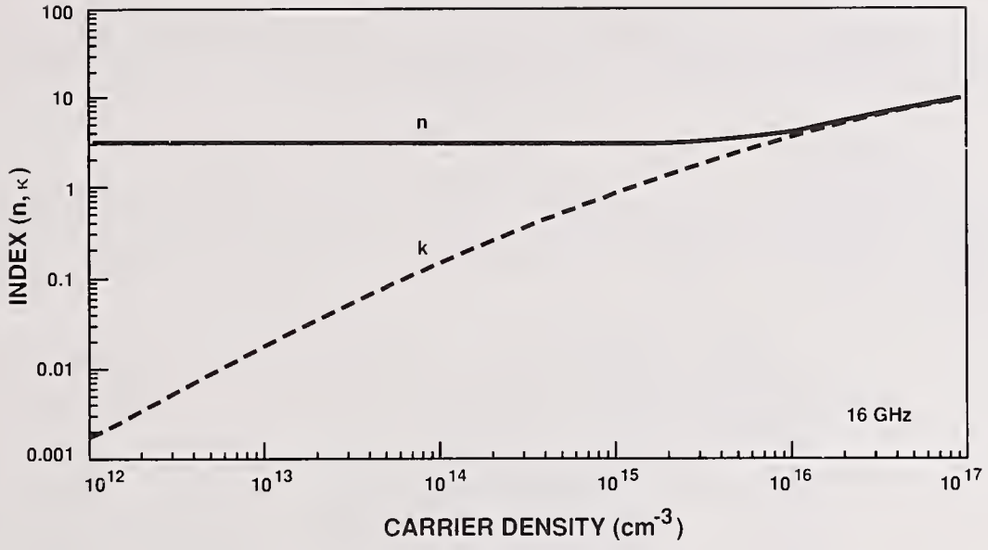

Figure 3. Complex index of CdTe as a function of plasma density at 16 GHz

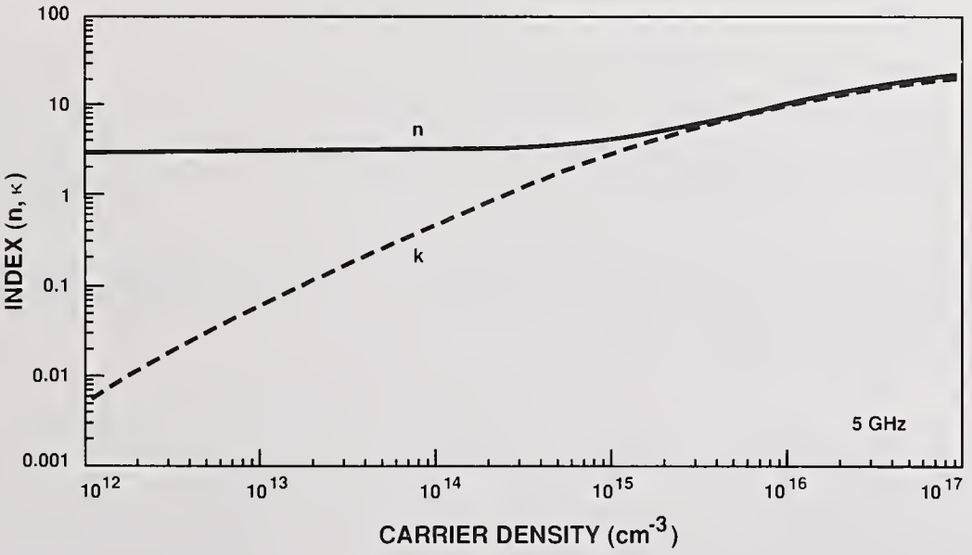

Figure 4. Complex index of CdTe as a function of plasma density at 5 GHz

The significance of eq (28) is that the effective microwave conductivity is equal to the dc conductivity. Using this value of conductivity, we can go back to Maxwell's equations and derive the propagation constant and impedance using the transmission line theory.

Table 2 lists the complex index and surface impedance for a 30 μm thick resistive sheet of heated CdTe at 5 GHz and 16 GHz. The surface impedance Z_s is defined as the inverse of the product of the "complex" conductivity and the conducting sheet thickness:

$$Z_s = \frac{1}{t}\left(\frac{1}{j\omega\epsilon_0\epsilon_r}\right) \tag{29}$$

here ϵ_0 and ϵ_r are the vacuum and relative (complex) permittivities, respectively. In a highly conductive medium, the "complex" conductivity $j\omega\epsilon_0\epsilon_r \rightarrow \omega\epsilon_0\epsilon'' = \sigma_{eff}$ and we have the more familiar expression for surface resistance $R_s = 1/(t \times \sigma)$. The impedances in table 2 are in $\Omega/\square$ and are for sheet thickness=30 μm.

Table 2. Complex Index (n_r) and Surface Impedance (Z_s) for CdTe

Carrier density	5 GHz		16 GHz	
(10^{16} cm^{-3})	$n_r = n - j\kappa$	$Z_s = r_s - jx_s$	$n_r = n - j\kappa$	$Z_s = r_s - jx_s$
0.100	$4.28 - j2.82$	$4192 - j1800$	$3.41 - j1.11$	$1714 - j2354$
0.316	$6.17 - j5.26$	$1800 - j288.5$	$4.07 - j2.49$	$1464 - j749$
1.000	$9.43 - j8.87$	$713.7 - j43.7$	$5.64 - j4.63$	$689.8 - j137.0$
3.160	$14.34 - j13.98$	$298.7 - j7.6$	$8.25 - j7.60$	$296.6 - j24.4$
10.00	$20.92 - j20.67$	$138.6 - j1.67$	$11.89 - j11.41$	$138.6 - j1.67$

3. Microwave Reflection Measurements of Metallic Disks Inside Waveguides

To estimate the microwave reflection from a laser heated semiconductor, simulations of a plasma using disks of different surface resistance inside a waveguide were performed. These measurements were carried out at 5 GHz using a 5.47 cm x 2.17 cm C-band waveguide. Different diameter copper disks were used at first. Figure 5 shows the position of a metallic disk (a), its equivalent circuit (b), and the one port equivalent circuit for microwave reflection. Reflection measurements were made with a microwave source incident from the left end of the waveguide with the right end of the waveguide terminated in a waveguide load. Figure 6 is a plot of 10 times the common logarithm of the voltage reflection coefficient r vs. disk diameter in cm (squares). For a disk diameter of about 8.4 mm, the voltage reflection coefficient is about -10 dB, which translates to a power reflection of about 1 %. The solid line in the figure represents the calculated absolute values of the reflection coefficient r (eq (32) in the following) using an expression for the shunt susceptance B to represent the disk inside a waveguide [13]. The shunt susceptance B normalized to the waveguide admittance Y_0 is

$$B' = \frac{8\pi\epsilon_r}{3}\frac{(2r_0)^3}{ab}\frac{\lambda_g}{\lambda_0^2} \tag{30}$$

where r_0 is the disk radius, a and b are the waveguide transverse dimensions, λ_0 and λ_g are the free space and guide wavelengths, respectively.

The normalized reactance X' is given by: $X' = X/Z_0 = -1/B'$, where X is the reactance and Z_0 is the waveguide impedance. Therefore, the input impedance Z_i for the combination of the shunt and the terminated waveguide is the shunt impedance $Z = jX$ in parallel with the waveguide impedance Z_0 with $Z' = Z/Z_0 = jX/Z_0 = jX'$

$$Z_i = \frac{Z_0 Z}{Z_0 + Z} = \frac{Z_0 \cdot Z'}{1 + Z'} \tag{31}$$

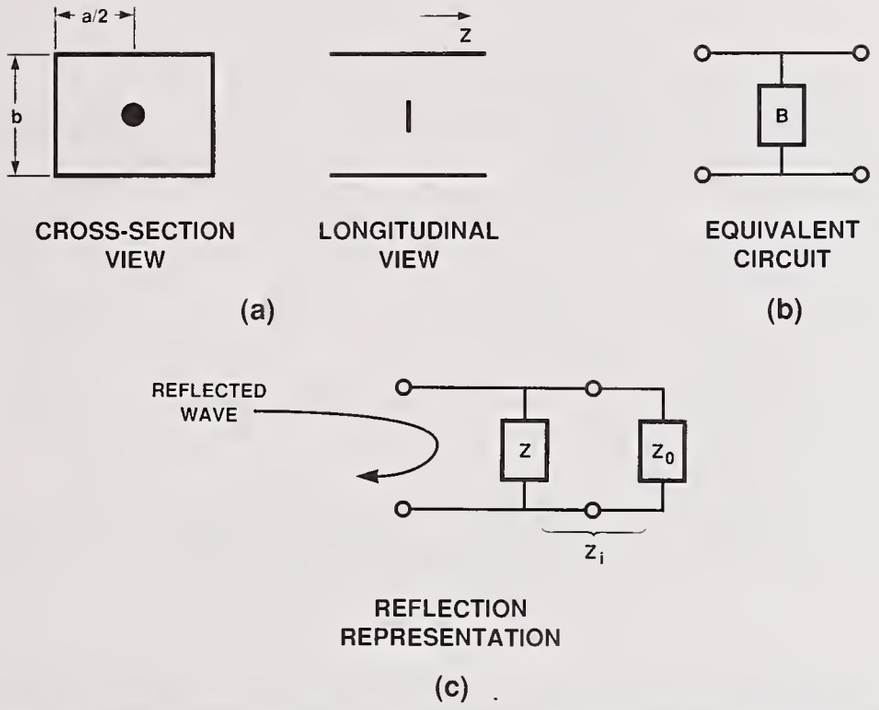

Figure 5. Position of a metallic disk in a microwave waveguide (a), its equivalent circuit (b), and microwave reflection representation (c)

Next, the reflection coefficient r is obtained

$$r = \frac{Z_i - Z_0}{Z_i + Z_0} = \frac{-1}{2Z' + 1} \tag{32}$$

Note that the reflection coefficient is a function of the normalized impedance Z' only. Since the normalized impedance is implicitly given by eq (30), the effect of the waveguide medium on the reflection coefficient is then a function of the relative permittivity given in eq (30). The relative permittivity was not present in the original expression in [13]; we have included it in this memorandum for the CdTe dielectric waveguide application.

Next the reflection coefficients for four different resistive sheets were also measured. These are plotted in figure 6 with the triangles, crosses, diamonds, and stars for the surface resistances of 100, 200, 377, and 1000 $\Omega/\square$, respectively. As expected, the more conductive the sheet, the closer is the reflection coefficient to that of the metallic disk. The measured reflection coefficients obtained for small resistive disks are higher than that of the metallic disk. This is probably due to uncertainties in measurements at small reflection coefficients. Figure 7 shows the voltage reflection as a function of the surface resistance for a 1.4 cm diameter disk. The lowest value of surface resistance is that of copper, less than 0.1 $\Omega/\square$. It represents the maximum reflection for this size of disk. Next, we extended our calculations to the 16 GHz regime and used the actual size of the 5.4 mm x 5.4 mm CdTe–filled waveguide modulator. Figure 8 shows the results for a disk with the resistivity of copper. Note that for a 3–mm diameter disk, the voltage reflection is between -2 and -3 dB, which translates to a power reflection greater than 25 %. This is much greater than that shown in figure 6 for the observed data for the C–band rectangular waveguide.

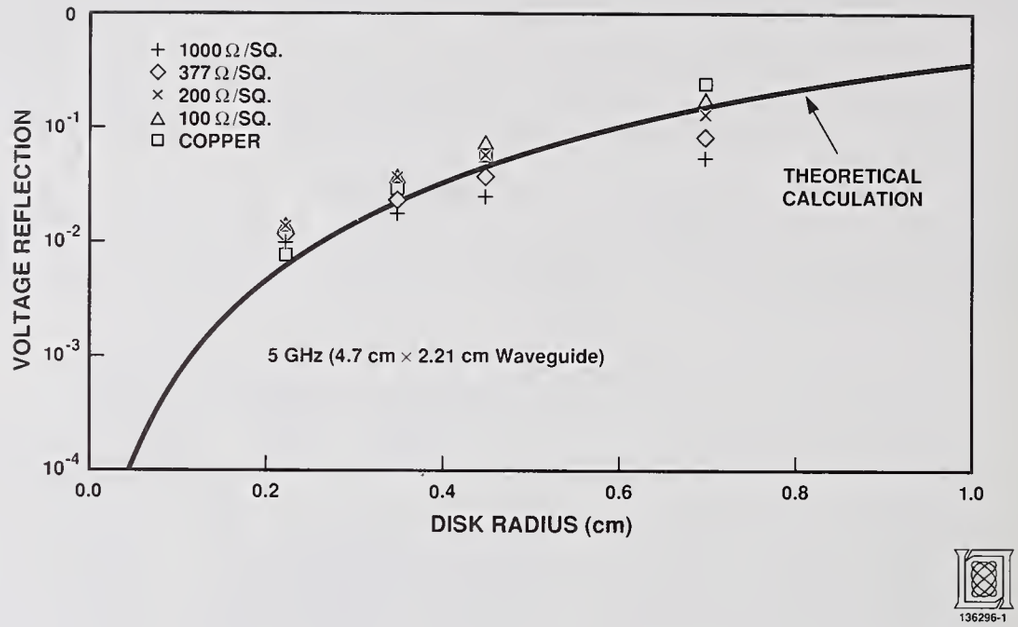

Figure 6. Voltage reflections from circular disks in an air-filled C-band waveguide

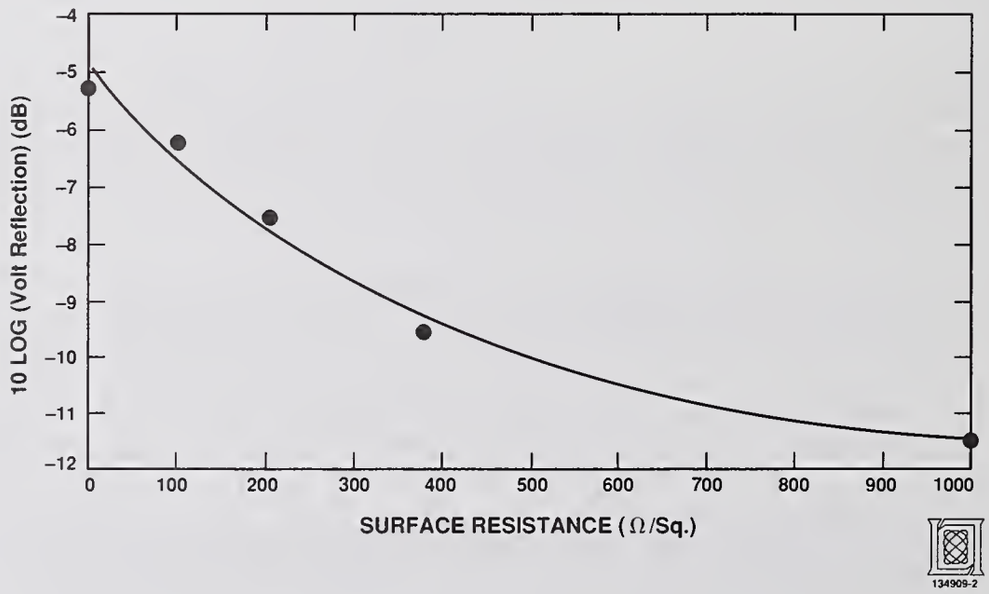

Figure 7. Voltage reflection at 5 GHz as a function of the surface resistance for a 1.4 cm diameter disk

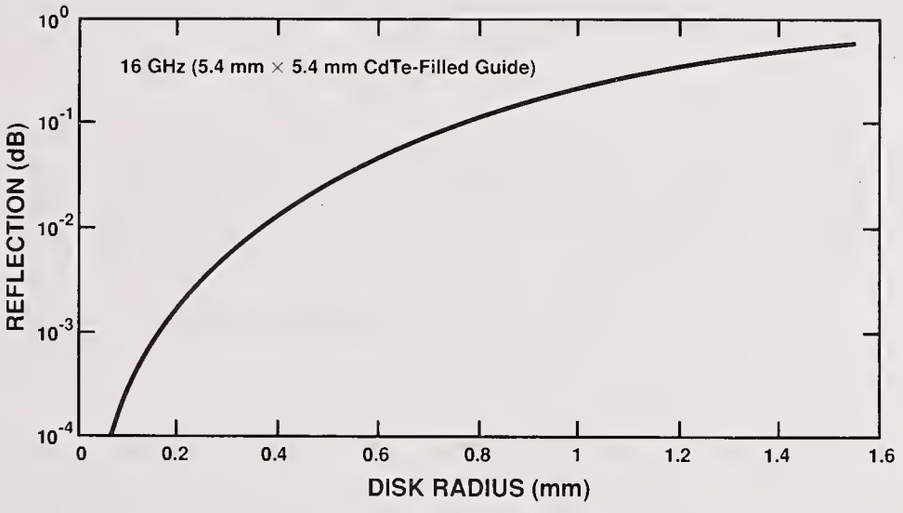

Figure 8. Voltage reflection at 16 GHz as a function of copper disk diameter

4. Estimate of Microwave Reflection from Heated CdTe Modulator Crystal

In Section 2, we discussed how a heated semiconductor medium could have a very high free carrier density and that under this circumstance the semiconductor could be characterized as a metallic–like medium with a corresponding complex relative permittivity. In Section 3, we have shown that when an electrically conducting sheet or resistive sheet is placed inside a rectangular waveguide to simulate such a plasma, microwave reflection is present; the reflections were measured for different degrees of conductivity and were accurately predicted for the purely metallic case. In this section we will attempt to combine the preceding two sections and estimate the magnitude of microwave reflection from a heated semiconducting sheet placed inside a waveguide. Although we were able to obtain a closed form expression in the case of a metallic disk suspended inside a rectangular waveguide, as far as we know there is no method available for the resistive sheet. In the following, A transmission line method is used to estimate the microwave power reflection from a semiconductive sheet placed inside a waveguide.

4.1. Transmission Line Method

In measurements of surface resistance described in Ref. [14], a formula was used for determining the surface resistance by measuring the microwave voltage reflection from a thin sheet of resistive material placed inside a waveguide. This formula relating the microwave reflection R to a thin sheet of resistive material with surface impedance Z_s located at a quarter of a waveguide wavelength from a waveguide short is given by:

$$\frac{1-R}{1+R} = \frac{120\pi}{\sqrt{1-(\frac{\lambda_0}{2a})^2}} \cdot \frac{1}{Z_s} \tag{33}$$

Since the waveguide impedance Z_g is

$$Z_g = \frac{120\pi}{\sqrt{1-(\frac{\lambda_0}{2a})^2}} \tag{34}$$

solving for the reflection R from eq (33) leads to:

$$R = \frac{Z_g - Z_s}{Z_g + Z_s} \tag{35}$$

In electro-optic modulator applications, the waveguide is terminated in its own characteristic impedance Z_g; as a result, at the location of the sheet impedance, the incident microwave field sees not just a shunt impedance Z_s, but Z_s in parallel with Z_g. We denote this parallel combination of impedance by Z_p. Therefore, eq (35) becomes:

$$R = \frac{Z_g - Z_p}{Z_g + Z_p} = \frac{Z_g(Z_g + Z_s) - Z_s Z_g}{Z_g(Z_g + Z_s) + Z_s Z_g} = \frac{Z_g}{Z_g + 2Z_s} = \frac{1}{1 + 2\frac{Z_s}{Z_g}} = \frac{1}{1 + 2Z_s'} \tag{36}$$

where $Z_s' = Z_s/Z_g$ is the normalized sheet impedance.

To evaluate this approach, we first assume a resistive sheet with surface impedance of about 713.7 Ω (corresponding to a carrier density of about 1 x 10^{16} cm^{-3} as shown in table 2) filling the cross section of a 4.76 cm x 2.21 cm C band waveguide at 5 GHz as will be subsequently discussed. The waveguide impedance is given by:

$$Z_g = \frac{120\pi}{\sqrt{1-[\frac{6}{(2)(4.76)}]^2}} = 486\ \Omega \tag{37}$$

Using eq (36), we next obtain a voltage reflection of about

$$R = \frac{1}{1 + 2(Z_s)/486} = 0.254 \tag{38}$$

The power reflection is then about 6.4 %.

Since the resistive sheet does not cover the entire cross section of the guide, we must multiply the 6.4 % by the ratio of the effective area of the sheet optical power impinging on to that across the whole waveguide cross section. This factor is calculated as follows: The sheet disk radius w is taken to be 0.7 cm; so the area of the disk is $\pi(0.7)^2\ cm^2$. The C-band waveguide internal dimension is 4.76 cm x 2.21 cm.

So we have

$$\text{Correction Ratio} = 4\int_0^w \sqrt{w^2 - x^2}\cos^2(\frac{\pi}{a}x)\,dx \cdot [\int_0^b dy \int_0^a \sin^2(\frac{\pi}{a}x)\,dx]^{-1} \tag{39}$$

where a and b are the rectangular waveguide internal dimensions and the electric field distribution is that of a TE_{10} mode. Substituting the numerical values into eq (39) and performing the integration yield the correction ratio

$$\text{Correction Ratio} = \frac{4(0.365)}{2.21 * (4.76/2)} = 0.278 \tag{40}$$

The effective power reflection is 0.064 x 0.278 =1.77 %. This value is in fair agreement with the measured voltage reflection of approximately −10 dB (see Fig. 6), which corresponds to a power reflection of about 1 %, for a 1.4 cm diameter 713 Ω/□ resistance disk suspended inside a C-band square waveguide. The discrepancy is probably caused by neglecting the effect of diffraction in obtaining the correction factor.

Having achieved satisfactory agreement between the calculated and the experimental results for a resistive sheet partially covering a C-band rectangular waveguide, we want to extend the present calculations to a dielectric-filled (CdTe) 5.4 mm x 5.4 mm waveguide at 16 GHz.

We assume that the resistive sheet is a plasma sheet of dense free carriers excited thermally by a pulsed laser beam. In particular, at a carrier density of 1 x 10^{16} cm^{-3} occurring at a medium temperature of 694 °C, the plasma sheet as an electric circuit can be characterized as:

$$n_r = n - j\kappa = 5.64 - j4.63 \tag{41}$$

The corresponding surface impedance Z_s for a 30 μm thick sheet is:

$$Z_s = 689.8 - j137.0 \ \Omega \tag{42}$$

The only other required parameter is the waveguide impedance, which is $Z_g = 139\ \Omega$; the value of guide impedance is lower because the permittivity is about 10.4.

Next, we substitute numerical values for Z_g and Z_s in eq (36) to determine the microwave voltage reflection R as follows:

$$R = \frac{1}{1 + 2(Z_s)/139} = 0.090 \tag{43}$$

The power reflection is then about 0.0081. For a $1/e^2$ optical beam diameter of 3 mm impinging on the modulator crystal inside a 5.4 mm x 5.4 mm square waveguide, the reduction in power reflection using an expression similar to eq (40):

$$\text{Correction Ratio} = \frac{4(0.0147)}{0.54 * (0.54/2)} = 0.40 \tag{44}$$

Therefore, the effective power reflection is about 0.32 % at 16 GHz for a carrier density of about 1 x 10^{16} cm^{-3}. Extending the calculations to other cases, we obtain the results shown in tables 3 and 4 for the calculated power reflections at 5 GHz and 16 GHz, respectively for various carrier densities. In table 3, the observed reflections are also given for comparison purposes.

Table 3. Microwave power reflection at 5 GHz

Temperature (°C)	Carrier density (10^{16} cm^{-3})	Calc. power reflection	Power reflection from figure 7
528	0.100	0.0007	not extrapolated
604	0.316	0.0038	not extrapolated
694	1.000	0.0177	0.0080
804	3.160	0.056	0.0190
940	10.000	0.113	0.0450

5. Microwave Absorption

The imaginary part of the refractive index, κ, listed in table 2 is a measure of the microwave attenuation. The microwave absorption coefficient, α, is given by

$$\alpha = \frac{4\pi\kappa}{\lambda_0} \tag{53}$$

Table 4. Microwave power reflection at 16 GHz

Temperature (°C)	Carrier density (10^{16} cm^{-3})	Calc. power reflection
528	0.100	0.00022
604	0.316	0.00065
694	1.000	0.00320
804	3.160	0.01400
940	10.000	0.04400

The microwave transmission T_r is then

$$T_r = e^{-\alpha \ell} \tag{54}$$

where ℓ is the thickness of the plasma sheet. For small values of $\alpha\ell$, the loss is simply $\alpha\ell$. Table 5 lists the microwave losses, $\alpha\ell$, for different carrier densities at 16 GHz. In calculating the losses, we used the same correction factor that was used previously for the microwave transmission, namely, 0.40 at 16 GHz.

Table 5. Microwave absorption at 16 GHz

Temperature (°C)	Carrier density (10^{16} cm^{-3})	Frac. power absorbed
528	0.100	0.0087
604	0.316	0.020
694	1.000	0.036
804	3.160	0.060
940	10.000	0.090

In a CdTe modulator housing containing three CdTe crystals, there are six end faces where possible high absorptions occur. Therefore, one percent absorption per surface is perhaps too high for proper modulator operation. Based on the results presented in table 5, it appears that microwave absorption is a more severe problem than microwave reflection. For detection of optical microwave interaction effects in CdTe, a method based on microwave absorption is perhaps more sensitive. For example, if the detection sensitivity for microwave absorption is as high as 0.1 %, a free carrier density of 1 x 10^{14} cm^{-3} can then be detected which translates to a temperature of about 400 °C or about 1/3 of the melting point of CdTe.

6. Experiments with Electro-Optic Modulator and Discussions

The effects of optical beam heating on microwave propagation in CdTe are being investigated experimentally in our laboratories. In particular, methods of reflection and absorption measurement have been devised which appear to be sensitive enough for detecting the effects that have been estimated. The CO_2 MOPA system in the MIT Plasma Fusion Center has been reactivated for the present optical microwave interaction study. This MOPA system is a TEA CO_2 laser system which is capable of delivering more than tens of joules. Because of the presence of a leading edge spike in the output pulse shape, a time delay technique will be used to minimize this effect and create a pulse of a few microseconds by amplifying the tail of the oscillation. Figure 9 is a schematic diagram of the TEA CO_2 laser MOPA system. All components are standard manufactured items from Lumonics Inc. Modifications have been made to produce single frequency operation for far IR pumping applications. The laser beam profile in general is slightly elliptical.

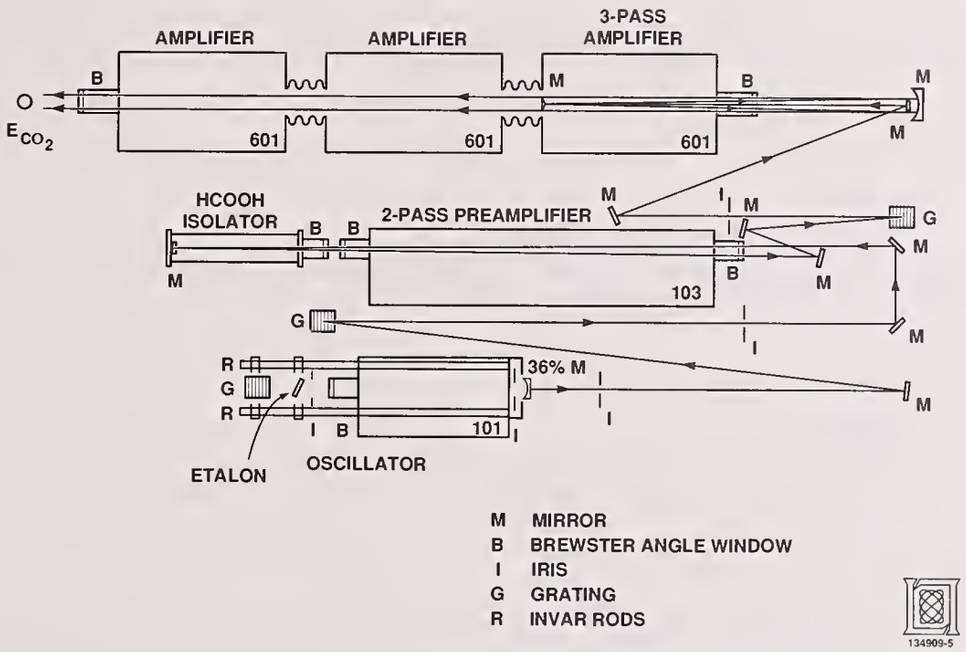

Figure 9. Schematic diagram of a TEA CO_2 laser MOPA system

So far we have considered only the microwave reflection and attenuation problems. Examining table 2 shows that the microwave phase shift can also be affected because of the change in the index from the room temperature value. For example, for a change in the refractive index value of 5 occurring at a free carrier density of about 3 x 10^{16} cm^{-3}, the total change in phase is about 0.12 radian for a modulator section containing three CdTe crystals with six possible absorption segments each 30 μm thick at the ends of the crystals. Because a proper microwave phase is required for effective interaction with the optical beam, the effect of a small perhaps not negligible phase shift on the modulator conversion efficiency is deemed complicated and must be investigated carefully using the modulator interaction theory. We plan to pursued this topic in future work.

Finally, we have not considered the effect of laser beam heating on the semiconductor compensation doping; it is possible that additional free carriers due to the doping ions are generated which may further reduce the medium impedance.

7. Summary and Conclusions

Based on theoretical analysis and plasma simulation using conducting disks inside a C-band waveguide, it appears that the microwave propagation in CdTe can be affected at temperatures lower than the melting temperature. The degree of degradation in microwave propagation depends on the maximum temperature reached and the plasma sheet thickness assumed. Based on the known value of thermal diffusion, a sheet thickness of 30 μm is a reasonable estimate. Assuming this thickness and that the hot region has about the same radial extent as the laser beam, it appears that a temperature of about 730 °C will give rise to a reflection of about 1 % and about 4 % at 940 °C and an absorption on the order of 1 % would occur at a temperature of about 550 °C and about 10 % at 940 °C. Measurements of microwave transmission can be used as a diagnostic to study the damage process. For example, a measurement of the change of microwave

reflectivity as a function of number of pulses for fixed laser pulse energy might be used to study possible changes in thermal conductivity. Other effects to be investigated are the microwave losses associated with continuous heating at moderate temperatures [15].

8. Acknowledgment

The authors would like to thank L. J. Sullivan, W. E. Keicher, B. E. Edwards, and B. Lax for helpful discussions. This research was supported by the Department of the Navy for SDIO under contract F19628-85-C-0002.

9. References

[1] J. R. Myer, F. J. Bartoli, and M. R. Kruer, "Optical heating in semiconductors," Phys. Rev. 21B, 1559(1980).

[2] J. R. Myer, M. R. Kruer, and F. J. Bartoli, "Optical heating in semiconductors: Laser damage in Ge, Si, InSb, and GaAs," J. Appl. Phys. 51, 5513(1980).

[3] R. S. Eng, J. G. Grimm, J. Greene, J. A. Daley, and N. W. Harris, "Measurements of Ultra-wide Pulse Damage Thresholds of Anti-reflection Coated IR Materials at 10.6 μm," Paper presented at the Eighteenth Annual Symposium on Optical Materials for High Power Lasers," Boulder, Colorado(Oct. 26–28, 1987).

[4] J. G. Grimm, R. S. Eng, C. Freed, and R. G. O'Donnell, "Measurements of Pulse Damage Thresholds of AR Coated CdTe at 10.6 μm," Paper presented at the Nineteenth Annual Symposium on Optical Materials for High Power Lasers," Boulder, Colorado(Oct. 26–28, 1988).

[5] T. W. Walker, A. H. Guenther, and P. Nielsen, "Pulsed Laser-induced Damage to Thin-Film Optical Coatings–Part I: Experimental," IEEE J. Quantum Electron. QE–17, 2041(1981); T. W. Walker, A. H. Guenther, and P. Nielsen, "Pulsed Laser-induced Damage to Thin-Film Optical Coatings–Part II: Theory," IEEE J. Quantum ELectron. QE–17, 2053(1981);

[6] H. S. Bennett and C. D. Cantrell, "Absorbing precipitates in cadmium telluride: estimates for catastrophic laser-damage thresholds," Appl. Opt. 16, 2931(1977).

[7] M. Kruer, L. Esterowitz, R. Allen, and F. Bartoli, "Thermal models for laser damage in InSb photovoltaic and photoconductive detectors," Infrared Phys. 16, 375(1976).

[8] R. Doussain and H. P. LeBodo, "Thermal diffusivity of germanium, gallium arsenide, and cadmium telluride," in Laser Induced Damage in Optical Materials: 1975, A. J. Glass and A. H. Guenther, eds. (NBS Special Publication 435), p. 98.

[9] G. A. Slack, "Thermal Conductivity of II–VI Compounds and Phonon Scattering by Fe^{2+} Impurities," Phys. Rev. B, 3791(1972).

[10] C. H. Lee, P. S. Mak, and A. P. DeFonzo, "Optical Control of Millimeter-Wave Propagation in Dielectric Waveguides," IEEE J. Quantum Electron. QE–16, 277(1980).

[11] A. J. Strauss, "The physical Properties of Cadmium Telluride," Rev. Phys. Appl. 12, 167(1977).

[12] R. K. Willardson and A. C. Beer, Semiconductors and Semimetals, Vol. 13, Cadmium Telluride, K. Zanio, ed. Academic Press, New York, 1978, Chapter 2.

[13] A. A. Oliner, "Equivalent Circuits for Small Symmetrical Longitudinal Apertures and Obstacles," IRE Trans. on Microwave Theory and Techniques, Vol. MTT-6, 72(1960).

COMMENTS

Question: A recent article I saw on silicon carbide concluded that, although its a nice material, it's still too expensive even for government work. Would you comment on the cost?

Answer: The reaction bonding process is a cheap process. You make up a slip; you cast it into a mold of whatever shape you want; you can include leachable cords to make closed-back mirrors; you can get very precise shapes. This process in itself is very cheap compared to, say, the CVD process where you do have a large chamber and depositions take place over a long period of time. So the facilities are not as expensive. The starting materials are relatively cheap; the silicon carbide powder itself for the highest purity material is only about $25.00 a pound. It's a low cost material. The expense primarily comes in the polishing, and we're looking to reduce that with these polishing methods. We think that we can bring the price down substantially.

Question: In your IBS process, you used a beta silicon carbide target, if I remember. Did you try an alpha-mixed target; did you notice any difference in the target as far as a deposit?

Answer: With the IBS process, we only use the beta because it was available in a fully dense sheet form so we could get a decent sized target. We did not try using an alpha target for the IBS. With the ion-assisted deposition, we used alpha and beta as a source material from the E-beam gun and found no difference in the deposit, which was amorphous. We feel that since we did an amorphous deposit with the IBS process as well, it probably won't make a difference in the source material.

Question: Is there any difference in the thermal expansion with thermocycling? Is there any hysteresis effect in the multiphase material?

Answer: We haven't seen anything at room temperature. We've cycled up to 400°C and down to liquid nitrogen and have only made the measurement at room temperature. We see no change. We're going to be doing some cryogenic testing of bare and coated 6 inch spheres where we'll be doing interferometry at about 100 K and perhaps some intermediate temperatures.

Question: Is the thermoexpansion coefficient just a weighted average of the silicon and the silicon carbide?

Answer: To a first order, yes.

[14] M. D. Abouzahra, "Automatic Wide-Band Surface Resistivity Measurements of Resistive Sheets," IEEE Trans. Instru. and Measurement, IM-36, 1031(1987).

[15] D. M. Wong, private communications.

Question: In many situations where you have multiple phases or different crystal orientations in a polycrystalline substrate, you can sometimes even out the removal rates by the addition of chemical agents in a mechanical-chemical process. Have you studied that at all in these reaction bonded systems?

Answer: No, we haven't. We've looked strictly at diamond removal with essentially a fixed-in hard lap.

Question: We've done some polishing of silicon carbide and also noticed a difference between a mechanical profile versus an optical measurement, which we attributed in part due to the difference in optical properties between the various phases that were present. I would assume that if you were to use a Wyko or any kind of interferometric method that this will show up and contribute to the differences in height which you see, unless you were to silver the part of metallize it first. And of course the scattering results, maybe that was the other topic or other paper that you were referring to. When you look at scattering, you see a scatter difference that doesn't correlate with a profile measurement.

Answer: Yes. What we have seen is that when we aluminize the two-phase material, we get the same Wyko profiles and roughness, but the BRDF changes drastically.

Question: Following up on the earlier question on cost, you're probably in a unique position to comment on the relative cost for beryllium versus silicon carbide optics. Of course it's a function of the construction; lightweight or solid. If you made a lightweight face sheet or mirror and were making one out of silicon carbide and one out of beryllium, could you give a relative sense based on your own gut feeling as to where things are today? The difference between silicon carbide and beryllium today, is it roughly like 2 to 1 in cost?

Answer: Today, because the maturity of the silicon carbide is not there, it's more expensive than the beryllium. It's just not a mature process as yet. But with very little development, I think silicon carbide should be comparable in price or less than beryllium.

Manuscript received
4-2-90

Laser-Induced Damage to Silicon Photosensor Arrays

Chen-Zhi Zhang, Thierry Benchetrit, Steve E. Watkins, Rodger M. Walser,
and Michael F.Becker

Center for Materials Science and Engineering and
Department of Electrical and Computer Engineering
The University of Texas at Austin
Austin, Texas 78712

Laser-induced damage in two types of silicon photosensor array has been studied. The samples were MOS CCD time delay integration (TDI) sensors with a 2048x96 element array of pixels and CID photodiode arrays of 512x1 pixels. The laser source was a Q-switched 1064 nm Nd:YAG laser (10 Hz rep rate, 10 ns pulses with a 250 μm spot radius). Tests for morphological and electrical damage to the CCD arrays have been reported previously. In new experiments, the micro-damage morphology is examined and correlated with both the observed electrical degradation and newly observed stress effects. We report the observation of surface deformation and lattice defects due to laser-induced stresses in the SiO_2 and poly-silicon thin films on the silicon substrate. Measurements of damage for the CID arrays show them to be more resistant to laser damage than MOS structures such as CCD arrays. In addition, electrical degradation of these arrays was observed which affected the video output signal from the devices.

Key words: laser damage; silicon photosensor arrays; laser-induced electrical degradation

1. Introduction

In this work, we have carried out a series of laser damage and diagnostic tests on CCD and photodiode array imaging devices, including the detection of performance degradation by sensitive electrical measurements and the observation of morphological or microstructural changes using Normarski microscopy, SEM and TEM techniques. So far, the previous data seemed to be insufficient to analyze the possible effects of laser interaction and to clarify the laser damage mechanisms of these devices [1-3]. Solid-state sensors of this type are widely used in video cameras because of their high-performance and long lifetime. Recently, these devices are of great interest in laser-related applications, such as inter-satellite laser communications and laser-related imaging measurements.

The most commonly used solid-state imagers fall into two major categories according to their basic structure and physical principals: charge-coupled devices (CCDs) and photodiode arrays. CCDs have low-noise levels and are qualified for use in low light level imaging. Photodiodes, on the other hand, have the advantages of high quantum efficiency, high dynamic range, and no smearing between pixels [4]. Since they are both used in laser related applications, it is necessary to examine laser-induced performance changes and find their tolerance to laser-induced degradation or damage. Better understanding of the damage mechanisms of these sensors will allow improvements in their damage resistance and related systems' reliability.

Two main objectives of this paper are (1) to present the experimental results from this work to gain insight into laser-induced damage processes and possible physical mechanisms; and (2) to compare the related laser damage resistances and mechanisms between these two devices and to correlate the morphological damage with the electrical performance degradation for each kind of device. The next section describes the samples tested and the experimental setup and procedures. Section 3 gives the results obtained from the measurements of electrical performance and the micro-evaluation of laser-induced morphological damage to these two different devices. In section 3 we also correlate electrical degradation with morphological damage thresholds and discusses the damage mechanisms. Finally, in the fourth section, several conclusions are drawn from this work.

2. Samples and Experimental Procedures

The CCD samples used in these experiments were 2048x96 pixel, n-channel TDI CCD arrays with 13 x 13 μm pixel size, as shown in figure 1. The devices were fabricated on 100 mm diameter wafers by standard MOS-LSI processes [5], including two level poly-silicon gates with individual thicknesses of 0.5 to 0.6 μm, field oxide of 1.25 μm, and thin gate oxide of 0.1 μm. Figure 2a shows a schematic cross-section view of the CCD active area. Another type of sample tested, photodiode arrays, were packaged devices (EG&G RL-512S), containing 512 x 1 pixels with 25 μm x 2.5 mm pixel size and 3 μm thick cap oxide, as shown in figure 2b.

The laser source for these tests was a 1.06 μm Q-switched Nd:YAG laser with a pulse length of 10 ns (FWHM) at a 10 Hz repetition rate. The incident energy on the samples was controlled by an attenuator consisting of a rotating halfwave plate followed by a fixed thin-film polarizer. A 76 cm focusing lens was used to obtain Gaussian spot sizes on the sample with a radii about 250 μm. The computer calibrated the detectors, recorded the beam spot size, recorded the energy of each incident pulse, and controlled the shutter which blocked the laser beam after the desired number of pulses. During the testing process, the samples were positioned using a coaxial HeNe beam and a 20x alignment microscope which was used to check for gross surface damage.

Following laser irradiation, both CCDs and photodiode arrays were arranged to be tested in the following sequence: first electrical measurements, and then morphological observations, some of which were destructive to the samples. For CCDs, the leakage currents and breakdown voltages between the two adjacent poly-silicon clock lines were measured with a HP 4145B semiconductor parameter analyzer and a probe station. Since these two parameters are very sensitive to laser-induced degradation as compared to those obtained from the other on-wafer test patterns, such as resistor bars, MOS capacitors and MOSFETs [6], the extent of electrical damage can best be described in terms of them. After electrical evaluation, careful morphological examination of the poly-silicon lines was done under a 50-1000x Nomarski optical microscope. As in our previous work, morphological damage has been defined as any visible change on the sample, especially color change within the laser spot observed under the Normarski microscope. In order to observe the microstructural changes of poly-silicon films before and after laser irradiation, some samples were investigated by SEM and TEM. Those samples were prepared by conventional methods. The major procedures were: (1) for SEM samples, polishing a cross-section of the devices at a 30^{o} angle and removing the top and isolating oxides in a buffered HF solution; (2) for TEM observations, etching the silicon substrate from the backside of the CCD active area as well as removing the top oxide as described above.

The performance of the photodiode arrays was tested at dark, half- and saturation illumination levels using an EG&G RC1000/RC1001 evaluation board. Electrical degradation of the devices was characterized by the dark leakage current in each junction element. The detailed experimental setup and typical video signal waveforms measured at each test point on the evaluation board are shown in figure 3. The dark leakage current corresponding to each pixel element was determined from these video signals. The unprocessed video test point on the evaluation board gave the best correspondence to the degree of electrical damage as it is most closely correlated to the raw recharge current of the pixel. After signal processing (integrating the recharge current, sampling, and holding), the change in the video signal output due to laser-induced leakage in each pixel was recorded. Operation of the imagers at half- and saturated illumination was then carried out to characterize the their functional degradation in terms of photo response. These techniques are appropriate for determining local pattern noise and for correlating dark-current increase with physical defects on a pixel-by-pixel basis.

3. Results and Discussion

3.1 CCD Arrays

It is apparent that the electrical isolation between two adjacent poly-silicon lines is sensitive to laser irradiation. Shown in figures 4a and 4b, respectively, are the leakage current and breakdown voltage for adjacent poly-silicon clock lines in the CCD active area as a function of laser fluence. The onset of changes of both parameters started at laser fluences as low as 0.3 J/cm^2. Both high leakage and low breakdown voltage occurred at fluences above 0.4 J/cm^2. Such degradation would usually lead to electrical failure since during normal operation the peak-to-peak voltage between the lines is about 12 V. The electrical damage threshold for the clock lines can be defined as the laser fluence at which the leakage current is above 1 μA or the breakdown voltage is below 25 V, which are drawn with the broken straight lines in figures 4a and 4b at about 0.55 J/cm^2 in both cases.

Figure 5 gives a typical SEM micrograph for a sample irradiated at 0.7 J/cm^2. It is clear that the edges of the poly-2 lines were broken and very ragged, while the same parts for undamaged areas look straight and smooth. Such minor morphological changes indicate that melting has occurred and deformed those edges These changes in turn appear to be related to the increase of leakage current and the decrease of breakdown voltage.

After laser irradiation at the morphological damage threshold, the poly-silicon grain size changes are remarkably different in the four sections of poly-silicon lines, as shown in figure 6a. For unirradiated regions, the average grain sizes of both poly-silicon lines were nearly the same (about 0.8 to 1 μm). Over the thick oxide or field oxide the grain size of poly-Si 2 (5 μm wide) was changed to very fine particles 20 to 30 nm in size, and the grain structure of poly-Si 1(8 μm wide) became long horizontal cells or columnar grains 0.2 x 1μm in size. Over the thin oxide or gate oxide, very slight melting at grain boundaries was observed, but no significant grain size change occurred. Figures 6b-6d illustrate typical TEM diffraction rings corresponding to the changes in grain structure in the different regions. In figure 6d for example, the diffraction pattern looks much denser due to the fine grain size. In figure 6a, changes are also visible in the oxide between the clock lines. Many poly-silicon inclusions have been formed in the oxide by the laser irradiation. These inclusions, which may be responsible for the electrical leakage between clock lines, were most probably formed when the edges of the poly-silicon lines melted.

The above phenomena can be explained in terms of local temperature extremes in different parts of the devices induced by transient laser heating. These temperature rises depend strongly on the thermal parameters and device structure. The absorption length at 1.06 μm has been found to be about several μm for heavily doped or implanted silicon and poly-silicon, while it is about 300 μm for high resistivity single crystal silicon [7-8]. Our results show that strong absorption in the heavily doped poly-silicon films results in a higher surface temperature response. Since the thermal conductivity of Si is about one order of magnitude higher than that of SiO_2, thicker oxide isolation of the poly-silicon from the substrate gave less heat conduction, which in turn led to a higher transient temperature response. For the narrower poly-silicon lines (poly-Si 2) on the thicker oxide, the highest temperature peak was expected. In this case, a grain fine structure was produced during rapid quenching following fast melting. Within the wider poly-Si 1 line on the field oxide, the major heat flux flowed along the line direction, which resulted in the observed columnar grain structure parallel to the line. The poly-silicon lines on the gate oxide suffered less extreme heating because the thinner oxide conducted much more heat into silicon substrate. Computer simulations of transient heating in this structure are in progress to further analyze the effects of materials, structures, and variable laser energy absorption mechanisms.

In addition to thermal properties, process related stress induced by the intra-granular oxidation of the poly-silicon films may play a role in the morphological damage threshold. Since the volume increases by a factor of two during the growth of silicon oxide on silicon, a compressive stress may be generated along the grain boundaries during oxidation [9]. When transient laser heating relived surface stress, the poly-silicon surface appeared significantly rougher and more uneven under the cap oxide when observed using an optical microscope. The degree of roughness was reduced for a series of samples which were prepared by etching the cap oxide to different thicknesses in a buffered HF solution before laser irradiation. This phenomena was probably related to the relief of process-induced stress at the poly-silicon film surface.

3.2 Photodiode Arrays

The electrical degradation of the photodiode arrays was investigated by studying the video signals obtained from test points on the evaluation circuit card. Signals from damaged and undamaged pixels at dark-, half-, and saturated-illumination are shown in figures 7a-c, where the top curve is the raw video signal from the test point immediately following the pre-amplifier, the middle curve is after charge integration, and the bottom one is the final sample-and-held video output signal. This site was irradiated at 2.2 J/cm^2 which was just above the onset of electrical damage but well below the onset of visible morphology change. For those pixels located near the center of the laser spot, significant dark leakage was measured, and no photo response was present. The video output signal from these damaged pixels was at the saturated white level. In figure 7d, the raw video signal from the same damage site is examined for two different charge integration times, 10 ms and 40 ms. Both the peak recharge current voltage drop, $\Delta V_{recharge}$ (negative spike) and the equilibrium recharge current voltage drop, $\Delta V_{leakage}$ (plateau after the spike) gradually increased (negative signal) from the edge to the center of the laser irradiation spot. These two signal features are related to the loss of stored charge in each damaged pixel during the integration time and to the voltage drop due to leakage during the recharge period respectively. Note that the longer 40 ms integration time curve in figure 7d revealed a slight increase in the recharge spike for the third pixel which was not evident for the shorter integration time. Although other sites were irradiated at 1.8, 1.9, 2.0 J/cm^2 and higher fluences, only those sites irradiated at 2.0 J/cm^2 or higher showed electrical damage similar to that in figure 7. All of the sites irradiated at fluences below 2.0 J/cm^2 showed no degradation, and none were observed to have any small leakage increases of the type observed at the edges of the clearly damaged sites, even when observed at long integration times. Thus, the electrical damage threshold was abrupt at 2.0 J/cm^2.

In order to compare the magnitudes of these changes in electrical parameters and quickly assess the degree of damage, a bar chart representing the two leakage components described above was prepared as shown in figure 8. The results on the left sides of the damage sites show that ,at the onset of electrical performance changes, the recharge current peak is the most sensitive parameter to laser-induced change. This is only clear when the scan direction (from left to right in the figures) is taken into account. On the right side of the damage sites, a finite recovery time for the recharge circuitry is observed in the form of a finite $\Delta V_{leakage}$ at one or more undamaged pixels. Furthermore, those pixels showing morphological changes are denoted in figure 7 by a darker shading on their $\Delta V_{recharge}$ bars. For the heavily damaged central pixels at site 3 there was no recharge peak visible, and presumably those sites are showing more resistor-like than capacitive, diode-like behavior and are practically shorted.

A sequence of micrographs showing laser-induced morphological changes on photodiode arrays as a function of increasing laser fluence are shown in figures 9a-9c. This device has a 3 μm thick cap oxide and showed damage behavior which was dependent on the heating behavior of the silicon below it. The examples shown in figure 9 include: (a) plastically deformed bump at F = 2.9 J/cm^2; (b) cracks at the spot center at F = 3.0 J/cm^2; and (c) fractures and ruptures at F = 3.5 J/cm^2 and above. From these results we deduce that a very high vapor pressure existed under the thick cap oxide during transient heating. At 2.9 J/cm^2 the resulting high temperature and pressure induced plastic deformation of the cap oxide which resulted in a permanent bump after cooling. At higher fluences, the pressure was high enough to break the oxide, while some evidence of plastic deformation remained around the edge of oxide opening. However, for multi-shot damage, all evidence of plastically deformed edges around the oxide window have been removed as shown in figure 9d. Perhaps the multiple temperature cycles propagated cracks and removed the deformed oxide area.

To explain the above electrical and morphological damage behavior, the following damage mechanism is considered to be responsible for the electrical damage. At laser fluences near the electrical damage threshold, a limited number of defects are introduced into the surface junction region due to the rapid heating and cooling rates. In a previous study of PIN photodiodes, those defects consisted of point defects which acted as deep levels within the energy gap [2]. For higher fluences, shallow melting of the silicon surface occurred, and rapid resolidification left a large number of defects at the junction termination. The presence of these defects greatly increased the the leakage and resulted in saturated video output. In severe damage cases, surface melting or even boiling at the silicon surface resulted in an electrical connection between adjacent pixels as observed in [10]. In such cases, it was impossible to detect individual pixel damage because leakage from adjacent pixels could smear together and increase the total leakage current.

As a summary of this section, table I gives the results of 1-on-1 laser-induced damage for all samples. It also shows the trend of sheet resistance change in poly-silicon films by laser heating [6]. Both types of imaging devices were found to have lower thresholds for electrical damage than for morphological damage. These data are consistent with our proposed damage models: (1) for CCDs, poly-silicon films have a large optical absorption coefficient so that the isolating oxide between poly-silicon lines was easily damaged; and (2) for photodiodes, the surface termination of the p-n junction was degraded and resulted in increased leakage current.

4. Conclusions

We have studied laser-induced damage effects on two kinds of silicon imaging arrays and have investigated both electrical performance degradation and morphology changes. The strong optical absorption in and thermal isolation of the poly-silicon films leads to much lower damage thresholds for CCD arrays than for bulk silicon photodiodes. Electrical degradation of the isolation oxide between adjacent CCD poly-silicon clock lines was due to laser-induced heating and quenching cycles and to changes which these cycles caused in the microstructure of the poly-silicon lines. These effects were related to the thermal isolation of the lines and built-in stress from the fabrication process. For photodiode arrays, a detection and test technique for evaluating dark leakage current has been described. It was found that the electrical degradation threshold for photodiode arrays is somewhat lower than the onset of visible morphological damage but considerably higher than the onset of electrical degradation in CCDs. The electrical damage onset for photodiode arrays was also found to be lower than that in discrete photodiodes in which the surface junction termination was not irradiated. These results have further verified that the laser-induced defects in the p-n junction region are responsible for the increase of the dark leakage current in many types of photodiode devices.

We acknowledge the assistance of Bob Maddoux of EG&G Reticon in providing us with the photodiode array samples.

5. References

[1] D. L. Parker, F.-Y. Lin, S.-J. Zhu, D.-K. Zhang, and W. A. Porter, "A comparison of Nd:YAG fundamental and second-harmonic Q-switched laser-beam lifetime doping in single-crystal silicon," IEEE Trans. on Elect. Dev. **ED-30**, 1322 (1983).

[2] S. E. Watkins, C.-Z. Zhang, R.M. Walser, and M.F. Becker, "Laser-induced electrical parameter degradation in silicon photodiodes," Proceedings of the 20th Annual Symposium on Optical Materials for Higher Power Lasers, NIST (NBS) Special Publication #775, 288, Boulder CO (1989).

[3] C.-Z. Zhang, S.E. Watkins, R.M. Walser, and M.F. Becker, "Laser-induced changes in the electrical performance of silicon MOS device structures," Proceedings of the 20th Annual Symposium on Optical Materials for Higher Power Lasers, NIST (NBS) Special Publication #775, 105, Boulder CO (1989).

[4] H.-F. Tseng, J. R. Ambrose, and M. Fattahi, "Evaluation of the solid-state image sensor," J. Imaging Sci. Vol. **29**, 1 (1985).

[5] J.P. Ellul, H.-Y. Tsoi, J.J. White, M.I. King, and W.C. Bradley, "State-of-the-art imaging arrays and their applications," Proceedings of SPIE **501**, 117 (1984).

[6] M. F. Becker, C.-Z. Zhang, S. E.Watkins, and R. M. Walser, "Laser-induced damage to silicon imaging sensors," SPIE **1105** Materials for Optical Switches, Isolators, and Limiters, 68 (1989).

[7] M. F. Becker, F. E. Domann, A. F. Stewart, and A. H. Guenther, "Charge emission and related precursor events associated with laser damage," Fifteenth Annual Symposium: Optical Materials for High Power Lasers, NBS Special Publication #688 (1984); and F. E. Domann, M. F. Becker, A. H. Guenther, and A. F. Stewart, "Charged particle emission related to laser damage," Applied Optics, Vol.**25**, 1371 (1986).

[8] J. D. Chlipala, L. M. Scarfone and C.-Y. Lu, "Computer simulated explosion of poly-silicide links in laser-programmable redundancy for VLSI memory repair," IEEE Trans. on Elect. Dev. **ED-36**, 2433 (1989).

[9] E. A. Irene, E. Tierney, and D. W. Dong, "Silicon oxidation studies: morphological aspects of the oxidation of polycrystalline silicon," J. Electrochem. Soc. **127**, 705 (1980).

[10] S.S. Cohen, P.W Wyatt, G.H. Chapman, and J.M. Canter, "Laser-induced diode linking for wafer-scale integration," IEEE Trans. on Elect. Dev. **ED-35**, 1533 (1988).

Table I: Summary of 1-on-1 Laser-induced Damage

Device	Fluence (J/cm^2)	Electrical Change	Morphological Change
	< 0.2	No Change	No Change
	0.2 - 0.3	Poly-Si: sheet R decrease; Clock lines: breakdown V decrease and leakage I increase	No Change
CCD	0.5 - 0.6	Electrical failure (clock lines becoming shorted)	Grain surfaces melted
	0.7 - 0.9	Electrical failure (clock lines shorted)	change in color (surface height increase); oxide damage pits
	1.0 - 1.2	Electrical failure (clock and Al lines melted, open circuit)	Top oxide broken
	< 1.9	No Change	No Change
Photo-diode	1.9 - 2.0	Junction leakage increases, no photo response	No Change
	2.9 - 3.0	Severe leakage	Oxide bump & crack Si surface melting
	> 3.5	Melting and total pn junction failure	Open oxide window

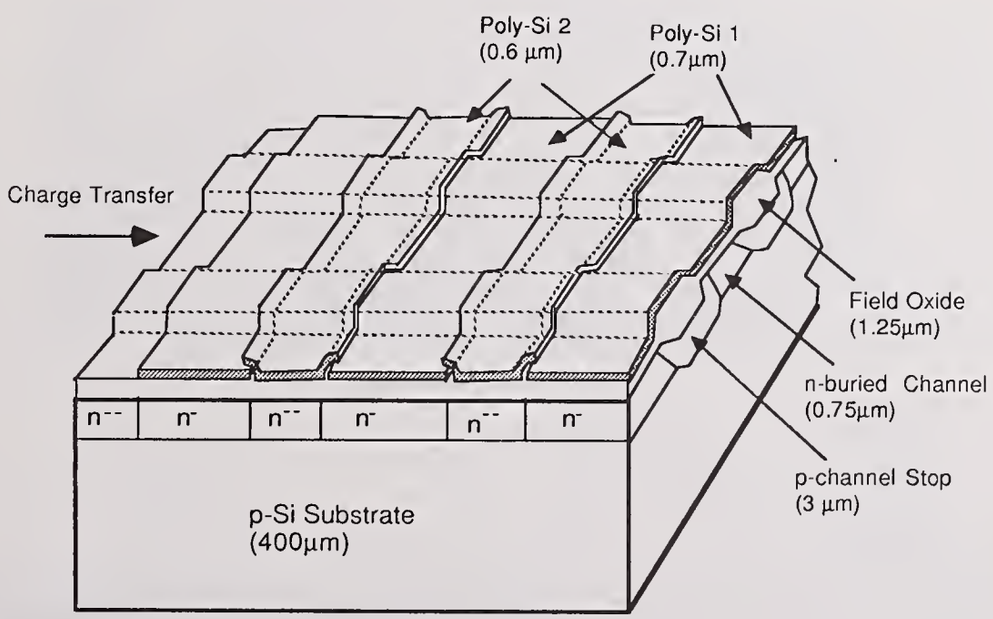

Figure 1. Projection view of the CCD active area.

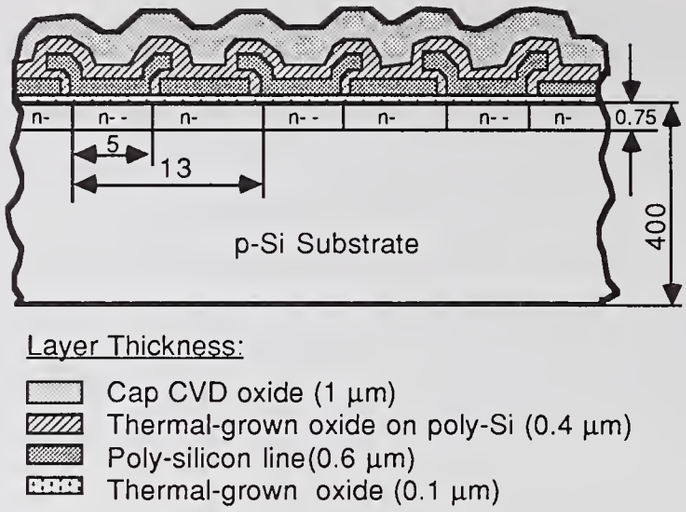

a.

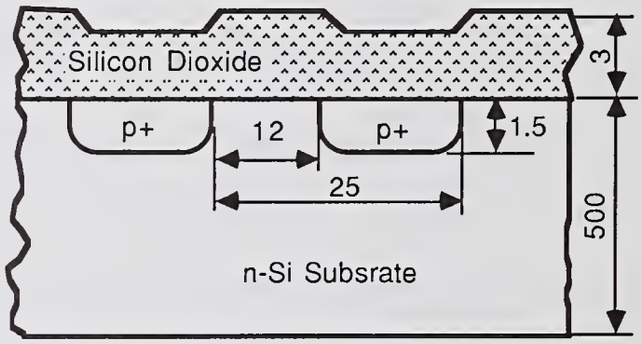

b.

Figure 2. Cross-section views of the test devices: a. CCD imaging array; b. photodiode array.

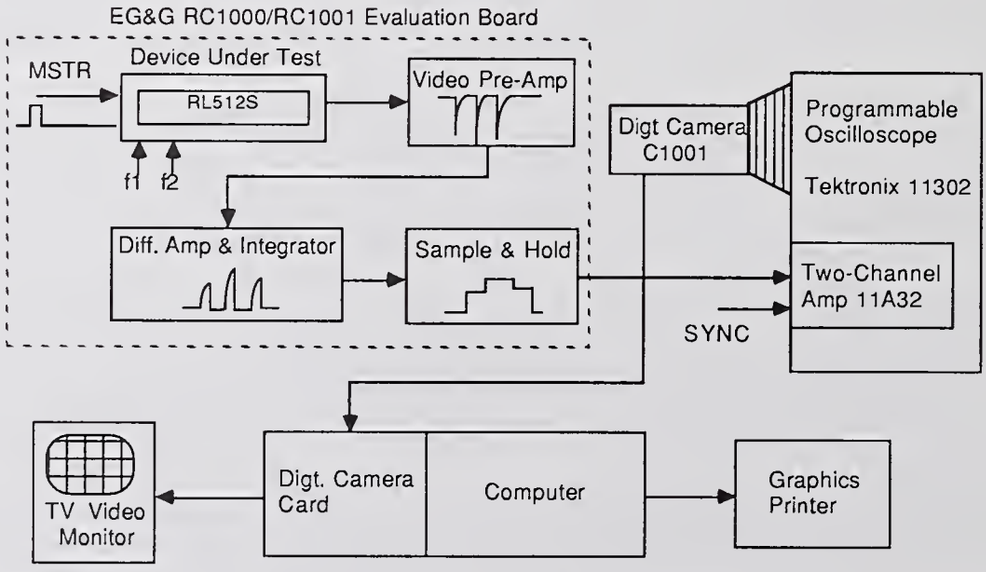

Figure 3. Block diagram of the measurement setup for photodiode arrays, where MSTR is a pulse signal starting a scan operation, f1 and f2 are two properly timed clock phase signals, and SYNC is an oscilloscope synchronizing signal.

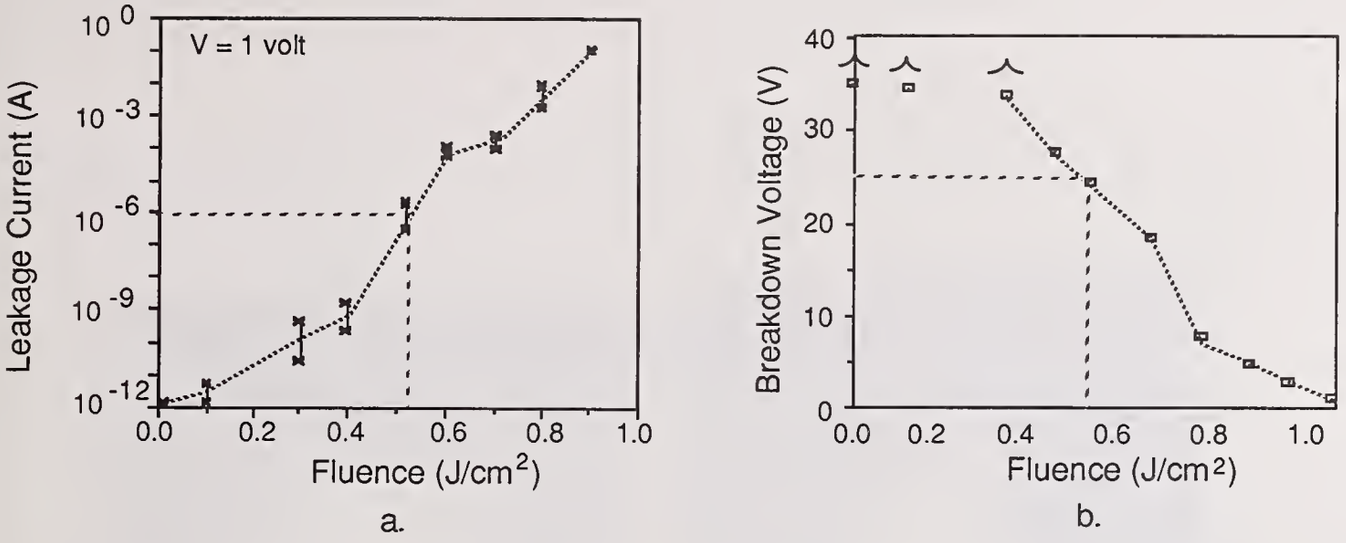

Figure 4. Measured clock line electrical parameters vs. laser fluence: a. leakage current between adjacent poly-silicon lines measured at 1 V applied voltage; b. breakdown voltage between adjacent poly-silicon lines. For fluences below 0.3 J/cm^2, the breakdown voltage was greater than 35 V.

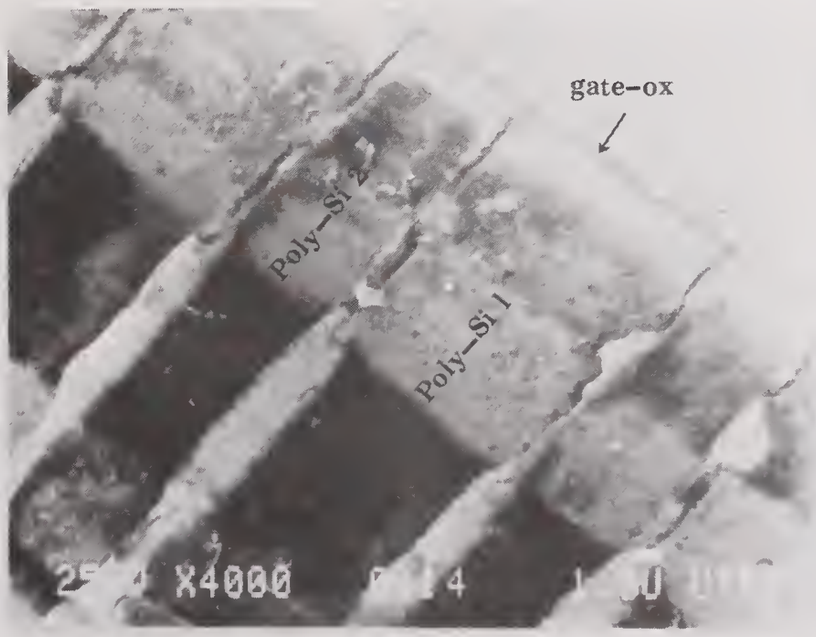

Figure 5. SEM micrograph of the CCD active area after irradiation at 0.7 J/cm^2. The cap oxide has been etched away; and in the upper-right half of the photo, the sample has been polished at a 30^o angle.

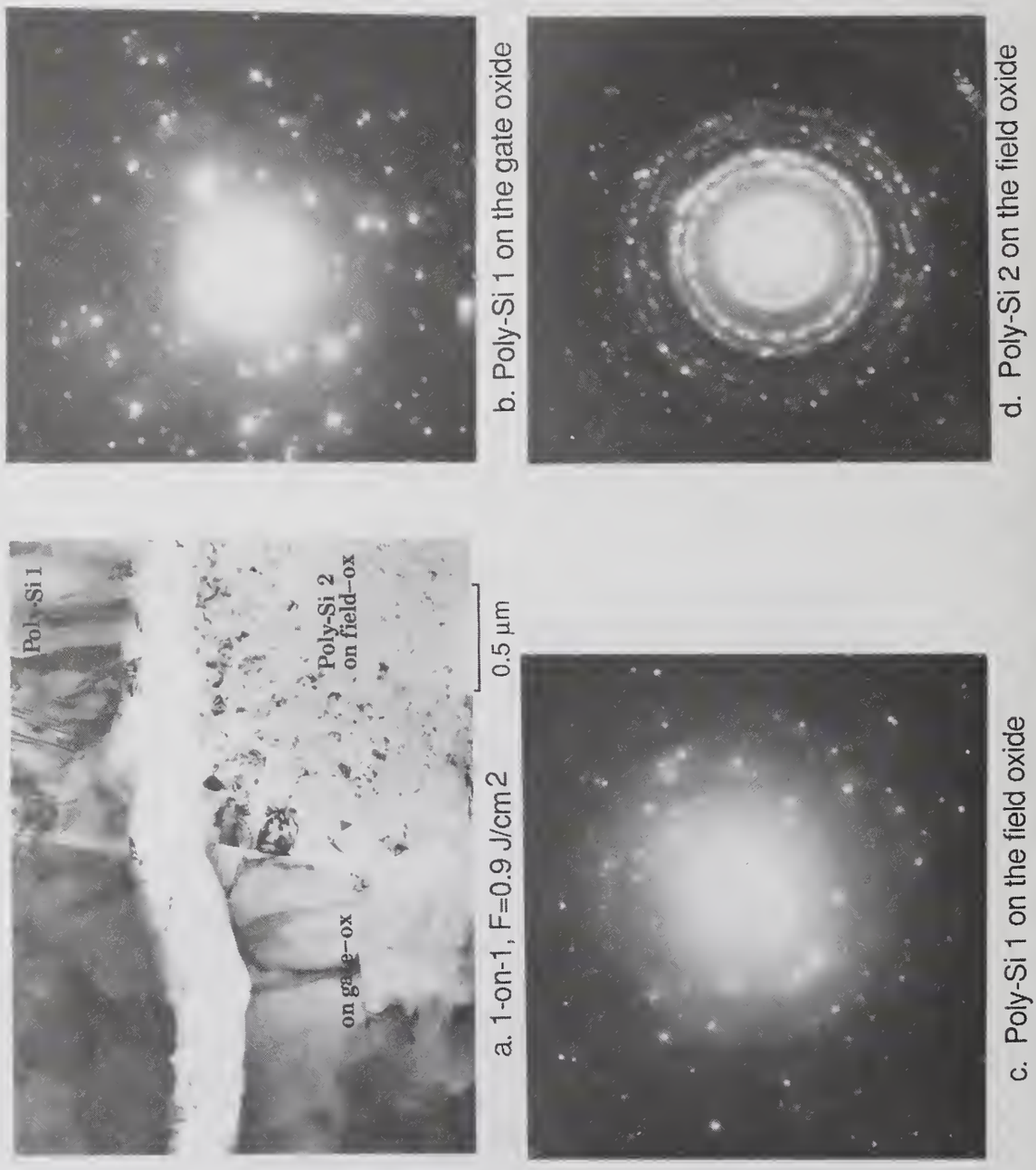

Figure 6. TEM micrographs of CCD poly-silicon lines: a. different grain size changes within the four regions after irradiation at 0.9 J/cm^2; b-d. typical TEM diffraction rings corresponding to three regions shown in figure 6a.

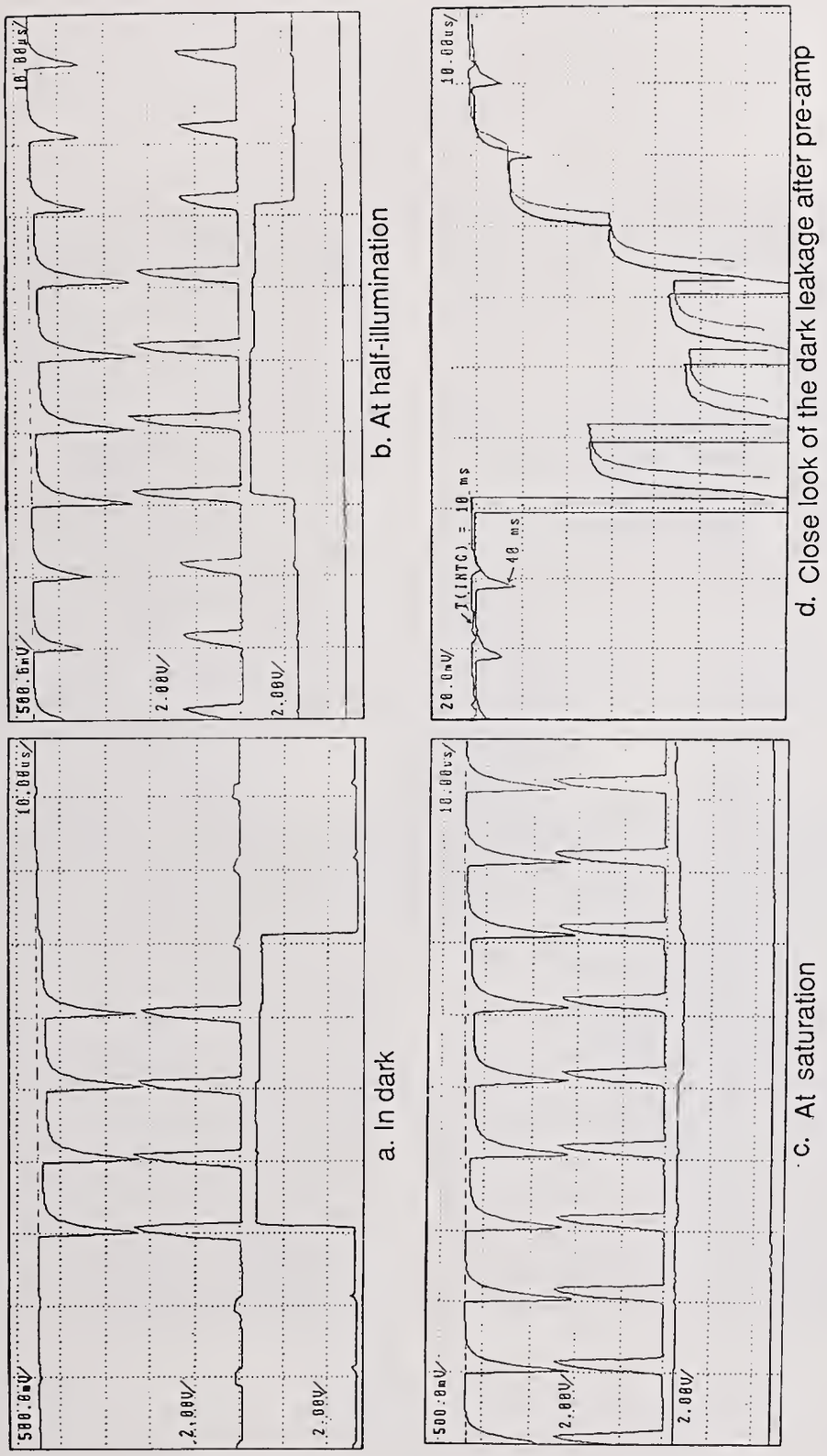

Figure 7. Video signals form photodiode pixels irradiated at 2.2 J/cm^2: a-c. correspond to the conditions of dark-, half-, and saturated-illumination respectively, where the top curve is the raw video signal from the test point immediately following the preamplifier, the middle curve is after charge integration, and the bottom curve is the final sample-and-held output signal; d. an expanded view of the dark leakage video signal for integration times of 10 and 40 ms.

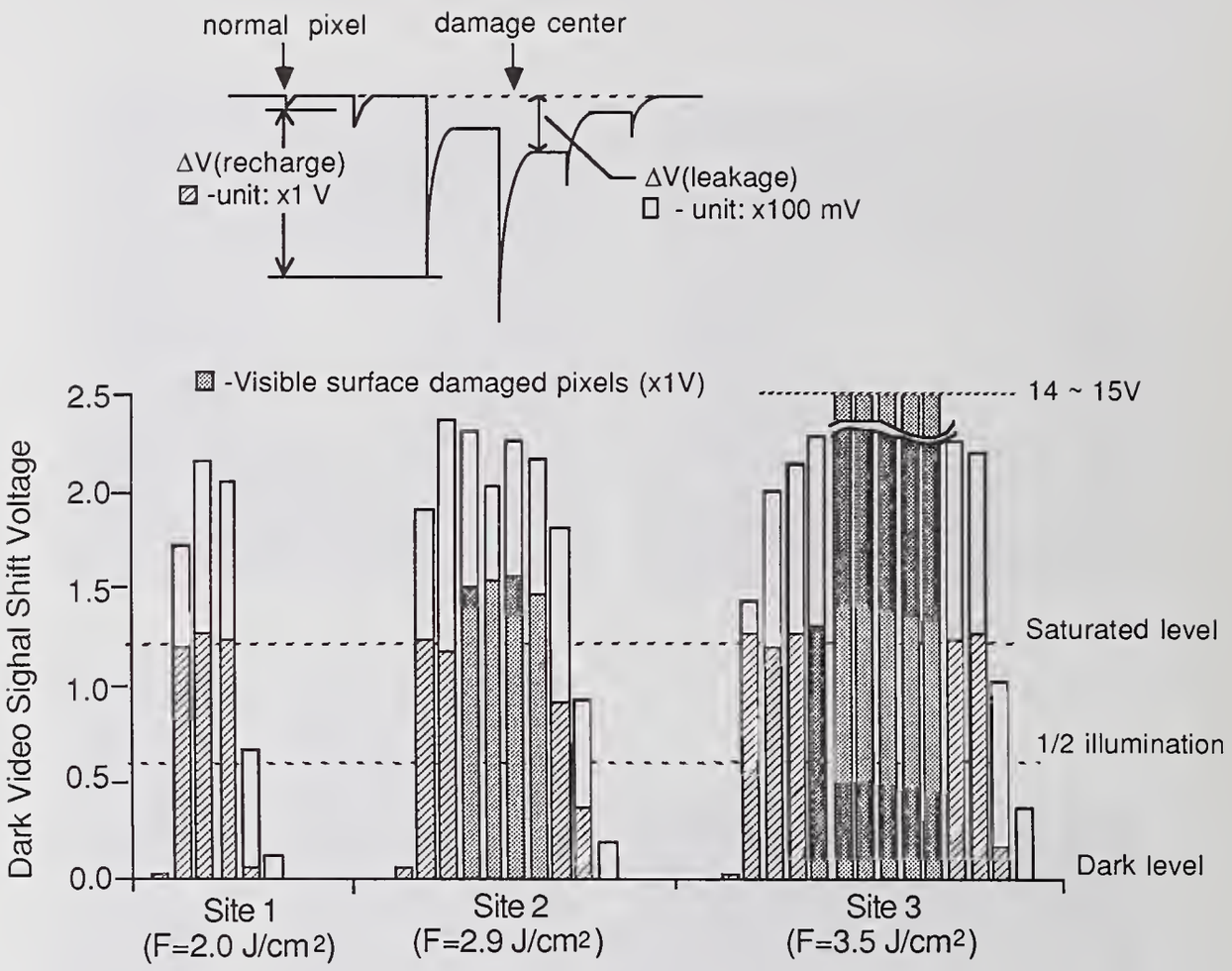

Figure 8. A bar chart representing the two leakage components, $\Delta V_{recharge}$ and $\Delta V_{leakage}$, from pixels at three damage sites of increasing laser fluence.

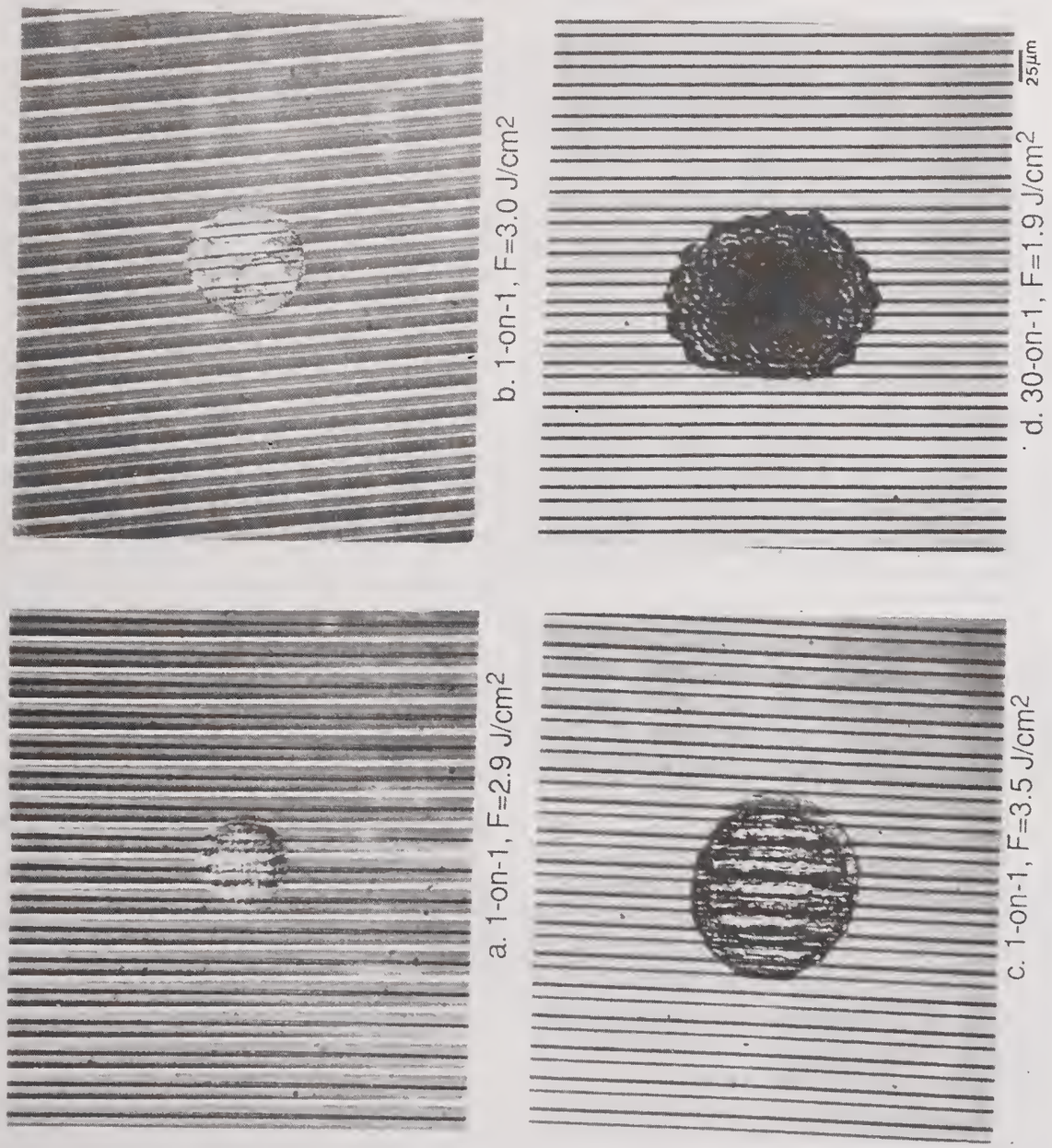

Figure 9. A sequence of Nomarski optical micrographs showing laser-induced morphological changes on photodiode arrays as a function of laser fluence.

Manuscript received
3-8-90

SENSITIVE n_2 MEASUREMENTS USING A SINGLE BEAM

M. Sheik-Bahae, A.A. Said, T.H. Wei,
D.J. Hagan, E.W. Van Stryland and M.J. Soileau

CREOL
Center for Research in Electro Optics and Lasers
University of Central Florida, Orlando, FL 32826

We present a sensitive single beam technique for measuring nonlinear refraction in a variety of materials that offers simplicity, sensitivity and speed. The transmittance of a sample is measured through a finite aperture in the far-field as the sample is moved along the propagation path (z) of a focused Gaussian beam. The sign and magnitude of the nonlinearity is easily deduced from such a transmittance curve (Z-scan). Employing this technique a sensitivity of better than $\lambda/300$ wavefront distortion is achieved in n_2 measurements of BaF_2 using picosecond visible laser pulses.

Key words: BaF_2; CS_2; experimental technique; Kerr effect; nonlinear refraction; Z-scan

1. INTRODUCTION

We have recently reported a single beam method, which we refer to as a Z-scan, for measuring the sign and magnitude of the nonlinear refractive index n_2.[1] In practice we have found that this method has a sensitivity comparable to interferometric methods. Here we describe this method in detail and demonstrate how it can be applied and analyzed for a variety of materials. We also present a simple method to minimize parasitic effects due to the presence of linear sample inhomogeneities.

Previous measurements of nonlinear refraction have used a variety of techniques including nonlinear interferometry [2], [3], degenerate four-wave mixing [4], nearly-degenerate three-wave mixing [5], ellipse rotation [6], beam distortion measurements [7], [8], and our recently reported Z-scan technique. The first three methods, namely nonlinear interferometry and wave mixing are potentially sensitive techniques but require a relatively complex experimental apparatus. Beam distortion measurements, on the other hand, are relatively insensitive and require detailed wave propagation analysis. The Z-scan technique is based on the principles of spatial beam distortion but offers simplicity as well as very high sensitivity.

We will describe this simple technique in Section II. Theoretical analyses of Z-scan measurements are given in Section III for a "thin" nonlinear medium. It will be shown that for many practical cases, nonlinear refraction and its sign can be obtained from a simple linear relationship between the observed transmittance changes and the induced phase distortion without the need for performing detailed calculations. In Section IV we present measurements of nonlinear refraction in a number of materials such as CS_2, and transparent dielectrics at wavelengths of 532 nm, 1.06 μm and 10.6 μm. In CS_2 at 10 μm, for example, both thermo-optical and reorientational Kerr effects were identified using nanosecond and picosecond pulses respectively. We also describe how effects of linear sample inhomogeneities (eg. bulk index variations) can be effectively removed from the experimental data.

2. THE Z-SCAN TECHNIQUE

Using a single Gaussian laser beam in a tight focus geometry, as depicted in Fig. 1, we measure the transmittance of a nonlinear medium through a finite aperture in the far field as a function of the sample position z measured with respect to the focal plane. The following example will qualitatively elucidate how such a trace (Z-scan) is related to the nonlinear refraction of the sample. Assume, for instance, a material with a negative nonlinear refractive index and a thickness smaller than the diffraction length of the focused beam (a thin medium). This can be regarded as a thin lens of variable focal length. Starting the scan from a distance far away from the focus (negative z) the beam irradiance is low and negligible nonlinear refraction occurs; hence, the transmittance (D_2/D_1 in Fig. 1) remains relatively constant. As the sample is brought closer to focus, the beam irradiance increases leading to self-lensing in the sample. A negative self-lensing prior to focus will tend to collimate the beam, causing a beam narrowing at the aperture which results in an increase in the measured transmittance. As the scan in z continues and the sample passes the focal plane to the right

(positive z), the same self-defocusing increases the beam divergence leading to beam broadening at the aperture and, thus, a decrease in transmittance. This suggests that there is a null as the sample crosses the focal plane. This is analogous to placing a thin lens at or near the focus, resulting in a minimal change of the far field pattern of the beam. The Z-scan is completed as the sample is moved away from focus (positive z) such that the transmittance becomes linear since the irradiance is again low. Induced beam broadening and narrowing of this type have been previously observed and explained during nonlinear refraction measurements of some semiconductors.[9],[10] A similar technique was also previously used to measure thermally induced beam distortion of chemicals in solvents.[11]

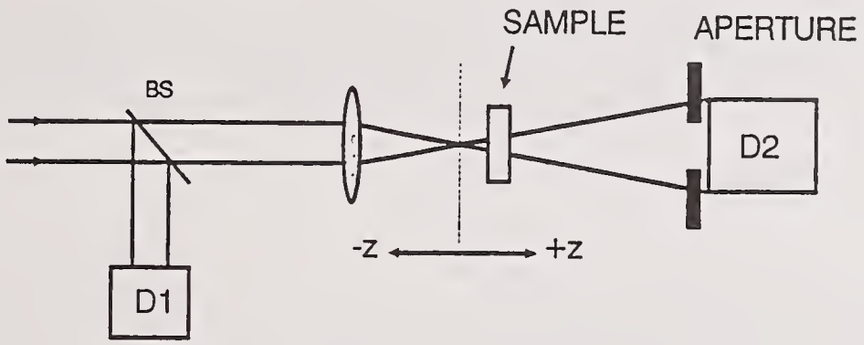

Fig.1 The Z-scan experimental apparatus in which the ratio D2/D1 is recorded as a function of the sample position z.

A pre-focal transmittance maximum (peak) followed by a post-focal transmittance minimum (valley) is, therefore, the Z-scan signature of a negative refractive nonlinearity. Positive nonlinear refraction, following the same analogy, gives rise to an opposite valley-peak configuration. It is an extremely useful feature of the Z-scan method that the sign of the nonlinear index is immediately obvious from the data, and as we will show in the following section the magnitude can also be easily estimated using a simple analysis for a thin medium.

In the above picture describing the Z-scan, one must bear in mind that a purely refractive nonlinearity was considered assuming that no absorptive nonlinearities (such as multiphoton or saturation of absorption) are present. Qualitatively, multiphoton absorption suppresses the peak and enhances the valley, while saturation produces the opposite effect. The sensitivity to nonlinear refraction is entirely due to the aperture, and removal of the aperture completely eliminates the effect. However, in this case the Z-scan will still be sensitive to nonlinear absorption. Nonlinear absorption coefficients could be extracted from such "open" aperture experiments.

3. THEORY

Much work has been done in investigating the propagation of intense laser beams inside a nonlinear material and the ensuing self-refraction [12], [13]. Considering the geometry given in Fig. 1, we will formulate and discuss a simple method for analyzing the Z-scan data based on modifications of existing theories.

In general, various order nonlinearities can be considered; however, for simplicity, we first examine only a cubic nonlinearity where the index of refraction n is expressed in terms of nonlinear indices n_2(esu) or $\gamma(m^2/W)$ through:

$$n = n_0 + \frac{n_2}{2}|E|^2 = n_0 + \gamma I \qquad (1)$$

where n_0 is the linear index of refraction, E is the peak electric field (cgs), and I denotes the irradiance (MKS) of the laser beam within the sample. [n_2 and γ are related through the conversion formula, $n_2(esu)=(cn_0/40\pi)\gamma(m^2/W)$, where c (m/sec) is the speed of light in vacuum]. Assuming a TEM_{00} Gaussian beam of beam waist radius w_0 traveling in the +z direction, we can write E as:

$$E(z,r,t) = E_0(t)\ \frac{w_0}{w(z)} \exp\left(-\frac{r^2}{w^2(z)} - \frac{ikr^2}{2R(z)}\right) e^{-i\phi(z,t)}\ , \tag{2}$$

where $w^2(z)=w_0^2(1+z^2/z_0^2)$ is the beam radius, $R(z)=z(1+z_0^2/z^2)$ is the radius of curvature of the wavefront at z, $z_0=kw_0^2/2$ is the diffraction length of the beam, $k=2\pi/\lambda$ is the wave vector and λ is the laser wavelength, all in free space. $E_0(t)$ denotes the radiation electric field at the focus and contains the temporal envelope of the laser pulse. The $e^{-i\phi(z,t)}$ term contains all the radially uniform phase variations. As we are only concerned with calculating the radial phase variations $\Delta\phi(r)$, the slowly varying envelope approximation (SVEA) applies, and all other phase changes that are uniform in r are ignored.

If the sample length is small enough that changes in the beam diameter within the sample due to either diffraction or nonlinear refraction can be neglected, the medium is regarded as "thin", in which case the self-refraction process is referred to as "external self-action". Such an assumption simplifies the problem considerably, and the amplitude $\sqrt{I}$ and phase ϕ of the electric field as a function of z′ are now governed in the SVEA by a pair of simple equations:

$$\frac{d\Delta\phi}{dz'} = \Delta n(I)\ k\ , \tag{3}$$

and

$$\frac{dI}{dz'} = -\alpha\ I\ , \tag{4}$$

where z′ is the propagation depth in the sample and α is the linear absorption coefficient. Note that z′ should not be confused with the sample position z. In the case of a cubic nonlinearity, Eqns. 3 and 4 are solved to give the phase shift $\Delta\phi$ at the exit surface of the sample, which simply follows the radial variation of the incident irradiance at a given position of the sample z. Thus,

$$\Delta\phi(z,r,t) = \Delta\phi_0(z,t) \exp\left(-\frac{2r^2}{w^2(z)}\right), \tag{5-a}$$

with

$$\Delta\phi_0(z,t) = \frac{\Delta\Phi_0(t)}{1+z^2/z_0^2}\ . \tag{5-b}$$

$\Delta\Phi_0(t)$, the on-axis phase shift at the focus, is defined as,

$$\Delta\Phi_0(t) = k\Delta n_0(t)\ \frac{1-e^{-\alpha L}}{\alpha}\ , \tag{6}$$

where L is the sample length, and $\Delta n_0 = \gamma I_0(t)$ with $I_0(t)$ being the on-axis irradiance at focus (ie.z=0). Again we take $I_0(t)$ as the irradiance within the sample to account for Fresnel reflection losses.

The complex electric field after the sample, E′, now contains the nonlinear phase distortion,

$$E' = E(z,r,t)\ e^{-\alpha L/2}\ e^{i\Delta\phi(z,r,t)}\ . \tag{7}$$

By virtue of Huygen's principle one can obtain the far field pattern of the beam at the aperture plane through a zeroth order Hankel transformation of E′.[14] We will follow a more convenient treatment applicable to Gaussian input beams which we refer to as the "Gaussian Decomposition" (GD) method given by Weaire et. al.[15], in which they decompose the complex electric field at the exit plane of the sample into a summation of Gaussian beams through a Taylor series expansion of the nonlinear phase term $e^{i\Delta\phi(z,r,t)}$ in Eq. 7. That is,

$$e^{i\Delta\phi(z,r,t)} = \sum_{m=0}^{\infty} \frac{[i\Delta\phi_0(z,t)]^m}{m!}\ e^{-2mr^2/w^2(z)}\ . \tag{8}$$

Each Gaussian beam can now be simply propagated to the aperture plane where they will be resummed to reconstruct

the beam. When including the initial beam curvature for the focused beam, we derive the resultant electric field pattern at the aperture as:

$$E_a(r,t) = E(z,r=0,t)\, e^{-\alpha L/2} \sum_{m=0}^{\infty} \frac{(i\Delta\phi_0(t))^m}{m!} \left[g^2+\frac{d^2}{d^2_m}\right]^{-\frac{1}{2}} \exp\left[-\frac{r^2}{w^2_m} - \frac{ikr^2}{2R_m} + i\theta_m\right], \tag{9}$$

where d is the propagation distance in free space from the sample to the aperture plane, and g=1+d/R , R=R(z) being the beam radius of curvature at the sample. As long as the far field condition is met, d can be considered independent of the sample position z resulting in symmetric Z-scans. The remaining parameters in Eq. 9 are expressed as:

$$w^2_{mo} = \frac{w^2(z)}{2m+1}, \qquad d_m = \frac{kw^2_{mo}}{2}, \qquad w^2_m = w^2_{m0}\left[g^2+\frac{d^2}{d^2_m}\right],$$

$$R_m = d\left[1- \frac{g}{g^2+d^2/d^2_m}\right]^{-1}, \quad \text{and } \theta_m = \tan^{-1}\left[\frac{d/d_m}{g}\right].$$

The expression given by Eq. 9 is a general case of that derived in Ref. [15] where they considered a collimated beam (R=∞) for which g=1. We find that this GD method is very useful for the small phase distortions detected with the Z-scan method since only a few terms of the sum in Eq. 9 are needed. The method is also easily extended to higher order nonlinearities.

The transmitted power through the aperture is obtained by spatially integrating $E_a(r,t)$ up to the aperture radius r_a, giving,

$$P_T(\Delta\Phi_0(t)) = \frac{c\epsilon_0 n_0}{2}\int_0^{r_a} |E_a(r,t)|^2\, r\,dr\,. \tag{10}$$

Including the pulse temporal variation, the normalized Z-scan transmittance T(z) can be calculated as:

$$T(z) = \frac{\int_{-\infty}^{\infty} P_T(\Delta\Phi_0(t))\, dt}{S\int_{-\infty}^{\infty} P_i(t)\, dt}, \tag{11}$$

where $P_i(t) = \pi w_0^2 I_0(t)/2$ is the instantanous input power (within the sample) and S is the aperture transmittance in the linear regime.

We first consider an instantaneous nonlinearity and a temporally square pulse to illustrate the general features of the Z-scan. This is equivalent to assuming cw radiation and the nonlinearity has reached the steady state. The normalized transmittance, T(z), in the far field, is shown in Fig. 2 for $\Delta\Phi_0 = \pm 0.1$ and a small aperture (S=0.01). They exhibit the expected features, namely a valley-peak (v-p) for the positive nonlinearity and a peak-valley (p-v) for the negative one. For a given $\Delta\Phi_0$, the magnitude and shape of T(z) do not depend on the wavelength or geometry as long as the far field condition for the aperture plane is satisfied. The aperture size S, however, is an important parameter since a large aperture reduces the variations in T(z). This reduction is more prominent in the peak where beam narrowing occurs and can result in a peak transmittance which cannot exceed (1-S). Needless to say, for very large aperture or no aperture (S=1), the effect vanishes and T(z) = 1 for all z and $\Delta\Phi_0$. For small $|\Delta\Phi_0|$, the peak and valley occur at the same distance with respect to focus, and for a cubic nonlinearity this distance is found to be $\simeq 0.85z_0$. With larger phase distortions ($|\Delta\Phi_0|>1$) this symmetry no longer holds and both peak and valley move toward ±z for the corresponding sign of nonlinearity ($\pm\Delta\Phi_0$) such that their separation remains relatively constant given by,

$$\Delta Z_{p-v} \simeq 1.7 z_0\,. \tag{12}$$

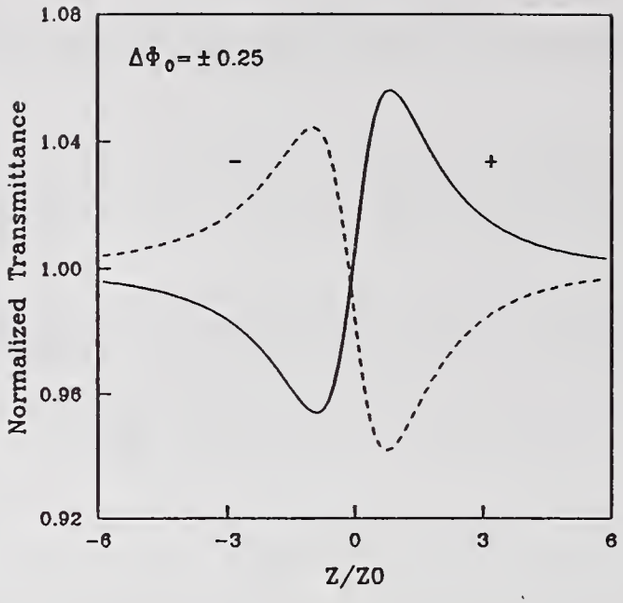

Fig.2 Calculated Z-scan transmittance curves for a cubic nonlinearity with either polarity and a small aperture (S=0.01).

We can define an easily measurable quantity ΔT_{p-v} as the difference between the normalized peak and valley transmittance: $T_p - T_v$. The variation of this quantity as a function of $|\Delta\Phi_0|$, as calculated for various aperture sizes is illustrated in Fig. 3. These curves exhibit some useful features. First, for a given order of nonlinearity, they can be considered universal. In other words, they are independent of the laser wavelength, geometry (as long as the far field condition is met) and the sign of nonlinearity. Second, for all aperture sizes, the variation of ΔT_{p-v} is found to be linearly dependent on $|\Delta\Phi_0|$. Particularly for on axis (S≃0) we find,

$$\Delta T_{p-v} \simeq 0.406\,|\Delta\Phi_0| \quad \text{for} \quad |\Delta\Phi_0| \leq \pi\,, \tag{13-a}$$

to be accurate to within 0.5 percent. As shown in Fig. 3, for larger apertures, the linear coefficient 0.405 decreases such that with S=0.5 it becomes 0.34 and at S=0.7 it reduces to 0.29. Based on a numerical fitting, the following relationship can be used to include such variations within a ±2% accuracy;

$$\Delta T_{p-v} \simeq 0.406(1-S)^{0.25}\,|\Delta\Phi_0| \quad \text{for} \quad |\Delta\Phi_0| \leq \pi\,. \tag{13-b}$$

The implications of Eqns. 13-a and 13-b are quite promising in that they can be used to readily estimate the nonlinear index (n_2) with good accuracy after a Z-scan is performed. What is most intriguing about these expressions is that they reveal the highly sensitive nature of the Z-scan technique. For example, if our experimental apparatus and data acquisition systems are capable of resolving transmission changes ΔT_{p-v} of ≃1%, we will be able to measure phase changes corresponding to less than $\lambda/250$ wavefront distortion. Achieving such sensitivity, however, requires relatively good optical quality of the sample under study. We describe in the experimental section IV a means to minimize problems arising from poor optical quality samples.

We can now easily extend the steady state cw results to include transient effects along with pulsed radiation by using the time averaged index change $\langle\Delta n_0(t)\rangle$ where,

$$\langle\Delta n_0(t)\rangle = \frac{\int_{-\infty}^{\infty} \Delta n_0(t)\, I_0(t)dt}{\int_{-\infty}^{\infty} I_0(t)dt}\,, \tag{14}$$

The time averaged $\langle\Delta\Phi_0(t)\rangle$ is related to $\langle\Delta n_0(t)\rangle$ through Eq. 6. With a nonlinearity having instantaneous response and decay times relative to the pulsewidth of the laser, one obtains for a temporally Gaussian pulse:

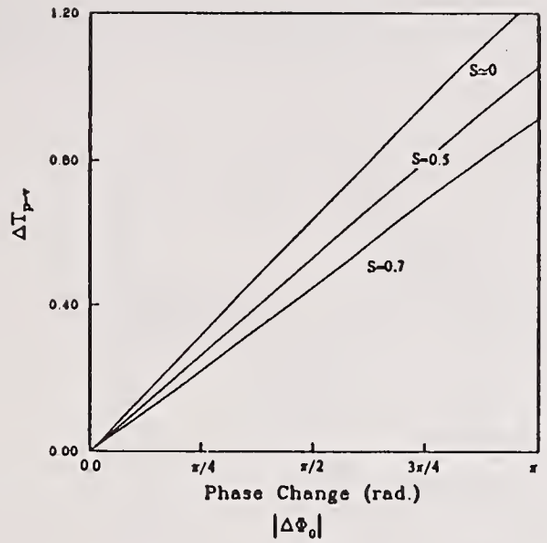

Fig.3 Calculated ΔT_{p-v} as a function of the phase shift at the focus ($\Delta\Phi_0$). The sensitivity, as indicated by the slope of the curves, decreases slowly for larger aperture sizes (S>0).

$$\langle \Delta n_0(t) \rangle = \Delta n_0/\sqrt{2} \ , \tag{15}$$

where Δn_0 now represents the peak-on-axis index change at the focus. For a cumulative nonlinearity having a decay time much longer than the pulsewidth (eg. thermal), the instantaneous index change is given by the following integral:

$$\Delta n_0(t) = A \int_{-\infty}^{t} I_0(t')dt' \ , \tag{16}$$

where A a constant which depends on the nature of the nonlinearity. If we substitute Eq. 16 into Eq. 14 we obtain a fluence averaging factor of 1/2. That is,

$$\langle \Delta n_0(t) \rangle = \frac{1}{2} A F \ , \tag{17}$$

where F is the pulse fluence at focus within the sample. Interestingly, the factor of 1/2 is independent of the temporal pulse shape.

4. EXPERIMENTAL RESULTS

We examined the nonlinear refraction of a number of materials using the Z-scan technique. Fig. 4 shows a Z-scan of a 1 mm thick cuvette with NaCl windows filled with CS_2 using 300 ns TEA CO_2 laser pulses having an energy of 0.85 mJ. The peak-valley configuration of this Z-scan is indicative of a negative (self-defocusing) nonlinearity. The solid line in Fig. 4 is the calculated result using $\langle \Delta\Phi_0 \rangle = -0.6$ which gives an index change of $\langle \Delta n_0 \rangle \simeq -1 \times 10^{-3}$. As mentioned earlier such detailed theoretical fitting is not neccessary for obtaining $\langle \Delta n_0 \rangle$ (only ΔT_{p-v} is needed). The defocusing effect shown in Fig. 4 is attributed to a thermal nonlinearity resulting from linear absorption of CS_2 ($\alpha \simeq 0.22$ cm^{-1} at 10.6 μm). The risetime of a thermal lens in a liquid is determined by the acoustic transit time, $\tau = w_0/v_s$, where v_s is the velocity of sound in the liquid [17]. For CS_2 with $v_s \simeq 1.5 \times 10^5$ cm/sec and having $w_0 \simeq 60$ μm, we obtain a risetime of $\simeq$40 ns which is almost an order of magnitude smaller than the TEA laser pulsewidth. Furthermore, the relaxation of the thermal lens, governed by thermal diffusion, is of the order of 100 ms.[17] Therefore, we regard the nonuniform heating caused by the 300 ns pulses as quasi-steady state, in which case, from Eq. 17, the average on-axis nonlinear index change at focus can be determined in terms of the thermo-optic coefficient, dn/dT, as:

$$\langle \Delta n_0 \rangle \simeq \frac{dn}{dT} \frac{F_0 \alpha}{2\rho C_v} \ , \tag{18}$$

where F_0 is the fluence, ρ is the density, C_v is the specific heat and 1/2 denotes the fluence averaging factor. With the known value of $\rho C_v \simeq 1.3$ J/^{0}Kcm^3 for CS_2, we deduce $dn/dT \simeq -(8.3 \pm 1.0)\times10^{-4}$ $^0C^{-1}$ which is in good agreement with the reported value of -8×10^{-4} $^0C^{-1}$.[16]

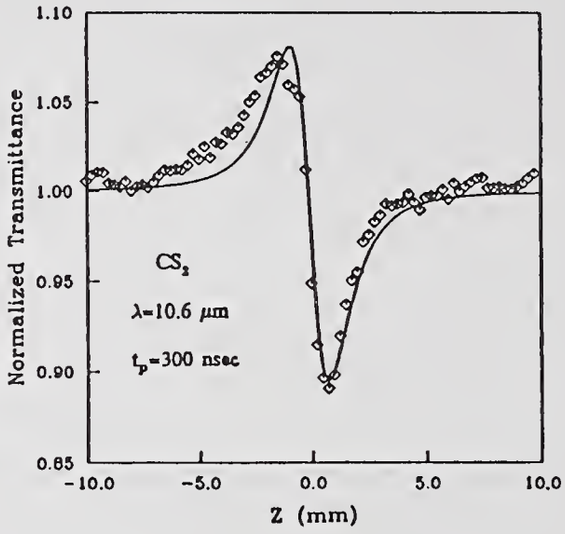

Fig.4 Measured Z-scan of a 1mm thick CS_2 cell using 300 ns pulses at λ=10.6 μm indicating thermal self-defocusing. The solid line is the calculated result with $\Delta\Phi_0$=-0.6 and 60% aperture (S=0.6).

With ultrashort pulses, nonlocal nonlinearities such as thermal or electrostriction are no longer significant. Particularly, in CS_2, the molecular reorientational Kerr effect becomes the dominant mechanism for nonlinear refraction. CS_2 is frequently used as a standard reference nonlinear material.[18, 19] We have used picosecond pulses at 10.6 μm, 1.06 μm and at 0.53 μm to measure n_2 in CS_2. We obtain the same value of n_2, within errors, at all three wavelengths, $(1.5\pm0.6)\times10^{-11}$ esu at 10.6 μm, $(1.3\pm0.3)\times10^{-11}$ esu at 1.06 μm and $(1.2\pm0.2)\times10^{-11}$ esu at 0.53 μm. The external self-focusing arising from the Kerr effect in CS_2 is shown in Fig. 5, where a Z-scan of a 1mm cell using 27 ps (FWHM) pulses focused to a beam waist w_0 of 26 μm from a frequency doubled Nd:YAG laser is illustrated. Its valley-peak configuration indicates the positive sign of n_2. With ΔT_{p-v} = 0.24, and using Eq. 13-b with a 40 percent aperture (S = 0.4), one readily obtains a $\langle\Delta n_0\rangle = 5.6 \times 10^{-5}$. Using the peak irradiance of 2.6 GW/cm^2, this value of $\langle\Delta n_0\rangle$ corresponds to an $n_2 \simeq (1.2 \pm 0.2)\times 10^{-11}$ esu.

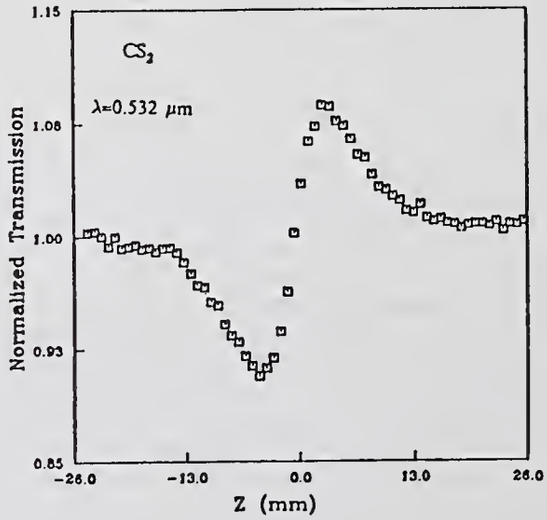

Fig.5 Measured Z-scan of a 1mm thick CS_2 cell using 27 ps pulses at λ=532 nm. It depicts the self-focusing effect due to the reorientational Kerr effect.

The main source of uncertainty in the value of n_2 is the absolute measurement of the irradiance. A plot of ΔT_{p-v} versus peak laser irradiance as measured from various Z-scans on the same CS_2 cell is shown in Fig. 6. The linear behavior of this plot follows Eq. 13 as derived for a cubic nonlinearity.

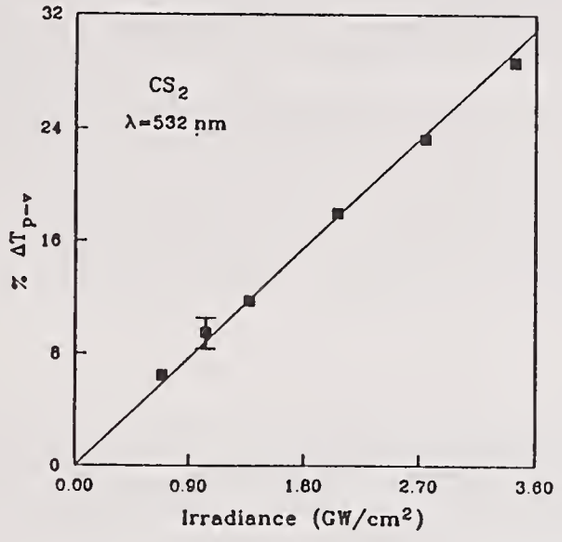

Fig.6 T_{p-v} in percent as a function of the peak irradiance from the Z-scan data of CS_2 at 532 nm, indicative of the reorientational Kerr effect.

Transparent dielectric window materials have relatively small nonlinear indices. Recently, Adair et. al. [20] have performed a careful study of the nonlinear index of refraction of a large number of such materials in a nearly degenerate-three-wave-mixing scheme at $\lambda \simeq 1.06$ μm. Using the Z-scan technique, we examined some of these materials at 532 nm. For example, the result for BaF_2 (2.4mm thick) is shown in Fig.7, using the same beam parameters as for CS_2. This Z-scan was obtained by purposely lowering the pulse energy to 2 μJ in order to observe the resolution and the sensitivity of this measurement. With a $\Delta T_{p-v} \simeq 0.035$, this Z-scan corresponds to a $\lambda/75$ induced phase distortion. For a unity signal-to-noise-ratio for our particular laser system, it is seen from Fig. 7 that the sensitivity to phase distortion is better than $\lambda/300$. For laser systems having better amplitude and pulsewidth stability, the sensitivity should be correspondingly increased.

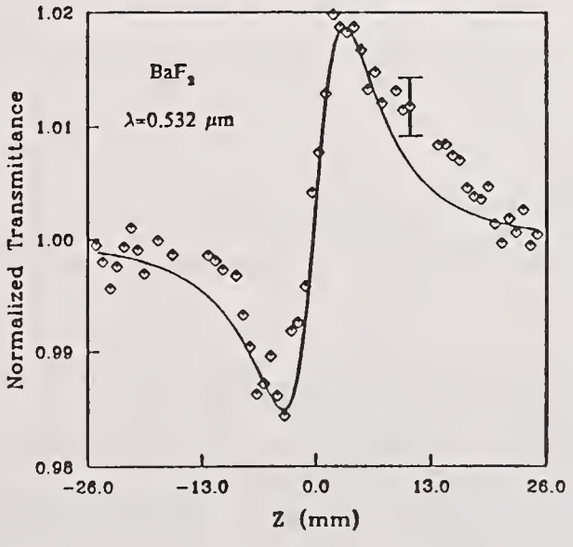

Fig.7 Measured Z-scan of a 2.4 mm thick BaF_2 sample using 20 ps pulses at λ=532 nm indicating the self-focusing due to the electronic Kerr effect. The solid line is the calculated result with $\Delta\Phi_0$=0.085 corresponding to $\simeq\lambda/75$ total phase distortion. The error bar shown corresponds to approximately $\lambda/480$ induced phase distortion.

Aside from the statistical fluctuations of the laser irradiance, surface imperfections or wedge in the sample may lead to systematic transmittance changes with z that could mask the effect of nonlinear refraction. We found, however, that such "parasitic" effects may be substantially reduced by subtracting a low irradiance background Z-scan from the high irradiance scan. A simple computer simulation of this process assuming that the surface imperfections do not disturb the circular symmetry of the beam or cause any beam steering, indicated that background subtraction indeed recovers the original ΔT_{p-v} arising from the nonlinear refraction effect even for quite large surface disturbances $\Delta\phi_s$ of up to π.

Returning to the Z-scan of Fig.7, we obtain $n_2 \simeq (0.8\pm.15)\ x10^{-13}$ esu for BaF_2 at 532 nm, which is in close agreement with the reported values of $0.7x10^{-13}$ esu [20] and $1.0x10^{-13}$ esu [3] as measured at 1.06 μm using more complex techniques of nearly degenerate-three-wave-mixing and time-resolved-nonlinear-interferometry, respectively. Similarly for MgF_2, we measure $n_2 \simeq 0.25x10^{-13}$ esu at 532 nm as compared to the reported value of $0.32x10^{-13}$ esu at 1.06 μm for this material as given in [20]. Dispersion in n_2 for these materials between 1 and 0.5 μm is expected to be minimal. It should be noted that the n_2 values extracted from the Z-scans are absolute rather than relative measurements. If the beam parameters are not accurately known, however, it should be possible to calibrate the system by using a standard nonlinear material such as CS_2.

5. CONCLUSION

We have demonstrated a simple single beam technique that is sensitive to less than $\lambda/300$ nonlinearly induced phase distortion. Using the Z-scan data the magnitude and sign of the nonlinear refraction can be simply determined. We have derived relations that allow the refractive index to be obtained directly from the Z-scan data without resorting to computer fits. We have applied this technique to several materials displaying a variety of nonlinearities on different time scales. It is expected that this method will be a valuable tool for experimenters searching for highly nonlinear materials.

6. ACKNOWLEDGEMENT

We gratefully acknowledge the support of the National Science Foundation grant #ECS-8617066, and the support of DARPA/CNVEO and the Florida High Technology and Industry Council. We also wish to thank Alan Miller for helpful discussions.

7. REFERENCES

1. Sheik-Bahae, M.; Said, A.A.; Van Stryland, E. W. "High Sensitivity Single Beam n_2 Measurement," Opt. Lett. 14,955-957(1989)
2. Weber, M.J.; Milam, D.; Smith, W.L. "Nonlinear Refractive Index of Glasses and Crystals," Optical Engineering, 17, 463-469 (1978).
3. Moran, M.J.; She, C.Y.; Carman, R.L. "Interferometric Measurements of Nonlinear Refractive-Index Coefficient Relative to CS_2 in Laser-System-Related Materials," IEEE J. Quantum Electron. QE-11, 259-263 (1975).
4. Friberg, S.R.; Smith, P.W. "Nonlinear Optical Glasses for Ultrafast Optical Switches," IEEE J. Quantum Electron. QE-23, 2089-2094 (1987).
5. Adair, R.; Chase, L.L.; Payne, S.A. "Nonlinear refractive index measurement of glasses using three-wave frequency mixing," J. Opt. Soc. Am. B 4, 875-881 (1987).
6. Owyoung, A. "Ellipse Rotations Studies in Laser Host Materials," IEEE J. Quantum Electron. QE-9, 1064-1069 (1973).
7. Williams, W.E.; Soileau, M.J.; Van Stryland, E.W. "Optical Switching and n_2 Measurements in CS_2," Opt. Comm. 50, 256-260 (1984).
8. Williams, W.E.; Soileau, M.J.; Van Stryland, E.W. "Simple direct measurements of n_2," Proc. 15th Annual Symp. on Optical Materials for High Power Lasers, Boulder, CO (1983).
9. Hill, J.R.; Parry, G.; Miller, A. "Non-linear Refraction Index Changes in CdHgTe at 175K with 1.06 μm Radiation," Opt. Commun., 43, 151-156 (1982).
10. Boggess, T.F.; Moss, S.C.; Boyd, I.W.; Smirl, A.L. "Picosecond Nonlinear-Optical Limiting in Silicon," in Ultrafast Phenomena IV, edited by D.H. Huston and K.B. Eisenthal (Spriner-Verlag), (New York, 1984). pp. 202.
11. Harris, J.M.; Dovichi, N.J. "Thermal Lens Calorimetry," Analytical Chem. 52, 695-700(1980).
12. Akhmanov, S.A.; Sukhorokov, A.D.; Khokhlov, R.V. "Self-focusing and Diffraction of Light in a Nonlinear Medium," Sov. Phys. Vspekhi; English Translation, 10, 609 (1968).
13. Smith, W.L.; Bechtel, J.H.; Bloembergen, N. "Dielectric-Breakdown Threshold and Nonlinear-refractive Index Measurements with Picosecond Laser Pulses, Phys. Rev. B 12, 706-714 (1975).
14. Gaskill, J.D. Linear Systems, Fourier Transforms, and Optics, John Wiley & Sons, New York, 1978.

15. Weaire, D.; Wherrett, B.S.; Miller, D.A.B.; Smith, S.D. "Effect of Low-Power Nonlinear refraction on laser beam propagation in InSb," Opt. Lett., 4, 331-333 (1974).
16. Raman, V.; Venkataraman, K.S. "Determination of the adiabatic piezo-optic coefficient of liquids." Proc. Roy. Soc. A, 171, 137 (1939).
17. Hayes, J.N. "Thermal Blooming of Laser Beams in Fluids," Appl. Opt. 2, 455-461 (1972).
18. Ho, P.P.; Alfano, R.R. "Optical Kerr effects in Liquids," Phys. Rev. A, 20, 2070-2087 (1979).
19. Thomas, P.; Jares, A.; Stoicheff, B.P. "Nonlinear Refractive Index and "DC" Kerr Constant of Liquid CS_2," IEEE J. Quantum Electron. QE-10, 493-494(1974).
20. Adair, R.; Chase, L.L.; Payne, A. "Nonlinear Refractive Index of Optical Crystals," Phys. Rev. B, 39, 3337-3350(1989).

COMMENTS

Question: Are your results affected by surface nonuniformity?

Answer: If the scatter is homogeneous then it's no problem. If it's grossly inhomogeneous or if the surface is corrugated or something, then it really effects the technique quite a bit. In fact, you can use it to measure surface quality as well if you turn the radiance down to very low values. We have done experiments where we had rough surfaces and just took data from lower radiance values. Then we took the data from higher radiance values and just divided it up. We still get good signal, but it does degrade as the quality of the optics degrade.

Manuscript received
8-20-89

OPTICAL BREAKDOWN IN PARTICLE SUSPENSION

Kamjou Mansour, M.J. Soileau and E.W. Van Stryland

Center for Research in Electro-Optics & Lasers (CREOL)
University of Central Florida
12424 Research Parkway, Orlando, FL 32826

We have characterized the nonlinearities observed in suspensions of carbon black particles in liquids (CBS). We have developed a preliminary explanation of the optical limiting characteristic of the CBS that qualitatively explains the low limiting thresholds. We have found that the limiting depends primarily on the input optical fluence (J/cm^2) rather than irradiance (W/cm^2). We have monitored transmission, side scattered light, and the photoacoustic response of the CBS simultaneously. The nonlinear scattered light appears to be the dominant nonlinearity. Additionally, we have observed that the nonlinearities disappear after repeated laser firings. Thus, in essense, we are performing a laser induced damage experiment, and we have prepared a material with a low damage threshold. These data have led us to the following model. The carbon first linearly absorbs the input light efficiently. The carbon is rapidly heated, vaporizes and ionizes to form a rapidly expanding microplasma. This plasma absorbs and scatters subsequent light, thus limiting the transmittance.

Key words: carbon black suspension; nonlinear absorption; nonlinear scattering; nonlinear transmission; nsec pulses; optical limiting; psec pulses; .53 μm, 1.06 μm.

1. INTRODUCTION

Recently there has been a growing interest in the use of microparticle suspensions as nonlinear media. Here, we demonstrate and review the dynamics of limiting in a suspension of absorbing microparticles that exhibit primarily nonlinear scattering and nonlinear absorption. The absorbing microparticles of interest are carbon black particles which are $\simeq$ 35 nm in diameter with agglomerates up to 500 nm in diameter. We demonstrate an optical limiting threshold as low as 80 watts peak power for 0.532 μm and 160 Watts for 1.06 μm using pulses of 14 nsec and 20 nsec (FWHM), respectively.

Because of the structure of these dispersions, different mechanisms including nonlinear absorption, nonlinear refraction (self-focusing, self-defocusing), nonlinear scattering and combinations of these mechanisms could be the source of the optical nonlinearity leading to such a low optical limiting threshold.[1] In order to investigate the relative contributions of these mechanisms we perform a series of experiments. We first perform optical limiting experiments in the CBS and in the carbon black particles which are deposited on the surface of a glass substrate at 0.532 μm and 1.06 μm for nanosecond pulses. We present transmission measurements which directly show the fluence dependence of limiting in CBS. We also perform a measurement that monitors the absorptance, transmittance and fraction of side scattered light simultaneously. As will be demonstrated, we are performing a laser-induced-damage experiment on a material with an extremely low damage threshold. This leads us to discuss and show the repetition rate dependence of the CBS, and carbon black particles deposited on the glass substrate.

2. OPTICAL LIMITING

The optical geometry often used as a screening test, as it is sensitive to both nonlinear absorption and nonlinear refraction, is shown in Figure 1.[1] We used this arrangement with pulses from an Nd:YAG laser operated in the TEM_{00} mode of 14 ns (FWHM) duration at 0.532 μm and 20 ns at 1.064 μm. These pulses were focused by either a 40mm (.532μm) or 50mm (1.064μm) "best form" lens, shown as L_1. This results in calculated beam radii of 3.5 μm at a wavelength of .532 μm and 7 μm at 1.064 μm inside the 1 cm cuvette. The spot radii quoted in this paper are half-widths at the $1/e^2$ maximum in irradiance. The transmitted pulse was then collected by a 102 mm focal length "best form" lens L_2 placed behind the sample. The laser beam then passed through a 400 μm aperture placed in front of a silicon photodiode. This system had an overall low input transmittance of 70 percent for both wavelengths.

Using this optical geometry we have looked at optical limiting in various concentrations of CBS and a known standard sample, CS_2, which has been previously used as an optical limiting material [2]. Optical limiting in CS_2 is primarily due to molecular reorientation of the molecules athough a small contribution from electrostriction may be

present for nanosecond pulses and tight focusing geometries. The optical limiting of CBS and CS_2 in a 1 cm thick cuvette is shown in Figure 2 for nanosecond laser pulses at 0.532 μm. In order to resolve the onset of limiting, the measurement was performed for lower input powers as shown in Figure 3. The CBS begins clamping the transmitted fluence above approximately 80 watts input power and continues clamping for $\simeq$5 orders of magnitude of increased input power. It is important to note that each laser firing irradiates "new" material as discussed in Section 5. The limiting of the CBS at 1.064 μm is shown in Figures 4 and 5. As is shown, the onset of limiting for 1.064 μm laser pulses is approximately 160 watts. The optical limiting in a film of carbon black particles deposited on a glass substrate at 1.06 μm is shown in Figure 6. The sample was moved to a new site for each laser firing. As is shown, the onset of limiting for 1.064 μm laser pulses is approximately 600 watts.

The observed optical limiting using the geometry shown in Figure 1, could be due to several mechanisms including nonlinear absorption, nonlinear refraction and nonlinear scattering. Below we describe a series of experiments performed to determine the dominant nonlinearity.

3. NONLINEAR TRANSMITTANCE MEASUREMENT

We have studied the fluence dependence of the transmittance of CBS at 0.532 μm and 1.064 μm. The optical goemetry used is shown in Figure 7. Both a one meter and 50 centimeter "best form" lens were used to focus the nsec pulsed input beams at the two wavelengths. This resulted in measured spot sizes of 108 μm and 254 μm for 0.532 μm light. The transmitted signal was collected by a large area uniform response Si photodiode located very close to the cell. The diameter of the detector is 1 centimeter and the beam radius at the detector is approximately 1mm in diameter. The difference between this geometry and the optical limiting geometry of Figure 1 is that we are not using tight focusing and the aperture has been removed so that this experiment is insensitive to nonlinear refraction. The results of the transmittance measurements are plotted as a function of incident fluence and incident power in Figures 8, and 9 for 0.532 μm. For incident fluences above 200 mj/cm^2 for 0.532 μm, the transmission becomes increasingly nonlinear and is essentially identical for both beam radii at a given wavelength as shown in Figure 8. However, the onset of a change in transmittance appears at two different incident power levels for these beam radii as shown in Figure 9. Similar results are observed for 1.06 μm laser pulses. We also observed that the onset of limiting for both nanosecond and picosecond measurements occurs approximately at the same fluence. The experiments indicate that the nonlinear transmittance observed is fluence dependent.

4. MEASUREMENT OF TRANSMITTANCE, SCATTERING AND ABSORBTANCE

In order to understand the nature of this fluence dependent nonlinear transmittance, we have set up an experiment which enables us to monitor for a single pulse , the absorptance and the fraction of side scattered light simultaneously with the transmittance measurement. This simultaneous measurement was conducted using the Q-switched Nd:YAG laser. The laser light was focused by a 1 meter focal length "best form" lens L_1 into a one centimeter cuvette cell. (See Figure 7) The transmitted light was monitored as previously described. The absorption of the incident light was directly monitored by a sensitive piezoelectric transducer which was placed in contact with the bottom of the cuvette with silicone grease. Photoacoustic measurements have been used to directly detect very small changes in absorption.[3] The side scattered light was collected by a two-inch diameter, 98 mm focal length lens and detected by a Si photodiode. The optical geometry for this measurement is shown in Figure 11.

The results of the simultaneous measurement of absorptance, transmittance, and the fraction of side scattered light (side scattering light divided by incident light) are plotted as a function of incident fluence for 1.064 μm laser pulses in Figure 11. For very low input fluences the CBS behaves linearly and there is no change in the three quantities monitored. However, for input fluences close to 360 mj/cm^2 for 1.064 μm light, the transmittance begins to decrease nonlinearly as is shown by squares in Figure 11. The absorptance increases nonlinearly for incident fluence close to this threshold value (i.e., onset of change of transmittance) and levels off at a higher value even for input fluences two orders of magnitude above threshold. The scattered fraction increases nonlinearly as the transmittance decreases as shown by circles in Figure 11. This trend continues for at least two orders of magnitude above threshold. Similar results observed for .532 μm light. From these results we see that blocking of the light by the CBS above threshold is primarily due to nonlinear scattering.

5. NONLINEAR SCATTERING

The blocking of the incident light by scattering can readily be photographed as shown in Figure 12. These pictures were taken by looking at the side window of the cuvette perpendicular to the direction of the incident light. For low input fluences, top picture, the bright region in the photograph represents the input pulse which is linearly scattered (Mie scattering) by carbon black particles. However, for incident fluences above 200 mj/cm^2, the light is nonlinearly scattered to the sides and thus, blocks the incident light from being transmitted. This is shown in the lower picture.

The dynamics of the transmittance loss is studied by time resolved transmission measurements conducted using nanosecond pulses. By delaying the transmitted pulse with respect to the input pulse we are able to monitor both the incident and transmitted pulses shown in Figure 13. For an incident fluence above 200 mj/cm^2, there is a sharp cut off in time of the transmitted pulse (shown in graph b). The transmitted laser pulse is most strongly attenuated during the

later portions of the pulse, thus, the pulse appears advanced in time. This experiment again suggests that the attenuation of the laser beam is produced by a laser-induced-breakdown plasma.

Under this assumption, the attenuation is dominated by scattering losses of the laser light by the plasma as seen in Figures 11. Thus, we are performing a laser-induced-damage experiment, and we have prepared a material with an extremely low damage threshold. This is consistent with having high linear absorption, and is also consistent with the disappearance of the nonlinearities after repeated laser irradiation as discussed in the next section.

6. REPETITION RATE DEPENDENCE

Recently, we reported the repetition rate dependence of the CBS.[4] In that report we indicated that the onset of the limiting threshold for 1 and 10 Hz repetition rate laser pulses is considerably different and is higher for the 10 Hz repetition rate. This repetition rate dependence was removed by flowing the material at such a rate that virgin material was exposed to each laser pulse.

This bleaching or reduction of limiting of the laser light in the nonflowing liquid after repeated irradiation on the same region of the sample can be observed by monitoring the transmitted signal and scattered signal at a fixed fluence above the single shot threshold for limiting. Using the geometry shown in Figure 11 and setting the incident fluence at 350 mj/cm^2 for 0.532 μm laser pulses and a 1 Hz repetition rate, we can observe that the transmitted signal increases as the number of the incident pulses irradiating the sample increases. The transmittance levels off to a value that is less than the linear transmittance of the solvent as shown in Figure 14. The scattered signal reduces and levels off after repeated laser firings. This is shown as circles in Figure 14. For flowing liquid, stirred liquid or a long elapse time between the laser pulses irradiating the liquid, we have observed that the transmitted signal and scattered signal remain fixed as shown in Figure 15. The maximum limiting capability is for the first laser firing and recovery of the irradiated region of the sample is due to convection in the liquid at room temperature which for the spot size used is a slow process in comparison with the repetition rate of 1 Hz. Note that using a tight focusing geometry and a 1 Hz repetition rate that we do not see these cumulative effects. We observed that this recovery time is proportional to the radius of the laser beam in the cell, consistent with convection.

The bleaching of CBS can also be monitored as shown in Figure 16 where we have used a very large spot size of more than 254 μm. Here, we have used a HeNe laser beam expanded to illuminate the region close to the front surface of the cell. The scattering of the HeNe beam by the suspended microparticles is readily observable. We irradiated the CBS using an incident fluence of 350 mj/cm^2 and photographed the scattered light after 10 seconds. This is shown in Figure 17. The dark spot appearing in the middle of the bright screen is the irradiated region showing that the scattering centers have been "removed" by the laser pulse. We find that this excited volume is slowly replaced by fresh CBS after approximately two minutes due to convection. The conjecture is that the microparticles have been considerably reduced in size or "atomized" so that they no longer efficiently scatter the HeNe light. The carbon particles deposited on glass are blown off the surface with repetitive firings and therefore, limiting also disappears.

7. NONLINEAR REFRACTION

In order to investigate contributions of phase distortion due to a thermooptic effect, electrostriction, or other nonlinear refractive mechanism, we monitored the far field profile of the transmitted beam using a vidicon tube with an optical multichannel analyzer. For incident fluences below threshold and up to an order of magnitude higher than threshold, we have not observed any broadening of the spatial profile of the transmitted beam. Therefore, the change in index of refraction of the CBS is very small and the phase distortion due to this index change is less than 0.2 λ which is the sensitivity of our detection system. From this measurement we conclude that the contribution of nonlinear refraction is small in comparison with the nonlinear scattering observed. In order to further validate this point we removed the aperture in the original limiting geometry shown in Figure 1 and observed no change in limiting threshold.

8. MODEL

It appears from our experimental results that the dominant mechanism in the CBS is nonlinear scattering. The nature of this nonlinear scattering is consistent with the formation of microplasmas by laser-induced-breakdown of the carbon particles. Therefore, the dynamics of limiting in CBS can be described by a simple model. The carbon linearly absorbs the incident light very efficiently. The carbon is rapidly heated to several thousand degrees Celcius. A simple calculation of the particle temperature at threshold gives a few thousand degrees Celcius. The carbon then vaporizes and ionizes to form a rapidly expanding microplasma which absorbs and scatters later portions of the laser light and blocks the transmission. This model is also consistent with the disappearance of the nonlinearities after repeated laser firings as the carbon particles will have undergone vaporization.

9. CONCLUSION

We have characterized the nonlinearities observed in a suspension of carbon black particles (CBS) in liquid. We have developed a qualitative model based on laser-induced breakdown to explain the low limiting threshold of the CBS. From our results, we conclude that nonlinear scattering due to rapidly expanding microplasmas is the dominate mechanism leading to limiting. While the evidence obtained is insufficient to give details of this damage process, the

mechanism leading to limiting. While the evidence obtained is insufficient to give details of this damage process, the predictions closely match our observations. We note that the broad-band nature of the nonlinearity is primarily due to the fact that carbon is black, i.e., it absorbs all wavelengths.

10. ACKNOWLEDGEMENTS

This research was supported with funds from the DARPA/CNVEO and the Florida High Technology and Industry Council.

11. REFERENCES

1. E.W. Van Stryland, Y.Y. Wu, D.J. Hagan, M.J. Soileau, and K. Mansour, JOSAB, Vol. 5, 1980, September 1988.

2. M.J. Soileau, Williams E. Williams, and Eric W. Van Stryland, IEEE J. Quantum Electronics, QE 19, No. 4, 731, April 1983.

3. A.C. Tam and C.K.N. Patel, Appl. Opt. 18(19), 3348, 1979.

4. M.J. Soileau, Kamjou Mansour, E.W. Van Stryland, E. Canto, and David J. Hagan, Joint U.S. - U.K. Conference on Sensor Protection, Malvern, England, 1987.

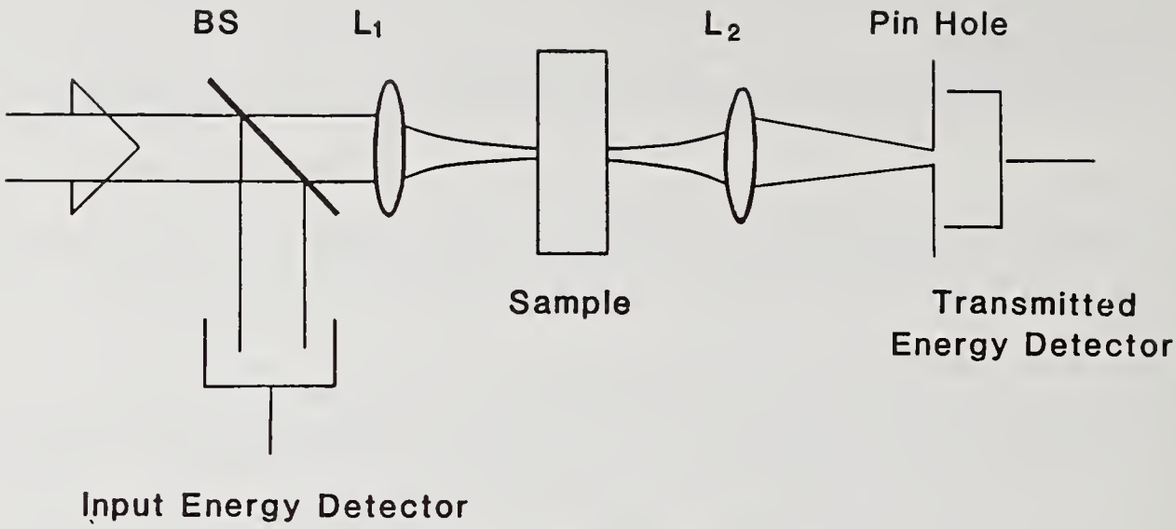

Figure 1. Optical limiting geometry.

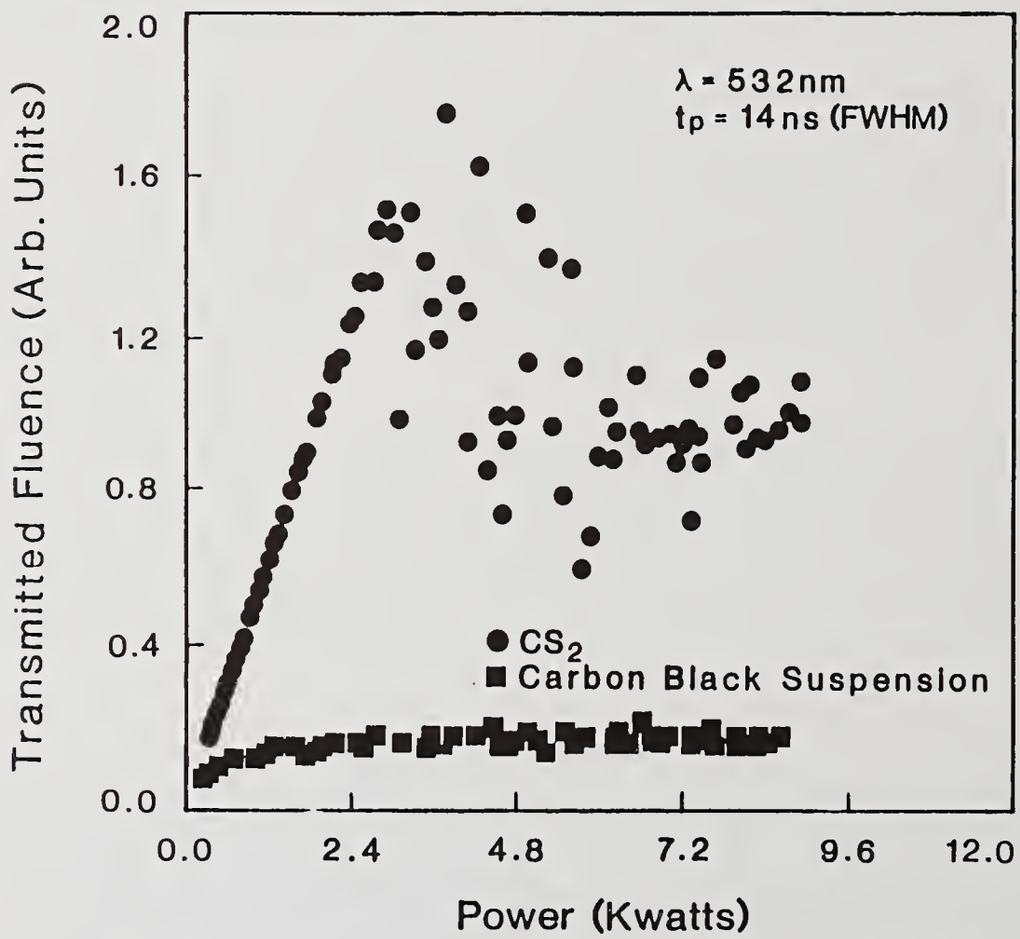

Figure 2. Plot of the limiting of CS_2 (circles) and CBS (squares) as a function of input power for 14 ns (FWHM), 0.532 μm pulses.

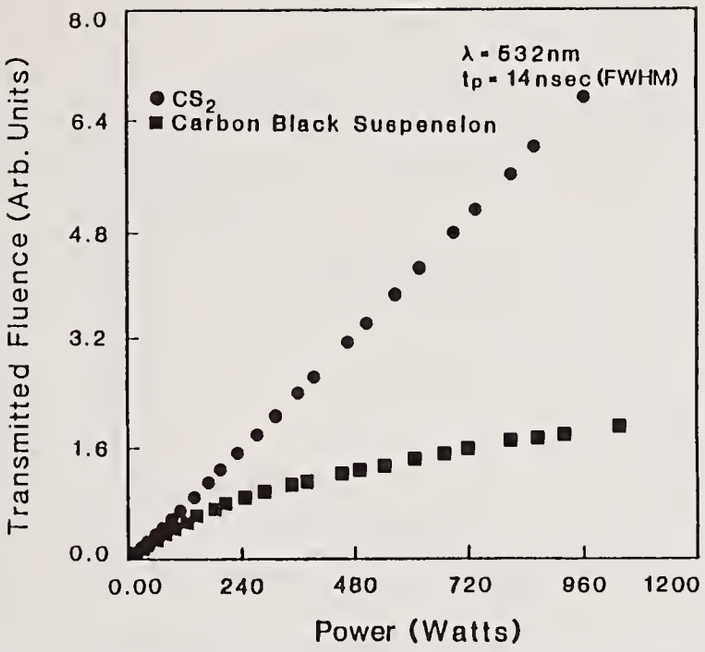

Figure 3. Plot of onset of limiting of CS_2 (circles) and CBS (squares) as a function of input power for 14 ns (FWHM), 0.53 μm pulses.

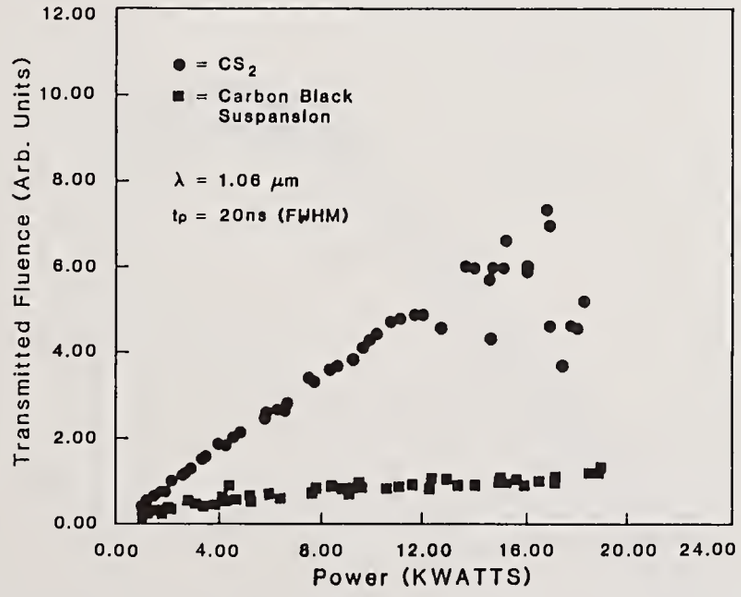

Figure 4. Plot of limiting of CS_2 (circles) and CBS (squares) as a function of input power for 20 ns (FWHM), 1.06 μm pulses.

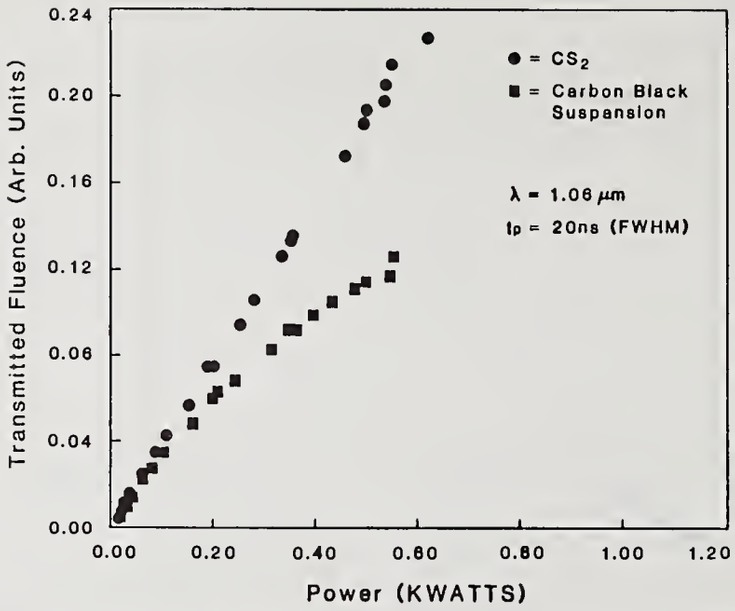

Figure 5. Plot of on set of limiting of CS_2 (circles) and CBS (squares) as a function of input power for 20 ns (FWHM), 1.06 μm pulses.

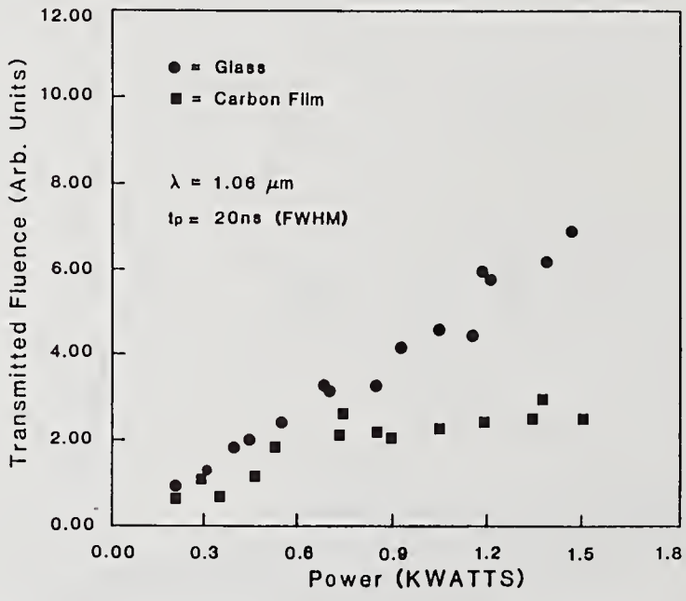

Figure 6. Plot of limiting of Carbon Particle on glass (squares) and glass as a function of input power for 20 ns (FWHM), 1.06 μm pulses.

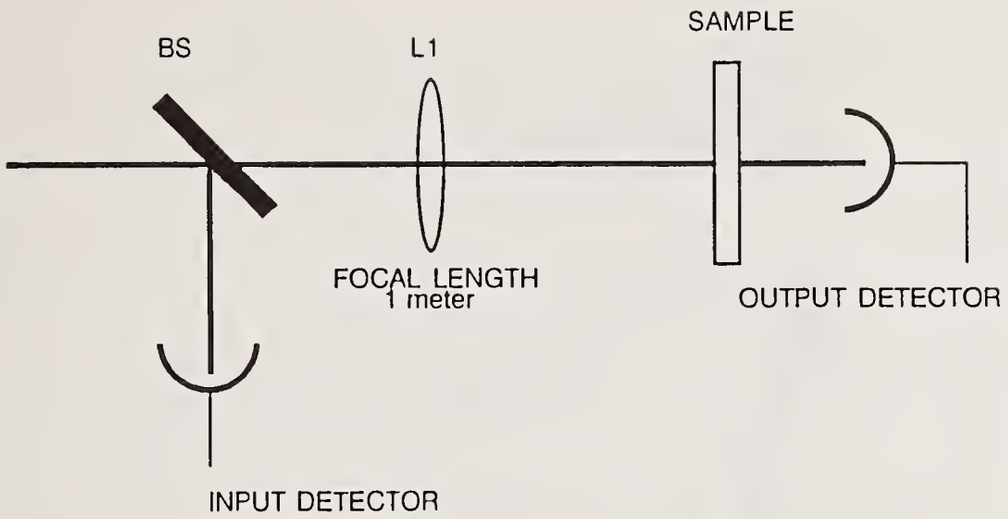

Figure 7. Optical geometry for transmission measurement.

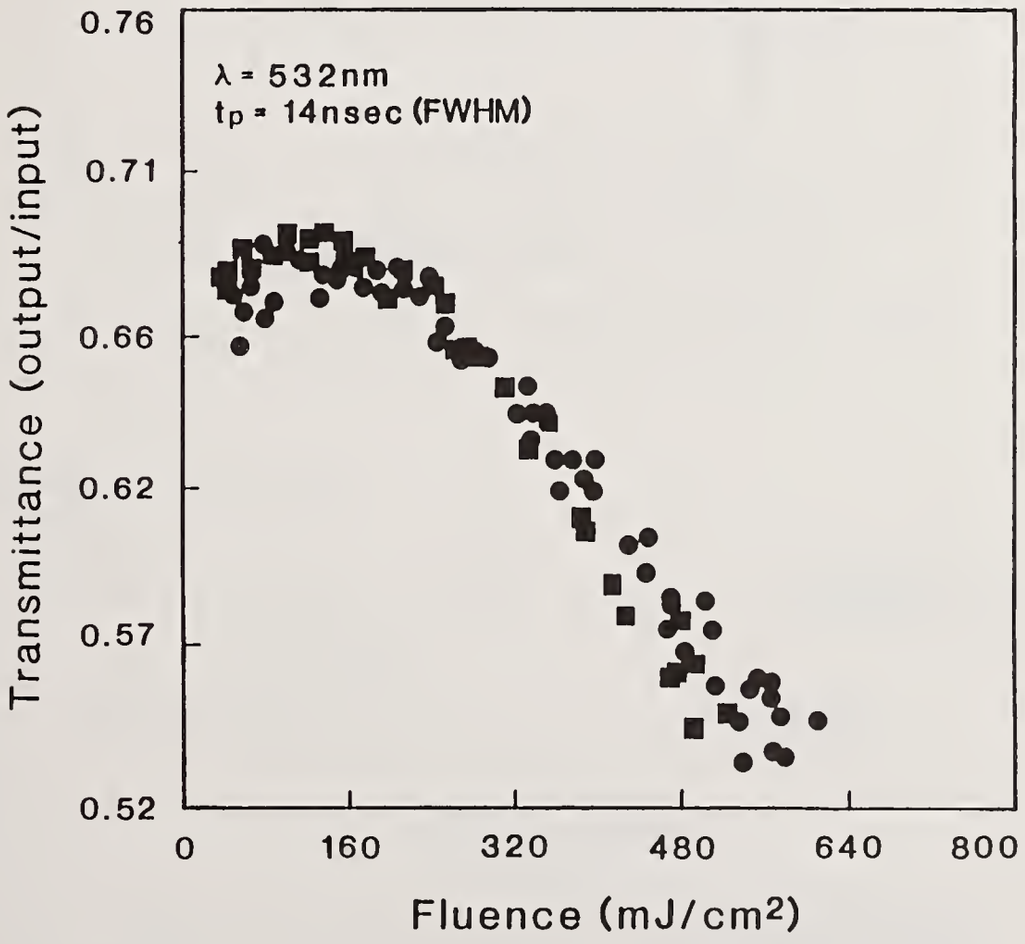

Figure 8. Measured CBS transmittance as a function of incident fluence (mj/cm²) for 108 μm (circles) and 254 μm (squares) spot sizes at 0.532 μm.

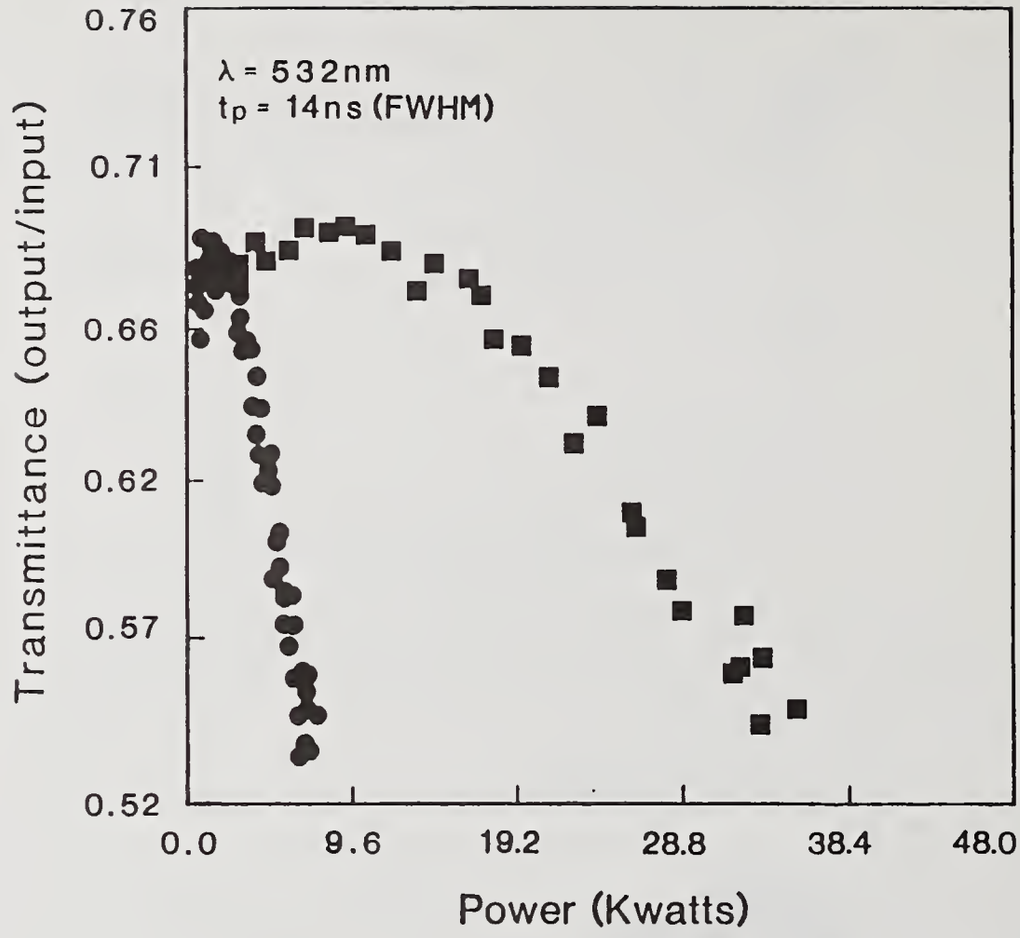

Figure 9. Measured CBS transmittance as a function of incident power (KW) for 108 μm (circles) and 254 μm (squares) spot sizes at 0.532 μm.

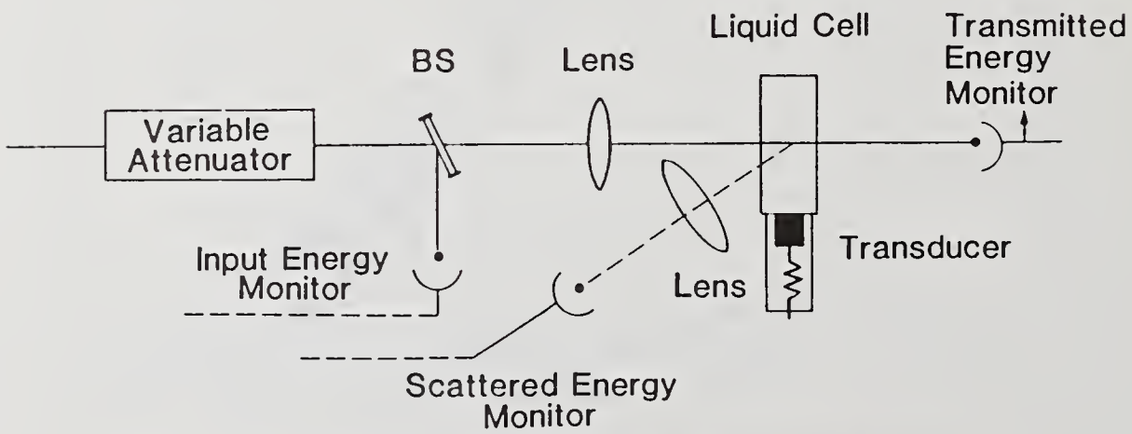

Figure 10. Optical geometry used to monitor the transmittance, absorptance and side scattered light.

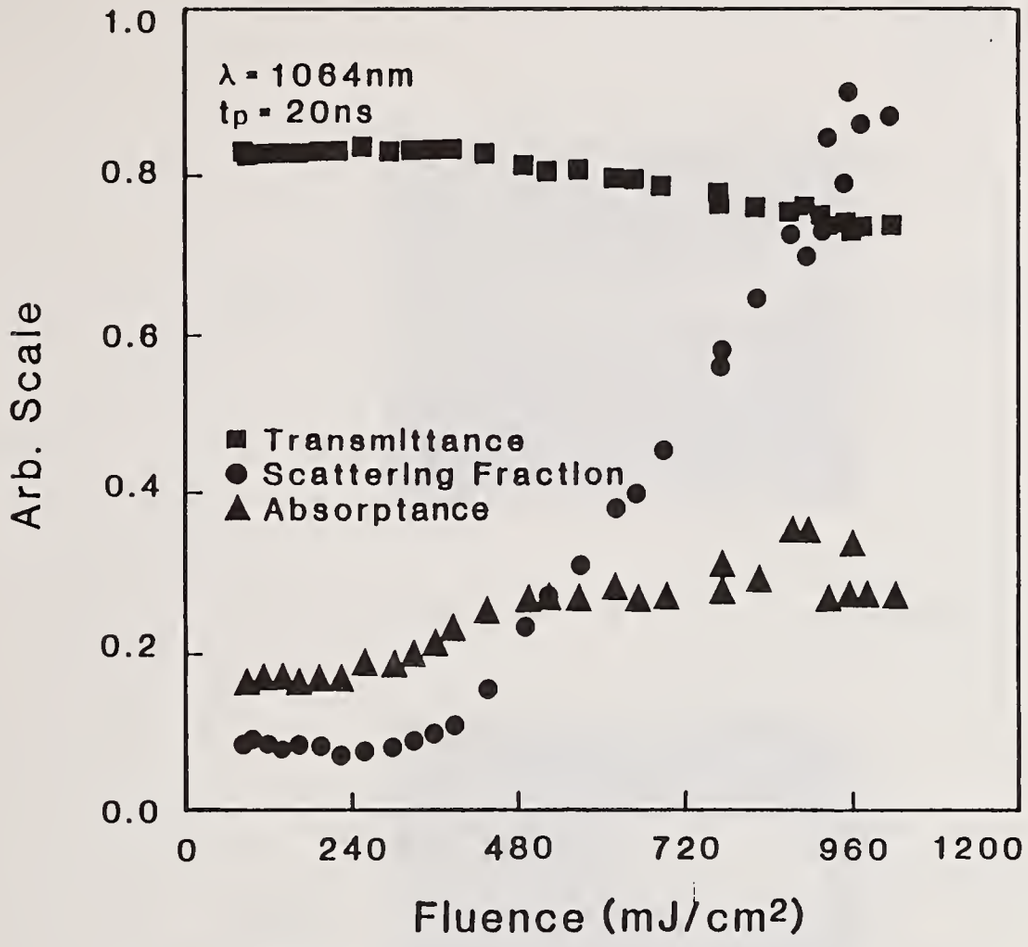

Figure 11. Plot of change of transmittance (squares), absorptance (triangle) and scattering fraction (circles) as a function of incident fluence (mj/cm^2) for 1.06 μm, 20 ns pulses.

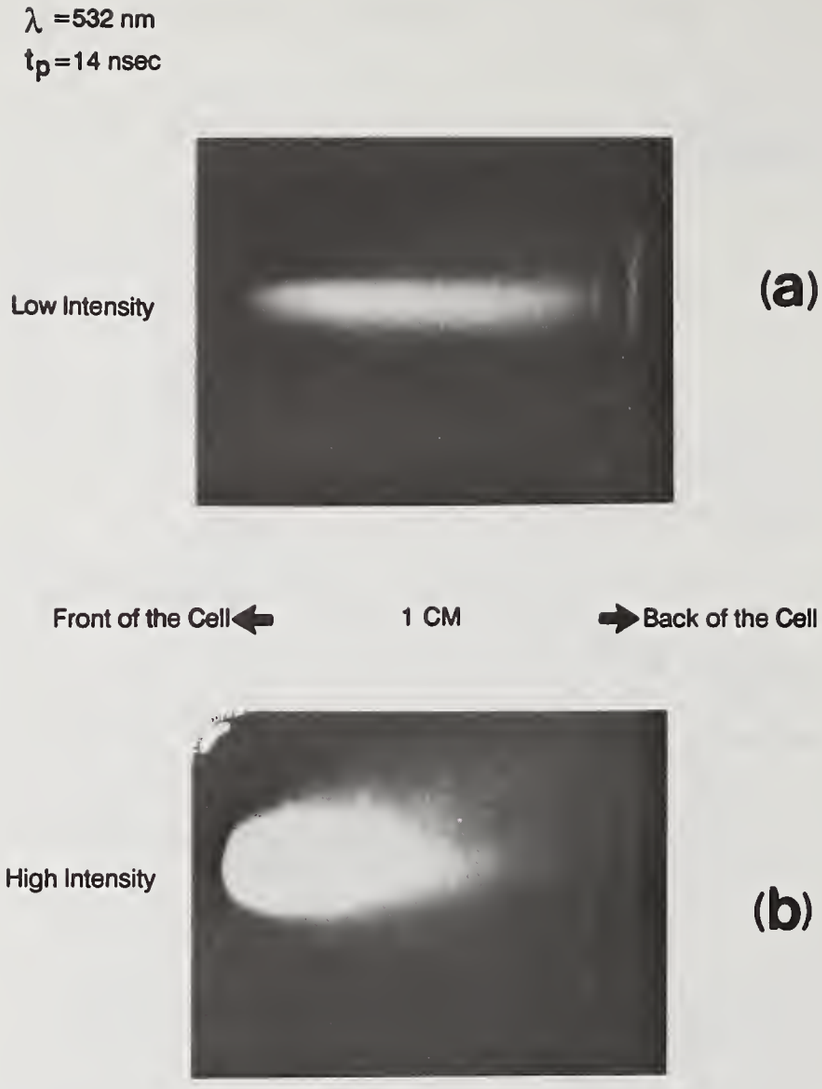

Figure 12. Photographs A and B represent the input pulse which is scattered by CBS for low and high incident fluences respectively.

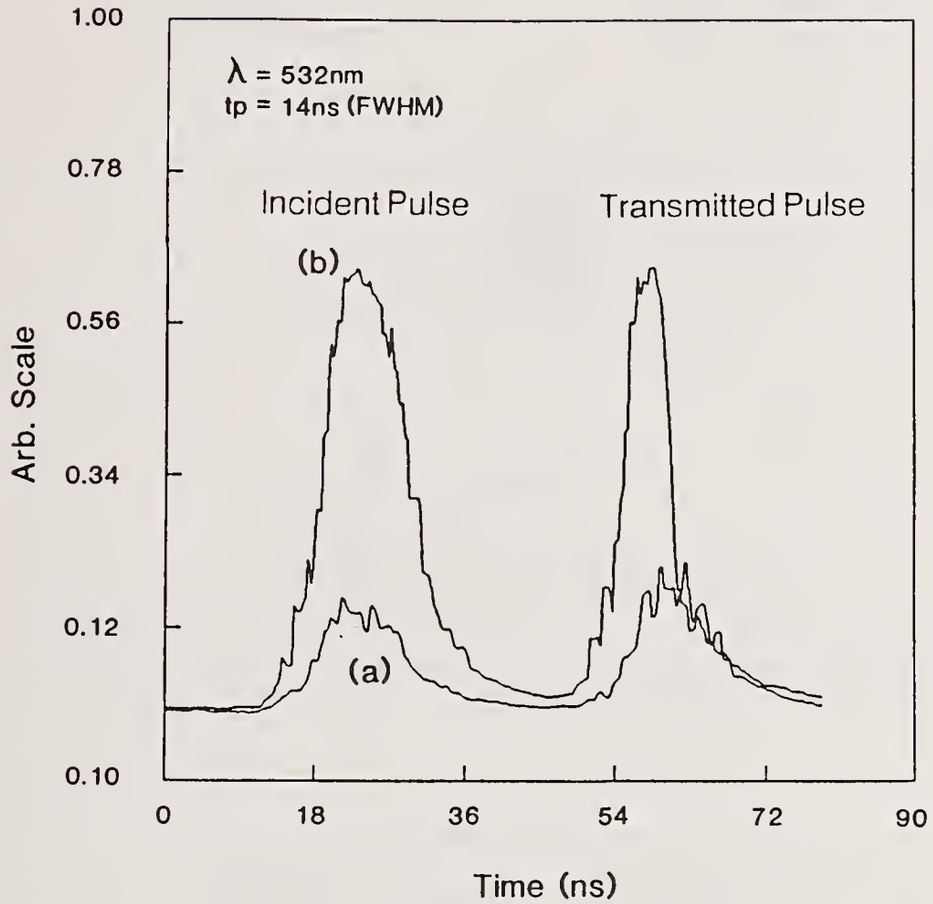

Figure 13. Graphs A and B represent the incident and transmitted pulse for fluence levels below and above the threshold. Incident pulse in graph B has been attenuated by a factor of 10 in respect to the transmitted pulse.

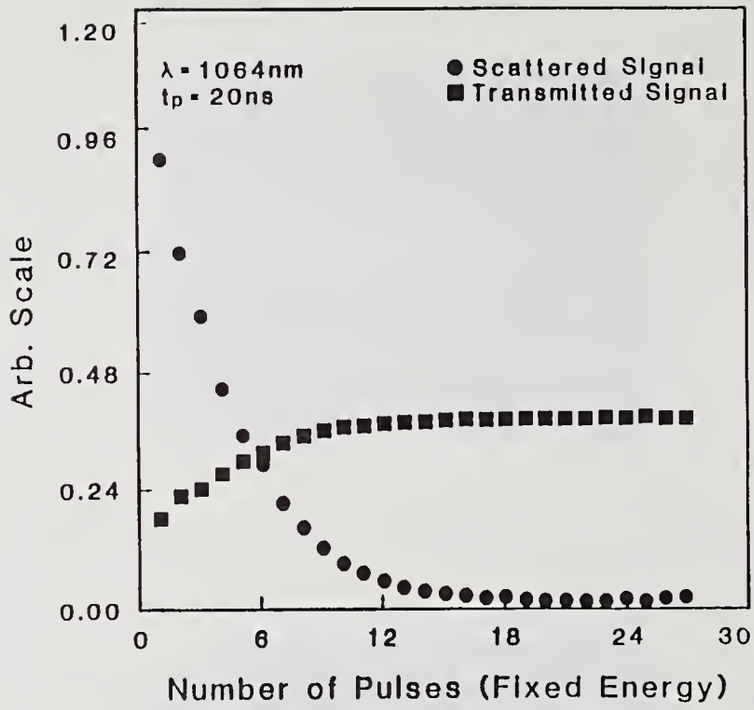

Figure 14. Plot of fraction of scattered light (circles) and transmittance (squares) as a function of the number consecutive laser pulses for 1.06 μm, 20 ns pulses at a fluence of 450 mj/cm^2.

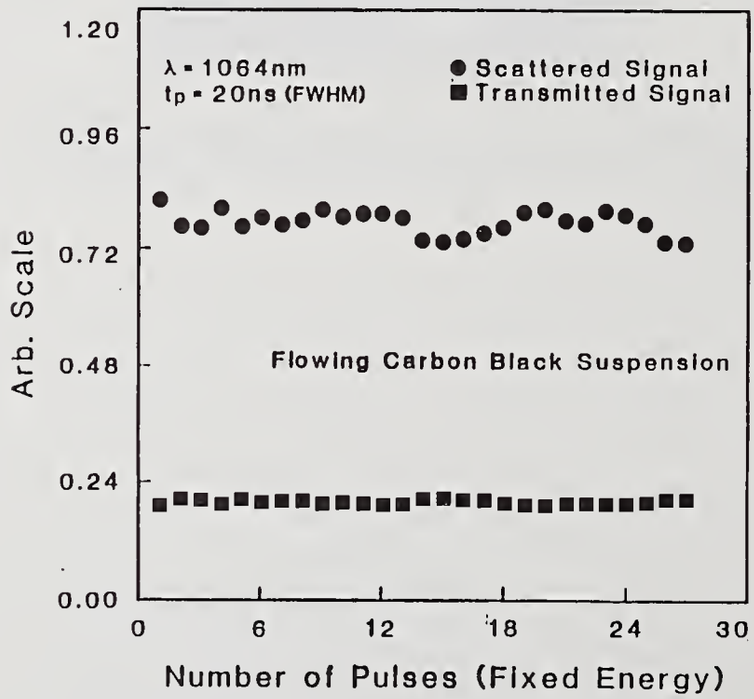

Figure 15. Plot of fraction of scattered light (circles) and transmittance (squares) in flowing CBS as a function of the number of consecutive laser pulses for 1.06 μm, 20 ns pulses at a fluence of 450 mj/cm^2.

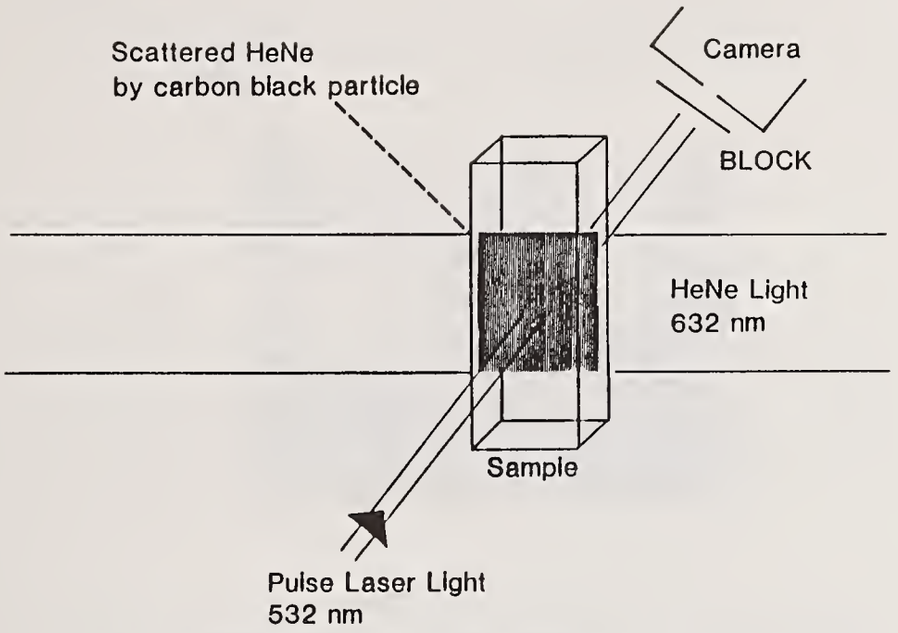

Figure 16. Optical geometry to monitor "bleaching" of carbon particles in CBS.

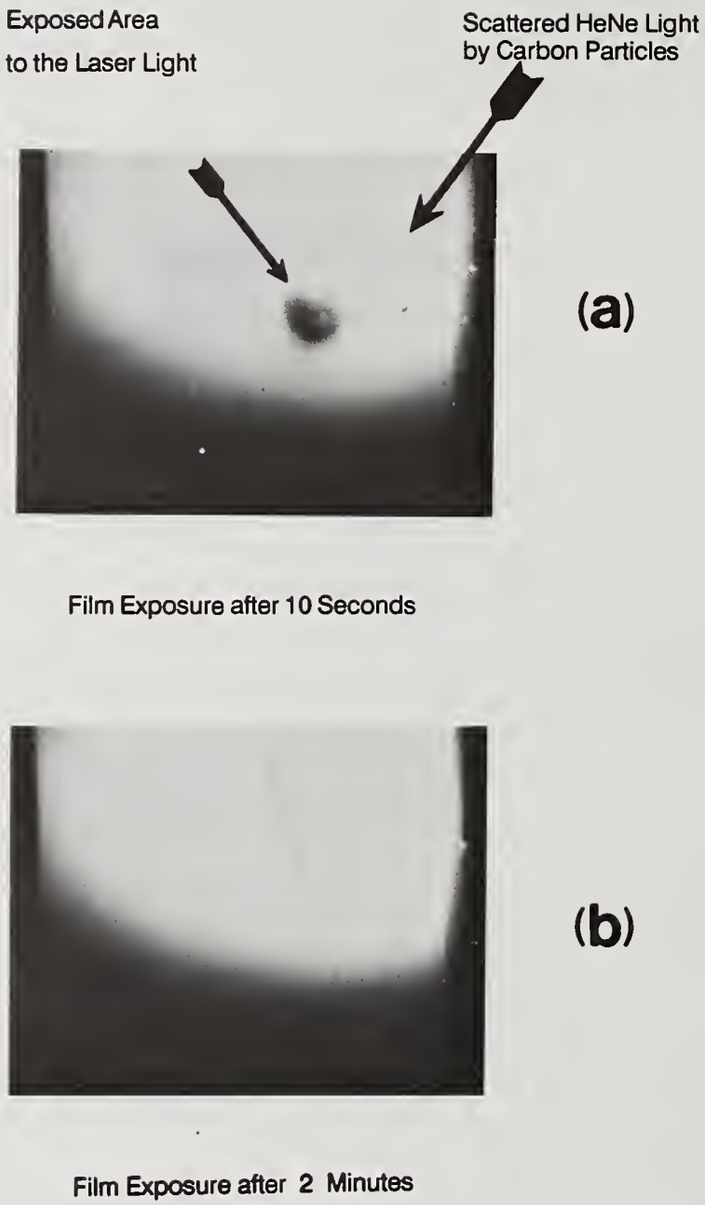

Figure 17. Photographs A and B represent the "bleaching" of carbon particles within the irradiated region and replacement of the irradiated region with fresh liquid, respectively.

Manuscript received
3-21-90

ANNEALING OF INDUCED DAMAGE IN FLUORIDE GLASS COMPONENTS

OSAMA H. EL-BAYOUMI AND MICHAEL J. SUSCAVAGE

Solid State Sciences Directorate
Rome Air Development Center
Hanscom AFB, MA 01731

AND

L. PIERRE DE ROCHEMONT

SpecTran Corporation
Sturbridge, MA

Heavy metal fluoride (HMF) glasses are of considerable interest for use as multispectral optical components. HMF glass samples of different compositions were prepared and subjected to different doses of gamma radiation at room temperature. Optical absorption measurements showed that strong damage occurred in the UV and visible regions and no significant losses were detected in the infrared region.

1.0 INTRODUCTION

Heavy metal fluoride (HMF) glasses are of considerable interest for use as multispectral mid-infrared/visible shared aperature optical components [1 & 2]. The primary characteristics are continuous transparency from the mid-ir (~8.5 μm) to near-uv (~0.25 μm), a low refractive index, (< or = 1.5), low dispersion over both the ir and visible (Abbe # = 80), low rayleigh scattering (less than silica glasses), low thermal distortion, low non-linear coefficient and resistance to chemical attack by gases and halide acids as reported by El-Bayoumi, et al. (3). An envisioned application for this glass family is in ionizing radiation environment. HMF glasses offer potentially lower intrinsic loses and lower susceptibilities to nuclear radiation than do silica-based glasses. (4).

Impurities and imperfections exist in all optical components and can contribute significantly to intrinsic optical losses. For some applications, a certain level of imperfections can be accepted under quiescent conditions which may become absorbing centers when subjected to ionizing radiation. The susceptibility of silica-based bulk glasses and fibers to nuclear radiation has been extensively studied and reviewed [5]. In oxide glasses, loses observed in the near-ir are due to the long radiation-induced absorption tails that are centered in the visible and near-uv spectral regions. The formation of the color-centers depends primarily on the total radiation dosage, dose rate, temperature, glass composition, and exposure time. These losses, which usually have both transient and permanent characteristics, can significantly compromise the performance of optical components in nuclear environments. HMF glasses, on the other hand, may be less susceptible to ionizing radiation because the induced absorption bands usually peak at shorter wavelengths and have tails which decrease rapidly at longer wavelengths.

In this paper, we report the effect of ionizing gamma radiation on the optical properties of bulk HMF glasses in the spectral region 0.2μm to 9.0μm. The concentration of InF_3 on NaF and, consequently, the content of fluorine ions on the radiation induced damage in the fluorozirconate glass family (ZBLA) is examined. Irradiated glass samples were annealed at 100°C to increase the fluorine ion mobility without grossly affecting the glass structure and at temperatures near the glass transition temperature (Tg) where structural relaxation can occur. However, within two hours after irradiation, annealing at room temperature also became significant in the visible region. The primary objective of this work is to determine parameter required to anneal some or all of the radiation induced damage without compromising the integrity of the optical component.

2.0 EXPERIMENTAL

In this study, four compositions based on fluorozirconate (ZBLA) glass having a molar ratio $57ZrF_4$ - $36BaF_2$ - $3LaF_3$ - $4AlF_3$ were selected. This particular ZBLA glass was selected because of its stability and it has been extensively characterized [6-8]. The glass compositions and the modulated fluorine ion content of the base glass (a) are listed in table 1. Glass

transition tempertures (Tg) and crystallization temperatures (Tx) were determined using a Perkin-Elmer 7500 differential scanning calorimeter (DSC) at a heating rate of 10°C/min in an argon atmosphere.

Commercially available anhydrous fluorides were used as starting materials: ZrF_4 (99.0% or better, Cerac) was sublimed in-house to remove carbon and oxide impurities. The sublimation procedure is reported elsewhere [9]. BaF_2 and NaF ("Optipur" grade, EM Laboratories), LaF_3 (99.9%, Rare Earth Division, American Potash and Chemical Corporation), AlF_3 and InF_3 ("Optical grade, 99.5% Cerac) where melted without further refining. All chemicals were handled, weighed and mixed in an argon filled glovebox, with less than 20 ppm oxygen and water.

GLASS SAMPLE I.D.	GLASS COMPOSITION (MOLE%)						MOLE % F^-
	ZrF4	BaF2	LaF3	AlF	InF3	NaF	
A	57	36	3	4	--	--	0
1402	57	36	3	3	1	--	0
1430	53	20	4	3	--	20	28
D	57	36	3	4	--	2	-2

Tg = (265 - 320) C

Tx = (315 - 400) C

Table 1. Composition, Fluorine ion Variation, Glass Transition (Tg), Crystallization (Tx) Temperature Range.

Fluoride glass batches were melted in vitreous carbon crucibles using a radio frequency heated assembly. The furnace is sealed to the bottom of the glovebox allowing the top to be opened to an atmosphere controlled area as shown in figure 1. All glass batches were melted for two hours at 770°C. At the end of the melting cycle, the molten glass was stirred and allowed to cool to 575°C before being poured into a brass mold preheated to Tg-15°C (glasses A&D) or crucible cooled (glasses 1402 & 1430). All glasses were annealed at Tg for two hours and cooled to room temperature over four hours. The glasses were cut and polished to a 1.0 micron finish using diamond paste.

Glass samples were irradiated at Rome Air Development Center's radiation facilities at Hanscom AFB, MA using cobalt-60 gamma source at room temperature for roughly 20 minutes, depending upon the dose required. All absorption measurments started within ten minutes of the irradiation to minimize the effect of room temperature annealing. A seperate experiment, discussed later in this text, was conducted to measure the extent of room temperature annealing. The optical absorption measurements in the spectral region 190nm to 3200nm were conducted on each sample before and after irradiation using Perkin-Elmer Lambda 9 UV/VIS/NIR spectrophotometer. The infrared transmission spectra of all samples in the optical region 2.0μm to 10μm were measured on a Perkin-Elmer 1600 series FTIR. A typical optical transmission spectra of ZBLA and thorium fluoride based families are shown in figure 2 compared with the optical transmission of fused silica glass.

Polished samples were measured for baseline absorption prior to irradiation. These test samples were then gamma irradiated with 1.0/Mrad. Trial irradiation runs showed that no induced optical damage could be detected beyond 1500nm. Irradiated samples were annealed at 100, 150, 200, 230, and 270°C for twenty four hours in a tube furnace under argon temperature.

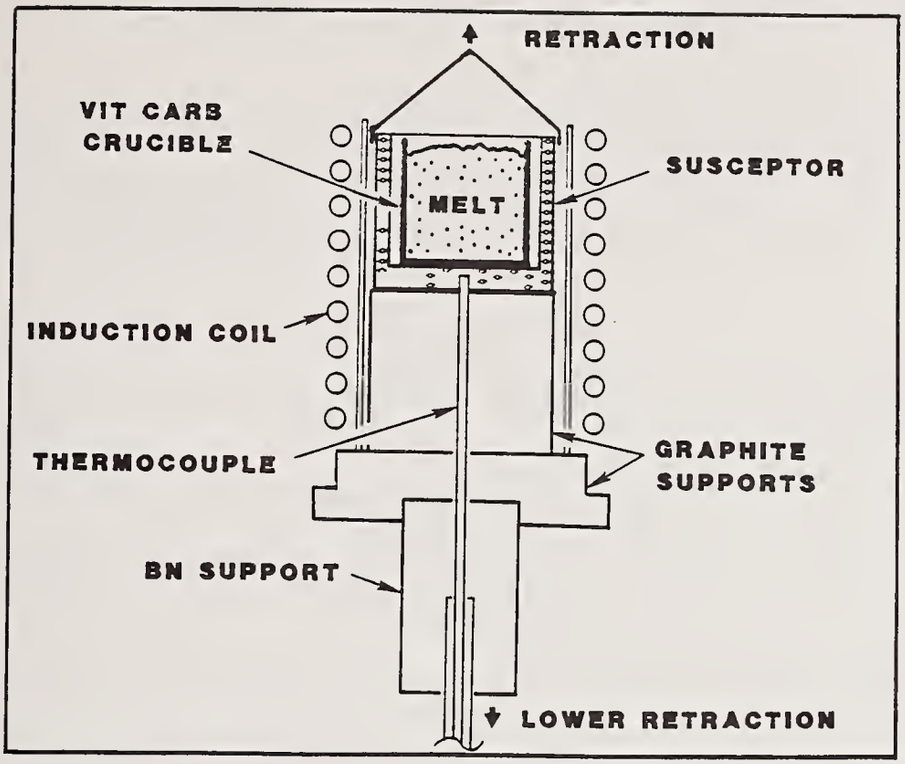

Figure 1. Fluoride Glass Melting Furnace Assembly

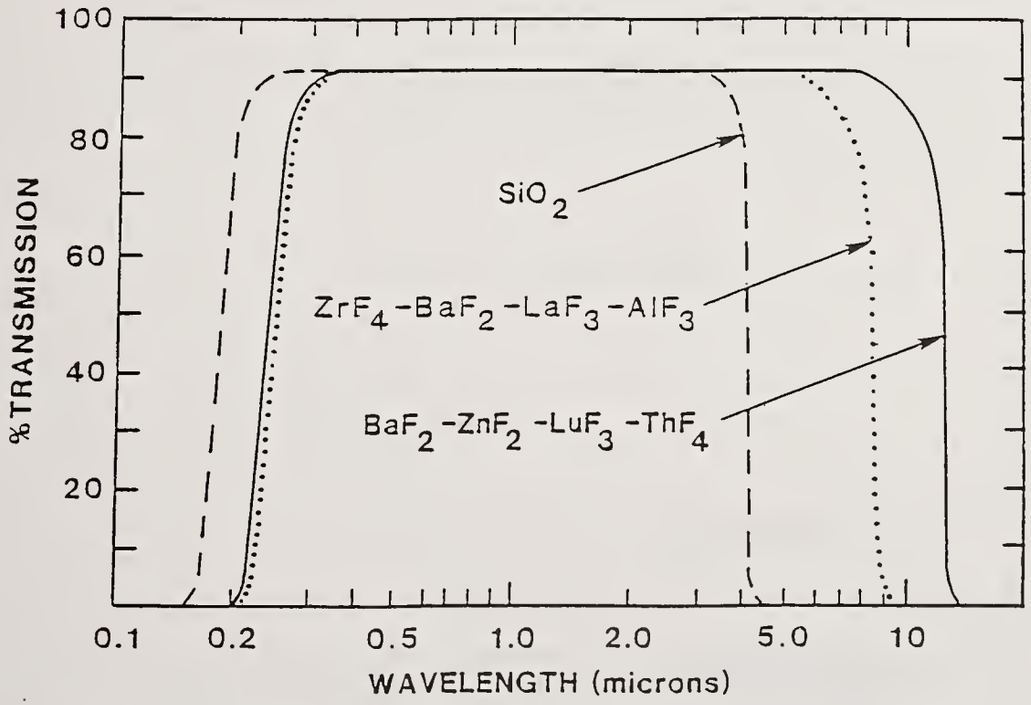

Figure 2. Comparison of UV-VIS-IR Transmission Windows in Silica and Heavy Metal Fluoride Glasses.

3.0 RESULTS AND DISCUSSION

The glass compositions, listed in table 1, were chosen to study the effect of InF_3 and NaF on the radiation induced damage in a fluorozirconate glass family. The effect of NaF addition on

the optical transmission of the base glass ZBLA (A) prior to irradiation is a slight shift in the infrared absorption edge towards shorter wavelength. Doping the base glass with InF_3 has no effect on the optical transmission spectra prior to irradiation.

Figure 3a is the optical transmission as a function of wavelength covering the range 2. 0-10.0μm for sample A before and after 1.0 Mrad gamma irradiation. It shows that this dose of radiation did not affect the optical transmission of this glass over this spectral region. This infrared hardness was observed in all fluoride glasses irradiated to 1.0 Mrad. Since no significant color-center peaks were observed over the spectral range 850nm and 3200nm in any of these glasses, as shown in figure 3b, discussion will focus on results obtained over the 200-850nm window, figure 3c.

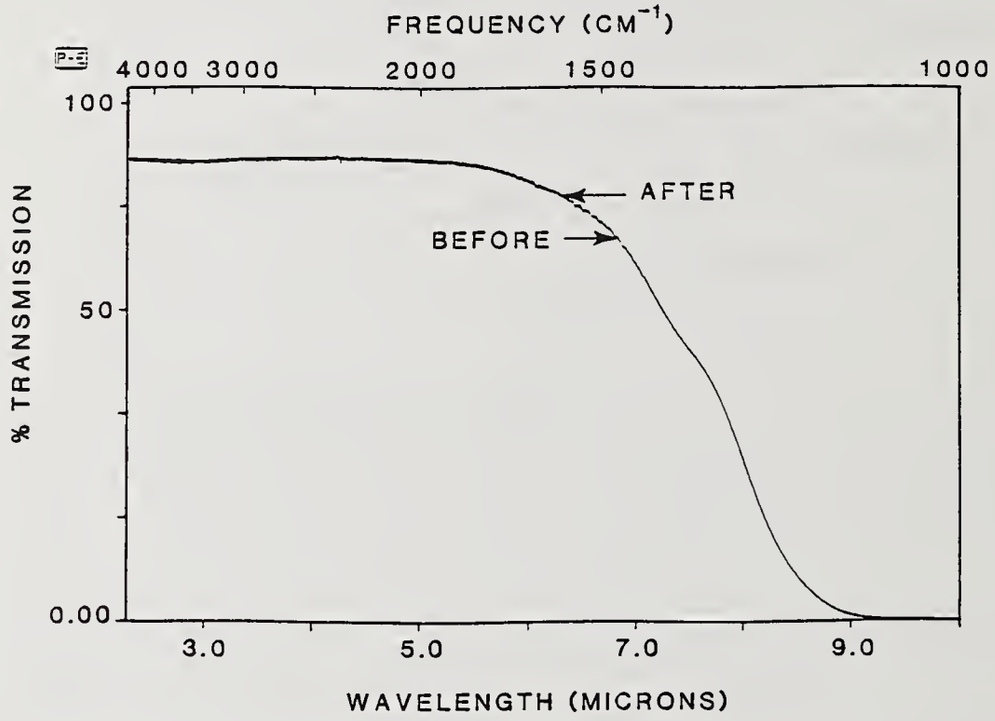

Figure 3a. ZBLA Infrared window before and after 1.0 Mrad Irradiation.

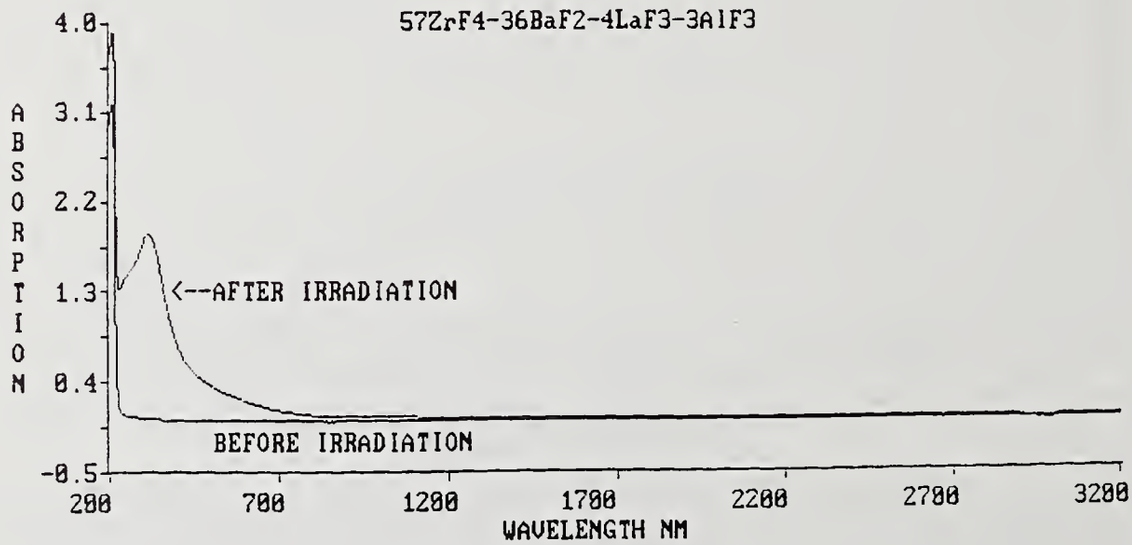

Figure 3b. ZBLA UV-VIS-NIR Window before and after 1.0 Mrad Irradiation.

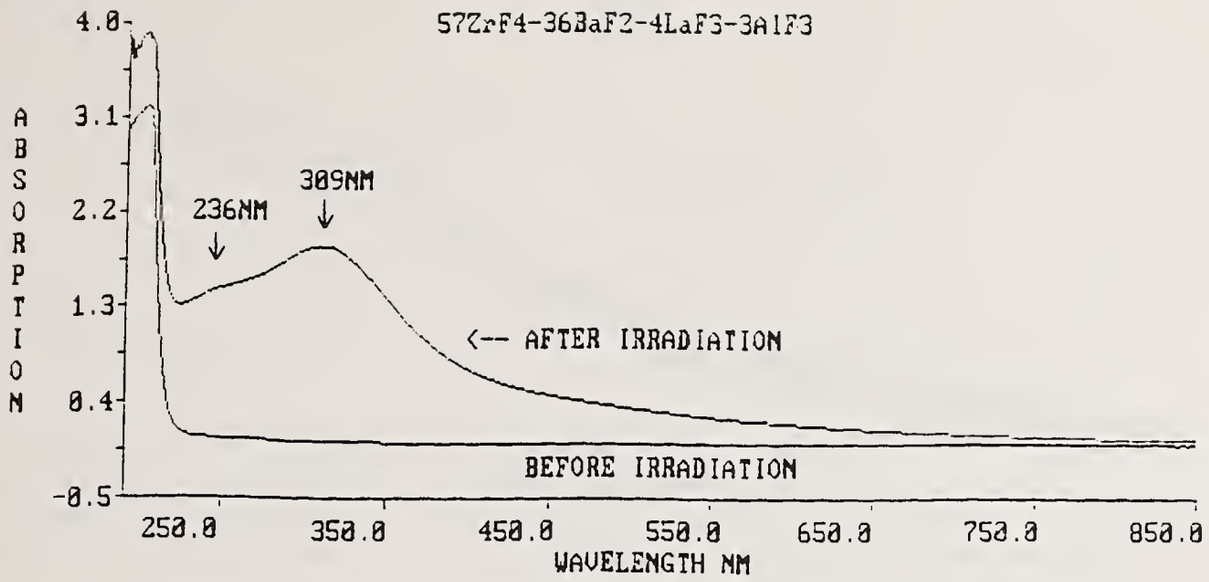

Figure 3c. Ultraviolet Color-Centers at 236 and 309nm Induced by 1.0 Mrad Irradiation in ZBLA Fluoride Glasses.

After 1.0 Mrad irradiation, the base glass ZBLA, and the sodium fluoride doped glasses ZBLAN, had dark brown and light brown tints respectively, whereas the indium fluoride doped glass ZBLAI, was nearly colorless. The optical absorption over the 200-850nm region in 1.0 Mrad damaged ZBLA and ZBLAN had similar profiles, as shown in figure 4a. Both glasses exhibited two strong absorption bands centered at 309 and 236 nm, which most closely match the assignments for Cl_2 FCI prescribed by Tanimura, et. al [10]. The uv edge shifted slightly towards longer wavelength and absorption below 206nm increased. The glass containing 1.0 mole% InF3 behaved far differently from ZBLA or ZBLAN glass shown in figure 4a. Induced absorption peaks were not observed at 309 or 236nm. However, growth of a color-center peak either in or close to vacuum-uv occurred as shown in figure 4b. The proximity of this absorption to the ultraviolet cut-off of the spectrometer precluded assessing damage in terms of shifts of the uv edge to longer wavelengths.

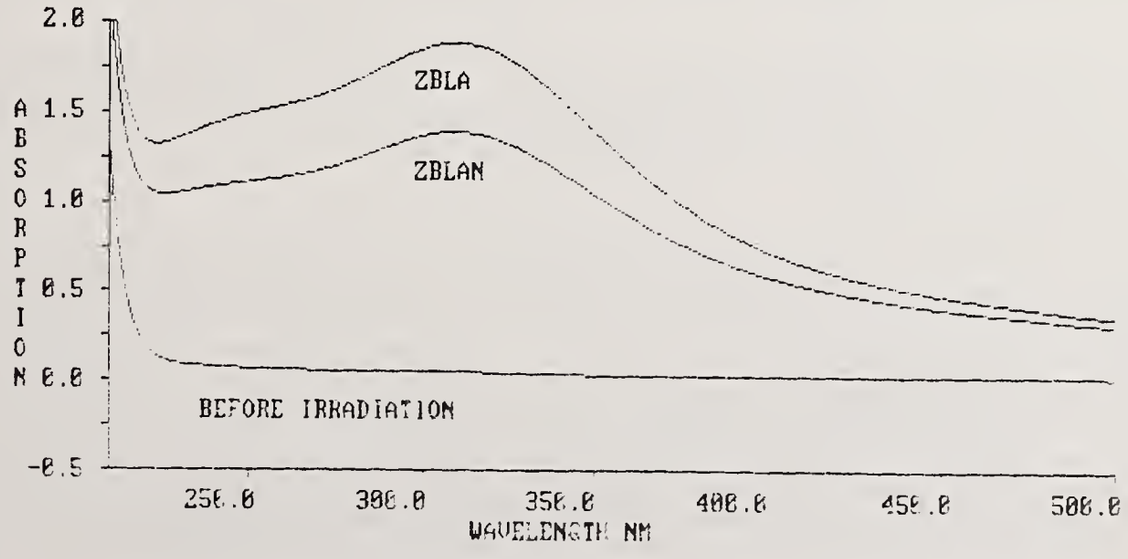

Figure 4a. Comparison of UV Color-Centers Induced in ZBLA and ZBLAN (2.0 mole% NaF).

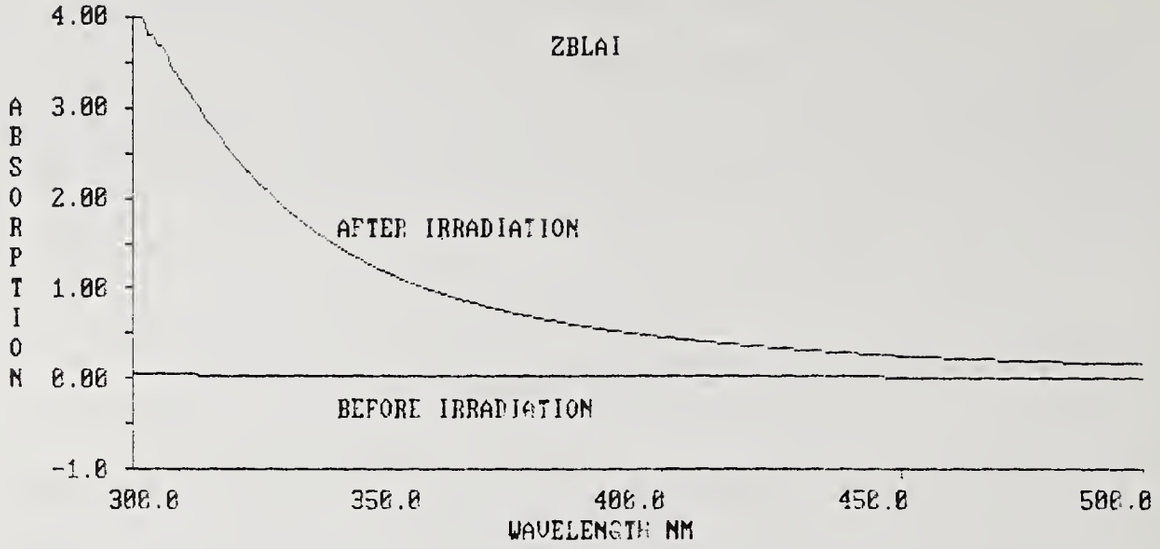

Figure 4b. Induced Damage in ZBLAI (1.0 mole% InF_3) Showing the UV Edge Shift.

3.1 LIFE TIME ANNEALING

Damage induced in all glasses by exposure to gamma irradiation could not always be completely annealed. However, room temperture annealing, (life time annealing), does start to occur as soon as the samples are removed from irradiation chamber. Life time annealing of the induced damage was performed on a ZBLAN glass sample irradiated to 1.0 Mrad as a test to determine a suitable heat treatment schedule. The absorption spectra in the 190-3200nm range was measured every ten minutes for two hours. The absorption spectra was scanned again four hours after irradiation. All fourteen scans are shown in figure 5. The most significant life time annealing of the induced damage over two hours occurred below 350nm.

Figure 6 is a plot of the percent change in absorption before and after 1.0 Mrad gamma irradiation as a function of life time annealing of the induced damage starting immediately after removal of the sample from the irradiation chamber. Seven traces are shown in figure 6 representing different wavelenghts in the UV and visible optical region. It is clear from this figure that induced damage is more significant at shorter wavelengths in the UV region. As expected, a decrease in the absorption of the induced color centers was measured with increasing annealing time. After one hour, significant annealing occurred at shorter wavelenghts. This annealing was less pronounced in the visible region. However, after two hours, room temperature annealing also became significant at longer wavelength.

As it was mentioned early in this text, the time required to measure a spectra over the region 190nm-3200 was ten mniutes. Life time annealing of induced damage occured after ten minutes from the time the sampe was removed from the irradiation chamber. This effect, however small, can be calculated for the purpose of precise qualitative analysis.

3.2 ROOM TEMPERATURE ANNEALING

The stability of the 309nm and 236nm induced absorption in ZBLA and ZBLAN glasses due to 1.0Mrad gamma irradiation was monitored as a function of room tempertaure annealing time ranging from 30 minutes to 31 days. Figure 7 is the optical absorption spectra of ZBLAN glass #1430 annealed at room temperature. The eleven traces represent the spectra of the glass sample before irradiation (bottom), immediately after irradiation (top) and after annealing at room temperature for 30 min, 60 min, 120 min, 180 min, 24 hrs, 48 hrs, 9 days and 31 days. It is clear that the 236nm absorption peaks has almost disappeared after 3 hours of room temperature annealing. The difference between 9 and 31 days annealing was negligible. This may suggest that the 236nm band is related to fluorine ion mobility and the 309nm band is due structural damage. In the case of ZBLAI glass, 50% of the induced damage due to 1.0 Mrad gamma irradiation was annealed after 31 days at room temperature as shown in figure 8.

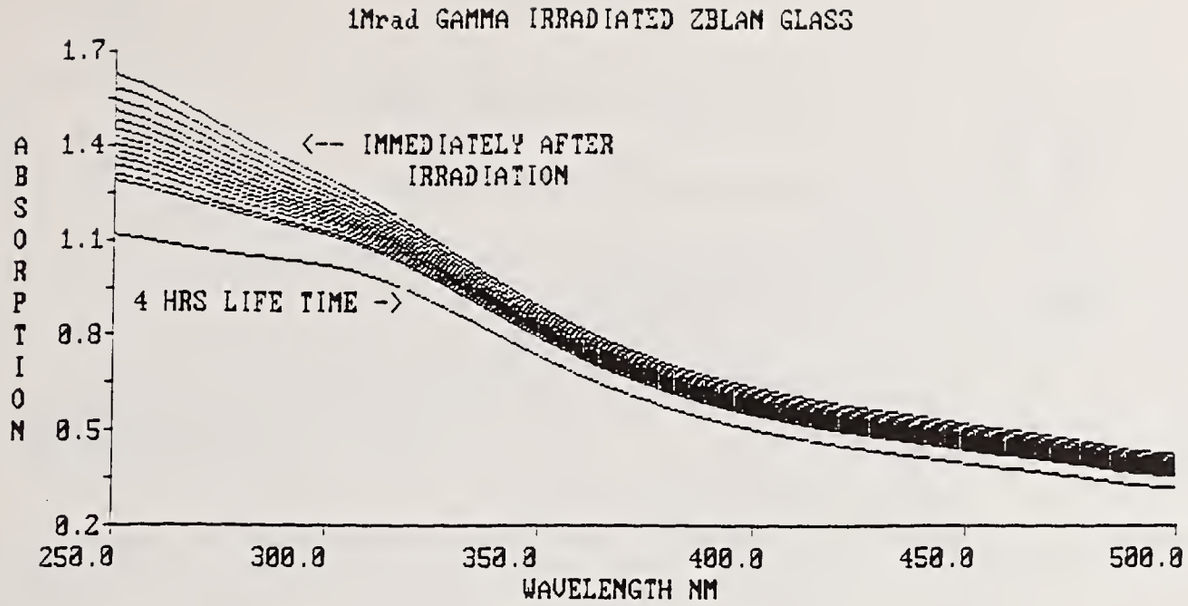

Figure 5. Four Hours Room Temperature Annealing of Induced Damage in 1.0 Mrad Gamma Irradiated ZBLAN Glass (20.0 mole% NaF).

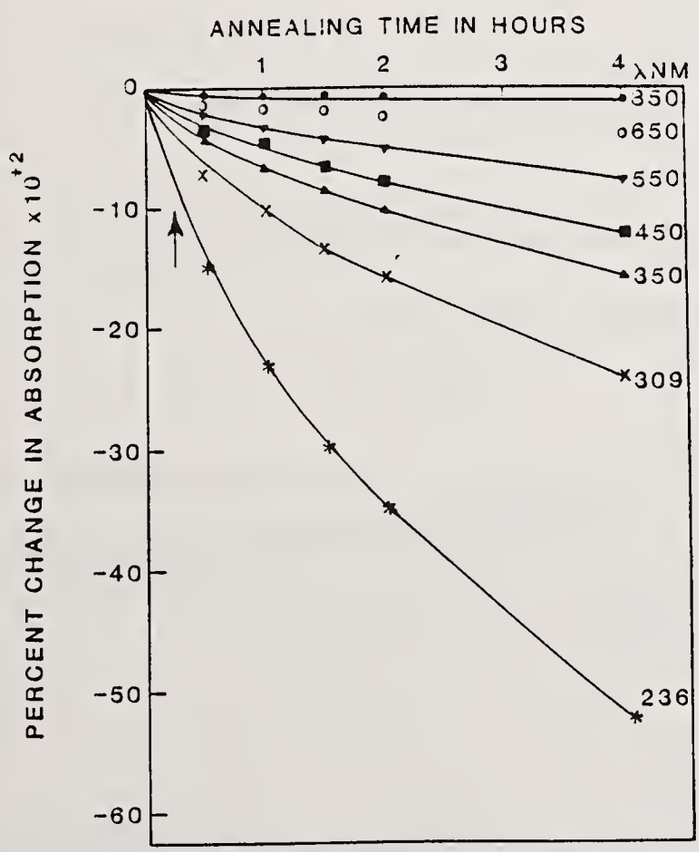

Figure 6. Room Temperature Life Time Annelaing of Induced Damage in ZBLAN Glass in the Visible and UV Regions.

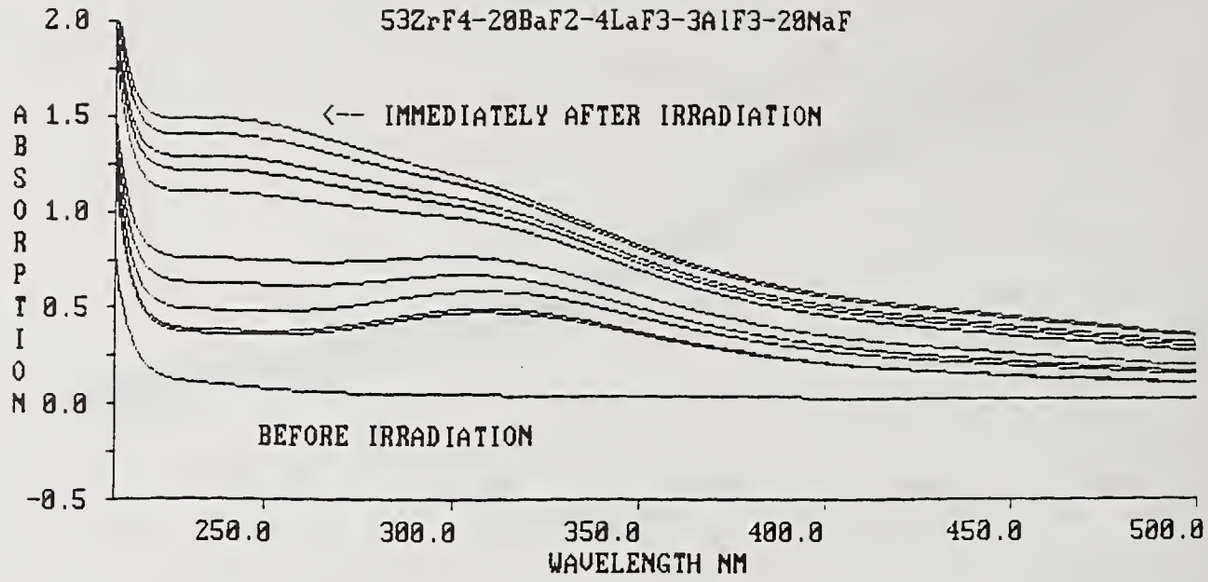

Figure 7. Thirty One Days Room Temperature Annealing of Induced Damage in ZBLAN (20.0 mole% NaF).

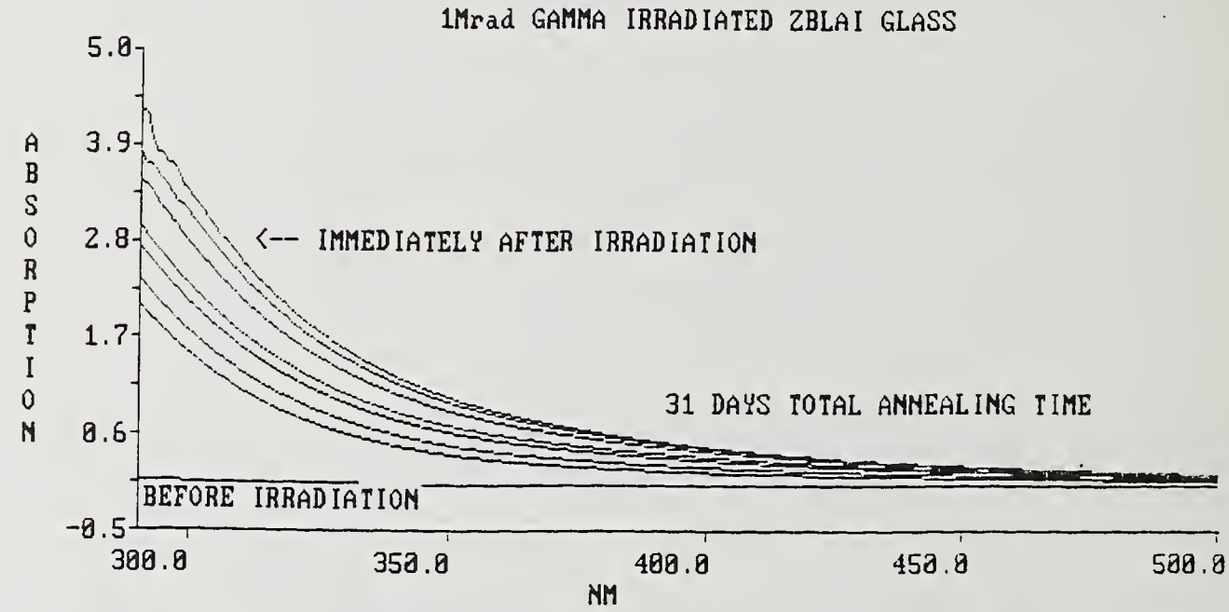

Figure 8. Thirty One Days Room Temperature Annealing of Induced Damage in ZBLAI Glass.

3.3 HIGH TEMPERATURE ANNEALING

The ZBLAN and ZBLAI glasses, after having been annealed for 31 days at room temperature, were heated for 24 hours at 100, 150, 200, 230, and 270°C. The absorption spectra of these glasses after heat treatment are shown in figures 9 and 10. Also shown in the same figures, for comparison, are the spectra before gamma irradiation and after annealing at room temperature for 31 days. It is clear that the induced damage was not completely annealed even when the glass samples were heated at or near the glass transition temperature where structural relaxation occurs.

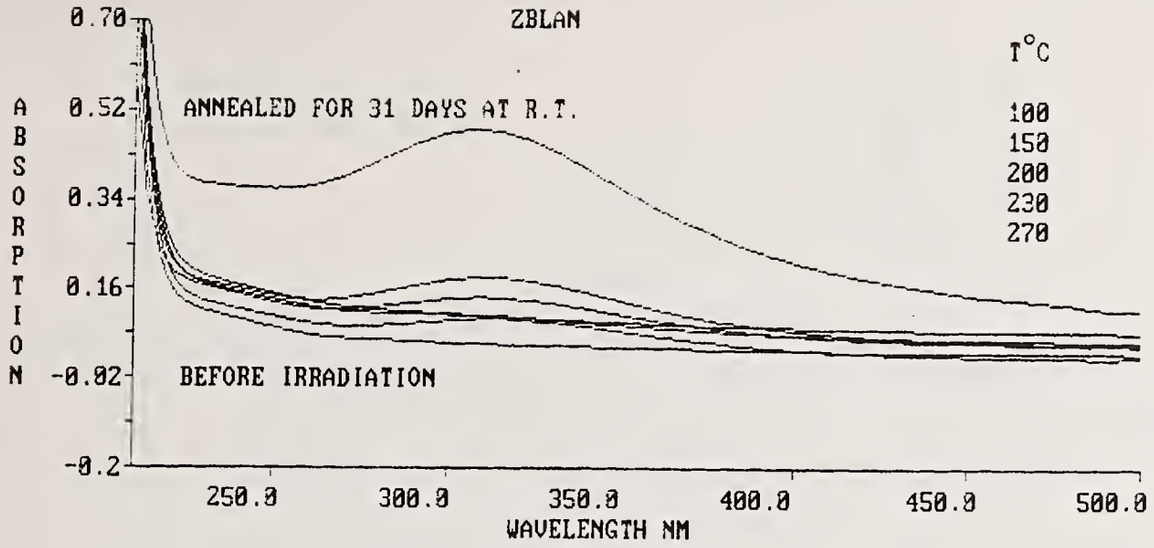

Figure 9. Twenty Four Hours Annealing of Induced Damage at Different Temperatures in ZBLAN Glass.

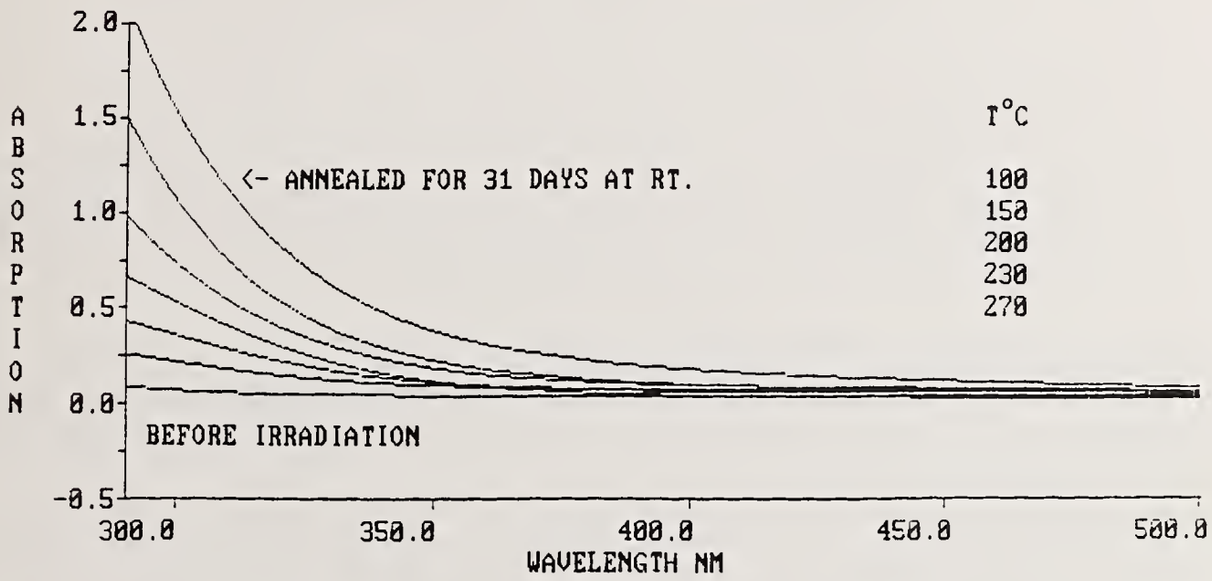

Figure 10. Twenty Four Hours Annealing of Induced Damage at Different Temperatures in ZBLAI.

The results in figure 9 and 10 are summarized in figure 11 where the percentage change in absorption before and after irradiation are plotted as function annealing temperature. The induced damage observed in ZBLAN glass was annealed to 15% of the original damage when the glass was heated at 100°C. The annealing process slowed markedly even after heating at the high temperature. In contrast, the recovery of the original absorption before irradiation of ZBLAI glass was gradual. Most of the damage was annealed only after heating the glass at 270°C, below the glass transition temperature.

4.0 CONCLUSIONS

Although the limited results presented in this work are not sufficient to present a complete characterization of radiation effect on the optical properties of heavy metal fluroide glasses, some interesting relationships can be highlighted. Induced damage due to 1.0Mrad gamma irradiation was not observed in the region 1.0-8.0μm. However, the tail of the UV and visible damage affected the absorption in the near infrared region (1.0-1.2μm). Strong induced damage was observed at 309 and 245nm in ZBLA glass and 309 and 236nm in ZBLAN containing 20.0 mole% NaF. The ultraviolet absorption edge was shifted towards longer wavelength as in the ZBLAI glass containing 1.0 mole% InF3.

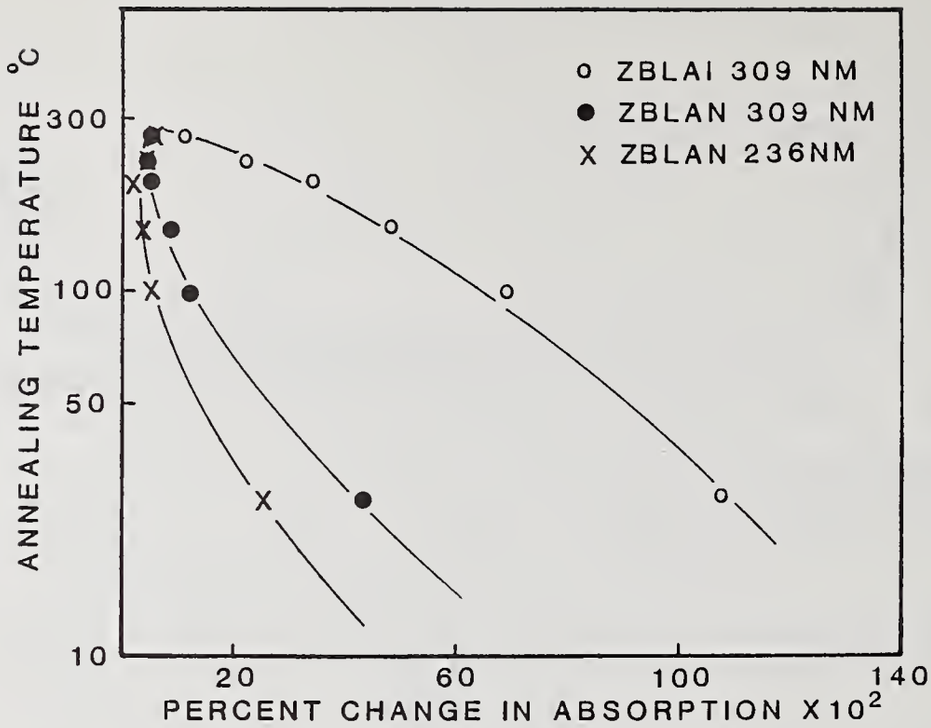

Figure 11. High Temperature Annealing of Induced Damage in ZBLAN and ZBLAI Glasses

In all these glasses, damage observed in the spectral region 1.0-1.2μm was completely recovered after a short room temperature anneal. When the glasses were annealed at 100°C for 24 hours, 90% of the damage was annealed in ZBLA and ZBLAN samples and only 60% of the transmission was recovered in ZBLAI glass. Most of the induced damage was recovered in ZBLAI glass. Most of the induced damage was recovered in ZBLA, ZBLAN and ZBLAI glasses when the samples were heat treated at near the glass transition temperature.

In conclusion, heavy metal fluoride glasses in the ZBLA family are susceptible to 1.0Mrad gamma irradiation in the ultraviolet and visible spectral region. Induced damage can be significantly reduced by annealing. High temperature annealing is effective for damage that occurs in the ultraviolet and visible region. Further work is necessary to identify sources and mechanisms of induced damage and to identify dopants that may eliminate or reduce damage and enhance transmission recovery below 100°C.

The authors would like to express their appreciation to Bruce L. Gilpin and John R. Cappelli for irradiating the glass samples and Steven D. Mittleman for valuable suggestions.

REFERENCES

[1] Drexhage, M.G.; Quinlan, K.P.; Moynihan, C.T.; Saleh-Boulos, M. Advances in Ceramics. Vol 2. Edited by Bendow, B. and Mitra, S., The American Ceramic Society, Columbus, OH, 57; 1981.

[2] Gannon, J.R. Proc. SPIE, (266): 63: 1981.

[3] El-Bayoumi, O.H.; Suscavage, M.J.; Bendow, B.J., Non-Crystalline Solids. 73 (1-3): 613; 1985.

[4] Gannon, J.R. J., Non-Crystalline Solids. (43): 239; 1981.

[5] Frieble, E.J., Opt. Tng. (18): 552; 1979.

[6] Drexhage, M.G.; El-Bayoumi, O.H.; Moynihan, C.T., Proc. SPIE (320): 27; 1982.

[7] Polain, M.; Lucas, J. Verres refract. (32): 505; 1978.

[8] Miyashita, T.; Manabe, T., IEEE J. Quan. Elec. (QE-18): 1432; 1982.

[9] Hutta, J.J.; Suscavage, M.J.; Drexhage, M.G.; El-Bayoumi, O.H., Proc. SPIE (484): 83; 1984.

[10] Tanimura, K.; Ali, M.; Feuerhelm, L.F.; Sibley, S.M.; Sibley, W.A.; J. Non-Crystalline Solids. (70): 397; 1985.

COMMENTS

Question: Some place between 10 and 15 years ago, an experiment was performed at the Air Force Weapons Laboratory to study subsurface influences on the damage of fused silica surfaces. Let me briefly describe what was done. We started off with a rather rough course grind and, as you know, the general rule of thumb is that subsurface fractures are produced that of three times what the grit size is. After grinding the samples we would remove a sample and continue the process with the next finer grit size, removing three times the previous grit size, and then remove a sample until we got down to about a 3 micron grit. We then took all of those samples which had various levels of subsurface damage and polished all of them in the same way. We obtained surfaces, if I recall, on the order of 7 angstroms RMS, certainly not a super polish but not bad. After performing the laser damage experiments, we saw no difference in the damage threshold with all these varying degrees of subsurface fracture. The damage measurements were done at 1 micron and 30 nanoseconds, just for the audience's interest.

Answer: In those days when people were doing subsurface damage studies, there was no technique that really revealed what the surface conditions were. The only criteria that they were using was a stamped-on particle size and they were assuming by the "rule of thumb" to remove a certain amount of material. What we are saying here is that for brittle material, and especially optical material and semiconductor material, which is quite fragile, when you don't remove all the subsurface damage during polishing, there are crack propagations in the surface which drive deeper and deeper beneath the surface, resulting in this sense in surface damage. So in some of the earlier studies, what we think is that it made no difference because whatever polish was used, it did not eliminate this subsurface damage layer. The damage threshold was basically saturated in terms of subsurface damage. So you didn't see any difference no matter what you did. We are proposing here that the technique described in this paper is the only time that we have had a nondestructive technique that allows you to qualify and to characterize what the surface looks like before you try to damage it. It should now be possible to get some meaningful data and see if there is any difference caused by subsurface damage on other levels.

Question: Could you tell me how you concluded that there are impurity clusters in the defects?

Answer: Well, we have done Secondary Ion Mass Spectroscopy.

Question: On fused silica?

Answer: Not on fused silica; there's a lot of charging on fused silica. On fused silica, the impurity cluster is looked at by some sort of a chemical etch technique to delineate the etch and look at the strain patterns using high resolution electron microscopy to see what the strain looks like. We don't know, certainly, what kind of contaminants we have in those impurity clusters.

Question: So you don't have any direct evidence that there are impurities in those defects?

Answer: Right.

Question: I think you need to tell us a little more about your experiment. If I understand from your abstract, the damage measurements were made in the ultraviolet at 2480 angstroms, which might have some effect on the sort of damage that you see. The other thing is what you mean by "standard polish" and "super polish." Quite honestly, I have never seen this sort of "pits" in the standard polish samples that you seem to be seeing. When looking at it, say for example, under Nomarski microscopy, the defects look like etch pits.

Answer: The surface that you look at has been subjected or has been exposed to a delineation etch. You don't see anything on the Nomarski microscope until after you etch it. Then you expose all the pits and scratches.

We etch the surface for a specific time to remove a specific amount of material, and then we look at the surface using a Nomarski microscope and see what type of features are brought out or decorated by the etch.

Question: So all the pictures you showed were after etching?

Answer: They have been etched.

Question: Can you tell us a little bit about your etch?

Answer: The etch is different from the HF base etch. This is another area of the topic that I presented some data on at the ASPE meeting. It's a very, very elaborate chemical screen to look at the kinetics. By using different proportions of chemical oxidizing agent and complexing agent to desoften the material one can bring out this subtle damage. People using the HF alone might see some damage, but they don't really have the high resolution of the etch that we have developed. And I will not reveal the etch formulation at this time.

Comment: I see. It makes it difficult to check your work.

Answer: That's fine. We are not here trying to exchange information; we are more doing business. We will not reveal the etch.

Comment: This is a scientific meeting by the way.

Answer: We are building a photon backscattering system from a commercial point of view. Once we build that, we will reveal all the information we have found for the past eight years. That is because of people who steal the data and don't give us credit.

Comment: I guess I would disagree most vigorously. We are here to exchange information. That's the nature of scientific meetings. Second thing I would say is that criminology, first and only, doesn't leave much maneuvering room. I congratulate you in patenting photon backscattering, but there have been many people at this meeting that have reported various optical techniques for examining the quality of optical surfaces prior to damage. "Frustrated Total Internal Reflection" by Paul Temple is one example that I think stands out. I think the people at Rochester had developed a very elegant system also for using small scale photo acoustic techniques for mapping out surfaces. Finally, I would note that the terminology of super polish and nonsuper polish was one, too, that about 15 years ago we decided was not very quantitative. One man's super polish is often another man's fine grind.

Answer: True. That's why we developed the KBS system. The super polish is a commercially available optic. It's not what we're doing. So we're here just to bring out to you that this work has been done extensively in the semiconductor industry. The optical industry is not really open to evaluating this technique, and they're trying to invent other techniques that are not really sensitive enough to determine what the surface characteristics are on the surface they're looking at.

Manuscript received
2-12-90

The Effect of Laser Annealing on Laser Induced Damage Threshold

N.C.Kerr and D.C.Emmony

Department of Physics
Loughborough University of Technology
Loughborough
Leicestershire
U.K.

A significant enhancement of the single shot Laser Induced Damage Threshold of CaF_2 and fused silica and a moderate enhancement for GaAs and Al has been observed as the result of laser annealing using an excimer laser operating at 248 nm. This phenomenon is primarily attributed to a reduction of the residual surface roughness of the samples.

Key words: Excimer laser; Laser beam annealing; Laser induced damage

1. Introduction

In the context of Laser Induced Damage (LID) laser annealing refers to irradiating samples at non damaging fluences with the intention of raising their Laser Induced Damage Threshold (LIDT).

This effect has been reported by several authors. Swain et al [1] reported upto a factor of 2 increase in the single shot threshold of colloidal silica antireflection (AR) coatings if they are processed by typically 10 non damaging pulses. Temple et al [2,3] have reported more than a factor of 2 increase in the LIDT on samples of fused silica processed by a cw CO_2 laser and then damage tested by a pulsed 1.06μm wavelength laser.

Two mechanisms are thought to be responsible for this effect. Temple et al have proposed that the cracks and scratches left on the surface after mechanical polishing are reduced by the heating effect of the laser whereas, Swain et al have suggested that the heating effect removes surface contaminants. Both of these mechanisms result in a more "ideal" surface and thus will increase the surface damage threshold.

Qualitative enhancement of the LIDT of a range of UV and IR materials; such as fused silica, CaF_2, GaAs, Si, Ge, and MgF_2 by laser annealing have been observed by the authors whilst using the damage test facility at Loughborough University of Technology [4]. To determine if either of the proposed mechanisms dominates the annealing process we endeavoured firstly to quantify the increase in LIDT for a variety of annealing regimes and then to make careful observations of how the surface composition, morphology and structure had been altered by the annealing process.

2. Experimental

The damage facility centres around a Lambda Physik model EMG 200 excimer laser. This is operated with a Krypton and Fluorine gas mix and produces a nominal 1J pulse of

30ns duration at a wavelength of 248nm. A 20cm focal length fused silica lens was used to focus the beam such that the full width at the $1/e^2$ points in the horizontal and vertical directions was respectively 1.5mm and 0.5mm. Control of the pulse energy was achieved by means of a liquid dye cell attenuator, filled with rhodamine 6G in distilled water, whilst measurement of beam energy was performed using a Gentek joulemeter calibrated using a Laser Instrumentation Calorimeter. The spatial profile of the excimer beam and hence the on-target fluence levels were measured using a computer-controlled video framestore system [5] that essentially images the fluorescence that the excimer beam produces in a thin piece of absorbing glass. The beam which had no localised hot spots had an approximately gaussian profile in the vertical direction but was almost rectangular in the horizontal direction. Peak fluence in the beam is quoted throughout this paper.

The surface morphology of the samples was investigated using a Scanning Electron Microscope (SEM), optical microscopy, and following Temple [6] Total Internal Reflection Microscopy (TIRM). The surface structure was investigated using a Scanning Transmission Electron Microscope (STEM) for electron beam diffraction whilst the surface composition was determined using Secondary Ion Mass Spectroscopy (SIMS) and Laser Induced Mass Analysis (LIMA).

A High Resolution Schlieren imaging system utilising a computer controlled video framestore and camera [7] was used to detect the onset of damage. The apparatus was arranged as shown schematically in figure (1). A 5mW HeNe laser was used as the source of the surface probe. Damage is defined as a significant measurable change between an image in the framestore of the surface before an incident excimer pulse and an image taken after the pulse.

Measurements of the single shot LIDT were made on samples of Ge, Al, Si, GaAs, fused silica and CaF_2. Prior to testing these samples underwent no special treatment except to have their surfaces wiped with methanol to remove dust etc. Two types of Si were used during this work. The first consisted simply of boron doped single crystal wafers used for the initial damage threshold measurements. At a later stage thin sputtered amorphous Si films were used for the electron diffraction work. These films were formed by dc planar magnetron sputtering onto ICI 'o' grade 50μm thick polyethylene tetraphthalate. This flexible polymer was handled in the vacuum web coater of Ridge et al [8] and coated from the 100mm exposed pole magnetron described by Spencer et al [9]. The film thickness was approximately 60nm. The sputtering was performed by Dr R.Spencer and R.Howson of the University Vacuum Coating Group [10].

Firstly the samples were damage tested to determine their initial, unannealed single shot damage thresholds. The excimer fluence incident upon the sample surface was gradually increased and at each fluence 6 individual sites on the sample surface were damage tested. Usually for an accurate determination of damage threshold more surface sites are irradiated but because in this experiment large changes in threshold level were expected fewer sites could be used. The damage threshold was defined as the fluence which produced damage on 50% of the sites tested at that fluence.

The same process was then repeated, but prior to irradiation the area being tested was given a series of annealing laser pulses. These were varied in intensity from just below the untreated surfaces damage threshold to less than a tenth of the value and in number from one to a hundred. The damage threshold was again set at the 50% survivability level for each of the different annealing regimes used.

3. Results

Modification of the LIDT for fused silica and Al are shown graphically in figure (2) and figure (3). CaF_2 showed results similar to those of fused silica whilst GaAs showed results similar to those of Al. Annealing Si and Ge gave no measurable increase in LIDT but a clear decrease in the amount of damage caused by the excimer pulses. This effect is

more clearly seen on dielectric surfaces were the annealing pulses were of very low fluence, see figure (4). Annealing pulses with fluences in the range of 60- 80% of the untreated single shot LIDT produced the most significant changes in LIDT. At fluences much below 50% of this level no significant rise in the single shot LIDT was observed for annealing regimes involving up to several hundred pulses. The relative change in LIDT for the Al and GaAs samples was not as large as for dielectric materials.

Analysis of single crystal wafer samples of Si before and after annealing using SIMS showed an order of magnitude change for the sodium line at mass number 23, figure (5). Typical LIMA results are shown in figure (6).

Using optical microscopy to examine the morphology of the annealed surfaces showed that for every surface which had been annealed the degree of roughness upon it was reduced. In some cases it appears that nearly all surface marks have been totally removed over the area of interaction of the laser beam whereas in others the roughness has been greatly reduced but not entirely removed, see figure (7).

The very smooth CaF_2 and fused silica surfaces showed no detail using dark field microscopy but using TIRM it is clear that laser annealing has removed surface marks, figure (8).

Investigations of annealed, specially prepared amorphous silicon surfaces using electron beam diffraction showed that the crystal structure of the sample had changed significantly during the annealing process, see figure (9).

4. Discussion

Inspection of dark field images for an annealed Al surface such as that in figure (7) would indicate by the reduced number of bright spots in the image that the sharp edges on the sample surface have been removed, however care must be taken in the interpretation of these photographs. Using interference contrast microscopy, figure (10) it is clear that rather than removing the two scratches running across the laser interaction area the annealing has simply rounded off their sharp edges. Note also the "doughnut" shaped structures around points in the annealed area. These are characteristic of melting and subsequent resolidification of a localised region on the surface of a material where the density of the liquid phase is less than the density of the solid [11]. These regions appear localised around what we assume to have been sharp points on the unannealed samples surface. It should be noted that dark field images are obtained using a type of Schlieren process which stops off the zeroth order, and some of the lower orders in the light forming the image of the surface. For this reason dark field imaging shows up the high frequencies due to sharp points on the surface but not the more smoothly varying contours.

The theory by Bloembergen [12] demonstrates that sharp edged cracks or defects on a surface lead to the largest enhancement of the local surface electric field and consequently a reduction of the surface LIDT over the bulk. The removal of such sharp edges will effect the magnitude of this field enhancement and therefore the damage threshold of the surface.

It is the authors' contention that the reduced effect of annealing on metal or semiconductor surfaces compared to that on dielectrics can be explained in terms of their differing interactions with the incident radiation. In a dielectric the absorption of the incident energy is small with the result that the small increase in absorption due to the enhanced electric fields around local surface roughness can be a significant fraction of the total absorption. Thus a small change in surface roughness can cause a large change in LIDT. In the case of a metal nearly all of the laser energy is absorbed within 100nm

of the surface (the skin depth). The increased absorption due to the enhanced electric fields at the surface are thus relatively insignificant compared to the total absorption of energy in the sample and hence annealing has little effect on the surface LIDT.

Removal of contaminants by any method can certainly be expected to raise the damage threshold of a surface. Clark [7] notes that the removal of absorbed contaminants from the atmosphere in Sol-Gel coatings by cleaning with Methanol can greatly increase their damage threshold. To this end analysis using LIMA was performed at low laser fluences and at a wavelength of 266nm, nearly equal to that of the excimer laser. Initially it was hoped that the low fluence pulses would simulate the situation encountered during laser annealing with the excimer laser. The resulting mass analysis would then indicate the species being evolved from the sample during the annealing process. However, for LIMA to function it must always vapourize and ionize a small volume of the sample, hence damaging the surface. The results would seem to indicate that common surface contaminants, absorbed from the atmosphere, can be expected to be evolved during the annealing process, at the typical laser fluences used.

Similarly, our results from SIMS analysis can be interpreted to demonstrate that surface contaminants in the form of sodium are being burnt off the surface by low fluence laser pulses.

Liu [13] and Leamy [14] have demonstrated that it is possible to change polycrystalline Si to single crystal material by laser annealing. Intuitatively we feel that such an annealing process could be used to raise the surface damage threshold of semiconductors, this is confirmed by Cullis [15]. It is noted that any process which will produce a single crystal layer on a sample surface will result in a larger resistance to laser induced damage. However after reading the papers by Liu and Leamy it is clear that the fluences they were using to produce their changes were well above the damage threshold level of the samples. It is however pointed out by Vitali [16] that even at low laser fluences, well below the surface damage threshold, as used here changes in crystal structure can be expected such as from amorphous to polycrystalline, or polycrystalline to single crystal depending upon the exact fluence used and the number of laser pulses. The results reported herein would certainly confirm this observation. The amorphous silicon structure as indicated by the diffuse ring pattern in figure (9a) has clearly been transformed by laser annealing into a polycrystalline pattern as indicated by the well defined rings in figure (9b).

This transformation was induced by multiple laser pulses with fluences of $0.25 Jcm^{-2}$, well below the melting threshold for Si of $0.65 Jcm^{-2}$ at 248nm quoted by Jellison [17]. It should be noted however that Vitali clearly demonstrates that structural transitions such as the above can gradually occur without the material being constrained to melt by irradiating with successive laser pulses which lead to a cumulative effect.

5. Conclusions

Laser annealing can significantly improve the LIDT of a sample surface. The dominant process leading to this would appear to be removal or reduction of the severity of surface roughness. Strong indications of the removal of surface contaminants and changes to the surface crystal structure means that these mechanisms cannot be ruled out as contributing processes in raising the LIDT.

Acknowledgements

N.C.K. acknowledges the financial support of SERC and BDH Ltd, Poole, Dorset. We are indebted to Dr. Alison Chew and D.Sykes of Loughborough Consultants Ltd. for the use of their SIMS. We would also like to thank J.Bates, Angela Kerr and Anne Waddilove for helpful discussions and technical assistance.

References

[1] J.E.Swain, W.H.Lowdermilk, D.Milam,"Raising the Surface Damage Threshold of Neutral Solution Processed BK-7 by Pulsed Laser Irradiation," Natl. Bur Stand. (U.S.) Spec. Pub. 669 (1982), pp292

[2] P.A.Temple, W.H.Lowdermilk, D.Milam,"Carbon Dioxide Laser Polishing of Fused Silica Surfaces for Increased Laser-Damage Resistance at 1064 nm," Applied Optics, Vol. 21, No 18, pp3249, (1982).

[3] P.A.Temple, W.H.Lowdermilk, D.Milam,"CO_2-Laser Polishing of Fused Silica Surfaces For Increased Laser Damage Resistance at 1.06μm," Natl. Bur. Stand. (U.S.) Spec. Pub. 568 (1979) pp229.

[4] S.E.Clark, I.Laidler, D.C.Emmony, B.A.Omar, M.J.Shaw,"U.V. Laser Beam Diagnostics using a Computer Controlled Video Framestore System," Natl. Bur. Stand. (U.S.) Spec. Pub. 746 (1985), pp35.

[5] B.A.Omar, S.E.Clark, D.C.Emmony, D.B.Hollis, M.J.Shaw,"The Application of Doped Glass Fluorescers to the Recording of Pulsed Ultra-Violet Laser Beam Profiles," Optics and Laser Technology, Vol. 20, No 4, pp193, (1988).

[6] P.A.Temple,"Total Internal Reflection Microscopy: A Surface Inspection Technique," Applied Optics, Vol. 20, No 15, pp2656, (1981).

[7] S.E.Clark,"Excimer Laser Induced Modification of Optical Surfaces," Ph.D. Thesis, Loughborough University, England, (1988).

[8] M.I.Ridge, R.P.Howson, C.A.Bishop, Proc. SPIE, Vol. 325, Optical thin films, pp46, (1982).

[9] A.G.Spencer, C.A.Bishop, R.P.Howson, Vacuum, 37, pp363, (1987).

[10] Vacuum Coating Group, Loughborough Consultants Ltd, University of Technology, Loughborough, Leicestershire, (U.K.).

[11] D.C.Emmony, N.J.Phillips, J.H.Toyer, L.J.Willis,"The Topography of Laser-Irradiated Germanium," J. Phys. D: Appl. Phys., Vol. 8, pp1472, (1975).

[12] N.Bloembergen,"Role of Cracks, Pores and Absorbing Inclusions on Laser Induced Damage Threshold at Surfaces of Transparent Dielectrics," Applied Optics, Vol. 12, No 4, pp661, (1973).

[13] P.L.Liu, R.Yen, N.Bloembergen, R.T.Hodgson,"Picosecond Laser-Induced Melting and Resolidification Morphology on Si," Appl. Phys. Lett., Vol. 34, No 12, pp864, (1979).

[14] H.J.Leamy, G.A.Rozgonyi, T.T.Sheng, G.K.Celler,"Periodic Regrowth Phenomena Produced by Laser Annealing of Ion-Implanted Silicon," Appl. Phys. Lett., Vol. 32, No 9, pp535, (1978).

[15] A.G.Cullis,"Transient Annealing of Semiconductors by Laser, Electron Beam and Radiant Heating Techniques," Rep. Prog. Phys., **48**, (1985), p1155-1233.

[16] G.Vitali, "On some less evident aspects of laser annealing," Phys. Letts., vol. 78A, No 4, pp387-390, (1980).

[17] G.E.Jellison, D.H.Lowndes, D.N.Mashburn, R.F.Wood, "Time resolved reflectivity measurements on silicon and germanium using a pulsed excimer KrF laser heating beam", Physical Review B, Vol. 34, No 4, pp2407-2415, (1986).

Figure captions.

Figure (1).
Experimental arrangement used to measure Laser Induced Damage Thresholds for a metal or semiconductor surface. For a transparent dielectric sample the surface was viewed in transmission.

Figure (2).
Laser Induced Damage Thresholds for Fused Silica.
(a) Unannealed surface.
(b) Surface annealed with five 2.8 J/cm^2 laser pulses.
(c) Surface annealed with one hundred 2.8 J/cm^2 laser pulses.

Figure (3).
Laser Induced Damage Thresholds for Al.
(a) Unannealed surface.
(b) Surface annealed with twenty 2.8 J/cm^2 laser pulses.

Figure (4).
An example of how laser annealing can decrease the amount of damage caused by the excimer laser pulse.
(a) Damage caused on an unannealed CaF_2 surface by one incident excimer pulse with a fluence of 6 J/cm^2.
(b) Damage caused on the same sample by a 6 J/cm^2 excimer pulse incident after 1000 annealing pulses of 0.15 J/cm^2 each.

Figure (5).
The results of a SIMS analysis of a Si sample.
(a) SIMS trace before annealing.
(b) SIMS trace after annealing, showing very little change.

Figure (6).
The results of LIMA performed on Al and Ge samples showing the evolution of common surface contaminants.

Figure (7).
Typical dark field images taken of an Al and Ge surface after annealing. Note the discontinuity of scratches across the centrally located black annealed region.

Figure (8).
TIRM images taken on a CaF_2 surface.
(a) Video image of the surface before annealing.
(b) Video image of the same area after annealing. Note the reduction of surface scattering points in the region which has been annealed
(c) Computer processed image of (b)-(a). This shows more clearly that only areas on the surface irradiated by the annealing pulses have had their scatter reduced.

Figure (9).
The results of STEM and electron diffraction measurements on silicon both (a) before and (b) after laser annealing. The insets show the respective electron diffraction patterns. Clearly the unannealed silicon surface was amorphous in nature as indicated by its diffuse ring type diffraction pattern. After annealing the diffraction pattern is made up of discrete well defined rings indicating a polycrystalline structure.

Figure (10).

An interference contrast image showing the annealed region of Figure (7a) where the two scratches cross it at higher magnification. Note that the scratches do appear to have been erased in some parts but more generally have become rounded off. At the foot of the photograph corresponding to the edge of the annealed region the scratches are still well defined.

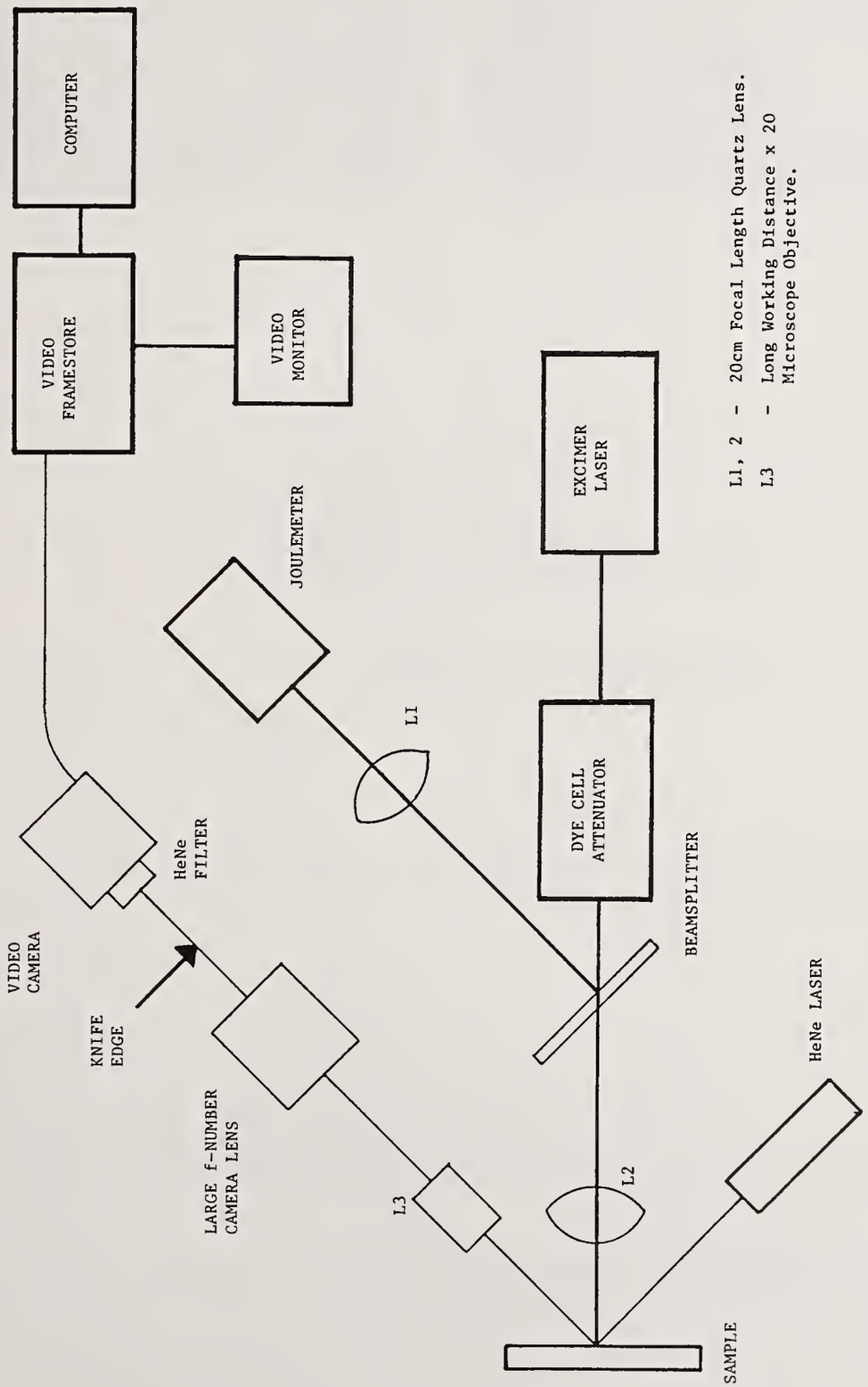

Figure 1

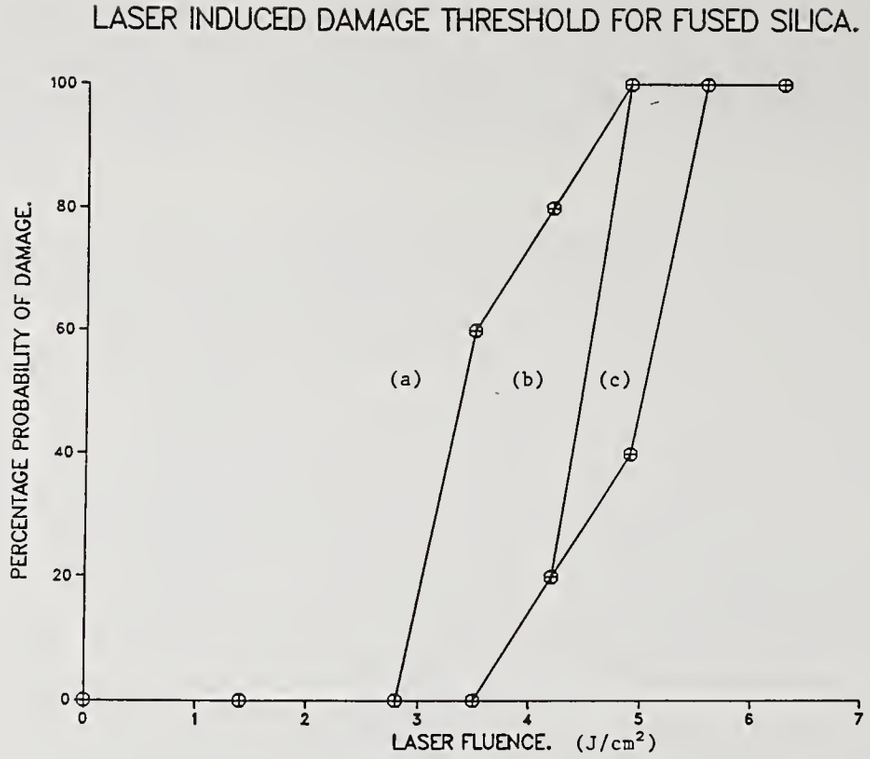

Figure 2

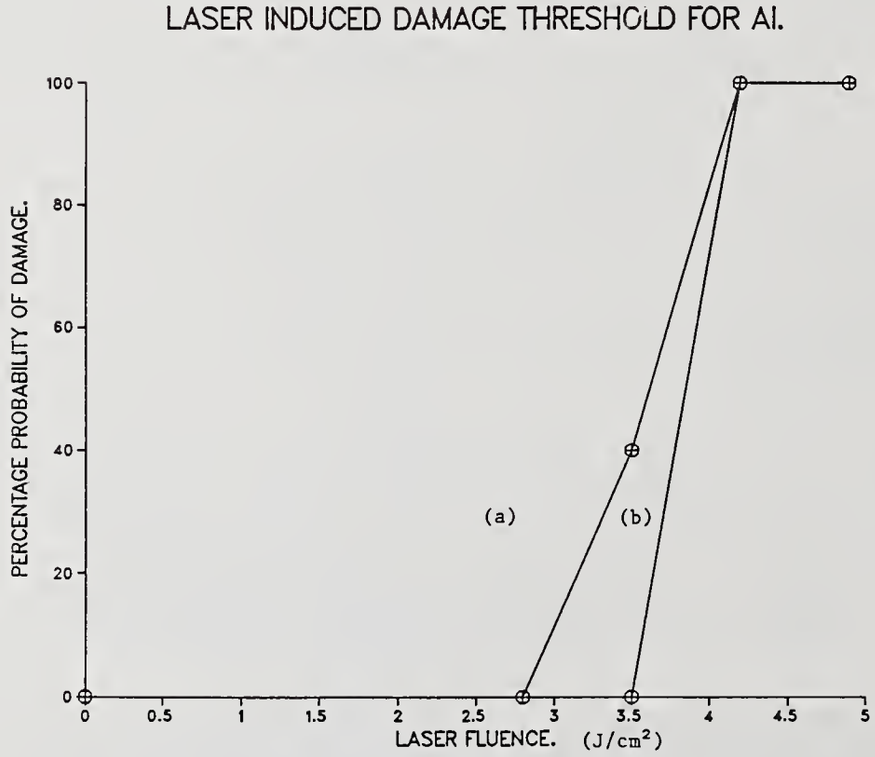

Figure 3

Figure 4a

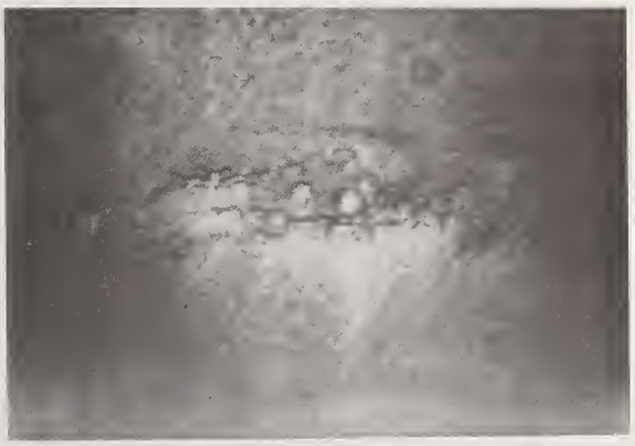

Figure 4b

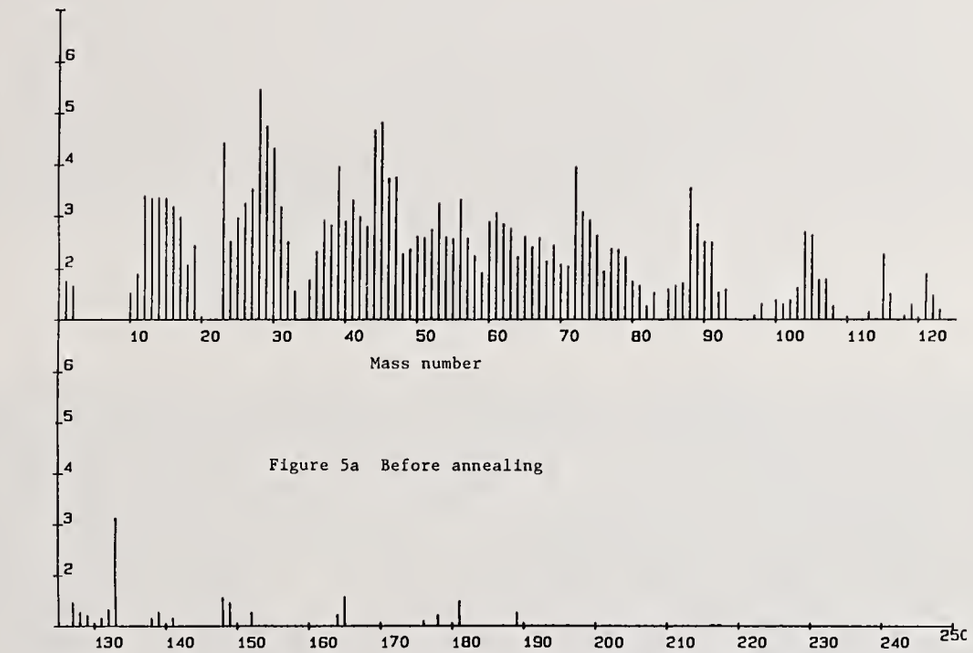

Figure 5a Before annealing

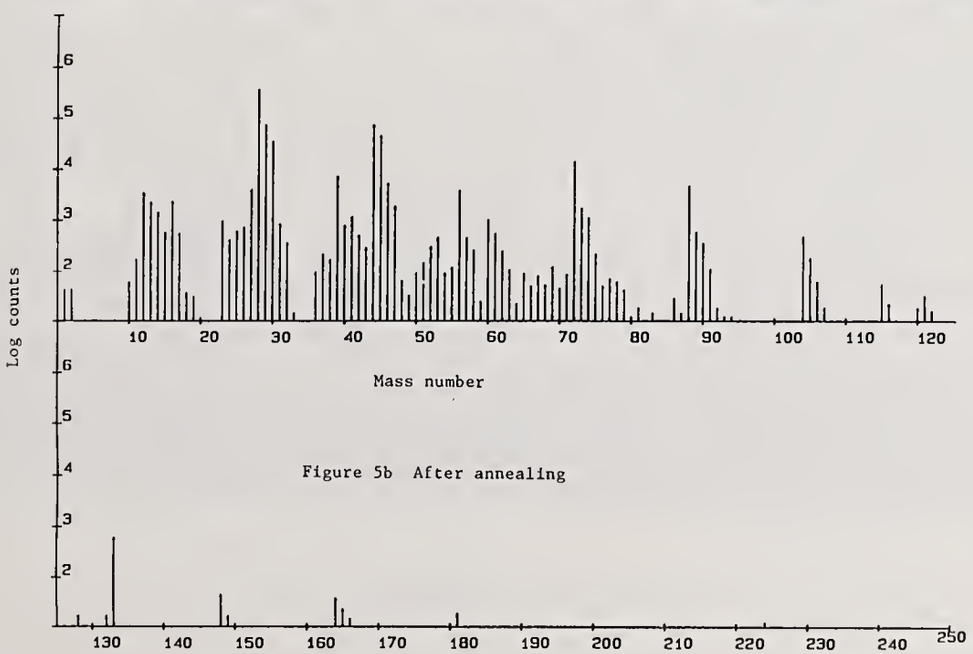

Figure 5b After annealing

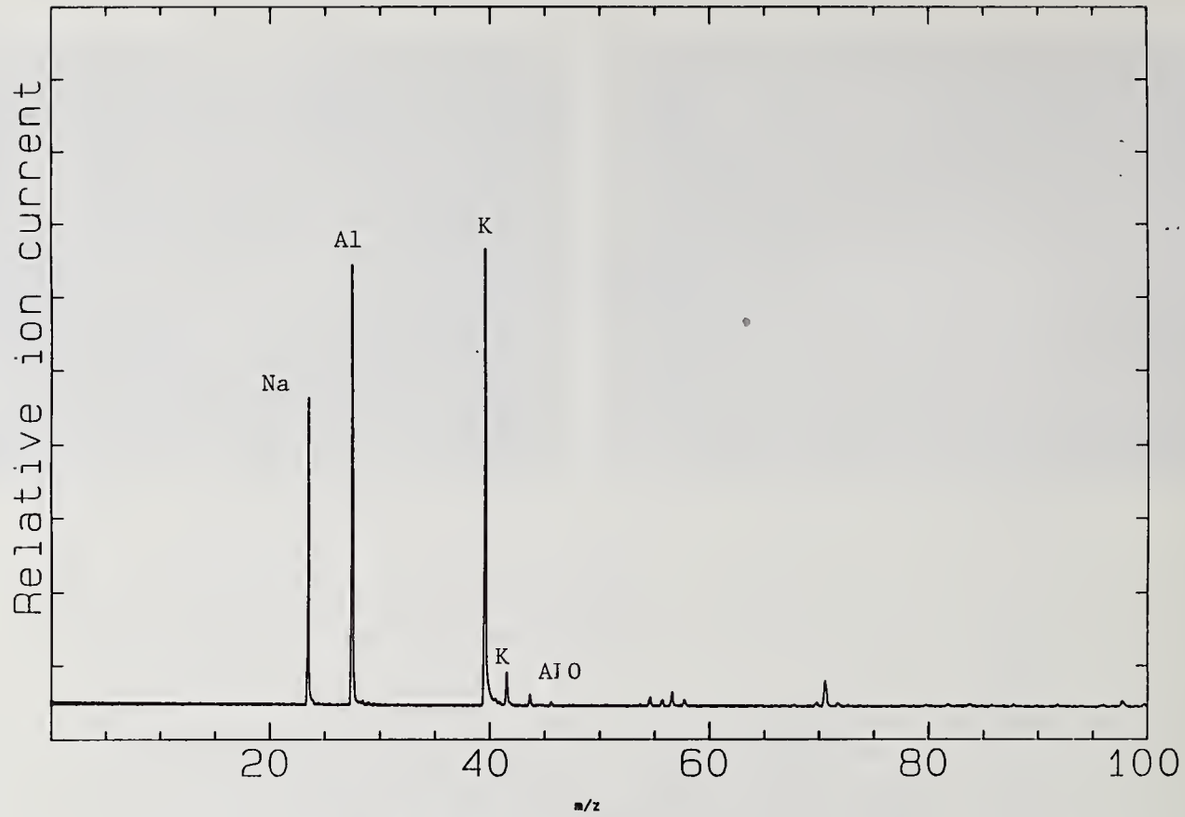

Figure 6a Aluminium

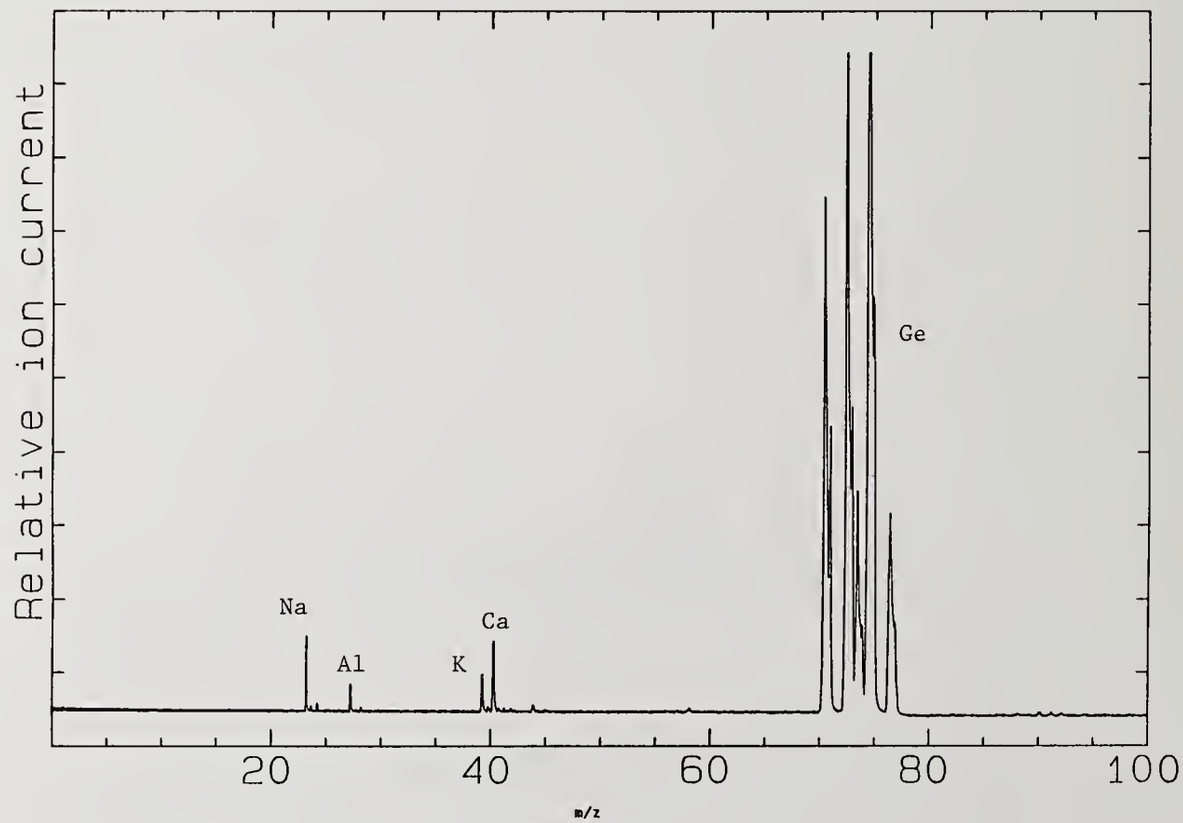

Figure 6b Germanium

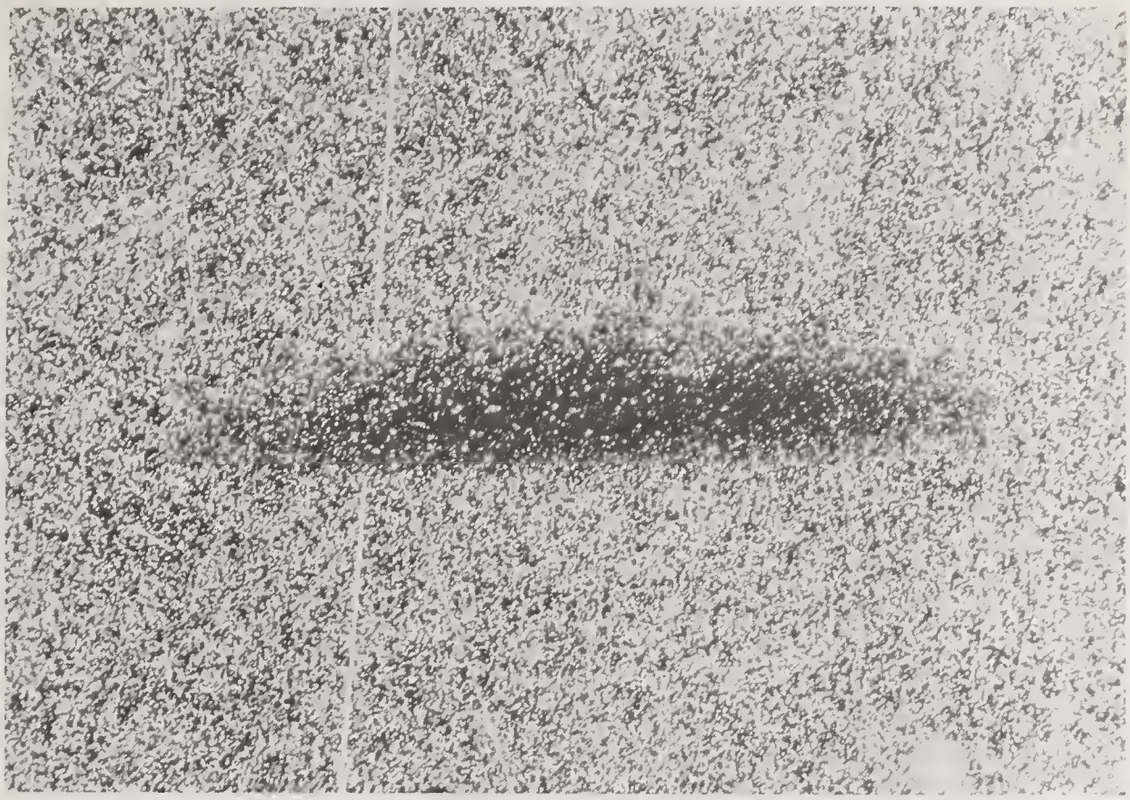

Figure 7a Aluminium

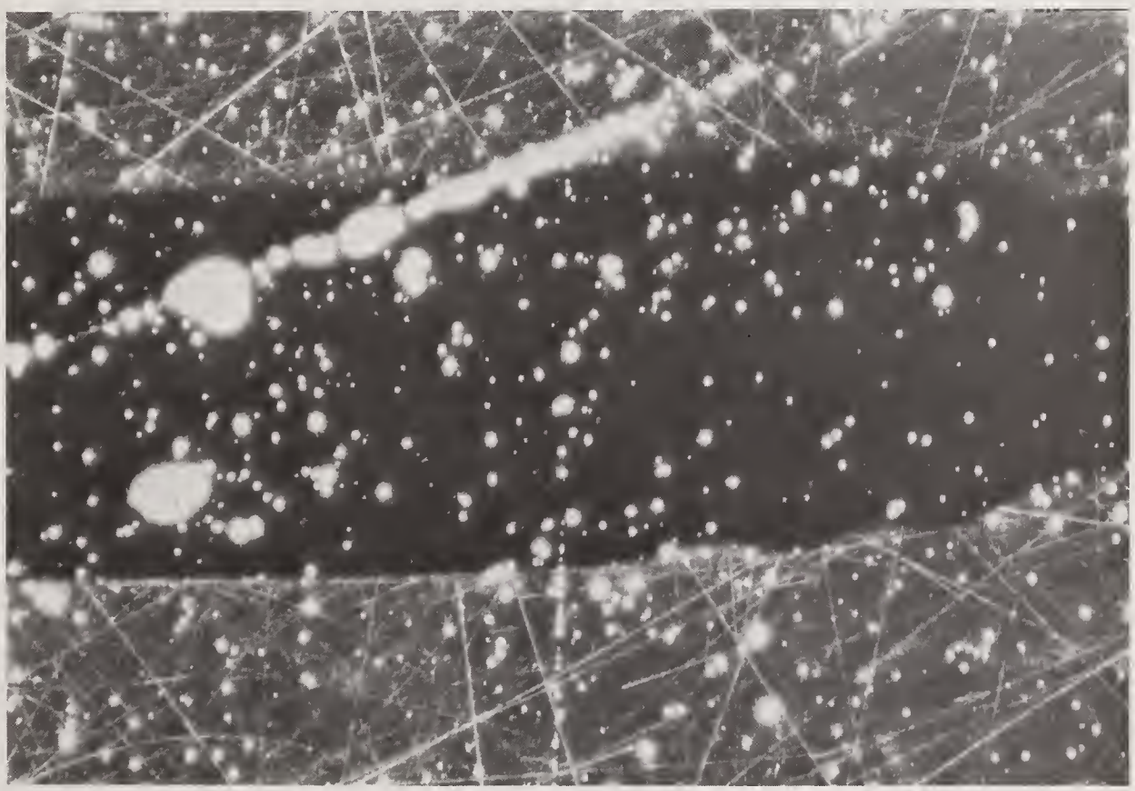

Figure 7b Germanium

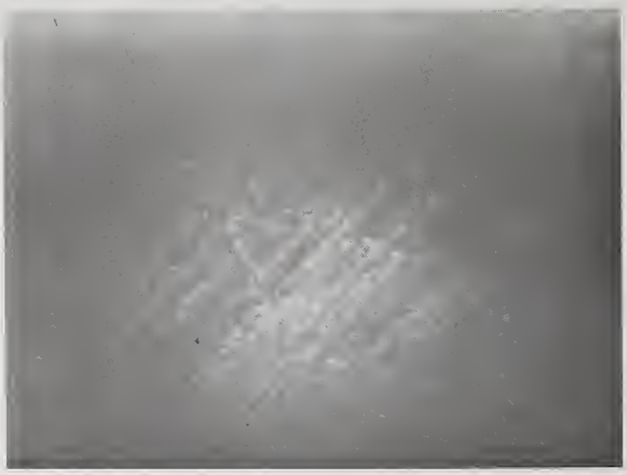

Figure 8

(a) CaF_2 before annealing

Video image

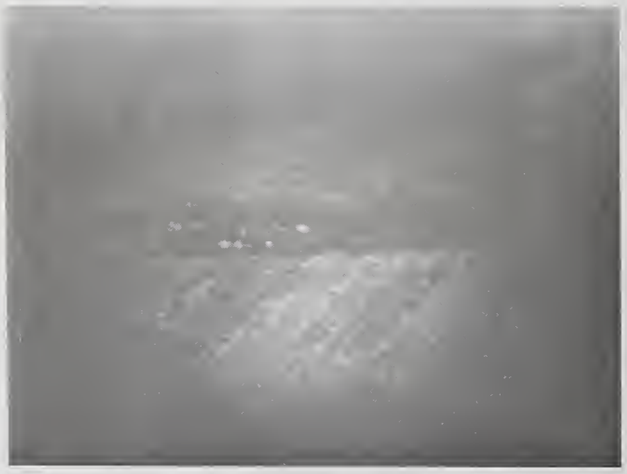

(b) After annealing

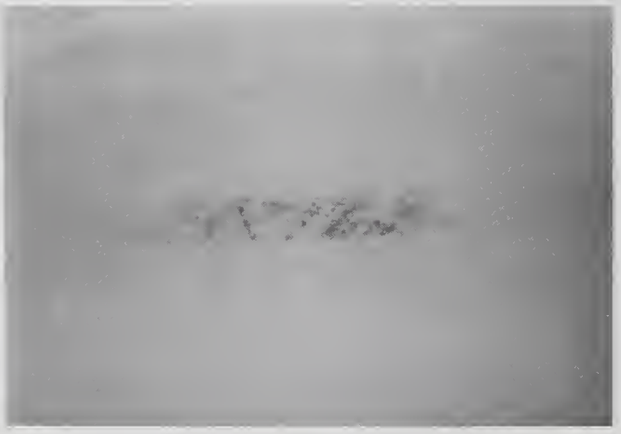

(c) Computer subtracted
(b - a)

Figure 9 (a) STEM image

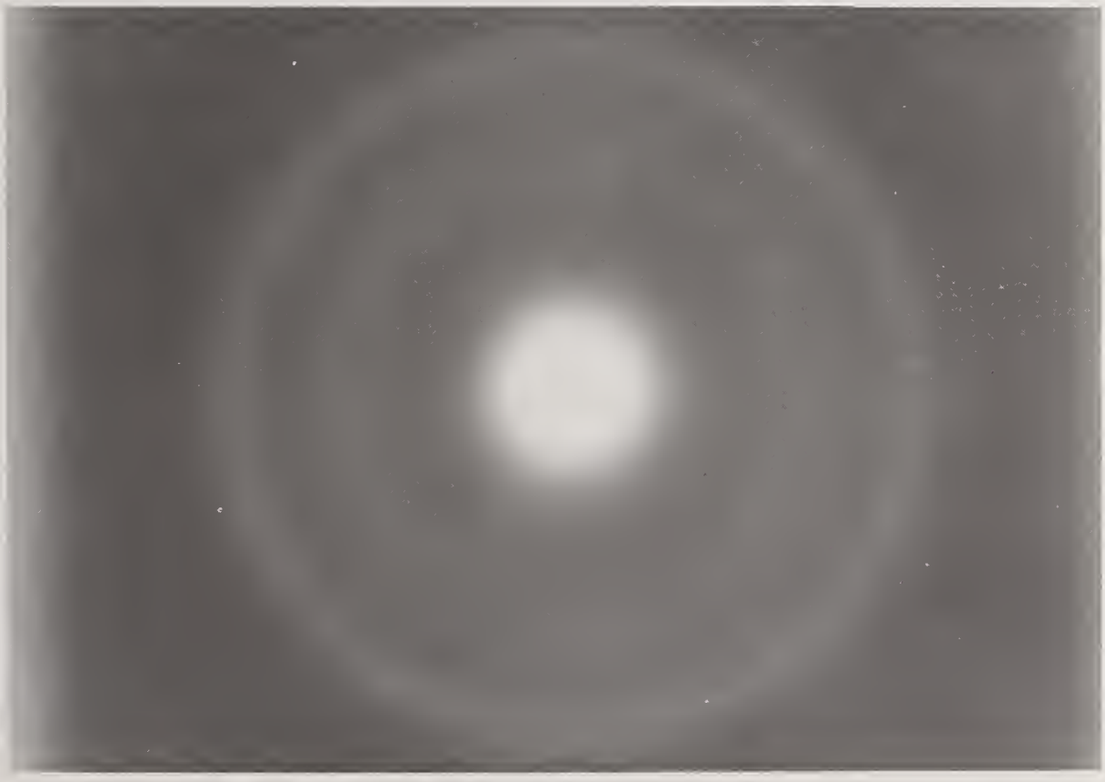

Figure 9 (a) Electron diffraction pattern

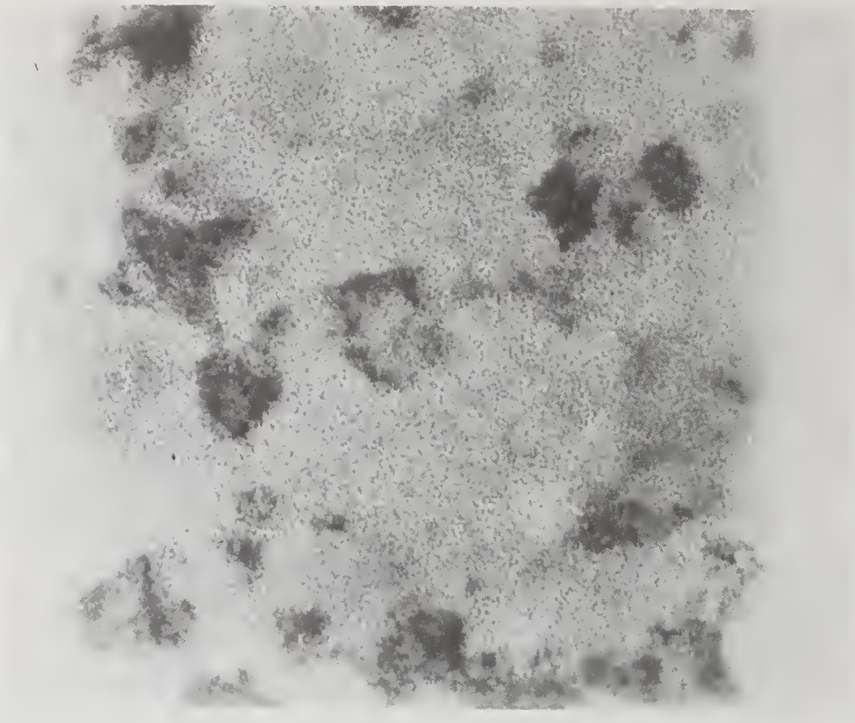

Figure 9 (b) STEM image

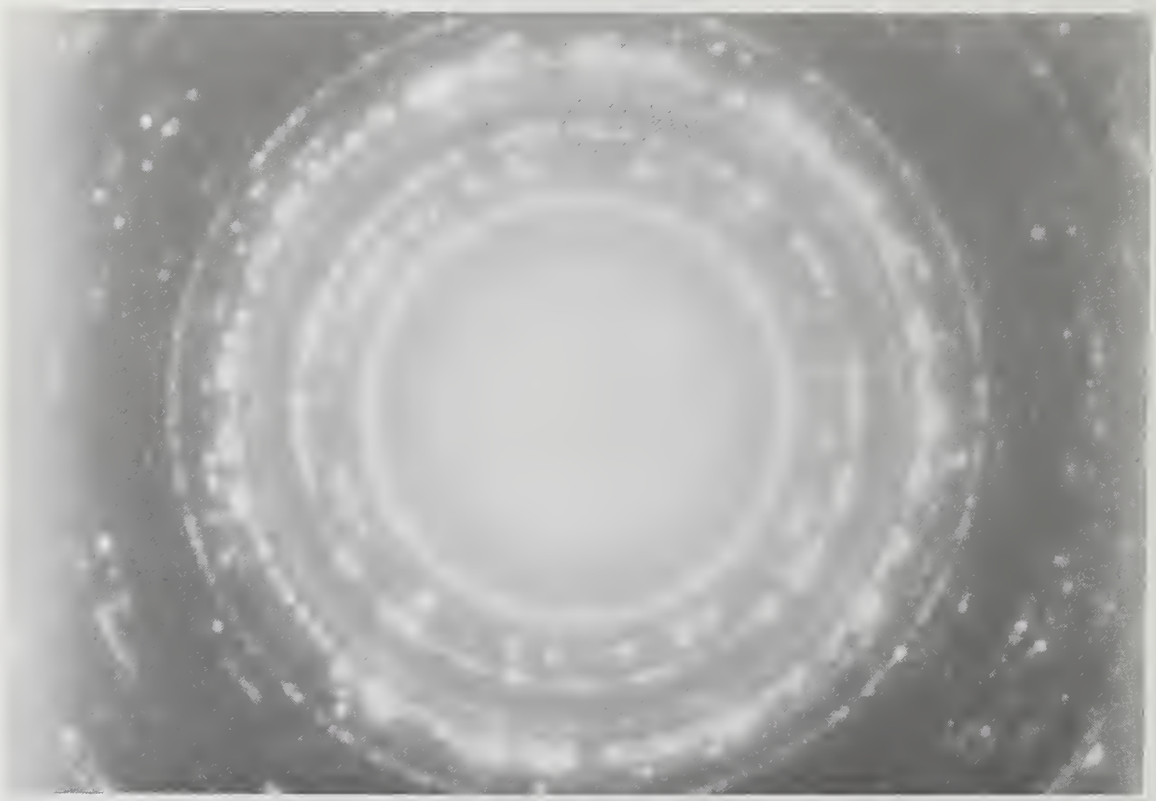

Figure 9 (b) Electron diffraction pattern

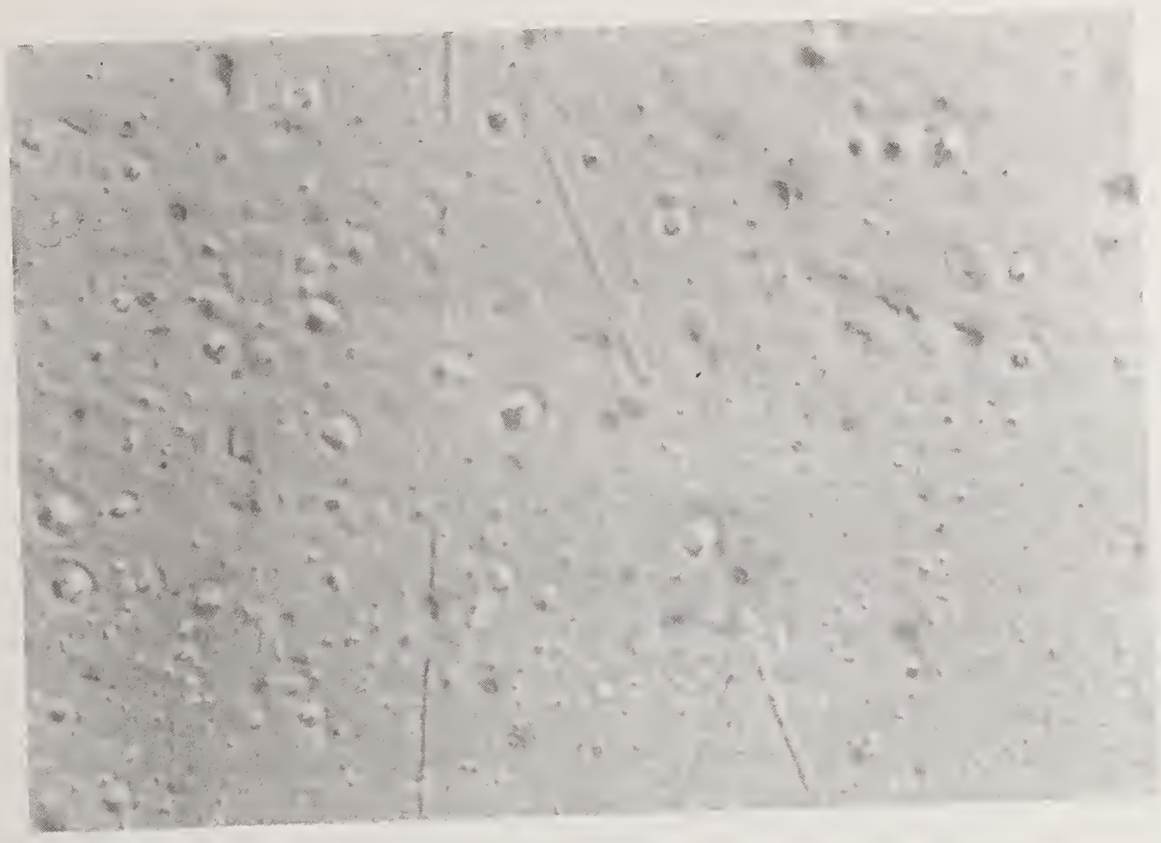

Figure 10

Manuscript received
2-27-90

SHOCKWAVE DETECTION, AN EFFICIENT WAY TO DETERMINE MULTIPLE-PULSE DAMAGE THRESHOLDS

S. Petzoldt, A.P. Elg, J. Reif, and E. Matthias
Fachbereich Physik, Freie Universität Berlin
Arnimallee 14, D-1000 Berlin 33, FRG

The detection of damage associated shock pulses via the deflection of a probe laser beam is exploited to study multiple-shot damage thresholds in CaF_2, PMMA, copper, and aluminium. We find a reduction of threshold intensity as compared to single-shot conditions. The experimental results point towards deviations from the previously postulated fluence dependence $F_N = F_1 N^{S-1}$ [see Ref.4]. They are, however, compatible with a simple model relating the threshold reduction to defect accumulation via non-linear energy absorption.

Key words: Multi-shot damage, probe beam deflection, defect accumulation

Optical systems for high-power pulsed lasers are limited by damage to the optical components. In practical applications, the maximum usable intensity is most often determined by the multiple-shot damage threshold. Due to accumulative effects [1,2], this threshold is frequently considerably *lower* than the single-shot threshold, in contrast to observations in multiple dielectric layers [3]. For a classification of different materials, it is important to know the number of pulses at a given intensity, that can be applied before damage occurs. In other words: The relation between the N-pulse damage threshold and the intensity of the laser beam is of great interest for a reliable prediction of the longevity of optical components. Presently, several laboratories are working on that question. E.g., M.F. Becker et al. [4] have measured single- and multiple-pulse damage thresholds of copper to investigate damage morphologies and damage accumulation, and to determine the damage mechanism. From their data, they derived the cumulative equation

$$F_N = F_1 N^{S-1} \qquad (1)$$

where F_1 is the single-shot damage threshold fluence, F_N is the threshold for N laser pulses, and S is a material specific parameter derived from the experimental data.

In Fig. 1 a schematic of such accumulative curves is represented. The total energy (number of pulses times threshold fluence) is plotted in a log-log scale as a function of the number of shots. In this plot the data should represent a straight line with slope S, according to Eq.(1). A slope of S=1 is standing for the absence of incubation effects. Normally, the measured data provide a slope smaller than 1. The difference between slope 1 and slope S is the reduction of the total threshold energy, and should be a measure for incubation. Becker et al. explain the incubation for metals as a storage cycle of thermal stress-strain energy, induced by the laser pulses.

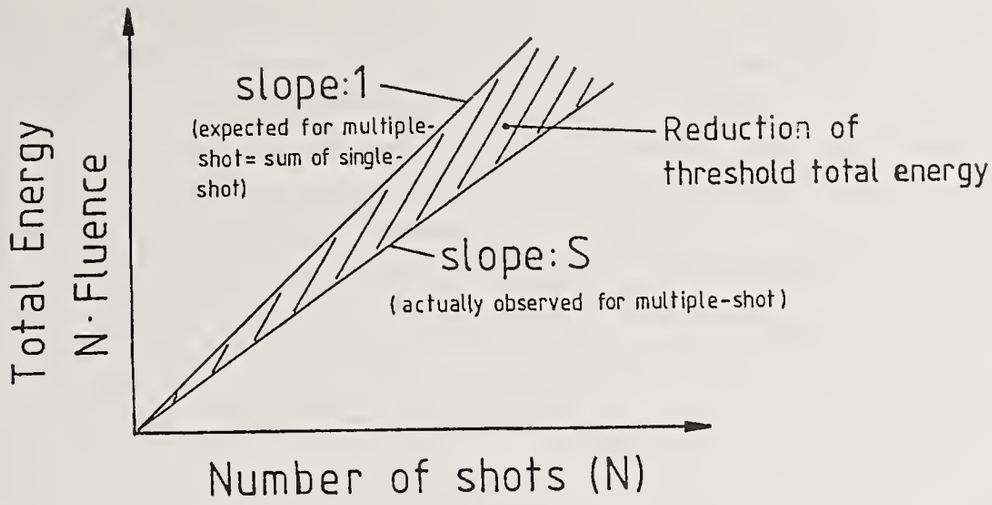

Figure 1: Schematic of the incubation effect according to Eq. (1): The total absorbed energy is plotted versus the number of pulses (log-log coordinates).

In the following we report on measurements of the multiple-shot damage thresholds of PMMA, CaF_2, Cu, and Al for ns pulses of green (530 nm) laser light and present a simple phenomenological model to account for the accumulation effect. In our experiments we use the probe beam deflection technique [5] to detect the shockwave connected with surface damage. As shown previously [5,6], this is quite appropriate to rapidly yield laser damage thresholds. The method utilizes a probe laser beam passing at short distance parallel to the sample surface (see Fig. 2). In case of damage, a shock pulse emerges from the sample, and the associated transient change of refractive index causes the deflection of the probe beam. This is monitored via the intensity variation behind a narrow slit placed on one slope of the spatial beam profile. The shock pulse energy derived from this intensity variation was shown to be a function of the degree of damage.

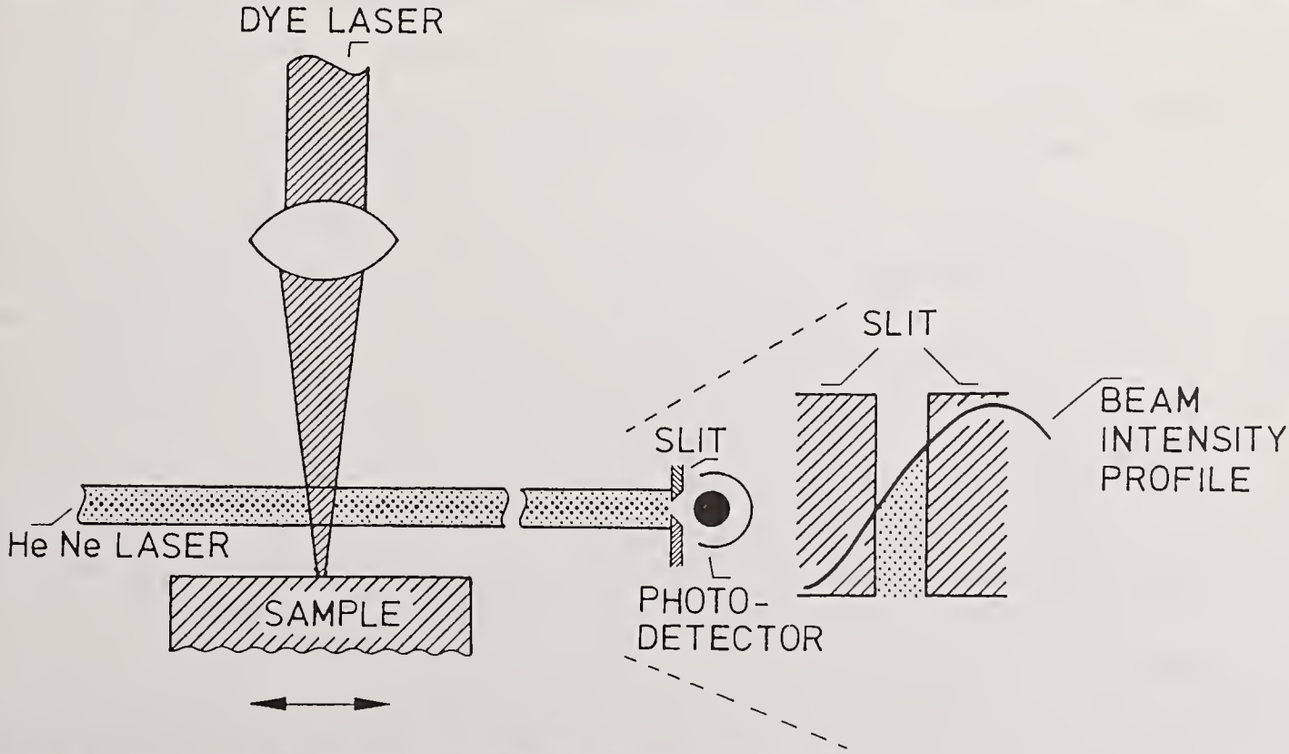

Figure 2: Principle setup for the beam deflection technique

In a preliminary experiment, we measured the intensity dependence of the damage thresholds on CaF_2 and PMMA for comparison, which are shown in Fig. 3. In part a), of both cases, 1-on-1 measurements are displayed. In part b) the data of measurements with overlapping spots are plotted. Here each laser shot hit a predamaged area. For CaF_2 there is a big difference in threshold and slope between isolated and overlapping spots. The change in slope indicates, that the process is changing from avalanche breakdown to multiphoton ionization [7]. In the case of PMMA, however, the threshold is decreasing but the slope above threshold is not changing very much pointing to only one process responsible for single- and muliple-shot damage.

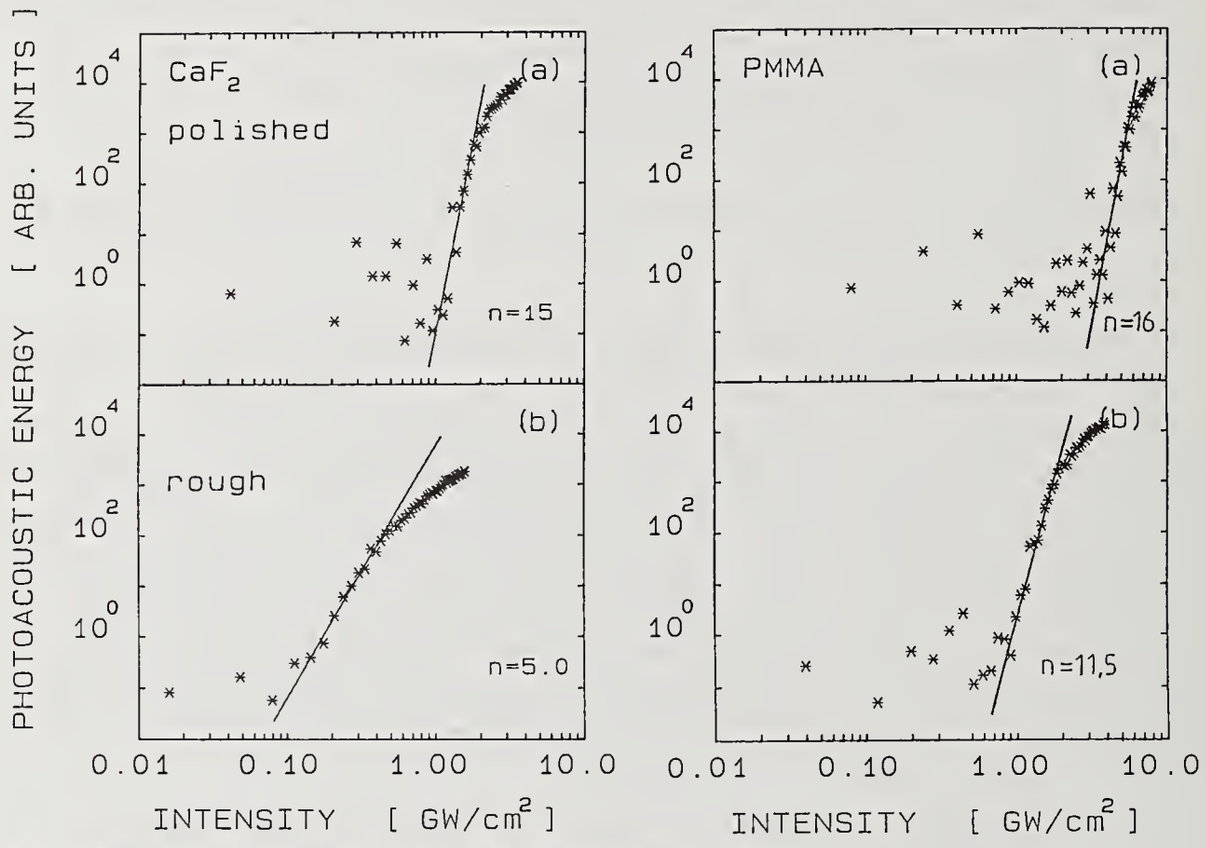

Figure 3: Damage thresholds for CaF_2 (left) and PMMA (right)
(a): isolated spots (1-on-1); (b): overlapping spots (predamaged).

The accumulation effect was studied by measuring multi-shot damage thresholds. For this purpose, we illuminated the sample with a repetition rate of 3 Hz at fixed laser intensity, and counted the number of shots needed for a first damage event to occur, i.e., the counter was stopped by the first detectable deflection signal. This experiment is fully computer controlled, and so we are able to rapidly collect substantial quantities of data, quite in contrast to conventional techniques like, e.g., microscopic inspection. Therefore we have the possibility to do these measurements for a high number of different intensities and to use relatively low intensities where up to 10,000 shots are needed before damage occurs. In Fig. 4 the data of CaF_2, PMMA, copper, and aluminium are shown. Along the lines of Ref. [4], the accumulative energies $N \cdot F_N$ are plotted as a function of the number of pulses N. The solid line is a fit of Eq.(1) to these data. The parameter S was determined to be 0.88 for copper, 0.91 for aluminium, 0.84 for PMMA, and 0.95 for CaF_2. Obviously, for high values of N this kind of data analysis becomes highly insensitive. Therefore, in Fig. 5 the actual threshold intensity is plotted as a function of the number of laser pulses to damage.

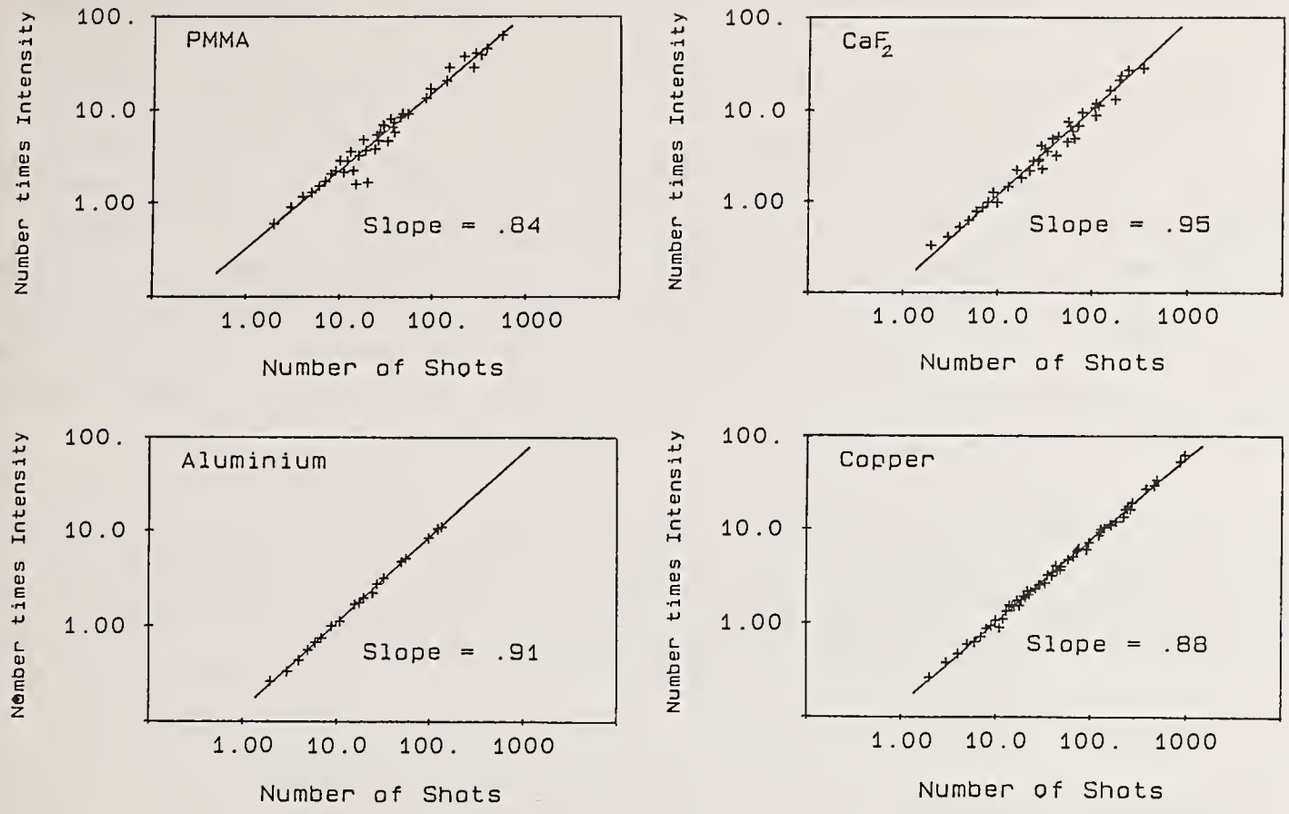

Figure 4: Analysis of incubation effect according to Eq. (1) for PMMA, CaF_2, Al, and Cu.

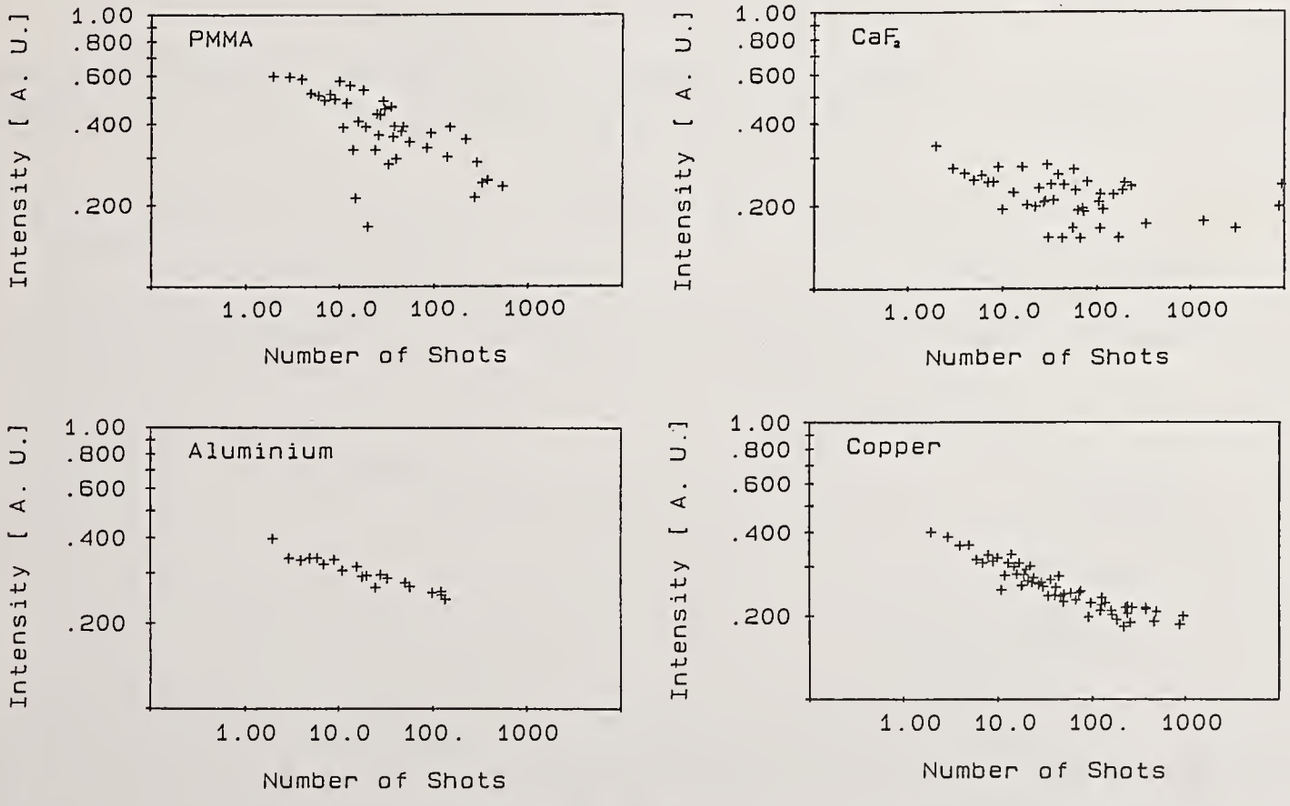

Figure 5: Log-log plot of damage threshold vs. number of shots. Note the deviation from straight lines, which are expected from Eq. (1).

According to Eq. (1), this should yield straight lines again, with slopes of (S-1). Closer inspection of Fig. 5, however, shows deviations from this expectation. For CaF_2 and copper there is a change to greater S-values for higher numbers of shots and smaller intensities. That points to a *decreasing* incubation for lower intensities. The data of PMMA contrarily provide a decrease of the S-value for a greater number of shots. That looks like an *increasing* incubation effect. The differences between the species may be the result of different incubation processes. If incubation is interpreted by defect creation [1,8], in the case of CaF_2 and copper a decay rate of defects would explain the observed behavior. In the other case of PMMA, permanent defects and an increase of the defect creation cross-section with the density of defects would be an explanation for the deviation from the straight line. So, Eq. (1) is a description of the coarse behavior only, but there are deviations in the fine structure. These deviations, we think, depend on the different materials.

In the following, we try to present a simple phenomenological model to account for a more detailed analysis of the effect of energy accumulation leading to reduced damage thresholds.

For this purpose, let us assume the energy absorption in the material to occur via k individual absorbers, e.g. defects. Then, we have the absorbed energy per pulse

$$E_{abs} = k \cdot \epsilon \tag{2}$$

where the energy per absorber

$$\epsilon = (\sigma_n I^{n-1}) F \tag{3}$$

may depend non linearly on intensity I and fluence F. Further, we postulate that the absorbed energy primarily leads to the generation of additional absorbers, i.e., after the i-th pulse we have

$$k_{i+1} = k_i + \Gamma(\epsilon) k_i \epsilon. \tag{4}$$

So, the increment in number of absorbers per number of pulses is proportional to the energy absorbed

$$\frac{dk}{di} = \Gamma(\epsilon) k \epsilon. \tag{5}$$

Integration of Eq. (5) yields

$$\ln k + \text{const} = \Gamma(\epsilon) \epsilon i. \tag{6}$$

Defining damage to occur when the energy absorbed during one pulse equals the threshold energy E_o, the number of absorbers at threshold is given by

$$k_{th} = E_o / \epsilon. \tag{7}$$

Combining Eqs. (6) and (7), we obtain the number of shots N, required for damage at single absorber energy ϵ:

$$N = \frac{\text{const} + \ln E_0 - \ln \epsilon}{\Gamma(\epsilon)\,\epsilon} \tag{8}$$

In order to evaluate the absorber creation rate $\Gamma(\epsilon)$ let us think of the following simple model: In the simplest case, $\Gamma(\epsilon) = \Gamma_0$ would be a constant. If we allow, however, for a portion of energy to be trapped at the absorber, as would be done by a barrier for energy transfer, we try the ansatz of a reduced rate

$$\Gamma(\epsilon) = \Gamma_0 - 1/a\epsilon \tag{9}$$

We can refine this by replacing

$$1-1/(a\epsilon\Gamma_0) \approx \exp\left[-\frac{1}{a\epsilon\Gamma_0}\right] \tag{10}$$

and obtain from Eq. (8):

$$N = \frac{C - \ln \epsilon}{\Gamma_0\,\epsilon}\exp\left[\frac{1}{a\epsilon\Gamma_0}\right]. \tag{11}$$

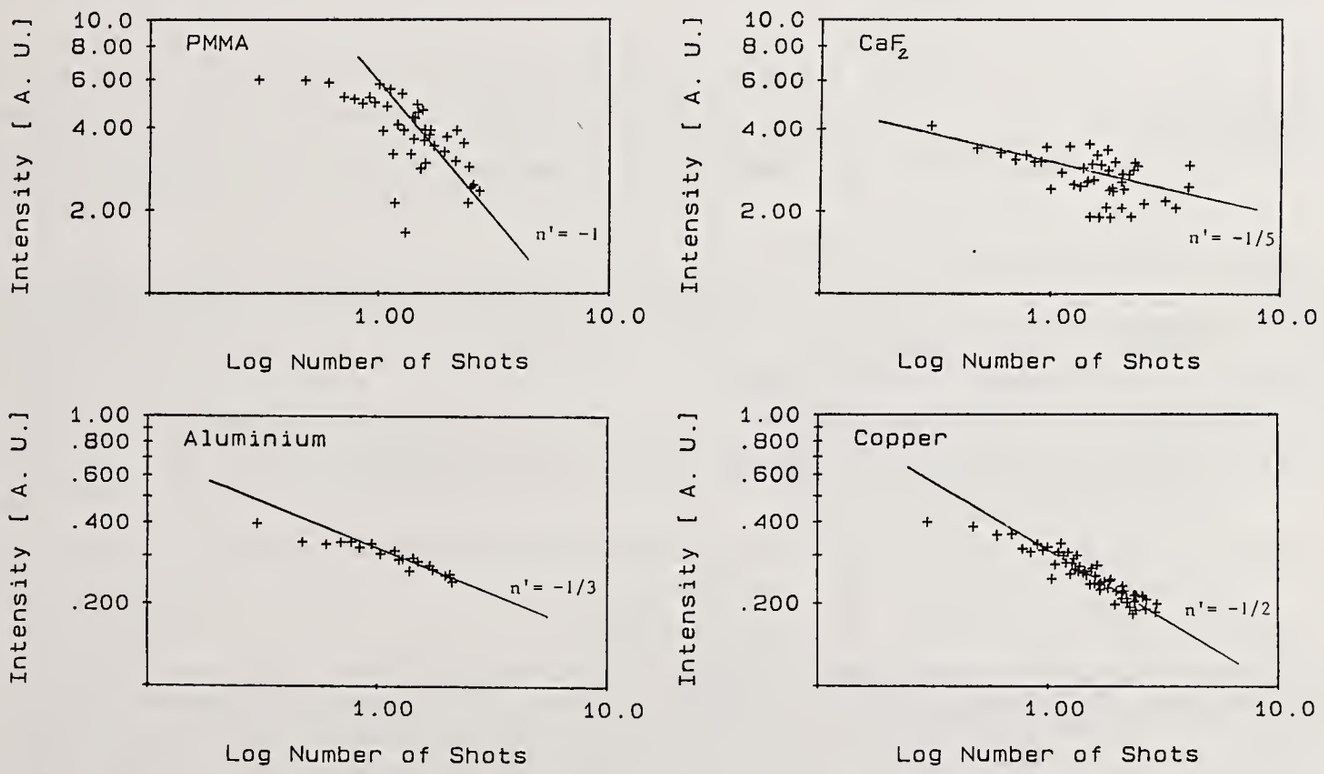

Figure 6: Analysis of incubation effect along the lines of the defect creation model (log [threshold intensity] vs. log[log(number of shots)]). For large N, all data may be represented by Eq. (12). The slopes n' are obtained by assuming integer orders of nonlinear energy input.

If we keep, as a limit at low intensities, only the exponential contribution

$$N \approx \text{const} \exp(1/b\epsilon) \qquad (12)$$

we can indeed compare this with our data, as shown in Fig. 6, by assuming very simple integer nonlinearities n in Eq. (3). These are indicated in Fig. 6 by straight lines with slopes 1/n. It should be remembered here, however, that this model does not yield any insight into the microscopic processes of energy dissipation and defect creation, as is tried in [1] for alkali halide crystals. Instead, it is intended to provide a phenomenological parameterization of the incubation effect.

In conclusion, the probe beam deflection technique is a useful tool to investigate multi-shot damage thresholds, providing us with the possibility of rapidly collecting statistically significant quantities of data. The function $F_N = F_1 N^{S-1}$ of Ref.[4] is fitting our data but closer inspection provides some deviations. A simple model, relating the accumulation effect to defect creation via non-linear energy input, is compatible with our experimental results.

We gratefully acknowledge support from the Deutsche Forschungsgemeinschaft, Sfb 337, and the BMFT, contract No. 13N5627.

References:

[1] S.C. Jones, P. Braunlich, R.T. Casper, X.-A. Shen, and P. Kelly; Opt.Eng. 28, 1039 (1989)

[2] S. Küper and M. Stuke; Appl.Phys. A49, 221 (1989)

[3] C.R. Wolfe, M.R. Kozlowski, J.H. Campbell, F. Rainer, A. Morgan, and R. Gonzales; "Laser Pre-Conditioning of Optical Thin Films", this volume

[4] Y. Jee, M.F. Becker, and R.W. Walser J.Opt.Soc.Am. B5(3), 648 (1988)

[5] S. Petzoldt, A.P. Elg, M. Reichling, J. Reif, and E. Matthias; Appl.Phys.Lett. 53, 2005 (1988)

[6] E. Matthias, S. Petzoldt, A.P. Elg, P.J. West, and J. Reif; NIST Special Publication 756, 217 (1987)

[7] S. Petzoldt, A.P. Elg, J. Reif, and E. Matthias; NIST Special Publication 1988, in press

[8] R.T. Williams; Opt.Eng. 28, 1024 (1989)

Manuscript received
2-20-90

Application of the Ronchi Ruling Beam Profiling Method to Axially Symmetric Laser Beams

Robert M. O'Connell
and
Cheng-Hao Chen

Electrical and Computer Engineering
University of Missouri-Columbia
Columbia, MO 65211

The application of the Ronchi ruling beam characterization method to axially symmetric optical beams is analyzed. Specific results are derived for the Airy and focused annulus diffraction patterns. Plots of the ratio of minimum to maximum transmitted optical power versus the first null radius of the beam functions show that for the Airy pattern and other focused annuli with obscuration ratios smaller than approximately 0.30, the method should be just as useful as with Gaussian beams.

Key words: Airy pattern; axially symmetric beam; beam profiling; focused annulus; Gaussian beam; Ronchi ruling.

1. Introduction

Although many of the lasers used in laser damage studies emit non-Gaussian beams, they are often assumed to be Gaussian for beam profiling purposes because it is very easy to apply the standard beam profiling methods (e.g., pinhole, slit, knife-edge) to a Gaussian beam. Unfortunately, this approach can lead to significantly inaccurate profiles (and, thereby, to incorrect damage thresholds) when, for example, the beam contains substantial sidelobes. Such is the case when the beam in question is the focused output of a laser with a confocal unstable resonator, i.e., a focused annulus.

While such axially symmetric beams can be profiled with the knife-edge method [1], doing so requires a large number of accurately positioned data readings over a wide range of power levels, which can introduce significant measurement error. Another approach is to use the Ronchi ruling method, which has previously been applied successfully to Gaussian beams [2-4]. In this paper, we consider its application to axially symmetric beams in general and to the focused annulus beam function in particular. We review the application of the method to Gaussian beams and then derive analogous results for the axially symmetric focused annulus, a special case of which is the Airy pattern. The results will show that the method appears to be most useful for focused annuli with obscuration ratios smaller than approximately 0.3.

2. The Ronchi Ruling Method: Application to Gaussian Beams

2.1. Analysis

The Ronchi ruling method can be most easily understood in terms of its application to a specific beam function. As applied to a Gaussian beam, the method consists of moving a ruling (reflective or transmissive) of known optical characteristics transversely through the beam and measuring the ratio K of the minimum total power P_{min} reflected or transmitted to the maximum total power P_{max} reflected or transmitted. The $1/e^2$ beam radius r_0 can then be obtained from a graphical relationship between K and r_0 that results from an analysis of the optical power reflected or transmitted when a Gaussian laser beam illuminates a Ronchi ruling with specific optical characteristics (period, duty cycle, and reflectance or transmittance).

The appropriate graphical relationship for an ideal Ronchi ruling and a Gaussian beam can be derived with the aid of figure 1. As shown in the figure, the bars and spaces in the ruling are assumed to be infinitely long, of equal width L, and to have 100% reflectance and transmittance, respectively. Assuming that the bars

and spaces of the ruling are oriented parallel to the y-axis, expressions for the transmitted powers P_{min} and P_{max} can be obtained from parts a) and b) of the figure, respectively.

Assuming that the Gaussian beam has been focused and the measurement is to be made in the focal plane, the intensity I(x,y) of the beam is expressed as

$$I(x,y) = I_0 \, e^{-2(x^2 + y^2)/r_0^2} \quad , \tag{1}$$

where I_0 is the intensity at the center of the beam. The optical power P in any portion of the focused beam can be obtained by integrating eq (1), i.e.,

$$P = I_0 \int_x e^{-2x^2/r_0^2} \, dx \int_y e^{-2y^2/r_0^2} \, dy \quad . \tag{2}$$

The limits on x in eq (2) are different for P_{min} and P_{max}, but the limits on y are from $-\infty$ to $+\infty$ in both cases. The integral on y is thus

$$\int_{-\infty}^{\infty} e^{-2y^2/r_0^2} \, dy = r_0\sqrt{\pi/2} \quad , \tag{3}$$

and eq (2) becomes

$$P = I_0 r_0 \sqrt{\pi/2} \int_x e^{-2x^2/r_0^2} \, dx \quad , \tag{4}$$

which can be used to determine expressions for both P_{min} and P_{max}.

Using figure 1a and eq (4), it is evident that

$$P_{min} = 2I_0 r_0 \sqrt{\pi/2} \left[\int_{L/2}^{3L/2} e^{-2x^2/r^2_0} \, dx + \int_{5L/2}^{7L/2} e^{-2x^2/r^2_0} \, dx \right.$$

$$\left. + \int_{9L/2}^{11L/2} e^{-2x^2/r^2_0} \, dx + \ldots\ldots \right]$$

$$= 2I_0 r_0 \sqrt{\pi/2} \left[\int_0^{3L/2} e^{-2x^2/r^2_0}\, dx - \int_0^{L/2} e^{-2x^2/r^2_0}\, dx \right.$$

$$\left. + \int_0^{7L/2} e^{-2x^2/r^2_0}\, dx - \int_0^{5L/2} e^{-2x^2/r^2_0}\, dx + \ldots\ldots \right] . \qquad (5)$$

Similarly, figure 1b and eq (4) yield

$$P_{max} = 2I_0 r_0 \sqrt{\pi/2} \left[\int_0^{L/2} e^{-2x^2/r^2_0}\, dx + \int_{3L/2}^{5L/2} e^{-2x^2/r^2_0}\, dx \right.$$

$$\left. + \int_{7L/2}^{9L/2} e^{-2x^2/r^2_0}\, dx + \ldots\ldots \right]$$

$$= 2I_0 r_0 \sqrt{\pi/2} \left[\int_0^{L/2} e^{-2x^2/r^2_0}\, dx + \int_0^{5L/2} e^{-2x^2/r^2_0}\, dx \right.$$

$$- \int_0^{3L/2} e^{-2x^2/r^2_0}\, dx + \int_0^{9L/2} e^{-2x^2/r^2_0}\, dx$$

$$\left. - \int_0^{7L/2} e^{-2x^2/r^2_0}\, dx + \ldots\ldots \right] . \qquad (6)$$

If the variable change $u = 2x/r_0$ is made, eq (5) and (6) become, respectively,

$$P_{min} = \pi I_0 r^2_0 \left[\int_0^{3L/r_0} \frac{e^{-u^2/2}}{(2\pi)^{1/2}}\, du - \int_0^{L/r_0} \frac{e^{-u^2/2}}{(2\pi)^{1/2}}\, du \right.$$

$$+ \int_0^{7L/r_0} \frac{e^{-u^2/2}}{(2\pi)^{1/2}}\,du - \int_0^{5L/r_0} \frac{e^{-u^2/2}}{(2\pi)^{1/2}}\,du + \ldots\ldots \Big] \quad , \tag{7}$$

and
$$P_{max} = \pi I_0 r_0^2 \Big[\int_0^{L/r_0} \frac{e^{-u^2/2}}{(2\pi)^{1/2}}\,du + \int_0^{5L/r_0} \frac{e^{-u^2/2}}{(2\pi)^{1/2}}\,du$$

$$- \int_0^{3L/r_0} \frac{e^{-u^2/2}}{(2\pi)^{1/2}}\,du + \int_0^{9L/r_0} \frac{e^{-u^2/2}}{(2\pi)^{1/2}}\,du - \int_0^{7L/r_0} \frac{e^{-u^2/2}}{(2\pi)^{1/2}}\,du \Big] \quad . \tag{8}$$

The integrals in eq (7) and (8) are related to the well-known normal distribution function, for which tabulated values are available [5]. Defining

$$\Phi(ARG) = (2\pi)^{-1/2} \int_0^{ARG} e^{-u^2/2}\,du \quad , \tag{9}$$

eq (7) and (8) become, respectively,

$$P_{min} = \pi r_0^2 I_0 \Big[\Phi(3L/r_0) - \Phi(L/r_0) + \Phi(7L/r_0) - \Phi(5L/r_0) + \ldots\ldots \Big]$$

$$= \pi r_0^2 I_0 \sum_{m=1}^{\infty} \Big[\Phi(\,(4m - 1)\,L/r_0\,) - \Phi(\,(4m - 3)\,L/r_0\,) \Big] \quad . \tag{10}$$

and
$$P_{max} = \pi r_0^2 I_0 \Big[\Phi(L/r_0) + \Phi(5L/r_0) - \Phi(3L/r_0) + \Phi(9L/r_0) + \ldots\ldots \Big]$$

$$= \pi r_0^2 I_0 \Big[\Phi(L/r_0) + \sum_{m=1}^{\infty} \Big[\Phi((4m + 1)\,L/r_0) - \Phi((4m - 1)\,L/r_0) \Big] \Big] \tag{11}$$

Finally, using eq (10) and (11), the ratio K of P_{min} to P_{max} is obtained as

$$K = \frac{\sum_{m=1}^{M\to\infty} \left[\Phi((4m - 1)\, L/r_0) - \Phi((4m - 3)\, L/r_0) \right]}{\Phi(L/r_0) + \sum_{m=1}^{m\to\infty} \left[\Phi((4m + 1)\, L/r_0) - \Phi((4m - 1)\, L/r_0) \right]} \qquad (12)$$

where $\Phi(\ )$ is defined in eq (9) and the quantity M has been introduced into the summations in order to limit the sums in computations.

2.2. Results

A computer-generated plot of K versus r_0/L obtained with eq (12) is shown in figure 2. Clearly, if L is known, a single measurement of K will determine r_0 from such a plot. Repeated trials showed that most of the curve in figure (2) can be produced with values of M = 3 or 4 in eq (12). Larger M are needed only to show that the curve approaches 1 for large r_0/L. Also, increasing M in eq (12) causes no detrimental effects to the curve at small r_0/L. As will be seen below, in the case of axially symmetric beams, increasing M to improve one end of the curve will reduce the accuracy of the other end. Finally, note that the curve in figure (2) is approximately linear from r_0/L = 0.6 to 1.45. Using a 400 line per inch ruling, it should thus be possible to accurately measure Gaussian beam $1/e^2$ radii in the range from approximately 19 μm to 46 μm. Of course, larger radii can be accurately measured with rulings have larger L.

3. Application to Any Axially Symmetric Beam Function

As with a Gaussian beam, characterizing any beam with the Ronchi ruling method requires a graphical relationship between the optical power ratio K and some property that characterizes the beam (e.g., the $1/e^2$ beam radius in the Gaussian case). A unique relationship has to be derived for each ruling - optical beam function combination. For an ideal Ronchi ruling and any axially symmetric beam, an expression for K can be obtained with the aid of figure 3. The circles in the figure represent the beam, whose optical intensity function and arbitrary radial extent are I(r) and R, respectively.

To calculate P_{min} and P_{max}, note first that the beam power P in the area A to the right of any vertical line and above the x-axis in figure 3 can be obtained from the expression

$$P = \int I(r)\, dA \qquad (13)$$

Using polar coordinates, in which $dA = rdrd\theta$, and referring to figure 3, eq (13) can be rewritten as

$$P = \int_x^R rI(r)\, dr \int_0^{\cos^{-1}(x/r)} d\Theta = \int_x^R rI(r)\cos^{-1}(x/r)\, dr$$

Since the last form is a function of x, we define it as $\phi(x)$, i.e.,

$$\phi(x) = \int_{x}^{R} rI(r)\cos^{-1}(x/r)\, dr \quad . \tag{14}$$

Referring once again to figure 3, it can be seen that P_{min} and P_{max} can respectively be expressed in terms of $\phi(x)$ as

$$P_{min} = 4[\phi(L/2) - \phi(3L/2) + \phi(5L/2) - \phi(7L/2) + ...]$$

$$= 4 \sum_{m=1}^{\infty} [\phi((4m - 3)L/2) - \phi((4m - 1)L/2)] \quad ,$$

and

$$P_{max} = 4 \left[\phi(0) - \phi(L/2) + \phi(3L/2) - \phi(5L/2) + \phi(7L/2) + ... \right]$$

$$= 4 \left[\phi(0) - \phi(L/2) + \sum_{m=1}^{\infty} [\phi((4m - 1)L/2) - \phi((4m + 1)L/2) \right] \quad .$$

Using these forms, the ratio $K = P_{min}/P_{max}$ becomes

$$K = \frac{\sum_{m=1}^{\infty} [\phi((4m - 3)L/2) - \phi((4m - 1)L/2)]}{\phi(0) - \phi(L/2) + \sum_{m=1}^{\infty} [\phi((4m - 1)L/2) - \phi((4m + 1)L/2)]} \quad , \tag{15}$$

where $\phi(\ )$ is defined in eq (14).

Equations (14) and (15) are valid for any axially symmetric beam and an ideal Ronchi ruling. To be practically useful, however, they must be applied to a specific beam intensity function I(r) and expressed in terms of some parameter characteristic of that function. This is done specifically for the Airy diffraction pattern and the focused annulus in the following section. Since the Airy pattern is just a special case of focused annulus, the analysis will be done for the more general focused annulus, and the results simplified appropriately for the Airy pattern.

4. Application to the Focused Annulus and Airy Diffraction Patterns

4.1. Analysis

The output of a laser based on the confocal unstable resonator design [6] is a uniform beam in the shape of an annulus [7]. As illustrated in the inset of figure 4, the annulus consists of a circular aperture of radius α and a central circular obstruction of radius $\epsilon\alpha$, where ϵ is defined as the obscuration ratio. When an annular beam is focused, the intensity function of the resulting Fraunhofer diffraction pattern can be written as [8]

$$I(r) = I_0/(1 - \epsilon^2)^2 \left[\frac{2J_1(rc)}{rc} - \epsilon^2 \frac{2J_1(\epsilon rc)}{\epsilon rc} \right]^2 , \tag{16}$$

where I_0 is the intensity at the center of the beam, $J_1(\ )$ is the Bessel function of the first kind, first order, and c is a shorthand constant for the expression

$$c = 2\pi\alpha/f\lambda \quad . \tag{17}$$

In eq (17) α is the radius of the diffracting aperture, f is the lens focal length, and λ is the wavelength of the diffracted light. Note that when $\epsilon = 0$ the diffracting aperture shown in figure 4 becomes a simple circle for which the diffraction pattern is the well-known Airy pattern. Accordingly, eq (16) reduces, as expected, to

$$I(r) = I_0[2J_1(rc)/rc]^2 \quad . \tag{18}$$

The Airy pattern is an important special case because it occurs frequently in most laser systems due to the common use of circular apertures and lenses.

Figure 4 shows normalized plots of eq (16) for the cases $\epsilon = 0.0$ (the Airy pattern) and 0.5. Note that as ϵ increases, an increasing fraction of the total energy in the beam appears in the sidelobes. Thus, the error inherent in characterizing this beam function by assuming it to be approximately Gaussian becomes more significant with increasing ϵ.

Application of eq (14) and (15) to the focused annulus begins by using eq (16) in eq (14) and defining a new variable y = rc. Equation (14) thus becomes

$$\phi(xc) = 4I_0/(1-\epsilon^2)^2c^2 \int_{y=xc}^{y=Rc\to\infty} \left[J_1(y) - \epsilon J_1(\epsilon y) \right]^2 (1/y)\cos^{-1}(xc/y)\, dy \quad . \tag{19}$$

The upper limit of eq (19) is written $R\to\infty$ because, although the Airy pattern has infinite radial extent, the integral has to be terminated at some finite point for purposes of computation. Since the argument of the function $\phi(\ )$ in eq (14) has been changed from x to xc in eq (19), all the arguments of $\phi(\ )$ in eq (15) must also be multiplied by the shorthand constant c. Also, it is evident that when eq (19) is used in eq (15) the factor $4I_0/(1-\epsilon^2)^2c^2$ will be common to every term and thereby cancel. It is convenient, therefore, to define a new function to be used in eq (15), i.e.,

$$\Theta(z) = \frac{\phi(z = xc)}{4I_0/(1-\epsilon^2)^2c^2} = \int_z^{Rc\to\infty} \left[J_1(y) - \epsilon J_1(\epsilon y) \right]^2 (1/y)\cos^{-1}(z/y)\, dy \quad . \qquad (20)$$

In terms of eq (20), eq (15) can be rewritten as

$$K = \frac{\sum_{m=1}^{M\to\infty} \left[\Theta((4m - 3)Lc/2) - \Theta((4m - 1)Lc/2) \right]}{\pi(1-\epsilon^2)/4 - \Theta(Lc/2) + \sum_{m=1}^{M\to\infty} \left[\Theta((4m - 1)Lc/2) - \Theta((4m + 1)Lc/2) \right]} \qquad (21)$$

where the quantity M has been introduced in the summations for computational purposes and the first term in the denominator has been replaced by its actual value, i.e.,

$$\Theta(0) = \frac{\pi}{2} \int_0^{\infty} \left[J_1(y) - \epsilon J_1(\epsilon y) \right]^2 (1/y)\, dy$$

$$= \frac{\pi}{2} \left[\int_0^{\infty} \frac{J_1^2(y)}{y}\, dy + \epsilon^2 \int_0^{\infty} \frac{J_1^2(\epsilon y)}{y}\, dy - 2\epsilon \int_0^{\infty} \frac{J_1(y)\, J_1(\epsilon y)}{y}\, dy \right]$$

$$= \pi/2\, (1/2 + \epsilon^2/2 - \epsilon^2) = \pi(1 - \epsilon^2)/4 \ ,$$

where the tabulated integral [9]

$$\int_0^{\infty} \frac{j_n(at)\, J_n(bt)}{t}\, dt = \frac{(b/a)^n}{2n}$$

was used to evaluate the three integrals in the calculation.

The final step in applying eq (15) to the focused annulus is to replace the quantity c in eq (21) with a parameter that characterizes the beam function. In analogy with the use of the $1/e^2$ beam radius r_0 in the case of Gaussian beams, the radial distance r_1 to the first null of the focused annulus is defined here as that

characteristic parameter. It is evident in figure 4 that the first zero of the focused annulus depends on the value of ϵ. We therefore define $g(\epsilon)$ as the value of rc corresponding to the first null of the intensity function in eq (16), i.e., $g(\epsilon) = r_1 c$, so that the form of c to be used in eq (21) is

$$c = g(\epsilon)/r_1 \quad . \tag{22}$$

From eq (16) it can be seen that $g(\epsilon)$ is the smallest solution of the transcendental equation

$$J_1(rc) - \epsilon J_1(\epsilon rc) = 0 \quad , \tag{23}$$

which can be solved iteratively. For example, for $\epsilon = 0.0$ and 0.5, solution of eq (23) yields $g(\epsilon) = 3.833$ or 1.220π and 3.145 or 1.001π, respectively. Substitution of eq (22) into eq (21) yields the required result for K, i.e.,

$$K = \frac{\displaystyle\sum_{m=1}^{M\to\infty} \left[\Theta((4m-3)g(\epsilon)L/2r_1) - \Theta((4m-1)g(\epsilon)L/2r_1) \right]}{\pi(1-\epsilon^2)/4 - \Theta(g(\epsilon)L/2r_1) + \displaystyle\sum_{m=1}^{M\to\infty} \left[\Theta((4m-1)g(\epsilon)L/2r_1) - \Theta((4m+1)g(\epsilon)L/2r_1) \right]} \quad , \tag{24}$$

where $\Theta(\ )$ is defined in eq (20).

4.2. Results

Equation (24) provides the desired relation between the measured ratio K and the radial distance r_1 characteristic of a specific focused annulus. For comparison with the results shown in figure 2 for Gaussian beams, eq (20) and (24) were used to obtain plots of K versus r_1/L. The repeated integrations of eq (20) required in eq (24) were done numerically using Simpson's one-third rule [10]. To ensure that the upper limit Rc of every integral was always larger than the lower limit, it was necessary to require that Rc be at least as large as the largest argument in eq (24), which is $(4M+1)g(\epsilon)L/2r_1$. This leads to the condition

$$r_1/L \geq (4M + 1)\, g(\epsilon) / 2Rc \quad , \tag{25}$$

which reveals a computational tradeoff between the minimum r_1/L for which eq (24) can be evaluated and the number of terms M used in the summations. Note that no such tradeoff was present in the Gaussian beam case. Fortunately, the difficulty imposed by this tradeoff could be essentially eliminated by a sufficiently large choice of the upper limit Rc (200), which also guaranteed that most of the energy in the beam was accounted for in the computations.

In reference [8], it is shown that the fraction of the total power or energy of the Airy pattern (the $\epsilon = 0$ case) contained in the axial circle of radius R is given by the expression

$$P(R) = 1 - J_0^2(Rc) - J_1^2(Rc) \quad , \tag{26}$$

where $J_0(\ )$ and $J_1(\ )$ are Bessel functions of the first kind, orders zero and one, respectively. Using large argument formulas [11] for $J_0(\ )$ and $J_1(\ )$ in eq (26), it was found that for Rc = 200, P(R) = 99.68%. For values of ϵ other than zero, P(R) is slightly less, as can be seen in the normalized curves of figure 4, where the sidelobe energy content increases with ϵ. The fraction of total energy contained within a finite radius of a focused annulus with arbitrary ϵ can be calculated by numerically integrating eq (20) with z = 0. This has been done previously [12-14], and the results of reference [14] show that for Rc = 200, at least 99% of the beam energy is included if $\epsilon \leq 0.5$ and at least 98% is included if $\epsilon \leq 0.8$. Furthermore, with Rc = 200 in eq (20) and as few as three terms ($M \geq 3$) in the summations of eq (24), plots of K versus r_1/L were found to be virtually identical for values of r_1/L up to approximately 2.5. At that point $K \simeq 0.99$, which is well beyond the useful portion of a given plot.

Figure 5 shows plots of K versus r_1/L for ϵ = 0.0, 0.25, and 0.50, which were obtained with Rc = 200 in eq (20) and M = 5 in eq (24). The lower ends of the curves terminate at $r_1/L \simeq 0.20$ due to the limitation imposed by eq (25). Fewer terms ($M < 5$) in the summations would allow the curves to extend to smaller values of r_1/L. On the other hand, larger M are needed to show how the upper ends of the curves approach 1.0 asymptotically with increasing r_1/L. Therefore, the use of M = 5 represents an acceptable compromise that yields the useful portion of the K versus r_1/L relationship.

As is the case with Gaussian beams, a K versus r_1/L Ronchi ruling plot is most useful if it varies smoothly, monotonically, and approximately linearly over as wide a range of (r_1/L, K) values as possible. The curves in figure 5 (and others not shown here) show that, beginning with $\epsilon \simeq 0.45$, a portion of the K versus r_1/L data exhibits a non-monotonic behavior that becomes more pronounced with increasing ϵ. Thus, the method is most useful for smaller ϵ, i.e., $\epsilon \leq 0.45$. For example, Curve (a) in figure 5 for the Airy pattern (ϵ = 0) is smooth and reasonably linear over the approximate range of (r_1/L, K) values from (0.75, 0.1) to (2.25, 0.9). Thus, using a 400 line per inch Ronchi ruling (L = 31.8 μm), it should be possible to accurately measure first nulls of Airy patterns ranging in size from approximately 24 μm to 71 μm. This result is similar to that discussed earlier for Gaussian beams (see Section 3). Also, since the behavior of Curve (b) in figure 5 for ϵ = 0.25 can be seen to be similar to that of Curve (a), similar comments can be made about it and other curves corresponding to relatively small ϵ. Thus, the Ronchi ruling method should be at least as useful with those beams as with Gaussian beams.

Curves of K versus r_1/L for larger ϵ can also be used, but in a somewhat restricted manner. For example, Curve (c) in figure 5 for ϵ = 0.50 is monotonic and roughly linear over two relatively small ranges of (r_1/L, K), i.e., from approximately (0.29, 0.12) to (0.50, 0.42) and from approximately (1.4, 0.55) to (2.0, 0.97). In terms of a 400 line per inch ruling, these two ranges would enable measurement of first null radii ranging from approximately 9.2 μm to 15.9 μm and from approximately 44.5 μm to 63.6 μm.

Determining the r_1 of a focused annulus from a plot of K versus r_1/L depends upon whether the value of ϵ is known. If ϵ is known, the procedure is the same as in the case of Gaussian beams. A single measurement of K with a Ronchi ruling of known L allows r_1 to immediately be read from the appropriate plot of K versus r_1/L. If the value of ϵ is unknown (the more likely situation), measurements of K with two different Ronchi rulings of known bar and space widths (L_1 and L_2), are needed to determine r_1. The first measurement of K with the known L_1 will determine a set of possible r_1 values, one from each of a set of curves of K versus r_1/L for different ϵ. With the known L_2, a set of r_1/L_2 ratios can then be formed and used with the set of K versus r_1/L curves to predict the value of K to be measured with L_2. The second measurement should agree with only one of those predictions, thereby establishing both ϵ and r_1.

Note, finally, that a measurement of r_1 also determines the outer radius α of the diffracting aperture. This becomes evident when eq (17) and (22) are compared, which shows that

$$\alpha = g(\epsilon) f\lambda / 2\pi r_1 \quad , \tag{27}$$

where the lens focal length f and the wavelength λ of the diffracted light are presumably known.

5. Summary and Conclusions

We have reviewed the application of the Ronchi ruling method to Gaussian beams and analyzed its application to axially symmetric beams. Equations (14) and (15) express the ratio K of minimum to maximum transmitted optical powers in terms of the ruling parameter L and the beam function I(r) of an arbitrary axisymmetric beam. Equations (14) and (15) are converted to eq (20) and (24), respectively, when applied to the focused annulus beam function (eq (16)), a special case of which is the Airy pattern (eq (18)).

In analogy with previous Ronchi ruling analyses of Gaussian beams [1-3], eq (20) and (24) were used to generate plots of K versus r_1/L, where r_1 is the first null of the specific beam function. Typical examples are given in figure 5. The results suggest that the Ronchi ruling method is most useful for focused annuli with relatively small obscuration ratios i.e., $\epsilon \leq 0.30$ (approximately). In such cases the K versus r_1/L plots are similar in behavior to the results obtained for Gaussian beams, i.e., monotonic and roughly linear over a relatively wide range of (r_1/L, K) values.

It should be possible to quickly and accurately characterize beams with first nulls larger than or equal to approximately 25 μm. If ϵ is known, one measurement of K with a ruling of known L determines both r_1 (from a K versus r_1/L plot) and the outer radius α of the diffracting aperture (from eq (27)). If ϵ is unknown, a second measurement with a different known ruling will determine ϵ, r_1, and α.

6. References

[1] R. M. O'Connell and R. A. Vogel, "Abel inversion of knife-edge data from radially symmetric pulsed laser beams", Appl. Opt. 26, 2528 (1987).

[2] L. D. Dickson, "Ronchi ruling method for measuring Gaussian beam diameter", Opt. Eng. 18, 70 (1979).

[3] E. C. Broockman, L. D. Dickson, and R. S. Fortenberry, "Generalization of the Ronchi ruling method for measuring Gaussian beam diameter", Opt. Eng. 22, 643 (1983).

[4] M. A. Karim, "Measurement of Gaussian beam diameter using Ronchi rulings", Electron. Lett. 21, 427 (1985).

[5] Standard Mathematical Tables (The Chemical Rubber Co., Cleveland, 1965), p.258.

[6] W. F. Krupke and W. R. Sooy, "Properties of an unstable confocal resonator CO_2 laser system", IEEE J. Quantum Electron. QE-5, 575 (1969).

[7] J. T. Verdeyen, Laser Electronics (Prentice-Hall, Englewood Cliffs, 1981), p.106.

[8] M. Born and E. Wolf, Principles of Optics (Pergamon, Oxford, 1975), pp.395-418.

[9] G. N. Watson, A Treatise on the Theory of Bessel Functions (Cambridge, New York, 1944), p.405.

[10] R. G. Stanton, Numerical Methods for Science and Engineering (Prentice-Hall, Englewood Cliffs, 1961), p.116.

[11] Standard Mathematical Tables (The Chemical Rubber Co., Cleveland, 1965), p.350.

[12] W. T. Welford, "Use of annular apertures to increase focal depth", J. Opt. Soc. Am. 50, 749 (1960).

[13] B. L. Mehta, "Total illumination in an aberration-free annular aperture", Appl. Opt. 13, 736 (1974).

[14] H.F.A. Tschunko, "Imaging performance of annular apertures", Appl. Opt. 13, 1820 (1974).

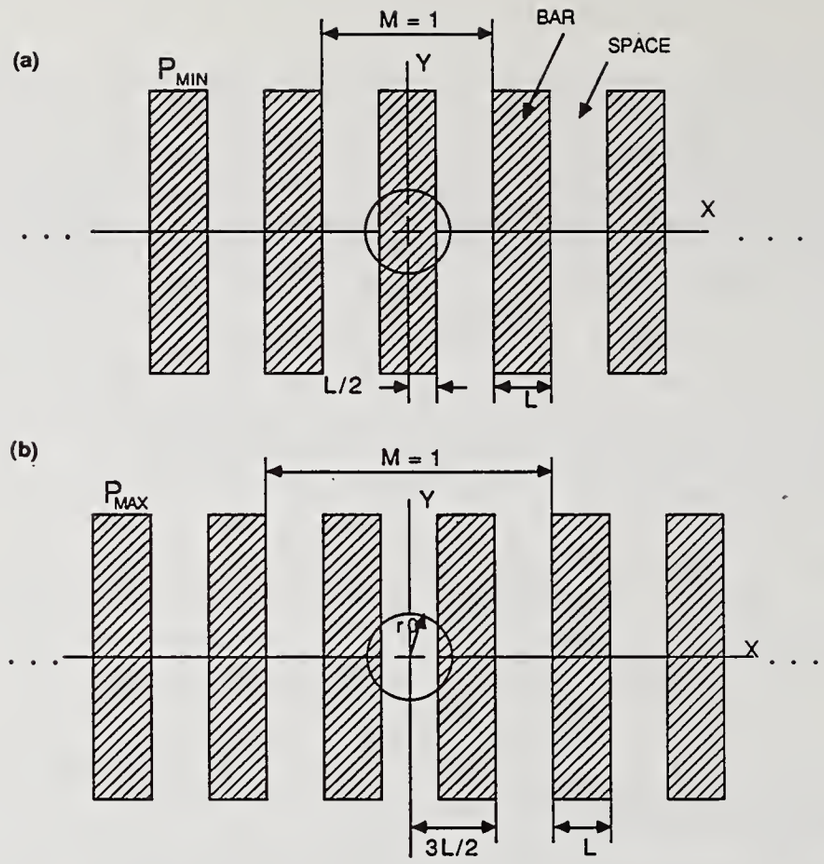

Figure 1. Geometry used to analyze the characterization of a Gaussian beam with an ideal Ronchi ruling: (a) for the calculation of P_{min} ; (b) for the calculation of P_{max} .

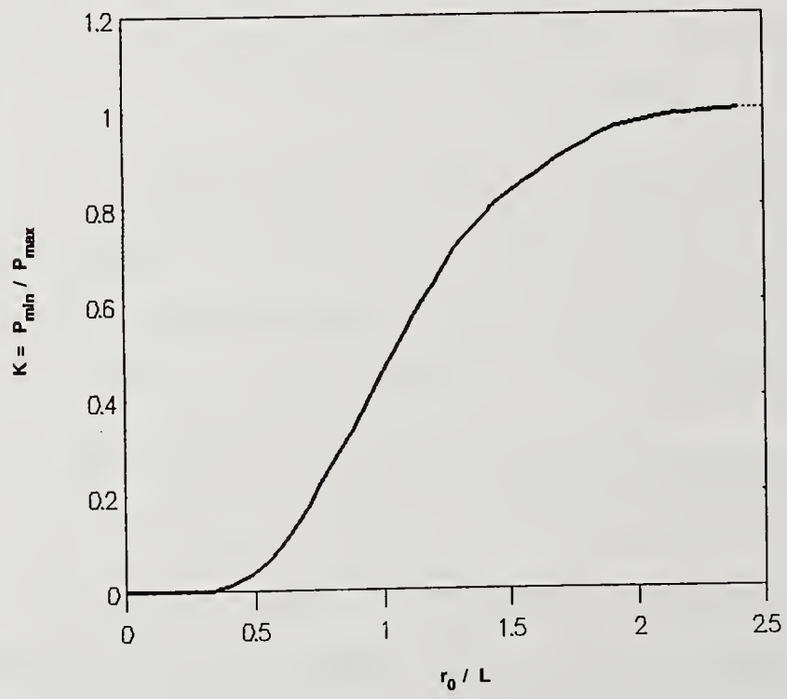

Figure 2. Plot of K versus r_0 / L for a Gaussian beam (Equation (12)).

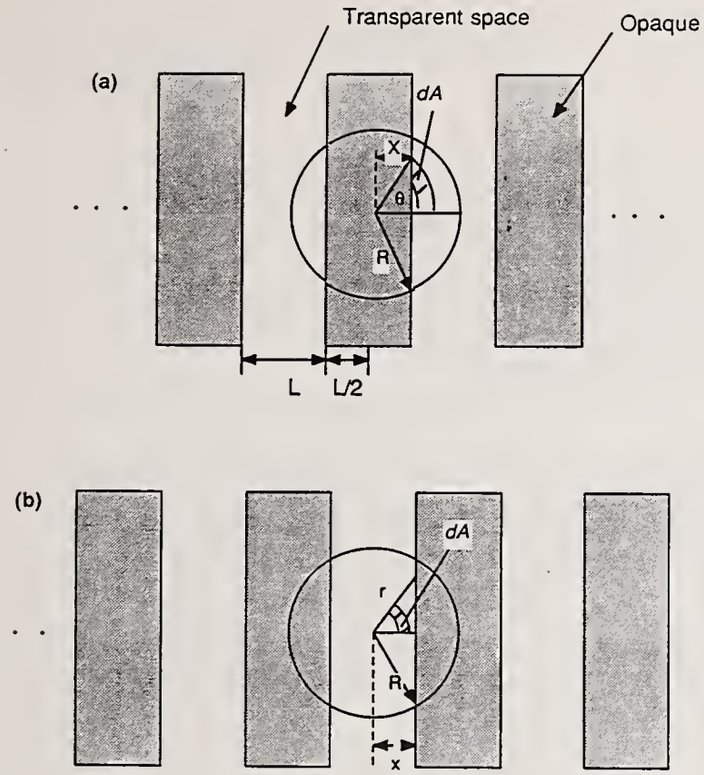

Figure 3. Geometry used to analyze the characterization of an arbitrary axially symmetric beam with an ideal Ronchi ruling: (a) for the calculation of P_{min} ; (b) for the calculation of P_{max}.

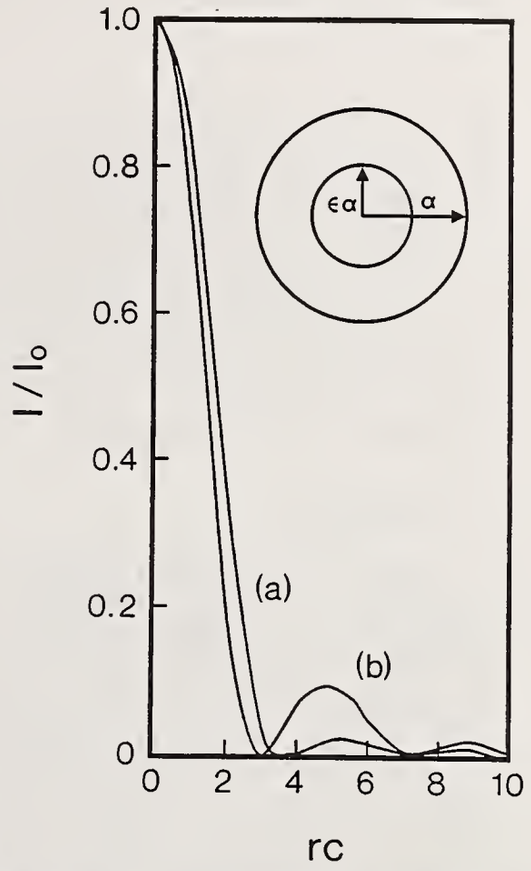

Figure 4. Geometry of an annular aperture (inset) and normalized cross-sections of two axially symmetric beam functions: (a) the Airy pattern (Equation (18)) or focused annulus (Equation (16)) with ϵ = 0.0; (b) the focused annulus (Equation (16)) with ϵ = 0.5.

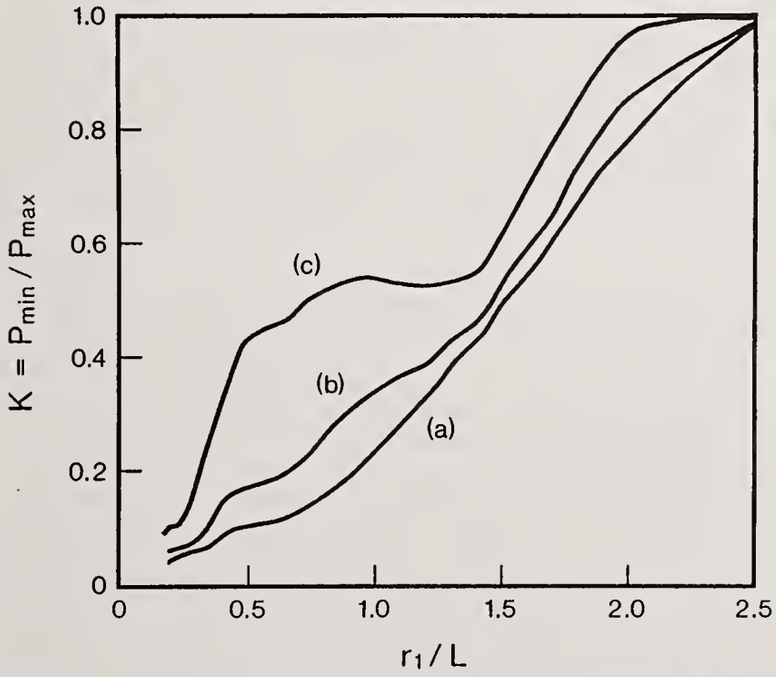

Figure 5. Plots of K versus r_1 / L obtained using Rc = 200 in Equation (20) and M = 5 in Equation (24) for various focused annuli: (a) ϵ = 0.0 (the Airy pattern); (b) ϵ = 0.25; (c) ϵ = 0.50.

Manuscript received
1-29-90

Prediction Of Laser Induced Damage By Comparison Of Laser Fluence Profile To Damage Spot Radius

R. Goedert, T. Whittaker and D. Templeton

U.S. Army Tank-Automotive Command
Countermeasures Branch
Warren, MI 48397-5000

In this method, the laser induced damage threshold for a material is obtained by determining the fluence within the damaging beam at a radial distance equal to the radius of the damage spot. The energy profile of the laser pulse is determined by translating a slit across the beam and reading the energy passing through the slit with position. The laser profile is then quantified into fluence squares of area 400um^2 in a two dimensional fluence grid. The radius of the damage site is then applied to the fluence grid, indicating the fluence square that corresponds to the edge of damage and it is this value that is the predicted damage threshold.

Key Words: Laser Induced Damage, Profile, Fluence Grid, Surface Pitting

1. Introduction

Damage threshold measurements are often very time consuming and expensive, but for many applications, all that is needed is a good approximation of the threshold for a given set of parameters. This paper presents preliminary results of a method for determining the damage threshold of an optical glass by relating the size of the damage site to the energy profile of the damaging pulse of light. It is the goal of this work to develop and narrow the process sufficiently such that very few damage sites will be needed to make an accurate prediction of the single shot damage threshold of the glass.

The optical glass used in this investigation was Schott Glass Corporation's OG-550 absorption glass. This glass is a cut-on filter with its 50% transmission point at 550nm while it absorbs very strongly at 532nm. Figure 1 is a transmission curve of OG-550. The single shot and multiple pulse laser induced damage thresholds of OG-550 to Q-switched 532nm radiation have been determined by this laboratory, Whittaker et. al. [1], and presented at the 1989 Symposium on Optical Materials for High Power Lasers, National Institute of Standards and Technology in Boulder, Colorado in a paper entitled, "Laser Induced Damage In Schott's OG-550 Optical Absorption Glass." The results of that investigation are summarized in table 1 and figure 2.

The primary hypothesis of this work is that each particular portion of the damaging beam is mostly responsible for the damage done to the target over that area which it impacts. Heating of other areas of the target by other portions of the beam may contribute to the damaging of any particular area, but this aspect is ignored for the single shot damage threshold determination (heat propagation does not appear to be significant until about the sixth pulse of multiple shot irradiance at 10 Hz for the energy levels utilized). Figure 3 pictorially displays the concept. Filbert et. al. [2], presented work showing a direct correlation between the shape of damage within a damage site and the shape of the fluence distribution within the laser spot. They used a 100x100 pixel array camera to capture the multimode fluence distribution of the laser spot. This distribution contour plot was then compared with an enlarged picture of the damage site. Their example showed that sections of common fluence within the contour plot had the same shape as sections of damage within the damage site.

2. Damage Requirement

Since the method requires that the average radius of the damage site be measured, energy levels must be set to cause damage that is roughly circular. In addition, since the method

relies on matching the damage site to the energy profile of the beam, damage sites with radii larger than the $1/e^2$ radius of the beam are not desirable. The type of damage referred to in this investigation is surface pitting. Figure 4 displays photographs of a typical damage site.

3. Experimental Setup

Figure 5 shows the laser damage optical setup. The laser source is a Quantel International model 581 Q-switched Nd:YAG with doubler lasing at 532nm with a pulse length of approximately 10nsec. The pulse energy is measured using a Laser Precision Corporation silicon detector, model RJP-765. The f/2 lens is used to bring the laser spot size to a diameter on the order of 600um at the sample surface.

4. Fluence Within the Laser Pulse

Two separate processes were developed which use common one-dimensional single slit energy profile data and translate it into two dimensional fluence data. The laser beam profile is obtained by translating a 120um slit perpendicular to the beam (x-direction) in increments of 60um or 120um and measuring the energy passing through the slit. Figures 6 and 7 show the energy profile obtained with the slit method for our data. The first method, 'The Common Area Method', yields a fluence value for the common area between the slit and a beam of diameter $1/e^2$, for the slit at any location. The second method, the 'Fluence Grid Process', quantizes the single slit profile data into a two dimensional grid of fluence squares of the same area. The Common Area Method assumes only that the beam is circular while the Fluence Grid Process assumes that it is gaussian. The Fluence Grid Process is preferred, but the Common Area Method deserves some discussion since it does not require a gaussian beam and for comparison between the two methods.

4.1 Fluence Grid Process

Very simply, the method quantifies the laser spot into a grid of squares of varying fluences. One then measures the diameter of the damage site and matches the point on the glass at the diameter of the damage to the square within the beam that caused the damage. That particular square has a fluence associated with it and that fluence is considered the damage threshold of the glass.

Again, the beam is characterized by translating a 120um slit across the beam in 60um or 120um increments and the energy passing through the slit recorded. This data is then interpolated so that we have a value for the energy passing through a 120um slit for every 20um increment across the beam (note that this adds extra data points such that when you add them up you have a value larger than the actual total energy; the solution is simply to divide the total by the number of added data points within the 120um range). The beam is assumed to be gaussian and therefore we can find a best fit gaussian curve through our data. Figures 6 and 7 show the gaussian best fit through our slit profile data. Using a computer spread sheet, we construct a two dimensional array with a data point (cell) every 20um in both the x and y directions (the beam travels in the z direction). The values in the cells represent a rotation of the gaussian best fit curve. Each cell contains the equation for a gaussian in the form:

$$\text{Cell Energy} = \frac{C}{2*PI*sigma^2} * e^{-((x^2 + y^2)/2*sigma^2)} * 400um^2 \qquad \text{eq (1)}$$

where, x & y indicate the cell position within the array &

$$C = \frac{2*PI*sigma^2}{Area} * (\text{Peak Energy})$$

The total energy of the damaging laser pulse is known and the interpolated energy profile is adjusted such that the total energy under its curve is equal to this value. Then C is adjusted until the total of all the elements in the array equals the energy of the damaging pulse. At this point the values in the fluence grid are the correct values for the given damaging pulse, and the damage threshold can be found using the damage site radius. Figure 8 is a schematic diagram of the process. Note that the choice to interpolate the data every 20um, and therefore have a fluence square area of $400um^2$, is completely arbitrary; our

limiting factor is the memory of our computer.

4.2 The Common Area Method

In this method the objective is to determine the fluence in the slice of the beam that intersects with the edge of the damage site; it is this fluence that we assume to be the damage threshold for the glass. That is, if our profiling slit is of width 120um and our damage site has radius 200um, then we want the fluence in the slice of width 120um centered at 200um from the center of the laser spot. After determining the energy profile of the beam by the slit translation method, we interpolate this data to obtain a curve of energy through the slit with position. A BASIC program written at the Tank-Automotive Command entitled, "Profiles" is utilized to calculate the common area between the slit and the beam for the slit at a given position within a beam of $1/e^2$ radius. Since we have the total amount of energy passing through the slit at any position across the beam, we can determine the fluence for any slice of the beam. However, there are two boundary conditions that apply. The first is that damage sites used in this method must not have a radius larger than 90% of the beam spot radius. This is because the area calculation tends quickly to zero after this point, since we are not allowing the inclusion of any area outside the $1/e^2$ radius. Although there is energy in the wings of the gaussian beyond the $1/e^2$ point, a logical limit had to be placed on the common area calculation. The second boundary is that a damage site radius can not be any smaller than the slit width. As the damage site gets smaller, tending to zero, the common area calculation tends to its maximum value (that of the slit positioned at the center of the beam). This causes a diverging discrepancy between the immediate area around the edge of the damage site (the area over which we are interested in the fluence) and the area calculated by the program. This divergence needs a limit then, which should probably be larger than the slit width, but this limit is at least obvious.

5. Results

When comparing the results of this investigation to the damage threshold values stated by Whittaker *et. al.* in table 1, compare with the values given for microscopic damage.

5.1 Results of Fluence Grid Process

There are two data sets presented here, each using a different beam radius. The beam radius for data set A was 325um and for data set B it was 295um. Figures 9 and 10 show the damage thresholds achieved for each beam diameter using the accepted method of decreasing the fluence until no damage is seen. While the threshold achieved for data set A agrees well with the data presented in table 1, it is not understood why the threshold achieved for data set B is higher.

Table 2 shows the predicted single shot damage thresholds achieved using the Fluence Grid Process, along with the radius of the damage site used to obtain the value and the number of laser pulses that caused the damage. Note that while there is considerable variation within the data, the average value for data set B, 6.16 J/cm^2, is very close to the accepted value for data set A of 6.3 J/cm^2. Also the average value of data set A, 7.97 J/cm^2, is reasonably close to the accepted value for data set B of 9.9 J/cm^2.

Single shot and two shot data are presented in the table. It was noted that two shots yielded a more uniform damage site in most cases and therefore this data is presented to examine the influence of the second shot on the prediction of the damage threshold. It appears that the two shot data yields a threshold value close to that obtained for the single shot data. While it may be desirable to use two shot data (since the damage is more uniform), it is still unclear how to handle two shots of slightly varying energies and for this reason the use of two shot data requires further study.

Figure 11 is a plot of the total fluence on site versus damage radius. This demonstrates that there is a region over which the diameter of the damage spot increases linearly with increasing fluence on site. The data obtained with the 325um radius beam, data set A, appears better behaved than that from data set B with a beam diameter of 295um. Figure 12 is a plot of the predicted single shot damage threshold versus the damage spot radius. This plot seems to demonstrate that our premise that the edge of the damage sight will point directly to the threshold fluence is flawed. There is, however, a definite linear relationship that is worth exploring. We will examine this relationship further to see if the y intercept is some function of the threshold value for several different materials.

5.2 Results of Common Area Method

Figures 13 and 14 present the predicted damage threshold values versus damage spot radius

for data sets A and B using the Common Area Method. The data within the boxes is considered 'allowed' because it meets the boundary conditions that the damage site cannot have radius larger than 90% of the beam spot radius or smaller than the slit width. The average predicted damage threshold for data set A is 16.98 J/cm^2 and for data set B is 7.66 J/cm^2. Again, these values are to be compared with 6.3 J/cm^2 for data set A and 9.9 J/cm^2 for data set B. While the value of 7.66 J/cm^2 is considered a good approximation, it is not understood why the threshold obtained for data set A is roughly twice as large as the accepted value. Note that the threshold data within the allowed regions of figures 13 and 14 does not increase or decrease with increasing damage site radius. This is the result that is desired. This shows that while the fluence within the beam changes quickly with increasing radius from the center of the beam (as it does with a gaussian beam), the threshold value determined with this method remains fairly constant.

6. Conclusions

While it is too early yet to draw a definite conclusion on the utility of the methods, they appear to yield, on average, good approximations to the accepted damage threshold value. The goal of the method, however, is to closely approximate the threshold value using very few data points, and this has not yet been accomplished. Figure 12 indicates that the initial hypothesis is not correct, at least for the glass used in this work. It remains to be seen if this method will apply to coated optics and metalized mirrors. Other hypotheses should be tested with the data in figure 13, from the Common Area Method, since this data behaves as expected.

Since it is expected that the large spread within the damage threshold region (the overlap between 'damage' & 'no damage' in figures 9 & 10) is inherent to the material and that this parameter cannot be changed, other aspects of the experiment such as beam quality must be known to a high degree. It also appears that this same variation may be manifesting itself within each damage site resulting in less than circular damage. We are planning to measure multiple radii for each damage site and then average these values to see if this may be a method to obtain a reasonable average value from only a few damage sites. We are also planning to utilize a 256X256 array camera and framegrabber system to capture the shape of each damaging pulse. It is suspected that hot spots within the laser beam may be contributing to the variation in our data and the framegrabbing system should help to expose this problem. The camera system also displays a fluence value for each pixel. If the laser spot and damage site can be imaged together, fluence values could be given that literally outline the damage site. It is expected that the average of these many values for a single damage site will yield a close approximation to the true threshold value, and thus only a few damage sites will be needed for an accurate threshold determination.

Other additional work will include the application of this method to other optical glasses, thin film coatings and metallized mirrors. It is clear that if this process can be refined such that only a few damage sites are needed for a damage threshold determination, the method will find great utility in areas such as testing of one-of-a-kind parts, testing expensive materials or coatings, or a quick quality control measure.

Special thanks to Dr. John Bennett who helped us develop the fluence grid process, and to Mazin Kashat and Gerald Koenig who wrote the Profiles program which calculates the common area between a beam of $1/e^2$ radius and a slit of width x at any given position.

7. References

[1] Whittaker T.A., Goedert R., Templeton D., "Laser Induced Damage in Schott's OG-550 Optical Absorption Glass," National Inst. of Standards & Tech. Laser Damage Symposium, 1989.

[2] Filbert P.C., Guttman J.L., Navoda C.L., Watson B.A., "Application of a Computer-Automated IR Sensitive Camera to the Determination of Pulsed Laser Surface Damage Thresholds," Natl. Bur. Stand. (U.S.) Spec. Publ. 727, pp. 77-84, 1984.

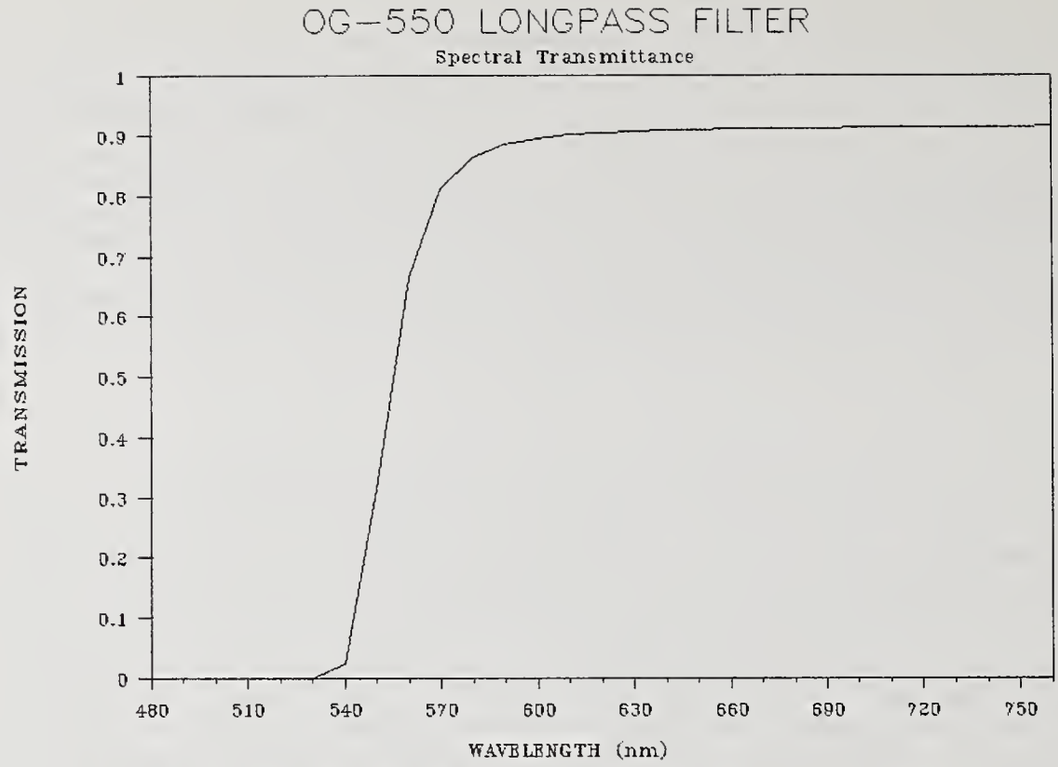

Figure 1. Spectral transmission of OG-550 absorption glass.

TABLE 1. TYPE OF DAMAGE: Surface pitting

SINGLE SHOT DAMAGE THRESHOLD (J/cm²)			
SAMPLE #	LASER SPOT SIZE (RADIUS μm)	DAMAGE CRITERION Visual	Micro (100X)
3	432	6.0	4.9
6	442	6.7	6.0
9	626	9.7	8.6
10	626	7.9	6.6
11	626	7.3	6.8
12	626	7.0	4.9
	AVERAGE	7.4	6.6

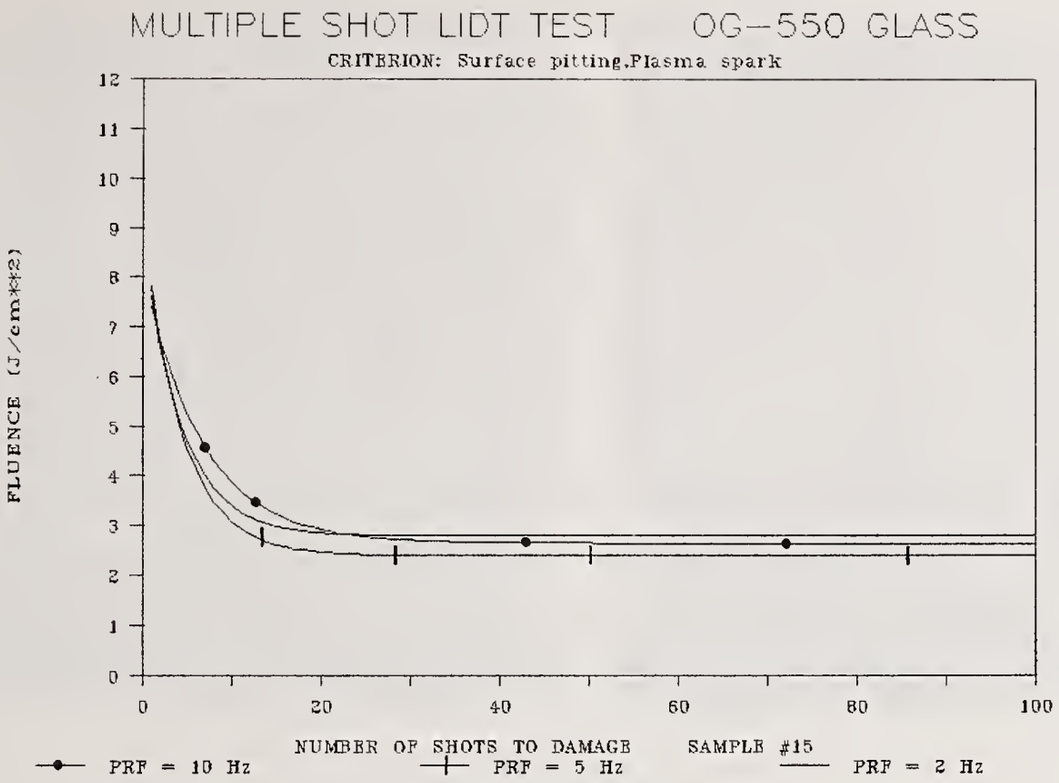

Figure 2. Multiple shot laser induced damage threshold (LIDT) results presented by Whittaker et. al.

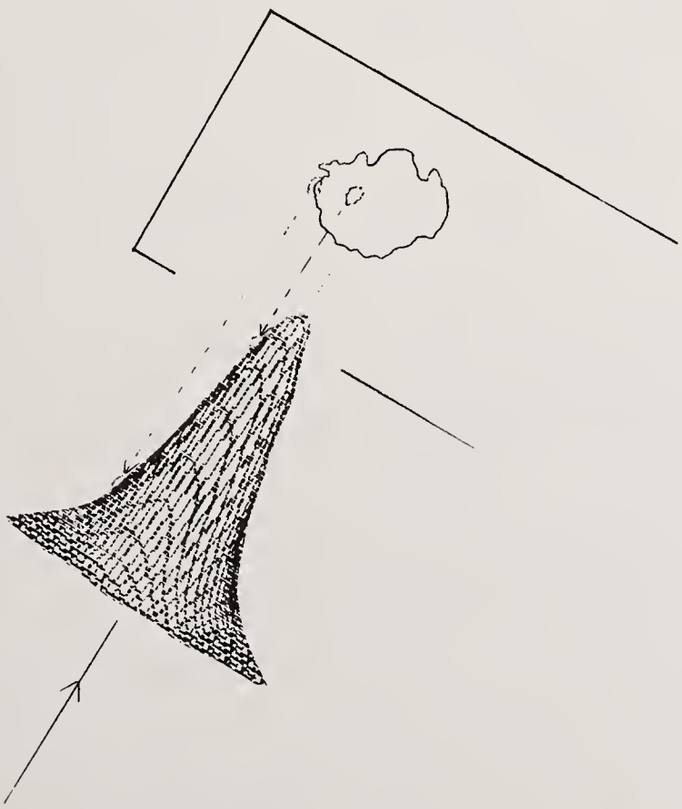

Figure 3. The drawing displays the concept that particular portions of the beam are responsible for particular portions of damage within the damage site.

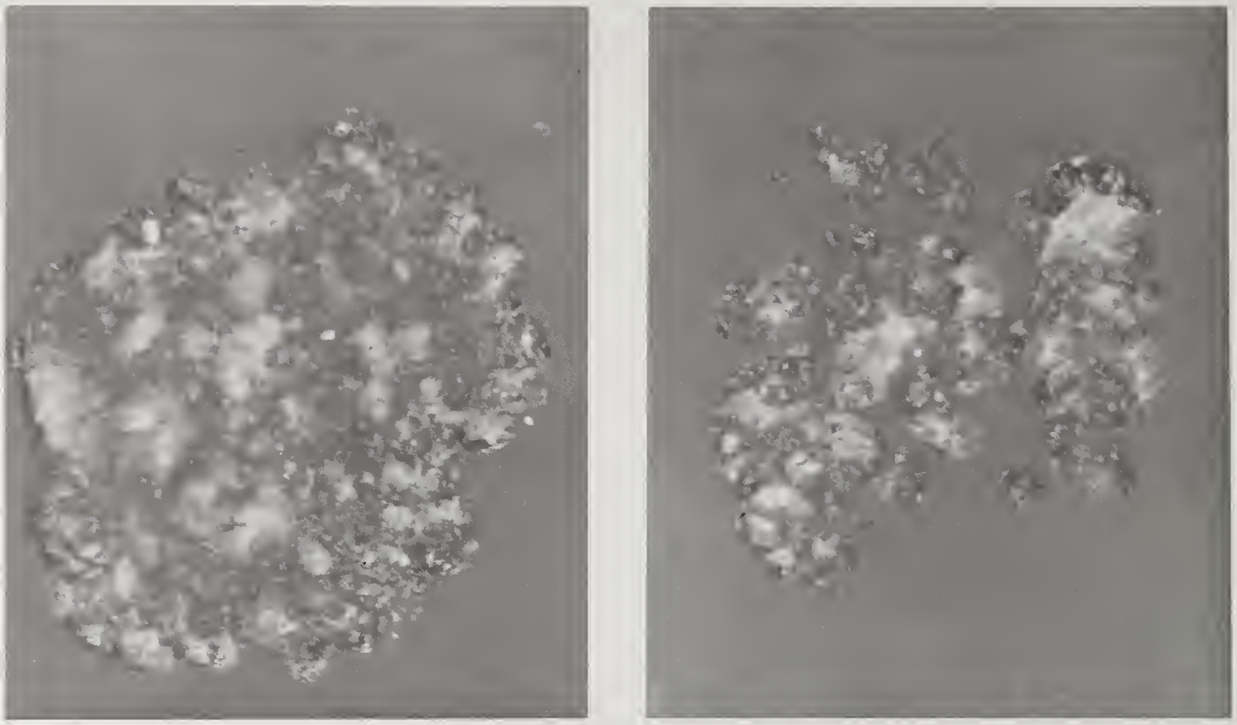

Figure 4. Typical damage sites. The damage appears as pits in the surface.

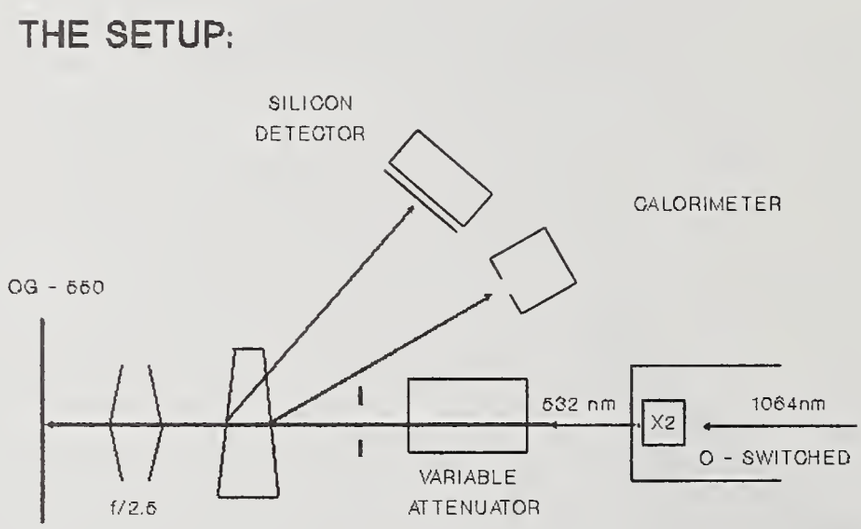

Figure 5. The laser damage optical setup.

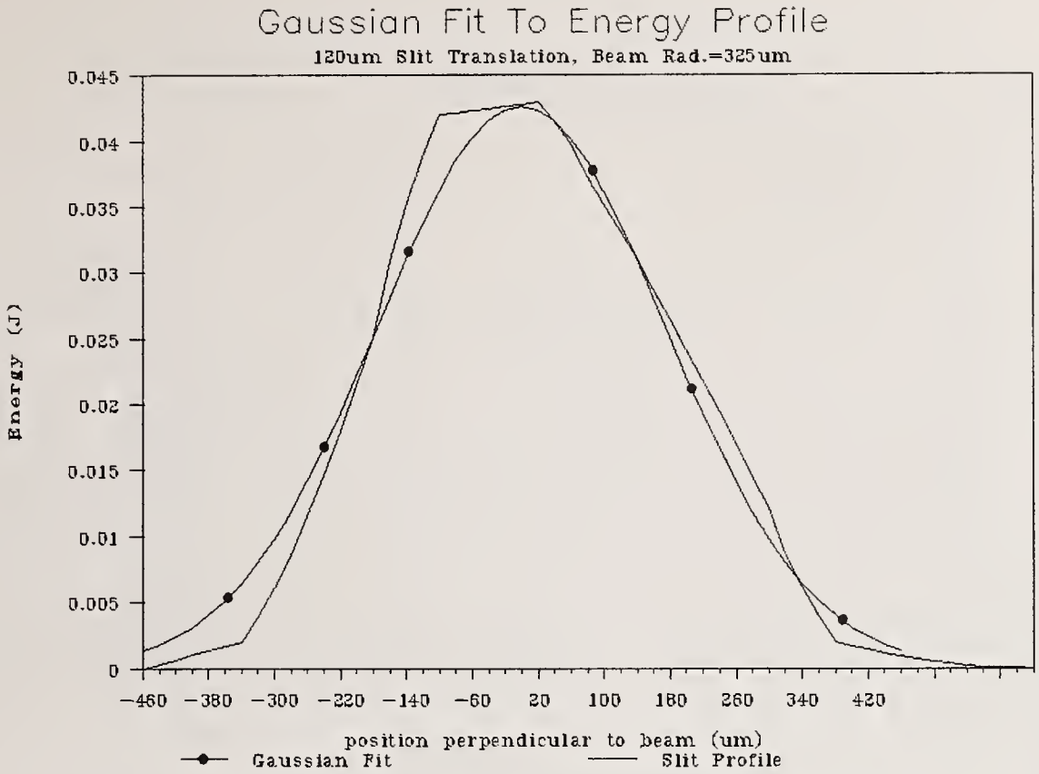

Figure 6. Gaussian, fit to the energy profile, derived from the slit translation method, for data set A.

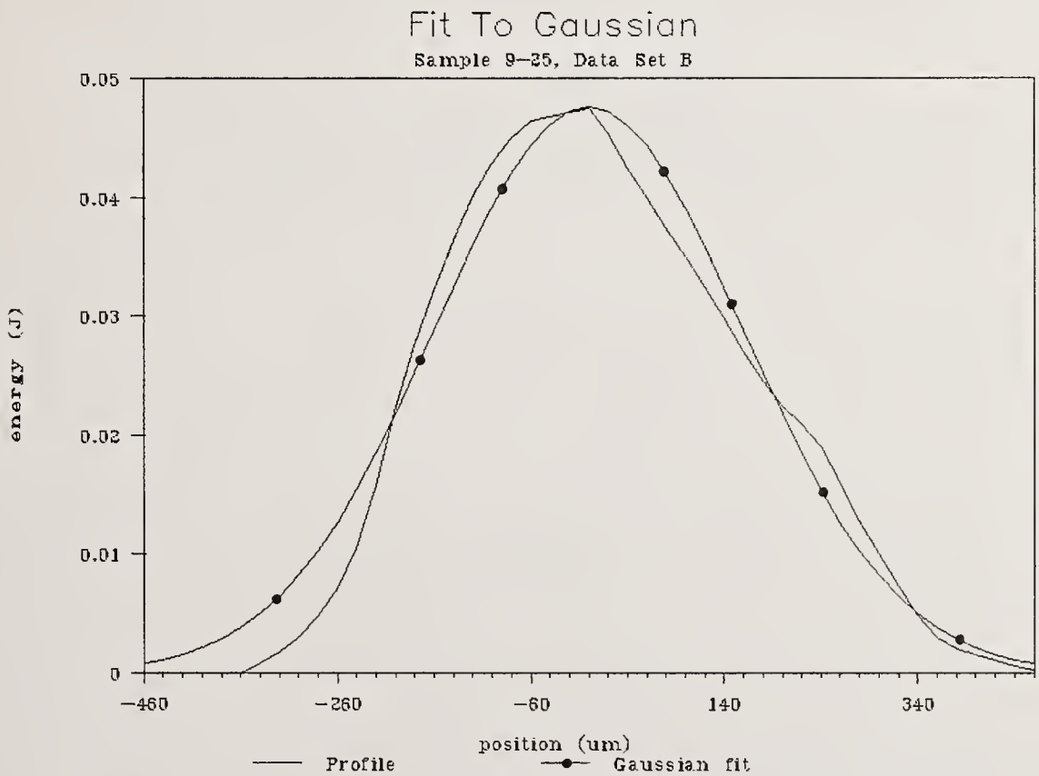

Figure 7. Gaussian fit to the energy profile for data set B.

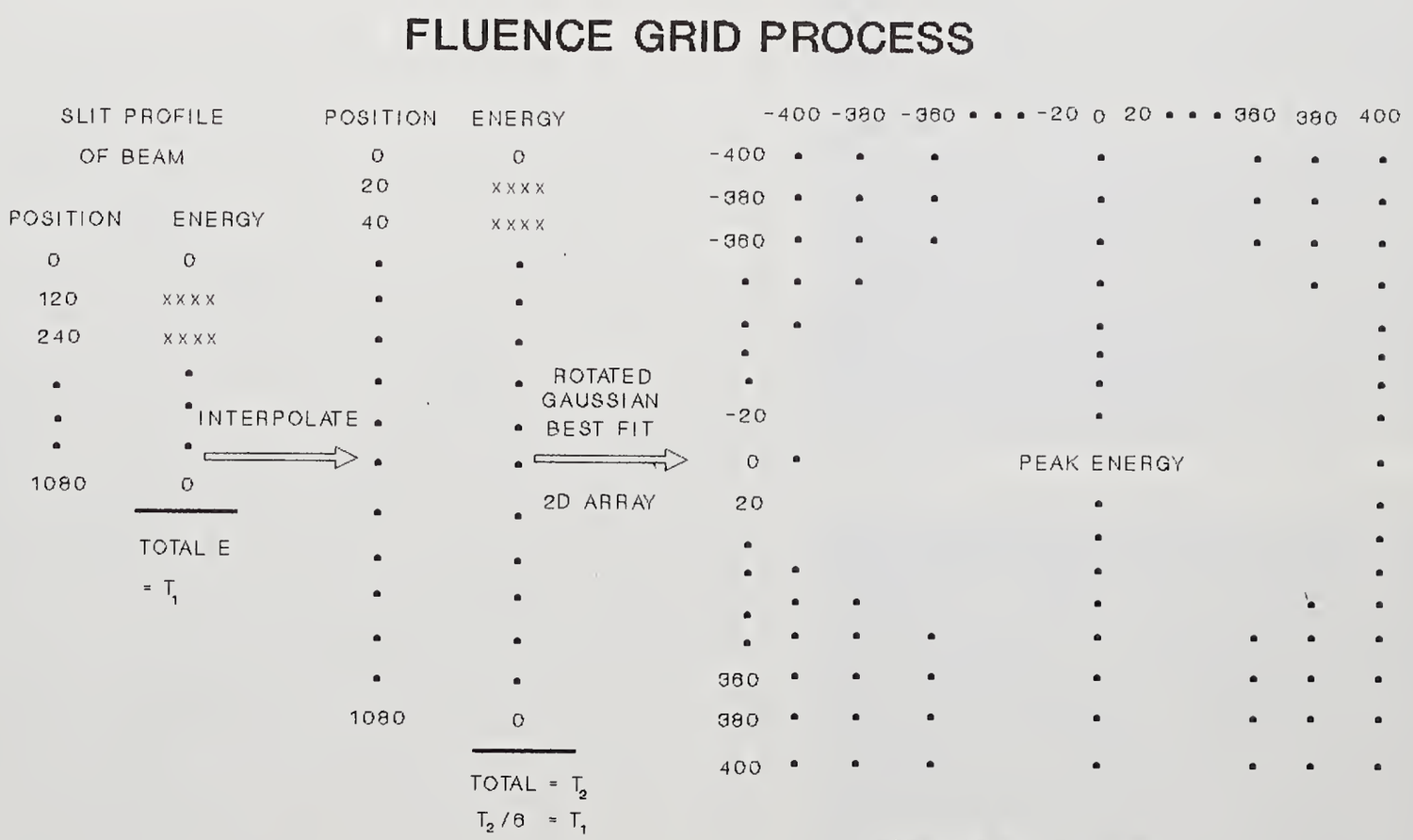

Figure 8. A schematic diagram of the Fluence Grid Process.

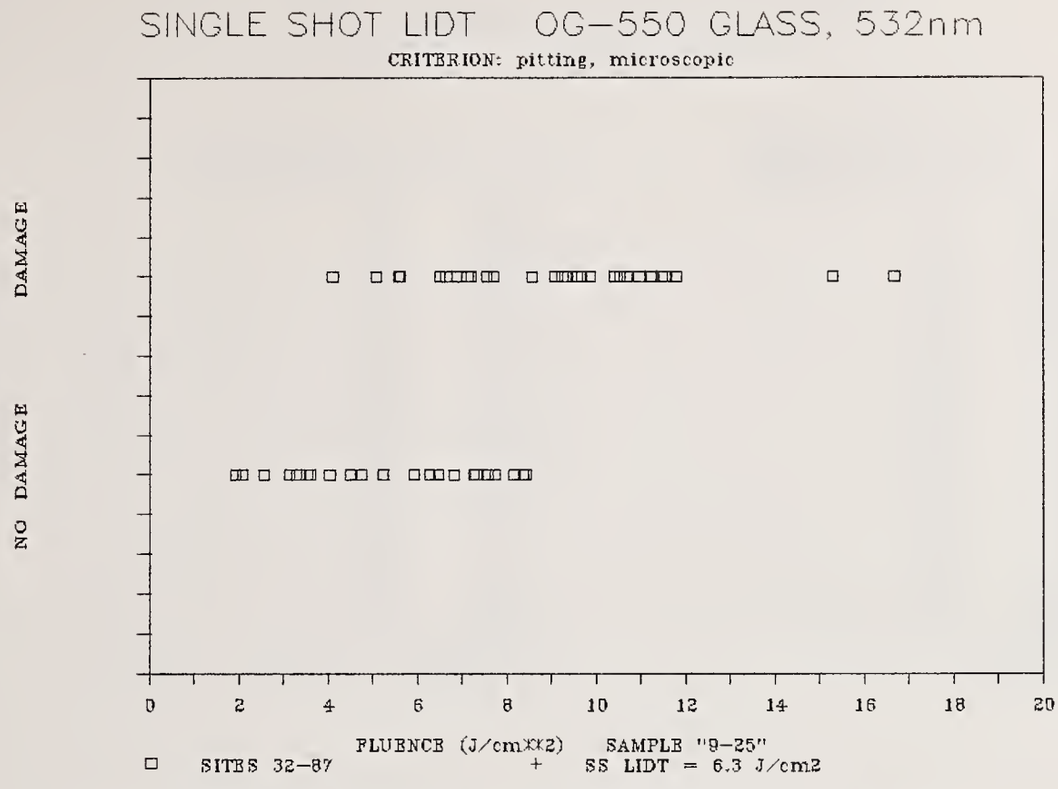

Figure 9. Single shot damage threshold results for data set A using the standard method. Threshold is 6.3 J/CM^2.

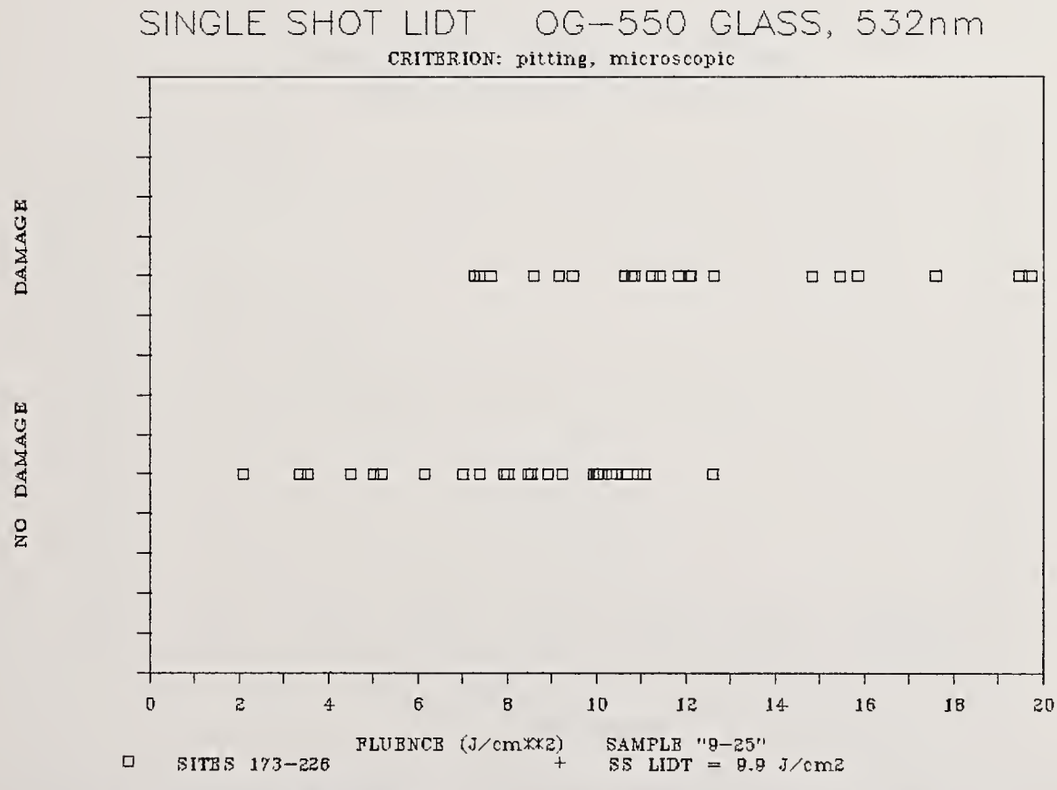

Figure 10. Single shot damage threshold results for data set B using the standard method. Threshold is 9.9 J/CM^2.

TABLE 2. PREDICTED SS LIDT

DATA SET A BEAM RADIUS=325 um

LIDT	DAMG. RAD.	# OF SHOTS
8.313	45	1
7.790	80	2
18.13	130	1
14.38	140	1
11.98	160	1
12.79	160	1
11.75	160	2
11.98	185	1
11.98	190	1
11.42	200	1
9.010	213	1
8.583	250	1
4.584	275	1
5.375	275	1
3.200	295	2
3.250	300	1
3.687	300	1
3.135	305	1
3.177	305	1
2.670	315	2
1.302	325	1
3.498	325	1
2.380	325	2

AVERAGE = 7.414 J/CM^2

AVERAGE OF SS DATA ALONE = 7.97 J/CM^2

DATA SET B BEAM RADIUS=295 um

LIDT	DAMG. RAD.	# OF SHOTS
18.04	90	1
13.21	175	1
8.540	210	1
8.690	215	2
8.790	225	1
8.040	235	1
5.170	240	1
8.580	240	1
5.980	245	1
4.125	250	1
4.790	250	1
3.420	260	1
3.670	260	1
3.170	260	2
3.530	264	1
3.750	270	1
3.830	270	2
8.125	275	1
4.080	280	1
3.398	285	1
3.730	285	1
2.750	290	2
2.500	300	2

AVERAGE = 5.840 J/CM^2

AVERAGE OF SS DATA ALONE = 8.18 J/CM^2

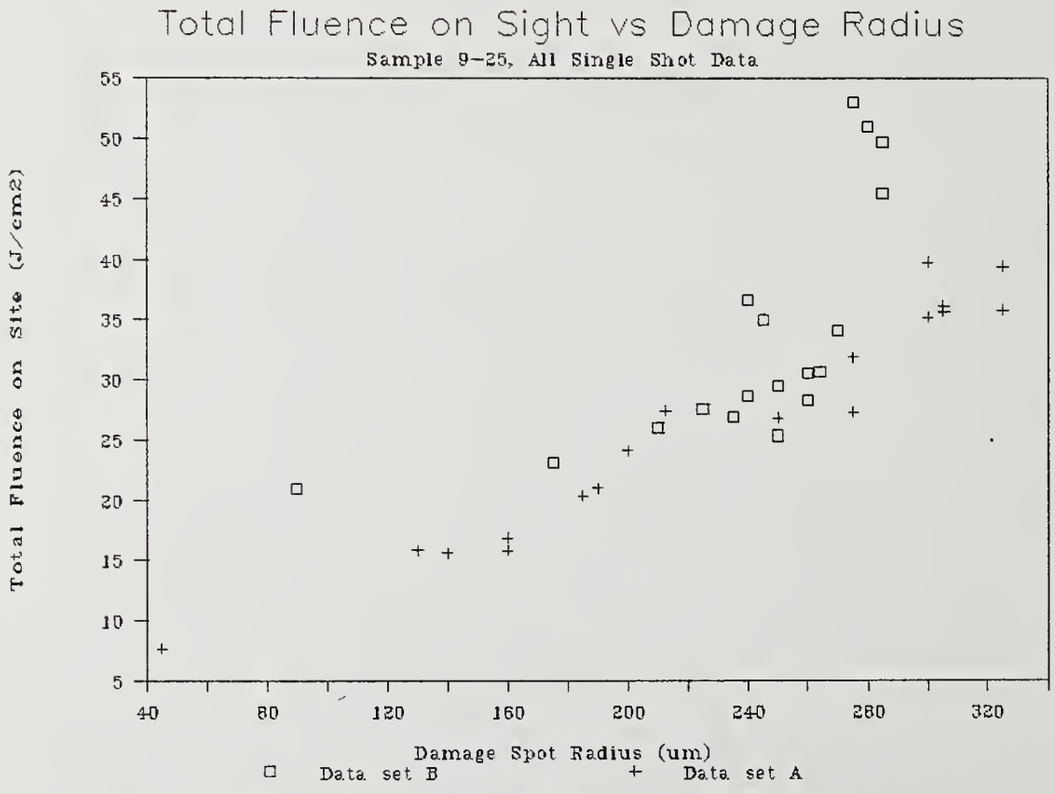

Figure 11. The total fluence (over the entire $1/e^2$ radius of the beam) on site versus the damage site radius.

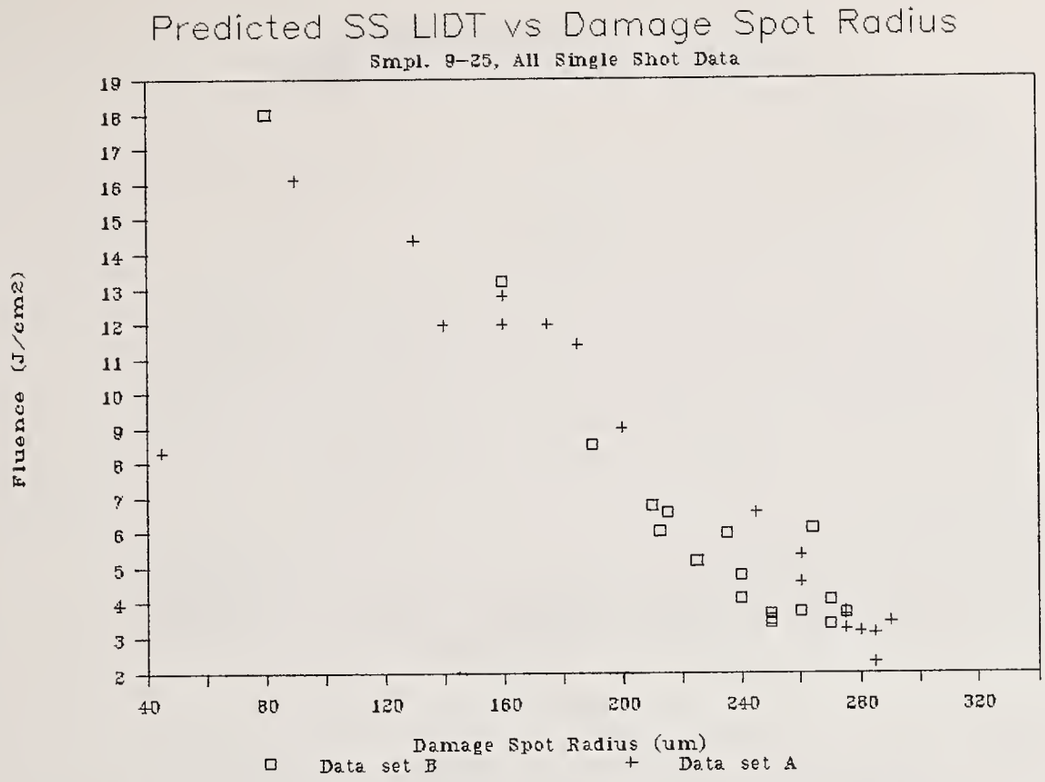

Figure 12. The predicted damage threshold versus the damage site radius using the Fluence Grid Process.

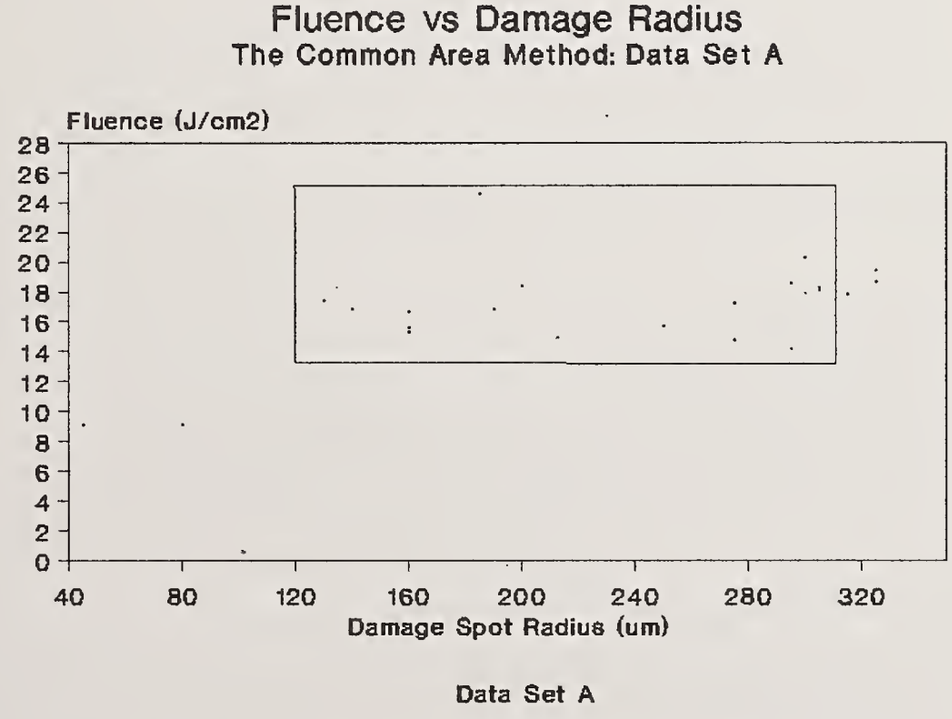

Figure 13. The predicted damage threshold versus damage site radius for data set A using the Common Area Method.

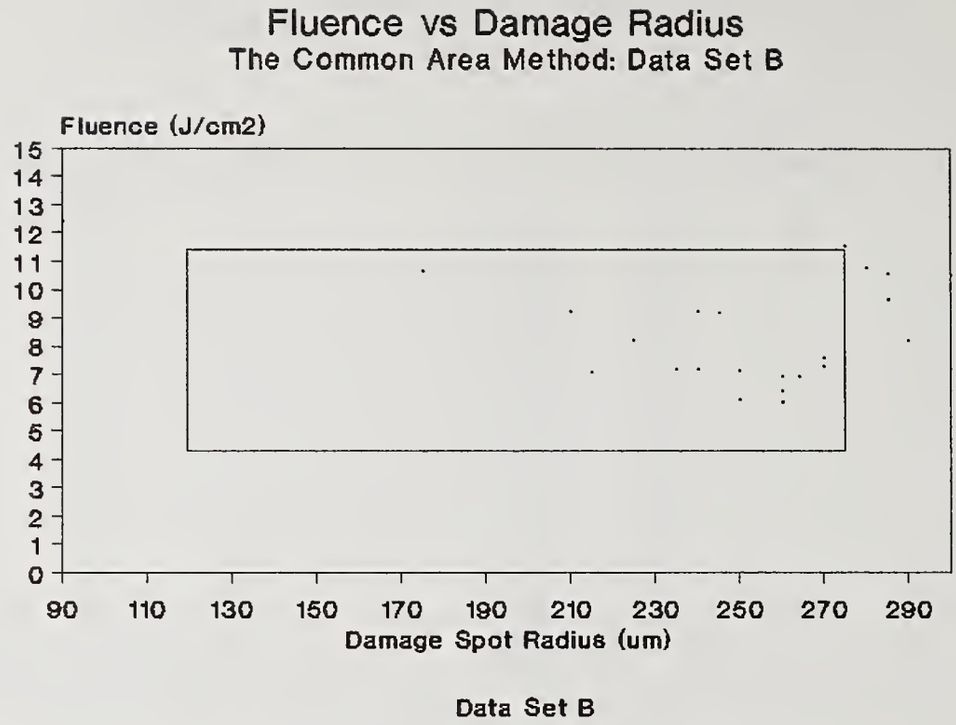

Figure 14. The predicted damage threshold versus damage site radius for data set B using the Common Area Method.

COMMENTS

Question: In about 1980, somewhere in that time frame, OCLI provided Livermore with silica titania reflectors that had thresholds in excess of 20 joules per square centimeter at 1 nanosecond. These parts should be in the archives somewhere, I suppose. Have any parts with that high a damage threshold initially been conditioned to see if you get even a higher threshold?

Answer: I don't believe our initial coatings were quite that high, but recently we have made good titania coatings and conditioned them. Our problem with titania is that over a period of a couple of years we get good and bad results from titania. It's not a very controllable material, at least not as controllable as the other dielectrics I've mentioned.

Question: There are applications where optics are sold and they go on the shelf for three or four years before they're put into systems in field rework. I wonder if you have any data or if you've looked at any data carefully enough to extrapolate your claim that this enhancement is permanent to longer time frames than I've heard mentioned so far? It has important economic consequences, if this is possible. Have you got data like that? Are you looking at that? Will you be mapping it over a period of years.

Answer: No. At this point, we've been following this conditioning in a low absorption stoichiometric films for maybe nine months, and we see it as an important thing. I believe there's a good chance that it is permanent for longer times, but the coatings have to be kept in a very controlled environment if they are going to be stored. I think they'd have to be kept clean, in a generic sense.

Question: Have you given any thought to comparing your laser annealing to just baking or thermal annealing, which is maybe not practical for the 1 meter optics, but a lot cheaper.

Answer: Yes. We've thought about it, and that is something that would be very revealing to do. We haven't done that experiment yet. We're also attempting other kinds of annealing. The laser annealing may be the most awkward way to do it. We've tried flash lamp annealing, for example, and you'll hear a little more about that, I think, from the next speaker. But we're certainly interested in other techniques. The laser annealing may not be the best way to do this at all.

Manuscript received
2-12-90

IR Laser Beam Profiling Using Quenched Fluorescence

N.C.Kerr, S.E.Clark and D.C.Emmony

Department of Physics
Loughborough University of Technology
Loughborough
Leicestershire
U.K.

The construction and performance of a system for the spatial characterization of a CO_2 pulsed laser beam is described. Using thermally quenched fluorescence a direct imaging technique has been developed for single shot CO_2 laser pulse beam profiling. A CCD video camera and framestore interfaced to a PC computer are used to image the spatial intensity distribution produced by a CO_2 pulse incident upon a temperature dependent luminescent screen. The resolution is similar to much more expensive pyroelectric detector array techniques with all the advantages of two dimensional beam processing.

Key words: beam profiling, CO_2 laser, pulsed.

1. Introduction

Laser beam profiling is a problem as old as the laser itself, with many methods of varying degrees of success having been reported. Methods such as photographic film, scanning pinhole and linear array techniques have been used. Whilst references can be found in the paper by Rose et al [1] it is worth while to note that all of these methods suffer from the long time scale required to perform the measurements. Using a CCD video camera, a 2-dimensional image of the laser beam profile can be obtained quickly with only a single laser pulse.

A fast, single shot, focal zone beam profiling system has previously been built for use with UV, visible and near infrared lasers at the Loughborough University laser damage facility by Clark et al [2]. These authors based their technique on a CCD video camera linked to a computer controlled video framestore. In cases where the laser wavelength is within the response band of the camera (40-1100nm) the beam is imaged directly, but at shorter wavelengths, fluorescent glasses which produce visible light if excited by UV light are used. To extend this technique to longer wavelengths e.g. 10.6 μm, a mechanism to linearly convert the IR to visible radiation must be found.

To enable near linear conversion of the IR to visible, thermal imaging plates, such as those marketed by Optical Engineering were used. These plates make use of what is known as thermal quenching of induced fluorescence. In this process, the plates are made to flouresce by illumination with a cw UV light. If the plates are heated, e.g. by a CO_2 pulse, the fluorescence decreases in proportion to the local temperature, i.e. the local fluence and hence in proportion to the beam intensity.

2. Experimental

Figure 1 shows a schematic layout of the beam profiling/interaction zone. The pulsed output of a Laser Applications TEA CO_2 laser operating at 10.6μm is focused in the plane X-X using a 15cm focal length CaF_2 lens. This plane is then imaged onto the luminescent screen using a second CaF_2 lens. The two lens combination is used both to provide a suitable magnification of the profile for imaging and to arrive at a suitable energy density for the luminescent screen.

The luminescent screen [3] has a normal sensitive range of 0.4-2.4 W/cm^2, a damage threshold of 24 W/cm^2 (under cw illumination) and a resolution of 4 lines/mm. By magnifying the image incident upon the screen (using the second CaF_2 lens), the resolution in the luminescent image is effectively increased by a factor equal to the magnification. A fourfold magnification was used to give the system a resolution of about 16 lines/mm in the damage zone, which is a figure comparable to that stated for much more sophisticated and expensive CO_2 beam profiling systems using arrays of pyroelectric detectors. The degree of quenching, i.e. darkening of the screen is linearly dependent upon the incident CO_2 intensity to within 10% over the stated ranges.

To be sure which plane through the focus of the first lens was being imaged, a graticule was placed at X-X and illuminated using a HeNe laser and the image focused on the luminescent screen. As well determining which plane is in focus, this process enables the physical extent of the image as seen on the video monitor to be calibrated.

The CCD camera imaged the luminescent screen using a 50mm camera lens at as near normal incidence as possible to reduce depth-of-field problems. The signal from the camera was sent to an Eltime Image III framestore where it was digitised and stored. The resulting video images which are made up of 256x256 pixels each having 6 bit (64 greylevel) resolution, can be displayed on a video monitor and/or processed using a PC computer. Ideally, to specify the beam profile to an accuracy of say 5%, at least 160 grey levels are required. Such 8 bit frame grabbers are available but we were constrained by the Eltime, which was the only frame grabber available to us.

The luminescent screen is flood-illuminated using a 125W UV lamp that covers the peak excitation wavelength (360 nm) of the screen. The fluorescence which is in the yellow/green region of the spectrum is easily detected by the CCD camera, however the decrease in brightness caused by the heating due to the CO_2 laser pulse corresponded to a change of at best 4 greylevels compared to the constant background signal. Such a small change does not produce enough dynamic range to perform beam profiling measurements such as determining the $1/e^2$ points.

Simple amplification of the video signal is not satisfactory as it would also amplify the background. It was therefore necessary to build a circuit which selectively amplified the signal of interest, the block diagram of which is illustrated in figure 2. The dc component in the video signal associated with the background illumination is removed from the signal due to the quenching of the fluorescence by firstly amplifying the whole signal. The output of this amplifier stage is then passed to the base of a fast transistor. Only signals above the 0.7v turn on level of the transistor are passed to its output. By careful adjustment of the amplifier gain and dc offset it is ensured that only the component of the signal corresponding to the quenched fluorescence is above this level. The amplification is variable upto x10 and has the effect of increasing the contrast of the resultant video image. This circuit also accommodated the laser and framestore trigger and synchronised the capture of a video image to the start of a video field from the CCD camera.

Using the computer and suitable processing routines it is possible to rapidly process images in the framestore. Subtraction of images can be used to remove fixed pattern noise in the video image, this is due to dark current non-uniformities in the sensitive element of the camera. Further, it is possible to average the signals for any number of frames, which reduces the random electronic noise introduced by the selective amplifier circuit.

Laser beam profiling can simply involve the recording of a single frame of the quenched fluorescence and subsequent computer processing. However because of the speed of operation of the system as a whole, the routine method adopted is to average the video signal over 16 laser pulses. Figure 3 shows a typical processed video image after it has been intensity inverted during the processing. This inversion allows the image to be processed directly by profiling routines previously written for use with UV beam images, as well as giving a more acceptable picture of the laser beam.

Figure 4 shows the intensity along the cursor drawn horizontally in the previous figure. For comparison,the intensity profile obtained in an identical image plane using a scanning pinhole in conjunction with an integrating pyroelectric detector is also shown. The two profiles are normalised to the same peak intensity. Excellent agreement is clearly evident between the two sets of data. It should be noted that figure 3 contains all of the 2-dimensional information necessary to obtain any desired horizontal or vertical profile across the CO_2 pulse. The time taken to obtain this data, including image processing time, was less than 5 minutes. To obtain a similar resolution and number of profiles using a scanning pinhole would take in excess of 6 hours and several thousands of laser pulses. The Laser Applications laser has particularly good shot to shot reproducibility otherwise the scanning pinhole technique would not even be applicable .

3. Conclusion

Using thermally quenched fluorescence, a direct imaging technique has been developed for single shot CO_2 laser pulse beam profiling. The resolution is similar to much more expensive pyroelectric detector array techniques with all the advantages of two dimensional beam processing.

Acknowledgements

The authors would like to acknowledge the technical assistance given by Mr M. Pancholi and Mr R. Pancholi of the Physics Department Electronics Workshop and Angela Anne Kerr in the preparation of this manuscript. NCK would especially like to acknowledge the financial support of BDH Ltd and SERC.

4. References

[1] Rose A., Nie Y.-X. and Gupta R. Laser Beam Profiling Measurement by Photothermal Deflection Technique. Appl. Opt., 25 1738-1741 (1986)

[2] Clark S.E. Excimer Laser Induced Modifications of Optical Surfaces, Ph.D. Thesis, Loughborough University, 1988.

[3] Optical Engineering Inc., Santa Rosa, CA 95401, U.S.A., model 23-7 CO_2 beam probe.

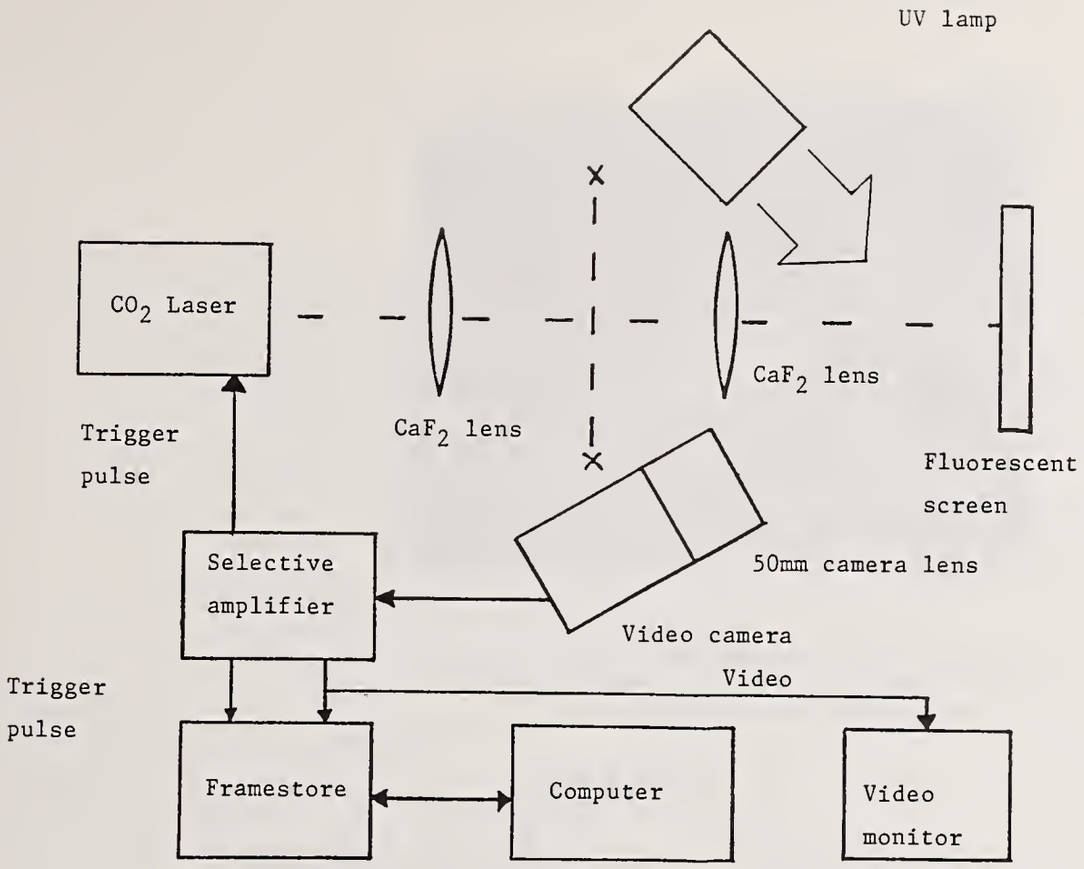

Figure 1. Experimental arrangement of apparatus.

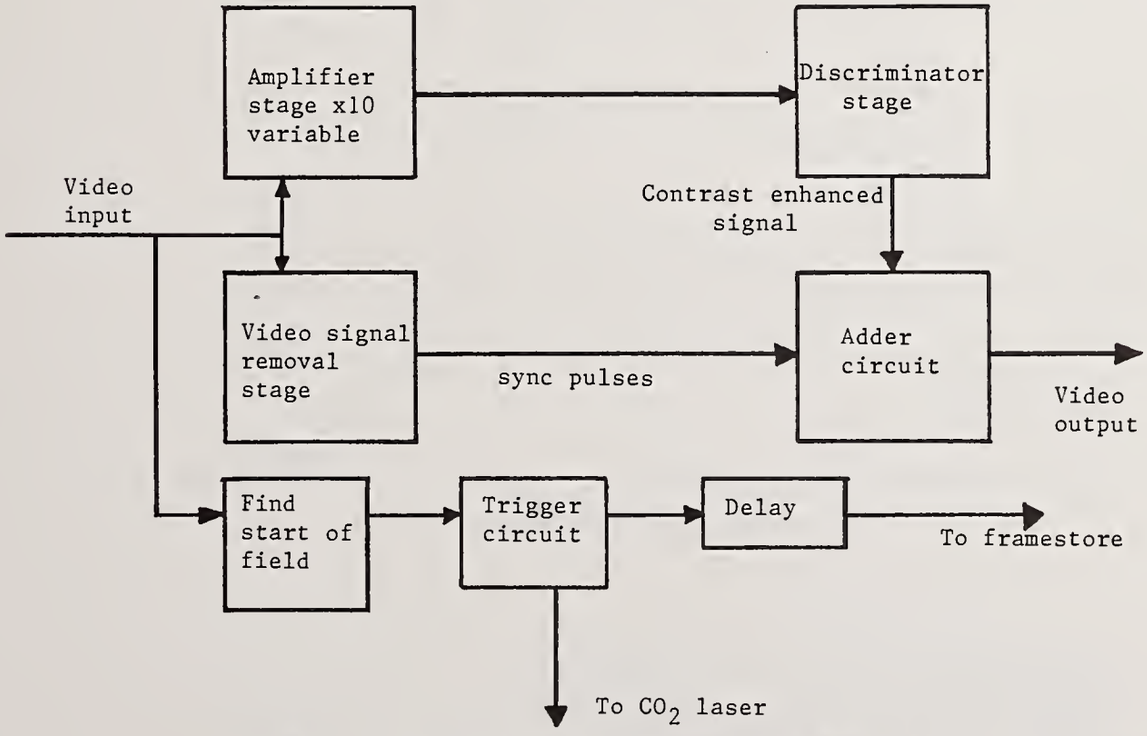

Figure 2. Block diagram of the selective amplifier and trigger circuits.

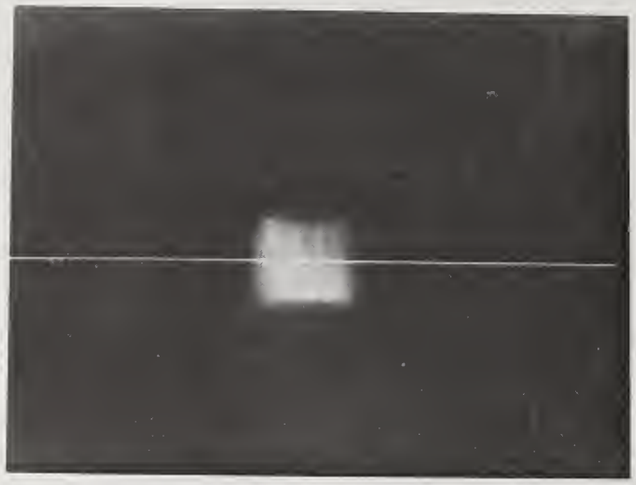

Figure 3. Intensity inverted video picture of CO_2 laser quenched fluorescence. The rectangular focal zone is approximately 5mm X 5mm.

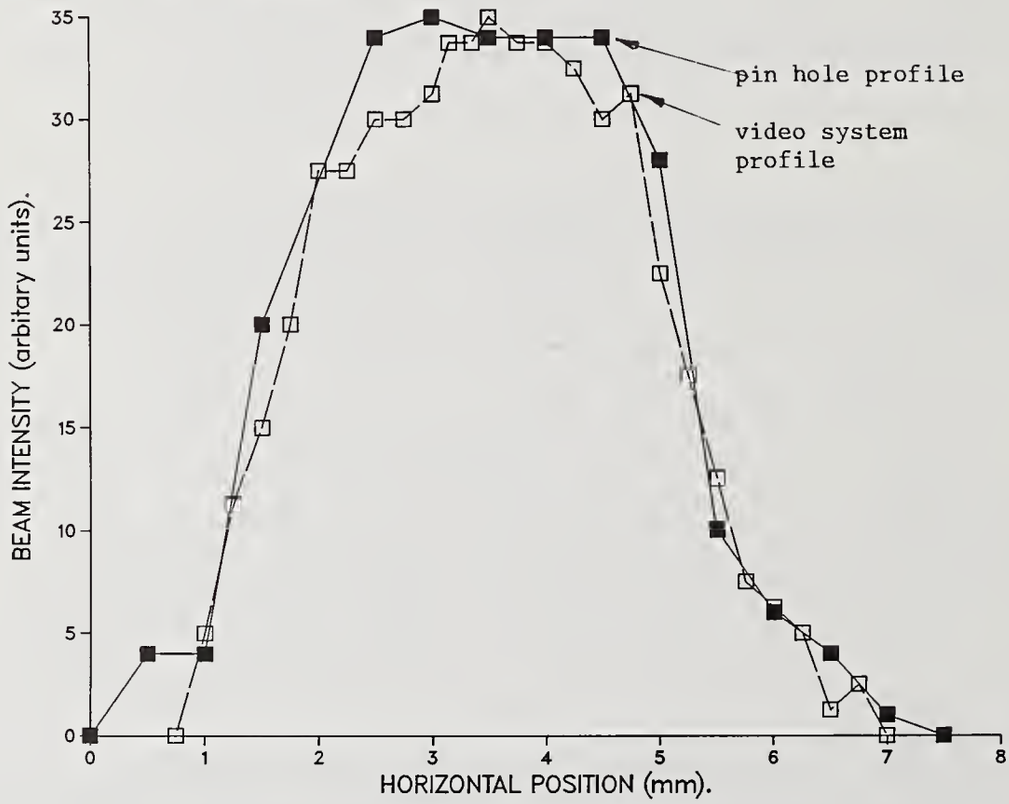

Figure 4. Intensity profile across the focal zone corresponding to the curser in figure 3. For comparison a scan using a pinhole was made along the same line. The pinhole scan points are each the average of 5 laser pulses.

COMMENTS

Comment: Annealing glass certainly can remove color center damage; however, some studies we've done previously have shown that residual structural damage still persists in the glass. For example, in the case of heavily irradiated yttrium phosphate glasses, we have done some vibrational spectroscopy and have shown that, even after annealing, changes in the chemical bond angle between the atoms assumes a wider distribution then in the undamaged glass. I suspect the same may be occurring in your fluoride glass. We are not talking about the mechanism, but it could be also due to impurities. Remember this is a fluoride glass and it's a biconic glass and the fluorine is immobile, so that we can have color centered fluorine. One of the things that we would like to do is to take the samples and <u>reradiate</u> them again and measure and see if there is permanent damage that happens to them. We are interested in looking at mechanisms.

Questions: What was the energy of your gamma?

Answer: One megahertz in cobalt 60.

Question: Do you think that the energy of the gammas has the effect of just producing electron hole pairs or is it doing knock on type of damage in your material?

Answer: I am not sure. We did not take extra precautions to minimize the impurities like earth and iron in these glasses, so we are not sure about the source of color centers.

Question: Can you give us some idea about the optical quality of your glass? I notice that you are not stirring your melt or are you liable to have striae inhomogeneities, seeds and other things?

Answer: We supplied large samples of these for laser testing and we did take an extra precaution for stones and things. This fluoride glass is very fluid. In this experiment we cast them but in general we don't cast them, we leave them in the crystal to be annealed inside the crystal. Stones are not common in fluoride glasses.

Manuscript received
3-6-90

Laser-Induced Failure in Biased Silicon Avalanche Photodiodes

Steve E. Watkins*, Chen-Zhi Zhang, Rodger M. Walser, and
Michael F. Becker

Center for Materials Science and Engineering and
Department of Electrical and Computer Engineering
The University of Texas at Austin
Austin, Texas 78712

The characteristics of laser-induced electrical failure in biased silicon avalanche photodiodes have been observed. The samples were RCA reach-through avalanche photodiodes with antireflection coatings. They were biased at typical operating voltages during irradiation. The laser source was a Q-switched 1064 nm Nd:YAG pulsed laser operating at 10 Hz with a 10 ns pulse length and with a 300 μm spot radius.

The current-voltage characteristics were monitored for permanent change as a function of laser fluence and the degradation thresholds were found. Two types of change were observed. The first type was a large increase in bulk leakage current. It may be modeled by the introduction of defects into the depletion region by deep melting transients. The second type was catastrophic failure in which the devices were electrically shorted after irradiation. It may be modeled by excessive current density in the photodiode junction. The type of failure was determined by the parameters of the biasing circuit.

Key words: avalanche photodiodes; electrical degradation; laser damage; and silicon photodiodes.

1. Introduction

Laser damage to photodetectors is an important concern. Photodetectors are particularly susceptible to damage as compared to other optical system elements since they are highly absorbing at their operating wavelengths and are often subjected to focused irradiation. Laser-induced phase changes have been modeled thermally for PbS, PbSe, and HgCdTe infrared detectors [1, 2]. Laser damage in silicon solar cells has caused electrical degradation without the observation of a surface phase transformation [3]. Laser-induced changes in current characteristics, breakdown voltage, light spot profiles, and noise characteristics have been observed in silicon photo-transistors, p+ n photodiodes, and avalanche photodiodes [4, 5, 6]. Fluence thresholds for microscopic damage and loss of responsivity as a function of irradiation pulse length have been reported [7]. In our previous work, laser-induced electrical degradation of silicon high performance PIN and avalanche photodiodes was characterized for nanosecond optical pulses [8, 9, 10].

* The author's address is currently the Department of Electrical Engineering, University of Missouri- Rolla, Rolla, Missouri 65401.

In this paper, we examine the electrical degradation mechanisms in silicon avalanche photodiodes for irradiation by nanosecond pulses. The photodiodes were irradiated while under typical bias voltages by a near band gap, laser source in order to approximate typical operating conditions. Two types of electrical failure were observed. The first type was a large increase in bulk leakage current. The second type was catastrophic failure in which the detectors were electrically shorted after irradiation. Models which include the effects of biasing are proposed for the degradation.

2. Experimental Procedures

The experimental configuration for irradiating the samples is shown in figure 1. The laser source was a 1064 nm, stable resonator Q-switched Nd:YAG laser operating at a repetition rate of 10 Hz and with a pulse length of 10 ns (FWHM). The incident energy on the samples was controlled by an attenuator consisting of a rotating half-wave plate followed by a fixed, thin-film polarizer and monitored by a reference energy meter. The standard deviation of the pulse-to-pulse energies was two percent or less.

The spatial profile of the Gaussian beam was measured by the scanning slit method and the FWHM was determined. The $1/e^2$ beam-spot radius w_o was obtained using the equation $2w_o = \text{FWHM}\ (\ln 2/2)^{1/2}$. A 76 cm focusing lens was used to achieve spot radii on the samples of about 300 μm. The peak-on-axis irradiation fluences were calculated using $F = 2E/\pi w_o^2$, where E is the pulse energy. The reference energy meter was calibrated and the spot size was determined during each test session.

In the damage testing process, the samples were positioned using a HeNe alignment laser and a 20X alignment microscope. The computer recorded the energy of each incident pulse, controlled the shutter which blocked the beam after the desired number of pulses, and calculated the peak-on-axis fluence. Detailed morphological examinations and micro-photography were done subsequently with a 50-500X optical Nomarski microscope. Morphological damage was defined as any visual change in the surface as observed under the Nomarski microscope. Reverse saturation current and breakdown voltage were the electrical parameters monitored for permanent change. A Keithley Model 617 Electrometer, a Tektronix Model 577 Curve Tracer, a Fluke Model 77 Multimeter, and a custom current measurement circuit were used to make the measurements.

During irradiation, the avalanche photodiodes were biased at a typical operating point of about fifty volts below the breakdown voltage. This bias voltage gives a multiplication gain of about one hundred. The biasing circuits are shown in figure 2. For both circuits, the photodiode is in series with a 50 Ω load resistance. Circuit # 1 has a 0.01 μF capacitor in parallel with the photodiode and load resistance series combination; circuit # 2 has a 1010 pF capacitance in parallel with the photodiode and load. Also, stray inductance was minimized in circuit # 2 by using stripline construction and low inductance components.

The test samples were supplied by RCA and were silicon avalanche photodiodes of type C30817. The device cross section is shown in figure 3. The detectors had the standard antireflection coating for 1.06 μm. Their active area was 0.5 mm^2.

3. Electrical Degradation and Morphological Damage

The avalanche photodiodes were irradiated over a range of laser fluences at single and multiple pulses per device while under typical bias voltage. The reverse-biased current-voltage characteristics were measured before and after irradiation. One set of detectors used circuit # 1 in figure 2 and was biased at 336 V which is approximately 50 V below the breakdown voltage. The second set of detectors was biased using circuit # 2 in figure 2. The bias voltage was set individually to be 50 V below the breakdown voltages for each photodiode.

The irradiation fluences and leakage currents for the sample set using bias circuit # 1 are shown in table 1. Devices A, B, C, and D were irradiated with a single pulse per device, i.e. 1-on-1 tests, at 2.1 J/cm^2, 5.7 J/cm^2, 6.5 J/cm^2, and 9.7 J/cm^2, respectively. The current-voltage characteristics are shown in figure 4. The predamage characteristic, as shown by the initial curve, has an almost constant leakage current at bias voltages below the breakdown voltage. The current characteristics were not significantly changed for devices A and B, but were greatly changed for devices C and D. The leakage current at the operating voltage increased by almost three orders of magnitude for device C and by more than five orders of magnitude for device D (table 1). The threshold for electrical change is then between 5.7 J/cm^2 and 6.5 J/cm^2. Electrical degradation of identical avalanche photodiodes which were unbiased during irradiation occurred at similar fluences, i.e. greater than 6.5 J/cm^2, but the

change in the leakage current was much less severe [8, 9]. The characteristic for unbiased photodiodes irradiated between 6.5 J/cm^2 and 9.5 J/cm^2 is also included in figure 4.

The damage morphologies of devices A, B, C, and D are shown in the micrographs of figure 5. At these fluences, the antireflection coating has been shattered in the irradiated area. The damage spots show melting and boiling surface morphologies which are identical to those obtained for unbiased photodiodes. Note that the surface may have severe physical damage (see fig. 5.a. and b.) without any associated change in the current characteristic.

Table 1. Electrical Degradation Test Results for Bias Circuit # 1

Device Designation	1-on-1 Irradiation Fluence	Leakage Current at 336 V Predamage	Postdamage
A	2.1 J/cm^2	77 nA	77 nA
B	5.7 J/cm^2	77 nA	80 nA
C	6.5 J/cm^2	77 nA	5.5 μA
D	9.7 J/cm^2	72 nA	>20 nA

The fluence thresholds and damage characteristics for the sample set using bias circuit # 2 are shown in table 2. This set contained twenty photodiodes which were subjected to tests of one pulse per device and thirty thousand pulses per device. All devices irradiated below 0.4 J/cm^2 were not morphologically damaged or electrically degraded. All detectors irradiated above 0.5 J/cm^2 were electrically shorted, i.e. the reverse-biased photodiodes passed a current on the order of milliamperes with a very small voltage drop. Some of the photodiodes, but not all, irradiated between 0.4 J/cm^2 and 0.5 J/cm^2 were degraded. All photodiodes were either electrically unchanged or shorted. For the single-pulse tests, no morphological damage was observed in the irradiated area below 1.0 J/cm^2. However, a melting morphology occurred at the edge of the active area for every shorted detector and only for shorted detectors. This morphology is shown in figure 6.a. At higher fluences, the damage morphologies also included the typical melting and boiling spot, a separation of the antireflection coating from the surface in a dentritical pattern, and a melt channel (see fig. 6.b.). For the tests of thirty thousand pulses per device, pitting was observed without any electrical degradation below 0.4 J/cm^2. Edge melting morphologies, the typical center melt spot, and a melt channel were observed above this degradation threshold as shown in figure 6.c.

Table 2. Electrical Degradation Test Results for Bias Circuit # 2

N-on-1 Test	Fluence Threshold	Damage Characteristics
1-on-1	~ 0.4 J/cm^2	Electrical Short Junction Spike Edge Melt Morphology
30,000-on-1	~ 0.4 J/cm^2	Electrical Short Junction Spike Edge and Surface Morphology

Several of the avalanche photodiodes in both sample sets were disassembled, etched to remove the contact metalizations, and polished to give cross sections. No unusual morphologies were observed on the devices for which degradation consisted of an increase in leakage current. However, every diode which failed catastrophically had a deep hole on the back, or junction side (see fig. 6.d.). The cross section of such a photodiode is depicted in figure 7. The hole was three to five microns in depth and was filled with metal before the etch. This junction spike was presumably the reason the devices were shorted. Typically, it was directly beneath the melting morphology at the edge of the front metalization. Although for the higher fluences as in figure 6.b., it was below the center boiling spot.

4. Discussion

The degradation of electrical performance in avalanche photodiodes was clearly a function of biasing voltage and biasing circuit parameters. The degradation was more severe for detectors which were biased during irradiation than for unbiased detectors. All photodiodes in which electrical change was observed were rendered useless by the degree of the degradation. The type of electrical change was dependent upon the circuit parameters. The devices suffered either degraded current characteristics or catastrophic failure.

The former type of degradation was an increase in the leakage current at high bias voltages. The data suggests that this increase can be attributed to the introduction of deep level defects in the depletion region of the photodiodes. Rapid regrowth of the crystal during deep melting transients leaves defects in this electrically sensitive region and thereby increases the bulk leakage current. Morphological change is initially confined to the thin electrically-inactive surface layer by nonlinear limiting.

The fluence threshold for current degradation and the damage behavior of the biased detectors were roughly equivalent to those of unbiased detectors. The proposed model was originally developed for unbiased photodiodes [8]. The much lower morphological damage threshold and the extensive surface melting at the degradation threshold indicate that deep laser-induced melting is required to cause this type of change in the electrical performance. The degraded current characteristics (see figure 4) are indicative of an increase in bulk leakage current due to defects in the p- depletion region of figure 3. [9, 10]. At bias voltages below about 170 V, the p-region is not depleted near the surface and defects located there will not contribute to the leakage current [11]. Hence, the current characteristics are unchanged at low bias voltages and degraded at high bias voltages. The behavior of the biased photodiodes only differed from that of the unbiased photodiodes in the much larger current increase induced at a given fluence above threshold. The responsible mechanism is not clear.

The other type of degradation was catastrophic failure in which the photodiodes were electrically shorted after irradiation. This type of failure was not observed for unbiased avalanche photodiodes or for PIN photodiodes [9]. It only occurred for biased avalanche photodiodes using circuit # 2. This failure may be modeled by excessive current densities in the photodiode junction. Crystal defects and nonuniformities in the diode structure can lead to localized concentrations of current, i.e. current filaments. For a large laser-induced current transient, excessive current density may result and cause localized heating. The local temperature may enter the intrinsic range of the doped silicon in which the carrier concentration depends on the temperature and not the doping density. Then, additional carriers are generated by the temperature increase and the current density is increased further. The higher current density gives more local heating which generates more carriers. Positive thermal feedback is thereby established and the devices eventually fails [12]. This proposed mechanism is similar to the failure mechanisms for transistors under some conditions and for avalanche photodiodes which are biased above their breakdown voltage [12, 13, 14].

The metal spike from the back contact metalization was apparently the immediate cause of failure. The spike probably formed when local heating of a current filament melted the silicon and the adjacent contact metalization. The junction was thereby shorted. The melt morphology at the edge of the front contact metalization was probably caused by the large steady-state current occurring after the device shorted. The separation of the antireflection coating and the melt channel only occurred for high fluences. It is unclear whether these morphologies are directly related to the failure mechanism or are incidental effects. The junction spike was always located opposite the edge of the front surface metalization for fluences near the threshold. The physical origin of this behavior is unclear. At high fluences, the spike was beneath the irradiated area and may have been photo-initiated.

Only biasing circuit # 2, which had the fastest rise time due to its stripline design and low-inductance components, allowed catastrophic failure. Because of its slower response, circuit # 1 presumably prevented the peak of the current transient from reaching the excessive levels necessary for catastrophic failure.

5. Summary

The electrical degradation of biased avalanche photodiodes is more severe than for unbiased photodiodes. The biased devices may fail from laser-induced degradation of bulk leakage current characteristics or from laser-induced shorting of the device, i.e. catastrophic failure. The type of failure appears to be determined by the rise time of the biasing circuit. The fluence threshold for degraded current-characteristics was about 6 J/cm^2 which is approximately equal to the threshold for similar degraded current characteristics in unbiased detectors. This current increase may be modeled by the introduction of defects in the depletion region during melting transients. The fluence for catastrophic failure was about 0.4 J/cm^2 which is slightly less than the threshold for single-pulse surface morphological damage of 1.0 J/cm^2. This failure may be modeled by excessive current density transients which induce junction spikes.

6. References

[1] M. Kruer, L. Esterowitz, F. Bartoli, and R. Allen, "Thermal Analysis of Laser Damage in Thin-Film Photoconductors," J. Appl. Phys. 47, 2867 (1976).

[2] F. Bartoli, L. Esterowitz, R. Allen, and M. Kruer, "A Generalized Thermal Model for Laser Damage in Infrared Detectors," J. Appl. Phys. 47, 2875 (1976).

[3] Y. Matsuoka and A. Usami, "Normal Laser Damage of Silicon Solar Cells without Phase Change," Appl. Phys. Lett. 25, 574 (1974).

[4] J.F. Giuliani and C.L. Marquardt, "Electrical Effects in Laser-Damaged Phototransistors," J. Appl. Phys. 45, 4993 (1974).

[5] D.L. Parker, F. Lin, S. Zhu, D. Zhang, and W.A. Porter, "Selective Lifetime Doping in Silicon by Laser Scanning," IEEE Trans. Electron Devices 29, 1718 (1982).

[6] M.A. Acharekar, "Laser Damage in Silicon Avalanche Photodiode," Laser Induced Damage in Optical Materials: 1987, Nat. Inst. of Standards and Technology (US) Spec. Publ. 756, 50, (1988).

[7] M. Kruer, R. Allen, L. Esterowitz, and F. Bartoli, "Laser Damage in Silicon Photodiodes," Optical and Quantum Electronics 8, 453 (1976).

[8] S.E. Watkins, C. Zhang, R.M. Walser, and M.F. Becker, "Laser-Induced Electrical Parameter Degradation in Silicon Photodiodes," 20th Symposium on Optical Materials for High Power Lasers, Boulder, Colorado, 25-28 October 1988 (Proceedings to be published by NIST).

[9] S.E. Watkins, C. Zhang, R.M. Walser, and M.F. Becker, "Electrical Performance of Laser Damaged Silicon Photodiodes," Appl. Opt. 29(6), 827 (1990).

[10] S.E. Watkins, "Electrical Parameter Degradation of Silicon Photodiodes Induced by Nanosecond 1.06 μm Laser Pulses," Ph.D. Dissertation, The University of Texas at Austin, 1989.

[11] P.P. Webb, R.J. McIntyre, and J. Conradi, "Properties of Avalanche Photodiodes," RCA Review 35, 234 (1974).

[12] A. Blicher, Field-Effect and Bipolar Power Transistor Physics, Academic Press, New York, 186-193 (1981).

[13] R.A. Sunshine and M.A. Lampert, "Second-Breakdown Phenomena in Avalanching Silicon-on-Sapphire Diodes," IEEE Trans. Electron. Devices ED-19 (7), 873 (1972).

[14] M.W. Muller, "Current Filaments in Avalanching PIN Diodes," Appl. Phys. Lett. 12 (6), 218 (1968).

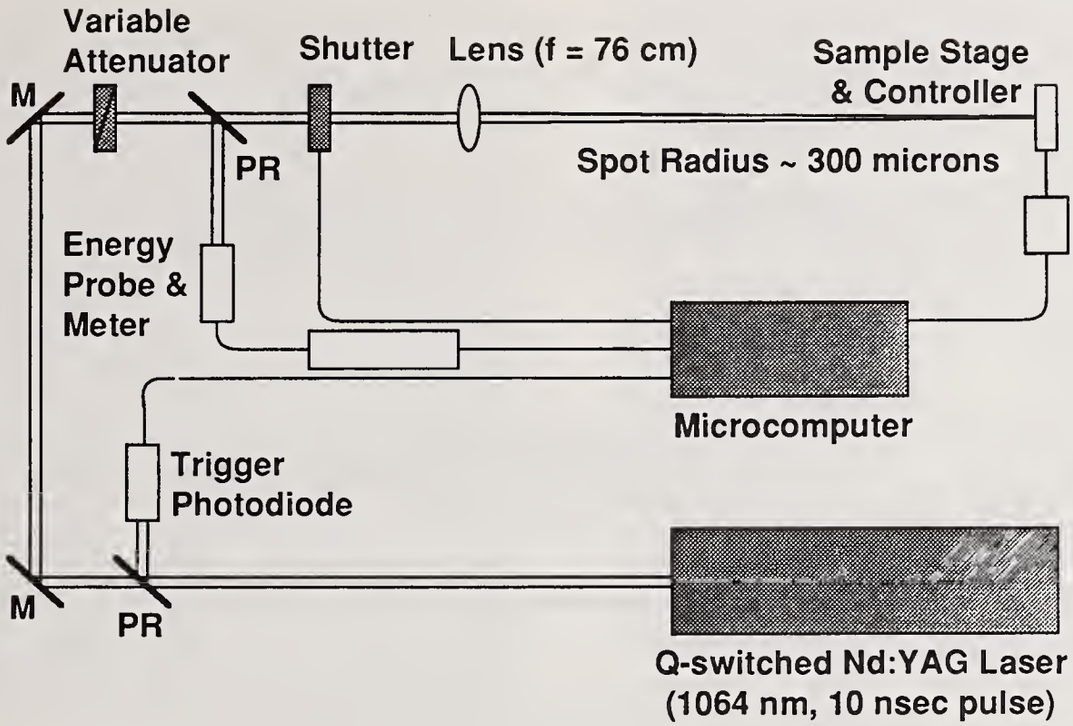

Figure 1. The experimental configuration for irradiating the photodiodes. During the tests, the devices were biased. M and PR indicate mirrors and partial reflectors, respectively.

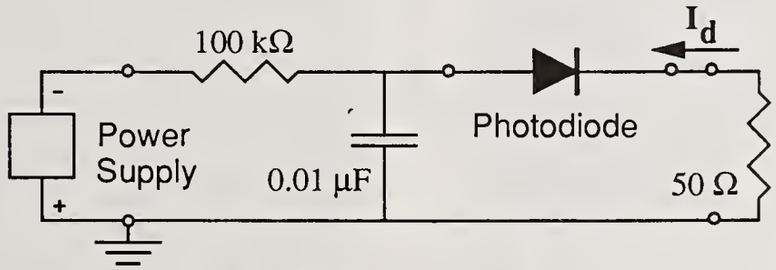

a. Biasing Circuit # 1

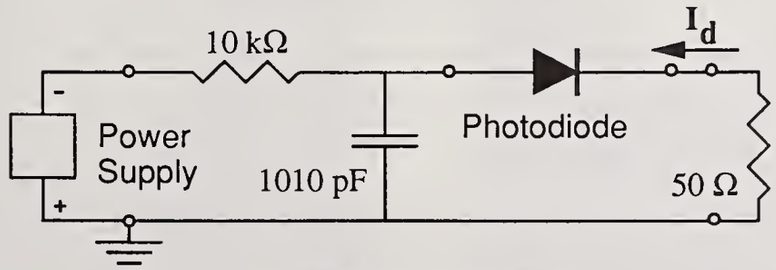

b. Biasing Circuit # 2

Figure 2. Biasing circuit # 1 (diagram a.) and biasing circuit # 2 (diagram b.) for the avalanche photodiodes. Biasing circuit # 2 was of stripline design.

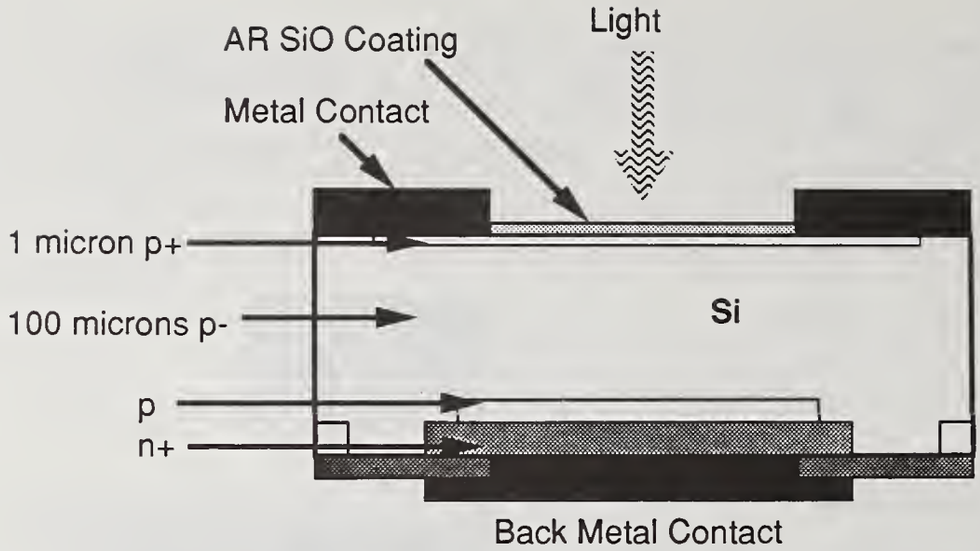

Figure 3. Cross section of the RCA avalanche photodiode type C30817 with reach-through structure. The devices had antireflection coatings.

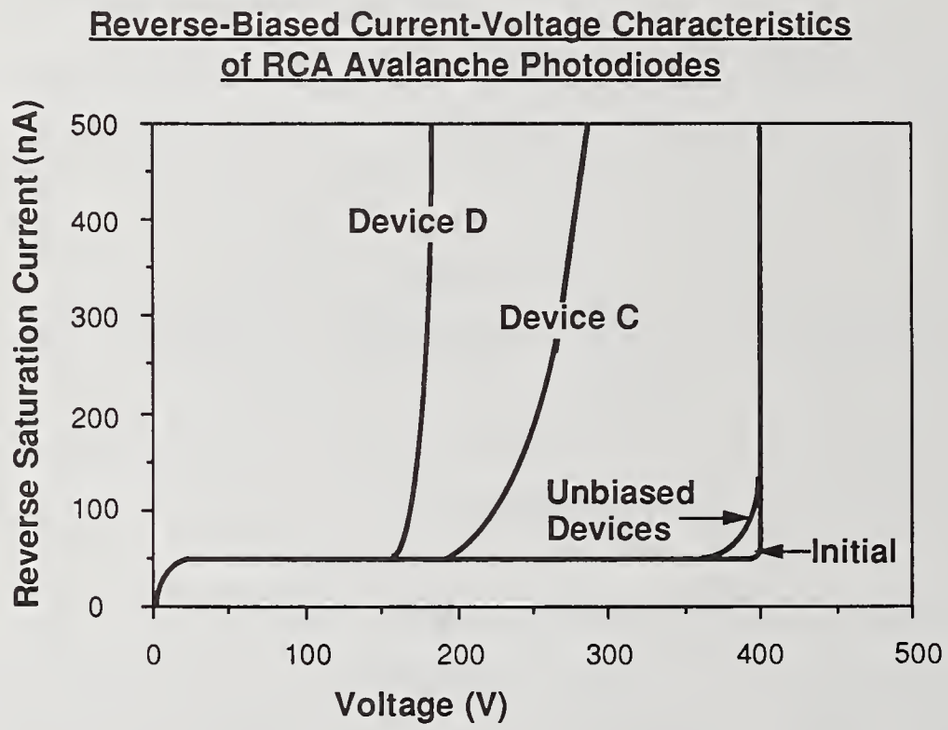

Figure 4. Reverse-biased current-voltage characteristics of irradiated photodiodes. The initial curve is the characteristic before irradiation and degradation. Devices A, B, C, and D were irradiated while biased using circuit #1. The characteristics of devices A and B were unchanged, i.e. the initial curve. The postdamage characteristics of devices C and D are shown. The typical postdamage characteristic of unbiased devices irradiated between 6.5 and 9.5 J/cm2 is also shown.

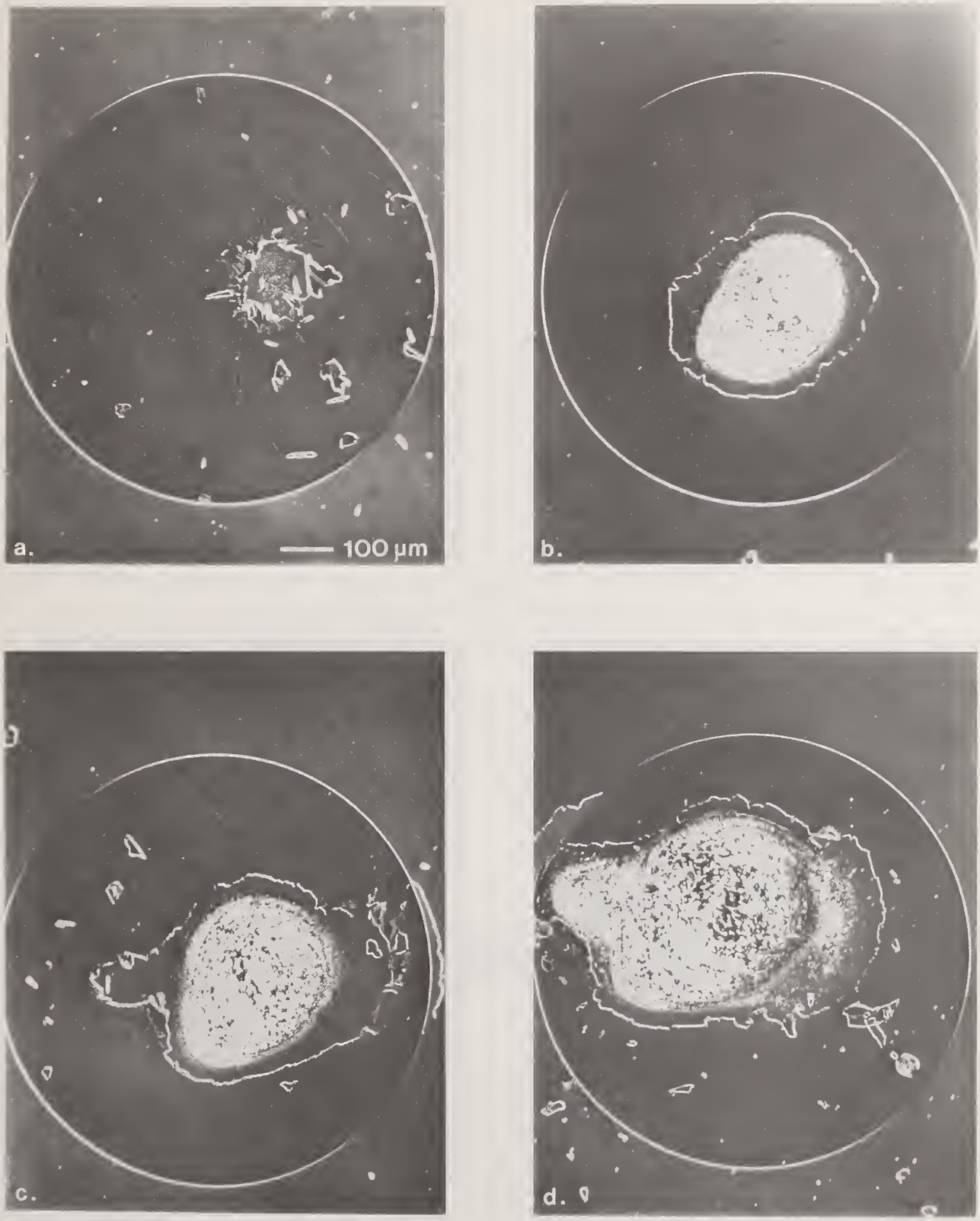

Figure 5.

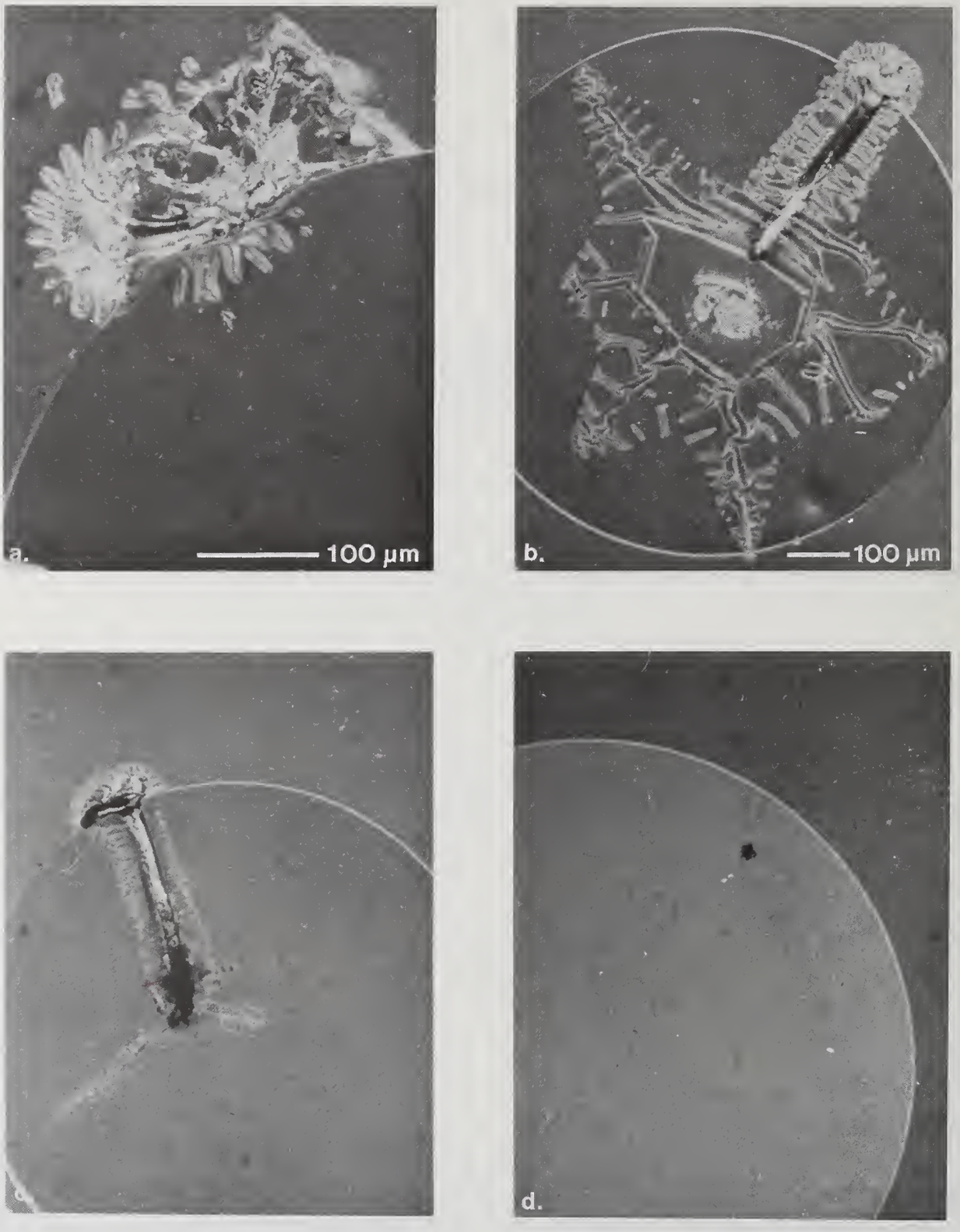

Figure 6.

Figure 5. Damage morphologies of RCA avalanche photodiodes which show deep melting. Biasing circuit #1 was used during irradiation. The current characteristics were not changed for devices A and B (a. and b.). For device C (c.), the leakage current at 336 Volts increased from 77 nA to 5.5 μA. For device D (d.), the leakage current increased from 72 nA to over 20 mA. Nomarski micrographs.

a. Device A 1-shot at 2.1 J/cm2
b. Device B 1-shot at 5.7 J/cm2
c. Device C 1-shot at 6.4 J/cm2
d. Device D 1-shot at 9.7 J/cm2

Figure 6. Damage morphologies of RCA avalanche photodiodes which failed catastrophically. Biasing circuit #2 was used during irradiation. Micrographs b., c., and d. have the same scale. Nomarski micrographs.

a. Edge morphology for 1-shot at 0.4 J/cm2
b. 1-shot at 3.9 J/cm2
c. 3000-shots at 0.4 J/cm2
d. Back side of shorted device

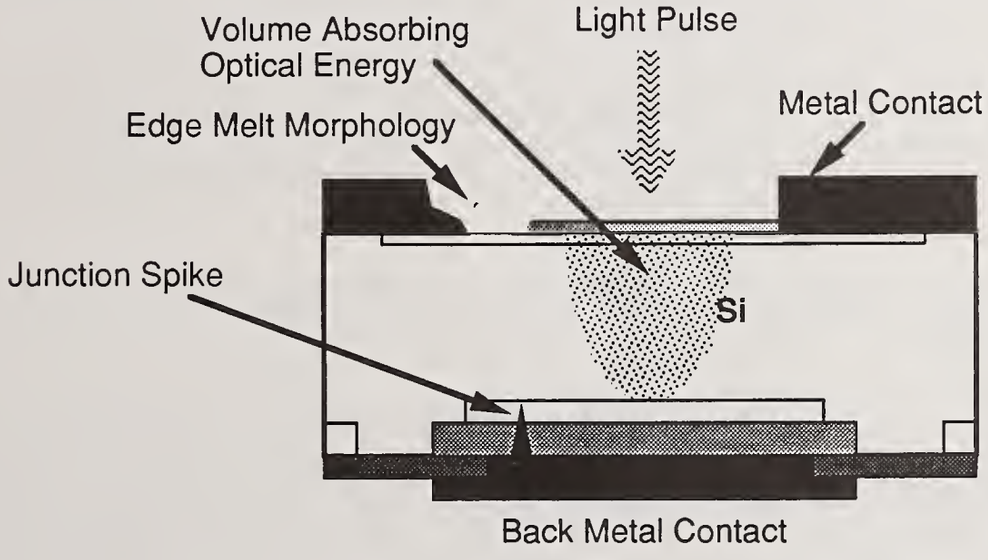

Figure 7. Cross section of a shorted avalanche photodiode. This catastrophic failure only occurred for devices biased using circuit # 2. The morphologies resulting from near-threshold fluences are the junction spike from the back contact metalization and the melt morphology at the edge of the active area. Neither of these morphologies are located in the volume which absorbs the optical energy.

Manuscript received
1-29-90

The Effect of Subsurface Defects on "Incipient" (Below Threshold) Laser Damage Nucleation In Fused Silica Optical Flats

T. J. Magee and C. S. Leung
XMR Inc.
Santa Clara, California 95054

F. D. Orazio, Jr.
VTI Inc.
Dayton, Ohio 45431

J. D. Boyer, B. R. Mauro, and V. E. Sanders
Los Alamos National Laboratory
Los Alamos, New Mexico 87545

The development of subsurface defects in optical components has been extensively investigated by the authors and others over the past few years. Investigation of optical components using nondestructive photon backscattering (PBS_{TM}), delineation etch/optical microscopy and charge decoration/delineation techniques has shown laterally variable spatial distributions of subsurface defects in the form of lineated remnant polishing traces, voids, and microscopic impurity clusters introduced during the surface finishing process. In this paper, we report on the correlation between nondestructive PBS_{TM} mapping and delineation etch/optical microscopy techniques for detection of subsurface defects, as well as the effect of subsurface defects on the initiation of microscopic or "incipient" laser damage (λ = 248 nm) at levels below the point of macroscopic or catastrophic failure observed at the surface. The detection of laser induced microscopic cracking on nucleation sites within nondestructively identified areas provides additional insight into the progressive development of failure sites in distributed subsurface regions of low RMS, optically finished surfaces.

Key Words: fused silica; incipient laser damage nucleation; microscopic impurity clusters; subsurface defects

1. Introduction

Damage to optical materials under intense photon irradiation has always been a major problem [1]. The proceedings of the annual Boulder Damage Symposium document 20 years of progress in resolving various key fundamental issues in understanding the laser induced damage mechanism [2]. Although tremendous research effort has been made to understand the laser damage mechanism in optical materials, defining the state-of-the-art laser resistant material is often difficult. It has been shown that it is difficult to conduct laser damage tests and to predict laser induced damage thresholds for the same materials from sample to sample [3,4]. In addition, the "apparent" laser damage threshold may vary spatially across the surface.

The occurrence of incipient damage beneath the surface at laser energy levels far below the observable macroscopic "damage" point has been identified recently by the authors for various optical materials such as fused silica, alexandrite rod, and potassium titanyl phosphate (KTP) crystals. Although the role of cracks, pores, and absorbing inclusions on laser induced damage thresholds has been discussed previously [5], it should be noted that the highly localized subsurface damage regions present in a well-polished optical surface has a more dramatic effect on avalanche breakdown by the high power laser pulse. The subsurface defect commonly found in the otherwise optically smooth surface of optical materials is

introduced by conventional lapping/polishing processes through propagation of the damage into near-surface regions of a super smooth surface depending on the fabrication schemes as well as the characteristics of the material [6].

One of the major problems in predicting laser damage thresholds is the lack of nondestructive techniques to characterize the test surface extensively prior to the damage test procedure as well as the criteria of laser-induced damage threshold that are based on phenomenological observations and statistical data at the test sites. Nondestructive mapping techniques are needed for measuring spatial surface quality and subsurface defects on the test parts, otherwise anomalous effects are seen in determining surface damage threshold of optical materials that leads to erroneous assumptions in laser damage mechanism modeling.

The objective of this paper is to report on the correlation between nondestructive photon backscattering mapping and selective etch delineation techniques for detection of subsurface defects, as well as the effect of subsurface defects on the initiation of microscopic or "incipient" laser induced damage in fused silica. Although the relation of subsurface structure in fused silica and laser damage threshold has been reported previously [7,8,9], with some form of controlled grinding/polishing procedures, the lack of surface and subsurface defects characterization techniques on these test parts makes predicting damage thresholds erratic. Conventional grinding/polishing procedures can produce severe subsurface damage, impurity clusters, as well as other subsurface imperfections in the near-surface region of the processed parts. Nondestructive techniques are needed to identify the nature of subsurface defect structure that has eluded investigators for a long time. Recently, a nondestructive photon backscattering technique has been develop to map subsurface defects found in optical blanks such as fused silica and sapphire [10]. Spatially varying subsurface damage from a super-polished surface has densities far below that of a standard polish. Using a selective delineation etch, all the UV laser exposure spots (248 nm) on a standard polished surface can be revealed at energy fluences ranging from 4.7 - 9.5 J/cm^2 and the catastrophic damage can be found to be associated with the high scatter regions of the PBS map.

2. Results and Discussion

The fused silica optical flat used in the nondestructive testing photon backscattering (NDT-PBS_{TM}) mapping was a one-inch diameter flat with a super polish on one side and a standard polish on the other. The fused silica optical flat was subjected to NDT-PBS_{TM} measurements on both sides. The PBS_{TM} instrumentation used is a very sensitive patented technique that measures scattering of HeNe laser light as a function of angle and produces a plot of scattering level as a function of position on the optical flat. The PBS maps of the super polished and standard polished surface of the fused silica optical flat are shown in figures 1 and 2. In the super polished surface of the optical flat, very few features can be found in the PBS_{TM} map with a low average scatter level (.0252). In comparison, in the standard polished surface of the optical flat, the lineated features of high-scatter intensity are distributed across the test area with a high average scatter level (1.0221). These features are caused by the buried spatially varied subsurface damage produced by the conventional polishing process. The subsurface defects have very distinct characteristics, dependent upon material properties and the specific fabrication procedures used to produce the ultra smooth surface.

Following the NDT-PBS_{TM} mapping, the fused silica flat was subjected to laser damage tests at Los Alamos National Laboratory. Damage threshold measurements after exposure to 23 ns, 248 nm laser pulses were made on both sides of the one-inch diameter fused silica blank. The super-polished side was tested with a laser energy fluences ranging from 6.4 - 16.2 J/cm^2 while the fluence on the standard finished side ranged from 4.7 - 12.0 J/cm^2. Each site was exposed to 100 shots at a specific fluence using a laser pulse repetition rate of 50 Hz. The spot size was approximately 0.20 x 0.75 mm

for all sites. Damage was detected by visual examination of the test sites using a microscope equipped with white-light, bright-field illumination at 100X. Using the observable surface change as a criteria for laser damage, the damage thresholds were 8.0 and 6.3 J/cm^2 for the super-polished and standard finished sides, respectively.

After the laser damage threshold measurements, the fused silica optical flat was subjected to a sensitive etch delineation procedure. In this etch procedure for fused silica, approximately 2 um of material was removed at a faster rate in the matrix material having a high density of defects. Nomarski micrographs showing the representative etch delineated subsurface defect features found on the super polished and standard polished surface are shown in figure 3. As shown in figure 3, it can be seen that the density of subsurface defects (voids and scratches) on the standard polished surface is higher than the super polished surface.

Of particular interest in the sensitive etch delineation procedure is the delineation of all laser damage sites on the standard polished surface with energy fluences exposure as low as 4.7 J/cm^2. On the contrary, except for the catastrophic damage sites, no etch delineated test sites can be seen on the super-polished surface even with higher energy fluence exposures. Upon careful examination of the etch delineated laser damage test sites on the standard polished surface, it is apparent that incipient laser damage has been induced in the subsurface defect regions on the standard polished surface. The "incipient" laser damage induced in the subsurface regions at various laser fluences after exposure to selective etch is shown in figure 4. Delineated laser induced subsurface defects are seen at all laser fluences on the standard polished surface.

These results clearly demonstrate the occurrence of "incipient" damage beneath the surface at energy levels far below the macroscopic/catastrophic failure point. In this respect, both the definition of "laser damage" threshold and the understanding of damage nucleation at subsurface sites will require serious reconsideration. The approach to predict laser damage threshold by considering statistical data and phenomenological observations is limited by the lack of availability of controlled experimental data such as sensitive nondestructive test techniques on the surface quality of the test samples. Most laser damage tests have been performed without any extensive characterization of the spatially varying subsurface defects.

The influence of subsurface defects on laser damage is illustrated in figure 5 for fused silica at a specific site. In this case, the laser damage initiated at a site containing a relatively high density of absorbing macroscopic inclusions and subsurface damage, resulting in conchoidal fracture generated by the thermal gradients within the matrix material. Depending on the characteristic of these absorbing inclusions and subsurface damage, the laser damage threshold can change drastically since the initial interaction of laser pulses with these defects will have a direct impact on various material properties upon exposure to subsequent laser pulses.

3. References

[1] Guenther, A.H. A chronology of laser damage research. Lasers & Applications. 3(5):87-92; 1984.

[2] Proceedings of the Annual Symposium on Optical Materials for High Power Lasers (Boulder Damage Symposium): available at National Bureau of Standards Special Application.

[3] Seitel, S.C. Planning a laser damage test. Photonics Spectra. 19(8): 84-92; 1985.

[4] Soileau, M.J. Laser induced damage. Photonics Spectra. 21(11):109-114; 1987.

[5] Bloemberger, N. Role of cracks, pores, and absorbing inclusions on laser induced damage threshold at surfaces of transparent dielectrics. Applied Optics. 12(4):661-664.

[6] Magee, T.J.; Leung, C.S. Overview of subsurface damage in brittle materials - evolution of concepts and current status. Park, R.E., ed. Proceedings of ASPE spring conference on subsurface damage in glass. 1989 April 25-27; Tucson, AZ. 15-55.

[7] House II, R.A.; Bettis, J.R.; Guenther, A.H. Subsurface structure and laser damage threshold. IEEE J. of Quant. Elect., EQ-12, No. 5:363-364.

[8] Temple, P.A.; Lowdermilk, W.H.; Milam, D. Carbon dioxide laser polishing of fused silica surfaces for increased laser-damage resistance at 1064 nm. Applied Optics 21(18):3249-3255 (1982).

[9] House, R.A.; Bettis, J.R.; Guenther, A.H. Preparation techniques and hydroxyl concentration vs. surface damage threshold. NBS Special Publication 462, Laser induced damage in optical materials, p. 310 (1976).

[10] Magee, T.J.; Leung, C.S.; Orazio Jr., F. Nondestructive and destructive analysis of spatially distributed subsurface damage in quartz and sapphire optical flats. Parks, R.E. ed. Proceedings of ASPE Spring Conference on subsurface damage in glass; 1989 April 25-27; Tucson, AZ 147-173.

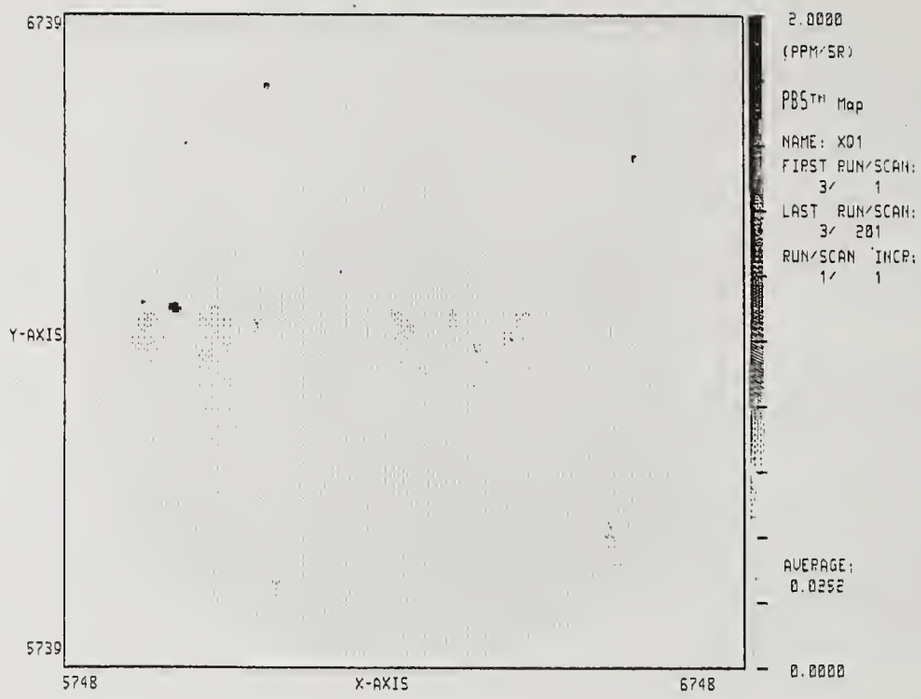

Figure 1. Photon Backscattering (PBS_{TM}) map of super-polished fused silica optical flat (Original map is on multicolor plot)

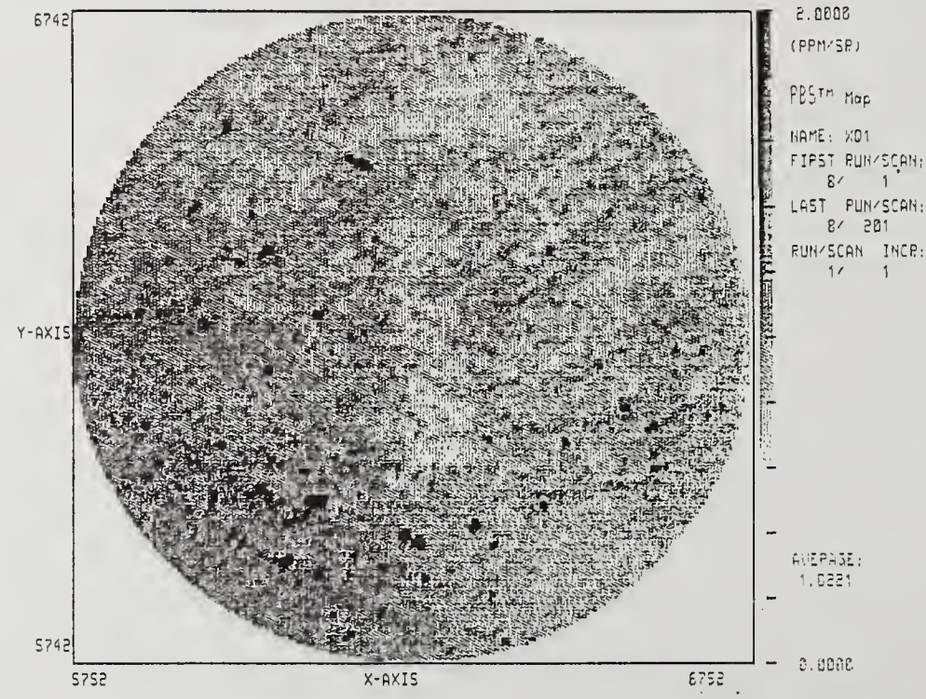

Figure 2. Photon Backscattering (PBS_{TM}) map of standard polished fused silica optical flat (Original map is on multicolor plot)

(a) Super Polish

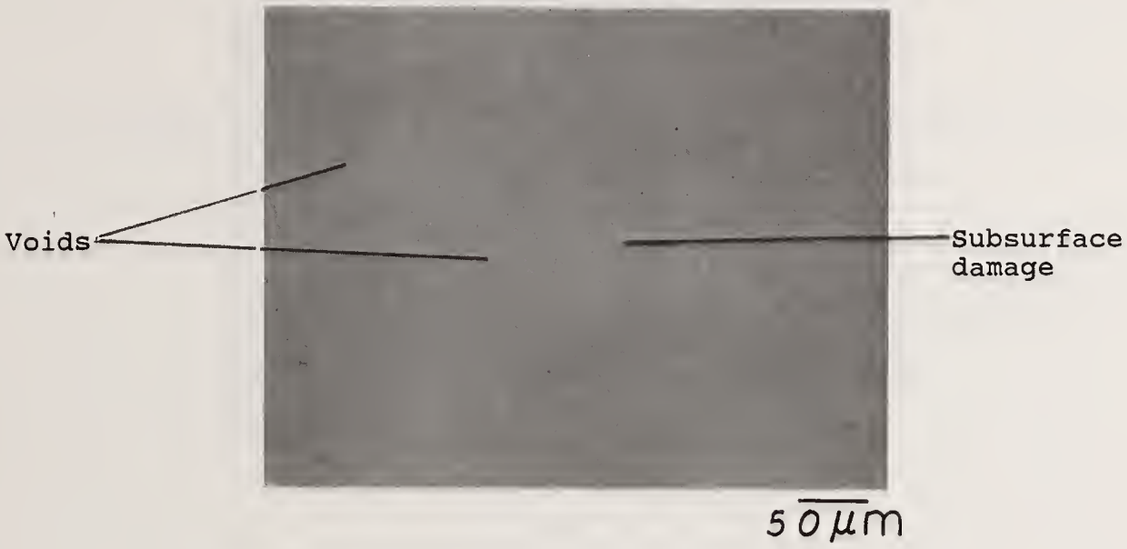

(b) Standard Polish

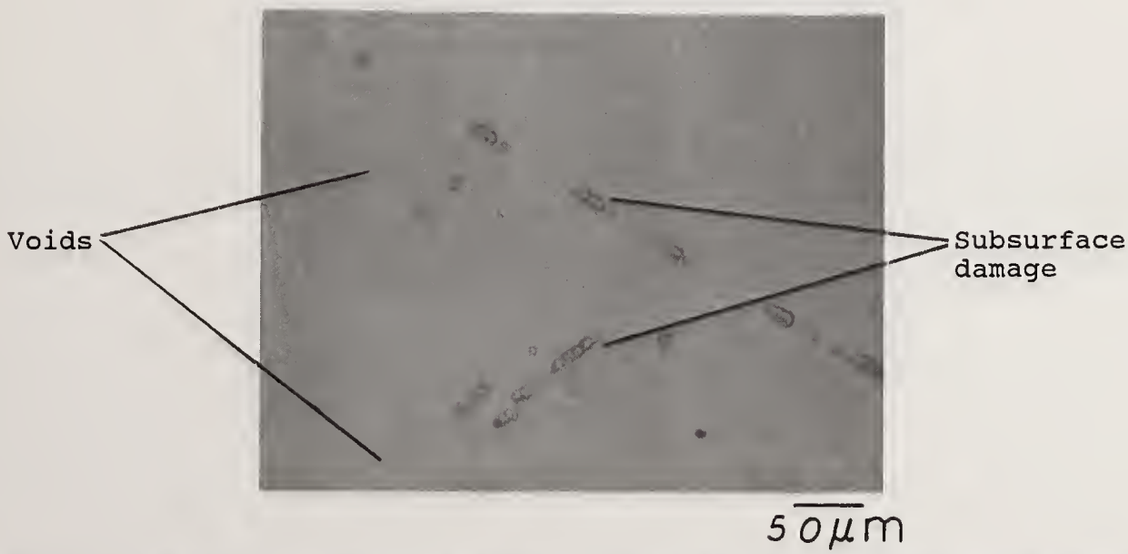

Figure 3. Nomarski micrographs showing representative subsurface defect on fused silica surface after exposure to selective delineation etch (a) super polish, (b) standard polish

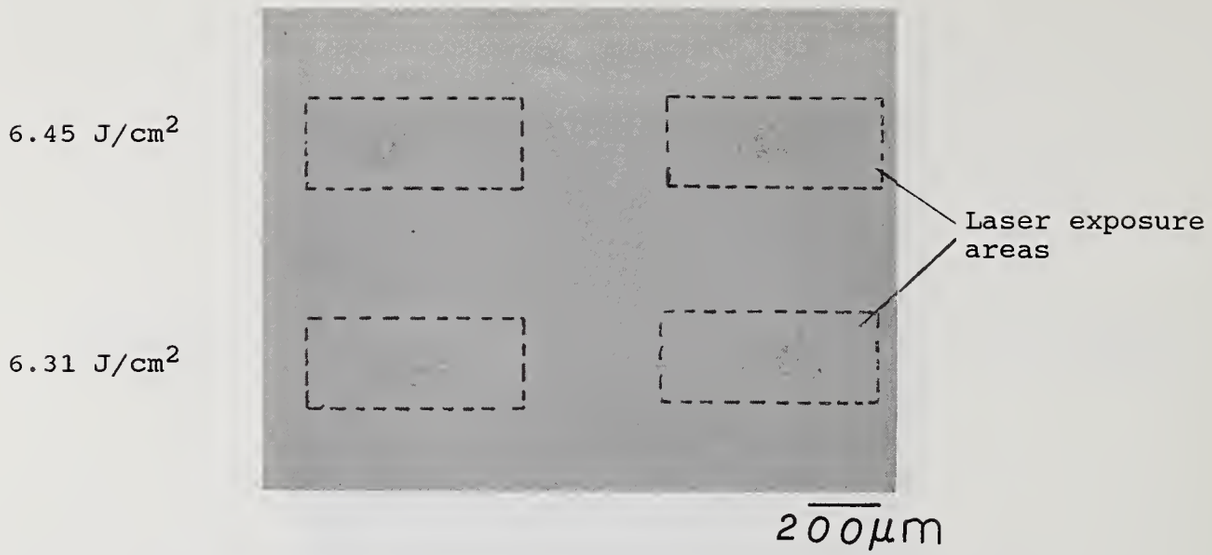

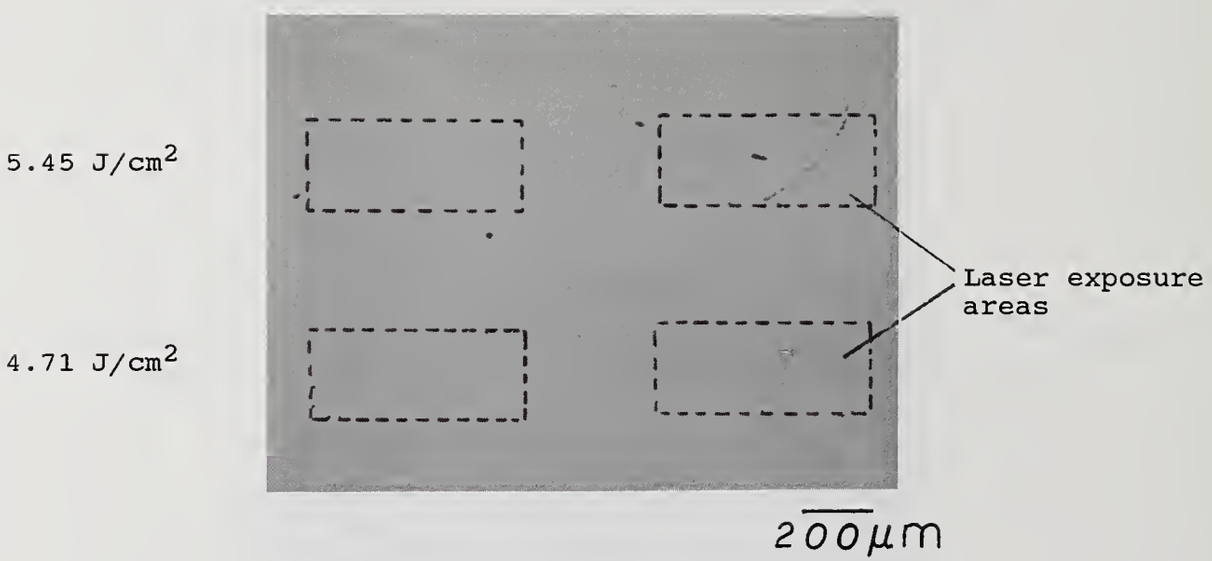

Figure 4. Nomarski micrographs showing "incipient" laser damage in subsurface regions (etch delineated after laser exposure) at various laser fluences for standard polish surface

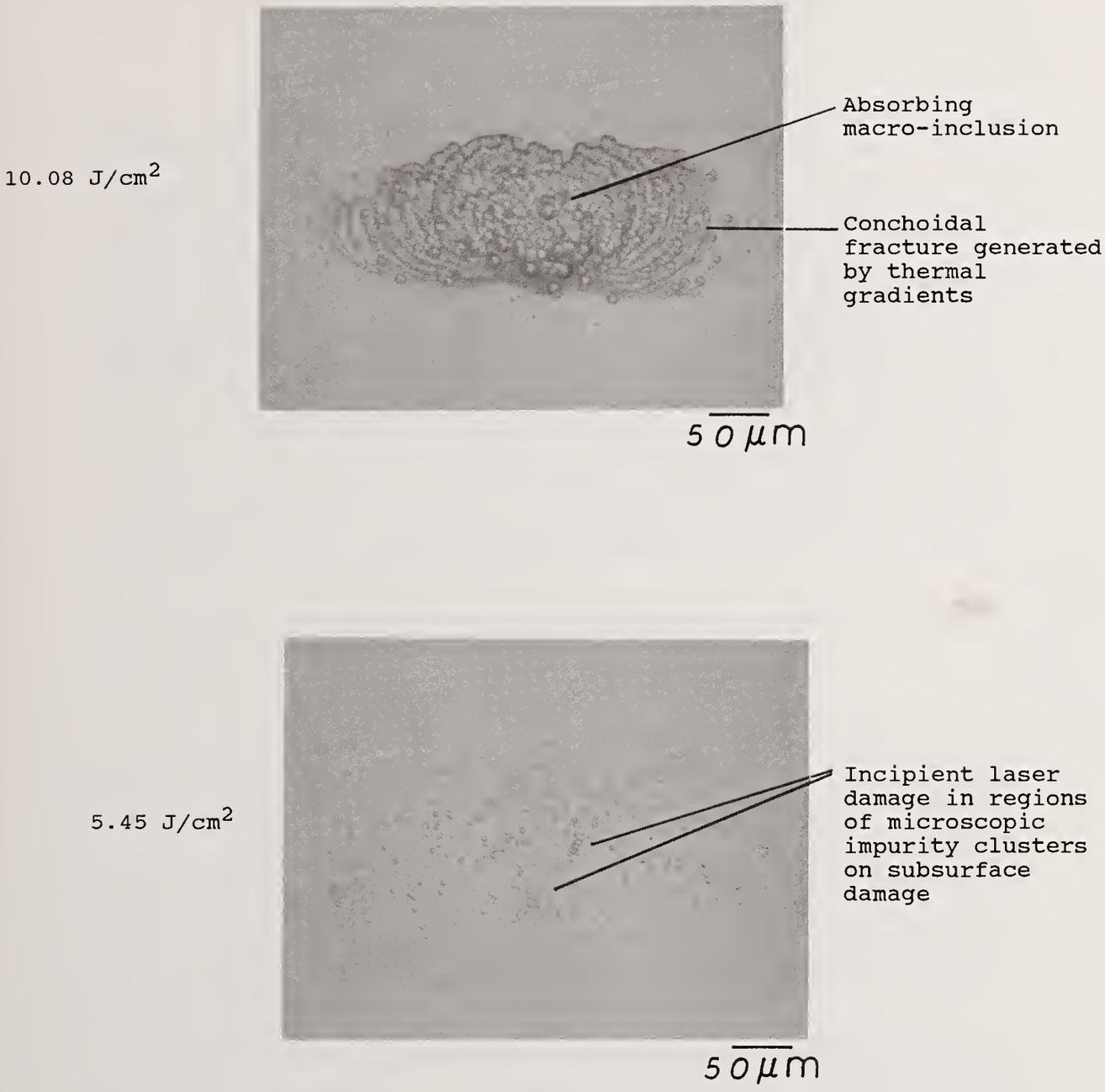

Figure 5. Nomarski micrographs showing "incipient" damage initiated at (a) macroscopic absorbing inclusion sites and (b) lineated subsurface damage sites

COMMENTS

Question: If I understand correctly, your characterization of the films does not allow for a variation in crystallite size as the film grows or as you get additional films. Now in fact for many films you do get an increase in structure as you go to thicker films. Doesn't that require that one extend this theory to consider that effect?

Answer: We do not detect interference from variations in microstructure. It is due to the range of measurable special frequencies. Even if you measure at 80°, the peak defects are ten times higher than the thickness of the layer. Maybe, if we used longer wavelengths it would be possible to detect possible correlation or interference.

Manuscript received
12-29-89

Quantitative Analysis of Surface Trace Metal Contamination on Substrates and Films by TXRF

R. S. Hockett

Charles Evans & Associates
301 Chesapeake Drive
Redwood City, CA 94063

The damage to optics from high power laser radiation depends in part upon the surface films on the system optics. Approaches to hardening these surfaces to these types of radiation have focused on layered film compositions and upon the reduction of structural defects in the films and the substrates. The importance of heavy metal contamination at trace levels (less than one thousandths of a monolayer) in the top few monolayers of the surfaces, or at the film interfaces, has been minimized because of insufficient analytical technology to detect these impurities. These localized heavy metals may absorb radiation, ionize to high positive states, and become the source of defects leading to damage. This paper will describe a new analytical technique, Total Reflection X-Ray Fluorescence (TXRF), which is capable of quantitatively detecting heavy metals (Z>11) on the surface (top few nm's) of the substrates or films, with detection limits down to 10^{11} atoms/cm^2 (in most cases several orders of magnitude better than ESCA or AES, and quantitative, in contrast to SIMS.)

Key Words: Contamination; Damage; Defects; Films; Metals; Surfaces; Total Reflection X-Ray Fluorescence

1. Introduction

The damage to optics from high power laser radiation depends in part upon the surface films on the system optics. Approaches to hardening these surfaces to these types of radiation have focused on layered film compositions and upon the reduction of structural defects in the films and the substrates [1]. The importance of heavy metal contamination at trace levels (less than one thousandths of a monolayer) in the top few monolayers of the films, or at the film interfaces, has been suspected by not studied because of insufficient analytical technology to detect these impurities. These localized heavy metals may absorb radiation, ionize to high positive states, and become the source of defects leading to damage. These heavy metals may even be part of the explanation for the major discrepancy between bulk thermal conductivities and theoretical damage thresholds in thin film coatings [2].

The effect of bulk trace impurities in some films has been studied [3-5], as well as the effect of surface cleaning [6], but the effect of surface (top few monolayers) impurities, at levels below the detection capability of Auger Electron Spectroscopy (AES) or Electron Spectroscopy for Chemical Analysis (ESCA), upon the damage threshold has not been studied. The reason is until recently there has been no analytical instrument capable of quantitatively detecting these highly localized (in depth) impurities. The theory of small metallic inclusions (1-20 nm diameter) in the bulk of the films has also been addressed [7], but the effect of aggregated surface impurities in the top few monolayers has not.

The difficulty in quantitatively detecting trace metals localized in the surface (top few monolayers) has been great. AES and ESCA, which can provide semi-quantitative measurements, are sensitive to these depths, but only have detection limits on the order of 1 to 0.1 atomic % at best. This is about 10^{14} to 10^{13} atoms/cm^2, or roughly one tenth to one hundreth of a monolayer, respectively. Other analytical techniques, such as laser ionization mass

spectrometry , electron probe, secondary electron microscopy equipped with energy dispersive x-ray analysis, and Rutherford backscattering spectrometry do not have the depth resolution. Secondary ion mass spectrometry has the depth resolution, but the non-linear ion yields from the sputtering process in the first few monolayers makes quantification not possible. The same problem (i.e., the difficulty in quantitatively measuring the trace impurities in the top few monolayers) has also existed in the semiconductor industry for processes which polish and clean substrates and thin films.

2. Total Reflection X-Ray Fluorescence

Recently in 1987 a new surface sensitive analytical technique was developed [8] to meet this need in the semiconductor industry. The technique called Total Reflection X-Ray Fluorescence (TXRF) has detection limits, when using a Molybdenum anode, on the order of 10^{11} atoms/cm^2 for heavy metals on silicon and SiO_2 surfaces, as shown in Figure 1. This is about two orders of magnitude more sensitive than AES or ESCA for the heavy metals.

In the TXRF technique x-rays from a conventional x-ray anode strike the substrate surface at grazing incidence and totally reflect from the substrate surface. The atoms in the top few monolayers emit fluorescence x-rays depending upon the incident x-ray energy and the energy levels of the surface atoms. The fluorescence radiation is detected then by an energy dispersive x-ray spectrometer, a conventional Li-drifted silicon detector which is cooled by liquid nitrogen.

The TXRF technique has been shown to detect heavy metals even on ultra-clean commercial quality silicon substrates [8,9] and has been applied to cleaning process development of silicon substrates by integrated circuit (IC) manufacturers [10,11]. Figure 2 shows a TXRF spectra (detected fluorescence x-rays versus the fluorescence x-ray energy) for a commercial silicon wafer. The substrate was not intentionally contaminated with the detected Fe, Cu and Zn at levels in the mid 10^{11} to low 10^{12} atoms/cm^2 range. These impurities arise from the cleaning process, are localized in the top few monolayers of the substrate, and are not detectable by AES or ESCA. Figure 3 shows a TXRF spectra of an SiO_2 layer on a silicon substrate where the SiO_2 was cleaned using semiconductor grade processing equipment; here we see Cr, Cu and Zn at levels of 10^{11} atoms/cm^2. Figure 4 shows a TXRF spectra of a commercial GaAs semiconductor substrate with Fe and Cu surface levels in the 10^{11} to 10^{12} atoms/cm^2 range also. The technique is also capable of detecting metal contamination on diamond films [12]. The TXRF technique is being rapidly accepted in the semiconductor and IC industry and is expected to become a standard technique [13] for surface analytical measurements.

2.1 Quantification

Quantification is achieved using a silicon substrate which has been intentionally contaminated with Ni of a known areal density using a diluted wet chemistry standard. Once the calibration for Ni is completed, the calibration for the other metals is completed using sensitivity factors which were measured once when the instrument was manufactured.

Correlation of TXRF with nitrogen-beam Rutherford backscattering spectrometry (RBS) and vapor phase decomposition followed by atomic absorption spectroscopy (VPD/AAS) has validated the quantification approach. The correlation between TXRF and VPD/AAS is shown in Figure 5 for Fe, Ni, Cu and Zn on silicon wafer surfaces. The multi-point TXRF measurements were made using XSA-8000 instruments at Charles Evans & Associates on one set of wafers and at GeMeTec (Munich, West Germany) on another set of wafers. The intentionally contaminated wafers and VPD/AAS measurements were provided by Kyushu Electronic Metals Co. Ltd., Japan. A BLANK was measured at Charles Evans & Associates for 5.6 hours to check for instrumental background; only Cu at 7×10^{10} atoms/cm^2 was detected. The correlation between TXRF, RBS (nitrogen beam), and VPD/AAS for the sum of the metal contamination is shown in Figure 6. The reason for summing the metals is RBS cannot mass resolve these metals, but detects them as one mass.

2.2 Stability

Analytical statistical process control (SPC) is completed using periodic TXRF measurements on two 100 mm diameter silicon samples. The SPC measurements are made daily, since a within-day time study revealed the measurements were stable over a one day time period. The first sample is the calibration standard which contains Ni and Bi. The Ni is used to derive the calibration constant which gives the quantification. A drop in this value outside of SPC may indicate the x-ray tube is losing power. The Bi is monitored for SPC of the high energy calibration. The second sample is a commercial wafer with Cu, Fe and Zn plated from its original cleaning. (The TXRF signal versus angle variation reveals the metals are plated.) The Cu is monitored for SPC of the angle calibration, the Fe for SPC of the detection limit, and the Zn for SPC of the energy resolution (the ability to separate the Zn k-alpha line from the Cu k-beta line).

Figure 7 shows a plot of the Ni calibration (counts/sec) and Bi measurement over a 3 month period. Figure 8 shows a plot of the measurement of Cu, Fe and Zn over the same period of time. The measurements on the Cu, Fe and Zn contaminated sample were terminated after this period of time when the Cu, Fe and Zn measurements went out of SPC control, and an angle scan revealed particulate contamination had been introduced to the sample, i.e., a special cause could be assigned to the out-of-SPC measurement. The Cu readings in Figure 8 shows a drop with time that is also out of SPC control, while the Fe and Zn do not. The drop has a slope of 0.35% per day, and may be detectable for the Cu because of its high signal level, while the lower levels of Fe and Zn result in too much variability to identify a statistically valid drop. This same drop can be created by inserting a similar wafer into the instrument for a series of 50-90 sequential measurements in one day without removing the wafer between measurements. A similar experiment was tried where a Co contaminated 125 mm diameter wafer was sequentially measured for 49 times in one day without removal from the clamp. The Co was localized on the surface and in the subsurface; in this case there was no drop. Recent radiotracer studies have shown Cu can be activated at room temperature to diffuse into crystalline silicon. In any case a drop of only 0.35% per day (or per measurement) is not a practical problem for the measurement precision itself.

Precisions (one relative standard deviation) depend upon the specific element and its amount. For the SPC contaminated wafer the precisions are 5% for Cu at 4×10^{12} atoms/cm^2 (linear drop removed); 29% for Fe at 0.5×10^{12} atoms/cm^2, and 18% for Zn at 0.4×10^{12} atoms/cm^2. The precisions for the Ni counts/sec and Bi reading are 3.8% and 6.4% respectively.

3. Applications

We anticipate that since there is heavy metal contamination at these levels on commercial silicon, SiO_2, and GaAs substrates manufactured for the IC industry, then there will most likely also be heavy metal contamination at these levels, or higher, on substrates and films used for high power laser optics. There is the opportunity then to apply this new TXRF technique to high power laser optical structures in order to reduce the heavy metal contamination from processing and to show a reduction in optics damage. The two generic application areas are:

(1) the polishing and cleaning process development for high power laser optical substrates before film growth, and

(2) the cleaning process development of the film surfaces after film growth

The approach works for silicon and GaAs substrates and films. However, development work is required in order to apply TXRF to other critically important high power laser optical substrates and films. The reason is there are some differences between the semiconductor applications and the non-silicon optical materials applications, i.e., the matrix signals, the optimum excitation source, the critical angle, matrix interferences, optimum angle for signal-to-background, and quantification.

Group I - TXRF Immediate Applications

I.1 Silicon

I.2 Fused Silica

I.3 Silicon Carbide

Group II - TXRF Expected Applications

II.1 Be on Silicon Carbide

II.2 Be on Fused Silica

II.3 Low Z Dielectric Stacks with and without Al Baselayer on ULE, Silicon Carbide and Silicon.

II.4 Low Z Coatings

II.4 NaCl on Al

Group III - TXRF Anticipated Applications

III.1 Heavy Metal Fluorides

III.2 MgO and AlN coatings on Heavy Metal Fluorides

III.3 Zinc Selenide

III.4 Mo and Au films on Al

III.5 Ag on Silicon

III.6 Au on Be on Fused Silica

3.1 Development

Group II Samples: Be on Silicon Carbide; Be on Fused Silica; Low Z Dielectric Stacks with and without Al Baselayer on ULE, Silicon Carbide and Silicon; Low Z Coatings; and NaCl on Al.

The Group II samples are different from Group I samples in that the surfaces are low Z and therefore do not provide matrix signals with which to experimentally determine the critical angle for total reflectance. There are two approaches to overcoming this difficulty.

One approach is to calculate the critical angle for the low Z surface; a table of calculated critical angles for a range of low Z materials already exists. Then the approximate angle of incidence can be found using a high Z sample (like a silicon substrate) which is already well understood. The low Z sample can then be inserted into the TXRF instrument and the angle setting from the high Z sample calibration will be used. The drawback from this approach is the repeatability of the measurement will not be as good as if we could directly measure the critical angle for the low Z surface.

A second approach is to deposit a high Z coating (less than one monolayer) onto the low Z sample surface and use the high Z coating to in situ calibrate the angle settings and then use the calculated angle setting for the low Z matrix. The drawback here is that the deposition process may itself add surface contamination. We have at Charles Evans & Associates an electron beam heated silicon deposition system by which we can attempt to add very low levels of silicon to the low Z surface. Previous studies have indicated that this can be done without adding heavy

metal contamination, but the rate control may be difficult for a submonolayer deposition.

Group III Samples: Heavy Metal Fluorides; MgO and AlN coatings on Heavy Metal Fluorides; Zinc Selenide; Mo and Au films on Al; Ag on Silicon; and Au on Be on Fused Silica.

The Group III samples are different from the Group II samples in that they will produce a desirable matrix signal for critical angle calibration (as with the Group I samples), but the matrix signal may increase the background levels and introduce interferences. This in effect is what happens with GaAs. Observation of Figure 4 indicates there are major Ga and As fluorescence peaks in the spectra and these interferences restrict the heavy metals which can be detected on GaAs. Some of this problem can be reduced by using different energy x-rays for the incident x-rays, if the excitation of the matrix can be avoided or dampened.

4. References

[1] Abstracts from the High Power Laser Optical Components Topical Meeting, sponsored by SDIO, NWC and AFWL, October 24-25, 1988, Boulder, CO.

[2] Arthur H. Guenther, Laser Induced Damage in Optical Materials: 1986, NIST Special Publication 752, ASTM STP 1028, (U.S. Department of Commerce/National Institute of Standards and Technology), Proceedings of the Symposium, November 3-5, 1986, Boulder, CO (September 1988), p. xiii.

[3] S. C. Seitel and L. G. DeShazer, ibid., p. 65.

[4] Ian Laidler and David C. Emmony, ibid., p. 151.

[5] Larry D. Merkel and Pradip K. Bandyopadhyay, ibid., p. 677.

[6] D. J. Gallant, Marilyn Law and Brad Pond, ibid., p. 159.

[7] W. Becker, J. K. McIver, and A. H. Guenther, ibid., p. 603.

[8] Peter Eichinger, Heinz J. Rath, and Heinrich Schwenke, Semiconductor Fabrication: Technology and Metrology, ASTM STP 990, Dinesh C. Gupta, editor, American Society for Testing and Materials, 1988.

[9] R. S. Hockett, S. M. Baumann, and E. Schemmel, Diagnostic Techniques for Semiconductor Materials and Devices, ECS Vol. 88-20, edited by Thomas J. Shaffner and Dieter K. Schroder, published by the Electrochemical Society (Pennington, NY), p. 113 (1988); "Comparison of wafer cleaning processes using total reflection x-ray fluorescence (TXRF)," R. S. Hockett and William Katz, J. ECS, November 1989.

[10] "An evaluation of wafer cleaning: suppression of oxidation induced stacking faults and control of oxide thickness," A. Hariri of Siliconix, Inc., and R. S. Hockett, Semiconductor International, August 1989.

[11] V. Penka and W. Hub of Siemens Ag, "Detection of metallic trace impurities on Si (100) surfaces with total reflection x-ray fluorescence (TXRF)," Fresenius Z. Anal. Chem. 333, 586 (1989); "Application of total reflection x-ray fluorescence in semiconductor surface analysis," Spectrochimica Acta 44B, 483 (1989).

[12] R. S. Hockett and James Knowles, "Characterization of heavy metal contamination on diamond films using SIMS and Total Reflection X-Ray Fluorescence (TXRF)," to be presented at the Fall Meeting of the Materials Research Society, Boston, 1989 (abstract F3.2).

[13] "The application of TXRF to semiconductor surface analysis," R. S. Hockett, invited presentation for the ASTM F104 annual workshop, February 1, 1989, San Diego, CA.

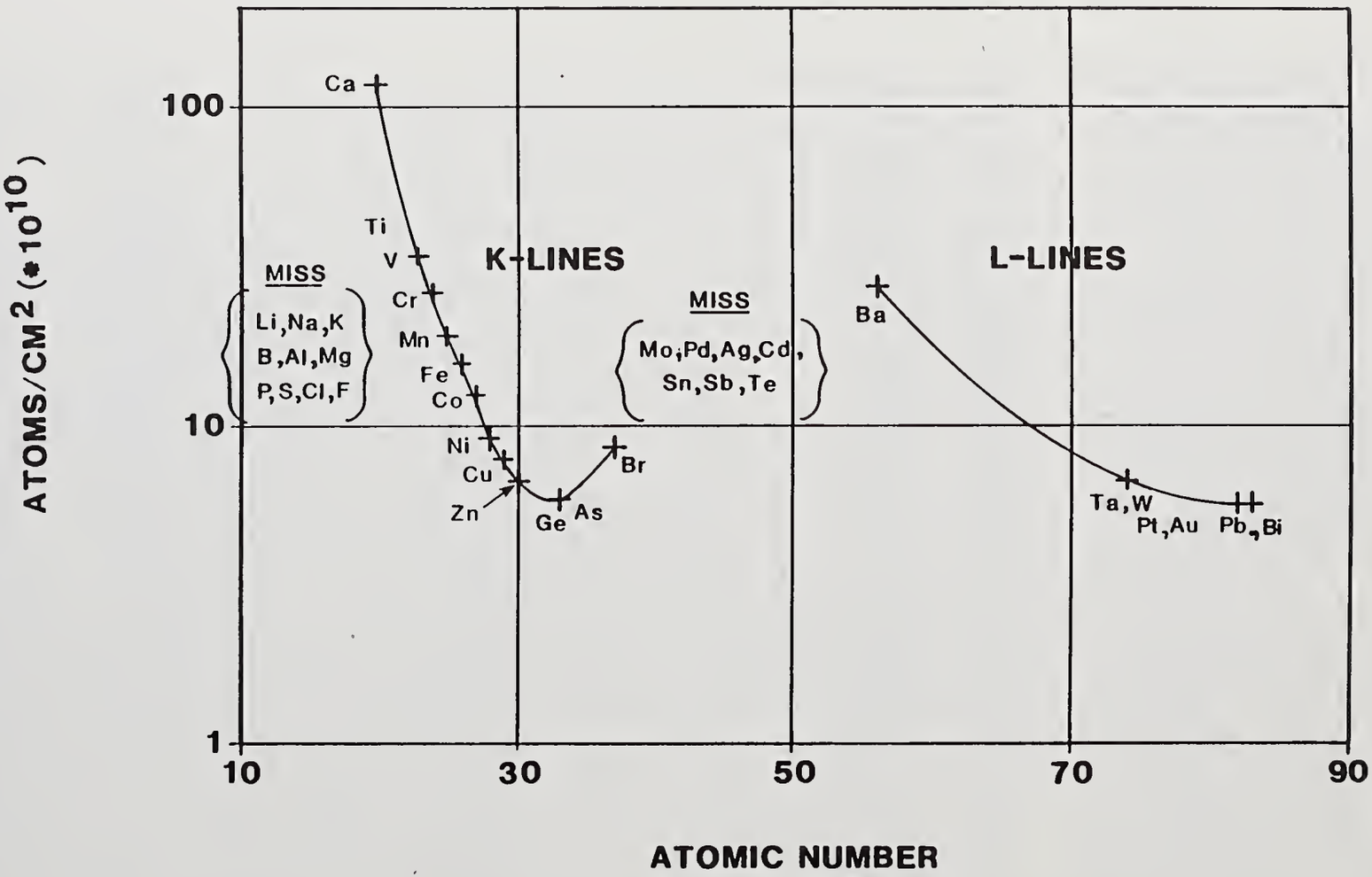

FIGURE 1. OPTIMUM TXRF DETECTION LIMITS ON SILICON USING A MO X-RAY ANODE

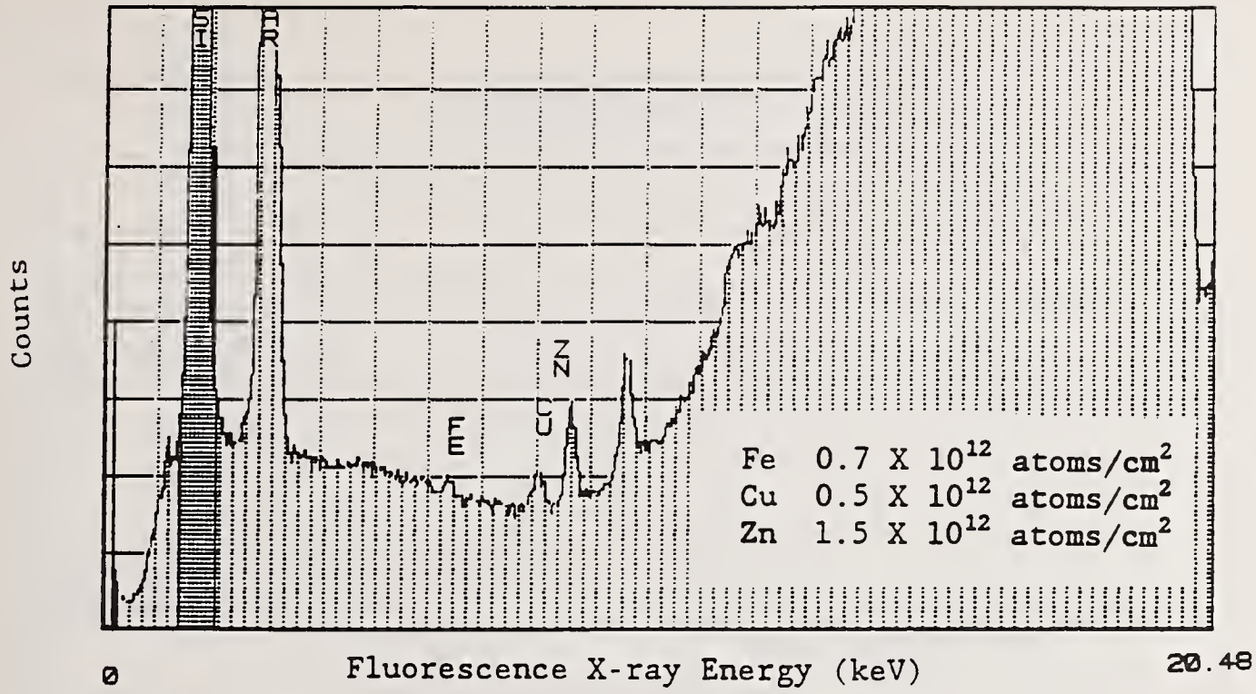

Figure 2. TXRF Spectra for a Commercial Silicon Wafer

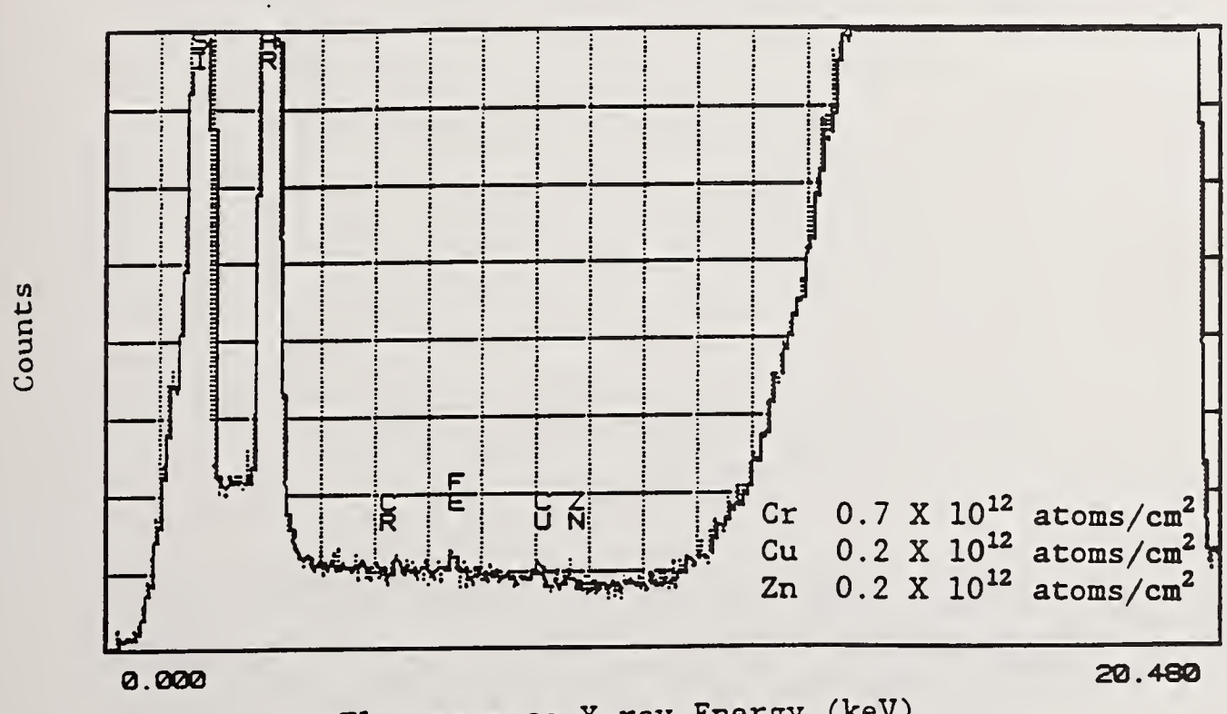

Figure 3. TXRF Spectra for an SiO_2 Film on Silicon after Cleaning

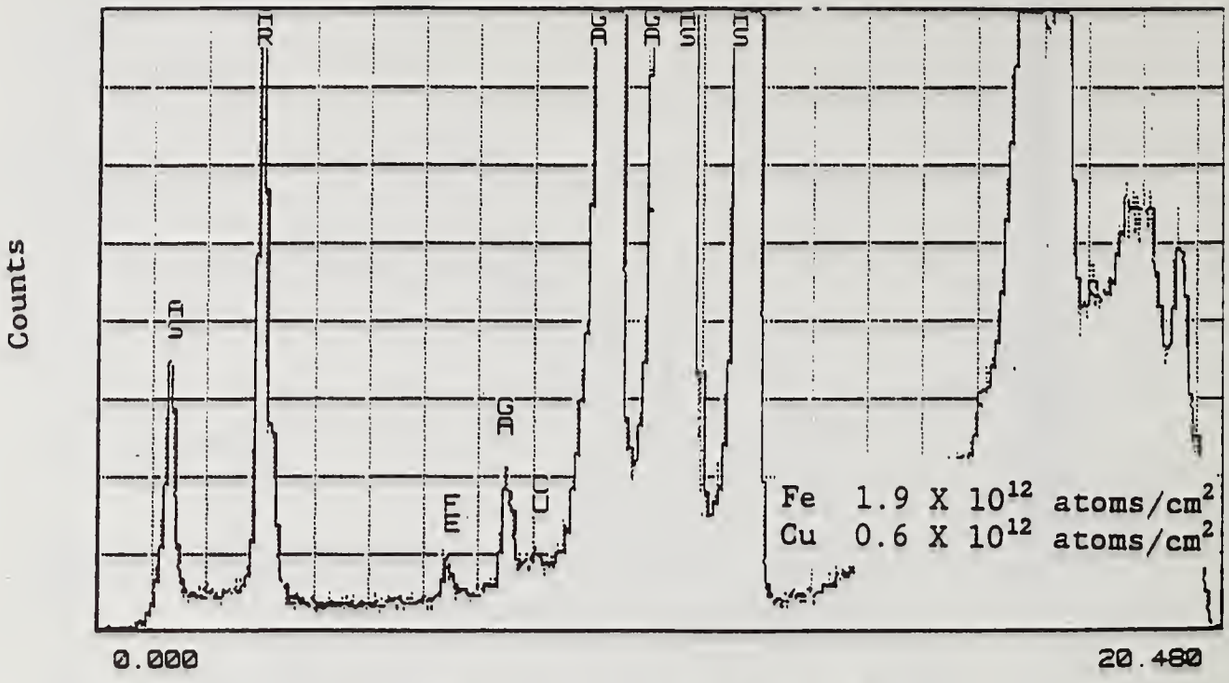

Figure 4. TXRF Spectra for a Commercial GaAs Wafer

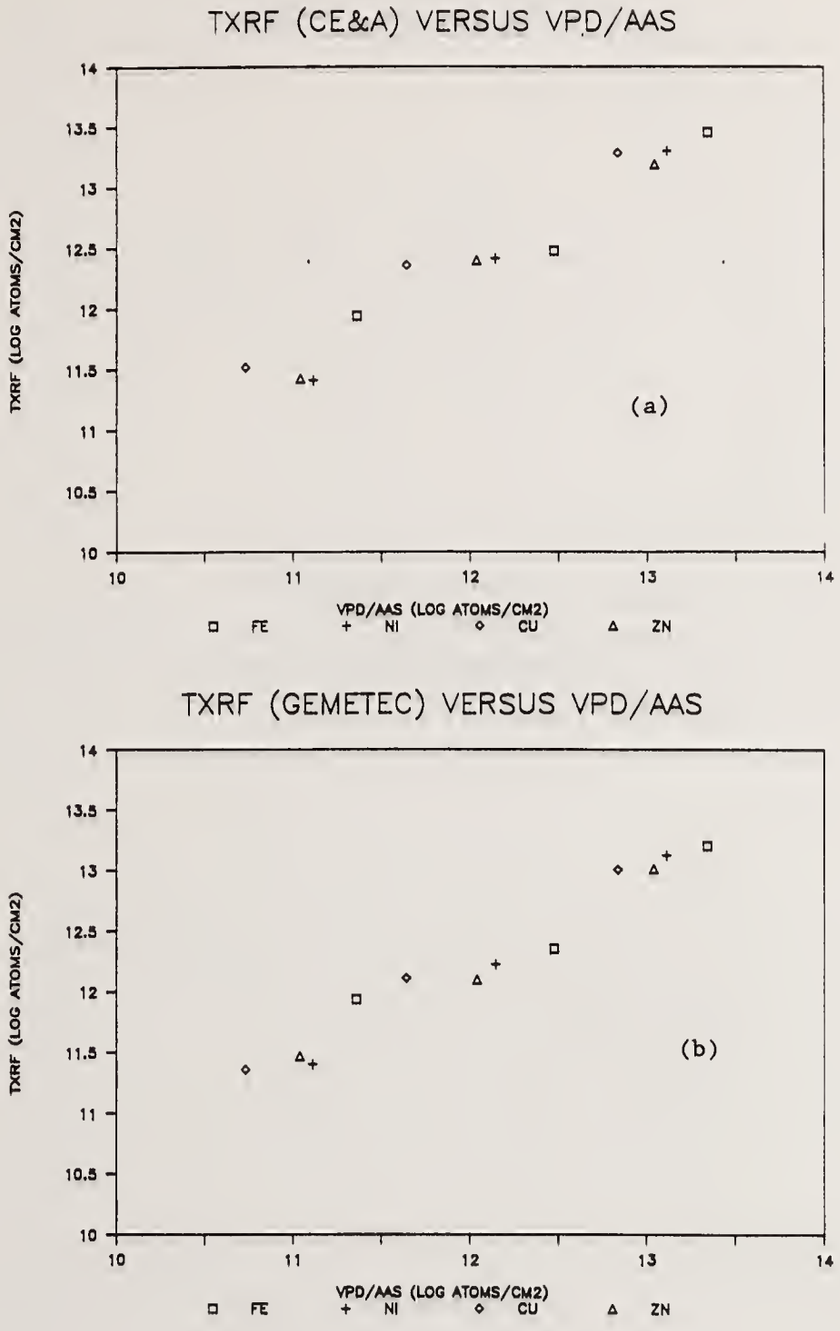

Fig. 5 Correlation between TXRF and VPD/AAS (Kyushu Electronic Metals Co., Japan) for Fe, Ni, Cu and Zn on spin-coated silicon wafers: (a) TXRF and wafers at Charles Evans & Associates, (b) TXRF and wafers at GeMeTec (Munich, West Germany). The spin coating and VPD/AAS were done by Kyushu Electronic Metals Co., Japan. The TXRF instruments were Perkin-Elmer XSA-8000.

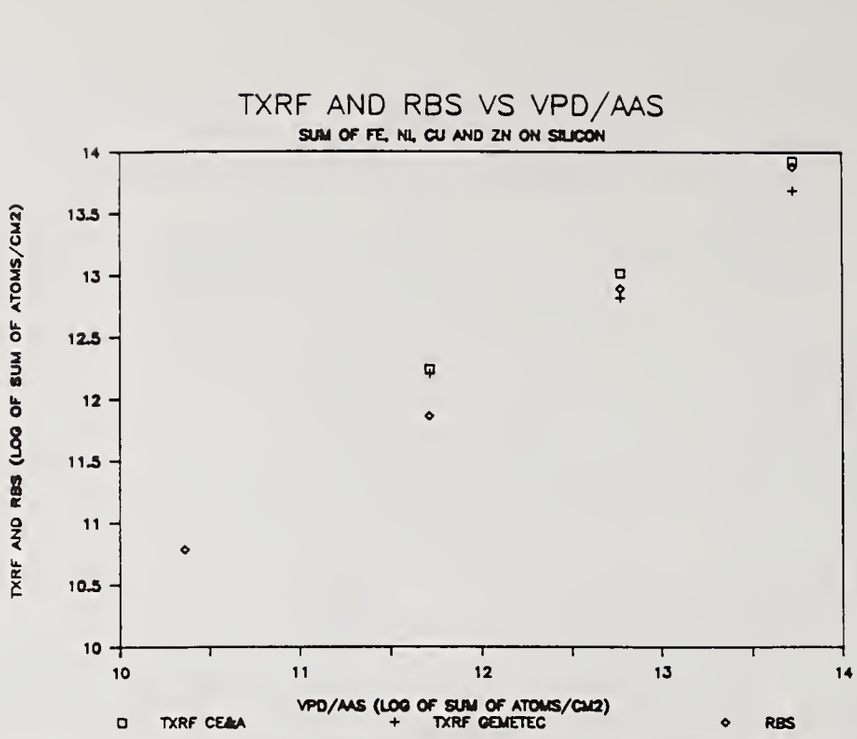

Fig. 6 Correlation between TXRF (Charles Evans & Associates and GeMeTec), RBS (GeMeTec), and VPD/AAS (Kyushu Electronic Metals Co.) for summed Fe, Ni, Cu, and Zn contamination on spin-coated silicon wafers.

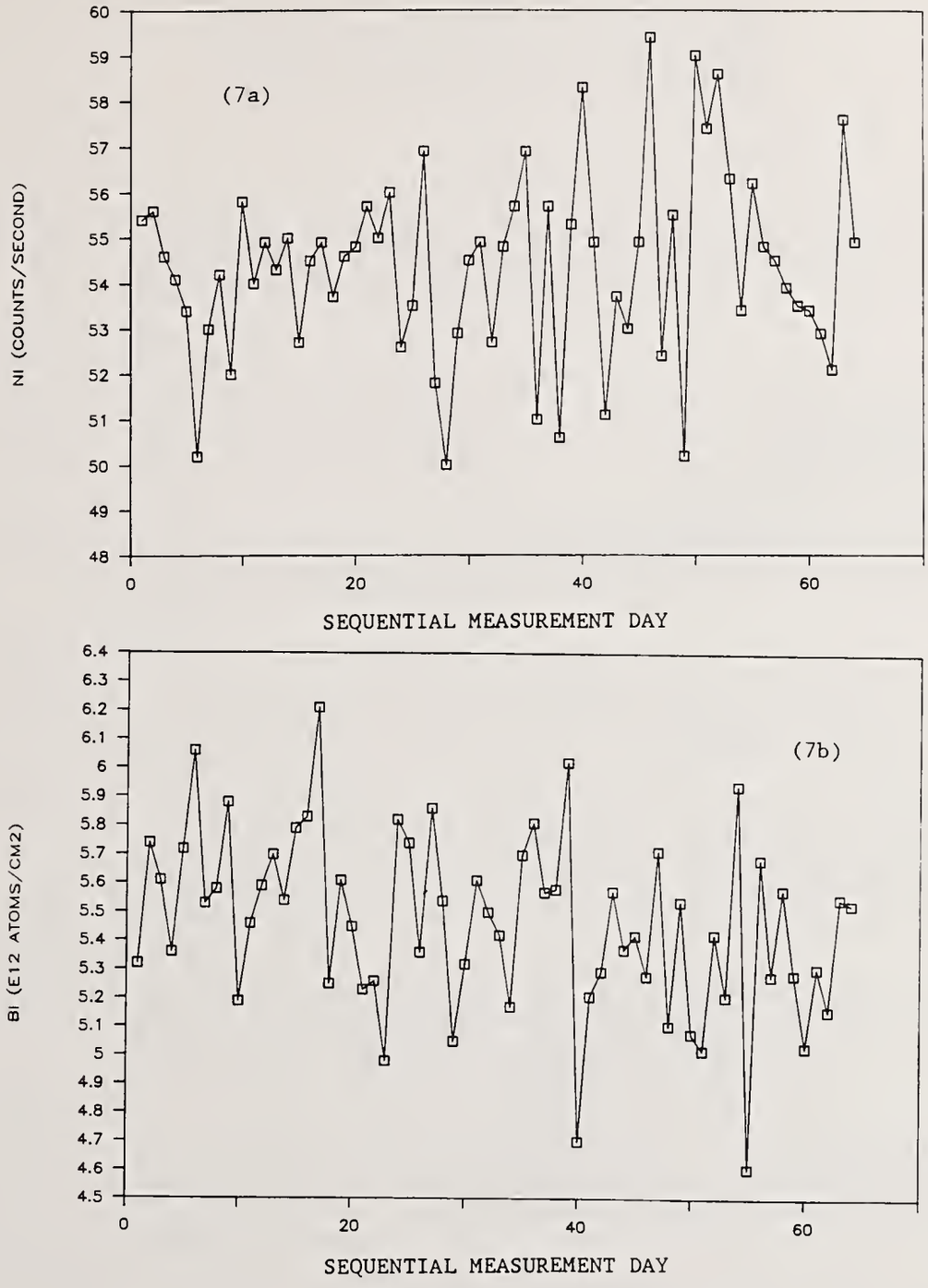

Fig. 7 TXRF signals versus measurement day over 3 months for residue-contaminated calibration wafer: (5a) counts/sec for Ni standard (1 ng Ni) tracks x-ray power; (5b) measured Bi atoms/cm^2 tracks high energy calibration. (50 sec integration, 30 kV, 60 mA, air, 200 micron Mo filter)

Fig. 8 TXRF areal density (atoms/cm^2) versus measurement day over 3 months for prime silicon wafer: (6a) Cu tracks angle calibration; (6b) Fe tracks detection limit; (6c) Zn tracks energy resolution. (700 sec integration, 30 kV, 60 mA, air, 50 micron Mo filter).

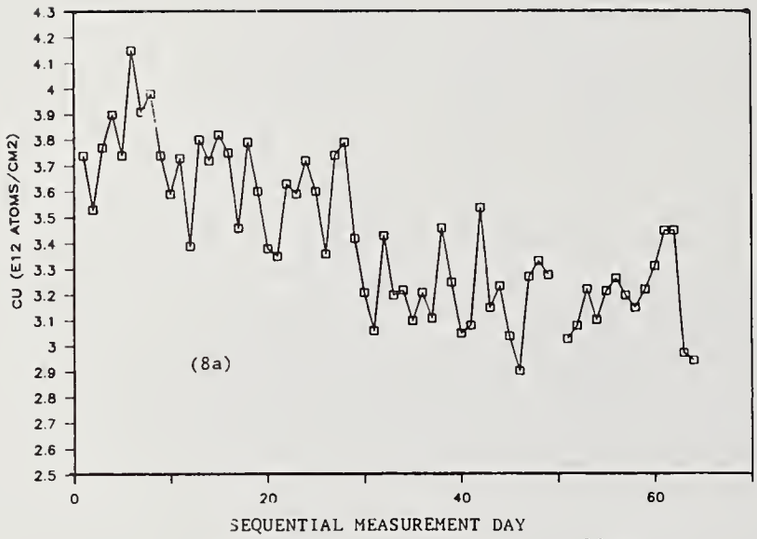

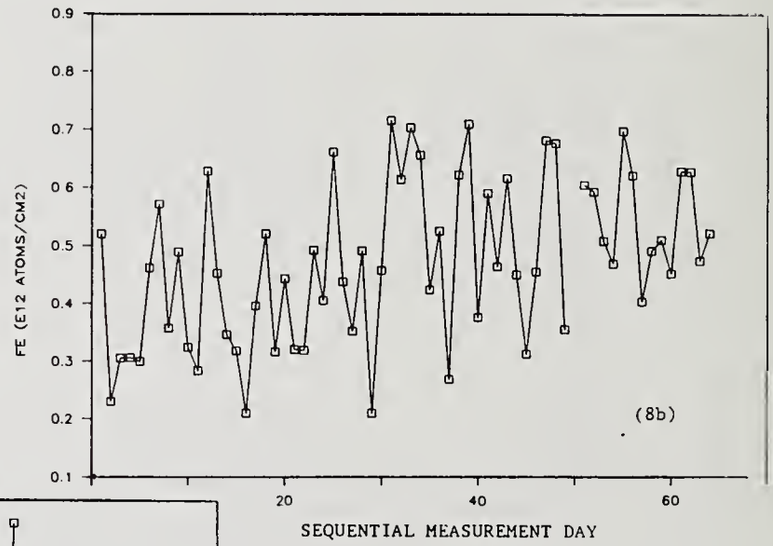

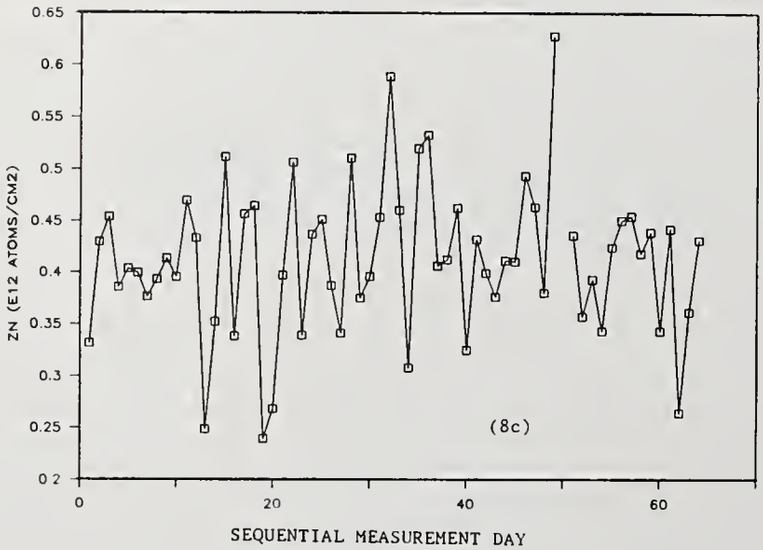

COMMENTS

Question: When you were running along the raster of preconditioning, did you ever encounter anomalously weak sites that failed in the preconditioning process itself?

Answer: No.

Question: First question is how many samples of each species did you test?

Answer: The data was from the average of two to three samples for each raster program, and the results were comparable to within about 15%

Question: The other thing is, have you done any preconditioning in other than an air environment, say in vacuum or nitrogen or hydrogen or forming gas or anything like that?

Answer: No.

Question: Do you have a rough idea of how high the temperature gets at the surface when you do the conditioning? Is it like 200°C is it like 500°C?

Answer: From looking at the older NOAA films which have damage, you can see that the particles back down onto the surface of the mirrors. The particles are in some cases spheres, which indicates that the films did in fact melt. And Fluoresced, too, which is the lower melting component of the films, I think that melting temperature is about 1800°C.

Question: In your electronic defects model I assume that the defect states before and after preconditioning are the same - you don't create any new ones or you don't destroy any old ones? The only thing changing is the population of the deep levels, right?

Answer: Yes. We're not expecting that the preconditioning illumination is strong enough to create or destroy states. It's been shown that with UV illumination you could change the actual defects involved, but not a lot of work has been done to study these defects at 1 micron.

Question: With regard to your postulated deep level defects, if you are changing the charge state of these defects, then you might expect a metastable situation. How long would you expect preconditioning to last before the defect states might return to the original charge state?

Answer: Well, I think that the metastable state exists when the defects are charged. It's been shown by, I believe, Schwartz and Hughes at the University of Houston. He's used EPR to look at SiO_2 films put down by several different techniques, and the less equilibrium

techniques, like E-beam deposition or R sputtering, show that these states were filled. The equilibrium techniques, like high-temperature CVD, showed that those defects were empty. So I think that the films that we're looking at were nonequilibrium to start with, and the conditioning is moving them toward equilibrium. So they shouldn't revert back.

Question: It is well-known that for wide-band gap uncoated materials, the same action of multiple-shot laser radiation leads to reduction of the damage threshold instead of the increase that you observe for your thin films. One possible idea is that you are creating electronic states which promote the damage threshold.

Answer: I think maybe the key difference here is, again, the wavelength of the illumination. What you're talking about, is that at 1 micron or at some higher energy photon?

Question: Well, observations like this have been observed at 1 micron as well as higher photon energies. So for example, we measure at half the wavelengths of 500 nanometers, which is not so short wavelengths, anyway.

Answer: You can't just generalize. We're not proposing that the mechanism that we're proposing here is a general conditioning mechanism for all materials.

Question: But the uncoated materials are just behaving the opposite way.

Answer: Uh-huh. Well, it's definitely possible that we might be also creating further defects, but with these dielectric films, we're not seeing a decrease in the threshold. We're seeing only an increase.

Comment: M. J. Soileau, University of Central Florida: I might say that it is not a universally observed fact that preconditioning of wide-band gap dielectrics lowers the threshold. I've done countless experiments myself where we've seen the same effects reported in this paper with uncoated dielectric surfaces. You radiate at low intensities and then you have an increase in damage threshold. Its not universally observed that the damage threshold decreases. In fact, there are good examples where the same results reported here are seen.

Question: Is the fact that you didn't see any conditioning with the xenon lamp somewhat inconsistent with your hypothesis of electronic defects?

Answer: I think the key difference there is probably the fact that you're also hitting the sample with UV photons at the same time. It's been shown for silica films that if you illuminate them with UV radiation, you fill those defects. And so, we're trying to condition with both UV and IR radiation at the same time. And we're not going to see any effect.

Comment: I might say we did some experiments on bulk zirconia, where we were, by multiphoton absorption, populating defects. And there were lots of them so you could measure their absorption and then could easily remove them at lower radiance, multiple shots at lower radiance, removing carriers from those defects. I think there are some close parallels to the model that you're proposing there. I might just add, it's a very complicated process. You've got a multiphoton process to generate defects and perhaps single-photon process to remove them. And with a wide-band source, you could have lots of things going on simultaneously.

MANUSCRIPT NOT RECEIVED

An Error Analysis of the Wyko TOPO Noncontact Surface Profiler

Van A. Hodgkin

Physics Division, Research Department
Naval Weapons Center, China Lake, CA 93555-6001

ABSTRACT

An increasingly important tool in the characterization and measurement of optical materials and components in the Wyko TOPO Noncontact Surface Profiler. Optically, it consists of a low- to medium-power microscope in which the objective, depending upon the power, is a visible light interferometer of either Michelson, Mireau, or Linnik design. By integrating a detector array into the viewing system and attaching the reference arm of the interferometer to a piezoelectric transducer, the technique of surface profiling by phase shifting is accomplished by computer.

The potential utility of this system to the investigator interested in the fundamental mechanisms of laser-induced damage is enormous, provided that the user is aware of its proper use and limitations. This paper is intended to act as a user's guide to the TOPO system in such cases and to document its precision and accuracy limitations given a variety of surface types and measurement configurations.

MANUSCRIPT NOT RECEIVED

Ultra-Precision Grinding of LHG-8 Laser Glass and Laser Damage Thresholds

Y. Namba

Chubu University
1200 Matsumotocho, Kasugai
Aichi 487, Japan

K. Yoshida, H. Yoshida, and S. Nakai

Institute of Laser Engineering
Osaka University
2-6 Yamadaoka, Suita
Osaka 565, Japan

ABSTRACT

It has been very important to reduce the machining cost of optical materials in the laser fusion program. LHG-8 laser glass was ground with the ultra-precision surface grinder having a glass-ceramic spindle of zero-thermal expansion in order to remove or shorten the optical polishing process in manufacturing high power laser optics. The laser damage thresholds were measured at 1 ns and 30 ns in pulse width and 1.053 μm in wavelength on ground surfaces as well as optically-polished surfaces. 0.5 nm rms in surface roughness was measured on the ground surface with WYKO's TOPO-3D. The laser damage thresholds on the ground surface were very similar to that on the optically-polished one.

Manuscript received
3-2-90

Low Scatter Surfaces on Silicon Carbide

Roger A. Paquin and Matthew B. Magida

Hughes Danbury Optical Systems, Inc.
Danbury, CT 06810-7509

Reaction bonded silicon carbide (RB SiC) can be readily fabricated to near net shape and mirror blanks produced by this method can potentially be less costly than those fabricated by chemical vapor deposition (CVD). However, RB SiC is two phase, SiC and up to 30% silicon (Si), and can not normally be directly polished to low scatter and roughness levels due to the difference in hardness of the two phases. We have investigated the polishability of RB SiC as a function of Si content and microstructure. Our results show that with a favorable microstructure, RB SiC can be polished to less than 10Å rms. For reduced roughness and lower scatter surfaces, we have developed low temperature deposition techniques to apply polishable, single phase coatings to the figured two phase surfaces. Scatter and roughness measurements show levels are comparable to CVD SiC.

KEY WORDS: BRDF; coatings; finishing; grinding; ion assisted deposition; ion beam sputtering; low scatter; microstructure; mirrors; polishing; reaction bonded silicon carbide; silicon; silicon carbide; surface roughness.

1. Introduction

Silicon carbide (SiC) is an excellent material for laser mirrors primarily due to its superior properties relative to other often used mirror materials. Table 1 shows that the various forms of SiC have low thermal expansion, high thermal conductivity, very high mechanical properties and high transition temperature. These properties lead to distortion coefficients that compare favorably with the low expansion dielectrics, while far exceeding them in fracture strength. For cooled mirrors, SiC is superior to molybdenum (Mo) in both thermal and mechanical properties.

As shown in the table and in figure 1, there are a number of types of SiC. Chemically vapor deposited (CVD) SiC is a pure form of the cubic beta phase that is grown on a mandrel and has a columnar grain structure. It has been polished to super low levels of scatter and roughness. There are no fully dense and pure forms of hexagonal alpha SiC, since it requires about two percent of additives such as boron and aluminum to achieve full density. Both CVD and alpha are difficult to form into complex shapes. Reaction bonded (RB) SiC is a polycrystalline two phase material consisting of interpenetrating networks of silicon (Si) and alpha SiC. The Si content can range from twelve to forty percent. Reaction bonded SiC can readily be formed into complex mirror shapes and can be polished to reasonably low roughness and scatter levels. The major reason that RB SiC has not been used more extensively is that the mirror surface, when polished by conventional methods, exhibits a topologically differential microstructure. This

is shown in figure 2, where the Si phase is 300 to 700Å below the level of the SiC.

Table 1. Selected Mirror Material properties* at 20°C

Material	a 10^{-6}/°C	k W/cm-°C	E GPa	p g/cc	F MPa	T °C	a/k 10^{-6}cm/W
CVD SiC	2.5	1.10	445	3.21	>200	1300	2.3
Alpha SiC	3.2	1.40	435	3.22	>300	1800	2.3
RBSiC (30%Si)	2.64	1.58	324	2.93	>200	1400	1.7
RBSiC (12%Si)	2.68	1.75	386	3.11	>200	1400	1.5
ULE	0.008	0.013	67	2.21	7	800	0.6
Zerodur	0.015	0.016	92	2.53	10	500	0.9
Molybdenum	5.0	1.40	324	10.21	400	500	3.6
Beryllium	11.4	1.93	287	1.85	280	500	5.9

*a-coefficient of thermal expansion; k-thermal conductivity; E-elastic modulus; p-density; F-fracture strength: modulus of rupture except 0.2% yield strength for Mo and Be; T-transition temperature: highest usable temperature for optics, in protective atmosphere and exclusive of optical coatings.

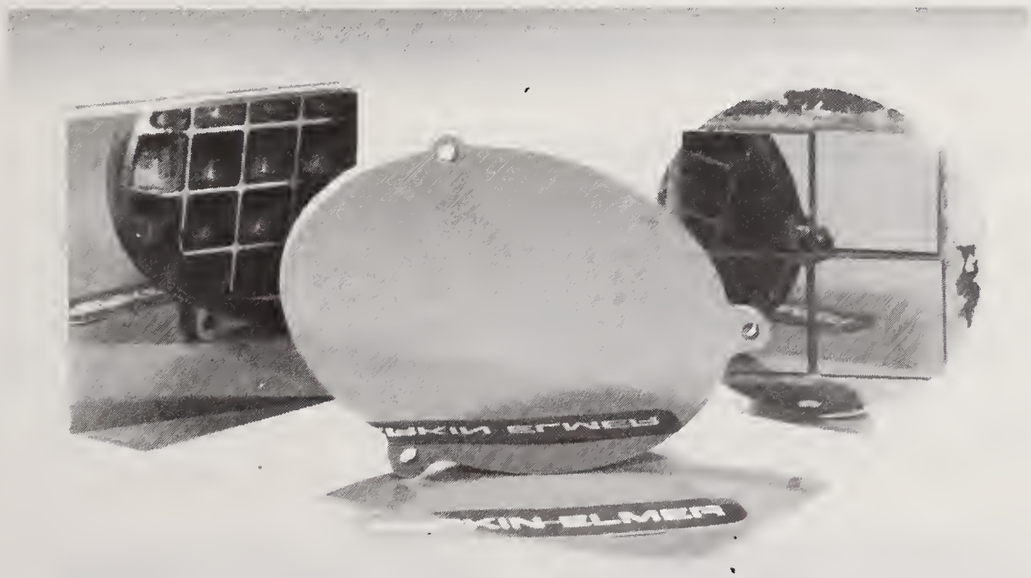

Figure 1. Silicon carbide substrates, formed by three different processes, shown polished: (a) square hot pressed alpha SiC; (b) lightweight isoformed reaction bonded SiC (alpha SiC + Si); (c) four squares of CVD beta SiC.

Given this limitation, we decided to investigate this promising new mirror material because of the following factors: (1) near net shape capability of RB SiC fabrication methods that allows the formation of internal cavities, such as used in heat exchanger mirrors, (2) the potential for

modifying the microstructure for better polishability and (3) the potential for ultra-low scatter by overcoating with a polishable SiC coating to bury the two phase microstructure, as we have successfully demonstrated with beryllium [1].

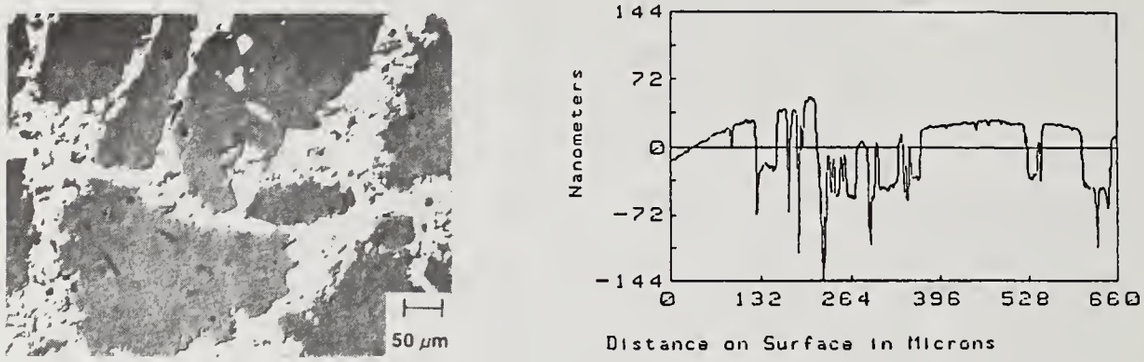

Figure 2. Microstructure and Wyko surface profile for polished reaction bonded silicon carbide mirror specimen showing step heights of 300 to 700Å at phase boundaries.

2. Experimental Approach

We concentrated our investigation in two areas: (1) substrate finishing, including substrate material effects and processing approaches, and (2) coatings for ultra-low scatter. The techniques developed were used to demonstrate low scatter surface finishing. These topics are described in the following sections.

2.1. Substrate Finishing Development

During our investigation we worked with a number of different microstructures. We varied the Si content and at a given Si level, varied the grain size and grain size distribution of the SiC as described previously [2]. Typical microstructures are shown in figure 3 for a monomodal SiC grain size in a 30% Si material, and a multimodal distribution with 12% Si. Our optical fabrication experiments were carried out using a number of lap materials, grinding and polishing abrasive grits and fluid media, while varying the applied pressure and relative velocities.

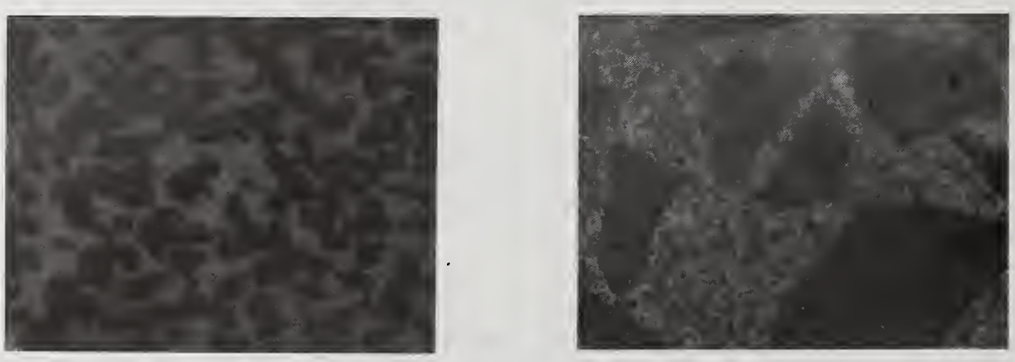

Figure 3. Microstructures of reaction bonded silicon carbide (SiC): (a) 30% silicon (Si) with monomodal SiC grain size distribution, (b) 12% Si with multimodal SiC distribution.

2.2. Silicon Carbide Coating Development

Coatings that are normally applied to RB SiC to obtain low scatter finishes include CVD SiC and PVD Si. The CVD SiC is deposited at elevated temperatures, in excess of 1000°C, and yields a polycrystalline beta (cubic) material with fine columnar grains. The Si can be deposited using any of several physical deposition methods such as evaporation from thermal or electron beam sources. The Si can be either polycrystalline or amorphous depending on deposition conditions. The Si can be finished to very low scatter levels but has a mismatch in properties with SiC.

We chose to investigate processes that utilize ion beams for higher energy deposition to deposit pure SiC at or near room temperature. The higher energy results in better adhesion, lower defect concentration, higher packing density for near bulk properties and reduced residual stress, and broad substrate applicability. We investigated two of these methods, shown schematically in figure 4, ion assisted deposition (IAD) and ion beam sputtering (IBS). For the former, an electron beam is used to evaporate pure alpha SiC chunks while an argon ion source bombards the substrate. For the latter, the argon ion beam sputters SiC from a CVD target onto the substrate. In IAD, the ions add energy to the arriving atoms, while with IBS, the sputtering mechanism results in SiC with high kinetic energy.

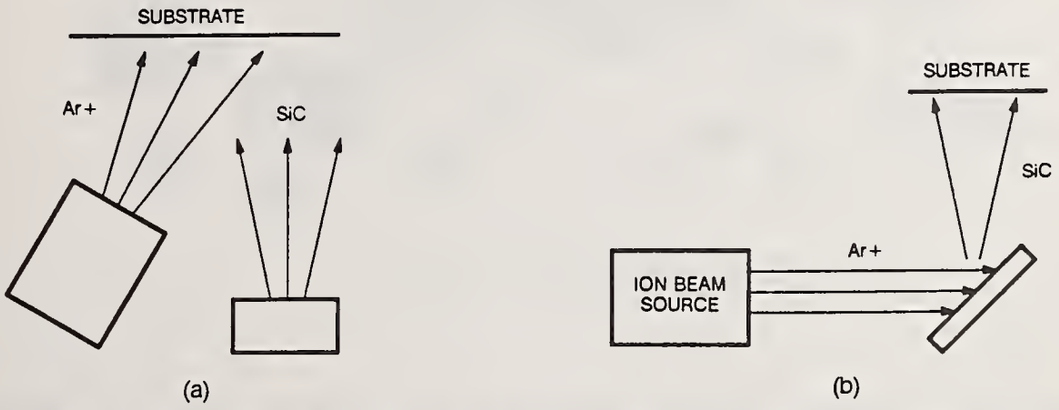

Figure 4. Low temperature silicon carbide coating methods: (a) argon ion assisted electron beam evaporation, (b) argon ion beam sputtering.

2.3. Polishing Demonstration

To demonstrate the low scatter polishing methods developed during the program, bare and SiC coated 76mm flat and 152mm spherical mirrors were prepared in addition to the 25 and 38mm diameter flat mirrors. Some of these mirrors are shown in figure 5.

3. Results

We developed a baseline optical finishing process similar to that of Fuchs and Brown of LLNL [3], in which grinding and figuring are carried out on metal/epoxy composite laps with successively finer diamond grits with water and diamond extender, while polishing utilizes pitch with sub-micron diamond. We were able to achieve figures of better than 0.1 visible wave without difficulty on all of the 25 and 38mm flats. Achievable surface

roughness, as measured by Wyko, was dependent on the microstructure. On 30% Si material, we were able to achieve 20-30Å rms with large grain monomodal grains, 15Å with fine monomodal grains, as shown in figure 3a, and 15Å with a multimodal grain size distribution. When 12-15% Si RB SiC was polished, the multimodal grain distribution yielded surfaces with roughness less than 10Å rms. This investigation shows that low scatter and roughness (<10Å rms) mirror surfaces can be produced on RB SiC with tailored microstructures. A preferred microstructure with reduced Si content and fine multimodal grain size has been shown for RB SiC.

Figure 5. Silicon carbide substrates of various sizes and shapes which have been optically finished to demonstrate our low scatter finishing process. Shown are 25, 38, 76mm diameter flats, 152mm diameter spheres and a 254mm oval shaped targeting mirror blank.

Coating deposition experiments were carried out to determine optimum parameters for the two techniques and to evaluate differences between coatings produced by the two methods. We found that in our initial approach involving IAD, we were unable to identify a combination of parameters that would repeatedly produce smooth, stoichiometric SiC. Parameter ranges investigated included: coating thicknesses from <1 to >5 microns; ion assist levels from zero to the sputter regime; substrate temperature from 30 to 200°C; and source material of high purity alpha chunks to a CVD plate. Although good adhesion was achieved, the coatings contained high defect densities (associated with spatter) and were typically off-stoichiometry, being Si deficient.

In our alternate approach, ion beam sputtering, we were more successful. Defect free, stoichiometric, amorphous coatings up to six microns thick

]were deposited. While the coatings were readily polishable to very low roughness and scatter levels, some compressive stress was observed in the coatings. We are continuing our investigation in an effort to eliminate this stress.

The results of our polishing efforts on bare and coated samples are shown in table 2 and figure 6. The data represent the best sample mirrors measured to date. The 12% Si material, called reaction bonded in the figure, has significantly smaller surface roughness and lower scatter than the 30% Si material. The BRDF at one degree is very low for this two phase material. While not described peviously, we polished some CVD SiC which has much lower BRDF than the best RB SiC, but note that the Wyko roughness falls between the two bare materials. The IBS coating however has the lowest numbers for both scatter and roughness, and in fact, is the lowest scatter surface ever measured in our laboratory. The variance between roughness and scatter data is similar to that observed for beryllium, and is the subject of investigations in our laboratory and others. If overcoated with an opaque metal film, the scatter, but not necessarily the roughness, should drop. The two phase RB SiC should show the greatest change. This study is a subject for future presentations.

Table 2. Summary of SiC Surface Quality Results for Bare and Coated Surfaces

Material	Roughness* Å rms	BRDF Slope 1° to 10°	BRDF at 1° from slope
30% Si	9.4	-2.4	1.3 E 0
12% Si	5.8	-1.1	8.4 E-2
IBS Coating	2.9	-1.8	3.3 E-3
CVD Coating	8.2	-1.3	7.4 E-3

* Roughness measured by Wyko

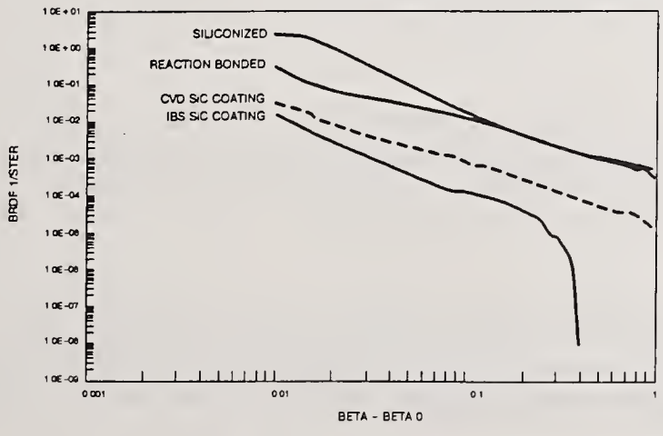

Figure 6. Bidirectional reflectance distribution function (BRDF) measurements at 633nm comparing polished bare and coated silicon carbide. Siliconized is 30% Si and reaction bonded is 12% Si.

The polishing and IBS coating processes have been applied to 152mm diameter spherical mirrors with radius of curvature of 610mm, fabricated from 12% Si reaction bonded SiC. To date, one-tenth wave figure has been achieved on bare surfaces, and two mirrors have been IBS coated with approximately four microns of amorphous SiC. Surface roughness and scatter measurements have not yet been performed on the bare mirrors and the coated ones are not yet polished.

4. Conclusions

In this experimental program we have shown that reaction bonded silicon carbide is a viable laser mirror material when the silicon content is low (22-15%) and a multimodal, small, SiC grain distribution is employed. This preferred material is polishable to 10Å rms with one-tenth wave or better figure using diamond slurries on pitch laps after grinding and figuring with diamond on composite laps.

We have developed an ion beam sputtering process for overcoating the polished RB SiC with amorphous SiC that can be polished to ultra-low scatter and roughness (<5Å rms) levels.

The processes described in this paper are scaleable to complex shapes, aspheric surfaces and to very large sizes.

This work was performed with Hughes Danbury (formerly Perkin-Elmer) IR&D funding. We acknowledge the continuing support of Gerry Weaver, Carborundum Specialty Products, in the development of the SiC materials investigated in this program. We would also like to thank Max Bruckenthal of Hughes Danbury who performed all of the optical finishing.

5. References

[1] Paquin, Roger A.; Gardopée, George J.; Peterson, James "Hot Isostatic Pressed Beryllium Mirrors," in Proceedings of the Topical Meeting on High Power Laser Optical Components, Hopkins, Alan, ed. 1987 October 29-30; Boulder, CO. Weapons Laboratory, AFWL-CP-88-01, 1988 May. Pp 23-32.

[2] Magida, Matthew B; Paquin, Roger A. "Silicon Carbide Mirror Surface Technology," in Proceedings of the Topical Meeting on High Power Laser Optical Components, Stanford, James L., ed. 1988 October 24-25; Boulder, CO. Naval Weapons Center, NWC TP 7017 Part 1, 1989 July. Pp 52-58.

[3] Fuchs, B. A. "Removal Rates, Polishing and Subsurface Damage of Chemical Deposited Silicon Carbide," presented at the OSA Workshop on Optical Fabrication and Testing, 1987 October 20-23; Rochester, NY.

Manuscript received
12-29-89

PHYSICAL LIMITS ON ULTRA-HIGH ALBEDO DIFFUSE REFLECTORS

Perry Miles, R & D Associates
Marina del Rey, CA

1.0 INTRODUCTION

While the theoretical possibility of achieving near-perfect diffuse reflectance in a purely scattering material is longstanding[1], no attempt seems to have been made to develop scatterers with albedos of 0.999 and beyond. Such ultra-high albedo diffuse scatterers are now of interest because they offer the possibility for the development of shields against high levels of laser radiation[2].

The simple two-stream model[3] for a thickness, L, of such a material gives an albedo:

$$A = \frac{k_s L(1 - R) + 2R}{k_s L(1 - R) + 2} - k_a L \left[1 + \frac{2R}{k_s L(1 - R) + 2}\right], \quad k_a \ll k_s$$

where k_a describes attenuation by absorptive processes and k_s describes the total scatter, assumed to be equal, forward and reverse, per unit length (volume) of material, and where, for the sake of simplicity, we have ignored the Fresnel reflection at the front surface, but have included a rear surface reflection R to take into account the effect of any opaque substrate material such as a metal plate. For all practical values of substrate reflectance ($R < 0.95$), and for $k_s L > 10^3$, we may use the approximation

$$A = 1 - \frac{2}{k_s L} - k_a L$$

Accordingly, the achievement of A = 0.9999, in a 1 cm thick plate, for example, calls for a scatter coefficient, k_s, greater than $2X10^4$ cm^{-1} together with a residual absorption coefficient, k_a, less than 10^{-5} cm^{-1}. The issues for this paper are first, whether such levels are achievable, even at low irradiance levels below 10^3 W/cm^2, and second, whether this performance can be preserved at time average irradiance levels above 10^4 W/cm^2 in pulsed wavetrains where the <u>instantaneous</u> irradiance levels may exceed 10^7 W/cm^2.

2.0 CANDIDATE MATERIALS

At first sight, these requirements seem attainable with careful attention to cleanliness in the preparation of the matrix material and in its treatment to develop a porous or other inhomogeneous structure. As we pointed out in Reference 2, inorganic glasses have already been developed for use in fiber optic transmission lines (Figure 1) with attenuation constants less than 1 db/km (2.3×10^{-6} cm^{-1}).

In some spectral ranges, these attenuation levels are dominated by <u>scatter</u> losses, which are not a limiting factor in the present context. Even OH impurity generated <u>absorption</u> can be kept to below 10^{-5} cm^{-1}, while the intrinsic (linear) electronic and

---

[1]Stokes, G.G., Proc. Roy. Soc. (London) <u>11</u>, 545 (1862)

[2]Miles, P., "Conceptual Bases for Ultimate Hardening Against CW and RP Lasers," AIAA/DNA Laser Effects and Target Response Conference, March 1988

[3]Schuster, A., Astrophys. J. <u>21</u>, 1 (1905)

Figure 1

(U) LOSS BREAKDOWNFOR AN ULTIMATE LOW-LOSS SINGLE-MODE FIBER

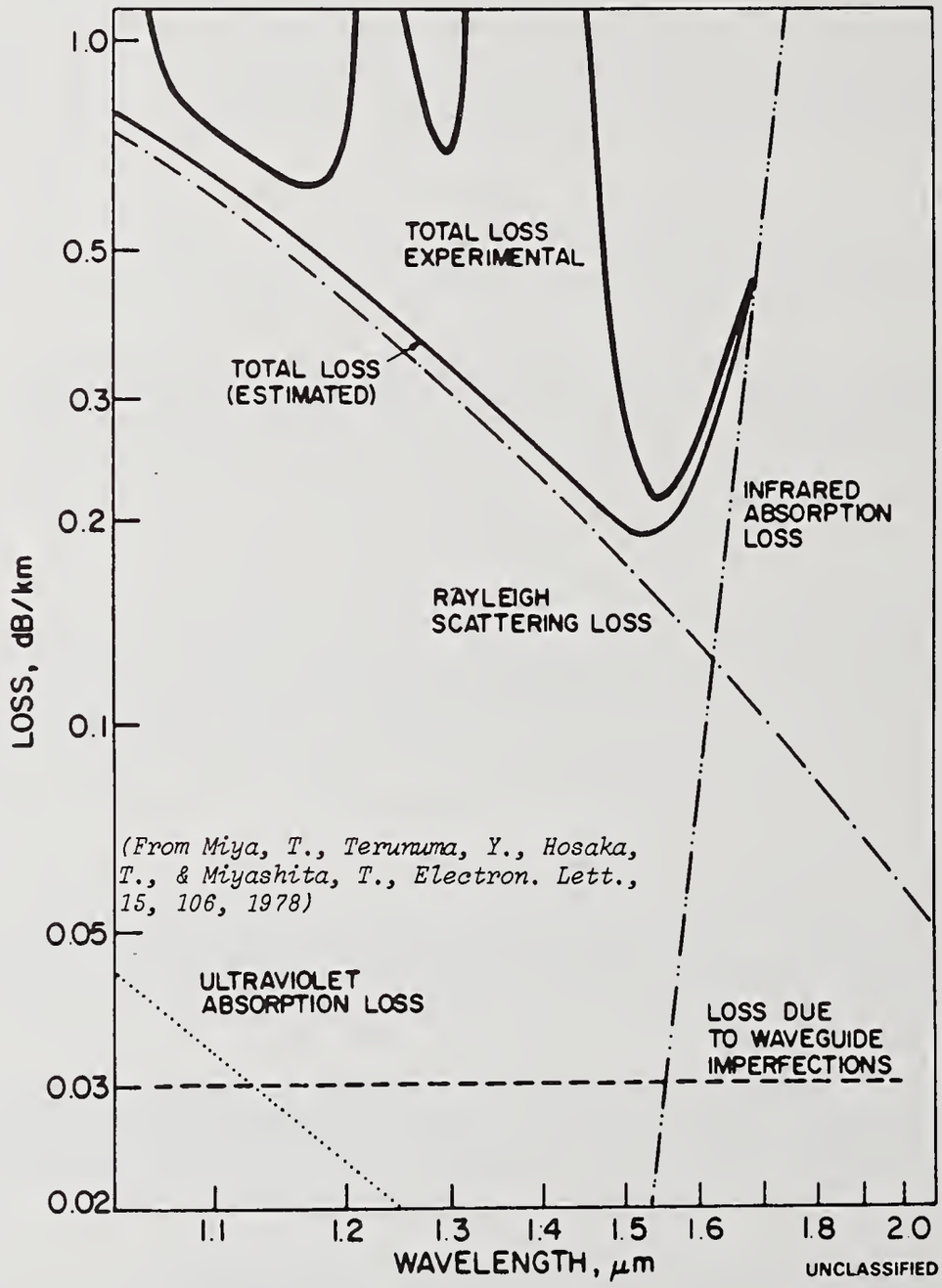

lattice phonon excitations may give absorption coefficients two orders of magnitude lower still--at least at room temperature.

At higher levels of heating, we are concerned both with changes in the optical properties of the matrix and with the possibility of thermally induced fractures. These are the same concerns that, in the past, have faced the designers and developers of window and lens elements for high power laser optical trains. It is highly likely, therefore, that the best materials for the UHA protective shields may well be scattering forms of materials already developed for those same high power laser weapon and IR optical components. Alkali halides, CaF_2, ZnSe, fluoride glasses, and possibly sapphire, spinel, fused silica, high purity forms of SiC, as well as the host glasses for Nd:glass laser components are all likely candidates.

Over the period 1970-1975, the absorption coefficients of fully dense forms of many of these materials were reduced by careful processing techniques[4] to levels so low that conventional transmission spectroscopy was unable to provide accurate measurements of absorption in the transparent spectral range between the visible/UV and IR absorption edges. In its place, a variety of vacuum calorimetric techniques were developed with sensitivities down to 10^{-6} fractional loss, both linear and non-linear, along with photo acoustic techniques with even greater sensitivities[5,6]. These same techniques will be needed to assess the quality of UHA materials.

3.0 LIMITS ON PERFORMANCE

Beyond the fundamental limitation imposed by the finite thickness of the scatter plate, the most obvious problem comes from residual absorption throughout the material. In fact, heating of the scattering material, either as a linear process or one accelerated by increases in the absorption coefficient itself, may set the limits on its ability to withstand high levels of incident laser radiation. Thus, an alumina scattering shield with an areal density 2 gm/cm^2, a specific heat of 1 J/gm/K and an albedo of 0.9999 would heat up at the rate of 5 X 10^{-5} I_0 K/s. For $I_0 = 10^5$ W/cm^2 this is 5 K/s or 200 K in 40 s. At $I_0 = 10^4$ W/cm^2, it would take 400 s to reach 200 K--even longer, if a deliberate attempt were made to transfer heat out of the irradiated area.

For pulsed irradiation, on the other hand, much higher temperature excursions would occur at absorbing impurity centers and in their immediate surroundings. For absorbing centers less than 1 μm in diameter, however, significant heat diffusion could extend to ten diameters from the center during pulse lengths greater than 10 ns, thereby reducing the maximum temperature excursion at the site itself. Apart from the well-known case of Pt inclusions in laser glasses[7], the specific origin of the damage threshold under pulsed irradiation of highly transparent materials has been an unresolved issue for many years. Recent work in the field[8] is shedding more light on the intrinsic nonlinear free carrier absorption and heating that precedes detectable damage in wide bandgap materials, but while intrinsic multiphoton excitation of carriers has been observed at UV and visible

---

[4]Miles, P., Opt. Eng. 15, 451 (1976)

[5]Hordvik, A., App. Opt. 16, 2827 (1977)

[6]Tam, A.C., Rev. Mod. Phys. 58, 381 (1986)

[7]Hopper, R.W., Uhlmann, D.R., J. App. Phys. 41, 4023 (1970)

[8]Chen, X.A., Jones, S.C., Braunlich, P.F., Phys. Rev. Letts. 62, 2711 (1989)

wavelengths[9,10], the initiation of damage in such materials at infrared wavelengths is still likely to be associated with impurities and structural defects.

The single pulse damage level for wide bandgap materials is of the order of 20 J/cm^2 in a 1 ns pulse, that is, at instantaneous irradiance levels of 2 X 10^{10} W/cm^2. Whether these levels will be achievable in scatterers is an open question.

The possible augmentation of the internal radiation field strength in the vicinity of micropores and microcracks--particularly in high index materials--was also pointed out long ago[11], and in the present case, where pores and scattering discontinuities are an explicit aspect of the material design, this effect can be expected to be of great importance. The preparation of external optical surfaces with fractional loss factors below 10^{-6} is rare and these residual surface losses are also assumed, though without proof, to be due to structural imperfections and the accumulation of absorptive impurities. It remains to be seen whether internal surfaces can be made any better. If they cannot, a material with a 10^{-6} loss every micrometer of path would result in a limiting albedo of the order of 0.99--the apparent present state-of-the-art[12], interestingly enough--and of no use as a high power laser shield.

Quite apart from the geometric intensification of the field at crack tips that might also be impurity sites, the question arises whether the internal surfaces or discontinuities themselves exhibit nonlinear behavior to a far greater degree than the bulk material. Indeed, the careful study of ultra-high albedo materials where the surface to volume ratio has been increased by many orders of magnitude over comparable solid, non-porous, materials may lead to new understanding of the optical properties of surfaces and interfaces per se.

4.0 SUMMARY

Past efforts to develop low loss, damage resistant window, lens and optical fiber materials provide the starting point for the development of near-zero absorption scatter reflective coatings. Designs can be envisioned with absorption coefficients less than 10^{-4} cm^{-1} and with external albedos greater than 0.999. Achievable limits of absorption will presumably depend on the same factors that determine the damage threshold for transparent laser optical components--namely residual impurities, intrinsic absorption mechanisms and non-linear responses to pulsed radiation. In particular, the linear and nonlinear optical properties of internal surfaces and interfaces may turn out to be the most important limiting factor for strongly scattering materials. Explicit studies of the properties of surface discontinuities may become essential.

5.0 ACKNOWLEDGEMENT

This work was carried out under the Defense Nuclear Agency's Contract Number DNA001-88-C-0046.

---

[9]Nathan, V., Guenther, A.H., Mitra, S.S., JOSA, B2, 294 (1985)

[10]Jones, S.C., Chen, X.A., Braunlich, P.F., Kelly, P., Epifanov, A.S., Phys. Rev. B 35, 894 (1987)

[11]Bloembergen, N., App. Optics 12, 661 (1973)

[12]Weidner, V.R., Hsia, J.J., JOSA 71, 856 (1981)

Manuscript received
2-8-90

Optical Damage on SiO_2 Cavity Mirrors Produced by High-Power VUV Laser Irradiation

Y. Takigawa

Department of Solid State Electronics, Osaka Electro-Communication University, Neyagawa, Osaka 572 Japan.

K. Kurosawa and M. Okuda

Department of Electronics, University of Osaka Prefecture, Sakai, Osaka 591, Japan.

W. Sasaki

Department of Electrical Engineering, Miyazaki University, Miyazaki 889-21 Japan.

K. Yoshida, E. Fujiwara and Y. Kato

Institute of Laser Engineering, Osaka University, Suita, Osaka 565 Japan.

Y. Inoue

R/D Engineering Department, Scientific Equipment Division, Shimadzu Co., Kyoto 604 Japan

We report observation results about damages on SiO_2 mirror surfaces. The damages were made when the mirrors were used as a cavity reflector for the Ar and Kr excimer lasers. The surface profile, transmission and reflectance spectra, and X-ray photoelectron spectra show that bulk Si is isolated in the surface layer which was exposed to 9.8eV photons from the Ar excimer laser. The Kr excimer laser, whose photon energy is 8.5eV, does not induce such a phenomenon. The Ar excimer laser photons, surmounting the fundamental band gap of SiO_2, 9eV, are considered to create high density excitons that induce the Si-O bond breaking and Si isolation.

Key words: VUV laser, rare gas excimer laser, quartz glass mirror, mirror damage, x-ray photoelectron spectroscopy.

1. Introduction

High-purity synthetic SiO_2 glasses are the most promising materials for mirrors, windows and lens in a wide spectral region from visible to ultraviolet (UV) wavelength. It has been observed, recently, that UV excimer lasers whose photon energies are higher than 5eV generate absorbing color centers in SiO_2 [1-2]. In addition to a fact that, in cases of ArF and KrF excimer lasers, two photons could surmount the fundamental band gap energy of 9eV [3], the resultant number of color centers follows a $(power)^2$ dependence, so that excitons that are created via a two-photon generation process is capable of creating color centers. Since the color centers created by the sub-band gap excimer laser radiation are the same types as those created by ionizing radiation such as X-rays, γ -rays or E-beams [4-5], the generating mechanisms are inferred to be the same.

We have been developing high power argon (Ar) and krypton (Kr) excimer lasers for applications to plasma diagnostics, photo-chemistry, lithography, and others [6-8]. On the course of the project, SiO_2 glass plate surfaces which were used as the laser cavity reflector, suffered damages (beam patterns) even at relatively low output power [9]. Apparently the surface temperature rises up beyond its melting point and the surfaces are observed to be roughened. In addition to the thermal effect, isolated Si was detected, when the mirrors were used for the Ar excimer laser [10]. The Si isolation is considered to originate from electronic excitation, because the photons of 9.8 eV must excite electrons from the valence band to the conduction band and generate efficiently electron-hole pairs. In this paper, we show observation results of the surface damages, which are induced by the Ar and Kr excimer lasers, with surface topography, transmission and reflectance spectra, and X-ray photoelectron spectroscopy. Discussion about the Si isolation mechanism is also described.

2. Electron Beam Pumped Rare Gas Excimer Lasers

Prior to the description about the laser induced damages, we should note the high-power rare-gas excimer lasers as illustrated in figure 1. High purity Ar or Kr gas was filled in a stainless steel pipe of 5 mm diameter, 80 cm length and 80 μ m thickness. This pipe acted as an anode for an electron beam accerelated at 700 kV. The laser cavity, located at both ends of the anode pipe, was composed of a SiO_2 glass reflector and a MgF_2 output coupler. The output mirror had 63% transmittance and 8% reflectance at 126 nm. The output energy of the laser beam of 5 mm in diameter, which was came out through the output mirror and window of MgF_2, was measured in vacuum. The surfaces of the SiO_2 reflector were observed to be suffered damages even when the laser output energy was relatively low, around 5 mJ. The energy stored in the cavity was calculated from the laser output energy by taking account of the transmittance of the output mirror and window. The energy was considered to correspond to that in front of the mirror surface. It should be noted, furthermore, that clear beam patterns with 5 mm diameter were observed even by only one shot, and that the patterns became clearer by multiple shots. In this paper, we observed the beam patterns made by 2 - 5 shots of the Ar or Kr excimer laser, which provides the output energy of about 10 mJ.

3. Observations of Mirror Damages

3.1 Surface topographic observations

The beam patterns were observed clearly with naked eyes and also with an optical microscope. The scattered light by the surface roughness probably enables us to see the beam patterns, but since their contrast was very faint, we could not show you clear photos. The beam patterns were more clearly seen by using a surface topographic method, as shown in figure 2. These were taken with an optical interferometric profilemeter (Wyko Co., NCP-1000). The peculiar feature of the beam patterns is wrinkles along the peripheral, that is, remarkable ripples near the edges are observed. Such features are observed for both of the laser radiation. The surface temperature was estimated to be far beyond the melting temperature by the 10 mJ laser radiation. Therefore, it seems us that the molten layer moves toward the peripheral of the beam pattern and the wrinkles were formed along the edges.

3.2 Optical properties

In order to have more detailed insight into the observed damages, we have taken transmission and reflectance spectra of the SiO_2 mirrors in the visible to VUV regions using synchrotron radiation [11]. Figure 3 shows the transmission spectra, in which curve (a) is taken from a non-irradiated part of the mirror, curve (b) from the Ar excimer laser induced damage, and curve (c) from the Kr excimer laser induced damage. The tramsmittance just above the optical band gap wavelength decreases significantly for both of the laser induced damages. This is probably partly because of the surface roughness enhanced by the laser radiation.

Figure 4 shows the reflectance spectra of the mirror, in which curve (a) is taken from a non-irradiated part, curve (b) from the Ar excimer laser induced damage, and curve (c) from the Kr excimer laser induced damage. In curve (a), there appear four distinct peaks, at 10.4, 11.7, 14.0, and 17.3eV, which are assigned to transitions between s-p hybrid orbitals with Si-O bonds [12]. In curve (c) four peaks still appear besides for slight decreasing of the reflectance. However, in curve (b), their peaks become very weak and almost disappear. This result indicates that Si-O bonds are broken in the surface layer of the SiO_2 mirror due to high power Ar excimer laser irradiation. In addition to the peak disappearance, the reflectance spectrum from the Ar excimer laser induced damage (curve (b)) has found to have a peculiar feature. The reflectivity in the UV region becomes significantly enhanced and has a broad peak around 200nm. With respect to the profile of the spectrum is concerned, the spectrum resembles that of bulk Si [13]. If bulk Si is isolated in the surface layer of the Ar excimer laser induced damage, it is explained well that the reflectance peaks disappear and also that the reflectivity increases in the UV region. It should be pointed out here that such a phenomenon has not been observed in the Kr excimer laser induced damages.

3.3 X-ray photoelectron spectroscopic studies

For studying such phenomena, one of the most promising methods is X-ray photo-electron spectroscopy (XPS), which provides an information about chemical bonding

nature. An ordinary XPS analysis offers only an average value over the exposed area by X-ray radiation. Sometimes spatially resolved spectra are required. Several techniques for this purpose have been offered and realized. Yamaguchi et al. have developed an electromagnetic lens system which collects the photoelectron and also which makes focused beam onto an entrance slit of the photoelectron energy analyzer [14]. By using an appropriate aperture at the slit, photoelectron coming from a selected area is analyzed. The smallest area analyzable is about 0.20mm in diameter onto the sample surface. It is interesting furthermore that a precisely controlled X-Y stage for the sample holder is installed and thus two-dimensional images have become possibly obtained. In this paper, we used MgK α emission at 1253.6 eV for the excitation and the electron energy was analyzed by a 180 ° hemispherical electron energy analyzer.

X-ray photoelectron spectra were taken from several different points at intervals of 1mm along a line including two beam patterns induced by the Ar and Kr excimer lasers. In figure 5 are shown the respective XPS spectra. Curves 4 to 9 are taken from points in the Ar excimer laser induced beam pattern, and curves 11 to 16 from points in the Kr excimer laser induced beam pattern. The others are from non-irradiated area. The strong peaks, which are seen in all of the spectra, are assigned as the Si-2p emission in SiO_2 glass, because of the binding energy of 103.4 eV. In addition to their peaks, a relatively small peak appears only in the spectra 4 to 9. Its binding energy is 99 eV and thus it is identified as the Si-2p emission of bulk Si. It is worthwhile at this stage that Si-O bonds are broken and thus bulk Si appears macroscopically in the surface layer of the SiO_2 glass due to the strong Ar excimer laser irradiation but not due to the strong Kr excimer laser irradiation.

With the precisely controlled translational stage, two dimensional distribution of photoelectrons having a given binding energy is obtained. Figure 6(a) shows such an image taken with 103.4 eV emission of Si-2p in SiO_2 glass. The brighter spots in the figure indicate the higher density of the photoelectrons emitted from them. On the other hand, the darker spots correspond to them with the lower density. In this figure, all surface area except for the circular area in the left hand side of this figure is seen in white, which indicates that SiO_2 is the predominant species in this area. On the other hand, in the circular area, relatively small amount of SiO_2 is included. Figure 6(b) shows another image taken with 99 eV emission of Si-2p in bulk Si. This figure shows that bulk Si is included only in the circular area which just corresponds to the beam pattern exposed to the Ar excimer laser irradiation. It should be noticed that the bulk Si appears only in the beam pattern made by the Ar excimer laser radiation, and further that is isolated uniformly in the beam pattern, at least with a spatial resolution of 200 μ m. The Si isolation could not be observed in the beam pattern irradiated by the Kr excimer laser.

In general, glasses usually include much more defects and impurities than crystals. We are very interested in whether the Si isolation in SiO_2 is a peculiar phenomenon in glasses or not. In order to this point, we observed the beam patterns of a crystalline SiO_2. Figures 7(a) and (b) show two dimensional distribution images with 103.4eV photoelectrons (a) and with 99eV photoelectrons (b). In these figures, two beam patterns are included, one in the left hand side induced by one shot of the Ar excimer laser and one in the right hand side induced with five shots. These images show that both of the patterns include bulk Si isolated and deficient SiO_2. Nevertheless, the five shots induce much larger amount of bulk Si than the one shot. It can be concluded here that the Si isolation by 9.8eV photons is a

common phenomenon in both of amorphous and crystalline SiO_2, namely, that the Si isolation is a fundamental property in SiO_2.

4. Discussion

The penetration depth of the Ar excimer laser radiation is calculated to be 52 nm, from data about the optical constants of SiO_2 glass [12]. The laser radiation with 200 mJ/cm^2 fluence onto the mirror surface, corresponding 10 mJ output energy, include 1.2×10^{17} photons/cm^2. Taking account of reflectivity of 14% at 126nm, we can estimate that these photons hit the small volume of SiO_2. If one photon excites one electron from the valence band to the conduction band, an extremely high density of electrons, about $10^{22}/cm^3$, are generated. Even though a part of the photons are required to rise up the mirror surface temperature, still a large amount of electrons are present in the conduction band. In the case of the Kr excimer laser, the intrinsic SiO_2 property shows almost transparent at 146nm [12], but the SiO_2 glass usually show strong absorption around 146 nm. In fact, the optical band edge shown in figure 3 was 165 nm, 7.5 eV. The SiO_2 glass mirror used here shows strong absorption even around 146 nm, and thus the damage patterns were observed for the Kr excimer laser irradiation. Therefore, if high density of electrons excited have a capability to break Si-O bonds and isolate bulk Si, the Kr excimer laser photons could induce the same phenomenon of Si isolation as the Ar excimer laser. It should be noted here that the difference of the photon energies is remarkable, that is, 9.8 eV photons break the Si-O bonds but 8.5 eV photons not. Presumably the electron excitation directly from the valence band to the conduction band and thus creation of excitons is of importance for this phenomenon.

In summary, with selected area X-ray photoelectron spectra, Si-O bonds have been observed to be broken in SiO_2 glass by the Ar excimer laser radiation, but not by the Kr excimer laser radiation. The two dimensional distribution images with given energies show the uniformly distributed pattern of the Si isolation within the beam pattern induced by the Ar excimer laser irradiation. The Si isolation, that is, Si-O bond breaking, is considered to be caused by excitons created by the Ar excimer laser photons, in addition to the thermal effect appearing as the wrinkles along the beam pattern periphery. This point has not een confirmed yet. The detailed mechanism on the Si isolation will be discussed in future.

5. References

[1] Arai, K.; Imai, H.; Hosono, H.; Abe, Y.; Imagawa, H. Two-photon processes in defect formation by excimer lasers in synthetic silica glass. Appl. Phys. Lett. 53(20): 1891-1893; 1988.

[2] Tsai, T. E.; Griscom, D. L.; Friebele, E. J. Mechanism of Intrinsic Si E'-Center Photogeneration in High-Purity Silica. Phys. Rev. Lett. 61(4): 444-446; 1988.

[3] DiStefano, T. H.; Eastman, D. E. The band edge of amorphous SiO_2 by photoinjection and photoconductivity measurements. Solid State Commun.; 9(24): 2259-2261; 1971.

[4] Griscom, D.L. Defect Structure of Glasses. J. Non-Cryst. Solids. 73(1): 51-77; 1985.

[5] Feigl, F. J.; Fowler, W. B.; Yip, K. L. Oxygen vacancy model for the E_1' center in SiO_2. Solid State Commun. 14(3): 225-229; 1974.

[6] Sasaki, W; Uehara, Y.; Kurosawa, K.; Fujiwara, E.; Kato, Y.; Yamanaka, M. High power tunable coherent radiation around 126nm with an argon excimer laser. Rev. Laser Engineer. 14(5): 370-377; 1986.

[7] Sasaki, W.; Kurosawa, K.; Herman, P. R.; Yoshida, K.; Kato, Y. "Intense coherent radiation in the VUV and XUV region with electron beam pumped rare gas excimer lasers," in Proceedings of the OSA topical meeting on Short Wavelength Coherent Radiation: Generation and Applications, R. W. Falcone; Kirz, J., ed. 1988 Sep. 26-29; North Falmouth; Cape Cod, MA. pp. 184-188.

[8] Kurosawa, K; Sasaki, W.; Fujiwara, E.; Kato, Y. High power narrow band operation and Raman frequency conversion of an electron beam pumped krypton excimer laser. IEEE J. Quantum Electron. 24(9): 1908-1914; 1988.

[9] Takeuchi, K.; Kurosawa, K.; Sasaki, W.; Takigawa, Y.; Yoshida, K.; Fujiwara, E.; Kato, Y. Output characteristics of Ar excimer laser with various cavity mirrors. Rev. Laser Engineer. 16(10): 691-698; 1988. (in Japanese)

[10] Takigawa, Y.;Kurosawa, K.; Sasaki, W.; Fujiwara, E.; Yoshida, K.; Kato, Y. Si-O bond breaking in SiO_2 by vacuum ultraviolet laser radiation. J. Non-Crystal. Solids (in press).

[11] This reseasrch was supported by the Joint Studies Program of the Institute for Molecular Science.

[12] Phillipp, H. R. Optical properties of non-crystalline Si, SiO, SiO_x and SiO_2. J. Phys. Chem. Solids 32(8): 1935-1945; 1971.

[13] Philipp, H.R. Silicon dioxide (glass). in Handbook of Optical Constants of Solids. E.D.Palik, ed. Orlando, Fl: Academic press; 985. 749-763.

[14] Yamaguchi, M.; Goto, H.; Mitamura, S.; Kato, I.; Hattori, T.; Shimizu, H.; Kajikawa, T.; Nagaso, T. Development of X-ray photoelectron spectroscopy ESCA-1000. J. Shimadzu Scientific Instruments 1(2): 62-66; 1989.(in Japanese)

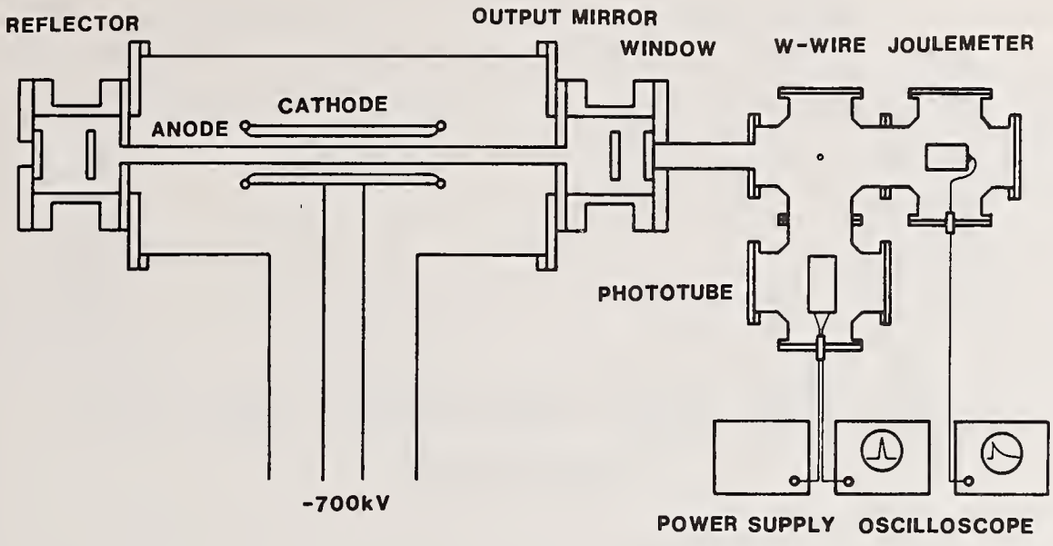

Figure 1 Schematic illustration of the electron beam pumped rare gas excimer laser.

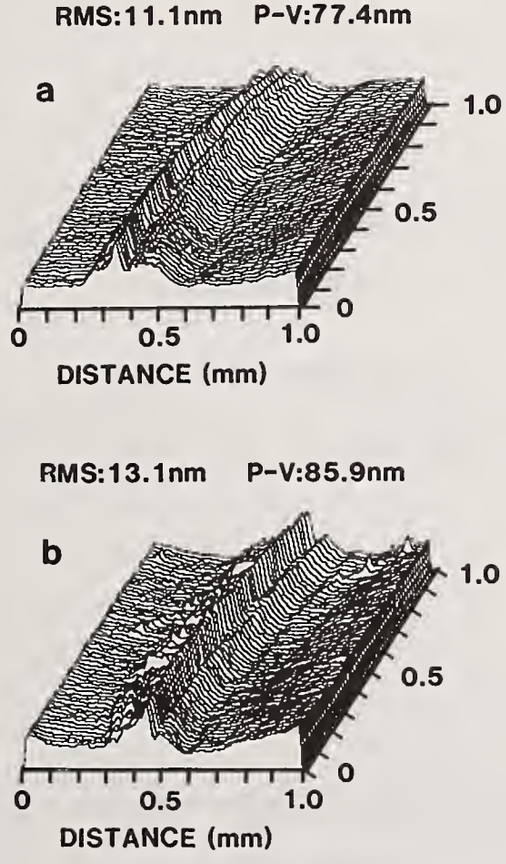

Figure 2 Surface topographic images of the beam patterns induced by the Ar excimer laser (a) and by the Kr excimer laser (b).

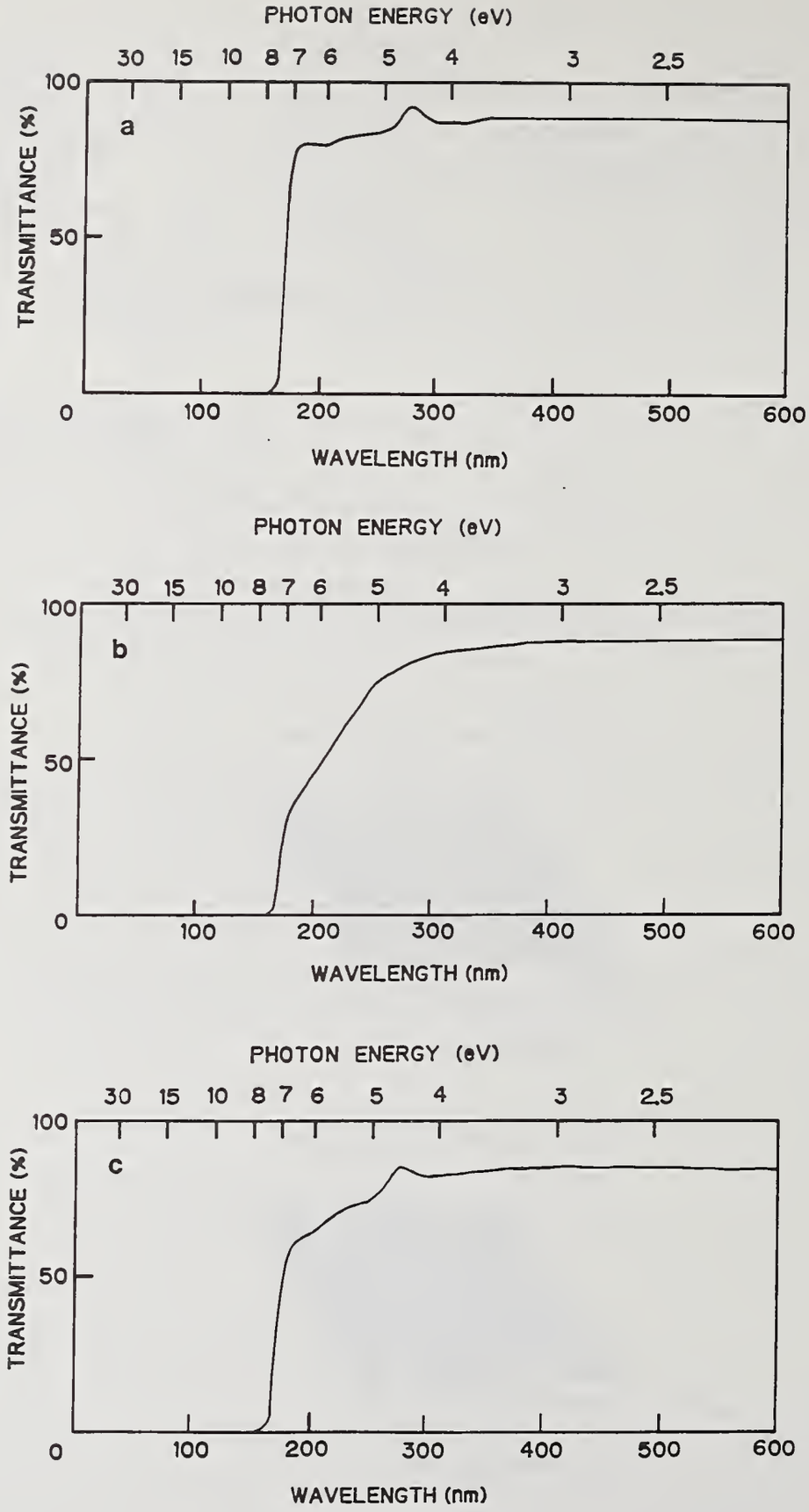

Figure 3 Transmission spectra of the SiO_2 glass mirror: curve (a) is taken from a non-irradiated part of the mirror surface, curve (b) from a beam pattern induced by the Ar excimer laser, and curve (c) from a beam pattern induced by the Kr excimer laser.

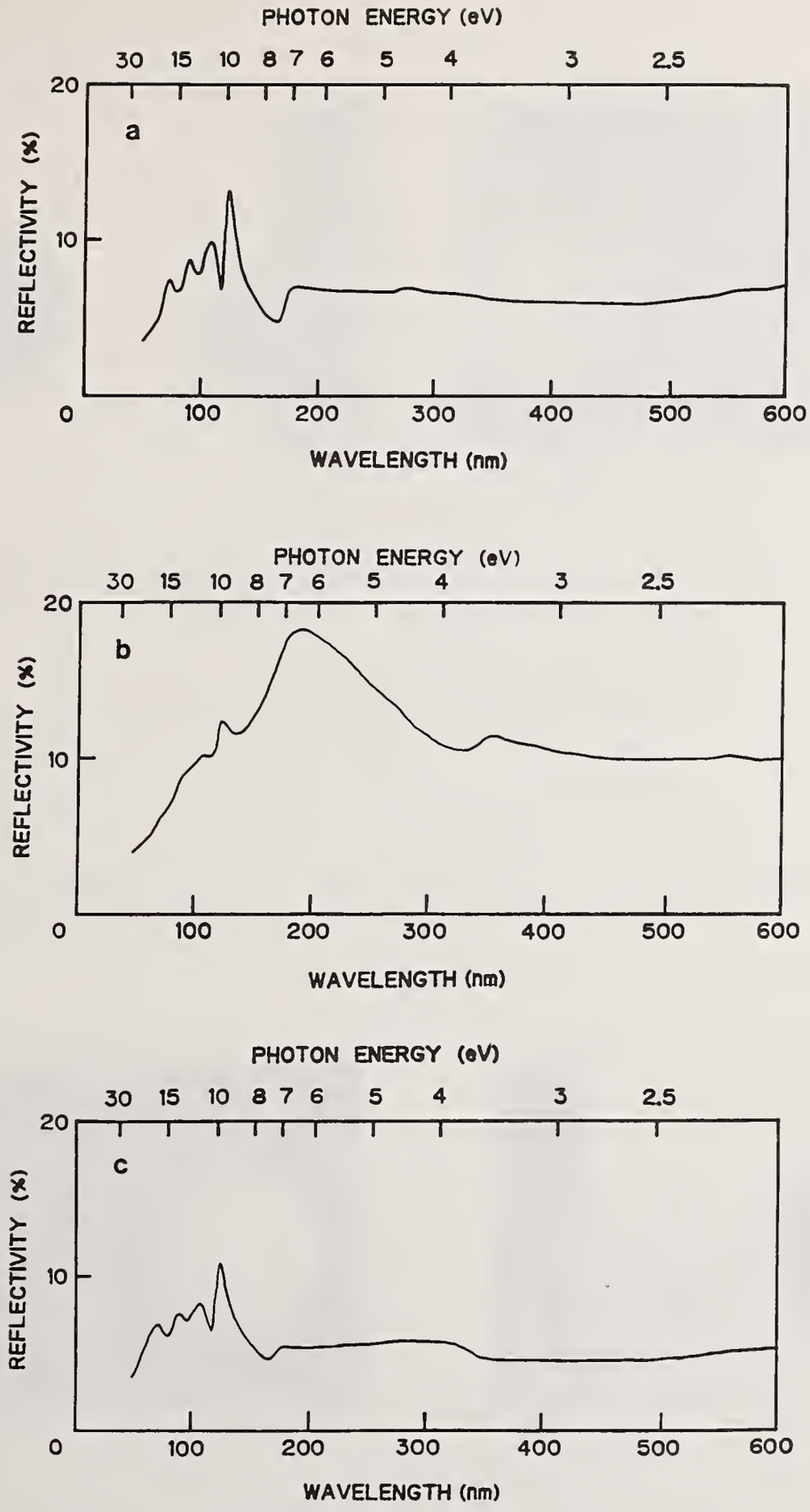

Figure 4 Reflectance spectra of the SiO_2 glass mirror: curve (a) is taken from a non-irradiated part of the mirror surface, curve (b) from a beam pattern induced by the Ar excimer laser, and curve (c) from a beam pattern induced by the Kr excimer laser.

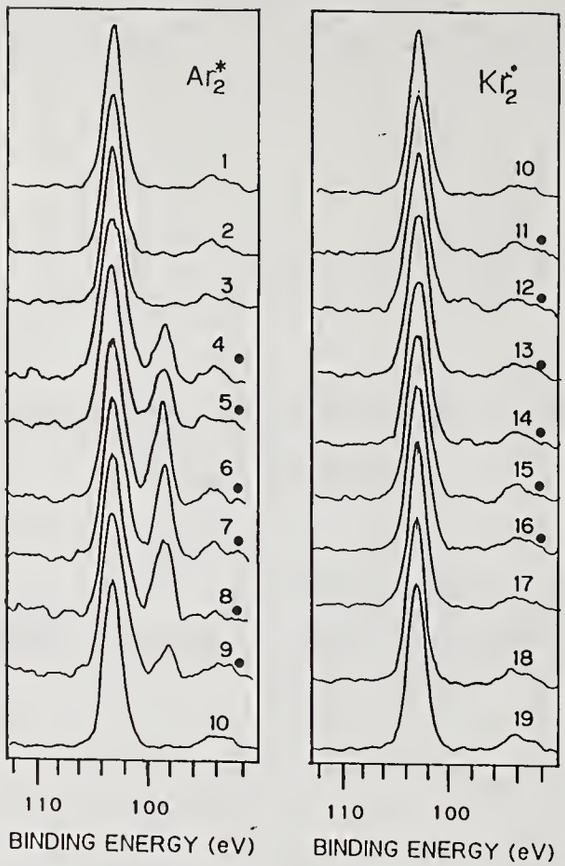

Figure 5 XPS specrta of Si-2p emission from several points on the SiO_2 glass mirror surface.

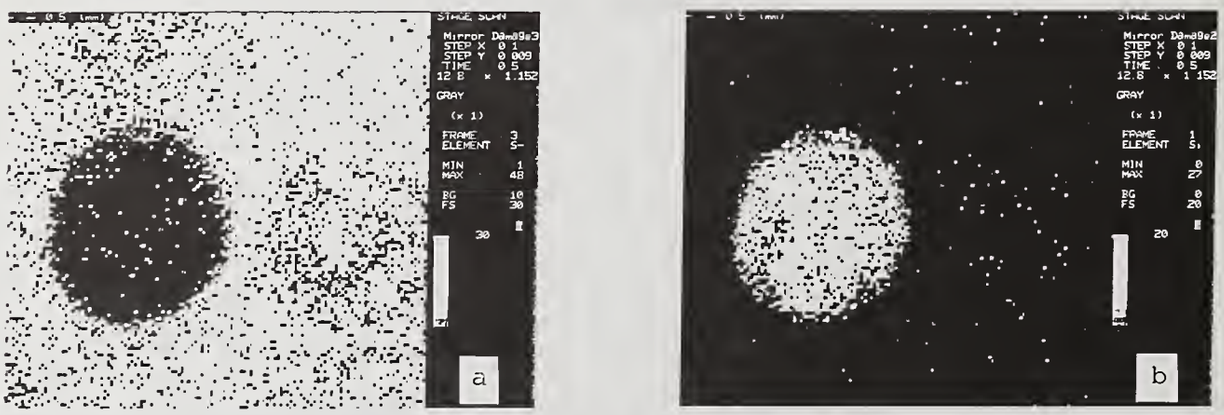

Figure 6 Two dimensional images of the SiO_2 glass mirror surface taken with 103.4eV Si-2p emission of SiO_2 (a) and with 99eV Si-2p emission of bulk Si (b).

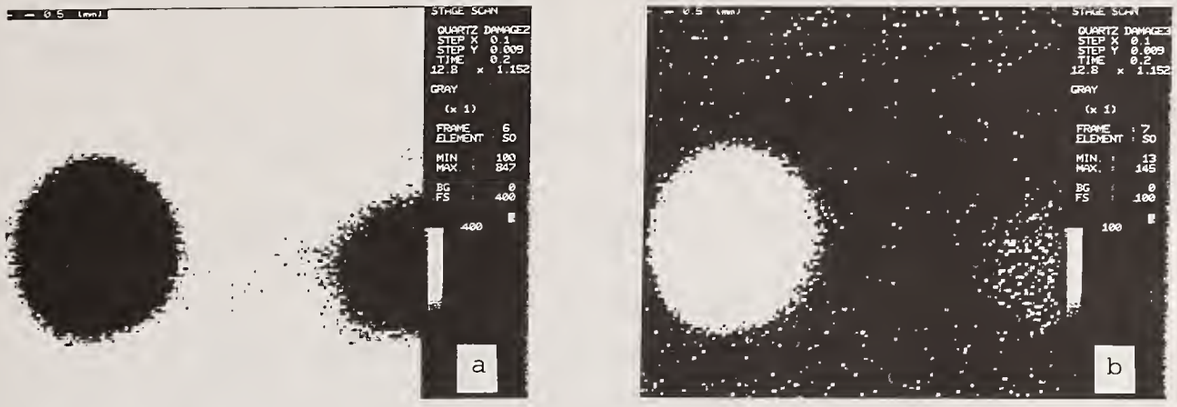

Figure 7 Two dimensional images of the crystalline SiO_2 mirror surface taken with 103.4eV Si-2p emission of SiO_2 (a) and with 99eV Si-2p emission of bulk Si (b).

Manuscript received
3-20-90

Damage Assessment and Possible Damage Mechanisms to 1-Meter Diameter Nova Turning Mirrors*

G. Edwards, J. Campbell, R. Wolfe, E. Lindsey

University of California
Lawrence Livermore National Laboratory
P.O. Box 5508, L-490
Livermore, California 94550

A major concern in the operation of the LLNL 120 kJ Nova laser system is damage to the nominal 1-meter diameter mirrors (i.e. HR coatings). The damage appears to originate from microscopic defects that vary in size up to approximately 30 μm in diameter. These defects produce damage sites up to 250 μm and, in some cases, covering 20% or more of the mirror surface. Defects due to particulates that are in or under the coating are highly unlikely due to the fact that coating thickness is only 5 μm thick and particles up to 30 μm would produce surface roughness that could be easily detected. Consequently, the defects must be plate-like (i.e. "2-D") in nature. A by-product of the damage is a haze left on the surface of the mirror. This haze is analyzed and shown to be blown-off particles of ZrO_2/SiO_2 coating material. The particle morphology suggests nucleation from a vapor phase which implies localized heating in the coating to temperatures on the order of 3000°K. Some possible damage mechanisms are also explored.

1. Introduction/Background

Since the early 1970's, LLNL has designed, constructed and operated a succession of six increasingly powerful Nd:glass laser systems to support fusion energy research. The latest of these is the Nova laser facility, a nominal 120-TW, 120-kJ system that became operational in 1985 [1]. A continuing problem with all large, high-peak-power laser systems is damage to key optical elements. The high reflectivity, dielectric coatings that are used on Nova to steer the output laser beams to the target chamber are perhaps the weakest elements (in terms of damage) on the system. In this paper we assess the damage to these mirrors and possible damage mechanisms.

---

*Work performed under the auspices of the U.S. Department of Energy by Lawrence Livermore National Laboratory under Contract No. W-7405-ENG-48.

The Nova HR coatings receiving the highest fluences are located at the mirror denoted by the letters "C" and "E" in figure 1 [2]. For example, for a nominal 125 KJ, 1-ns shot, the average fluence on these mirrors is about 4 J/cm^2. Assuming a modulation of the beam intensity of 1.5:1 this corresponds to peak fluences of roughly 6 J/cm^2.

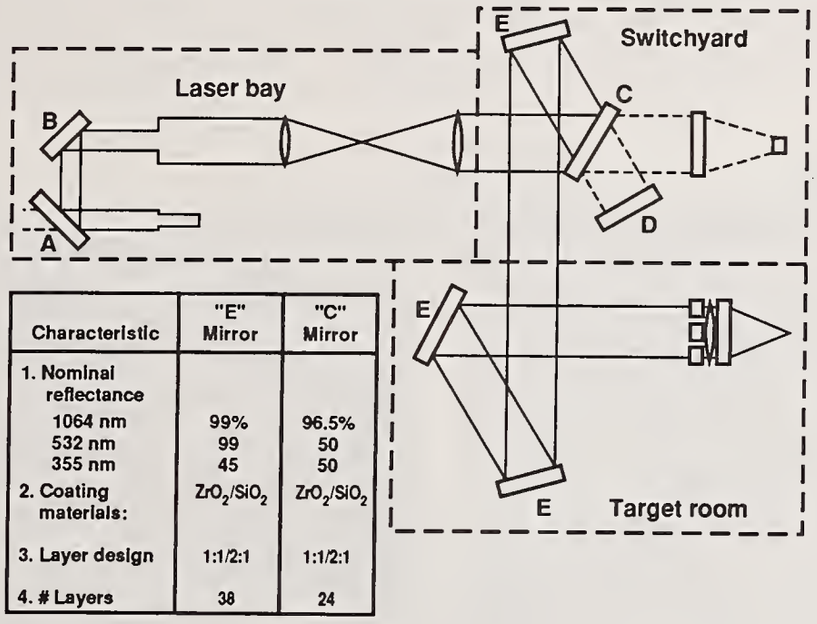

Characteristic	"E" Mirror	"C" Mirror
1. Nominal reflectance		
1064 nm	99%	96.5%
532 nm	99	50
355 nm	45	50
2. Coating materials:	ZrO_2/SiO_2	ZrO_2/SiO_2
3. Layer design	1:1/2:1	1:1/2:1
4. # Layers	38	24

Figure 1. Schematic diagram of a Nova beamline showing the positions of various mirrors. The mirrors in the high fluence positions are labeled as "C" and "E" and their key characteristics are summarized in the insert.

The "C" and "E" mirrors both have the same HR coating materials. However, the "C" mirrors serve a diagnostic function that allows some light transmittance and consequently they have fewer layers.

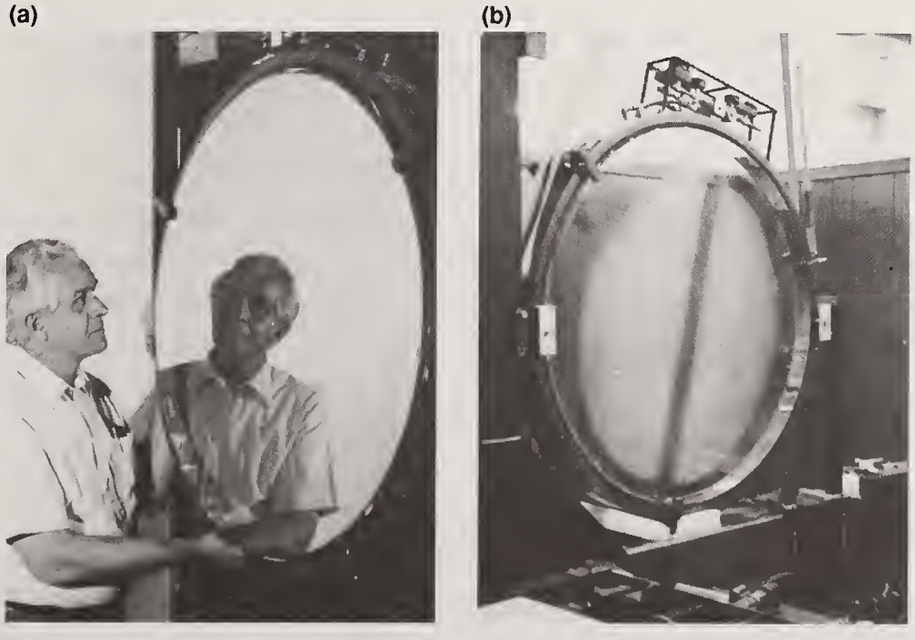

Figure 2. Photograph of the 1.0 m mirror on Nova beamline 4 (a) before, and (b) after four years of service on the laser system. The beam imprint is clearly seen as the "hazy" region that is left after damage.

Recently an "E" mirror that had been badly damaged (fig. 2) was removed from the system. The measured reflectivity across the mirror surface is shown in figure 3. In the most heavily damaged regions the reflectivity had dropped to roughly 66%. In addition, the mirror had a uniform "haze" layer over the area of the beam imprint. This layer could be easily removed by wiping and contributed about 5% to the overall drop in reflection. Microscopic inspection of undamaged areas of the HR coating (that is, areas outside of the beam path) showed a large number of "particles" with diameters up to 30 μm.

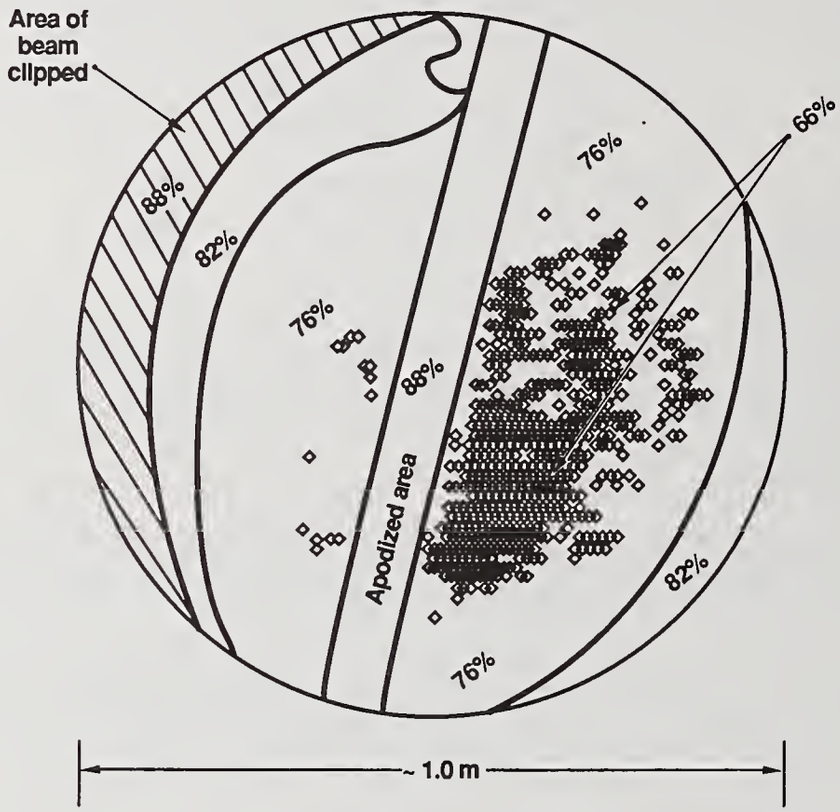

Figure 3. Measured reflectivity at 1.06 μm at various locations on the mirror surface[2]. This is for the same mirror as shown in figure 2. Wiping the haze from the surface increases the reflectivity about 5% above the values shown. The small diamonds indicate areas of heavy damage.

Inspections of other mirrors on Nova showed similar results although the other mirrors do not seem to be as badly damaged. Furthermore, microscopic inspections of the other HR coatings show that "particles" are always present in the coatings. Consequently we assume that the assessment given here of the damage to the one of the Nova mirrors is a fair representation of that expected for the other high fluence mirrors on Nova.

2. Analysis of Nova HR Coating Damage

2.1 Density and morphology of coating defects

Microscopic inspection of undamaged HR coating regions shows a large number of visible defects (fig. 4a). Based on the photomicrographs of the coating, we estimate there are about 80 to 100 per mm^2 in the 5-30 μm range. From the shape of the defects (i.e. circular) one naturally draws the conclusion that these are small particles embedded

in the coating. But are they? We suggest that they are not particles simply because they are too large relative to the coating thickness and thus would not give the observed smooth coating surface. This point is illustrated in figure 5 where the total coating thickness (about 5 μm) is shown relative to an embedded 30 μm particle. Note that if many particles of the 30-μm size were embedded in the coating one should be able to easily see them when looking at the coating surface from an oblique angle. Since the coating surface is very smooth (less than 25-50 Å rms surface roughness) then it is assumed that the defects are not particles (i.e. "spheres") but are more nearly two-dimensional (i.e. plate-like).

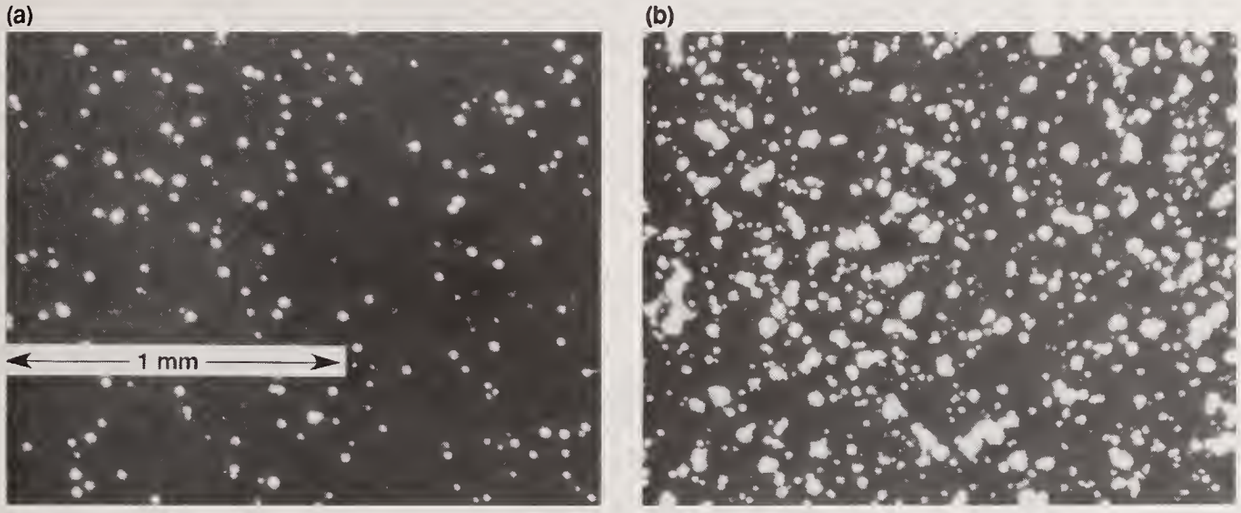

Figure 4. Photomicrographs of the (a) undamaged and (b) damaged region of the Nova mirror HR coating.

Of course the next obvious question is what are they if they are not particles? So far that remains unknown; all our attempts to quantitatively analyze such defects have failed.

2.2 Correlation of damage with observed defects

Figure 4b is a photomicrograph taken of the damaged region of the mirror coating. This is to the same scale as the photograph in figure 4a allowing a one-to-one visual comparison of damaged and undamaged regions of the coating. It is clear that the average damage "spot" is larger than the average defect and that in many instances the damage at one or more adjacent sites coalesced into a larger area. It is also apparent that the density of damage spots is greater than the density of defects. For example, the density of damage spots in figure 4b is about 300 per mm^2 or about three times the defect density shown in figure 4a.

The fact that one does not observe any defects remaining undamaged in figure 4b leads one to conclude that visually observed defects do indeed cause damage. However, they don't seem to occur in sufficient numbers to account for all the damage. This latter observation has to be tempered with two facts: first the photos are of two different regions on the mirror surface and the defect density may have been slightly different at

the two sites; second, a number of "barely visible" defects (< 2 to 4 μm) can be seen in the undamaged coating that were not included in the original (undamaged) defect-density estimate.

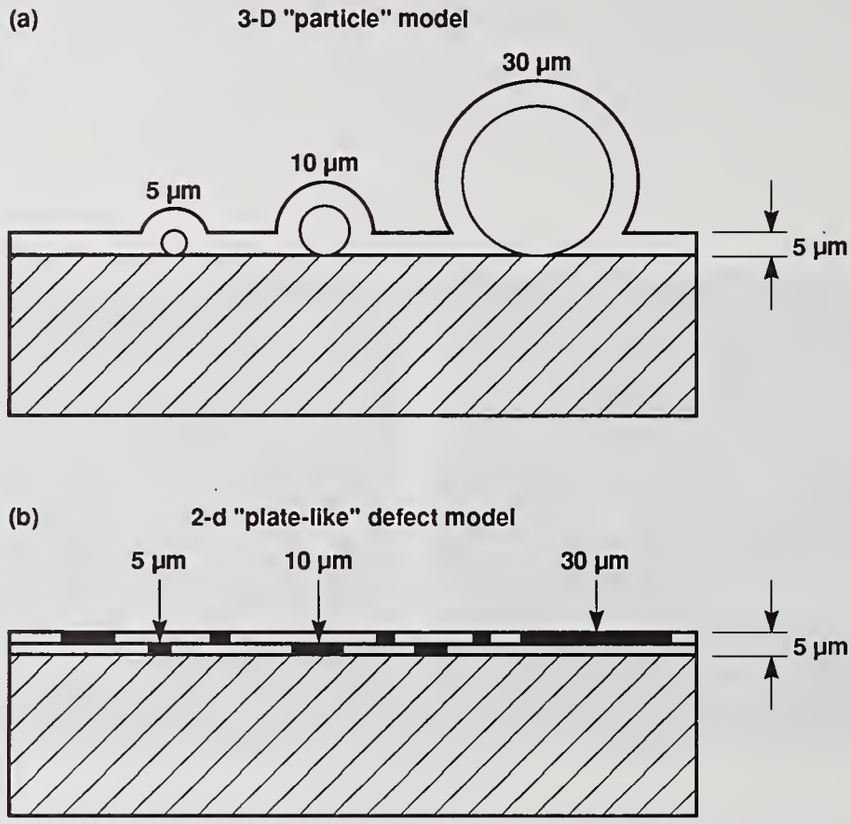

Figure 5. Schematic diagrams showing the effects of (a) spherical or (b) plate-like defects on a nominally 5μm-thick Nova HR coating. Note the large amount of surface roughing that would be easily visible for the case of the spherical (3-D) defects.

2.3 Source of the "haze" on the mirror surface

Analysis of the particles that produced the haze on the surface of the mirror show they are ZrO_2 and SiO_2, the same materials as the coating (fig. 6a). Thus the coating material blown off during damage created particles of ZrO_2/SiO_2 that litter the damaged surface.* SEM images of the particles show that they are less than about 1 μm in diameter and have both jagged and smooth surface morphologies (fig. 6b). The smooth particles probably nucleated and grew from a vapor phase whereas the jagged particles are simply ejected solid debris, i.e. not vaporized.

One possible scenario for the damage process is shown in figure 7. Before damage, the coating contains a number of defects that, when irradiated, heat to a temperature high enough to vaporize the surrounding ZrO_2/SiO_2 coating. Based on the normal boiling points of these materials this has to be greater than 3000°K. The ejected material 1

---

* We analyzed a number of particles and were unable to detect other elements that might be associated with some source of external contamination.

consists of a mixture of solid fragments and molten or vaporized SiO_2 and ZrO_2. The vapor cools, nucleates and forms either single or agglomerated particles.

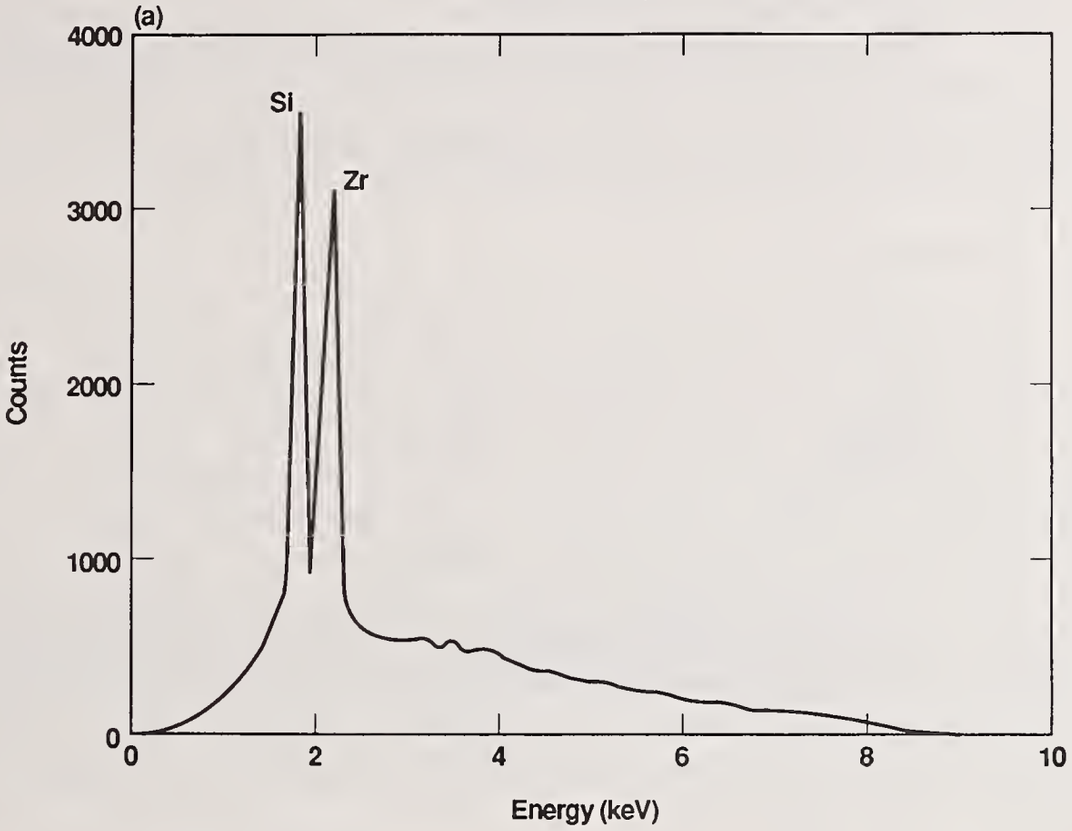

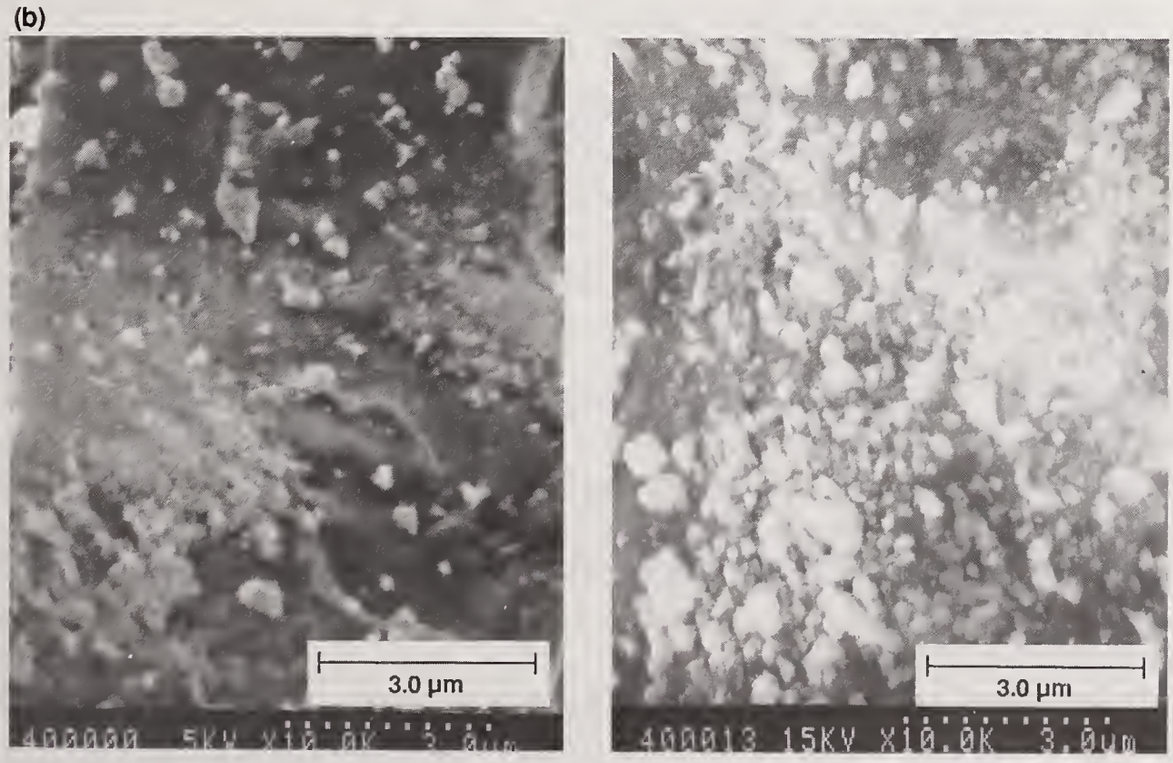

Figure 6. Energy Dispersive X-ray (EDX) analysis and SEM photographs of the particle debris removed from the damaged Nova HR coated surface.

Based on the extent of damage (about 20-30% of the coating area) and the original coating thickness of about 5 μm, one can estimate the thickness of the debris layer. This is about 2 μm assuming a porosity of 50%.

The observation that the vaporized SiO_2 and ZrO_2 nucleates, grows and agglomerates is not surprising. Simple thermodynamic theory [3-5] shows that growth will occur once a molecular cluster exceeds a critical radius, r_c, given by:

$$r_c = 2GV/(RT\ln[p/p_e]) \qquad (1)$$

where G is the surface energy (erg/cm^2), V is the molar volume (cm^3/mole), R the molar gas constant (erg/mol K) and T the temperature (K). The driving force for nucleation and growth is the departure from equilibrium represented by the ratio of measured and equilibrium vapor pressures, i.e. p/p_e. Assuming SiO_2 vaporization at 3000K and subsequent cooling to 1000K, it is easy to show that the critical cluster radius is less than the SiO_2 molecular dimension. This unphysical result simply implies that the system is so far from equilibrium under these conditions that nucleation occurs almost instantaneously. The point here is that simple theory predicts that the SiO_2 (or ZrO_2) vaporized during damage rapidly nucleates and grows forming many of the small particles that comprise the debris we see littered on the mirror surface. Moreover the debris particle size distribution (< 1.0 μm) and morphology is consistent with this observation.

3. Damage Mechanism in the Nova HR Coatings

It is clear from the data presented above that damage is caused by localized heating at defect sites in the coating. The question that always remains is: exactly how is the laser energy coupled into the material? One mechanism that is generally accepted for thin films is the so-called impurity model that simply assumes bulk absorption of the energy by some extrinsic defect, e.g. "dirt" buried in the coating. In the case of e-beam evaporated coatings this "dirt" model is often invoked because of the observed particulate spatter that occurs from the source material in the evaporation crucible. A number of papers have been published on modeling spherical impurities embedded in thin films or bulk material and the associated analytic (or numerical) solutions to the heat transport equations in this geometry. There is little that we can add to this literature. However, one question that is rarely asked in relation to the impurity model is what could the impurity be? In other words, what materials have a bulk absorption high enough to give the temperatures required for vaporization (i.e. damage) and is it likely they would be in the coating?

To assist in our search for such materials, we used a simple 1-D heating model in figure 8a to help bracket the probable range of absorption coefficients. This model assumes an absorption profile through the defect given by

$$\frac{I}{I_o} = \exp(-\alpha x) \qquad (2)$$

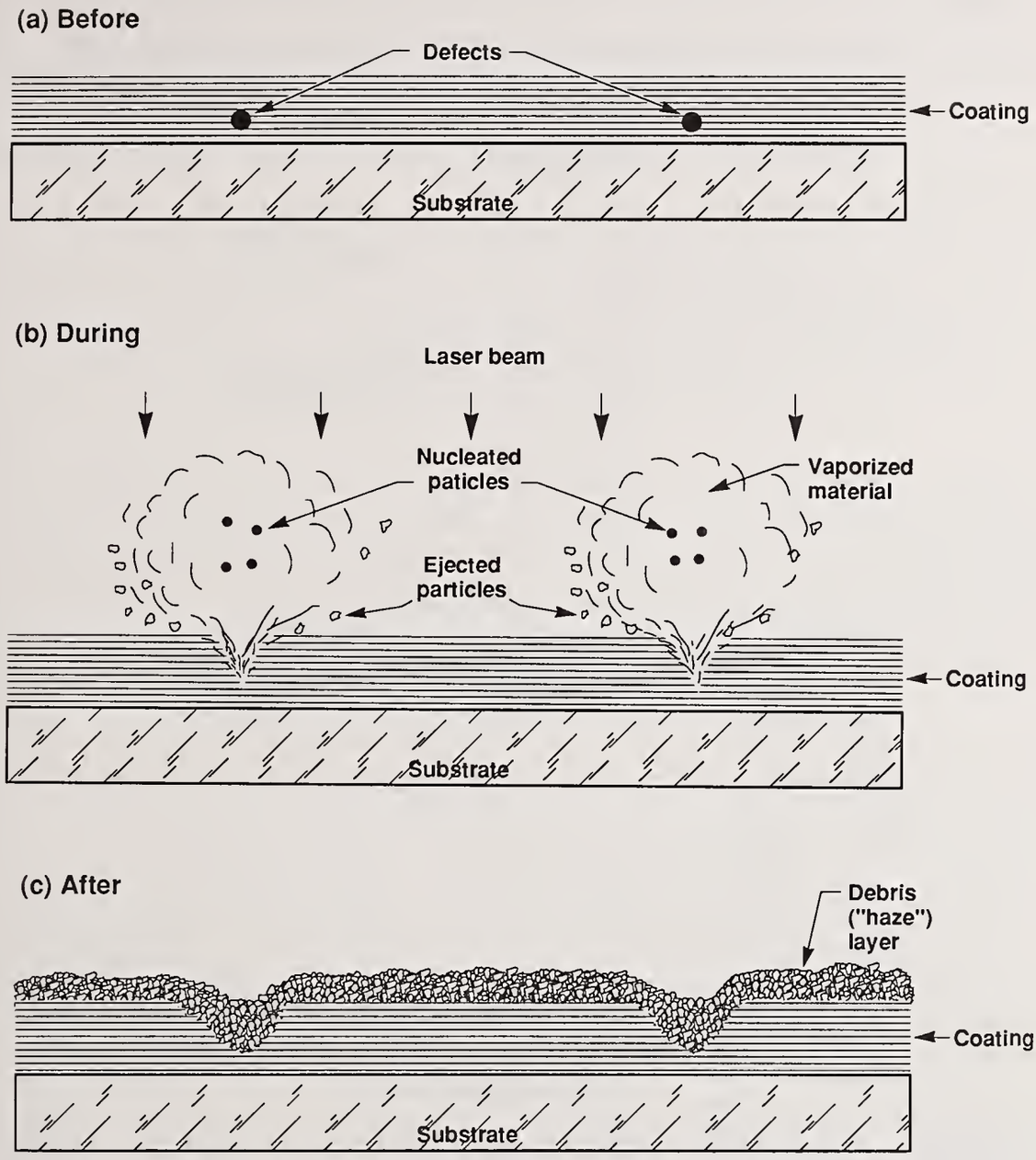

Fig. 7. Simple physical picture of the proposed process for damage to Nova HR coatings (a) before, (b) during and (c) after damage.

where I_o (J/cm^2) is the incident laser fluence, I is the fluence at position x (cm), and α (cm^{-1}) is the absorption coefficient of the impurity. It is straight-forward to show that the corresponding temperature rise through the absorbing region is:

$$\Delta T(x) = \frac{\alpha I}{\rho C_p} \exp(-\alpha x) \qquad (3)$$

with a maximum at the front surface (x = 0):

$$\Delta T(o) = \frac{\alpha I}{\rho C_p} \qquad (4)$$

where ρ is the material density (g/cm^3) and C_p is the specific heat (J/g•K). Thus for a given laser fluence one can get a reasonable idea of the impurity absorption required to heat the sample to the boiling point of the coating materials (i.e., SiO_2 and ZrO_2) and then, in turn, bracket possible impurity materials that might be present.*

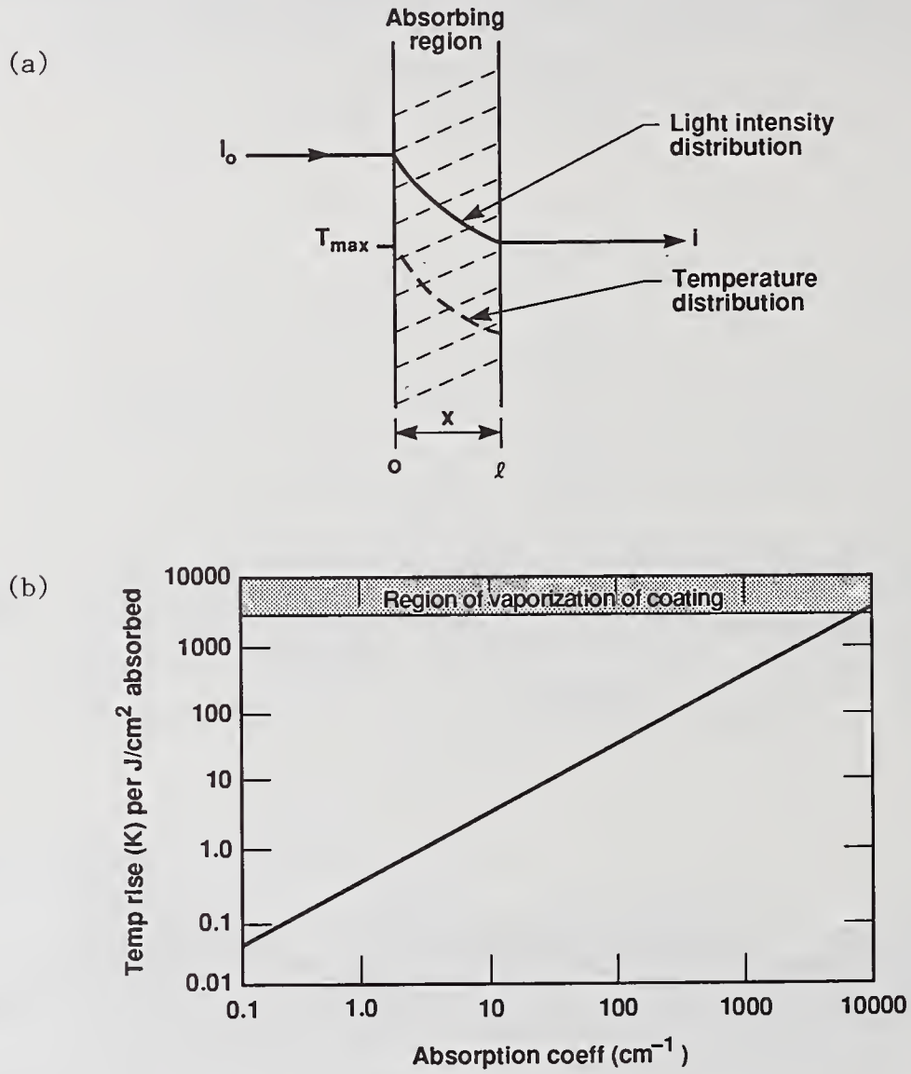

Figure 8. (a) Simple 1-D model of laser heating at an absorbing impurity and (b) predicted temperature rise at the incident surface of an impurity vs. the impurity absorption coefficient. The calculated temperature rise is per joule/cm^2 of absorbed incident laser energy. Thus, for example, for 10 J/cm^2 of absorbed incident fluence, simply multiply the temperature rise by 10.

Before proceeding there is one thing to note about equation (4), that is, it is pulse length independent. This is valid only if the characteristic absorption depth (i.e. $1/\alpha$) is long compared to the characteristic thermal diffusion distance $\bar{x}$:

$$\bar{x} = 2(\kappa t)^{1/2} \qquad (5)$$

where κ is the thermal diffusivity (cm^2/s) and t is the laser pulse width (s). This is a very important point because it is well known that damage thresholds generally seem

*For these "back-of-the-envelope" estimates we have neglected the enthalpy change associated with melting (i.e. heat of fusion).

to scale with laser pulse width somewhere between $t^{0.25}$ to $t^{0.5}$. In table 1 is a list of common coating materials with their associated thermal physical properties; these data are from Lang, et. al.[6] The calculated characteristic thermal transport distance ($\bar{x}$) for a 1-ns pulse is given in the far right column; for these dielectrics the thermal transport is typically less than 0.1 to 0.2 μm. Consequently if the absorption coefficients are significantly less than $1/\bar{x}$ (i.e. < 10^5 cm^{-1}), the damage threshold should scale only weakly with pulse length in the nanosecond-or-less region. As will be shown below, even relatively strongly absorbing dielectrics have absorption coefficients less than this at 1.06 μm. Thus, one would expect a very small pulse-length-dependence for the damage threshold if this impurity-heating model is valid. (In the case of the original Nova HR coatings we have found a negligible pulse length scaling of the 1.06 μm damage threshold between 1 and 10-ns [10].

For comparison, we've also included a list of metals in table 1 with their thermal-physical properties and characteristic diffusion depth in 1-ns. Note that for metals the optical absorption depth (< 10^{-2} μm) is much less than the thermal diffusion distance (~ 1 μm). Thus one would expect damage due to metal particles to scale as approximately $t^{0.5}$ in the ns region (for particles > 1 μm). This is indeed observed, as in the case of the Pt-inclusion damage in glasses [7,8].

Table 1. Summary of thermal-physical properties reported by Lange et al.[6] for a number of crystalline dielectrics often used in optical thin films and, for comparison, several metals.

Material	Index	k (J/cm•s•K)	C_ρ (J/g•K)	ρ (g/cm^3)	T (melting) (K)	T (Boiling) (K)	κ (cm^2/s)	$\bar{x}$ (μm)
I. Dielectrics								
Al_2O_3	1.72	0.346	0.774	4	2325	3250	0.112	0.21
HfO_2	2.25	~0.017	0.168	8.68	3137	~5600	0.012	0.068
LaF_3	1.59	0.0508	0.462	5.94	1763	~2600	0.019	0.086
LiF	1.37	~0.017	1.61	2.635	1121	1950	0.004	0.040
MgF_2	1.43	0.116	0.394	3.176	1536	2512	0.093	0.193
MgO	1.83	0.6	0.92	3.77	3098	3870	0.173	0.263
SiO_2	1.44	0.14	0.737	2.32	1696	2500	0.082	0.181
ThF_4	1.59	0.1	0.359	6.32	1380	~2000	0.044	0.133
ThO_2	1.90	0.142	0.234	10	3540	4670	0.061	0.156
Y_2O_3	2.10	0.0246	0.451	5.01	2683	--	0.011	0.066
ZrO_2	2.25	0.011	0.46	5.7	2950	4570	0.0042	0.041
II. Metals								
Au	--	2.97	0.131	19.3	1336	3243	1.17	0.69
Pt	--	0.69	0.131	21.45	2042	4803	0.24	0.31
Cu	--	3.94	0.380	8.96	1356	2868	1.15	0.68
Ag	--	4.18	0.234	10.49	1233	2483	1.70	0.83
Al	--	2.04	0.896	2.71	--	--	8.42	0.58

We return now to the question of what dielectrics have absorption coefficients high enough to cause thermal heating to ~ 2000-3000 K? Figure 8b is a plot of maximum temperature rise (per J/cm^2 absorbed) vs. absorption coefficient. Since the Nova mirrors damage at roughly 7-8 J/cm^2 then the impurity absorption would have to be

> 1000 cm^{-1} to give the observed thermal heating. So, what are some possibilities? One is SiO, a suboxide of silica that is often proposed to be present in e-beam SiO_2 coatings. SiO has an absorption coefficient of < 100 cm^{-1} at 1 μm [9] so it would not give the required temperature rise. Some other common dielectrics that are also strong absorbers at 1.0 μm include FeO, Fe_2O_3, CuO_2, CuO, and NiO. Based on absorptions at 1.0 μm for these materials when doped in glass, we have <u>estimated</u> bulk absorptions (table 2). Note that almost all of these have absorptions greater than 1000 cm^{-1}. So one could propose that the coating is contaminated by numerous inclusions of materials of this type. But is that likely? Remember that the defect density is about 100/mm^2 so there would have to be a fairly large contamination problem within the coating chamber. Moreover, the contaminants would have to be flat-plates (not particles) to agree with the observation that the defects are largely 2-dimensional, producing negligible surface roughening.

This leads us to two main conclusions regarding the mechanism for damage to Nova HR coatings. First, a damage mechanism based solely on absorbing dielectric particles (i.e. dirt) is possible but unlikely, even though it does predict a negligible pulselength dependence as is reported for Nova. However, it requires plate-like (2-D) particles that have very high absorption coefficients. The possible candidates for these impurities are probably not suboxides of the coating material (e.g. SiO) but rather some external impurities. In addition, the very high absorption values that are required eliminate all but the most strongly absorbing dielectrics as impurities. The concentration of defects in the Nova coatings is so high it is difficult to believe there is an outside contamination problem of this magnitude.

Table 2. Estimated absorption coefficients at 1.0 μm for several possible dielectrics contaminants.

Material	Absorption Coefficient (cm^{-1})
SiO	< 100
FeO	5200
Fe_2O_3	960
Cu_2O	2180
CuO	3490
Ni	2640

Second, it is clear from the data that visible defects do lead to damage so they must be absorbing energy by some mechanism. We believe it may be due to electron donor (or acceptor) states lying close enough to the conduction (or valence) band to undergo excitation by linear absorption. High densities of these states may be associated either with the bulk or boundaries of the observed defects leading to sufficient absorption to produce the heating observed. Thus one would expect the damage to be associated with observed physical defects. Notice that the scale length of the region containing these absorbing states; would need to be > 0.1 to 0.2 μm to explain the negligible pulse length scaling that is observed. This is on the order of a single-layer coating thickness suggesting a plate-like defect region equal to the coating thickness and up to about 30 μm in diameter.

Acknowledgments

The authors gratefully acknowledge the efforts of the late George Watchmaker (TID Photo Department) in taking the photographs of the damaged and undamaged Nova mirror coatings. Also, the assistance of George Greiner on several aspects of this effort, are greatly appreciated.

References:

1. H. T. Powell, J. H. Campbell, J. T. Hunt, W. H. Lowdermilk, J. R. Murray, and D. R. Speck, "High Power Nd:Glass Lasers as Drivers for Inertial Confinement Fusion", Lawrence Livermore National Laboratory report UCRL-99517 in Proceedings of the Workshop on Inertial Confinement Fusion, 1988 (in press).

2. G. R. Wirtenson, "Coatings for High Energy Applications - The Nova Laser", Lawrence Livermore National Laboratory report UCRL-99517 in Proceedings of SPIE - International Society of Optical Engineering Meeting, Jan. 19-24, 1986.

3. G. D. Ulrich, "Theory of particle formation and growth in oxide synthesis flames", Combustion Science and Technology, 4, pp. 47-57, (1971).

4. J. Bloem, "Nucleation and growth of silicon by CVD", J. of Crystal Growth, 50, pp. 581-644 (1980).

5. A. P. George, R. D. Murley, and E. R. Place, "Formation of TiO_2 aerosol from the combustion supported reaction of $TiCl_4$ and O_2", Faraday Symposium of the Chemical Society on Fogs and Smokes, London, England, p. 63, 1973.

6. M. R. Lange, J. McIver, A. Guenther, Laser Induced Damage in Optical Materials: 1983, NBS special publication 688, pg. 454.

7. R. Gonzales and D. Milam, "Evolution during multiple-shot irradiation of damage surrounding isolated Pt-inclusions in phosphate laser glass", Proceedings of the Boulder Damage Symposium, Oct. 1985, NBS special publication 746, p. 128.

8. J. Pitts, "Modeling laser damage caused by Pt-inclusions in laser glass", Proceedings of the Boulder Damage Symposium, NBS special publication 746, p. 537.

9. Handbook of Optical Constants of Solids, E. D. Palik, ed; Academic Press, Inc. (1985) p. 767.

10. D. Milam, Lawrence Livermore National Laboratory, private communication (1989).

Manuscript received
1-30-90

Thermal Transport Studies of Optical Coatings, Interfaces and Surfaces by Thermal Diffusion Wave Interferometry

Randall T. Swimm and Gary Wiemokly
Center for Laser Studies
University of Southern California
Los Angeles, CA 90089-1112

Thermal transport data on thin metal coatings are presented. The data illustrate the ability of the measurement technique to characterize the thermal transport properties of single samples. The method offers insight on coating survivability.

key words: adhesion; coatings; damage; delamination; laser hardness; laser-induced damage; nondestructive evaluation; nuclear hardness; optical coatings; thermal conductivity; thermal diffusivity; thermal properties; thermal transport; thin films.

Introduction

The unifying characteristic of thin-film coating studies is the need to separate the surface and interface properties of the coating from the bulk properties of the coating. Frequently this separation is accomplished by varying a characteristic length of the system. Methods of doing so fall into at least two classes. The first class of measurement methods is based on varying the sample thickness. By plotting the measured value of an appropriately chosen property of the samples as a function of sample thickness, the sum of the surface and interface contributions may be extracted as the ordinate intercept of the data at zero thickness, and the bulk contribution may be obtained as the slope or the reciprocal of the slope of the data. A tacit assumption of this approach is that the sample properties are independent of coating thickness. An additional requirement is that the material properties be repeatable among samples. Finally, the signal to noise ratio and the data reproducibility must be adequate. In practice, it may be difficult to satisfy all of these conditions, especially with regard to material properties repeatability. As a consequence, data are occasionally reported which show nonphysical results such as negative slopes or negative intercepts. Unless the substrate polishing and coating deposition processes are under sufficient control to yield repeatable coating properties, the attempt to obtain meaningful results by utilizing measurement techniques based on multiple samples of different coating thickness is futile.

An alternative class of measurement methods is based on varying a characteristic length imposed by the measurement process, and obtaining separate surface, bulk and interface contributions for a single coated sample. Such techniques may include those based on varying a spot size, the physical offset between pumped and probed regions, a wavelength or a diffusion length. The present work falls into this latter class of measurement methods. The goal of this paper is to show that a great deal may be learned about the thermal transport properties of a single sample.

Background

The measurement and analysis techniques have been described in earlier proceedings[1,2]. Briefly, the physics of the measurement is as follows. Under steady-state conditions of sinusoidally modulated surface heating, thermal waves generated at the sample surface diffuse through the sample and partially reflect at abrupt discontinuities of the thermal effusivity (equal to the thermal conductivity divided by the square root of the thermal diffusivity[3]). Reflected thermal waves that return to the sample surface interfere with the instantaneous thermal waves being generated at the surface, causing the surface temperature response to be out of phase with the response that would occur in the absence of reflected thermal waves. In the present work, a metal coating or a bare metal substrate is used to ensure the required condition that the thermal waves be generated in a depth that is small compared to the local thermal diffusion length in order to preserve interference contrast. The thermal waves are generated by heating the sample using a sinusoidally-modulated argon ion laser beam. The temperature response is detected using an unmodulated helium neon laser beam reflected from the center of the heated region, based on the fact that the metal reflectivity is temperature dependent. The weak intensity modulation induced on the HeNe laser beam is measured using a silicon detector and lock-in detection. The system electronic phase is separately calibrated by directing the pump beam into the probe detector. The measured phase of the temperature response constitutes the data. The data are modelled using the boundary value solution for the presumed sample structure, in which the material properties are included as adjustable parameters. In the present modelling, the piecewise constant approximation is used, and the thermal contact resistance is included. A key consideration is the uniqueness of the solution. This can be inferred only by individually studying a sufficient range of different sample types so as to exclude alternative possibilities.

The present measurement system is an upgraded version of that described in the earlier proceedings[1,2]. A Coherent, Inc. model 90-6 Innova argon ion laser is used as the pump laser. A second probe beam line has been added to allow the temperature response at the coating-to-substrate interface to be determined for samples with a transparent substrate. Various other refinements have been added to avoid systematic errors. These include improved detector shielding, optical baffling to minimize light scattered into the detectors, and careful optical alignment to avoid stray reflections. A custom-built Lasermetrics, Inc. electro-optic modulator with reduced crystal spacing is used to avoid thermal lensing in the index matching fluid at high pump-beam power (3 W at 514.5 nm). Data are recorded using an automated system.

Recent related work by other authors is listed in the references[4-11].

Results and Discussion

Results for a 1 μm rf sputtered Ni coating deposited on fused silica are presented in Fig. 1. The sample was sinusoidally heated at the coating surface. The phase of the sinusoidal temperature response is plotted as a function of the logarithm of the modulation frequency. The circles show the response at the coating surface. The squares show the response at the coating-to-substrate interface. The upper curve shows the results of a zero-parameter fit (i.e. no adjustable parameters), based on a one-dimensional heat flow model assuming the handbook values for thermal conductivity and thermal diffusivity of Ni in bulk format, and also assuming a thermal contact resistance equal to zero. The

lower curve shows the theoretical response at the interface under identical assumptions. Several conclusions may be drawn from the data and the model agreement.

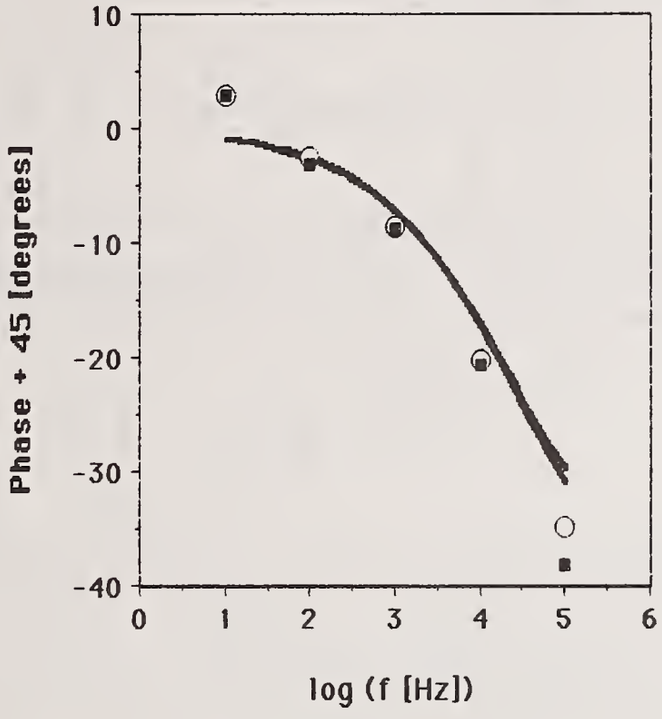

Fig. 1. 1 μm RF Sputtered Ni Coating on Fused Silica

First consider the near-equality of the surface and interface data at low modulation frequencies. The phase of the temperature response at the surface and the interface is expected to be equal at modulation frequencies for which the coating thickness is much less than the thermal diffusion length in the coating. The observed near-equality is a strong indicator of whether the data are due to the temperature modulation of the coating reflectance as assumed. Because of the small values typical of the thermal coefficient of the reflectance, numerous synchronous background signals giving rise to systematic errors had to be eliminated before the observed agreement of surface and interface response was attained.

Attempts to fully account for the data in terms of a one-dimensional heat flow model with a non-zero thermal contact resistance failed. However, the one-dimensional model is known to fail at frequencies for which the thermal diffusion length is not small compared to the pump spot diameter. The tentative interpretation of the data is that the Ni coating is displaying essentially bulk-like thermal transport behavior, with negligible thermal contact resistance, and with three-dimensional heat flow exhibited at low modulation frequencies. In order to verify the signature of three-dimensional heat flow in the simplest possible case, a solid metal mirror was studied.

Results for a solid Mo mirror, using a 1.90 mm diameter gaussian pump spot are considered next. The surface of the mirror was visibly oxidized. Mo is known to form sub-oxide surface layers several hundred angstroms thick[12]. The model calculation assumes no oxide layer, and uses handbook values for the Mo thermal transport parameters. The theoretical derivation follows that of Carslaw and Jaeger[13], except that the temporally modulated gaussian pump intensity distribution is used for the heat flux instead of a constant flux over a circular region as treated by Carslaw and

Jaeger. Consider the cylindrically symmetric heat diffusion equation for a homogeneous isotropic medium (assuming small temperature excursions, and therefore ignoring temperature dependence of thermal transport coefficients), for the region $z \geq 0$

$$\frac{\partial^2 T}{\partial r^2} + \frac{\partial^2 T}{\partial z^2} - \frac{1}{\kappa}\frac{\partial T}{\partial t} = 0 \qquad (1)$$

where T equals temperature, κ equals thermal diffusivity, z equals depth, r equals radial distance and t equals time. For a solution of the form $T = T\, e^{i\omega t}$, where T is temperature amplitude, i is the square root of minus one and ω is angular frequency, a Fourier transform yields the steady-state equation:

$$\frac{\partial^2 T}{\partial r^2} + \frac{\partial^2 T}{\partial z^2} - \frac{i\omega}{\kappa} T = 0. \qquad (2)$$

For a gaussian pump beam, Eq. (2) is to be solved subject to the following boundary conditions:

$$-K\left[\frac{\partial T}{\partial z}\right]_{z=0} = I_0\, e^{-2\left(\frac{r}{r_0}\right)^2}, \qquad (3)$$

where K equals thermal conductivity, I_0 equals intensity and r_0 equals the $1/e^2$ radius of the pump beam. Applying a Hankel transform of order zero to Eq. (2) yields the equation:

$$\frac{d^2 V_0}{dz^2} - \sigma^2 V_0 - \frac{i\omega}{\kappa} V_0 = 0 \qquad (4)$$

where

$$V_0 = \int_0^\infty r\, T(r,z)\, J_0(\sigma r)\, dr. \qquad (5)$$

and σ is the transform variable conjugate to r. Eq. (4) is subject to the following transformed boundary conditions.

$$-K\left[\frac{\partial V_0}{\partial z}\right]_{z=0} = I_0 \int_0^\infty r\, e^{-2\left(\frac{r}{r_0}\right)^2} J_0(\sigma r)\, dr \qquad (6)$$

It follows by inspection that the following is a solution to Eq. (4), subject to Eq. (6) and vanishing as $z \to \infty$

$$V_0 = \frac{I_0}{K} \int_0^\infty r'\, e^{-2\left(\frac{r'}{r_0}\right)^2} J_0(\sigma r')\, dr' \, \frac{e^{-\sqrt{\sigma^2 + \frac{i\omega}{\kappa}}\, z}}{\sqrt{\sigma^2 + \frac{i\omega}{\kappa}}}, \qquad (7)$$

and therefore by inversion that the following is a solution to Eq. (2), subject to Eq. (3) and vanishing as $z \to \infty$.

$$T = \frac{I_0}{K} \int_0^\infty \int_0^\infty r' e^{-2\left(\frac{r'}{r_0}\right)^2} J_0(\sigma r')\, dr' \frac{e^{-\sqrt{\sigma^2 + \frac{i\omega}{\kappa}}\, z}}{\sqrt{\sigma^2 + \frac{i\omega}{\kappa}}} \sigma J_0(\sigma r)\, d\sigma \tag{8}$$

This integral may be simplified as follows[14].

$$T(r,z) = \frac{r_0^2 I_0}{4K} \int_0^\infty \frac{\sigma}{\sqrt{\sigma^2 + \frac{i\omega}{\kappa}}} e^{-\frac{\sigma^2 r_0^2}{8}} e^{-\sqrt{\sigma^2 + \frac{i\omega}{\kappa}}\, z} J_0(\sigma r)\, d\sigma. \tag{9}$$

Eq. (9) expresses the temperature at a general point in a semi-infinite solid with gaussian heating at the surface. In the experiments, the temperature is measured at the center of the heated spot. Therefore, the point of interest has coordinates r=0, z=0. Consequently, the temperature response simplifies to the following expression (after converting the integral to dimensionless variables)[15]:

$$T\Big|_{\substack{r=0 \\ z=0}} = \frac{r_0^2 I_0}{4K} \sqrt{\frac{\omega}{\kappa}} \int_0^\infty \frac{s}{\sqrt{s^2 + i}} e^{-b^2 s^2}\, ds, \tag{10}$$

where $s = \sigma\sqrt{\kappa/\omega}$, and $b = (r_0/2)\sqrt{\omega/2\kappa}$. The phase ϕ of the temperature response relative to the sinusoidal pump-beam modulation may be obtained as the arctangent of the quotient of the imaginary component divided by the real component, as follows.

$$\phi(\kappa, r_0; \omega)\Big|_{\substack{r=0 \\ z=0}} = \tan^{-1}\left\{ (-) \frac{\int_0^\infty \frac{s}{\sqrt[4]{s^4+1}} \sqrt{1 - \left[\frac{s}{\sqrt[4]{s^4+1}}\right]^2}\, e^{-b^2 s^2}\, ds}{\int_0^\infty \frac{s}{\sqrt[4]{s^4+1}} \sqrt{1 + \left[\frac{s}{\sqrt[4]{s^4+1}}\right]^2}\, e^{-b^2 s^2}\, ds} \right\} \tag{11}$$

Calculations based on this expression (with no adjustable parameters) are presented in Fig. 2.

Reference to Fig. 2 shows that most of the measured phase variation is accounted for by the model. On the basis of one-dimensional calculations, the departure of the data from the model is con-

sistent with that expected, due to the presence of the surface oxide layer. The form of the three-dimensional numerical calculations also supports the hypothesis that the low-frequency departure of the measured phase from the one-dimensional model presented in Fig. 1 is due to the onset of three-dimensional heat flow.

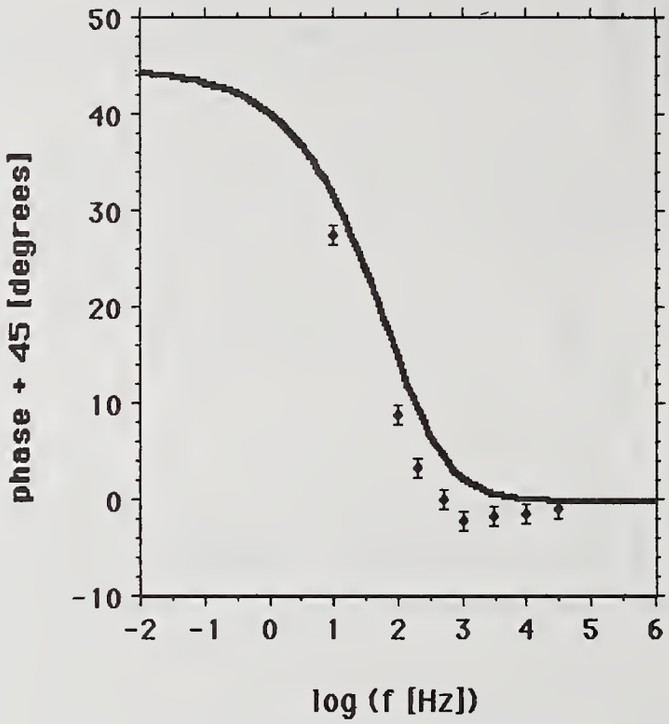

Fig. 2. Solid Mo Mirror

In an effort to obtain data free from three-dimensional heat flow effects, a metal coating of lower thermal diffusivity was studied. Results for a 1 μm rf sputtered Ti coating deposited on fused silica are presented in Fig. 3. The phase of the sinusoidal temperature response is plotted as a function of the logarithm of the modulation frequency. The circles show the response at the coating surface. The squares show the response at the coating-to-substrate interface. The upper curve shows the results of a zero-parameter fit (i.e. no adjustable parameters), based on a one-dimensional heat flow model assuming the handbook values for thermal conductivity and thermal diffusivity of Ti in bulk format, and also assuming a thermal contact resistance equal to zero. The lower curve shows the theoretical response at the interface under identical assumptions.

The near equality of the of the surface and interface data at low modulation frequencies again confirms the absence of a large class of potential systematic errors. Note also that the low modulation frequency data are in agreement with the one-dimensional heat flow model calculations. The gradual increase of the phase difference between the temperature response at the surface and the interface is expected, on the basis of thermal transit-time effects. The agreement of the experimental and theoretical differences between surface and interface response per se is fair. Unfortunately, the data show additional, unexpected structure in the modulation-frequency range above 10 kHz. The authors originally suspected that this structure may have been due to the presence of an additional stratified layer with an abrupt interface. Possible explanations in terms of a thermally-thick interface layer, a coating surface oxide layer, and a sub-surface substrate polishing damage layer were all examined via modelling. However, additional measurements were performed on a number of samples, including a Ni

coating e-beam deposited onto a sapphire substrate, a Ti coating dc magnetron sputtered on to a fused silica substrate that had been argon-ion beam milled after polishing to remove a graded layer two to

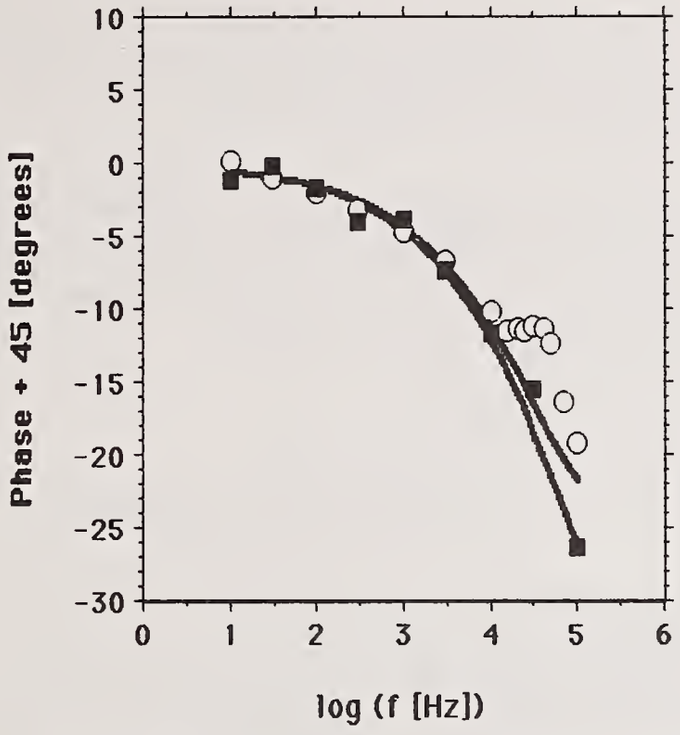

Fig. 3. 1 μm RF Sputtered Ti Coating on Fused Silica

ten micrometers thick[16], and the Mo mirror at a finer grid of modulation frequencies. In every case, structure was observed in the same modulation frequency interval. Since the unexplained data structure occurs at the same modulation frequency in many dissimilar samples, it is quite likely to be the result of a systematic error. Further work to identify the cause is under way. Notwithstanding the presence of the unexplained structure, the tentative interpretation of the data is that the Ti coating is displaying essentially bulk-like thermal transport behavior, with negligible thermal contact resistance (much less than 10^{-2} K/(W/cm^2)), and with one-dimensional heat flow exhibited at all modulation frequencies employed.

Conclusion

Thermal-wave interferometry can produce a wealth of thermal transport information on a single sample. Onset of three-dimensional heat flow, contributions due to thermal contact resistance, evidence of transit time effects, and the presence of unanticipated stratified layers are some of the phenomena that may be seen. As the preceding results imply, the present agreement with plausible models based on handbook transport data suggests that quantitative modelling using adjustable parameters should also be possible, provided that the physical origin of the observed data is understood. The natural consequence of the sensitivity to the detailed transport physics that is shown is that great care must be taken while interpreting the data. However, the revealed detail ensures that essential effects are not overlooked.

Acknowledgments

Productive discussions with Alan Stewart (Battelle PNL), Kent Stowell (Weapons Laboratory) and Patricia White (Battelle PNL) are gratefully acknowledged. This research was funded by grant AFOSR-88-0038 from the Air Force Office of Scientific Research.

[1]R.T. Swimm and L. Hou, NIST Special Publication **752**, Laser Induced Damage in Optical Materials: 1986 (Government Printing Office, Washington, DC, 1988), p. 251.

[2]R.T. Swimm, NIST Special Publication **756**, Laser Induced Damage in Optical Materials: 1987 (Government Printing Office, Washington, DC, 1988), p.328.

[3]R.T. Swimm, Appl. Phys. Lett. **42**, 955 (1983).

[4]J. Baumann and R. Tilgner, J. Appl. Phys. **58**, 1982 (1985).

[5]C.A. Paddock and G.L. Eesley, J. Appl. Phys. **60**, 285 (1986).

[6]Akira Ono, Tetsuya Baba, Hiroyuki Funomoto and Akira Nishikawa, Jpn. J. Appl. Phys. **25**, L808 (1986).

[7]L.J. Bortner, R.S. Newrock and D.J. Resnick, J. Appl. Phys. **61**, 4452 (1987).

[8]E.T. Swartz and R.O. Pohl, Appl. Phys. Lett. **51**, 2200 (1987).

[9]B.M. Clemens, G.L. Eesley and C.A. Paddock, Phys. Rev. B **37**, 1085 (1988).

[10]H.P.R. Frederikse and X.T. Ying, Appl. Opt. **27**, 4672 (1988).

[11]J.C. Lambropoulos, M.R. Jolly, C.A. Amsden, S.E. Gilman, M.J. Sinicropi, D. Diakomihalis and S.D. Jacobs, J. Appl. Phys. **66**, 4230 (1989).

[12]Ray Bell (Lockheed, Inc.), private communication.

[13]H.S. Carslaw and J.C. Jaeger, in Conduction of Heat in Solids (Oxford University Press, Oxford, 1959), Chap. XVII, p. 461.

[14]M. Abramowitz and I.A. Stegun (ed.), in Handbook of Mathematical Functions, U.S. Dept. of Commerce, Nat. Bur. of Stand., Appl. Math. Series **55** (Government Printing Office, Washington, DC, 1964), Eq. 11.4.29, p. 486.

[15]The $\exp(-\sigma^2 r_0^2/8)$ factor in the integrand of Eq.(9) keeps the integral and its derivatives with respect to r and z well behaved as $r \to 0$ and $z \to 0$.

[16]In collaboration with Patricia White.

Erratum

A systematic error that entered during the system phase calibration was discovered in the data presented in [2]. Consequently the data and data analysis in that paper are invalid.

Investigation of Thin Films Using Total Internal Reflection Microscopy

F.L. Williams, C.K. Carniglia and B.J. Pond

S. Systems Corporation
Developmental Optics Facility
P.O. Box 9316
Albuquerque, NM 87119

W.K. Stowell

Weapons Laboratory
WL/ARCB
Kirtland AFB, NM 87117

The application of total internal reflection microscopy (TIRM) to the inspection of subwavelength optical features on surfaces has been well documented.[1-3] This paper discusses recent experiments testing the feasibility of using TIRM to study dielectric coatings in the nucleation stage. Samples were coated with thin films of different thicknesses to allow optical scattering levels to be determined as a function of coating thickness. An increase was observed in scatter levels with increasing coating thickness, and is assumed to be related to thin film microstructure. Thus, TIRM provides a means of detecting film defects in the early stages of coating growth, as well as identifying possible precursors to nodules that are often observed in thin and thick films.

Key Words: surface inspection technique, thin film defects, optical scatter

1. Introduction

Total internal reflection microscopy (TIRM) has been shown to be an effective technique for observing subwavelength features on surfaces.[1-3] Scattered light is easily detectable from scratches and pits on an optical surface, as well as from subsurface microcracks. In addition, scattering from optical coatings can be viewed.[2] The purpose of this study is to investigate the practicality of examining scattered light from thin films using TIRM.

The basic configuration for TIRM is illustrated in figure 1. A laser beam is directed into a prism by means of an adjustable mirror. The beam is then coupled into an optic through a thin layer of index matching fluid, and is incident on the top surface of the optic at an angle slightly greater than the critical angle θ_c for total internal reflection. Thus, there is no specular beam in the region above the optic. However, light scattered by surface and subsurface defects can escape from the optic and be observed by an optical microscope focused on the surface from above. For visual observation, a laser with several hundred mW of power is required for inspecting most surfaces.

Figure 2 illustrates a plot of the intensity (i.e., the square of the electric field) at the surface of the optic for a beam polarized in the transverse or s direction and with an incident angle slightly greater than θ_c. The standing wave present in the optic has a maximum intensity which is four times the incident intensity. The evanescent field extends a few wavelengths into the region on the other side of the interface. Note that for this and other intensity plots, a wavelength of 514 nm is used.

For a very thin film on the surface, the intensity profile is essentially unchanged, as shown in figure 3a. Here a film with a thickness of 100 Å and a refractive index n = 1.85 has been added to the surface of a fused silica optic with index n_s = 1.45. If the film is thicker, the intensity profile is altered and depends on the film thickness, as illustrated in figure 3b.

Scalar scattering theory applied to surfaces predicts that for s polarization, the total integrated scatter is proportional to the electric-field intensity.[4] Therefore, the scatter as a function of film thickness may be estimated by integrating the intensity over the thickness of the film. Figure 4 shows the estimated relative scatter as a function of film thickness for a ZrO_2 film having a refractive index of 1.85 on a silica substrate. The incident angle is slightly greater than θ_c and the wavelength is 514 nm. As expected, the scatter increases with increasing film thickness, but there are oscillations in the curve resulting from the standing-wave nature of the electric field. For very thin films (thickness < 200 Å), however, the intensity is nearly unchanged, so the scatter is proportional to the film thickness. This calculation does not include effects due to variations in scattering-site density within the coating, which have been observed in dielectric films.[5,6]

2. Experiment

Thin films of ZrO_2 were simultaneously deposited on 2-in-diam fused-silica substrates of "standard-grade" (SG) surface quality and "super-polished" (SP) surface quality. All substrates were cleaned using detergent, deionized water and organic solvents before being loaded in the coating chamber.

Electron-beam evaporation was used to produce the thin films analyzed in this study. The coatings were produced in an ultra-high vacuum chamber that was brought to a pressure of ~1 x 10^{-9} torr prior to deposition. The films were deposited at a rate of ~0.2 Å s^{-1} in an atmosphere of ~6 x 10^{-5} torr O_2. Coatings having nominal uniform thicknesses of 50 Å, 250 Å, 500 Å and 1000 Å were produced. The substrates were masked so only half the surface became coated during deposition. This allowed characterization of both the coated and uncoated surface of each sample generated in this study.

After being coated, the substrates were removed from the vacuum chamber and analyzed by TIRM. The TIRM apparatus was located directly under a high-efficiency particle air (HEPA) filter to minimize surface contamination during characterization. An argon-ion laser operating at 514 nm was used as the illumination source, and the laser was light-monitored to produce a stable output of 500 mW. A cube polarizer was situated in the beam just prior to the input mirror to insure that only s-polarized light illuminated the sample. A standard microscope with a camera attachment was used to produce micrographs of the surfaces using TIRM. The exposure time for all micrographs was fixed at 30 secs.

It is important to note that it is very difficult to characterize by photography the nature of scatter images that can be observed using TIRM. Exposure time, laser power, the type of photographic film used and the photographic development process all have dramatic effects on the recorded image quality. These parameters must be carefully optimized to achieve even an approximate reproduction of the quality of TIRM images that are easily observed by the naked eye. Consequently, TIRM is an inspection technique that must be personally experienced to be fully appreciated.

3. Results

Figure 5a is a TIRM micrograph of an SG optic that has half of its surface coated with ~50 Å of ZrO_2. The figure is a photograph taken near the edge of the coating such that the left half of the micrograph is an image of the coated portion of the optic, while the right half depicts the uncoated surface. All TIRM micrographs presented in this report were produced in the same manner.

Figure 5b is a micrograph produced by Nomarski microscopy of the same region characterized in figure 5a. While the TIRM micrograph of this region reveals the presence of scattering defects, there is virtually no detail observable in the Nomarski micrograph.

This comparison emphasizes the sensitivity of TIRM and its utility in examining surface and subsurface imperfections.

The samples examined in this study exhibit two general types of optical scatter observable by TIRM:

a) "Background scatter," which appears as a form of diffuse graininess that is not localized and occupies the entire field of the image.

b) "Point scatter," which is visible as distinct bright points of light.

Figures 6a and 6b are TIRM micrographs obtained from optics that have been coated with ~50 Å of ZrO_2. For these and the rest of the photos presented in this report, the micrographs designated by "a" are taken from SG optics while "b" micrographs are taken from SP optics. In both figures 6a and 6b, it can be seen that the coated side exhibits more point scatter than does the uncoated side. This is especially true for the SP optic, which is practically devoid of point scatter on the uncoated side. In addition, the SP optic displays considerably less background scatter compared to the SG optic.

These trends continue and become more pronounced as film thickness increases. In figures 7a and 7b, TIRM micrographs of SG and SP optics coated with ~250 Å of ZrO_2 are presented. Figures 8a and 8b are TIRM micrographs taken from optics coated with ~500 Å of ZrO_2, and figures 9a and 9b show TIRM micrographs taken from optics coated with ~1000 Å of ZrO_2. Inspection of these micrographs reveals that an increase in film thickness is accompanied by an increase in the number and photodensity of point scatter sites in the coated region. The SG optics also appear to generate point scatter sites at a faster rate than SP optics.

The background scatter does not behave in the same manner. In fact, when using s-polarized illumination, the background scatter level of the coated region generally decreases as film thickness increases.

4. Discussion

It is a well-known phenomenon that coating defects increase in size as thin film growth progresses.[7] These defects in dielectric films are usually in the form of nodules.[8,9] The point scatter observed in this study most likely originates from such nodules.

Several researchers have reported the result that nodules in general begin at the substrate/film interface and grow in size as the film thickness increases.[7-9] As described above, however, the TIRM point scatter, which is presumed to be evidence of film nodules, is seen to increase with increasing film thickness. This fact appears to indicate that, while nodule growth may begin only at the substrate/film interface, the size of nodules generated is non-uniform. This could yield the observed result that point scatter level increases with increasing film thickness, since nodules not detectable at the onset of film growth could expand to detectable size as the film becomes thicker. This conclusion is supported by Liao et al. (1988), who observed that nodules in thin films are indeed nonuniform in size.[9]

It has been theorized that nodule growth originates only from surface contaminants such as dust, residual polishing compounds and evaporant spatter.[9] These particles act as seeds located at the substrate/film interface. In the current study, coatings deposited on SG optics generate point scatter sites at a greater rate compared to SP optics. Since SP optics exhibit less surface defects compared to SG optics, we conclude that nodule generation in this study depends on the surface quality of the optic. It is not known at this time, however, if nodule generation is occurring directly from surface defects acting as seeds, or if the poorer surface quality of SG optics makes them more prone to accumulate nodule seeds in the form of surface contamination.

The dependence of background scatter on whether the surface is coated or not may be explained by considering the intensity near the substrate/film interface. Figure 10 shows the value of the s-polarized intensity determined at the interface as a function of film thickness. As discussed above, the intensity is four times the incident value for an uncoated substrate. By depositing film material on the optic, however, the value of the

intensity at the interface is seen to decrease. Thus, there is a direct correlation between the interface intensity and the background scatter level observed from coated surfaces analyzed in this study. This fact leads us to conclude that the background scatter detected by TIRM originates from substrate defects at and just interior to the optic surface. The fact that SP optics exhibit considerably less background scatter than do SG optics supports this finding.

5. Conclusion

Total internal reflection microscopy has been used to characterize thin films of ZrO_2 deposited on SG and SP optics. Point scatter sites are presumed to represent evidence of thin film nodules in the coating, while background scatter most likely originates from surface and subsurface defects in the optic. Both forms of TIRM scatter are seen to depend on film thickness and on the surface quality of the optic. Consequently, TIRM has been shown to be a sensitive method of surface analysis capable of detecting the effects of coating process parameters and optical surface quality in thin films.

6. Acknowledgements

This effort was sponsored by the Weapons Laboratory, Kirtland AFB, NM, 87117, and was funded by the Air Force Office of Scientific Research.

Some of the figures were generated using a program provided by Thin Film Designer Software.®

7. References

1) M. Hercher, "Virometer - an instrument for the measurement of the size of viruses using an optical microscope," in Clever Optics, Proc. SPIE 126, 17 (1977).

2) P.A. Temple, "Examination of laser damage sites of transparent surfaces and films using total internal reflection microscopy," in Laser Induced Damage in Optical Materials: 1979, Natl. Bur. Stand. Spec. Publ. 568, 333 (1980).

3) M. Law, J. Bender and C.K. Carniglia, "Characterization of calcium fluoride optical surfaces," in Laser Induced Damage in Optical Materials: 1986, Natl. Inst. Stand. Technol. Spec. Publ. 752, 532 (1988).

4) C.K. Carniglia, "Scalar scattering theory for multilayer optical coatings," Opt. Eng. 18, 104 (1979).

5) R.E. Klinger and P. Swab, "Evolution of surface roughness and scatter in evaporated zirconia/silica multilayer coatings," in Optical Thin Films II: New Developments, Proc. SPIE 678, 41 (1986).

6) K.H. Guenther, H.L. Gruber and H.K. Pulker, "Morphology and light scattering of dielectric multilayer systems," Thin Solid Films 34, 363 (1976).

7) R. Messier, "Toward quantification of thin film morphology," J. Vac. Sci. Technol. A 4, 490 (1986).

8) K.H. Guenther, "Nodular defects in dielectric multilayers and thick single layers," Appl. Opt. 20, 1034 (1981).

9) B. Liao, D.J. Smith and B. McIntyre, "The formation and development of nodular defects in optical coatings," in Laser Induced Damage in Optical Materials: 1985, Natl. Bur. Stand. Spec. Publ. 746, 305 (1988).

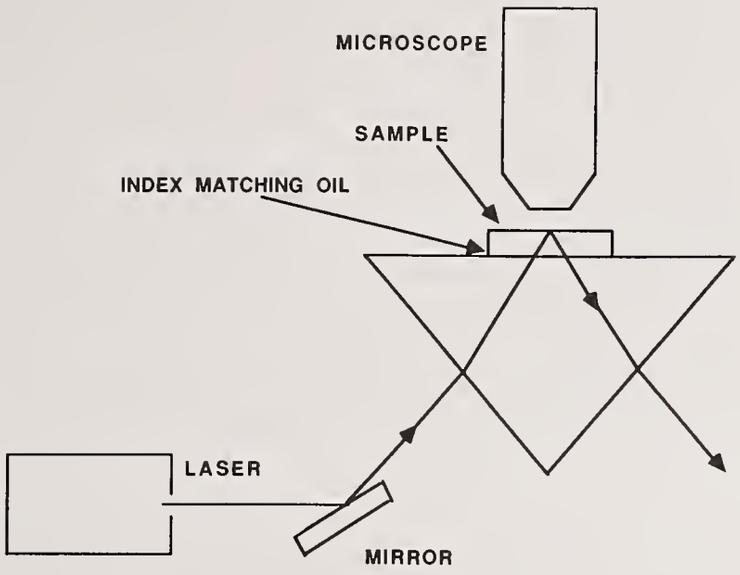

Figure 1. Total Internal Reflection Microscopy

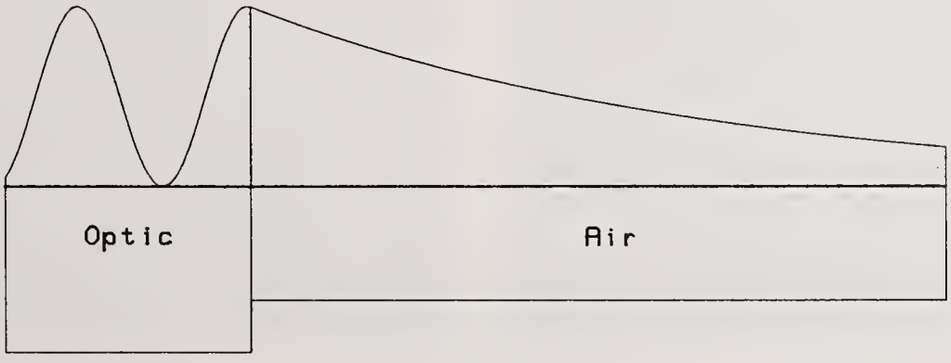

Figure 2. Intensity near the surface of the optic for total internal reflection

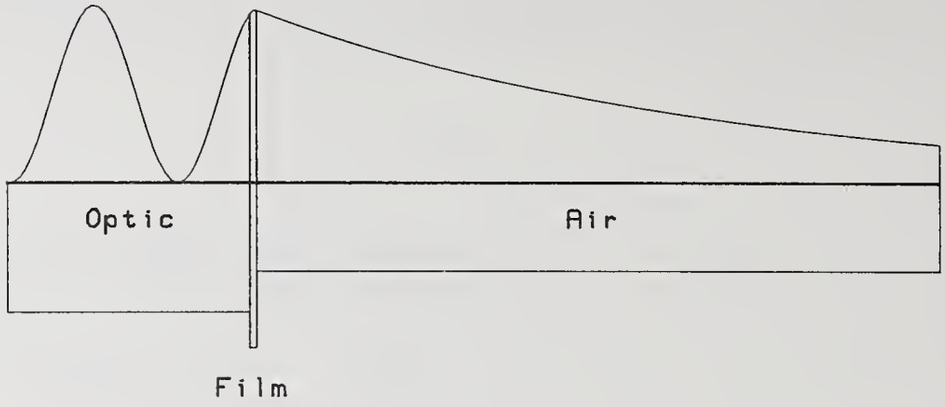

(a). 50-Å-thick coating

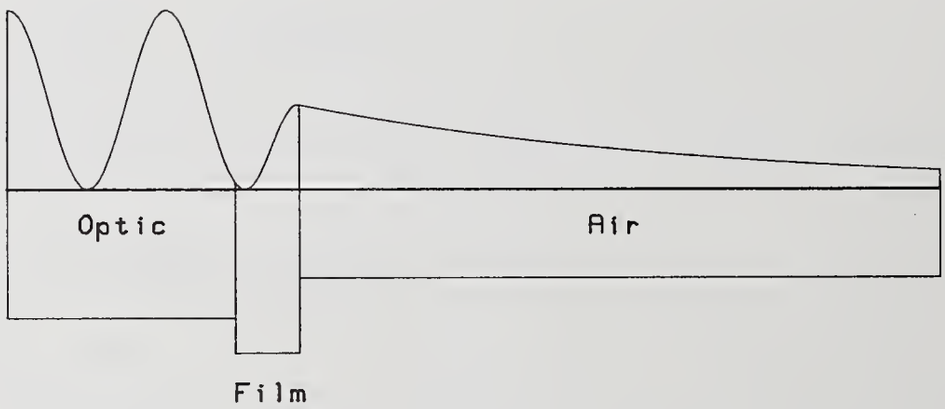

(b). 1000-Å-thick coating

Figure 3. Intensity near the surface of a coated optic for different film thicknesses

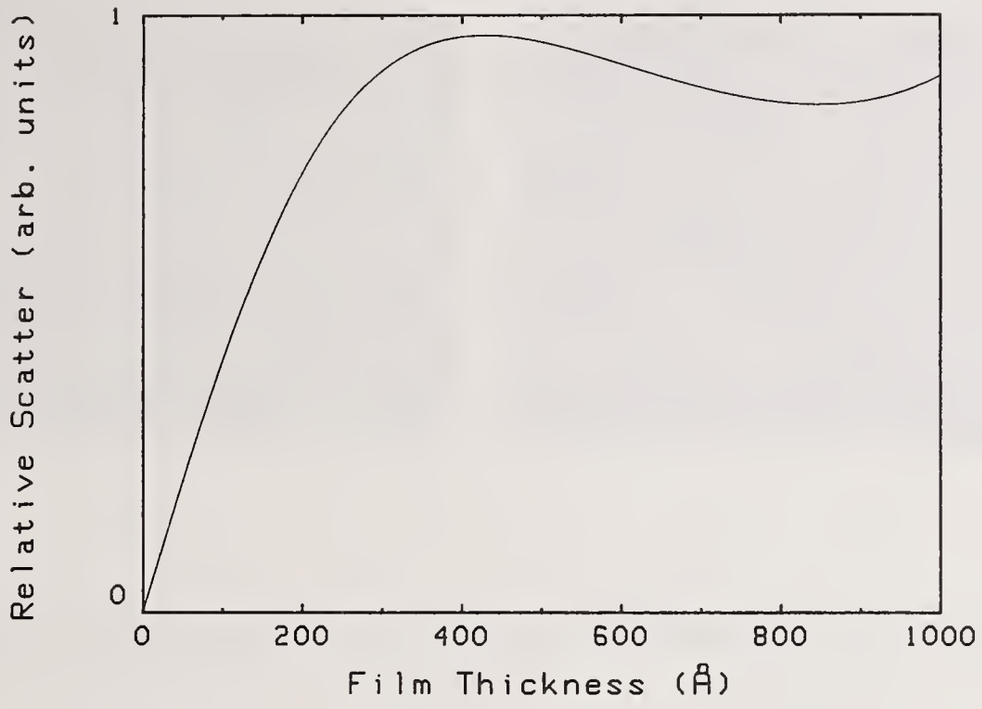

Figure 4. Estimated relative TIRM scatter from a ZrO_2 thin film as a function of film thickness

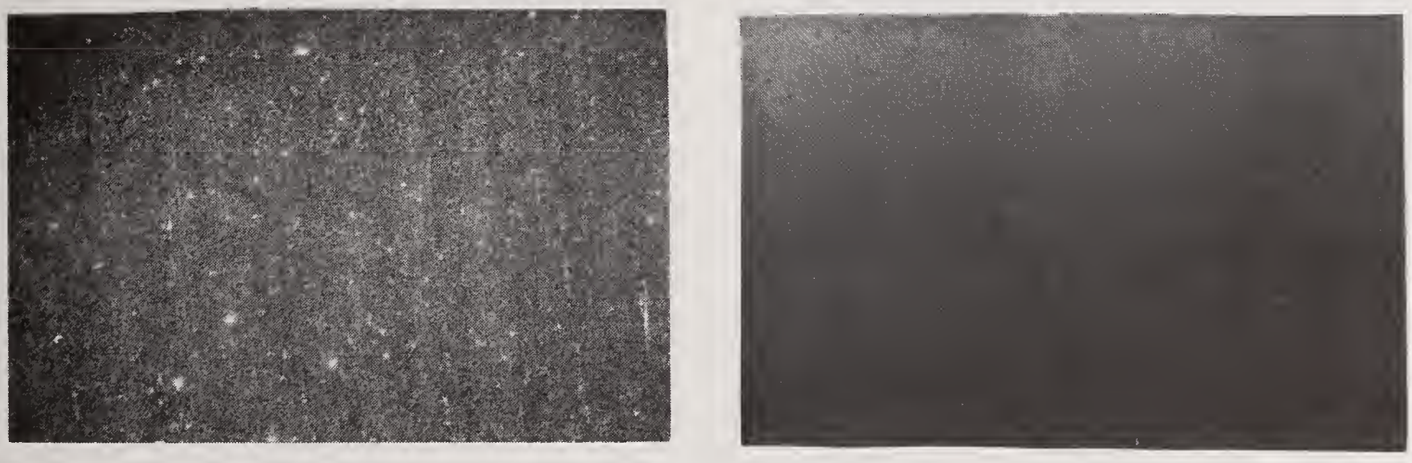

(a) (b)

Figure 5. Micrographs of the same surface taken by (a) TIRM and (b) Nomarski microscopy

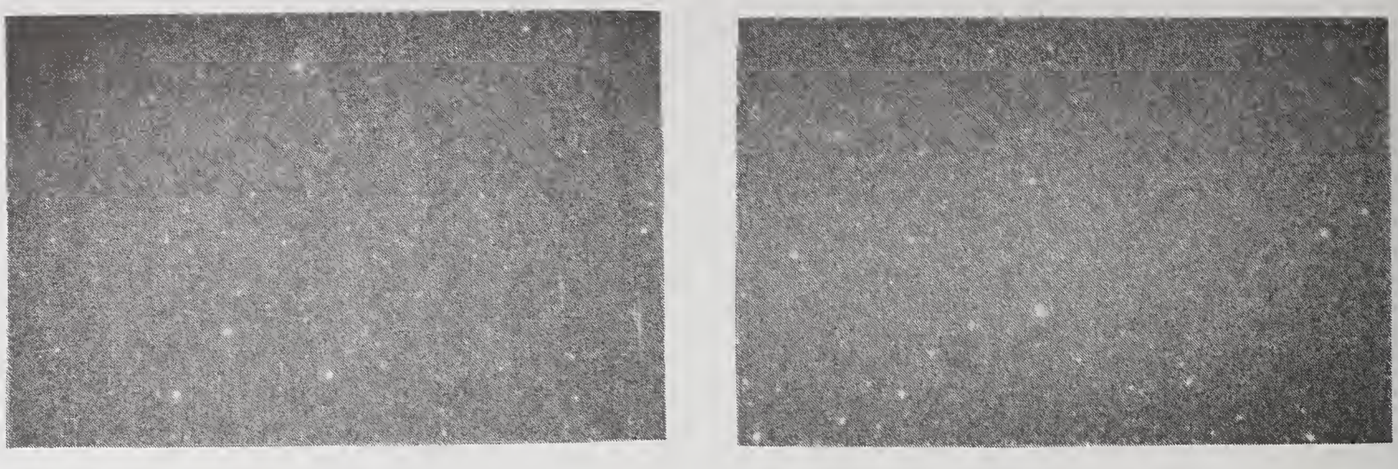

(a) (b)

Figure 6. TIRM micrographs of (a) SG and (b) SP optics coated with ~50 Å of ZrO_2

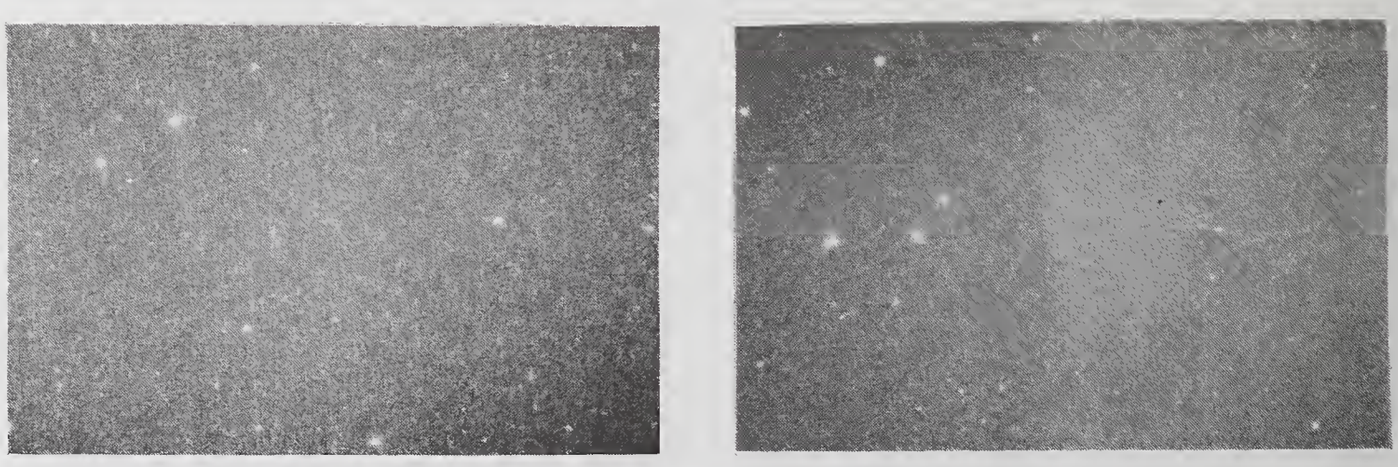

(a) (b)

Figure 7. TIRM micrographs of (a) SG and (b) SP optics coated with ~250 Å of ZrO_2

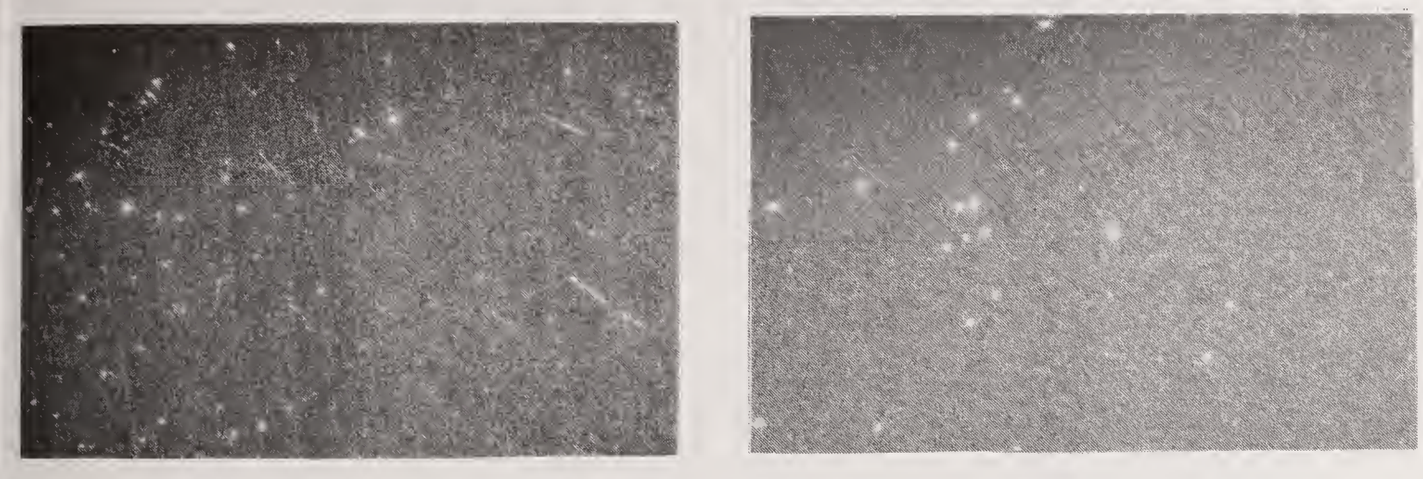

(a) (b)

Figure 8. TIRM micrographs of (a) SG and (b) SP optics coated with ~500 Å of ZrO_2

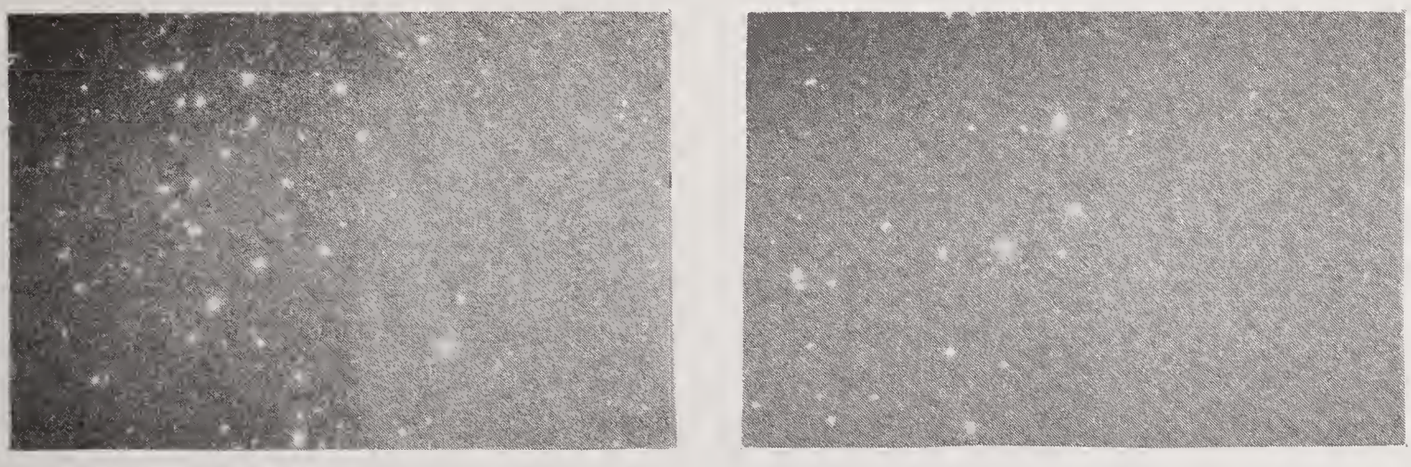

(a) (b)

Figure 9. TIRM micrographs of (a) SG and (b) SP optics coated with ~1000 Å of ZrO_2

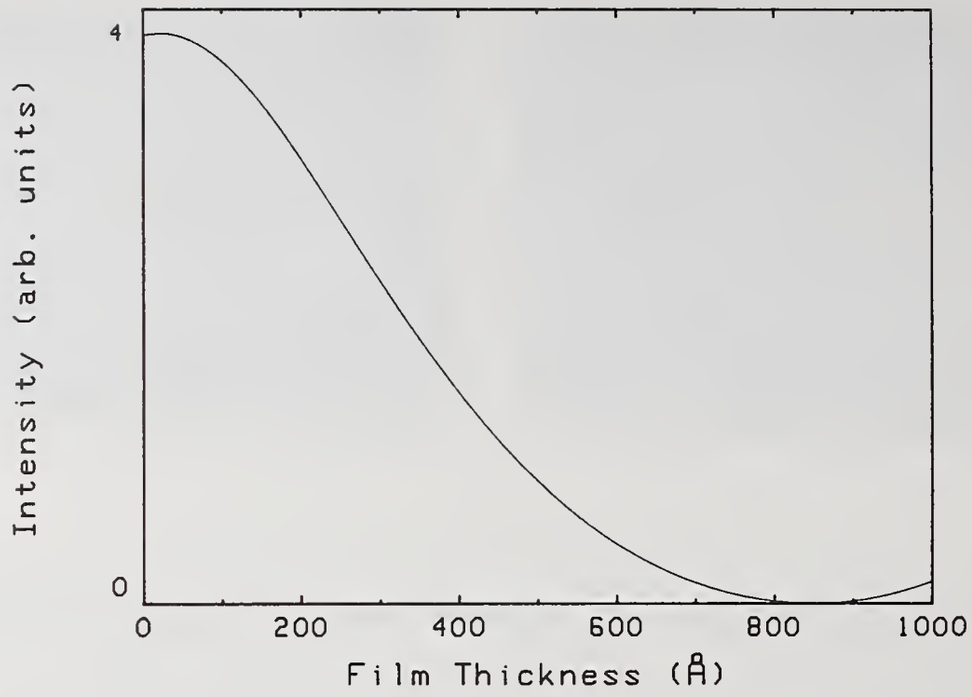

Figure 10. Intensity at the optic/film interface as a function of ZrO_2 thickness

Manuscript received
2-12-90

Scattering Characterization of Materials in Thin Film Form

C. Amra

Laboratoire d'Optique des Surfaces et des Couches Minces - Unité Associée au CNRS - Ecole Nationale Supérieure de Physique de Marseille - Domaine Universitaire de St Jérôme - 13397 Marseille Cedex 13 - France

The "scattering characterization" that was developed in Marseilles enables us today, with the help of complementary tools (causal model, isotropy degree, ...), to point out the origin of micro-roughness in optical coatings without any ambiguity. Each material can be associated to a key parameter that characterizes its scattering. These parameters can be determined through measurements performed on one single layer, and then can be used to predict scattering in more complex systems.

Experimental results (IAD, IP) are presented and show that in most cases, scattering measurement of substrate is sufficient to predict scattering from any coating with a high accuracy. However, at very low scattering levels (under 10^{-6}), this prediction is limited by the presence of local defects in the coatings.

key words: cross-correlation laws; Ion Assisted Deposition; isotropy degree; local defects; microroughness; optical coatings; scattering; thin films;

1. Introduction

It is well known today that if we want to establish an accurate energy balance in multilayer optical coatings, we have to take account of numerous factors that are connected more or less directly with the microstructure of materials in thin film form [1, 2, 3]. We will be interested here in surface scattering, and will say first that, at low loss levels, it is not easy to separate the effects of intrinsic absorption A (connected with extinction coefficients of materials) from the effects of scattering (due to roughness). Indeed, according to the method which is involved to measure the absorption (spectrophotometric measurements [4] or photodeflection technique [5] ...), we will have respectively access to intrinsic absorption plus external scattering (which is the quantity of scattered light that is measurable between 0° and 90°), or to intrinsic absorption plus other losses connected with internal scattering (which is the quantity of scattered light embedded inside the coating). For instance, if we consider a half-wave layer made of a material which extinction coefficient is 10^{-4}, a roughness of 1.8 nm at the two interfaces will give rise to more

scattering than absorption, and therefore we will have access to an apparent absorption A' which is in fact equal to the scattering D (A' = A + D ≅ D). The consequence is that in some cases, we will observe unexpected variations of absorption versus wavelength [6], since we know that scattering can vary in phase or in phase cancellation with reflection, according to the correlation between interfaces [7, 8].

The distribution of scattered light from an optical multilayer obviously depends on the design of the coating, but also on the roughness of each interface of the stack and on cross-correlation laws between these roughnesses [9, 10]. It is then possible, provided that we use adequate experimental and theoretical tools, to extract from scattering measurements numerous information (two dimensional roughness spectrum and autocorrelation function, isotropy degree variations ...) concerning each interface defect. This information is closely connected with material microstructure (at the scale of optical frequencies), and therefore scattering investigation appears to be an accurate method to characterize materials in thin film form.

The "scattering characterization" that was developed in Marseilles enables us today, with the help of complementary tools (causal model [8] for cross-correlation laws, isotropy degree variations [11], ...) to point out the origin of micro-roughness in optical coatings without any ambiguity relative to the choice of the parameters (roughness and cross-correlation coefficients). Each material can be associated to a key parameter that characterizes its scattering. These parameters can be determined through measurements performed on a single layer, and then can be used to predict scattering in more complex systems.

We present here our methods of investigation and give the results for coatings produced by Ion Assisted Deposition (IAD) [12] and Ion Plating [13] (IP).

2. Cross-correlation laws

2.1. Some recalls about the theory

According to the vector theories [9, 10], the scattered light from an optical coating can be written as:

$$BRDF \cdot \cos\theta = \sum_{i,j} C_i \bar{C}_j \, \alpha_{ij} \, \gamma_{jj} \qquad (1)$$

where:

- $BRDF.\cos\theta(\theta,\phi)$ is the scattered flux per unit of surface and solid angle, normalized to the incident flux.
- θ and ϕ are the angles that characterize a scattering direction (θ from the sample normal, ϕ polar angle).

- The ideal coefficients C_i [10] depend only on the design of the coating, and on illumination and observation conditions. They take account of the magnitude of the scattering sources at each rough interface, as well as of the multiple reflections of each scattered wave inside the multilayer.

- γ_{jj} is the roughness spectrum of interface j and contains all information relative to the defects of this surface: it is the Fourier Transform of the autocorrelation function of the profile of surface (j). Its integral over the range of measurable spatial frequencies gives the square of the roughness δ_j of this surface.

- α_{ij} is the cross-correlation coefficient between interfaces (i) and (j), and takes account of interference phenomena between the waves scattered by these two surfaces. It can be seen as a degree of coherence between the two scattering sources (i) and (j), or as a degree of similitude between the two interface profiles (i) and (j).

Usually the roughness spectrum is taken as the sum of the Hankel Transform (for isotropic surfaces) of a gaussian and an exponential function [11], which requires 4 parameters. Since most of the time cross-correlation coefficients and roughnesses are considered as independent parameters, therefore prediction of scattering from a p-layer stack requires the knowledge of 5p+4 parameters. In these conditions, there are always several solutions to fit the experimental results, which explains the limited number of non-ambiguous conclusions that can be found in the literature [7, 14, 15]. For instance, even in the case of a single layer, one can explain the distribution of scattered light (in the whole angular range) by considering correlated or uncorrelated surfaces (fig. 1).

Now we will show how the use of a causal model together with isotropy variations of scattering enables us to eliminate any ambiguity relative to the choice of the parameters.

2.2. A causal model

Correlation is certainly the key parameter of scattering since it enables destructive interferences to occur between the scattering sources inside the stack (provided that the design is adequate), which permits reduction of scattering losses. If we have uncorrelated roughnesses for instance, scattering will practically always increase with the number of layers of the stack. On the contrary case (perfectly correlated roughnesses), scattering can strongly be reduced after coating (antiscattering effect [15]). In a more general way, scattering in narrow-band filters will vary by a factor 50 according to the value of correlation between interfaces (with a high sensitivity to these parameters).

Usually the correlation is considered to be a real constant number between 0 and 1. In fact we have to take account of a more realistic model and write that the profiles of interfaces (i) and (i-1) are connected by the following relationship:

$$h_i = a_{i,i-1} * h_{i-1} + g_i$$

where (*) is a convolution product. This means that the defects of interface (i) are due to two different phenomena, that are reproduction (perfect or partial) of

interface (i-1) defects and addition of residual roughness that characterizes the grain size of the material in thin film form. Therefore the "filtering" function $a_{i,i-1}$ describes the action of the material at the interface, and g_i is due to the material microstructure (notice that these two functions can be connected).

The question is to know whether one or the other term will be predominant in scattering phenomena; for this we will first consider coatings produced on rather rough substrates (of the order of 1.5 nm) so that we can be sure that residual roughness is negligible compared to reproduction of substrate defects (experiment will prove this situation). In these conditions correlation is the Fourier Transform of the filtering function and varies with spatial frequency. Consequently the parameters are no more independent, since cross-correlation laws and roughness spectra are connected by:

$$\gamma_{ii} = |\alpha_{ij}|^2 . \gamma_{jj}$$

Therefore, and provided that the substrate is measured before coating, prediction of scattering from a p-layer stack (with two H and L materials) requires only the knowledge of two functions $\alpha_H(\sigma)$ and $\alpha_L(\sigma)$ [σ is the spatial frequency]. Indeed, if we look at expression (1), we can notice that:

- The ideal coefficients C_i are given by the theory when the design of the coating is known.
- The roughness spectrum γ_{jj} of interface (j) is given as a function of the roughness spectrum γ_s of the substrate, provided that correlation is known:

$\gamma_{jj} = f(\gamma_s)$

- The roughness spectrum γ_s of the substrate can be measured before coating.
- The correlation α_{ij} is given as a function of the successive cross-correlation coefficients $\alpha_{k,k-1}$:

$$\alpha_{ij} = \prod_{k=0}^{i-j-1} \alpha_{i-k,i-k-1} \qquad (j < i)$$

Since we can assume that the same material will have the same effect on interfaces whatever the layer of the stack, we can write: $\alpha_{2k,2k-1} = \alpha_L$ and $\alpha_{2k-1,2k-2} = \alpha_H$, where $\alpha_H(\sigma)$ and $\alpha_L(\sigma)$ are relative to the high and low index materials that constitute the multilayer.

Moreover, we must not forget that with an incident wavelength of 0.6 µm, scattering in the direction $\theta = 5°$ is due to the presence, on the rough interfaces, of sinusoïdal gratings of period $C \cong 7$ µm. It is then very probable that, whatever the material microstructure, the layer will perfectly reproduce a grating of period nearly one hundred times its thickness (for visible applications)(**fig.2**). For this reason, we will assume that correlation is perfect at least for large period defects (that is, to explain scattering at small angles), and that it decreases with decreasing period defects. Therefore the materials act as low-pass filters, and the filtering functions α_H and α_L can be characterized with only one parameter which is a cut-off frequency. Briefly, scattering from a p-layer stack can be predicted with only two cut-off frequencies (σ_H and σ_L) if the substrate is measured before coating.

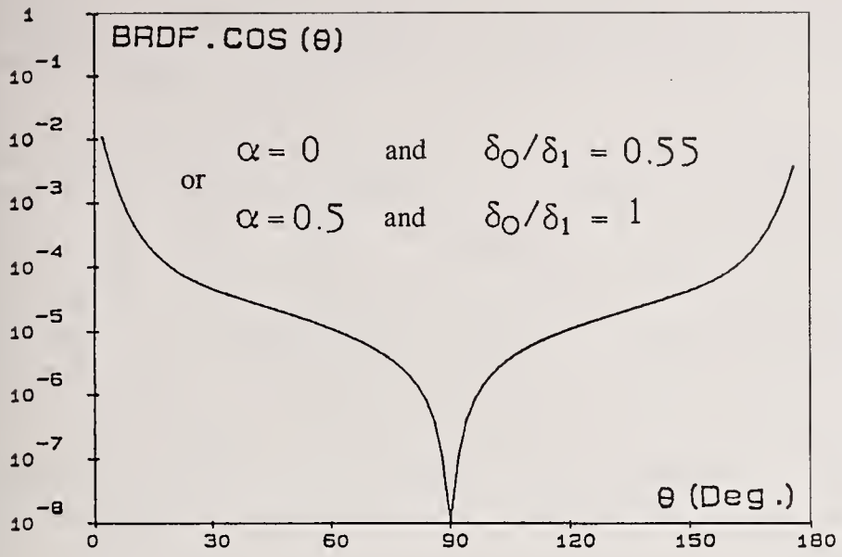

Figure 1:

Scattering from a single $\lambda_0/2$ high index layer. The angular distribution can be explained in the whole range (0° → 180°) assuming one or the other of the following cases:

- The two roughnesses are identical and correlation is partial, that is: $\delta_o/\delta_1 = 1$ and $\alpha_{10} = 0.5$.
- The roughnesses are different and correlation is zero, that is: $\delta_o/\delta_1 = 0.55$ and $\alpha_{10} = 0$.

Note that λ_0 is the wavelength of incident light.

For θ = 5°

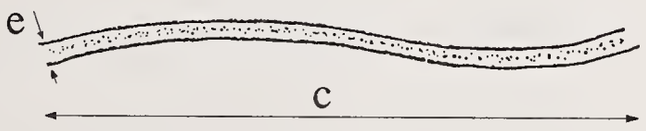

Figure 2:

Schematic representation of the ratio C(θ)/e, where C(θ) is the grating period responsible for scattering in the direction θ. The layer thickness is e.

For θ = 60°

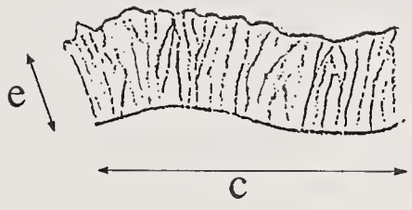

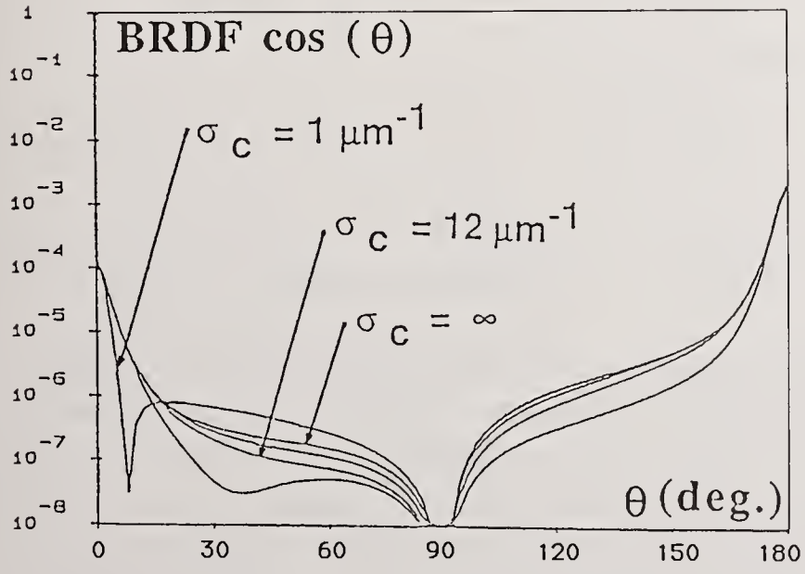

Figure 3:

Influence of cut-off frequency σ_c on the angular scattering curve of a single layer.

These parameters can be determined through measurements performed on single layers, and then can be used to predict scattering from more complex optical systems.

Fig.3 shows how the angular distribution of scattering is modified when the cut-off frequency is varied. The case where σ_c is infinite is that of perfect correlation for all period defects (no cut-off frequency).

Experimental results are in complete agreement with this causal model (see section IV) in the case of coatings produced on rather rough substrates (1.5 nm). In a second stage, we will have to decrease the substrate roughness in order to see whether this model remains valid or not (negligible residual roughness?). But in order to obtain a very detailed investigation and eliminate any ambiguity on the origin of micro-roughness, we will first present a complementary tool that is isotropy properties of scattering.

Notice here that we have worked with classical quarter-wave coatings (all layers of same material have identical thicknesses), for which reason we did not investigate dependence of correlation with thickness.

3. Isotropy variations of scattering

With the preceding causal model, we have seen that the substrate is privilegied since its defects are responsible for the roughness of each interface. In fact, many substrates present privilegied directions that give rise to non-isotropic scattering, which can be pointed out through level maps (**fig.4**). This information can be very helpful for investigation of microroughness.

3.1. Uncoated surfaces

Instead of limiting ourselves to the qualitative view of **fig.4**, we can define a quantitative value of anisotropy through considerations on the angular autocorrelation. Starting from the measurements of scattering in whole space, we can extract the bidimensional roughness spectrum and calculate the normalized angular autocorrelation $F(\alpha)$ of Autocorrelation function of surface defects. In the case of an isotropic surface, the angular function $F(\alpha)$ is constant and we say that the isotropy degree is equal to unity. In the contrary case (**fig.5**), $F(\alpha)$ is first decreasing, and we define the isotropy degree as the minimum of the curve. In other words, isotropy degree is analogous to autocorrelation length but from a point of view of rotation.

If we want to obtain more information and work with each spatial frequency, we can perform the same calculation for each period defect and plot the variations of isotropy degree with spatial frequency (or scattering angle) (**Fig. 6**). For this, the surface profile is seen as an infinite sum of sinusoïdal gratings, and we calculate the isotropy for all gratings that have same period but different orientations. This is a real advantage against the preceding angular function $F(\alpha)$ which integrates all

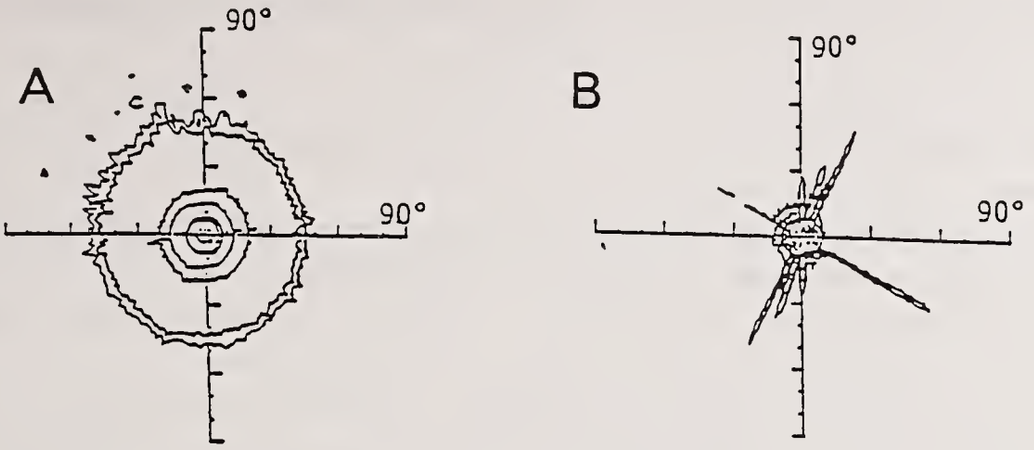

Figure 4:
Level maps of scattering from an isotropic (A) and a non isotropic (B) substrate. Departure from perfect circles is due to the presence of privilegied directions on the surface.

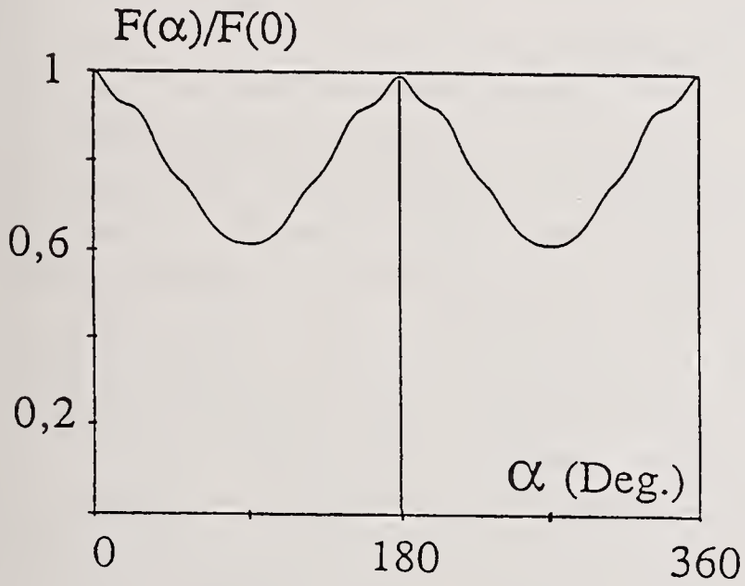

Figure 5:
Angular function F(α) calculated from the measurements of scattering. Notice the perfect symmetry of the curve at 180°. The isotropy degree is near 0.6 in this case. The presence of local extrema is due to the existence of several directions on the surface.

Figure 6:
Variations of isotropy degree versus spatial frequency σ (or scattering angle). Large period defects show a more pronounced anisotropy.

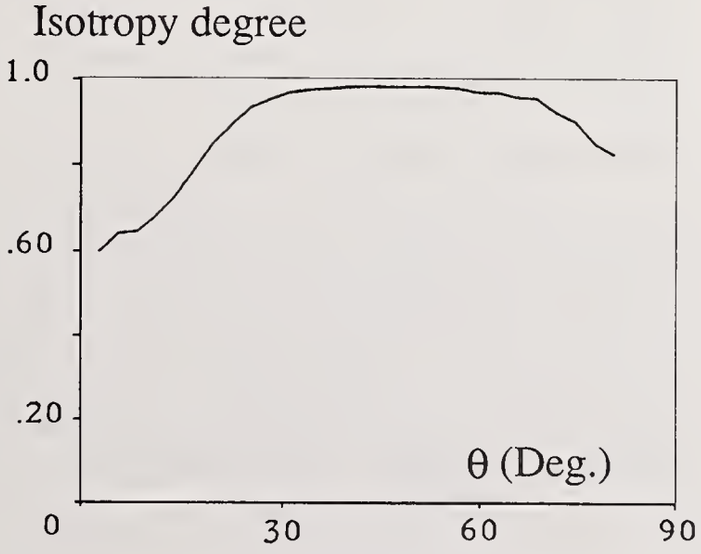

period defects simultaneously (as an analogy, the roughness spectrum gives more detailed information than only the roughness).

3.2. Optical coatings

Isotropy variations of scattering is a real signature of the substrate roughness and can be used to investigate the origin of microroughness in optical coatings. In fact, the preceding angular function $F(\alpha)$ cannot be directly used here since it is relative to the defects of only one surface. For this reason, we use a different angular function $F'(\alpha)$ related to scattering and not to roughness spectrum. Therefore the method of investigation is the following: starting from a substrate which scattering has been measured in whole space, we extract the bidimensional roughness spectrum and therefore we calculate (using the causal model) the distribution of scattered light in whole space from any coating produced on this substrate. In this way, we have access to the angular function $F'(\alpha)$ which is relative to the predicted scattering. At the same time, the coating is produced and its scattering is measured in whole space, so that we can compare directly the calculated and measured angular functions $F'(\alpha)$.

The use of isotropy degree variations is more convenient since we can show that it is independent of the design of the coating, provided that these coatings are produced under quasi-normal incidence deposition [8]. This means that, due to the fact that all functions are normalized, the isotropy degree variations calculated with the substrate scattering are identical to those calculated with the scattering of the coating (assuming that residual roughness is negligible). This presents two real advantages: first, it is not necessary to calculate the scattering from the coating (measured isotropy degree variations can be directly compared before and after coating and must be the same if residual roughness is negligible, whatever the values of cut-off frequencies). Secondly, since isotropy variations are independent of the design of the coating, the comparison of the curves before and after coating is valid even if there are errors on the layer thicknesses. As a summary, we will say that isotropy of scattering is a precious complementary tool, since any difference observed between the curves measured before and after coating will point out the limit of the causal model. This tool will be very useful to investigate the experimental results of section IV.

As for a remark, we will also say that this tool permits an eventual columnar growth of materials to be detected [8]. Indeed, for a coating produced at oblique incidence deposition, the substrate defects are reproduced with a lateral shift, which modifies the interference phenomena between the scattered waves (in this case, the correlation has a phase term). The consequence is that the isotropy variations will be modified and can therefore be easily detected (fig. 7): even if all surfaces of the stack are isotropic, scattering will not be isotropic.

4. Application to experiment

Experimental results are relative here to TiO_2 and SiO_2 materials obtained with IAD. We will not present the results for Ta_2O_5 and SiO_2 materials obtained by I.P., since the conclusions are exactly the same (no difference between these two techniques and materials for the scattering behavior).

4. 1 Classical stacks

Fig. 8 shows that the agreement between calculation and measurements is excellent for a single layer, and this in the whole range of angular scattering. The predicted angular scattering curve was calculated with the measured roughness spectrum of the substrate (using the causal model), and the superimposition to experiment is obtained for an infinite cut-off frequency (no cut-off frequency): this means that we can explain the experimental results assuming a perfect correlation for all period defects.

This is first confirmed using the angular autocorrelations of **fig. 9**, since there is no difference between calculation and measurements. At last, if we observe the variations of isotropy degree before and after coating (**fig. 10**), we have perfect agreement between the two curves at low scattering angles (large period defects) and a slight difference at large angles. It is not obvious that such difference is due to the limit of the causal model because, at this stage of accuracy, we could implicate some errors due to the linearity of the detector (notice that we have a linear scale). Anyway, these three curves (**fig. 8, 9, 10**) prove that correlation is quasi-perfect in the whole range of measurable spatial frequencies and that residual roughness can be neglected here.

Fig. 11 and **12** show that these conclusions remain valid in the case of multilayer stacks (19-layer mirror and 9-layer Fabry-Perot filters). Therefore measurement of substrate is sufficient to predict scattering from these coatings with a high accuracy.

4.2. Specific stacks

The preceding coatings were produced on rather rough substrates (near 1.5 nm). Now we can wonder whether the causal model remains valid or not in the case of very low roughnesses; in other words, will the reproduction of substrate defects be predominant if we use highly polished substrates? Moreover, we could say that some coatings are more or less sensitive to the correlation (depending on their design), and that it is the reason why we do not detect shifts for perfect correlation at large scattering angles. In order to solve these two problems, we have produced specific stacks that are very sensitive to correlation [16] (a variation of correlation of 1% near unity increases the total scattering losses by a factor two), and these stacks were produced on very different substrate qualities (1.5 nm, 0.5 nm, 0.1 nm -

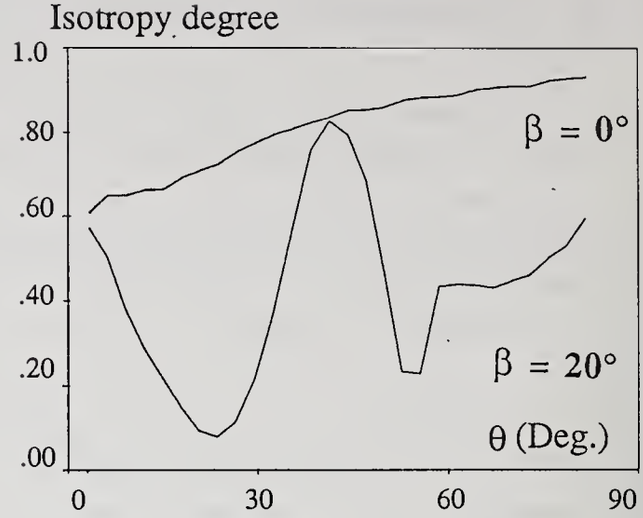

Figure 7:

Variations of isotropy degree calculated for a layer produced at normal ($\beta = 0$) and oblique incidence deposition ($\beta = 20°$). The calculation is performed using the causal model together with the measurements of a non isotropic substrate.

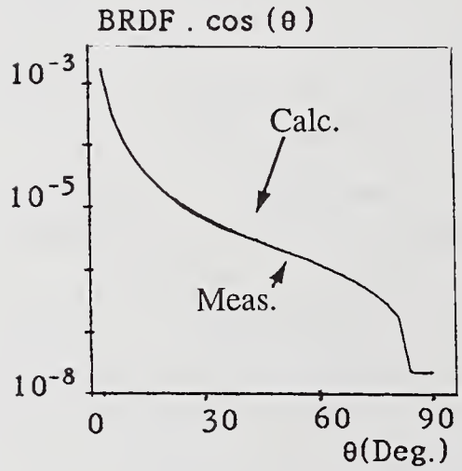

Figure 8:

Calculation and measurements of angular scattering curve of a single $6\lambda_0/4$ layer of SiO_2 produced by I.A.D.

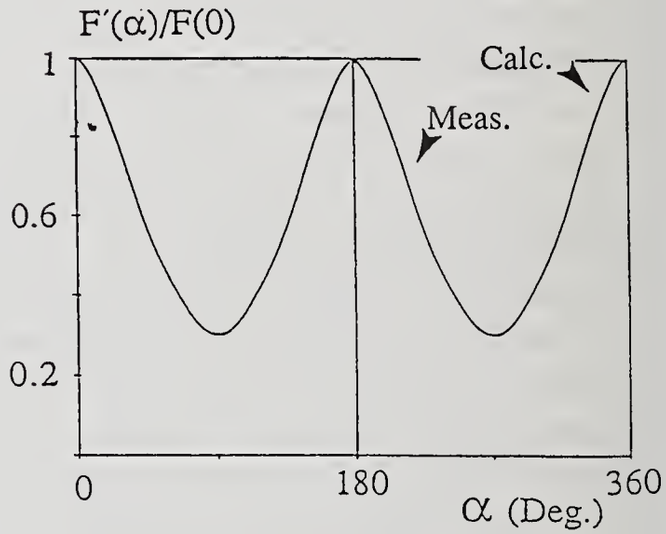

Figure 9:

Calculation and measurement of angular function $F'(\alpha)$ relative to the scattering from a (6L) SiO_2 layer.

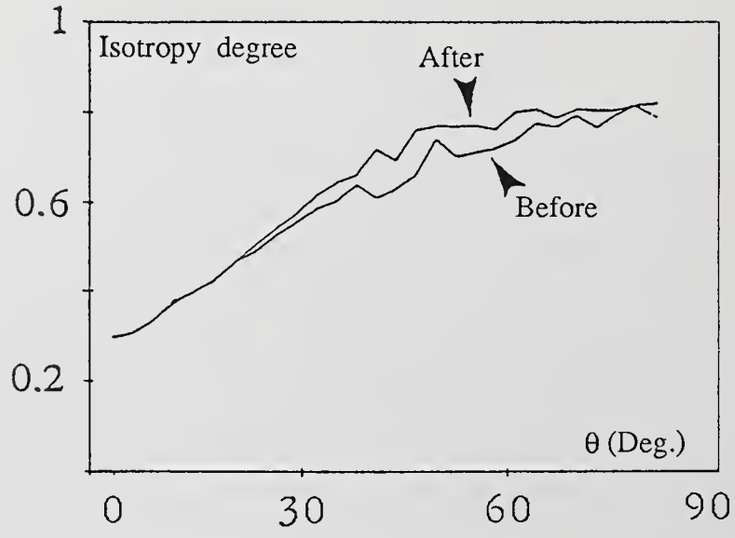

Figure 10:

Isotropy degree variations before and after coating by a (6L) SiO_2 layer.

the case of 0.1 nm is relative to a silicon wafer substrate). For these coatings, the theory predicts that the two angular scattering curves measured before and after coating must be the same if correlation is perfect in the whole range of scattering. The results are presented in **fig. 13**, and must be discussed now.

Whatever the substrate roughness, we can first notice that for the three coatings (**Fig. 13**), the curves before and after coating are superimposed at low scattering angles, which proves that correlation is perfect at least for large period defects. Concerning the disagreement observed at large angles, this could be explained *a priori* by involving scattering due to residual roughness or even to the volume of materials, but in these cases the scattering would be isotropic for these large angles. In fact, for **fig. 13a and 13b**, we can verify that the isotropy degree is very similar before and after coating (and different of unity) whatever the scattering angle, which proves that the disagreement is not due to residual roughness or bulk scattering. On the other hand, we demonstrate that the disagreement is due to a 1.5% error on the thickness of the layers (**fig. 14**), which is indeed the accuracy limit obtained with optical monitoring (for this stack). This error thickness was completely verified using spectrophotometric measurements [4] and guided wave techniques [17]: thickness given by scattering measurements is as accurate as thickness given by these two techniques. This accuracy is due to the fact that scattered light can see the layer thickness at all directions.

However, such reason cannot explain the disagreement observed in **fig. 13c**. In this case (0.1 nm substrate roughness), scattering levels are so low that the scattering due to local defects in the layers becomes predominant (compared to the scattering due to reproduction of substrate roughness). Usually, such presence of pits in the coating (that can be seen with Nomarsky microscope) has no influence on the scattering if the BRDF.cos θ is greater than 10^{-6}, which is not the case for the stack produced on the silicon wafer substrate. Nomarsky microscope reveals the presence of one pit (diameter 1µm) in a 350 µm diameter microscope field: in these conditions we have approximately 100 pits in the illuminated region (diameter $\phi \cong 2$ mm) of the sample. **Fig. 15** shows how the scattering from local defects can be quantified on a substrate. Unfortunately it is very difficult, even if we start from a perfectly clean substrate, to eliminate the presence of local defects in the volume of the layers: the presence of pits occurs during deposition, and their number increases with deposition time (or number of layers).

As a summary, we will say that reproduction of substrate defects is predominant for a substrate roughness of 1.5 nm or 0.5 nm. For lower substrate roughnesses, an eventual residual roughness (due to the grain size of materials) is not easy to detect since the scattering is due to local defects in the volume of the layers.

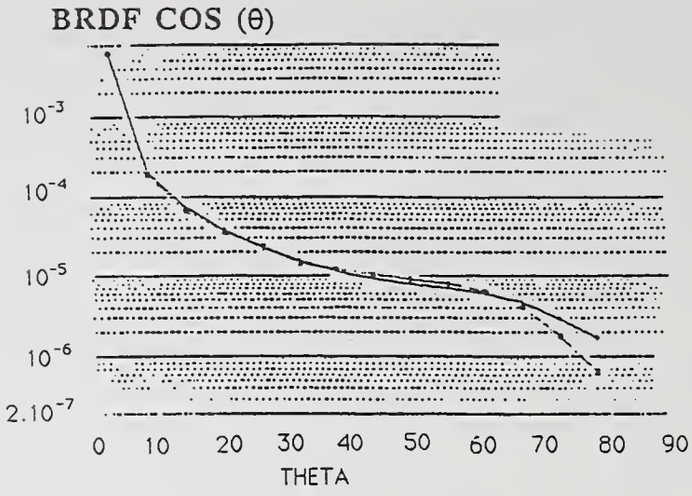

Figure 11:

Calculation and measurement of the angular scattering curve from a 19-layer quarterwave mirror produced by I.A.D. Materials are SiO_2 and TiO_2. Calculation is performed with an infinite cut-off frequency ($\frac{1}{\sigma_c} = 0$) for both materials.

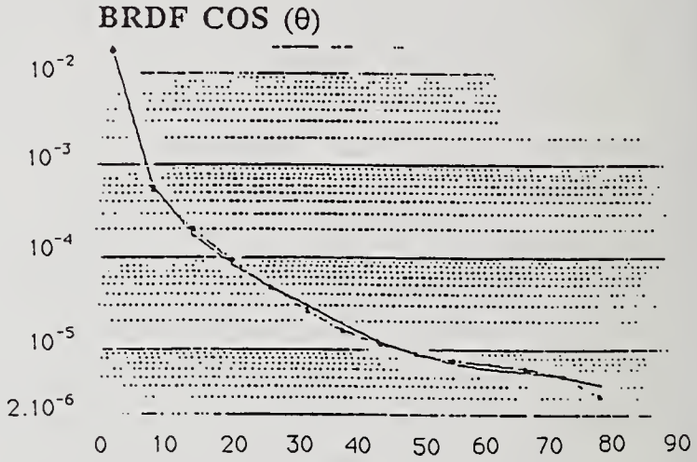

Figure 12:

Calculation and measurements of the angular scattering curve from a 9-layer Fabry-Perot filter ($\frac{1}{\sigma_c} = 0$).

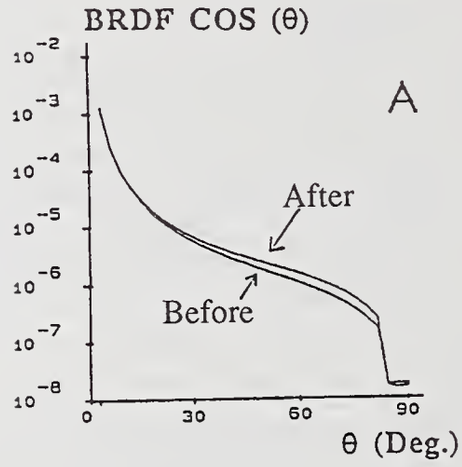

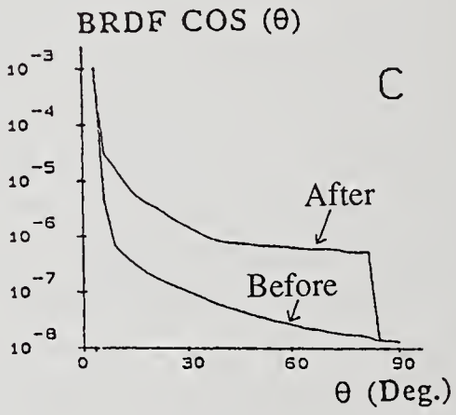

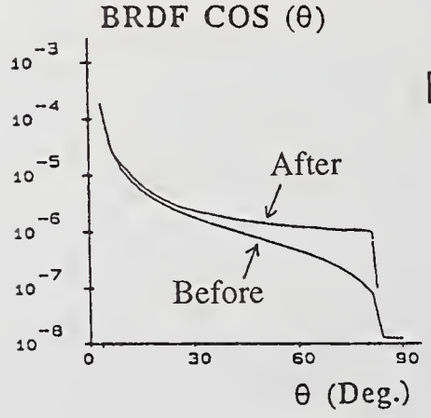

Figure 13:

Angular scattering curves before and after coating by an absentee layer stack (2H 2L 2H) produced on a substrate which roughness is 1.5 nm (A), 0.5 nm (B) and 0.1 nm (C).

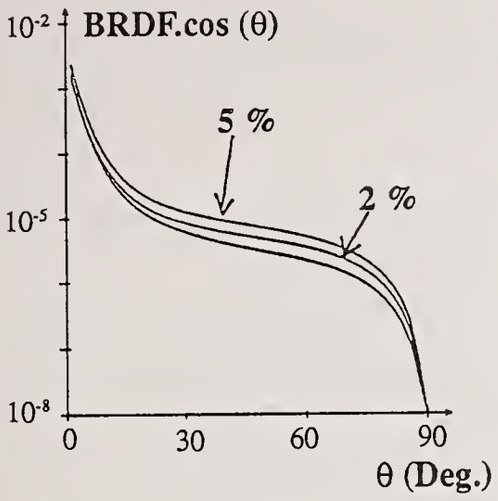

Figure 14:
Influence of thickness errors on the angular scattering curve of a single layer.

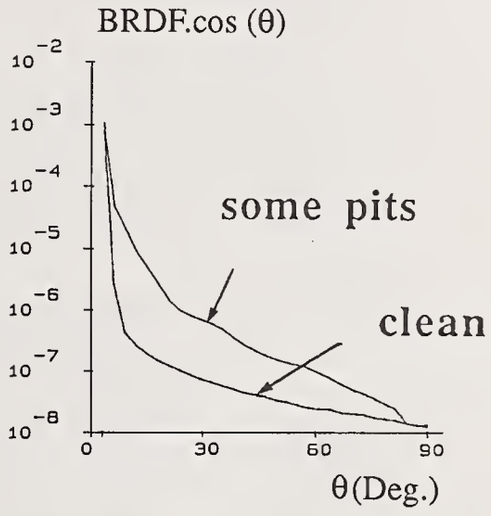

Figure 15:
Scattering from a perfectly clean silicon wafer substrate and from the same substrate with one defect (1 μm diameter) in a 350-μm diameter microscope field.

5. Conclusion

With materials such as TiO_2 and SiO_2 obtained by IAD, as well as Ta_2O_5 and SiO_2 obtained by IP, scattering phenomena in optical coatings are well understood and measurements of the substrate is enough to predict scattering from a coating of any design with high accuracy. Residual roughness due to the materials appears to be negligible and therefore correlation is perfect in the whole range of measurable spatial frequencies ($0.6\ \mu m^{-1} \rightarrow 20\ \mu m^{-1}$).

Isotropy variations of scattering constitute a precious tool to study the origin of microroughness in optical coatings, and leads to elimination of any ambiguity relative to the choice of the parameters (roughness and cross-corelation laws). The conjoint use of isotropy and causal model gives also access to the thickness of the layer.

Investigation of residual roughness requires the use of substrates with roughnesses near 0.1 nm or less. But in these conditions, scattering levels are so low that scattering due to local defects in the coatings (depending on materials and deposition technique) becomes predominant.

References

1 K.H. Guenther, H.K. Pulker, "Electron microscopic investigations of cross sections of optical thin films," Applied Optics, **15**, 2992 (1976)
H.K. Pulker and E. Jung, "Correlation between film structure and sorption behaviour of vapor deposited ZnS, cryolite and MgF_2 films," Thin Solid Films, **9**, 57 (1971) - Thin Solid Films, **10**, 163 (1972)

2 H.A. Macleod, "The microstructure of optical thin films", Proc. SPIE, **325**, 21 (1982)
M. Harris, M. Bowden, H.A. Macleod, "The relationship between optical inhomogeneity and film structure", Thin Solid Films, **57**, 173 (1979)

3 J.M. Bennett, "Optical scattering and absorption losses at interfaces and in thin films," Thin Solid Films, **123**, 27 (1985)

4 J.P. Borgogno, B. Lazaridès, P. Roche, "An improved method for the determination of the extinction coefficient of thin film materials," Thin Solid Films, **102**, 209-220 (1983)

5 M. Commandré, L. Bertrand, G. Albrand, E. Pelletier, "Measurement of absorption losses of optical thin film components by Photothermal Deflection Spectroscopy," SPIE **805**, Optical Components and Systems, 128-135 (1987)

6 J.P. Borgogno, E. Pelletier, "Determination of the extinction coefficient of dielectric thin films from spectrophotometric measurements," Applied Optics, **28**, 2895-2901 (1989)

7 J.M. Eastman, "Surface scattering in optical interference coatings", Thesis, Univ. of rochester, Rochester, N.Y. (1974)

8 C. Amra, P. Bousquet, "Scattering from surfaces and multilayer coatings: recent advances for a better investigation of experiment", SPIE Proceedings, vol 1009 "Surface Measurement and Characterization"p. 82-97

9 J.M. Elson, "Angle resolved light scattering from composite optical surfaces," Proc. Soc. Photo. Opt. Instrum. Eng. **240**, 296 (1980)

10 P. Bousquet, F. Flory, P. Roche, "Scattering from multilayer thin films: theory and experiment.," J. Opt. Soc. Am.,**71**, 1115-1123 (1981)

11 C. Amra C. Grèzes-Besset, P. Roche, E. Pelletier, "Description of a scattering apparatus- Application to the problemes of characterization of opaque surfaces," Applied Optics, **28**, 2723-2730(1989)

12 F. Flory, E. Pelletier, G. Albrand and Y. Hu, "Surface optical coatings by Ion Assisted Deposition techniques: study of uniformity," Applied Optics, **28**, 2952-2959 (1989)

13 B.G. Bovard and al., Silicon nitride thin films by low voltage reactive Ion plating: optical properties and composition", Applied Optics, **28**, 4436-4441, (1989)

14 J.M. Elson, J.P. Rahn and J.M. Bennett, "Light scattering from multilayer optics: comparison of theory and experiment," Appl; Opt. **19**, 669 (1980)

15 C. Amra, G. Albrand,P. Roche, "Theory and application of antiscattering single layers; antiscattering antireflection coatings," Appl. Opt. **25**, 2695-3915 (1986)

16 C. Amra, " Minimizing scattering in multilayers: technique for searching optimal realization conditions," "Laser induced damage in optical materials", **756**, 265-271 (1987)

17 E. Pelletier, F. Flory, Y. Hu, "Optical characterization of thin films by guided waves." Applied Optics, **28**, 2918-2924 (1989)

COMMENTS

Comment: We shouldn't forget Alex Glass's comment that whatever turns you off is the definition of laser damage.

Comment: I would like to make a remark concerning damage thresholds. I think what we should, in any case possible, measure predamage phenomena. They should finally lead up to damage and we should measure them as a function of photon flux or whatever unit you want to use that gives not only the appreciation of what the mechanism is, but will also help to clearly define what the damage threshold means at that point at which one observes some changes.

Secondly, I would want to warn people about using high energy electrons particularly in scanning electron microscopy to search for damage on surfaces. This pertains mostly to halides. You will create primarily defects starting with excitons which have a severe photochemical reaction following and you will simply alter the surface with an electron beam of kinetic energy larger than the bandgap, this process is usually extremely efficient. So you will damage your surface by looking for damage.

Answer: Thank you. I think that shows up a good point here. There is the dichotomy of bifurcation of science and engineering, in regard to laser damage. The engineering definition is whatever turns you off, or we need to use the part until it is broke, or can I deliver hardware with these optics. However, a threshold needs to be defined through science and I think that fits nicely with your comments.

Comment: I do really hope that our co-workers from China do show up here because on a recent visit there, earlier this year, where they were using photothermal deflection in a different way then I have observed any place else, I think I observed for the first time a 100% reliable indicator of precatastrophic damage.

Manuscript received
12-29-89

Optical Properties and Laser Damage Measurements of Inorganic Polymer Films

Gregory J. Exarhos
Pacific Northwest Laboratory
Richland, WA 99352

Kevin M. Crosby
Beloit College
Beloit, WI 53511

Linear phosphorus-nitrogen based polymers have been synthesized and deposited as thin films from solution on silica or silicon substrates using dip-coating or spin-casting methods. Most materials transmit well into the ultraviolet region of the spectrum and have refractive indices (1.5 to 1.7 at 500 nm) which are controlled by the functionality of chemical substituents introduced at the phosphorus atom. Films exposed to pulsed laser irradiation (1064 nm , 8ns pulsewidth) exhibit damage morphologies ranging from severe cratering to delamination. The chloro-substituted polymer shows a spheroidal surface morphology after exposure to a 25 J/cm^2 pulse suggesting melting or condensation of ablated material. The relative stability of these materials to laser irradiation will be discussed in terms of chemical bond ionicity which is influenced by atom electronegativity and the nature of substituent groups. Preliminary measurements of the non-linear optical response observed in several of these materials (SHG) will also be discussed.

Key Words: inorganic polymers; laser damage; optical polymers; phosphazene; second harmonic generation; thin film.

1.0 Introduction

Fundamental studies of composition/structure/property relationships in linear high-molecular-weight polymers which contain inorganic atoms in their backbone chains can lead to development of new materials for optical coating applications. Such inorganic polymers as the isoelectronic and isostructural polysiloxanes, $-[O-SiR_2]_x$, and polyphosphazenes, $-[N=PR_2]_x$, where R signifies a particular chemical functional group, offer improved physical properties over fully organic based polymer materials. This is in part due to the presence of electronegative atoms such as nitrogen or oxygen in the backbone which tends to perturb chemical bonding along the chain. Alcock discusses some of the new inorganic polymer systems and current materials applications in a recent review article [1]. These range from new elastomers which do not embrittle at low temperatures used for pipeline applications, and fast ion conducting polymers for solid state batteries, to bioactive polymers designed as drug delivery systems. While many of these materials can be deposited as thin films, their optical properties are not well known.

A number of factors suggest that phosphazene polymers may be attractive alternatives for optical coating applications. Polyphosphazenes exhibit good solubility properties in both hydrophilic and hydrophobic solvents depending on the nature of the substitutional group on the phosphorus atom. This not only facilitates sample purification and solution deposition of thin films, but simplifies polymer derivitization. Since many of these materials exhibit enhanced thermal stability over organic polymer analogs, their tendency to degrade under high laser fluences may also be proportionally higher.

Chemical bonding along the backbone chain involves overlap between the phosphorus d and nitrogen p electronic orbitals. As a result of the symmetries of the participating orbitals and the high electronegativity of nitrogen, electron density is localized at the nitrogen atom centers. Electron delocalization along the polyphosphazene chain is frustrated, in contrast to the organic polyacetylene system, and the polymer becomes a wide bandgap insulator. A zwitterionic model has been proposed to describe the chemical bonding in this system [2]. Two consequences of this bonding model are apparent: phosphazene polymers should

exhibit good transmission properties in the ultraviolet region of the spectrum; and the chain nitrogen atom basicity should promote attachment of phosphazene polymers to hydroxylated surfaces through a hydrogen bonding mechanism. The latter prediction has been verified by ^{31}P magnetic resonance measurements of phosphazene molecules adsorbed on colloidal alumina surfaces [3]. In addition, the polarizability of the -P=N- bond is controlled by the nature of chemical groups substituted on the phosphorus atom [4]. This suggests the possibility for non-linear optical effects in these materials driven by the electron withdrawing power of the substitutional group.

Recent work in this laboratory has been directed toward the design, synthesis, and characterization of phosphazene polymers, and the development of techniques for solution deposition of polymer films. The real and imaginary parts of the refractive index for several polyphosphazene films deposited on silica substrates have been determined from measured transmission spectra. Polymer films exposed to high fluence pulsed irradiation or high intensity CW irradiation exhibit catastrophic damage morphologies characterized by severe cratering, film delamination, and melting. Results for five polymer systems will be discussed. Initial observations of non-linear optical behavior in several systems will also be presented.

2.0 Synthesis of Phosphazene Polymers

Preparation of phosphazene-based polymers and cyclic ring polymer precursors has been an active area of research for the past twenty five years. Principal work has focused on development of new synthetic methods, characterization of chemical bonding, and kinetic measurements of the polymerization reaction [5]. Synthetic routes for the polymerization of phosphazenes contrast procedures used for the preparation of fully organic based polymers. Figure 1 illustrates the ring-opening polymerization mechanism commonly used to prepare high molecular weight inorganic polymers. Usual precursors include the cyclic bis-dichlorophosphazene trimer or tetramer. At moderate temperatures, 500 K, an equilibrium between ring and chain moieties is established in the melt. Upon cooling, the solidified mixture can be separated into high molecular weight polymers and a low molecular weight fraction which consists of short oligomers and small cyclic rings.

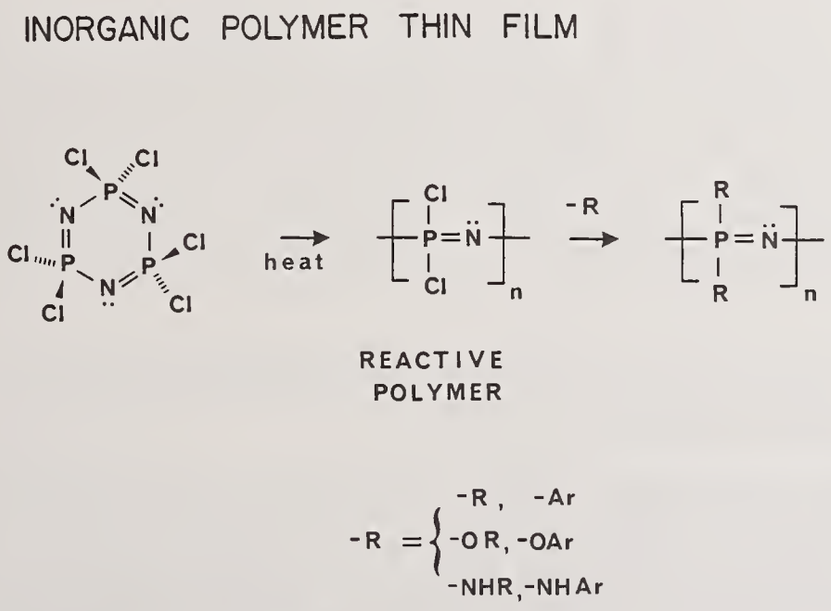

Figure 1. Thermally induced polymerization route to the synthesis of phosphazene polymers.

Owing to the reactivity of the phosphorus-chlorine bond and the ease of dissolution of the polymer in non-polar solvents, nucleophilic substitution reactions readily occur. This allows preparation of well characterized derivatives in good yield. The nature of the substituted chemical group determines the physical properties of these polymers. Amine and alkoxy derivatives of poly bis-dichlorophosphazene have been prepared and can be deposited as thin films from solution. The five materials chosen for this investigation are listed in table 1.

Table 1. PHOSPHAZENE POLYMERS, $-[N=PR_2]_x-$, AND SOLVENT COMPATIBILITY

Name	Chemical Formula of R Group	Designation
Chlorophosphazene (toluene, tetrahydrofuran)	-Cl	CP
Methylaminophosphazene (water, trifluoroethanol)	$-N(CH_3)_2$	MAP
Phenylaminophosphazene (tetrahydrofuran)	$-NHC_6H_5$	PAP
Piperidinophosphazene (chloroform, benzene)	$-NC_5H_{10}$	PP
Trifluoroethoxyphosphazene (acetone)	$-OCH_2CF_3$	TFEP

3.0 Experimental

Polymers were prepared by nucleophilic substitution of poly bis-dichlorophosphazene using published methods [5]. The initial chloro-polymer was purified by sublimation of lower molecular weight species followed by successive recrystallization. Derivatized materials were also subjected to multiple recrystallizations from appropriate solvents to insure highest purity as determined from High Performance Liquid Chromatography (HPLC) and ^{31}P magnetic resonance measurements. All materials studied were fully substituted high molecular weight homopolymers as indicated by a single ^{31}P line in the magnetic resonance spectrum, and were thermally stable to 580 K.

Films were deposited onto cleaned silica substrates using dip-coating or spin casting methods. Polymer solutions were filtered through 0.2 micrometer Gelman fluoropolymer membranes prior to use. Substrate surfaces were cleaned and hydroxylated by treatment with NaOH/methanol followed by a hydrochloric acid and deionized water rinse to remove any sodium chloride that might be present on the surface. The dip-coating procedure involved immersing cleaned substrates in the appropriate polymer solution for 30 seconds and then withdrawing the substrate from solution at a rate of 1 mm/sec. Spin coated films were prepared using an Integrated Technologies Inc. Model P6204 system. Spin parameters included a 2 sec acceleration time followed by a hold at 4000 rpm for 150 seconds and a 4 second deceleration time. Polymer concentrations averaged approximately 0.3 normal for deposition of 1 micrometer thick films.

Transmission spectra were recorded over the wavelength range from 190 to 900 nm. Analysis of measured spectra using the methods of Manifacier, et.al. [6] allowed determination of film thickness and refractive index.

Films were subjected to pulsed laser radiation from a Quantel Model 581C Nd:YAG laser (1064 nm, 8 nsec pulsewidth, 0.65 J/pulse, 30 Hz). A 50 mm diameter 700 mm focal length laser focusing singlet (Melles Griot 01LFS055) optimized for 1064 nm radiation was used to image the beam onto the sample. Spot sizes on the polymer coatings ranged from 1 mm to 5 mm in diameter. Following irradiation, samples were examined using an optical microscope. The effect of CW irradiation on polymer coatings was also evaluated using a Raman microprobe (Spex Model 1482). A 488 nm probe beam from an argon ion laser at power levels up to 2 watts was directed through the microscope optics and imaged directly onto the coating. Spot sizes averaged 5 micrometers in diameter and irradiations were conducted for fixed time intervals.

The observation of green emission during polymer film irradiation with 1064 nm pulsed irradiation prompted preliminary measurements of non-linear effects in these materials. Several phosphazene polymers and polymer precursors were mechanically powdered (5 micrometer particle size), compressed to 2.0 cm diameter pellets under a pressure of 0.1 GPa, and evaluated for their ability to generate second harmonic light. The powder technique originally developed by Kurtz and Perry [7] was used. This method has been successful in the

evaluation of nonlinear optical properties of organic polymer systems [8]. A 0.25 m focal length monochromator and diode array detector replaced the photomultiplier and optical filters used in the original experiment.

4.0 Optical Properties of Polyphosphazene Films

The optical transmission spectra of several phosphazene polymers deposited on cleaned silica substrates are shown in figure 2. Most of these materials, even when exposed to the ambient laboratory atmosphere for one month, exhibited negligible change in measured optical transmission. However, the chloro-substituted polymer film began to degrade after a period of two weeks due to reaction with oxygen and water vapor in the atmosphere. This instability is attributed to the high reactivity of the phosphorus-chlorine bond resulting in hydroxyl addition to the chain and eventual crosslinking of the network. While the dimethylamine polymer is water soluble, the other materials are all hydrophobic, and show no measurable reactivity with water. Optical measurements of dried films following immersion in water reveal no changes in measured transmission spectra.

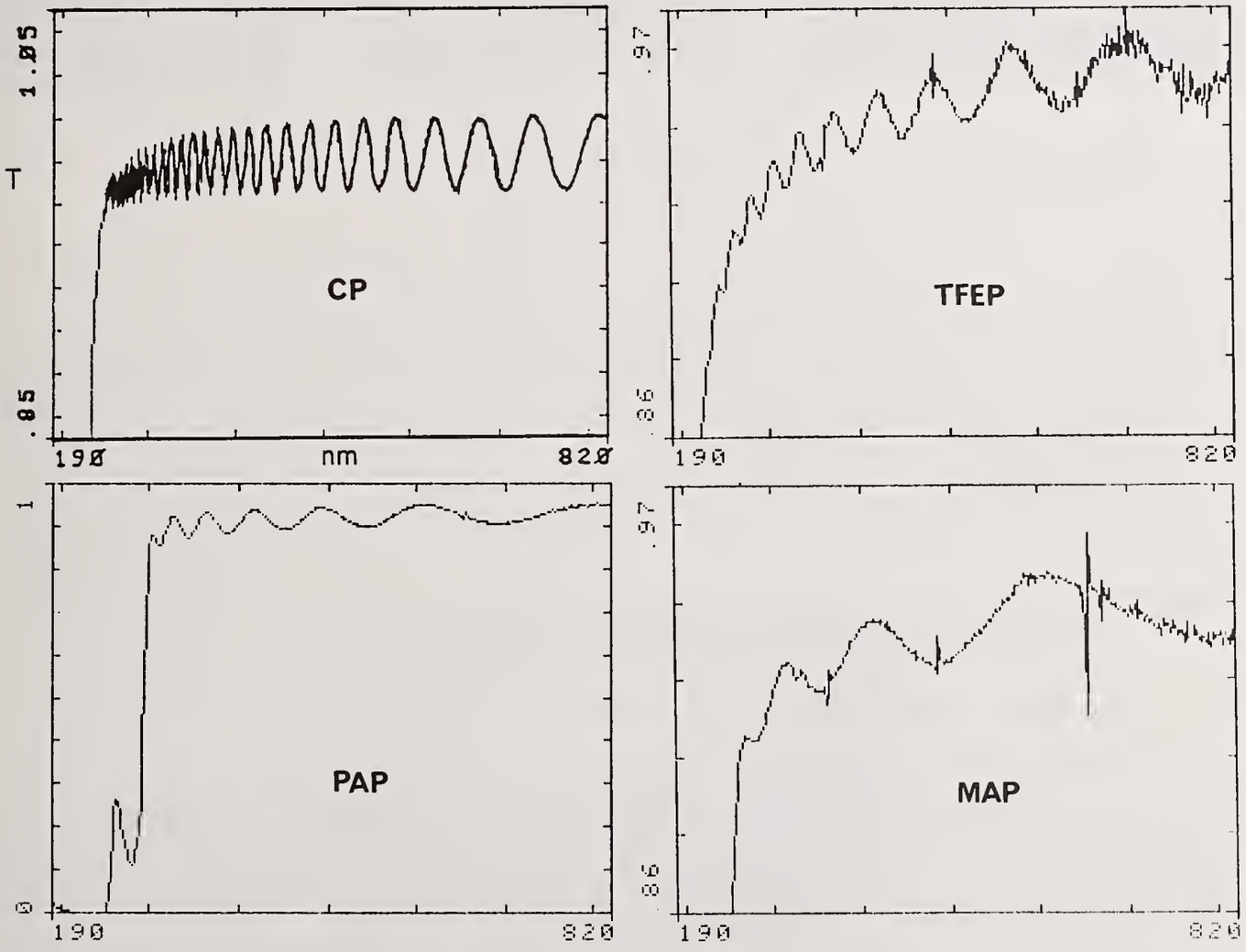

Figure 2. Transmission spectra of several phosphazene polymers deposited on cleaned silica substrates.

The fringe patterns observed in the transmission spectra attest to the uniformity of film thickness over the 1 cm^2 measurement area. Four polymer films, (CP, MAP, PP, TFEP) transmit significantly at wavelengths as short as 250 nm, while PAP begins to absorb strongly at 300 nm due to the presence of the conjugated phenyl groups in the polymer. The optical properties of these films were determined by analysis of the interference fringes according to the method described by Manifacier, et.al. [6]. The optical constants for these materials are reported in table 2, and the dispersion in refractive index as a function of wavelength for the phenyl-substituted polymer is displayed in figure 3.

Table 2. Real (n) and Imaginary (k) Parts of the Refractive Index Measured at 500 nm for Polyphosphazene Films

POLYMER	n	k	THICKNESS (nm)
CP	1.584	1.34E-3	2492
CP	1.625	0.78E-3	1604
CP	1.642	0.80E-3	233
PAP	1.632	1.16E-3	756
MAP	1.494	1.26E-3	379
PP	1.542	1.32E-3	1221
TFEP	1.574	0.67E-3	1083

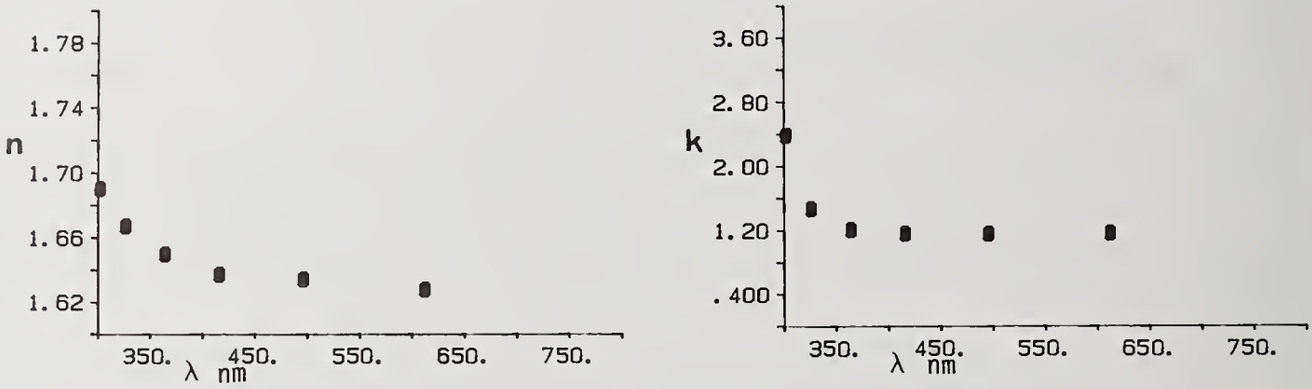

Figure 3. Wavelength dependence of the real and imaginary parts of the refractive index for the phenylamine-substituted phosphazene polymer.

5.0 Laser Damage in Phosphazene Polymer Films

5.1 Pulsed Irradiation Damage

Polymer films deposited on silica substrates were exposed at normal incidence to pulsed 1064 nm radiation at fluences from 1 - 25 J/cm^2. Single and multiple shot (30 second exposure) irradiation at fluences less than 3 J/cm^2 resulted in no observable microscopic damage. Figure 4 exhibits three distinct damage morphologies for the phenylamine, piperidine, and chloro substituted polymers at higher fluences.

Catastrophic damage in PAP results in the formation of a large ablated region surrounded by a series of irregular but distinctly bounded shelves. Debris from ablated material appears randomly distributed over the damaged area. The damage region for PP consists of a similarly cratered region. However, a street-like fracturing of the undamaged region away from the periphery of the damage crater is also evident. The fracturing may indicate a greater degree of polymer chain orientation present in the PP dip-coated film. A distinct damage morphology is also observed for CP dip-coated films. The periphery of the damage crater consists of a random arrangement of well-formed spheres which apparently condensed following ablation. Further measurements are needed to determine the nature of these decomposition species. It is likely that the spheres may be smaller phosphazene chain or ring oligomers formed by laser-induced depolymerization of the film as suggested by laser Raman characterization of the damage region.

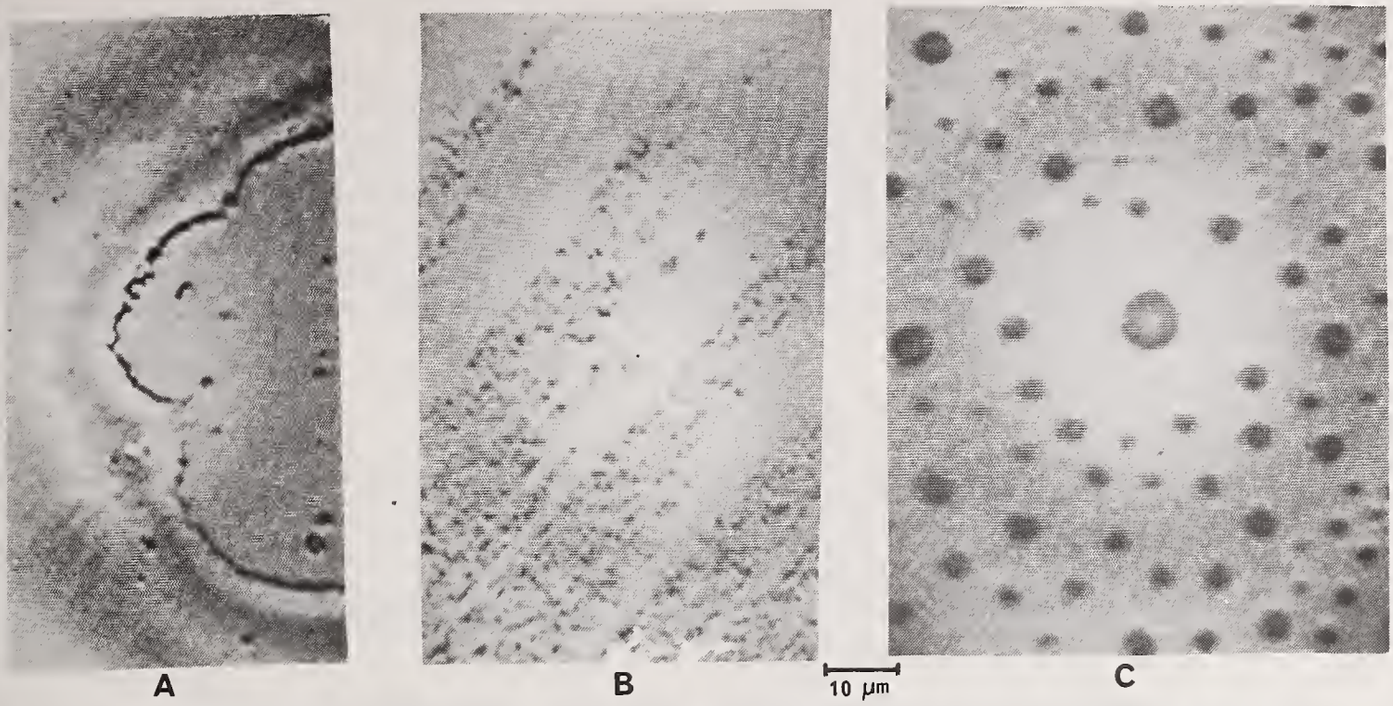

Figure 4. Catastrophic single pulse irradiation damage to several polyphosphazene films deposited on silica. (A) PAP, 6 J/cm^2; (B) PP, 9 J/cm^2; (C) CP, 25 J/cm^2.

5.2 CW Laser Irradiation Damage

The three polymer films discussed above were also subjected to CW laser irradiation (488 nm) at relatively high power densities. The damage morphology depicted in figure 5 for the PAP polymer film is representative of that observed in all films that failed. A 5 micrometer crater was seen in PAP, and PP films exposed to CW irradiation for periods of 60 seconds at power densities of 0.24 and 0.29 MW/cm^2. No damage was observed for polymer films irradiated for less than 60 seconds at these measured power densities. In addition, the chloropolymer (CP) failed to show any sign of damage at power densities approaching 1 MW/cm^2 and exposure times up to 300 seconds. The stability of this material attests to the high purity of the polymer and absence of chromophores which might absorb at 488 nm leading to localized heating.

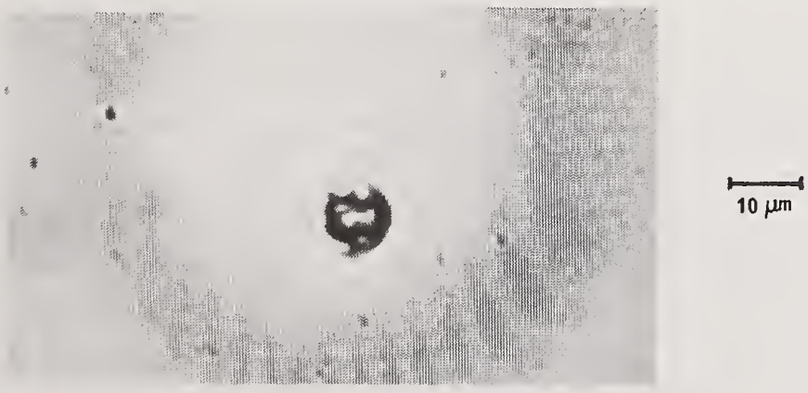

Figure 5. CW laser damage to a PAP film irradiated for 60 seconds at a power density of 0.24 MW/cm^2.

6.0 Second Harmonic Generation in Phosphazenes

Several phosphazene polymers and polymer precursors were observed to emit green light when irradiated with 1064 nm pulsed radiation from a Nd:YAG laser (ca. 1 mJ/pulse at 30 Hz). Figure 6 shows the intensity dependence of SHG on excitation laser pulse energy for the bis-dichloro phosphazene trimer. Emission measured at 532 nm and the observed quadratic power dependence confirm the non-linear optical response of this material. Continuing measurements on derivatized phosphazenes indicate that the magnitude of the SHG effect is controlled by the electron withdrawing power of the substituent groups on the phosphorus atom as well as the molecular conformation.

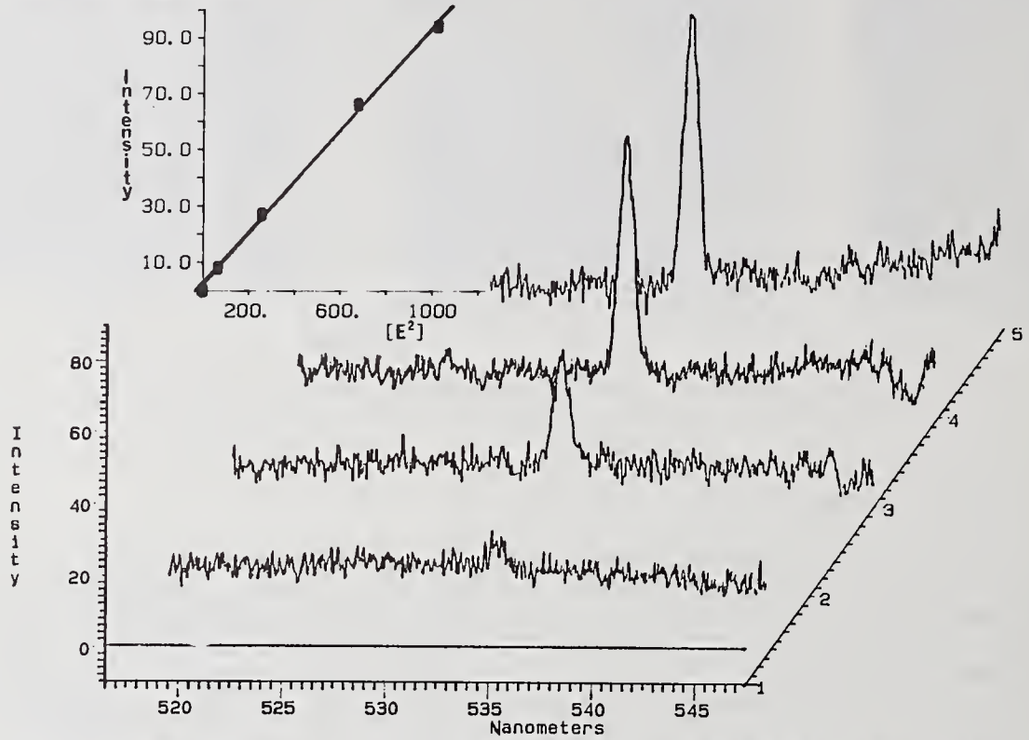

Figure 6. Second Harmonic Generation in the bisdichlorophosphazene trimer under pulsed 1064 nm excitation.

7.0 Conclusions

Optical properties of substituted polyphosphazenes are determined by the nature of the d-p pi bonding along the inorganic polymer chain, which tends to localize electron density around nitrogen centers. Three-center bonds are formed at the nitrogen atoms, and the symmetry of the molecular orbitals precludes electron conjugation along the chain. The nature of chemical functional groups which can be substituted on phosphorus perturbs the charge distribution along the chain and modifies the electronic structure of the polymer. Lowest energy allowed electronic transitions probably occur between filled pi bonding orbitals and empty pi antibonding orbitals, although weaker transitions originating from the nitrogen nonbonding orbitals are also expected. These constraints suggest that polyphosphazene materials should behave like wide band-gap insulators, and offer an explanation for the relatively high ultraviolet transparency. However, electronic transitions localized on the substitutional groups can also modify the electronic structure of the polymer as seen in the phenylamine substituted material where absorbtion at 300 nm is significant. These concepts suggest that perturbation of polyphosphazene optical properties can be achieved through suitable derivatization, and provide an avenue for design of new materials.

A contrast in chemical bonding and associated electronic structure between organic polymers and inorganic polyphosphazenes has been demonstrated in a recent theoretical paper [?]. Preliminary measurements of inorganic polymer optical properties are reported in this paper and suggest their use in dielectric film applications. The solubility of phosphazene polymers facilitates purification and deposition from solution as uniform films. Laser damage appears in polyphosphazene films at thresholds comparable with organic polymer materials. Improvement in damage susceptibility can be expected with increased attention to polymer purity and deposition procedures. The first observation of non-linear behavior in phosphazenes is reported and warrants further study from both experimental and theoretical modeling studies.

8.0 Acknowledgments

This work has been supported by the Materials Sciences Division of the Office of Basic Energy Sciences, U. S. Department of Energy. Inorganic polymer and polymer precursors have been synthesized by Dr. W. D. Samuels whose assistance is gratefully acknowledged. The authors also acknowledge the contribution of Mr. Joel Drews who assisted in the development of solution deposition procedures and measurement of polymer film optical properties.

9.0 References

[1] H. R. Allcock, "Inorganic Macromolecules", Chem. Engin. News 63(11), 22-36 (1985).

[2] K. F. Ferris, P. M. Friedman, and D. M. Friedrich, "Electronic Structure of the Phosphonitrilic Trimer - Role of d Orbitals in Chemical Bonding", Int. J. Quantum Chem: Quantum Chemistry Symposium 22, 207-218 (1988).

[3] G. J. Exarhos, K. F. Ferris, D. M. Friedrich, and W. D. Samuels, "^{31}P NMR Studies of Aqueous Colloidal Dispersions Stabilized by Polyphosphazene Adsorption", J. Am. Ceramic Soc. 71(9), C406-407 (1988).

[4] L. S. Dake, D. R. Baer, and D. M. Friedrich, "Auger Parameter Measurements of Phosphorus Compounds for Characterization of Phosphazenes", J. Vac. Sci. Technology A 7(3), 1634-1638 (1988).

[5] H. R. Allcock, Phosphorus-Nitrogen Compounds, Cyclic, Linear, and High Polymeric Systems, Academic Press, New York, pp. 73-87 (1972).

[6] J. C. Manifacier, J. Gasiot, and J. P. Fillard, "A Simple Method for the Determination of the Optical Constants n, k, and the Thickness of a Weakly Absorbing Thin Film", J. Phys. E 9, 4002-4004 (1976).

[7] S. K. Kurtz, and T. T. Perry, "A Powder Technique for the Evaluation of Nonlinear Optical Materials", J. Appl. Phys. 39(8), 3798-3813 (1968).

[8] D. Chen, N. Okamoto, and R. Matsushima, "Second Harmonic Generation from Organic Nonlinear Materials of N-Alkyl-4-Nitroaniline", Optics Commun. 69(5,6), 425-428 1989).

COMMENTS

Question: Pages of questions; start with some simple ones. What about the rather voluminous amount of data on temperature dependence of laser induced damage in wide band gap dielectrics and also frequency dependence of laser induced damage in wide band gap dielectrics that are absolutely totally inconsistent with multiphoton initiated damage?

Answer: That's what you think. We have measured temperature dependence and it's a difficult experiment. When you have avalanche you get a very steep temperature dependence; Manenkov has done that and has calculated that. When you use intrinsic properties and study intrinsic damage, the steep temperature dependence is not there. They have been able to do between 50 K and 300 K. These experiments have actually been published in one of the Boulder Conferences. We have done more work since then. Frequency dependence there was the basic thing. We have two frequency dependencies in this kind of physics and the multiphoton cross section is a drastic function of frequency. Free carrier heating is a function of rms electric field strengths and thus laser field strengths. When you increase the wave length you get more efficient free carrier heating.

Question: Is that observation consistent with other free carrier absorptions measurements in other materials?

Answer: We have measured the cross section of that and we feel we are right. The problem in this business is that people draw conclusions by measuring damage thresholds alone and they have no idea whether they are chasing an extrinsic or intrinsic phenomena. You should never trust any of these experiments unless they have proven through subthreshold damage experiments what the flux dependence is that leads up to damage. I'm firmly convinced that aside from the data which you singled out, that Manenkov data is intrinsic. Nobody here in this business, in the colloquium has ever reported intrinsic damage events except our prebreakdown experiments that finally get led up to intrinsic damage. So don't believe the volume dependencies, the wavelengths dependencies, the temperature dependencies, which people have measured with extrinsic material and have interpreted them with intrinsic theories. It simply doesn't work and 99.9% of all the data is in this category.

Question: There has been a lot of early data that supports avalanche breakdown at DC in dielectrics as a mechanism for breakdown. Quite extensive work that dates back decades. How do you reconcile that? Finally, what is the breakdown in SiO_2? You must have some multiplication of electrons or else it is still an insulator?

Answer: Ok, that's a loaded question. What my talk implies and what the people from IBM also believe is that we have to throw out literally 60 years of work of DC breakdown experiments. That's what that means, nothing less. The IBM people are in the same boat. Now when do they see damage? When they increase their voltage. Sometimes at certain points, at certain voltages, the sample simply goes because of electron photon collisions.

Comment: I would like to comment on your question. Most of the work we did was on SiO_2. The situation was like this, that the DC breakdown field increased exponentially with the improvement of technology. The breakdown field is now like 25 megavolts per centimeter. At the time when Fröhlich was doing his model, which is a nice model, breakdown fields were something like 6 megavolts per centimeter. You could explain these results within his model. Then the breakdown field increased and you had to add new stuff to the model, so that's the situation now. I think something else is going on in laser physics here. I am not an expert in laser physics but I think that the purer the material gets and the more care you take results in the breakdown field being pushed higher and higher. It seems that for SiO_2 the avalanche breakdown field actually is very high and that we haven't seen it with our DC experiments, which go up to 25 megavolts. If we use our theory and extrapolate to higher fields, we would expect to avalanche at higher values. The avalanche then still exists. It just doesn't some into play in our experiments. It comes in at far higher field strengths so that it may exist when you shoot the laser with pulse that is a factor of ten above the damage threshold. You have avalanche even when you have discharge in gases. That's not what we want to dispute, we want to simply tell you that we haven't found it and the reason is that the acoustic phonon scattering has stabilized.

Question: How much of your data is on crystalline quartz and how much on amorphous silica and are they different?

Answer: We have only looked at the amorphous silica.

Question: It seems to me that about seven or eight years ago there was a Russian group that did a two frequency experiment, or something like it, and came to completely opposite conclusions. Do you have any comment on their data and the interpretation?

Answer: Well that's the same thing I always say, you have to prove first that you have intrinsic materials in front of you because otherwise you are beset by problems due to imperfect materials. This extrinsic damage is a totally different picture.

Question: Can we extrapolate your results to other materials?

Answer: Yes, we have thought about it. We were in the process of writing a proposal but you know how that goes. We thought it would be marvelous to take these experimental techniques and study relevant optical materials such as calcium fluoride. The Harshaw people

told us that they have a huge contract from SDI to make the biggest most perfect calcium fluoride crystal. I don't know whether it ever happened but I think some of these crystals now are getting so good that you can reach the intrinsic damage limit. If you don't know what you have you may already have the materials perfected to the point where you have reached the intrinsic limit and you may still plough millions into make more perfect material. Our techniques should be carried over to other materials, particularly to those which we know how to make in a very perfect way. Those which have practical applications or practical importance are barium fluoride, calcium fluoride, magnesium fluoride, the oxides, maybe even materials which are used in dielectric coatings. For coatings the physics if far more complicated because we have lots of failures due to film mismatch and all these things, but at least we could find out what is the temperature that you dump into you coating.

I think in this area the physics has just begun. We should come to the conclusion that taking something and firing at it and measuring a histogram of how it damages is simply no good, We don't understand at all what's going on. It may be good for engineers that want to get better coatings but if you want to get to the limit of what you can do this is not good enough.

Question: Does your theory support the material variation throughout the alkali halides in damage threshold?

Answer: We have not done all alkali halides-these experiments are very involved and it is very difficult to get clean samples. We didn't have the time to measure them all but I have not the slightest doubt that given a perfect material, they will all behave in a similar way.

Question: Well actually I didn't mean the measurement. Will your theory predict a variation in alkali halides?

Answer: It flatters me that you consider me a theoretician. We are experimentialists. The theories are from other people; Epifanov; Sparks, and Fischetti are the main players. All we try to do is do clean experiments which demonstrate predamage energy deposition. That gives you a chance to compare experiment with theory.

Question: Have you talked with Nicolaas Bloembergen about your results to find out what he sees?

Answer: No, his articles claim that since they studied damage in say, <u>covalent</u> materials (in diamond) our theory must be wrong. Nicolaas Bloembergen does not believe in this and I simply can not help him.

Manuscript received
2-22-90

Interfacial Stability in Optical Coatings

K L Lewis, A M Pitt, A G Cullis and K Welford
Royal Signals and Radar Establishment
Malvern, Worcestershire WR14 3PS
England

I T Muirhead
OCLI Optical Coatings
Ridgeway, Hillend Industrial Park,
Fife, Dunfermline KY11 5FR
Scotland

As optical coatings become more complex, partly due to improved deposition processes and more stringent design criteria, the number of layers in the coating increases, with a corresponding risk of interfacial instability. This can lead to partial film delamination, arising from residual stress effects, from interdiffusion of different chemical species across the film boundaries, or from the presence of impurity species at the interface itself. These effects are very relevant to the application of such coatings in laser systems, especially where the newer digital techniques are used to synthesise graded designs. One useful way of exploring the effect is to incorporate a large number of interfaces within a Fabry-Perot etalon cavity, and to temperature cycle the structure, whilst measuring its spectral response. The changes observed can be correlated with information derived from X-ray photoelectron spectroscopic examination of discrete interfaces specifically fabricated to simulate those present in the etalon cavity.

INTRODUCTION

The problem of interfacial stability is becoming of increasing importance as optical coatings become more complex, with greater numbers of component layers. Several factors can influence the behaviour of such interface regions under high flux levels. Firstly, these are regions at which impurities or particulates often segregate because of interruptions in the fabrication process. or movement of furniture (eg masks) within the coating chambers. This can then result in regions of porosity as the following layer tries to accommodate the impurity or inclusion, with risk of increase in stress levels. A second characteristic is that most interfaces are atomically rough as a result of the polycrystalline nature of the component materials. This can serve to weaken the interfacial bond in certain cases and increase the risk of delamination. A third factor that arises is related to the possibility of material diffusion across the interface, with formation of new phases with different optical constants. This can modify the optical characteristics of the component, perhaps degrading its performance under critical conditions.

In previous work [1], this latter process was identified as a possible explanation for reduction in reflection band intensity in distributed Bragg reflectors. Here, evidence was provided for the formation of a separate interface species from the results of depth profiling X-ray photoelectron spectroscopy, and from reverse analysis of the reflector design. The relative magnitude of such chemical diffusion processes will be associated with the temperature at which the films were deposited, and on the different materials present.

Some new techniques are proposed to explore the fundamental issues involved in determining the stability of interfaces, emphasising the different types of failure to be expected. The first addresses the mechanical stability of the interface, whilst the second explores chemical reaction processes by

directly observing the changes occuring at an engineered surface interface. The remainder of the work is concerned with an assessment of the optical stability of the interface expected and observed as a result of thermal cycling.

MECHANICAL STABILITY OF INTERFACES

Many of the conventional tests applied for film adhesion are concerned with the bond between coating and substrate. For example, in the case of the Scotch tape test, failure mostly results in separation at the coating-substrate interface, and only occasionally within a given multilayer. More quantitative techniques, such as the scratch test, involve drawing a stylus across the film under successively increasing loads. Although the flakes of material delaminated in this test can be microscopically examined, their form is not amenable to cross-sectional transmission electron microscopy (XTEM) to reveal the origins of failure within the coating.

In this work, as-deposited multilayers have been cross-sectioned by cleaving, epoxy mounting and abrasive thinning to 100μm in thickness. Higher than usual levels of mechanical stress used during these operations can serve to introduce a degree of controlled microcracking in the multilayer. Thin foils are then produced by further thinning of the cross-section by argon ion milling, culminating in the use of reactive iodine etching to remove extrinsic dislocation loops and other ion-beam damage artefacts.

Figure (1) shows a cross-sectional transmission electron micrograph of a digital BaF_2/ZnS multilayer produced by molecular beam evaporation as described previously [2]. This technique ensured freedom from background impurity species at all stages during film deposition, with partial pressures of water vapour in the 10^{-12} mbar range. The level of stress introduced during foil preparation has led to fracture of the film and delamination at interfaces at different levels in the film. Close examination of regions of the micrograph in figure (1) show that the separation <u>always</u> occurs beneath the darker contrast layers in the coating. These are the BaF_2 layers, as more clearly shown in figure (2). This is a somewhat surprising observation, since it would be expected that the chemical interaction occurring at all BaF_2/ZnS interfaces would be identical. Clearly this is not the case and there is a significant difference between the way in which BaF_2 nucleates onto fresh ZnS surfaces, and the reverse process of ZnS nucleating onto BaF_2.

Examination of the cross-section in figure (2) at sufficiently high magnification to resolve the individual lattice planes does not reveal any major differences between the two types of interface.

DIRECT ASSESSMENT OF INTERFACE REACTIVITY

It is difficult to explore the chemical processes occurring at interfaces without the risk of the probe technique used influencing the interaction taking place. The interfaces of greatest interest are frequently those within a multilayer structure and these are only accessible by profiling or cross-sectioning. In order to avoid any uncertainty, a new approach has been taken, in which the interface chemistry has been reconstructed at an accessible surface. This involves covering a freshly grown surface of one material with a monolayer of a second in ultra-high vacuum and following the subsequent reactions using a surface sensitive technique such as X-ray photoelectron spectroscopy (XPS). The molecular beam facility previously described [3] is ideally suited for such studies, since it allows the deposition of high purity films in any desired configuration, and their subsequent analysis at any stage *in situ* without exposure to the atmosphere.

The engineered interface is shown schematically in figure (3), highlighting the various possibilities for material reaction and/or transport. On an atomistic scale, real surfaces are far from smooth, incorporating ledges, kinks and hillocks which act as favourable sites for material incorporation. Deposition of a second material to the extent of a monolayer or so is not going to achieve complete coverage of the surface, and there will always be sites where the underlying material is exposed. Material transport can occur as a result of desorption, surface diffusion, chemical reaction or diffusion into the underlying film material. Although XPS is a surface sensitive technique, it actually provides information on the constituents in the top few atomic layers. Further detail can obtained by angle resolution if required. Such interfaces can easily be studied for different materials combinations, but most attention to date has been focussed on the BiF_3/ZnS system, using films deposited from molecular beams of BiF_3, Zn and S_2. The latter species were obtained as a result of the congruent evaporation of high purity ZnS.

Figures (4a) and (4b) compare the spectrum of a fresh ZnS surface with that obtained when that same surface is covered with a nominal monolayer of BiF_3. The major changes apparent are the reduction in intensity of the Zn and S related signals, and the appearance of Bi and F related features. On standing in UHV, the F related peaks gradually decay over a period of several hours, with no change in the intensities of the other peaks, and no absorption of other background species such as oxygen (peak at 532eV). In 2.7 hours, the integrated area for the F 1s peak had reduced by 14%, whilst in 48 hours, the reduction was considerably greater to give the spectrum shown in figure (4c). A slight increase in the Zn Auger signal is apparent in this latter case, but of more significance is the complete change in the form of the doublet near 160eV. This spectral region is expanded in figure (5) clearly highlighting the changes occurring. It is notable that there is no change here in the intensities of the Zn Auger peaks at 240.50 and 263.75eV, nor for that matter in the S 2s peak at 225.75eV. This implies that the Zn and S concentrations in the analysed volume do not change with time. The characteristic 2p signal for sulphur at 162eV virtually coincides with the Bi 4f peaks, but this still allows the evolution in the surface chemistry to be followed clearly as a function of time. When freshly deposited, the Bi $4f_{7/2}$ peak overlaps the sulphur peak. After 160 minutes, a gradual shift in the Bi binding energy occurs, revealing the S 2p signal as a more defined shoulder. Within 2 days standing, the Bi 4f $_{7/2}$ peak has moved to 156.75eV, some 4eV lower than its original position, whilst the Bi $4f_{5/2}$ peak is now coincident with the S 2p signal. This explains the overall trend in general appearance of the doublet.

The changes observed are entirely attributable to a shift in the chemical environment of the Bi from a configuration centred on Bi-F bonding to one centred on Bi-S bonding. This is accompanied by the reduction in surface fluorine coverage observed. It is believed that the fluorine reduction occurs as result of diffusion into the underlying ZnS film. The formation of bismuth sulphide is notable and has important implications from an optical point of view, because of its difference in refractive index to that of BiF_3.

This concept of using a model interface is applicable to a wide range of materials combinations, and can be used to select those likely to show the greatest stability. It is limited only in cases where spectral features are difficult to resolve due to line overlap. Temperature effects can be explored at a fundamental level providing some insight into processes likely to occur during laser irradiation.

EFFECT OF INTERFACE REACTIVITY ON STABILITY OF COMPLEX FILTER STRUCTURES

In the selection of materials combinations for complex filter designs, it is important to address the effect of material interaction on the resulting

increased risk of significant change as a result of chemical interaction. It is of interest to explore the magnitude of the changes likely to be encountered and to compare the results of those studies with observed behaviour. Chemical reaction effects can be accelerated by increase in temperature, so allowing a candidate filter structure to be assessed for any permanent changes in characteristic simply by heating and subsequent cooling to its original temperature.

Previous work [4] has highlighted the use of etalons for assessing the thermal stability of thin film structures. That study was concerned with the behaviour of resonant cavities containing one uniform spacer material. Such structures are ideal for measuring the temperature coefficient of refractive index of thin films, simply by determining the transmission spectra at different temperatures and calculating the value of dn/dT from the spectral shifts observed. Any permanent changes in the spacer material appear as permanent line shifts on cooling the filter back to room temperature. By using an etalon in high order, the spectral shifts can be determined over a range of wavelengths simultaneously, providing a measure of the dispersion in dn/dT. The etalon fringes are of course characteristic only of the spacer medium, and slight changes in the end mirrors do not have a major effect on line position. It is not strictly necessary to use an etalon with high reflectivity mirrors for these measurements, although these serve to sharpen the interference maxima observed. The fundamental interference processes still occur in single layers of material giving rise to the well-known maxima and minima in transmission spectra. Careful measurement of their position also allows a determination of refractive index and its temperature dependence. Some results obtained on 5μm thick films of ZnSe produced in UHV are presented in figure (6), and clearly show the trend obtained with increase in temperature. Values obtained from successive temperature cycling experiments merely overlay on the curves shown, demonstrating the inherent stability of such material even in thin film form.

The etalon technique is extended in this work to explore interfacial stability by fabricating filters with spacer layers containing a large number of interfaces. One configuration adopted contains a repeat structure of 20 individual layer pairs within the etalon cavity and is based on the design $(HL)^4/(HH0.24L)^{20}/(HL)^4$/sub. The periodic form of the spacer gives a Bragg resonance peak at the centre design wavelength, but the etalon fringes at longer wavelengths are characteristic of the average index of the entire etalon cavity. The calculated transmission of such a structure using H = 2.5 (ZnSe) and L = 1.5 (BaF_2) is shown in figure (7a) for a design cetred on 500nm. Sharp transmission maxima are clearly delineated at 612.5 and 635.0nm. Increase in the value of refractive index of the ZnSe component of the filter as a result of heating can be readily expored by substituting different values for H in the design, and re-running the matrix calculation for the film ensemble. For example, a change in H from 2.5 to 2.55 results in the above two etalon fringes shifting to 625 and 647.5nm respectively as shown in figure (7b).

Experimental results for a real filter of similar design, but centred at a slightly different wavelength are presented in figure (8). Here the characteristic fringes at 561, 585, 606 and 631nm shift by 3nm to longer wavelengths on heating the filter from 25°C to 150°C in air. This is indicative of a change in refractive index Δn of the ZnSe of about 0.015, a value in good agreement from that obtained above on single films of ZnSe. It also shows that the changes in transmission spectra are dominated by the temperature dependant properties of the ZnSe component of the filter. On cooling to 25°C, the filter characteristic returns to its original position, with evidence of a slight decrease in absorption implied by increase in intensity of the 561nm peak. This wavelength is close to the absorption edge of the ZnSe, and the decrease in absorption suggests that an annealing of lattice defects in the film may be occuring. A second

heating of the film to 200°C as shown in figure (9) accentuates the changes observed in the 150°C case , but also highlights a larger permanent change in characteristic on cooling to 25°C. This is indicative of a permanent

reduction in average refractive index of the spacer layer, and is presumed to be due to the result of interface reactions since the effect is not observable in the case of ZnSe alone. Clearly the shift in wavelength in this case is quite small and for most applications insignificant.

It is difficult to model the peak shift without some *a proiri* knowledge of the extent of material diffusion across interfaces, and the resulting phase composition of the materials produced as a result of reaction. However, the assessment technique is adequate for demonstrating whether a particular interface configuration is stable or not, and for providing guidance in the selection of materials for use in complex filter designs.

CONCLUSIONS

Three techniques have been explored for assessing interface stability. The first reveals delamination processes induced by mechanical stress within multilayer films by direct observation in cross sectional transmission electron microscopy. The second addresses chemical reactivity by analysis of an engineered interface accessible to surface analysis techniques in UHV. The effect of such processes on the resulting optical characteristics of complete filter structures is explored in the final technique, by measurement of temperature induced shifts in etalon characteristics whose spacer layers contain a large number of interfaces.

The interface between BiF_3 and ZnS appears to be unstable as a result of diffusion of fluorine into the ZnS and formation of a bismuth sulphide phase. In comparison, structures containing ZnSe and BaF_2 are comparatively stable, with only slight changes observable after temperature cycling in air to 200°C.

REFERENCES

1. K L Lewis, I T Muirhead, A M Pitt, A G Cullis and G M Williams: Proc 1988 Boulder Damage Symposium

2. K L Lewis, A M Pitt, N G Chew, A G Cullis, T J Wyatt-Davies, L Charlwood, O D Dosser and I T Muirhead: Proc 1986 Boulder Damage Symposium, NIST Sp Publ 752 365 (1988)

3. K L Lewis, I T Muirhead, A M Pitt, A G Cullis, G M Williams and T J Wyatt-Davies: J Vac Sci Technol a7 1413 (1989)

4. K L Lewis, A Miller, I T Muirhead and J Staromlynska: Proc 1987 Boulder Damage Symposium, NIST Sp Publ 756 338 (1988)

Figure 1. Cross sectional transmission electron micrograph (XTEM) showing stress induced failure of BaF_2/ZnS digital multilayer.

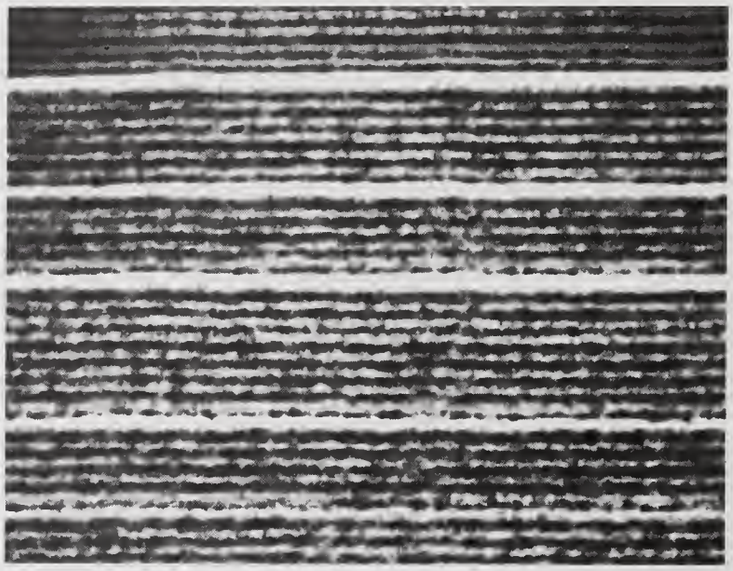

Figure 2. Detail of stressed BaF_2/ZnS digital multilayer showing occurrence of delamination beneath BaF_2 layers.

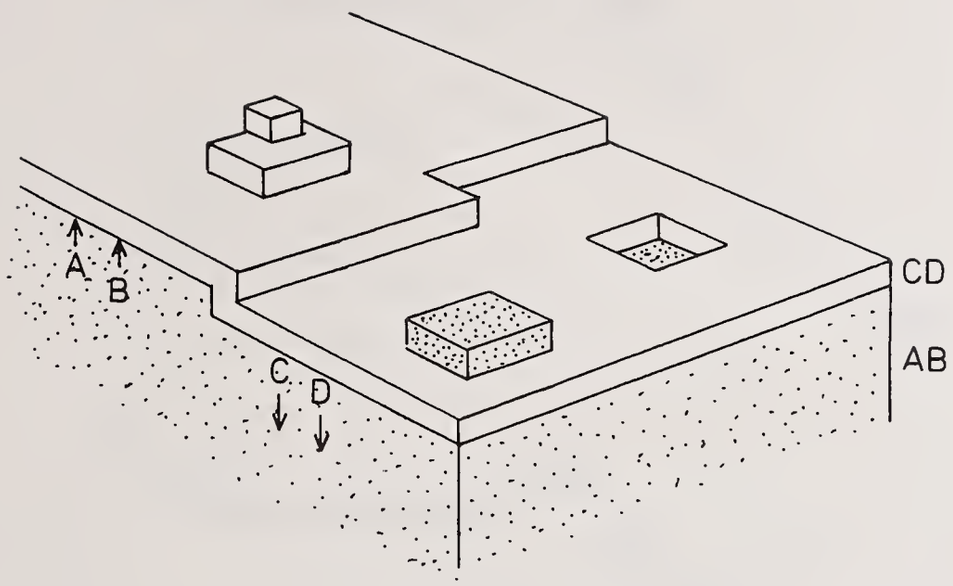

$$AB + CD = ABCD$$

$$AB + CD = ABC + D$$

$$AB + CD = ABD + C$$

$$AB + CD = ACD + B$$

$$AB + CD = BCD + A$$

$$AB + CD = AC + BD$$

$$AB + CD = AD + BC$$

Figure 3. Schematic diagram of interface constructed between two generic binary materials AB and CD, using one monolayer of CD. Various possibilities for chemical interaction/material transport are highlighted.

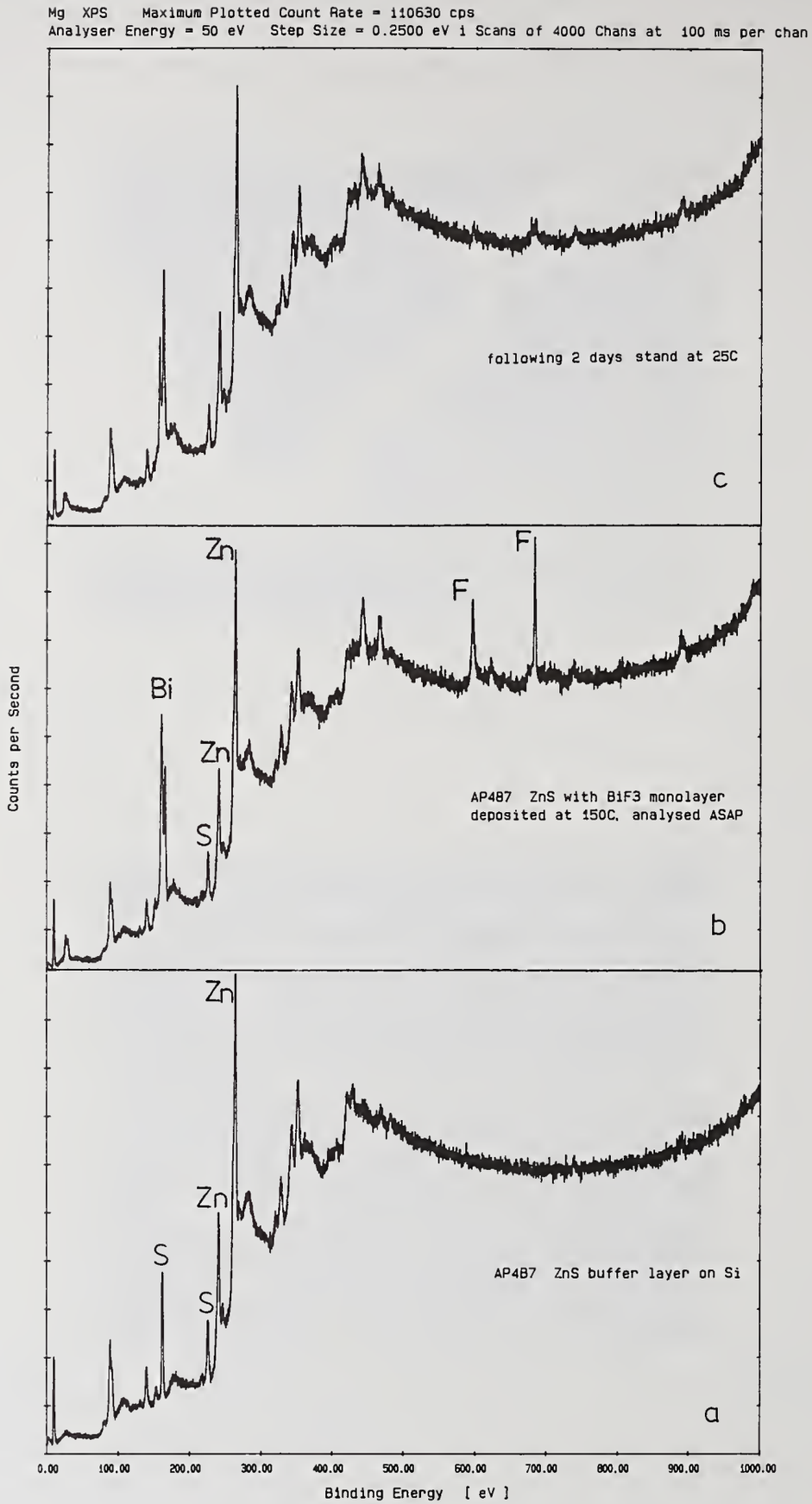

Figure 4. X-ray photoelectron spectra (XPS) of ZnS films (a) as grown, (b) with a monolayer of BiF_3 deposited at 150°C, (c) as (b) after 48 hours in UHV at 25°C.

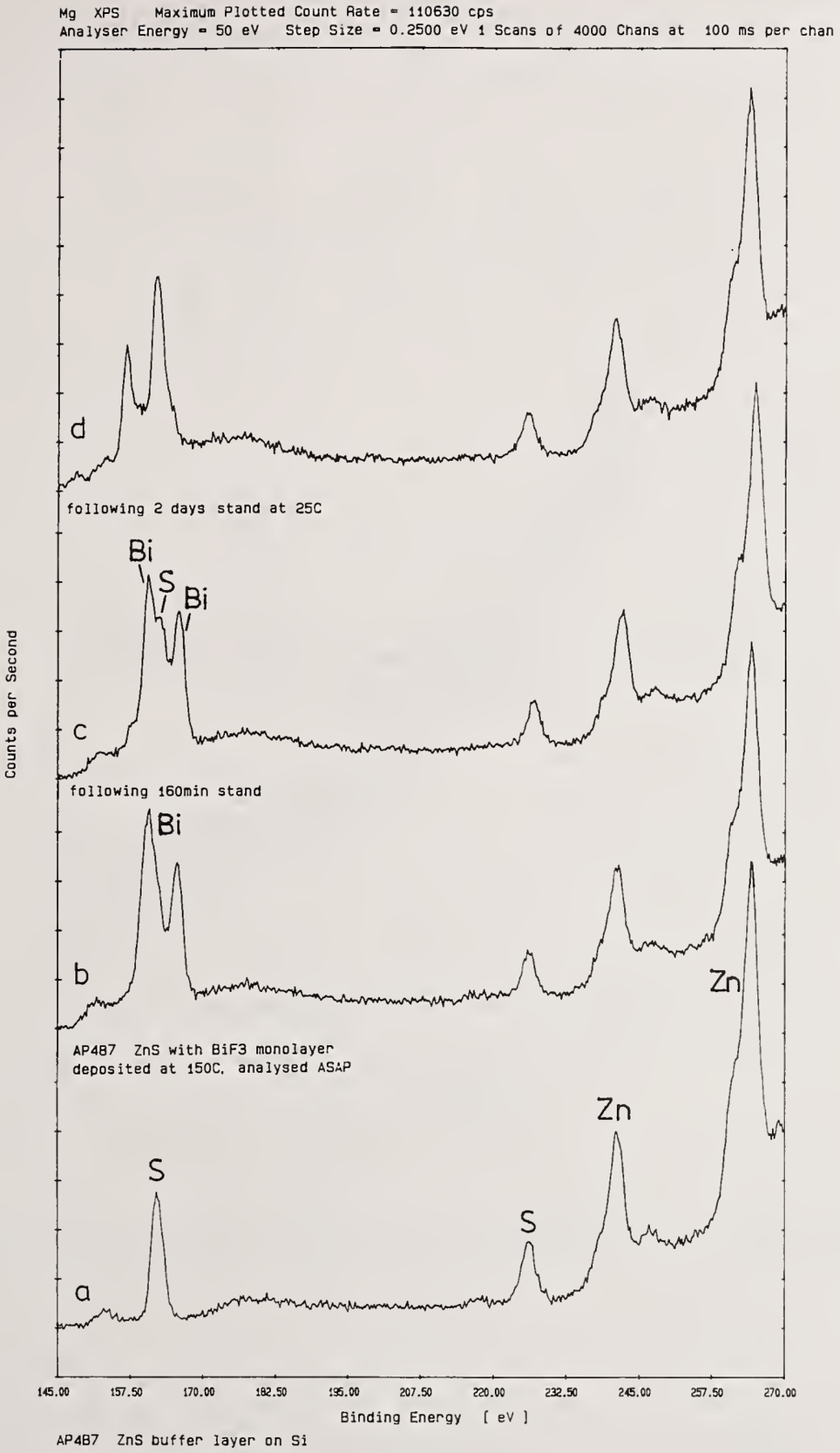

Figure 5. Detail of X-ray photoelectron spectra of ZnS films (a) as grown, (b) with a monolayer of BiF_3 deposited at 150°C, (c) as (b) after 160 minutes in UHV at 25°C, (d) as (b) after 48 hours in UHV at 25°C.

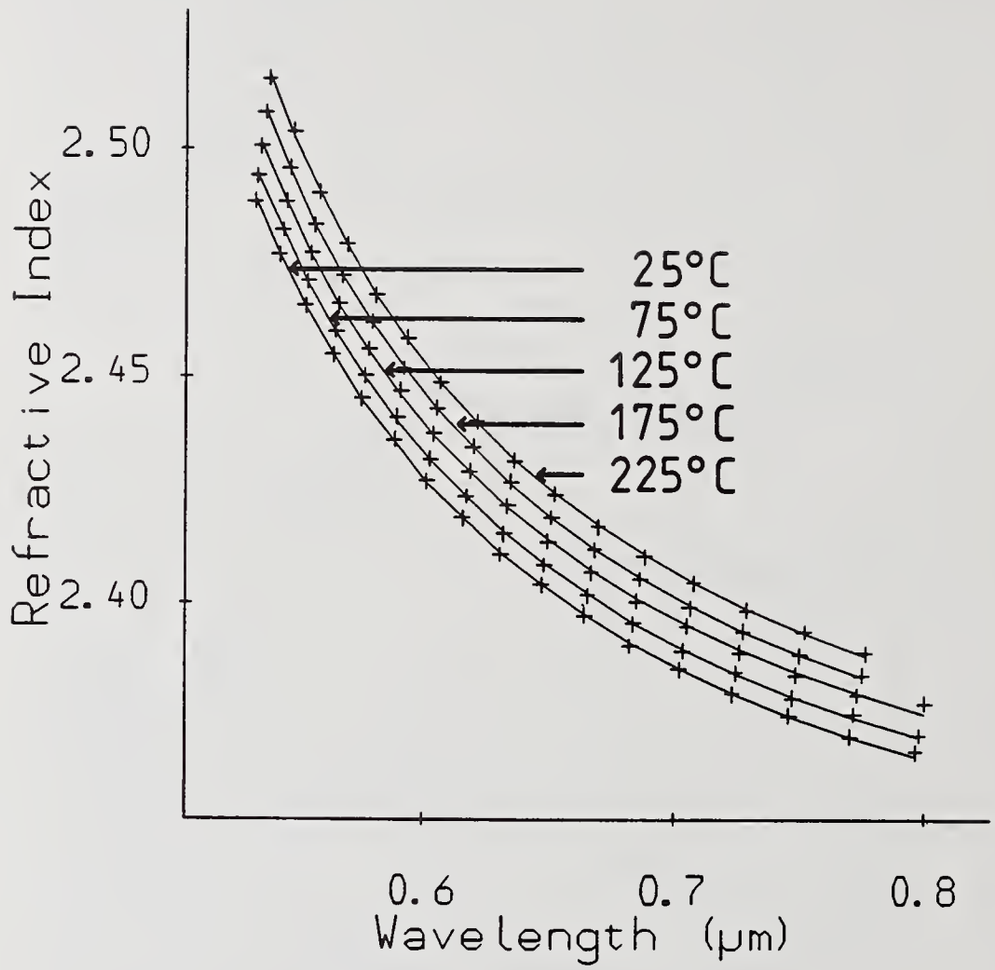

Figure 6. Temperature dependence of refractive index of ZnSe.
x - experimental, line is fitted to three parameter Sellmeier equation.

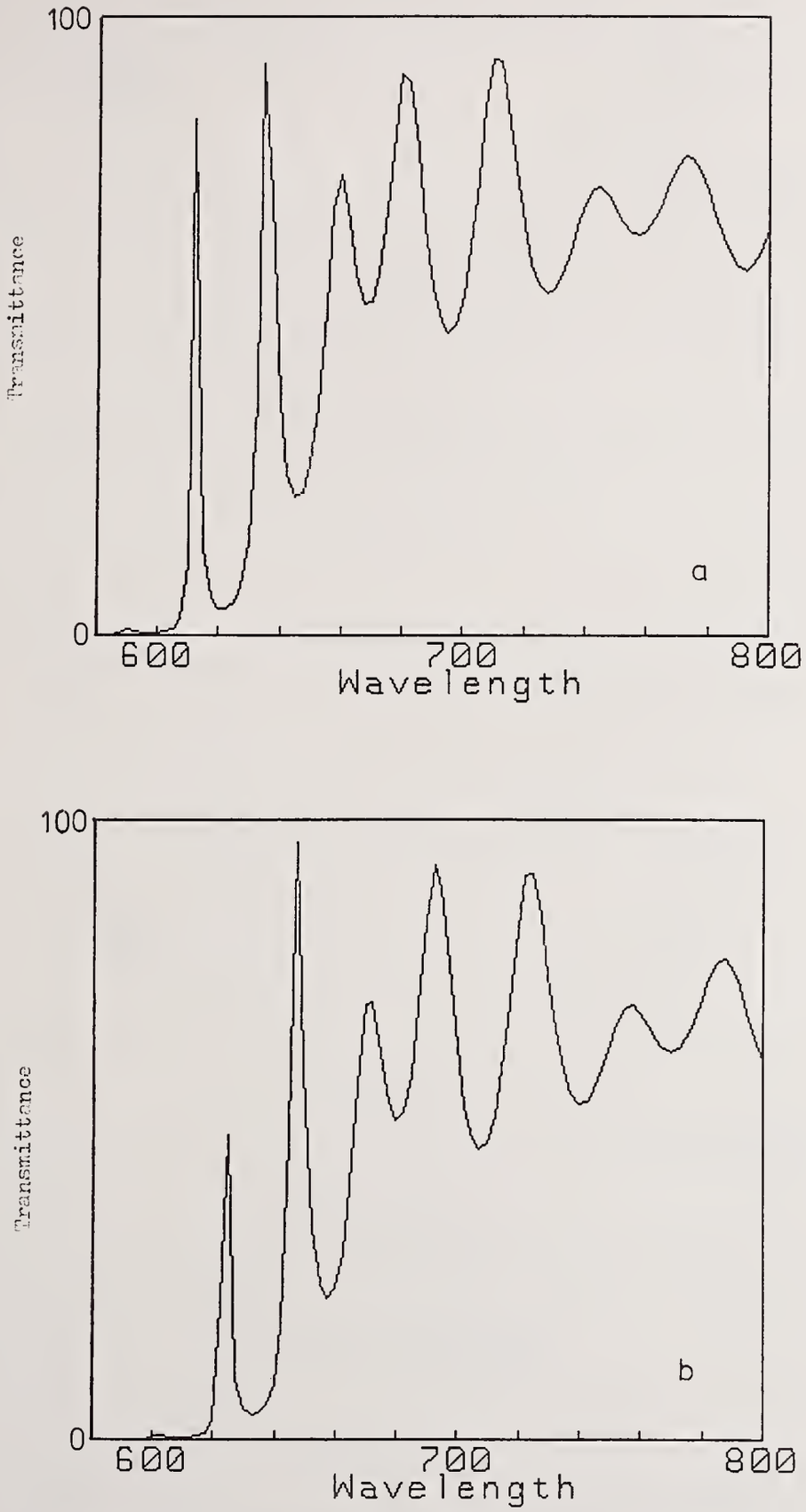

Figure 7. Theoretical transmittances of etalon containing $(HH0.24L)^{8}$ structure (see text). (a) with H = 2.5, L = 1.5, (b) with H = 2.55, L = 1.5

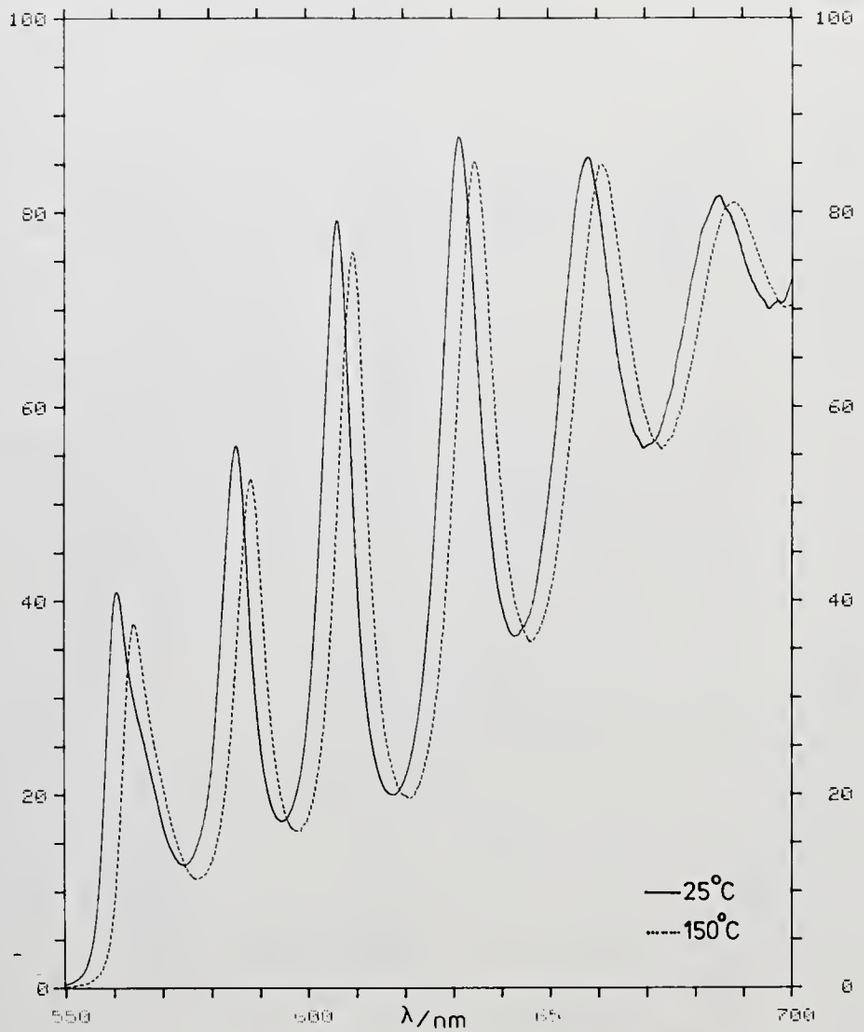

Solid line 25°C, dotted line 150°C

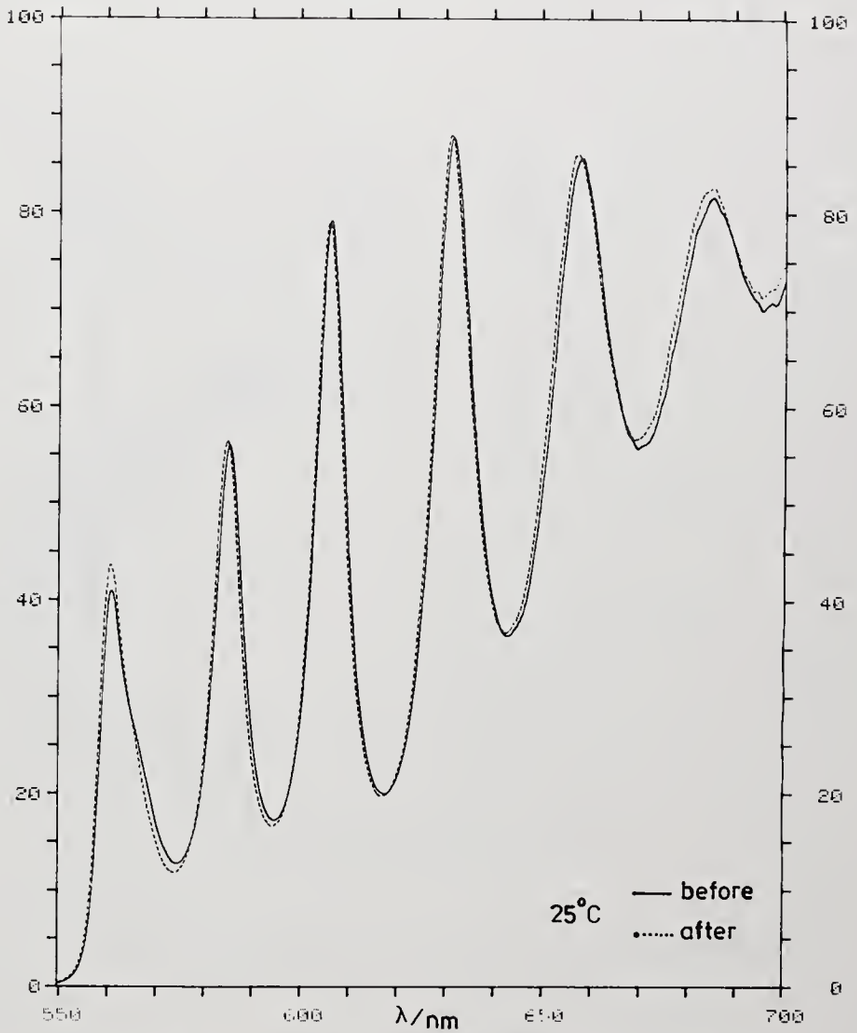

Solid line before heating
Dotted line after cooling from 150°C

Figure 8. Experimental transmission spectra for etalon similar to that of figure (7), measured at different stages of heating.
(a) solid curve 25°C before heating, dotted curve 150°C
(b) solid curve 25°C before heating, dotted curve 25°C after cooling from 150°C.

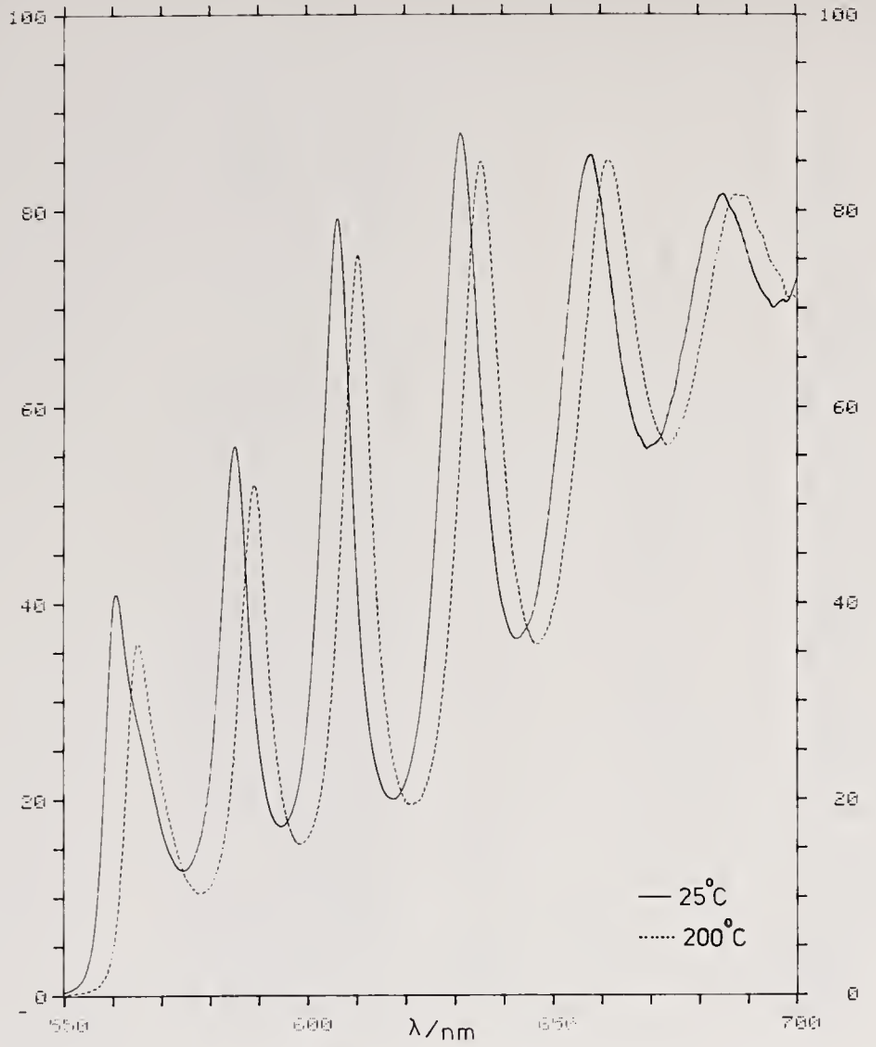

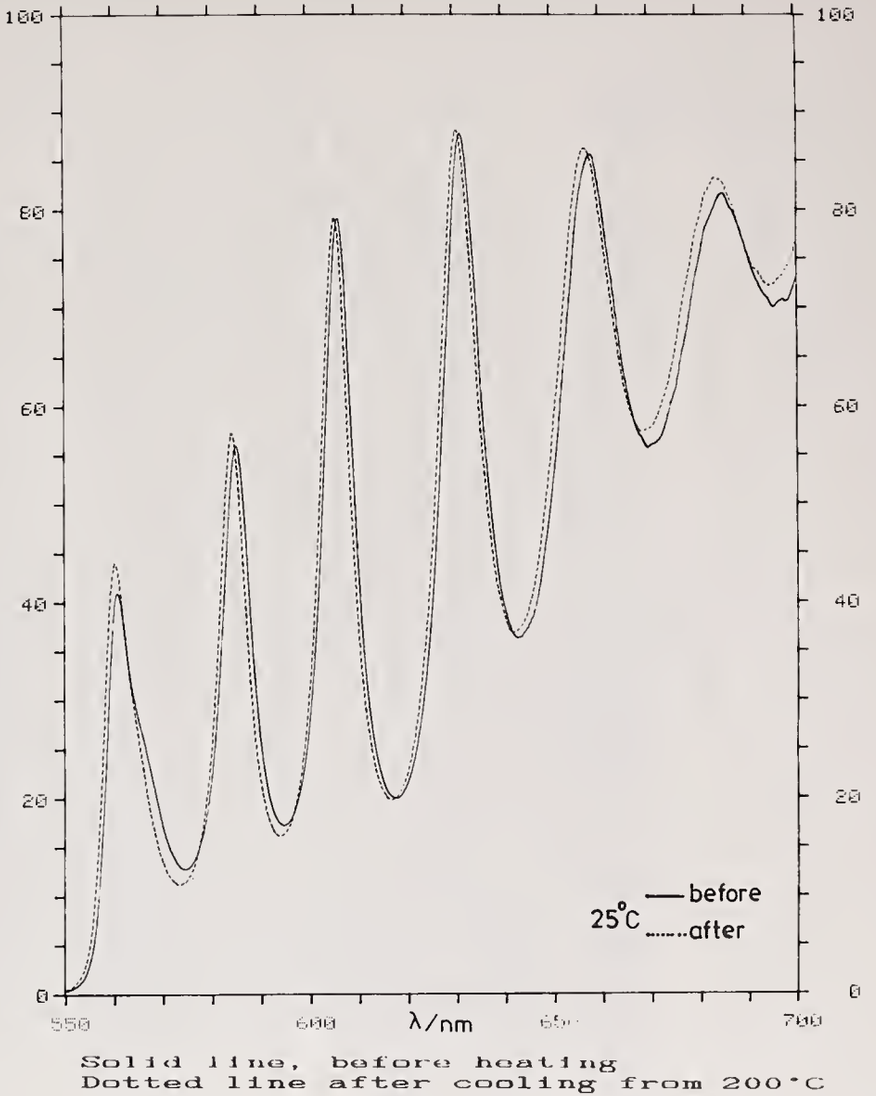

Figure 9. Experimental transmission spectra for etalon similar to that of figure (7), measured in a second heating cycle.
(a) solid curve 25°C before heating, dotted curve 200°C
(b) solid curve 25°C before heating, dotted curve 25°C after cooling from 200°C

Question: Do you have any feeling for how long this condition effect lasts, first of all? And secondly, if it does last, do you feel it is a useful process for improving an operational threshold?

Answer: Absolutely. You are going to get a lot more detail on this tomorrow and I don't want to take away the thunder from the people who are doing that. We have shown that conditioning does in fact last. We've looked at an over annealed sample, for example, annealed the entire substrate, and after 10 weeks still see no degradation in the damage threshold. We still have that sample around and doing a lot of testing on it. The conditioning does indeed last and we're certainly hoping that this is a good way to be able to get these thresholds up higher because the improvement is in the order of factors of 2 or 3. We've seen that on KDP crystals where we've looked at the bulk. That's practically six, seven, eight years ago, that we did that. It's only been in the last few years that people have talked about coatings. The thought was that it doesn't really last. Well, I think that Bob Wolfe and Mark Kozlowski tomorrow will explain what we think is really happening when we do this conditioning and indicate why we feel this is a permanent phenomena.

Question: In relation to this conditioning, what procedure do you go through in cleaning the sample before you do these retesting.

Answer: The sample is cleaned the same way each time unless we have specific requests from somebody to clean something in an exotic fashion.

Question: What is that procedure?

Answer: We do an ethanol wipe with a lens tissue several times.

Question: That's it?

Answer: That's it.

Question: Is this independent of rep-rate even going into very high rep-rates?

Answer: This is something that we are working to determine. How many shots do you need in order to condition and what rep-rate you need to do that. Typically, in our single shot systems, it's very difficult to put too many shots on to a system. On REPTILE where we typically are now firing at 10 Hz and we radiate for a minute, we will ramp up from zero fluence up to the maximum fluence where we want to go to in a continuous step-wise fashion. This doesn't mean that you have to put 600 shots on there.

Question: Will the threshold possibly go down for very high rep-rates?

Answer: The highest rep-rates we have typically gone to are 120 Hz on a REPTILE laser when we used four lasers. We are not running at 120 Hz anymore, with one laser I can run at 30 Hz, so we have not done any of that testing. There really has been no effect observed of difference between 120 Hz testing and 30 Hz testing. If there is an effect, it's not because the rep-rate but it's because of the number of shots we put on it. For instance, titania coatings are notorious in that you put more shots on there and the damage will get more, get larger. This is not a rep-rate effect but a shot-rate effect. On a kilohertz tester we have not been able to test things to an extreme, but basically there is no rep-rate effect.

Question: Do you understand the difference between LAP and KDP and its performance?

Answer: I know that they are different crystals and one of them is a hydrocarbon. Other than showing you the chemical formula, again I'm not a chemist and I would really not like to speculate on those differences.

Comment: This DLAP data has been corroborated by a Japan group here last year. They reported very high damage thresholds for DLAP. We grew some in our own lab first time out and also measured extremely high damage threshold for that material.

Manuscript received
12-29-89

Surface Analytical Methods for the Assessment of Damage in Optical Thin Films

James R. Hoenigman

University of Dayton Research Institute
Dayton, Ohio 45469

With the recent advances in surface analytical instrumentation, a methodology now exists which enables optical thin films to be studied in considerable detail. Scanning Auger spectroscopy with argon ion etching capabilities in conjunction with scanning electron microscopy, backscatter electron microscopy, optical microscopy, and light element energy dispersive x-ray spectroscopy have been successfully used at the University of Dayton to study coating defects and radiation induced damage in a variety of specimens. A brief description of the capabilities and limitations of some of these techniques will be given. Ball cratering, a relatively obscure technique by which underlying layers in an optical stack can be exposed, has proven to be a powerful tool which has extended the range of the above mentioned analytical techniques. Some examples of adhesion failures, crack phenomena, substrate and film failures, and Auger depth profiling will be presented.

Key words: Auger depth profiling; Auger spectroscopy; Ball cratering; Dielectric films; Energy dispersive x-ray spectroscopy; Optical coatings; Radiation damage.

1. Introduction

Over the past 25 years instrumentation for Auger electron spectroscopy (AES) has evolved from infancy to its present fourth generation state. AES has contributed significantly to advances which have occurred in most thin film technologies over the same period of time. A synergistic relationship has developed between AES and the microelectronics industry. The result has been that as more sophisticated digital electronic microcircuitry has been developed it has been incorporated into each new generation of AES instrumentation.

A typical state-of-the-art scanning Auger microprobe is designed to be an Auger spectrometer as well as a scanning electron microscope with secondary and backscatter electron imaging capabilities. Allowances are made for the addition of an energy dispersive x-ray detector which extends its analytical capabilities to include bulk analysis. A differentially pumped ion gun, which enables Auger depth profiles to be acquired, is an essential part of an Auger microprobe. These components are enclosed in an ultrahigh vacuum chamber with a rapid sample insertion interlock which enables specimens to changed in a few minutes. Finally, computer control has become an integral part of this instrumentation. Hardware and software has been developed which enables complete instrument control with full data acquisition and data processing capabilities.

Auger spectroscopy has traditionally been used on conductive or semiconductive specimens. Lower operational beam currents, however, which can be used in state-of-the-art Auger microprobes, now permit nonconductors to be successfully studied in many cases. We have taken advantage of this to study dielectric thin films on glass, silicon, and metal substrates. The objective of this paper is to demonstrate how the complementary analytical capabilities of a state-of-the-art scanning Auger microprobe can be used effectively to study damage mechanisms in optical thin films.

2. Analytical Techniques

The fundamental principles relating to Auger spectroscopy, scanning electron microscopy (SEM), and energy dispersive x-ray spectroscopy (EDS) are adequately described in the literature [1-4]. One point, however, which often is not emphasized enough is the complementary nature of these techniques, especially as they apply to the study of damage in optical thin films.

When an energetic beam of electrons is focused on a solid surface of interest, several processes occur, each of which provides the analyst with specific information about the specimen. Figure 1 shows the well known "teardrop" model which is commonly used to describe the interaction of an energetic electron beam with a solid surface. It is immediately apparent that different sampling depths are associated with each process. The information generated in

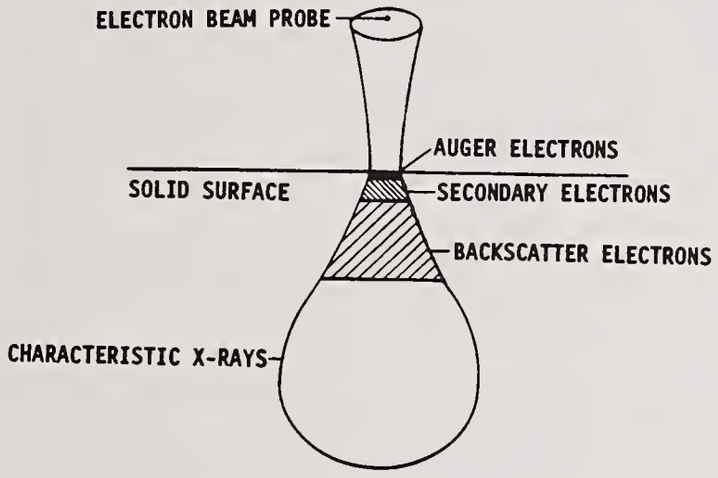

Figure 1. Teardrop model for electron beam initiated processes within solid specimens. Each process is restricted to a specific sampled volume.

each instance is in some way dependent upon the primary beam energy and is limited to a specific sampled volume. Table 1 summarizes the type of information and the approximate depth resolutions of each of these processes for typical primary beam energies. An Auger microprobe equipped with the appropriate detectors enables the analyst to sequentially probe deeper into a specimen by selecting different detectors.

Table 1. Depth restrictions and type of information which results from electron beam initiated processes

Auger	0 to ~5 nm	Elemental (Li to U), qualitative and quantiative
Secondary electrons	0 to ~50nm	Compositional contrast, imaging and morphology
Backscatter electrons	0 to ~300 nm	Compositional contrast, imaging and morphology
X-rays	0 to ~1 μm	Elemental (B to U), qualitative and quantitative

In the discussion which follows, the term "surface" is used in conjunction only with information generated by the Auger process. In dielectric films this is on the order of 5 nm or less into the specimen. The surface of a specimen can be etched with an argon ion beam exposing new surface deeper into the specimen. Using suitable thin film standards of known thickness, etch rates can be determined for dielectric films of interest enabling a composition versus depth profile to be constructed. Etch rates on the order of 20 nm/min are achievable. An example of an Auger depth profile will be shown later.

The analytical techniques described thus far are applied to exposed exterior surfaces of a specimen. With most multilayer optical stacks, Auger depth profiling is a very time consuming process to use to probe buried layers and interfaces, especially if the substrate interface is of interest. We have successfully employed a mechanical erosion technique to expose buried layers and interfaces in optical stacks. The method is called "ball cratering" and is described in detail elsewhere [5,6]. Briefly, a polished spherical metal ball is mechanically rotated at a point of interest on a specimen. A slurry, made from diamond paste, is prepared and applied at the contact point of the ball with the specimen before rotation begins. The result is a spherical crater in the specimen which appears as a set of concentric rings in a two dimensional SEM image or optical photograph as will be shown later. If the diameter of the ball is known, the ring diameters can be measured from a photograph of known magnification and the thickness of each layer calculated from the spherical geometry. By exposing successive layers in an optical stack, access is gained to each layer and the interfaces between them. Craters can be located to intersect damage sites and in undamaged regions enabling comparative measurements to be made. With optical microscopy and SEM imaging, missing coatings, film delaminations, and crack penetration can be readily observed at cratered damage sites.

A new generation of thin window or windowless EDS detectors for ultrahigh vacuum applications has enabled light element detection down to boron in some cases. Quantification, however, is difficult because of x-ray overlap problems and difficulties associated with determining true peak intensities using the reduced beam energies which are required to enhance light element detection. Valuable qualitative information can be gained, however, in high purity thin films. Since Auger is more sensitive to light elements, it can be used effectively in conjunction with EDS to quantify elemental compositions in such films even though it samples only a few monolayers compared to perhaps 0.5 μm for light element EDS.

3. Strengths and Limitations

The characterization of optical films by nonoptical methods was reviewed by K. H. Guenther in 1981 [7]. Most of what was said at that time is still true regarding the relative strengths and weaknesses of many of the methods reviewed. The lower operational current densities which are possible in state-of-the-art Auger microprobes, however, have resulted in reducing some of the specimen charging problems associated with acquiring Auger spectra from uncoated dielectric films. Further, Auger spatial resolution has increased dramatically in recent years. Auger spectra can be acquired routinely from submicron features under certain circumstances. Specimen charging, however, remains the principal problem in using electron excitation techniques to evaluate dielectric films.

Ball cratering can expose buried layers and interfaces within an optical stack for subsequent Auger and EDS analyses. Craters on the order of 1 mm in diameter are required. It is difficult, however, to accurately position craters to intersect regions of interest. Further, specimens must be cleaned after cratering to remove the abrasive slurry. This, in some cases, can introduce contamination and produce delamination in fragile films. By locating craters at both damaged and undamaged sites on a specimen, cleaning induced damage can usually be distinguished from radiation induced damage by comparing photographs of the craters. By its nature, ball cratering is destructive and should be used only on post mortem specimens. Ball cratering used in conjunction with AES, EDS, and SEM imaging provides a powerful analytical approach for evaluating damage deep within dielectric stacks.

The methodology we have employed for evaluating radiation damage in post mortem optical specimens consists of using Auger spectroscopy, light element EDS, and SEM and backscatter

imagining in conjunction with ball cratering and optical microscopy. Craters are made at damaged sites and in undamaged regions where comparative studies have proven useful in identifying damage mechanisms. Ball cratering in conjunction with Auger depth profiling and light element EDS, has enabled the detailed study of substrate/stack interfaces and the bulk compositions of subsurface dielectric films to be determined directly.

4. Crack Damage

A specimen which consisted of several alternating thin films of Si_3N_4 and Al_2O_3 was ball cratered at a radiation damage site and at an undamaged site. Figure 2 shows images of both

A

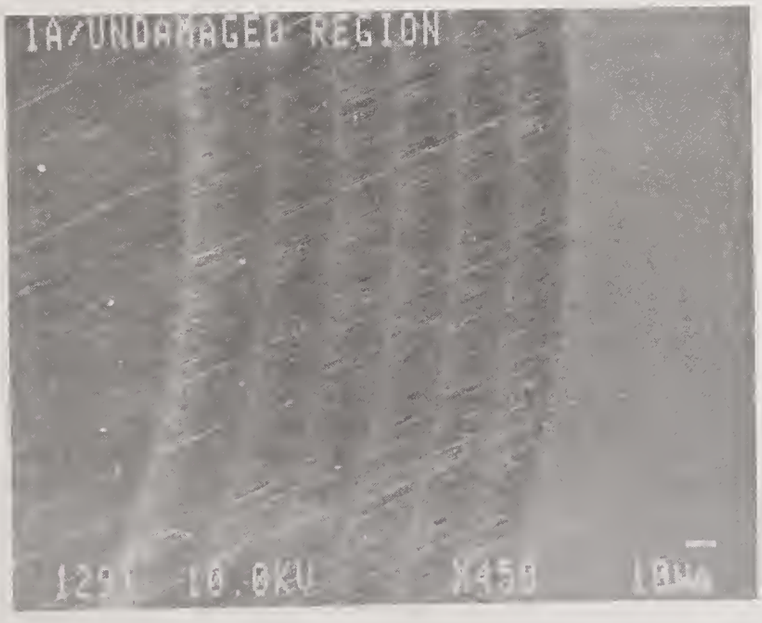

B

Figure 2. SEM image of a ball crater at a radiation induced site (A) and in an undamaged region (B). It is clearly evident that damage occurred within the optical stack.

sites. It is immediately apparent that cracking and delamination has occurred at the radiation damage site, whereas, the undamaged site, which experienced the same cratering and cleaning procedures, does not show evidence of cracking. In this example the cracking and subsequent delamination is typical of what occurs as a result of stress relief cracking in thin films. The exact layer or interface at which the damage occurred can be located by counting the rings and using Auger spectroscopy to identify the exposed surface. Figure 3 shows a crater from a different specimen where substrate failure is clearly evident. Hence, ball cratering together with optical microscopy and/or SEM imaging can be used effectively to determine whether cracks terminate within dielectric stacks or penetrate through to the substrate and to identify where delamination occurs.

Figure 3. An SEM image of a ball crater acquired at a radiation damage site. Cracks are observed which penetrate the optical stack into the glass substrate. A large wedge of glass (lower portion of image) was removed either during cratering or in the cleaning process which followed. A large amount of wear debris is also observed within the crater.

5. Substrate Interfaces

In another example, a specimen was ball cratered at a radiation damage site. The specimen consisted of a stack of alternating Si_3N_4/Al_2O_3 layers on a 100 nm film of Al on a glass substrate. Information regarding the Al_2O_3/Al/glass region was of interest. Auger spectroscopy was used in conjunction with ion etching to produce a depth profile (Figure 4) of the last two interfaces after exposure by ball cratering. For this profile, the ion beam was turned on for 30 sec, then turned off while the Auger spectra were acquired. This sequence was repeated until the profile was completed. Each pair of data points, one each from the oxygen peak and the aluminum peak, corresponds to a single sputter time. Peak shapes at selected times for this profile are shown in Figure 5. The stable position of the oxygen peak (~510 eV) indicates that specimen charging did not occur. The Al peak shape change from oxide to metal is evident in the Al KLL peak (~1380 eV) as the Al_2O_3/Al interface is traversed.

Interfacial broadening as a result of radiation induced damage can be measured by comparing depth profiles using identical ion beam parameters from a damaged and undamaged site on the same specimen, although this was not done in this example. This can be considered a first order approach to study radiation damage induced interfacial broadening. It is assumed that

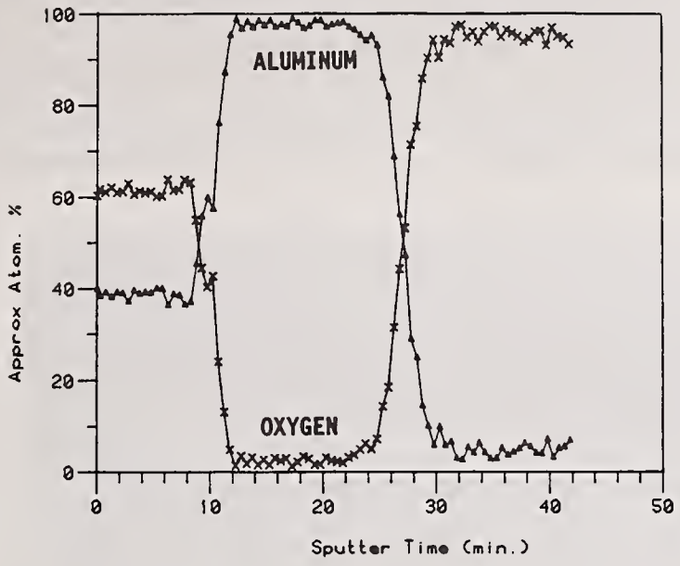

Figure 4. An Auger depth profile acquired from an Al_2O_3/Al/glass region after ball cratering. The interfaces are quite sharp and the Al region is almost devoid of oxygen.

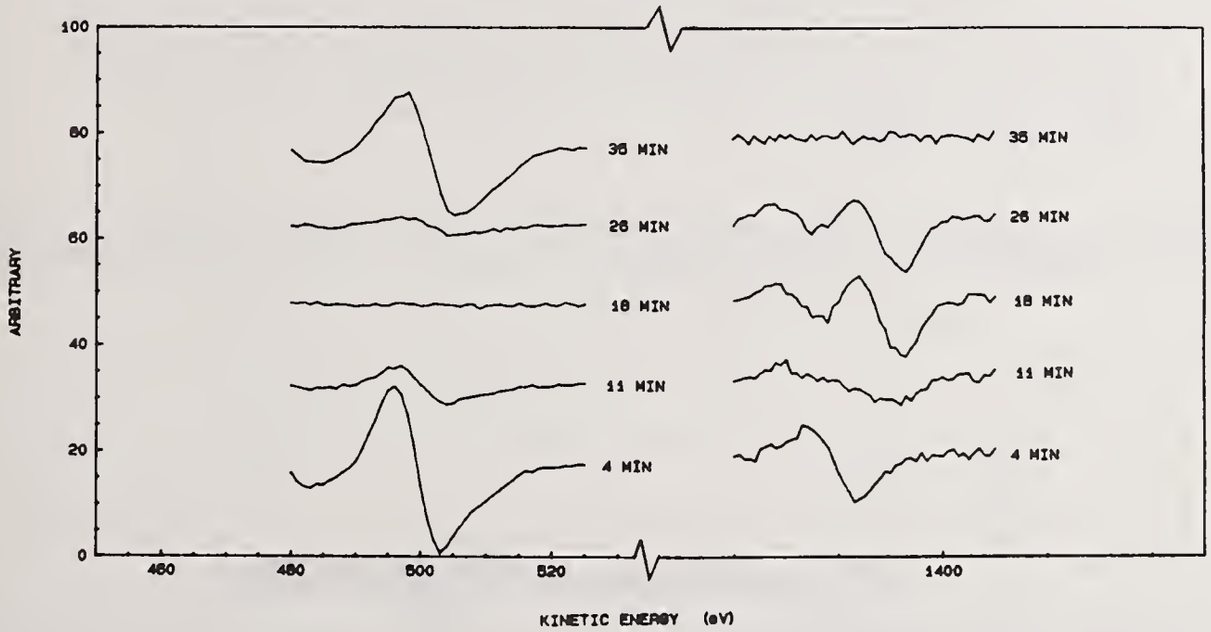

Figure 5. Auger peak shapes at specific times during the depth profile in Figure 4. The aluminum peak shape changes as expected as the metal oxide to metal interface is penetrated.

ion beam induced effects in both profiles are constant and any observed differences result from radiation induced effects. More basic research is required to enable ion beam induced effects to be measured directly in different dielectric films so that radiation induced interdiffusion at interfaces can be more accurately measured and modeled.

In another example, Auger spectroscopy was used to study an Al/glass interface after depth profiling. Figure 6 shows the sputtered region of interest, the textured region at the left

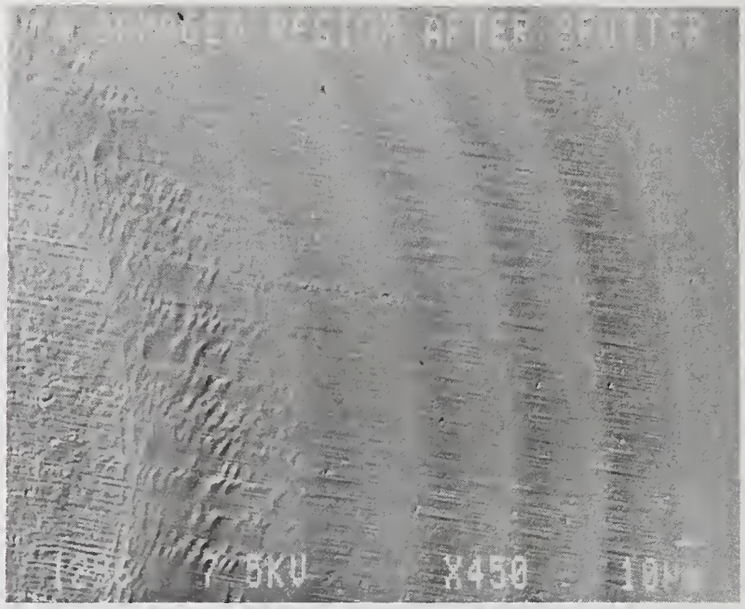

Figure 6. An SEM image acquired from a ball cratered optical stack after ion sputtering. The innermost ring near the left edge shows evidence of ion beam texturing which is not observed in other dielectric films in this stack. This suggests a sputtering anomaly which could be related to compositional differences.

center of the photograph. An Auger spectrum acquired within this region (Figure 7) showed the presence of carbide formation. The formation of metal carbides by low energy ion bombardment

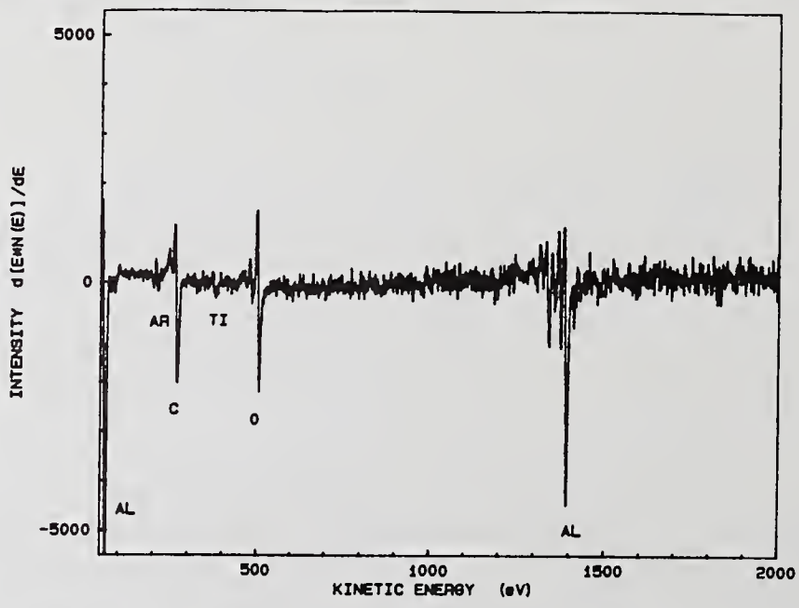

Figure 7. An Auger spectrum acquired from the textured region in Figure 6. The carbon peak shape indicates the formation of a carbide. Carbon was not observed outside the textured ring.

has been reported in the literature [8] and has been observed in our laboratory with clean titanium surfaces. Whether the observed carbide, in this example, formed as a result of ion bombardment or radiation induced damage is not known. These data do suggest, however, that efforts should be made to eliminate carbon contamination from substrate surfaces before the deposition of metal films and subsequent dielectric films. Even small amounts of carbon (a few monolayers) trapped at the metal/substrate interface on a poor thermally conductive substrate could result in carbide formation if elevated temperatures are anticipated during the service life of the specimen. Power densities of just a few watts/cm^2 are capable of initiating carbide formation if the absorbed thermal energy is not rapidly dissipated in the substrate.

6. EDS of Thin Films

Ordinarily EDS is considered a bulk analytical technique which can sample at least a micron into a specimen under typical operating conditions. For dielectric stacks with layers of 0.5 μm or less, the technique can be modified to produce valuable qualitative data at both damaged and undamaged sites on a specimen. This is accomplished by selecting a thin film of interest in a dielectric stack and reducing the primary electron beam excitation energy while observing the resulting EDS spectrum. When x-rays from atomic species are no longer observed from an underlying layer, the resulting EDS spectrum is being generated entirely within the selected layer of the stack. If a ball crater is made in a stack of films, each successive layer can be probed by adjusting the primary beam energy in the manner described. We have applied this technique to an optical stack which allegedly contained alternating boron nitride and alumina films each about 0.5 μm thick to demonstrate its usefulness. The specimen was ball cratered. Figure 8 shows an EDS spectrum which was acquired from the first alumina film. Aluminum and oxygen are clearly observed. An EDS spectrum acquired from the second alumina film was identical.

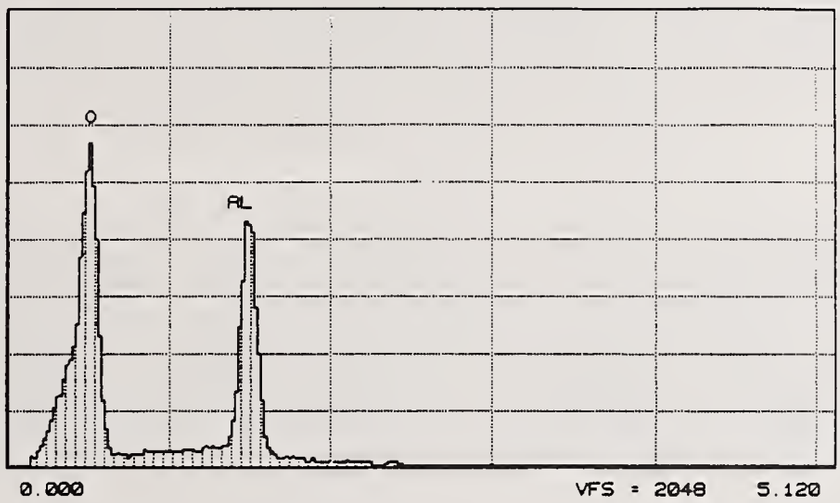

Figure 8. Light element EDS spectrum from the first alumina film in a dielectric stack after adjusting the primary electron beam energy so that only the alumina layer is sampled.

Figure 9 shows an EDS spectrum acquired from the outermost boron nitride film. Boron cannot be observed with our EDS detector, although a subsequent Auger spectrum confirmed its presence. The nitrogen signal from the boron nitride film is clearly evident. In addition, silicon and oxygen are observed. An EDS spectrum from the second boron nitride film was identical indicating that the boron nitride films in this stack had a silicon/oxygen bulk component. Auger spectra acquired from the boron nitride films along the ball cratered surface confirmed the presence of silicon and oxygen in the boron nitride. Hence, the usefulness of light element EDS for evaluating the bulk composition of thin dielectric films has been

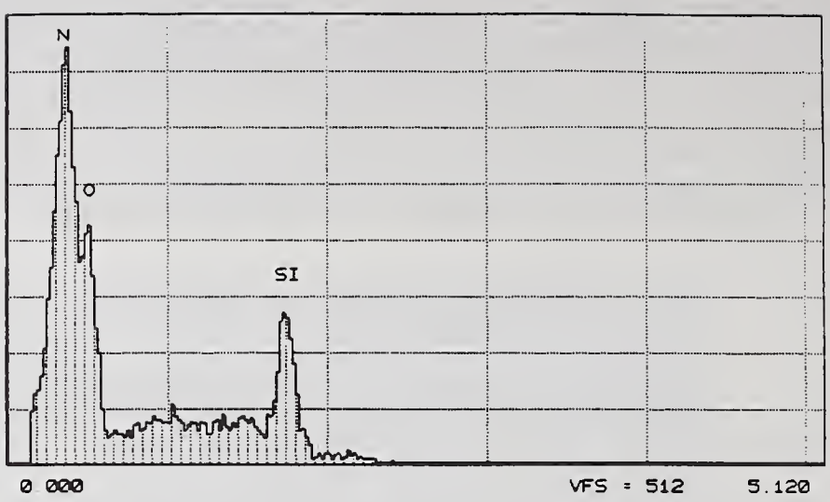

Figure 9. Light element EDS spectrum from the outermost boron nitride film. film. Silicon and oxygen are observed in this film in addition to nitrogen from the boron nitride.

demonstrated. Together with ball cratering and AES, a powerful methodology has been developed for probing bulk compositions of individual layers deep within optical stacks. The approach we have described has to be modified slightly if one or both of the films in the stack contain heavier elements which cannot be excited with reduced primary beam energies such as were used in the above example. We have also used light element EDS to determine the composition of micron size particulates within dielectric films, to identify surface debris, and to analyze ring defects in optical films. Further, in conjunction with ball cratering and AES, valuable qualitative data from radiation induced bulk damage sites has been obtained.

7. Summary

The usefulness of AES, EDS, SEM, and Auger depth profiling in evaluating dielectric thin films has been demonstrated. Further, ball cratering allows these techniques to applied sequentially to underlying layers deep within an optical stack. Stress relief cracking, substrate failure, and film delamination can be studied by ball cratering at damaged and undamaged sites and comparing the results using optical microscopy and scanning electron microscopy. Collectively, these analytical techniques when used in conjunction with ball cratering enable a powerful methodology for the study of radiation induced damage in optical thin films. Much more basic research needs to be done on dielectric thin films to enable fully quantitative results to be achieved using a combination of these techniques.

The author wishes to acknowledge the financial support of the Naval Weapons Center, China Lake, California for this work and the enthusiastic support given the author by T. M. Donovan.

8. References

[1] Joshi, A.; Davis, L. E.; Palmberg, P. W. Auger electron spectroscopy, chapter 5 in Methods of surface analysis, A. W. Czanderna, ed. Amsterdam: Elsevier Scientific Publishing Company; 1975. 159-222.

[2] Briggs, D; Seah, M. P. Practical surface analysis by Auger and x-ray photoelectron spectroscopy. New York, NY: John Wiley & Sons; 1983.

[3] Murr, L. E. Electron and ion microscopy and microanalysis. New York, NY: Marcel Dekker, Inc; 1982.

[4] Reed, S.J.B. Energy-dispersive x-ray spectrometer, chapter 4 in Quantitative electron-probe microanalysis, Scott, V. D.; Love, G., ed. Chichester, England: Ellis Horwood Limited; 1983. 81-100.

[5] Walls, J. M.; Brown, I. K.; Hall, D. D. The application of taper-sectioning techniques for depth profiling using Auger electron spectroscopy. Appl. Surf. Sci. 15(1-4): 93-107; 1983 april.

[6] Walls, J. M. The application of surface analytical techniques to thin films and surface coatings. Thin Solid Films 80: 213-220; 1981.

[7] Guenther, K. H. Nonoptical characterization of optical coatings. Appl. Optics 20(20): 3487-3502; 1981 October 15.

[8] Okuyama F.; Fujimoto, Y. Direct evidence for a thermal effect of Ar^+ ion bombardment in a conventional sputtering mode. J. Vac. Sci. Technol. A4(2): 237-238; 1986 March/April.

COMMENTS

Question: Can you say anything about the cost of the facility?

Answer: The capital equipment cost to field the coater is about $350,000. The cost does not include the costs of any personnel working on it. The facilities have run about $50,000 so I'd say that the total cost is roughly about $400,000 to $500,000.

Manuscript Received
5-8-90

Laser Conditioning of Optical Thin Films*

C. R. Wolfe, M. R. Kozlowski, J. H. Campbell, F. Rainer,
A.J. Morgan, and R.P Gonzales

University of California
Lawrence Livermore National Laboratory
P.O. Box 5508, L-490
Livermore, CA 94550

Results are presented that show the damage thresholds of e-beam deposited multilayer HfO_2/SiO_2 thin films can be permanently increased by a factor of 2 to 3 by illumination with subthreshold fluences of laser light. This sub-threshold illumination procedure is referred to as "laser conditioning". The films used in this study were prepared by three different physical-vapor-deposition techniques: ion-beam sputtering, plasma plating and e-beam evaporation. Only the e-beam deposited films showed consistent and significant improvement with laser conditioning. Of the material pairs examined (HfO_2/SiO_2, ZrO_2/SiO_2 and TiO_2/SiO_2), HfO_2/SiO_2 gave the greatest and most consistent damage improvement with conditioning. The number of layers and the reflective or transmissive characteristics of the HfO_2/SiO_2 films were found to have little impact on laser conditioning of the film. The results show that the damage thresholds of a wide range of e-beam deposited coatings (e.g. HR's, polarizers, etc.) can be improved by laser conditioning. Several possible conditioning mechanisms are examined.

Key words: "annealing", band-gap states, conditioning, damage, damage thresholds, dielectric oxides, laser conditioning, laser damage, optical thin films, paramagnetic states, point defects.

1. Introduction

At LLNL we are improving processes for fabricating damage resistant optical coatings for use on high-peak-power lasers such as those used in inertial confinement fusion (ICF) research. The coating fabrication processes under study are physical vapor deposition (PVD), plasma assisted chemical vapor deposition (PCVD), and sol-gel processing. Each alternative has certain advantages. However at the present time only PVD involving e-beam evaporation in vacuum is a fully scaled and practical process capable of fabricating the high-quality, large-aperture optical coatings needed for ICF research.

A significant limitation on the operating fluence (or peak power) of high-peak-power lasers is the laser damage threshold of the optical components. Over the last two decades laser conditioning, or "annealing", using sub-threshold illumination has been reported as a method to increase the damage threshold of optical thin films and bulk optical materials [1-10]. In most cases, details of the process and materials involved have been sketchy. In addition, little effort has been made to apply such a process to improve the threshold of optical components installed in operating laser systems. In general, two mechanisms have been proposed as responsible for the observed conditioning effects. The first mechanism involves "laser cleaning", whereby volatile contaminants (especially atmospheric water) are removed either from the surface [1-4, 7, 8] or from the bulk of the material [5, 9]. It has been proposed that

* Work performed under the auspices of the U. S. Department of Energy by Lawrence Livermore National Laboratory under Contract No. W-7405-ENG-48.

absorption by these contaminants leads to laser damage. This conditioning process appears to be reversible for surfaces [3] but permanent for bulk materials [9]. The second mechanism involves laser heating of the material until a change in crystallinity is observed [6] or polishing damage is removed [10]. The mechanism applicable to a particular system appears to be dependent on the optical material and the laser conditioning wavelength.

It has been shown by Wilder and Thomas that dielectric multilayer coatings similar to those used as turning mirrors in the LLNL Nova laser system show a laser conditioning effect [5]. In our study a number of different optical coatings were prepared in an attempt to identify the importance of different film parameters on both conditioned and unconditioned damage thresholds for materials used on the Nova laser. These film parameters are: dielectric material, deposition method and multi-layer film design. In the following pages we examine each of these three parameters. In addition we examine possible changes in the coating material that may lead to laser conditioning. Specifically we present evidence that absorption/desorption of contaminants and laser induced phase changes are not responsible for the conditioning effect observed in the films studied here. Also we observed that the conditioning effect is permanent for these films. Finally in a concluding section we propose an electronic defect mechanism to explain the laser conditioning effect in the dielectric films.

We intend to employ conditioning in the near future to increase the damage threshold of one meter diameter replacement mirrors for the Nova laser. Fabrication of these new mirrors with HfO_2/SiO_2 highly reflective (HR) coatings is scheduled to begin during the 1990 fiscal year.

2. Damage testing

The "figure-of-merit" for coating serviceability continues to be damage threshold. Damage thresholds measured at 1064 nm on three different facilities at LLNL are reported here. The repeatability on different lasers adds to the credibility of our conclusions. The Nd:YAG laser systems used are:

i. A variable pulselength laser which operates in a single shot mode with pulselengths varying from 1 to 16 ns.

ii. A rep-rated laser that operates at pulse-repetition frequencies (PRF) of 10, 15 or 30 Hz with a pulselength of 10 or 16 ns.

iii. A rep-rated laser that operates at 18 Hz with a pulselength of 8 ns and is capable of rastering large aperture optics automatically.

The laser fluence is determined using calorimetry measurements and the measured beam profile recorded with a CCD video camera. Commercial software is used to calculate the peak fluence from these data. The laser spot size is usually greater than 1 mm diameter ($1/e^2$). Damage is defined as any visual change in the sample after laser irradiation when viewed by 100X Nomarski microscopy. To observe the on-set of microscopic damage, photographs of the test area are taken before and after testing and compared for evidence of damage to the surface. A detailed description of damage testing apparatus and procedures is presented in an accompanying paper in this symposium by Rainer et al. [11].

The damage thresholds reported here were determined by one or more of the four test sequences shown in figure 1. The four test sequences differ in the number of shots, the time between shots, and the range of fluences used. The damage threshold measured by 1:1 and S:1 shot programs are reported as "unconditioned" thresholds; these shot programs expose each site to only one fluence level. The 1:1 test uses a single shot per site. The S:1 test uses a series of constant-fluence shots on each fresh (i.e. unexposed) site with the time between shots being short (equal to 1/PRF). Conditioned thresholds are measured by R:1 and N:1 tests. The R:1 test uses a series of shots separated by short intervals as in S:1, but the fluence is varied from zero to a pre-set upper bound in a linear ramp. The N:1 test uses a series of single shots, the fluence of each shot is increased step-wise until a pre-set upper bound is reached. The time between shots for N:1 testing can be rather long, generally several minutes. Uncertainty in the threshold measurement is typically ± 15%.

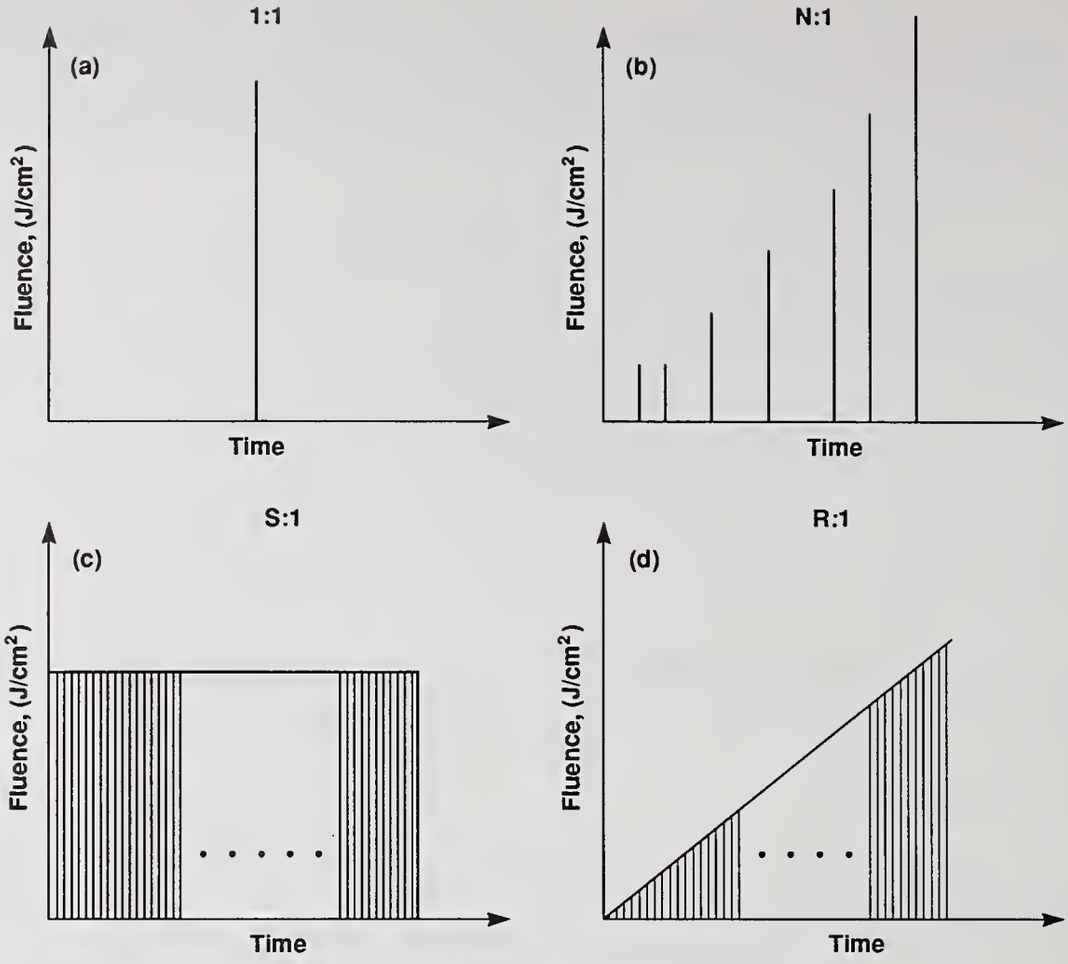

Figure 1. Four methods used to measure damage threshold: (a) single shot per site (1:1), (b) multiple shots per site with large increments in fluence between shots (N:1); (c) multiple shots per site at constant fluence (S:1), and (d) multiple shots per site with a ramped increase in fluence (R:1). Note that N:1 and R:1 tests give "conditioned" damage thresholds.

3. Results and discussion

3.1 Damage threshold dependence on film materials

SiO_2 was used as the low-index dielectric for all multilayers prepared in the course of this work. High-index dielectrics considered were: HfO_2, ZrO_2, TiO_2 and Ta_2O_5. Ta_2O_5 was rejected because of the need to bake coated parts in O_2 after deposition to achieve full oxidation and low absorption. Baking at elevated temperatures is not practical for massive (250 kg) Nova-scale optics.

HfO_2, ZrO_2 and TiO_2 paired with SiO_2 were directly compared in simple"quarterwave" HR designs, the optical performance of the HfO_2/SiO_2 coating is shown in figure 2. Inconsistent damage thresholds were obtained from TiO_2/SiO_2 mirrors fabricated both during this study and in the past. The formation of highly absorbing sub-oxides of TiO_2 [12] is difficult to avoid during high vacuum deposition and may be the reason for the inconsistent damage thresholds. Therefore TiO_2 was also eliminated as a potential film material, leaving only HfO_2 and ZrO_2 as high-index materials of interest.

E-beam evaporated HR coatings of both HfO_2/SiO_2 and ZrO_2/SiO_2 were prepared in order to study the influence of laser conditioning on the damage threshold. Upon conditioning, both material combinations produced a marked improvement in damage threshold for 1-ns pulses, as shown by the data in figure 3. These results indicate that HfO_2/SiO_2 and ZrO_2/SiO_2 have essentially equivalent damage resistance; the unconditioned thresholds are 6-8 J/cm² and conditioned thresholds are as much as 3 times greater.

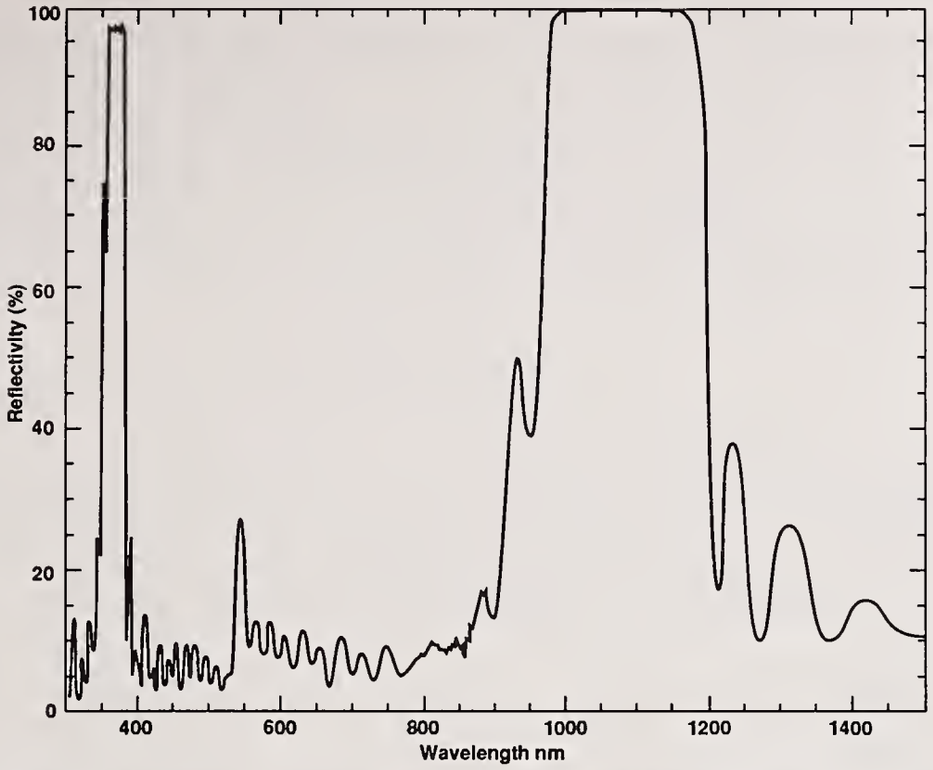

Figure 2. Measured reflectance vs. wavelength for a simple HfO_2/SiO_2 quarter-wave stack that was prepared as part of this study. The reflectance at 1064 nm is > 99.5%.

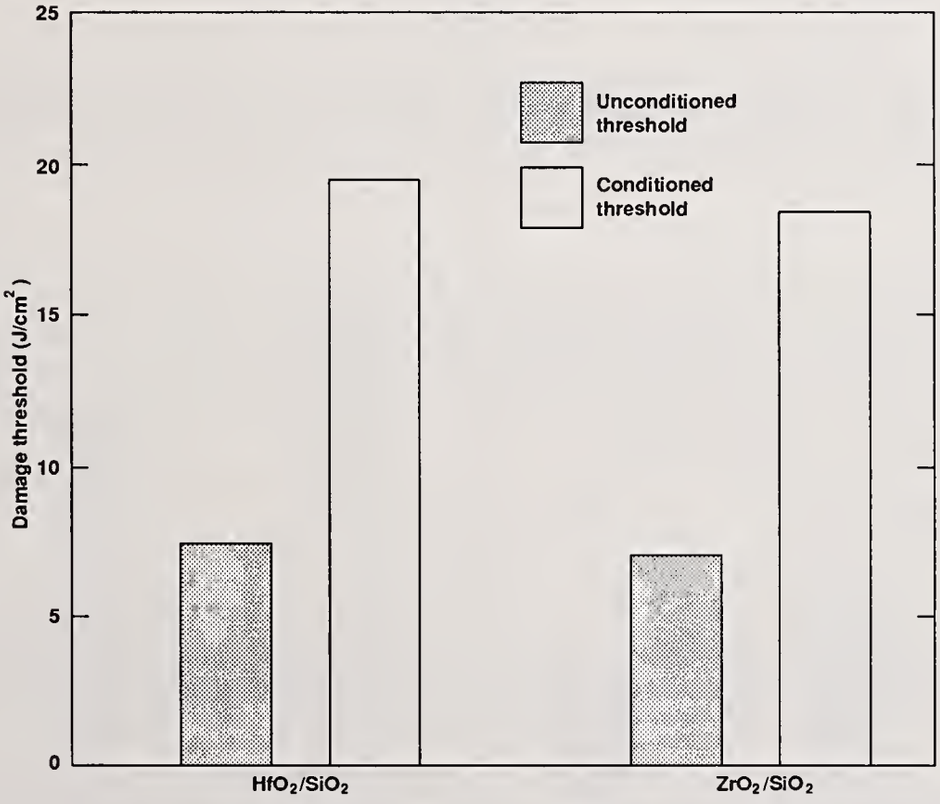

Figure 3. Comparison of unconditioned and laser-conditioned damage thresholds for HfO_2/SiO_2 and ZrO_2/SiO_2 HR quarterwave stacks for 1-ns pulses, 1064 nm. The unconditioned values are from 1:1 tests and the conditioned values are for N:1 measurements.

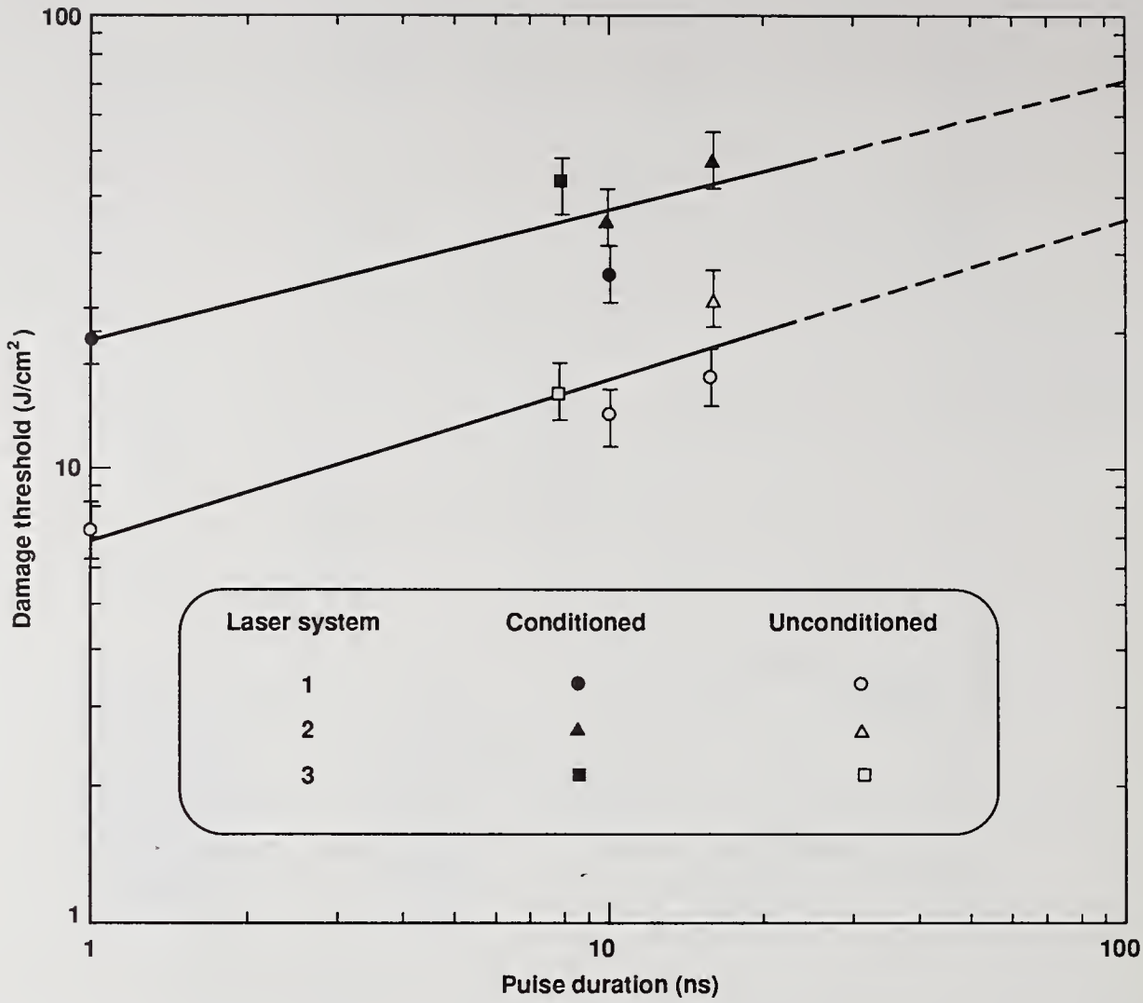

Figure 4. Measured pulselength scaling for conditioned and unconditioned damage thresholds of HfO_2/SiO_2 quarterwave HR coatings at 1064 nm. The data are from measurements on the three different laser systems described in section 2 and the solid line represents a least squares fit to the data.

The HfO_2/SiO_2 coating thresholds are very reproducible and show about the same factor of improvement due to conditioning over a broad pulselength range, as shown in figure 4. The reproducibility of the threshold measurements was remarkably consistent considering three different laser-damage-test systems were used in the study. Based on the data in figure 4 for the HfO_2/SiO_2 coatings, the damage threshold scales with pulse-length as approximately:

unconditioned: $D_t \simeq 7\ t_p^{0.35}$

laser conditioned: $D_t \simeq 19\ t_p^{0.30}$

where D_t is the damage threshold in J/cm^2 and t_p is the laser pulselength in ns. This pulselength scaling of the damage threshold falls within the range typically reported by others studying damage to thin films (i.e. between about $t_p^{0.25}$ and $t_p^{0.4}$) [see for example reference 13].

In contrast to the HfO_2/SiO_2 thresholds, we found that the ZrO_2/SiO_2 coatings showed significant site-to-site variability in threshold measurements. In some tests the ZrO_2/SiO_2 showed marked improvement with conditioning (as in figure 3) while in other tests they showed no improvement.

The reason for the difference in damage performance of the ZrO_2- vs. HfO_2-based coatings used in this study is unclear. When the ZrO_2/SiO_2 films did condition, the threshold improvement was comparable

to that observed for the HfO_2/SiO_2 films. We therefore suggest that HfO_2/SiO_2 and ZrO_2/SiO_2 have similar intrinsic film properties. However, in the case of ZrO_2, the damage threshold is often controlled by extrinsic properties such as visible defects. These extrinsic defects lead to the site-to-site variability observed in the damage threshold. Using Nomarski microscopy, we found that the ZrO_2- and HfO_2-based films have about the same density of visible defects; however, the defects tend to be somewhat larger in the ZrO_2/SiO_2 films. As was pointed out by Kozlowski et al. [14], it is unlikely that modest differences in size or density of defects, per se, leads to different damage threshold. Rather these differences probably indicate different types of defects that may be more or less susceptible to either laser damage or conditioning or both.

3.2 Damage threshold vs. film deposition method

During the course of this study we prepared HR films of HfO_2/SiO_2 by three different deposition techniques: (1) conventional e-beam evaporation, (2) ion-beam sputtering (IBS), and (3) plasma plating (PP). In addition, for the case of e-beam evaporation, we examined the effects of scale-up by preparing coatings in a small (1.2-m diameter) research-scale chamber as well as the large 3-m diameter production-scale chamber used to fabricate the current 1-m diameter, 250-kg Nova mirrors.

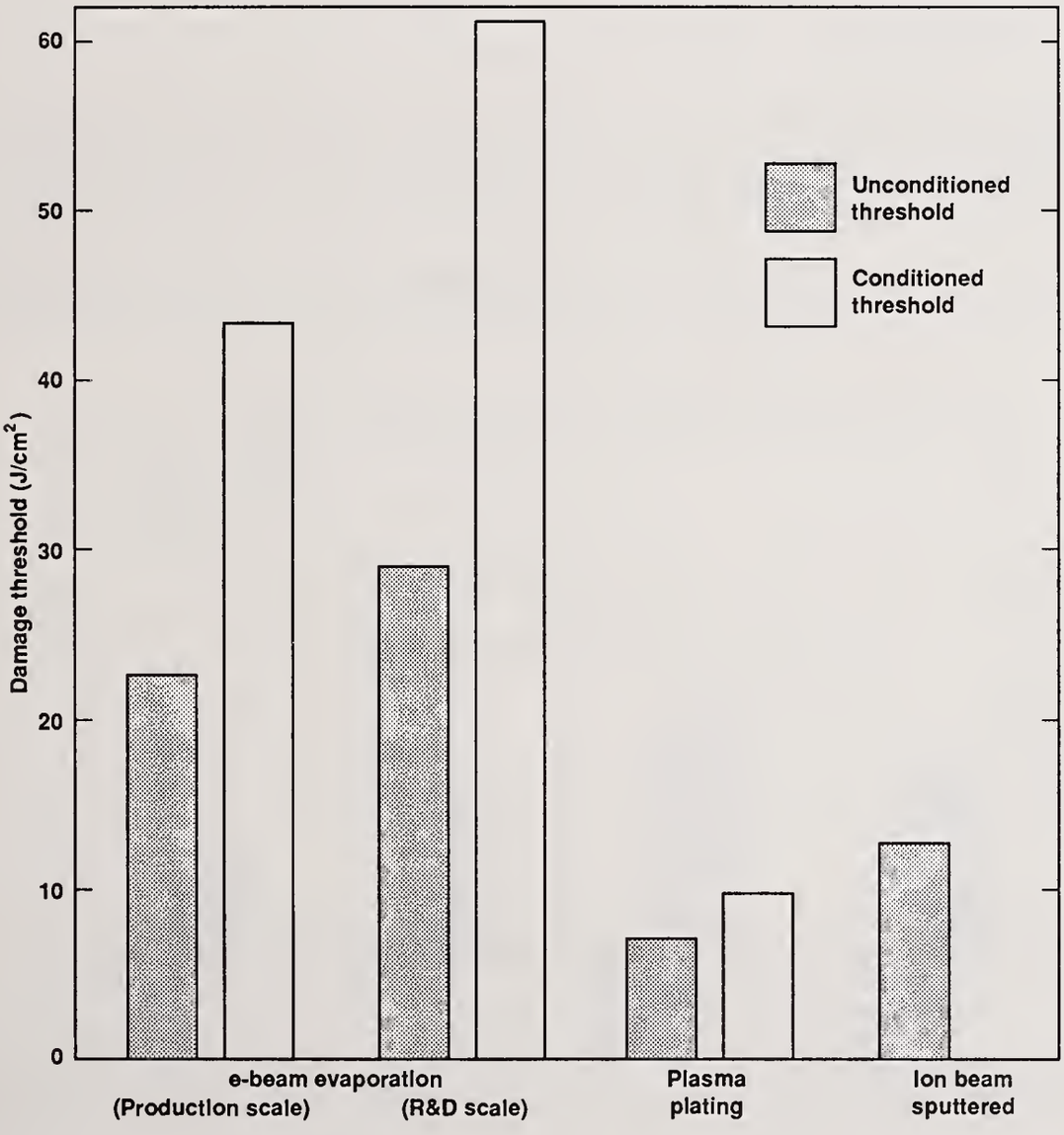

Figure 5. Unconditioned (S:1) and conditioned (R:1) damage thresholds (16 ns, 1064 nm) for HfO_2/SiO_2 HR coatings prepared by e-beam evaporation, plasma plating, and ion-beam sputtering. The e-beam data are for coatings prepared on both the small scale R & D coater and the large scale (3-m diameter) production coater.

The choice of IBS and PP as coating methods was based on the observation that coatings produced by these methods have less porosity (i.e. higher density) and therefore have greater mechanical strength and environmental durability [15-19]. This latter quality was thought to be particularly important because of previous reports of film conditioning (and laser damage) being related to water-vapor absorption [1, 3, 4]. However, our measurements show that HR films of HfO_2/SiO_2 deposited by IBS and PP have lower damage thresholds than those made by conventional e-beam evaporation. Figure 5 compares the measured damage thresholds of coatings made by e-beam evaporation, IBS and PP. Laser conditioning does not significantly increase the damage threshold of the PP coatings. In addition, threshold measurements of IBS films were very inconsistent and the conditioning effect was not always observed, consequently no laser conditioned value is reported in figure 5. In this study laser conditioning was consistently observed only in e-beam-deposited coatings. In addition we note that the film absorption at 1064 nm, measured by calorimetry [20], was 500-5000 ppm for PP, 100-250 ppm for IBS and ~100 ppm for e-beam deposition.

Figure 5 also compares measured damage thresholds for coatings made in a small and a large e-beam coating chamber. The results show that conditioning is observed for the films produced in these two chambers; therefore the conditioning characteristics of the HfO_2/SiO_2 films are preserved in scale-up. The conditioned and unconditioned thresholds for the coatings produced in the small coater are 30-40 % higher than those made in the production coater, however.

3.3 Damage threshold dependence on coating design

The data in the previous section describes laser conditioning effects in HR coatings consisting of a simple optical quarterwave stack of high- and low-index materials. We also found that the conditioning effect occurs in both transmissive and reflective coatings and in single as well as multilayer films. In other words, the conditioning effect appears independent of the coating design for HfO_2/SiO_2 film materials.

Figure 6 shows the unconditioned and conditioned damage thresholds for: (a) single-wavelength (1064 nm) HR coatings each consisting of a 27-layer quarterwave stack, (b) complex, 64-layer trichroic HR

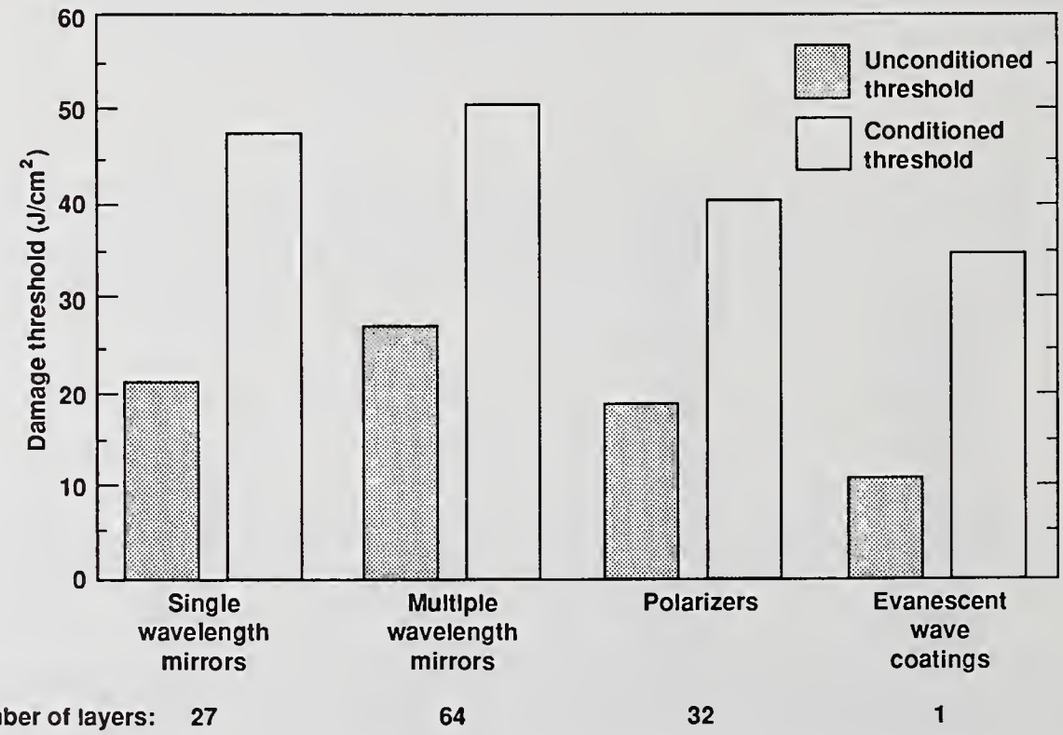

Figure 6. Comparison of conditioned and unconditioned damage thresholds for HfO_2/SiO_2 multilayer HR's, polarizer and single-layer evanescent wave coatings; all data are for 1064-nm laser irradiation. The HR data are for pulse lengths of 16 ns and the polarizer and evanescent wave coatings are for 10-ns pulses.

coatings designed to reflect at 1064, 532 and 355 nm, (c) 1064-nm polarizers with a rejection ratio of about 300 to 1, and (d) a single-layer SiO_2 evanescent wave coating 1400 nm thick. Note that for this series of coatings there appears to be no correlation between the threshold improvement via conditioning and the coating design. In addition, the degree of improvement by conditioning is also largely independent of the number of layers (or interfaces) within the coating for these HfO_2/SiO_2 coatings.

3.4 Effects of material changes on laser conditioning

Laser conditioning of thin films has previously been linked to the removal of adsorbed water or other atmospheric contamination [1, 3, 21-23]. When such a "cleaning" mechanism was reportedly involved, the enhancement of the damage threshold by conditioning was often found to be temporary [3].

Experiments performed at LLNL on HfO_2/SiO_2 mirrors indicate that the laser conditioning effect is permanent for these films and not related to the presence, or removal, of atmospheric water. To demonstrate this, HfO_2/SiO_2 mirrors made by conventional e-beam deposition were allowed to equilibrate with ambient air (20°C, relative humidity ~50%) and were then damage tested at 1064 nm. Both the unconditioned and conditioned damage thresholds were determined. The coatings were then desiccated for 10 weeks over P_2O_5 to remove physically absorbed water [24]. The removal of water was observed as a shift in reflectance to shorter wavelengths (table 1). The occurrence of spectral shifts in optical filters upon drying is well known [25]. The conditioned and unconditioned thresholds of the dried coatings were then measured and compared to the thresholds of the same samples before they were dried. No change in threshold was observed (fig. 7). Furthermore, the reflectance shift caused by drying was found to be reversible. When the dried coatings were re-exposed to moist air their reflectance shifted back to longer wavelengths and the original performance was recovered. Figure 8 shows the gradual shift in the reflectance at 950 nm of one of the dried mirrors as it was re-equilibrated with ambient air. The optical absorption at 950 nm was used to monitor the slight shift in coating performance because a pronounced minimum in reflectance occurred at this wavelength (fig. 2). This structure allowed the slight reflectance shift to be accurately monitored. The time scale for equilibration is about 4 weeks. (Measurement of water absorption at 3350 cm^{-1} verified that the change in reflectivity was due to changes in the water content.)

Table 1. Measured Short Wavelength Shift of HfO_2/SiO_2 HR Coatings After Drying Over P_2O_5 for 10 weeks

Deposition method	Spectral Shift (nm)
E-beam evaporation: R&D-scale chamber	25
E-beam evaporation: Production-scale chamber	5
Ion beam sputtering	7
Plasma plating	3

The role of photolytic vaporization of contaminants in conditioning was investigated also. We attempted to "clean" and thus condition HfO_2/SiO_2 mirrors by exposure to broadband flashlamp light [26]. The lamp output fluence is about 10 J/cm^2 in 0.5-ms pulses, although it is over a very broad spectral range (~ 350 to 2000 nm). No increase in damage threshold was observed for the mirrors processed in this way, we therefore tentatively rule out "photolytic cleaning" of contaminants as a conditioning mechanism. Additional discussion of these experiments as they relate to electronic defects is given by Kozlowski et al. [14].

X-ray analyses of the HfO_2/SiO_2 HR coatings also indicate that conditioning does not involve any obvious material phase change. A diffractometer scan of an unconditioned mirror (using Cu, Kα x-rays

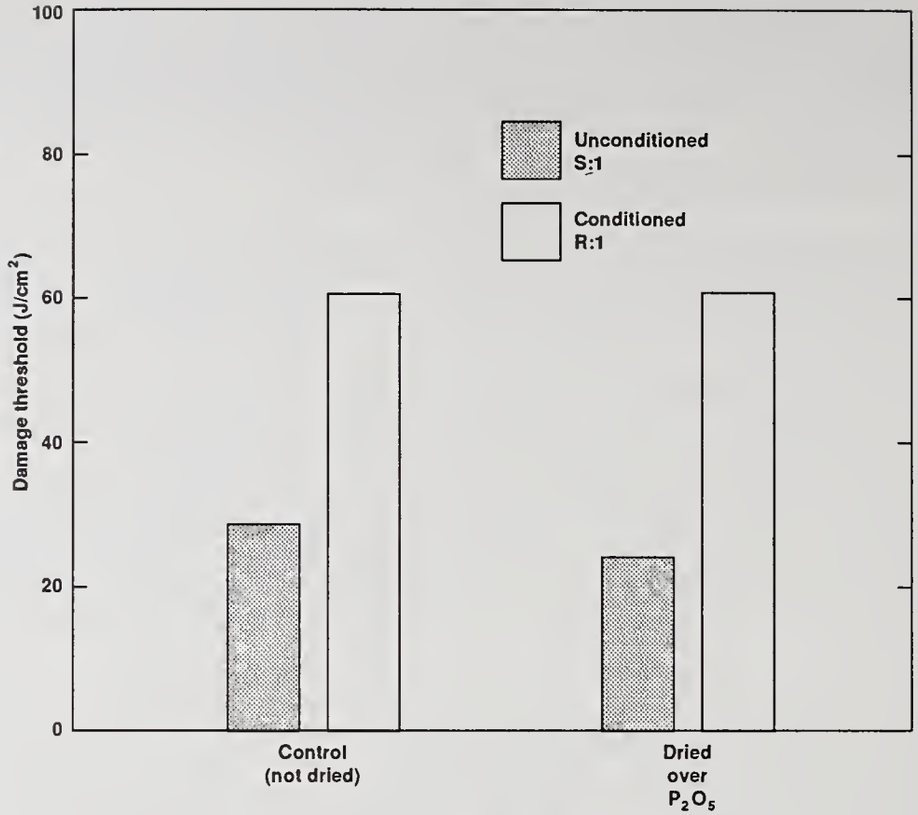

Figure 7. Conditioned (R:1) and unconditioned (S:1) damage thresholds (1064 nm, 16 ns) for HfO_2/SiO_2 HR coatings equilibrated in ambient air and desiccated over P_2O_5.

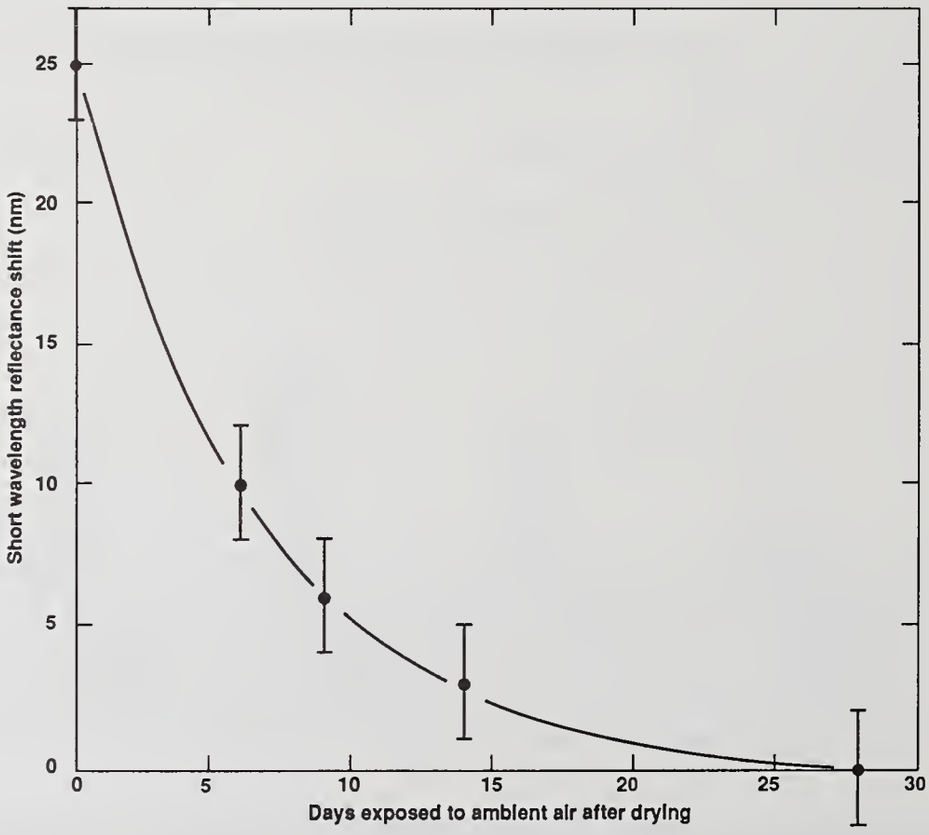

Figure 8. Time dependence of the spectral shift, to short wavelength, of a desiccated HfO_2/SiO_2 HR upon exposure to air.

with wavelength of 1.5405 Å) is shown in fig. 9a. Peak assignment indicates that the HfO_2 is partially crystalline. The crystalline fraction appears as mostly the monoclinic phase and a trace of cubic present on a high amorphous background. TEM analysis has shown that the HfO_2 layers are initially amorphous, but as the deposition continues, the crystal size increases so that at about halfway through the deposition columnar growth is observed. In contrast, SiO_2 is entirely amorphous. Diffractometer scans of the conditioned and unconditioned coatings showed no detectable change (± 5-10%) in the quantities or types

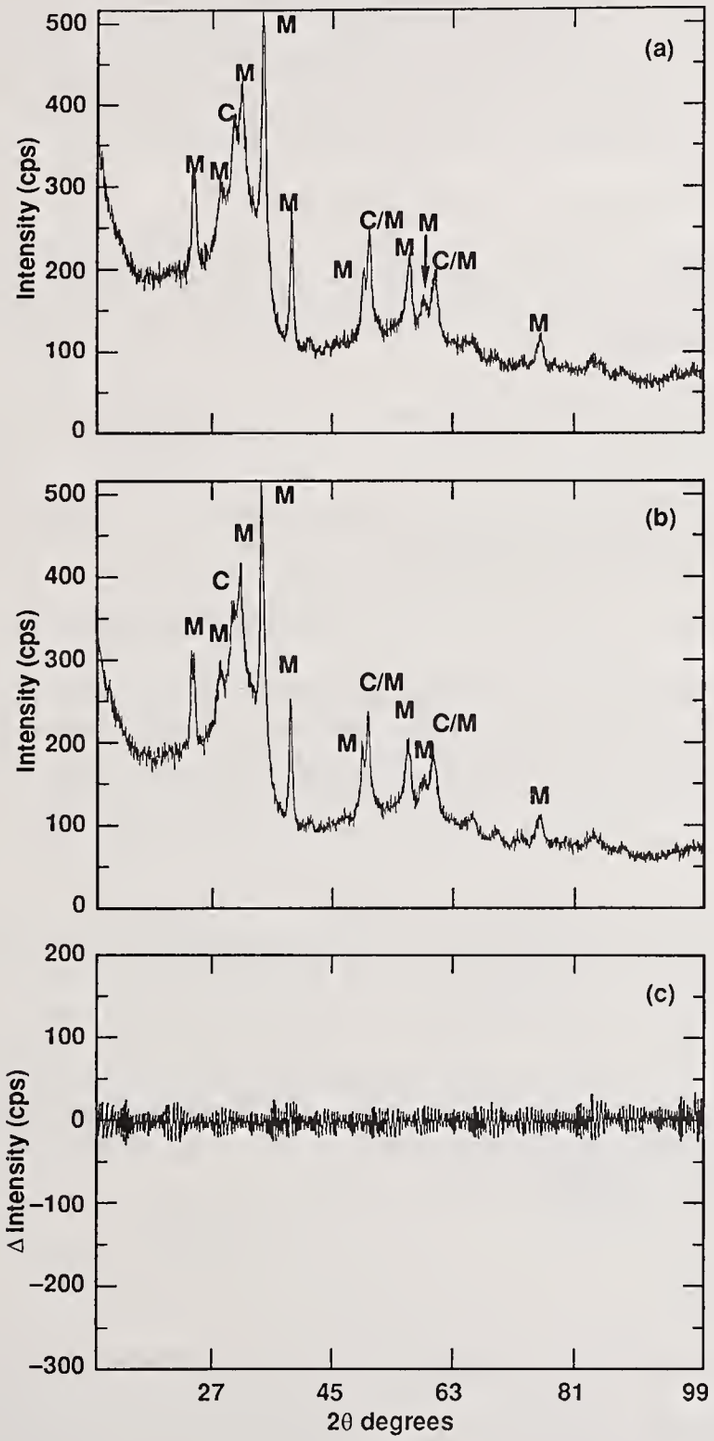

Figure 9 X-ray diffractometer signal vs. 2θ for (a) an unconditioned and (b) a conditioned HfO_2/SiO_2 HR coating. 'M' and 'C' identify peaks associated with the monoclinic and cubic phases of crystalline HfO_2, respectively; (c) the difference between the two spectra as determined by subtracting (b) from (a).

of phases present (fig. 9). Therefore we conclude that no phase change, that is measurable by this technique, accompanies laser conditioning of these coatings.

As a final note we report that the enhancement of damage threshold by laser conditioning is permanent in the HfO_2/SiO_2 e-beam deposited films. To determine this, a large area (~ 4-cm diameter) of an HR coating was conditioned using the Nova laser. The conditioned threshold of this sample was then monitored by subsequent small-aperture tests over a period of about 10 weeks. Details of this experiment and the results are given in the companion paper by Kozlowski et al. [14]. The results indicate that the pre-conditioned threshold was increased > 2 times over the unconditioned threshold and remained unchanged, within experimental error, over a period of 10 weeks. As shown above (fig. 8), the time scale for complete reabsorption of water in a desiccated film is only about 4 weeks. Thus film conditioning caused by laser induced water (or other contaminant) desorption, followed by reabsorption can be eliminated. We conclude that for all practical purposes the conditioning effect is permanent.

3.5 Thoughts on the mechanism for laser conditioning

Before proceeding to describe what may cause the conditioning effect, it is worthwhile to state what it does not depend on (at least for the films discussed in this work). The results in the preceding sections indicate the conditioning effect is:

i. not associated with the removal of absorbed moisture or other atmospheric contamination,

ii. not clearly dependent on the number of coating layers or the transmissive or reflective characteristics of the optical design,

iii. not associated with measurable recrystallization within the film.

The results therefore indicate that the often proposed "laser cleaning" or phase change mechanisms are not the dominant mechanisms responsible for the conditioning phenomena occurring in the dielectric films of interest here. In a paper by Edwards et al. [27] we further show that linear absorption by contaminating particles [5] does not cause damage. We instead propose below that the laser conditioning effect observed in high quality optical thin films is associated with intrinsic electronic defects in the films.

Of the materials we have tested, conditioning is only consistently observed in HfO_2/SiO_2 films deposited by conventional e-beam evaporation. One significant characteristic of e-beam coatings, that distinguishes them from films made by other processes, is the low energy of the material being deposited (<< 1 eV). In addition, the condensation process is one of extremely rapid quenching from a high temperature vapor to a much cooler substrate ~100-300°C; this can be thought of as "splat cooling". This rapid quenching can result in porous films dominated by intrinsic defects [28]. We believe that the "non-equilibrium" state of these e-beam films is associated with their laser conditioning properties. In the following paragraphs we speculate on the nature of these intrinsic defects and on how they may be associated with the laser conditioning process.

We propose that the laser damage of unconditioned films deposited by e-beam evaporation occurs by a four step process:

i. photo-excitation of electrons from shallow electronic gap states into the conduction band,

ii. excitation of the free carriers to high energy by acceleration under the optical electric field or by free carrier absorption,

iii. subsequent transfer of the excess energy to the lattice via avalanche [29] or an electron-phonon interaction (lattice heating) [30],

iv. heating of the film to some critical damage temperature such as the melting or boiling point of the dielectric material.

The importance of conduction band electrons to optical damage is not a novel concept. In fact, the dependence of the laser damage threshold on the presence of conduction electrons has been demonstrated for bulk SiO_2 [30], as well as for silicon and glass [31]. The novel concept is the connection between the conduction band electrons and the conditioning effect. We suggest that laser conditioning occurs due to the removal of the source of conduction band electrons in step (i) above. That is, when the dielectric material is illuminated at a low fluence, the electrons in the defect levels are excited to the conduction band. Since the optical electric field is not large enough to cause damage (steps (ii) to (iv)) the electrons decay into deep levels from which they cannot be easily excited into the conduction band on subsequent illuminations. When the 'conditioned' dielectric is subsequently illuminated at intensities above the unconditioned damage threshold, the number of electrons available for transfer to the conduction band is low and, therefore, the net energy transferred to the lattice is too low to cause damage; hence the observed laser conditioning effect.

E-beam deposited dielectric coatings are known to have a high concentration of electronic defects in the band-gap [32]. Point defects in amorphous and crystalline SiO_2 are well characterized because of their importance to solid state electronic technology [33-35]. Very little is known however about similar defects in other wide band gap dielectrics such as HfO_2, ZrO_2, and TiO_2. As shown schematically in figure 10, energy bands in amorphous solids can be thought of as distorted by local variations in bonding. In general, this produces discrete states in the band gap that are distributed randomly in the amorphous material [36]. Wide band gap dielectrics deposited by e-beam evaporation are highly disordered and electronically metastable. A high concentration of occupied gap states located above the Fermi level may result from this type of disorder. An example of such defects, paramagnetic point defects, have been observed in amorphous SiO_2 [37]. It has been demonstrated that these states can be filled by electrons as a result of UV illumination and then subsequently emptied by thermal treatment [38].

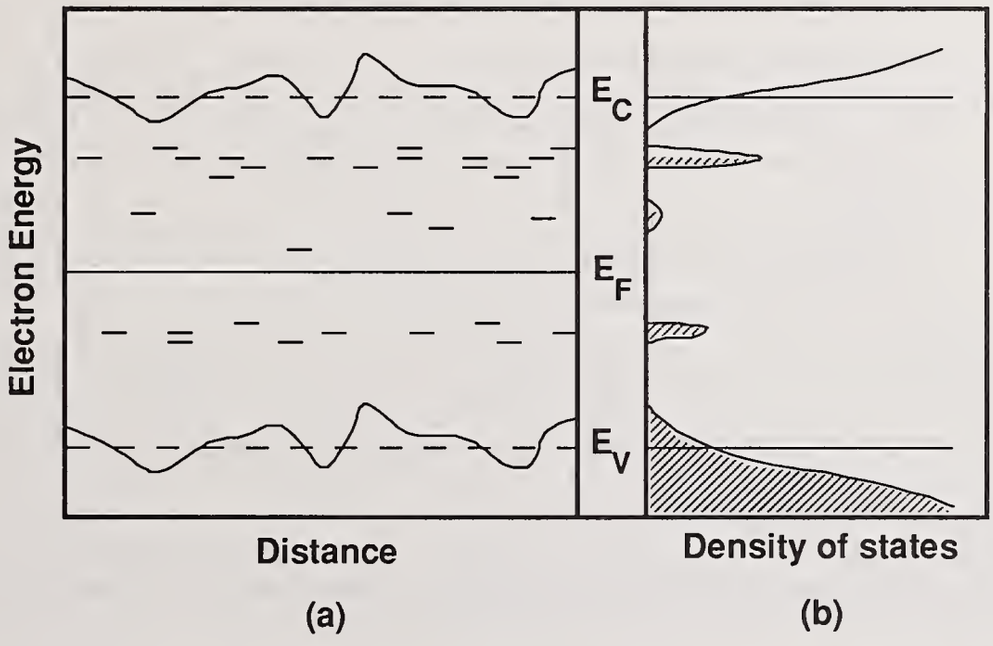

Figure 10. (a) Schematic diagram showing the model representation of the energy bands of an amorphous dielectric solid including gap states. E_v, E_f and E_c refer to the energies associated with the valence band, Fermi level and conduction band, respectively; (b) schematic representation of the corresponding density of states. The shaded regions represent occupied levels.

The independence of the laser conditioning effect on film design and number of layers suggests that the electronic defects of interest are bulk defects and not associated with interfaces. Further discussion of

the nature of the electronic defects and the mechanism by which energy is transferred to the crystal lattice is given by Kozlowski et al. [14].

As shown above, "non-equilibrated" films produced by e-beam deposition produced consistent conditioning effects. In contrast, films of SiO_2 prepared by high temperature PCVD [39, 40] have very high unconditioned thresholds, comparable to those for conditioned films of e-beam deposited SiO_2. We believe that the PCVD process produces inherently more equilibrated films, which are not susceptible to the damage/conditioning mechanisms important to unconditioned e-beam coatings. Unfortunately the PCVD coating technology is not yet developed to the scale required to fabricate large-aperture optical components for fusion research lasers.

Because of their non-equilibrium deposition conditions, the plasma plating and ion-beam sputtering processes examined in this study might be expected to produce electronically highly defective films with a high concentration of electronic defects similar to those produced by e-beam deposition. The IBS and PP films, however, showed negligible improvement in the damage threshold upon laser conditioning. The low unconditioned threshold and lack of a conditioning effect suggests that a damage mechanism other than the electronic defect mechanism described above might be dominant for these films.

4. Conclusions

The results of experiments reported here show that optical thin films of SiO_2 or HfO_2/SiO_2 deposited by conventional e-beam processes can be laser conditioned to significantly increase their laser damage threshold. This is accomplished by illuminating the coating at fluences below the damage fluence. Our results indicate that:

i. the damage threshold can be increased by factors as great as 2-3x,

ii. the conditioning effect is permanent,

iii. the conditioning effect is dependent on the dielectric material and the deposition technique, but shows little dependence on coating design or the size of the deposition chamber

v. conditioning may be related to the removal of electrons from intrinsic defects energetically close to the conduction bands in these materials.

Through the use of the conditioning process the damage threshold of e-beam deposited optical coatings can be made to exceed the operating fluences required by current and future fusion laser systems. Currently, e-beam deposition is the only process by which large-aperture, high-quality, optical coatings can be made. Results presented here show that the conditioning properties of e-beam deposited films are not influenced by scale-up to a production scale deposition chamber. In a paper by Kozlowski et al. [14] we further show that the laser conditioning process can be used to increase the damage threshold over entire large area optical components. These laser conditioned e-beam coatings will comprise the next generation of large aperture optical thin films used on the LLNL Nova laser system.

5. Acknowledgements

The coatings studied in the course of this work were prepared under contract to the Advanced Products Division and Research Department of Optical Coatings Laboratory, Inc. (OCLI) in Santa Rosa, Ca. and Spectra- Physics Optics Co. in Mountain View, Ca. The authors gratefully acknowledge the assistance of Dr. M. Shinn in measuring the water absorption spectra, Dr. M. Sattler in performing the TEM analysis, and L. Summers in making the x-ray measurements on the HfO_2/SiO_2 films. The efforts by A. Clasen in preparing this manuscript for publication are also deeply appreciated.

6. References

[1] Porteus, J. O.; Faith, W. N.; Allen, S. D. Laser desorption analysis of H_2O and other contaminants from optical surfaces. Nat. Bur. Stand. (U.S.) Spec. Publ. 638; 1981 November. 273 p.

[2] Swain, J. E.; Lowdermilk, W. H.; Milam, D. Raising the surface damage threshold of neutral solution processed BK-7 by pulse laser irradiation. Nat. Bur. Stand. (U.S.) Spec. Pub. 669; 1982 November. 292 p.

[3] Frink, M. E.; Arenberg, J. W.; Mordaunt, D. W.; Seitel, S. C.; Babb, M. T.; Teppo, E. A. Temporary laser damage threshold enhancement by laser conditioning of anti-reflection coated glass. Appl. Phys. Lett. 51 (1987) 415.

[4] Arenberg, J. W.; Mordaunt, D. W. Experimental investigation on the role of wavelength in the laser conditioning effect. Nat. Inst. Stand. & Tech. (U.S.) Spec. Pub. 775; 1988 October. 516 p.

[5] Wilder, J. G.; Thomas, I. M. Effect of n on 1 laser treatment on damage threshold of selected optical coatings. Nat. Inst. Stand. & Tech. (U.S.) Spec. Pub. 756; 1987 October. 369 p.

[6] Stewart, A. F.; Guenther, A. H.; Domann, F. E. The properties of laser annealed dielectric films. Nat. Inst. Stand. & Tech. (U.S.) Spec. Pub. 775; 1988 October. 259 p.

[7] Wang, V.; Rudisill, J. E.; Giuliano, C. R.; Braunstein, M.; Braunstein, A. Pulsed CO_2 laser damage in windows, reflectors and coatings. Nat. Bur. Stand. (U.S.) Spec. Publ. 414; 1974 May. 59 p.

[8] Foltyn, S. R.; Newnam, B. E. Multiple-shot laser damage thresholds of ultraviolet reflectors at 248 and 308 nanometers. Nat. Bur. Stand. (U.S.) Spec. Publ. 620; 1980 September. 265 p.

[9] Swain, J. E.; Stokowski, S. E.; Milam, D.; Kennedy, G. The effect of baking and pulsed laser irradiation on the damage threshold of potassium dihydrogen phosphate crystals. Appl. Phys. Lett. 41 (1982) 12.

[10] Temple, P. A.; Lowdermilk, W. H.; Milam, D. Carbon dioxide laser polishing of fused silica surfaces for increased laser-damage resistance at 1064 nm. Appl. Opt. 21 (1982) 3249.

[11] Morgan, A. J.; Rainer, F.; De Marco, F. P.; Gonzales, R. P.; Kozlowski, M. R.; Staggs, M. C. Expanded damage test facilities at LLNL. Nat. Inst. Stand. & Tech. (U.S.) Spec. Publ.; (Laser Induced Damage in Optical Materials: 1989) - these proceedings.

[12] Sorensen, O. T., ed. Non-stoichiometric oxides, Chapters 1, 2 and 7; Academic Press, New York, 1981.

[13] Rainer, F.; Vercimak, C. L.; Milam, D.; Carniglia, C. K.; Tuttle-Hart, T. Measurements of the dependence of damage thresholds on laser wavelength, pulse duration and film thickness. Nat. Bur. Stand. (U.S.) Spec. Publ.688; 1983 November. 268 p.

[14] Kozlowski, M. R.; Staggs, M. C.; Wolfe, C. R.; Campbell, J. H. Large area laser preconditioning of dielectric thin film mirrors. Nat. Inst. Stand. & Tech. (U.S.) Spec. Publ.; (Laser Induced Damage in Optical Materials: 1989) - these proceedings.

[15] Iscoff, R. Ion assisted deposition. Lasers and Optronics 7 (1988) 53.

[16] McNeil, J. R.; Al-Jumaily, G.; Jungling, K. C.; Barron, A. Properties of TiO_2 and SiO_2 thin films deposited by ion assisted deposition. Appl. Opt. 24 (1985) 490.

[17] Martin, P. J. Review - Ion based methods for optical thin film deposition: Journal of Materials Science 21 (1986) 1.

[18] Allen, T. H. Reactive ion beam sputtered coatings: Society of Vacuum Coaters, Proceedings of the 30th Annual Technical Conference, April 27-May 1, 1987, Boston, MA.

[19] Rancourt, J. D. "Future Prospects", Chapter 7 in Optical Thin Films Users Handbook. Macmillan, New York, 1987.

[20] Rancourt, J. D. Optical Thin Films Users' Handbook, Section 5.1.10 "Measuring Absorption by Calorimetry", p. 153. MacMillan, New York, 1987.

[21] Tam, A. C.; Schroeder, H. Laser induced thermal desorption of moisture from a surface in atmospheric conditions. Appl. Phys. 64 (1988) 3667.

[22] Kovalev, V. I.; Faizullov, F. Influence of adsorbed water on the optical strength of infrared optics elements. Sov. Quant. Elect. 7 (1977) 326.

[23] Brauns, B.; Schafer, D.; Wolf, R.; Zscherpe, G. Effect of the substrate preparation with CO_2 laser radiation on the laser resistance of optical layers. Thin Solid Films 138 (1986) 157.

[24] Voorthuyzen, J. A.; Keskin, K.; Bergveld, P. Investigations of the surface conductivity of silicon dioxide and methods to reduce it. Surface Science 187 (1987) 201.

[25] Macleod, H.A. Thin Film Optical Filters, 2nd Edition, Chap. 11, especially p. 456 "Environmental Resistance"; Chapter 9, especially p. 398, "Factors Affecting Layer Properties", MacMillan, ed., 1986.

[26] Wolfe, C. R.; Campbell, J. H.; Lyon, R. E.; Pitts, J. H.; Powell, H. T. Optical damage in epoxy polymers by millisecond light pulses. Nat. Bur. Stand. (U.S.) Spec. Publ. 752; 1986 September. 194 p.

[27] Edwards, G.; Campbell, J. H.; Wolfe, C. R.; Lindsey, E. F. Damage assessment and possible damage mechanisms to 1-meter diameter Nova turning mirrors. Nat. Inst. Stand. & Tech. (U.S.) Spec. Publ.; (Laser Induced Damage in Optical Materials: 1989) - these proceedings.

[28] Beauchamp, W. T.; Hichawa, B. P.; Innus, M. H. Systematic design approach leads to better optical coatings. Laser Focus/Electro-Optics, 24(5) (1988) 109.

[29] Bloembergen, N. Laser induced electric breakdown in solids. IEEE J. Quantum Electron., QE-10 (1974) 375.

[30] Jones, S. C.; Braunlich, P.; Casper, R.; Shen, Xiao-An; Kelly, P. Recent progress on laser induced modifications and intrinsic bulk damage of wide band-gap optical materials. Opt. Eng. 28 (1989) 1039.

[31] Kerr, N. C.; Clark, S. E.; Emmony, D. C. U.V. seeding of I.R. laser induced damage. Nat. Inst. Stand. & Tech. (U.S.) Spec. Publ.; (Laser Induced Damage in Optical Materials: 1989) - these proceedings.

[32] Schwartz, R. N.; Clark, M. D.; Chamulitrat, W.; Kevan, L. Electron paramagnetic resonance studies of intrinsic bonding defects and impurities in SiO_2 thin solid films: in Defects in Glasses, Mat. Res. Soc. Symp. 61 (1986), 359.

[33] DiMaria, D. J. Defects and impurities in thermal SiO_2: The physics of SiO_2 and its interfaces, Proceedings of the international topical conferences, Pantelides, S. T., ed. Perganon Press 1978, Chapter 4.

[34] Griscom, D. L. Defects in noncrystalline oxides: in Defects and their structure in non-metallic solids, Henderson, B.; Hughes, A. E., eds. Plenum Publishing Co., New York, 1976, p. 323.

[35] Griscom, D. L. Point defects in amorphous SiO_2: What have we learned from 30 years of experimentation?, Materials Res. Soc. Sym. Proc. 61 (1986) 213.

[36] Fuhs, W. Transport properties of amorphous semiconductors, in Physics of structurally disordered solids, Mitra, S. S., ed. Plenum Press, New York, 1976, p. 411.

[37] Stathis, J. H. Identification of native defects in amorphous-SiO_2: in The Physics and Technology of Amorphous SiO_2, Devin, R. ed. Plenum Publ. Co., New York, 1988, p. 141.

[38] Stathis, J. H.; Kastner, M. A. Photoinduced paramagnetic defects in amorphous silicon dioxide. Materials Res. Soc. Sym. Proc., 61 (1986) 161.

[39] Campbell, J. H.; Emmett, J. L.; Brusasco, R. M.; Rainer, F.; Gonzales, R. P.; Morgan, A. J.; Kersten, R. T.; Paquet, V.; Etzkorn, H.-W. Damage resistant optical coatings prepared using high temperature plasma chemical-vapor-deposition. Nat. Inst. Stand. & Tech. (U.S.) Spec. Publ.; (Laser Induced Damage in Optical Materials: 1989) - these proceedings.

[40] Paquet, V.; Etzkorn, H.-W.; Kersten, R. Th.; Emmet, J. L.; Campbell, J. H.; Brusasco, R. M.; Rainer, F. Laser damage resistant coatings by plasma-impulse-CVD: Proceedings of the ECO2, April 24th-28th, 1989; Ninth European Symposium on Optoelectronics, Paris, France.

Manuscript received
3-20-90

Large Area Laser Conditioning of Dielectric Thin Film Mirrors

M.R. Kozlowski, C.R. Wolfe, M.C. Staggs, J.H. Campbell

Lawrence Livermore National Laboratory
University of California
P.O. Box 5508
Livermore CA 94550

The laser conditioning of dielectric thin film HR coatings has been studied as a practical method for the improvement of the damage thresholds of large area (1.1 m dia.) high power 1064 nm laser mirrors on the LLNL 120 kJ, 100 TW Nova laser system. Both HfO_2/SiO_2 and ZrO_2/SiO_2 HR coatings were conditioned by rastering with a small (~0.2 mm) diameter beam from a pulsed (18 Hz, 8 ns) Nd-YAG laser (1064 nm). The samples were rastered at various fluences below the unconditioned damage threshold and subsequently damage tested. Large area conditioning studies were also performed using a large aperture beam of the Nova laser. The laser conditioning effect was found to be permanent. Improvements in damage threshold due to conditioning were as high as a factor of 2.7 and were dependent on the conditioning parameters. A model for the conditioning effect is proposed based on the emptying of electronic defect levels within the bandgap of the dielectric materials.

Key Words: electronic defects; halfnia; HR coatings; laser conditioning; laser damage; silica, zirconia.

1. Introduction

The cost of optical components for high power laser systems, such as those used in fusion energy research, increases dramatically with the size of the optic. In order to keep the power delivered by the laser high while keeping the cost of the system low, high damage threshold optical materials are needed. Presently, increases in the output of the 120 kJ Nova laser system used for inertial confinement fusion research at Lawrence Livermore National Laboratory are limited in part by the damage threshold of the dielectric multilayer turning mirrors. These mirrors have diameters of 96 and 109 cm and are deposited on 16 cm thick BK-7 glass substrates.

Over the last two decades many researchers have reported that the laser damage threshold of both bulk [1-5] and thin film [4-10] optical materials can be increased by first illuminating the material at a sub-threshold fluence. Threshold increases have been observed for photon wavelengths ranging from 10.6 μm [5] to 0.248 μm [6]. This sub-threshold illumination has been referred to as "laser conditioning" or "laser annealing". Increases in damage thresholds by a factor of three are typical but increases as high as a factor of 10 have also been reported [5]. A few studies have attempted to determine which conditioning parameters provide the largest increase in the damage threshold. Arenberg et al. [9] have studied the laser conditioning effect as a function of the conditioning fluence for 1064 nm/532 nm antireflection coatings of undisclosed composition. Laser conditioning at 1064 nm increased the 1064 nm damage threshold by 40% but did not influence the 532 nm threshold. The probability of damage occurring at fluences slightly above the unconditioned damage threshold was found to decrease as the conditioning fluence approached the unconditioned damage threshold. The conditioning effect in Arenberg's study was also found to last only 4-5 days. The 532 nm damage threshold was not influenced by conditioning at either 532 nm or

*Work performed under the auspices of the U.S. Department of Energy by Lawrence Livermore National Laboratory under contract number W-7405-ENG-48.

1064 nm. The authors suggested that the conditioning effect was due to removal of water from the films. Stewart et al. [8] have studied the effect of rastering single layer dielectric films with a CW CO_2 laser. For fluences ranging from 25 W/cm^2 to 100 W/cm^2 they observed indications, from both optical and structural measurements, of recrystallization of the dielectric materials. They reported a correlation between the crystallization and a small (< 40%) increase in the damage threshold for thin films of rf-sputtered Ta_2O_5 and sol-gel TiO_2. Areas conditioned in these earlier studies were typically the size of the damage test laser beam, no larger than a few mm in diameter. To our knowledge, the only direct test of the practicallity of laser conditioning large area optical materials was a study of KDP crystals [3]. It was shown that the 1064 nm damage threshold of KDP could be increased by rastering a large area of the crystal with a small area beam from a rep-rated laser. The conditioning effect was observed for sub-threshold fluences of either 1064 or 350 nm light. In contrast to Arenberg's AR coatings, the conditioning effect on KDP has been shown to be permanent over more than a month [2]. Clearly the laser conditioning phenomena is complex and generalizations must be made carefully.

This paper presents the preliminary results of a study to determine how the laser conditioning effect could be used to increase the damage threshold of the Nova turning mirrors. Laser conditioning of 1064 nm dielectric high reflective coatings was first reported by Wilder and Thomas [10]. In a companion paper in the present volume, Wolfe et al. [11] has reported on the influence of materials and coating design on the increase in the laser damage threshold due to laser conditioning. Here we concentrate on large area conditioning studies on two types of HR coatings: a) the present Nova mirrors: ZrO_2/SiO_2 reflectors designed for 1064, 532, and 355 nm light, and b) R&D HfO_2/SiO_2 reflectors designed for 1064 nm light. Both coatings were deposited by OCLI* using electron beam deposition in a 3-m diameter planetary coater. This production coater is designed to handle up to three 1-m diameter substrates and was purchased and installed by LLNL during the construction of the Nova laser. The ZrO_2/SiO_2 coatings were made in 1983 while the HfO_2/SiO_2 coatings were made in 1989. The two principal large area conditioning methods examined were i) rastering a small area beam back and forth across the sample surface, and ii) illuminating a large area optic using a large aperture laser beam such as that available on the Nova laser. Laser conditioning parameters examined included the illumination fluence and the number of illumination pulses. We also performed preliminary conditioning tests using broadband flashlamps.

Several mechanisms have been proposed in the literature to explain the conditioning phenomenon observed for bulk materials, surfaces, and thin films. These mechanisms include the desorption of water or other contaminants from the surface [7,9], melting or recrystallization of structural defects [8], and the slow volatilization of absorbing inclusions from within the films [10]. Wolfe et al. [11] has experimentally demonstrated that for the HR coatings of interest here the first two of these mechanisms do not seem to apply. Edwards et al. [12] has similarly presented arguments against the applicability of the absorbing inclusion model to damage in the Nova mirrors of interest here. We instead propose that the conditioning effect in the dielectric HR coatings is related to the emptying of electronic defect states in the bandgap. These electronic defects serve as the source of conduction band electrons required to produce damage in the dielectric layers. We will discuss this damage/conditioning mechanism in detail in Section 6.

2. Standard damage testing of present and R&D Nova mirror coatings:

All damage tests were made using a 1064 nm Nd:YAG laser with a beam diameter of 0.2 mm at 80% of the peak fluence. The pulse length was 8 ns and the repetition rate was 18 Hz. The damage threshold was chosen as the lowest fluence which caused a light flash at the coating surface and a visible change in the oxide surface properties, as determined by the sensitive "breath test" [13]. The breath test relies on water vapor condensation patterns to identify damage areas. The damage thresholds obtained in this way are in good agreement with those obtained using x100 Nomarski microscopy. Two types of damage tests were performed using the 18 Hz laser:

S-on-1: multiple shots of the same fluence at a single site.

R-on-1: multiple shots of increasing (ramped) fluence at a single site.

For the R-on-1 tests the laser fluence was increased at ~0.2 J/sec until damage was observed. This rate corresponds to a fluence increment per shot of ~0.013 J/cm^2. For S-on-1 tests the samples were illuminated for about 30 seconds (~530 shots) unless damage was observed, in which case illumination was stopped immediately. In nearly all S-on-1 tests where damage was observed it occurred during the first couple of pulses. The damage threshold values reported are ±15%. Each reported threshold represents the average of 1 to 4 tests.

---

*Optical Coatings Laboratories Inc., Santa Rosa, Ca

S-on-1 damage tests showed that the two HR coatings studied had similar thresholds (fig. 1). The thresholds at 8 ns were 12 J/cm² for the present Nova coating and 16 J/cm² for the R&D coating. These values are essentially the same given the accuracy of the measurement. The R-on-1 tests, however, produced quite different results for the two coatings. For the present Nova coatings the R-on-1 threshold was 18.5 J/cm², a factor of 1.5 increase over the S-on-1 (i.e. unconditioned) threshold. For the new coatings the R-on-1 threshold was 44 J/cm², corresponding to a factor of 2.7 increase in the damage threshold. In most cases the damage in these coatings is observed to occur at microscopic (< 50 μm) defects in the coatings. (The 8 ns R-on-1 and S-on-1 thresholds reported here for the R&D coatings agree well with values of 16 (S-on-1) and 37 (R-on-1) J/cm² predicted from data obtained at different pulse lengths on other LLNL damage test systems [11]).

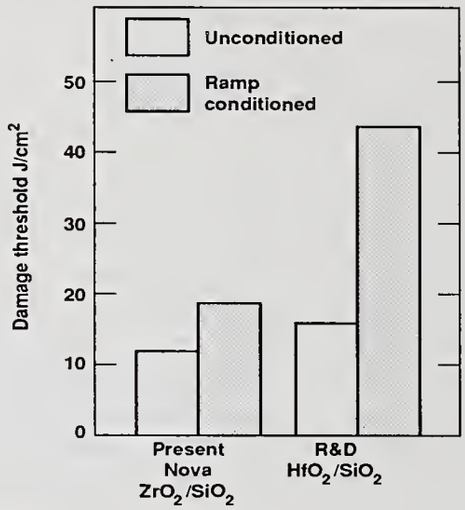

Figure 1: Unconditioned and ramp conditioned 1064 nm damage thresholds (18 Hz, τ_p=8ns) of Nova ZrO_2/SiO_2 and R&D HfO_2/SiO_2 HR coatings. Conditioning performed using damage test laser.

The R-on-1 tests clearly showed that laser conditioning had a larger effect on the R&D coatings than on the present Nova coatings. There are three major differences between the R&D and current Nova HR coatings that may cause the differences in their damage performance: i) change of high index material (HfO_2 vs. ZrO_2), ii) change of high reflectivity design wavelength, and iii) decreases in the size, density, and perhaps type of film defects due to advances in coating technology since the present Nova coatings were made. Damage measurements on R&D HfO_2/SiO_2 and ZrO_2/SiO_2 of various designs indicate that the material or design dependence of the conditioning effect is small [11]. Therefore we conclude that items (i) and (ii) above have a negligible effect on the conditioning of the films used in this study. This leaves item (iii), differences in defects, as the likely explanation for the conditioning effect differences. This also agrees with our observation that damage in both films (R&D and Nova) typically originate at the site of visible defects.

Measurements were made of the film defect sizes using dark field, bright field, and Nomarski microscopy. All three techniques showed that the defects in the R&D coatings were smaller than those in the Nova coatings: nominally 5 to 10 μm vs. 10 to 30 μm, respectively. The R&D coatings also had a slightly lower defect density (about 30 to 80 per mm²) compared to the current Nova coatings (about 100 per mm²). It is unlikely that these modest changes in size or areal density of the defects, per se, influences the damage threshold. Rather, these differences probably indicate different types of defects, with one type of defect being more susceptible to conditioning than the other.

Differences in the performance of the two coatings is also indicated by the dependence of their damage threshold on laser pulse length. For the present Nova mirrors no pulse length dependence is observed [14]. For the HfO_2/SiO_2 R&D coatings, however, the damage threshold, D_T (J/cm²) is dependent on the pulse length, τ_p(ns) as [11]

$$D_T = 7.1\ \tau_p^{0.355}. \qquad (1)$$

The differences in the pulse length dependence and the extent of threshold enhancement due to conditioning for the two coatings may indicate a change in the laser damage mechanism. It should be emphasized that without conditioning the damage thresholds of the two films studied are approximately the same at 8 ns. The threshold improvements for the R&D coating is apparent only after conditioning.

3. Large Area Conditioning via Raster-scanning:

In the R-on-1 tests described above an area only the size of the test beam (~0.2 mm) was conditioned. We are interested, however, in laser conditioning coatings the size of the Nova mirrors (1.1 m), therefore other, more practical, methods of laser preconditioning were studied. Here we present the results of conditioning studies performed by rastering a large coating surface with a small area beam (~0.2 mm) at laser fluences below the S-on-1 damage threshold. The rastering was done using the damage test laser and a programmable x-y stage. The x-y stage velocity was chosen such that the sample was shot every 0.1 mm in both the x and y directions. This scan rate corresponds to four shots/site for a 0.2 mm diameter beam. Areas of ~4 cm² were rastered with various fluences below the S-on-1 damage thresholds of both coatings. Four types of pre-conditioning programs were examined in this study:

a) raster at 10% of the S-on-1 threshold

b) raster at 63% or 55% of the S-on-1 threshold

c) raster at 85% of the S-on-1 threshold

d) consecutive rasterings at five fluences increasing from 37 to 85% of the S-on-1 damage threshold (hereafter referred to as "step conditioning").

These conditioning programs, along with that for ramp conditioning, are shown graphically in fig. 2. For the 5-step conditioning the time between individual illuminations was approximately 1 hr. This is in contrast to the ramp conditioning where the time between shots is ~0.1 s. Note also that the increment in fluence between shots in the ramp is only ~0.05% of the S-on-1 damage threshold.

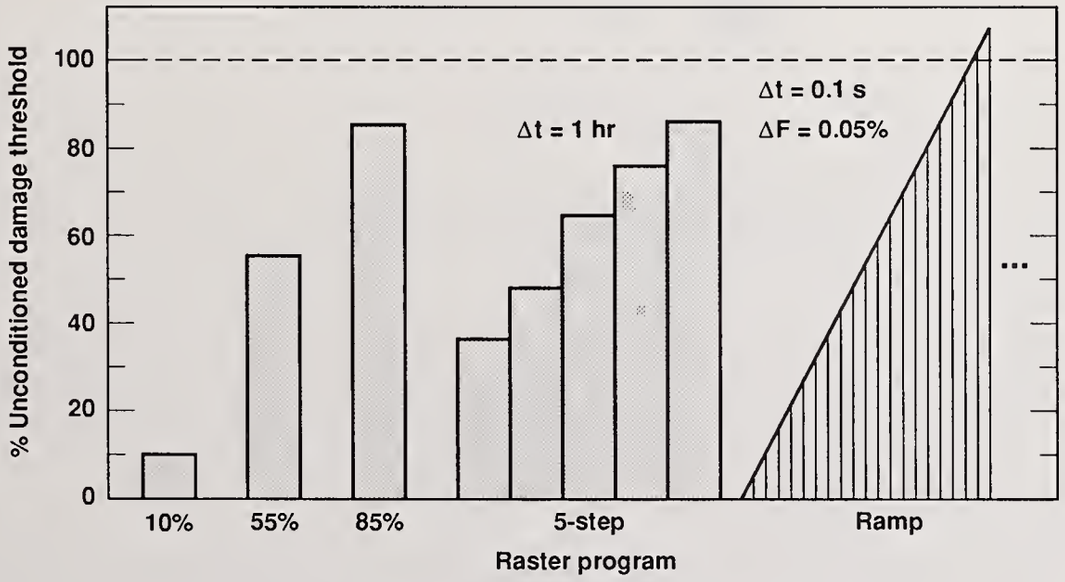

Figure 2: Laser conditioning program used in raster conditioning and ramp conditioning experiments.

For both the R&D and present Nova coatings, single or multiple fluence raster conditioning resulted in an increase in the S-on-1 threshold. The average damage thresholds measured for the different conditioning programs are shown in fig. 3. Conditioning increased the damage threshold of the present Nova mirror by a factor of 1.2 to 1.3. For the R&D coatings, however, conditioning increased the threshold by a factor of 1.2 to 2.4. It is not clear at this time which type of raster conditioning program would provide the largest increase in the damage threshold. It appears, however, that no clear advantage is gained by step conditioning. The most important conclusion reached was that for both coatings all raster conditioning programs resulted in conditioning factors less than that obtained by the ramped fluence technique (i.e. R-on-1).

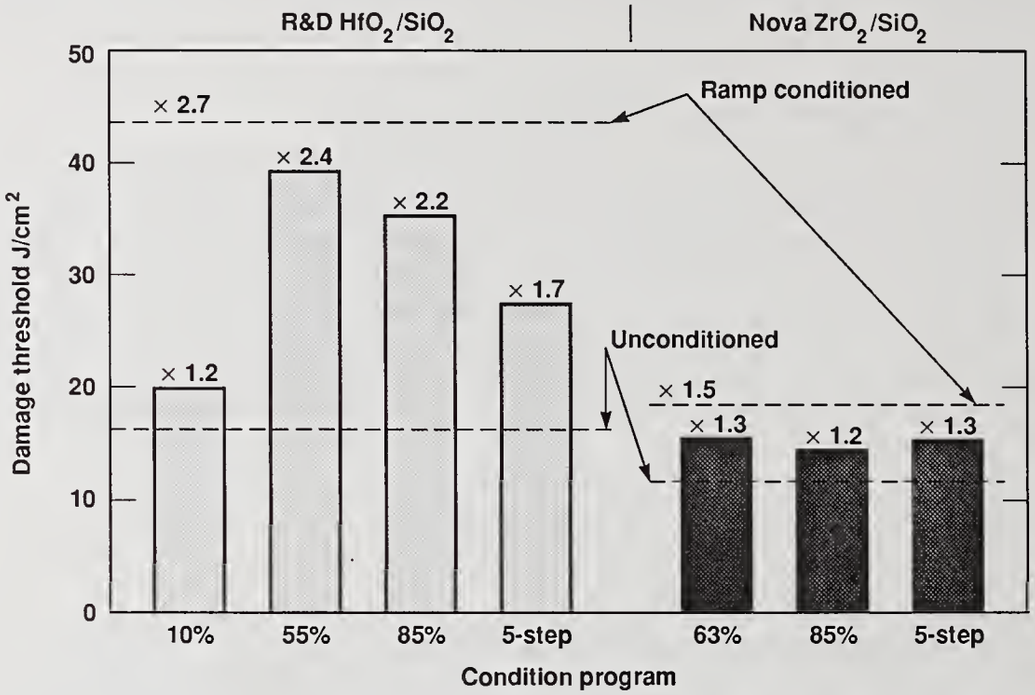

Figure 3: Conditioned 1064 nm damage thresholds (18 Hz, τ_p= 8ns) of Nova ZrO_2/SiO_2 and R&D HfO_2/SiO_2 HR coatings for various raster conditioning programs. Unconditioned and conditioned thresholds are included for reference.

In all tests we defined the damage threshold as the lowest fluence at which damage occurred. Below that threshold we assume that there is zero probability of damage. As the fluence is increased above the threshold the probability of damage increases until a fluence is reached at which any location would damage. We observed that the range of fluences over which the damage probability changed from 0% to 100% was dependent on the conditioning history of the sample. For S-on-1 thresholds the 0-100% damage probability transition range was ~10 J/cm2, while for the R-on-1 tests the range was > 40J/cm². For raster conditioned samples the range was intermediate between the S-on-1 and R-on-1 cases. The change in the abruptness of the damage threshold indicates that the film properties which control the damage threshold after conditioning are not uniform across the sample. It should be noted that since the damage threshold is not abrupt for the conditioned samples, the choice of the lowest damage fluence as the reported damage threshold results in a conservative value for the conditioned damage threshold. In some areas R-on-1 testing increased the damage threshold by more than a factor of four.

4. Large Aperture Nova Conditioning

Using the beam size and raster rate used above, it would take nearly two months to raster a 109 cm diameter mirror. Obviously a more practical large area conditioning technique is required. We therefore next examined the effectiveness of using a large aperture beam from the Nova laser (1ns, 1064 nm) for the conditioning illumination.

If this method is effective, Nova mirrors can be conditioned in-situ. Two 5-cm samples were examined in this study: a HfO_2/SiO_2 1064 nm HR and a ZrO_2/SiO_2 1064 nm HR. It has been shown that the 1-on-1 (single pulse at a given site) damage thresholds for these two coatings at 1064 nm are both ~7 J/cm² at 1 ns [11]. During testing the coating samples were mounted down line from a condensing lens which focussed a mid-chain Nova beam down to a 4 cm-diameter spot. Shot energies were measured using a calorimeter and the beam profile was recorded on film. Densitometer traces of the developed film were used to measure beam modulation and the average fluence. After each shot the sample was removed from the holder and visually inspected under a microscope at magnifications up to 40X using bright-light illumination. The whole coating surface was also photographed for macroscopic changes using a 35-mm close-up camera. At the completion of inspection, the sample was drag-wipe-cleaned using methanol and remounted in the test system. A fiducial mark was used to insure the sample alignment remained the same from one shot to the next. At the completion of the tests on Nova, the samples were again photographed at magnifications up to 400X using both Nomarski and bright and dark field illumination.

A total of seven laser shots were fired at the HfO_2/SiO_2 and one at the ZrO_2/SiO_2 coating. Figure 4 shows the illumination history in terms of the average fluence for each shot and fig. 5 shows a typical fluence profile for the Nova beam. Note that the peak-to average modulation of the beam intensity is about 1.3-to-1. In the case of the HfO_2/SiO_2 coating, we slowly increased the laser fluence from a value of about 3.5 J/cm² up to about 12 J/cm²; 12 J/cm² is about 1.5 to 2 times the 1-on-1 damage threshold. Microscopic and large area inspection of the HfO_2/SiO_2 coating after each shot showed no change. Furthermore, the "breath-test" also showed no change in the sample. The final Nova shot was fired on the ZrO_2/SiO_2 coating. This single shot, having a mean fluence of about 10.6 J/cm² was significantly above the single-shot damage threshold (7 J/cm²). As expected, the sample damaged; this was clearly seen by both our microscopic inspection and the "breath-test". These Nova test results show that large area optics can be conditioned using the Nova laser beam.

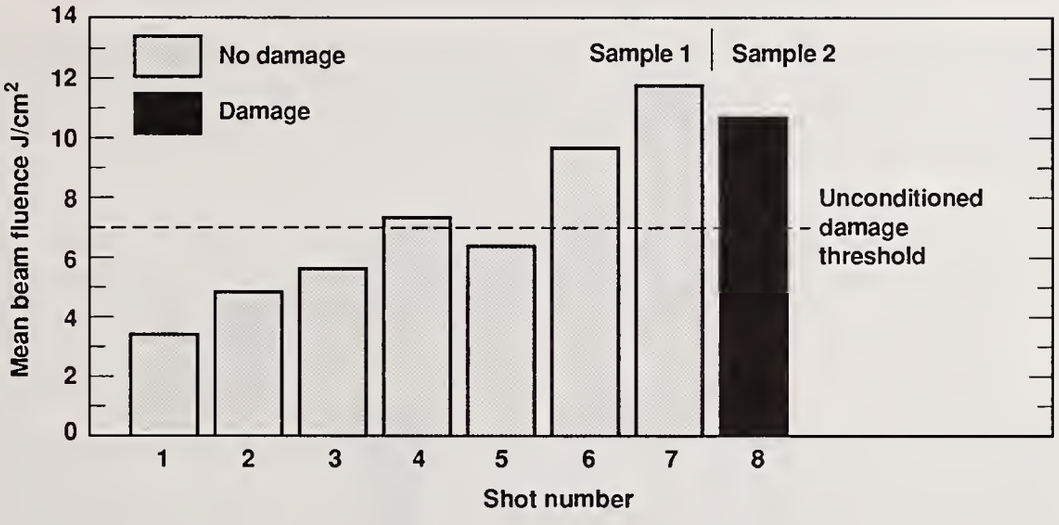

Figure 4: Beam fluence vs. shot number for large aperture Nova conditioning experiment. λ=1064nm, τ_p= 1 ns.

Previous small-area damage tests had shown that the conditioned damage threshold for the HfO_2/SiO_2 coating should be about 18-20 J/cm² (at 1-ns) vs. an unconditioned (1-on-1) threshold of 6-8 J/cm². We decided not to test the HfO_2/SiO_2 sample on Nova above about 12 J/cm². This was for two reasons: first, it provided us with a conditioned, yet undamaged large area sample that could subsequently be tested to determine if the conditioning effect was permanent. Second, because of beam modulation the peak fluence seen by the test sample may have been as much as 1.3-times the mean fluence. Thus at a fluence of 12 J/cm², some regions for the sample could be subjected to fluences near the maximum damage threshold expected from conditioning.

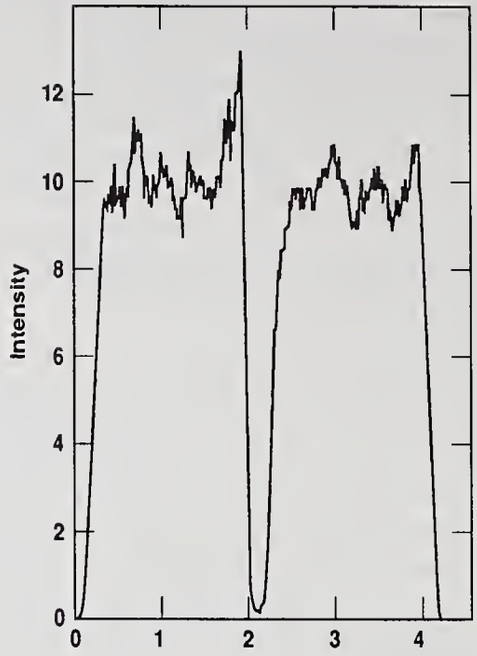

Figure 5: Example of typical Nova arm-9 beam profile showing degree of modulation. The split down middle of beam is due to an apodizer.

In order to compare the damage thresholds obtained by Nova and raster conditioning we damage tested, at 8 ns, the Nova conditioned sample. Figure 6 shows that the Nova conditioned sample has a damage threshold in the range obtained by raster conditioning. Note once again that all the large-area conditioned thresholds are lower than that obtained by ramp conditioning.

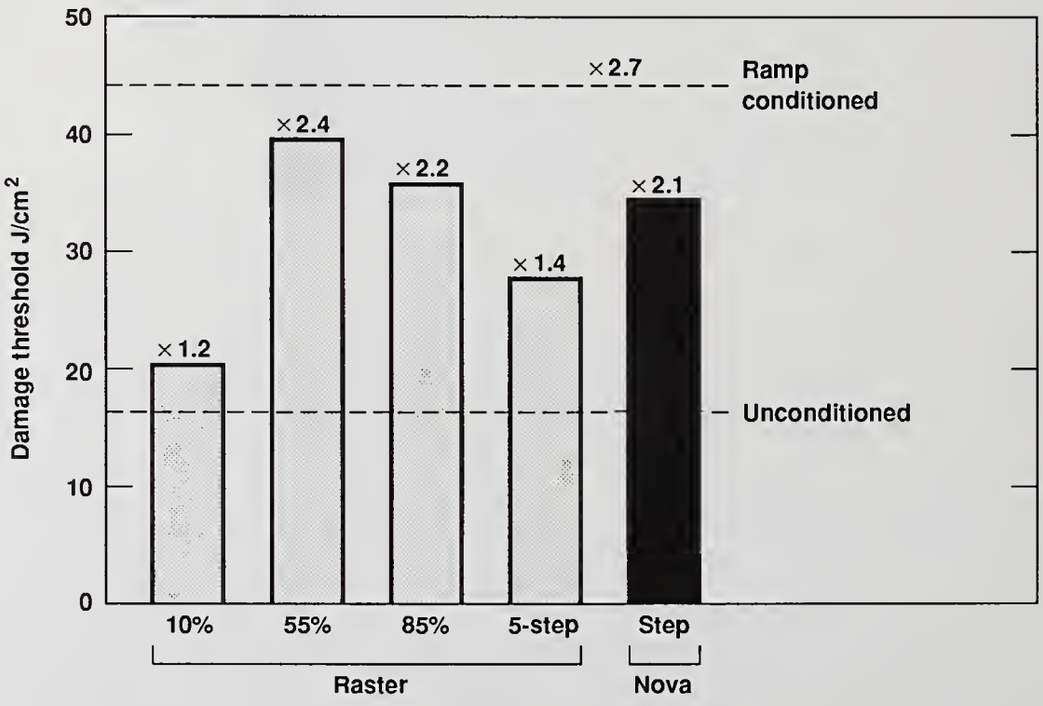

Figure 6: 1064 nm damage thresholds (18 Hz, τ_p=8ns) of R&D HfO_2/SiO_2 HR coatings conditioned by raster scanning and large aperture Nova illumination.

The HfO_2/SiO_2 coating that was conditioned on Nova was further damage tested to determine if the effect was permanent. These damage tests were done at 1064 nm and 10 ns; the results are shown in fig. 7. Tests conducted over a period of about 10 weeks showed no drop in the conditioned damage threshold.

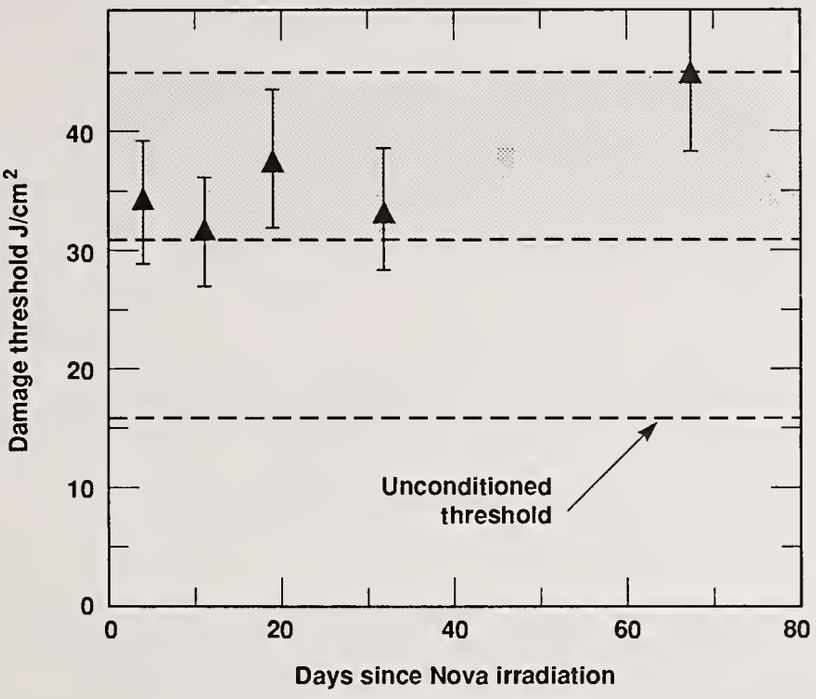

Figure 7: 1064 nm damage thresholds (τ_p = 10 ns) vs. time after conditioning for the R&D HfO_2/SiO_2 HR coatings illuminated on Nova.

Independent conditioning tests performed by Floch (at Commissariat a l'Energie Atomique, France) using HfO_2/SiO_2 coatings prepared by Matra (France) showed no change in damage threshold for up to six weeks [15]. Damage threshold improvements of a factor of 2-3 were observed in the French study.

5. Flashlamp Conditioning Experiments

Besides the raster and Nova conditioning methods, we also attempted to condition the thin film dielectrics by broadband flashlamp illumination. Broadband illumination is commonly used to decompose or outgas contaminants from vacuum systems. Similarly, we intended this process to remove organic contaminants from our thin films. The flashlamp study consisted of illuminating a HfO_2/SiO_2 HR sample with 20 flashes of a Xenon arc lamp. The illumination intensity was about 10 J/cm² for each shot and the pulse length was 0.5 ms. The spectral output of the lamp is given in fig. 8. Subsequent S-on-1 damage tests to the sample showed that flashlamp illumination did not change the damage threshold of the HR coatings. Two obvious differences between the flashlamp and the laser illumination are the range of photon wavelengths involved and the magnitude of the electric field produced in the sample. The long pulse length of the flashlamp results in a low electric field since

$$E=[2\ F_L/\ \tau_p\ n\ y]^{0.5} \qquad (2)$$

where E is the electric field (V/cm), F_L is the fluence (J/cm²), τ_p is the pulse length (sec.), n is the refractive index (1.45 for SiO_2), and y is the admittance in free space (2.66×10^{-3} F/s). For F_L=10 J/cm² and τ= 5×10^{-4} sec., the electric field is 3×10^3 V/cm. This field is less than 1% of the field associated with an 8 ns laser pulse of the same fluence. Possible connections between illumination wavelength, electric field, and the conditioning effect are discussed in Section 6.

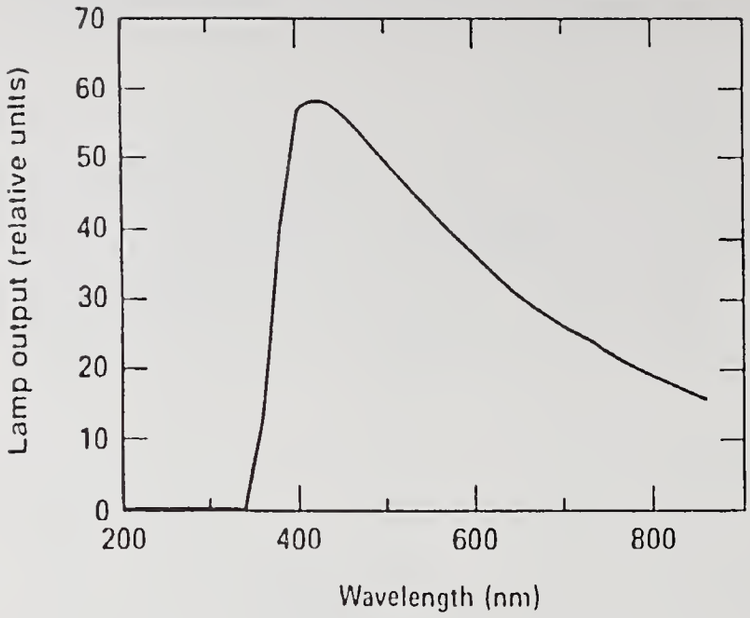

Figure 8: Time integrated Xe flashlamp output spectra [36]. Outut below 350 nm is suppressed by Ce dopant contained in the flashlamp envelope.

6. Electron Defect Model

Several different mechanisms for laser conditioning have been suggested in the literature (film crystallization, water desorption, etc.). Different mechanisms may apply for different combinations of materials, deposition methods, illumination wavelength, etc.. A complete review of the conditioning mechanism literature is outside the scope of this text. We are interested here primarily in the laser conditioning of 1064 nm dielectric HR films of HfO_2/ SiO_2 deposited by e-beam evaporation.

We are presently examining a possible mechanism for laser induced optical damage in which conduction band electrons are heated by interaction with the laser beam and subsequently transfer energy to the crystal lattice. Damage occurs when the film temperature reaches some critical value such as the melting point of the dielectric material. There are two conditions that must be met for film damage to occur: (i) electrons must be available in the conduction band, and (ii) the laser intensity must be high enough to transfer sufficient energy to the lattice to cause damage. We propose that the source of conduction band electrons is the photo-excitation of electrons from shallow defect levels located below the conduction band edge. We further propose that laser conditioning occurs due to the removal of this source of conduction band electrons. When the dielectric material is illuminated at a low fluence, the electrons in the defect levels are excited to the conduction band. Since the optical electric field is not large enough to cause damage the electrons decay into deep levels from which they cannot be easily excited into the conduction band on subsequent illuminations. A diagram of the proposed band structure for the unconditioned and conditioned dielectrics are shown in fig. 9. When the 'conditioned' dielectric is subsequently illuminated at intensities above the unconditioned damage threshold, the number of electrons available for transfer to the conduction band is low and, therefore, the net energy transfered to the lattice is too low to cause damage. This increase in the damage threshold is the observed laser conditioning effect.

The importance of conduction band electrons to optical damage to bulk dielectric samples has been demonstrated by other investigators. Jones et al. [16] have shown that no heating of a-SiO_2 occurred by 1064 nm illumination unless the sample was simultaneously illuminated with 266 nm light. The 266 nm light provided

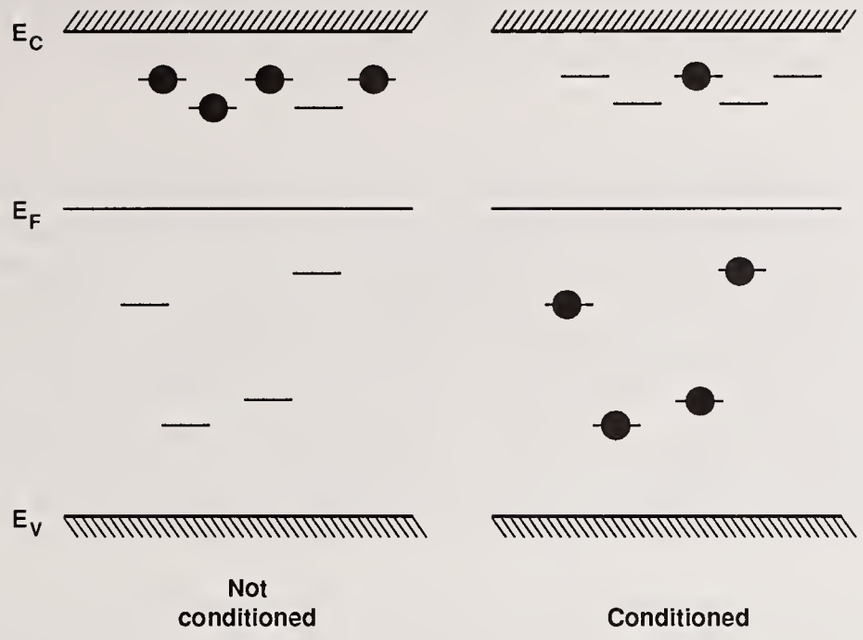

Figure 9: Schematic energy band diagram of the location of electrons (•) in traps (-) for unconditioned and laser conditioned dielectric films.

conduction band electrons by multiphoton excitation from the valance band. Once these electrons were present in the conduction band, they could be heated by the 1064 nm photons (i.e. free carrier absorption). Similarly, Kerr et al. [17] has shown that the 10.6 μm damage threshold for silicon and glass is decreased by simultaneous illumination by UV light. Also, Soileau et al. [18] has shown that the damage threshold of bulk fused SiO_2 can be decreased by inducing electronic defects in the material by gamma irradiation. These defect levels serve as a source of conduction band electrons leading to laser damage. In that study the electrons were excited to the conduction band by two photon absorption of 532 nm photons. In the following paragraphs we consider the nature of the defect levels in the HR films of interest to Nova and discuss the mechanisms by which energy is transferred from the laser pulse to the lattice via the conduction band electrons.

6.1. Free carrier generation

Assuming a one photon (1064 nm) excitation process, the defect states contributing electrons to the conduction band of our dielectric films could be up to 1.2 eV below the band edge. In the presence of the large optical electric field (~10^6 V/cm^2) produced by the laser pulse, activation barrier lowering associated with the Poole-Frenkel effect may occur however [19]. The magnitude the the barrier lowering, ΔE_b (eV), is given by

$$\Delta E_b = [e^3E/\pi\varepsilon_o\varepsilon]^{1/2} \qquad (3)$$

where E is the magnitude of the electric field (V/cm), e is the charge on an electron, and ε is the dielectric constant, and ε_o is the permitivity of vacuum (F/cm). The resulting decrease in the activation energy of the trap-to-conduction band transition would be as much as 0.6 eV for the materials of interest here. The Poole-Frenkel effect would therefore allow a 1064 nm photon to excite electrons from states nearly 2 eV below the conduction band edge.

Electron paramagnetic resonance has been used to demonstrate that occupied defect levels may be present between the Fermi level and conduction band in amorphous SiO_2 [20]. If the defect levels are occupied by only one electron they are paramagnetic and produce an EPR signal. Stathis et al. [21] has shown that these defect levels in high quality a-SiO_2 are normally empty but can be filled by illumination with UV photons. One particular type of

defect, generally associated with a peroxide radical, can be made paramagnetic by illumination with 7.6 eV photons. If the electrons excited into the defects by the 7.6 eV photons come from the valance band, these defect levels must be about 1-2 eV below the conduction band of the ~ 9 eV bandgap SiO_2. It should therefore be possible to excite the electrons from these paramagnetic states into the conduction band by the absorption of a single 1064 nm photon (1.2 eV).

In its most stable state high purity a-SiO_2 should not have any occupied electronic levels above the Fermi level. Occupied states can be induced in this material by UV, x-ray, or charged particle irradiation. Schwartz et al. [22] has shown, however, that paramagnetic bonding defects are present in some as-deposited thin film SiO_2. Since e-beam and rf-sputter deposition techniques are accompanied by soft x-rays and energetic particles, electrons and holes can be generated during deposition. These charge carriers could then become trapped at appropriate precursor sites resulting in the formation of paramagnetic point defects. For techniques such as hot wall low pressure chemical vapor deposition (LPCVD) and plasma enhanced chemical vapor deposition (PECVD), which do not have attendant soft x-rays or energetic particles, no paramagnetic states are observed. Cold wall LPCVD, which produces non-equilibrium films, have paramagnetic states but they can be annealed out by heating the samples to 300°C. Optical absorption measurements on rf-sputtered films of SiO_2 have also shown that the electronic properties of thin films are dependent on deposition parameters [23]. Paramagnetic defect densities on the order of $10^{16}/cm^2$ have been measured [21].

It has often been suggested that damage in dielectric multilayers occurs first in the high index material. Studies of single layer materials have shown that the damage threshold of HfO_2 and ZrO_2 are typically below that of SiO_2[24]. Unfortunately there is little information available in the literature regarding defect levels in HfO_2 and ZrO_2. It has been shown, however, that structural defects produced by ion implantation can reduce the bandgap of HfO_2 by as much as 2 eV [25]. In general, the electronic band structure of materials are more sensitive to long range structural disorder the smaller their bandgap [26]. Therefore the electronic properties of HfO_2 and ZrO_2 are more likely to be influenced by structural defects than those of SiO_2. For the HfO_2/SiO_2 films studied here, x-ray diffraction studies have shown that the SiO_2 layer is amorphous. The HfO_2 layer, however, is amorphous at the SiO_2 surface but as the HfO_2 layer thickens, oxide with a predominantly monoclinic structure is produced [27]. This same type of structural transition has been reported for thin films of ZrO_2 [28].

The model presented here assumes that charged defects are the primary source of conduction band electrons in the dielectric films. There are, however, four other sources of conduction electrons which we must consider:

1. Thermal detrapping from shallow levels in the dielectric. Since the large bandgap insulators of interest have very low conductivities, this source of electrons is unlikely.

2. Multiphoton absorption by valance band electrons. For the 1064 nm irradiation 5 photons would be needed for ionization in HfO_2 and 8 photons would be required for SiO_2. It has been suggested in the literature that multiphoton ionization is unlikely for n>4 [16]. Photoacoustic measurements by Jones et al.[16] have indicated that no multiphoton ionization occurs in high purity a-SiO_2 for 1064 nm photons. Three photon absorption is observed however for 266 nm light. The number of photons required for multiphoton absorption in SiO_2 and HfO_2 given above are based on the bandgaps of the near perfect crystalline materials. These bandgaps are 9.0 eV and 5.1 eV, respectively. For highly defective thin films, however, bandgaps several eV lower have been measured for both HfO_2 [25] and SiO_2 [23]. For these lower bandgap films multiphoton processes may become more significant. Photoacoustic measurements are planned which will determine if multiphoton absorption is important at 1064 nm for the e-beam films of interest here.

3. Electron-impact ionization and subsequent avalanche formation. Recent photoacoustic measurements [16] indicate that avalanche ionization does not occur in KBr, NaCl, KI, or a-SiO_2. Furthermore, experimental and computer modeling studies by DiMaria et al. [29,30] have shown that the distribution of energies of conduction electrons in SiO_2 is not high enough to allow impact ionization to occur. No comparable measurements have yet been reported on HfO_2 or ZrO_2, however.

4. Electrons produced by laser induced defect formation (i.e. F-centers). It is believed that if F-centers were produced by the laser pulse illumination, an accumulation effect would be apparent, i.e. single shot damage thresholds would be higher than multiple shot thresholds [16]. Such an accumulation effect has not been observed for the dielectric stacks of interest here, but has been observed in sol-gel processed TiO_2 coatings [31].

Based on the available literature, it therefore seems likely that laser damage in our dielectric materials is associated with conduction band electrons and that the source of these electrons is shallow defect levels.

6.2.. Energy transfer

There are three commonly discussed mechanisms for transfer of energy between the laser beam and the crystal lattice of a dielectric material. In the classic electron-avalanche model of Bloembergen and Yablanovitch [32], the lattice heating mechanism was taken from the Drude model for AC conductivity in metals [33]. In the Drude model, electrons are accelerated by the optical electric field and then lose energy to the lattice by electron-phonon interaction (i.e. Joule heating). The other two mechanisms for lattice heating: (a) free-electron heating and (b) polaron heating, involve the direct absorption of photons and subsequent transfer of energy to the lattice by electron-phonon interactions. Free electron heating is more likely for the ionic materials and the short wavelengths of interest here [16]. The three mechanisms can be experimentally differentiated by the relationship between the energy absorbed and the laser pulse energy. For example, the energy absorbed by the free-electron model has a non-linear dependence on pulse energy while for the polaron mechanism the dependence is linear. Jones et al. [16] have shown that for SiO_2, and for many alkali-halides, lattice heating occurs by the electron-heating mechanism.

7. Discussion of Results

The laser conditioning experiments reported here demonstrated that the damage thresholds of the dielectric multilayer stacks could be increased as a result of as few as one subthreshold illumination pulse. Based on the simple laser conditioning mechanism discussed above, it might be expected that the effect of conditioning should increase with fluence or number of pulses until the cumulative photon flux has removed all the electrons from the defect levels near the conduction band. Further illumination should have little effect. Some of our data suggests this picture is correct whereas other results suggest that the conditioning mechanism is more complex than this. Clearly more data is required in order to understand the relationship between the conditioning program and the increase in the damage threshold fluence.

We have observed that damage in the dielectric stacks tends to occur at the sites of film defects visible by Nomarski microscopy. The defect driven damage is likely the result of either of two mechanisms: (i) the defects are regions of high concentrations of occupied defect levels which serve as the source of conduction band electrons, or (ii) the defect areas are regions of enhanced electric fields, as described by Bloembergen [34], and therefore allow damage to occur at lower fluences than that of a perfect material.

An interesting observation reported by Wolfe et al. [11] is that the pulse length dependence of the damage threshold for both unconditioned and ramp conditioned materials are the same. The thresholds are proportioned to τ_p^x where x is approximately 0.3. This result may suggest that the damage mechanism remains the same after conditioning.

Our attempts to condition the HR films by flash lamp illumination were not successful. There are three possible explanations for this lack of a damage threshold increase. The first explanation is related to the broadband nature of the flashlamp. The optical film is simultaneously being irradiated with both UV and IR irradiation. Stathis [35] has shown that paramagnetic states can be generated by UV illumination. The UV photon may therefore counter the emptying effect of the IR illumination. The second explanation is related to the low electric field produced by the long pulse length (~1 ms) flashlamp output The field produced by the flashlamp is a factor of 10^3 lower than that of the 8 ns laser pulses. If barrier lowering by the Poole-Frenkel mechanism is required for the excitation of trapped electrons, then the flashlamp illumination would not result in a conditioning effect. Third, the flashlamp output produces a much lower energy density over a given wavelength interval than does a laser. Consequently, if the absorption cross section associated with the conditioning process is small (and wavelength specific) then the effect of the flashlamp would be expected to be negligible. In addtion, flashlamp illumination has also been shown not to alter the damage threshold of laser conditionable KDP [2].

It may be possible to empty the paramagnetic defects by thermal excitation as well as optical excitation.

Several paramagnetic states in a SiO_2 can be emptied by thermal treatments at temperatures below 700°C [35]. No information is available on thermal detrapping from states in HfO_2. For dielectric multilayers thermal conditioning is limited by thermal stress build up and may not be practical for thin films prepared by physical vapor deposition methods.

8. Conclusions

The damage threshold of HfO_2/SiO_2 high reflection coatings can be increased by a factor of about 2.7 by ramped-fluence laser conditioning (i.e. R-on-1 damage tests). This laser conditioning effect can be used to permanently increase the damage threshold of large area optics. Large areas were conditioned by either rastering a surface with a small beam or by illumination with a large aperture beam such as that available on the Nova laser. In order to be practical, these large area conditioning methods require illumination in fairly large incremental steps in laser fluence. Such discrete illumination techniques produced smaller increases in damage threshold than can be obtained by the small step, ramped-fluence techniques. Increases of a factor of about 2 can be expected for discrete step, large area conditioning. Further study is needed to determine the optimum discrete fluence illumination program. In the case of practical conditioning of Nova turning mirrors, the large aperture conditioning procedure is the most attractive since the mirrors can be conditioned in-situ on Nova. In contrast, raster conditioning of a 1.1 m diameter mirror with the damage test beam would take several weeks and a dedicated facility.

The mechanism proposed here for the laser conditioning phenomenon is based on the presence of sub-bandgap electronic defect levels that are intrinsic to the e-beam deposition process. This is in contrast to extrinsic mechanisms, such as absorbing inclusions and water contamination, that have been suggested in the past. The move toward intrinsic mechanisms may indicate that thin film processing techniques have improved over the years, as should be expected. We are currently involved in using the EPR technique to identify the electronic defects that are present in the dielectric films and to determine if the charge state of the defects are altered by the sub-threshold conditioning illumination. If the electronic defect model is correct, further improvements in film properties might be gained by using deposition techniques that are more "equilibrated" (in a structural or electronic sense). Plasma-assisted CVD is one such possible coating method.

References:

1. B. Newnam, A. Nowak, and D. Gill, " Short pulse CO_2-laser damage studies of NaCl and KCl windows",Laser Induced Damage in Optical Materials: 1979, NBS Spec. Pub. 620, p. 209.

2. J. Swain, S. Stokowski, D. Milam, and G. Kennedy, The effect of baking and pulsed laser irradiation on the damage threshold of potassium dihydrogen phosphate crystals", Appl. Phys. Lett. 41 (1982) 12.

3. R. Gonzales, M. Staggs, M. Singleton, D. George, C. Weinzapfel, S. Weinzapfel, "Variations with laser pulse duration of the thresholds at 350 nm and 1064 nm for bulk damage in crystals of KDP", UCLR-95284, presented at the Boulder Damage Conference, 1986.

4. V. Wang, J. Rudisill, C. Giuliano, M. Braunstein and A.Braunstein, "Pulsed CO_2 laser damage in windows, reflectors and coatings", Laser Induced Damage in Optical Materials: 1974, NBS Spec. Pub. 414, p. 59

5. B. Brauns, D. Schafer, R. Wolf, and G. Zscherpe, "Effect of the substrate preparation with CO_2 laser radiation on the laser resistance of optical layers", Thin Solid Films, 138 (1986) 157.

6. F. Rainer, D. Milam, and W. Lowdermilk, "Laser damage thresholds of thin film optical coatings at 248 nm",Laser Induced Damage in Optical Materials: 1981, NBS Spec. Pub. 638, p. 339.

7. J.E. Swain, W.H. Lowdermilk, and D. Milam, "Raising damage thresholds of gradient -index antireflecting surfaces by pulsed laser irradiation" Appl. Phys. Lett. 41 (1982) 782.

8. A. Stewart, A. Guenther, F. Domann, "The properties of laser annealed dielectric films", Laser Induced Damage of Optical Materials: 1987, NBS Spec. Pub. 756, p. 369.

9. J. W. Arenberg and D. Mordaunt, "Experimental investigation of the role of wavelength in the laser conditioning effect", Laser Induced Damage in Optical Materials: 1988, NBS Spec. Pub. (to be published).

10. J. Wilder and I. Thomas, "Effect of n-on-1 laser treatment on damage threshold of selected optical coatings", Laser Induced Damage of Optical Materials: 1988, NBS Spec. Pub. (to be published).

11. C. R. Wolfe, M. Kozlowski, J. Campbell, F. Rainer, A. Morgan, and R. Gonzales, "Laser pre-conditioning of optical thin films", Laser Induced Damage of Optical Materials: 1989, NBS Spec. Pub. (to be published).

12. G. Edwards, J. Campbell, R. Wolfe, and E. Lindsey, "Damage Assessment and possible damage mechanisms to 1-meter diameter Nova turning mirrors" Laser Induced Damage of Optical Materials: 1989, NBS Spec. Pub. (to be published).

13. T.J. Baker, "Breath figures", Phil. Mag., 44 (1922) 752.

14. G.R. Wirtenson and F. Rainer, LLNL intermal memorandum SOC 88-005 (Feb. 1988).

15. Herve Floch, Commissariat a l'Energie Atomique, Villeneuve Saint Georges, France, private communication.

16. S. Jones, P. Braunlich, R. T. Casper, X.-A. Shen, and P. Kelly,"Recent progress on laser-induced modifications and intrinsic bulk damage of wide-gap optical materials", Optical Engineering 28 (1989) 1039.

17. N. C. Kerr, S. E. Clark, and D. C. Emmony, "UV seeding of IR laser induced damage" abstracts to the Laser Induced Damage of Optical Materials: 1989, Boulder CO., Oct. 1989.

18. M. J. Soileau, N. Mansour, E. Carlo, and D. L. Griscom, "Effects of radiation induced defects on laser-induced breakdown in SiO_2", Mat. Res. Soc. Symp. Proc., Vol. 61 (1986) 205.

19. A. R. Newark and U. Stimming, "Photoinduced electron transfer involving localized electronic states", Electrochimica Acta, 32 (1987) 1217.

20. E.P. O'Reilly and J. Robertson, "Theory of Defects in Vitreous Silicon Dioxide", Phys. Rev. B, 27 (1983) 3780.

21. J. H. Stathis and M. A. Kastner, "Photoinduced Paramagnetic Defects in Amorphous Silicon Dioxide", Mat. Res. Soc. Symp. Proc., Vol. 61 (1986) 161.

22. R. N. Schwartz, M. D. Clark, W. Chamulitrat, and L. Kevan, "Electron Papamgnetic Resonance Studies of Intrinsic Bonding Defects and Impurities In SiO_2 Thin Solid Films" in 'Defects in Glasses', Mat. Res. Soc. Symp. Vol. 61 (1986), 359.

23. T. Hickmott and J. Baglin, "Stoichiometry and atomic defects in rf-sputtered SiO_2", J. Appl. Phys., 50 (1979) 317.

24. A. Guenther and T. Humphreys, "Physical aspects of laser-induced damage of optical materials" , Proc. SPIE, Vol. 401 (1983) p. 247.

25. J. W. Schultze, B. Danzfuss, O. Meyer, and U. Stimming, "Electrochemical investigations of ion-implanted oxide films", Mat. Sci. Eng. 69 (1985) 273.

26. J. Tauc, "Optical properties of non-crystalline solids" in Optical Properties of Solids, F. Abeles ed.,North Holland Pubs., Amsterdam, 1972.

27. Tom Allen, Optical Coatings Laboratory Inc., private communication.(1989).

28. N.V. Krizosheen, N.N. Zapleshko, and N.F. Fedorov, "Interrelationship between the structure and optical properties of zirconium dioxide thin films", Inorg. Mater., 19 (1983) 825.

29. D. J. DiMaria and M. V. Fischetti, "Hot electrons in silicon dioxide: Balistic to steady-state transport", Appl. Surface Sci., 30 (1987) 278.

30. D. J. DiMaria, M. V. Fishetti, M. Arienzo, and E. Tierney, "Electron heating studies in silicon dioxide: Low fields and thick films", J. Appl. Phys. 60 (1986) 1719.

31. I.M. Thomas, J.G. Wilder, and R.P. Gonzales, "HR coatings prepared from colloidal suspensions", Laser Induced Damage of Optical Materials: 1987, NBS Spec. Pub. 756, p. 286.

32. E. Yablonovitch and N. Bloembergen, "Avalanche Ionization and the limiting diameter of filaments induced by light pulses in transparent media", Phys. Rev. Lett. 29 (1972) 907.

33. N.W. Ashcroft and N.D. Mermin, Solid State Phyics, Saunders College, Philadelphia (1976).

34. N. Bloembergen, "Role of Cracks,Pores, and Absorbing inclusions on laser induced damage thresholds at surfaces of transparent dielectrics", Applied Optics, 12 (1973) 661.

35. Stathis, J. H., "Identification of native defects in a-SiO_2" in 'The Physics and Technology of Amorphous SiO_2', Edited by R. Devin (Plenum Publ. Corp., 1988), p. 141.

36. C.R. Wolfe, J.H. Campbell, R.E. Lyon, J.H. Pitts, H.T. Powell, "Optical damage in epoxy polymers by millisecond light pulses", Laser Induced Damage in Optical Materials: 1986, NBS Spec. Pub. 752, p. 194.

COMMENTS

Question: You said you did the abrasion with the diamond slurry. Did you ever find any carbon from the diamond? Are you concerned about the imbedding of the diamond in the film or the pick up of water by the films?

Answer: There are several questions there. Do we see diamond paste or diamond particles in the crater itself. We were unable in these craters to pick up carbon. The analysis goes down to parts per thousand so that if there is a particle there we should see a half micron or the tenth micron size particle. We should see a significant carbon signal if we hit one of those particles. Probing around I have never seen the evidence of diamond imbedded in that way. I would expect perhaps to see diamond in the ULE glass simply because it is softer. In answer to the second part of your question, we do not clean these specimens with water after we crater them. We use organic solvents and essentially what we do is to use the organic solvent to clean the specimen and then we go back and lightly etch with perhaps a 1000 angstrom argon ion beam to clean that up. I would not believe what I see at an interface that was cleaned in that fashion. I would step back and depth profile away from that maybe a thousand angstrom. I would have to go through a thousand angstroms of the layer above in order to get to the interface. I tried to stay away for the exposed interfaces and then move back, if you understand what I mean.

Question: There is a danger in coming back to that same point. If you are using a steel ball, might you not be getting carbon from the high carbon steel embedded in the process.

Answer: If that were true we should see it all over the crater and we don't. In the example I showed you where we had ion beam texturing, if the carbon would have been uniform all over the crater we should have seen that texturing all over the crater. It did not appear all over the crater, it appeared at the interface.

Question: What is the energy resolution of your Auger spectrometer and can you distinguish different crystals in phases in the material?

Answer: No, we can not distinguish crystals in phases. Energy resolution, that question is best answered this way. Peaks are broad, we are looking at 15 or 20 electron volts wide, the energy resolution of this spectrometer is usually way below the width of the peak. So we are somewhere, I really forget the spec on the instrument, but the peak shifts that we would expect to see are much, much larger than the energy resolution of the spectrometer. However, I would say this: we very seldom try to correlate peak shift information in Auger data with chemical state. If you want to do that, go to XPS.

Question: You mentioned that you didn't see any charging on this particular film; is that a general result do you think or will it depend strongly on the materials?

Answer: No that's magic, straight and clear. There are a number of tricks one can use to get rid of the charging on these films. First, we do these specimens at perhaps 60° to 70° degrees incidence. So the charge tends to deflect off. Second, in the first generation Auger instruments beam currents on the order of seven or eight microamps were common. These spectra were taken at perhaps thirty nanoamps so the beam current has been reduced significantly. Finally, if you want to pull some other tricks what you can do is to broaden out the spot and defocus it slightly. It doesn't affect the peak shapes at all. What it does is to decrease the energy density, which gets red of the charging. But every material is different.

Manuscript received
2-14-90

Population Distribution of Conditioned Damage Thresholds on AR Coated BK-7 Glass with Varying Laser Spot Size

D. W. Mordaunt and J. W. Arenberg*
Hughes Aircraft Company
P. O. Box 902, Bldg. E1/MS B129
El Segundo, CA 90245

In this paper we report on an empirical study of the population distributions of conditioned laser damage thresholds on antireflection (AR) coated BK-7 glass while varying the laser spot size. Two different 1.06 μm AR coating designs were tested. All damage tests were conducted at the design wavelength of 1.06 μm. To obtain the population distribution, 20 determinations of the conditioned damage threshold were performed. This procedure was repeated for each spot size on each of the samples. For control purposes, the unconditioned damage threshold was also measured for each spot size and coating design. The data was analyzed statistically by describing the population distribution and testing for differences as a function of spot size and coating design.

Key Words: laser damage; damage test; laser conditioning; preconditioning; prepulsing

1. Introduction

This paper reports an empirical study of the population distributions of conditioned laser damage thresholds on antireflection (AR) coated BK-7 glass while varying the laser spot size. The phenomenon of laser conditioning consists of an enhancement in the laser induced damage threshold due to exposure of the sample to subthreshold fluences and has been well documented in the literature [1-8]. This conditioning effect (also referred to as preconditioning) has been attributed to various effects including the desorption of adsorbed contaminants in thin film coatings, the annealing of surface defects and the annealing of molecular defects such as electron traps in a crystalline substrate. The conditioning effect is particularly interesting because of the possibility of permanently increasing the damage threshold of critical laser optics and thereby obtaining an increase in the lifetime and reliability of the laser system. In this report we continue our previous efforts to understand and quantify the laser conditioning effect. We investigated the conditioning of two different designs and report the dependence of the conditioning on the laser spot size. The results were analyzed to provide information about the distribution and density throughout the coatings of the main actor in the laser conditioning effect.

2. Experimental Results

The damage test facility is shown in figure 1. It consists of a Nd:YAG oscillator and two Nd:YAG amplifier heads which are capable of generating up to 1.5 J of near diffraction limited energy at the 1.06 μm Nd:YAG fundamental. The energy is polarization outcoupled and focused onto the target plane where the sample is located. A wedge is used to generate two equivalent target planes where the beam energy and spatial profile are measured. The sample is observed on line with a 25X magnification microscope and video system and can be illuminated with up to 25 mW of He-Ne laser power to observe changes in the surface scatter. We typically used about 2.5 mW of He-Ne power in our experiments. The experimental test parameters are summarized in table 1. All of our testing was performed at 1064 nm and damage

* Current address: TRW Space and Technology Group, One Space Park Drive, 01/1210, Redondo Beach, CA 90278.

was defined as the first observable change that occurred when the sample was observed on line at 25X magnification under illumination by a 2.5 mW He-Ne laser. All of the test samples consisted of multilayer dielectric thin film coatings deposited on BK-7 glass using electron beam evaporation. Sample A was a MgF_2/Al_2O_3 multilayer antireflection (AR) coating deposited on unheated substrates while sample B was a Al_2O_3/ZrO_2 multilayer AR coating for which the substrates were heated prior to deposition.

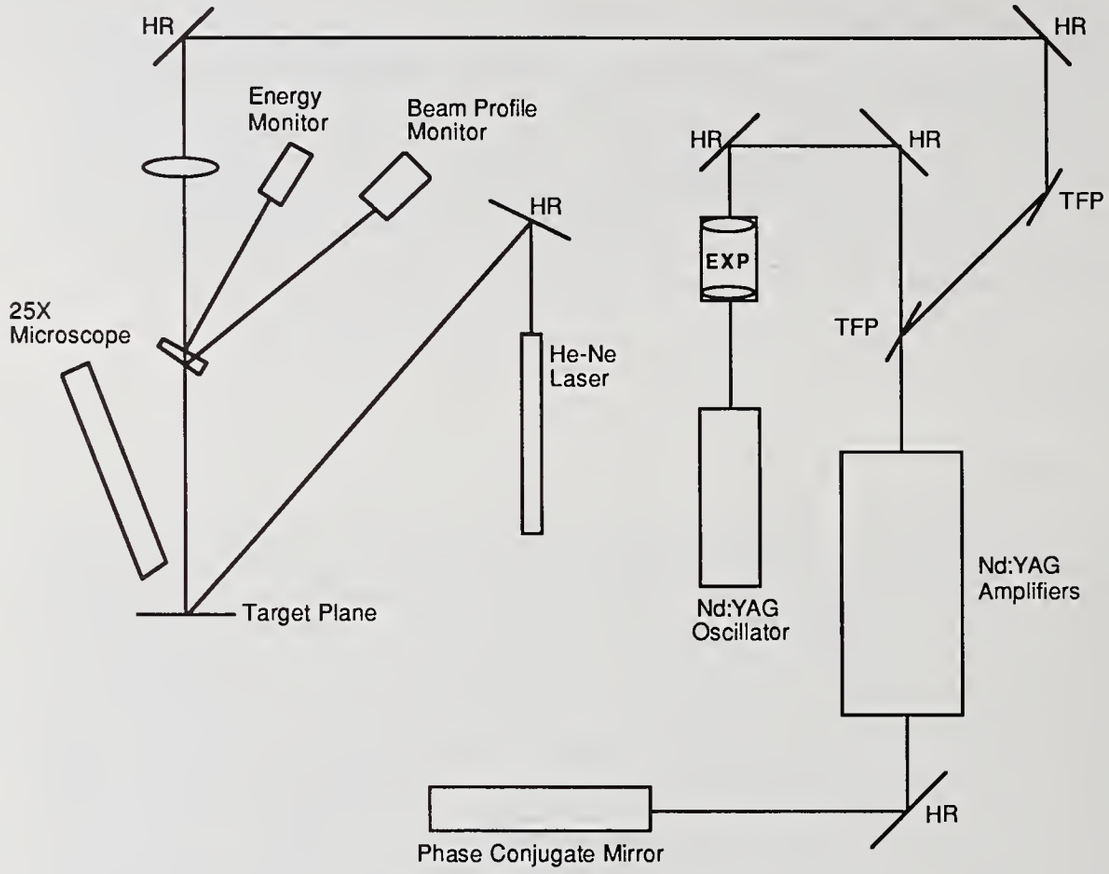

Figure 1. Layout of the damage test facility.

The unconditioned and conditioned thresholds were measured for both samples. For the unconditioned test procedure, each site on the surface was exposed to only a single fluence. The test sites were separated by at least three times the diameter of the laser spot and each site was exposed to 25 shots or until damage was observed. For the conditioned test procedure, each site was initially exposed to 1/2 the unconditioned threshold and then the fluence was slowly ramped up stepwise until damage was observed. The sites were exposed to 25 shots at each fluence level before increasing to the next higher level. All threshold measurements are accurate to ±10%.

The results of the unconditioned threshold measurements are presented in table 2. The unconditioned threshold shows some dependence on spot size, particularly for the smallest spot size of 0.25 mm. These results were fairly typical of off-the-shelf production laser optics, with sample B being considerably more durable than sample A. The unconditioned damage test results are presented in figures 2 and 3 as a plot of the test result (damage or no damage) versus fluence. The unconditioned testing showed considerable overlap between damaging and non-damaging fluences.

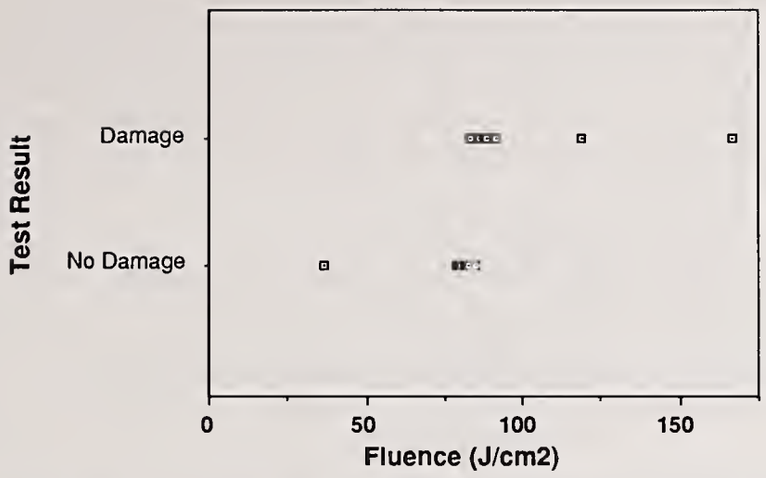

Figure 2a. Unconditioned results for sample A with a 0.25 mm spot size.

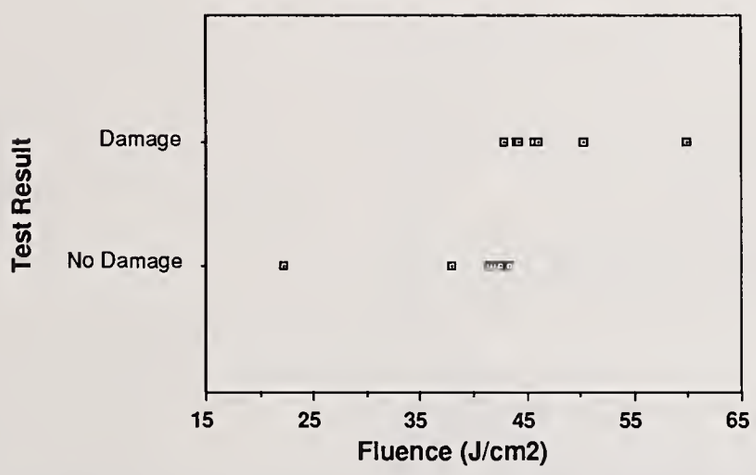

Figure 2b. Unconditioned results for sample A with a 0.5 mm spot size.

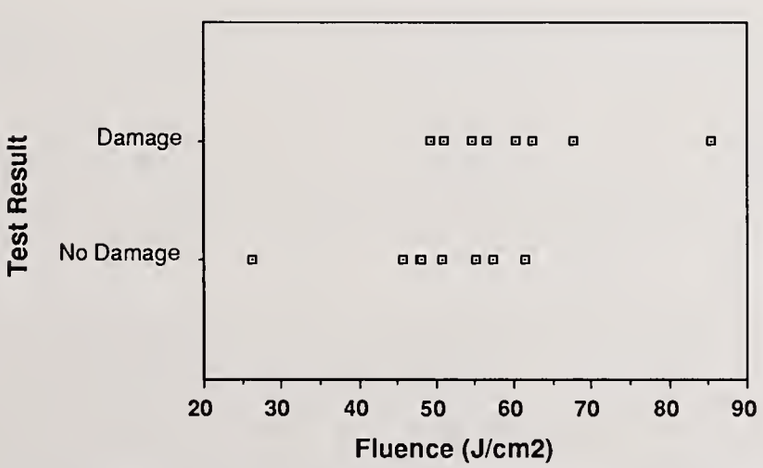

Figure 2c. Unconditioned results for sample A with a 1.00 mm spot size.

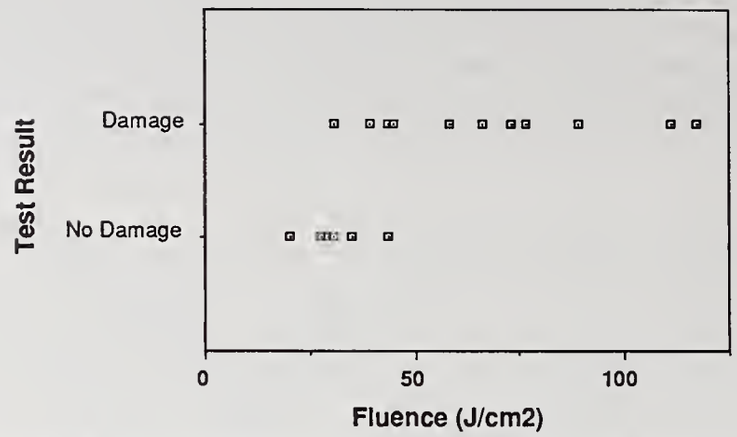

Figure 3a. Unconditioned results for sample B with a 0.25 mm spot size.

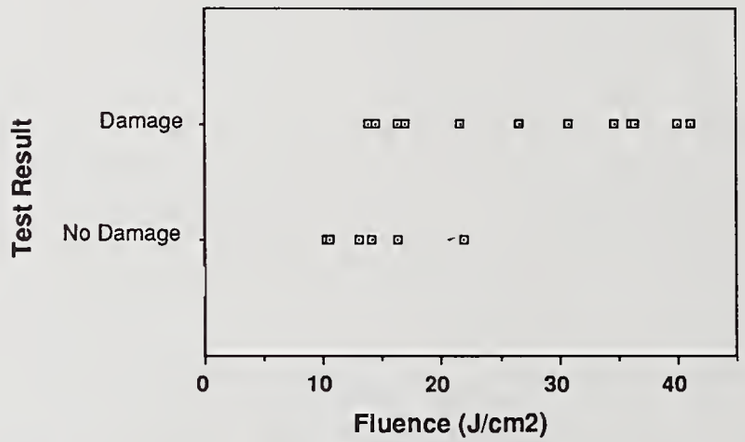

Figure 3b. Unconditioned results for sample B with a 0.5 mm spot size.

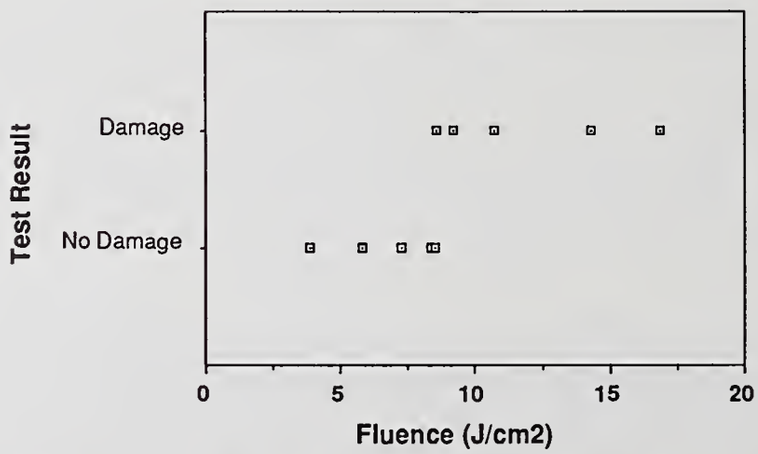

Figure 3c. Unconditioned results for sample B with a 1.00 mm spot size.

The results of the conditioned damage threshold measurements are presented in the histograms of figures 4 and 5 for samples A and B, respectively. Approximately 20 spots per sample were tested at each spot size to allow a statistical analysis of the defect distribution. A comparison of the conditioned and unconditioned measurements is provided in figure 6. The conditioning increased the damage threshold for the smaller spot sizes but provided little improvement at the 1.0 mm diameter spot size. The standard deviation of the conditioned threshold vs spot size is shown for both samples in figure 7. The deviation was largest for the smallest spot size and also was largest for coating A, which had the lowest overall damage threshold. These results are consistent with a defect dominated damage mechanism in which the defect spacing is on the order of 1 mm. In this case, the smaller spot sizes would exhibit a large variation in the conditioned threshold, depending on whether the laser spot happened to intersect a coating defect. If the spacing is on the order of 1 mm, then as the spot size approaches the defect spacing, the measured thresholds will become more tightly grouped, as was observed.

Table 1. Laser test parameters.

Laser Parameter	Value used for testing
Wavelength	1064 nm
Pulsewidth	15 nsec FWHM
Temporal Profile	Smooth with minimal mode beating
Pulse Repetition Frequency	1 Hz
Spot Size	0.25 to 1.0 mm full width at $1/e^2$
Spatial Profile	Approximately Gaussian (monotonically increasing to a central on-axis peak)
Angle of Incidence	Normal
Laser Polarization	Linear
Sample Substrate	BK-7 Glass
Coating Sample A	Multilayer AR with $MgF_2/Al2O_3$
Coating Sample B	Multilayer AR with $Al2O_3/ZrO_2$
Irradiation History	Both Conditioned and Unconditioned

Table 2. Unconditioned damage threshold measurements.

Spot size (FW in mm at $1/e^2$)	Sample A (J/cm^2)	Sample B (J/cm^2)
0.25	29.2	82.5
0.50	13.1	42.5
1.00	8.5	48.2

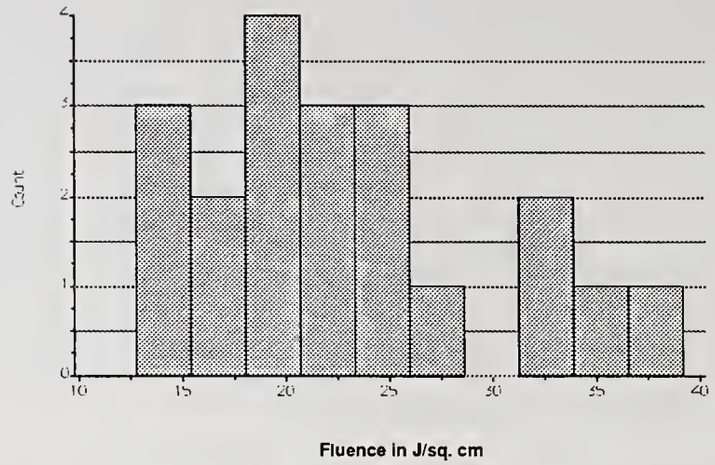

Figure 4a. Histogram of conditioned failures for sample A with a spot size of 1.0 mm.

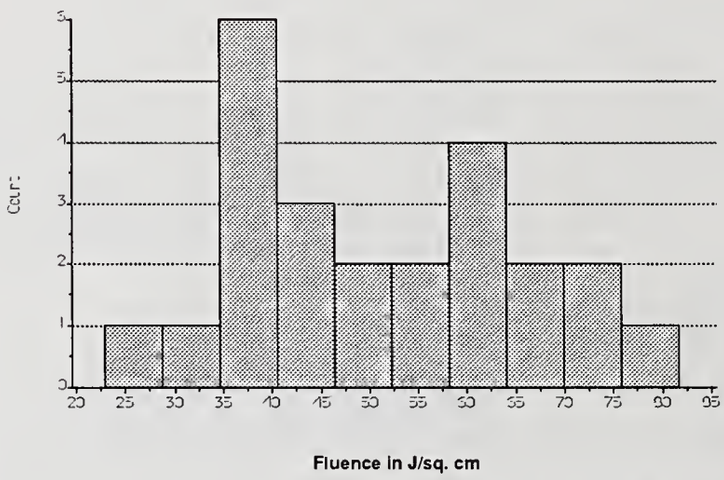

Figure 4b. Histogram of conditioned failures for sample A with a spot size of 0.5 mm.

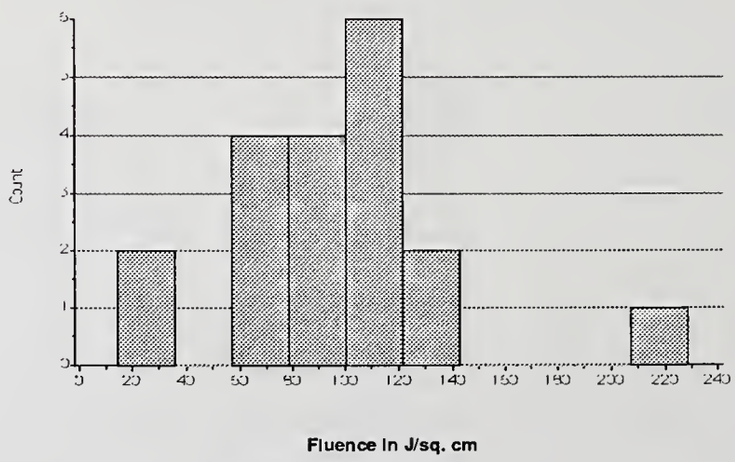

Figure 4c. Histogram of conditioned failures for sample A with a spot size of 0.25 mm.

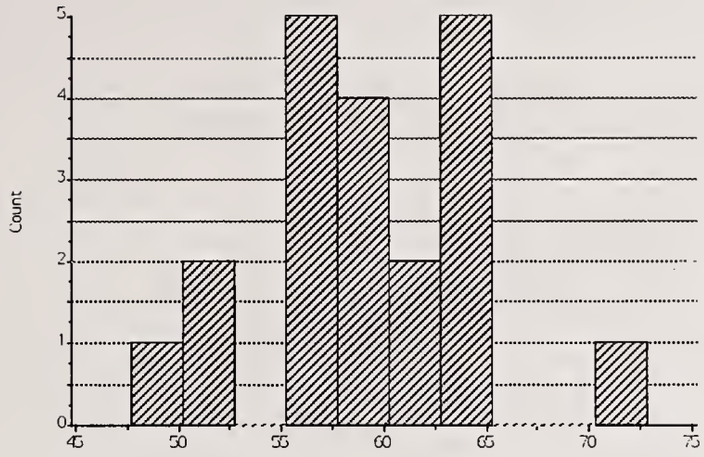

Figure 5a. Histogram of conditioned failures for sample B with a spot size of 1.0 mm.

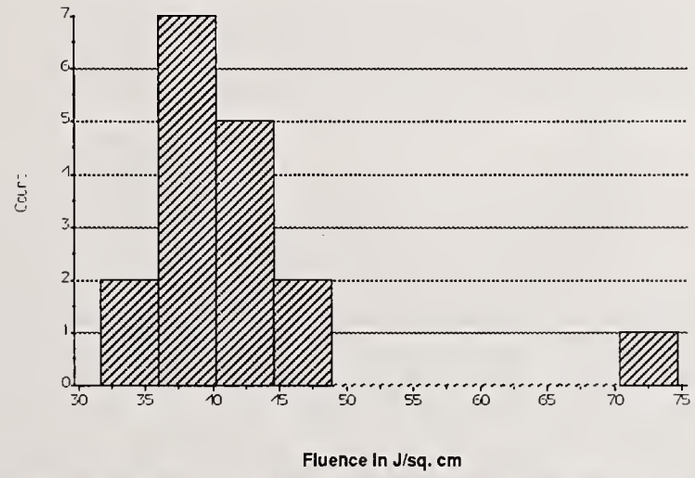

Figure 5b. Histogram of conditioned failures for sample B with a spot size of 0.5 mm.

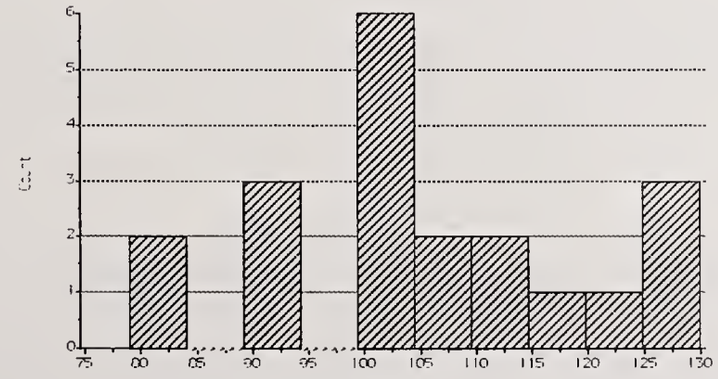

Figure 5c. Histogram of conditioned failures for sample B with a spot size of 0.25 mm.

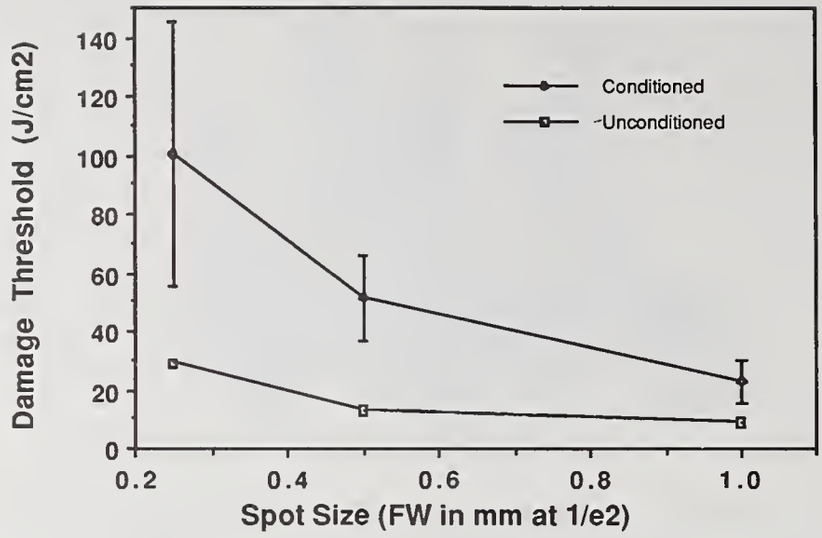

Figure 6a. Conditioned and unconditioned performance of sample A.

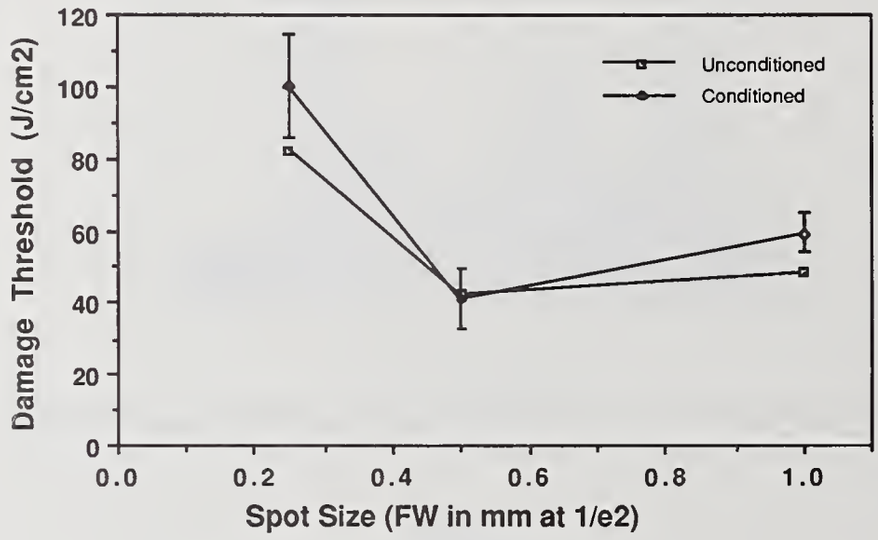

Figure 6b. Conditioned and unconditioned performance of sample B.

Figure 6. Comparison of the conditioned and unconditioned test results for the three different spot sizes.

3. Conclusions

In summary, we have verified that the threshold enhancement due to conditioning is largest for small spot sizes and decreases as the spot size is increased. The variability in the conditioned threshold measurements was also largest for the small spot size, with the distribution becoming more tightly grouped as the spot size was increased.

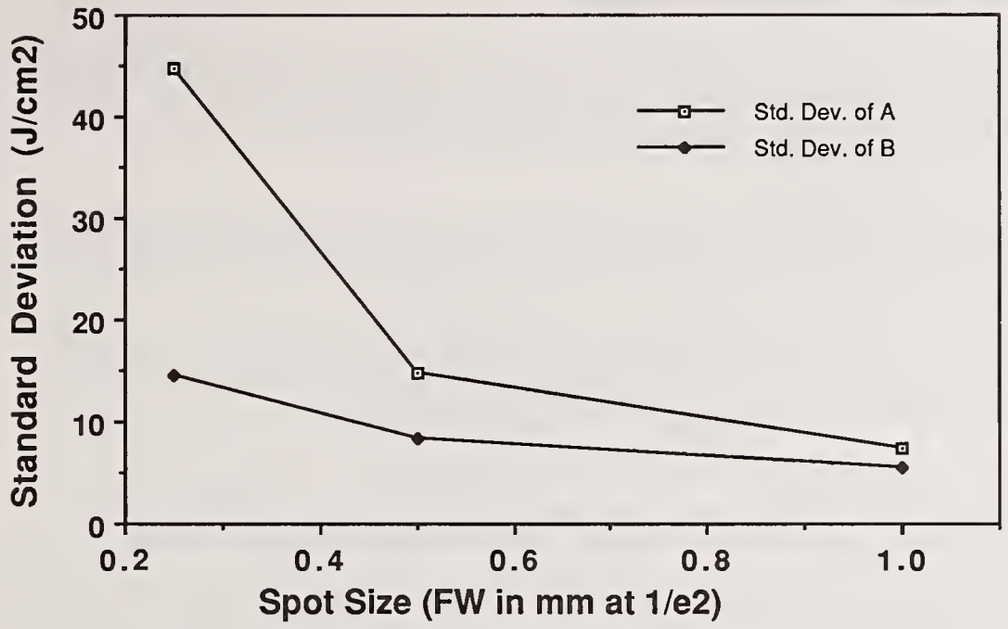

Figure 7. The standard deviation of the conditioned threshold was largest for the smallest spot size.

This evidence indicates that the spacing of the coating defects that were responsible for the damage was on the order of 1 mm.

These results demonstrate the variability in damage threshold and laser conditioning with variations in the coating design, materials and deposition parameters. Although both coatings were multilayer, dielectric coatings deposited on BK-7 glass, the designs and materials were different for the two samples. A significant change in deposition processes was that coating A was deposited on a cold substrate while coating B was deposited on a preheated substrate. Our experience with production laser optics indicates that preheating the substrates tends to yield a higher density coating which is harder, more durable, and has a a higher damage threshold. Because of the process variations used in the production of our two samples, we expect that coating A will be lower density and therefore more porous than coating B. Our results are consistent with this conclusion since sample A had a lower damage threshold and exhibited a much higher level of conditioning than did sample B. This empirical evidence supports previous efforts to establish a link between coating porosity, adsorbed contaminants and the laser conditioning effect [3, 5-7].

4. References

[1] Wolfe, C. R.; Kozlowski, M. R.; Campbell, J. H.; Rainer, F.; Morgan, A.; Gonzales, R. "Laser Preconditioning of Optical Thin Films", presented elsewhere in this symposium.

[2] Kozlowski, M. R.; Staggs, M.; Wolfe, C. R.; Campbell, J. H. "Large Area Laser Preconditioning of Dielectric Thin Films", presented elsewhere in this symposium.

[3] Arenberg, J. W.; Mordaunt, D. W. "Experimental Investigation on the Role of Wavelength in the Laser Conditioning Effect", presented at the 20th Symposium on

Optical Materials for High Power Lasers (Boulder Damage Symposium), Boulder, CO, October, 1988, proceedings to be published.

[4] Wilder, J. G.; Thomas, I. K. "Effect of n on 1 Laser Damage Threshold of Selected Optical Coatings", presented at the 20th Symposium on Optical Materials for High Power Lasers (Boulder Damage Symposium), Boulder, CO, October, 1988, proceedings to be published.

[5] Arenberg, J. W.; Frink, M. E. "On the Role of Water in the Laser Conditioning Effect", Laser Induced Damage in Optical Materials: 1987, NIST Special Publication 756; October 1988, p. 430.

[6] Frink, M. E.; Arenberg, J. W.; Mordaunt, D. W.; Seitel, S. C.; Babb, M. T.; Teppo, E. A. "Temporary Laser Damage threshold enhancement by laser conditioning of antireflection-coated glass", Appl. Phys. Lett. 51, (6), 415 (1987).

[7] Frink, M. E.; Arenberg, J. W.; Mordaunt, D. W.; Seitel, S. C.; Teppo, E. A. "Quantification of the Magnitude and Duration of the Preconditioning Effect in AR Coated BK-7 Glass", Laser Induced Damage in Optical Materials: 1986, NIST Special Publication 752, September 1988, p. 279.

[8] Swain, J. E.; Lowdermilk, W. H.; Milam, D. Nat. Bur. Stand. (U. S.) Spec. Publ. No. 669, 292 (1982).

COMMENTS

Question: In your germanium data, showing a linear plot of damage threshold versus the square of the field, there was a roll off at the high values. Do you have an explanation for that?

Answer: We might be changing the optical thickness through simply binding the fields and that wouldn't be covered by the simple model.

Question: Can you give some information concerning scattering?

Answer: Scattering, I don't really know about. We didn't take that kind of loss into account in the field calculations. A quick calculation shows that it is not going to be important for this model. But it probably will have an effect, a small effect. That also might help to account for the roll off at the high energy end of the scale.

MANUSCRIPT NOT RECEIVED

Damage Threshold Measurements of Reflective and Transmissive Optics at 130 nm

C.H. Muller, III and C.E. Hamilton

Spectra Technology, Inc.
Bellevue, Washington 98004-1495

ABSTRACT

The GLORIA VUV facility at Spectra Technology, Inc. has been used to measure the damage threshold and reflectivity of first surface Al+MgF_2 mirrors and second surface MgF_2+Al+MgF_2 mirrors. The mirrors were illuminated by high power VUV coherent radiation at 130 nm. Mirror reflectivity was monitored for several thousand pulses for each optic studied. Two nanosecond long pulses and energy densities as high as 20 mJ cm^{-2} were used for the measurements. In addition, measurements of "color center" formation rates in transmissive optics have been obtained. The GLORIA VUV facility, experimental measurement system, and damage results will be discussed in detail.

Work supported by Sandia National Laboratory

Manuscript received
2-1-90

Laser Induced Damage Thresholds of Dielectric Coatings at 193 nm and Correlations to Optical Constants and Process Parameters

J. Kolbe, H. Müller, H. Schink, H. Welling

Institut für Quantenoptik, Universität Hannover,
Welfengarten 1, D-3000 Hannover 1, FRG

and

J. Ebert

Laseroptik GmbH, 3008 Garbsen 8, FRG

Laser-induced damage thresholds of dielectric single layers and reflectors were measured at 193 nm. Layers of Al_2O_3 and SiO_2 were prepared by electron beam evaporation and by ion beam sputtering; layers of NaF, AlF_3, MgF_2, GdF_3, LaF_3, NdF_3 and YF_3 were prepared by thermal evaporation. Spectrophotometric methods were used to evaluate optical constants and inhomogeneity coefficients in the spectral range between 150 nm and 250 nm. The dependence of refractive indices and absorption coefficients on process parameters and deposition methods was analyzed in order to prepare low loss reflectors for 193 nm and 157 nm.

Key words: fluoride layers; UV coatings; UV laser damage; excimer laser mirrors; ion-beam sputtered UV coatings; UV losses in dielectric layers.

1. Introduction

In the last few years, the number of laser applications in material processing has increased by an appreciable amount [1]. It has turned out that in many applications, the use of ultraviolet laser radiation has considerable advantages in comparison to visible or infrared light. The interaction mechanism between light and matter is dominated by photoablation rather than by thermal processes; so the interaction is restricted to very thin surface layers, which is extremely useful, for example, in eye surgery. - In semiconductor applications, the shorter wavelength of ultraviolet light facilitates an improved resolution in chip fabrication.

The KrF eximer laser which operates at 248 nm has already proven as a powerful tool to produce intense ultraviolet light. Nevertheless, the use of even shorter wavelengths would be connected with further progresses in the above mentioned applications. This affords, however, the availability of high-quality optical components. For this reason, a study has been initiated to develop dielectric mirrors with high reflectivities and damage thresholds at 193 nm (ArF excimer laser). Additionally, mirrors for 157 nm (F_2 excimer laser) have been deposited and analyzed.

In the first step of our study, we deposited single layers of coating materials with absorption edges below 250 nm. The optical properties of the

layers were measured and evaluated by spectrophotometric methods. The deposition processes and parameters were optimized in order to minimize absorption and scatter losses. To get some insight into the microstructure of the layers, their cosmetic appearance, water content, and inhomogeneity were investigated. Finally, the damage thresholds at 193 nm were measured.

In the second step, high reflecting quarterwave stacks were deposited. The reflection and transmission coefficients were measured and compared with theoretical data which had been computed with the single layer values of the refractive indices and extinction coefficients. The damage thresholds were determined and compared with the results for the single layers.

2. Experimental Apparatus

Fluoride and oxide coatings were deposited by thermal and electron beam evaporation. The vacuum chamber was equipped with an oil diffusion pump and a liquid nitrogen-cooled Meissner trap; the base pressure was smaller than $5*10^{-6}$ mbar; the substrates could be heated up to 400 °C; the layer thickness was controlled by an optical monitoring system.

Additionally, oxide coatings were deposited by ion beam sputtering. This was performed in a cryo-pumped coating plant. Two 5 cm Kaufman ion guns with hollow cathodes and one common hollow cathode neutralizer were used to sputter the targets. These consisted of the oxide materials to be coated; their diameter was 20 cm; the angle between the targets and the ion beams was 45°. Each gun produced an argon ion beam of 130 mA with an ion energy of 1000 eV. The Ar backpressure due to the gas flow through the ion guns and the hollow cathode neutralizer was 10^{-4} mbar; an amount of 10^{-4} mbar oxygen was added to produce fully stoichiometric oxide coatings. The deposition rate was 0.4 nm/s for silica and 0.3 nm/s for alumina.

The reflection and transmission measurements were made with a Perkin-Elmer Lambda 9 spectrophotometer (wavelengths above 190 nm), and with a self-constructed VUV-spectrophotometer (wavelengths between 140 nm and 240 nm).

The damage threshold measurements were performed by the "Laser-Laboratorium Göttingen e.V.". A Lambda Physik EMG 202 MSC excimer laser was used to produce pulses at 193 nm with a pulse length of 25 ns. The beam profile was approximately gaussian. The beam cross-section at the probe was elliptical and had a $1/e^2$ area of 0.65 mm^2. The energy densities given below are the mean values within the $1/e^2$ area; the peak energy densities are higher by a factor of about 2.5. Damage was detected by in-situ-microscopy in connection with digital image processing. Further details of the arrangement are given in a recent paper by K. Mann [2].

3. Experimental results

3.1 Single layers

Only few data about the basic optical properties (refractive index and extinction coefficient as functions of wavelength) of dielectric thin films for the deep ultraviolet are available from the literature [3]...[10]. For this reason, a series of suitable materials was selected for further investigations. Single layers were deposited by different processes and process parameters in order to minimize their scatter and absorption losses. The wavelength-dependent refractive indices (n) and extinction coefficients (k) of the

optimized layers were evaluated by an envelope method described in ref. [21]. Finally, the damage thresholds were measured and compared with the extinction coefficients.

3.1.1 Oxide materials

Layers of silica and alumina with thicknesses of about 400 nm were deposited onto fused silica substrates by electron beam evaporation and by ion beam sputtering. For the e-beam coatings, well established process parameters (substrate temperature: 300 °C, deposition rate: 0.5 nm/s; oxygen backpressure: $2*10^{-4}$ mbar) were used. For the IBS coatings, the optimized parameters are given in section 2.

Figure 1 shows the evaluated n and k values of alumina as functions of wavelength. The deviations of the values for n from those reported in refs. [4] and [19] are smaller or equal to 0.02 for the evaporated layers and 0.01 for the ion-beam sputtered layers. The extinction coefficients are comparable to the results given in ref. [19].

The e-beam deposited silica layers had a refractive index almost identical to the fused silica value; the index of the IBS-coatings was slightly higher (see fig. 1), which agrees with the information given in ref. [20]. In both cases, the extinction coefficient was smaller than 10^{-4} for wavelengths down to 190 nm.

The damage thresholds of the deposited oxide coatings are plotted in figure 8. The low values of the alumina layers are obviously caused by their high absorption losses. Generally, the thresholds of the IBS coatings are slightly higher than those of the e-beam coatings, which may be attributed to their higher packing density and better mechanical stability.

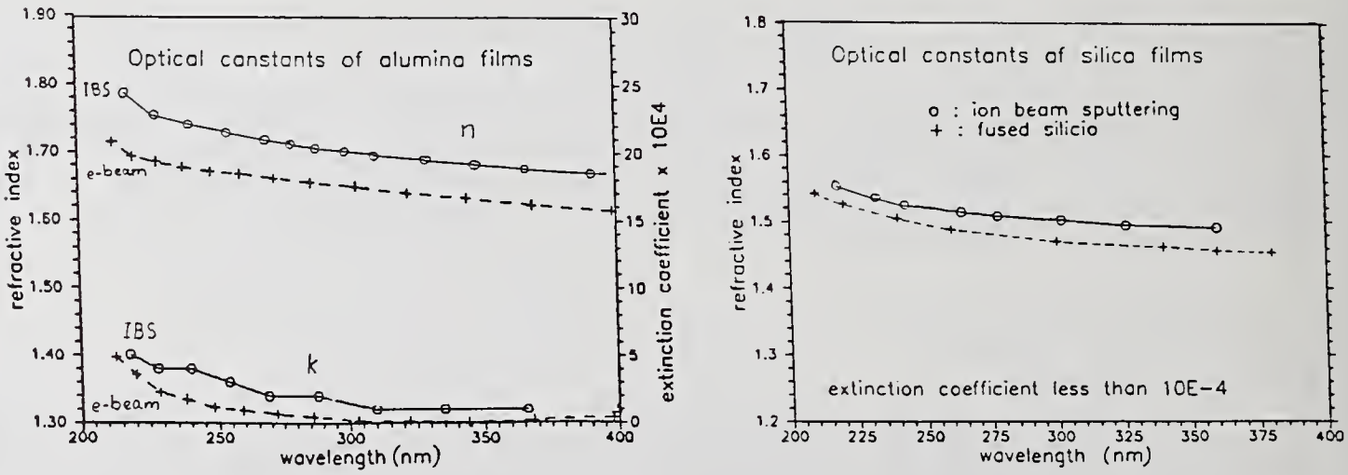

Fig. 1. Refractive indices and extinction coefficients of oxide films deposited by electron-beam evaporation and by ion-beam sputtering. The film thicknesses are about 400 nm.

3.1.2 Fluoride Materials

In the deposition of dielectric coatings consisting of fluoride materials, internal stresses as well as scatter losses arising from the microstructure of the layers impose severe limitations. To get a first insight into the mechanical and optical properties of fluoride coatings, single layers of different thicknesses (2, 8, 14, 20, 26 QWOT at about 200 nm) were deposited onto substrates of BK-7 glass, fused silica, and calcium fluoride. This was done for several substrate temperatures between 100°C and 400°C. The materials were evaporated from molybdenum boats (deposition rates in nm/s: 3 {AlF3}, 0.8 {MgF2}, 0.25 {NdF3}, 0.5 {other materials}).

The layers were examined by visual inspection (with illumination by intense white light) and by dark field microscopy (magnification 125 times). The results are given in table 1 and can be summarized as follows:

- All single layers of NaF and YF_3 had an inferior quality. While it is well known that NaF is very hygroscopic, the reason for the results with YF_3 is not quite clear.

- In layers of MgF_2, GdF_3, LaF_3, and NdF_3 which were deposited onto substrates heated up to 400 °C, cracks have been observed in some cases. In NdF_3 layers, the maximum layer thickness without cracks strongly depends on the substrate material: while the thermal expansion coefficient of the substrate (values are given in table 2) increases, the maximum layer thickness increases, too. Similar tendencies can be observed in MgF_2 and GdF_3 layers.

- Layers of AlF_3 have a good quality if deposited onto substrates of fused silica or calcium fluoride at high substrate temperatures. The reason for the inferior quality of the layers deposited on BK-7 glass is not understood yet.

- Thick Layers of GdF_3, LaF_3, and NdF_3 show a hazy appearance if deposited at a low substrate temperature (100 °C). As can be seen in figure 2, the optical losses are almost proportional to the layer thickness. So the change from "+" to "-" with increasing thickness just reveals the increase of the losses; it is not connected with a qualitative change in the structure of the layers.

A strong dependence on the substrate temperature is observed in several properties of the single layers. The extinction losses drop significantly with increasing substrate temperature (fig. 3). The inhomogeneity as well as the shift of optical thickness before/after venting with atmospheric air increase significantly at low substrate temperatures (figs. 4, 5). Although the data shown in these figures only refer to GdF_3 layers, similar tendencies have been observed in most of the other fluoride materials. These facts clearly demonstrate that the optical losses of the layers are closely connected with their internal microstructure.

The results presented above show that the deposition of fluoride coatings with low optical losses can be performed only at high substrate temperatures. These, however, may lead to cracking of the layers caused by internal stresses. The results in table 1 indicate that cracking can in some cases be avoided by choosing a substrate material with an appropriate thermal expansion coefficient.

Table 1. Morphology of evaporated fluoride single layers.

Layers marked with "+" showed no defects;
layers marked with "(+)" were damaged by rubbing with lens tissue and acetone;
layers marked with "-" showed one of the following defects:
- cracks (mean separation is given in brackets);
- extremely high pinhole densities;
- hazy appearance without any detectable fine structure.

Material; substrate temperature	Layer quality vs. layer thickness [QWOT at 200 nm]					Substrate material [F.S.= fused silica]	Morphology [explanations are given below]
	2	8	14	20	26		
NaF; 400 °C	-	-	-	-	-	all	pinholes
NaF; 100 °C	-	-	-	-	-	all	pinholes
AlF_3; 400 °C				+		CaF_2	
	+	-	-	-	-	BK-7	pinholes after ageing > 10 days
	+	+	+	+	-	F.S.	** ** **
AlF_3; 100 °C				-		CaF_2	pinholes after ageing > 10 days
	+	-	-	-	-	BK-7	pinholes
	+	+	-	-	-	F.S.	pinholes after ageing > 10 days
MgF_2; 400 °C				+		CaF_2	
	+	+	+	+	+	BK-7	
	+	+	-	-	-	F.S.	cracks (50 μ)
MgF_2; 100 °C				(+)		CaF_2	
	+	+	(+)	(+)	(+)	BK-7	
	+	+	-	-	-	F.S.	cracks (10 μ)
YF_3; 400 °C	(+)	-	-	-	-	all	pinholes
100 °C	(+)	-	-	-	-	all	pinholes
GdF_3; 400 °C				+		CaF_2	
	+	+	+	+		BK-7	
	+	+	-	-		F.S.	cracks (10 μ)
GdF_3; 100 °C							
	+	+	-	-		BK-7	hazy
	+	+	-	-		F.S.	hazy
LaF_3; 400 °C				-		CaF_2	cracks (5 μ)
	+	+	-	-	-	BK-7	cracks (10 μ)
	+	+	-	-	-	F.S.	cracks (5 μ)
LaF_3; 100 °C				-		CaF_2	pinholes
	+	+	+	-	-	BK-7	hazy
	+	+	+	-	-	F.S.	hazy
NdF_3; 400 °C				+		CaF_2	
	+	+	-	-	-	BK-7	cracks (20 μ)
	+	-	-	-	-	F.S.	cracks (10 μ)
NdF_3; 100 °C				-		CaF_2	hazy
	+	+	+	-	-	Bk-7	hazy after ageing > 10 days
	+	+	+	-	-	F.S.	** ** **

Table 2. Optical properties and thermal expansion coefficients of substrate and film materials.

The data have been taken from references [10] to [18] and refer to the bulk materials; abbreviations: (o), (e): ordinary, extraordinary ray; o.a.: optical axis.

Material	n (550nm)	Band Edge [nm]	Thermal expansion coeff. [10^{-6} °K^{-1}]
LiF	1.39	105	37
NaF	1.33		36
MgF_2	1.38 (o) 1.39 (e)	113	9 ⊥ o.a 14 ∥ o.a.
CaF_2	1.43	124	24
AlF_3	1.38	–	–
YF_3	1.55	–	17
LaF_3	1.60	135	14
NdF_3	1.60	–	14
GdF_3	1.58	–	–
SiO_2 (cryst.)	1.55 (o) 1.56 (e)	148	13.4 ⊥ o.a 8.0 ∥ o.a.
SiO_2 (fused)	1.46	160	0.55
Al_2O_3 (cryst.)	1.77 (o) 1.76 (e)	141	5.0 ⊥ o.a 6.7 ∥ o.a.
BK-7 glass	1.52	315	7.1

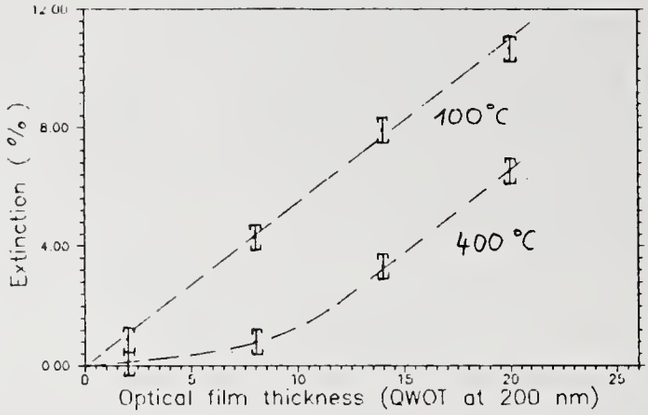

Fig. 2. Extinction losses at 200 nm versus layer thickness in GdF_3 single layers evaporated at substrate temperatures of 100 °C and 400 °C.

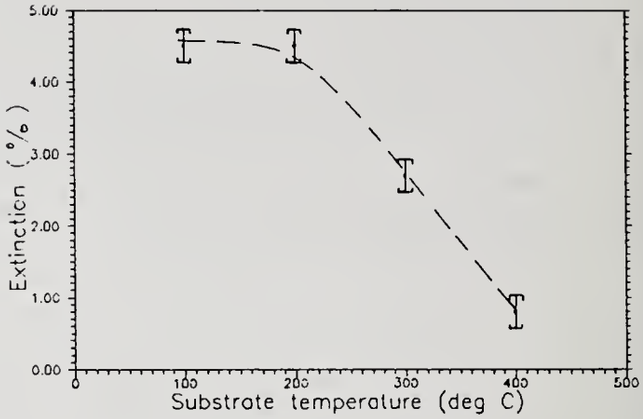

Fig. 3. Extinction losses at 200 nm versus substrate temperature in GdF_3 single layers (thickness: 2 QWOT at 200 nm).

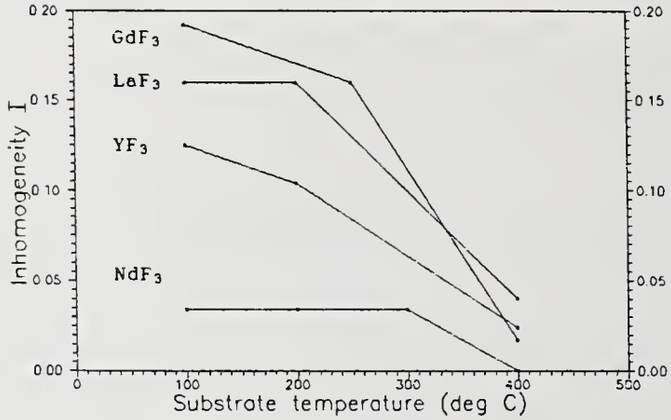

Fig. 4. Inhomogeneity I versus substrate temperature for the high-index fluoride materials.
$I:=(n_2-n_1)/n_2$;
n_2: film refractive index at the interface substrate-film;
n_1: film refractive index at the interface substrate-air.

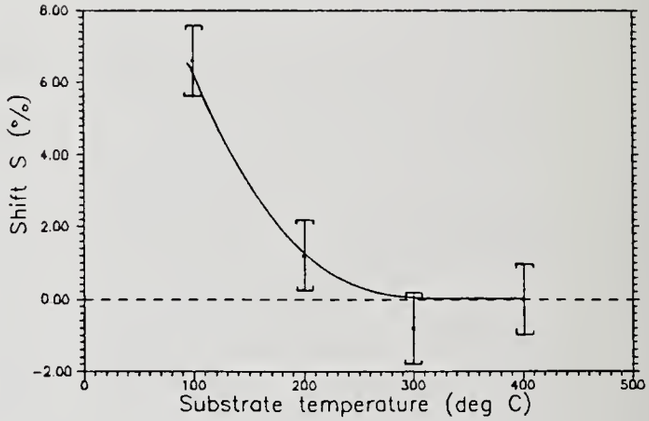

Fig. 5. Shift S of optical film thickness before/after venting with atmospheric air in 240 nm thick GdF_3 films.
S:={nd(after v.)-nd(before v.)}/nd

The evaluated refractive indices and extinction coefficients of fluoride layers deposited at 400 °C are shown in figures 6 and 7. - In references [3], [7] and [9], extinction coefficients of LaF_3 layers are given for wavelengths between 220 nm and 250 nm. The values given in [3] are almost identical to our results, while those from refs. [7] and [9] are somewhat higher. The extinction coefficients of MgF_2 and AlF_3 given in ref. [5] are comparable to our values; those from ref. [6] are higher by more than a factor of 2. In each case, the layers with relatively high losses had been deposited by electron beam evaporation. This is in accordance with our observations.

The damage thresholds of single layers are plotted in figure 8 together with their extinction coefficients. It can be seen that layers with high losses have low damage thresholds, and vice versa. Furthermore, it is observed that the damage thresholds of the high-index fluoride materials are much higher than those of the high-index oxide materials.

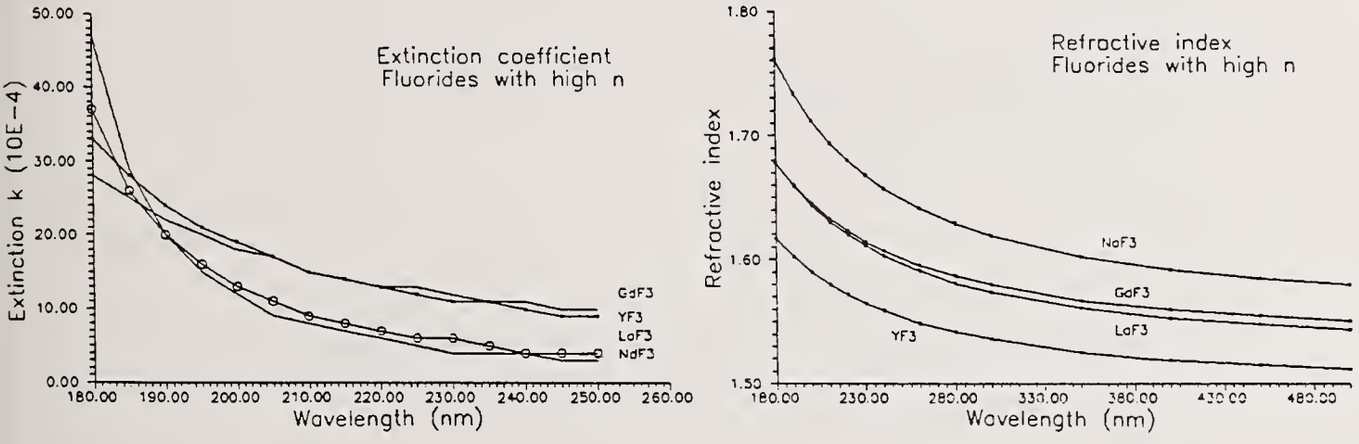

Fig. 6. Refractive indices and extinction coefficients of high-index fluoride single layers (thickness: about 400 nm) versus wavelength.

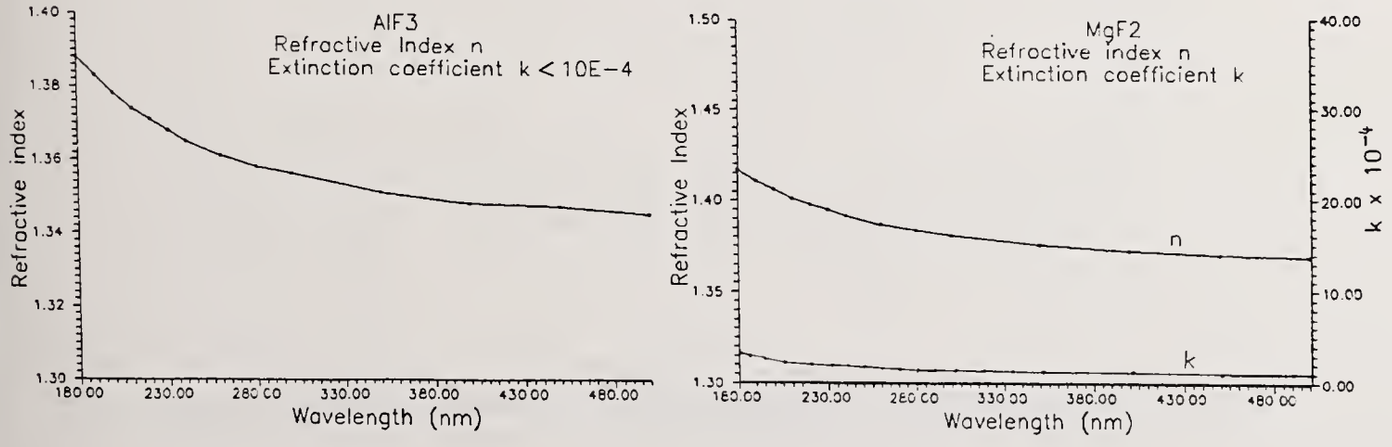

Fig. 7. Refractive indices and extinction coefficients of low-index fluoride single layers (thickness: about 400 nm) versus wavelength.

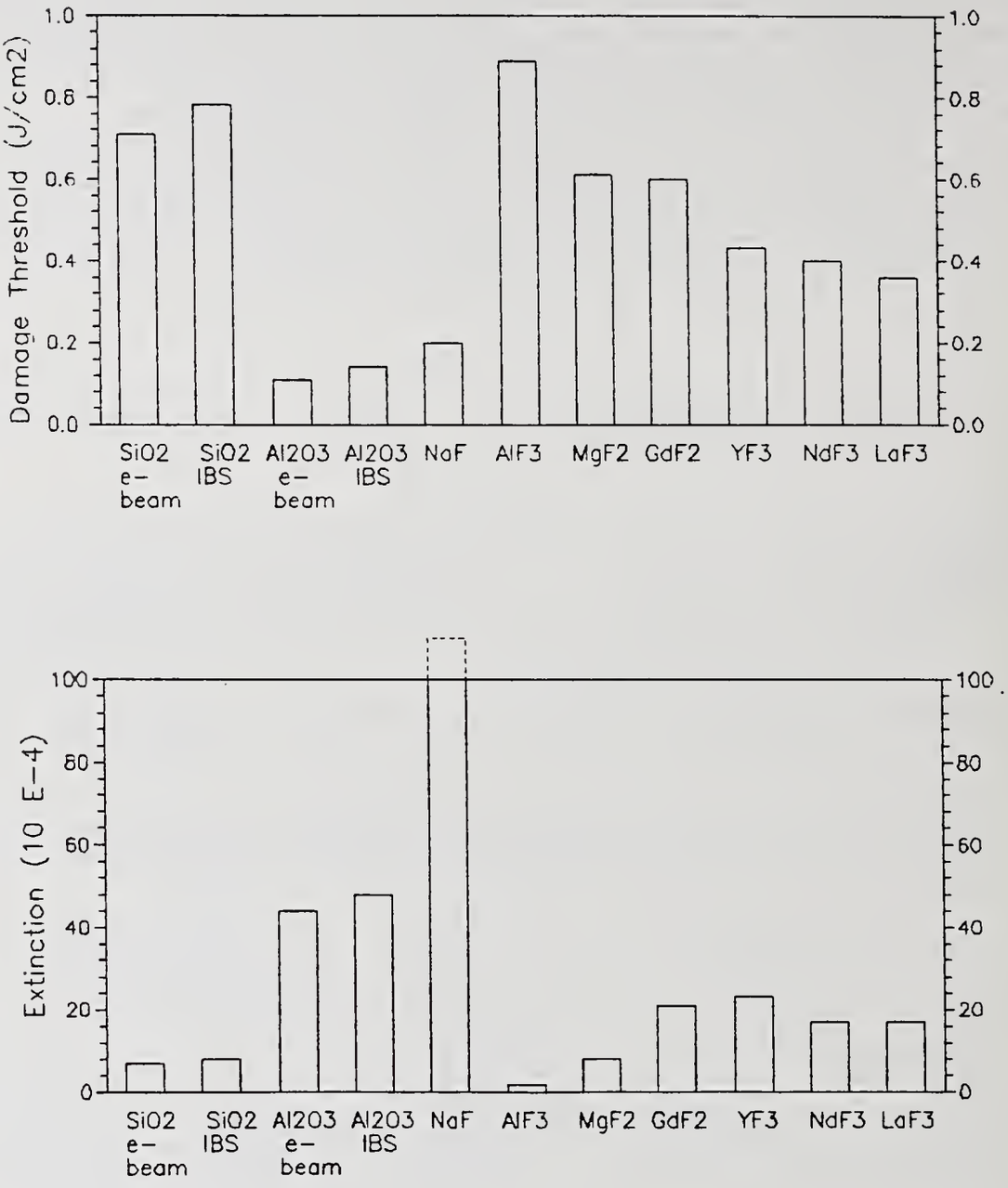

Fig. 8. Damage thresholds and extinction coefficients at 193 nm of single layers (thickness: typically 400 nm).

3.2 High-reflecting quarterwave stacks

From a series of appropriate material combinations (see table 3), high-reflecting quarterwave stacks were deposited. The systems (except the pure oxide systems) were deposited simultaneously onto heated substrates of fused silica, BK-7 glass, and calcium fluoride. The substrate temperature was between 300 °C and 400 °C. All systems (except the pure oxide systems) had cracks when deposited onto fused silica, but it was not difficult to deposit coatings without visible defects onto calcium fluoride and BK-7 substrates. These facts support the hypothesis that the internal stresses in fluoride coatings are strongly dependent on the thermal expansion coefficients of the substrates. - Figure 9 shows a typical transmittance and reflectance spectrum of a high reflecting multilayer stack.

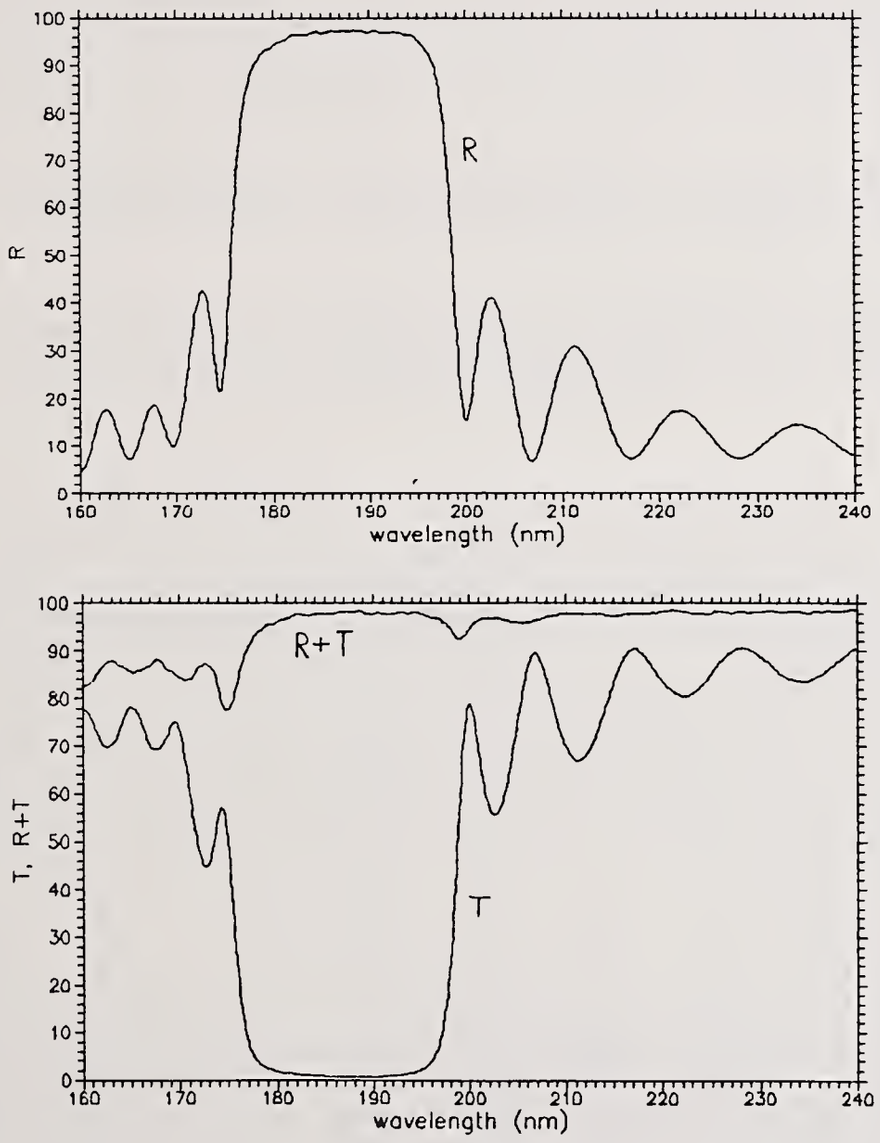

Fig. 9. Reflectivity (R), transmittance (T), and R+T versus wavelength of a high-reflecting quarterwave stack consisting of 41 layers NdF_3/AlF_3.

In table 3, some optical data of the HR-coatings are listed. The measured reflection and transmission values at the central wavelength are compared with theoretical values computed from the single layer data for n and k. A good agreement (differences less than 1 %) is observed in the combinations Al_2O_3/SiO_2, LaF_3/MgF_2, and LaF_3/AlF_3. In all other cases, however, the measured reflectivities are significantly lower than the computed ones. Two possible explanations can be given for this behaviour:

- Deviations of a real design from an ideal quarterwave stack may reduce its reflectivity (while the transmittance increases). This is observed in the systems made of LaF_3/AlF_3, GdF_3/AlF_3, NdF_3/AlF_3, and NdF_3/MgF_2.

- Interface losses which are relatively small in single layers, may contribute significantly to the total losses in a multilayer system. In this case, the reflectivity as well as the transmittance are smaller than the theoretical values. This may be caused either by the surface roughness of the substrates which is probably reproduced at each interface, or by interface defects caused by the chemical/physical properties of the layer materials.

In the deposited systems, both mechanisms seem to contribute significantly to the optical losses. Their better understanding as well as their reduction will be the subject of further investigations.

The damage thresholds of the HR coatings are shown in figure 10. It can be seen that the thresholds of the coatings with Al_2O_3 as the high-index material have relatively low damage thresholds. The best values were obtained with the systems made of NdF_3/MgF_2, LaF_3/AlF_3, and LaF_3/MgF_2. These results

Table 3. Optical data of the deposited multilayer HR stacks.

In some cases, the central wavelength L_c is different from 193 nm. For these coatings, the R and T data were taken at the individual values of L_c.

Materials	L_c (nm)	No. of layers	R_{exp} (%)	R_{th} (%)	T_{exp} (%)	T_{th} (%)	E_{dam} (J/cm²)
Al_2O_3/SiO_2	193	61	92.7	93.5	<0.1	0.2	0.26
Al_2O_3/SiO_2 (IBS)	193	41	93.5	94.6	0.2	0.2	
Al_2O_3/AlF_3	193	39	92.2	97.9	<0.1	<0.1	0.20
Al_2O_3/MgF_2	199	41	96.2	98.4	0.1	<0.1	0.07
NdF_3/AlF_3	193	41	97.6	99.0	0.3	<0.1	0.64
NdF_3/MgF_2	187	39	96.5	98.1	0.3	0.1	1.14
LaF_3/AlF_3	188	41	97.6	98.3	0.5	0.1	1.35
LaF_3/MgF_2	193	41	97.2	97.6	0.5	0.4	1.52
GdF_3/AlF_3	200	41	80.4	98.3	2.1	0.2	0.71

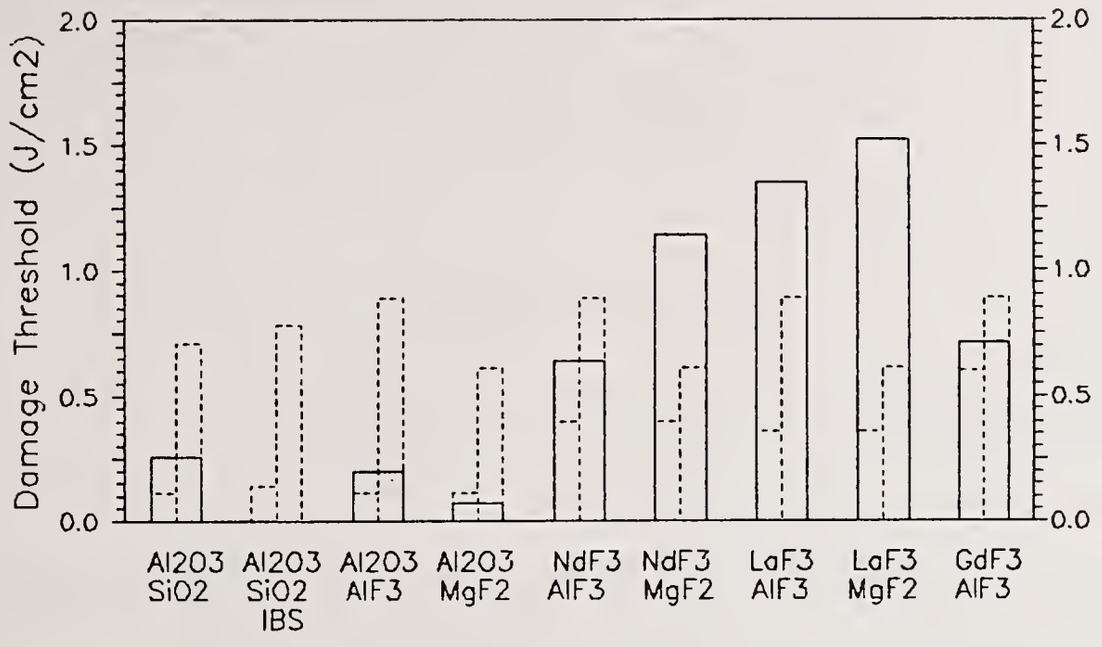

Fig. 10. Laser induced damage thresholds at 193 nm of high-reflecting multilayer stracks. - The dashed lines indicate the thresholds of the corresponding single layer results.

are consistent with the fact that the single layer damage thresholds of the high index fluoride materials are considerably higher than those of the alumina single layers. - The intermediate values for the NdF_3/AlF_3 and GdF_3/AlF_3 systems do not correlate with the single layer results. We suppose that they are caused by unfavorable deposition conditions. So it should be possible to get increased values by further optimization of the process parameters.

On the basis of the results described above, high-reflecting quarterwave stacks centered at 157 nm were deposited. They consisted of 41 layers of LaF_3/AlF_3 and had measured peak reflectivities of about 95 %. Their environmental resistance against the discharge gas of a F_2-excimer laser was tested by LAMBDA PHYSIK, Göttingen (FRG). A very good durability of the coatings has been observed there.

4. Conclusion

The purpose of the presented work has been to develop dielectric mirrors with low optical losses and high damage thresholds at 193 nm. Coatings of alumina and silica were deposited by electron beam evaporation and by ion beam sputtering. It has been shown that the IBS coatings had absorption losses and damage thresholds comparable to those of the e-beam coatings. The measured reflectivities and damage thresholds of the deposited high-reflecting quarterwave stacks were 93 % and 0.3 J/cm², respectively. - Quarterwave stacks consisting of alumina as high-index material and AlF_3 or MgF_2 as low-index material showed no significant improvements in comparison to the pure oxide coatings.

The highest reflectivities (97.6 %) and damage thresholds (1.5 J/cm²) were obtained with pure fluoride stacks. It has been shown that a decisive requirement for the production of high quality fluoride coatings is their deposition onto heated substrates. This, however, leads to high internal stresses which often cause cracks or other severe defects in the layers. While it seems to be impossible to deposit high reflecting fluoride stacks onto fused silica substrates heated up to 300 °C or even more, good results have been achieved with BK-7 and calcium fluoride substrates. This is attributed to their higher thermal expansion coefficients which tend to reduce the internal stresses in the coatings.

The measured peak reflectivities of the investigated fluoride stacks have values up to 97.6 % at 193 nm, and 95 % at 157 nm. On the other side, significantly higher values were calculated from single layer data on n and k. Presently, the reasons for these differences are not known exactly and will be a subject of further investigations.

5. Acknowledgements

We gratefully acknowledge the technical assistance of Mr A. Starke in the deposition of the ion-beam sputtered coatings, and the collaboration of Mr K. Mann (Laser-Laboratorium Göttingen e.V.) in the measurement of the damage thresholds. The work was supported by the BMFT (F&E-Vorhaben Nr. 13 N 5408).

6. References

[1] T. Znotins, SPIE 710, 55 (1986)
[2] K. Mann, to be published in: NIST (U.S) Spec. Publ. (1988)
[3] G. Hass, J.B. Ramsey and R. Thun, J. Opt. Soc. Am. 49, 2, 116 (1959)
[4] J.T. Cox, G. Hass and J.B. Ramsey, J. Physique 25, 250 (1964)
G. Hass, J.B. Ramsey and R. Thun, J. Opt. Soc. Am. 49, 2, 116 (1959)
[5] A.S. Barriere and A. Lachter, Appl. Opt. 16, 11, 2865 (1977)
[6] O.R. Wood II et al., Appl. Opt. 23, 20, 3644 (1984)
[7] D. Smith and P. Baumeister, Appl. Opt. 18, 1, 111 (1979)
[8] H.K. Pulker, Appl. Opt. 18, 12, 1969 (1979)
[9] F. Rainer et al., Appl. Opt. 24, 4, 496 (1985)
[10] Landolt-Börnstein, Physikalisch-chemische Tabellen, II, 912 (1923)
[11] E.D. Palik, Handbook of Optical Constants of Solids, Academic Press, Orlando (1985)
[12] A.J. Moses, Optical Materials Properties, in: Handbook of Electronic Materials Vol. 1, IFI/Plenum, New York (1971)
[13] A. Smakula, Einkristalle, Springer Verlag, Berlin (1962)
[14] Gmelin Handbuch der anorganischen Chemie, 8. Auflage, Teil C3, Springer Verlag, Berlin (1976)
[15] Melles-Grillot, Optics Guide 3, p.51 (1985)
[16] M.L. Scott, NBS Spec. Publ. 688, 329 (1983)
[17] J.S. Browder and S.S. Ballard, Appl. Opt. 16, 12, 3214 (1977)
[18] L.G. Van Uitert et al., Mat. Res. Bull. 12, 307 (1977)
[19] B. Pond et al., NIST Spec. Publ. 752, 410 (1986)
[20] T. Raj, J.S. Price and C.K. Carniglia, NBS Spec. Publ. 746, 325 (1985)
[21] C. K. Carniglia, J. Opt. Soc. Am. A3 (13), P40 (1986)

Angular Dependence of Thin-Film Dielectric Coating Damage Thresholds Revisited

J. D. Boyer, S. R. Foltyn, B.R. Mauro, and V. E. Sanders

Los Alamos National Laboratory
Chemical and Laser Science Division
Los Alamos, New Mexico 87545

Newnam et al. [1] reported experiments showing that the angular dependence of 351-nm laser damage thresholds in HfO_2/SiO_2 multilayer dielectric reflectors was much weaker than even the $1/\cos\theta$ expected from simple geometric fluence dilution. Several plausible explanations were suggested, but none were convincing. We propose a simple geometric model based on a cylindrical form for the coating defect responsible for damage initiation. We have measured 248-nm damage thresholds for bare fused silica, evaporated aluminium films, and HfO_2/SiO_2 and Al_2O_3/SiO_2 dielectric reflectors at angles out to 85°. The measured data agree well with our simple model.

Key words: angular dependence; aluminium oxide; coating defects; evaporated aluminium; fused silica; hafnium oxide; laser damage thresholds; multilayer dielectric reflectors; silicon dioxide.

1. Introduction

Before the experiments of Newnam et al. [1], it was believed that the laser damage thresholds for an S-plane polarized beam would increase with incident angle (θ) due to simple geometric fluence dilution and also due to the decrease in S-polarization electric field within the film. Geometric fluence dilution alone predicts a $1/\cos\theta$ increase in damage threshold and peak electric field calculations predicted an even more dramatic increase. Figure 1 compares the laser damage thresholds of HfO_2/SiO_2 reflectors reported in ref. 1 with a $1/\cos\theta$ angular dependence. If these results are general for multilayer dielectric reflectors, we have an opportunity to extend our understanding of laser induced damage.

We wished to verify the weak angular dependence and also utilize this behavior to gain further understanding of damage phenomena. In addition to verification, several other questions beg answers. Is this phenomena unique to HfO_2/SiO_2 multilayers or will it also occur in others such as Al_2O_3/SiO_2? Does it occur in bulk material such as fused silica? Is it sensitive to polarization? Of course the big question is, why do we not observe at least the simple $1/\cos\theta$ increase in laser damage thresholds with increasing incident angle. In this paper we propose an extension of geometric fluence dilution by considering the interaction of the diluted fluence with an absorbing defect. In addition we report experiment results which answer some of the questions raised above. The role of absorbing defects in laser damage has an observational basis [2] and additional support from theoretical work [3,4].

2. Proposed Model

A model which accounts only for geometric fluence dilution at the surface or within the bulk cannot account for the experimentally observed angular dependence of laser damage thresholds in some multilayer dielectric reflectors. It is apparent that the interaction cross-section does not decrease as rapidly as it would for a uniformly absorbing spherical defect. A simple extension of the uniformly absorbing spherical defect model is that which considers a uniformly absorbing cylindrical defect embedded in the film with the cylinder axis orientated normal to the film surface. Additional assumptions in this model are that the total energy which the defect must absorb for damage to occur is a constant independent of incident angle and that the cylinder height is the thickness of the film.

We now consider not only fluence at the film surface, but in the medium as well. Refraction modifies the beam geometric cross-section slightly. The following expression gives the ratio of the incident fluence to fluence in the medium of refractive index n as a function of angle.

$$B = \frac{\left(1 - \sin^2\theta / n^2\right)^{1/2}}{\cos\theta} \qquad (1)$$

This modification of the $1/\cos\theta$ behavior is modest (about twenty percent for HfO_2 at 85°) and is included primarily for completeness. A cylindrical defect of radius r embedded in a film of index n and thickness t presents a cross-sectional area

$$A = (2rt/n)\sin\theta + \pi r^2 \cos\theta \qquad (2)$$

to the incoming beam. As the film is tilted the fluence in the medium is diluted and the defect area is modified. The area may increase or decrease depending on the aspect ratio of the cylinder. The aspect ratio therefore becomes the chief free parameter of this model. When we impose the condition that the absorbed energy required to initiate damage at the defect is independent of angle, we arrive at an expression relating the damage threshold fluence at any angle $F(\theta)$ to the normal incidence damage threshold fluence F_0.

$$F(\theta) = \frac{F_O}{(2t/\pi nrB)\sin\theta + \cos\theta} \qquad (3)$$

This model is compared with the laser damage thresholds of HfO_2/SiO_2 reflectors from reference [1] in figure 2. We note that for small aspect ratios this model overestimates the increase in thresholds at large angles, but not so much as the $1/\cos\theta$ model. For large aspect ratios the present model predicts a decrease in damage thresholds over a broad range of angles before thresholds rise. Given the simplistic nature of many of our assumptions and also experimental uncertainties in the experimental results, this model is quite successful in explaining the weak angular dependence observed. We performed additional experimental tests of this model which comprise the remainder of this paper.

3. Test Procedures and parameters

The test setup and procedure was the standard multiple-shot used at Los Alamos and described in some detail previously.[1,5,7] Significant modifications include thin-film polarizers, a low intensity uv diagnostic illumination beam picked off before the beam attenuator, two-dimensional beam profile characterization generated by scanning a reticon array across the focal plane, computerized fluence measurement and control, and computerized data reduction. Table 1 below details specific test parameters.

Table 1. Damage Test Parameters

Wavelength:	248 nm
Pulselength:	23 ns
Repetition Rate:	50 Hz
Spot Size:	0.2 x 0.8 mm at normal inc.
Shots/Site:	100
Polarization Ratio:	1000:1 for S-polarization experiments

With the exception of the evaporated aluminium film test samples, the damage diagnostic was the telescope and video camera with the uv diagnostic beam for illumination. The fluence in the diagnostic beam was 5-10 mJ and too small to contribute to damage. The telescope was maintained at an angle of fifteen degrees with respect to the sample normal in an effort to maintain constant diagnostic sensitivity. For the aluminium films we found that visual examination with a low-power stereo microscope and white light provided the best reliability.

4. Test Samples

We tested four groups of samples. All samples were two inches in diameter. Bare evaporated aluminium films on BK7 were chosen to represent the case where damage is expected to occur at the surface due to bulk absorption. Fused silica(Corning 7940) was chosen to represent a non-absorbing bulk material. The HfO_2/SiO_2 multilayer reflectors were shipped by a coating vendor instead of the Al_2O_3/SiO_2 reflectors ordered. HfO_2 films are absorbing at 248 nm and do not represent defect dominated laser damage initiation. The HfO_2/SiO_2 reflectors were designed for seventy-five degree angle of incidence and coated in a single run. The S-plane polarized reflectance band for this design angle is broad enough that these coatings are good reflectors at all test angles. The Al_2O_3/SiO_2 multilayers were also designed for seventy-five degrees, but were coated in several coating runs. The Al_2O_3/SiO_2 multilayer reflectors are expected to behave at 248 nm as the HfO_2/SiO_2 reflectors did at 351 nm in ref. [1].

5. Experimental Results

The normalized laser damage threshold test results for the Corning 7940 fused silica are shown in figure 3. All samples are from the same lot and normal incidence damage thresholds were obtained by measurements on the 45 and 60 degree test samples. Most of these data are for unpolarized light and only the simple 1/cosÈ geometric fluence dilution enhancement of the damage threshold is expected. The damage thresholds obtained with unpolarized light follow a 1/cosθ scaling quite well. We also measured a few samples with S-polarized light to see if the stronger enhancement due to decreased peak electric field was present.[1] The results do indicate some additional enhancement, but the present data are insufficient to characterize this additional enhancement.

Figure 4 gives the normalized damage thresholds for evaporated aluminium on BK7. The normalization is the normal incidence damage threshold for this lot (0.12 J/cm^2). These results for the test with unpolarized light show at least the 1/cosθ geometric fluence dilution scaling. Tests with S-polarized light again show an additional enhancement. We do not understand why the scatter for the test with polarization is so much greater.

Figure 5 displays normalized damage thresholds for both the HfO_2/SiO_2 and Al_2O_3/SiO_2 multilayer reflectors. All of these results are for s-polarized light and the normalization is chosen to make the sixty degree points fall on the 1/cosθ curve for comparison. We immediately see that the HfO_2 damage thresholds follow the 1/cosÈ curve quite well at 248 nm. The Al_2O_3/SiO_2 damage threshold values, however, increase more slowly. We note that this implies that our normalization constant is probably too large and that the eighty five degree thresholds are more likely about four or five times greater than the normal incidence thresholds. Figure 6 compares the multilayer dielectric damage thresholds with spherical and cylindrical defect models. Here the Al_2O_3/SiO_2 damage thresholds are normalized so that the value at sixty degrees agrees with our model and chosen aspect ratio and the average values at each angle are plotted for clarity.

6. Summary

We have verified that multilayer dielectric reflector laser damage thresholds may not scale with simple geometric fluence dilution at the film surface. Figure 6 shows that the Al_2O_3/SiO_2 laser damage thresholds scale less rapidly than 1/cosθ and are in good agreement with our cylindrical model with r/t = 0.4. Our model and assumptions would imply a defect radius of about 10 nm and that melting of the defect would require absorption of about one percent of the incident energy. The results for aluminum films, bare fused silica, and the HfO_2/SiO_2 multilayers which are absorbing at 248 nm do scale with geometric fluence dilution at the sample surface. For the aluminium and HfO_2/SiO_2 multilayers, it is probable that bulk absorption is more important than local defects. The 1/cosθ scaling of the fused silica damage thresholds implies that either the defects are more spherical or that the energy-absorption mechanism is different than in multilayer dielectric films.

7. References

[1] Newnam, Brian E.; Foltyn, Stephen R.; Gill, Dennis H.; Jolin, L. John Angular dependence of multilayer-reflector damage thresholds. Nat. Bur. Stand. (U.S.) Spec. Publ. 727; 1984. 342-351.

[2] Gorshkov, B. G.; Danieliko, Y. K.; Nikolaev, U. N.; and Sidorin, A. V. Sov. J. Quant. Elect. 13 (3); 388; 1983.

[3] Lange, M. R.; McIver, J. K.; and Guenther, Arthur H. An initial study of: The inclusion model for repetitively pulsed laser damage. Nat. Bur. Stand. (U.S.) Spec. Publ. 727; 1984. 382-393.

[4] Becker, W.; McIver, J. K.; and Guenther, A. H. Initiation of laser induced damage by small metallic particles. Nat. Bur. Stand. U.S.) Spec. Publ. 752; 1986. 603-610.

[5] Newnam, B. E.; Foltyn, S. R.; Jolin, L. J.; Carniglia, C. K. Multiple-shot ultraviolet laser damage resistance of nonquarterwave reflector designs for 248 nm. Nat. Bur. Stand.(U.S.) Spec. Publ. 638; 1983. 363-371.

[6] Foltyn, S. R.; Jolin, L. J.; Newnam, B. E. Progress in ultraviolet damage testing at Los Alamos. Nat. Bur. Stand.(U.S.) Spec. Publ. 669; 1984. 266-273.

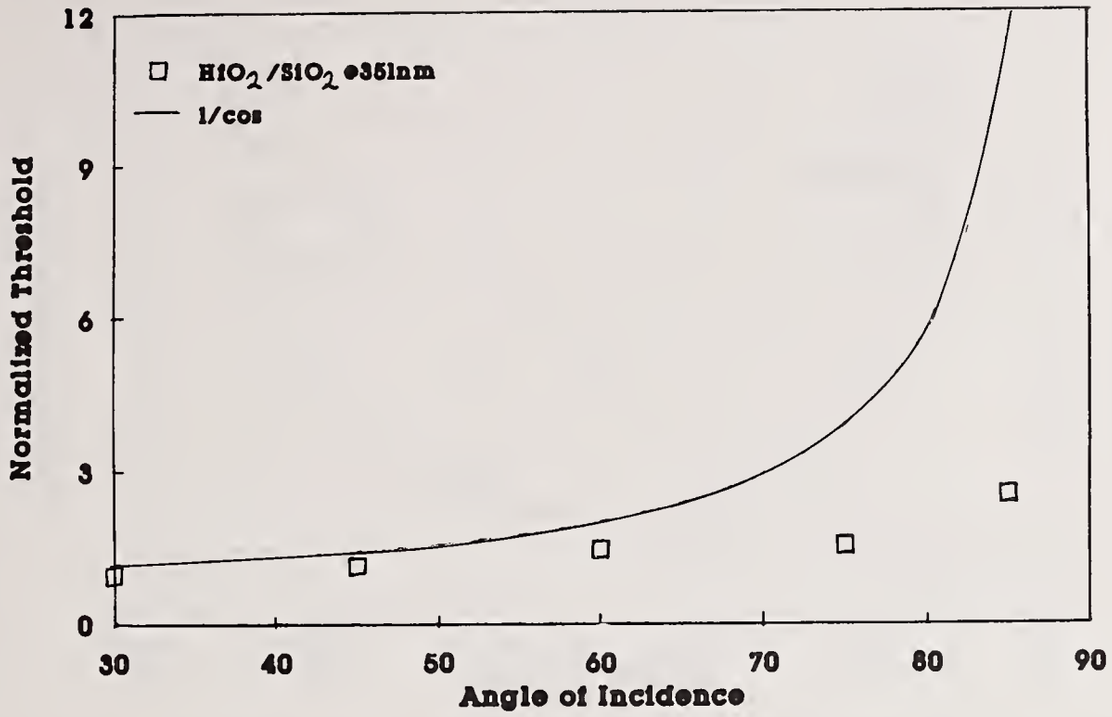

Figure 1. Comparison of the experimental damage threshold values from reference [1] with the $1/\cos\theta$ expected from simple geometric scaling

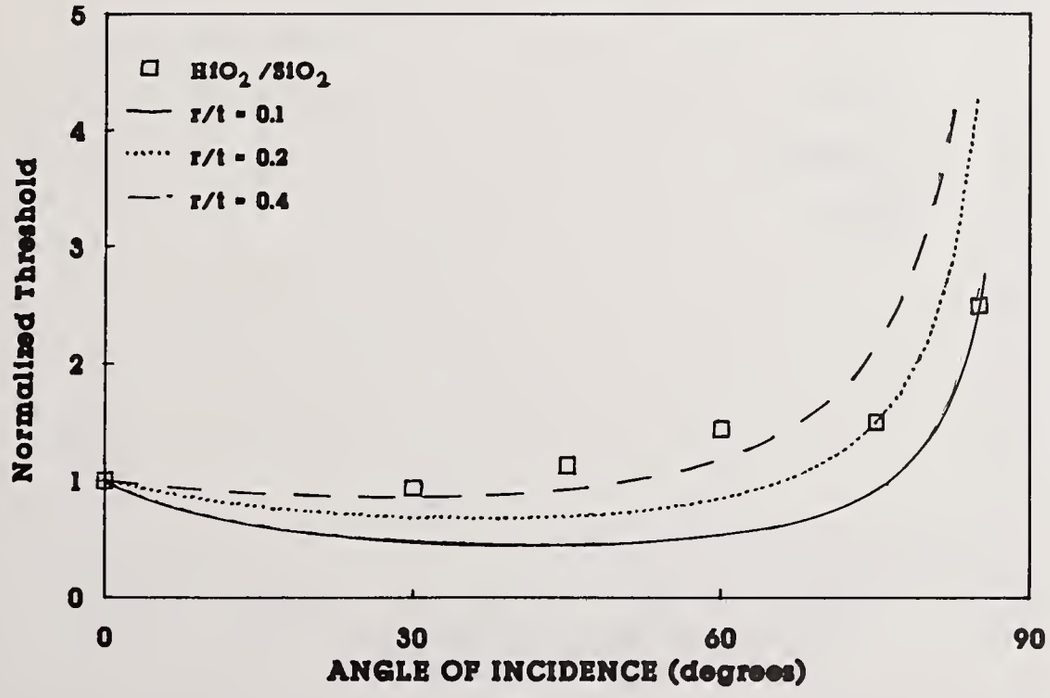

Figure 2. Comparison of the experimental damage threshold values from reference [1] with the cylindrical defect extension to simple geometric scaling

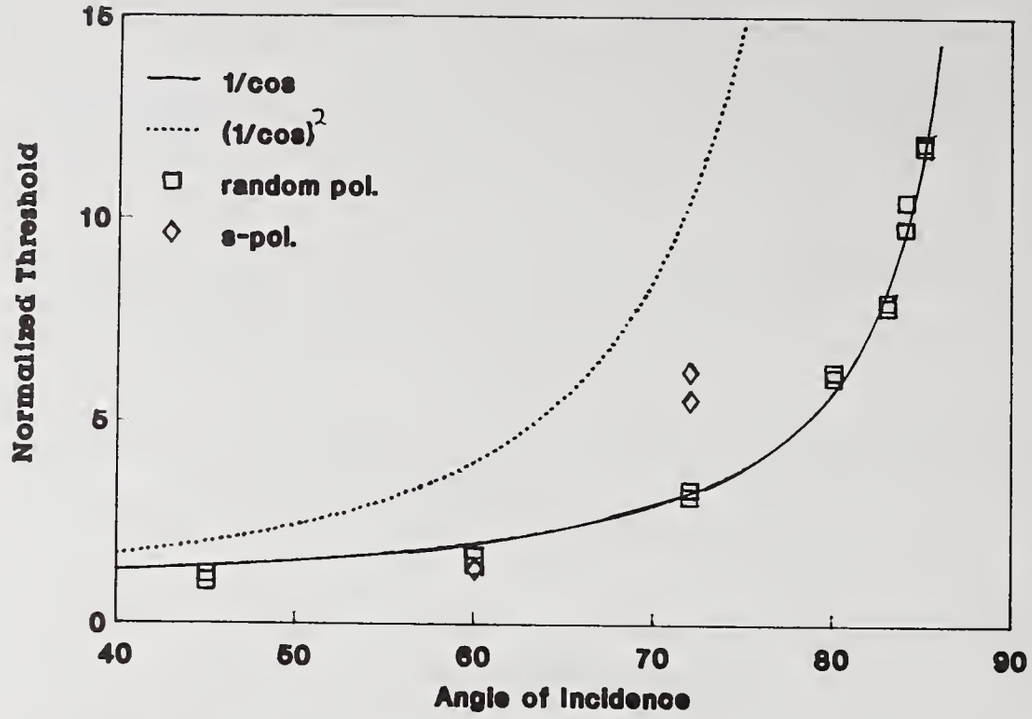

Figure 3. Laser damage threshold values for uncoated Corning 7940 fused silica with random polarization scale as 1/cosθ. The S-polarization results are further enhanced.

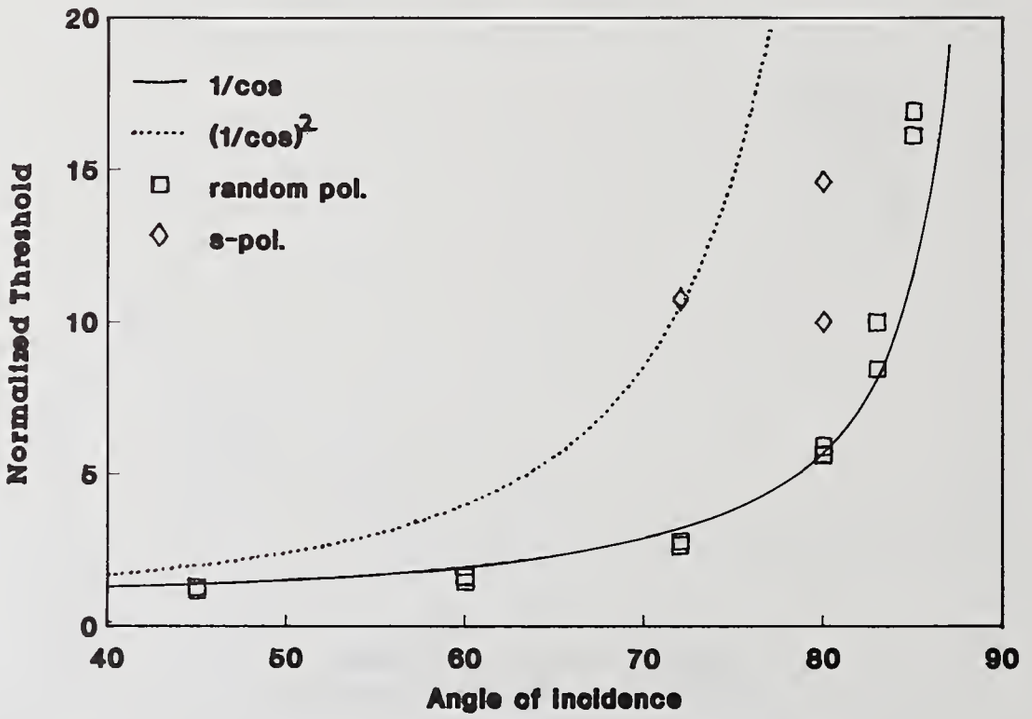

Figure 4. Laser damage threshold values of evaporated aluminium with random polarization scale as 1/cosθ. The thresholds for the S-polarization results are enhanced more than the uncoated fused silica.

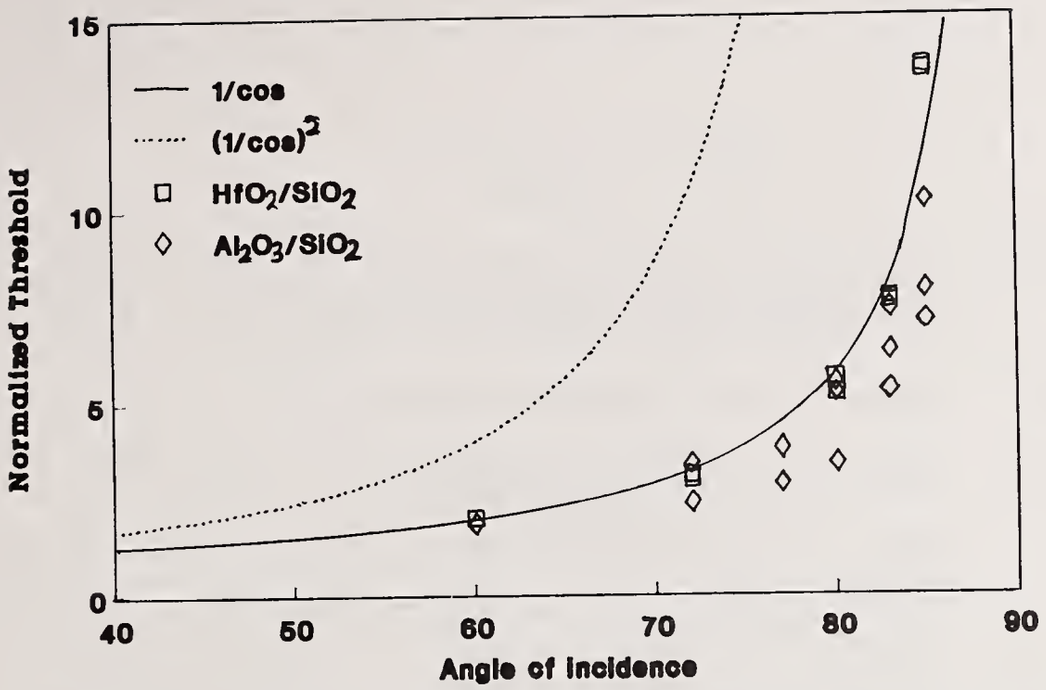

Figure 5. The laser damage threshold values for HfO_2/SiO_2 and Al_2O_3/SiO_2 multilayer dielectric reflectors are compared with $1/\cos\theta$ and $1/\cos^2\theta$.

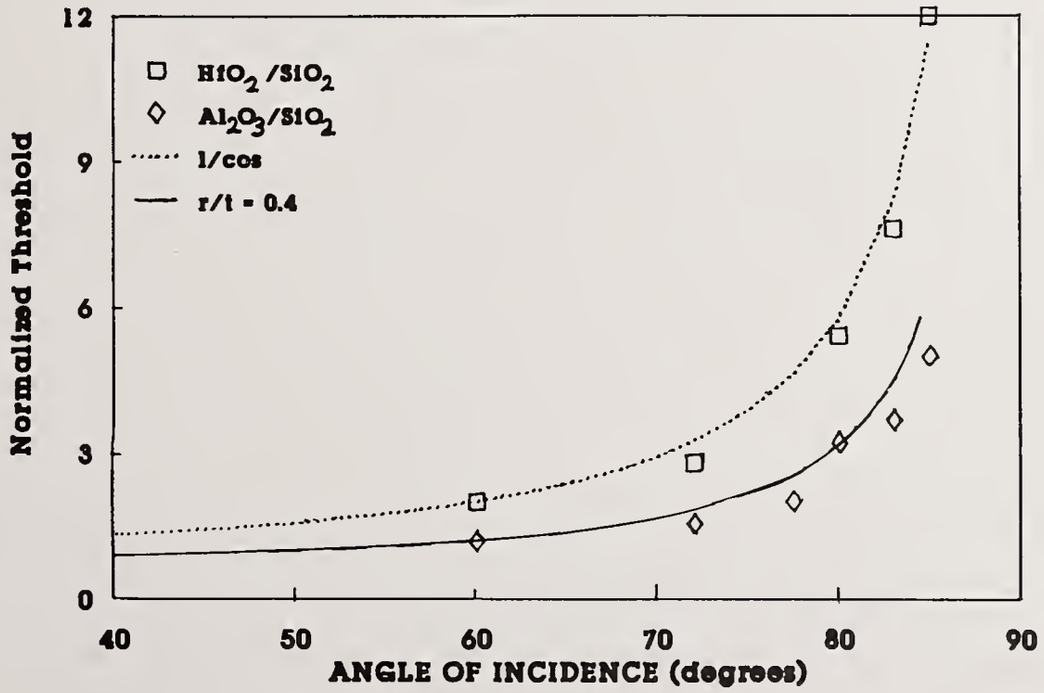

Figure 6. The laser damage threshold values for HfO_2/SiO_2 and Al_2O_3/SiO_2 multilayer dielectric reflectors are compared with $1/\cos\theta$ and the cylindrical defect model with $r/t = 0.4$.

COMMENTS

Comments: Several years ago, when the defect-initiated damage modeling was done, McIver and his people looked at the cylindrical impurities and, in fact, came up to the same conclusion you have, namely, that it was the aspect ration that was important.

Answer: Thank you, I wasn't aware of that work.

Question: Do you expect any dependence on pulse length, width, shape? It looked like you were doing everything for 23 nanoseconds.

Answer: Right. The pulse-length dependence of damage thresholds, I think, is entirely another question. And I do expect something. I think results have shown that you can get a pulse length dependence all the way from a basically nonpulse-length dependence on out to a square root of pulse-length dependence. And which you'll see depends on the particular wavelength and experimental setup.

MANUSCRIPT NOT RECEIVED

Pulse-width Dependence of Optical Coating Damage at 1052 nm

K. Yoshida, S. Ikunishi, H. Yoshida, Y. Kato, and S. Nakai

Institute of Laser Engineering
Osaka University
Suita, Osaka 565
Japan

ABSTRACT

Pulse-width dependence of optical coating damages at 1053 nm laser wavelength is studied. Quarterwave-thick single layer films of high-index materials of Al_2O_3, ZrO_2 and TiO_2, and low-index materials of MgF_2 and SiO_2 were tested. Damage thresholds of the MgF_2 and SiO_2 films follow the square root dependence on the pulse-width τ ($\sqrt{\tau}$ scaling) over the pulse widths of 0.35-90 ns. Although the damage thresholds of the Al_2O_3, ZrO_2 and TiO_2 films followed the $\sqrt{\tau}$ scaling from 0.35 to 1 ns, they become independent of the pulse-width for the pulse-widths longer than 6 ns. That is, the pulse-width dependence of the damage threshold is determined by the absorption property of the coating layer, which controls the damage mechanism.

Manuscript received
7-9-90

Damage Resistant Optical Coatings Prepared Using High Temperature, Plasma Chemical-Vapor-Deposition*

J.H. Campbell, J.L. Emmett, R.M. Brusasco and F. Rainer
University of California
Lawrence Livermore National Laboratory
P.O. Box 5508, L-490
Livermore, California 94550

R. Th. Kersten, V. Paquet and H. -W. Etzkorn
Schott Glaswerke
D-6500 Mainz
West Germany

Multilayer dielectric optical coatings, nominally consisting of 1000 or more optical-quarterwave layers, have been prepared by reacting $SiCl_4$ and a halogenated dopant (e.g. $GeCl_4$) with O_2 in a microwave-driven plasma. The dopant concentration is such that the index difference (Δn) between adjacent quarterwave layers is about 0.02 or less. The deposition is carried out at high substrate temperatures (850 to 1100°C) producing a fully dense, fused silica coating. Surface damage thresholds of high reflectivity (HR) coatings prepared by this plasma process are comparable to those for fused silica. For example, at 1.06 μm and 16-ns we measure surface damage thresholds greater than 45 J/cm^2 compared to about 45-60 J/cm^2 for super-polished optical fused silica.

I. Introduction

The output of high-peak-power lasers is often limited by the damage threshold of the multi-layer dielectric coatings that are deposited on various optical elements in the system. In this paper we discuss the results of experiments using high temperature (T > 850°C) plasma-assisted chemical vapor deposition to produce damage resistant optical coatings. The coatings typically consist of several thousand quarter-wave layers of fused SiO_2 lightly doped with a glass network modifier or network former (e.g. GeO_2, F) to give an interlayer index variation.

Currently, most multilayer dielectric optical coatings used in high power laser systems are prepared using

---

* Work performed under the auspices of the U.S. Department of Energy by Lawrence Livermore National Laboratory under Contract No. W-7405-Eng-48.

physical vapor deposition techniques (e.g. e-beam evaporation) and typically consist of a stack of alternating layers of metal oxides and/or fluorides. Although the exact mechanism for laser induced damage in these coatings is still widely debated, there are a number of inherent weaknesses in the deposited structure that have been proposed to lead to optical damage. These include (but are not limited to) the following:

- Thermal-mechanical and/or chemical incompatibility between layers [1].
- Bulk and localized regions of high optical absorption (often $>10^5$ times the natural, pure material) due to process-induced defects in the coating materials [2,3,6,7].
- Incorporation of light absorbing particulates (e.g. dust and other contaminates) in the coating during deposition [4-9].
- The presence of voids or microstructural defects formed in the coating layer that enhance the local electric field [8,9].

To achieve high damage thresholds in an optical coating one would like to develop a coating and an associated deposition technique that is not plagued by the above weaknesses. It is well known that optical fused-silica produced by a high temperature CVD process, such as that used by Corning, has high thresholds for both surface and bulk laser damage [10-12]. In the Corning CVD process, SiO_2 is formed by vapor-phase hydrolysis of $SiCl_4$ and then deposited layer-upon-layer until a boule of SiO_2 is formed [13]. Thus, in a general sense, the SiO_2 is a monolithic CVD "coating".

We believe the excellent damage resistance of optical fused silica is because it lacks the potential damage causing weaknesses outlined above. First, the material is compositionally uniform. Consequently there are no distinct material interfaces with thermal-mechanical or chemical incompatibility. Second, the chemical stoichiometry is uniformly controlled throughout the material by use of high-temperature, oxidizing deposition conditions. Third, any dust, dirt or other particulate contamination is fully oxidized and either dissolved directly in the glass or incorporated as an insigificant, low absorption, scattering center. Finally, the fused silica is a fully dense, amorphous body without the high density of microstructural defects that are often produced by conventional physical vapor deposition processes.

In principle then, if one could prepare an optical coating via the CVD technology used to prepare fused silica, it should have excellent resistance to laser damage. Figure 1 illustrates one such coating concept. In brief, various low concentrations of either network modifiers or network formers are added to alternating layers of the silica glass matrix. Doping the SiO_2 with these materials produces the index difference needed to achieve the desired optical characteristics, yet the dopant concentration is low enough that the bulk SiO_2 glass remains largely unaltered. Thus there are no distinct material interfaces. The coating is produced under the same high temperature (>1000°C), oxidizing conditions used for preparing bulk SiO_2 and therefore is amorphous, fully dense, with very low optical absorption and essentially defect-free. Since the dopant concentration is low, a large number of layers are required to produce the desired optical effect. This is shown in figure 2 where predicted reflectance curves are shown for multilayer coatings containing small dopant concentrations (< 10%) of GeO_2, F, or B_2O_3 in the silica matrix. In summary then, the coating is a silicate glass monolith comprised of several thousand alternating optical-quarterwave layers of slightly different glass composition (i.e. refractive index).

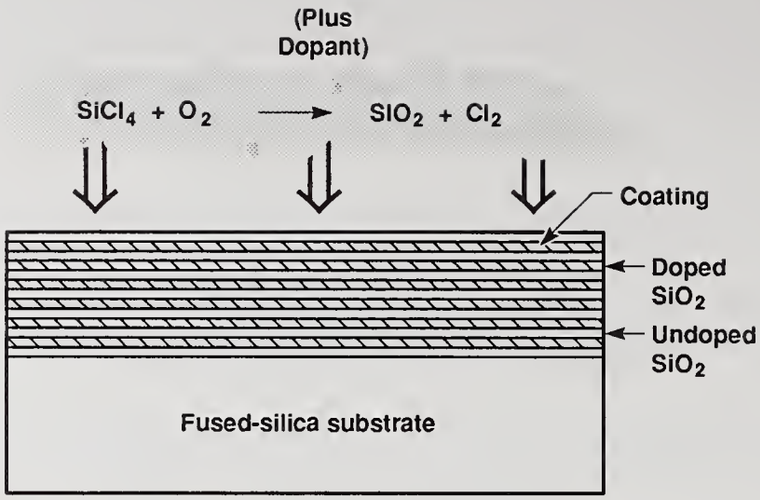

Figure 1. Conceptual view of multilayer optical coatings prepared by chemical vapor deposition of alternating layers of doped and undoped fused SiO_2.

2. Selection of a CVD coating process

The CVD processes used to prepare the preforms for silica optical fiber fabrication can, in principle, also be used to prepare optical coatings such as those described above. Typical fiber-preform processes operate at high temperatures under highly oxidizing conditions and at high deposition rates. Dopants are usually added to achieve variable refractive index control for the required optical fiber performance.

The optical fiber CVD processes can generally be broken down into two types. One is the so-called "soot" process in which the silica precursor ($SiCl_4$) is reacted thermally with O_2 to produce fine (0.1 to 1.0 μm) particles of SiO_2; these particles then deposit on the substrate wall and are subsequently sintered to a fully dense, amorphous SiO_2 monolith [14-16]. The second general deposition process is plasma driven. In this case the reaction of the precursor and O_2 are driven by a microwave or rf initiated plasma [17-19].

The plasma processes have the advantage that the thickness of a single deposition layer can be controlled to the angstrom level. In contrast, the layer thickness resolution of the "soot" process is at best several SiO_2 particle-diameters (a few tenths of a micron) and thus impractical for deposition of typical quarter-wave thick layers used in optical coatings.

Of the current plasma processes, the one having the best thickness control at high deposition rate is the Schott plasma-impulse chemical vapor deposition process (PICVD) [19-21]. Control of the deposition layer thickness (and hence refractive index profile) to within a few angstroms is possible while at the same time achieving deposition rates of a few microns per minute. This is the process we have selected for demonstration of the optical coating concept outlined here. The coatings have been deposited on the inside of a 1.7 cm id SiO_2 tube since that is the configuration of the presently available plasma CVD systems. Work is underway to adapt this process to large planar substrates.

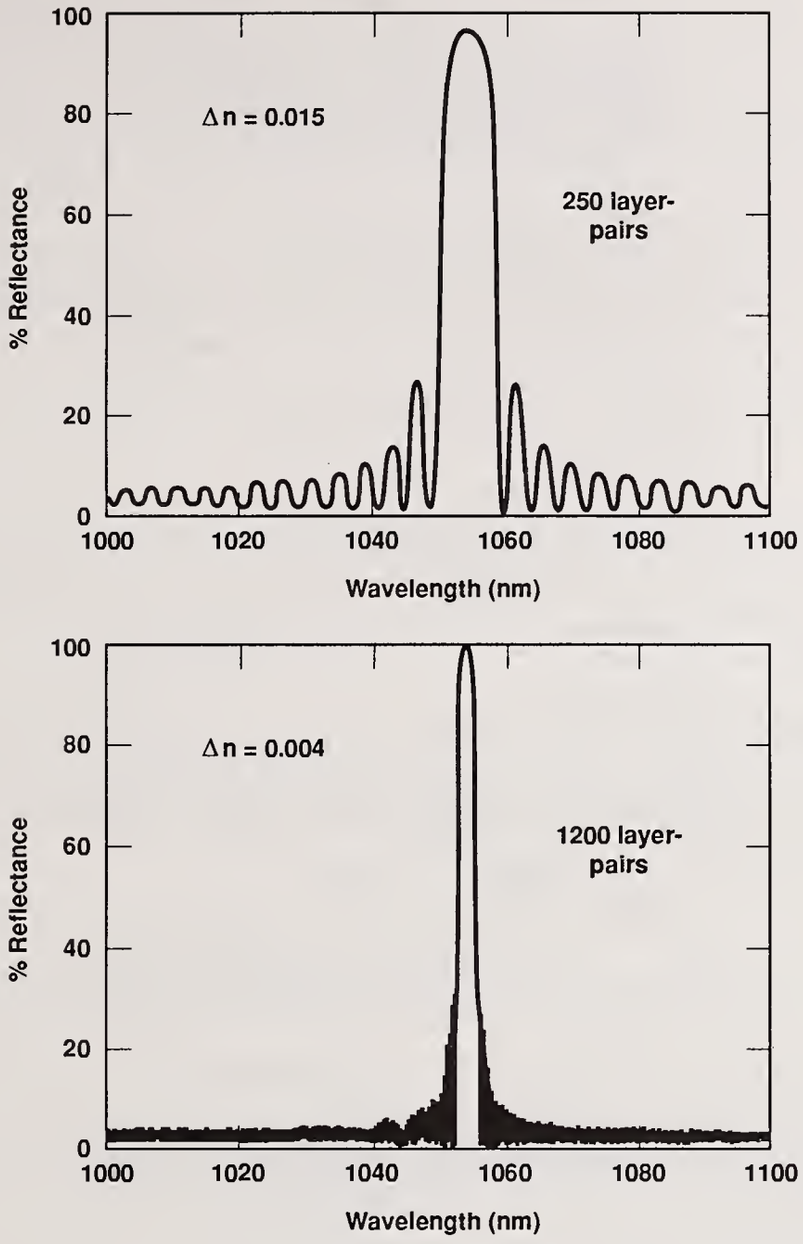

Figure 2. Examples of expected optical performance calculated for two HR coatings comprised of (a) 500 and (b) 2400 alternating quarterwave layers of SiO_2 and SiO_2 containing small additions of a glass network modifier. The index difference between quarterwave layers is 0.015 and 0.004, respectively.

3. Preparation of Plasma CVD Coatings

The optical coatings were prepared using the plasma-impulse-CVD process developed by Schott Glaswerke. Further details of the process are described elsewhere [19-21]. The PICVD process is shown schematically in figure 3. It consists of three major components: a gas supply system, the deposition unit and vacuum pump. All three units are under computer control. Reactant gases are continuously supplied to a 1.7 cm id x 120 cm longSiO_2 glass tube which serves as both the reaction vessel and deposition substrate. Immediately surrounding the quartz tube is a coaxially positioned microwave cavity. This entire assembly is located in a tubular furnace that typically heats the substrate to 800-1100°C.

The output from a 2.45 GHz magnetron, triggered by a pulse generator, is used to drive the deposition process. The deposition process consists of a sequence of four steps (fig. 4). First the SiO_2 tube is filled with gas reactants (e.g. $SiCl_4$, O_2), second, plasma is ignited and sustained by a pulse from the magnetron. The plasma ignition occurs at the end of a short inner tube and the plasma then serves as a lossy inner conductor that enables the coaxial propagation of the microwave down the length of the outer conductor. In the next step the plasma ignited inside the tube drives a gas-phase reaction between $SiCl_4$ and O_2 and ultimately produces a thin, amorphous deposit on the tube wall. Previous studies have shown that there is gas phase deposition of SiO at the walls followed by heterogenous reaction with O_2 forming SiO_2 (versus particulate formation and then deposition). Therefore, excellent thickness coating control is possible by controlling the reactant gas composition and pressure. The final step of the process consists of pumping out product gas (e.g. Cl_2 and unreacted O_2) and since the flow is continuous, also simultaneously refilling the tube. Experience has shown that the deposition efficiency is nearly 100%.

Typical deposition conditions used for these experiments are given in Table 1. Deposition rates were generally about 2 μm/min over the length of the tube (~50 cm); this corresponds to single-pulse layer thickness of about 30Å at the nominal 100 Hz pulse repetition rate. The substrate temperature was generally kept about 1000°C to reduce inclusion of product gases in the film and enhance the film quality.

The multilayer optical coating was prepared by periodically mixing SiO_2 precursors gas (i.e. $SiCl_4$) with a halogenated dopant gas. Dopant gases where chosen that are known to give stable silicate glasses and produce the desired index change without producing unacceptable thermomechanical stresses (fig.5). In most cases, co-dopants of Ge and F were used to produce the desired index change.

Table 1: Typical deposition conditions for preparing multilayer doped SiO_2 coating using Schott's PICVD process.

Substrate:	SiO_2, Heralux WG
Substrate geometry	
diameter:	1.7 cm ID, 2.0 cm OD
length:	> 50 cm
Substrate temperature:	850 to 1100°C
Pressure:	3 mbar
O_2 mass flow:	200 sccm
$SiCl_4$ mass flow:	50 sccm
Dopant flow:	< 10 sccm
Dopants:	GeO_2, F
Dopant Source:	$GeCl_4$, CCl_2F_2
Pulsed plasma repetition rate:	100 Hz
Microwave frequency:	2.45 GHz
Microwave power (avg.):	0.6 kW
Deposition rate:	~ 2 μm/min.
Incremental thickness:	~ 30 Å
Index profile:	sinusoidal or square wave
Quarterwave thickness: (at 1.06 μm)	1800 Å

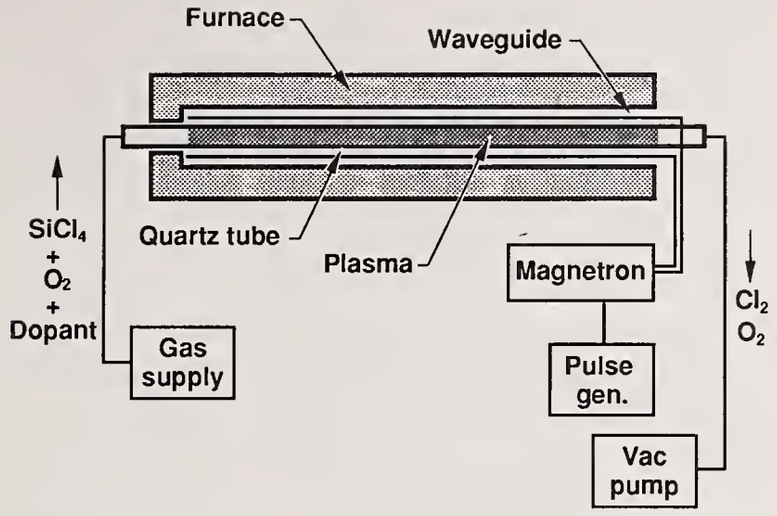

Figure 3. Schematic of the PICVD deposition system.

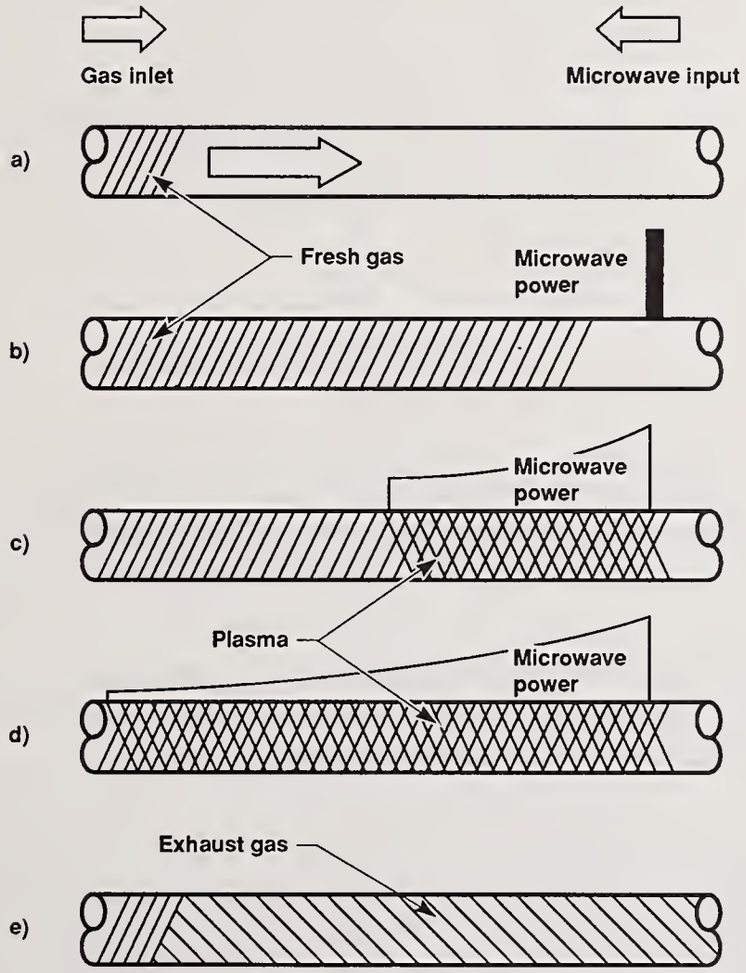

Figure 4. Four main phases of the PICVD deposition process on the inside of a tubular substrate: (a) filling reactant gases (eg. $SiCl_4 + O_2$), (b) ignition, (c and d) propagation of the plasma causing reaction and then deposition of the gas phase products, and (e) exhaust of residual gas to the pump system.

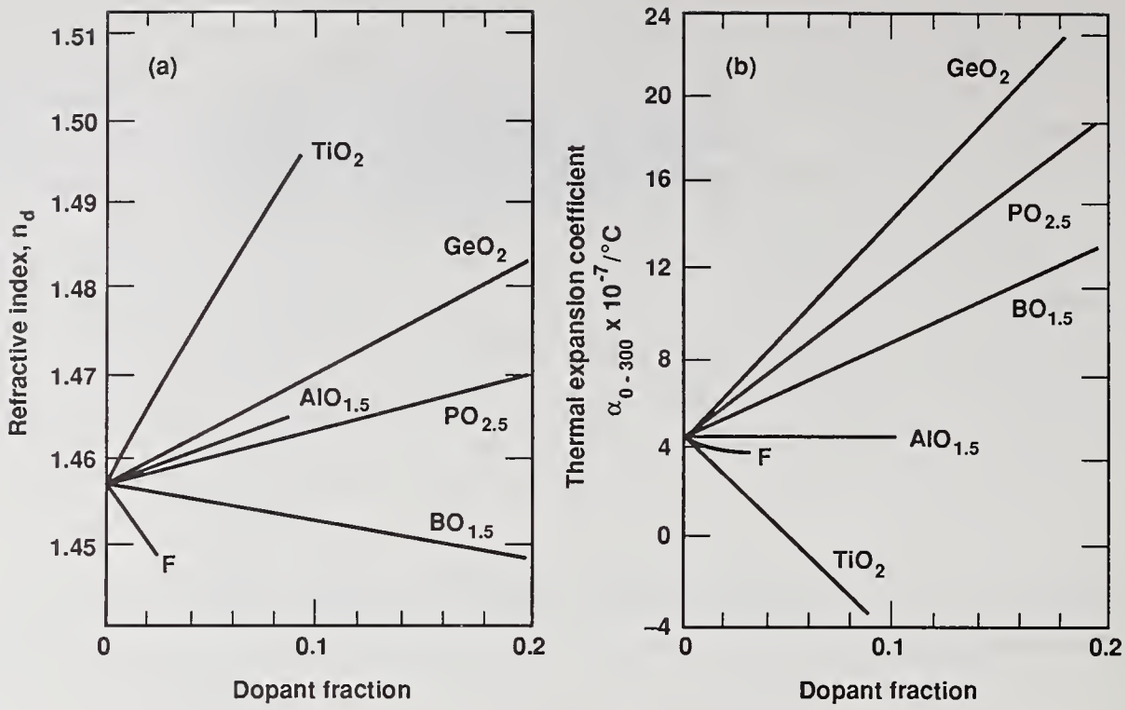

Figure 5. Variation of (a) refractive index and (b) thermal expansion coefficient vs. dopant ion concentration in SiO_2. The data are from ref. 22.

4. Characterization of Optical Coatings Prepared by PICVD

4.1 Optical Characterization

The measured transmission of two typical PICVD coatings is shown in fig. 6. The peaks in the curves (i.e. regions of low transmission) indicate reflection bands. The first coating (fig. 6a) consists of approximately 1000 optical quarterwave layers with a sinusoidal index variation and a maximum Δn of about 0.01 between adjacent layers. The layer thickness was adjusted to give a single maximum reflectance at 1064 nm. The shoulder on the short-wavelength side is due to small process variabilities. In general the measured bandwidth of the PICVD coatings is about 2-3 times the theoretical value. This suggests that with future improvement in process control, narrower bandwidth coatings with fewer layers should be possible.

The coating shown in fig. 6b consists of about 5000 quarterwave layers with roughly every 1000 layers designed to reflect a different wavelength (hence 5 reflectance maxima). In this case, the tail on the short-wavelength side is due to bulk absorption by the glass matrix and is not due to process variability. Since the deposition process is fully automated it is possible to create coatings having any number of peaks either fully or partially reflecting. Moreover by closely grouping the peaks such that they overlap, reflective coatings of any arbitrary bandwidth can be achieved. In principle a "white light" HR coating (i.e. a coating reflective over the entire visible region) could be fabricated with this technology.

Note that the use of a sinusoidal index profile produces a single reflectance band. Consequently reflections at harmonic wavelength are strongly suppressed except for the small amount ($\leq 5\%$) introduced by small process variations.

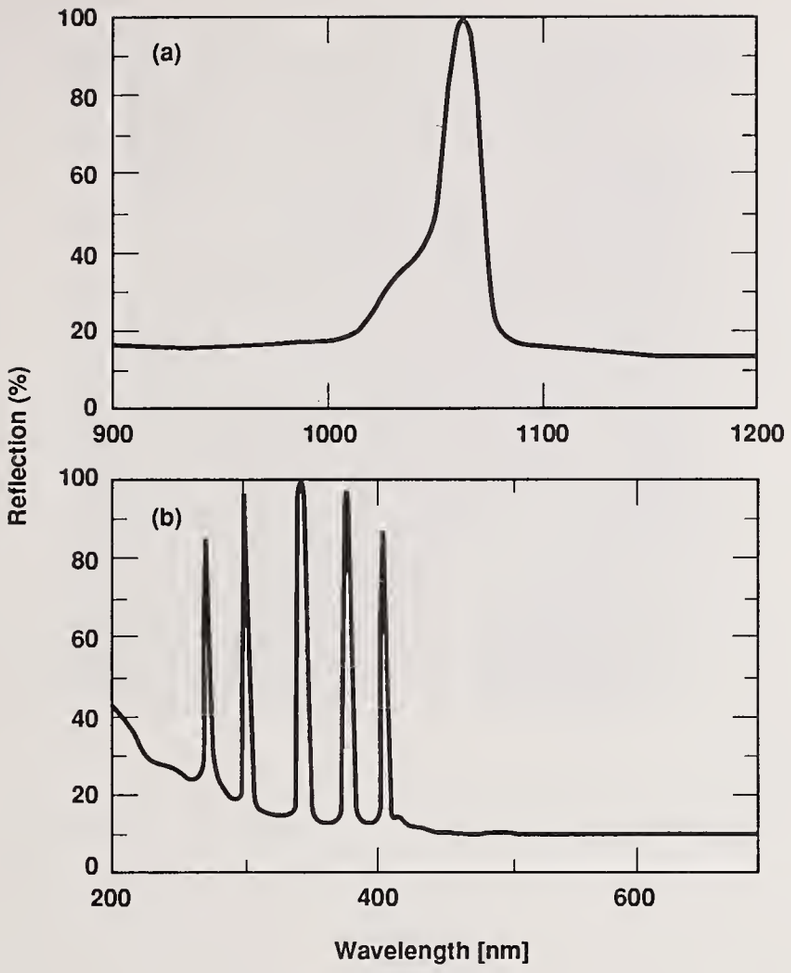

Figure 6. Measured transmission versus wavelength for (a) 1000 and (b) 5000 quarter-wave-layer optical coatings prepared by the PICVD process. The dopant profile was sinusoidal in both cases with the amplitude of the index variation about 0.01.

The overall absorption loss in optical thin films produced by the PICVD process is near the theoretical limit of that expected for the pure bulk material. The reason for this is clear; these coatings were made using the same deposition process used to prepare the full-density optical preforms used to fabricate optical fibers. The reported loss spectrum for the GeO_2-doped SiO_2 material used to prepare these coatings is shown in fig. 7; the measurements were made on a fiber drawn from the material. Note that the loss at 1.0 μm is approximately 1 dB/km corresponding to ~ 10^{-6} cm^{-1}. This absorption loss is about 5 orders of magnitude lower than that for high quality thin-films produced by current e-beam evaporation processes (fig. 8).

4.2 Compositional and Structural Characterization

Figure 9 is a SEM photograph showing the cross-section of a portion of an approximately 2000-layer coating designed to reflect at 1064 nm. The line-to-line spacing (corresponding to two quarterwaves) is about 365 nm. The deposited film is fully dense showing no visible defects.

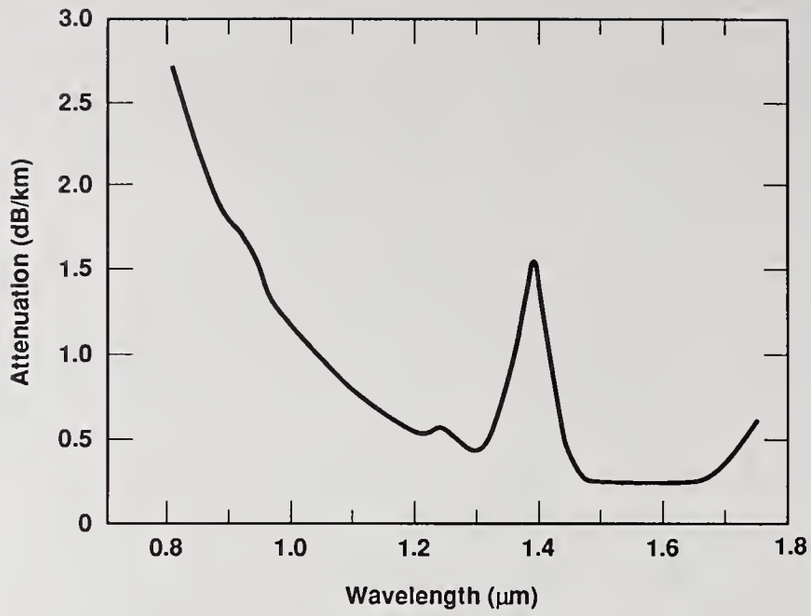

Figure 7. Loss spectrum for a Ge-doped, graded index SiO_2 fiber drawn from a preform made by the PICVD process (see ref. 19).

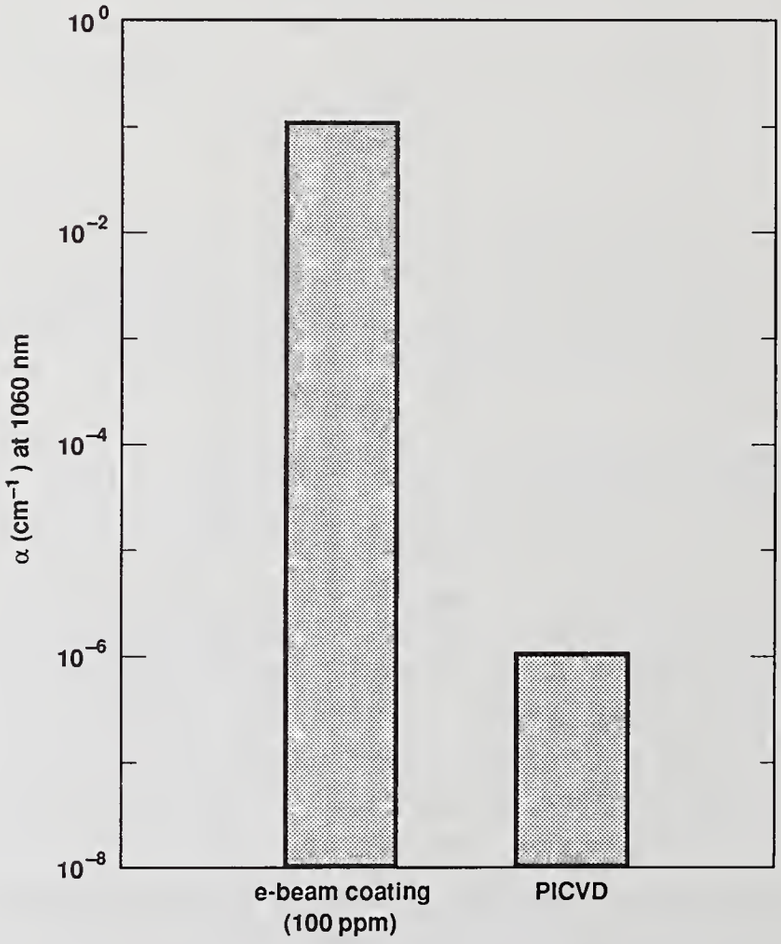

Figure 8. Comparison of typical optical absorption for Ge-doped SiO_2 made by high temperature plasma CVD [19] with that typically reported for high quality thin films produced by e-beam evaporation (see for example ref. 7 and 23).

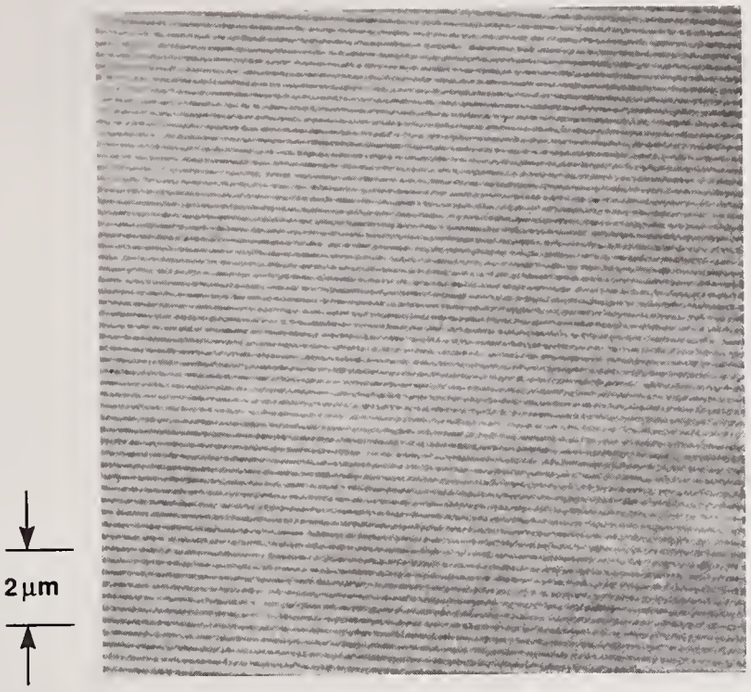

Figure 9. SEM photograph showing the cross-section of a portion of a 2000-layer Ge-doped SiO_2 coating deposited by the PICVD process. Note the 2 μm scale marker.

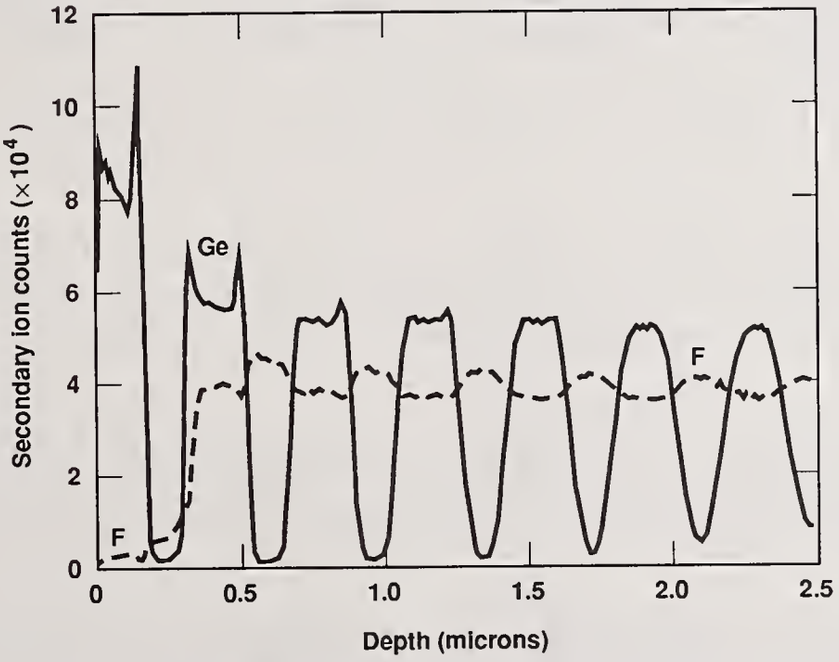

Figure 10. Results from SIMS analysis of the top 12-13 layers of a F, Ge co-doped SiO_2 coating.

We have analyzed the dopant concentration profile through several of the PICVD layers using secondary-ion-mass-spectrometry (SIMS). Figure 10 shows one example of SIMS data from the top approximately 12-13 layers of a 2000 layer Ge-F co-doped SiO_2 coating. The dopant concentration variation gave a peak-to-valley refractive index differences of 0.016. The SIMS data were collected using an oxygen primary-ion beam of 7 keV and current of 400 nA directed at the sample at a 60° angle of incidence. A 300 x 300 μm flat-bottomed crater was formed by rastering the beam while the data were collected in a 30-μm diameter spot at the crater center. Charging of the substrate was eliminated using a charge neutralization technique. The depth resolution is about 4 nm near the surface and becomes gradually poorer with increased sputter depth. Nevertheless the individual coating layers are clearly resolved. The lobes seen on the leading and trailing edges of the first few Ge-doped layers are probably real and a result of variability in the dopant mass flow controllers during this particular run. A calculated transmission spectrum, using the layer thickness determined from the SIMS data, is in good qualitative agreement with the measured transmission spectrum. The coating did show a reflection at the second harmonic that we believe is due to the GeO_2-doped layers being systemmatically thicker than required for a perfect optical quarterwave.

5. Damage Threshold Measurements

Most damage threshold measurements of the PICVD coatings were carried out at 1064 nm, with a 16-ns pulse width and 30 Hz repetition rate. The details of the damage test system (termed REPTILE) are described in a companion paper at this conference [24]. The REPTILE damage test system is one of five systems currently in use at LLNL to provide a data base of damage measurements to support our optical materials research efforts.

In brief, the damage measurements are carried out using the set-up shown schematically in figure 11. The output from a commercial (Quantel) Nd:YAG laser is directed through an attenuator and long focal length lens (~2 m) onto the test sample. The attenuator is used to vary the test fluence. The sample is located in a near field region where the beam spot diameter is about 1 mm in diameter. The test sample is examined both before and after laser irradiation using 100X Nomarski microscopy; we define damage as any observed change in the sample under these viewing conditions. The beam profile and energy are recorded using a calorimeter and video camera as shown in figure 11a. The fluence profile of the beam was then calculated using a commercially available software package.

The PICVD coatings were deposited on the inside of a 17.2 mm fused silica tube as described in a previous section. In order to properly test the coating, the tube was cut lengthwise into four pieces (fig. 11b). The laser beam was directed onto the inner coated surface of the sample at about a 10° angle of incidence.

Not all of the coatings that were damage tested were designed to reflect at 1064 nm leading to significant transmission through the sample. This often caused damage at the output surface and significant retroreflections. Thus, we feel our measurements represent a lower bound or conservative value of the damage thresholds that can be expected for the PICVD coatings.

Figure 12 compares the measured damage thresholds of the PICVD coatings* with the surface damage thresholds of super-polished (Zygo) fused silica and Ge-doped fused silica prepared using very high temperature (~ 1800°C) chemical vapor deposition. The undoped fused silica is the same high quality material used to fabricate

*bulk thresholds are much higher than the surface damage thresholds.

lenses, debris shields and other transmissive optical elements on the current 120 kJ LLNL Nova laser. Fused silica has the highest surface damage threshold of any material or coating on the Nova laser and consequently we use it as a "bench mark" to compare with new optical materials. The kilolayer PICVD coatings are nearly equivalent in damage threshold to the surface threshold of super-polished fused silica. The pulse length scaling for damage to fused SiO_2 is approximately:

$$D_T = 19\, t_p^{0.4}$$

where D_T is the damage threshold (J/cm^2) and t_p is the laser pulse width (ns).

Unfortunately we only tested one PICVD coating at 1 ns where it gave a damage threshold of about $13 J/cm^2$. This is somewhat lower than fused silica but is probably inconclusive without further tests (i.e. more sample statistics).

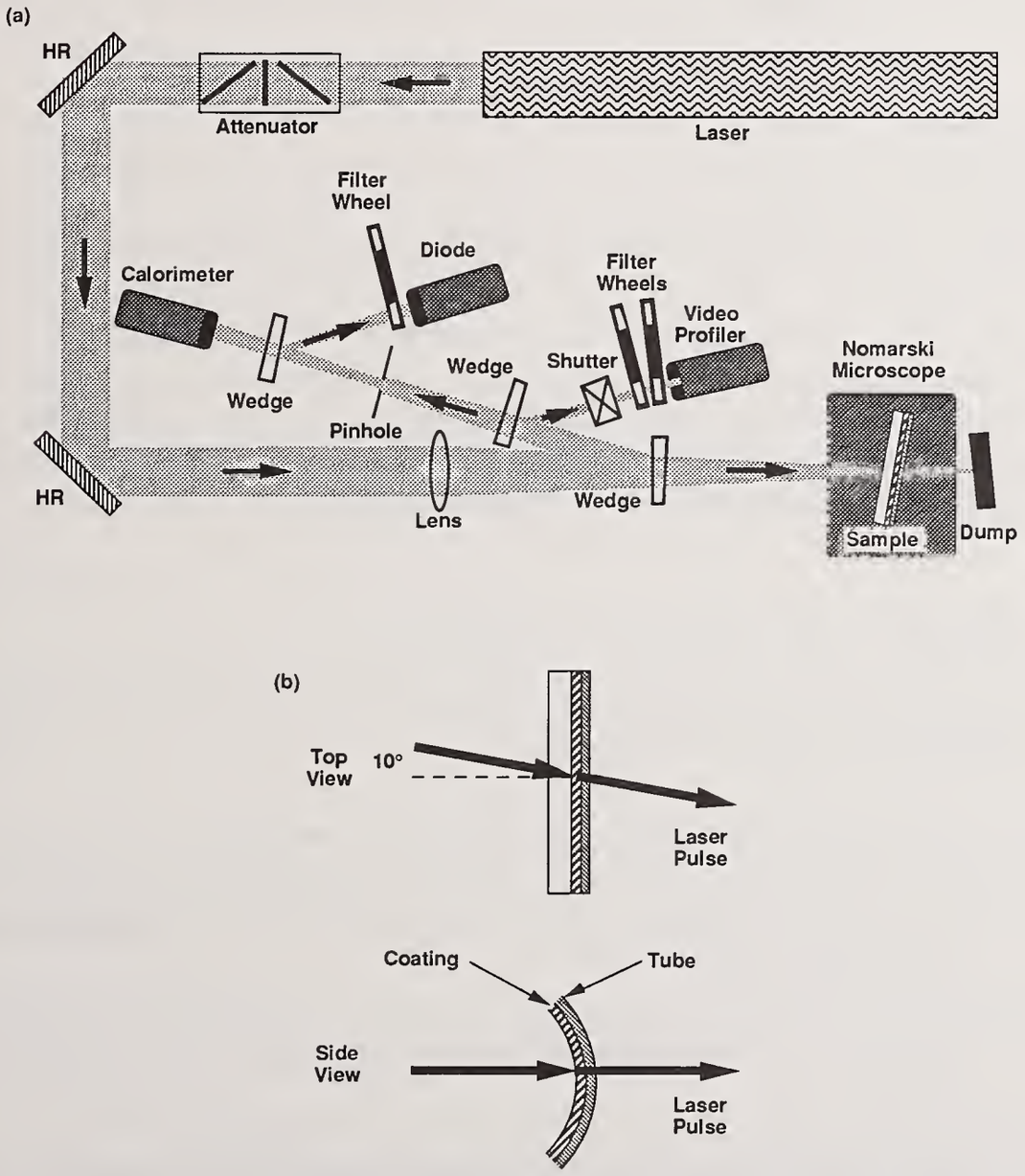

Figure 11. (a) Schematic representation of the 1064 nm laser damage test system used to test the PICVD coatings, and (b) configuration of the damage test sample cut from the 17.2 mm ID SiO_2 tube used as a substrate for the coating process.

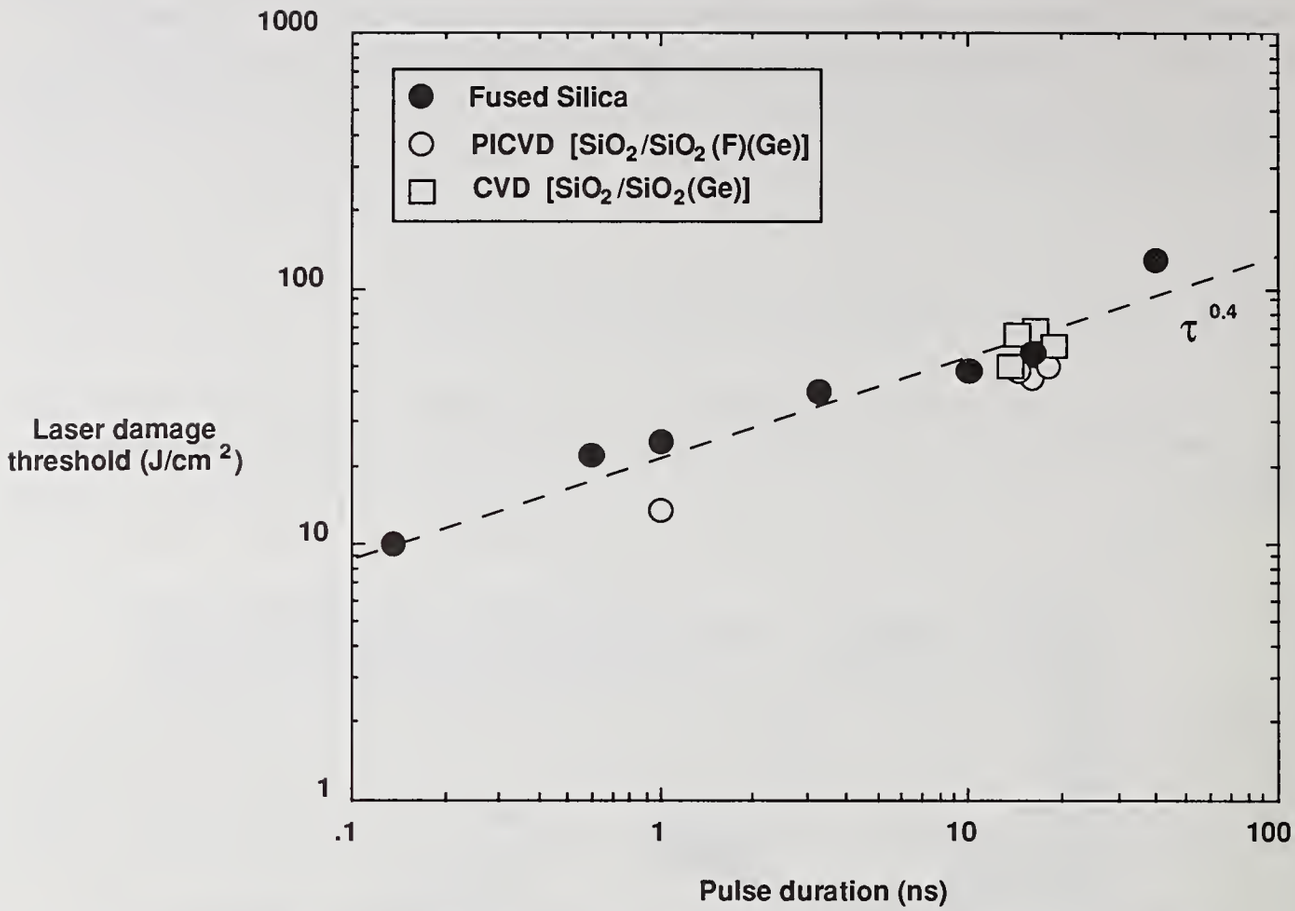

Figure 12. Measured damage threshold at 1064 nm versus pulse width for super-polished, bare fused silica and coatings prepared by either PICVD or very high temperature (~ 1800°C) CVD. The data for the bare fused silica are from ref. 10, 11 and 12. The PICVD coating samples consisted of 1000 or more quarter wave layers of doped SiO_2.

6. Extending the PCVD Coating Process to Flat Substrates

There are three major technical advances that must be made before the high temperature PICVD process can be used to prepare optical coatings on flat substrates:

1. Achieve uniform deposition over large, flat areas ($\geq$ 10 cm diameter),

2. Maintain the same high deposition rates and efficiencies that were used in preparing coatings on the inside of tubular substrates, and

3. Uniformly heat large areas to temperatures near 1000°C while maintaining a uniform reaction plasma.

In a companion paper [25] we discuss each of these issues further in light of our recent progress in designing and building a planar, high-temperature PCVD system.

7. Conclusions

High reflectivity (HR) coatings, nominally consisting of 1000 to 2000 optical-quarterwave layers, have been prepared by reacting $SiCl_4$ and a halogenated dopant (e.g. $GeCl_4$) with O_2 in a microwave-driven plasma. The dopant concentration is such that the index difference (Δn) between adjacent quarterwave layers is about 0.02 or less. The deposition is carried out at high substrate temperatures (about 900 to 1100°C) producing a fully dense, fused silica coating. The motivation for using the high temperature conditions is the observation that commercially available CVD deposited fused silica (used for making focusing lenses and other high fluence laser optical components) has very high surface and bulk damage thresholds.

Measured damage thresholds of HR coatings prepared by this plasma CVD process are comparable to those for super-polished fused silica surfaces. For example, at 1.064 nm and 16-ns we measure PICVD coating damage thresholds of about 45 J/cm^2 compared to about 45-60 J/cm^2 for the surface of super-polished Corning optical fused silica. The plasma CVD coatings have the highest N-on-1 damage threshold of any optical coating tested to date by the LLNL Laser Program.

The present coating method is an adaptation of a process developed by Schott Glaswerke for producing optical fiber preforms. Besides the advantage of operating at high temperature and under highly oxidizing conditions, this process offers: (1) high deposition rates (about 2-3 μm/min.), (2) control of the refractive index profile to within dopant diffusion limits, and (3) ultra-pure starting materials giving extremely low bulk absorptions. Consequently, low-scatter, essentially defect-free coatings consisting of several thousand quarterwave layers can be deposited in a few hours. Furthermore, the index profile can be easily tailored to be sinusoidal, square-wave, etc.

The major disadvantage of the present deposition process is that it was developed for coating the inside of fused silica tubes about 2-cm in diameter (used in making optical fiber preforms). Therefore it must be modified to coat flat substrates; extensive efforts are currently underway at LLNL and Schott to develop such a coating system.

Acknowledgements:

The authors gratefully acknowledge the efforts of Ms. A. Clasen in preparing this finished manuscript.

References:

[1] R. R. Austin, R. C. Michaud, A. H. Guenther, J. M. Putman and R. Harniman, "Influence of Structural Effects on Laser Damage Thresholds of Discrete and Inhomogeneous Thin Films and Multilayers", Laser Induced Damage in Optical Materials: 1972, NBS Pub. 372, pg. 135.

[2] M. R. Kozlowski, M. Staggs, C. R. Wolfe and J. H. Campbell, "Large Area Laser Conditioning of Dielectric Thin Film Mirrors", in Laser Induced Damage in Optical Materials: 1989, (this proceedings).

[3] C. R. Wolfe, M. R. Kozlowski, J. H. Campbell, F. Rainer, A. Morgan, and R. Gonzales, "Laser Conditioning of Optical Thin Films", in Laser Induced Damage in Optical Materials: 1989, (this proceedings).

[4] D. Milam and R. A. Bradbury, "Laser Damage Threshold for Dielectric Coatings as Determined by Inclusions", Appl. Phys. Lett. 23, 654 (1973).

[5] T. W. Walker, A. H. Guenther, and P. Nielsen, "Pulse Laser-Induced Damage to Thin-Film Optical Coatings-Part I: Experimental" and "Part II: Theory", IEEE, J. Quantum Electron., QE-17, 2041 (1981).

[6] W. H. Lowdermilk, D. Milam, and F. Rainer, "Optical Coatings for Laser Fusion Applications", Thin Solid Films, 73, (1980) 155-166.

[7] W. H. Lowdermilk and D. Milam, "Laser-Induced Surface and Coating Damage", J. Quantum Electron. QE-17, 1888 (1981).

[8] D. M. Aikens and J. R. Taylor, "Cause of Damage in Multilayer Dielectric Coatings Exposed to High Average Power Visible Laser Radiation", in Laser Induced Damage in Optical Materials: 1987, NIST Spec. Pub. 756, p. 419.

[9] N. Bloembergen, "Role of Cracks, Pores and Absorbing Inclusions on Laser Induced Damage Thresholds at Surfaces of Transparent Dielectrics", Applied Optics, 12 (1973), 661.

[10] S. Stokowski, D. Milam, and M. Weber, Laser Induced Damage in Optical Materials: 1978, NBS Spec. Pub. 541, (1978) p. 99-108.

[11] D. Milam, "1064 nm Laser Damage Thresholds of Polished Glass Surfaces as a Function of Pulse Duration and Surface Roughness", in Laser Induced Damage in Optical Materials: 1978, NBS Spec. Publication 541 (1978), p. 164-167.

[12] F. Rainer, R. P. Gonzales and A. J. Morgan, "Laser Damage Database at 1064 nm", in Laser Induced Damage in Optical Materials: 1989, NIST Spec. Publication (this proceedings).

[13] J. F. Hyde, "Method of Making a Transparent Article of Silica", US patent 2,272,342 (Feb. 10, 1942).

[14] S. R. Nagel, J. B. MacChesney and K. L. Walker, "An Overview of the Modified Chemical Vapor Deposition (MCVD) Process and Performance", IEEE J. Of Quant. Elect. QE-18, (1982) p. 459-476.

[15] H. Suda, S. Hibuta, and M. Nakahara, "Multiflame VAD Process for High-Rate Fabrication of Optical Fiber Preforms", Transactions of the IECE of Japan E69 (1986) 1206-1202.

[16] P. C. Schultz, "Fabrication of Optical Waveguides by the Outside Vapor Deposition Process", Proceedings of the IEEE 68 (1980), p. 1187-1190.

[17] H. Lydtin, "PCVD: A Technique Suitable for Large-Scale Fabrication of Optical Fibers", J. Lightwave Techn. LT-4 (1986), p. 1034-1038.

[18] J. Irven and A. Robinson, "Optical Fibers Produced by Plasma Augmented Vapour Deposition", Phys. and Chemistry of Glasses, 21 (1980), p. 47-52.

[19] Th. Hunlich, H. Bauch, R. Th. Kersten, V. Paquet, and G. F. Weidmann, "Fiber Preform Fabrication Using Plasma Technology: A Review", J. Opt. Commun. 8 (1987), p. 122-129.

[20] H. Bauch and V. Paquet, "Fibers with Pure SiO_2-Core Made by PICVD", J. Opt. Commun. 8 (1987), p.136139.

[21] H. Bauch, V. Paquet and W. Siefert, "Preparation of Optical Fiber Preforms by Plasma-Impulse CVD", Conf. Proc. SPIE, Optical Fiber Characteristics and Standards, SPIE Vol. 584, p. 33-37; Cannes (1985).

[22] P. C. Schultz, "Recent Advances in Optical Fiber Materials", Proceedings of Second Interntional Otto-Schott Colloquium, Jena, DDR, July 12-16, 1982, p. 215-225.

[23] D. Milam, W. H. Lowdermilk, F. Rainer, J. E. Swain, C. K. Carniglia and T. Tuttle Hart, "Influence of Deposition Parameters on Laser Damage Thresholds of Silica-Tantala AR Coatings", Applied Optics 21 (1982), p. 3689-3694.

[24] A. Morgan, F. Rainer, F. P. DeMarco, R. P. Gonzales, M. R. Kozlowski and M. C. Staggs, "Expanded Damage Test Facilities at LLNL," in Laser Induced Damage in Optical Materials: 1989, LLNL report UCRL-101642 (these proceedings).

[25] R. Brusasco, J. A. Britten, C. B. Thorsness, M. S. Scrivener, W. G. Unites, J. H. Campbell and W. L. Johnson, "A High Temperature, Plasma-Assisted Chemical Vapor Deposition System," in Laser Induced Damage in Optical Materials: 1989, LLNL report UCRL-101766 (these proceedings).

COMMENTS

Question: Did you consider other mechanisms other than the Drude model, for example band filling?

Answer: No, we just used a simple Drude model.

Question: Certainly in the 10 micron region the overwhelming contribution to the refractive index is not the Drude contribution but the contribution due to band filling, so you might want to have a look at that.

Answer: We shall look at that then, thank you.

Question: Could you tell us a bit more about the deep level impurities, what they might be, and how you diagnosed them?

Answer: We've done a number of tests on those in the discrete photodiode devices through cd measurements. That is how we know that they are deep levels about mid band and not shallow levels in the band gap. These levels were induced by melting transients in the discrete diodes. When we see this electrical damage onset that we have melted to the surface of the silicon.

Question: How do you know that you have introduced new defects rather than allowing the Fermi level to shift and change the charge state of an existing defect?

Answer: The cd measurements as a function of frequency will tell you that you really have not changed the charge state, but that these are bulk not surface defects. In the discrete devices we are looking at a junction that is below the surface, so we weren't really looking at traps in thick surface states. The defect level of an undamaged device was very low as measured by cd measurement before laser radiation.

Manuscript received
3-20-90

A High Temperature, Plasma-Assisted Chemical Vapor Deposition System*

R. M. Brusasco, J. A. Britten, C. B. Thorsness,
M. S. Scrivener, W. G. Unites, and J. H. Campbell

University of California
Lawrence Livermore National Laboratory
P.O. Box 5508, L-490
Livermore, CA 94550

W.L. Johnson
Prototech Research, Inc.
106 South 54th Street
Chandler, AZ 85226

We have designed and built a high-temperature, plasma-assisted, chemical vapor deposition system to deposit multilayer optical coatings of SiO_2 and doped-SiO_2 on flat substrates. The coater concept and design is an outgrowth of our recent work with Schott Glaswerke demonstrating the use of plasma assisted CVD to prepare very high damage threshold optical coatings. (That work is reported in a companion paper at this Symposium).

The coater is designed to deposit up to several thousand alternating quarterwave layers of SiO_2 and doped SiO_2 on SiO_2 substrates at deposition rates up to several microns per minute. The substrate is resistively heated to about 1000°C during the deposition phase of the process. The plasma is driven by a 13.56 MHz RF unit capable of producing power densities of up to 140 W cm^{-3} in the reaction zone. The coater is designed to be adaptable to microwave generated plasmas, as well as RF. Reactant gas flow rates of up to 10 slm can be achieved at a 10 torr operating pressure. Reactants consist of O_2, $SiCl_4$ and a volatile halogenated dopant (e.g. $GeCl_4$ or CCl_2F_2). These gases react in the plasma volume producing SiO_2 with dopant concentrations (e.g. GeO_2) of up to a few percent. A variable dopant concentration is used to produce index differences (nominally about 0.01) between adjacent optical layers.

*Work performed under the auspices of the U.S. Department of Energy by Lawrence Livermore National Laboratory under contract number W-7405-ENG-48.

Some of the major technical problems associated with the design and construction of this coater are discussed. These include flow distribution and its effect on deposition uniformity, substrate heater design and operation, choice of RF vs. microwave driven plasma and diagnostics design and placement. To address many of these issues, we have relied heavily on numerical and experimental modeling of the fluid flow, reaction kinetics, and heat transfer within the coater. Furthermore, preliminary experiments carried out on prototype designs were used to guide our development efforts.

1.0 Introduction

High reflectivity (HR) coatings for the next generation laser fusion driver will require laser damage thresholds not less than 40 J/cm^2 at 1.06 μ wavelength[1]. Considering that bulk fused silica possesses a high laser damage threshold and is made by high temperature chemical vapor deposition, an effort has been initiated to apply a high temperature deposition method to the creation of a multilayer HR reflector. This so-called "kilolayer" concept, and its success in a circular tube geometry, is described more fully in another paper in this publication[2]. The key processing issue now is to translate this process to one suitable for flat substrates.

The task requires separation into four roughly concurrent efforts; preliminary experimentation with the coating process, examination of heat and mass transport issues, investigation of fundamental plasma characteristics and hardware production and evaluation. With respect to mass transport, Wilcock et al.[3] and Law and Masliyah [4] have successfully used naphthalene sublimation in the analysis of mass transport uniformity. Since, mathematically, naphthalene sublimation (removal) is equivalent to deposition in terms of uniformity, we constructed a test bed to model the mass transport in the proposed reaction chamber geometry. We wished to determine whether the proposed geometry would lead to a uniform deposition and what the critical parameters were that would assure uniform mass transport.

With respect to plasma characteristics, we have demonstrated deposition of up to ≈5000 quarter wave layers inside a 3.0 cm diameter tube[2] using 2.45 GHz radiation to excite the plasma. However, the ability to scale plasma applicators at 2.45 GHz uniformly for large flat substrates, the cost of such scale-up and possible use of other radiation frequencies remain unresolved issues. As an example of frequency dependence, two literature studies concerning a photoresist stripping process can be used to compare RF versus microwave plasmas. The papers by Dzioba et al.[5] and Degenkolb et al.[6,7], describe experimental systems that are nearly identical, with similar reaction volumes, pressures, and oxygen flow rates. However, the study utilizing 2.45 GHz exhibited a more highly-excited oxygen plasma environment, inferred from the optical emission spectrum, and an order-of-magnitude increase in the stripping rate compared to the study which used 13.56 MHz radiation. The extent to which differences such as this would affect our CVD coating apparatus is unknown at this time, but could have a large impact in terms of hardware development and coating performance, particularly laser damage resistance. We have constructed a plasma test bed to investigate the differences between RF and microwave plasmas and to refine plasma diagnostic techniques.

Among the diagnostic techniques being considered for monitoring the coating environment are residual gas analysis for mass balance and impurity monitoring and determination of the electron density (n_e) and electron temperature (T_e) [8] with a Langmuir probe.

2.0 Experimental

Preliminary deposition studies were carried out in a horizontal silica tube reactor, shown schematically in figure 1. The tube was 7.62 cm in diameter (expanded to 12 cm in the reaction zone) and approximately 61 cm long. The tube was contained in a radiantly heated furnace with the heating zone approximately 30 cm long. A thimble containing a fused silica substrate, a graphite susceptor and a boron nitride insulator was inserted into the hot zone of the reaction tube. The graphite served as the absorber in the radiant furnace and as the driven electrode for the application of RF at 13.56 MHz. Gas flows of oxygen, silicon tetrachloride and germanium tetrachloride were established using mass flow controllers. Pressures were monitored with Baratron gauges and controlled by a butterfly valve controller. Typical operating parameter ranges are given in table I.

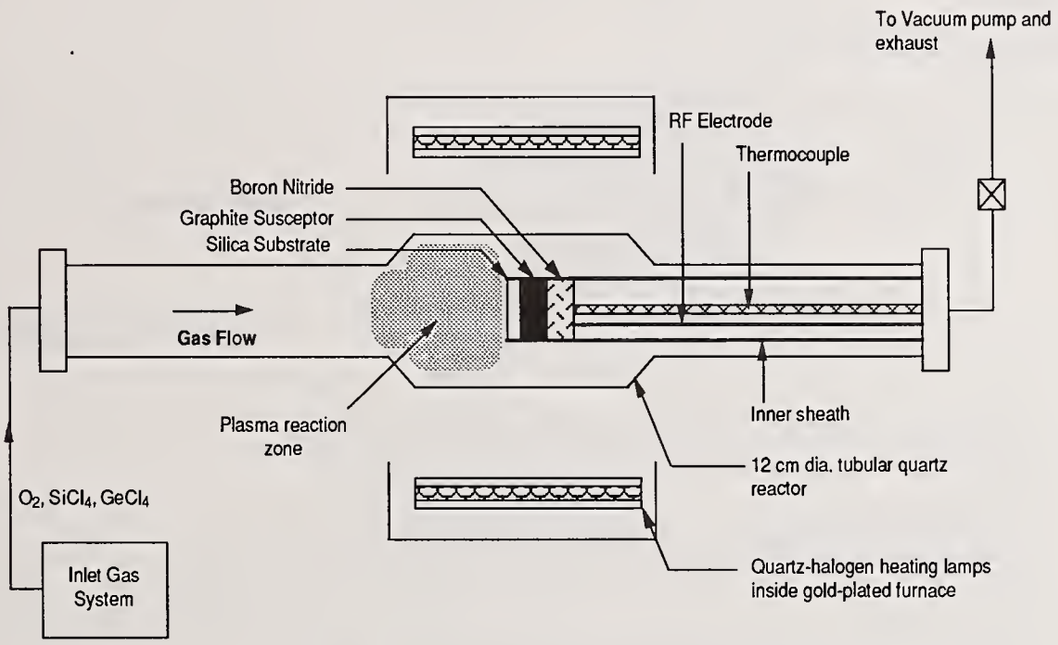

Figure 1. Schematic of radiantly heated plasma CVD reactor.

Mass transfer experiments were performed in a 1:1 scale model of the proposed coater (fig. 2) with a reaction volume of approximately 800 cm^3 [9]. The substrate-to-injection plate spacing could be adjusted with appropriately sized spacers. A Duo Seal 1398 vacuum pump allowed pumping rates as high as 5 slm through the reactor at reaction chamber pressures from 200 to 2000 Pa. A gas distribution plate consisting of a square array of 237 holes of 0.0635 cm diameter on 1 cm centers or 72 holes of 0.229 cm diameter on 1 cm centers was studied. Substrates were prepared by hot pressing naphthalene at approximately 78°C and 68 MPa pressure into aluminum molds. The substrates were weighed before and after the sublimation experiment to determine the mass of naphthalene that sublimed and from this an average rate of removal was calculated. The substrate surface was also profiled before and after a run on a Moore profilometer (resolution 3 X 10^{-4} cm) to determine uniformity of sublimation.

Table 1. Summary of typical operating conditions used in our preliminary radiant heating plasma CVD experiments

Pressure	0.3-3.0 torr
Flow rate oxygen	100-500 sccm
Flow rate $SiCl_4$	20-90 sccm
Flow rate $GeCl_4$	0-10 sccm
RF power (CW exp.)	300 Watts
RF power (peak)	57-94 Watts
RF power (average)	8.5-15 Watts
Pulse width	10-15 X 10^{-3} sec
Pulse Repetition Frequency	10-30 Hz
Temperature	1050-1250°C
Reaction time	60 min.
Number of experimental runs	16

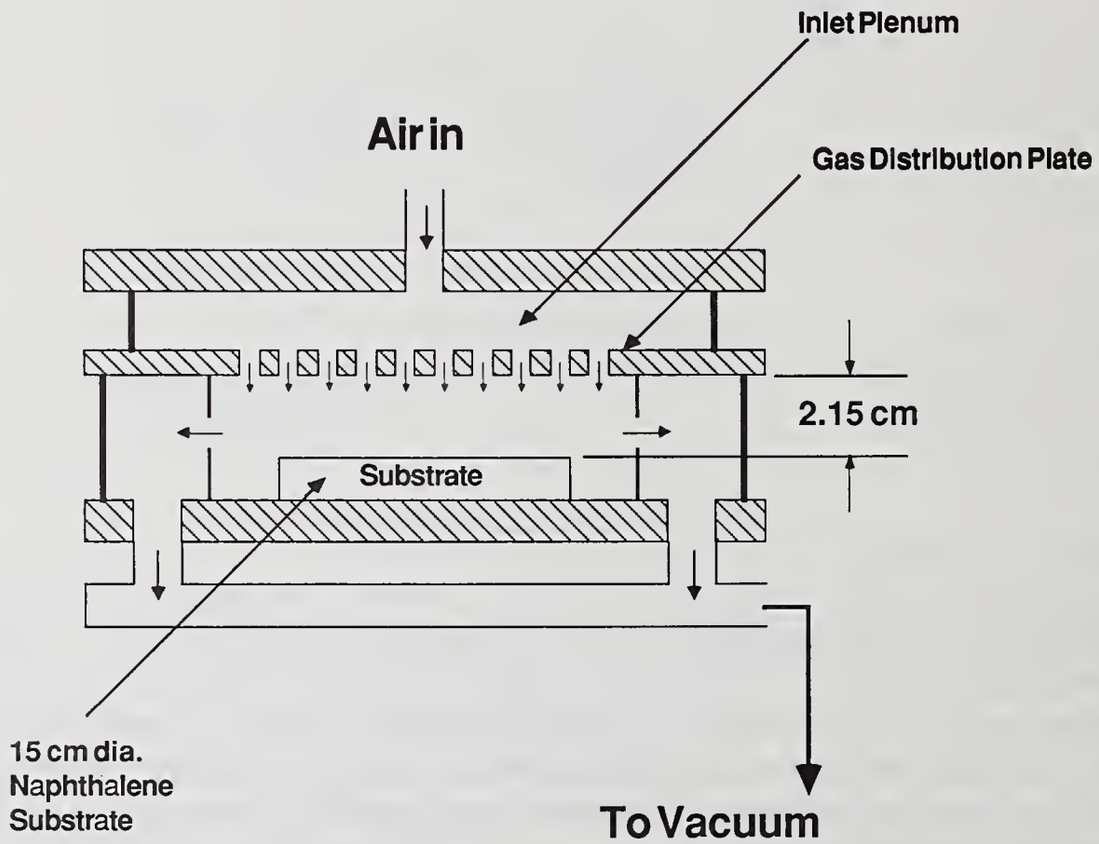

Figure 2. Schematic of the mass-transfer test system

Initial experiments on plasma characteristics were carried out in a silica reactor. Langmuir probe experiments were done in a horizontal fused silica tube of 15 cm diameter in the reaction zone and an overall length of 90 cm, as shown in figure 3. The plasma was excited by RF at 13.56 MHz using 2.5 cm wide strips of metal as electrodes that were attached to the outside of the reactor tube in a clam-shell arrangement. The Langmuir double probe was constructed as described by Chen [10] and placed as close to the electrodes as possible and extended into the plasma region approximately 5 cm. Presently, diagnostics experiments are conducted in a full scale mock-up of the proposed PCVD coater geometry as shown in figure 4, with a diameter of 15 cm and a height adjustable from 1 to 7 cm. The plasma is excited by either a parallel plate RF electrode arrangement, with the driven electrode at the bottom of the chamber, or with a waveguide applicator for 2.45 GHz radiation. A residual gas analysis system using an Inficon Quadrex 100 Residual Gas Analyzer (RGA) was attached to the exhaust port of the test chamber.

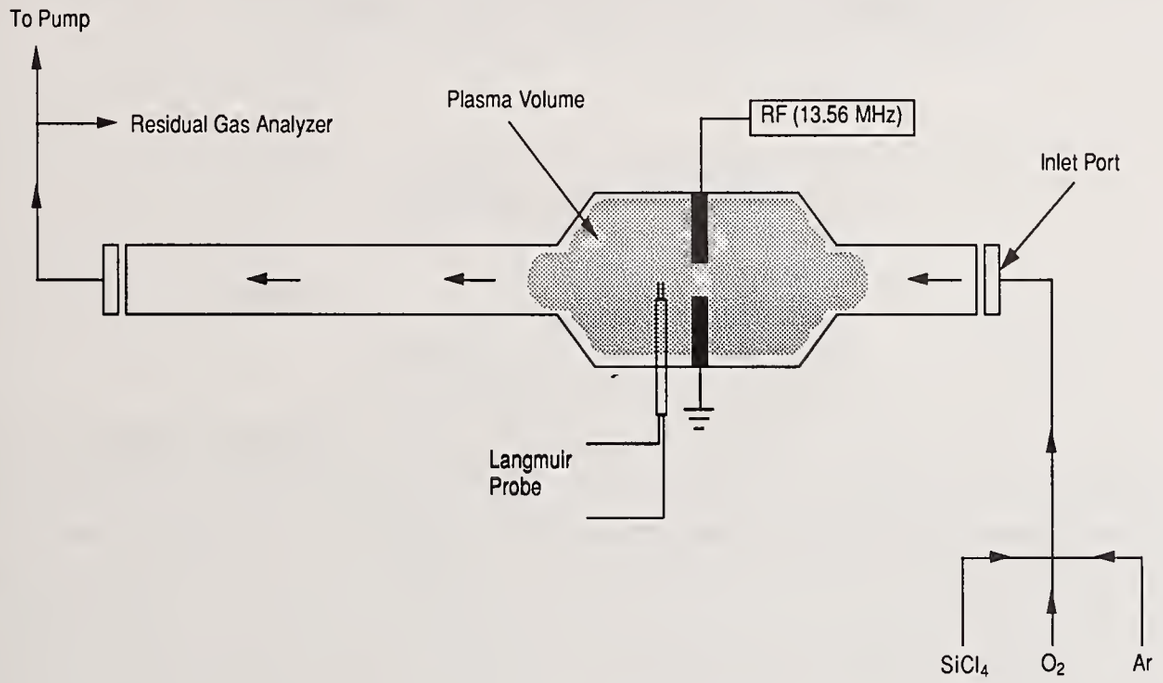

Figure 3. Schematic of tubular plasma test bed

3.0 Results and Discussion

3.1 Preliminary Deposition Experiments

Preliminary deposition experiments using 13.56 MHz RF to drive the reactive plasma in the horizontal, radiantly heated furnace pointed out several significant problem areas. First, the substrate temperature was difficult to determine. The thermocouple monitor could only read the back of the susceptor and was influenced by the driving RF electric field. Second, the deposited layers were uneven and contained particulates. The existence of cold walls in contact with the process caused generation of particulate silica, which found its way onto the growing film. Also, there was considerable leakage of the plasma into undesirable areas of the reactor, such as directly behind the susceptor and along the walls of the thimble. This leakage significantly reduced the plasma power density available in the reaction volume. In addition, the total RF power available was only 1 kW.

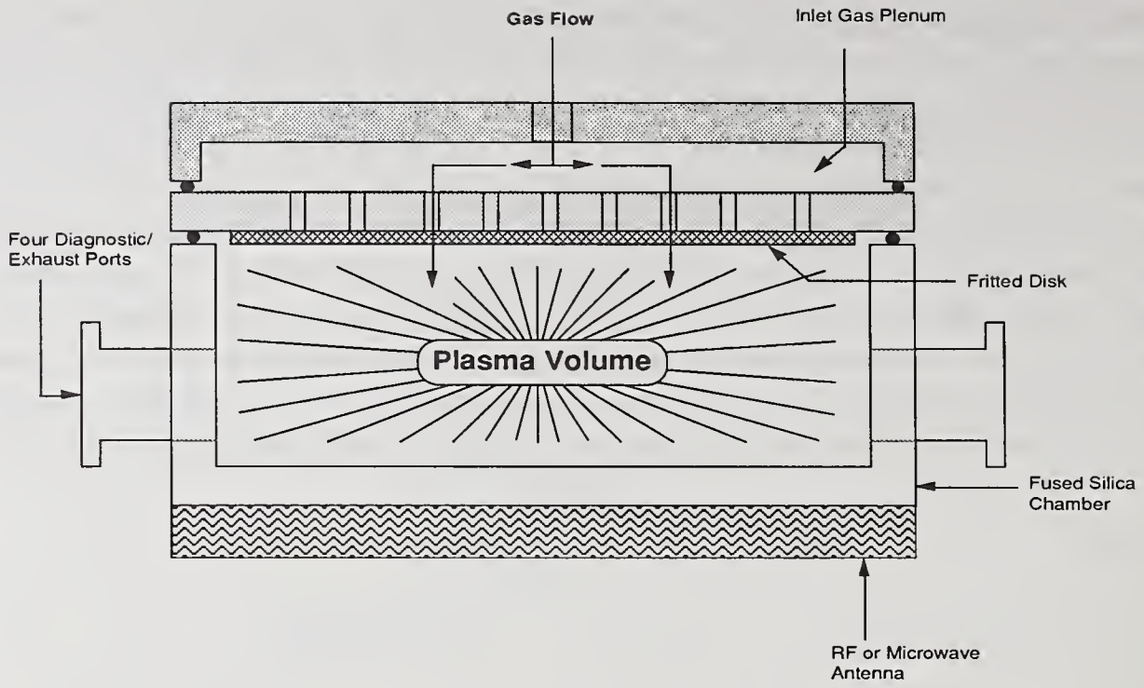

Figure 4. Schematic of parallel-plate plasma test bed.

3.2 Mass Transport

Figure 5 shows the surface profile of a naphthalene disk before and after a sublimation run where the disk was exposed to 2 slm flow for 5 hours to remove approximately 50% of the naphthalene material. The increased surface roughness following sublimation is attributed to the crystalline nature of the naphthalene causing preferential removal based on grain orientation. The mass removal rate was greater at the outer edge of the disk than at the center due to edge effects associated with a finite disk size. An analysis of the radial removal rate versus total amount of material removed, neglecting the outer 1.5 cm edge, shows the uniformity to be $\pm$5%. Figure 6 compares the dimensionless mass transfer rate versus Reynolds number (Re) for experiment with that predicted by stagnation flow theory assuming uniform gas injection through the top plate. Here we define the Reynolds number as,

$$R_e = \frac{HV}{\eta} \tag{1}$$

where H is the distance separating the gas injection plate and substrate (cm), V is the superficial axial injection velocity (cm/sec) and η is the kinematic gas viscosity (cm^2/sec).The mass transfer rate is made dimensionless by,

$$y' = \left(\frac{W}{tA}\right)\left(\frac{P}{P_{sat}}\right)\left(\frac{H}{\mathcal{D}\rho M}\right) \tag{2}$$

where:

W = Mass loss (gm)
t = time (s)
A = Naphthalene surface area (cm^2)
P = Pressure (torr)
P_{sat} = Naphthalene vapor pressure (torr)
H = Reactor height (cm)
$\mathscr{D}$ = Naphthalene diffusivity in air (cm^2/s)
ρ = Gas density (g/cm^3)
M = Molecular weight naphthalene (gm)

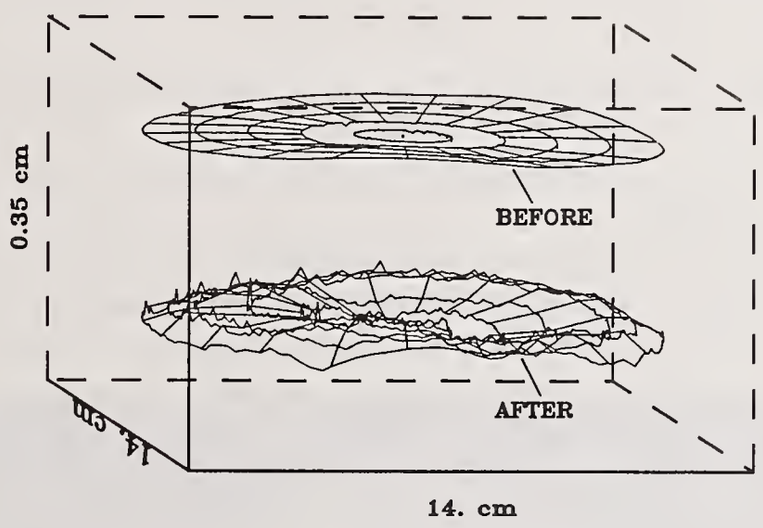

Figure 5. Plot of the naphthalene disk surface contour before and after evaporation.

For low Reynolds numbers, the mass transfer rate agrees with the stagnation flow theory [11] and the removal of naphthalene is uniform. Above a Reynolds number of about 3 the mass removal rate increases sharply due to jet impingement as shown in figure 7. Here, jet impingement has caused locally high mass removal directly under the inlet orifices, causing a dimpling of the naphthalene surface. These studies have defined flow rate ranges, for a given reactor and gas distribution geometry, that lead to radially uniform mass transfer in the reactor; further details of this work are given in ref. 9.

3.3 Plasma Characterization

Figure 8 shows some preliminary data taken from Residual Gas Analysis of a mixture of O_2 and $SiCl_4$ exposed to an RF plasma. A very low baseline of oxygen gas is compared with a mixture of O_2 and $SiCl_4$ without plasma, which reveals the fragmentation pattern of silicon tetrachloride. Upon striking the plasma, the fragmentation pattern indicates a dramatic increase in the signal at mass 70, attributed to Cl_2

parent ion, with corresponding decreases in the masses of the lower silicon halides. Residual gas analysis will be useful in characterizing the stable volatile reaction products as well as monitoring the presence of impurities in the gas streams. The major improvement here will be the calibration of the instrument to provide a mass balance for the reactants and products and to increase the mass range such that all fragments of $SiCl_4$ and dopants can be monitored routinely.

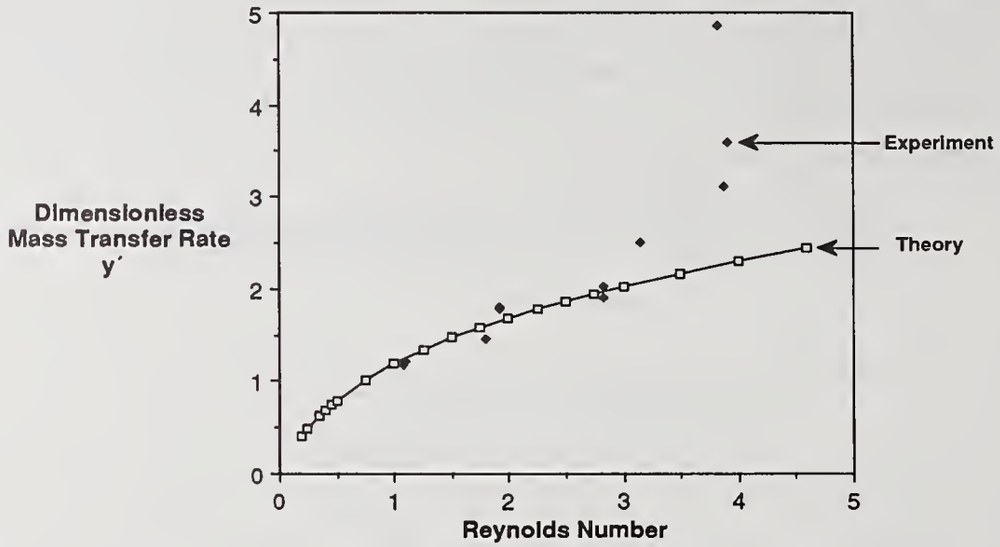

Figure 6. Dimensionless mass transfer rate versus Reynolds number

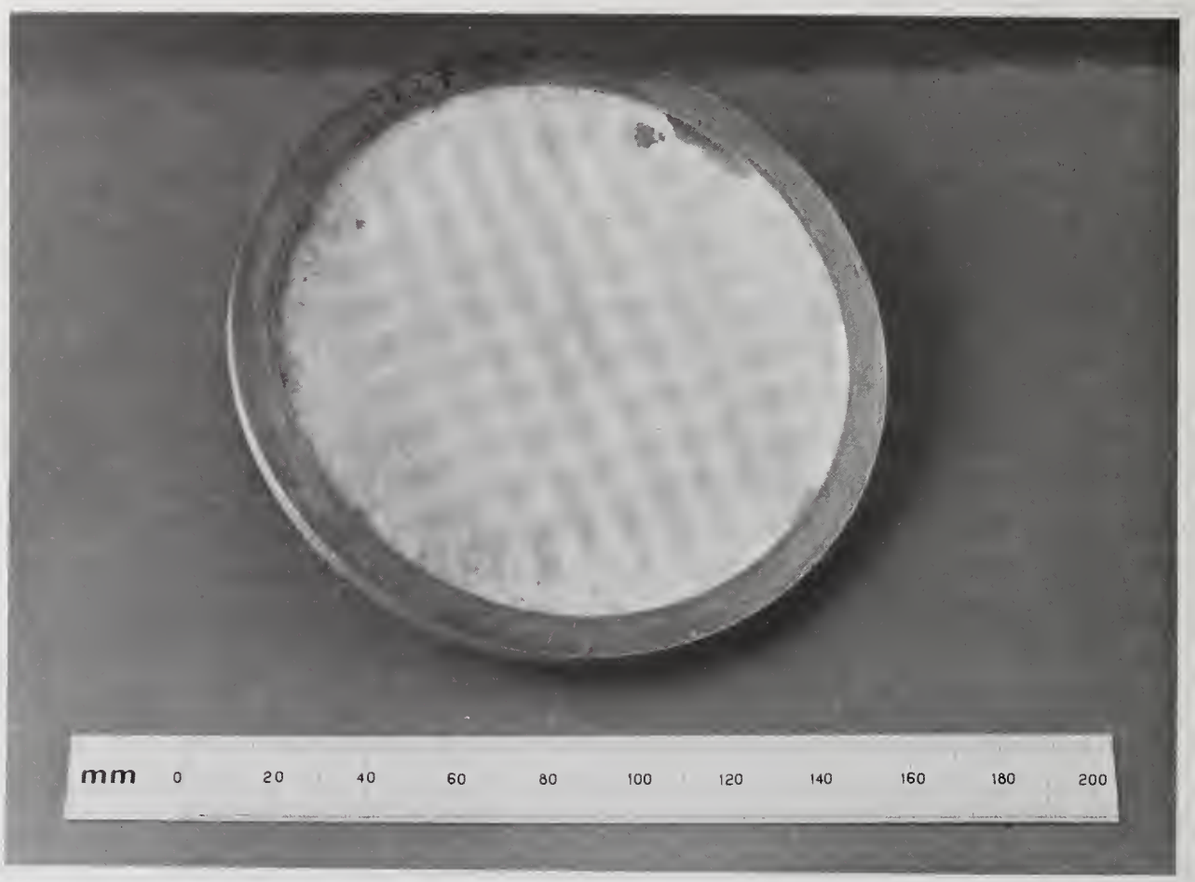

Figure 7. Photo of jet impingement on a naphthalene disk.

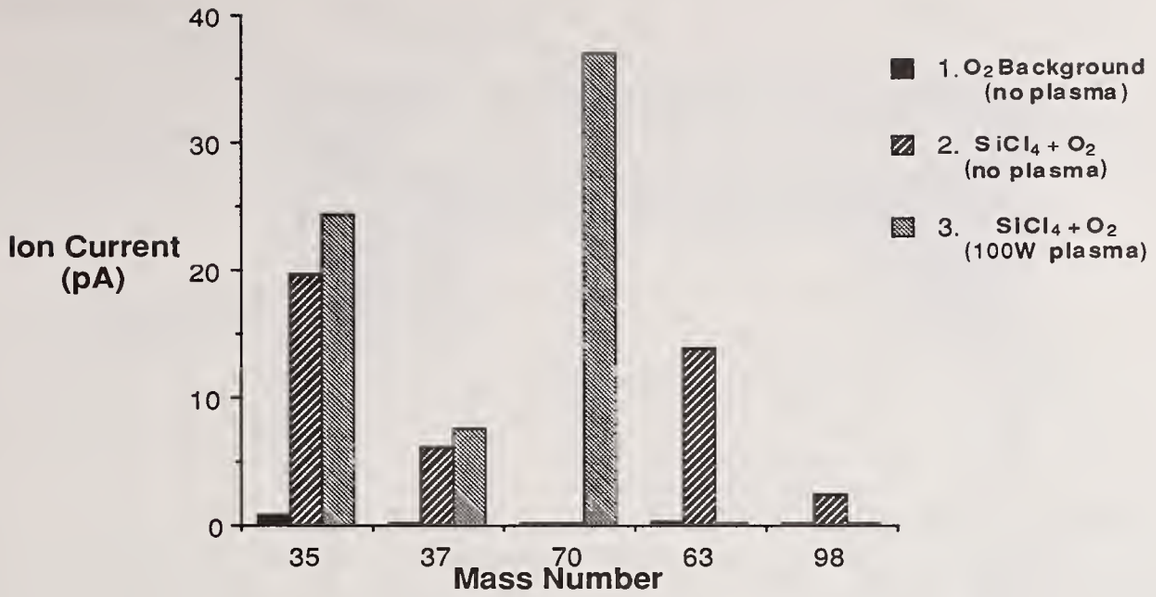

Figure 8. Residual Gas Analysis of coater effluent with and without plasma.

Current-voltage data were taken with a Langmuir double probe in oxygen at 1 torr pressure at several 13.56 MHz RF power levels. Figure 9 shows that with increasing RF power, the electron temperature increases from about 4 eV at 50 watts to approximately 6 eV at 150 watts. Similarly, the electron density increases from about 6.0 X 10^9 cm^{-3} at 50 watts to 1.3 X 10^{10} cm^{-3} at 150 watts. These data are in qualitative agreement with data from Heidenreich et al. [12] investigating oxygen microwave afterglows and Yamagishi et al. [13] investigating air-helium plasmas excited by several methods. The key developments in Langmuir probe measurements will be to extend their operation at high power densities and in the electronegative plasmas anticipated in the coater environment.

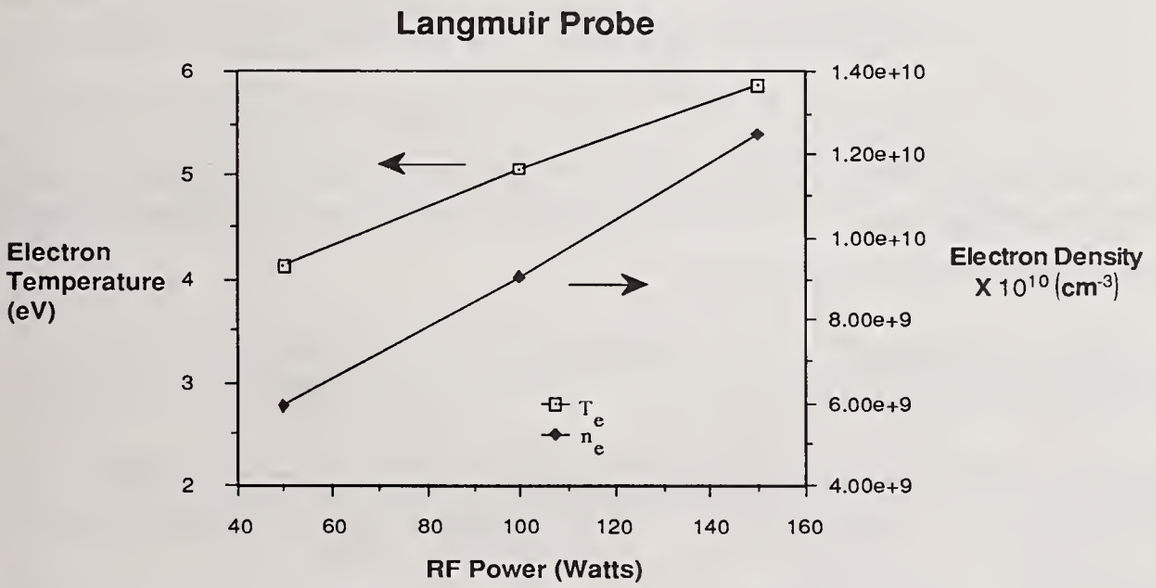

Figure 9. Plot of electron temperature and electron density versus RF power for oxygen gas in a 1 Torr pressure plasma as determined by Langmuir probe.

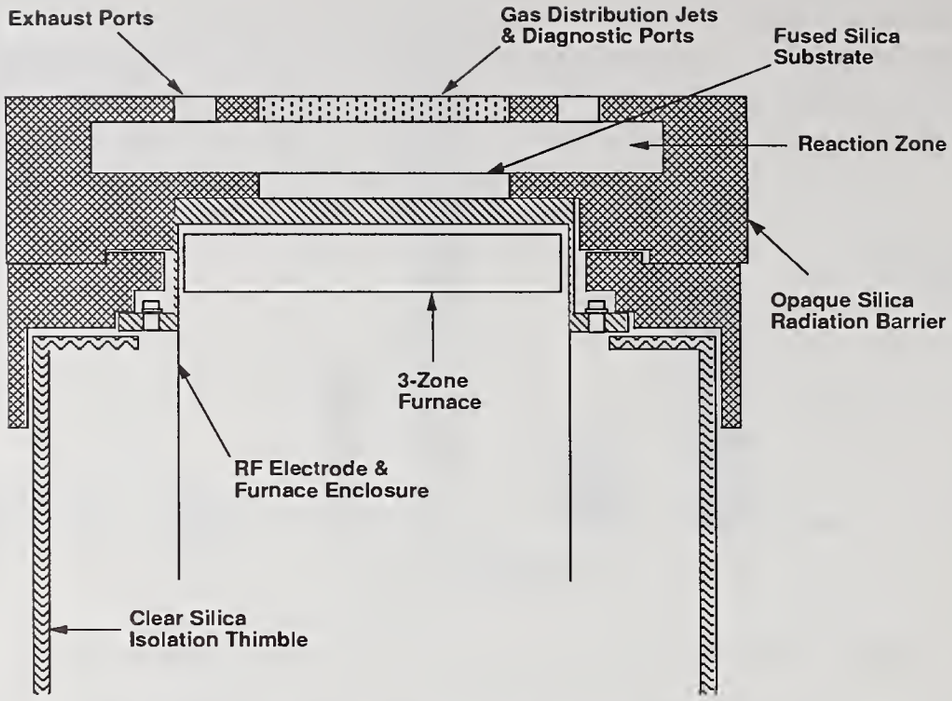

Figure 10. Schematic drawing of PCVD coater reaction chamber.

3.4 Hardware Development

Building on the results of the preliminary investigations, a coating system was specified by LLNL and designed and built by Prototech Research Inc. A schematic of the coating chamber is shown in figure 10. It is capable of handling fused silica substrates up to 15 cm in diameter and 1 cm thick. The furnace is a 3-zone back-heating system designed to heat the substrates to about 1000°C. Some details regarding the reaction environment are described in table 2. The "hot wall" reactor is formed by using closed-cell porous silica glass to enclose the reaction volume and absorb radiant energy from the furnace. Gas is injected through a top plate via an array of gas injection ports and exhausted out the top at the periphery of the substrate. The containment vessel for the furnace acts as an electrode for a 24 kW 13.56 MHz RF generator. Plasma confinement is achieved by isolating the walls of the electrode with a silica thimble which is evacuated to less than 10^{-4} torr. The absorbing silica provides dielectric insulation to suppress plasma breakdown outside of the reaction chamber. The coating apparatus is located in a clean box to prevent particulate contamination. This coater is designed to be as flexible as possible to allow for design changes to meet coating process demands.

Table 2. Summary of designed operating characteristics of the high temperature, plasma CVD coating system

Substrate Size	15 cm dia. X 1 cm thick
Oxygen Flow Rate	0-8 slm
$SiCl_4$ Flow Rate	0-2 slm
$GeCl_4$ Flow Rate	0-500 sccm
RF Power	24 kW maximum
Substrate Temperature	1000°C nominal, 1200°C max.

4.0 Conclusions

We have recently shown that very high damage threshold dielectric coatings can be made using plasma CVD at high temperatures (≈1000°C) [2]. In this paper we discussed our efforts at scaling this process to large, flat substrates (> 10 to 50 cm diameter). There are four main technical issues that must be solved to successfully implement this coating process:

1. Uniform deposition over a large area (± 1-5%)
2. High deposition rates (1-4 $\mu m\ min^{-1}$)
3. Uniform substrate heating at temperatures up to about 1000°C
4. Minimal dopant diffusion

To address these technical issues we have designed, built and operated a series of test bed reactors to look at mass transport, plasma chemistry, and substrate heating issues. We have identified a flow regime that provides uniform radial mass transfer and hence should give uniform deposition. In this work we have used mathematical models to guide and interpret the experiments. In addition, work is in progress to look at the effects of RF versus microwave driven plasmas on the deposition process and we have begun to identify and refine plasma characterization techniques. Based on these results we have built a large coating system designed to coat substrates up to about 15 cm in diameter with several thousand quarter-wave layers of alternating doped and undoped SiO_2. Details of the coater design specifications have been formulated and given. The system is expected to be fully operational by mid-1990.

References

[1] Powell, H.T., J.H. Campbell, J.T. Hunt, W.H. Lowdermilk, J.R. Murray and D.R. Speck, Proceedings of the Workshop on Inertial Confinement Fusion, Varenna, Italy (Sept. 1988). LLNL report UCRL-99517. High Power Nd:Glass Lasers as Drivers for Inertial Confinement Fusion.

[2] Campbell, J.H., J.L. Emmett, R.M. Brusasco, F. Rainer, R.Th. Kersten, V. Paquet and H.-W. Etzkorn, Laser Induced Damage in Optical Materials, 1989. NTIS special publication (in press). Damage Resistant Optical Coatings Prepared Using High Temperature Plasma-Chemical-Vapor-Deposition.

[3] Wilcock, D., C.C. Wright and B.L. Button, Proc. 8th Int. Heat Transfer Conf., **3**, 1199, 1986. Multijet Inclined Heat Exchanger Modules: Mass/Heat Transfer and Pressure Loss Characteristics.

[4] Law, H.S. and J.H. Masliyah, Ind. Eng. Chem. Fundam., **23**, 446, 1984. Mass Transfer Due to a Confined Laminar Impinging Axisymmetric Jet.

[5] Dzioba, S. G. Este and H.M. Naguib, J. Electrochem. Soc., **129(11)**, 2537, 1982. Decapsulation and Photoresist Stripping in Oxygen Microwave Plasmas.

[6] Degenkolb, E.O., C.J. Mogab, M.R. Goldrick, and J.E. Griffiths, Appl. Spectrosc., **30(5)**, 520, 1976. Spectroscopic Study of Radiofrequency Oxygen Plasma Stripping of Negative Photoresists. I. Ultraviolet Spectrum.

[7] Griffiths, J.E. and E.O. Degenkolb, Appl. Spectrosc., **31(2)**, 134, 1977. Spectroscopic Study of Radiofrequency Oxygen Plasma Stripping of Negative Photoresists: II Visible Spectrum.

[8] Steinbruchel, Ch., B.J. Curtis, H.W. Lehmann and R. Widmer, IEEE Trans. Plasma Sci., **PS-14(2)**, 137, 1986. Diagnostics of Low-Pressure Oxygen RF Plamsas and the Mechanism for Polymer Etching: A Comparison of Reactive Sputter Etching and Magnetron Sputter Etching.

[9] Thorsness, C.B. and J.A. Britten, LLNL Report, UCRL-102041, October 1989. Mass Transfer Characteristics in Radial-Flow Multijet CVD Reactors.

[10] Chen, F.F., "Electric Probes", Plasma Diagnostic Techniques, Chapter 4, pp. 113 ff, Academic Press, NY, 1965.

[11] Houtman, C., D.B. Graves and K.F. Jensen, J. Electrochem. Soc., **133**, 961, 1986. CVD in Stagnation Point Flow.

[12] Heidenreich, J.E., III, J.R. Paraszczak, M. Moisan and G.J. Sauve, J. Vac. Sci. Technol. B, **5(1)**, 347, 1987. Electrostatic probe analysis of microwave plasmas used for polymer etching.

[13] Yamagishi, M., K. Mizuno and J. De Groot, J. Quant. Spectrsc. Radiat. Transfer, **40(4)**, 519, 1988. Spectroscopic Measurements of Air Plasma.

Manuscript received
1-29-90

The Evolution of Molecular Beam Deposition (MBD) from Laboratory to Production Usage

C C H Hale, I T Muirhead, S P Fisher, G J H Mathew

The use of molecular beam technology (MBD) under ultra high vacuum conditions (UHV) has proved to be a highly controllable process capable of producing dense films which are free of porosity, low in impurities and having bulk like optical properties. These distinctions are requisite for coatings which require a high laser damage threshold, low scatter and stable spectral characteristics. The application also lends itself to the formation of novel distributed Bragg reflectors (DBR) and rugate structures which require a highly controllable deposition process to form the many, often very thin, layers involved.

In order to further the research in this field and produce advanced optical coatings for applications requiring stringent specification beyond the capability of conventional technology, a VG Semicon V90H MBE system has been installed at OCLI, Scotland, purchased and operated under a joint venture between OCLI Ltd and Heriot Watt University. This facility can provide a thickness uniformity of better than +/- 0.5% over a 4" substrate.

This paper will review the current results from this unique deposition facility and describe the advances made in depositing complex multilayer coatings.

Key words: defect density; large substrates; low absorption and new equipment

Chris Hale and Ian Muirhead are with OCLI Optical Coatings Ltd., Ridge Way, Hillend Industrial Park, Fife, Scotland, KY11 5FR, United Kingdom.

Shari Powell Fisher is with Optical Coating Laboratory Inc., 2789 Northpoint Parkway, Santa Rosa, California 95407-7397, U.S.A.

Dr Gordon Mathew is with Heriot Watt University, Riccarton, Edinburgh, Scotland, EH14 4AS, United Kingdom.

1. Introduction

The continually increasing expansion in the field of optics and opto-electronics has placed great demands on thin film performance. Many applications demand a combination of low absorption, low scatter, high laser damage thresholds and enhanced environmental stability for thin film structures, which play an ever more critical part in the performance of optical or opto-electronic systems.

The requirement has lead to the development of various methods of improving the quality of optical thin films beyond that obtainable using conventional processes. Once such is to employ an ultra high vacuum (UHV) chamber in conjunction with Knudsen effusion cells to deposit material under strictly controlled conditions in a low contamination environment.

The technique was pioneered at the Royal Signals and Radar Establishment (RSRE) in the U.K (6) and the approach builds on the technology developed for molecular beam epitaxy (MBE) of crystalline semiconductors which has proved to be quintessential in providing ultra-pure material for advanced electronic devices. The approach described in this paper differs mainly in that the substrates are not lattice matched crystalline materials but rather polycrystalline or amorphous substances. As this is not, therefore, an epitaxial technique, it is described as molecular beam deposition (MBD).

The equipment used at RSRE was only suitable for laboratory usage but the results were sufficiently encouraging for the process to evolve further with the procurement of a larger and specialised UHV facility, which was situated at OCLI Optical Coatings Ltd, in the U.K. - Figure 1.

This new facility would allow the accelerated development of the process plus provide a small to medium scale production facility to manufacture advanced optical components for the market place which would exhibit the same qualities previously obtained on a smaller scale.

The UHV system was purchased largely from a grant from the Science and Engineering Research Council (SERC) obtained on behalf of Heriot Watt University, Edinburgh. The facility is operated under a joint venture between OCLI Optical Coatings Ltd and Heriot Watt University.

2. The Molecular Beam Technique

In recent years there has been increasing interest in Molecular Beam Deposition (MBD) and Ultra High Vacuum (UHV) thin film deposition for optical applications. Previously, this work had been primarily limited to electronic applications where extreme purity and a structure free of dislocations is paramount to enhanced electrical properties. There are many aspects of the process, however, which can potentially lead to improved optical thin films. The low defect level can reduce the amount of light scattered from the resulting film; bulk-like densities increase the refractive index over conventional thin films and a structure free of voids gives enhanced spectral stability (2) and increased environmental stability.

These improvements are a result of the very low levels of contaminants in the vacuum environment and of the evaporation techniques used. The residual gas encountered at the nominal pressures employed with conventional thermal evaporation (i.e. 10 E-6 mbar) is composed of a large fraction of water vapour, absorbed oxygen, organics (oils, etc) and/or process gasses (e.g. Argon). In comparison, in the UHV environment, the partial pressures of such sources of contamination are in the 10 E-11 mbar regime. Futhermore, the degree of control available allows the potential of techniques for microstructure control and refractive index synthesis to be realised at a sub-microscopic (nanoscopic) level.

In any vacuum deposition process, the degree of contamination of a surface by the residual environment of a coating chamber can be estimated from the Kinetic Theory of Gasses from which the number of molecules of species (i) striking and adhering to the substrate per unit area is given by:

$$R = \frac{S.P_i}{2.pi.M_i.kT)} = \frac{2.67.10\ E22.P_i}{(M_iT)}$$

where P_i = Partial Pressure of i, M_i = Molecular Weight of i, S = Sticking Coefficient. S is generally around 0.1 for permanent gasses.

An ideal coating process would be configured so that the residual flux is negligible compared with the incident flux of material to be deposited e.g. by using a very high incident flux of coating material or by decreasing the residual impurity flux by deposition under UHV conditions. In conventional evaporators, the rate incidence of water on a surface is equivalent to one monolayer every minute at 10 E-5 mbar. In the UHV environment (10 E-11 mbar) employed for MBD, this drops to less than one monolayer over the total length of a typical deposition run.

3. Description of Current Facility

The UHV/MBD facility installed at OCLI consists of the following three chambers, separated from one another by gate valves. Figure 2.

3.1 Growth Chamber

This is the main section of the equipment capable of a base pressure in the mid 10 E-11 mbar range. The substrate holder/manipulator can accommodate a single four inch substrate or a multiple of smaller, e.g. nine by one inch. The ultra-high vacuum provides an environment with residual active gas species e.g. O2, CO, H2O and CO2 in the sub 10 E-11 mbar range.

It is generally accepted that it is particularly important for the deposition of optical thin films to take place in an environment with a minimum H2O partial pressure. In particular, the absorption of moisture between columns of the thin film structure affects the morphology. (6).

3.2 Preparation & Analytical Chambers

One of the advantages of working in the UHV regime is that it allows access to a range of surface analytical facilities. This chamber also operates at 10 E-11 mbar and offers X-ray Photo-electron Spectroscopy. Further extension could provide Secondary Ion Mass Spectrometry (SIMS) and Auger Electron Spectroscopy (AES). Substrates can be studied at any stage in the loading/cleaning/deposition process. Substrate cleaning is achieved through the use of 0-3 KeV Ar ions from a de-focussed beam ion source, assuming uniform etching profiles.

A cassette of ten substrates can be stored under vacuum in this chamber allowing the movement of samples from preparation chamber to deposition chamber without having to open the system to atmospheric pressure.

3.3 Load Chamber

The substrates are loaded into the system via rapid entry load lock without disruption of work in the other chambers. Substrates are cleaned chemically prior to loading into the equipment. The load chamber is evacuated using a cryopump. Pressures of around 10 E-8 mbar are attained before transferring the substrate to the preparation chamber via an hydraulic valve.

3.4 Evaporation Sources

The requirement of the molecular beam generators is to provide a stable flux of ultra-high purity beams which is of a uniform and appropriate intensity. This is provided by Knudsen-cells of which there are four on the OCLI machine with the capacity for four more. In a Knudsen cell, the solid or liquid source material is held in an inert crucible source and a thermocouple is used to provide temperature feedback. These simple concepts belie the considerable design, development and experimentation which has been invested in perfecting the performance of such vital components in MBE equipment.

At typical Knudsen operating temperatures, the flux from the cell to the substrate can be considered as operating in the molecular flow regime as the mean free path of the constituent particles is of the order of one metre and hence interactions within the beam can be considered as negligible. The beams may be effectively interrupted by the interposition of fast mechanical shutters capable of reliable continuous cycling with open/close times less than 0.1 seconds with minimal associated vacuum degradation in the growth environment.

3.5 Layer Thickness Control

As optical thin films may often have an individual layer thickness of a few nanometres, monitoring thickness as the layer grows is of primary importance. This is often done by monitoring the change in reflection from a beam of narrow band-width light reflecting of the growing surface. In the OCLI facility, many wavelengths over the visible and near infrared spectrum is monitored simultaneously using a broad band optical monitor. As well as providing many wavelengths with which to monitor layer growth it also allows the visualisation of the optical performance of the device, as the layers are growing. A quartz crystal rate monitor is also used whenever optical monitoring is unsuitable.

4. Coating Materials and Film Microstructure

The choice of materials for optical coatings is wide and varied. Knudsen cells, however, have a limited temperature range and hence are usually used for the higher vapour pressure materials. This, nevertheless, permits the deposition of a considerable range of materials. These include group II-VI compounds, chalcogenides and flouride materials. Fluoride materials are of particular interest because of their low refractive indices and their wide spectral bandwidths. For example, PbF2 can be used in the 0.2 to 15 micron range. Although most fluorides are partially soluble in water, the actual moisture resistance of a film is dependent on the techniques used for its deposition. A characteristic feature of material grown under optimum conditions in the UHV/MBD system is high film density, resulting in reduced moisture uptake and laser damage thresholds $\sim$ 3 times that of conventional coatings. (5)

The techniques employed have also led to a high degree of interface perfection, the morphology of the films being then only substrate limited. As many of the problems encountered with thin films are related to the polycrystalline columnar microstructure, it would be ideal to avoid this by depositing the films epitaxially on to the substrate. Restrictions on the choice of substrate and thin film materials with their associated lattice constants makes this a difficult goal. This aim, nevertheless, can be partially achieved by the fabrication of "pseudo-amorphous" films using digital stratified designs. These films are synthesised by repeating discrete layers of different materials, the thickness of each component layer being negligible compared with the wavelength under consideration. The fast shuttering and stable fluxes afforded by MBD is ideal for this task. (5)

The high degree of control obtained over the growth process enables refractive index synthesis and the ability to deposit novel structures such as digital graded index films and rugate filters. By altering the mark space ratio of the two materials during deposition, a graded index layer can be achieved. Such designs can be used to avoid high electric field intensities at interfaces within the coating structure.

5. Unfiromity

Uniformity is an important parameter for optical thin film coatings because of the sensitivity of interferometric structures to thickness variations of even a fraction of a wavelength of light. In this work, the materials are evaporated from crucibles, the geometry of which corresponds to the axis of each K-cell being aligned such that the focus of the full K-cell set lies approximately 50mm behind the substrate plane.

The substrates that have been employed are glasses, fused silica or sapphire for the visible and germanium, silicon, chalcogenide or alkali-halide for infra red applications. Substrate temperatures ranged between 20°C to 350°C.

Deposition was performed using a single K-cell for each material with growth rates of typically 1 um/hour.

The variation of optical thickness across a coated surface was measured using standard spectroscopic techniques. With single layer films, the peaks and troughs in the reflection spectrum correspond to optical thicknesses equal to integral numbers of quarter and half wavelengths of the probe wavelength. Two spectroscopic instruments have been used for this work; a Monolight 6800 series scanning grating monochromator and a Bomen/Edinburgh - Instruments spatial scanning fourier transform spectrometer. The latter provides spectra with a typical resolution of 0.2nm in the visible and a spatial resolution of 1mm. Software has been developed for converting raw data into optical thickness contour maps.

5.1 Uniformity Results

Tests were performed using ZnSe in granular form (1 - 2mm size) and better than 99.9% purity level. Crucibles were filled to near maximum capacity and effusion could be considered to occur from a circular area of 40mm. With this full-cell configuration there is negligible focusing from the mouth of the cell. Crucibles with increased cone angles of 1° were used to determine whether better uniformity could be obtained over the standard cells but similar results were obtained and it was concluded that the standard 70cc crucible is close to the optimum design. Uniformity of +/- 1.2% across 100mm was routinely obtained with this configuration.

Improved uniformity was obtained by fine tuning of the source geometry. This can be achieved by exploiting the fact that the granular source material fuses in the crucible once the cell has been heated to deposition temperature. This solid surface is sloped due to the settling under gravity of the granules when a full crucible is first put into the system. It was found that by adjusting the plane of the material surface, with respect to the substrate plane, very high levels of uniformity were obtained. A thickness variation of +/- 0.2% over 100 mm was achieved over several consecutive runs. Figure 3. Similarly, complete interference filter structures have been fabricated using ZnSe and BaF2 with the spatial variation in the centre wavelength of the pass band indicative of only +/- 0.05% variation of the central spacer layer over 80mm diameter. In this case, the narrow interference fringes permit very accurate measurement of small fluctuations in thickness.

It was previously thought that without the use of a planetary rotation system, commonly used in conventional coating facilities, high levels of uniformity might be difficult to achieve. This work has shown that by using thermally stable Knudsen effusion cells, as opposed to heated boats used for conventional thermal evaporation and by optimising source/substrate geometries, excellent uniformity can be achieved.

6. Source Stability

Each Knudsen cell is heated by a series of resistive tantalum foil strips and these are powered by Eurotherm controllers with feedback from a thermocouple assembly which fits around the narrow end of the conical crucible. The temperature stability of this arrangement is +/- 0.1°C over the operating range of the cells (up to 1450 C°). The partial pressure of the coating flux from the cell can be measured by positioning a monitoring ion gauge (MIG) between the source and substrate. The ouput of the ion gauge controller reads to two decimal places.

Remarkable effusion stability has been recorded from the cells under normal operating conditions. Stability of source flux as measured on the MIG is stable to two decimal places during lengthy deposition times and remains constant for constant cell temperatures during subsequent deposition runs.

This feature of the equipment allows many of the multilayer designs to be fabricated using rate as the controlling factor. As an example of this, figures 4a and 4b show the theoretical and measured performance of a distributed Bragg reflector formed by alternating layers of ZnSe and BaF2. The filter performance shown was achieved from the first attempt, after individually calibrating the deposition rate for the two materials. The comparison shows close agreement between the theoretical and measured performance.

As an experiment to test the rate stability, the design was repeated with a slight variation in thickness in the first and last layers. This has the effect in theory of moving the ripple from the long wavelength side of the rejection band to the short. Figures 5a and 5b show the theoretical and measured characteristics for this test, which again show close agreement. The later deposition run was performed several days after the first with no further calibration of the sources.

This stability is a fundamental feature of the system and is vital for the production of devices requiring stringent specification. The fabrication of, for example, a rugate filter, requires an uncompromising process control but unless the coating process is sufficiently stable to respond to control parameters then the desired spectral performance of the filter will not be obtained.

7. Absorption

It has been shown previously that materials deposited under ultra high vacuum have lower levels of absorption than that measured for the same material deposited by conventional thermal evaporation. This is due to lower contamination levels and absence of porosity. The absorption coefficient of ZnSe for MBD layers was found to vary between 100 and 1000 1/cm between 676 and 521 nm. (1)

A thin film device which is highly sensitive to levels of absorption is a Fabry-Perot etalon which usually takes the form of, HLHL...(mHH)...LHLH where H indicates a quarter wave optical thickness layer of a high index material, (ZnSe, n=2.7 at 514nm) and L is a quarter wave layer of low index material, (BaF2, n=1.45 at 514nm). the integer, m, gives the etalon spacer thickness. (2)

Two etalons were fabricated, one using conventional thermal evaporation and the other using MBD. The transmission spectra near the ZnSe absorption edge is shown for each device in figure 6. It can be seen that the MBD device has a higher transmission in the transmissive region and that transmission extends further at the fundamental absorption edge. The absorption edge roll-off is dominated by impurities which affect the spectrum in a variety of ways but all have the effect of reducing the energy gap between the conduction and valence bands, which allows fundamental absorption to occur for longer wavelengths than would be the case for a pure material. (4)

This demonstration shows qualitatively the lower absorption coefficient for ZnSe prepared by MBD compared to the same prepared by conventional thermal evaporation.

8. Surface Quality

Another feature of the thermally stable Knudsen cells is that the emission of spatter is effectively eliminated. Spatter inclusions in a growing layer usually results in the formation of large nodular defects in the coating which can cause scatter and which are prime sites for laser damage effects. (3)

In order to demonstrate the improvement in surface quality between single layers produced by conventional thermal evaporation and MBD, figures 7a and 7b show photographs of ZnSe surfaces produced by the two techniques. The materials were of the same thickness, were deposited at similar rates and with the same substrate temperature. The photographs show a greater density of surface anomalies for the surface prepared by conventional evaporation. The traces from a surface profileometer show the absence of surface anomalies on the MBD layer and also reveals that the surface is smoother (the vertical scale for the MBD layer is 0 to 800 A and 0 to 4000 A for the other). The rms roughness for the MBD layer was 25 A whereas that for the other layer was 90 A.

The reduction of scatter in coatings is of primary importance when fabricating narrow band pass filters with very high optical densities. If the light to be rejected experiences scatter then it will have angle effects in the multilayer structure. For very narrow rejection filters this will mean that the scattered light "misses" the rejection band and is transmitted. This effect could reduce the actual optical density of the filter by orders of magnitude.

9. Laser Damage Thresholds

Due to the short time that the facility has been in operation, no quantified assessment of laser induced damage thresholds have been made although a test programme has been initiated. There is every reason to expect, however, that the laser damage thresholds should be as good, if not better, than those measured on films produced by MBD at RSRE. (5)

10. Future MBD Developments

The V90 was commissioned in late February, 1989 and the system is under constant test and development. A range of materials is being studied to assess their optical properties and the analysis of multilayer interfaces is in progress to select pairs of high and low index materials which will not form poor interface boundaries or unwanted alloys. Materials being studied include zinc sulphide, zinc selenide, barium fluoride, lead fluoride and a range of other fluoride compounds. The combination of barium fluoride and zinc selenide has consistently produced good results and is suitable for the microstructure engineering of multiple, very thin layers (kilo layers). Such engineering allows the synthesis of refractive indices between the high and low limit and is applicable to graded index coatings such as wide band AR and rugate designs.

The ability to produce tight tolerance filters introduces the opportunity to form optically bistable devices and agile filters, by the inclusion to the multilayer of non-linear materials. Optically bistable Fabry-Perot devices have been fabricated which operate at a number of laser wavelengths. (2)

The low absorption, low defect density, absence of porosity and high laser damage thresholds in MBD coatings makes the process suitable for the manufacture high power density laser optics. (5) The process is presently being used to fabricate laser mirrors for wavelengths ranging from UV to 10.6 um.

Although the V90 H represents a great advance in UHV equipment development for optical thin film fabrication, it still has limitations. The system was an "off the shelf" item developed primarily for the electronics industry and as such is limited, in this case, to a 100mm substrate diameter. The thermal sources are adequate for electronic materials but limit the range of optical materials which can be used. There is no reason, though, why the equipment (pumps, sources etc) should not be incorporated into a custom designed chamber, incorporating large susbstrate handling capabilities, load locks and the possibility of electron gun sources for the deposition of high temperature materials such as oxides. These possibilities are constantly under review.

11. Conclusion

A UHV facility for the manufacture of optical thin films by molecular beam deposition on 100mm diamter substrates has been sited at OCLI Optical Coatings Ltd in the UK. It has proved suitable for the production of thin film materials which exhibit low absorption, low defect density and good uniformity over 100 mm. The technique has been used to produce thin films with high laser damage thresholds. The deposition process is highly stable and is capable of being controlled for the formation of multiple, very thin layers. Multilayer devices comprising BaF2 and ZnSe have been fabricated in the system.

12. References

[1] Optical Bistability in II-VI Compounds. A Miller, J Staromlynska, I T Muirhead, K L Lewis, D Craig, G Steward. II-VI-87, Monteray, July 1987.

[2] Optical Bistability in Molecular Beam Deposited ZnSe/BaF2 Multilayer Interference Filters. A Miller, I T Muirhead, K L Lewis, J Staromlynska and D R Welford. Journal De Physique, Colloque C2, Supplement au No 6. Tome 49, juin 1988.

[3] Nodular defects in dielectric multilayers and thick single layers. K H Geunther, App. Op. Vol 20 No 6.

[4] Elementary Solid State Physics. Omar. Addison-Wesley. pp 292-300.

[5] Fabrication of Fluoride Thin Films Using Ultra High Vacuum Techniques. K L Lewis, A M Pitt, N G Chew, A G Cullis, T J Wyatt-Davies, L Charlwood, O D Dosser, I T Muirhead. Proc. Boulder Damage Symposium, 1986.

[6] Assessment of Optical Coatings Prepared by Molecular Beam Techniques. K L Lewis, J A Savage, A G Cullis, N G Chew, L Charlwood, D W Craig. Proc. Boulder Damage Symposium, 1984.

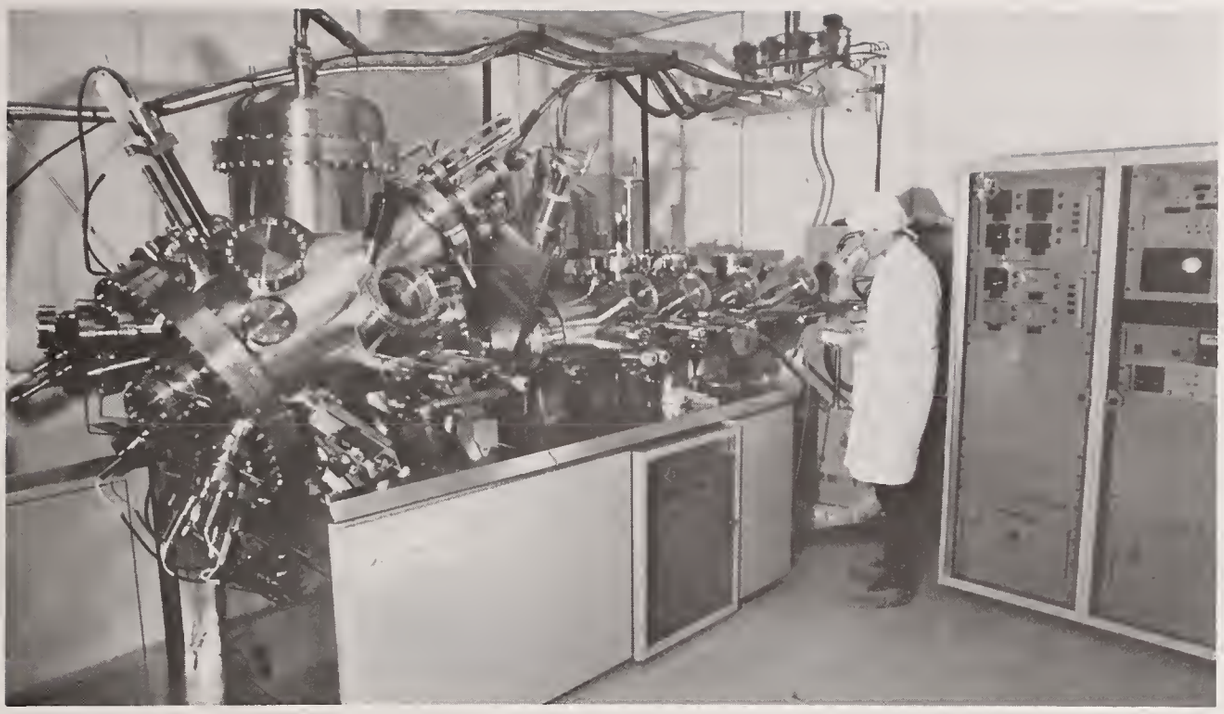

Figure 1: The OCLI/Heriot Watt University
V90H sited at OCLI Optical Coatings Ltd

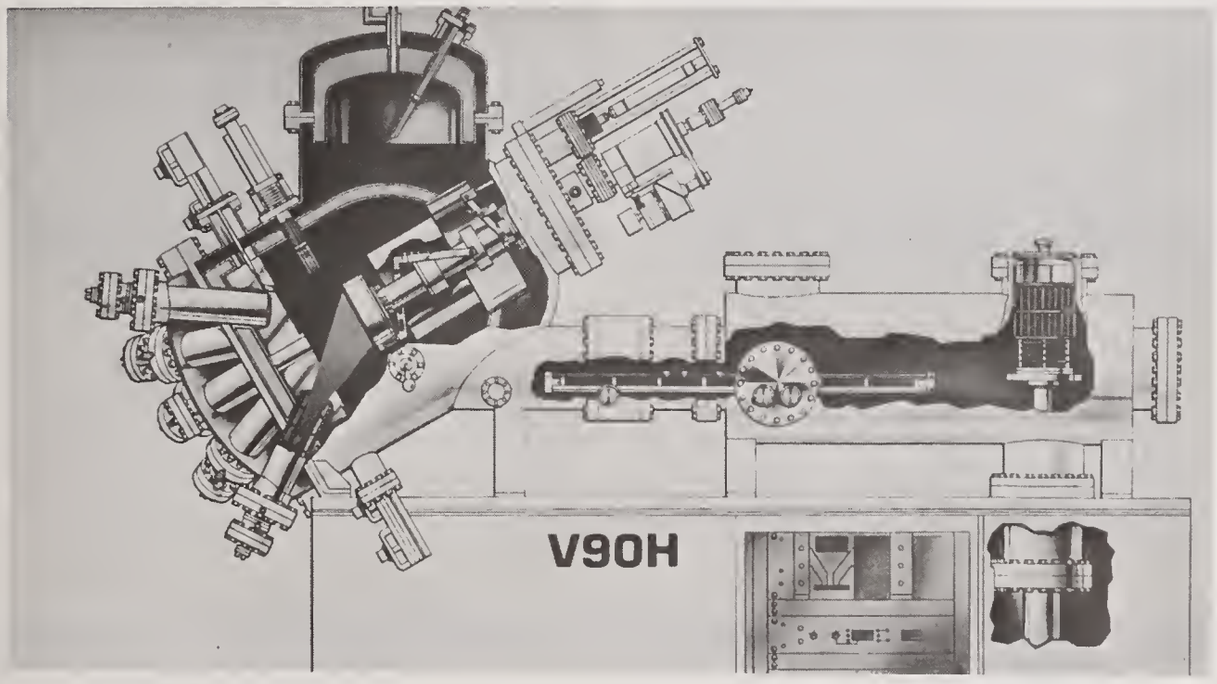

Figure 2: Schematic representation
of the basic V90H

UNIFORMITY RESULTS

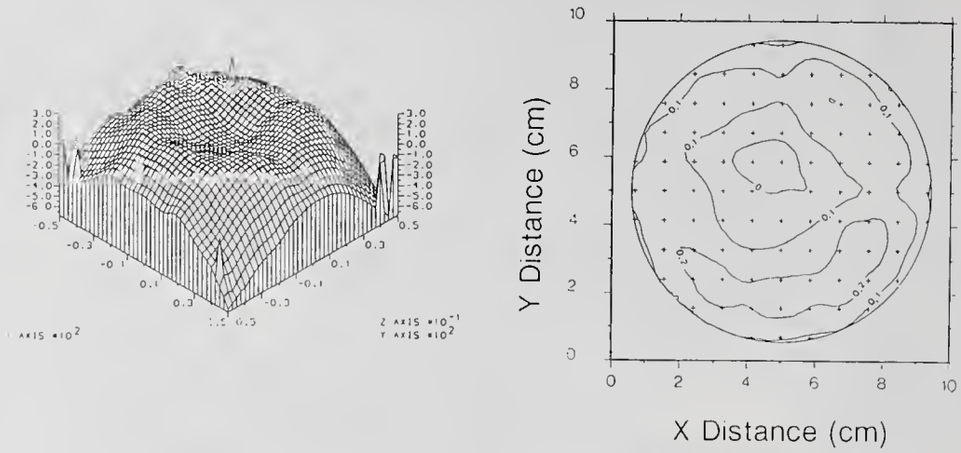

Figure 3: Uniformity of single layer ZnSe over 100 mm
Each contour line represents ±0.1% variation
in thickness from centre

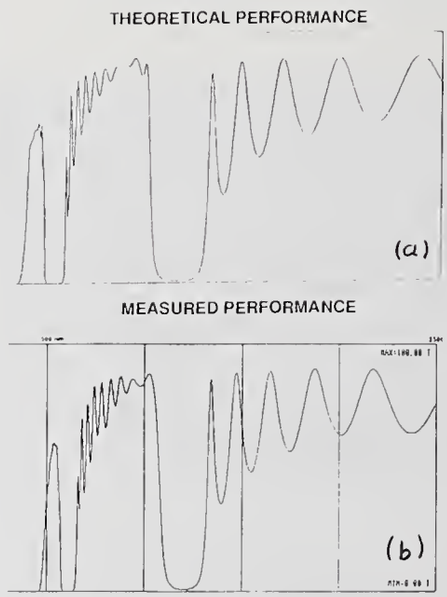

Figure 4: (a) Theoretical and (b) measured performance of DBR filter produced using rate as the controlling agent

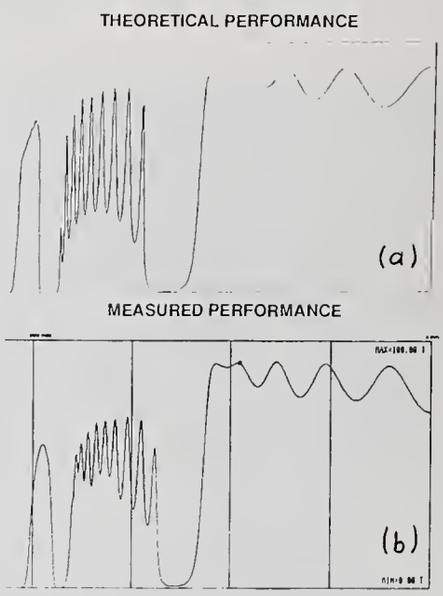

Figure 5: Theoretical and (b) measured performance of similar design with slight alteration to move ripple. Rate control again was used.

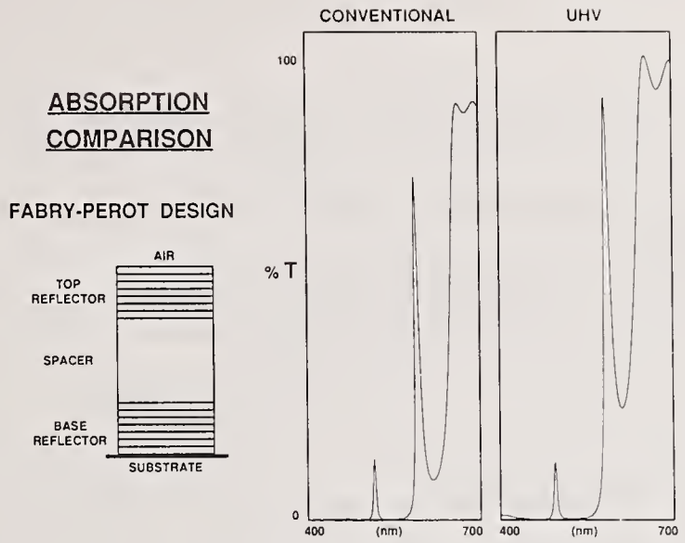

Figure 6: Transmission spectra for two etalons fabricated by conventional thermal evaporation and MBD. The MBD filter shows superior optical characteristics.

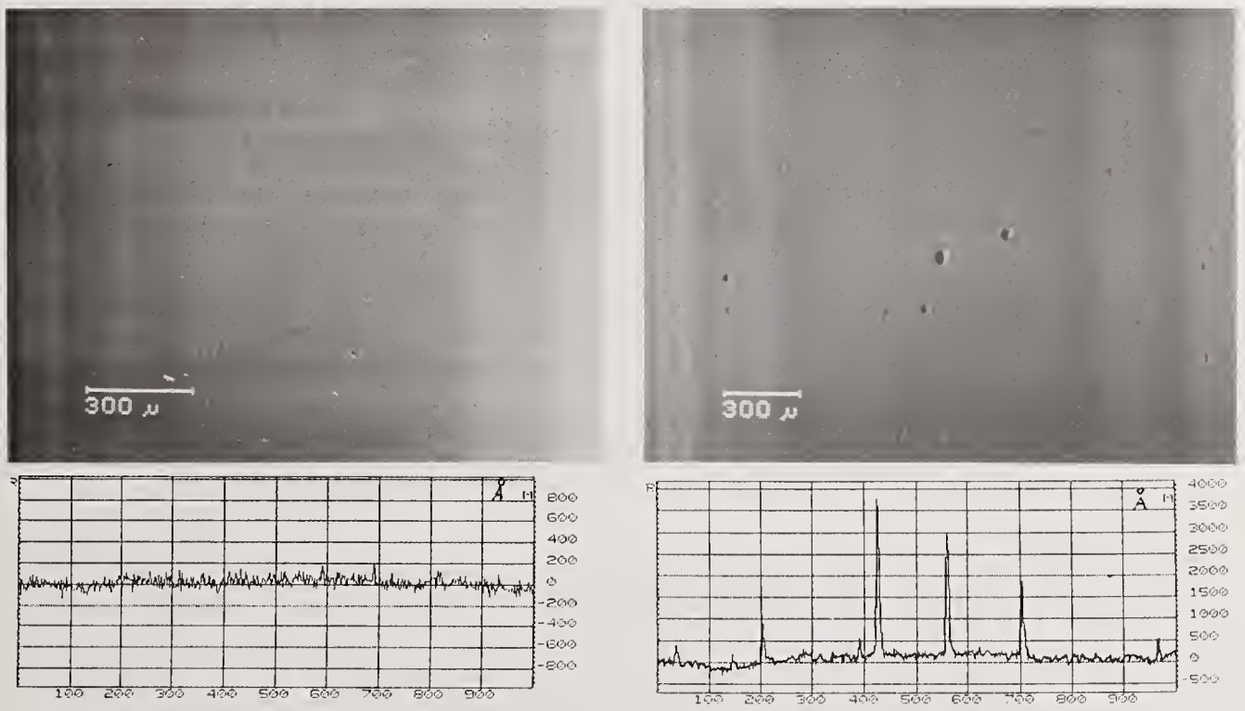

Figure 7: (a) Surface of ZnSe deposited by MBD plus surface profile

(b) Surface of ZnSe deposited by conventional thermal evaporation plus surface profile

COMMENTS

Question: First question is the same as the last speaker. What is the price tag?

Answer: The total price of the equipment you saw there including cleaning facilities, XPS, is about three-fourths of one million pounds.

Question: Have you quantified the absorption and defect densities yet?

Answer: We haven't qualified them from this machine. We are going back to the results from RSRE. The absorption could change from 1000 to 100 in inverse centimeters between wavelengths 647 nm to 521 nm.

Question: Can you get practical production throughput on normal reflectors in such a device or does it take a couple of days.

Answer: The deposition rates we have readily achieved are up to three microns an hour. These rates aren't particularly fast but a fast rate isn't necessary for the stability of the cells. We do have the ability to store up to twenty index cassettes under ultra-high vacuum. The system is thus designed with small scale production in mind.

Question: One of the advantages of Keith Lewis's system was that he was able to demonstrate that in a number of cases he did in fact get optical constants, particularly absorption coefficient, which were equivalent to the bulk material. I believe that is the first time that bulk optical properties had been achieved for some of these thin films. You have shown us qualitatively that you are getting significantly better results than those obtained for conventional films. But have you gotten quantitative results. Do you know how close you are to the bulk, optical properties of the materials?

Answer: We haven't quantified that as yet. That is why I showed only the qualitative results. It was only a visual representation of the difference in absorption. But we will get quantative results and report them.

Question: What fraction of the conventional coating materials do you think that you will ultimately be able to handle by this technique?

Answer: We bought an off the shelf system. The system is developed by VD Semicon for the electronics industry and you just fit it with cell sources. You have a temperature range of around 1450°C, considering the low pressures that we have. We can evaporate most materials, for example, ionic fluorides. There is no reason at all why we couldn't expand this system to take E-guns, larger sources, larger substrate handling capabilities. It just needs funding.

Manuscript received
2-22-90

Investigation and Modelling of Laser Damage Properties of Fabry-Perot Filters

A. McInnes, C.M. MacDonald, D.R. Gibson and A.D. Wilson

Applied Physics Group
Barr & Stroud Ltd
Pilkington Optronics
Anniesland
Glasgow G13 1HZ
Scotland, UK

The electric field distribution within a fabry-perot etalon is readily variable by changing the angle of incidence or the thickness of the etalon. The laser damage threshold (LDT) of Fabry-Perot etalons was measured as a function of electric field distribution, monitored through the transmittance. Two types of etalon were used - thin film Fabry-Perot devices with high finesse were investigated at 1.064μm, and a simple dielectric slab etalon (Germanium) was investigated at 10.6μm.

In the latter case the results show a correlation between the LDT and the inverse square of the calculated peak electric field ($1/E^2$) in the sample. For the thin film Fabry-Perot, the correlation is between the LDT and $1/E^2$ at the spacer boundaries. Subsequent sample analysis also suggests that damage was initiated at spacer boundaries.

It is concluded that the laser damage properties of such etalons are in agreement with theoretical expectations, and that their damage behaviour can be described by a single parameter.

Key words: Fabry-Perot etalons, Laser damage, CO_2 laser, Nd:YAG laser, electric field distribution.

1. INTRODUCTION

The laser damage behaviour of Fabry-Perot etalons (FPEs) of two types - thin film type was studied with a Nd:YAG laser at 1.064μm, and a simple dielectric slab etalon of Germanium was studied with a CO_2 laser at 10.6μm. It is found that the LDTs are highly variable, depending on the conditions of the measurement, but the behaviour can be explained and agrees with theoretical expectations.

FPEs are ideal devices to examine because their linear behaviour is well understood and their transmittance and reflectance can be changed by varying the angle of incidence, the thickness or the thin film design. Small changes in any of these parameters cause large changes in the electric field distribution within the device, so that by, for example, tilting a FPE, the peak fields can be varied in magnitude and position, and thus used to probe the interior of the FPE.

2. GERMANIUM ETALON

The measurements on this were carried out using a dedicated CO_2 laser damage testing system, whose parameters are shown in Table 1.

Table 1. CO_2 Laser System Parameters

Wavelength (μm)	10.6
Pulselength	100ns spike + 2μs tail
Spot size (μm)	210 $1/e^2$ diameter
Mode quality	TEM_{oo}

In these experiments, the LDT was measured as a function of optical thickness. This was controlled by varying the sample temperature, thus allowing it to be irradiated at normal incidence throughout. Angle could have been used, but would have introduced unnecessary complications such as beam walk-off. The measurements were carried out with the sample at the beam waist, where the beam is best collimated.

In order to find the internal electric field distribution we need to know the optical thickness, which is obtained through measurement of the device transmission.

Figure 1 shows transmission vs. temperature for the Germanium FPE. Note the large modulation, due to the high refractive index of Ge. Also, we see that it takes a temperature change of $\approx 14^{o}C$ to scan one complete free spectral range, which corresponds to an optical thickness change of $\lambda/2$. This means that tight temperature control is not necessary. This figure also illustrates the fact that measurements were carried out over more than one free spectral range.

Figure 2 shows the electric field distributions within the FPE in three different transmission states. High transmission means high internal fields, and low transmission means low internal fields. Other states are intermediate.

From earlier work [1], [2], [3] the LDT is expected to be related to the field distribution, and indeed a strong correlation is found between LDT and the inverse of the peak field squared.

Figure 3 shows the results. Up to $\approx 35 Jcm^{-2}$ they fit a straight line very well. This tells us that LDT x E^2 for these points is a constant. In other words, the value of E^2, the peak fluence inside the sample, is constant at the onset of damage, regardless of the combination of input fluence and optical thickness that give rise to it. This value is $11.5 Jcm^{-2}$. This means that if $>11.5 Jcm^{-2}$ exists within the sample, it will damage.

As for the two points not on the line, there are two possible explanations. Both involve the fact that energy is high. It could be that another process is beginning to limit the LDT, such as a surface effect perhaps, or possibly we are seeing a nonlinear change in refractive index, which leads to a change in the optical thickness and hence increases the peak field from the expected value.

There are few points to note here. Firstly, the range of LDT values observed is approximately a factor of 4. Bear in mind that this was all carried out with one sample. This large range is obtained purely by changing the optical thickness.

The next point is that it is the peak field squared that is important. It is known [4], [5] that damage in Ge is dominated by the effect of a surface layer with higher absorption than the bulk, due to polishing debris and absorbing defects. Yet it is not the field at the surface that determines the LDT, but the peak field which, as we see from Figure 2, can be up to $\lambda/4$ = 0.66μm inside the sample. This suggests that in this case, damage is initiated inside the sample. It therefore also suggests that the surface absorbing layer is at least 0.66μm thick.

3. THIN FILM ETALONS

These measurements were carried out using a dedicated Nd:YAG laser damage testing facility whose parameters are shown in Table 2.

Table 2. Nd:YAG Laser System Parameters

Wavelength (μm)	1.064
Pulselength (ns)	15
Mode Quality	TEM_{oo}

There were three different designs of thin film FPE, and they are shown in Table 3. All the "H" layers are ZnS, all the "L" layers MgF_2, and all were quarter-waves at 1070nm. This was chosen so that tilting the FPE by a few degrees would change it from a low to a high transmission state.

Table 3. Design of Thin Film Fabry-Perot Filters

Design 1	$(HL)^4$ 2H $(LH)^4$
Design 2	$(HL)^3$ 4H $(LH)^3$
Design 3	$(HL)^4$ 8H $(LH)^4$

The angular performance of the three filters is shown in Figure 4. The broader transmission maximum of design 2 is due to the fact that its mirrors have three repeat units rather than the four of designs 1 and 3. Design 3 has the narrowest peak and the

greatest angular peak position because it has the thickest spacer layer.

The effect of angle on the field distribution within design 1 is shown in Figure 5. On going from low to high transmission there is a very large increase in the peak field squared at the spacer layer boundaries.

Figure 6 shows typical damage site morphology, and this, in conjunction with the stylus profilometer trace, can be used to elucidate the position of initiation. Material has been removed from the beam area down to the depth of the spacer layer, suggesting that the point of damage was at the spacer boundary, which we would expect from the field distribution. Damage was seen to occur at one or other, or both, spacer layer boundaries.

The results (fig. 7) show good correlation again, but this time with the fluence at the spacer boundaries. Note that this plot includes data for all 3 filter designs. Again the product LDT x E^2 = constant, in this case equal to $25Jcm^{-2}$. There is an even larger range of LDT, due to the amplification of the field at the spacer boundaries.

Thin film interaces within the multilayer are regions of high defect and impurity density, and therefore regions of high absorption [6]. Also, the interfaces are regions of mechanical weakness. In combination with the high field, this results in preferential damage at the spacer interfaces.

The two points not on the line may be explained as follows. Both are design 3 data, and if we look at the field pattern for this case as shown in Figure 8, we see that there is another peak at the first layer boundary. This boundary, at the top of a 24 layer stack, is likely to be under stress, and indeed when we look at the morphology we see a quite different pattern, (fig. 9). The film has simply ruptured, and this is consistent with damage just below the surface.

4. CONCLUSIONS

In both cases it has been shown that the LDT is highly dependent on the exact measurement configuration. However, when field effects are taken into account, the behaviour is found to be as expected. In fact, a single number can be found to describe the LDTs of each device type; $25Jcm^{-2}$ at the spacer boundaries for the thin film FPE and $11.5Jcm^{-2}$ inside the sample in the case of germanium.

This has the well-known corollary that if a high LDT coating is desired then the peak fields should be kept away from the interfaces.

It also serves as a warning to be extra careful of measurement conditions when testing samples or devices which could act as etalons.

One last point is that there might be an application for the Ge etalon as a variable reflectivity high LDT mirror which does

not need coatings or depend on polarisation for its variability. It could possibly be used as an output coupler for high energy CO_2 lasers.

The permission of the management and directors of Barr & Stroud Ltd to publish this work is gratefully acknowledged.

5. REFERENCES.

[1] Apfel, J. H.; Matteucci, J. S.; Newnam, B. E.; Gill, D. H. Symposium on Laser Induced Damage in Optical Materials. Nat. Bur. Stand. (U.S.) Spec. Publ. 462; 1976 301p.

[2] Apfel, J. H.; Symposium on Laser Induced Damage in Optical Materials. Nat. Bur. Stand. (U.S.) Spec. Publ. 509; 1977 251p.

[3] Gill, D. H.; Newnam, B. E.; McLeod, J. Symposium on Laser Induced Damage in Optical Materials. Nat. Bur. Stand. (U.S.) Spec. Publ. 509; 1977 260p.

[4] Gibson, D. R.; MacDonald, C. M.; Wilson, A. D. Symposium on Laser Induced Damage in Optical Materials. Nat. Bur. Stand. (U.S.) Spec. Publ. 746; 1985 203p.

[5] McDonald, C. M.; McGeoch, S. P.; McInnes, A. A.; Nelson, C. H.; Wilson, A. D. "Laser-induced damage mechanisms in model optical materials." J. Phys. D.: Applied Physics (UK) 21; S85-S87; 1988.

[6] Ristau, D.; Dang, X. C.; Ebert, J. Symposium on Laser Induced Damage in Optical Materials. Nat. Bur. Stand. (U.S.) Spec. Publ. 727; 1984 298p.

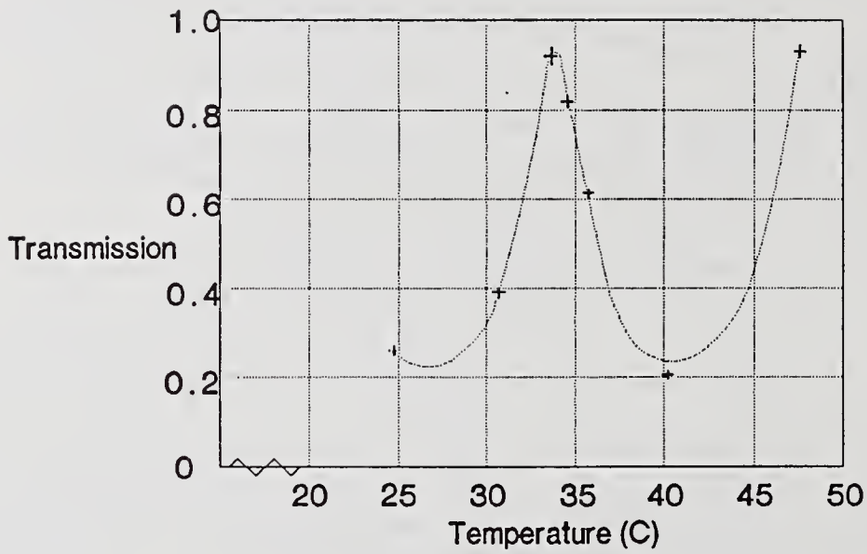

Figure 1 Transmission vs temperature for the germanium etalon at the temperatures used for the LDT measurements (experimental).

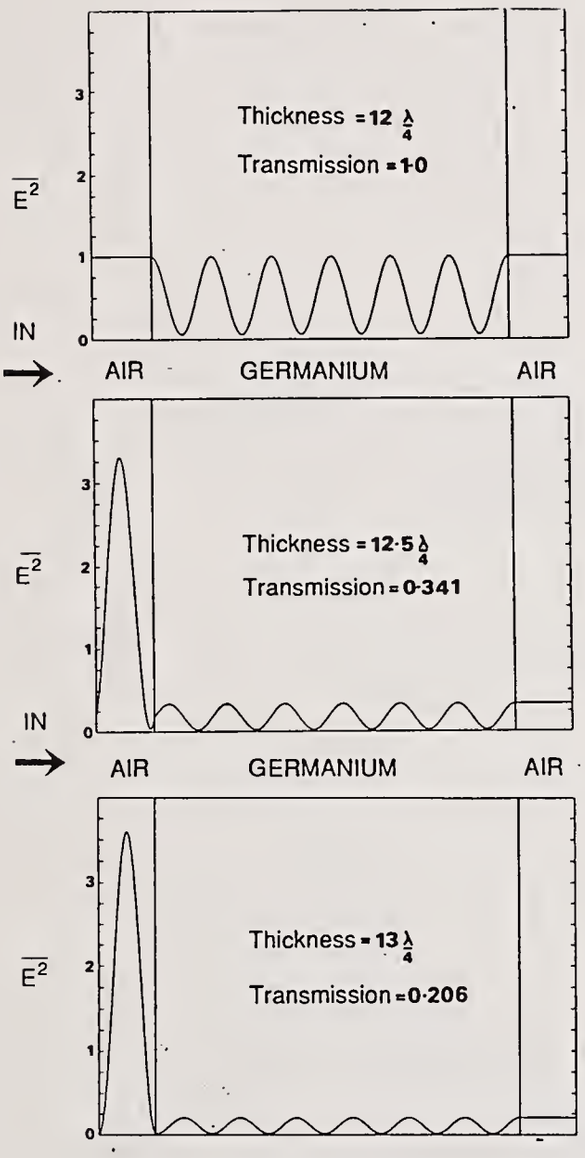

Figure 2 Time-averaged electric field distributions within the germanium etalon in different transmission states.

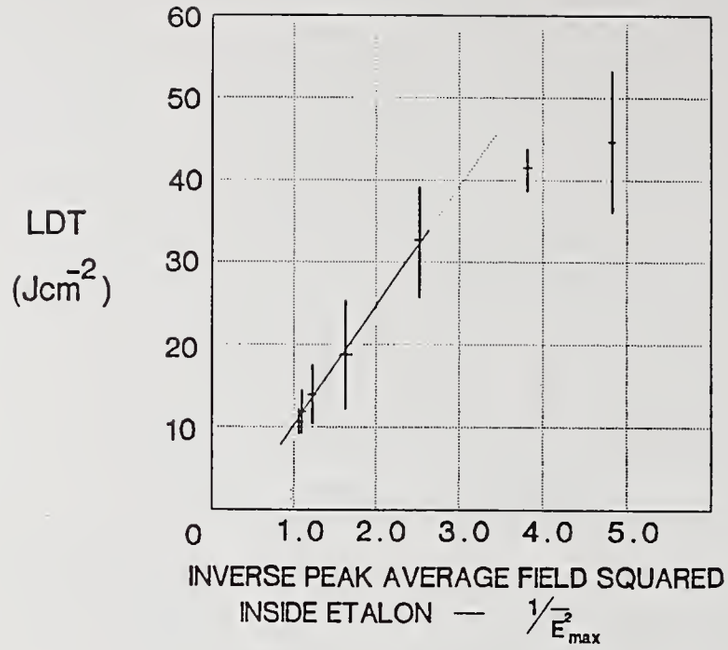

Figure 3 LDT vs 1/(peak time-averaged field squared) inside the germanium etalon.

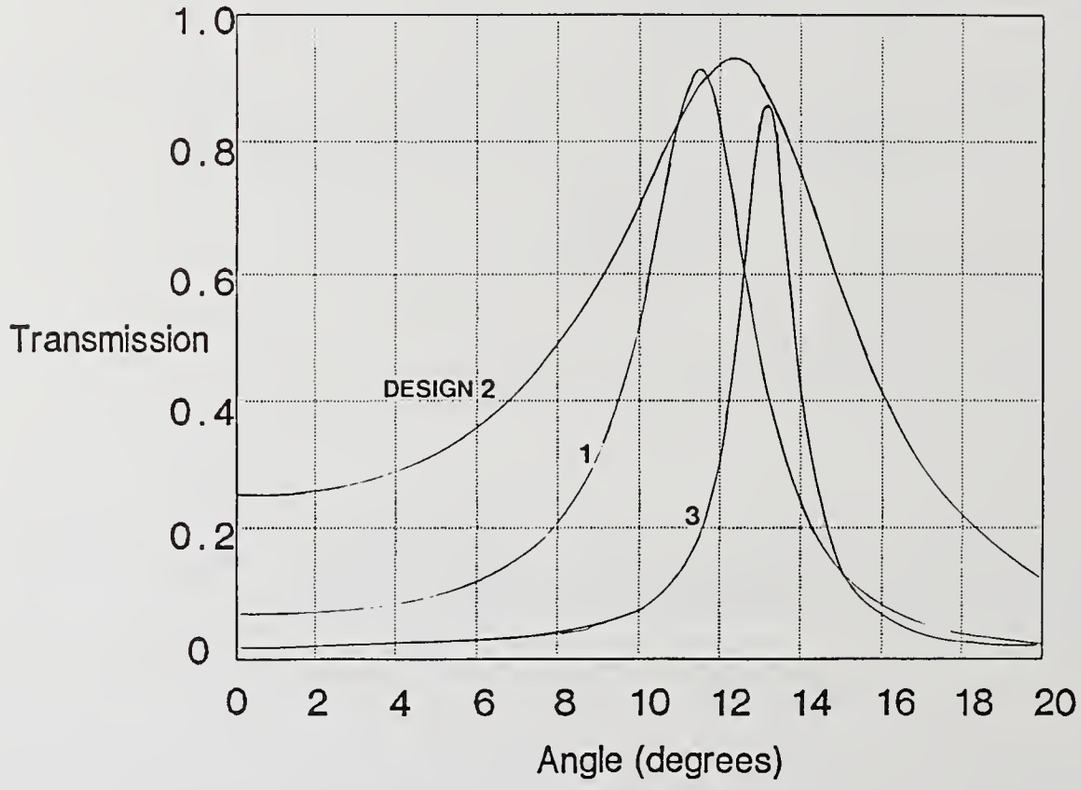

Figure 4 Transmission vs angle of incidence for the three thin film FPE designs, at 1.064μm.

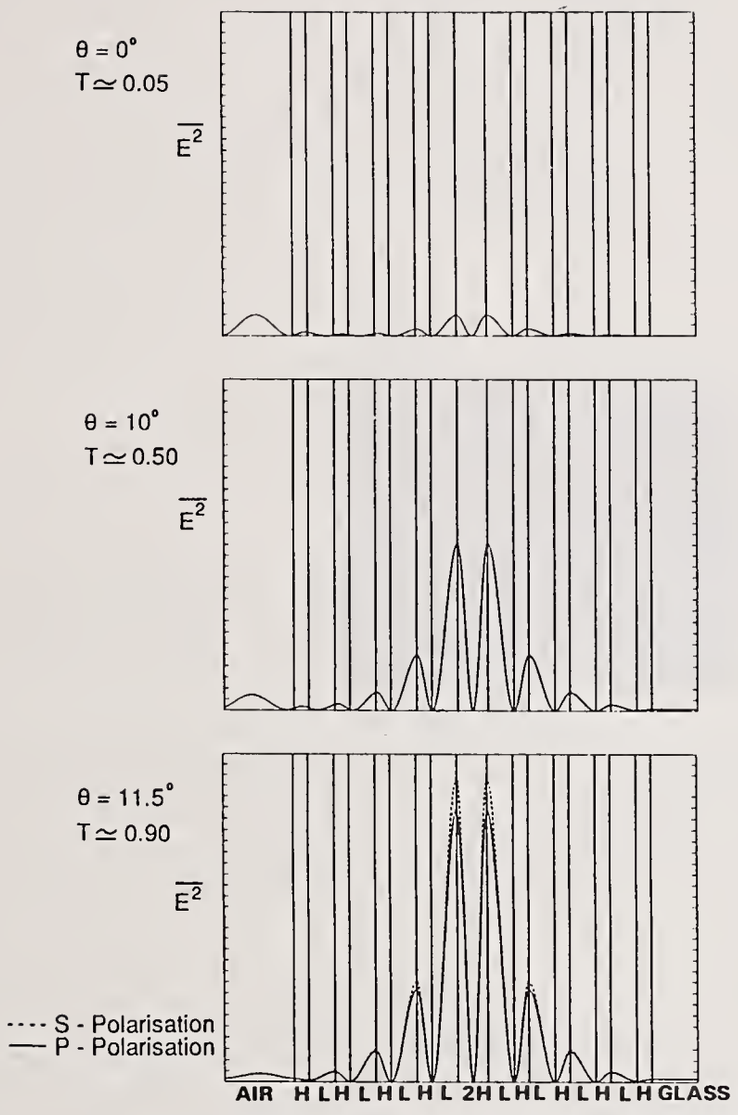

AVERAGE FIELD SQUARED vs. POSITION THROUGH A THIN FILM FABRY-PEROT FILTER FOR DIFFERENT ANGLES OF INCIDENCE

Figure 5 Time averaged field squared vs position through a thin film FPE (design 1) at different angles of incidence.

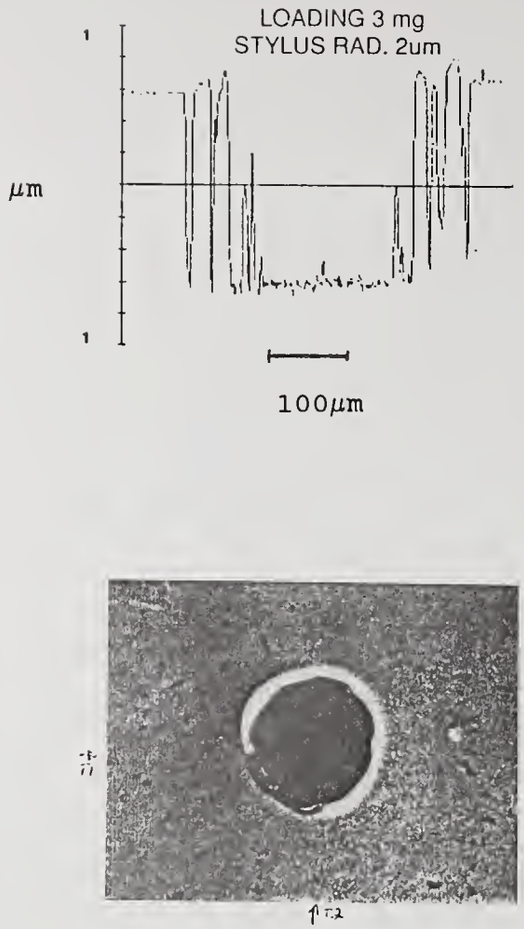

Figure 6 Stylus profilometer trace and Nomarski micrograph of a damage site on a thin film FPE.

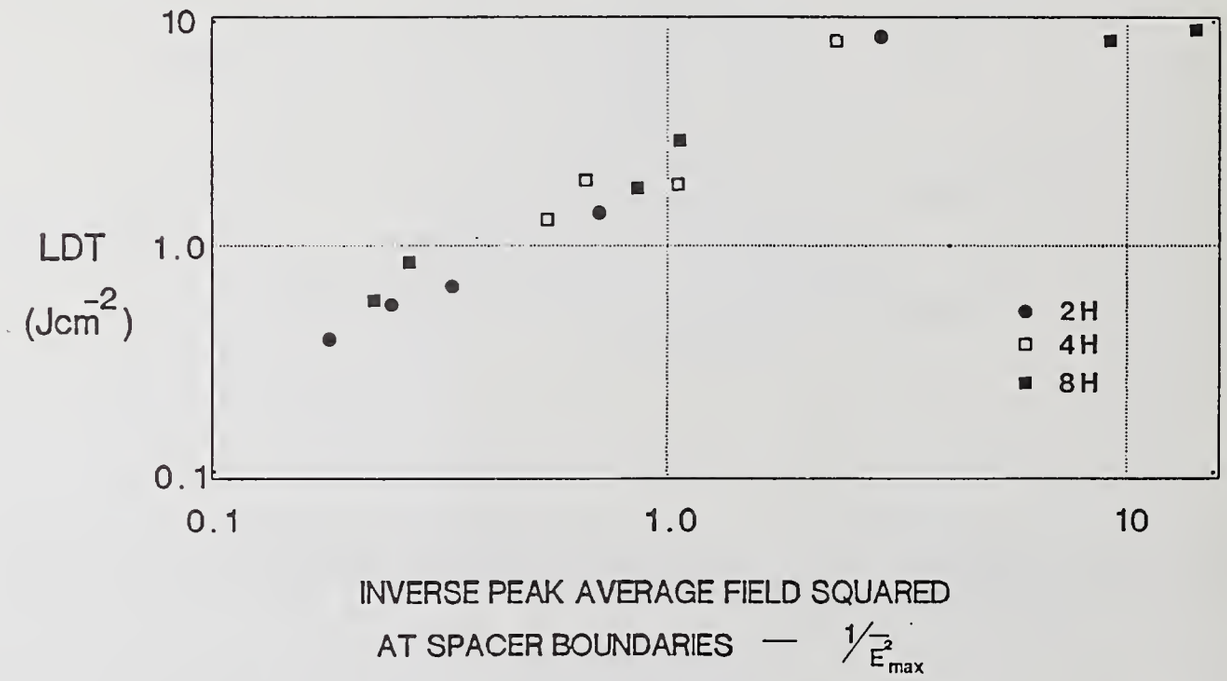

Figure 7. LDT vs 1/(peak time averaged field squared) at the spacer boundaries of the thin film FPEs).

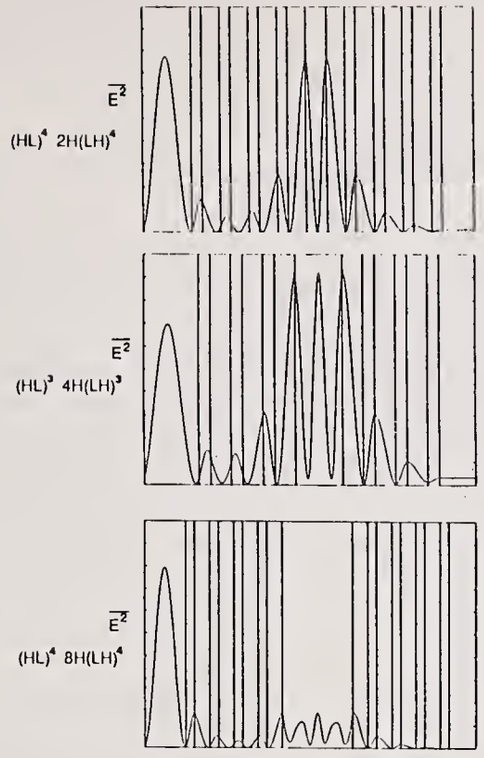

Figure 8 Time averaged field squared vs position through thin film FPEs of different designs all at normal incidence (low transmission, high LDT).

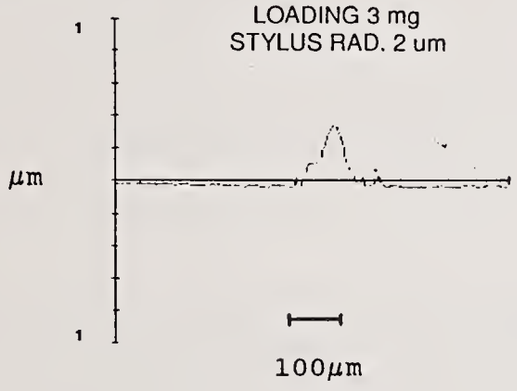

Figure 9 Stylus profilometer trace and Nomarski micrograph of a damage site on a thin film FPE.

COMMENTS

Question: I'm confused about the composition of aluminum oxide. I saw that boehmite and Al_2O_3 were both listed in your data.

Answer: Yes, I'm afraid I have been sort of lax. A boehmite is a crystallized form of dehydrated aluminum. It is quite a stable hydrate. You would have to heat to 500° before it dehydrates and it dehydrates to something like monohydrate alumina. There are two ways of writing the monohydrate. You can either call it AlOOH or call it $AL_2O_3 \cdot H_2O$. What we are doing now is we tend to call it AlOOH because I think that, that makes it easier to understand than when you see the H_2O on the end of alumina. But the monohydrate and boehmite are both recognized as fairly stable crystalline hydrates.

Question: What kind of thickness control do you have when you look at the different spin rates. Do you still get uniformity?

Answer: Yes, the thickness control is surprisingly good. We usually vary the thickness by varying the concentration of the applied solution rather than by varying the difference in spin rate. If you spin faster you will tend to get thinner coats because it spins off faster. So slow spinning gives you thick coats, faster spinning gives you thin. We like to spin reasonably fast to get the stuff right out to the side. You can vary the thickness also by varying the concentration in the material that you are adding. If you have a high concentration of course more stays on the substrate. Spin coating is almost idiot proof for getting things uniform. I was told that by an expert who knows about these things.

Question: Have you done any work at all with spin casting on curved surfaces?

Answer: Yes, we have spin coated lenses convex and concave. Now, I don't know exactly what the focal length was, but it was considerable and I thing g forces, the centrifugal force out seems to be much greater than 1g. We have never had any problem. It is very easy to see this because all these single coatings are colored so you can see how good the uniformity is just by looking at it. The human eye is pretty good for detecting nonuniformity. Things always turn out nicely uniform.

Question: Did you characterize the silica gel size?

Answer: Yes, silica particles vary from eight nanometers to 20 nm and they are roughly spherical. Our alumina particles are plates and they are roughly 30 nm by 30 nm and about 5 nm thick.

Question: Do you do anything to keep the particles from becoming aggregates in solution?

Answer: No, as long as you keep them in solution they are mainly monodispersed. One of the problems we do have, especially with the silica, is that if we dry it out and then try to resuspend it, it aggregates. That is a problem we have especially in a dip coating apparatus where the fluid goes up and down. A crude coat tends to form around the outside and it doesn't redisperse. The alumina does.

Manuscript received
3-20-90

High Damage Threshold AlO.OH-SiO_2 HR Coatings Prepared by the Sol-Gel Process*

Ian M. Thomas

University of California
Lawrence Livemore National Laboratory
P.O. Box 5508, L-483
Livermore, CA. 94550

Our study of highly reflective (HR) dielectric coatings prepared by the sol-gel process has indicated that hydrated alumina and silica are the materials of choice for the high and low index components respectively.

We can now prepare 32-36 quarter-wave-layer samples from colloidal suspensions of the relevant oxides by spin coating at room temperature. These have reflectivities of about 99% and damage thresholds in the range 30-40 J/cm^2 at 1064 nm with 16 ns pulses at 30 Hz. This threefold improvement in threshold over that reported earlier for this system was attributed to an improvement in the preparative technique particularly in regard to cleanliness. Coatings have been prepared recently on substrates up to 8" in diameter and scale-up development continues.

1. Introduction

The work described in this paper is part of a continuing study on the preparation of high damage threshold coatings suitable for use on the optical components in high power laser systems. Earlier investigations with the same objective on porous silica anti-reflective (AR) coatings [1], porous fluoride AR coatings [2], TiO_2 and TiO_2-SiO_2 high reflectivity (HR) coatings [3] and $Al_2O_3.H_2O$ and $Al_2O_3.H_2O$-SiO_2 HR coatings [4] have been previously reported.

Our investigation throughout has been based on the use of colloidal suspensions as coating media. These have the following advantages over other systems:

1. Liquid system which is easily applied at room temperature by conventional means.
2. No cure or heat required. Stress-free.
3. Rapid application
4. High purity product

---

*Work performed under the auspices of the U.S. Department of Energy by Lawrence Livermore National Laboratory under Contract No. W-7405-ENG-48.

5. Especially good for large substrates.
6. Low capital equipment cost.
7. Coating easily removed and replaced with no damage to substrate.

In our work with HR coatings we have always used SiO_2 as the low index component. Colloidal suspensions of SiO_2 are readily prepared and can be used to give high damage threshold, single layer SiO_2 coatings [1]. We have used these as AR coatings on substrates up to one meter in diameter. TiO_2, ZrO_2, HfO_2, Ta_2O_5, and AlO.OH were selected for investigation as the high index component. All but AlOOH were eventually rejected mainly because single coatings from each material had only low to moderate damage thresholds. The preparation of suitable colloidal suspensions of ZrO_2 and HfO_2 were also quite involved. These would have been difficult to prepare in quantities suitable for application to large substrates.

Suspensions of AlO.OH were found to be readily prepared and to give high damage threshold single layer coatings. The AlOOH-SiO_2 system was therefore chosen for further investigation. The initial work was carried out on 5 cm diameter substrates but our ultimate objective was to scale-up to much larger sizes.

2. Experimental Procedure

2.1 Colloidal Suspensions

Suspensions of AlOOH and SiO_2 were prepared by the hydrolysis of sec-butoxide aluminum and tetraethylsilicate respectively by methods previously described [1,4]. Both alkoxides were distilled prior to use to ensure a high purity product.

The SiO_2 suspension was prepared at 3% concentration in ethanol and then diluted to 2% with ethanol prior to use. The AlOOH suspension was prepared at 1% concentration in water. It was then adjusted to pH 5 with an ion exchange resin, evaporated under vacuum to 16% and finally diluted to 4% with methanol prior to use.

2.2 Coating Procedure

All coating suspensions were filtered through a 0.2 μm membrane filter. 5 cm diameter and 1 cm thick fused silica or BK-7 substrates were then coated using a spin coater in a 0.2 mm filtered, forced air horizontal flow clean hood. The first coat applied was always SiO_2 and this was followed with alternating AlOOH and SiO_2 coatings allowing about 10-15 minutes drying time between coats. The final coat was AlOOH. All coatings were prepared at an optical thickness of 266 nm corresponding to quarterwave at 1.06 μm.

The preparation and processing of both suspensions is illustrated in figures 1, 2 and 3.

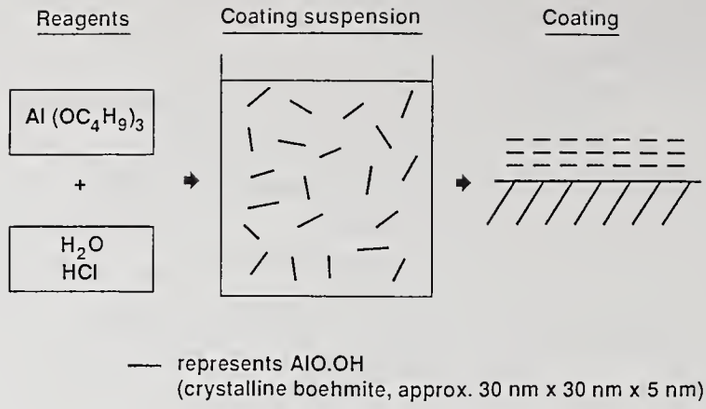

Figure 1. Preparation and application of colloidal AlO.OH.

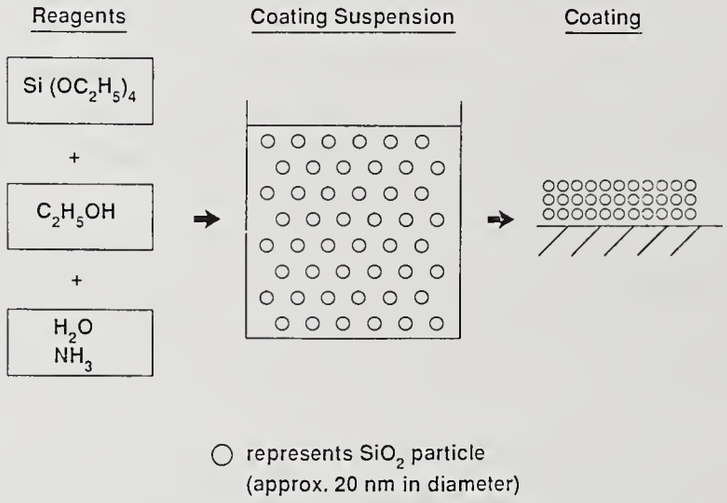

Figure 2. Preparation and application of colloidal SiO_2.

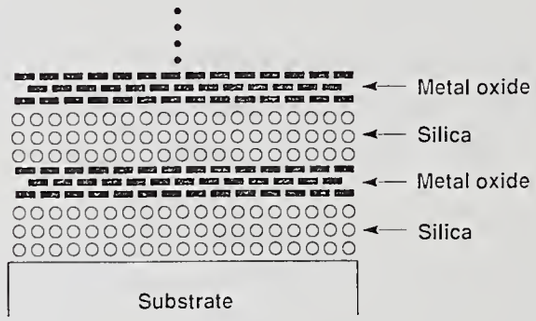

Figure 3. Multilayer HR coating.

2.3 Damage Threshold Measurements

Damage threshold measurements were carried out at 1064 nm using multishots at a pulse length of 16 ns at 30 Hz. The beam spot size was approximately 1 sq. mm. Each site on the sample was irradiated for 60 seconds (1800 shots) and then inspected for damage.

A new site was then selected and irradiation repeated. From a sequence of irradiations, the damage threshold was defined as the average of the highest fluence which caused no damage and the lowest fluence that did.

3. Discussion of Results

The refractive indices of the SiO_2 and AlO.OH prepared from colloidal suspensions have been shown to be 1.22 and 1.44 respectively [4]. A large number of alternating layers will therefore be required for high reflectance in a HR mirror system because of the low index difference. Calculations indicated that about 30-36 layers would be required to achieve reflectance greater than 99% on BK-7.

Table I shows the actual reflectances obtained for a variety of samples containing from 26 to 40 layers. It can be seen that at least 34 layers are required for 99% reflection. Figure 4 shows the transmission curve of a fused silica substrate coated with 36 layers. The reflectance of this sample is greater than 99% at 1064 nm. The narrow band third harmonic reflectance of about 95%, which is characteristic for this type of quarterwave stack is also present.

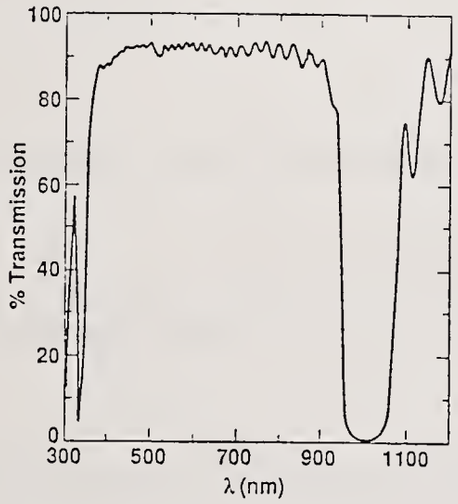

Figure 4. Transmission spectrum of 36-layer HR coating.

Laser damage threshold measurements at 1064 nm (16 ns pulse, 30 Hz) are also listed in Table I. These range from 21-50 J/cm^2 with an average of 37 J/cm^2 with no apparent dependence on number of layers. This perhaps is not unexpected as the first few layers in

all samples are exposed to, and reflect most, of the fluence. These damage thresholds are much higher than we have reported previously [4]. While the reason for this is not known for sure we suspect that improvement in technique, especially in regard to cleanliness, has made a major contribution.

Table 1. Reflectance and damage threshold of several HR coatings.

Layers	Reflection at 1.06 μm	Damage 1064 nm/16 ns
26	95.0 %	34 J/cm^2
30	98.0	45
30	98.5	28
32	98.0	38
32	98.5	50
34	99.0	21
36	99.0	37
40	99.5	40

Our efforts are now directed towards scaling-up the coating process. We are currently coating 8" diameter fused silica substrates and have encountered a few minor problems. These include an increase in the number of artifacts and "comets" in the coatings and, in some cases, radial lines have appeared. The artifacts mean that we must improve our cleanliness to an even greater extent and the radial lines are probably due to non-uniform drying and suspension instability during coating. These factors are all under investigation.

4. Conclusions

We have selected AlO.OH - SiO_2 over several other candidates for continuing evaluation as an HR coating system.

Our research on small 2" diameter samples has indicated that this system has high laser damage threshold and adequate optical performance but requires a large number of layers (32-36).

A coating system for 8" diameter substrates is under development.

5. References:

[1] Thomas, I. M. "High Laser Damage Threshold Porous Silica Antireflective Coating," Appl. Opt. 25, 1481 (1986).

[2] Thomas, I. M. "Porous Fluoride Antireflective Coatings," Appl. Opt. 27, 3356 (1988).

[3] I. M. Thomas, "Single Layer TiO_2 and Multilayer TiO_2-SiO_2 Optical Coatings Prepared from Colloidal Suspensions," Appl. Opt. 26, 4688 (1987).

[4] Thomas, I. M. "Single Layer $Al_2O_3.H_2O$ and Multilayer $Al_2O_3.H_2O$-SiO_2 Optical Coatings Prepared from Colloidal Suspensions," Appl. Opt. 28, 4013 (1989).

Manuscript received
3-8-90

1-on-1 And n-on-1 Laser Strength of Binder Aided ZrO_2 and ZrO_2-SiO_2 Reflective Sol-Gel Coatings

Hervé G. FLOCH and Jean Jacques PRIOTTON
Commissariat à l'Energie Atomique
Centre d'Etudes de Limeil-Valenton
94195 Villeneuve Saint Geroges Cedex
France

Abstract

In continuation to our search program on laser-damage resistant coatings and in synergy with the Lawrence Livermore National Laboratory, we have prepared porous single layer coatings of ZrO_2 on fused silica and BK-7 substrates from suitable aqueous colloidal suspensions of crystalline zirconia at room temperature. By adding judiciously a soluble inorganic binder to the suspension prior to application, it has been possible to increase substantially both the coating refractive index and the abrasion-resistance. The optimum binder concentration was about 30 % and at this level the optical properties and laser damage threshold of the zirconia coating were satisfactory. Multilayer high reflectivity dielectric coatings were also elaborated by laying down quaterwave-thick, alternating coats of this binder-aided zirconia with silica, also prepared from colloidal suspension. To achieve 99 % reflectivity, 17-19 layers were required. Single shot (1-on-1), laser damage tests at 1064-nm wavelength with a pulse length of 3-ns were carried out on both the single layer and multilayer systems. The thresholds averaged 8.6 and 8.2 J/cm² respectively. With a laser-annealing post-treatment, n-on-1 threshold values were higher than the 1-on-1 figures by a factor of about 1.5.

Key words : Laser damage, ZrO_2, zirconia-silica coatings, sol, binder, HR-coatings, sol-gel coatings.

1 - INTRODUCTION

The sol-gel process is a versatile route for the preparation of films or dense monolithic bodies of high purity glasses and ceramics. This field has been known for many years and has created a real excitement in the last decade within the research domain of materials. Indeed, the sol-gel process has allowed already to make better useful materials and even authorized the synthesis of unusual non-crystalline solids either by extending the normal glass formation limits or by obviating problem of phase separation. The main winning cards of the sol-gel process is likely the fact it avoids meltings of suitable precursors, and starts from solutions, therefore many "exotic" new composite systems with unusual microstructure can also be obtained. Most of the sol-gel innovations have been brought together through excellent books of papers submitted in basic symposia /1-7/ and through a recent book describing the principles, developments, techniques and applications of sol-gel processing /8/.

The uniqueness of the so-called "sol-gel" process is to go all the way from the precursor to the product, allowing better control of the whole process and the synthesis of "tailor-made"materials. Such an approach is basically articulated in three steps :

1. Preparation of a solution or colloidal suspension of the suitable(s) component(s). This step gives the *SOL*.

2. Gellation of the *SOL* by polymerization or coagulation. This step gives the *GEL*.

3. Conversion of the wet *GEL* to a useful product, generally through a thermal treatment.

So, at Limeil-laboratory we have prompted interest with the sol-gel technology since 1985, the year where we acquired and activated our 20 KJ - 1 ns neodynium : glass Phebus laser destinated to laser-fusion experiments (ICF-program), for high damage threshold optical coatings. Additionnally, since this time we have maintained an official collaboration with the Lawrence Livermore National Laboratory alike involved on ICF-program, and particularly with Ian M. Thomas for laser-resistant sol-gel coatings. Doctor Ian M. Thomas is probably the pioneer as for the promotion and the development of highly damage resistant sol-gel coatings presently used in the most powerful laser-systems operating at Livermore and Limeil laboratories and elsewere.

Previous investigations, with the imperative to develop highly damage resistant films on, porous silica antireflective (AR) coatings /9 , 10/, porous fluoride AR coatings /11/, ThO_2 and ThO_2-SiO_2 high reflectivity (HR) coatings /12/, TiO_2 and TiO_2-SiO_2 HR coatings /13 , 14/ and more recently on AlOOH and AlOOH-SiO_2 HR coatings /15/ have been essentially reported over these last five years by Thomas and Floch.

The work described in this paper is part of the continuing effort we maintain to achieve the laser-strength HR-coatings must have to withstand the high peak fluences delivered by current and future high-power lasers. It is now clearly established that dielectric multilayered mirrors must be built up from colloidal media (sols) and not from solutions as summarized and illustrated, in a recent survey /16/, primarily because the colloidal method gives stress-free coatings. Others main advantages of the route using colloids are the room temperature process, the low capital cost of equipment and the low cost of processing.

The TiO_2-SiO_2 HR system, while giving satisfactory optical performance, did not have the high laser damage threshold that was expected. The ThO_2-SiO_2 HR system, in spite of respectable results on both optical properties and laser-strength has been abandoned for safety reasons. The major hazard of thoria is its strong toxicity when organism-ingested and not its spontaneous radioactivity as often perceived. Moreover, to date, the AlOOH-SiO_2 HR system only has fulfilled the expected damage resistance requirement, but because of the relatively low refractive index difference between silica (1.22) and bohemite alumina (1.44) coatings, about 35 total layers are demanded to achieve reflectance greater than 99% onto BK-7. This last point is substantially detrimental for clean and scatter-free mirror realization. Thus, in order to get round this penalizing aspect, we decided to address new investigations on ZrO_2 high index material, knowing it is a stoutly refractory material, with adequate redox and phase diagrams. Such caracteristics could help to obtain damage resistant HR coatings, associated with less layers than in the alumina-silica combination.

II - COLLOIDAL ZIRCONIA SUSPENSIONS

A. Standard sol

Aqueous colloidal suspensions of zirconium oxide (also called zirconia) have received a consistent attention for many years and in many countries for the production of a variety of ceramics utilized in nuclear field. One of the first patents describing the synthesis of zirconia concentrated aqueous sols has been claimed by Alexander and Bugosh in 1961 /17/. Later in 1964 Clearfield precised chemical conditions to produce different crystalline forms of hydrous zirconia /18/. In both cases, these processes started from ionic precursors as oxychloride or oxynitrate salts which then were hydrolyzed in temperature for a sufficient period of time to allow cationic polymerization by an olation (or deprotonation) process until nucleation in colloidal dimension was reached and to induce crystallization of the grown solid phase. In 1968, Woodhead prepared zirconia aquasols by precipitating zirconium hydroxide from salts in alkaline medium and by subsequently digesting the fresh slurry in dilute acid conditions (peptization) /19/. Since these works, numerous detailed papers have been published about zirconia sols, clarifying experimental conditions and characterizations of produced powders, either with ionic /20 , 21/ and molecular /22 , 23/ precursors. The prementioned references are by no means complete, and should be considered exemplary only.

As a first evaluation, we decided to start our investigations on zirconia colloidal coatings using aquasols made from ionic precursors. By another way, we selected the zirconium oxychloride (zirconyl chloride) salt ($ZrOCl_2$) as the preparative source because the major absorption band of likely residual chloride anion is at about 180 nm and therefore is far away from the wavelength of our interest 1064 nm.

Before use, the zirconium oxychloride has been carefully recrystallized twice in strongly acidic HCl solutions, giving sparkling needle-like white prismatic crystals. The chosen preparative method for producing zirconia aquasols was an adoption of the one depicted by Clearfield /18/, and consisted in a controlled precipitation of the oxide through an hydrothermal treatment. Such an hydrolysis was carried out using osmozed deionized water and the zirconium solution was passed through a 0.2 μm Millipore teflon membrane to remove any suspended solid before processing.

The overall hydrolysis reaction can be represented by the following chemical equation :

$$ZrOCl_2 + H_2O \xrightarrow{\sim 100°C} ZrO_2 + 2HCl$$

The hydrolysis was conducted at reflux temperature to allow nucleation and oxide germination, and on the other hand to help the precipitated oxide to crystallize. An excellent paper adressed by Livage et *al* on the sol-gel chemistry of transition metal oxides gives a more detailed assessment about the polycationic condensation mechanism via olation /24/. Their quantitative analysis is based on the Partial Charge Model use /25/.

A typical zirconia suspension was prepared as follows : Recrystallized zirconium oxychloride octahydrate (65 g : 0.2 mole Alfa) was dissolved into stirred doubly distilled water (300 g) at room temperature and then filtered at 0.2 μm through a teflon membrane filter. This mixture was rapidly added into stirred deionized water (15 kg) contained in a 20-liter glass reactor. The temperature was then raised to the boiling point, establishing a smooth and regular reflux. Refluxing was continued over about 40 hours, until a slightly opalescent suspension was obtained. At this stage, the mixture was spontaneously cooled down until room temperature and then concentrated HCl (d = 1.18) was added in large excess inducing an agglomeration and a precipitation of zirconia particles. After the decantation was completed, the acidic supernatant liquor was eliminated meticulously and the fine powder was easily redispersed in about 500 mliters water by dialysis. The dialysis was performed using a cellulosic molecularporous membrane (Spectrapor 3, MWCO = 3500) in running water. In this way, the pH of the suspension could be increased from an initial 0-0.5 to about 5 with no decrease in colloidal stability or gelation appearance. The partially neutralized suspension was concentrated under reduced pressure (20 mmHg) by distilling off the water, until the product weighed 207g. This solution that corresponds to a colloidal suspension containing the equivalent of 12 % ZrO_2 was readily filtered through an hydrophylic 1.0 μm teflon membrane.

A scanning Electron Microscopy (SEM) of such a colloidal suspension using the grid analysis method revealed that the zirconia was obtained in the form of approximately spheroidal particles 300 - 500 Å in diameter. The micrograph presented hereafter illustrates the colloid morphology. See figure 1.

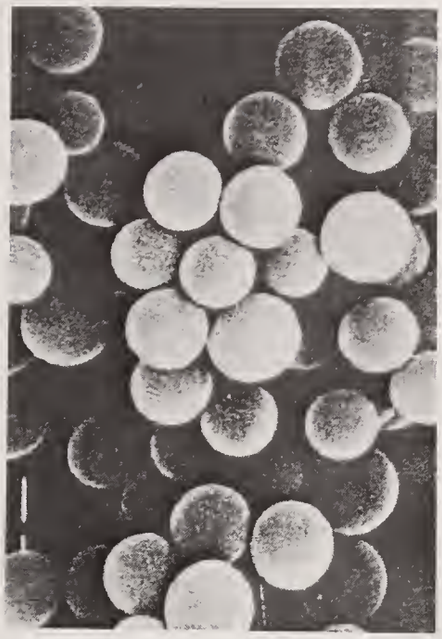

Fig. 1 : SEM of ZrO_2 particles obtained by forced - hydrolysis of a $1.3.10^{-3}$ M zirconium oxychloride solution.

Additionnally, an X-ray diffraction analysis of the zirconia agglomerates present in suspension showed that the oxide consisted in monoclinic microcrystals (baddeleyite allotropic variety).

B. Binder-aided suspension

The zirconia particles in the colloidal suspension prepared as described above have likely a significant number of peripheral surface hydroxyl groups which are firmly bound to the underlying zirconium atoms. These groups can be reacted with hydrolyzable zirconium compounds such as the oxychloride salt for example in the manner shown in figure 2. The zirconium dichloride oxide will then act as a binder to increase the adhesion between adjacent particles and we would expect a stronger, more abrasive-resistant coating to result. The degree of crosslinking will depend on the amount of reagent added. At some level the zirconium salt reagent will have linked up all the available particle hydroxyl groups and any excess will then go to fill up the air space between zirconia colloids. We would then expect at this stage a decrease in porosity and consequent increase in refractive index.

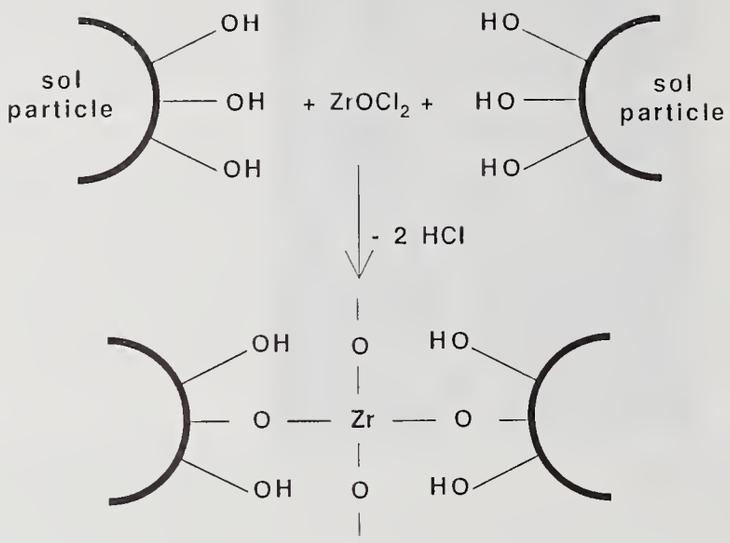

Fig. 2 : Surface hydroxyl groups can be linked by reaction with zirconium oxychloride.

This last point is particularly interesting owing to the fact that it implicates a possible flexibility on the final refractive index of the coating. So, by judiciously proportioning the level of binder added to the initial zirconia suspension, we could substantially raise the index of the coating and therefore reduce appreciably the number of total-layers in HR-films while maintaining high reflectivities. Moreover, such binder-aided coatings could possess an enhanced overall strength.

Compositions containing the standard suspension with various quantities of binder were then prepared by the addition of zirconium oxychloride to a sample of the standard sol. A typical preparation of a composition containing 70 % particles and 30 % inorganic binder was carried out as follows :

Recrystallized zirconium oxychloride (13.1g : 0.04 mole) was added into stirred 12 % zirconia standard aqueous suspension overnight. The pH of such a solution being about 1, it was necessary to reduce its acidity by the addition of an anion exchange resin as Amberlite IRA-93SP that corresponds to a secondary amine free-base. The mixture was partially neutralized by stirring with the anion exchange resin until the pH had been raised to a maximum of 4 otherwise at higher value coagulation took place progressively.

The final binder-contained coating mixture included a total of 15 % zirconia, 70 % of which was in the form of colloidal zirconia and the remaining 30 % in solution as a soluble zirconium oxo-hydroxo polycation. The coating-mixture was then readily filtered through a 1.0 μm teflon filter. A sketch of the chemical preparation is presented in figure 3.

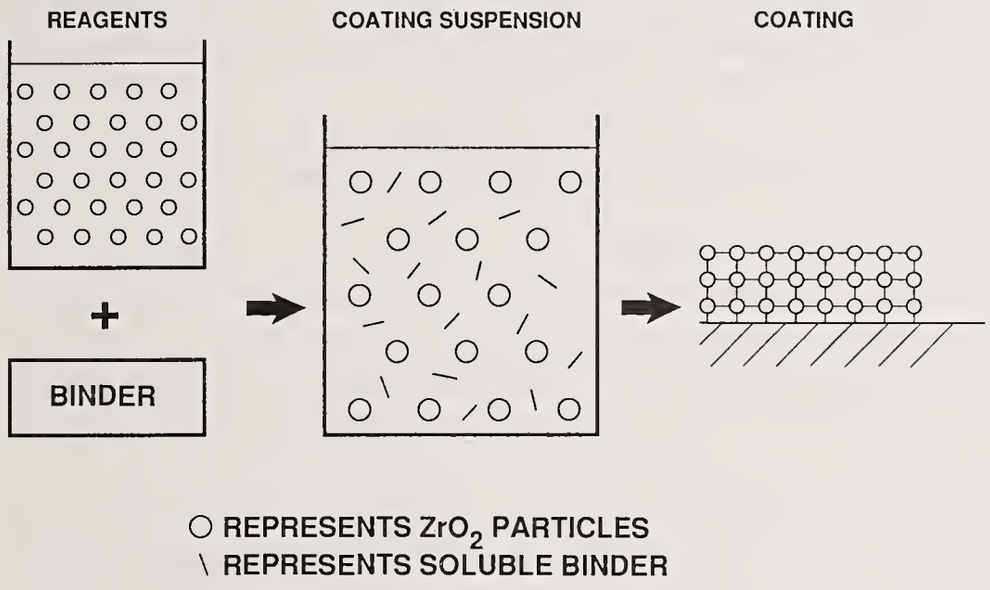

Fig. 3 : The preparation of binder-aided zirconia sols is basically simple

III - COLLOIDAL SILICA SUSPENSION

A typical silica sol was prepared by the base catalyzed hydrolysis of distilled tetraethylsilicate in pure ethanol or methanol by the method previously described /9,10/. In basic medium, hydrolysis of the silicate is prefered over condensation to soluble organosiloxane polymers /26/. The material was prepared at 3.0 % silica concentration, and consisted of monidispersed roughly spherical particles with a diameter of about 20 nm.

IV - COATING PROCEDURE

Before use, all coating suspensions were filtered through a teflon membrane filter of 1.0 μm pore size for zirconia coating-sols and 0.2 μm for silica. We have prefered to spin-coat rather to dip-coat because it uses much less material. Coatings were deposited on 5-cm diameter and 1-cm thick fused silica of BK-7 glass substrates using a spin-coater in a 0.2 μm filtered, forced air, clean hood. All coatings were prepared at an optical thickness of 266 nm, corresponding to quaterwave at the use wavelength of 1064-nm. All coating suspensions were applied at room temperature with a relative humidity in the range 50-60 %. Before coating-operation all substrates were $UV/O_2/H_2O_2$ cleaned using an ozone-photoreactor (PR-100 ; UVP.Inc), achieving hydrophilic surfaces.

Zirconia coatings were applied from various aqueous binder-aided sols containing 15 % ZrO_2 in which the binder ratios were incleased to 10 %, 20 %, 30 % and 40 %. We had no wetting problems with our aqueous mixtures because as mentioned before the UV-ozone treated surfaces remained very hydrophilic and this within about 20 minutes. So, such a coating procedure allowed us to avoid the use of a nonionic surfactant and therefore eliminated a risk of potential carbonaceous contamination leading to laser damage, and on another hand to avoid dilution with lower aliphatic alcohols, such as methanol or ethanol, which tend to thicken progressively the sols until complete gelation after a few days storage. One coat at 1500 rpm was required to give a coating of the correct thickness.

Silica coatings were applied from a suspension in ethanol containing 3.0 % SiO_2 in basic medium (pH ~ 10). One application at 1300 rpm was required to give a coating of the desired thickness. Such a coating was easily water-wetted contrary to n-propanol-diluted silica sols which were water-repellent. In the preparation of multicoated samples, both silica and zirconia coatings were air dried at room temperature for 10-min prior to the application of the next coat. Looking at the reflected color of the coated parts, we could appreciated with unaided eyes the uniformity of the films. The majority of our coatings had no discernible color variations.

V - LASER DAMAGE MEASUREMENTS

Damage threshold measurements were carried out on our W_0-facility at 1064-nm using single shots with a pulse length of 3-ns. The beam spot size was about 2.0-mm diameter. We conducted 1-on-1 (one shot of known fluence onto a selected site) and n-on-1 (n shots of ramped fluence onto a selected site) damage tests. Each sample site was inspected under a Vickers microscope and video-memorized before and after laser irradiation to allow a simple and performant photographic comparison. In like manner, we could attest if the sample damaged yes or no. Damage was defined to be any evolutive 5-10 micron size range alteration observable by our technique. From a sequence of irradiations, the damage threshold was defined as the average of the highest fluence which caused no damage and the lowest fluence which did. While in general, we do not wish to discount the significance of minute damage spots at low fluence levels, we feel that it is important and logical to differentiate the notion of very minor and nonevolutive damage from one of consistent and growing damage. Such an interpretation of damage threshold seemed to us more adequate to judge the suitability of a particular coating for practical application.

VI DISCUSSION OF RESULTS

A. Single Layer ZrO_2 Coatings

The refractive indices of the different binder-aided ZrO_2 coatings are shown in table 1. Note that the standard sol, binder-free, gave very low coating index value compared to the dense material. This indicates that coating was about 60 % porous. The 90/10 composition remained poorly affected by the binder presence just like its abrasion-resistance. The 80/20 composition revealed already a notable increase in refractive index and gave abrasion-resistant coating against an alcoholic drag-wipe. The 70/30 composition was the selected one for HR multicoated films because it has a relatively high index value associated with abrasion and adhesive tape resistance. Continuing to raise the binder-content, the refractive index still increased, but coatings appeared significantly stressed when observed under microscope, exhibiting some fractal cracks. Therefore such ZrO_2 coating-sols were useless for multilayered systems. Althought the 70/30 composition gave slightly stressed zirconia coatings, we found that this coating-formula was a good compromise for subsequent HR-coating build up. All the binder-aided ZrO_2 coatings exhibited a slight spectral evolution when heated at 100°C, consisting roughly in a 50-nm shift to shorter wavelengths.

This shrinkage phenomenon is likely due to water desorption associated with completing polycondensation and drying of the binder. There was no change in the optical spectrum when coatings were exposed for one day to varying relative humidity.

Particle - binder ratio	Refractive index
100 - 0	1.48
90 - 10	1.50
80 - 20	1.56
70 - 30	1.65
60 - 40	1.72

Table 1 : Refractive indices of various binder-aided ZrO_2 coatings

The refractive index values reported above have been deduced from spectrophotometrically measured transmission spectra of respective binder-aided single layer ZrO_2 coatings. Standard optics calculations indicated the corresponding refractive index assuming an index of 1.46 for the fused silica substrate. As a remark, we noticed that ZrO_2 single coat made from straight aqueous sol, binder-free, gave coating which was weakly antireflective onto BK-7 substrate and furthermore with an index value lower than the one reported by Thomas et *al* for the same material at the time of preliminary investigations ; his figure being 1.55 /27/.

Laser damage thresholds in a 1-on-1 mode ranged from a low of 6.3 J/cm² to a high of 11.7 J/cm² with an average of 8.6 J/cm² . We think the wide range of damage thresholds is probably attributed to local coating-contamination inherent to the process itself and consequently favoring damage. Samples with low thresholds generally showed only a few small defects in the beam area. Massive damage over the whole beam area did not occur until fluences in the range 14-15 J/cm² were applied. After fine observations under Reicher stereomicroscope, we observed that in all cases damage originated at visible artifacts. Clean areas appeared stonger to laser than those busy.

When laser-annealing was directed onto such sol-gel zirconia coatings, we obtained at the first try a consistent enhancement of the laser-strength. The laser-annealing or laser-conditioning consists to increase progressively the laser fluence, this procedure is called "n-on-1" mode. Figure 4 summarizes through an histogram the laser-resistance of both 1-on-1 and n-on-1 tested ZrO_2 films. N-on-1 thresholds were in the range 11.6-15.4 J/cm² and averaged 13 J/cm². In this irradiation mode the massive damage appeared at fluences up to 25 J/cm². Wilder and Thomas had recently suspected and reported that some evaporated and sol-gel dielectric coatings were laser-annealing sensitive /28/. Such an observation opened rapidly an interest and since this time, laser-annealing has been adapted systematically in our lab and elsewere. Even thought we do not know yet, what is the responsible mechanism involved in this phenomenon, we know for sure that the induced enhancement of the laser resistance was durable over at least 6 months. Notable effort are presently in progress in our lab and at LLNL in order to identify the reason of the observed damage improvement and previews were already advanced by Kozlowski et *al* /29/, based on possible electronic rearrangement in condensed dielectric materials. Regarding our sol-gel zirconia coatings, which must be in good thermodynamic-equilibrium as confered by the chemical nature of the sol-gel process itself, we think to date that the observed enhancement in laser-strength, by a factor of about 1.5, might be likely due to a gentle desorption of volatile absorbing contaminants through coating-porosity. A subsequente emission spectrographic analysis of our ZrO_2 coatings revealed a consistent but comprehensible amount of hafnium (< 5000 ppm), significant traces of iron (< 1000 ppm), silicon (<500 ppm) and aluminium (< 400 ppm). Most of these ionic impurities absorb at 1064-nm and therefore are particularly prejudical to high laser damage threshold achievement.

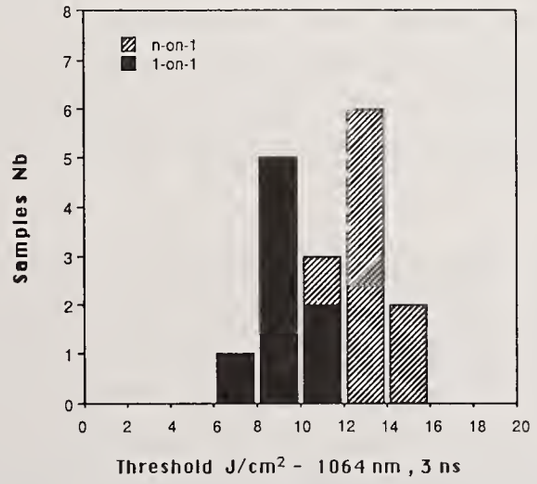

Fig.4 : 1-on-1 and n-on-1 laser strength of binder-aided ZrO_2 coatings

B. Multilayer coatings

Multilayer coatings were readily prepared at room temperature by applying alternating coats of 70/30 composition zirconia and silica. Layers were applied with approximately 5-min drying time under an IR-lamp between applications and with the substrate remaining in the spin coater. Occasional samples would contain comets as a result of coating over small artifacts on the surface of the previous layer. In multilayer applications the cleanliness criterion becomes drastically critical, so, stringently tidy conditions during coating deposition must be considered.

Calculations using Fresnel laws indicated that, with refractive indices of 1.22 for silica and 1.65 for binder-aided zirconia, about 17-19 layers would be required to achieve reflectance close to 99 % on fused silica, and this was experimentally confirmed. This coating-combination involved much less layers than within the reported alumina-silica system /15/. For multicoat build up, we have not been faced to any problem concerning the wettability of the silica coating by the aqueous zirconia sol. After about 5-7 layers were deposited onto well-polished substrates, coating surface aspect evidenced fine radial-lines testifying of an apparent inhomogeneous flow motion of coating-solution. Resulting HR-films including from 9 to 19 total layers were uniform in reflection performances over the entire coated diameter but were slightly disrupted in surface by the presence of such radial-lines. However, further relative-roughness measurements made on our Reicher device gave surprisingly good figures in the range 15-20 Å RMS. We plan to adress in the future, investigations in order to reduce the radial-lines phenomenon because it gave noticeably rise to laser-damage. All the 17 total layer mirrors made with the described coating procedure and reflecting about 99 % of the incident 1064-nm wavelength were unfortunately betrayed after microscope observation, revealing some isolated fractal cracks inside coating-stacks. These cracks rose significantly light scattering when exposed with an intense white light source. This last point perhaps fixes the limits of such a sol-gel coating-version for highly reflective films in the near-infrated spectral range. All made multilayered-mirrors were also abrasion-resistant.

1-on-1 laser-strength measurements gave thresholds varying from a low of 8.0 J/cm² to a high of 8.8 J/cm² with an average of 8.2 J/cm² . In contrast of what we observed with the others oxide systems /12-15/, these figures are conservative to those of the relevant single layers. We have so far no precise explanation for this noting, except maybe the possibility that the binder by covering the zirconia particles reduced substantially their specific area and consequently decreased their spontaneous chemical adsorption that is suspected as detrimental for laser-resistance.

As for single layer coatings, the use of laser-annealing has been very effective. N-on-1 thresholds, even though some mirrors were localy crazed, ranged from 10.5 J/cm² to 13.7 J/cm² with an average of 12.0 J/cm² . At threshold values, damage consisted of dispersed and tiny spots about 10-20 μm in size. In n-on-1 mode, massive damage was attained at 25-30 J/cm² with catastrophic failure about 300 μm diameter. In order to illustrate the laser -annealing efficiency onto a ZrO_2-SiO_2 coating, we present hereafter the difference in damage aspect of selected sites irradiated with laser impacts of 15.7 J/cm² , with 1-on-1 (figure 5) and n-on-1 (Figure 5 bis) damage tests.

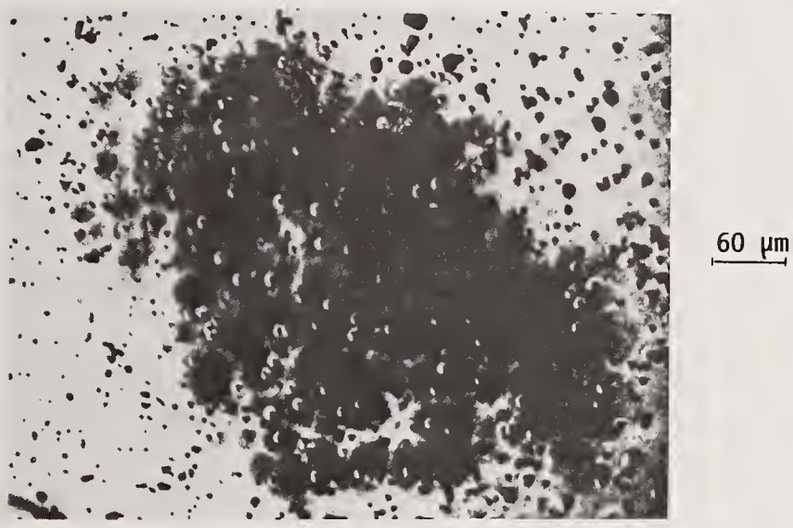

Fig. 5 : $(Zr\text{-}Si)^7$ - Zr sol-gel coating without laser-annealing post-treatment

60 µm

Fig. 5 bis : $(Zr\text{-}Si)^7$-Zr sol-gel coating with laser-annealing post-treatment

VII - CONCLUSION

We have prepared using the sol-gel process, porous abrasion-resistant m-ZrO_2 coatings on fused silica or BK-7 substrates from binder-assisted aqueous suspensions. These coatings were readily spin-applied at room temperature and required no subsequent processing after water evaporation. They had a refractive index increasing with binder adjunction. We found that the 70/30 colloidal-binder composition was the best compromise for ulterior multilayered mirror realization. Such a mixture gave zirconia coatings with an index of about 1.65 associated with 1-on-1 and n-on-1 laser damage thresholds of 8.6 and 13 J/cm² respectively for 1064-nm wavelength pulses of 3-ns duration.

Multilayer HR-coatings were also elaborated by stacking alternate quarterwave coatings of this zirconia with silica also prepared from a colloidal suspension. This operation was also conducted at room temperature, with about 5-min drying time under an IR-lamp between respective coats. About 17-19 total coats were required to give a reflectivity of 99 %. The 1-on-1 and n-on-1 thresholds of such mirrors averaged 8.2 and 12 J/cm² respectively in the same laser-conditions. HR-coatings were also abrasion-resistant to an alcohol drag-wipe operation but revealed some strain-induced fractal cracks due to binder drying.

From the technical point of view, it is true that when attempt is made to prepare large amount of zirconia coating-sol using such a cheminal method, we were confronted to a limitative aspect because hydrolysis of relevant precursor needs very large quantity of water and therefore clumsy devices. This is very penalizing when large size coated components have to be considered.

In endind, we think that if it was possible to start from molecular precursors as zirconium alkoxides rather than ionic salts for well defined coating-sol preparations, we should have more chance to achieve high laser damage threshold figures compared to the current moderate performances and that thing without having recourse to laser-annealing post-treatment.

Acknowledgements

The authors are very grateful to C. CORDILLOT for all damage measurments performed at Limeil-Laboratory. The author Hervé G. FLOCH is particularly indebted to Dr. Ian M. Thomas for his valuable and stimulating helping discussions and advices which have consistently contributed to orientate and finish this study off.

REFERENCES :

1. Better Ceramics Through Chemistry I, Edited by C.J. Brinker, D.E. Clark and D.R. Ulrich, (Mater. Res. Soc. Proc. 32, Albuquerque, New Mexico, 1984).

2. Better Ceramics Through Chemistry II, Edited by C.J. Brinker, D.E. Clark and D.R. Ulrich (Mater. Res. Soc. Proc. 73, Palo Alto, California, 1986).

3. Better Ceramics Through Chemistry III, Edited by C.J. Brinker, D.E. Clark and D.R. Ulrich (Mater. Res. Soc. Proc. 121, Reno, Nevada, 1988).

4. Ultrastructure Processing of Ceramics, Glasses and Composites, Edited by L. Hench and D.R. Ulrich (John Wiley and Sons, Inc., 1984).

5. Science of Ceramic Chemical Processing, Edited by L. Hench and D.R. Ulrich (John Wiley and Sons, Inc., 1986).

6. Ceramic Powder Science, vol 21, Edited by G.L. Messing, K.S. Mazdiyasni, J.W. McCauley and R.A. Haber (American Ceramic Society Inc., 1987).

7. Ceramic Powder Science, vol II A and II B, Edited by G.L. Messing, E.R. Fuller, Jr., H. Hausner (American Ceramic Society Inc., 1987).

8. Sol-Gel Technology, Edited by L. Klein (Noyes Publications, 1988).

9. I.M. Thomas, "High Laser Damage Threshold Porous Silica Antireflective Coating", Appl. Opt., 25, 1481 (1986).

10. H.G. Floch, J.J. Priotton, "Porous Silica Sol-Gel Coatings for Nd : Glass High-Power Pulsed Laser Uses", The Physics and Technology of Amorphous SiO_2, Edited by R.A. Devine, Plenum press, 561 (1988).

11. I.M. Thomas, "Porous fluoride Antireflective Coatings", Appl. Opt., 27, 3356 (1988).

12. H.G. Floch, J.J. Priotton, J.F. Mengue and C. Cordillot, "1064-nm and 350-nm Radiation Stability of Low Density ThO_2-SiO_2 High-Reflective Coatings Deposited from Sols", 19 th Boulder Damage Symposium Proc., 290 (1987).

13. I.M. Thomas, "Single-Layer TiO_2 and Multilayer TiO_2-SiO_2 Optical Coatings Prepared from Colloidal Suspensions", Appl. Opt., 26, 4688 (1987).

14. H.G. Floch, J.J. Priotton and I.M. Thomas, "TiO_2-SiO_2 colloidal HR-films for High-Power Lasers", Le vide, Les Couches Minces, vol 44, 245, 33 (1989).

15. I.M. Thomas, "Single-Layer Al_2O_3-H_2O and Multilayer Al_2O_3-H_2O-SiO_2 Optical Coatings Prepared from Colloidal Suspensions", Appl. Opt., 28, 4013 (1989).

16. H.G. Floch, J.J. Priotton and I.M. Thomas, "Optical Coatings Prepared from Colloidal Media", Thin Solid Films, 175, 173 - 178 (1989).

17. G.B. Alexander, J. Bugosh, "Concentrated Zirconia and Hafnia Aquasols and Their Preparation", U.S. patent 2,984,628 (1961) assigned to Du Pont de Nemours and Co.

18. A. Clearfield, "Crystalline Hydrous Zirconia", Inorg. Chem, 3, 146 (1964).

19. J.L. Woodhead, "Stabilized Zirconia Particles by Sol-Gel Processes", Science of Ceramics 4, 4, 105 (1968).

20. A. Garg and E. Matijevic, "Preparation and Properties of Uniform Coated Inorganic Colloidal Particles", J. Coll. & Interf. Sc., 126, 243 (1988).

21. A. Bleier and R.M. Cannon, "Nucleation and Growth of Uniform m-ZrO_2", MRS Symp. Proc., 73, 71 (1986).

22. T. Ikemoto, N. Mizutani, M. Kato and Y. Mitarai, "Synthesis of Monodispersed Zirconia Fine Particles ", Yogyo Kyokaishi 93, 585 (1985).

23. T. Ogihara, N. Mizutani and M. Kato, "Processing of Monodispersed ZrO_2 Powders", Ceram. Intern. 13, 35 (1987).

24. J. Livage, M. Henry and C. Sanchez, "Sol-Gel Chemistry of Transition Metal Oxides", Prog. Solid St. Chem., 18, 259 (1988).

25. J. Livage and M. Henry, "Ultrastructure Processing of Advanced Ceramics", Edited by J.D. Mackenzie and D.R. Ulrich, (Wiley, New York), 183 (1988).

26. B.E. Yoldas and D.P. Partlow, "Wide Spectrum Antireflective Coating for Fused Silica and Other Glasses", Appl. Opt., 23, 1418 (1984).

27. I.M. Thomas, J.G. Wilder and R.P. Gonzales, "HR Coatings Prepared from Colloidal Suspensions" 20 th Boulder Damage Symposium (Co), 1988.

28. J.G. Wilder and I.M. Thomas, "Effect of n-on-1 Laser Treatment on Damage Threshold of Selected Optical Coatings", 20 th Boulder Damage Symposium, (Co), 1988.

29. M.R. Kozlowski, M. Staggs, C.R. Wolfe and J.H. Campbell, "Large Area Laser Conditioning of Dielectric Thin Film Mirrors", 21 st Boulder Damage Symposium, (Co), 1989.

COMMENTS

Question: There has been quite a bit of work over the years, as I recall, in this area performed by people who are trying to get total scattering systems, people who are making magnesium oxide for integrating spheres. Actually, some of it was done here at the Bureau of Standards, I think. Have you looked into what sort of numbers they get?

Answer: As I say, the only numbers I've seen in handbooks for scatterers are at the 99% level. I'd appreciate any information that anyone can give me about the real state of the art of scattering surfaces.

Manuscript Received
3-2-90

Structural Modification of D_2O/H_2O-Dosed CaF_2 Optical Thin Films

J. B. Franck

Physics Division, Research Department
Naval Weapons Center, China Lake, California 93555-6001

Unusual behavior has been reported for D_2O/H_2O-dosed CaF_2 optical thin films. This behavior includes resistance to laser-induced damage at 2.7-μm radiation, improved damage morphology, and reduced optical absorption in the water band for even H_2O-dosed CaF_2 optical thin films. Analysis of the films strongly suggests that the modification of film properties is not the result of inclusion of the D_2O/H_2O into the film matrix or chemical contamination. Rather, the act of dosing has modified the structural properties of the films, thus producing the effects observed.

Key words: adsorption; calcium fluoride; D_2O; desorption; H_2O; laser damage; thin films.

Background

In work presented previously [1], it was reported that unexpected behavior had been found for ~1-μm-thick CaF_2 thin films produced by thermal evaporation in the presence of copious amounts of either D_2O or H_2O (called dosing). The CaF_2 films were evaporated onto a variety of substrates; however, most of the analysis was performed on films laid down onto single-point diamond-machined (SPDM) oxygen-free high-conductivity (OFHC) Cu substrates or SPDM ultrabright acid Cu (UBAC) plating on OFHC substrates. Several properties of these films were modified when compared to undosed films of CaF_2. Resistance to laser-induced damage at 2.7 μm was observed as well as improved damage morphology. Also observed was a reduced optical absorption in the water band. This was seen for both D_2O and H_2O dosing. A corollary to the above phenomena was that no evidence of optical absorption was found in Fourier transform infrared (FTIR) spectrometry for the heavy water band with D_2O dosing.

D_2O-dosed CaF_2 films were made initially in an attempt to produce a controlled sample set for laser-induced desorption experiments concerned with water contamination. The purpose of the D_2O dosing was to produce surfaces rich in a controlled desorbate. Dosing with D_2O resulted in films containing residual molecules behaving chemically in a manner very similar to water; however, the abundance of D_2O in nature is several orders of magnitude less than for H_2O. Surprisingly, the number of residual molecules (either adsorbed onto the surface or incorporated into the bulk) was too small to be seen in FTIR spectrometry in the heavy-water band. It was assumed that optical absorption in the water band would increase—not decrease. This was expected because the films were introduced into the atmosphere, and the dynamics of the adsorption/desorption process [2] strongly indicate that loosely bound surface D_2O will be replaced rapidly by the atmospheric H_2O. Evidence will be presented to suggest strongly that the altered film characteristics are due solely to film-structure modification and that, as the absorption data suggest, there is

little D_2O/H_2O incorporated into the matrix of the CaF_2 films. Rather, the residual D_2O/H_2O is due to the molecules being adsorbed onto the surface of the growth columns, which are the artifacts found in most optical thin films manufactured nonepitaxially. The reduced optical absorption, therefore, is a consequence of a reduced surface area for the film. X-ray crystallography data suggest that the dosed films are composed of larger, more ordered crystallites. For a given film area, the surface area of the film increases as the size of the crystallites decrease. This is analogous to increasing the surface area of a sample by crushing it into a powder.

Discussion

The absorption of H_2O onto the surface of CaF_2 has been studied by workers in the field from the early 1930s [3-5] to the present. Ogura [6], de Boer [7], and Gregg [8] have studied the adsorption/desorption process as well as the influence of microporosity on the adsorption/desorption process in a dynamical sense. Porteus *et al.* [9,10] have studied the dynamics of laser-induced desorption from CaF_2 surfaces. The present investigation was a direct result of an attempt to produce a sample set with controlled characteristics for laser-induced desorption study of CaF_2 optical coatings. The coatings were produced in a bell jar system by evaporation from a Mo boat. For each coating run, the coatings were deposited onto unheated substrates and the coating thickness was monitored by a quartz crystal monitor. After the coating run, a witness sample was measured by stylus profilometry to determine the coating thickness. The base pressure for the diffusion-pumped system was below 1×10^{-6} Torr. Dosing was performed by attaching one of two glass sampling cylinders to a leak valve. One cylinder contained H_2O, while the other contained 99.9% D_2O. The cylinders were outgassed in the following manner. One at a time, they were attached to a vacuum system operating in the mid 10^{-7} Torr range; during evacuation, they were placed in a dry-ice/methanol slurry. This caused the liquid in the sampling cylinder to slowly solidify as the vacuum system removed the more volatile elements.

Comparison studies were performed on undosed, H_2O-, and D_2O-dosed samples, and coating runs were always performed in that order. After the samples and system were cleaned, the runs were as follows: (1) undosed CaF_2 films; (2) H_2O-dosed CaF_2 films (introduction of H_2O into the system; since water is ubiquitous, it actually presented no additional contamination); and (3) D_2O-dosed CaF_2 films. Detailed coating-run information is available elsewhere [2].

Figure 1 shows a FTIR spectroscopy plot of a NaCl window used as a substrate for a test film. Figure 2 shows a FTIR plot of an Optovac CaF_2 window that was to be used as a coating material. Figure 3 shows a FTIR plot of a 1-μm-thick CaF_2 film. Absorption due to H_2O (OH) is seen, but there is no evidence of absorption due to D_2O (OD). This sample was dosed with D_2O, and the coating chamber was brought up to atmosphere with D_2O and taken immediately to the FTIR apparatus.

Laser-induced damage onset analysis at 2.7 μm was performed on a variety of samples. The data are presented in table 1. The highest damage onset was found for a D_2O-dosed CaF_2 film on a quartz substrate; H_2O-dosed CaF_2 on quartz was not tested. For a CaF_2 film on SPDM UBAC, the highest damage onset was found for H_2O dosing; D_2O dosing ranked next, and the lowest damage onset was with the undosed film. All Cu samples were baked in a low-vacuum oven for 12 hours at 115°C, with the exception of the first undosed sample that exhibited such a high residual stress that it self-fractured before baking. Spectral reflectance at 2.9 μm for three of the samples can be found in the fifth column of the table, and the accompanying spectral plots are shown in figures 4 through 6. Shown in

Table 1. Laser damage onset and morphology

CaF_2 doping	Substrate	Damage onset, J/cm^2	1-R at 2.9μm	R at 2.9μm	Damage morphology	Defect/ intrinsic
None	SPDM UBAC #12 run #14	5	10.4	89.6	fracture & delamination	intrinsic
H_2O	SPDM UBAC #13 run #15	30	7.5	92.5	ablation	intrinsic
D_2O	SPDM UBAC#15 run #17	22			ablation & fract at high fluence	intrinsic
D_2O	SPDM UBAC #16 run #18	12	9.5	90.5	ablation	intrinsic
D_2O	SPDM OFHC #3 run #6	12			ablation	intrinsic
D_2O	quartz #1 run #6	75			ablation	defect
None	quartz #4 run #10	20			fracture & delamination	defect

figure 7 is a plot of laser damage onset values versus spectral reflectance at 2.9 μm. The highest two additional points are for samples whose spectral reflectance is known but laser damage onset is unknown. The predicted value (which is quite high) may not actually be correct if failure is the result of defects at the higher fluence values. Defect-dominated failure was not seen for any of the CaF_2 films tested on the Cu substrates, as presented in table 1. Shown in figures 8 through 10 are photographs of laser-induced damage, showing the damage morphology for undosed CaF_2 films. Figures 8 and 9 are SPDM Cu substrates; figure 10 is a quartz substrate. Failure takes the form of fracture and delamination. For the quartz sample in figure 10, the CaF_2 film has been completely removed from the substrate in some regions. Figures 11 through 13 are photographs of laser damage sites showing the damage morphology for dosed CaF_2 on SPDM Cu substrates. The damage does not appear to be defect dominated. The damage morphology appears to be ablation and "orange-peel-like" surface roughening. A laser-induced desorption-onset and adsorption-site (called adsite for convenience) density analysis performed at 2.7 μm [2] showed that adsites, like laser damaging defects, tend to be distributed randomly about the surfaces under test. This was found for CaF_2 films on both dielectric and metal substrates. An attempt was made to compare the adsite density (found in laser-induced desorption-onset analysis) with damaging defect density (found in laser-induced damage-onset analysis) for CaF_2 on SPDM Cu. Surprisingly, it was found (table 1) that the films on SPDM Cu failed in a uniform manner while desorbing in an adsite-dominated fashion. There are two simple explanations for this phenomena: either the films are defect free or the defect density is so high that the failure is uniform because a defect is always encountered. We have taken the liberty to describe these surfaces as defect-domination free, since a defect is defined operationally as the element on a surface that fails prematurely. Regardless of one's operational definition,

the main point here is that the damaging defects did not correlate with the desorbing adsites.

Figures 14 and 15 are photographs of interference fringe patterns for undosed and H_2O-dosed CaF_2 on thin "stress measurement" samples, respectively. Fewer stress-induced fringes—a result of the bowing of the thin SiO_2 sample—can be seen on the H_2O-dosed film.

Figures 16 through 19 are spectral reflectance plots for undosed (unbaked and baked); and H_2O dosed (unbaked and baked) to determine the modification of optical absorption at 2.9 μm as a function of dosing and baking. While it was found that baking had a more pronounced improvement in reflectance at 2.9 μm, dosing also improved the reflectance.

Coating Analysis

A sample set was developed for the purpose of performing analytical tests. The CaF_2 films on SDPM UBAC (samples #1 through 12) as well as the CaF_2 films on graphite (samples #1 through 4) are listed in table 2, where the samples are listed by run number, substrate, type of dosing, thickness, and baking.

Table 2. CaF_2 SPDM analysis sample parameters

Sample #	Run #	Substrate	Dosing	Thickness	Baking
1	22	Cu	un	0.6 μm	baked
2	22	Cu	un	0.6 μm	un
3	24	Cu	un	0.5 μm	un
4	24	Cu	un	0.5 μm	baked
5	25	Cu	H_2O	0.34 μm	baked
6	25	Cu	H_2O	0.34 μm	un
7	25	Cu	H_2O	0.34 μm	un
8	25	Cu	H_2O	0.34 μm	baked
1	23	graphite	none	800 Å	baked
2	23	graphite	none	800 Å	un
9	26	Cu	D_2O	0.4 μm	baked
10	26	Cu	D_2O	0.4 μm	un
11	26	Cu	D_2O	0.4 μm	un
12	26	Cu	D_2O	0.4 μm	baked
3	26	graphite	D_2O	800 Å	un
4	27	graphite	DO	800 Å	baked

Shown in table 3 is a listing of the Auger data taken by A. Green of the Naval Weapons Center (NWC). The samples tested were SPDM OFHC Cu #1 & 2, 5 & 6, and 9 & 10. The data are tabulated by sample number, sputtering, dosing, baking, amplitude of the Ca peak, ratio of the oxygen peak to the Ca peak, and ratio of the Cu peak to the Ca peak. While data exist for the F peak, they are not presented in this table. This is because F is so mobile, that the peak values may have no fixed relationship with the actual amount of F present in the material.

Table 3. Auger parameters

Sample #	Case	Sputter	Dosed	Baked	Ca #	O/Ca	Cu/Ca
1	a	---	---	yes	3.357	0.212	0.043
	b	2 min	---	yes	3.337	0.134	0.048
2	a	---	---	---	3.038	0.153	0.03
	b	3 min	---	---	3.290	0.095	0.051
5	a	---	H_2O	yes	2.843	0.177	---
	b	3 min	H_2O	yes	3.128	0.081	0.032
6	a	---	H_2O	---	2.704	0.107	0.041
	b	3 min	H_2O	---	3.144	0.072	0.055
9	a	---	D_2O	yes	2.853	0.185	---
	b	3 min	D_2O	yes	3.165	0.101	---
10	a	---	D_2O	---	2.845	0.076	---
	b	3 min	D_2O	---	3.054	0.065	---

Oxygen is the first element that will be discussed. From table 3, the undosed/baked/unsputtered #1(a) sample (#1) can be seen to have the highest value for the oxygen peak. Since no sputtering has taken place, the surface remains unaltered; in fact, all of the unsputtered samples showed a greater oxygen peak compared to the same sample after sputtering has ablated the surface. The lowest oxygen peak was seen for the D_2O dosed/unbaked/sputtered coating #10(b). There are two points that come as a surprise: First, the baked samples show a higher oxygen peak than those unbaked. If one assumes that the presence of the oxygen peak is the result of adsorbed H_2O/D_2O, then baking should reduce the H_2O on the surface; hence, the oxygen peak should go down. The reverse was seen! Second, all four of the dosed coatings showed a lower oxygen peak than the undosed, with the exception of samples #5(a) and 9(a) (before sputtering)—as compared to sample #2(a) (before sputtering).

The highest peak for Cu was found for the H_2O-dosed/unbaked/sputtered sample #6(b), in contrast to the D_2O-dosed samples, which showed no demonstrable Cu peak. The data for the undosed/baked samples are very similar to sample #6(b) above. One important item is that the Cu peak always appeared to increase with sputtering depth into the coating.

Presented next will be the Auger data taken by R. Scheri of NWC. Two samples were chosen for detailed analysis, specifically on the basis of previous laser-induced damage performance tests on similar samples. The coatings that failed at the lowest fluence levels were the unbaked/undosed CaF_2 films, in contrast to the H_2O-dosed/baked CaF_2 films that withstood the highest fluences.

The peak heights found on the two samples were ratioed, as in the previous data, and are presented in table 4. Listed in the three columns are the sputter time, ratio of oxygen to Ca, and ratio of Cu to Ca. As in the previous results, the oxygen peak decreases with depth and the Cu peak increases with sputtering depth. However, there is an anomaly in the data points for both 20-min sputter times for the oxygen peaks. While the oxygen peak is steadily decreasing for the 5- and 10-min sputter times, the 20-min sputter value increases for both the undosed/unbaked and the H_2O-dosed/baked CaF_2 coatings. From table 4, it can be seen that this phenomenon is not seen for the Cu peak, which is monotonically increasing

for the undosed/unbaked film. At the same time, no evidence of the Cu peak is seen in the dosed/baked coating until 20 min of sputtering has occurred. In contrast to these anomalous data points, the previous Auger data saw no such effect for up to 10 min of sputter time. The sputter-ion current was much higher for the previous Auger data.

Table 4. Auger parameters

Sputter time	Oxygen/Ca	Cu/Ca
Sample #2, Undosed/Unbaked		
0 min	0.765	0.121
5 min	0.661	0.138
10 min	0.645	0.168
20 min	0.765	0.191
Sample #5, H_2O Dosed/Baked		
0 min	0.670	---
5 min	0.551	---
10 min	0.554	---
20 min	0.620	0.08

The x-ray analysis was particularly interesting. The samples tested were quartz #8, 10, and 12 and represented undosed, H_2O-, and D_2O-dosed CaF_2 on quartz, respectively. Plotted data from sample #8 are shown in figure 20. For all three samples, the first broad peak is seen as the result of the substrate. The first sharp peak at around 30 degrees is the (111) crystal orientation peak for CaF_2. The second sharp peak is the (220) crystal orientation peak attributed to CaF_2. For a powder sample, the (220) peak would be the 100% peak with the (111) at 92% of the (220) peak height. Clearly, the (111) peak is twice as high as the (220) peak for sample #8.

The plotted data for sample #10 are shown in figure 21. The same broad peak can be seen as in the previous data for the undosed CaF_2 film. However, the first sharp peak belonging to the (111) crystal orientation is approximately 11 times higher than the peak belonging to the (220) crystal orientation. This indicates that there is a much stronger preference for the (111) planes to be oriented parallel to the substrate for the H_2O-dosed film than for the undosed film.

The plotted data for sample #12 are shown in figure 22. There is a significant difference between this D_2O-dosed film and the H_2O-dosed film in that while the (111) is approximately the same height, there is only a small vestige of the (220) peak.

The analysis performed by C. Lowe-Ma of NWC was as follows. The average unit cell edge length for samples #8 and 12 were calculated to be 5.462 and 5.461 Å, respectively. C. Lowe-Ma cautioned that the F anion could be replaced by either an OH or OD anion in the crystal without any significant modification in unit cell size. From the ratio of the peak

heights, one can form a rough estimate of the relative portion of the material in the (111) versus the (220) crystal orientation. For sample #8, this means that about twice as much material is in the (111) as the (220) orientation. For sample #10, the amount of material in the (111) orientation is roughly a factor of 11 times that of the material in the (220) orientation; for sample #12, the ratio is on the order of 30:1. No evidence of $Ca(OH)_2$ or $Ca(OD)_2$ crystallites was found. BaF_2 powder was used as a standard for the determination of the average "crystallite size." The method utilized was the Warren-Averbach Fourier analysis approach. With this technique, an average size of about 284 Å was calculated for the crystallites of sample #8. For sample #12, an average crystallite size of 477 Å was calculated; for sample #10, it was 665 Å. It is interesting to note that the order of the average crystallite sizes parallels the order of optical absorption and laser damage.

Summary and Conclusions

The unusual properties observed for the dosed CaF_2 thin films required a substantial number of tests before a reasonable mechanism was determined. Evidence strongly points to modification of the film structure induced by the presence of H_2O or D_2O during the coating process. The low-temperature bakeout appears also to have played a role in some of the film properties observed.

From the analytical data discussed previously, it was observed that there was no evidence of residual D_2O in any of the films produced in the presence of copious amounts of D_2O. Only the laser-induced desorption onset experiment had the necessary sensitivity to consistently see the D_2O adsorbed onto the surface of the CaF_2 films randomly distributed in adsites. One first questions why no trace of D_2O was found, while substantial amounts of H_2O were present. Adsorption/desorption is a dynamic process. de Boer [7] shows that there are 1 x 10^{20} molecules/sec/cm^2 of H_2O bombarding a surface for even 10% humidity. For samples carried around in typically 35 to 40% humidity, it may seem more surprising that *any* residual D_2O was found. Ogura [6] discusses the problem of removing residual H_2O molecules from the pores frequently found in thin-film structures. He found that for pore sizes smaller than 13 Å it was quite difficult to remove the H_2O molecules. He also presents a pore modeled in the shape of an ink bottle. Such a pore would be very difficult to empty once filled. If such pores were filled with D_2O during the coating process, the dynamics of the adsorption/desorption process dictate that only the types of pore structures just discussed would tend to retain the trace amounts of D_2O found in the laser-induced desorption experiment. It also seems quite reasonable that pulsed irradiation could provide the stimulus to remove these trapped D_2O molecules.

We may now have a clue as to why the CaF_2 films made in the presence of H_2O/D_2O showed a decreased optical absorption in the water band while not absorbing in the heavy water band. While it is true that normal H_2O replaced the heavy water in the D_2O-dosed samples, the overall surface area would be reduced as well as the number of pores if the thin-film growth columns were larger. Does evidence exist that this has taken place? The answer is unequivocally, yes. From the x-ray crystallography data, it was determined that the grain size of the CaF_2 films on ultrabright acid Cu followed the optical absorption. The H_2O-dosed film had the lowest optical absorption and the largest grain size, while the undosed film had the highest optical absorption and the smallest grain size. The D_2O-dosed films exhibited an intermediate grain size and adsorption. Electron micrographs showed that the dosed CaF_2 films exhibited a larger columnar structure than the undosed films. This is probably the result of larger grain size. One concern that should be addressed here is the question of contamination. The analysis of the x-ray crystallography data indicates that $Ca(OH)_2$ was not present in the H_2O-dosed films. It is possible that an OH- ion can replace a F- in the CaF_2 with only a minor crystal distortion. The average unit cell edge length at 5.462 Å for both the undosed and D_2O-dosed films indicates that the two films are quite

similar in their unit cell structure. When the undosed film was retested to compare with a H_2O-dosed film, it was found to have an average unit cell edge length of 5.463 versus 5.465 Å for the H_2O-dosed CaF_2 film. Thus, the average unit cell edge length for all three samples was found to be quite similar. Crystallite size appears to determine the properties seen for the behavior of these films. Auger and secondary ion mass spectroscopy (SIMS) analyses did show that trace amounts of contaminants were found in both the dosed and the undosed CaF_2 films. There did not appear to be a significant difference in the contaminant level in the films as a function of dosing for most of the contaminants, but not for all of them. The exceptions were Cu and oxygen. The Auger and SIMS analyses were discussed earlier. If one assumes a more ordered system and, hence, larger crystallites and columnar structure than as stated earlier, an overall reduced surface area would follow. It is possible that Cu migrates up from the substrate along the surface of the growth columns toward the surface of the CaF_2 film. It is also possible that H_2O and, hence, oxygen migrate down from the top surface toward the substrate. Both of these phenomena should be impeded if the surface area is reduced. And, this is in general what was observed. The dosed films exhibited a reduced Cu migration from the substrate toward the surface and a reduced oxygen migration from the top surface toward the substrate.

We might wonder why dosing during the coating process caused the structural modification of the thin film without incorporating into the film. The process may be thought of as a "catalytic-like" one. If a simple model is permitted, figures 23 and 24 are cartoons showing CaF_2 molecules pictured as large circles and H_2O molecules pictured as smaller circles with a dot in the center. Figure 23(a) shows an ordered CaF_2 surface with an incoming CaF_2 molecule about to hit a corner region. Since the sticking coefficient is fairly high and the kinetic energy fairly low, the molecule adheres where it struck with a little additional movement, shown in figure 23(b). In contrast, the same CaF_2 surface is shown in figure 24 with two monolayers of H_2O on the bottom step. Figure 24(a), like the previous cartoon, shows an incoming CaF_2 molecule. This time, however, the in-bound molecule strikes both the CaF_2 molecule on the corner of a step as well the H_2O molecule in intimate contact with it. Now, after striking this surface [shown in fig. 24(b)], the molecule is attracted to both the CaF_2 and the H_2O molecule. With what little kinetic energy it has along with the high mobility of the H_2O molecule, the CaF_2 molecule moves around until it finds the most stable potential region, which happens to be the position in the surface that tends toward a crystalline structure. Additional support for this model can be found in figures 20 through 22, which show the result of the x-ray crystallography analysis. From these figures, it can be seen that one major effect of dosing the CaF_2 caused a considerable increase in the (111) crystal peak. This represents a set of crystalline planes "parallel" to the Cu substrate.

The small spot laser-induced technique provided information on the spatial distribution of the adsorbed gases. For the dosed coatings, it was found that H_2O/D_2O introduced during the coating process can act as a modifier of the structure of the film being deposited. Operationally, there are localized regions randomly distributed about the surface—adsites—where H_2O/D_2O aggregate.

From the conclusions drawn, one might expect that comparable results may be found for fluoride coatings produced in a manner similar to that described in this paper. However, often the coatings are deposited onto heated substrates. It seems likely that the increased temperature of the substrate will reduce the adsorption of H_2O/D_2O onto the surface being coated and thus reduce the action seen for unheated substrates. Also, since this study did not find the optimum operating substrate temperature, gas pressure, or even gas type, this work still remains to be performed.

References

[1] Franck, J. B.; Porteus, J. O.; Johnson, L. F.; Pentony, J. M.; Faith, W. N. "The consequence of doping optical materials with D_2O," presented at the 20th symposium on optical materials for high power lasers; Boulder, CO; 1988 26-28 October. (Proceedings in process.)

[2] Franck, J. B. "Laser-induced desorption and damage of water- and heavy-water-dosed optical thin films," Ph.D. Dissertation. Tucson, AZ; Optical Sciences Center; University of Arizona; 1989.

[3] de Boer, J. H.; Dipple, C. J. "Oberflachenbestimmung durch adsorption von wassermolekulen," Z. Phys. Chem. B 25; 399-411; 1934.

[4] Barraclough, P. B.; Hall, P. G. "Adsorption of water vapor by calcium fluoride, barium fluoride, and lead fluoride," J. Chem. Soc. Faraday Trans. 71; Part 11; 2266-2276; 1975.

[5] Porteus, J. O.; Franck, J. B.; Seitel, S. C.; Allen, S. D. "Defect characteristics of optical surfaces using pulsed laser damage methods," in Measurement and effects of surface defects and quality of polish, Baker, L. R.; Bennett, H. E., ed. Proc. SPIE, 525; 43-50; 1985.

[6] Ogura, S. "Some features of the behavior of optical thin films: A study of packing density, structure, and water sorption phenomena in optical thin films," Ph.D. Dissertation. England; Department of Physics and Physical Electronics; Newcastle Upon Tyne Polytechnic; 1975.

[7] de Boer, J. H. The dynamical character of adsorption. Oxford; Clarendon Press; 1968.

[8] Gregg, S. J.; Swing, K. S. W. Adsorption, surface area, and porosity, 2nd ed. San Diego, CA; Academic Press; 1982.

[9] Porteus, J. O.; Faith, W. N.; Allen, S. D. "Laser desorption analysis of H_2O and other contaminates from optical surfaces," in Laser induced damage in optical materials: 1981, Bennett, H. E.; Guenther, A. H.; Milam, D.; Newnam, B. E., ed. 1981 November 17-18; Boulder, CO. Nat. Bur. Stand. (U.S.) Spec. Publ. 638; 1983 September. Pp. 273-279.

[10] Allen, S. D.; Porteus, J. O.; Faith, W. N.; Franck, J. B. "Contaminant and defect analysis of optical surfaces by infrared laser induced desorption," Appl. Phys. Lett. 45; 997-999; 1984.

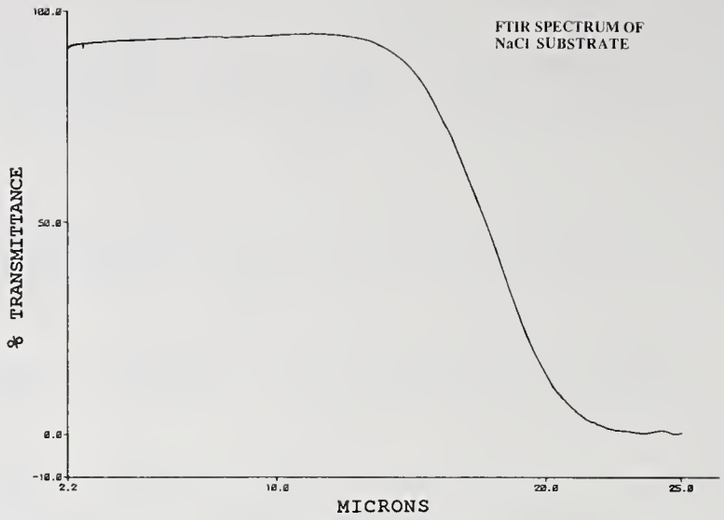

Figure 1. FTIR transmission plot of a NaCl substrate. The roll-off around 15 μm is due to the NaCl.

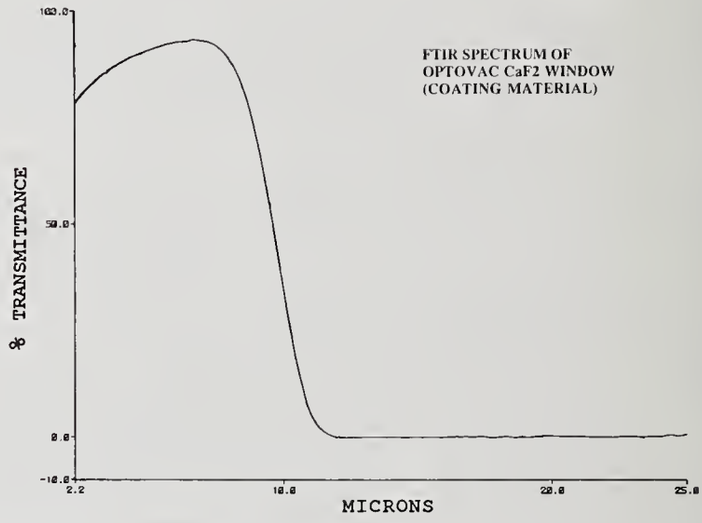

Figure 2. FTIR transmission plot of an Optovac window later broken for use as coating material. The slope on the short wavelength side is an instrumental artifact. The important consideration is that no absorption bands associated with either H_2O or D_2O can be seen.

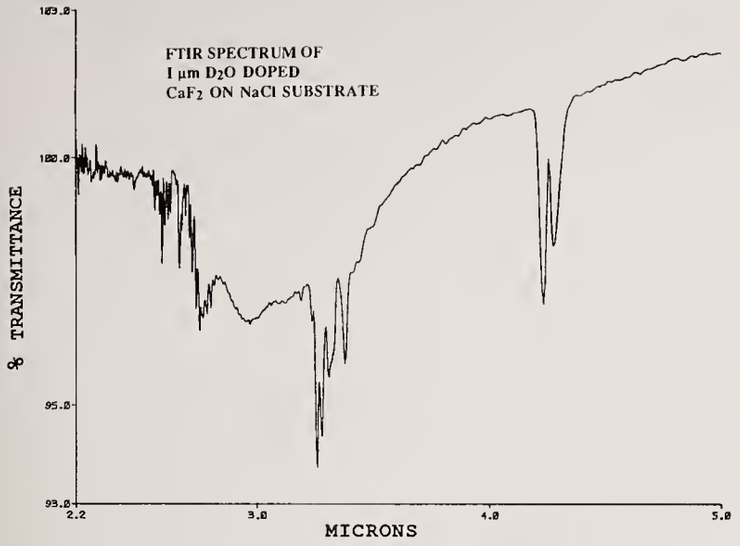

Figure 3. FTIR transmission plot of a D_2O-dosed 1-μm-thick CaF_2 film on the NaCl substrate presented in figure 2. The absorption band attributed to H_2O is seen with some fine structure associated with hydrocarbons around 3.3 μm as well as CO_2 around 4.3 μm. No evidence of the D_2O dosing can be seen at ~ 3.9 μm.

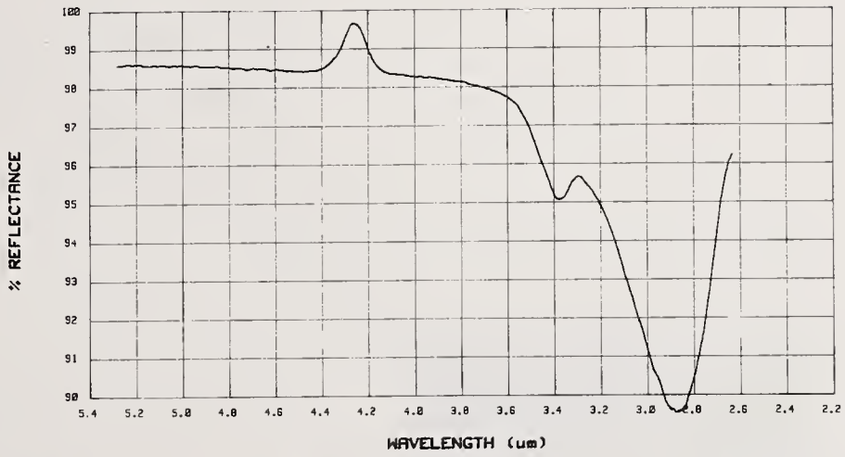

Figure 4. Plot of reflectance versus wavelength shown with wavelength decreasing from left to right for an undosed CaF_2 film on SPDM Cu. The sample has gone through a 12-hr bakeout. The reflectance minimum at 2.9 μm at around 89.5% is due to H_2O. The additional local minimum at 3.4 μm is due either to loosely bound OH^- or hydrocarbons. The bump around 4.3 μm is a calibration artifact.

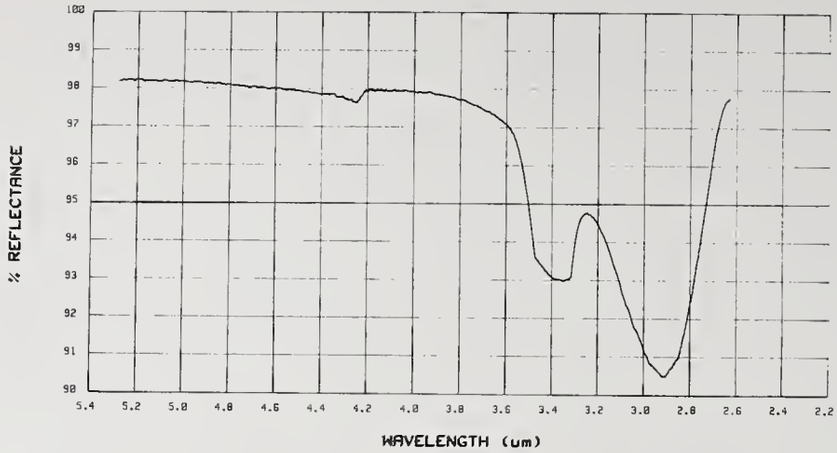

Figure 5. Plot of reflectance versus wavelength shown with wavelength decreasing from left to right for a D_2O-dosed CaF_2 film on SPDM Cu. The sample has gone through a 12-hr bakeout. The reflectance minimum at 2.9 μm, up from the coating discussed in figure 4 at around 90.5%, is due to H_2O. The additional local minimum at 3.4 μm has increased dramatically over the undosed film and has saturated the detector. No evidence of absorption related to the D_2O dosing is evidenced.

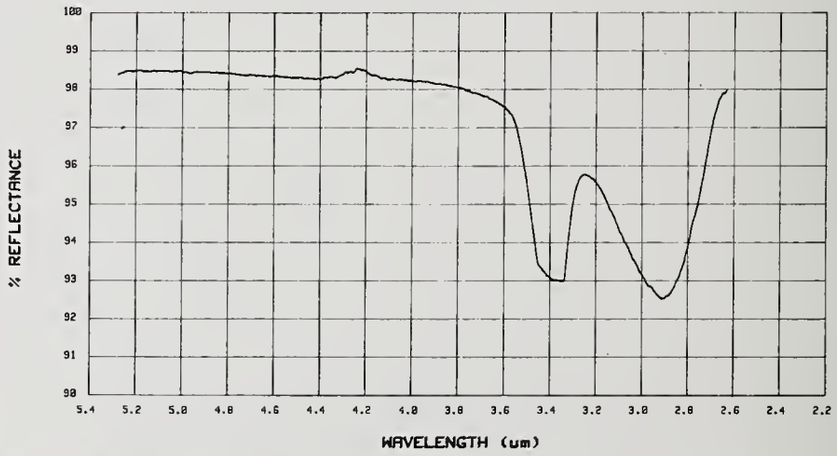

Figure 6. Plot of reflectance versus wavelength shown with wavelength decreasing from left to right for a H_2O-dosed CaF_2 film on SPDM Cu. The sample has gone through a 12-hr bakeout. The reflectance minimum at 2.9 μm, up from the reflectance of the undosed, dosed, or the D_2O dosed at around 92.5%, is due to H_2O. The additional local minimum at 3.4 μm has also increased dramatically over the undosed film and has saturated the detector.

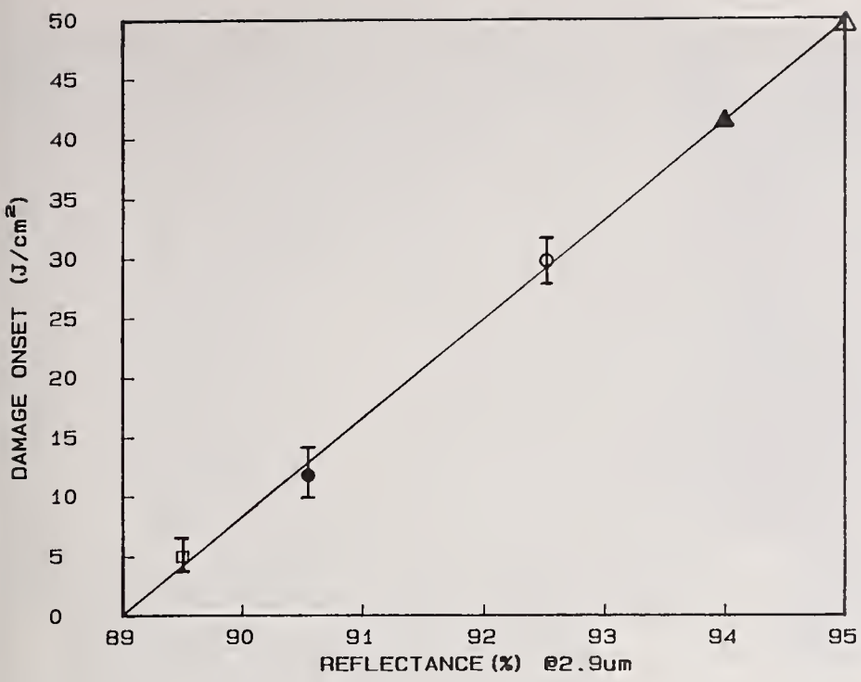

Figure 7. Plot of laser damage onset value versus spectral reflectance at 2.9 μm for the samples discussed in figures 4 through 6. A best-fit straight line passes through all three points: the hollow square, solid circle, and hollow circle. Two additional points—the solid triangle and hollow triangle—whose spectral reflectances are known but damage onsets are not known are placed on the line corresponding to their abscissa value for spectral reflectance. The corresponding laser damage onset value predicted in this fashion is quite high for 2.7 μm. This is, of course, only a prediction, as the straight line may roll off at higher fluences; however, the prediction made in this manner is certainly interesting.

Figure 8. Photograph of HF laser-induced damage of undosed CaF_2 on SPDM Cu. Damage morphology is fracture and delamination; 360X magnification.

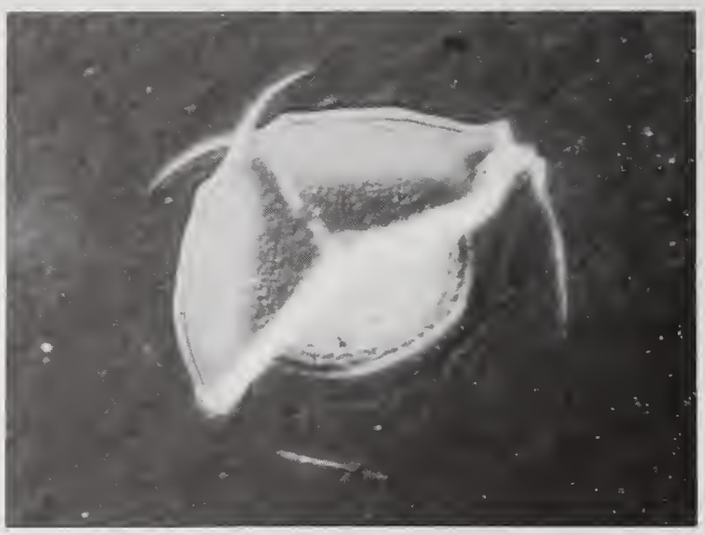

Figure 9. Photograph of HF laser-induced damage of undosed CaF_2 on SPDM Cu. Damage morphology is fracture and delamination; 360X magnification.

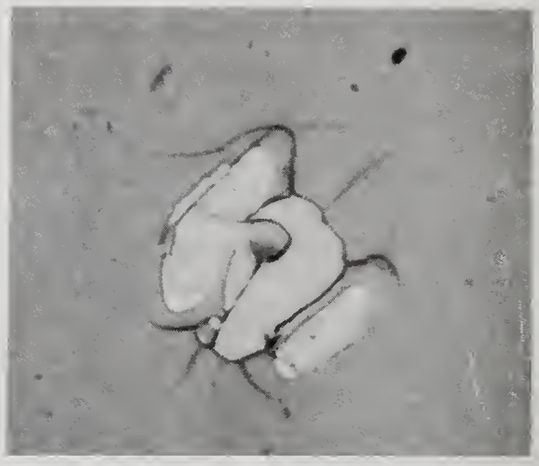

Figure 10. Photograph of HF laser-induced damage of undosed CaF_2 on quartz. Damage morphology is fracture and delamination; 360X magnification.

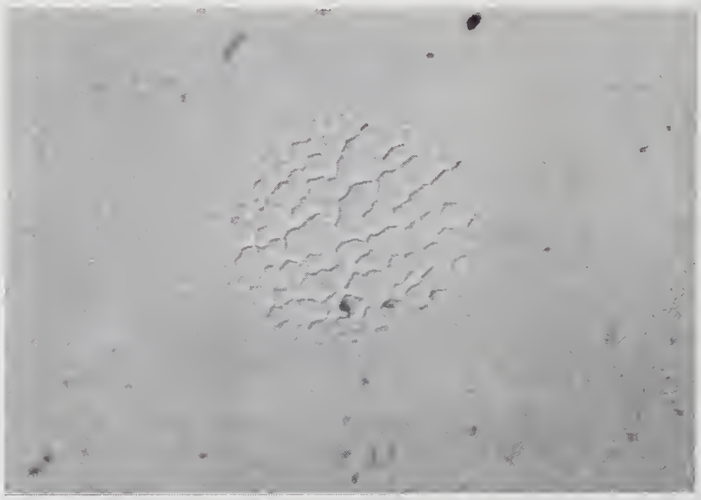

Figure 11. Photograph of HF laser-induced damage of H_2O-dosed CaF_2 on SPDM Cu. Damage morphology is ablation and "orange-peel-like" surface roughening; 360X magnification.

Figure 12. Photograph of HF laser-induced damage of H_2O-dosed CaF_2 on SPDM Cu. Damage morphology is ablation and "orange-peel-like" surface roughening; 360X magnification.

Figure 13. Photograph of HF laser-induced damage of H_2O-dosed CaF_2 on SPDM Cu. Damage morphology is ablation and "orange-peel-like" surface roughening. Damage has penetrated into the Cu without modifying the damage morphology; 360X magnification.

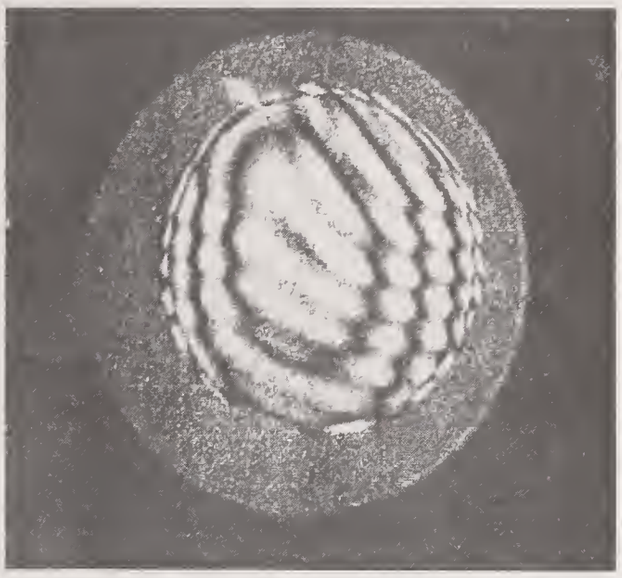

Figure 14. Photograph of the interference fringe pattern for undosed CaF_2 films on thin "stress measurement" sample. If the film is stressed, it will cause the thin, flat SiO_2 sample to bow either positively or negatively depending on whether the stress is compressive or tensile. A few fringes are visible, indicating some low residual stress in the coatings.

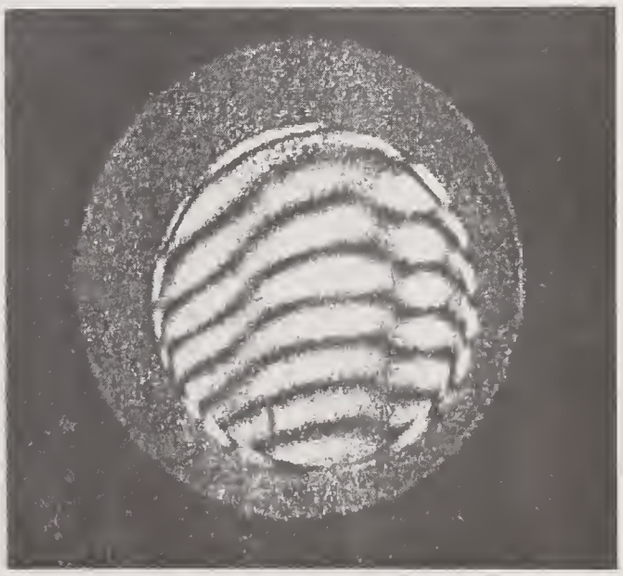

Figure 15. Photograph similar to figure 14 with the exception that it is H_2O dosed. Even fewer fringes can be observed with this sample, indicating less residual stress than in the undosed film.

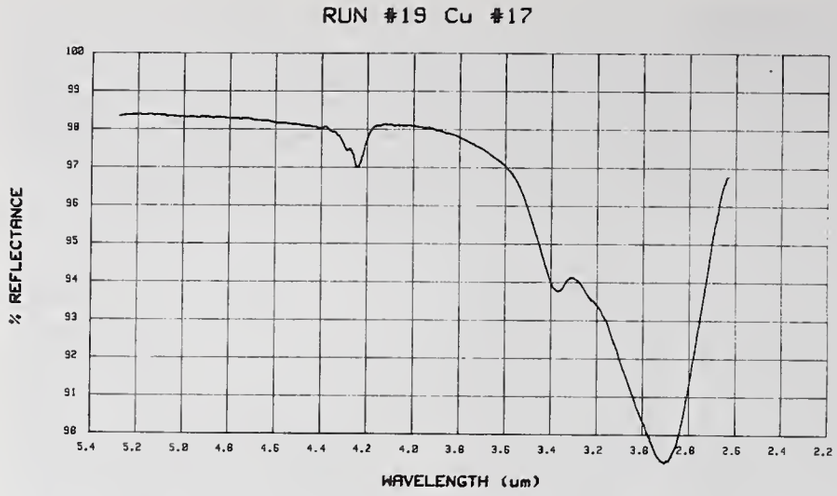

Figure 16. Plot of spectral reflectance versus wavelength shown with wavelength decreasing from left to right for an undosed CaF_2 film on SPDM Cu. The sample is unbaked. The reflectance minimum at 2.9 μm reflectance is around 89.5%. The additional local minimum at 3.4 μm can be seen.

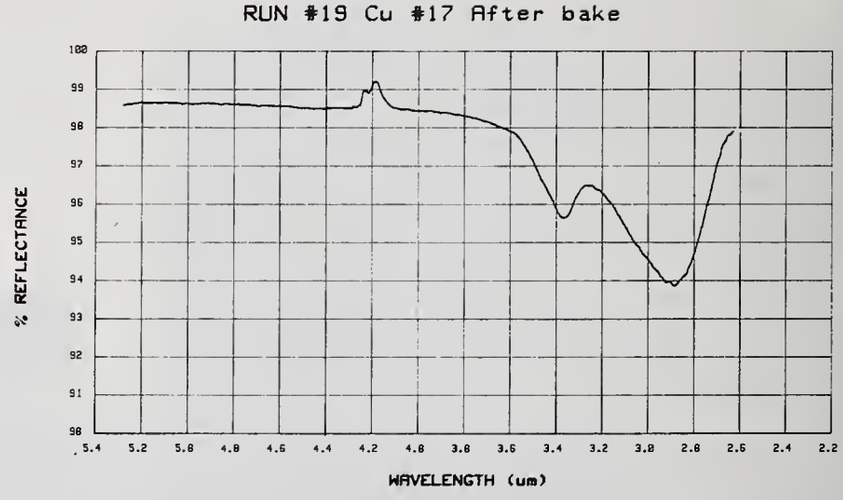

Figure 17. Plot of reflectance versus wavelength shown with wavelength decreasing from left to right for an undosed CaF_2 film on SPDM Cu. The sample has gone through an 18-hr bakeout. The reflectance minimum at 2.9 μm is up from the reflectance of the unbaked film at around 94.0%.

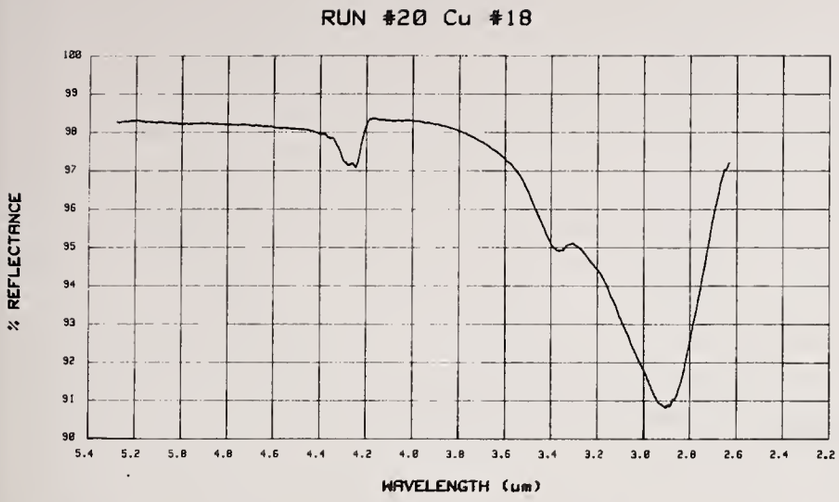

Figure 18. Plot of Reflectance versus wavelength shown with wavelength decreasing from left to right for a H_2O-dosed CaF_2 film on SPDM Cu. The sample is unbaked. The reflectance minimum at 2.9 μm is around 91.0%. The additional local minimum at 3.4 μm can be seen.

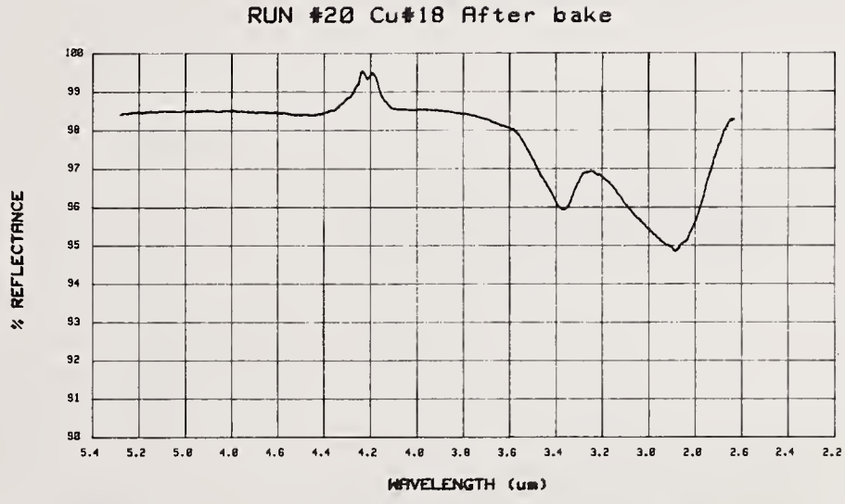

Figure 19. Plot of reflectance versus wavelength shown with wavelength decreasing from left to right for a H_2O-dosed CaF_2 film on SPDM Cu. The sample has gone through an 18-hr bakeout. The reflectance minimum at 2.9 μm is up to around 95.0%.

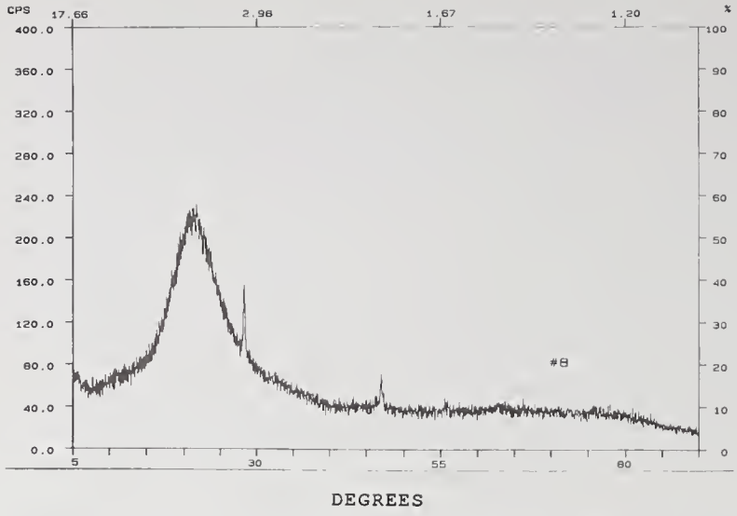

Figure 20. X-ray crystallography data shown plotted with counts per second for the ordinate and angle in degrees for the abscissa. The coating is an undosed/unbaked CaF_2 film on quartz. The broad peak around 22 deg is due to the substrate. There is a sharp peak around 29 deg associated with the (111) crystal orientation and a second peak around 47 deg associated with the (220) crystal orientation for CaF_2.

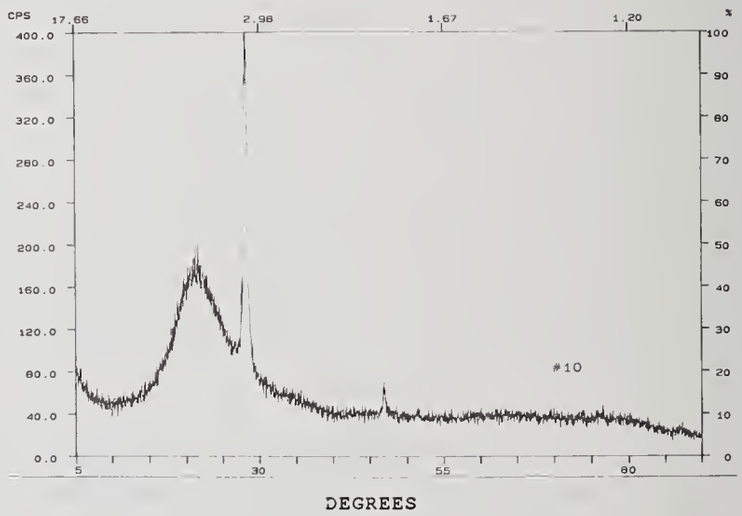

Figure 21. X-ray crystallography data shown plotted with counts per second for the ordinate and angle in degrees for the abscissa. The coating is a D_2O-dosed/unbaked CaF_2 film on quartz. The broad peak around 22 deg is due to the substrate. The sharp peak around 29 deg associated with the (111) crystal orientation is much higher for this coating than for the undosed coating. The second peak around 47 deg associated with the (220) crystal orientation appears the same.

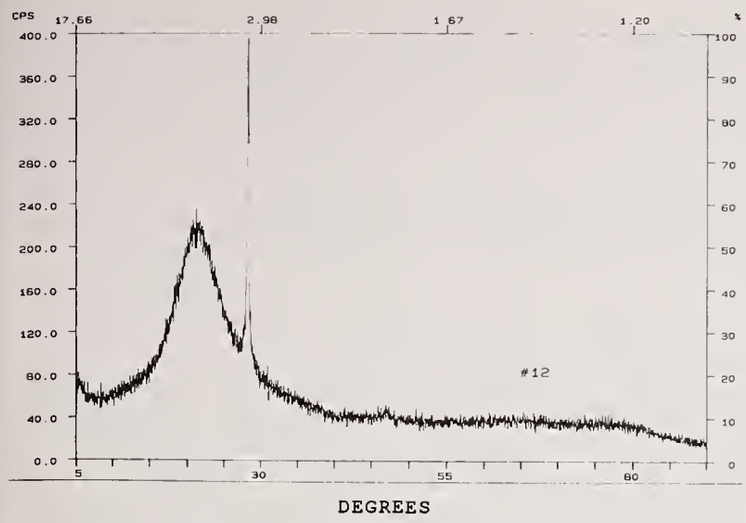

Figure 22. X-ray crystallography data shown plotted with counts per second for the ordinate and angle in degrees for the abscissa. The coating is a H_2O-dosed/unbaked CaF_2 film on quartz. The broad peak around 22 deg is due to the substrate. The sharp peak around 29 deg associated with the (111) crystal orientation is much higher for this coating than for the undosed coating. The second peak around 47 deg associated with the (220) crystal orientation appears much smaller than for the undosed or the D_2O-dosed film.

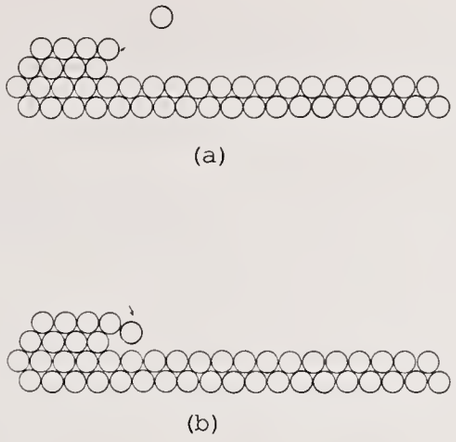

Figure 23. Cartoon representing a CaF_2 regular surface being impinged upon by a CaF_2 molecule shown in (a). After the impact, the molecule moves a little, but comes to rest in a manner such that a void is left behind, shown in (b). After several million iterations, the once ordered surface builds up into a strongly disordered surface.

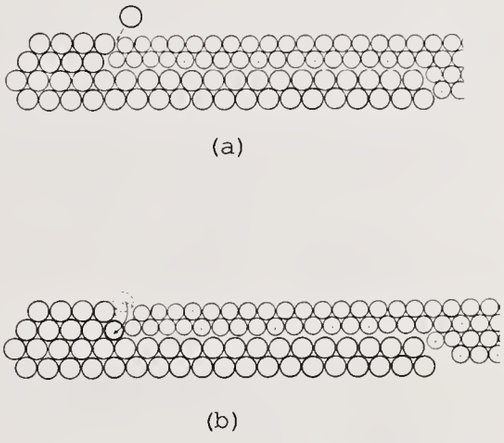

Figure 24. Cartoon representing a CaF_2 regular surface being impinged upon by a CaF_2 molecule shown in (a). Unlike the case in figure 23, this surface has H_2O molecules adsorbed onto it. After the impact, the molecule moves more freely and has the possibility of finding the lowest potential, hence building a more ordered surface, depicted in (b). After several million iterations, the once ordered surface builds up into a more ordered surface.

Manuscript received
4-2-90

Non-Avalanche Dielectric Breakdown in Wide-Band-Gap Insulators at DC and Optical Frequencies

P.Braunlich, S.C.Jones, X.A.Shen, and R.T.Casper

Dept. of Physics, Washington State University,
Pullman, WA 99164-2814

E.Cartier, D.J.DiMaria, and M.V.Fischetti

IBM T.J. Watson Research Center, P.O.Box 218,
Yorktown Heights, New York 10598

P.Kelly

Physics Division, National Research Council,
Ottawa, Canada K1A 0R6

It is the purpose of this paper to put recent novel experimental efforts to understand dielectric breakdown in wide-band-gap materials in various fields into a common framework and outline significant changes in the understanding of dielectric breakdown at optical frequencies and free electron heating under DC conditions. New experimental techniques used to measure multiphoton absorption and energy deposition in wide-band-gap alkali halides in the prebreakdown regime have led to hard evidence refuting the avalanche model of laser-induced damage at visible laser wavelength. The experiments show that virtually all lattice heating occurs via nonlinear absorption of laser photons by multiphoton excited free electrons. Direct measurements of free electron heating by DC fields in thin SiO_2-films and direct measurements of electron-phonon scattering rates of energetic free electrons impose a new understanding of carrier heating. The scattering of free electrons with non-polar acoustic phonons is found to be the dominant interaction in preventing the free carriers from reaching energies high enough to cause impact ionization and initiate avalanche breakdown. These results unambiguously show that the role of avalanche breakdown under DC conditions has been overestimated in the past.

avalanche breakdown; multiphoton absorption; electron heating; lattice heating; electron-phonon interaction; hot-electron transport.

1. Introduction

For several decades the phenomenon of dielectric breakdown in wide-band-gap insulators has been the subject of intense research in such different fields as the development of insulation in high power electrical equipment [1], of passivation layers in electronic devices [2], and of high power laser optics [3]. Due to the great technical importance of all these fields, the interest in the breakdown phenomena was kindled mainly by the desire to find materials which can withstand the voltage-, electrical field- or power-levels required for the specific technical applications. In all fields, breakdown manifests itself in a sudden, often totally destructive and irreversible material change. For a long period of time it was not possible to detect any precursors which would actually announce the catastrophic event. Therefore it is not surprising that in all technically relevant fields a vast literature exists, in which some sort of experimentally determined damage threshold, as the only easily measurable quantity, is taken as a test for various existing breakdown models.

In retrospect, this approach, justified from an engineering point of view, has actually provided little insight into the fundamental process leading to breakdown. By analyzing the literature, it is indeed possible to find theories - developed on the premise of a perfect intrinsic solid - which "predict" the highest, at the time available, breakdown strength as the "intrinsic" limit of the insulator under consideration. As purer solids and more perfect device structures become available, we are now in a situation where extrinsic breakdown (not due to the behavior of the perfect, ideal solid, but triggered by impurities, structural imperfection, etc.) is eliminated to a large extent. Therefore it has become possible to study dielectric breakdown not only as a sudden, statistically predictable destructive event but to investigate precursors to catastrophic breakdown such as electron heating [4-14] and lattice heating [3,15-19] well below the catastrophic damage threshold. A second important aspect which led, as we will review in this paper, to a new understanding of dielectric breakdown consists of the application of novel experimental techniques both in the field of DC [4-14] and laser [15-19] breakdown. Additionally, the development of new, more complete theories for the electron-phonon [20-23] and photon-electron-phonon interaction [24] as well as the application of advanced Monte Carlo techniques [21-23] to the electron transport problem in insulators have significantly contributed to this recent development.

The title of this contribution is intentionally provocative for the following reasons. The so called "avalanche breakdown" model in all its modifications has been, and still is, widely believed to be the ultimate and right answer to the dielectric breakdown phenomena in each community involved in dielectric breakdown in wide-band-gap insulators. This view point requires serious revision, since convincing experimental evidence has been gathered over the last years which shows that avalanche formation is not necessarily the limiting process for the dielectric strength of wide-band-gap insulators.

Laser experiments [3,15-19] have shown that in specially purified materials significant lattice heating can be detected at power levels as low as half the power for catastrophic breakdown. With increasing pulse power, the measured lattice heating becomes so strong that the insulator actually heats up close to its melting point in the center of the focal volume and thermo-mechanical destruction becomes inevitable [15-18]. Such a gradual energy deposition is totally incompatible with the avalanche breakdown model but can be consistently explained if virtually all lattice heating occurs via nonlinear absorption of laser photons by multiphoton excited free carriers. Measurements of free-carrier heating in a two-pulse experiment [19] directly confirm that lattice heating is indeed due to photon absorption by free carriers and the subsequent release of the excess kinetic energy to the lattice by phonon excitations. Again, catastrophic failure occurs when the temperature in the insulator approaches its melting point. These same results have been found in various ionic crystals as well as in SiO_2.

In the field of DC breakdown, the understanding of dielectric breakdown has been changed in a similarly dramatic way [1,4-14]. In SiO_2 with MOS(metal-oxide-silicon)-structures no indication for avalanche formation can be found up to DC fields as high as 16 MV/cm and breakdown has to be considered as an extrinsic event (mostly triggered by local imperfections of the MOS-structures), at least up to an oxide thickness of 500 Å. Direct measurements of the hot electron distribution at high electric fields [4-10] show that the electron distribution gets significantly heated at fields well below that for destructive breakdown. But the electron distribution is found to be stabilized well below the ionization threshold and an "average" electron cannot ionize the solid. The experiments, however, do not exclude that ionization and multiplication might indeed be the limiting factor in even more perfect MOS-structures or in bulk SiO_2 samples under DC conditions. An estimate of such a limiting field can be obtained from independent measurements of electron-phonon scattering rates [13] and subsequent simulations of electron heating using classical Monte Carlo techniques [21-22]. This procedure shows that the interaction of "hot" conduction band electrons with the SiO_2 lattice is so strong, that impact ionization is not expected for average electrons up to fields of 25 MV/cm, not only in thin oxide films but also in bulk SiO_2.

It is the purpose of this paper to review these recent novel experiments in different fields which have actually led independently to the conclusion that the role of avalanche breakdown has been overestimated as a limiting factor for the dielectric strength of wide-band-gap insulators both at optical frequences and under DC conditions.

However, we want to stress here that with the present bulk of experimental data it would be hasty to claim that avalanche breakdown is irrelevant for all wide-band-gap insulators. The critical field or power levels for avalanche breakdown under given experimental conditions (temperature, laser frequence, etc.) entirely depends on the properties of the solid via the electron-phonon interaction. It is this interaction which prevents runaway to energies high enough for impact ionization below some critical field. The crucial question simply is whether this interaction is weak enough to allow multiplication before some other fundamental or simply extrinsic process leads to breakdown. For DC breakdown, in possibly all wide-band-gap insulators studied, one can argue that there is no solid experimental proof that any published breakdown fields reprcsent an intrinsic threshold for avalanche formation. In laser breakdown a similar statement can be made, but here, at least in a few cases, strong evidence for another fundamentally limiting process has now been established.

The paper is organized as follows. In chapter 2, the results of single pulse laser experiments in the prebreakdown regime will be presented. In chapter 3, we review the electron-phonon interaction concepts in wide-band-gap insulators and show some results of Monte Carlo simulations to illustrate the consequences of the new understanding of free electron heating under high field conditions with SiO_2 as an example. In chaptcr 4, an experimental technique to determine electron-phonon scattering rates in a zero field experiment and results for SiO_2 will be prescnted. Finally, we

summarize the experiments which give direct access to the hot electron distribution under high DC fields. We only briefly outline the basic ideas of the experimental techniques and put more emphasis on the discussion of the results in order to outline the crucial role of a correctly chosen electron-phonon interaction scheme. The reader interested in experimental and theoretical details will find references for more detailed publications in each chapter.

2. Interaction of single high-power laser pulses with wide-band-gap insulators in the prebreakdown regime

The investigation of single-pulse laser damage discussed here has been ongoing for approximately the last 10 years, and the most significant results of the experimental program have been presented in detail at the 1986, 1987, and 1988 Boulder Laser Damage Symposia. We wish here to only briefly present the results as a unified discussion for purposes of review. A comprehensive review is available in Ref. [3].

Experiments were performed in all cases in specially purified alkali halide crystals prepared by the University of Utah Crystal Growth Laboratory. The laser system produced single pulses of approximately 80 psec (half width at 1/e) at 532 nm and 100 psec at 1064 nm. Data from photoacoustic and luminescence measurements were obtained only for pulse energies below the damage threshold, i.e., only prebreakdown processes leading up to damage were monitored.

Two types of experiments were performed in the prebreakdown regime to measure the absorption of laser beam energy, and these measurements were compared with models including processes that are known to occur in alkali halides following electron-hole pair production. Two alternative models for free-electron heating were investigated. The difference in (theoretical) heating efficiency of these two lead to conclusions regarding the relative importance of primary defects in single shot laser damage.

Calibrated photoacoustic measurements of prebreakdown energy absorption from 532 nm laser pulses in NaCl revealed that the primary process for the interaction is four-photon absorption. In figure 1 the peak temperature induced in the beam focal volume by a single pulse of peak photon flux density, F_p, is displayed. These results are compared with three models of the interaction.

They account in detail for the creation and recombination of e-h pairs, creation and annihilation of primary defects (V_k, STE, STH, F), and the resulting heating of the lattice. We allow for two possible pair generation processes, multiphoton absorption and impact ionization. The processes are depicted in figure 2. Generally, electrons are elevated to the conduction band either from the valence band or from ionized defects (STE's, F-centers). Free valence band holes are trapped rapidly, but may be freed again by hole absorption, then quickly retrapped. The net result is heat deposition of $\hbar\omega$ per event. V_k centers may orient themselves into directions relatively inert to the polarized laser light, thus the hole absorption does not occur for each V_k center throughout the duration of the laser pulse.

F-center formation is assumed to occur through the triplet STE state at high temperatures. This effect is included or excluded as to its interest in the particular experiment modeled.

The two treatments of free-carrier heating are called (1) the free-electron model, due to Epifanov *et al.* [24] a nonlinear absorption of electromagnetic energy by fairly energetic conduction electrons and (2) the polaron model, wherein low energy conduction electrons which are strongly coupled to lattice ions absorb photons linearly. The first is vastly more efficient theoretically, but there was no a priori reason to prefer one of these unproven models. For completeness, we also compared the data with a model including electron-impact ionization avalanche production of e-h pairs. Full details of these models are available in Ref. [15].

The calculations are superimposed on the data in figure 1. Both treatments of free carrier heating satisfactorily represent the measurements. The four-photon absorption cross section is ambiguous because the photoacoustic effect is a result of total absorbed energy. Allowing for secondary absorption processes (in addition to four-photon absorption) without a preference for one of the two alternatives, it cannot be determined which value of $\sigma^{(4)}$ is most correct, since both are satisfactory. We can see, however, that if model (1) is correct, then fewer electrons, and therefore, fewer primary defects are required to produce the effect. In fact, for model (1), $\approx$ 92 % of all energy absorption is via free electron heating. In model (2) defect absorption, primarily V_k center absorption, accounts for most of the heating (> 50 %). Further, the avalanche process does not account for the data.

In order to discover which model is most correct, and thus the importance of primary defects, it is necessary to model similar measurements with a known value of $\sigma^{(4)}$. This was accomplished using the self-trapped exciton recombination luminescence or STERL technique.

The STERL technique of measuring multiphoton excitation takes advantage of this intrinsic radiative relaxation of electron-hole (e-h) pairs in alkali halides. Since the process is intrinsic, the total light signal output is a measure of the number of e-h pairs generated in an excitation event. This then represents an improvement in measuring multiphoton cross sections over the photoacoustic method because, in a limited range of incident pulse intensities, the response of the sample to incident ionizing radiation is proportional only to the total number of excited carriers. This proportionality falls off when the crystal temperature exceeds that at which non-radiative recombination processes become important. This effect was used as a thermometer to determine lattice heating in KBr when pulse energies were increased beyond

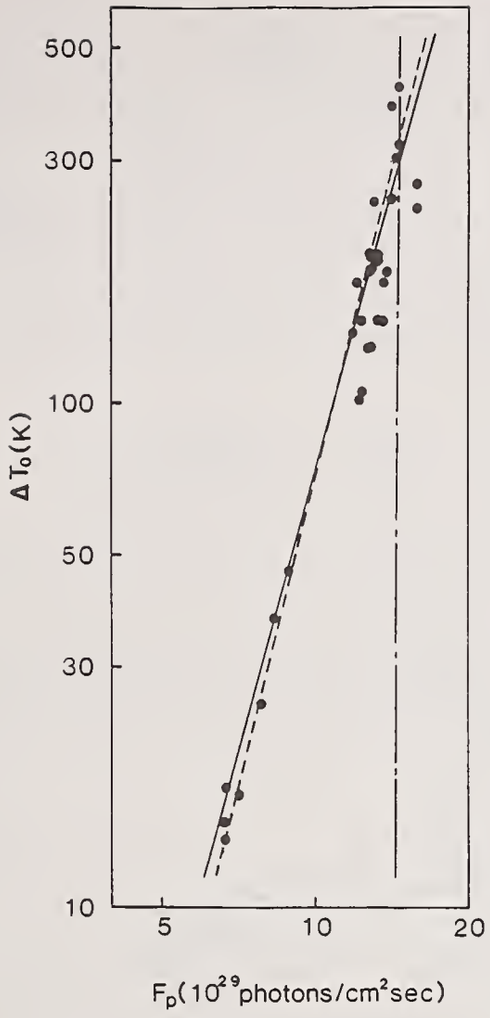

Figure 1. Composite double-logarithmic plot of the calculated temperature increase at the focal point vs incident energy of 532 nm pulses for two NaCl samples. The solid line is that calculated with the four-photon-polaron model, using $\sigma^{(4)} = 2x10^{-113} cm^8$ sec^3 ; the slope is $\approx$ 3.7. The dashed line is that obtained with the four-photon-free carrier model, using $\sigma^{(4)} = 1.5x10^{-114} cm^8$ sec^3 ; the slope is 3.93. The broken line was obtained with the avalanche-free carrier model, using initial carrier density $n_{c0} \approx 7x10^{10} cm^{-3}$.

the level where thermal quenching of the luminescence begins. Armed with the value of $\sigma^{(4)}$ obtained at low pulse intensities, the multiphoton-polaron and -free electron theories of energy absorption were compared with data, revealing that the polaron-defect absorption is simply too weak to account for the observed temperature increase, leaving the multiphoton-free-carrier model as a complete, satisfactory model of prebreakdown energy absorption. Further, temperature data indicate that the highest intensity nondamaging laser pulses induced heating in KBr to only a small amount below the melting point. These measurements could all be explained and modeled without any necessity of including avalanche generation. In fact, these measurements and calculations preclude the role of avalanche generation at least up to the melting point, even though electron densities greater than $10^{18} cm^{-3}$ are present. These results were verified in KI (three photon band gap at 532 nm). Details of the measurements and computations pertaining to KBr are available in Refs. [16-18]. Results of the model calculations, compared with data, are presented in figure 3. Only the σ-band of the STE emission was monitored due to interference of scattered laser light with the π-band.

The conclusion reached in the STERL study was bolstered by a third experiment. Pulses of 266 nm laser light were used to create e-h pairs in NaCl and SiO_2 (via 2-photon absorption), and photoacoustic signal was monitored as a function of coincident pulse energies of 1064 nm laser light, shown in figure 4. Details are presented in Ref. [19]. Since this wavelength is too long to create significant numbers of e-h pairs at these relatively low intensities, the only mechanism by which absorption could take place is via conduction carriers. The nonlinear nature of the resultant signal verified the correctness of the free-electron treatment of the conduction carrier absorption, thus relegating the participation of defects to a minor or possibly insignificant role in the single shot damage process. Exaggerating their roles in the model calculations showed that the models would cease to represent the data. Therefore, we conclude primary defects play at most a minor role in single pulse laser damage of pure alkali halides.

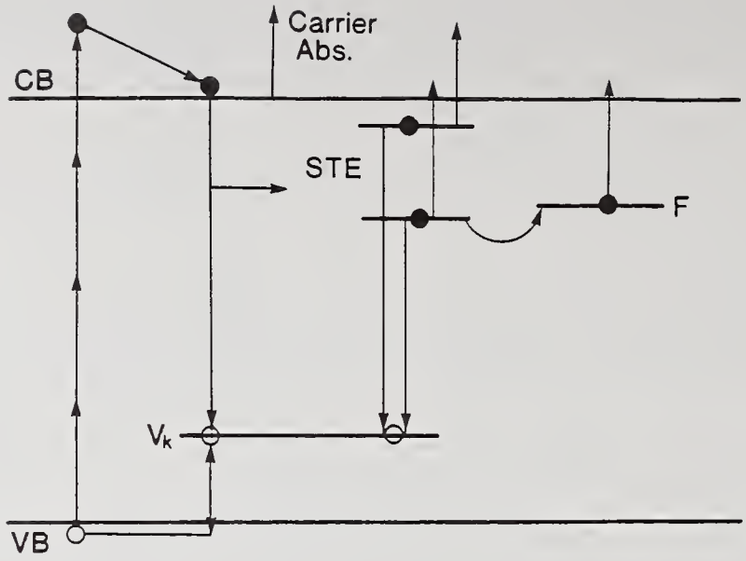

Figure 2. Processes considered in the model are production of electron-hole pairs by four-photon absorption, trapping of holes to form V_k centers, trapping of electrons by V_k centers to form self-trapped excitons (STE), and F-center production. Free carrier absorption, STE excitation, and defect ionization, and electron-hole recombination are also considered.

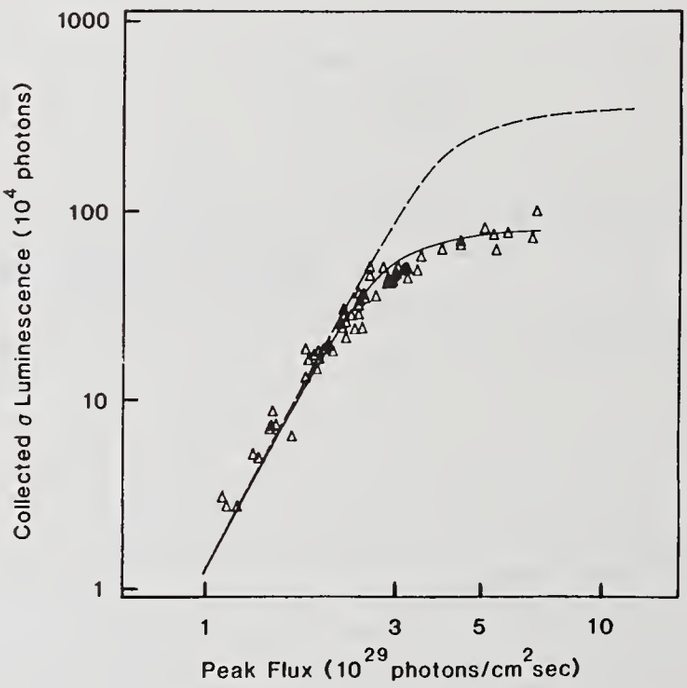

Figure 3. Calculated (solid and dashed lines) and measured (Δ) spatially- and temporally-integrated σ luminescence emission from KBr as a function of the peak photon flux in 532 nm laser pulses of 100 psec duration (1/e intensity halfwidth). The solid line is obtained using the free carrier heating model, while the dashed line is based on the polaron heating model. This luminescence is induced by four-photon exciton generation with subsequent radiative recombination of electrons and V_k centers.

The principal conclusions reached in these experiments are that, by monitoring prebreakdown processes up to the damage threshold, no generation of an electron impact ionization is observed, nor need it be invoked to explain the single

shot damage process. The principal avenue of energy absorption by the solid is photon absorption by multiphoton-generated free electrons. This was also observed in experiments at 1064 nm, where the conditions of high free-electron density and high field amplitudes failed also to show any evidence for avalanche formation, while revealing the predicted behavior for free electron absorption.

The free-electron theory of laser energy absorption by conduction band carriers in wide gap insulators, as developed by Epifanov *et al.* [24], concerns primarily the role of acoustic phonons in the scattering processes required for an electron to gain energy in an alternating electric field. We make no claims to have studied the details of this interaction for high frequency alternating fields, but in the following it is shown that in dc electric fields the acoustic phonon scattering mechanism prevents the formation of electron avalanche in SiO_2 at electric field strengths beyond the breakdown threshold. For purposes of comparison, we state measured breakdown threshold intensities [3] obtained in samples which demonstrated multiphoton absorption up to damage (i.e., samples which showed no evidence of avalanche formation at damage):

KI	$I_B = 75 GW/cm^2$,	$E_B = 6\ MV/cm$
KBr	$I_B = 245 GW/cm^2$,	$E_B = 10.9 MV/cm$
NaCl	$I_B = 745 GW/cm^2$,	$E_B = 19\ MV/cm$

Breakdown field values are the amplitudes, not rms values.

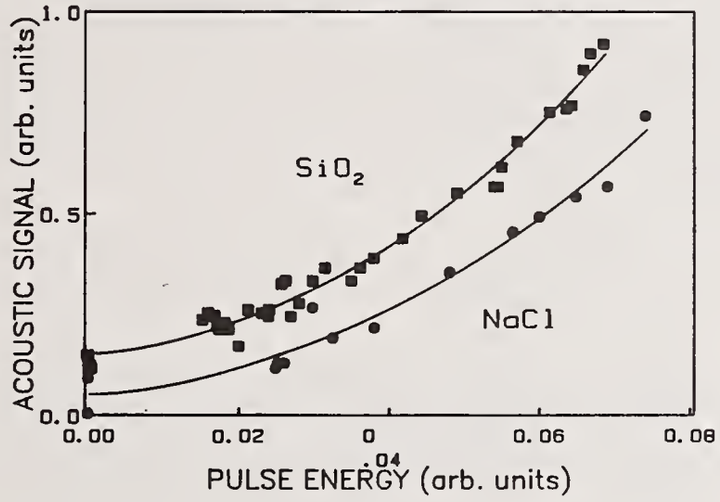

Figure 4. Photoacoustic signal as a function of the energy of the 1064 nm pulse obtained in NaCl and SiO_2 with a constant pump pulse (266 nm) energy. It clearly shows a nonlinear dependence on the energy of the heating pulse. The solid line is the fit to the experimental results [19].

3. Theory of high field electron transport

In this section, we will shortly review the present theoretical understanding of hot electron transport in wide band-gap-insulators [20-23]. We will focus the discussion on SiO_2 because SiO_2 is at present the best understood wide-band-gap insulator as far as hot electron transport goes and also because most of the experiments reviewed in this paper were obtained in this material.

Because of the wide band-gap of in SiO_2 ($E_{gap} \approx 9$ eV), an electron in the conduction band only interacts with the phonon modes over a wide energy range. Only at energies $E_{kin} > 9$ eV can electronic excitation and electron-electron scattering come into play. Consequently, any prediction about the behavior of a conduction band electron under the action of an applied electric field crucially depends on the correct modeling of the electron-phonon interaction over the whole energy range from near thermal energies up to typically 10 eV. Any prediction of an electron-avalanche theory entirely depends on the validity of the chosen electron-phonon interaction theory. All relevant phonon modes and the correct energy dependence of these scattering processes are crucial.

To illustrate this point, we give a short historic summary of the understanding of breakdown in SiO_2. It is interesting, that basically the same historic development can be seen in the field of laser breakdown. The present understanding of

hot electron transport in SiO_2 is indeed very similar to that proposed by Sparks *et al.* [20] in the context of avalanche breakdown in alkali halides as early as 1981. In this sense, the following discussion is indeed very general.

Until 1982, transport in SiO_2 was believed to be dominated by interaction of the electrons with only the polar-phonon modes of the lattice atoms through inelastic scattering [25,26]. The electrons were thought to lose the energy gained from the field in large amounts (0.153 and 0.063 eV for the dominant optical phonon modes in SiO_2) through the creation of these oscillations of the lattice atoms every 1-2 Å. Electrons were believed to stay at thermal energies, near the bottom of the conduction band, and to gain significant amounts of energy from the applied filed only near destructive breakdown of SiO_2 which typically occurred around 8 MV/cm. Destructive breakdown was believed to occur when the electrons gained enough energy to cause impact ionization which in turn caused the current density to become large enough to trigger melting and vaporization of the oxide. However even in the 1970's, there were some problems with this picture. Both experimentally [27-29] and theoretically [30], evidence was brought up, that the LO-phonon scattering length of 1-2 Å might in reality be a factor of 10 larger. Consequently, the LO-phonons could stabilize the electron energy distribution only up to 1.5 MV/cm and LO-phonon runaway would occur at this low field [30]. After 1982, our understanding of high-field steady state transport in SiO_2 began to change as direct studies of charge carrier energies [4-14] became possible and improved Monte Carlo techniques [21-23] were applied to study the transport of conduction electrons. From these studies a new picture for carrier transport in SiO_2 evolved. It became clear that the motion of electrons in the oxide layer is completely controlled by their interaction with the lattice and not by electronic excitations or defect and/or trapping states in the forbidden gap. Energy gained by the field is still lost mostly in large amounts to the polar modes. However, the non-polar phonons (quasi-elastic, large-angle scattering) help to stabilize the electron energy at high fields. They cause large angle scattering and therefore longer meandering paths characteristic of dispersive transport. Electrons stay at near-thermal energies only at fields lower then $\approx$ 1.5 MV/cm. At larger fields, the distribution heats up to a steady state condition where the average energy can be as large as 6 eV at the highest fields attained before destructive breakdown occurs. Before the work of Sparks *et al.* [20] and Fischetti *et al.* [21-23], the importance of the non-polar modes at high fields had been mostly neglected in insulators. This resulted in the incorrect idea that most electrons in SiO_2 and alkali halides were near thermal energies until breakdown, where the electrons accelerated to energies greater than that of the band-gap and caused impact ionization.

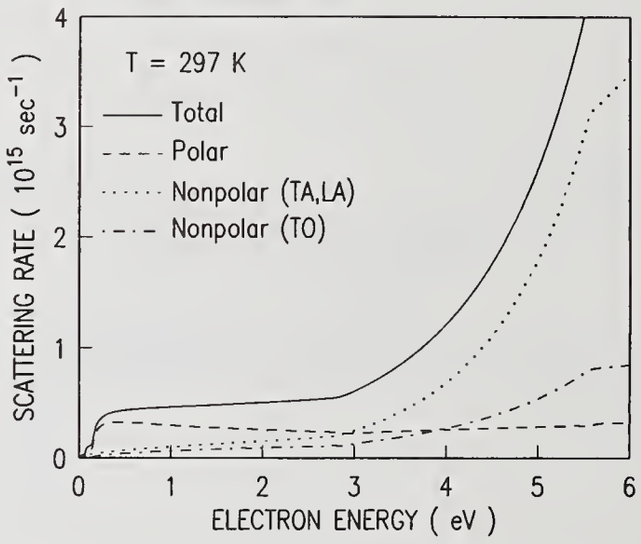

Figure 5. Electron-phonon scattering rates in SiO_2 as a function of electron energy at room temperature. Notice the strong increase of the acoustic-phonon scattering (nonpolar, TA, LA) rate with increasing electron energy. It is this interaction that stabilizes the electron energy distribution at high fields.

In figure 5, calculated electron scattering rates for the various phonon modes in a spherical-band model are shown. These rates reflect the present understanding of electron-phonon interaction in SiO_2 and are believed to be qualitatively true for polar inorganic and organic insulators in general [13]. Formal discussions of the calculation and the correct choice of electron-phonon coupling constants, the role of the conduction band structure, the electron-phonon interaction scheme etc. can be found in Refs. [21-23]. See also Sparks *et al.* [20] as well as Porod and Ferry [31] and Zakharov and Fiveisky [32]. All hot electron transport measurements presented below can be consistently explained with the scattering rates shown in figure 5. The polar electron-phonon interaction (dashed line in fig. 5) is due to the coupling between the electron and the dipole field with the LO-phonons of the crystal. Because of the Coulombic nature of the interaction, it shows a 1/k dependence (k is the electron wave vector) and is most important at the energy of the LO-phonon modes [25]. In contrast, the scattering rates for the non-polar collisions with the acoustic phonons (transverse (TA) and longitudinal (LA) acoustic dotted line in fig. 5) and the transverse-optical (TO-)phonons (dashed-dotted line in fig. 5) show

a completely different energy dependence. Non-polar scattering becomes more important as the electron gains energy. The role played by the two distinctly different scattering processes for high field transport can be seen most clearly in figure 6. In this figure, the electron trajectories using classical Monte Carlo simulations are shown. At low fields, "streaming-type" transport is observed where most of the electronic paths are in the direction of the applied field. The energy distribution is stabilized near thermal energies by LO-phonon emission. At fields significantly above the threshold for electron heating, dispersive transport dominates due to the large angle scattering caused by the acoustic phonons. Although the scattering rate for the polar phonon modes is decreasing with increasing electron energy, the distribution is stabilized against velocity runaway at energies of 2-6 eV by the rapid increase in the total path length due to the increasing scattering rate of the non-polar phonon modes. In the following sections, various experimental results which directly confirm this new understanding of electron transport in SiO_2 will be summarized.

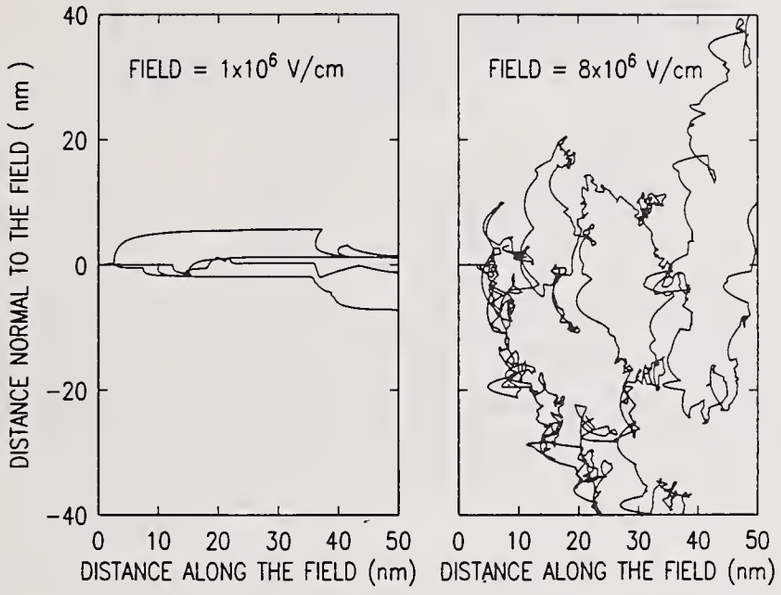

Figure 6. Trajectories of several electrons in SiO_2 in real space at two values of the electric field at room temperature. The low-field (1 MV/cm) trajectories show that transport is dominated by forward polar-scattering with LO-phonons. At high fields (8 MV/cm), the non-polar scattering at large angles with acoustic phonons randomizes the direction of motion and effectively increases the actual total path length of the electron. However, the large energy losses of the hot electrons are still dominated by polar, inelastic scattering with LO-phonons.

4. Experimental determination of energy dependent electron-phonon scattering rates

As outlined in the previous chapter, the prediction of any breakdown model depends crucially on the accurate knowledge of the energy dependent electron-phonon scattering rates for all relevant scattering processes. Over recent years, a technique called Internal Photoemission for Transport Analyses (IPTA) has been developed and applied to various insulators in order to provide exactly this information [11-14,33]. In simple terms, the technique operates as follows. Electrons of a well defined energy E_{kin} are injected via internal photoemission into thin dielectric overlayers on metal substrates. (In practice, a broad energy distribution with a well defined maximum energy will result from this process. But the simplification of monoenergetic injection is irrelevant for the presented discussion.) The metal simply acts as electron source and supports the thin films. The electron kinetic energy, E_{kin}, can be varied via the photon energy used for injection. During transport through the film, the injected hot electrons will be subject to phonon scattering (change direction, gain and lose energy) and eventually a certain fraction is emitted into vacuum. The number of emitted carriers as well as their energy distribution yields significant information on the electron-phonon interaction in the solid [14]. In the experiment, the electron energy distributions of emitted electrons are measured as a function of overlayer thickness and the scattering rates are extracted from the variations of the metal source distribution with thickness. This is done by solving the Boltzmann transport equation for the substrate overlayer geometry with appropriate boundary conditions either analytically [14] or with Monte Carlo techniques [21]. Independent of the details of the problem's solution it turns out that the injected current density, J_0, decreases exponentially with film thickness, d, $J(d,E_{kin}) = J_0 \exp(-d/\lambda^{eff})$. The effective scattering length, λ^{eff} (E_{kin}) depends on both LO-phonon and acoustic

phonon scattering via $1/\lambda^{eff} = 1/\lambda^{LO}(1/\lambda^{LO} + 1/\lambda^{ac})$. Here λ^{LO} and λ^{ac} are the inelastic and elastic scattering lengths at energy E_{kin} due to LO- and acoustic phonon scattering, respectively. These quantities are related to the scattering rates, $1/\tau$, discussed in the previous section via $1/\tau = v/\lambda$, where v is the electron velocity.

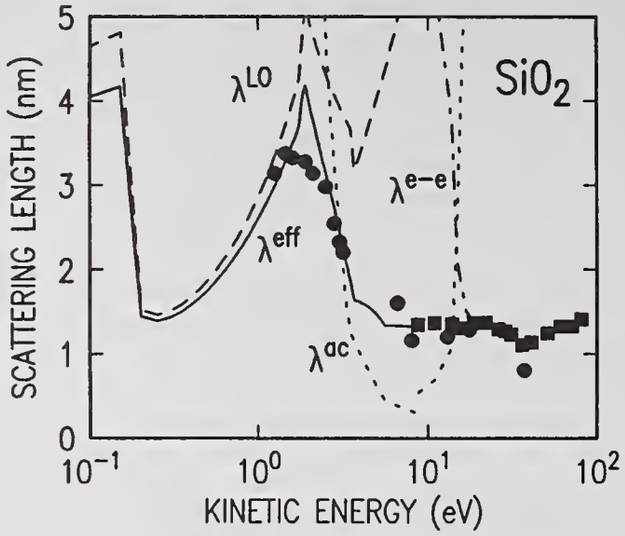

Figure 7. Experimentally determined effective scattering lengths, λ^{eff}, in SiO_2 for various electron kinetic energies [14,32]. The scattering lengths were measured with low energy electron transmission experiments through thin SiO_2 films. The scattering lengths for LO-phonon scattering, λ^{LO}, acoustic phonon scattering , λ^{ac} (and electron-electron scattering, λ^{e-e}) as obtained from electron-phonon interaction theory are shown for comparison. The solid line shows how the various scattering contributions combine to yield the effective scattering length, λ^{eff} , measured in the experiment.

Experimentally determined effective scattering lengths in SiO_2 are shown in figure 7 for electron energies ranging from 0.1eV to 100 eV. As can be seen, the effective scattering lengths show significant variations with energy and reflect the energy dependence of the various scattering processes discussed before. The solid line is calculated from the electron-phonon scattering rates shown in figure 5 using the equations mentioned above. As can be seen, the experiment confirms the calculation in detail. The various curves in figure 7 show how LO-phonon, acoustic phonon and electron-electron scattering contribute to λ^{eff} at various energies. It can be seen that quasi-elastic, large-angle, acoustic phonon scattering controls the transport of electrons in the energy range from 2-13 eV. Only at lower and higher energies do the inelastic processes of LO-phonon emission and impact ionization (and other electronic excitations), respectively, dominate. The observed strong increase of the acoustic scattering length above typically 13 eV energy is still subject to discussion. But it is most probably due to the fact that with increasing electron energy the electron scattering with acoustic phonons becomes more and more forward directed and thus reduces the momentum transfer per collision [23,33]. It can be shown that such a transition from isotropic to forward scattering yields an apparently smaller scattering rate in a transmission experiment [14].

5. Experimental determination of electron energy distributions at high fields

The most powerful techniques used to study carrier heating under the action of an electric field in SiO_2 are electroluminescence, carrier separation and vacuum emission [4-11]. Conceptually, all these experiments are very similar to the one described in the previous section. Electrons are injected (by Fowler-Nordheim tunneling) into thin layers of SiO_2 on one side of a MOS-capacitor structure. Under the action of the applied field these electrons are then transported to the opposite interface where there energy is measured in various ways. Electroluminescence and carrier separation measure only the average energy of the hot electron distribution. In contrast, vacuum emission measures the energy distribution itself. Each technique has its limitations, but their combination yields a quantitatively consistent picture for transport in SiO_2.

The electroluminescence [4,5] technique measures the spectra of light emitted from thin metal gates of MOS capacitor structures. These photons are due to radiating surface-plasmon-modes stimulated in the metal layer by hot electrons impinging on the oxide-metal interface after transport through the SiO_2 film. The information on the average electron energy in the oxide can then be extracted from the photon energies.

Carrier separation [6,7,10] measures the number of electron-hole pairs produced in single-crystal silicon by hot electrons injected after transport through the SiO_2 overlayer. The number of electron-hole pairs can be converted into the average energy of the incoming hot electron energy distribution.

Vacuum emission [6,8,10] directly measures the hot electron distribution ejected into vacuum through the thin metal gate of a MOS capacitor. Various types of standard electron energy analyzers can be used to collect and energy analyze these hot electrons. Average energies can be directly calculated from the measured distributions.

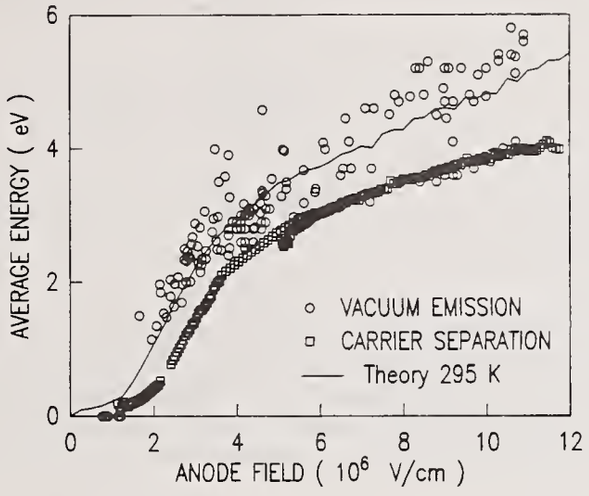

Figure 8. Average electron energy versus anode field from the experimental data (squares: carrier separation, circles: vacuum emission) in comparison with the result of Monte Carlo simulations (solid line). At fields below 1.5 MV/cm, the electron energy distribution can be stabilized close to thermal energies by LO-phonon scattering. Around 2 MV/cm LO-phonon runaway occurs, but the energy distribution gets stabilized against runaway at 2-6 eV by large angle acoustic phonon scattering via Umklapp processes.

In figure 8, average electron energies obtained by the three techniques mentioned above are shown as a function of applied field. The solid line shows the result of a Monte Carlo simulation as described in chapter 3. As can be seen, the Monte Carlo simulation reproduces the result in detail. Below 1 MV/cm the average electron energy is of the order of kT. The energy distribution is efficiently stabilized by LO-phonon emission. At about 1.5 MV/cm the average electron energy rapidly increases to about 2-4 eV. This phenomena known as "LO-phonon runaway" simply expresses the fact, that the electrons gain more energy from the field then they loose to the lattice via LO-phonon excitation. However, the average electron energy gets stabilized around 4 eV and only slightly increases towards higher fields. At all fields measured, the energy of an average electron stays well below the ionization threshold. As previously discussed, this stabilization is due to the rapid increase of the acoustic phonon scattering rate with increasing electron energy.

To conclude, let us present some results, which show that there are still some problems left to solve. Only the laser experiments were performed in bulk samples. All other experiments are done in thin film structures and it is not straight forward to extrapolate results obtained in thin film experiments to breakdown results in the bulk oxide.
This is illustrated in figure 9, where full energy distributions as obtained by the vacuum emission technique are shown for different electric fields and oxide thickness. As can be seen, the energy distributions start to develop a high energy tail both with increasing fields and increasing oxide thickness. Both trends would at least qualitatively be consistent with the ideas of avalanche breakdown. One would indeed expect, that energy distributions as shown in figure 9 lead to significant electron multiplication in a bulk sample. It is to date not entirely clear, whether these tails reflect an intrinsic property of SiO_2. First, the high energy tails cannot be reproduced in classical Monte Carlo simulation [21,22] using scattering rates compatible with the internal photoemission experiments presented above [13]. Second, above 20 eV electron energy, the inelastic mean-free path is less than 10 Å (see fig. 7) and involves energy losses of at least 8 eV per collision. These numbers show that the probability for electrons to have energies of 20 to 40 eV is extremely small. A field of 100 MV/cm (compared to the applied field of 10 MV/cm) would be required to keep an average electron above 20 eV energy. A collision-free flight of 300 Å (compared to a scattering length of 10 Å) would be needed in order to bring an electron out of the predicted Monte Carlo distribution up to 40 eV energy. Thirdly, it is believed that the electrons evolving into vacuum are emitted through small holes (inter-grain boundary cracks, missing grains, etc.) in the top metal contact of the MOS-capacitor. These imperfections in the MOS-structure lead to field distortions and allow some electrons to gain additional energy in vacuum. It can be shown that electrons emitted through the center of a missing grain in the top metal contact (modeled as a circular hole with 500 Å diameter on a 1500 Å thick oxide with an applied field of 10 MV/cm) can pick up an additional energy of typically 20 eV in vacuum. These arguments indicate

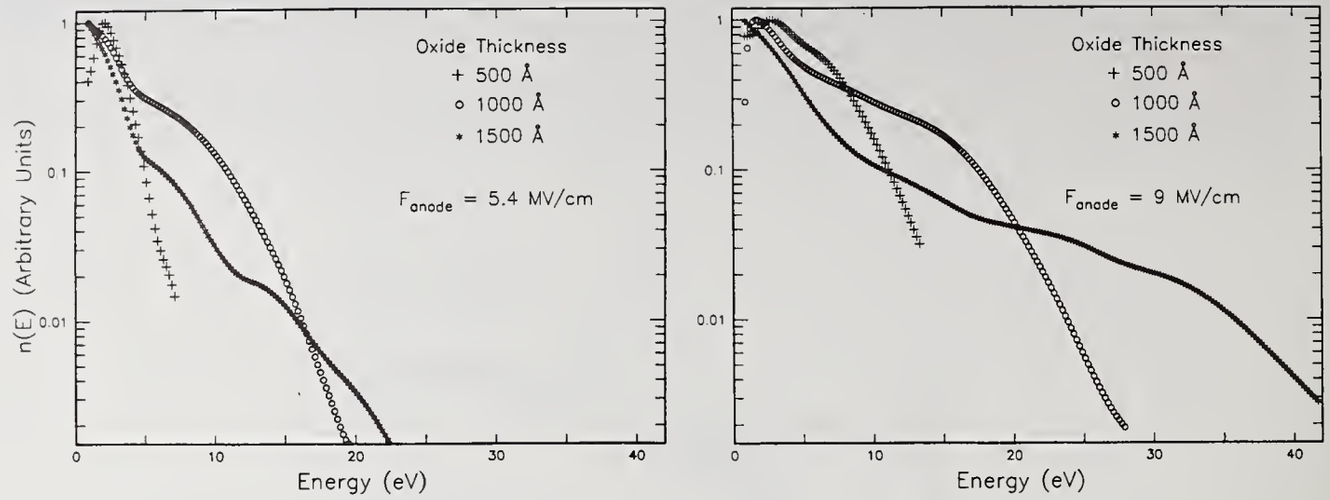

Figure 9. Comparison of electron energy distributions for varying oxide thickness (500-1500 Å) determined using vacuum emission for several electric fields at room temperature. Although the average energies deduced from these distributions are not strongly dependent on oxide thickness, a few "lucky" electrons out in a high energy tail are not stabilized against run-away. It is, at present, not clear whether this tail reflects an intrinsic behavior of SiO_2 or is due to imperfections of the oxide films (channel type defects) or possibly a side effect of the experiment (see text).

that the high energy tail could be an artifact of the vacuum emission technique, but this still must be unequivocally shown experimentally. Although we are cautious in drawing conclusions on the role of electron multiplication for breakdown in bulk samples, the Monte Carlo results would still be valid even for very thick oxides.

6. Conclusions

It was the intention of this paper, to put into a common framework recent experimental and theoretical effort from different fields but all related to the phenomena of dielectric breakdown in wide-band-gap insulators. Most of these efforts were, at least in an early stage, to some extent stimulated by the search for a experimental proof of the avalanche-breakdown model. Ironically, the experiments performed to achieve this goal now rather suggest that the avalanche concept for breakdown might play a more minor roll for solid state breakdown in wide-band-gap insulators than believed by most researchers for decades. In several ionic crystals and in SiO_2, the reviewed novel laser experiments give strong evidence that single pulse induced destructive breakdown at 532 nm wavelength is not initiated by electron multiplication and electron-avalanche formation, but is due to lattice heating by nonlinear photon absorption of free electrons generated by multiphoton absorption. In SiO_2, the presented results lead to a new understanding of hot electron transport. The existing experimental data conclusively eliminate the avalanche breakdown model for an oxide thickness smaller than 500 Å. Classical Monte Carlo simulations using experimentally determined energy dependent scattering rates for the various electron-phonon interactions do not predict any electron multiplication up to fields well above 20 MV/cm even in bulk SiO_2.

In the field of DC breakdown, especially with respect to MOS technologies, this is actually good news, since these new results clearly show that SiO_2 can indeed withstand the gradually increasing field strength inevitably occurring with device miniaturization (if the device fabrication and oxide quality can be improved accordingly). In the field of laser breakdown however, the new results show for the first time that there exists a mechanism inherent to the laser-field-insulator interaction which is different from avalanche breakdown but nevertheless fundamentally limiting the power density an optical dielectric can withstand.

7. References

[1] H. R. Zeller, T. Baumann, E. Cartier, H. Dersch, P. Pfluger, F. Stucki. The physics of breakdown in solid dielectrics. in; Festkörperprobleme (Advances in Solid State Physics), Volume 27, 223-240, P. Grosse (ed.), Vieweg, Braunschweig 1987

[2] P. Solomon, Breakdown in silicon oxide - A review, J.Vac.Sci.Technol. 14, 1122 (1977)

[3] S. C. Jones, P. Braunlich, R. T. Casper, X. A. Shen, P. Kelly, Recent progress on laser-induced modifications and intrinsic bulk damage of wide gap materials, Opt. Eng. 28, 1039 (1989).

[4] T. N. Theis, J. R. Kirtley, D. J. DiMaria, D. W. Dong, Light emission from electron-injector structures, Phys.Rev.Lett. 50, 750-754 (1983)

[5] T. N. Theis, D. J. DiMaria, J. R. Kirtley, D. W. Dong, Strong electric field heating of conduction-band electrons in SiO_2, Phys.Rev.Lett. 52, 1445-1448 (1984)

[6] D. J. DiMaria, M. V. Fischetti, E. Tierney, S. D. Brorson, Direct observation of the threshold for electron heating in silicon dioxide, Phys.Rev.Lett. 56, 1284-1286 (1984)

[7] D. J. DiMaria, T. N. Theis, J. R. Kirtley, F. L. Pesavento, D. W. Dong, S. D. Brorson, Electron heating in silicon dioxide and off-stoichionetric silicon dioxide films, J.Appl.Phys. 57, 1214-1238 (1985)

[8] S. D. Brorson, D. J. DiMaria, M. V. Fischetti, F. L. Pesavento, P. M. Solomon, and D. W. Dong, Direct measurement of the energy distribution of hot electrons in silicon dioxide, J.Appl.Phys. 58, 1302-1313 (1985)

[9] M. V. Fischetti, D. J. DiMaria, L. Dori, J. Batey, E. Tierney, J. Stasiak, Ballistic electron transport in thin silicon dioxide films, Phys.Rev. B 35, 4404-4414 (1987)

[10] D. J. DiMaria, M. V. Fischetti, M Arienzo, E. Tierney, Electron heating studies in silicon dioxide: Low fields and thick films, J.Appl.Phys. 60, 1719-1726 (1986)

[11] P. Pfluger, H. R. Zeller, J. Bernasconi, Hot-electron transport in polymeric dielectrics, Phys.Rev.Lett. 53, 94-97 (1984)

[12] E. Cartier and P. Pfluger, Transport and relaxation of hot conduction electrons in an organic dielectric, Phys.Rev. B34, 8822-8834 (1986)

[13] E. Cartier and P. Pfluger, Experimental determination of energy dependent inelastic and elastic scattering rates of hot electrons in large bandgap insulators, Physica Scripta T23, 235-241 (1988)

[14] J. Bernasconi, E. Cartier, P. Pfluger, Hot-electron transport through thin dielectric films: Boltzmann theory and electron spectroscopy, Phys.Rev. B38, 12567-12581 (1988)

[15] S. C. Jones, A. H. Fischer, P. Braunlich, P. Kelly, Prebreakdown energy absorption from intense laser pulses at 532 nm in NaCl, Phys. Rev. B37, 755-770 (1988).

[16] X. A. Shen, S. C. Jones, P. Braunlich, P. Kelly, Four-photon absorption cross section in potassium bromide at 532 nm, Phys. Rev. B36, 2831-2843 (1987).

[17] X. A. Shen, P. Braunlich, S. C. Jones, P. Kelly, Investigation of intrinsic optical damage in potassium bromide at 532 nm Phys. Rev. B38, 3494-3504 (1988).

[18] L. Simpson, X. A. Shen, S. C. Jones, P. Braunlich, P. Kelly, in Proc. 20th Annual Symposium on Optical Materials for High Power Lasers (Boulder, CO, Oct. 1988) Natl. Inst. Stand. Technol., in press.

[19] X. A. Shen, S. C. Jones, P. Braunlich, Laser heating of free elcctrons in wide-gap optical materials at 1064 nm, Phys. Rev. Lett. 62, 2711 (1989).

[20] M. Sparks, D. J. Mills, R. Warren, T. Holstein, A. A. Maradudin, L. J. Sham, E. Loh, Jr., D. F. King, Theory of electron-avalanche breakdown in solids, Phys.Rev. B24, 3519-3536, (1981)

[21] M. V. Fischetti, Monte Carlo solution to the problem of high-field electron heating in SiO_2, Phys.Rev.Lett. 53, 1755-1758, (1984)

[22] M. V. Fischetti, D. J. DiMaria, S. D. Brorson, T. N. Theis, J. R. Kirtlcy, Thcory of high-ficld transport in silicon dioxide, Phys.Rcv. B 31, 8124-8132 (1985)

[23] M. V. Fischetti and D. J. DiMaria, Quantum Monte Carlo simulation of high-field electron transport: an application to silicon dioxide, Phys.Rev.Lett. 55, 2475-2478 (1985)

[24] A. S. Epifanov, A. A. Manenkov, A. M. Prokhorov, Theory of avalanche ionization induced in transparent dielectrics by an electromagnetic field, Zh. Eksp. Teor. Fiz. 70, 728 (1976) [Sov. Phys. JETP 43, 377-382 (1976)].

[25] H. Fröhlich, On the theory of dielectric breakdown in solids, Proc.R.Soc.London.Ser. A 188, 521-531 (1947)

[26] D. K. Ferry, Electron transport and breakdown in SiO_2, J.Appl.Phys. 50, 1422-1427 (1979)

[27] C. N. Berglund and R. J. Powell, Photoinjection into SiO_2; Electron scattering in the image force potential well, J. Appl.Phys. 42, 573-579 (1971)

[28] R. Poirier and J. Olivier, Appl.Phys.Lett. 21, 334 (1972)

[29] J. Maserjian and N. Zamani, Behavior of Si/SiO_2 interface observed by Fowler-Nordheim tunneling, J.Appl.Phys. 53, 559-567 (1982)

[30] H. H. Fitting and J. U. Friemann, Monte Carlo study of electron mobility in SiO_2, Phys.Status Solidi A 69 349-358 (1982)

[31] W. Porod and D. K. Ferry, Monte Carlo study of high-energy electrons in silicon dioxide, Phys.Rev.Lett. 54, 1189-1191 (1985)

[32] S. I. Zakharov and Yu. D. Fiveisky, The influence of Umklapp processes on the hot carriers' relaxation, Solid State Commun. 66, 1251-1256 (1988)

[33] F. R. McFeely, E. Cartier, J. A. Yarmoff, and S. A. Joyce, Low energy electron escape length in SiO_2, accepted in Phys.Rev. B (1990)

Manuscript received
2-12-90

UV Seeding of IR Laser Induced Damage

N.C.Kerr, S.E.Clark and D.C.Emmony

Department of Physics
Loughborough University of Technology
Loughborough
Leicestershire
U.K.

The values of the laser induced surface damage thresholds for samples of silicon, fused quartz and soda lime glass at both 0.248μm (UV) and 10.6μm (IR) are presented. Experiments are then described where laser damage is induced using crossed UV-IR beams, with varying time delays imposed between the arrivals of the two laser pulses at the sample surface. The results of these crossed beam experiments are then discussed. Order of magnitude reductions in the IR damage thresholds of silicon and glass are observed when the beams are crossed, no such reduction is observed for quartz. Further, only in the case of glass samples is a reduction in the UV damage threshold seen when the beams are crossed. The reduction in IR threshold on silicon has been seen with delays between the laser pulses of up to 100ns. The reduction in IR threshold for glass was seen for delays up to 1.2ms. These results lead to a discussion of the role of so-called seed electrons in the damage process and the mechanisms operative at the different wavelengths.

Key words: excimer laser damage, CC_2 laser damage, crossed laser beams, seeding electrons.

1. Introduction

The laser induced damage of optical components is the basic limiting factor on the output power which a laser can develop. With the continuing need for ever more powerful yet compact lasers it is becoming critically important to find more damage resistant optical materials. As part of the search for such materials it is important to try to understand the mechanisms for laser induced damage.

Absorbing defects and inclusions, scratches and cracks are usually the dominant sources of bulk and surface damage respectively and reduce the threshold intensity at which damage begins. In practically all real situations these defects limit the laser induced damage threshold.

Intrinsic mechanisms set the ultimate optical strength of a material. Research has shown that the most probable mechanism for intrinsic breakdown is a mixture of both avalanche and multiphoton ionization [1]. The lowering of the surface damage threshold caused by such things as scratches and cracks is thought to be due mainly to the enhanced electric fields around such structures [2].

It is generally accepted that seed electrons which are necessary for the development of the electron avalanche due to collisional ionization arise from the photoionization of impurities and defects or the multiphoton ionization of the host atoms in the crystal lattice. The breakdown threshold is determined by the probability of the appearance of a seed electron within the electric field of the incident laser radiation.

The damage threshold due to avalanche ionization should not depend on the initial electron concentration n_o as long as $n_oV>1$, where V is the interaction volume. Under these conditions the artificial injection of excess carriers which can arise from the photoionization in the material caused by, say, auxilary UV irradiation should not effect the breakdown threshold since the probability of there already being a starting electron within the interaction volume is unity. However if $n_oV<1$ UV irradiation of the sample can exert a large influence on the damage threshold if the avalanche process is a dominant damage mechanism since a starting electron is unlikely to be already present within the interaction volume.

So-called crossed beam experiments, as outlined herein, are of interest in determining the role of seeding electrons and in attempting to make clear the nature of the damage mechanism operative at different wavelengths. Such knowledge is of interest since it allows a fuller understanding of the laser induced damage process.

Previous work [3,4] using crossed beam configurations has centered on using very tightly focused beams in an attempt to effectively get between defects and inclusions in the bulk of samples so that intrinsic damage thresholds are being measured and to satisfy the condition $n_oV<1$. In the work reported here results have been obtained using large spot sizes on the surfaces of materials. This is because of the constraints placed upon us by the availability of apparatus and the divergence of the UV laser beam. In a large spot size situation such as this, extrinsic damage mechanisms are likely to be dominant. It is felt that such a situation is however a more realistic example of real laser damage situations. If we consider that for an opaque sample the incident laser radiation penetrates the sample to a certain skin depth then we can still visualize a focal volume at the surface. For small focal volumes the starting electrons must be produced by multiphoton excitation of defect states; whereas, for large focal volumes, such as exist in this work, conduction band electrons initially present can initiate the avalanche process.

2. Experimental arrangement

The experimental arrangement of the apparatus is shown in figure 1. The damage facility at Loughborough [5] is based on a Lambda Physik KrF excimer laser working at 248nm and producing nominal 1J pulses of 30ns duration. Control of the on-target excimer energy is achieved by means of a liquid dye cell attenuator, whilst energy measurement is by use of a Laser Instrumentation calorimeter. To reach the required fluences a quartz lens was used to focus the beam, with spatial beam profiling being performed by means of a computer controlled video framestore system which images the fluorescence produced by absorbing the excimer laser radiation on a suitable glass fluorescer [6]. Using this system it is possible and is standard practice to quote the peak fluence in the excimer beam. The laser spot size at the surface is 1.5mm X 1.0mm.

IR laser pulses were obtained from a Laser Applications TEA CO_2 laser operating at 10.6μm. This gives the usual 100ns pulse followed by the long tail associated with the N_2 in the gas mixture. The nominal total laser pulse energy is 5J. The laser output is focused using a 15cm focal length CaF_2 lens and has a typical spot size on target of 3mm X 3mm. Control of the fluence at the target is obtained by using calibrated attenuating plastic films of varying thicknesses.

Damage detection was performed by use of high resolution Schlieren imaging (i.e. imaging with a suitable stop/filter in the focal plane of the imaging lens) with a CCD video camera linked to a computer controlled video framestore to enable fast and accurate processing of the images. The framestore is an Eltime Image III model linked to a Sperry PC/IT for image processing. Hard copy of video images is obtained from a 3M Dry Silver Copier. The target area is probed using a 10mW cw HeNe laser. The probe intensity was varied using a rotating polaroid filter.

Triggering pulses for the lasers are provided by a Lyons signal generator which has two independent outputs. These can be delayed relative to each other and were tailored to the requirements of the two lasers by a pair of fast transistor switches. The delay between the trigger pulses are set at the signal generator which has a measured jitter of less than 10ns. By modifying the CO_2 laser trigger input circuitry and careful adjustment of the thyratron reservoir voltage the jitter on the CO_2 laser trigger was reduced to less than 10ns. The jitter on the excimer laser trigger was so small as to be unmeasurable using the facilities at our disposal.

The relative time of arrival of each laser pulse at the target was monitored using beamsplitters and fast detectors suited to each wavelength used. For the IR pulses a silicon beamsplitter and integrating pyroelectric detector was used. For the UV a fused silica beamsplitter and fast silicon photodiode was used.

The two beams were arranged so that the smaller UV spot was positioned in the center of the larger IR spot. The imaging optics were arranged so that the IR spot just filled the image field of the Schlieren imaging camera.

3. Experimental technique

Firstly, by irradiating a series of sites on the sample surface with single UV laser pulses alone of increasing fluence the UV damage threshold was measured. The damage threshold for IR laser pulses alone was then measured in a similar manner.

The UV fluence was reduced in measured steps from this damage threshold value and for each fluence the corresponding IR damage threshold was remeasured. This process was performed on each sample with no delay between the end of the UV and the start of the IR laser pulses. The fluences of the two pulses were then fixed at values which were seen to have produced a marked decrease in damage threshold and the delay of the IR pulse was increased until no effect was observed. The alternate case of delaying the UV pulse relative to the IR was then investigated to see if any reduction in damage thresholds could be measured.

Measurements of the magnitude and decay of fluorescence induced in the glass were also made, the fused quartz exhibited no visible fluorescence. The fluorescence was monitored using a Hamamatsu IP28 photomultiplier tube. This covers the spectral range 185-650nm and has a response time of 2.2ns. The fluorescence was monitored through the glass slide. The fluorescence spectrum was measured for the glass sample using a scanning monochromator. The spectrum was constructed by shot to shot excitation of the glass slide. The signal from the photomultiplier was displayed on a fast oscilloscope with the input matched to the cable.

4. Results

Figure 2 shows a typical sequence of Schlieren images obtained on a sample of silicon using crossed UV and IR beams with no delay between the arrival of the pulses at the

sample. Image processing consisted simply of subtraction of an initial image of the surface and an image after the desired number of laser pulses had been incident at the surface. Figure 2a and 2b are processed images showing the effect on the surface of 10 UV and 10 IR pulses respectively. The fluences in each case were set at 75% of the respective wavelength's single shot damage threshold. Although there are low contrast artifacts associated with interlacing of video fields visible in these processed images no detectable damage can be seen. Figure 2c is the processed image obtained when the two beams are crossed. Damage is restricted solely to the region of overlap of the two beams in the center of the frame. Figure 2d is the processed image obtained if the UV fluence is reduced to 50% of the surface UV damage threshold. Clearly the damage is still localised to the region of overlap of the UV beam on the IR beam but the degree and extent of the damage has decreased.

The results for the variation of IR damage threshold with additional UV fluence are presented in figures 3, 4 and 5 for silicon, quartz and glass respectively. No time delay existed between the end of the UV and start of the IR laser pulses. Order of magnitude reductions in damage threshold are evident for the silicon and glass samples. No reduction was observed in the damage threshold for the quartz sample.

Figures 6 and 7 show the time dependencies of these effects as the delay between the end of the UV pulse and the start of the IR pulse is increased. For silicon the influence of the UV pulse persisted for only 100ns at most before it had no effect in reducing the IR damage threshold. In glass the effect persisted for between 500μs and 1ms.

If the IR pulse was incident before the UV pulse no reduction in the UV damage threshold was observed on samples of silicon and quartz. On glass the damage threshold of the sample was reduced with the effect persisting for times between the IR and UV pulse of upto 350ns. Limitations in the trigger electronics meant that this was the largest delay of its type available.

Fluorescence measurements on glass samples irradiated with UV pulses showed that the fluorescence was in the form of a wide band covering the wavelengths 375-570nm. The fluorescence decay time was typically 1.0 to 1.5ms at all wavelengths, see figure 8.

5. Discussion

For silicon, as a consequence of k, the complex part of its refractive index, being non zero the UV radiation is totally absorbed. The bandgap of the sample (1.1eV) is far less than the photon energy of the incident light (5.0eV) and so the dominant damage mechanism would be expected to be electron avalanche in the UV with the initial electrons being produced by photoionization.

At fluences below the UV damage threshold these electrons can only be expected to exist in the silicon for a short time, a value of hundreds of nanoseconds would not be unreasonable for heavily Boron doped samples such as those used [7]. If an IR pulse is incident within this time then these electrons would be expected to seed the IR damage process. Our results would tend to confirm this with the electrons produced by UV irradiation existing for up to 100ns. The UV radiation creates a dense electron plasma at the surface of the silicon. The plasma then absorbs the IR radiation by free carrier absorption. In the absence of the UV the intrinsic absorption is very low, in the presence of the plasma the coupling of the IR radiation to the surface is greatly enhanced. The plasma, heated by the IR cools down and transfers energy to the lattice in the form of phonons. For small delays between the pulses free carrier absorption probably dominates due to the heavy absorption of the UV but as the delay increases the plasma density decreases and the IR coupling decreases. The plasma density is increased for larger temperature rises due to the increasing absorption coefficient with temperature,

and hence for increasing fluences.

For silicon relatively little of the IR radiation is absorbed (imaginary complex refractive index equal to 1.27×10^{-4}) and the photon energy of the IR radiation is only 0.12eV making multiphoton ionization of electrons improbable. The few electrons promoted to the conduction band by either photoionization or thermal heating of impurity levels would not be expected to last very long or to significantly influence the threshold for subsequent UV pulses. These results confirm this since the UV threshold of silicon is not dependent upon auxilary IR irradiation fluences or time delays. The damage mechanism in the IR is probably thermal in origin for silicon in the large spot size condition.

For quartz the results clearly indicate that the damage mechanisms at each wavelength are different. In the IR a thermal mechanism is expected since quartz strongly absorbs IR. At wavelengths around 10.6μm quartz has a resonant absorption region leading to its strong absorption [8]. In the UV an avalanche mechanism must be invoked to explain the damage process. The relatively low absorbtion of UV and the large band gap for quartz, which is greater than 5eV, means that few electrons are expected to be produced by a low fluence UV laser pulse and hence the seeding effect of UV on IR pulses will be minimal. It is possible that the number of electrons produced by low fluence IR irradiation is too low to seed UV damage for fluences up to practically the IR threshold itself.

Glass absorbs both UV and IR radiation. Glass is an extended molecular network without symmetry or periodicity. The region of transmission for all types of glass is bounded at short wavelengths by the fundamental absorption edge and at long wavelengths by IR absorption bands. The UV irradiation obviously promotes a large number of electrons to the conduction band where they can stay for a long time, as indicated by the long fluorescence decay which is produced as they relax. Any seeding effect of the UV for IR pulses would be expected to persist for a time at least as long as the decay time of the fluorescence. This is confirmed experimentally.

Glass is very impure containing many metal impurities. These can be expected to be thermally heated by IR pulses and to excite electrons for quite a long time. For this reason subsequent UV pulses have their damage threshold reduced since their damage mechanism is already seeded by the previous IR pulse.

6. Conclusions

In silicon the damage mechanism for IR wavelengths is almost certainly thermal in origin. IR radiation cannot directly photoionize electrons unless an improbable number of steps are assumed. However the presence of a large number of seed electrons created by UV induced bandgap ionization increases the absorption coefficient for IR radiation and subsequent electron avalanche. The ability to modify the IR damage threshold by prior irradiation with UV up to 100ns before the IR pulse indicates that the seeding process has a lifetime around this value. For UV irradiation the damage mechanism is electron avalanche since direct photoionization of electrons is possible at these wavelengths. When the IR pulse preceeds the UV pulse it has no effect on the UV laser damage threshold in silicon.

In quartz the IR damage mechanism is almost certainly thermal in nature. It also seems that the heating by the IR pulse absorption does not modify the UV damage threshold up to the level where the IR heating itself causes permanent damage. The UV damage threshold is almost certainly determined by electron avalanche after multiphoton ionization.

In glass the IR and UV damage mechanisms are almost certainly thermal and electron avalanche in nature respectively for independent irradiation. As for silicon the large number of electrons excited by a UV pulse significantly modifies the absorption of a subsequent IR laser pulse. Unlike silicon an IR laser pulse can lower the UV damage threshold by reason of its heating effect at the glass surface.

Acknowledgements

NCK would like to acknowledge the financial assistance of BDH Ltd and SERC.

7. References

[1] A. Vaidyanathan, T. W. Walker, A. H. Guenther, The Relative Roles of Avalanche Multiplication and Multiphoton Absorption in Laser Induced Damage of Dielectrics, IEEE Journal of Quantum Electonics, Vol. QE-16, no. 1, 89-93, (1980).

[2] N. Bloembergen, Laser-Induced Electric Breakdown in Solids, IEEE Journal of Quantum Electronics, Vol. QE-10, no. 3, p375-386, (1974).

[3] B. G. Gorshkov, Yu. K. Danilelko, A. S. Epifanov, A. A. Manenkov, A. M. Prokhorov, A. V. Sidorin, Influence of Additional Ultraviolet Illumination on Breakdown of Alkali Halide Crystals by CO_2 Laser Radiation, Sov. J. Quantum Electron, **11**, (1), p85-86, (1981).

[4] B. G. Gorshkov, A. S. Epifanov, A. A. Manenkov, A. A. Panov, Studies of Laser-Produced Damage to Transparent Optical Material in the UV Region and in Crossed UV-IR Beams, NBS Spec. Publ. 688, US Government Printing Offices, Washington DC, p76-86, (1983).

[5] S. S. Wiseall, D. C. Emmony, A Laser Damage Facility in the Ultraviolet, NBS Spec. Publ. 669, US Government Printing Offices, Washington DC, p102, (1984).

[6] B. A. Omar, S. E. Clark, D. C. Emmony, D. B. Hollis, M. J. Shaw, The application of doped glass fluorescers to the recording of pulsed ultra-violet laser beam profiles, Optics and Laser Technology, vol. 20, no 4, p193-198, (1988).

[7] Private communication with Dr R.Howson and Dr D.Sykes, Loughborough University of Technology.

[8] F. Keilmann, Y. H. Bai, Periodic Surface Structures Frozen into CO_2 Laser Melted Quartz, Appl. Phys. A, Vol 29, p9-18, (1982).

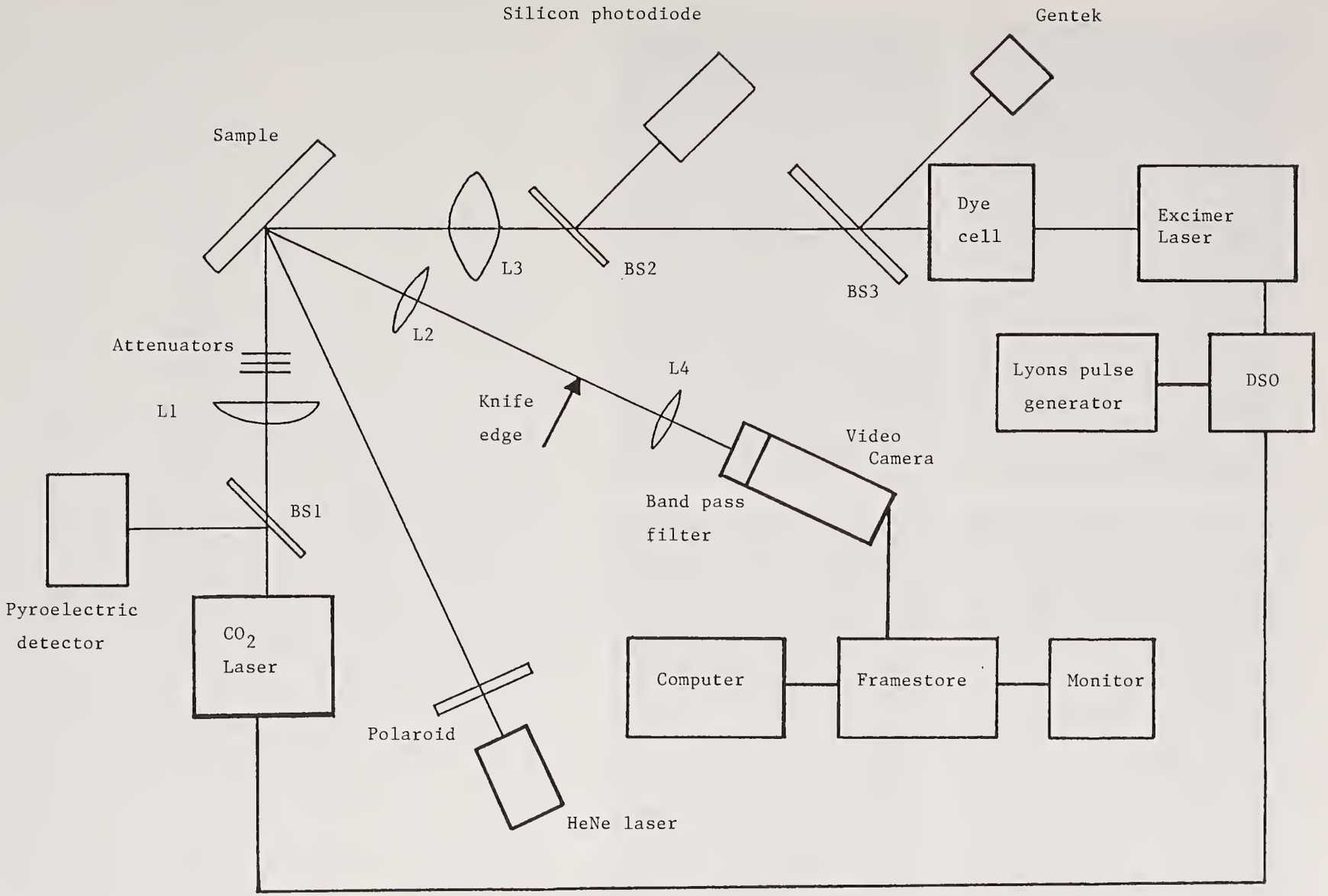

Fig 1 Experimental arrangement of the apparatus

Fig 2 A sequence of schlieren images of a silicon surface

2a (top left) Processed image showing the effect of 10 UV laser pulses with a fluence of 75% the single shot damage threshold

2b (bottom left) Processed image showing the effect of 10 IR laser pulses with a fluence of 75% the single shot damage threshold

2c (top right) Processed image showing the effect of a single pair of crossed UV-IR pulses with fluences as above

2d (bottom right) Processed image showing the effect of a single pair of crossed UV-IR pulses but with the UV fluence reduced to 50% of the single shot damage threshold

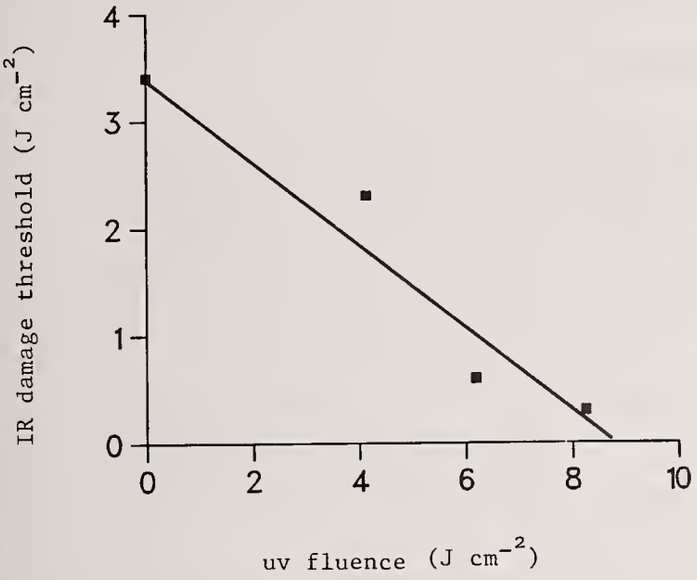

Fig 3 Variation of IR damage threshold for silicon with additional UV irradiation

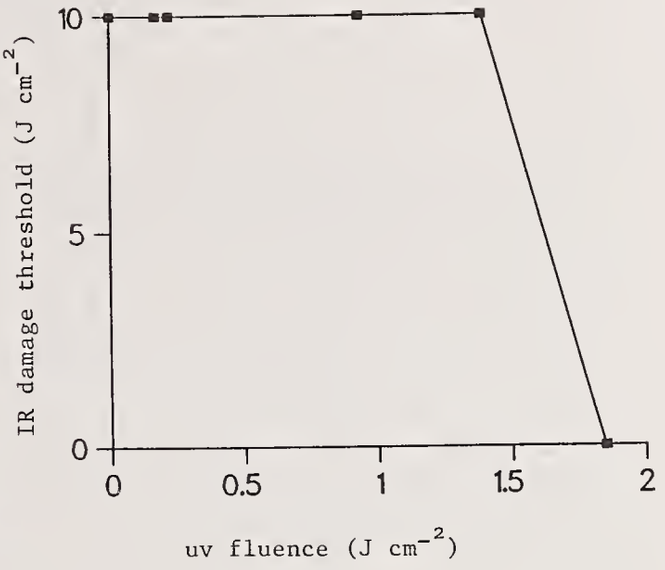

Fig 4 Variation of IR damage threshold for fused quartz with additional UV irradiation

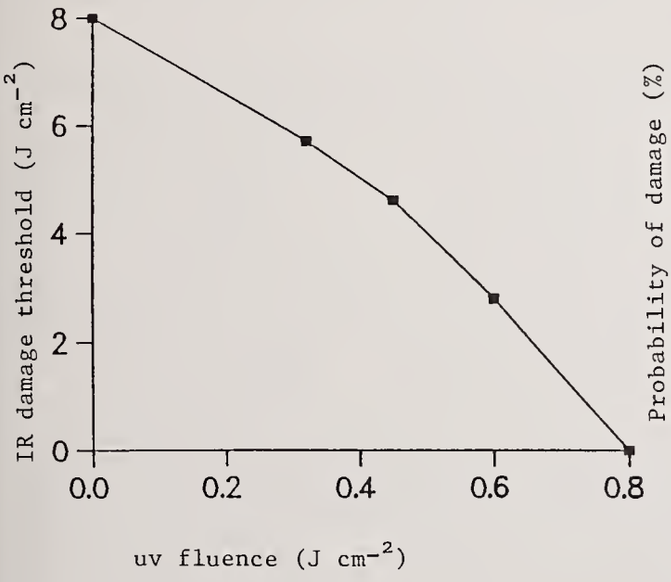

Fig 5 Variation of IR damage threshold for glass with additional UV irradiation

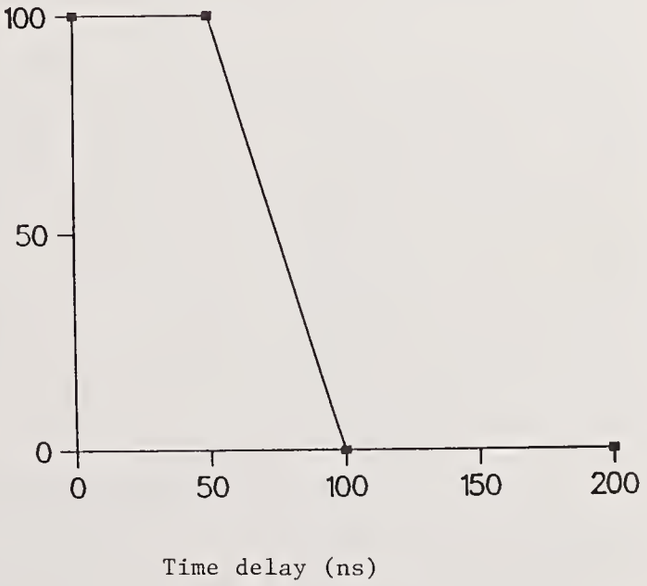

Fig 6 Variation of the probability of damage for differing delays between the UV and IR laser pulses on silicon

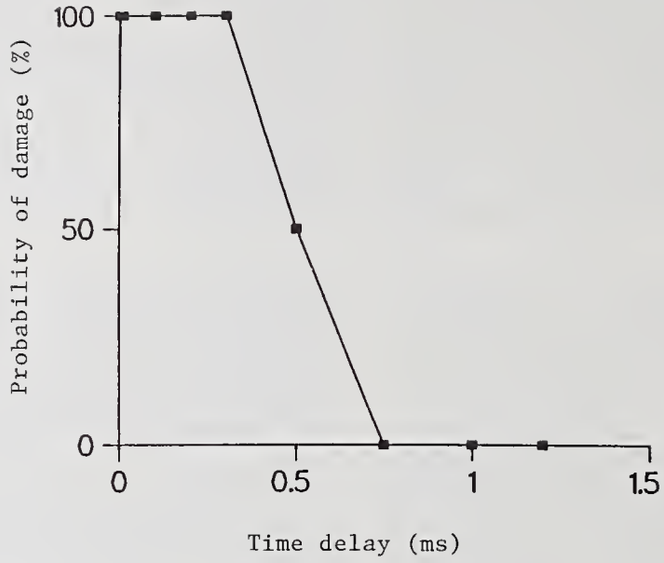

Fig 7 Variation of the probabilty of damage for differing delays between the UV and IR laser pulses on glass

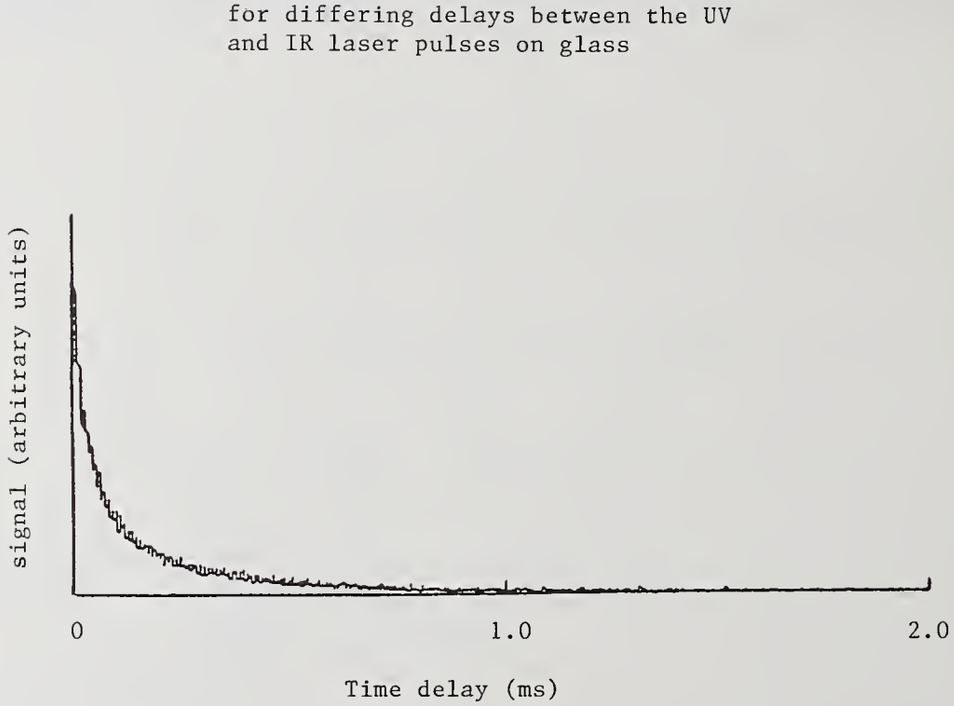

Fig 8 The decay of UV laser induced fluorescence in a glass slide

Manuscript received
12-29-89

Measurements of UV Induced Absorption in Dielectric Coatings

M.H. Bakshi, M. Cecere, D.A.G. Deacon, A.M. Fauchet[a)]

Deacon Research
2440 Embarcadero Way
Palo Alto CA 94304
(415) 493-6100

[a)]NSLS, Brookhaven National Lab, Upton NY 11973

We discuss the first results obtained from a new testing facility for measuring the induced absorption in multilayer dielectric coatings exposed to intense UV radiation. The absorption loss is measured in-situ during exposure, as a function of time for various UV photon energies, intensities, and sample materials. The sample is irradiated by the direct beam from the TOK undulator at NSLS and measured in-vacuo. The undulator is typically run at K = 1 (so that the harmonic emission is low) to simplify the data analysis. The test chamber is separated from the undulator beamline by a differentially pumped line which permits the introduction of carbonaceous gases into the chamber at pressures up to 10^{-5} Torr. By varying the current and energy of the stored electrons, one can adjust the intensity and photon energy of the undulator first harmonic in the range up to 1.2 w/cm^2, and between about 5 eV and 35 eV.

Key words: damage, dielectric coatings, free electron laser, harmonics, lossmeter, multilayer, optics, UV induced absorption

1. Introduction

Both free electron laser optics and space optics must perform well in the presence of intense UV irradiation. Progress in the current state of the art is needed for the applications planned in these fields. In this report, we describe the first results of an experiment designed to supply quantitative information on the rates and the scaling characteristics of these phenomena.

Spaceborne optics, thermal radiators, and detector surfaces are observed to degrade significantly [1] as a result of solar UV exposure. The space optics problem appears to be caused by the appearance of a carbonaceous deposit on the optical surface. Boller et al. [2] measured the thickness of the carbon layer which formed on metallic surfaces exposed to synchrotron radiation, and developed a model for the deposition rate. This model postulates that photo emission of electrons from the surface is primarily responsible for cracking adsorbed carbonaceous molecules which leave behind the observed residue. The model predicts different regions in parameter space in which the scaling of the deposition rate is either linear in intensity, or in the pressure of the carbonaceous precursor, or in the product of the two parameters. However, the rate of the process, and the boundaries between the different regions have not yet been determined. Stewart et al. [3] have verified the UV dependence of the mass deposition in space, and generated a quite similar model describing the transport of the contaminant molecules and the deposition of residue. Although information is available concerning the outgassing rates of many different materials used in spacecraft [4], the rates of UV induced carbonaceous film growth are unknown. As a result, it is not possible to calculate and optimize the lifetime of optical components exposed to significant solar UV. The performance of optical systems for missions such as SOHO, CLUSTER, OSL, UARS, ATLAS, ORFEUS, SUNLAB, and the Space Station depend on a design process which must rely on rules of thumb until the film growth process is understood in more detail.

Free electron laser performance has been severely affected [5-7] in experiments where the average UV flux is large enough to cause absorption changes in the resonator mirrors. Recent experiments [8,9] have demonstrated that the

harmonic generation process in FELs [10] can be described by a conversion efficiency for each harmonic. High average power FELs therefore produce a high average flux of UV radiation which will strike the optics. Table 1 shows values for the conversion efficiency measured and predicted for two types of FEL systems. The experimental results [12] for the odd harmonics are close to the theoretical predictions, and do not change their magnitude much for grossly different wiggler designs, as can be seen from the table. High power FEL

Table 1. FEL Harmonic Power

Harmonic Number	Relative Power Mark III FEL [11] (linear wiggler) Experimental Data [12]	Relative Power 360 periods (tapered wiggler) Theoretical Prediction [13]
1	1	1
2	2×10^{-3}	1×10^{-6}
3	8×10^{-4}	1×10^{-5}
4	7×10^{-5}	1×10^{-8}
5	1×10^{-6}	9×10^{-7}
6	3×10^{-7}	2×10^{-10}
7	3×10^{-8}	5×10^{-8}

optics will be irradiated by intense beams of UV photons. Since the higher power FELs also have a heat dissipation problem in the optics, UV induced absorption is of serious concern.

While carbonaceous films have been observed to form on FEL optics [5,6], additional phenomena are also observed. Fast time-constant, partially reversible loss changes were observed in the virgin mirrors of the Orsay FEL experiment [14]. An additional loss creation mechanism seems to appear when higher energy photons are present. Our experiment was developed to supply some additional information concerning the scaling and the mechanism of the various induced absorption processes. The previous work (which has been continued at Orsay [15]) was handicapped by the inability to measure the optical losses in situ. Typically, optics had to be exposed in the vacuum, and removed for later measurements in the air. This process had two large disadvantages. First, the labor and down time needed for the vacuum breaks exceeded the available resources. Second, the measurements were compromised by the fact that the damaged optics could only be measured after being exposed to the additional dust and hydrocarbons of the atmosphere. Some experiments were possible in-situ [14], but the measurement could only be done in the presence of the damaging UV photons.

In our experiment, loss measurement diagnostics have been incorporated into the vacuum chamber so that the optical absorption is measured independent of the other parameters of the system. Here, we report the results of our initial shakedown run.

2. Experiment

All measurements are done in an ultra-high vacuum system (10^{-10} Torr) to simulate the FEL and the space environments, and provide controlled surface conditions. The samples are exposed to the tunable UV beam produced by the TOK undulator [16] mounted on the UV storage ring at NSLS. The UV photon energy is adjusted between 6 and 35 eV by changing the ring energy. The bandwidth is determined primarily by the emittance of the ring, and varies between about 4% and 8% depending on the parameters of the stored beam. The photon flux of the fundamental depends on the stored current, but at 100 mA, varies from 200 mW/cm^2 to 86, 41, 17, and 5 mW/cm^2 for photon energies of 35 eV, 23, 16, 10, and 6 eV, respectively. The peak power is 75 times higher than the average

powers quoted above. The optical absorption measurements are made using a cavity ringdown approach [17]. A measurement is made of the photon lifetime in a resonator which incorporates the sample as one of the mirrors. This approach provides the desired loss coefficient, and is very sensitive due to the long mean lifetime of the photons captured in the cavity. The experimental system is described in more detail in reference [18].

Our samples in the first run were multilayer high reflectors made of a quarter wave stack of SiO_2 as the low index material and either TiO_2 or ZrO_2 as the high index material. In addition, most samples had a half wave of SiO_2 deposited on top to protect the high index material from direct exposure. The samples were optimized for reflectivity at either 633 nm or 432nm.

The cavity ringdown approach sums up the contributions from all the dissipation channels and determines the total loss. In principle, an observed change in loss could be due to changes in any combination of absorption, scatter, diffraction, and transmission of the sample. However, there is no known mechanism by which either the diffraction or the transmission could be sufficiently modified by the UV to produce the effects we see, and the possibility of a change in the scattering coefficient is very remote. In contrast with the above, there are many known channels for the induction of absorption in the coating material. The UV photons excite electrons into the conduction band, where they are mobile until becoming trapped at a defect, forming an absorption center. At the surface, adsorbed volatiles can be photolyzed into a permanent absorbing carbonaceous film. In addition, hard photons can excite the material in ways which lead to the creation of new defects, and therefore additional absorption. We have had scatter measurements made on samples exposed to UV photons, and on unexposed samples. We find that the loss due to scatter is only a few ppm, and that UV exposure does not change the scatter. The measured loss, and the induced change in it are almost entirely due to absorption in the present experiment.

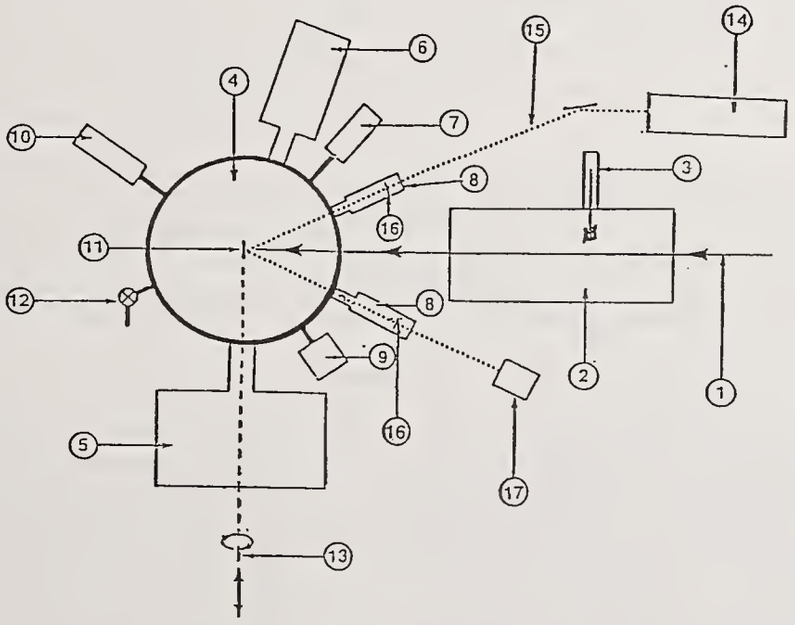

Figure 1. Schematic drawing of the experimental setup. The UV photons from the wiggler (1) pass through the differential isolation line (2) with photon shutter (3) into the spherical exposure chamber (4). The sample transfer chamber (5) allows samples to be exchanged into the measurement point (11) via the linear and rotary manipulator (13). A dye laser (14) is focussed (15) through the resonator mirrors (16) to the detector (17). Selected gasses can be introduced through the controlled leak valve (12). An RGA (10) and an XPS system consisting of X-ray source (7) and electron analyzer (6) can be used to determine the residual atmosphere and the surface constituents. An ion sputter gun (9) and electron flood gun are available for cleaning the sample surfaces.

3. Results

Figure 2 shows the results of a typical UV exposure. This sample mirror was fabricated with a total loss (at 432 nm) of less than 200 ppm per reflection. The UV photon beam was turned on for the first time at about 100 seconds into the scan. A rapid rise in loss is observed, followed by a slower relaxation to an equilibrium level about 500 ppm above the initial loss. The UV was turned off, on, and off again in this example, at about 410, 600, and 900 seconds, respectively. Each time the UV is turned off, the loss falls a small fraction of its initial rise (about 150 ppm in this case), with a similar time constant behavior as for the initial rise. Turning on the UV again boosts the losses back to the level attained earlier. Interestingly, the slow rise time component is not present in the subsequent exposures, although a slow fall time component is present in all the post-exposure relaxations. While the time constants can vary from sample to sample by about 50%, the fast and slow rise times are typically 1 s and 70 s, independent of the photon energy or intensity.

Apparently, the absorption of these samples consists of three parts: the initial loss (which is not pure absorption), a long lived "static" UV induced absorption, and a dynamic UV induced absorption which is present only during exposure. After the UV is turned off the absorption quickly falls back to its "static" level. Due to the lack of sufficient data, many questions remain concerning the dependence of the absorption on the exposure conditions. The next goal of this experiment is to determine the scaling of the static and dynamic components of the loss vs. UV photon energy and intensity, and as a function of the material.

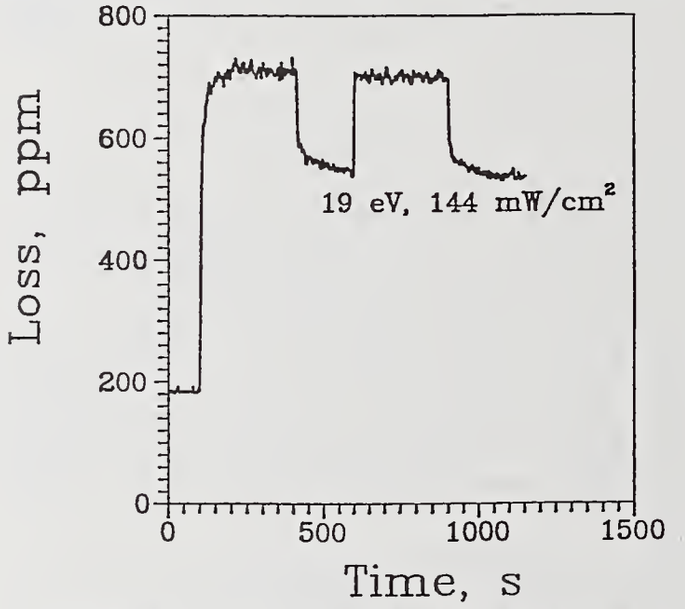

Figure 2. An example of the measured changes in optical absorption as a function of exposure time. The loss of an overcoated SiO_2/ZrO_2 multilayer mirror is measured at 432 nm, the design wavelength of the multilayer stack. A beam of 19 eV photons with an intensity of 140 mW/cm^2 (4.7×10^{16} photons/s-cm^2) is incident on the optic at the measurement point. The UV beam is turned on and off twice as described in the text.

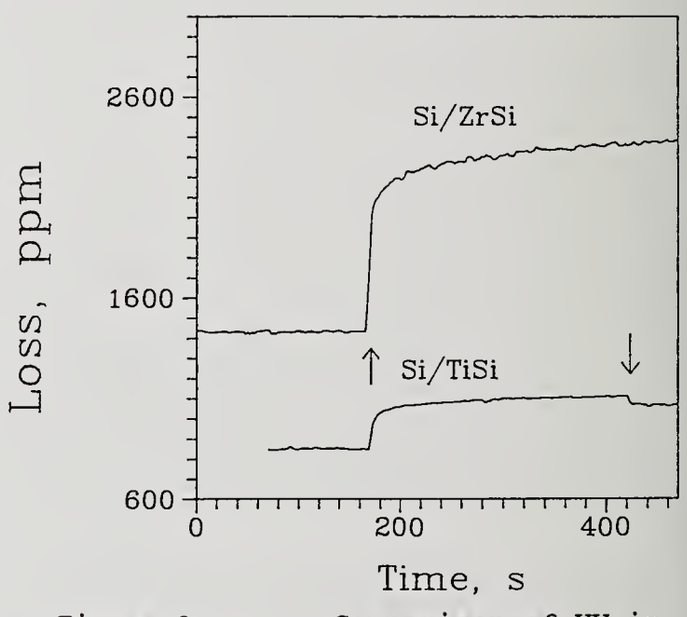

Figure 3. Comparison of UV induced absorption for two multilayer samples fabricated from different high index materials, TiO_2 and ZrO_2, and the same low index material, SiO_2. The UV photon energy is 23 eV and the loss measurement is made at 633 nm. While the initial absorption is of little significance, the magnitude of the UV induced rise for the ZrO_2/SiO_2 sample is seen to be a factor of four larger than the TiO_2/SiO_2 sample. Note that both samples have a half wave SiO_2 overcoat; the difference in induced absorption implies a good mobility for the solid state excitations which mediate the effect.

Figure 3 shows the performance of silica-titania samples along with that of silica-zirconia measured at 633 nm under similar exposure conditions. At this photon energy (23 eV), the initial rise of the loss is 240 ppm for the titania and 800 for the zirconia. This relative performance persists at lower UV photon energies. We plan to extend our measurements to additional materials so that we can build up a database of the static and dynamic losses. It would also be desirable to obtain this information as a function of the probe wavelength.

Several curves of loss vs. time taken at different photon energies are superposed for comparison in figure 4. This data was taken on SiO_2/TiO_2 mirrors with an SiO_2 overcoat. The form of the three curves is the same, but the amplitude of the initial rise grows rapidly with increasing photon energy. An independent measurement has shown that for our parameters, the magnitude of the initial rise is almost independent of flux: the initial rise at 16 eV barely doubled when the photon flux was increased by a factor of 20. Since the photon fluxes in these curves differed roughly by factors of two, (5.6, 3.6, and 1.4 x 10^{16} cm^{-2}, from top to bottom) we therefore ascribe the trend in the initial rise primarily to the energy change.

At least at the lower photon energies, as shown in figures 2 and 4, it would appear that the curve saturates: longer exposure times result in no additional absorption. This data leaves open the question of how long the absorption will remain flat, particularly if the photon flux were to be substantially higher than used here. Indeed, as the photon energy is increased as shown in figure 5, we discover a different absorption growth characteristic which must be due to a new mechanism.

Figure 5 shows absorption vs. time curves for three higher photon energies. As in figure 2, the 25 eV curve is interrupted twice by turning off the UV beam at 730 and 2150 seconds. The 29 eV curve is interrupted once at 1900 seconds, and the 35 eV beam once at 3200 seconds. Initially, these curves have the same form as the curves of figures 2 and 4: the loss jumps up sharply and flattens out. From there, the additional loss grows at an accelerating rate and ultimately reaches high levels. The 35 eV curve is shown to reach 1.6% absorption during its 50 min exposure. The initial absorption jump is dwarfed by the strong new loss creation mechanism. This latter sample was exposed to an intensity which dropped slowly from 1 W/cm^2 down to 800 mW/cm^2 due to the 4 hour lifetime of the beam during the experiment.

The key question remaining to be answered is the scaling of the new mechanism. It is clear that the growth rate drops rapidly with energy. But is there a threshold? If the mechanism is active at all energies, the question becomes: how many photons of a given energy does it take to produce, say, a 1% loss change? This is a serious issue for applications such as the free electron laser which produce a high intensity of UV radiation.

Figure 6 shows an entirely unexpected phenomenon which occurs in SiO_2/TiO_2 mirrors when exposed to high K undulator radiation. When the magnetic field is increased from K=1 to its maximum at K=5.6, the on axis intensity grows (approximately) linearly in K, and the spectrum changes drastically. The spectrum evolves from essentially a single peak at the undulator fundamental [19], to a series of overlapping peaks at all of the harmonics which approaches the spectrum of a bending magnet. The high K undulator therefore produces intense broadband radiation between about 3 eV and about 220 eV.

As can be clearly seen from the solid curve (taken at 600 ma beam current), the absorption loss is initially driven to higher levels, and then bleached or annealed away almost entirely. In the 600 ma case, the residual absorption is only 280 ppm (static losses, plus 300 ppm dynamic) above the unexposed value. If the exposure is stopped anywhere in the middle of the curve, the loss stabilizes near the current value. The initial exposures drive the losses up to more than 2% absorption. This gross absorption rise appears to be independent of the intensity, although its rate of rise has some intensity dependence. The loss reduction takes over from the induced losses fairly quickly, but the rate of improvement at 290 ma is much lower than that of the 600 ma data. Some of the bleaching effect may be permanent: in a reexposure 34 hours

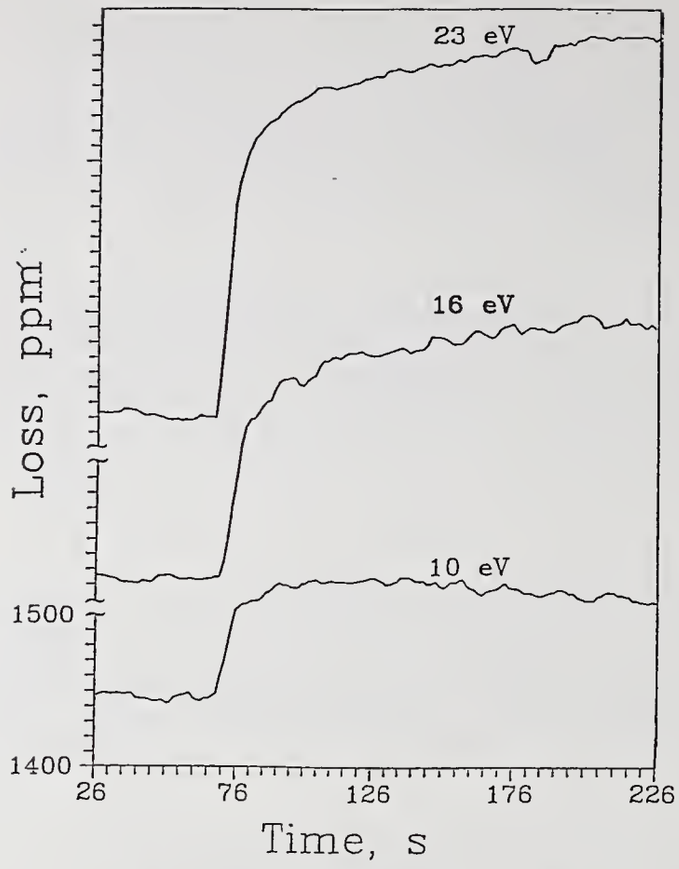

Figure 4. Initial exposure data is shown for overcoated SiO_2/TiO_2 mirrors exposed to three different photon energies and measured at 633 nm. As described in the text, the induced loss in this region is almost insensitive to the intensity, but shows an increase with photon energy.

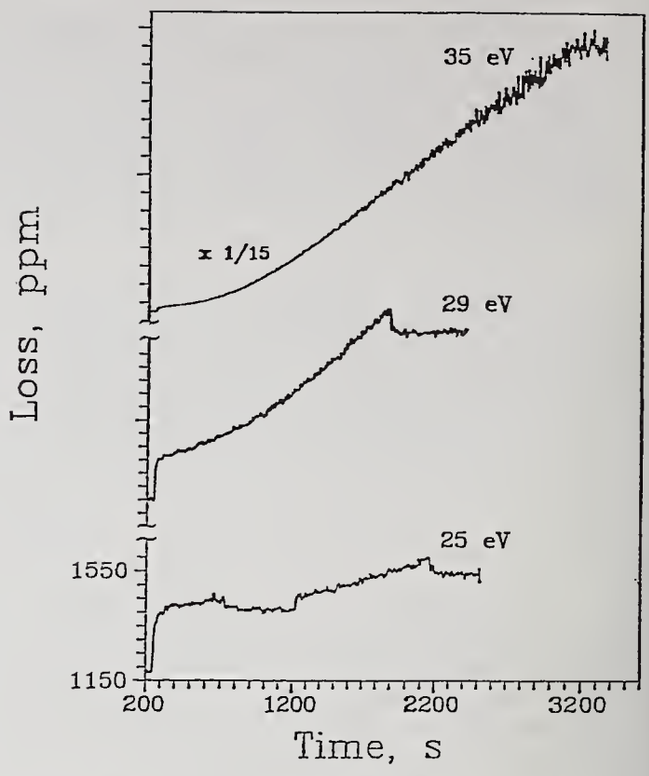

Figure 5. Exposure data is shown for higher photon energies where a new loss mechanism appears. The induced absorption varies in a nonlinear way with the fluence and can reach extremely high levels. The intensities were, from bottom to top, 300, 276, and 1000 mW/cm^2 respectively.

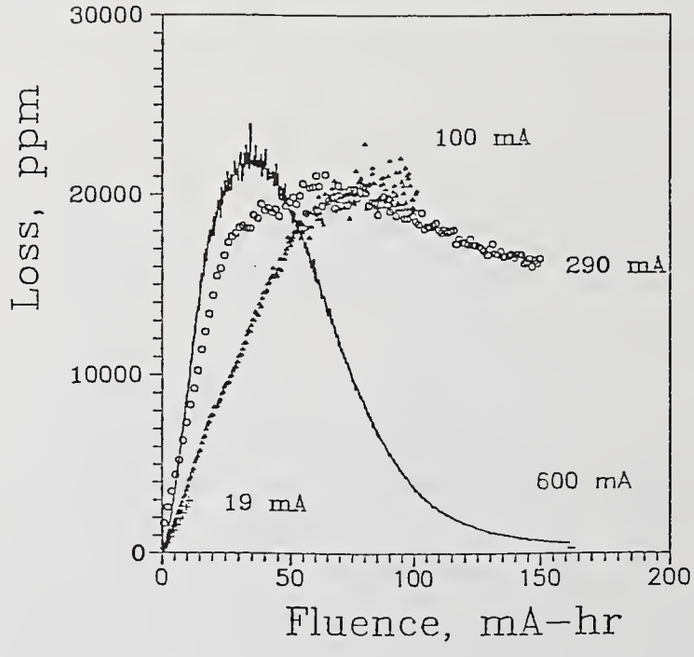

Figure 6. The solid curve shows UV induced absorption in overcoated TiO_2/SiO_2 followed by a UV induced reduction in the absorption measured at 632 nm. Four data sets taken under similar conditions are superimposed.

later, the maximum loss attained was only 25% of the initial maximum, and the time required for bleaching was only 10% of the initial time.

This effect is apparently due to a direct photon mediated bleaching process [21], but it is difficult to explain the intensity dependence, i.e. the fact that curves measured at different intensities do not show the same loss at the same fluence. We believe it is unlikely that the drop in the losses is due to thermal annealing, although the lower temperature rise produced by the lower intensity beams is consistent with the smaller effect on the loss. A rough calculation of the sample temperature indicates that the losses begin to drop before the surface temperature reaches about 150 ^{o}C in the initial exposures. In subsequent exposures, the estimated temperature at the time the losses begin to drop is much lower. At present we do not have the equipment to measure the sample temperatures during exposure.

4. Discussion

The reflected optical wave forms a standing wave in the multilayer stack [22]. The amplitude decays with depth so that appreciable field is present in only the first 5 or 6 layers. When illuminating the mirror at its design wavelength, the standing wave forms nodes at the surface, and at every low-to-high index interface within the stack. An antinode is formed in the middle of the surface layer, and at every high-to-low index interface. The UV photons, however, are absorbed exponentially at different rates depending on the layer material and the photon energy. The excitations created by the UV photons may also be mobile. The net absorption seen is related to the overlap of the local UV induced absorption coefficient and the local standing wave intensity.

The absorption coefficients for fused silica and crystalline TiO_2 (rutile) are known [23]. However, the properties of the ion sputtered amorphous films which make up our samples are somewhat different, since they are porous, may have a different stoichiometry, and contain a much higher concentration of dangling bonds and other defects than the solid material. The absorption of the higher energy photons should be similar to the bulk material, but the band edge will be broadened and shifted to lower energy.

At 35 eV, the absorption coefficient in fused silica is 0.11, which implies a 1/e penetration depth of 500 Angstroms. Since the SiO_2 surface layer thickness is 2170 (1470) Angstroms for the 633 (432) nm sample mirrors, only a few percent of the flux penetrates the surface layer into the next layer, which is the high index material TiO_2 or ZrO_2. (Note that the physical thickness of the layers is larger than quoted because of voids created during the coating process. Since the optical thickness is accurately 1/2 wave, the effective thickness quoted above is also accurate.) As the UV photon energy is reduced, the 1/e penetration depth drops rapidly to 480, 360, 195, 172, and 168 Angstroms at 35, 29, 23, 16, and 10.4 eV, respectively. Below 10.4 eV, the absorption of bulk fused silica drops rapidly, becoming essentially transparent under 6 eV. Thus, over the entire range of UV photon energies of interest here the silica layer is absorbing. The fraction of UV flux which penetrates the top SiO_2 layer is larger at higher UV photon energy and shorter probe wavelength. The TiO_2 layer underneath is highly absorbing [23] down to at least 3.7 eV. Essentially all of the photons which pass through the SiO_2 coating are absorbed in the TiO_2 layer. We do not have absorption data for ZrO_2, but we expect its behavior is comparable to the TiO_2.

In the 6 eV to 25 eV range, the majority of the incident photons are absorbed in the SiO_2 top layer. The small fraction of the photon flux which penetrates the SiO_2 layer follows a strong scaling behavior (from 10^{-6} to 10^{-2}, depending on the parameters) which is not at all followed by the induced absorption. Since the loss creation mechanism is not completely saturated, we conclude that the relevant excitations must be produced in the top layer. The absorption event promotes an electron to the conduction band, where it can find and get trapped at a localized state such as a dangling orbital near a vacancy. Such a center in turn absorbs over a range of wavelengths through low-lying excitations.

One of the questions our work raises is: what is the mobility of the UV induced excitations? Our results (Fig. 3) show that the size of the induced absorption depends strongly on the second layer material. The excitation centers are created in the top layer, but the sample response seems to depend on the nature of the buried layer. There are two factors which could lead to such a behavior: impurities and excitation mobility. We had our samples analyzed by charge-neutralized SIMS (Secondary Ion Mass Spectroscopy). Silica typically contains Na and K as impurities, which were found in the ppm range for all the samples tested [24]. There was also Ti present in silica layer at about the 1% level for the SiO_2/TiO_2 sample, and about the same amount of Zr for the SiO_2/ZrO_2 sample. (The intermixing resulted from spurious sputtering of adjacent anodes in the sample deposition chamber.) It is possible that the differences observed in Fig. 3 are due to the different oscillator strength for electrons trapped at the two different types of defects.

The other interesting possibility is that the excitations created by the UV photons in the top layer migrate to the lower layer where they form absorption centers. In this scenario, the characteristics of the absorption center depend on the lower layer material; the excitation is only required to transport energy to the center. It may be that the initial absorption rise is mediated by excitations generated in SiO_2 but which can propagate thousands of Angstroms to activate remote absorption centers.

At and above 25 eV, the growing penetration of higher energy photons into the high index layer may be partially responsible for the appearance of the new absorption mechanism, but it is not likely. The difference in penetration between the 25 and the 29 eV cases is a factor of 20, which is much larger than the times-three change in the induced absorption (after 25 min). Over the same 25 minute period, the change in penetration between the 29 and the 35 eV cases (a factor of 5) is smaller than the change in induced absorption (a factor of ten). It would appear that a threshold is being crossed which suddenly turns on the new mechanism visible in Figure 5.

When the UV induced excitation becomes trapped, the energy released depends on the UV photon energy. The excess energy can trigger a number of additional processes. One of the processes which comes in to play at higher photon energies is stimulated desorption [25]. For example, the threshold for O^+ desorption from silica lies between 18 and 31 eV depending on the number of O atoms bonded to Si in the sample [26]. Desorption contributes to defects by disrupting the local (ideally, tetrahedral) ordering. More sites become available than previously to trap an electron excited by UV photon absorption. These provide new absorption channels contributing to increased absorption. In view of the energy at which this new mechanism turns on, we conjecture that photo desorption of oxygen may be responsible.

We wish to thank Olive Lee and Larry MacNeil for their experimental and technical help during several of the night runs required to perform these experiments, and the NSLS staff for their efforts to help us interface the experiment with the beamline. This work was supported in part by the SDIO and managed by the ONR and the Los Alamos National Laboratory under contracts N00014-87-C-0154, 9-X28-1472G-6, and 9-LSH-1765G-1, and in part through the UV ring operating funds provided by the DOE through contract DE-AC02-76CH00016.

5. References

[1] D.F. Hall, T.B. Stewart, and R.R. Hayes, "Photo-enhanced Spacecraft Contamination Enhancement", ESA SP 232, 39 (1985).

[2] K. Boller, R.P. Haelbich, H. Hogrefe, W. Jark, C. Kunz, "Investigation of carbon contamination of mirror surfaces exposed to synchrotron radiation", Nucl. Instr. & Meth., 208 273-279 (1983).

[3] T. B. Stewart, G. S. Arnold, D. F. Hall, and H. D. Marten, "Absolute Rates of Vacuum-Ultraviolet Photochemical Deposition of Organic Films", J. Phys. Chem. 93, 2393 (1989).

[4] B. Campbell, NASA Ref. Pub. 1124, NASA Goddard Space Flight Center, Greenbelt MD 20771.

[5] M. Ambrosio, G.C. Barbarino, M. Castellano, N. Cavallo, F. Cevenini, M.R. 5Masullo, P. Patteri, "Dielectric mirrors damage due to the radiation of a high K undulator", Nucl. Instr. & Meth A250 289-292 (1986).

[6] M. Billardon, P. Elleaume, J.M. Ortega, C. Bazin, M. Bergher, M. Velghe, D.A.G. Deacon, Y. Petroff, "Free electron laser experiment at Orsay: a review", IEEE J. Quant. Elect. QE-21) 805-823 (1985).

[7] G.A. Kornyukhin, G.N. Kulipanov, V.N. Litvinenko, N.A. Mesentsev, A.N. Skrinsky, N.A. Vinokurov, P.D. Voblyi, "Status of the INP Optical Klystron", Nucl. Instr. & Meth. A237 281-288 (1985).

[8] D.J. Bamford, D.A.G. Deacon, "Measurement of the coherent harmonic emission from a FEL", Phys. Rev. Lett 62 1106-1109 (1989).

[9] B.A. Newnam, R.W. Warren, D.W. Feldman, W.E. Stein, "Harmonic generation-strength and mode shape", to be published in the Proceedings of the 11th International Conference on FELs, Naples FL, August 1989.

[10] A. Gover, A. Friedman, A. Luccio, Nucl. Instr. & Meth. A259 163-176 (1987).

[11] S. Benson, D.A.G. Deacon, J.N. Eckstein, J.M.J. Madey, K. Robinson, T.I. Smith, and R. Taber, J. Phys. (Paris), Colloq. 44, C1-353 (1983).

[12] D.J. Bamford and D.A.G. Deacon, "Measurement of the Harmonics Emitted in the MARK III Free Electron Laser", to be published in Nucl. Instr. & Meth. (1989); in Proceeding of Tenth International Free Electron Laser Conference, Jerusalem, Israel, August, 1988.

[13] M.J. Schmitt, C.J. Elliott, and B.E. Newnam, "Harmonic Power Implications on Free Electron Laser Mirror Design", Nucl. Instr. & Meth. A272, 586(1988).

[14] P. Elleaume, M. Velghe, M. Billardon, J.M. Ortega, "Diagnostic techniques and VUV induced degradation of the mirrors used in the Orsay storage ring FEL", Nucl. Instr. & Meth., A237 263-267 (1985).

[15] M.F. Velghe, M.E. Couprie, M. Billardon, "Specific optical properties of multilayer mirrors for FEL experiments", to be published in the Proceedings of the 11th International Conference on FELs, Naples FL, August 1989.

[16] A.M. Fauchet, G. Vignola, J.N. Galayda, C. Pellegrini, B.M. Kincaid, R.R. Freeman, F. De Martini, to be published in the proceedings of the 10th International FEL Conference, Jerusalem (1988).

[17] A. O'Keefe, D.A.G. Deacon, "Cavity ring-down optical spectrometer for absorption measurements using pulsed laser sources", Rev. Sci. Instr. 59 2544-2551 (1988).

[18] M.H. Bakshi, M.A. Cecere, and D.A.G. Deacon, "UV Photon Induced Absorption in Multilayer Dielectric Mirrors", submitted for publication in Nucl. Instr. & Meth. (1990); in the proceedings of the 11th International FEL Conference, Naples, FL, August 28-September 1, 1989.

[19] W.B. Colson, "The nonlinear wave equation for higher harmonics in FELs", IEEE Journ. Quant. Elect., QE-17 1417-1427 (1981).

[20] see for example, E. Ritter, "Dielectric Film Materials for Optical Absorptions", Phys. of Thin Films, 8, 1 (1975); P.W. Levy in Radiation Effects in Optical Materials, SPIE 541, 1 (1985).

[21] M. Born, E. Wolf, Principles of Optics, Pergamon Press, Oxford, (1975).

[22] E.D. Palik (ed.), Handbook of optical constants of solids, Academic Press, Orlando (1985).

[23] Evans East, Inc., Plainsboro, NJ, private communication; Deacon Research, unpublished results.

[24] M.L. Knotek, in Semiconductors and Insulators: Recombination Induced Defect Formation in Crystals, Gordon & Breach, ed. by F.C. Brown and N. Itoh, 5, 361 (1983).

[25] M.L. Knotek and J.E. Houston, J. Vac. Sci. Technol. B 1, 899 (1983).

Manuscript received
2-16-90

The Response of Multilayer Dielectric Coatings to Low Fluence Ultraviolet Light Exposure

V. E. Sanders, J. W. Early, and W. Leamon

Chemical and Laser Sciences Division
Los Alamos National Laboratory
Los Alamos, New Mexico 87545

Multilayer dielectric high-reflectance coatings were investigated for potential application in a high-average-power, 1-μm wavelength, free-electron laser oscillator. Of concern are the ultraviolet harmonics of the primary wavelength generated within the oscillator that tend to degrade the dielectric coatings. These coatings are required to be high reflecting and low absorbing with respect to the 1-μm wavelength and resist degradation/damage from the ultraviolet harmonics.

A KrF excimer laser was used to generate the low fluence ultraviolet light at 248-nm wavelength, a wavelength that simulates the fourth harmonic of the 1-μm free-electron laser. A variety of candidate dielectric oxide thin film materials are compared in this report. In each multilayer dielectric high reflector measured, a candidate high-index dielectric material is used in combination with SiO_2 as the low-index material. Damage test measurements are reported for the 248-nm wavelength with HfO_2 being the high-index material with significantly the best results.

Key words: excimer laser damage; free-electron laser optics; laser damage; multilayer dielectric coating; ultraviolet damage.

1. Introduction

Both metal and dielectric coatings are being developed for high-reflectance mirrors to be used in a 1-μm wavelength, high-average-power, free-electron laser. Silver metal coatings have been demonstrated [1] as meeting the requirements for these mirrors when applied to advanced designs for large cooled mirror substrates. Multilayer dielectric coatings have the potential for significant improvement over metal coatings owing to a demonstrated [2] significantly improved reflectance factor at the 1-μm primary wavelength. In both cases, metal and dielectric, the major portion of the 1-μm primary wavelength that is not reflected is absorbed in the coating and is transformed into heat. The heat may distort or destroy the mirror surface if not dissipated and carried away. Therefore, the potential improvement offered by dielectric coatings translates into improved laser beam quality, smaller/higher quality substrates, and significantly reduced cooling requirements.

Each of the dielectric thin film materials considered in this study is to some extent vulnerable to ultraviolet light. Therefore, the ultraviolet harmonics generated along with the 1-μm primary wavelength within the free-electron laser oscillator are a potential threat to a dielectric coating. The ultra-violet harmonic fluences relative to the primary wavelength are described/calculated in the free-electron laser literature [3]. The threat/damage of concern is from generation of color-centers [4] in the dielectric coating. This causes the absorption at 1-μm wavelength to increase, thereby negating the potential advantage over a metal coating that is not degraded by the ultraviolet light. This ultraviolet-induced degradation of dielectric mirrors in a free-electron laser has been observed in low-gain, low-power devices [5] and is therefore of much concern in proposed high-average-power free-electron lasers.

2. Experiment

A schematic diagram of the testing apparatus is shown in figure 1. The device is based on a high-precision reflectivity measurement technique for low-loss laser mirrors [6]. The operation and calibration of this device are described in the report [7] on the initial phase of this coating development study reported at the previous symposium on optical materials for high-power lasers. The candidate test mirror/coating is part of a continuous-wave helium-neon laser, lasing at 1.1 μm. This wavelength is near the nominal 1-μm primary wavelength of interest to the proposed high-average-power free-electron laser. The 1.1-μm high-reflectance test mirror is simultaneously and coincidentally exposed to ultraviolet laser radiation from an excimer laser. KrF lasing at 248 nm was used to simulate the fourth harmonic. As color-centers are generated in the dielectric coating from the ultraviolet exposure, the reflectivity at 1.1 μm decreases, causing the intracavity lasing power in the helium-neon laser to decrease.

The changing intracavity power is monitored by detecting a partial reflection from an internal window shown in figure 1. Not shown in the figure is a means of monitoring the transmittance of the test mirror via a similar photodiode and recorder as used with the indicated window. In addition, scatter is observed with a visible HeNe laser. In each measurement reported, neither transmittance nor scatter were observed to change significantly. Therefore, the measured change in reflectivity in each case is a result of changing absorption as expected from the creation of color-centers. As a result, the changing reflectivity (ΔR), i.e., changing absorption of the coating, is measured in real time. As demonstrated in reference 7, ΔR is measured to an accuracy near 0.01%.

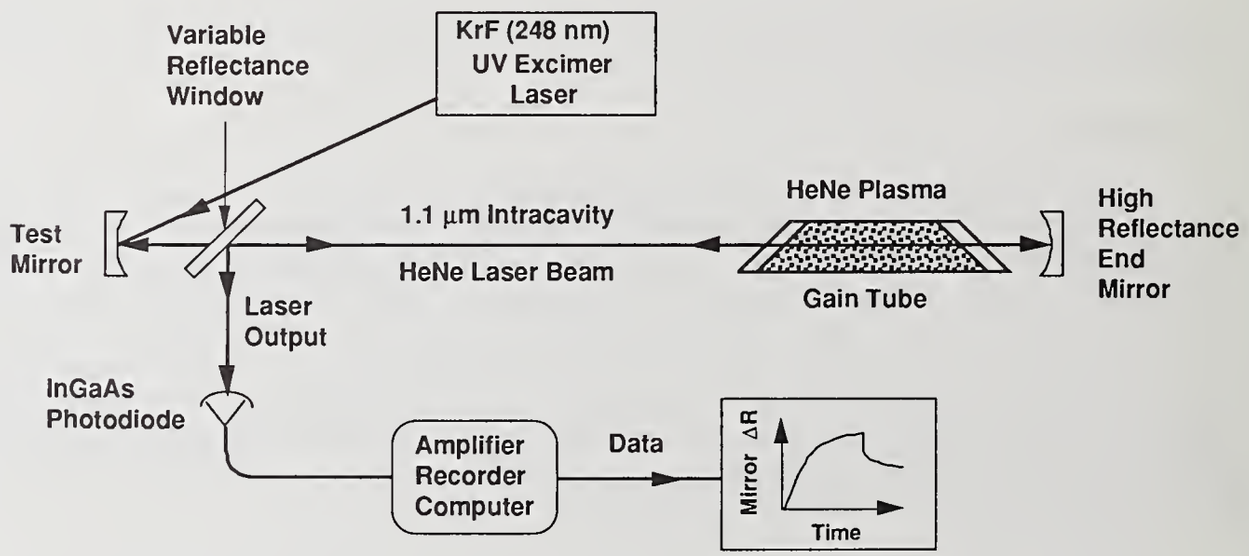

Figure 1. uv-damage testing apparatus

Figure 2 is a generic example of data from this apparatus. As the ultraviolet exposure of the test coating is initiated, a corresponding change in reflectivity is measured. When the ultraviolet laser is turned off, it is noted in time and again results in a corresponding change in reflectivity.

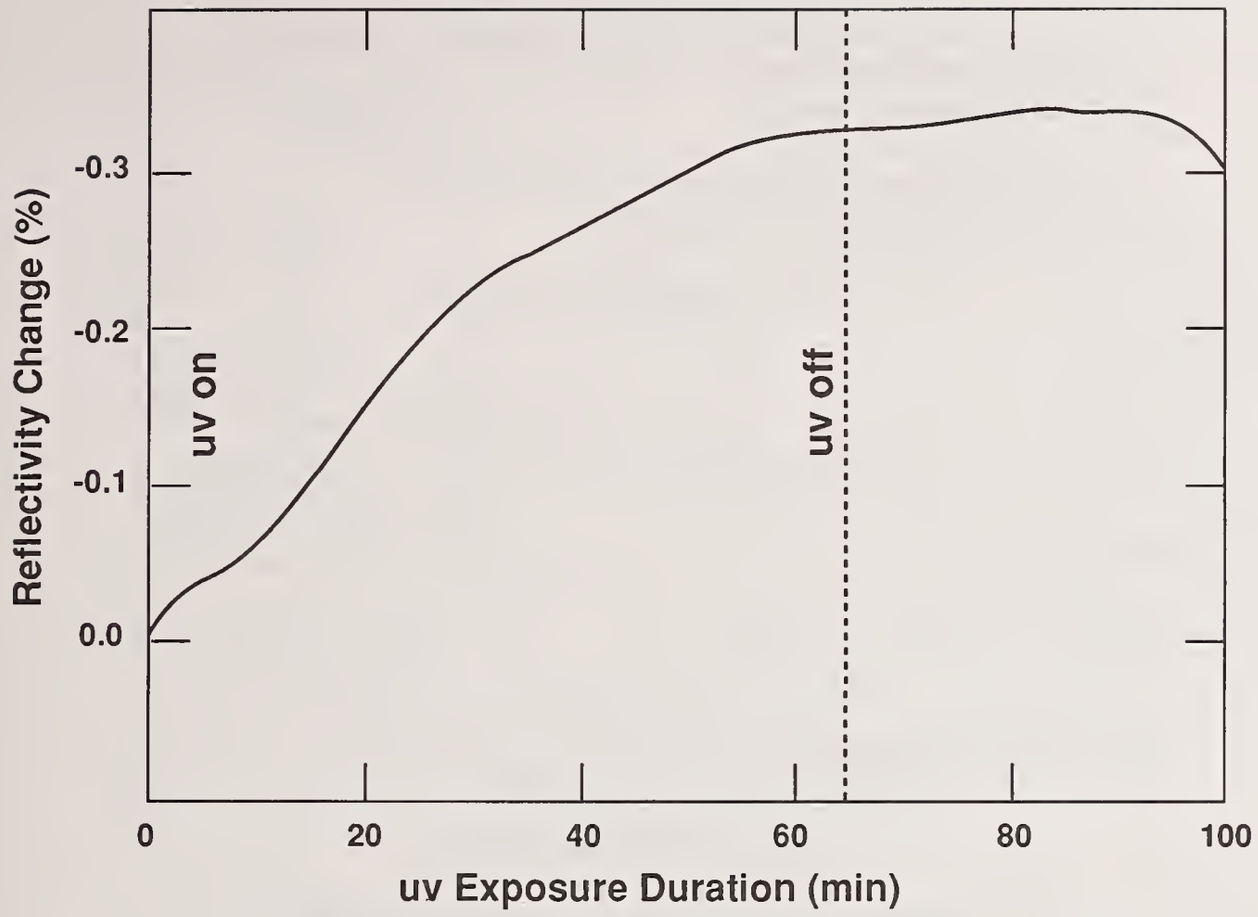

Figure 2. Generic data from testing apparatus

3. Results

The traditional lowest absorption, high-index dielectric thin film material for 1-μm wavelength coatings, TiO_2, does not fair well in this test or in the free-electron laser [5]. The specific task of this study has been to survey the alternate high-index coating materials that might make acceptable high-reflectance, low-absorbing coatings near 1-μm wavelength.

In each case tested the material is fabricated into a multilayer, high-reflectance stack in combination with SiO_2, the low-index material. Figure 3 shows a comparison of several high-index materials. The excimer laser parameters are indicated in the figure. The excimer laser spot on the test mirror is substantially larger, by a factor of three, than the 1.1-μm helium-neon spot providing a significant margin to consider a constant effect across the area sampled. These results indicate that pure (0.9997) HfO_2 is substantially the best choice at 248 nm. Note that this coating has degraded by only a factor of 0.03% after a one-hour exposure at the indicated fluence. In addition to the superior ultraviolet damage performance, the HfO_2/SiO_2 coating has demonstrated [2] reflectivity at 1.06-μm wavelength in excess of 0.9999 and damage thresholds that far exceed the free-electron laser requirement.

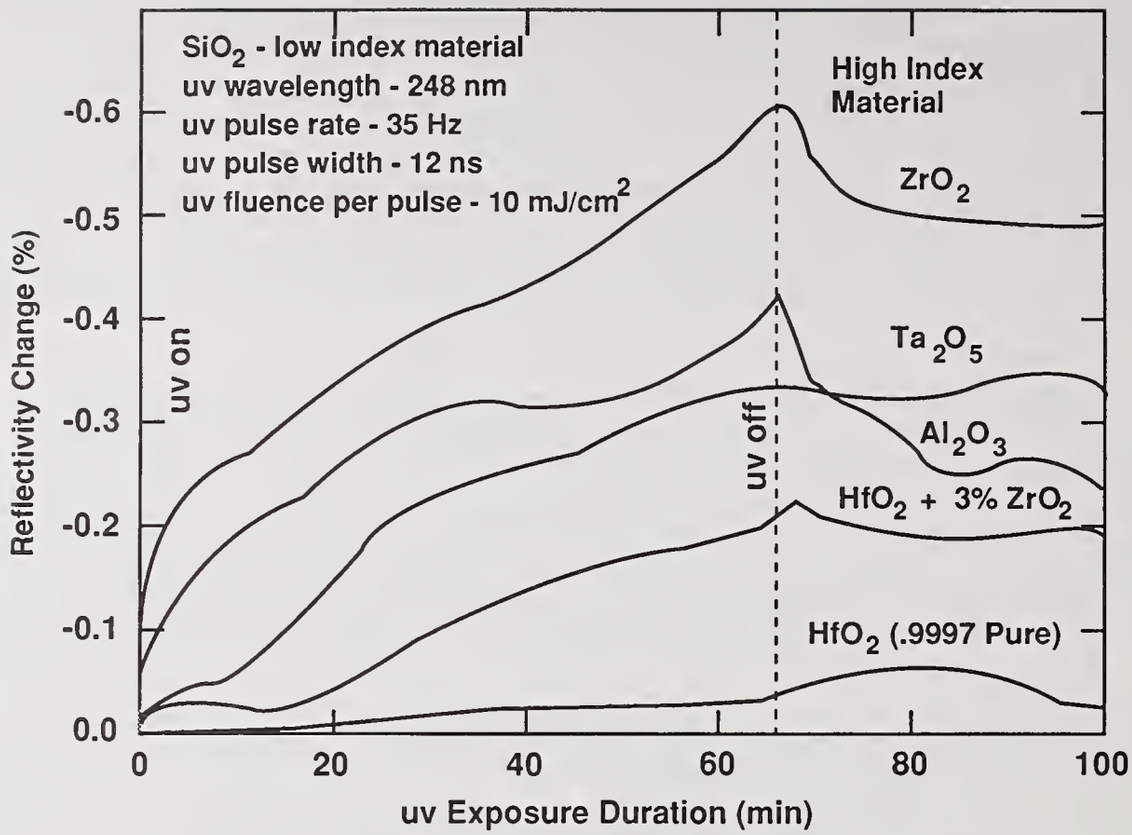

Figure 3. Comparison of high index materials in uv-damage experiment

In addition to a comparison of the indicated high-index materials in figure 3, this study demonstrated an unexpected relation between ultraviolet power density and induced damage, i.e., increased absorption at 1.1-μm wavelength. Figures 4, 5, and 6 show the relation. Figure 4 shows the continuous change in reflectivity during a 65-minute exposure at two separate pulse repetition rates (100 Hz and 8.4 Hz) associated with the excimer laser. In each case the individual pulse parameters are the same, as indicated in the figure. The pulse repetition rates differ by a factor greater than 10, but the rate at which absorption is being induced, i.e., the generation of color-centers, is nearly the same.

Figure 5 shows results from a single coating at separate sites on the coating. As indicated, the accumulated damage after 65 minutes of exposure is independent of ultraviolet pulse repetition rate for the given parameters.

Figure 6 indicates data from the same coating sample as represented in figures 4 and 5. In this case the reflectivity change after 65 minutes of exposure is indicated as a function of individual ultraviolet pulse fluence.

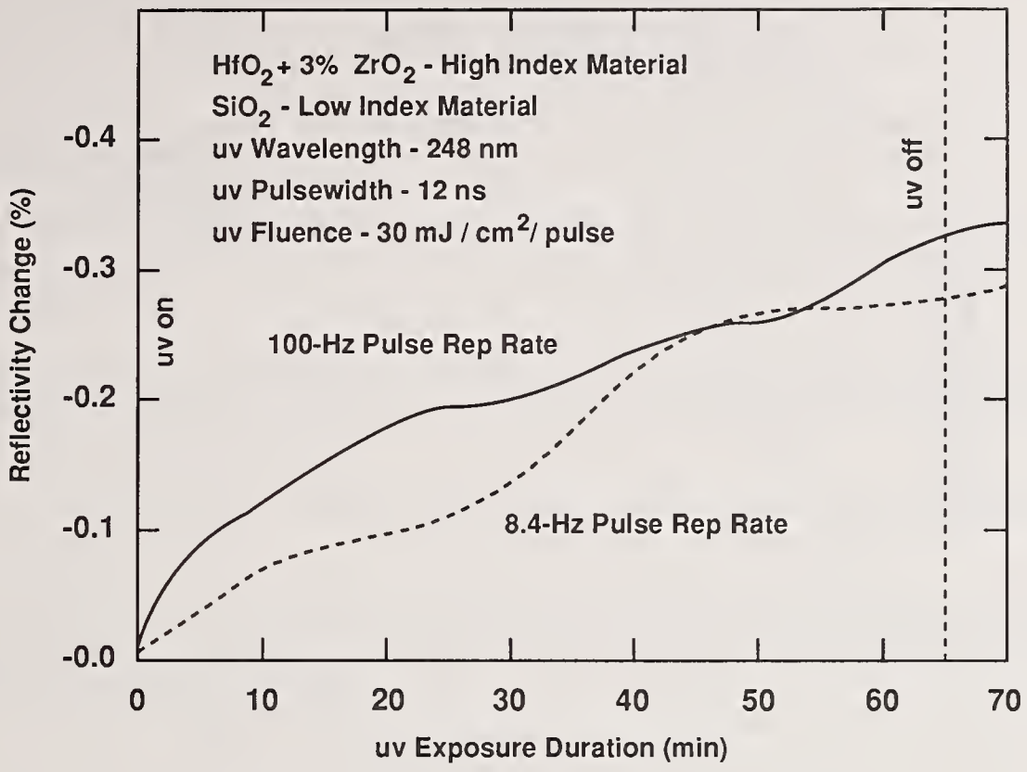

Figure 4. uv-induced reflectance change compared at two separate repetition rates

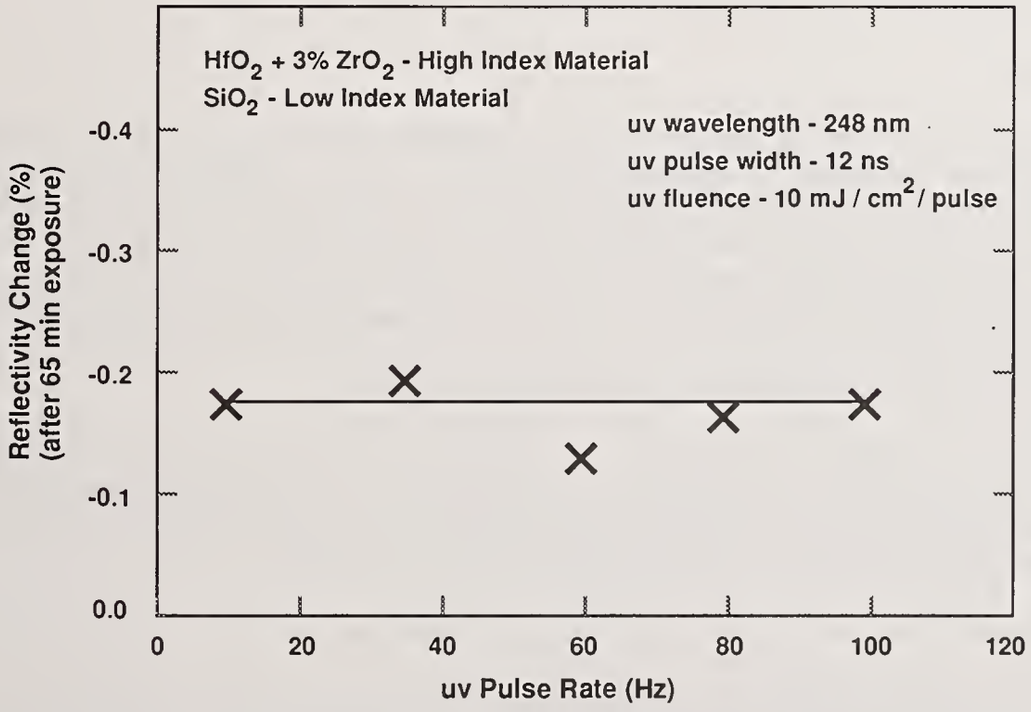

Figure 5. uv-induced reflectance change (after 65 minutes exposure) compared for several repetition rates

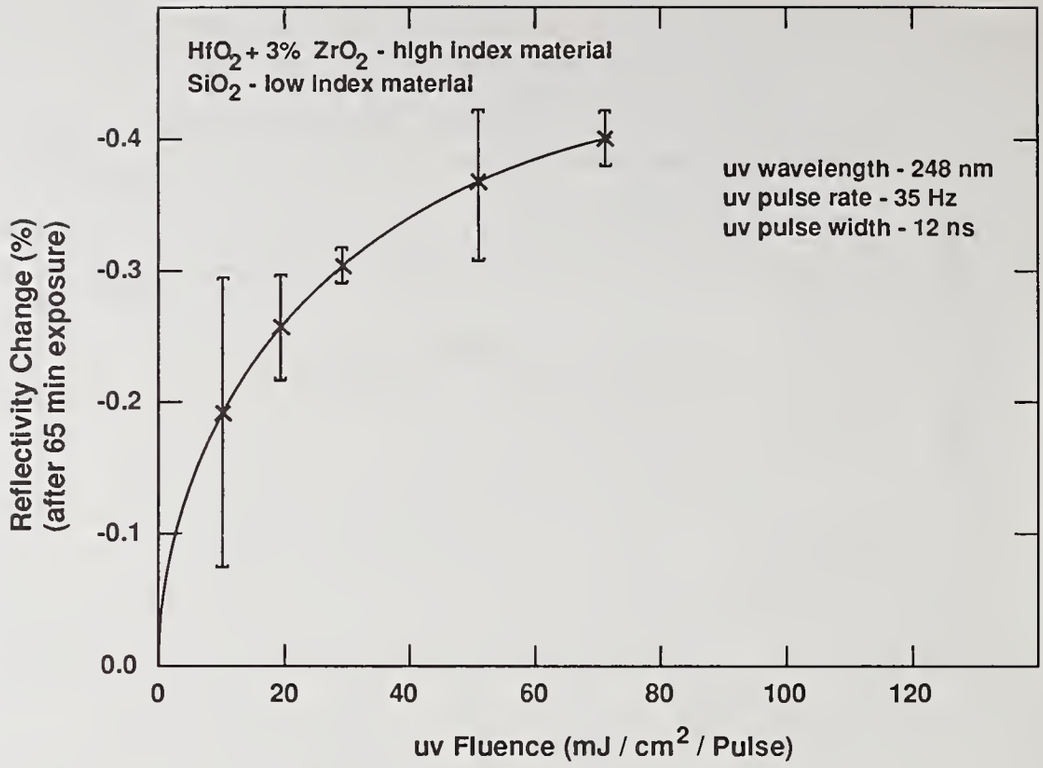

Figure 6. Coating reflectivity change as a function of peak uv fluence

We conclude from figures 4, 5, and 6 that the rate of induced absorption change or color-center generation is average power independent and peak power dependent. Each of the other materials indicated in figure 3 showed this same characteristic.

4. Conclusions

From the above-reported results and from the initial results at 351 nm reported in reference 7, we may conclude that the HfO_2/SiO_2 coating using pure HfO_2 is a good candidate for an ultraviolet- resistant coating. More particularly and in addition, given the results reported in reference 2 associated with 0.9999 reflectance and damage thresholds at 1-μm wavelength that far exceed the FEL system requirement, we conclude that this HfO_2/SiO_2 coating is a good candidate for a high-average-power free-electron laser. However, this study is not complete and will next obtain data at 193 nm using an ArF laser to simulate the fifth harmonic of 1 μm. Therefore, we consider our conclusions to be interim at this time in the study with respect to free-electron laser application.

In addition, we conclude that the average versus peak power nature of induced absorption as indicated in figures 4, 5, and 6 is significant. This relation has not been reported and is not resolved in the theoretical explanation of color-center generation in thin films. We conclude that this aspect of the study needs further consideration both experimentally and theoretically.

5. References

[1] Sanders, V.; Jolin, L.; Salazar, S. Damage to Silver Coatings from High Average Power 1-μm Laser. to be published in Laser Induced Damage in Optical Materials: 1988 (Boulder Damage Symposium Proceedings).

[2] Sanders, V.; Jolin, L.; Salazar, S. Laser Neutralizer Coating Validation Study. to be published in Proceedings of the Topical Meeting on High Power Laser Optical Components (1989).

[3] Schmitt, M.; Elliott, C.; Newnam, B. Harmonic Power Implications on Free-Electron Laser Mirror Design. Nuclear Instruments and Methods in Physics Research A272 (1988) 586-589.

[4] Levy, P. Overview of Nuclear Damage Processes; Phenomenological Features of Radiation Damage in Crystals and Glasses; Radiation Effects in Optical Materials. Levy, P., ed. Proc. SPIE 541; 1985 March 2-27.

[5] Elleaume, P.; Velghe, M.; Billardon, M.; Ortega, J. Diagnostic Techniques and UV-Induced Degradation of the Mirrors Used in the Orsay Storage Ring Free-Electron Laser. Applied Optics, Vol. 24, No. 17, September 1, 1985.

[6] Sanders, V. High Precision Reflectivity Measurement Technique for Low-Loss Laser Mirrors. Appl. Opt. 16 (1): 19-20; 1977.

[7] Early, J.; Sanders, V.; Leamon, W. The Response of Multilayer Dielectric Coatings to Low Fluence UV Light Exposure. to be published in Laser Induced Damage in Optical Materials: 1988 (Boulder Damage Symposium Proceedings).

Manuscript received
12-29-89

Radiation Damage in Single Crystal CsI(Tl) and Polycrystal CsI

O.Barnouin, A.Procoli, H.Chung and G.H.Miley

Department of Nuclear Engineering
University of Illinois at Urbana-Champaign
103 South Goodwin Avenue
Urbana, IL 61801

Radiation damage in single crystal CsI(Tl) and polycrystal CsI was assessed by measuring the changes in radioluminescent intensity caused by successive neutron and gamma ray pulses from a TRIGA nuclear reactor. The radioluminescent intensity from the single crystal decreases within nine pulses by 30% in the near infrared range (0.7-4.5 μm) and by 25% in the visible range (0.2-1 μm) before staying constant. For the polycrystal CsI, the emission in the visible range decreases by 60% within 6 pulses and then remains constant, whereas no measurable emission is observed in the infrared. Finally, a heating and cooling cycle is shown to repair the damage for both crystals.

Key words: Radiation damage, infrared radioluminescence, visible radioluminescence, cesium iodide, reactor irradiation, gamma ray irradiation, infrared window material

1. Introduction

CsI is a material that can be used for infrared detector windows and for making scintillators for high energy physics experiments (it is then doped with Thallium). This crystal may have to work in a harsh radiation environment which can cause an undesired signal to be sent to the detector or modify its calibration. It is therefore important to measure the response of this crystal to a flux of neutrons and gamma rays and to study the effects of dose accumulation. Such a study was conducted at the TRIGA nuclear reactor of the University of Illinois.

Radiation damage is most often studied through absorption measurements over the visible spectrum [1], rarely through radioluminescence measurements. Radioluminescence occurs [2] when an electron excited to the conduction band recombines radiatively, either directly to the valence band, or to a defect state (indirect, radiative recombination). Indirect recombination, however, can also occur without emission of a photon and the energy of the electron is lost through heating of the crystal lattice. The radioluminescent intensity then results from a competition between these processes. High energy radiations, by exciting electrons into the valence band and by creating new defects, modify the relative contribution of these recombination processes to the global recombination and leave the material in a state different from that before irradiation. One then speaks of radiation damage.

The investigation of radiation damage on CsI(Tl) has already been performed [3], although not extensively, with 1.25 MeV photons from a ^{60}Co source as gamma-ray source. The radioluminescence was due to irradiation

by a ^{137}Cs source. Although the total dose and dose rate were very much lower than in the present study (~500 rads, 100 rads per minute), a sizable reduction of the radioluminescence was observed (35% decrease of the emission at 500 rads). The damage was also found to be permanent.

It is the purpose of this paper to present results on radioluminescence measurements in both the visible and near infrared regions during a high-dose, pulsed irradiation of single crystal CsI(Tl) and polycrystal CsI by neutrons and gamma rays. It was found that, in both crystals, the radioluminescence decreases at first with increasing dose, but stabilizes after a few pulses. Also, heating the sample makes the radioluminescence decrease more rapidly in the single crystal CsI(Tl) than in the polycrystal. Finally, a cycle of heating and cooling is shown to repair the damage.

2. Experimental Setup

The samples underwent a series of pulses from the TRIGA pulsed nuclear reactor of the University of Illinois. The main characteristics of the pulse are shown in table 1 and the experimental setup is shown in figure 1.

Table 1. Pulse characteristics of the University of Illinois' TRIGA nuclear reactor

Pulse width	12.5 ms
Total power in a pulse	5.8 kWh
Total dose per pulse (SiO_2)	100 krads
Dose components: neutrons	5 krads
gammas	95 krads
Peak dose rate	6.7 Mrad/s
Pulse rate	4 pulses/hour

The CsI(Tl) sample was manufactured by Harshaw Company. It was grown from a solution and is a disk 25.4 mm diam., 2 mm thick. The polycrystal was made at the Oak Ridge National Laboratory and is made of a powder compressed uniaxially at 100 MPa at a temperature of 150°C. It is 25.4 mm in diameter and 10 mm in thickness.

The sample under test is placed in the middle of a nine-inch long aluminum rod mounted on a carriage. This carriage is positioned in the middle of a thruport adjacent to the reactor core (fig. 1). The rod is wrapped in a resistive heating tape used for raising the temperature of the sample. The rod is long enough to ensure a uniform temperature profile on the sample surface during the temperature rise. A thermocouple is attached to the carriage and is in direct contact with the sample to monitor its temperature carefully.

The light emitted by the sample impinges on a four-inch diameter, focussing aluminum mirror located at the exit of the thruport. The light is focussed onto an infrared, PbSe detector (detection range 0.7-4.5 μm) and onto a visible range, silicon detector (detection range 0.2-1 μm). A light chopper was used to account for the effect of the radiation on the detectors.

A typical reactor pulse gives a 0.1 Mrad dose in a SiO_2 sample. 0.5% of that dose (Table 1) comes from neutrons and 95% from gamma rays. The absorbed dose was not measured again in CsI, but a quick look at the

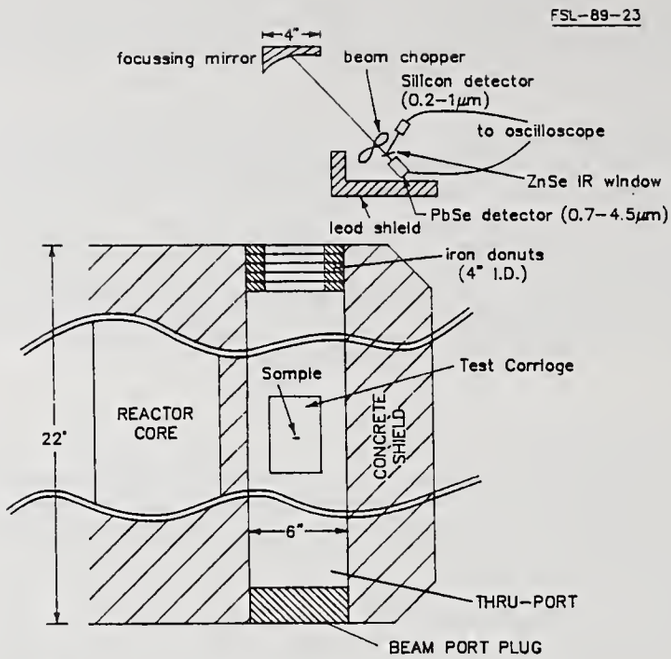

(NOTE: NOT TO SCALE)

Figure 1. Experimental setup

respective gamma absorption coefficients of SiO_2, Cs and I shows that the dose in CsI should not be larger than that in SiO_2 by more than a factor of two. Due to the higher atomic numbers of Cs and I with respect to SiO_2, the role of gamma rays will still be accentuated in CsI, making the neutron contribution to the radioluminescence and to the damage negligible.

3. Experiments performed and Results

Repetitive pulsing was performed for two consecutive days on the single crystal CsI(Tl) and for one day on the polycrystal. The pulses were spaced 17 minutes apart (this minimum time is imposed by NRC regulations).

3.1 Single crystal CsI(Tl)

The sample of single crystal CsI that had been delivered was found to contain Thallium impurities (20 to 30 ppm [4]). An emission spectrum was obtained with an OMA and revealed an emission peak at around 0.54 μm which is characteristic of the presence of Thallium [4,5] (whereas pure CsI only emits around 0.305 μm [4]). Apart from shifting the bulk of the emission to other wavelengths (as is desired in high-energy physics applications [5]), the presence of an impurity like Thallium can have important consequences for our measurements: it can "protect" against radiation damage "by scavenging free carriers before they can find a more damaging site" [6]. Further experiments will be needed with pure CsI to assess the role played by Thallium in the present results (apart, again, from the wavelength shift of the emission).

The change in radioluminescence for increasing dose in shown in figure 2 for the visible and infrared ranges (data taken at the peak of the pulse). In both ranges, the radioluminescence from CsI(Tl) at the peak of the pulse decreases and stabilizes after around nine pulses. The decreases amount to ~ 30% of the initial signal in the infrared and ~ 26% in the

visible range for data taken the first day. Due to the scatter of the data, a total of 16 pulses were taken to firmly establish the presence of this saturation level before the temperature of the sample was raised. The results as a function of temperature are shown in figure 3 for both wavelength ranges. The emission decreases by factors of 30-40 for a temperature rise of 100-125°C above room temperature.

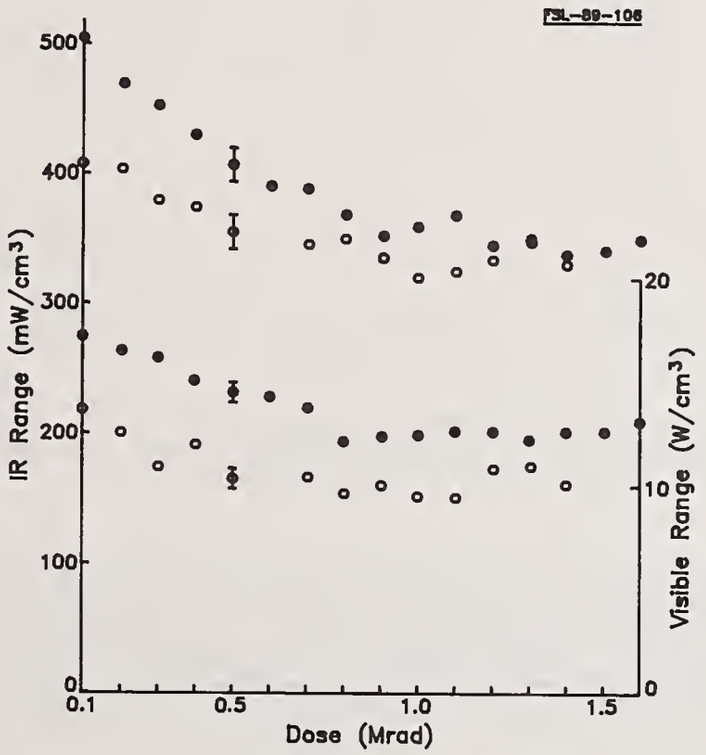

Figure 2. Radiation damage in single crystal CsI(Tl) at room temperature. Solid circles are data taken the first day, open circles to data taken the next day. Infrared data are at the top.

Data taken during the second day (fig. 2) show what may look like a recovery of the radioluminescence after the first day. The radioluminescence during the first pulse is higher than the stabilization level reached the day before. It then decreases for increasing dose until a constant level is reached that is slightly lower than observed the day before. We will analyze this behavior below, after taking a look at the results on polycrystal CsI.

3.2 Polycrystal CsI

This sample was first irradiated with a series of nine pulses. The resulting radioluminescence change at the peak of the pulse is shown in figure 4.a for the visible range emission. No measurable infrared emission was observed. The drop in figure 4.a is around 60% of the original emission and takes places within six pulses (compared with the 25% emission drop within nine pulses for CsI(Tl)). After stabilization of the radioluminescence (the scatter of the data is obviously less in this case than for the single crystal), the temperature was slowly increased to 170°C

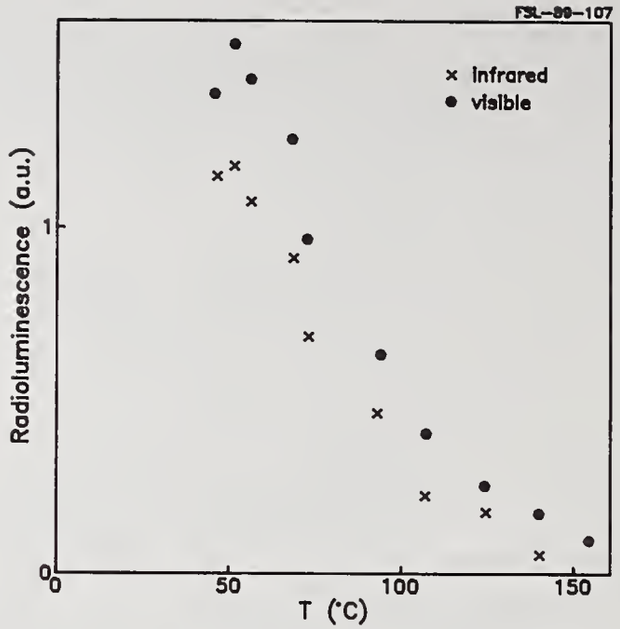

Figure 3. Radioluminescence intensity for increasing temperature. Data taken right after the data at room temperature.

and pulses were taken as the temperature was increased (fig. 4.b). The decrease of the emission is then due to thermal quenching. In contrast with the measurements on the single crystal, raising the temperature decreases the emission (relatively to the stabilization level obtained after 6 pulses) by only 60%. This represents a decrease by a factor of 2.5, whereas a diminution by 30 or 40 was observed for the single crystal. The emission from the polycrystal also remains constant between 150°C and 170°C.

The temperature was then brought down and some pulses were taken around room temperature. Obviously, the radioluminescence has recovered from the first series of pulses. It however decreases again when the irradiation goes on at room temperature (fig. 4.c) and it stabilizes at the same level as that observed in figure 4.a.

As a final experiment, the temperature was increased rapidly (in about 15 minutes) to 135°C and then brought down again after a pulse was taken at that temperature. The result is indicated by the two crosses in figure 4.b. Provided that there is no large temperature gradient at the surface of the sample (as might arise when heating the sample so fast), this experiment shows that the radioluminescence at higher temperature depends on the heating rate (fig. 4.b, lower cross). However, the cooling rate was the same as during the first cycle, and the radioluminescence then coincides with the previous data (fig. 4.b, upper cross).

4. Analysis

These experiments show that CsI, either single or polycrystal, does suffer radiation damage when irradiated by a pulse of neutrons and gamma rays. This radiation damage is evidenced by a decrease of the radioluminescent intensity for increasing dose. However, two important conclusions have been reached: 1) the radioluminescent intensity stabilizes

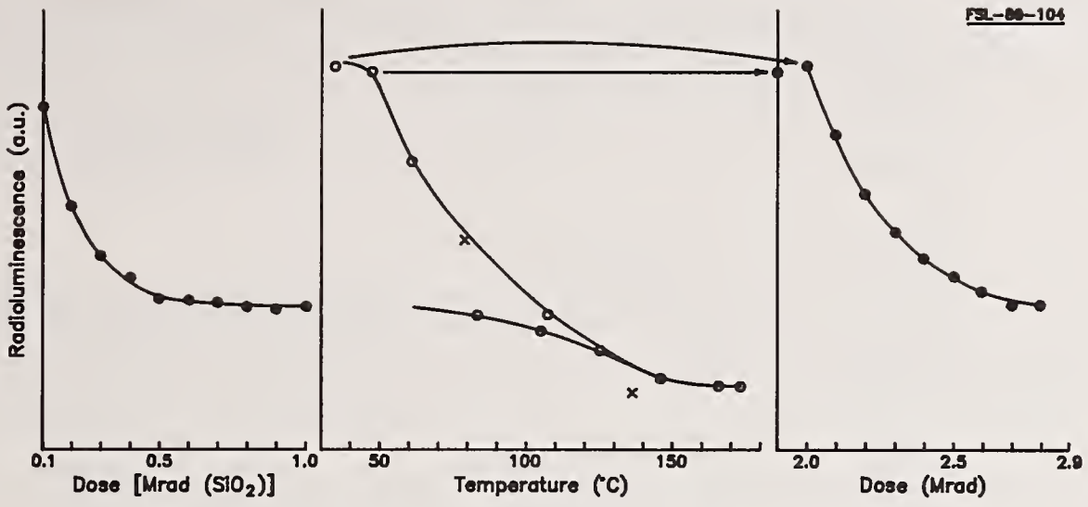

Figure 4. Radiation damage in polycrystal CsI. Chronological order is from left to right.

after a few pulses and, 2) the damage can be repaired by heating and cooling the sample, as is shown by the recovery of the radioluminescence after cooling.

The initial decrease of the radioluminescence might be due to several phenomena. First, an increase of the self-absorption during the irradiation. Absorption experiments performed at 0.633 μm show that the absorption at that wavelength increases during the whole pulse. However, the fact that the radioluminescence pulse is symmetric with respect to the peak of the pulse and is always proportional to the radiation pulse tells us that self-absorption does not play a more important role in the second half of the pulse than in the first half.

Second possibility, non-radiative recombinations can be favored by irradiation at high-energy. Available literature [7] does not give more precise explanations for the decrease of the radioluminescence for increasing dose. This decrease, together with the asymptotic behavior observed after 0.6-0.9 Mrad, can, however, be compared to the decrease and stabilization of the infrared transmission spectrum recorded after successive steady-state irradiations (0 Mrad (fresh sample), 1 Mrad,...) of a similar sample (fig. 5). The transmission decreases up to a dose of 1 Mrad (or less, since no data is available before 1 Mrad), and then remains constant for larger doses. Although the spectral range is different from that of the radioluminescence data, both kinds of results nevertheless evidence a saturation effect for the same total dose.

It is impossible for us to evidence the exact saturation mechanism from the data presented above. Considering the small contribution of neutrons to the total dose and the small kerma of CsI with respect to SiO_2, neutron creation of defects is not a determining factor in our results. However, traps can be filled by recombination of electrons located in the conduction band after ionization by gamma-rays. They can also be emptied by excitation. The number of electrons in traps influences the relative rates for radiative and non-radiative recombinations, hence the total radioluminescent emission. Whatever the real cause, figures 4 and 5 tell us that, after ~ 6 pulses, a kind of balance is reached in which the color centers would lose as many electrons by excitation as they would gain

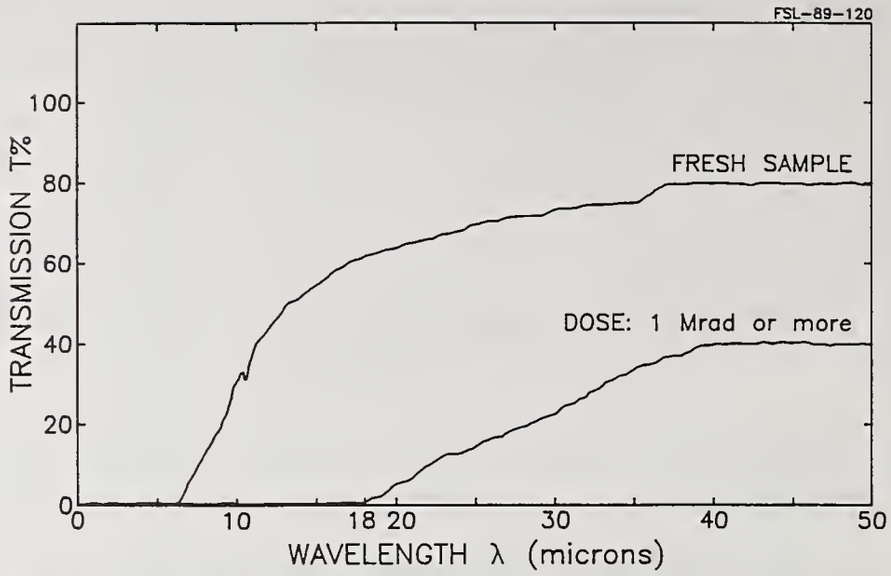

Figure 5. Transmission spectrum of polycrystal CsI before and after several irradiation from the TRIGA reactor at steady-state power.

through electronic capture. An increase in temperature alters that balance by exciting electrons out of the traps (quenching).

The remark about the recovery of the radioluminescence intensity after heating comes from the results on the polycrystal (fig. 4.c). The temperature rise, apart from quenching the emission, also modifies the number of electrons in traps, decreasing the possibilities for charge carriers to recombine non-radiatively, thereby increasing the radioluminescence at room temperature. This can also explain the recovery of the radioluminescence in the single crystal at the beginning of the second run, which took place after a temperature rise was performed at the end of the first day. The fact that the stabilization level reached during the second day is lower than that observed during the first day might be a real feature of radiation damage or be due to increased self absorption in the sample (due in particular to moisture absorbed during the night).

Thermal quenching of the emission is not as effective in the polycrystal as in the single crystal (fig. 3, 4.b). Furthermore, the emission from the polycrystal stabilizes above 150°C (there is no data above 170°C, however). This might be a sign that shallow traps have been emptied by the temperature rise and that the trap distribution is not continuous, whereas it would be continuous in the case of the single crystal.

5. Conclusions

This work shows that radiation damage in polycrystal CsI is stronger that in single crystal CsI(Tl). However, the presence of Thallium as a dopant in the single crystal clouds the issue. Further measurements on pure CsI are needed to determine whether Thallium effectively protects the crystal from radiation damage (or the opposite).

Several features of the radioluminescence exhibited by the samples are noteworthy: 1) the damage, as evidenced by radioluminescence measurements, stabilizes in either case after a dose of 0.6-0.9 Mrads provided at room

temperature; 2) a heating-cooling cycle repairs the damage by annealing some of the defects and, 3) heating the sample 120°C above room temperature decreases the emission in the polycrystal by only 60%, versus 98% in the case of the single crystal. The repair of the damage by heating is important since it means that the damage cannot be considered permanent, as long as one can afford to heat it up.

This work was performed under contract with the Oak Ridge National Laboratory and the U.S.A. Strategic Defense Command.

We thank the University of Illinois' TRIGA reactor crew for their assistance in the experiment.

6. References

[1] For example, Kubo, K. "Radiation Effects in LiF Crystals," Journal of the Physical Society of Japan 16; 2294; 1961.

[2] See, for example, McKeever, "Thermoluminescence of Solids", Cambridge University Press 1985.

[3] Bobbink, G.J.; Engler, A.; Kraemer, R.W. "Study of Radiation Damage to long BGO Crystals," Carnegie Mellon University Report CMU-HEP 83-13; 1983. Cited by Ref.4.

[4] Brad Utts, Harshaw Company, Solon (OH), private communication, September 21, 1989.

[5] Grassmann, H.; Lorenz, E.; Moser, H.G. "Properties of CsI(Tl) Renaissance of an Old Scintillation Material," Nuclear Instruments and Methods in Physics Research 228; 323; 1985.

[6] Williams, R.T. "Nature and Defects Generation in Optical Crystals," SPIE Radiation Effects in Optical Materials 541; 25; 1985.

[7] Levy, P. "Overview of Nuclear Radiation Damage Processes: Phenomenological Features of Radiation Damage in Crystals and Glasses," SPIE Radiation Effects in Optical Materials 541; 2; 1985.

Manuscript Received
5-17-90

Effects of Thermal Conductivity and Index of Refraction Variation on the Inclusion Dominated Model of Laser-Induced Damage

M. Z. Fuka and J. K. McIver

University of New Mexico Physics Department, Albuquerque, NM, 87131

A. H. Guenther

Los Alamos National Laboratory Los Alamos, NM, 87544

The inclusion-dominated model of laser-induced damage is reexamined in light of recent measurements of thin film thermal conductivities. In particular, the effects of varying the thermal conductivity and imaginary part of the index of refraction are explored. Two different values of the index of refraction are shown to be associated with a given damage threshold, and physical mechanisms are proposed for each value. Thermal conductivity is demonstrated to affect only weakly the value of the imaginary part of the index of refraction corresponding to a particular damage threshold.

Key words: Key words: laser damage, thin films, thermal conductivity, inclusion-thermal modeling, refractive index.

1. Introduction

The familiar [1] inclusion-dominated model of laser-induced damage in thin films incorporates a small localized region in the film that absorbs more incident radiation than the surrounding host film. The energy absorbed at the imperfections then diffuses into the main body of the film. Thus, the rate at which an inclusion can reach a critical damaging temperature depends in part on the cross section of the absorbing inclusion presented to the incident radiation and on the ability of the host thin film to diffuse heat.

Previous work [2,3] has shown that this model successfully describes the scaling of single-shot damage thresholds with respect to the laser pulse duration and the thermal properties of the film. In past laser damage calculations using this model [3], thermal property parameters approximating accepted values for bulk materials were used for the host and inclusion. Recent measurements [4], however, strongly suggest that thermal conductivities of materials in thin film form can be orders of magnitude less than bulk values. The first part of this present work considers the effects on laser damage thresholds of varying the thermal conductivities of host and inclusion.

The second part of this work discusses the effects on predicted damage thresholds of varying the imaginary part of the index of refraction of the inclusion. In particular, a given damage threshold can be achieved by two physical mechanisms, surface and bulk absorption by the inclusion, each associated with very different values of the imaginary part of the index of refraction. Since thus far comparisons of model predictions to experimental data have been limited to those cases where it was assumed that the incident radiation is absorbed uniformly by the inclusion, using various values of the index of refraction may therefore provide a means to approximate different inclusion absorption mechanisms.

2. Theory

A general description of the model is illustrated in Figure 1. A host thin film contains a spherical inclusion of radius a. The host film and inclusion are materials with different optical, thermal and mechanical properties. It is assumed that only the inclusion absorbs the incident radiation, and that the size of the absorbing inclusion is much smaller than the laser spot size. The absorption can thus be thought of as occurring in an optical field of constant radial intensity.

As shown in the figure, optical properties of the inclusion are specified by the complex index of refraction, $n = n_R + in_I$, where n_R and n_I are the real and imaginary parts of the index of refraction, respectively. The incident laser pulse is described by its intensity I, wavelength λ, and pulse duration t_1. The thermal properties of the system are described by the thermal conductivity, K, and the thermal diffusivity, D, of each region. These properties in concert with the rate at which radiation is absorbed are taken to be independent of the temperature. The system is considered damaged when the surface of the inclusion reaches some critical temperature, for example, the melting temperature of the film.

The temperature distribution T of the system is described by the thermal diffusion equations 3 :

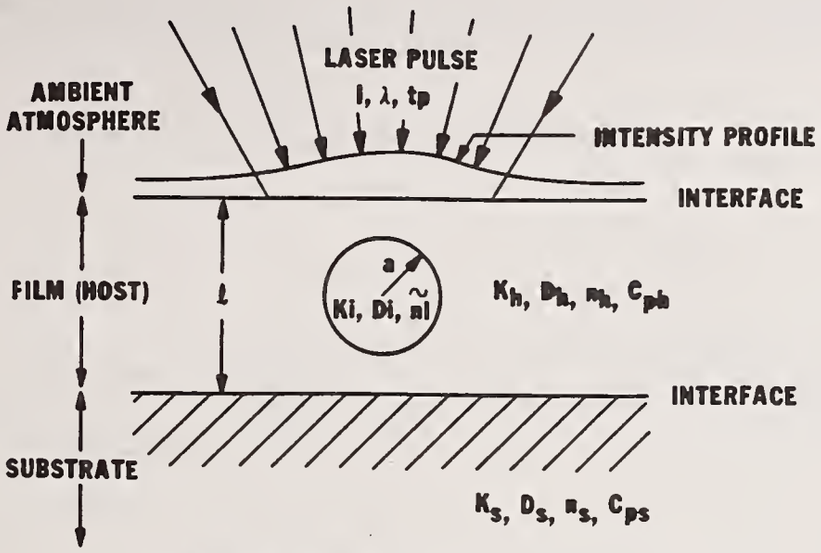

I - LASER INTENSITY (W/cm²)
λ - LASER WAVELENGTH (cm)
t_p - LASER PULSE WIDETH AT FWHM (sec)
n - INDEX OF REFRACTION
a - RADIUS OF SPHERICAL INCLUSION (cm)
K - THERMAL CONDUCTIVITY (W/cm - °K)
D - THERMAL DIFFUSIVITY (cm²/sec)
C_p - SPECIFIC HEAT AT CONSTANT PRESSURE (J/cm³ - °K)
ℓ - FILM THICKNESS (cm)

SUBSCRIPTS

i - INCLUSION
h - HOST
s - SUBSTRATE

Figure 1. The inclusion-dominated breakdown model.

$$\frac{1}{D_i}\frac{\partial T_i}{\partial t} = \frac{1}{r^2}\frac{\partial}{\partial r}r^2\frac{\partial T_i}{\partial r} + \frac{A}{K_i} \qquad 0 \le r \le a$$

$$\frac{1}{D_h}\frac{\partial T_h}{\partial t} = \frac{1}{r^2}\frac{\partial}{\partial r}r^2\frac{\partial}{\partial r}T_h, \qquad r > a \tag{1}$$

where the subscripts i and h refer to the inclusion and host, respectively. A is the source term. The interface between the impurity and the host is described by the boundary conditions:

$$T_i(a) = T_h(a),$$

$$K_i \left.\frac{\partial T_i}{\partial r}\right|_{r=a} = K_h \left.\frac{\partial T_h}{\partial r}\right|_{r=a} \tag{2}$$

The solution for this system of equations can be found by using a Laplace (temporal) transform or an integral (spatial) transform. The latter is more general, since it assumes no specific form of the temporal absorption profile. The solution for the temperature of the inclusion subject to the initial conditions

$$T_i(r, t=0) = T_h(r, t=0) = 0, \tag{3}$$

is given by [3]

$$T(r,t) = \frac{3QI}{4\pi K_i a}\left\{\frac{1}{3}\frac{K_i}{K_h} + \frac{1}{6}\left(1 - \frac{r^2}{a^2}\right) - \frac{2ab}{r\pi}\int_0^\infty e^{-y^2 t/\gamma} F(y)dy\right\}, \tag{4}$$

where

$$F(y) = \frac{(\sin y - y\cos y)\sin(ry|a)}{y^2\left\{(c\sin y) - y\cos y)^2 + b^2 y^2 \sin^2 y\right\}}$$

$$\gamma = \frac{a^2}{D_i} \quad c = 1 - \frac{K_h}{K_i} \quad b = \frac{K_h}{K_i}\sqrt{\frac{D_i}{D_h}}. \tag{5}$$

As in previous work, the source term A is written in terms of the incident intensity I

$$\int_{v_i} dr^3 A(r,t) = Q\left(\frac{2\pi a}{\lambda}, n_I\right) I(t), \tag{6}$$

where Q is the absorption cross section computed from Mie scattering theory [3] and n_I is the imaginary part of the index of refraction of the inclusion. The damage threshold is then defined as

$$E = \int_0^{t_p} dt I(t) \quad [Jcm^{-2}], \tag{7}$$

where t_p is the pulse length required to reach the critical temperature T_c at the radius a of the absorbing region. $T_c t_p = f(r, Q, E)$ is inverted to give $E = g(T_c, t_p, r, Q)$ in Joules per centimeter squared. For all calculations discussed in this work, the critical temperature is chosen to be 2000K, a typical value for the type of materials commonly used in dielectric thin films. The exact value of T_c is not critical because of the large value of dT_c/dt involved in the damage interaction.

3. Effects of Thermal Conductivity Variation

Figure 2 shows the results of reducing the thermal conductivities of the host (left-hand column) and the inclusion (right-hand column) in order of magnitude steps. Since conductivity and diffusivity are dependent on each other according to

$$\frac{K}{D} = \rho c_p, \tag{8}$$

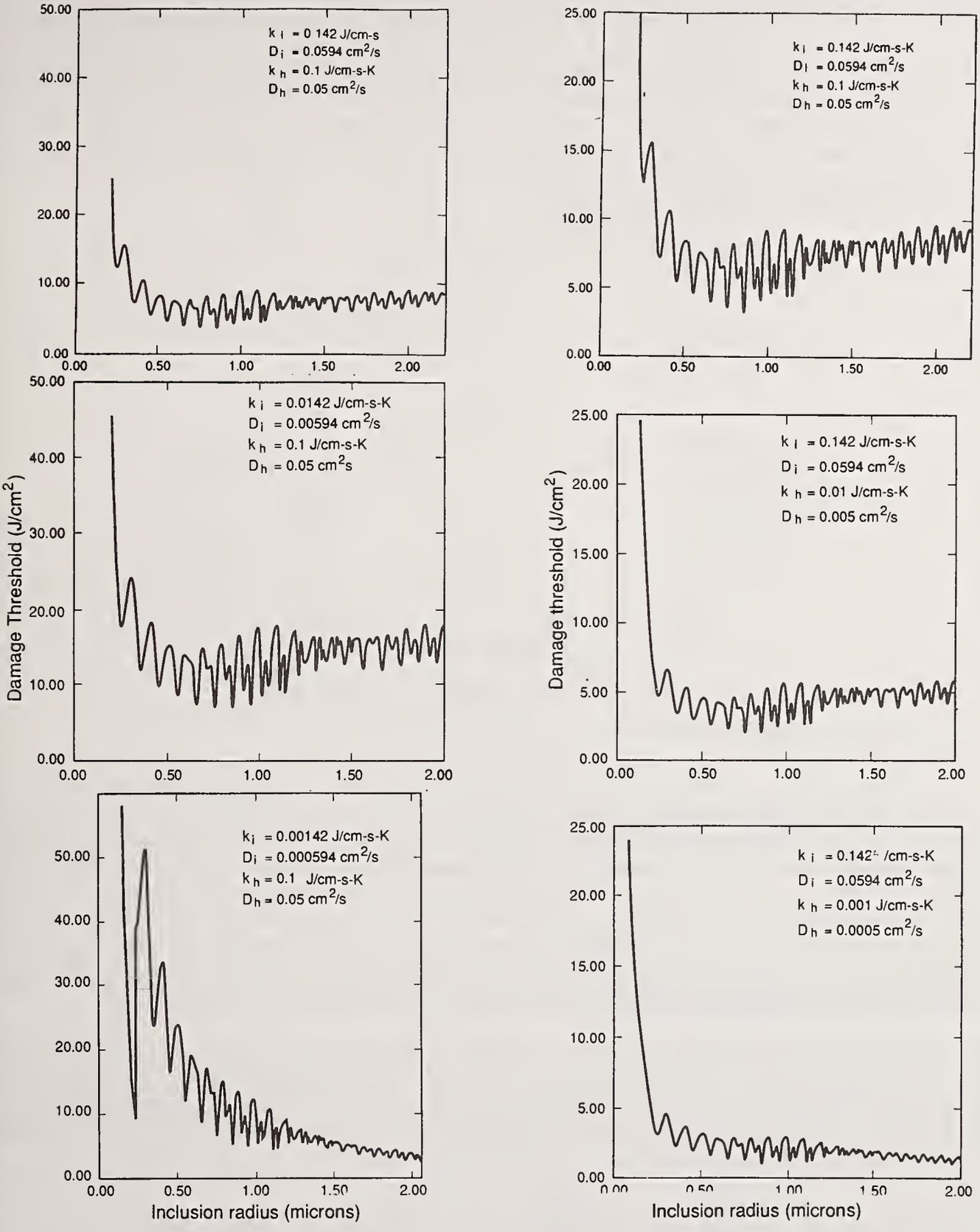

Figure 2. Effects of varying thermal conductivity on damage threshold. In the left hand column (a), host conductivity is held constant and inclusion conductivity and diffusivity are varied. In the right hand column (b) inclusion conductivity is held constant while host conductivity and diffusivity are varied.

they are reduced proportionally. The damage threshold is plotted as a function of the inclusion radius. As expected, damage thresholds decrease for decreasing host thermal conductivity. Conversely, thresholds increase overall for decreasing inclusion thermal conductivity. Damage thresholds change by roughly a factor of two for each order of magnitude change in conductivity. The damage threshold is therefore relatively weakly affected by large changes in host/inclusion thermal conductivities. This suggests that the use of this model remains appropriate for the much lower thermal conductivities recently observed. Note too that, as expected in the Mie absorption process, the minimum damage threshold occurs at the same inclusion radius as the thermal conductivities are varied. The thermal impedance mismatch between host and inclusion is not considered in these calculations since including the impedance would only complicate the calculations without effecting the qualitative results presented here.

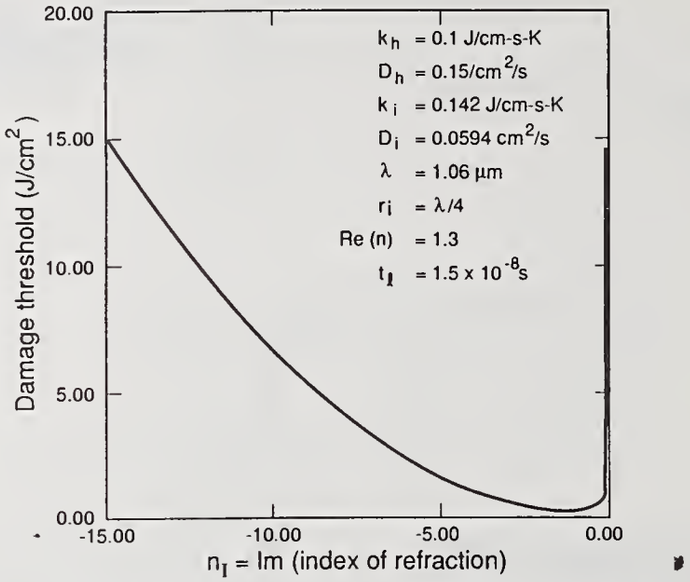

Figure 3. Damage Threshold as a function of n_I.

4. Variation of the Imaginary Part of the Index of Refraction

The damage threshold is shown in Figure 3 to be quite sensitive to changes in the imaginary part of the index of refraction n_I, particularly for n_I of magnitude much less than one. Normally in the use of this model the imaginary part of the index of refraction is taken to be a free parameter to be fitted to experimental damage thresholds. The sensitive dependence of the damage threshold to index of refraction variation may therefore provide a means to compensate for the changes in thermal conductivity discussed in the previous section. As can also be seen in the figure, a given damage threshold is predicted by two values of n_I. These values correspond in the model to two different physical mechanisms for damage one for n_I much less than one and one for n_I much greater than one. As shown in Tables 1 and 2 the values of n_I that predict a given damage threshold vary slowly for large thermal conductivity variations.

Table 1. Effects of varying inclusion thermal conductivity and diffusivity on the imaginary part of the refractive index.

$$K_h = .1(J/cm - s - K), \qquad D_h = .15cm^2/s$$

K_i	D_i	$n_{I(1)}$	$n_{I(2)}$
0.142	0.0594	−0.011	−14.0
0.0142	0.00594	−0.015	−12.0
0.00142	0.000594	−0.034	−8.2
0.000142	0.0000594	−0.029	−8.8

$n_{I(1)}$ = smallest magnitude root

$n_{I(2)}$ = largest magnitude root

Table 2. Effects of varying host conductivity and diffusivity on the imaginary part of the index of refraction.

$$K_h = .142(J/cm - s - K), \qquad D_i = .0594cm^2/s$$

K_h	D_h	$n_{I(1)}$	$n_{I(2)}$
0.1	0.15	−0.011	−14.0
0.01	0.15	−0.0040	−23.0
0.001	0.0015	−0.025	−27.0
0.0001	0.00015	−0.0015	−35.0

$n_{I(1)}$ = smallest magnitude root

$n_{I(2)}$ = largest magnitude root

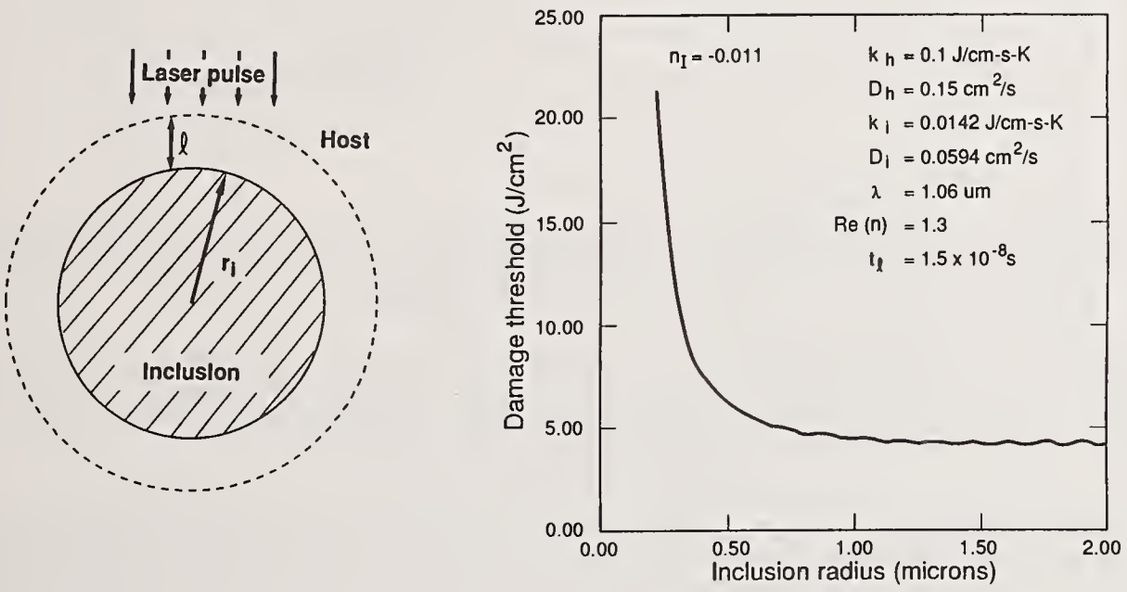

(a) (b)

Figure 4. Bulk absorption by the inclusion. The left hand side (a) illustrates the proposed mechanism. On the right hand side (b), damage threshold is plotted as a function of inclusion radius for $n_I = -.011$.

In the first proposed mechanism, an n_I of very small magnitude means that the skin depth δ of the inclusion is on the order of or greater than the radius of the inclusion r_i (Fig.4a). The inclusion can therefore be regarded as heating uniformly, absorbing some energy E_A proportional to the inclusion volume ('bulk' absorption). Energy diffuses some distance l (the diffusion length) into the host. The total energy diffused, E_D, is then proportional to $(r_i + l)^3$. The damage threshold is then proportional to E_D/E_A. This ratio approaches a constant for large inclusion radius, and infinity as the radius goes to zero (Fig. 4b).

For n_I of magnitude much larger than one, on the other hand, the skin depth δ of the inclusion is much less than the radius of the inclusion (Fig. 5a). The energy E_A absorbed by the inclusion is thus proportional to

$$E_A \propto 3r_i^2(\ell + \delta) + 3r_i(\ell^2 - \delta^2) + \ell^3 + \delta^3. \tag{9}$$

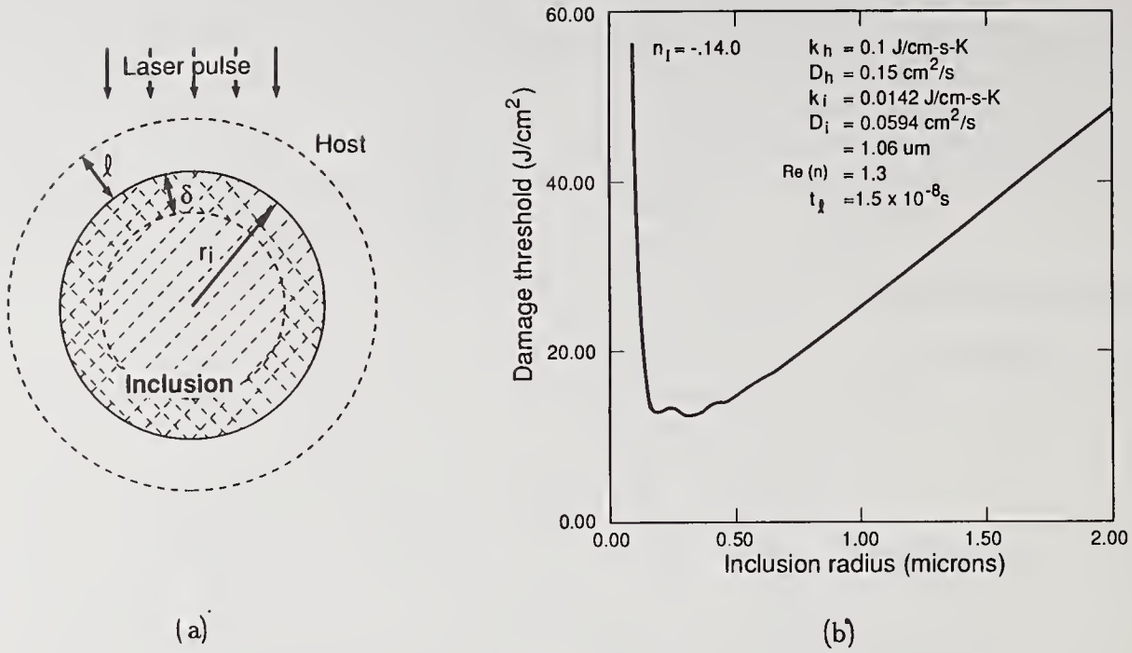

Figure 5. Surface absorption by the inclusion. The left hand side (a) illustrates the proposed mechanism. On the right hand side (b) damage threshold is plotted as a function of inclusion radius for $n_I = -14.0$.

This is referred to as 'surface' absorption. So in the limit of large r_i (assuming $\delta \ll r_i$) the ratio E_D/E_A that determines the damage now goes linearly in r_i (Fig. 5b). For very small inclusion radius, that is, for a skin depth of approximately r_i, the bulk absorption picture once again holds, yielding a damage threshold approaching infinity as r_i goes to zero (Fig. 5b).

This work does not propose that a specific inclusion material should be considered to have two very different indices of refraction. Rather it suggests that despite the fact that diffusion lengths for host and inclusion are not explicitly included in the model, two very different physical mechanisms for absorption can be investigated theoretically by using appropriate indices of refraction. Particularly interesting are the results of plotting laser damage as function of inclusion radius for the two n_I that yield a damage threshold of $13 J/cm^2$ (Fig. 6).

As can be seen in the figure, using an index of refraction yielding a surface absorption mechanism for the inclusion absorption gives qualitatively better agreement with experimental results [5]. On the other hand, a value of n_I chosen to model inclusion bulk absorption shows good agreement for large radii. For values of the imaginary part of the index of refraction between these two extremes, the correct mechanism represented by the model is most likely a composite of inclusion bulk and surface absorption. These results suggest that both types of absorption must be considered to obtain the best possible theoretical picture of laser damage. Changing the index of refraction, though nonphysical, provides a simple method to study the qualitative differences in the two mechanisms using the inclusion dominated model. These results further suggest that the inclusion dominated model could be adapted to make predictions of laser damage not only for those experimental cases where uniform absorption can be assumed, but also to cases where the absorption is nonuniform. Ideally, such an adaptation will include a more physically accurate method of including bulk and surface absorption mechanisms for inclusion absorption.

5. Summary

In conclusion, this work shows that the damage threshold predictions of the inclusion-dominated model for laser damage in thin films are relatively weakly affected by extremely large (order of magnitude) changes in the thermal conductivities. On the other hand, predicted damage threshold energies are rather sensitive to the imaginary part of the index of refraction n_I in this model. A given damage threshold is predicted by two different values of n_I, one of much smaller magnitude than the other. Different damage mechanisms can be associated with the two different indices of refraction. In the one, bulk absorption dominates, in the other, surface absorption. Through a combination of these mechanisms, it appears that the model can be adapted to yield realistic damage thresholds and indices of refraction for a variety of inclusion/host thermal conductivities.

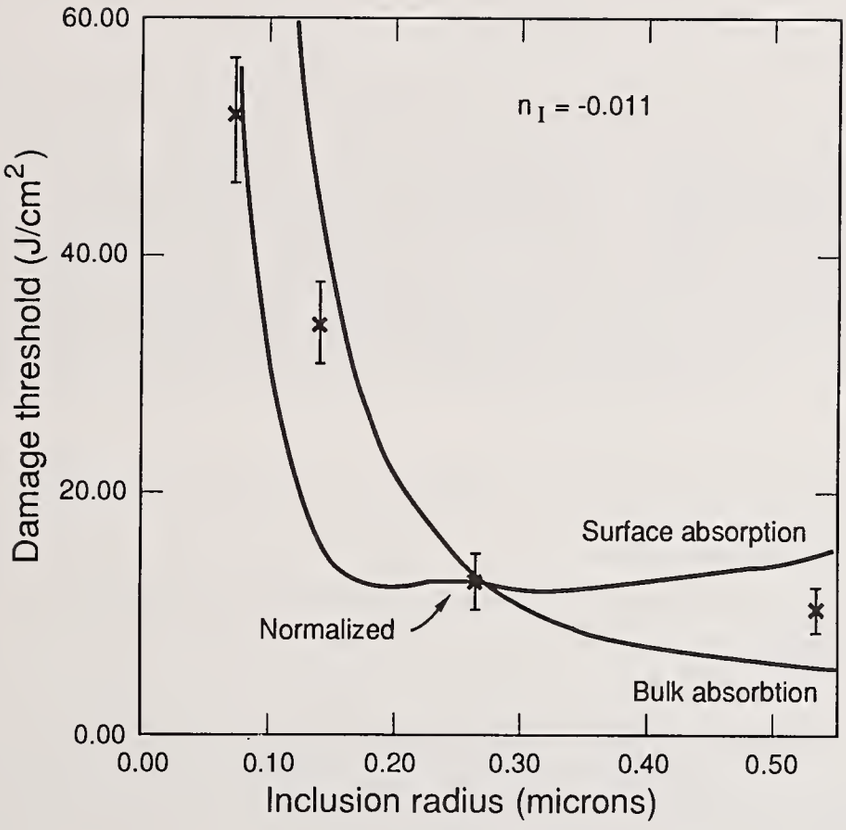

Figure 6. Comparison between experimental [5] data and model for ThF_4 films.

6. References

[1] H. Goldenberg and J. C. Trantor, "Heat Flow in an Infinite Medium Heated by a Sphere," Brit. J. Appl. Phys., **2**; 296-298; 1952 November.

[2] T. W. Walker, A. H. Guenther and P. Nielsen, "Pulsed Laser-IOnduced Damage to Thin-Film Optical Coatings Part II: Theory," IEEE J. Quant. Electr., **QE-17**; 2053-2065; 1981 October.

[3] M. R. Lange, J. K. McIver and A. H. Guenther, "Pulsed Laser Damage in Thin-Film Optical Coatings: Flourides and Oxides," Thin Solid Films, **125**; 143-155; 1985 April.

[4] D. C. Lambropoulos, M. R. Jolly, C. A. Amsden, S. E. Gilman, M. J. Sinicropi, D. Diakomihalis and S. C. Jacobs, "Thermal Conductivity of Dielectric Thin Films," J. Appl. Phys. **66**; 4230-4242; 1989 November 1.

[5] T. W. Walker, A. H. Guenther and P. Nielsen, "Pulsed Laser-Induced Damage to Thin-Film Optical Coatings Part I: Expeirmental," IEEE J. Quant. Electr., **QE-17**; 2041-2052; 1981 October.

Manuscript received
2-15-90

Theoretical Determination of the Nonlinear Optical Properties of Inorganic Polymers

Steven M. Risser and Kim F. Ferris
Pacific Northwest Laboratory[1], Materials and Chemical Sciences Center, Richland WA 99352

ABSTRACT

Third order hyperpolarizabilities were calculated using the Huckel Hamiltonian and third order perturbation theory for a series of phosphonitrilic compounds, $(X_2P\text{-}N)_n$, as a function of bond length alternation, ligand substitution and backbone conformation. Phosphonitrilic compounds show hyperpolarizabilities comparable to those reported for organic species, and are modulated by ligand group electronegativity. In contrast to organic polyenes, the difference in π orbital energy between phosphorus and nitrogen is critical to determining the onset of saturation and the magnitude of the hyperpolarizability. Conformation effects are smaller than those seen in polyenes.

Keywords: Nonlinear, hyperpolarizability, inorganic polymers, optical properties, phosphazenes

1.0 INTRODUCTION

While the search for materials with large macroscopic nonlinear properties has often focused on conjugated organic molecules, inorganic polymers feature many similar chemical bonding interactions and should also be viewed as viable candidates. Recent experiments on polyphosphazenes have shown that these polymers exhibit large bulk nonlinearities and high laser damage thresholds[2]. These properties combined with their transparency in the visible spectrum mark these compounds as potential alternatives for use in fabricating optical devices.

Most of the electronic properties of the polyenes, such as absorptions and both the linear and nonlinear optical properties[3], are governed by the conjugated π bonding electrons. Inorganic polymers such as the phosphonitrilic system feature two independent π-bonding networks, the normal π network which is constructed from out of the plane p_z orbitals, and a second, less highly conjugated π' network lying in the plane of the molecule[4]. The interaction of the two conjugated π electron systems has large effects on the electronic properties of the polyphosphazenes, increasing the optical transition energies of the out-of-plane π electrons[5] as compared to organic molecules, and making intrinsic contributions to the electronic hyperpolarizabilities of the molecule.

The similarities in the chemical bonding between organic and inorganic polymers would indicate that some features which affect the nonlinear optical properties of polyenes, such as degree of bond alternation and chain conformation, should be considered for their potential influences on inorganic polymers. In addition, characteristics such as the large electronegativity differences between atoms along the polymer backbone which are unique to the inorganic polymers, may also have large effects on the hyperpolarizabilities. This

electronegativity difference may restrict the delocalization of the π electrons and decrease the magnitude of the hyperpolarizabilities.

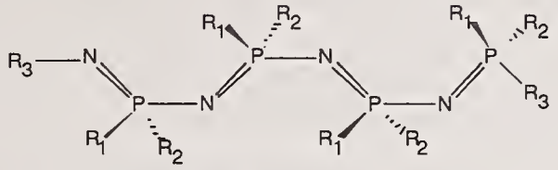

Figure 1. Schematic of phosphazene tetramer

We have calculated third order hyperpolarizabilities for a series of phosphazenes, $(X_2PN)_n$ (tetramer shown in Figure 1), as a function of its molecular parameters, that is, ligand substitutions, bond alternation and chain conformation. These effects of these parameters on the hyperpolarizability are compared to similar calculations for polyenes, and are interpreted in terms of the electronic structure and chemical properties of the phosphazene.

2.0 METHODS

The nonlinear optical properties of organic molecules are dominated by the conjugated π electrons, allowing them to be treated in a predictive sense by a π electron Hamiltonian for the determination of their hyperpolarizabilities[6]. The Huckel Hamiltonian was selected for this work based upon two features: 1) The chemical bonding of phosphonitrilic systems are dominated by π bonding interactions, and 2) The simplicity of the Hamiltonian allows also for calculation of the hyperpolarizabilities for a range of molecular parameters.

The Huckel Hamiltonian is a tight-binding π electron Hamiltonian allowing interactions between near neighbor atoms. In second quantized form, this Hamiltonian can be written as:

$$\hat{H} = \sum_{i,\sigma} \alpha_i c_{i\sigma}^{\dagger} c_{i\sigma} + \sum_{\substack{i \neq j \\ \sigma}} \beta_{ij} (c_{i\sigma}^{\dagger} c_{j\sigma} + c_{j\sigma}^{\dagger} c_{i\sigma})$$

where c_i ($c_i^{\dagger}$) is the destruction (creation) operator, which destroys (creates) a π electron on atom i. The second summation is restricted to bonded pairs of atoms i,j. Atomic p_z orbitals are assumed to be orthogonal, and molecular eigen states are formed as linear combinations of the atomic p_z orbitals. The ground state of the molecule is formed from the Slater determinant of the occupied molecular eigen states.

There are two sets of matrix elements which define the Hamiltonian, the Coulomb term α_i which is approximately equal to the ionization energy of a p electron atom i, and the hopping term β_{ij} describing the transfer of an electron from atom i to atom j. Ligand group effects at the phosphorus site were modelled by using a range of differences in the π orbital energy ($\Delta\alpha$) between the nitrogen and phosphorus centers. Structural parameters for the polyphosphazenes were taken from recent *ab initio* calculations for $(F_2PN)_4$. Because of the large role bond alternation plays in calculations of the hyperpolarizability for polyenes and the existence of bond length alternation in short chain length phosphazenes[4b,7], we have performed calculations

for a series of bond length alternations (0.00 $\beta_{PN} \equiv$ no bond alternation).

The third order hyperpolarizability can be determined by expanding the energy of the molecule in a Taylor series, and using perturbation theory to calculate the coefficients of the expansion. Thus, the third order hyperpolarizability can be shown to be:

$$\gamma_{\alpha\beta\lambda\delta} = P\Big\{ \sum_{i\,jk\neq o} \frac{\langle o|\mu_\alpha|i\rangle\langle i|\mu_\beta|j\rangle\langle j|\mu_\lambda|k\rangle\langle k|\mu_\delta|o\rangle}{(E_i-E_o)(E_j-E_o)(E_k-E_o)}$$

$$- \sum_{i\,j\neq o} \frac{\langle o|\mu_\alpha|i\rangle\langle i|\mu_\beta|o\rangle\langle o|\mu_\lambda|j\rangle\langle j|\mu_\delta|o\rangle}{(E_i-E_o)(E_i-E_o)(E_k-E_o)}$$

$$- 2 \sum_{i\,j\neq o} \frac{\langle o|\mu_\alpha|o\rangle\langle o|\mu_\beta|i\rangle\langle i|\mu_\lambda|j\rangle\langle j|\mu_\delta|o\rangle}{(E_i-E_o)(E_i-E_o)(E_k-E_o)}$$

$$+ \sum_{i\neq o} \frac{\langle o|\mu_\alpha|o\rangle\langle o|\mu_\beta|o\rangle\langle o|\mu_\lambda|i\rangle\langle i|\mu_\delta|o\rangle}{(E_i-E_o)(E_i-E_o)(E_i-E_o)} \Big\}$$

where α, β, λ, and δ refer to Cartesian coordinates in the molecular reference frame, P being the permutation operator for $\alpha, \beta, \lambda, \delta$; μ the one electron dipole operator, $|0\rangle$ is the ground state wavefunction, $|i\rangle$ $|j\rangle$ $|k\rangle$ are excited state wavefunction, E_o the ground state energy and E_i the excited state energy. Summations extend over all possible excited states. Because of the nature of the dipole operator, it is possible to restrict the first summation to single and double electron excitations. The latter three summations are restricted to single electron excitations.

3.0 RESULTS

The focus of the current investigation is to provide a theoretical basis for the nonlinear optical properties of phosphonitrilic polymers. While there are a number of similarities in the electronic properties between the organic and phosphonitrilic systems, one of the significant differences is the charge distribution along the polymer backbone. Although polarized chemical bonding situations are well known to exist in organic polymer systems, larger electronegativity differences are still possible when second row elements are included in the polymer backbone. The effects of these changes in the electron distribution and their interactions with bond alternation contributions are examined in the following discussion on the hyperpolarizability of the polyphosphonitrilic system.

Molecular Structure and Conformation

Crystallographic studies of the chloro-substituted polymer have shown the bonds to be of equal length within the resolution of the measurements[8], while recent *ab initio* calculations have shown the existence of bond length alternation in the small linear phosphonitrilic compounds. The existence or non-existence of bond alternation may be vital, as bond alternation has been firmly established as a principal factor in theoretical calculations of the

third order hyperpolarizabilities in polyenes. Previous theoretical calculations of the hyperpolarizability of trans and cis polyenes have shown that the magnitude of bond alternation plays a crucial role in deciding not only the magnitude but also the sign of the average hyperpolarizability[6]. The effects of possible bond alternation on the third order hyperpolarizability for a fixed difference in orbital energies ($\Delta\alpha=0.6\beta_{PN}$) are shown in Figure 2. The average hyperpolarizability per repeat unit for the cis-trans conformation is shown for five distinct amounts of bond alternation. The inclusion of bond length alternation has no qualitative effects on the third order hyperpolarizability, and causes only a slight decrease in magnitude. This is in contrast to the cis-trans polyenes, where greater degrees of bond alternation have been shown to increase the average hyperpolarizability.

The large amount of flexibility in the backbone of inorganic polymers gives rise to more than one possible conformation for the polymer. Both experimental and theoretical determinations of the hyperpolarizability of polyenes have shown that the hyperpolarizability

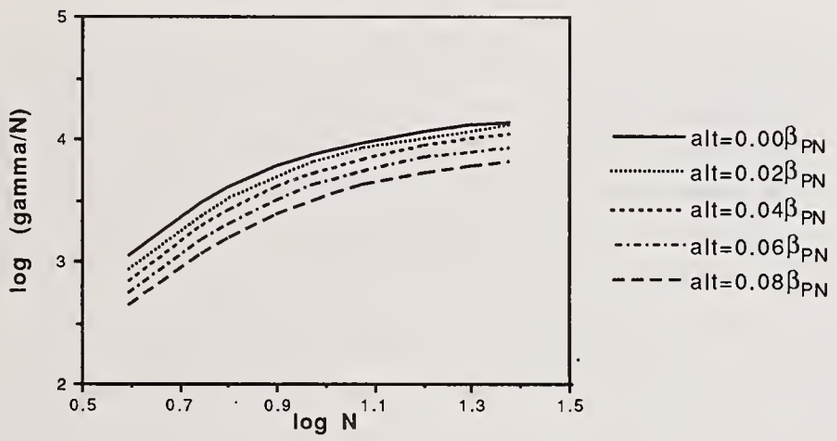

Figure 2. Hyperpolarizability per repeat unit of cis-trans conformation vs. number of repeat units. The energy difference between p_z orbitals is held constant at $\Delta\alpha=0.6\beta_{PN}$.

per repeat unit is dependent on the conformation of the polyene, but the magnitudes of the hyperpolarizability for the all-trans and cis-trans conformations are almost exactly identical per unit length along the primary axis of the molecule. Since inorganic systems commonly assume trans, cis-trans, and helical conformations due to their high backbone flexibility, the phosphazene conformation may also be significant in determining the hyperpolarizability of phosphazenes. To determine whether this same length dependence exists in phosphazenes, we have also performed calculations on the trans conformation of the polyphosphazene. The structural parameters were kept the same as for the cis-trans phosphazene. The hyperpolarizability per repeat unit for the trans conformation with varying degrees of bond

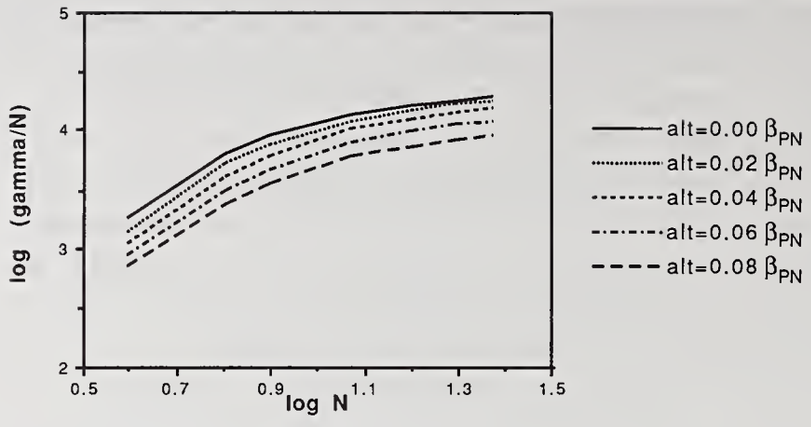

Figure 3. Hyperpolarizability per repeat unit of trans conformation vs. number of repeat units. The energy difference between p_z orbitals is held constant at $\Delta\alpha=0.6\beta_{PN}$.

alternation is shown in Figure 3. The difference in orbital energies was held constant at $\Delta\alpha=0.6\beta_{PN}$ to allow for direct comparisons with the cis-trans results in Figure 2. The magnitudes of the hyperpolarizability per repeat unit for the trans conformation are comparable to those of the cis-trans conformation indicating that the length of the conjugated system, and not the backbone conformation, is also the important feature for inorganic polymers.

The onset of saturation and the increase in nonlinearity per repeat unit determines the bulk nonlinearity for large molecular weight polymers. The rapid increase in the hyperpolarizability observed for small number of repeat units as shown in Figure 2 does not continue indefinitely, but instead quickly reaches saturation, where the nonlinearity becomes linearly dependent on the number of repeat units. Previous research in organic polymers has shown that the nonlinear optical properties saturate at a small number of repeat units, with the degree of bond alternation included in theoretical models being the key ingredient in determining when the models show saturation. The similarity of the shapes of the curves in Figures 2 and 3 indicate that bond alternation has no effect on the onset of saturation for the phosphonitrilic system. The decrease in the magnitude of the curves when bond alternation is included show that the existence of bond alternation in the polymer will decrease the magnitude of the bulk nonlinearity for either conformation of the polymer.

Electronic Interactions

The chemical bonding in phosphazenes has distinctly different electronic properties from organic polymers which may play a large role in determining their hyperpolarizabilities. Perhaps most important of these is the interaction of the substituent groups attached to the phosphorus with the in-plane and out-of-plane π bonding networks. The effects of varying substituent groups on the hyperpolarizability of phosphazenes was represented through variations in the energy of a p_z electron on the phosphorus atoms. Figure 4 shows the hyperpolarizability per repeat unit plotted against the number of repeat units for a number of energy differences, $\Delta\alpha$, between the nitrogen and phosphorus p_z orbitals, with the bond alternation held constant at $0.04\beta_{PN}$. Changing the energy difference between orbitals has a

very large effect on the hyperpolarizability. Decreasing the orbital energy difference increases both the magnitude of the hyperpolarizability and its rate of growth with increasing number of repeat units. This is most evident for the $\Delta\alpha$=0.0 curve, where the hyperpolarizability curve still exhibits significant curvature even for 60 repeat units.

The effects of conformation on these electronic influences were investigated by performing similar calculations on the trans conformation of the phosphazenes. Figure 5 shows the hyperpolarizability per repeat unit of the trans conformation plotted against the number of repeat units for a number of values for $\Delta\alpha$, with the bond alternation held constant at a value of $0.04\beta_{PN}$. The curves appear very similar to those of Figure 4, with the exception of for very small number of repeat units, where the $\Delta\alpha$=0.0 curve drops noticeably below that for the 0.5 eV curve.

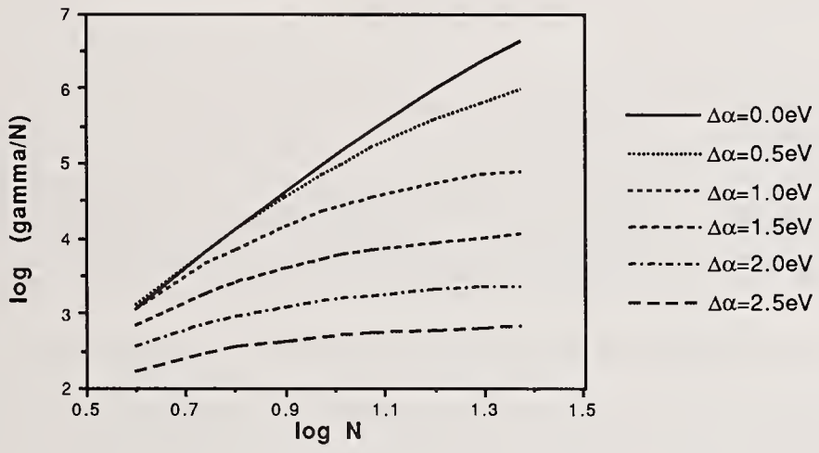

Figure 4. Hyperpolarizability per repeat unit of cis-trans conformation polyphosphazene vs. number of repeat units for various energy differences between p_z orbitals on nitrogen and phosphorus. The bond alternation is held at $0.04\beta_{PN}$.

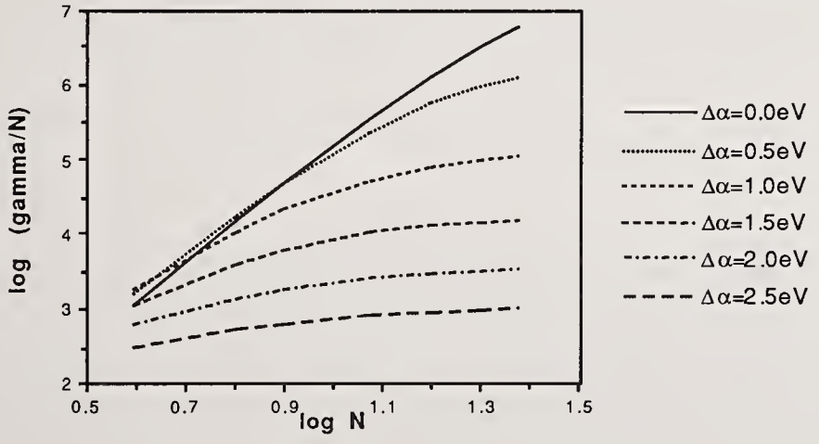

Figure 5. Hyperpolarizability per repeat unit of trans conformation polyphosphazene vs. number of repeat units for various energy differences between p_z orbitals on nitrogen and phosphorus. The bond alternation is held at $0.04\beta_{PN}$.

4.0 CONCLUSIONS

We have calculated the third order hyperpolarizability for phosphazenes of increasing length using the Huckel Hamiltonian and third order perturbation theory, using a series of possible bond alternations and representations of different substituent groups on the phosphorus. These calculations have shown that bond alternation does not appear to play a large role in determining the saturation of polyphosphazenes, in contrast to the results observed for organically based polyenes. Substituent effects on the electronic structure play crucial roles in determining the hyperpolarizability, with the largest magnitudes coming with weakly electron drawing groups.

5.0 REFERENCES

[1] The Pacific Northwest Laboratory is operated by Battelle Memorial Institute for the U.S. Department of Energy under contract DE-AC06 76RLO-1830.
[2] G.J. Exarhos and K. Crosby, Laser Induced Damage in Optical Materials: 1989, NBS Spec. Publ., (submitted).
[3] B.F. Levine and C.G. Bethea, J. Chem. Phys. 63, 2666 (1975).
[4] K.F. Ferris, P. Friedman, and D.M. Friedrich, Int. J. Quant. Chem. S22, 207, (1988); K.F. Ferris and C.B. Duke, Int. J. Quant. Chem. S23, (1989) in press.
[5] K.F. Ferris, S.M. Risser, A.K. Hanson, Proc. Mat. Res. Soc.: Electrical, Optical and Magnetic Properties of Organic Solid State Materials, ed. C. Liang, in press.
[6] S.M. Risser, S. Klemm, D.W. Allender and Michael A. Lee, Mol. Cryst. Liq. Cryst., 150b, 631 (1987).
[7] H.R. Allcock, N.M. Tollefson, R.A. Arcus, R.R. Whittle, J. Am. Chem. Soc. 107, 5166 (1985).
[8] H.R. Allcock in "Phosphorus-Nitrogen Compounds" New York: Academic Press (1972).

Manuscript received
3-8-90

RELATION BETWEEN n_2 AND TWO-PHOTON ABSORPTION

M. Sheik-Bahae, D.J. Hagan, E.W. Van Stryland,
T.H. Wei, A.A. Said, E. Canto, and A. Miller

Center for Research in Electro-Optics and Lasers
and the Department of Physics
University of Central Florida
Orlando, FL 32816

We present evidence from nonlinear refractive index measurements, two-photon absorption measurements, and four-wave mixing measurements on semiconductors showing that the bound electronic nonlinearity can be calculated from two-photon absorption dispersion via a simple Kramers-Kronig analysis. This analysis shows n_2 changing from positive to negative as the photon energy approaches the band-gap energy, consistent with observations. Additionally, this simple calculation, which assumes two parabolic bands, gives good agreement with measured values of n_2 in wide-gap dielectrics that are 2 to 3 orders of magnitude smaller than in semiconductors.

Key words: nonlinear refraction, two-photon absorption, Kramers-Kronig, four-wave mixing, semiconductors

Optical nonlinearities in semiconductors and transparent materials have been the subject of extensive studies during the past two decades. Of particular interest have been the third order effects in semiconductors. This interest has primarily dealt with the production of a real carrier plasma and the associated negative change in the refractive index. In this letter we will discuss the smaller and "faster" nonlinearities due to bound electrons which is positive for photon energies much less than the bandgap energy. The analogy in wide-gap dielectric materials is to self-focusing from the positive nonlinear refractive index n_2 (eg. self-focusing in glasses). Recently we found that measurements in semiconductors substantially above the two-photon-absorption (2PA) edge yield negative values for n_2.[1] This dramatic dispersion of n_2 can be partially explained using a nonlinear Kramers-Kronig (KK) relation between n_2 and the 2PA coefficient β, or between the real and imaginary parts of the third order nonlinear susceptibility $\chi^{(3)}$. The magnitude and dispersion of n_2 is of interest because of its importance in nonlinear propagation in fibers, fast optical switching, self-focusing and damage in optical materials, and optical limiting in semiconductors. Below, we describe our calculation of the bound electronic Kerr effect, n_2, and compare our results with data for a large number of materials, including semiconductors and dielectrics.

This n_2 arises from the real part of $\chi^{(3)}$, and is defined through the refractive index change Δn, where

$$\Delta n(\omega) = \gamma(\omega)\, I_\omega = \frac{n_2(\omega)}{2}|E_\omega|^2 , \qquad (1)$$

with I_ω and E_ω being the irradiance and electric field at frequency ω respectively and $n_2=(2\pi/n_0)\mathrm{Re}\{\chi^{(3)}\}$. The linear refractive index is n_0, and γ and n_2 are related by $n_2(\mathrm{esu})=(cn_0\gamma/40\pi)(\mathrm{MKS})$ with c the speed of light.

Most theoretical calculations of n_2 have been confined to the zero frequency limit.[2-6] Semi-empirical formulations have been most successful in predicting the magnitude of n_2.[5,6] For example, the formula obtained by Boling, Glass and Owyoung (BGO) in relating n_2 to the linear index (n_0) and the dispersion of n_0 in terms of the Abbe number has been successfully applied to a large class of transparent materials.[6,7] Their theory predicts the low frequency magnitude of n_2. We describe a KK method of calculation of n_2 that predicts the dispersion as well as the magnitude of n_2. This calculation assumes that 2PA gives the dominant contribution to n_2 and that other contributions from Raman and the AC Stark effect or virtual band-blocking are ignored. We will return to this assumption later.

Based on the principle of causality, the KK transformation states that a change in the refractive index (Δn) at ω is associated with changes in the absorption coefficient ($\Delta\alpha$) throughout the spectrum (ω') and vice versa. We write this as:

$$\Delta n(\omega;\xi) = \frac{c}{\pi}\int_0^\infty \frac{\Delta\alpha(\omega';\xi)}{\omega^2-\omega'^2}\,d\omega', \tag{2}$$

where c is the velocity of light in vacuum and ξ is a parameter (or parameters) denoting the "cause" of change in the absorption. The cause need not be of optical origin but of any external perturbation such as thermal excitation, etc. For cases where an electron-hole plasma is injected, the consequent change of absorption has been used to obtain the plasma contribution to the refractive index. In this case, the ξ parameter is taken as the change in plasma density (ΔN) regardlesss of the mechanism of generation of the plasma or the pump frequency.[8] In the case of 2PA the change is due to the presence of a pump field at Ω (ie. $\xi=\Omega$). The corresponding nonlinear refraction is $\Delta n(\omega,\Omega)$, which gives the dispersion of the index change with ω. For the case of self-refraction, $\omega=\Omega$, and this gives what is commonly referred to as n_2. Van Vechten and Aspnes [4] obtained the low frequency limit of n_2 from a similar KK transformation of the Franz-Keldysh electro-absorption effect where, in this case, ξ is the DC field. The bound electronic contribution to $\chi^{(3)}$ can originate from various absorptive counterparts that are quadratic functions of the pump field. Effects of this order may include 2PA, the electronic Raman effect, and the optical Stark effect. Here we consider only 2PA.

A wealth of experimental and theoretical work regarding 2PA in semiconductors and crystalline materials exists. In accordance with the predictions derived from either second order perturbation theory [9,10] or a Keldysh-type formalism [11], the 2PA coefficients of the semiconductors studied in Ref. [12] were found to be in good agreement with the theoretical expression given as:

$$\beta(2\omega') = K\frac{\sqrt{E_p}}{n_0^2 E_g^3}F_2(2\hbar\omega'/E_g)\ , \tag{3}$$

where K is a material independent constant and E_p (related to the Kane momentum parameter, a momentum matrix element) is nearly material independent and posseses a value of $\simeq$21 ev for most direct gap semiconductors. These data are shown in Fig. 1. Note $\beta=(4\pi\omega/n_0)\mathrm{Im}\{\chi^{(3)}\}$. The function F_2 is only a function of the ratio of the photon energy $\hbar\omega'$ to E_g (ie. the optically coupled states). The functional form of F_2 reflects the assumed band structure and the intermediate states considered in calculating the 2PA transition rate. The simplest model assumes a pair of isotropic and parabolic bands and intermediate states that are degenerate to initial (valence) or final (conduction) states. Neglecting the Coulomb interaction, this simple formalism yields:[10]

$$F_2(2x) = \frac{(2x-1)^{3/2}}{(2x)^5} \qquad \text{for } 2x>1\ . \tag{4}$$

Figure 2 shows the dispersion of β as given by Eq. 4.

The best fit to the data of Ref. 12 using Eqs. 3 and 4 gave $K=3.1\times10^3$ (see the line in Fig. 1) in units such that E_p and E_g were in eV and β was in cm/GW, while theory gave 5.2×10^3.[9] When nonparabolicity was included the average β was 26% lower than theory; however, the frequency dependence of β changed very little. Interestingly, Eqs. 3 and 4 also give a fair estimate of β for a number of transparent materials measured using the 3rd and 4th harmonics of picosecond Nd:YAG laser pulses.[13,14]

Equations 3 and 4 pertain to a degenerate case where the two photons involved are of the same frequency and source. For a KK transformation the nondegenerate 2PA coefficient for two distinct frequencies is needed (ie. Ω the "cause" and ω' the integration variable in Eq. 2). Extending the same simple model to obtain the non-degenerate 2PA coefficient has led to dispersion functions that are afflicted with "infrared divergences".[15,16] This has been a common problem originating from the use of the $\mathbf{A}\cdot\mathbf{p}$ perturbation to calculate the bound electronic nonlinear susceptibilities in solids.[15]

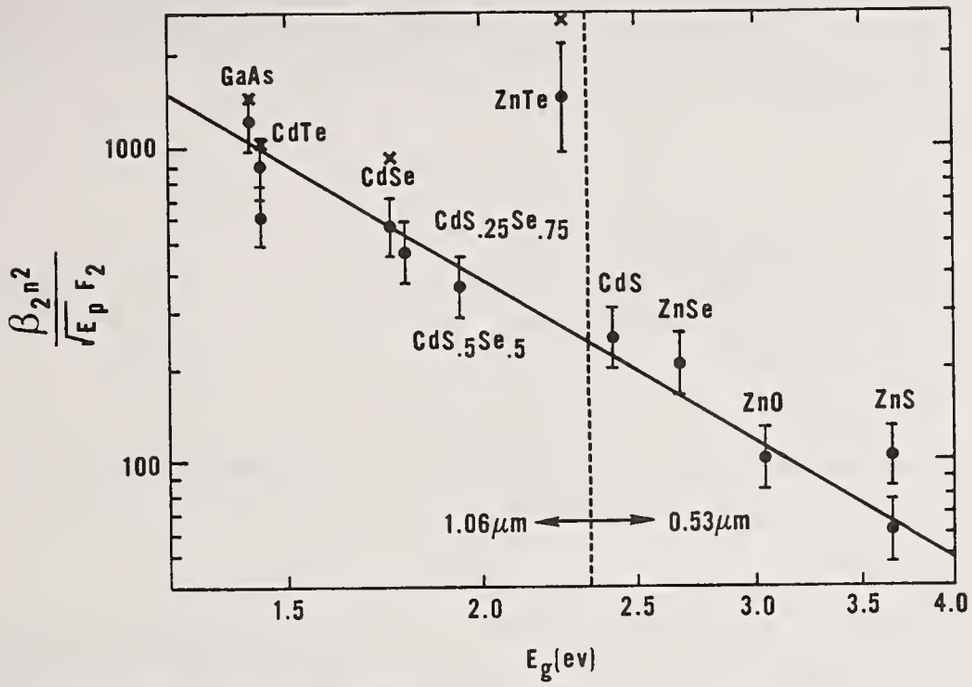

Figure 1. A log-log plot of the scaled value of β as a function of E_g to show the E_g^3 dependence. The line is a fit to the data using the F_2 of Eq. 4.

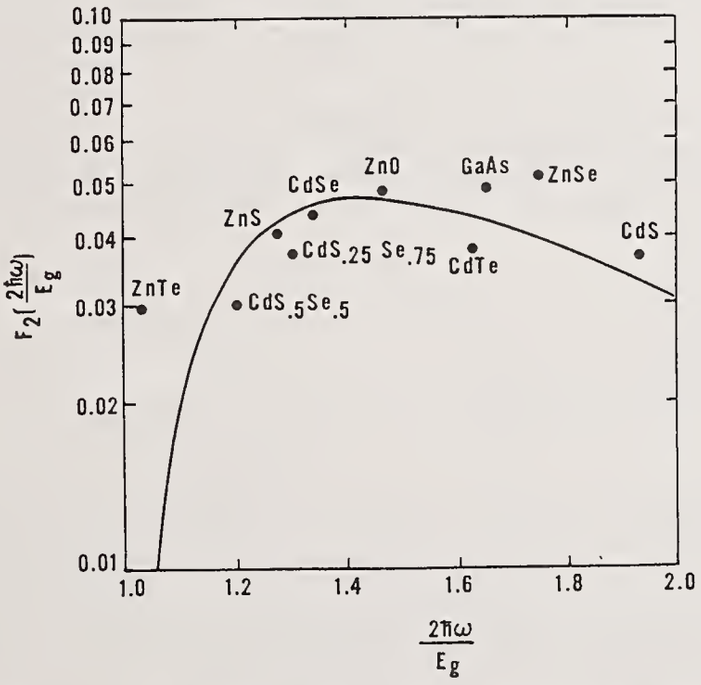

Figure 2. A semilogarithmic plot of F_2 as a function of $2\hbar\omega/E_g$ with the data of Fig. 1 superimposed.

Although special cases have been considered [17], a general theory that would rigorously address the proper scaling and dispersion of the non-degenerate 2PA is yet to be developed. For this reason we assume that the dispersion function F_2 for the nondegenerate 2PA coefficient, $\beta(\omega',\Omega)$, can be given by Eqn. 4 modified with the substitution of $2\hbar\omega'$ by $\hbar\omega'+\hbar\Omega$; thus, $F_2(2x)$ is replaced by $F_2(x'+X)$, where $x'=\hbar\omega'/E_g$ and $X=\hbar\Omega/E_g$, and $x'+X>1$. This substitution is strictly valid only for $x'=X$, however, the predictions resulting from this substitution show remarkable agreement with the data, as will be shown.

The change of the absorption spectrum (at ω') induced by the presence of a strong pump at Ω can be written for 2PA as $\Delta\alpha(\omega';\Omega) = \beta(\omega';\Omega)I_\Omega$, where I_Ω denotes the irradiance of the pump field. Similarly the change in refractive index at ω induced by the presence of a strong pump at Ω can be written as $\Delta n(\omega;\Omega) = \gamma(\omega;\Omega)I_\Omega$. Applying the KK transformation Eq. 2 at this point yields a relation between $\gamma(\omega;\Omega)$ and $\beta(\omega',\Omega)$. Using Eq. 3 with $F_2(x'+X)$ in Eq.2 we obtain for the degenerate case ($\omega=\Omega$):

$$\gamma = K \frac{\hbar c\sqrt{E_p}}{2n_0^2 E_g^4} G_2(\hbar\omega/E_g) , \tag{5}$$

where the dispersion function $G_2(x)$ is given by,

$$G_2(x) = \frac{-2+6x-3x^2-x^3-3/4x^4-3/4x^5+2(1-2x)^{3/2}\Theta(1-2x)}{64x^6} , \tag{6}$$

with $\Theta(x)$ being the unit step function.

Using the value of K obtained from the 2PA measurements, E_p=21 eV, and converting from γ to n_2, we obtain the final expression for n_2 as:

$$n_2(\text{esu}) = K' \frac{G_2(\hbar\omega/E_g)}{n_0 E_g^4} , \tag{7}$$

where $K'=3.4\times10^{-8}$ and E_g is in ev. Equation 7 explicitly shows an E_g^{-4} band-gap dependence for the magnitude of n_2, and the sign and the frequency dispersion of this quantity are given by the simple closed form function G_2. We can now readily compare the predictions of this theory with experiment.

Utilizing a newly developed technique (Z-scan) for n_2 measurements [1, 18] that can determine its magnitude and sign, we have measured n_2 for several materials at 1.06 and 0.53 μm. This simple technique has been shown to be an accurate and sensitive tool for measuring n_2 even in the presence of nonlinear absorption. We find, for example, in materials such as ZnSe at 0.53 μm, where 2PA is present, n_2 is negative, but that the sign changes at 1.06 μm.

Picosecond degenerate-four-wave-mixing (DFWM) measurements show this third order response (time resolution limited by the 30 ps pulsewidth), while at higher irradiances the slowly decaying 2PA generated free-carrier refraction is seen.[19] Figure 3 shows the DFWM experimental geometry. The DFWM signal as a function of backward pump delay is shown in Figure 4. This signal shows a "fast" third order nonlinearity followed by a slowly decaying "fifth" order nonlinearity.

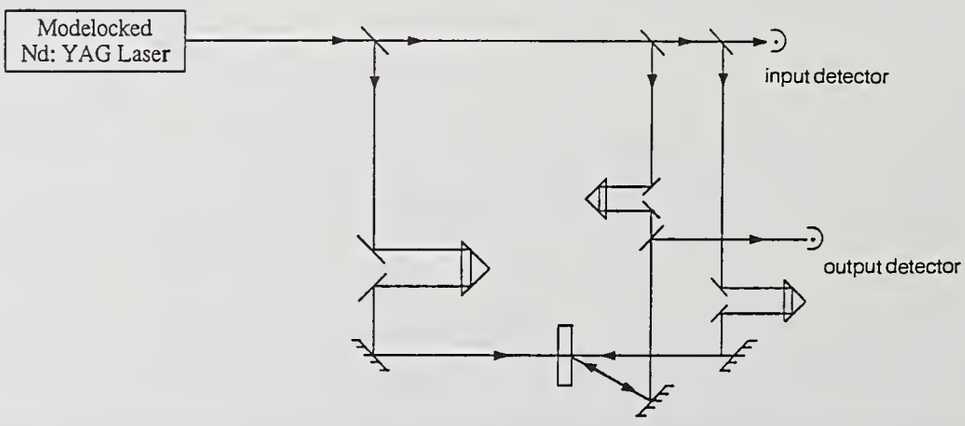

Figure 3. A schematic of the experimental geometry of the degenerate-four-wave-mixing experiment.

The order of the nonlinearity was determined by fixing the temporal delay at a) zero delay, or at b) long delay, and simultaneously varying the input energy of all three input beams. A log-log plot of the DFWM signal versus input energy (or irradiance) shows straight lines having slopes of three at zero delay (a) and five at long delay (b) as shown in Figure 5. The fast response of the third order nonlinearity at zero delay (time response limited by the 30 picosecond laser pulsewidth) indicate its bound electronic origin. The higher order nonlinearity observed at long delays is the

plasma nonlinearity due to carriers produced by 2PA, a sequential $Im\{\chi^{(3)}\}$:$RE\{\chi^{(1)}\}$ effect. This appears as an effective fifth order nonlinearity.

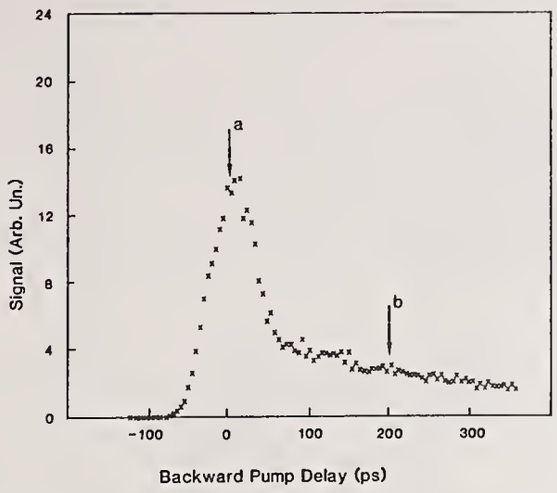

Figure 4. A plot of degenerate-four-wave-mixing signal as a function of backward pump beam temporal delay using the geometry of Figure 3.

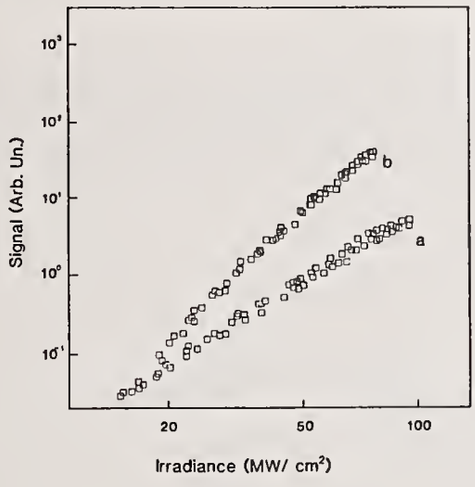

Figure 5. A log-log plot of the DFWM signal at delays a) and b) of Fig. 4 as a function of input with the energy of all three input beams varied simultaneously.

A graphical comparison of the data for n_2 is given in Figure 6 which shows the band-gap scaling law and in Figure 7 where the dispersion and sign of n_2 are explicitly compared to the G_2 of Eq. 7. Many of the experimental values for large gap optical crystals are obtained from recent measurements by Adair et.al. using a "nearly degenerate-three-wave-mixing" scheme.[7] We have also measured n_2 in a number of these wide-gap dielectrics using the Z-scan method and have obtained comparable results. The dispersive behavior of n_2 in Figure 6 is seen to be most significant within the range $E_g/2<\hbar\omega<E_g$ where 2PA is present and relatively small in the low frequency limit $\hbar\omega<<E_g$.

A noticeable difference between the magnitude of the measured and calculated values is seen near the one photon absorption edge. Considering the simplicity of the model in deriving Eq. 7, such deviations are not unexpected. The measured large negative values of n_2 as compared to the calculated values near the fundamental absorption edge may be attributed to the refraction due to the "optical Stark effect" which is also referred to as "virtual band-blocking" and has been ignored in our calculations. The contribution of this mechanism to the electronic nonlinear susceptibility has been shown to have a strong band-gap resonance and follows the same scaling as given in Eq. 7.[20] This effect, which is negative for all frequencies below the band-gap, vanishes quickly for longer wavelengths ($\hbar\omega<E_g/2$) and has negligible contribution in the transparency region of the material.

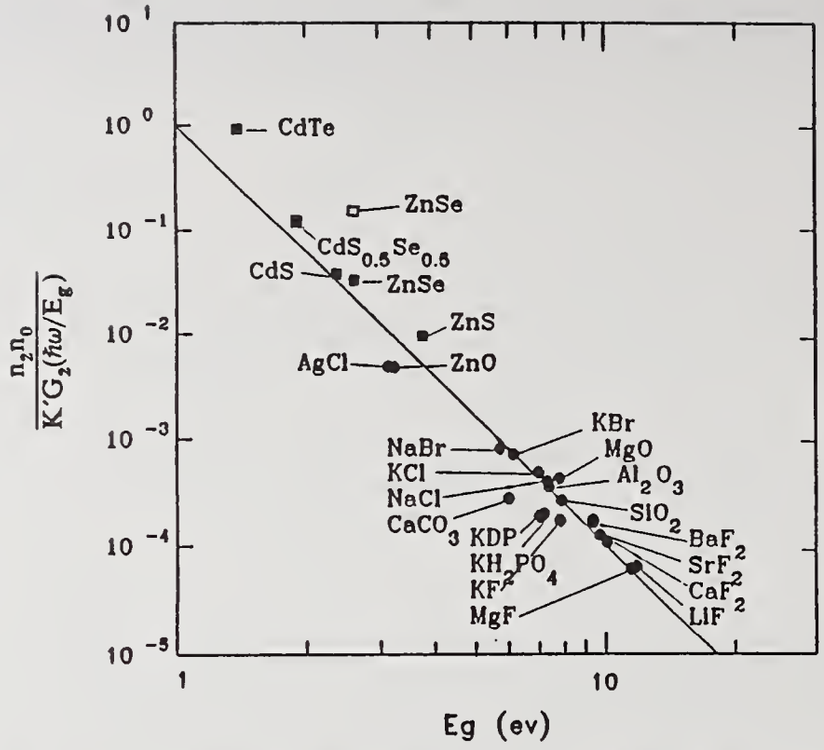

Figure 6. A log-log plot of the scaled n_2 versus energy gap (E_g) for a large class of optical materials. The solid line represents the theoretical result as obtained from Eq.(7) with no adjustable parameters and has a slope of -4. The solid circles represent the data from ref.[7] all obtained at λ=1.06 μm. The remaining data are our measurements using the Z-scan technique taken at λ=1.06 μm (solid squares) and at λ=.532 μm (open squares).

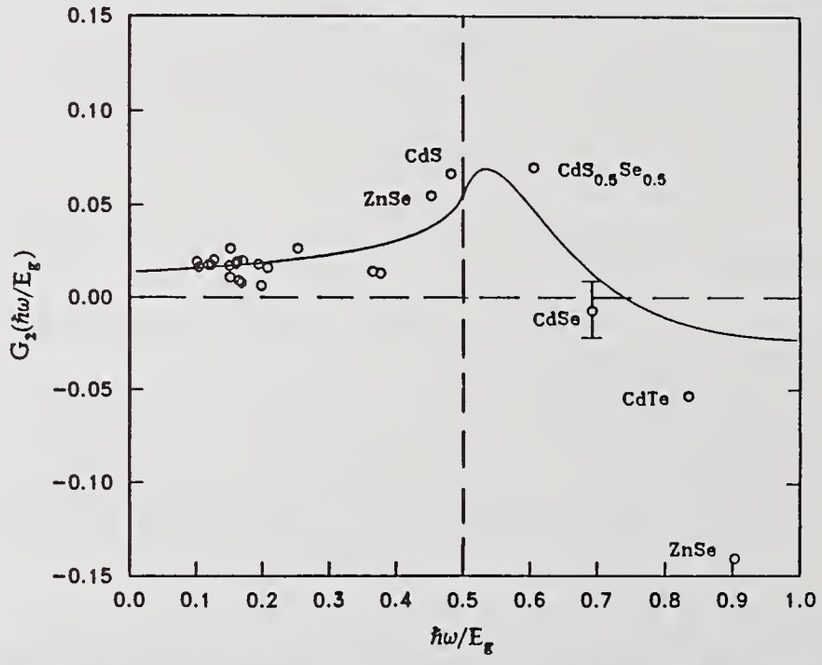

Figure 7. The calculated dispersion function G_2 versus $\hbar\omega/E_g$. The same n_2 data as in Figure 6, here scaled as $n_2 n_0 E_g^4/K'$, are compared with the theory. Only the semiconductor data within the highly dispersive region are labeled for comparison.

[16] G.D. Mahan, "Theory of Two-Photon Spectroscopy in Solids," Phys. Rev. 170, 825-838(1968).

[17] F.V. Bunkin, "Two Quantum Transitions in Optics," Sov. Phys. JETP, 23, 1121-1123(1966).

[18] M. Sheik-bahae, A.A. Said, and E.W. Van Stryland, "High Sensitivity, Single Beam n_2 Measurements," Opt. Lett. 14, 955-957(1989).

[19] D.J. Hagan, E. Canto, E. Miesak, M.J. Soileau, and E.W. Van Stryland, "Picosecond Degenerate Four Wave Mixing Studies in ZnSe," paper, TUX, pp.160, Technical Digest of the Conference on Lasers and Electro-Optics, Anaheim, CA, OSA Technical Digest Series, No. 7, 1988.

[20] B.S. Wherrett, A.C. Walker, and F.A.P. Tooley, "Nonlinear Refraction for CW Optical Bistability," in Optical Nonlinearities and Instabilities in Semiconductors, H. Haug, eds. (Academic Press, Inc. 1988.) pp.239-272.

Manuscript received
3-20-90

Photoconductivity of ZnS and ZnSe

B. E. Mason and C. D. Marrs

Physics Division, Research Department
Naval Weapons Center, China Lake, California 93555-6001

ZnS and ZnSe are important materials for laser windows and optical thin-film coatings. Understanding the laser-induced damage mechanism in optical materials provides the ability to make improved damage-resistant materials. Photoconductivity (PC) techniques have demonstrated the capability to provide information on carrier production that can lead to electron avalanche by single or multiple photon absorption processes produced by a high-intensity laser beam. A study of the linear PC using a monochromated Xe lamp and the nonlinear PC using various lasers as excitation sources will be presented for chemically vapor-deposited ZnS and ZnSe.

Key words: charge-production; CVD ZnS; CVD ZnSe; electron avalanche; impurity absorption; laser-induced damage; multiphoton absorption; photoconductivity

1. Introduction

ZnS and ZnSe are popular materials for optical components in high-power laser systems. Owing to the 3.8 and 2.7 eV band gaps for ZnS and ZnSe, respectively, excellent transmittance from the visible to IR and relatively high laser damage thresholds are observed. These properties make ZnS and ZnSe ideal materials for windows and coating materials in high-power laser systems. However, laser damage in these materials is observed by photons with less energy than the band gap energy. This damage may be due to charge-producing crystalline defects, even if present in low concentrations.

Photoconductivity (PC) measurements are a sensitive and nondestructive method of probing these charge-producing defects [1]. This paper presents and discusses the results obtained from linear and nonlinear PC measurements.

2. Samples

The samples used in this study were chemically vapor-deposited (CVD) ZnS and ZnSe and were supplied by CVD, Inc. The band gap energy of ZnS is 3.8 eV (326 nm), and the band gap energy of ZnSe is 2.7 eV (459 nm).

Sample-purity information was not available; however, typical impurities found in these CVD materials are Cu, Fe, Mg, Ni, Cr, Co, Al, Mn, Cl, Br, and I. The concentrations of these impurities range from sub-ppm to 3 ppm. The ZnS samples were 1 x 1 x 0.250 in. with all surfaces polished. The ZnSe sample was cylindrical in shape with a diameter of 1.5 in. and a thickness of 0.375 in. Two flat surfaces were polished on the edges at 180° from

each other to allow laser radiation to exit and enter the sample without any focusing of the beam by the sample.

3. Experimental Details

The experimental arrangement used in the PC measurements is illustrated in figure 1. The DC circuit is designed to measure photocurrents produced when photons are absorbed by crystalline or impurity-related defects and produce free charge carriers. The wide band gaps of ZnS and ZnSe crystals ensure that the electrodes are nonohmic, i.e., blocking electrodes. The photocurrent measured is the displacement current associated with the motion of photo-generated charge in the electric field produced by the bias voltage (VDC). The magnitude of VDC varied from -30 V for ZnSe to -1000 V for ZnS.

The samples investigated were mounted in an aluminum vacuum chamber that was typically evacuated to 10^{-5} torr to prevent electrode-to-electrode breakdown along the edges of the sample. The electrode arrangement was the same as that used by Lee *et al.* [2]. The ground electrode was brass, while the front or biased electrode was 28-mesh etched nickel screen supported by an aluminum ring. The nickel mesh provided a uniform electric field across the sample. Together, the sample holder and aluminum vacuum chamber constituted a guard ring to minimize the effects of ground loops.

For the linear PC measurements, light from a 450-W UV-enhanced Xe arc lamp was dispersed with a 2.6-nm bandpass McPherson 218 scanning monochromator before entering the vacuum chamber through a fused-silica window. The monochromator used in these measurements was a grating instrument, which necessitated the use of optical cut-off filters to prevent false PC readings from higher order wavelengths. Monochromated light from the arc lamp illuminated the ZnS and ZnSe samples through the nickel mesh electrode. By applying the DC voltage with the negative potential on the nickel electrode, any photoelectrons generated from the nickel mesh would be rejected, minimizing interference in detecting small internally generated photocurrents. The photocurrent was measured with a Keithley 642 electrometer. By interfacing the spectral position of the monochromator to the x-axis of an x-y recorder and using the electrometer to drive the y-axis of the recorder, a spectral scan of the photocurrent vs wavelength could be generated. The spectral scans presented and discussed have been normalized to the spectra of the Xe arc lamp. This normalized photocurrent is the photoresponse of the sample.

The nonlinear PC measurements were made using a Nd:YAG laser that was capable of emitting 1.064- and 0.532-μm radiation. The pulse width of the laser was 16.6 ns operating at 1.064 μm and 16.2 ns operating at 0.532 nm. The beam was passed through the fused silica window and focused to a spot size of 40 μm in the center of the sample. By using neutral density filters, the laser pulse energy was varied and monitored by a Gentek pyroelectric energy meter. By varying the laser pulse energy and recording resulting peak photocurrent, the peak photocurrent-vs-laser pulse energy curves were generated.

4. Discussion

4.1. Linear PC Data

Data presented here are in the form of linear x-y plots displaying normalized photocurrent or photoresponse vs wavelength. The wavelength range is 300 to 800 nm for the ZnS sample and 400 to 800 nm for the ZnSe sample.

The linear ZnS data are shown in figure 2. Two prominent peaks are located at 345 and 378 nm, followed by a broad spectral response from approximately 450 out to 800 nm. The origin of the peak at 345 nm is unknown at the present time. Georgobiani *et al.* [3] suggest the peak at 378 nm is due to an acceptor defect. This defect consists of a hole trapped at a Zn vacancy. The broad spectral response from 450 to 800 nm is associated with impurities, since the photoresponse occurs at energies below the band edge of ZnS. The specific impurities are unknown at the present time; however, Qidwai and Woods [4] suggest that Cu may be a contributor to the absorption-carrier production in this region.

The linear ZnSe data are shown in figure 3. Two prominent peaks are observed at 475 and 515 nm, followed by a monotonically decreasing spectral response. Lewis and Arthur [5] have attributed the peak at 475 nm to a transition from a Na acceptor defect to an unknown donor level. They observed this peak during photoluminescence excitation spectrum (PES) studies of ZnSe. In Lewis' model, a Zn site is occupied by a substitutional Na ion. However, Jones and Woods [6] report the same peak in their PES studies of ZnSe, which they attribute to a transition from the valence band to an acceptor state below the conduction band edge. It is suggested that the acceptor state may be associated with Cl ions. More work will be required to determine the correct model. The peak at 515 nm has been observed also in the PES studies of Lewis and Arthur. These authors suggest that the peak results from a deep acceptor site that consists of a substitutional Cu ion on a vacant Zn site. The spectral region of the monotonically decreasing photoresponse corresponds to the same region observed by Lewis in his PES studies and is attributed to the Cu-related defect.

4.2. Nonlinear PC Data

Nonlinear PC processes obey the equation

$$i_p \propto E_B^m$$

until electron avalance or laser-induced damage occurs, where i_p is peak photocurrent, E_B is laser pulse energy and m is the order of the absorption process. Therefore, data presented here are in the form of log-log plots that display peak photocurrent vs laser pulse energy, where m is the slope. Laser wavelengths of 1.064 and 0.532 μm were used with each sample in the nonlinear study.

4.2.1 Nonlinear ZnS Data at 1.064 μm

The plotted data in figure 4 show the laser pulse energy covering three decades and the peak photocurrent covering three decades. At pulse energies approximately less than 1.5×10^{-3} J, m = 0.61, indicating the presence of charge-producing defects that absorb 1.064-μm radiation. The nonlinear increase of photocurrent with increasing laser pulse energy above this value, suggests the onset of multiphoton-induced photocurrent. The band gap of ZnS is 3.8 eV, which corresponds to 3.3 times the photon energy of 1.064-μm radiation. The near vertical slope (m = 8.9) also suggests the onset of electron avalanche. At a laser pulse energy of approximately 2.2×10^{-3} J, laser-induced damage had occurred.

4.2.2. Nonlinear ZnS Data at 0.532 μm

The nonlinear PC data for ZnS is shown in figure 5. As for 1.064-μm excitation, the low pulse energies produce a slope less than 1 (m = 0.73), indicating charge production by defect states. The linear PC scans show significant photoresponse at 0.532 μm (see fig. 2). No nonlinear increase of photocurrent with increasing laser pulse energy is observed up to the energy producing damage to the sample. The band gap of ZnS corresponds to 1.6

times the photon energy of 0.532-μm radiation. If electron avalanche occurs, no greater than two-photon absorption would be required to generate valence-to-conduction-band transitions. Thus, the onset to avalanche would not require a dramatic increase in slope. This suggests that avalanche (damage) initiated from low-order absorption processes.

4.2.3. Nonlinear ZnSe Data at 1.064 μm

At low pulse energies, no observable PC signal was detected. This suggests that single-photon absorption producing free carriers does not occur at 1.064 μm. However, a PC signal was observed at high pulse energies, but the sample had sustained catastrophic damage. The fact that a PC signal and catastrophic damage were observed simultaneously supports electron avalanche as a damage mechanism. Since the band gap energy of ZnSe is 2.3 times the photon energy of 1.064-μm radiation, multiphoton (i.e., two-photon) absorption would be required to generate free carriers.

4.2.4. Nonlinear ZnSe Data at 0.532 μm

The linear PC of ZnSe shows a significant photoresponse at 0.532 μm. The nonlinear ZnSe data at 0.532 μm are shown in figure 6. At low laser pulse energies, m = 0.84, indicating free-carrier production from defects absorbing 0.532-μm radiation. With increasing laser pulse energies, no nonlinear increase in photocurrent was observed up to the energy producing damage to the sample. The band gap energy of ZnSe is 1.2 times the photon energy of 0.532-μm radiation. Analogous arguments to those presented for ZnS with 0.532-μm radiation incident also apply to ZnSe.

5. Summary

Linear and nonlinear photoconductivity have been observed in ZnS, while only linear photoconductivity has been observed in ZnSe.

Linear photoconductivity in ZnS and ZnSe is attributed to impurity-related defects. Cu is suggested as the prevalent impurity in both materials and the source of the 415- to 800-nm broad response in ZnS and the 515-nm peak in ZnSe. The 378-nm peak in ZnS is attributed to an acceptor defect associated with a Zn vacancy, while the origin of the peak at 345 nm is currently unknown. The literature suggests that the 475-nm peak in ZnSe may be associated with a Na- or Cl-ion-related defect.

Nonlinear photoconductivity, where $i_p \propto E_B{}^m$, shows charge generation at both 1.064 and 0.532 μm in ZnS and ZnSe. In ZnS at 1.064 μm, higher laser pulse energies yield a slope (m) >>1, indicating multiphoton avalanche charge production. For ZnS at 0.532 μm and ZnSe at 1.064 and 0.532 μm, data support the initiation of avalanche from low-order absorption processes, where $m \leq 2$.

6. Future Work

The direction of the future work will be to gain a better understanding of the morphology of the laser damage process.

A comparison of the photoresponse of crystalline and CVD materials (doped and pure) will be made to observe any changes in the linear damage thresholds PC spectra and the shape/behavior of the nonlinear PC spectra as related to the laser-damage thresholds.

Photoluminescence studies will be performed to gain an insight into the absorption mechanisms of the impurity related defects in crystalline and CVD (doped and pure) ZnS and ZnSe.

The temperature range of the PC experiments will be extended from 95-300 K in order to measure activation energies of the defects.

Time domain studies of carrier production will provide the time scale of the laser damage process in crystalline at CVD (doped and pure) ZnS and ZnSe.

7. References

[1] O'Connell, R. M.; Marrs, C. D. "Photoconductivity study of charge-producing defects in CaF_2," presented at the 20th Symposium on optical materials for high power lasers, Boulder, CO; 1988 October 26-28. (Proceedings in process.)

[2] Lee, R. S.; Merklin, J. F.; Marrs, C. D.; Richter, M. H. "Impurity photoconductivity of γ-irradiated LiF," Phys. Status Solidi (b) 103; 605; 1981.

[3] Georgobiani, A. N.; Maev, R. B.; Ozerov, Yu. V.; Strumban, E. E. "Deep traps in zinc sulfide single crystals," Bull. Acad. Sci. USSR, Phys. Ser. 40; 181-184; 1976.

[4] Qidwai, A. A.; Woods, J. "Deep level in In and Ga doped ZnS," J. Cryst. Growth 59; No. 1-2; 217-222; September 1982.

[5] Lewis, K. L.; Arthur, G. S. "Surface and free carrier absorption processes in CVD zinc selenide," in Laser induced damage in optical materials: 1982, Bennett, H. E.; Guenther, A. H.; Milam, D.; Newnam, B. E., ed. 1982 November 16-17; Boulder, CO. Nat. Bur. Stand. (U.S.) Spec. Publ. 669; 1984 January. Pp. 86-101.

[6] Jones, G.; Woods, J. "Luminescence of self-activated and copper-doped zinc selenide," J. Cumin.; 9(5); 389-405; 1974.

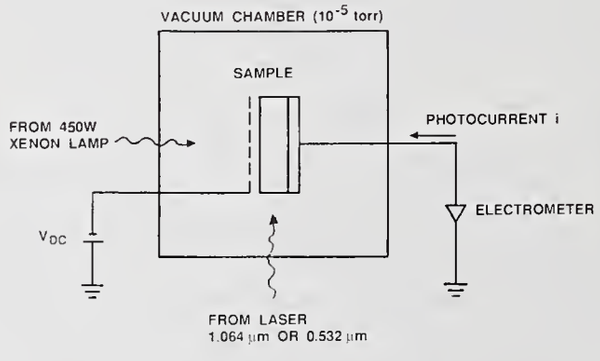

Figure 1. Experimental arrangement used in the photoconductivity measurements. Excitation source was either the xenon lamp or the Nd:YAG laser.

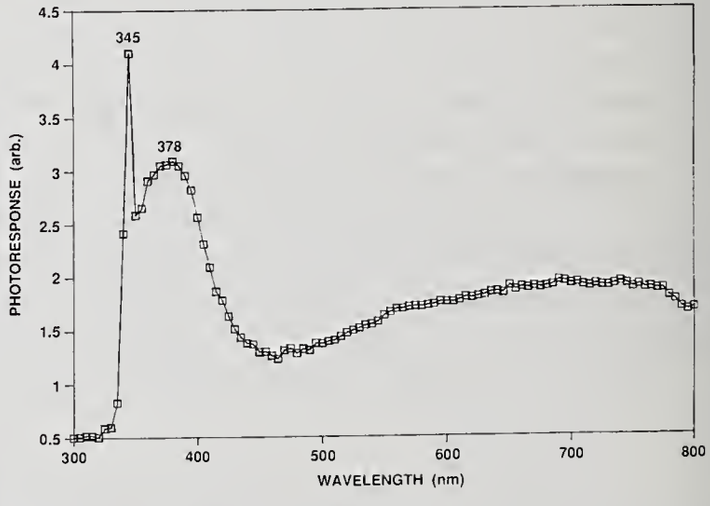

Figure 2. Linear PC spectrum from the CVD ZnS sample, bias voltage - 1000 VDC.

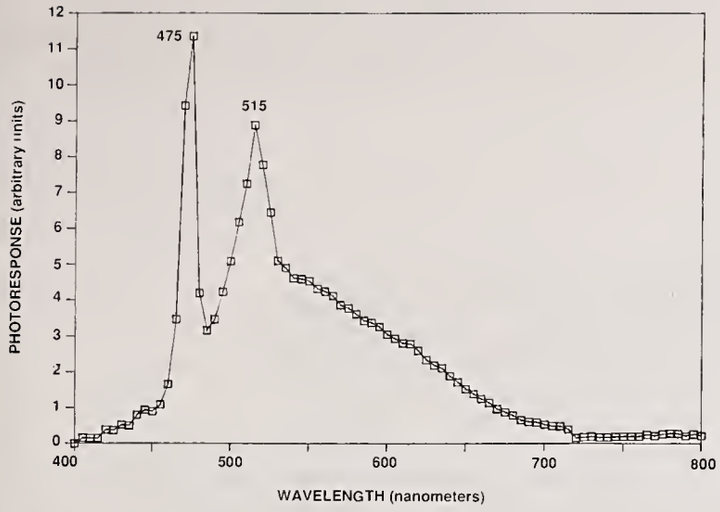

Figure 3. Linear PC spectrum from the CVD ZnSe sample, bias voltage - 30 VDC.

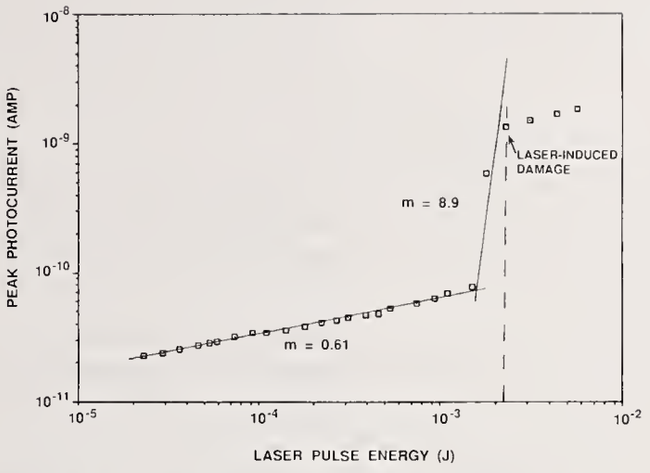

Figure 4. Nonlinear PC data from the CVD ZnS sample obtained with 1.064-μm radiation focused inside the sample.

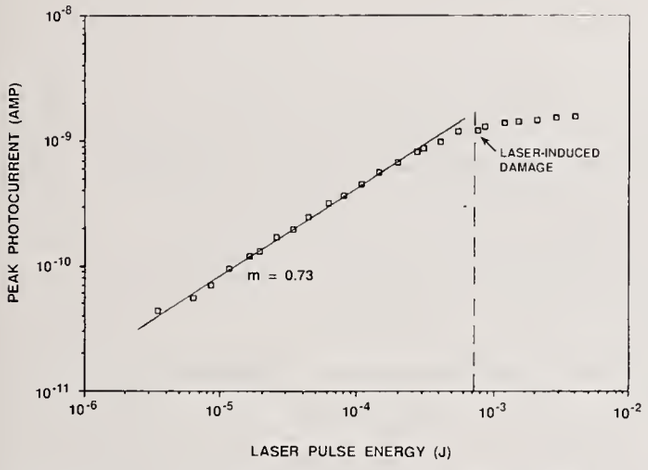

Figure 5. Nonlinear PC data from the CVD ZnS sample obtained with 0.532-μm radiation focused inside the sample.

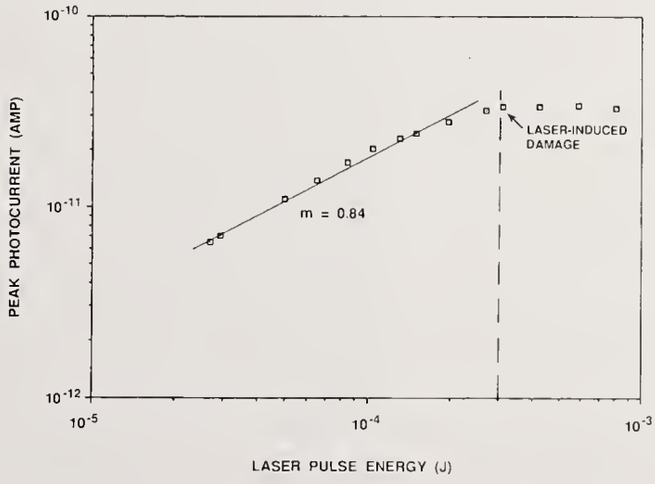

Figure 6. Nonlinear PC data from the CVD ZnSe sample obtained with 0.532-μm radiation focused inside the sample.

COMMENTS

Question: Could you say something about the long term environmental degradation of the optical properties of these materials, particularly the effect of solar radiation.

Answer: Right, let me point out two things. First of all, when we make these polymers we worry about residual organic solvents that might be deposited in the polymer films. For this reason we put the polymers we take in an oven at between 50°C and 100°C for varying amounts of time. We saw no change in the optical properties as a result of this heating. Secondly, we took some of these polymers and exposed them to the laboratory atmosphere for a period of a month. We then measured their optical properties and found that there was no discernable change in the fringe spacing over that period. I indicated that some of these polymers are soluble in water but they also form very nice films. One of the good attributes of the polymers is that once you get them down it is difficult for solvent molecules to grab onto them to pull them in solution, which attests to their enhanced stability.

Question: When you see the size of this polymer have you done the molecular size distribution?

Answer: The only thing that we've done is high performance liquid chromotrophy to try and get an idea of what the molecular weight of the material is. So far the materials measured here have had very high molecular weights with something like ten thousand repeat units along the chain. We currently are investigating techniques for making shorter chain materials using a boron trichloride catalyst to knock the chain link down. We think those materials will have different properties as well.

Question: I'm a little concerned about stress and temperature changes. Have you done any thermal cycling?

Answer: The only thermal cycling we have done is to put these in an oven at between 50°C and 100°C and look at the optical properties after we have withdrawn them. There appears to be no change. A lot of the materials that I have illustrated here are elastomers so they can stretch with temperature. Some of the other materials like the phenyl substituted material are quite brittle. That material is stable up to about 350°C and then it decomposes. One of the first slides I had, I showed a glass transition temperature of let's say the trifluoroethylene as minus 60°C. That material retains its elasticity to those temperatures. As a matter of fact that was one of the first commercial applications of these materials. It was used in the Alaskan pipeline as a gasketing material.

Question: I just wondered about the purpose of the second harmonic qeneration measurements. Do these have a crystallized phase so they might be useful as harmonic generation materials?

Answer: These polymers can be crystallized and I think they can be oriented. In an initial measurement we observed green emission when we hit the polymer with IR. It would be interesting to see if indeed the wavelength emitted was 532 nm. One thing we find out is when we substitute different groups on a polymer chain, for example, the isocyclamate, we observe the intensity to go up by over an order of magnitude. I think if we can affect some kind of orientation in the polymer it might be an attractive non-linear material.

Question: I just want to make a comment about the previous question. Organic polymers have been shown to have extremely high ratios that are associated with the conjugative systems in those molecules and you would expect that non-organic polymers could have similar affects. They should then have a lot of applications for waveguide structures.

Manuscript received
12-29-89

FORMATION OF A PREGIVEN REFLECTING SURFACE TOPOGRAPHY BY ELASTIC DEFORMATION OF THE MIRROR SUBSTRATE. NEW CONCEPT OF ADAPTIVE OPTICAL SYSTEM.

V.V.Apollonov, S.A.Chetkin, E.A.Ivanova, A.M.Prokhorov, G.V.Vdovin.

General Physics Institute, USSR Academy of Sciences
117942, Moscow, Vavilov street, 38, USSR

ABSTRACT

Complete model of a multiactuator flexible mirror,made as a thin plate with discrete piezo-actuators is described. Experimental results validated the efficiency of proposed model are presented.New concept of adaptive optical system with flexible mirror and linear wavefront sensor is developed.

INTRODUCTION

Adaptive mirror (AM) with continuous reflecting surface and discrete actuators have a series of advantages in comparison with other types of wavefront correctors. However, the control of the AM in adaptive optical system (AOS) is rather difficult because its influence functions (IF) are not orthogonal, no localized. Besides, the model, describing operation of AM, does not exist.

The purpose of this work is a description of analytic model of the AM, consisting of thin flexible substrate and an array of discrete actuators. This model is used for determination of AM parameters and numerical simulation of AM operation in AOS.

Effective algorithm of realization of phase conjugation in AOS with non-orthogonal influence functions is proposed.

1. NUMERICAL SIMULATION OF AM OPERATION.

Model of the AM

Theory of a thin plate is sufficient for description of elastic interaction of substrate and actuators. Within this theory the substrate deflection $W(\vec{r})$ under the action of load $P(\vec{r})$ satisfies the following equation:

$$\Delta\Delta W(\vec{r})=P(\vec{r})/D \qquad (1)$$

with the boundary conditions, corresponding to the method of substrate fixation. In (1) D is a cylindrical stiffness of the AM substrate [1].

We'll consider the circular AM with N actuators and clamped edge [2]. When the control signal is applied to the k-th actuator, it produces pointwise force P and other actuators produce reaction pointwise forces P q_i, where i is the actuator number. In this case the solution of the equation (1) is

$$W(r,\varphi)=PR^2/(16\pi D)\, f_k(r,\varphi) \qquad (2)$$

where R is the substrate radius, $f_k(r,\varphi)=\alpha_k(r,\varphi)+\sum_{i=1}^{N} q_i\alpha_i(r,\varphi)$,

$$\alpha_j(r,\varphi)=(1-r^2)(1-\rho_j^2)+(r^2+\rho_j^2-2r\rho_j\cos(\varphi-\theta_j))\ln((r^2+\rho_j^2-2r\rho_j\cos(\varphi-\theta_j))/(1+r^2\rho_j^2-2r\rho_j\cos(\varphi-\theta_j))$$

(ρ_j, θ_j) - coordinates of the j-th actuator. Reaction forces q_i, corresponding to the action of the unit force P, are defined from the system of linear equations:

$$\sum_{\substack{i=1 \\ i\neq k}}^{N} a_{ij} q_i = -\alpha_j(\rho_k, \theta_k) \qquad (j=1,\ldots,N; j\neq k) \qquad (3)$$

where $a_{ij} = \alpha_i(\rho_j, \theta_j) + \delta_{ij} G$, δ_{ij}- Kronecker symbol, $G = R^2/(16\pi D)\ K_a^{-1}$. K_a-actuator stiffness. Force, produced by the k-th actuator is equal to

$$P = \Delta l_0 / (K_a^{-1} + f_k(\rho_k, \theta_k) R^2/(16\pi D)), \qquad (4)$$

where Δl_0 is the elongation of the actuator under the action of the applied control signal at the free state (out of the mirror). The transverse piezoeffect is ordinary used for the control of the AM reflecting surface shape by piezoelectric actuators. In this case Δl_0 is related to the value of control voltage U by the equation:

$$\Delta l_0 = d_{31} l/d\ U, \qquad (5)$$

where d_{31} is piezoelectric constant of the actuator material, l is the length, d is transverse dimension of the actuator.

As the actuator influence on the AM surface is additive, profile, formed when voltages are applied to all the actuators, is the following

$$w(r,\varphi) = d_{31}\, l/d \sum_{i=1}^{N} \left(f_i(r,\varphi)/(f_i(\rho_i, \theta_i) + G)\ U_i \right) \qquad (6)$$

Normalized IF of two AM, - the first with 5 piezoelectric and the second with 19 magnetostriction actuators, found experimentally -(1,3) and calculated by the equation (2) - (2,4) are presented in Fig.1 and 2. Meansquare error of approximation of experimental IF by the model ones is about 0.08 of meansquare deviation of experimental IF from plane. Obtained accuracy proves the efficiency of the theory of a thin plate for description of the AM operation.

Efficiency of Actuator Operation

Efficiency of actuator operation in the AM is characterized by the ratio of actuator elongation in AM to actuator elongation in free state and by coefficient of transformation of control signal energy to the energy of substrate deformation. Actuator elongation in AM is equal to $W_k(\rho_k, \theta_k)$, hence, as following from (2)-(5):

$$\Delta l/\Delta l_0 = 1 - G/[G + f_k(\rho_k, \theta_k)] \qquad (7)$$

$\Delta l/\Delta l_0$ (G) dependencies for one-actuator mirror with different positions of actuator relatively to the center of AM are presented in Fig.3A. Increase of G leads to decreasing $\Delta l/\Delta l_0$, radial shift of actuator from mirror center also leads to decreasing $\Delta l/\Delta l_0$. $\Delta l/\Delta l_0$ (G) dependencies for actuators, located in hexagonal array with distance between actuators b=0.3R are presented in Fig.3B. For actuators, located at equal distances from AM center, the dependencies are identical. While the distance from the center increases, $\Delta l/\Delta l_0$ decreases as for the case of one actuator. Comparison of curves in Fig.3A and Fig.3B shows that increasing the number of actuators leads to increasing of effective substrate stiffness and, hence, to decreasing of displacement range of individual actuator.

Efficiency of control signal energy transform to the energy of substrate deformation is characterized by the value of energy transform coefficient(ETC),

equal to the ratio of substrate deformation energy to the summarized energy of substrate and actuators:

$$\eta = V_0 / \left(\sum_{i=1}^{N} V_i + V_0 \right) \qquad (8)$$

where V_0 - energy of substrate elastic deformation, V_i - potential energy of the i-th actuator. Dependence of η on the parameters of AM in case of actuators based on transverse piezoeffect is the following:

$$\eta = \left(f_k(\rho_k, \theta_k) - G \sum_{\substack{i=1 \\ i \neq k}}^{N} q_i \right) / \left(k_{31}^{-2} G^{-1} \left(f_k(\rho_k, \theta_k) + G \right)^2 - \left(f_k(\rho_k, \theta_k) + G \right) \right) \qquad (9)$$

where k_{31} is coefficient of piezomechanical coupling of actuator material [4]. Thus, ETC depends on the displacement, number of actuators and two dimensionless parameters - relative stiffness G and coefficient k_{31}.

$\eta(G)$ dependencies for actuators of 19-element AM (hexagonal array, b=0.3R, k_{31}=0.3) are presented in Fig.4. Dependencies of maximum value of ETC on the distance between actuators for the case of hexagonal array of 19 actuators are presented in Fig.5A, and the values of relative stiffness, corresponding to maximum ETC - in Fig.5B; k_{31}=0.3. The ETC dependencies on coefficient k_{31} are similar for actuators located at different distances from mirror center - - when k_{31} increases, ETC increases too. As an example, $\eta(k_{31})$ dependencies for 19-element mirror with hexagonal array of actuators are presented in Fig.6. (b=0.3R;G=0.2).

Numerical calculations have demonstrated that for effective operation of actuators in the AM, it is necessary to optimize their displacement and adjust their parameters with parameters of the substrate.

Correction of Seidel Aberrations BY AM

For effective correction of aberrations, the AM control system must provide control signals on actuators, producing forces, that form reflecting surface of given shape with certain accuracy.The degree of compensation can be characterized by meansquare error:

$$\mathcal{E} = \left[\int_0^{2\pi} \int_0^{A} (W_a - W_T^2) r dr d\varphi / (\pi A^2 W_{MAX}^2) \right]^{1/2} \qquad (10)$$

where $W_a(r,\varphi) = W_{MAX} \psi(r,\varphi)$ - the shape of aberration, $W_T(r,\varphi)$ - shape of AM reflecting surface, A - radius of operating aperture, that is the aperture at which conjugation is accomplished. Equation for W_T is written in the form $W_T = \sum_{i=1}^{N} Q_i \alpha_i(r,\varphi)$, where $Q_i = R^2/(16\pi D) P_i$, P_i is the force, produced by the i-th actuator. Q_i, providing minimum $\mathcal{E}$, are found from the system of linear equations:

$$\beta_{ik} Q_i = \gamma_k, \qquad (11)$$

where $\beta_{ik} = \int_0^{2\pi} \int_0^{A} \alpha_i(r,\varphi) \alpha_k(r,\varphi) r dr d\varphi$, $\gamma_k = W_{MAX} \int_0^{2\pi} \int_0^{A} \psi(r,\varphi) \alpha_k(r,\varphi) r dr d\varphi$. The results of numerical simulation of Seidel aberrations compensation are presented below [2].

Hexagonal array of actuators, defined by the distance between actuators b and the number of actuators N, is typical for the AM. $\mathcal{E}(b)$ dependencies for correction of Seidel aberrations by the AM with N=37, A=0.8R are presented in Fig.7. The arrangement of actuators powerfully influences on the value of compensation error, although hexagonal array is kept, therefore, it is necessary to optimize the actuators arrangement in order to provide effective correction of phase distortions.

$\mathcal{E}(A)$ dependencies for compensation of Seidel aberrations by the AM with N=37, b=0.32R are presented in Fig.8. While A decreases from R to 0.6R, $\mathcal{E}$ decreases in 5-50 times depending on type of aberration, hence, this way of increasing of compensation accuracy is very efficient.

Histogram, characterizing $\mathcal{E}(N)$ dependence for compensation of Seidel aberrations by the AM with N=7,19,37,61 in hexagonal array, is presented in Fig.9; b is optimum in each case, A=0.8R. It is evident that the increase of the number of actuators more than N=61 is not expedient when aberrations to be corrected are rather smooth.

Determination of demands to the AM alignment in the AOS is important for providing efficient compensation of phase distortions. Dependence of compensation error on the value of shift of beam axis relatively to the mirror center for the case of compensation of defocus by the AM with N=19, b=0.3R, A=0.6R. is illustrated in Fig.10. Even a small shift of the beam axis causes the critical error increase, therefore, the AM must be centered with high accuracy in the AOS. Fig.11 illustrates the dependence of accuracy of compensation of defocus and astigmatism by AM with N=19, b=0.48R, A=0.6R on the value of angle between the normal to the mirror surface and the axis of incident beam. Dependencies demonstrate that maximum accuracy of compensation corresponds to the case of normal incidence of radiation.

Results of numerical simulation of Seidel aberrations correction have demonstrated that compensation error for pregiven phase aberration can be essentially decreased by optimization of actuators arrangement, limitation of operating aperture of the AM in the AOS.

2. REALIZATION OF PHASE CONJUGATION BY MEANS OF ORTHOGONALIZATION OF WAVEFRONT SENSOR BASIS.

AOS Control Algorithm.

AOS under consideration includes linear wavefront sensor with M independent phase measuring channels and phase corrector with N control channels. Using wavefront corrector with nonorthogonal IF provides a considerable goal in correction quality, but it simultaneously complicates AM control in phase-conjugation AOS. Wavefront reconstruction from wavefront sensor response vector needs N^3 computer operatins, and using of initial assumptions about wavefront to be corrected. These assumptions lead to reconstruction error increasing. At the first (calibration) stage M-dimension wavefront sensor response vectors are measured for consecutive appling of unit signal to each control channel of corrector in the presence of model wavefront. Then orthogonal basis of vectors $\vec{\psi}_j$ is formed by mean of orthogonalization of response vectors $\vec{\varphi}_i$ and each of computed vectors is presented as a linear combination of response vectors:

$$\vec{\psi}_j = \sum_{i=1}^{N} \alpha_{ij} \vec{\varphi}_i \qquad (12)$$

Orthogonal basis $\vec{\psi}_j$ and coefficients α_{ij} are stored in control system memory.

At second (working) stage, vector of sensor response $\vec{\varphi}$ on aberrated wavefront is decomposed into basis vectors $\vec{\psi}_k$:

$$\vec{\varphi} \approx \sum_{k=1}^{N} \beta_k \vec{\psi}_k , \qquad (13)$$

where β_k is defined as $\beta_k = (\vec{\varphi}, \vec{\psi}_k)$.
Substitution of (12) to (13) gives:

$$\vec{\varphi} \approx \sum_{k=1}^{N} \beta_k \sum_{j=1}^{N} \alpha_{kj} \vec{\psi}_j \qquad (14)$$

here $\sum_{k=1}^{N} \beta_k \alpha_{kj}$ defines the value of control signal to be applied to the j-th control channel of corrector. The main advantage of proposed algorithm is that its realization needs only N^2 computer operations to determine all control signals in N-channel phase-conjugation AOS.

Numerical Simulation of AOS Operation

We have considered phase conjugation AOS, including Hartmann-type wavefront sensor and mirror-like phase corrector with discrete actuators. Efficiency of proposed control algorithm can be estimated by comparison of compensation error, provided by AM controlled by proposed algorithm and optimally controlled. The degree of compensation we'll characterize by residual meansquare error, devided by initial meansquare error of aberrated wavefront. Efficiency of proposed algorithm for 19-channel AM (hexagonal array, b=0.42R, A=0.8R) and 19-channel Hartmann-type sensor in comparison with optimal control in case of Seidel aberrations compensation is illustrated in Fig.12. The error of compensation for proposed algorithm is in 1.5 - 4 times high than that is for optimal control. So, proposed algorithm of phase conjugation, excluding initial assumptions about controlled wavefront, is effective. Definition of all control signals requires in this case only N^2 computer operations.

REFERENCES

1. Timoshenko S.P., Woinovsky-Kreiger S., Theory of Plates and Shells.- New York, 1959.

2. Apollonow V.V., Chetkin S.A., Ivanova E.A., Prokhorov A.M., Materials of Lasers '88 International Conference, Lake Tahoe, Nevada, pp.298-306

3. Apollonov V.V., Chetkin S.A., Ivanova E.A., Prokhorov A.M., Temnov S.N., Experimental Technic der Physic 37 (1989) 1, pp. 41-60.

4. Physical Acoustics ed. by W.P.Mason, v.1., part A., Moskow: Mir, 1966

5. M.Born, E.Wolf, Principles of Optics, Oxford, England: Pergamon Press,1965

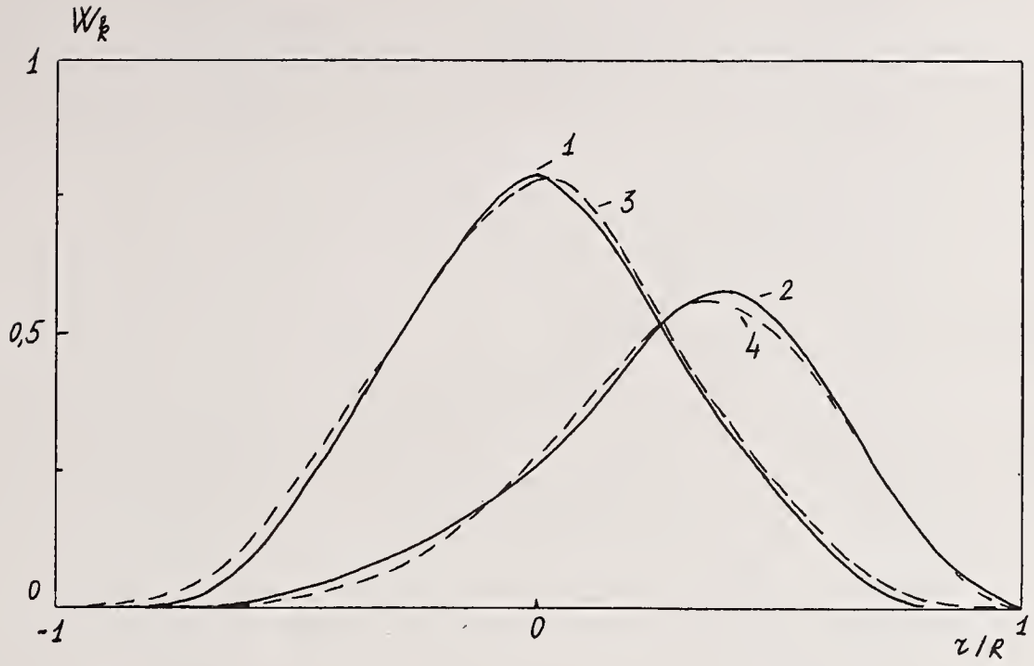

Fig.1. Experimental (1,3) and theoretical (2,4) IF of 5-element AM with piezoelectric actuators

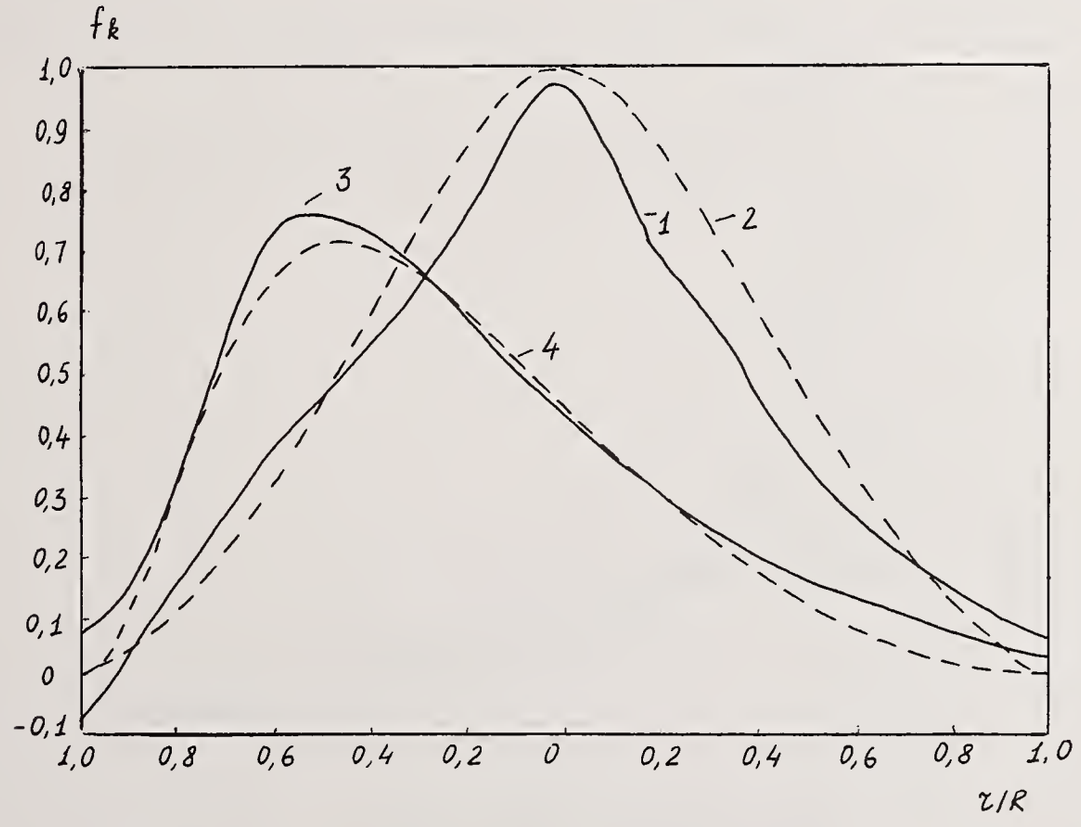

Fig.2. Experimental (1,3) and theoretical (2,4) IF of 19-element cooled AM with magnetostriction actuators

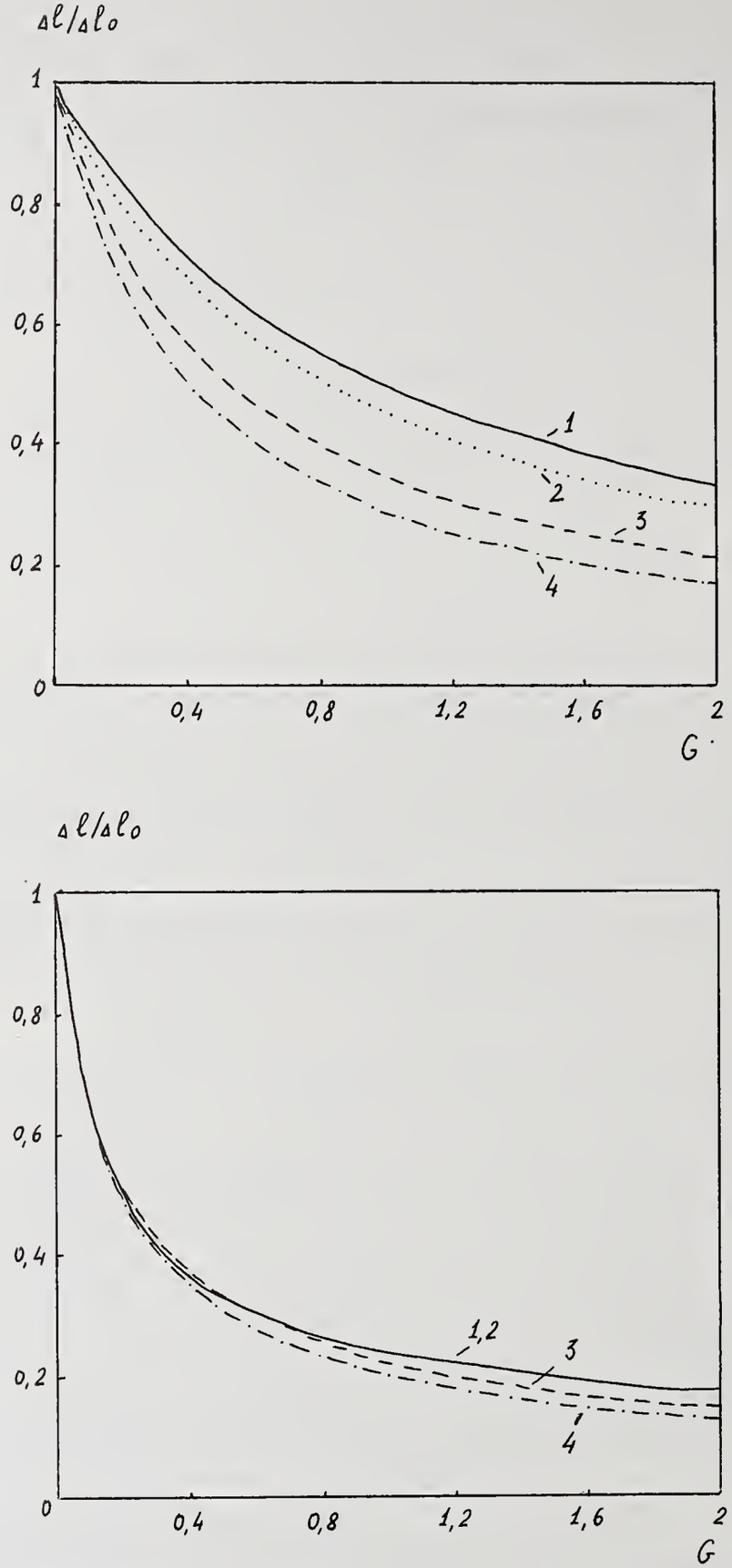

Fig.3. Relative elongation of actuators via relative stiffness G:
A) For 1-element AM
B) For 19-element AM with hexagonal array of actuators.
1 - ρ=0; 2 - ρ=0.3R ; 3 - ρ=0.52R; 4 - ρ=0.6R

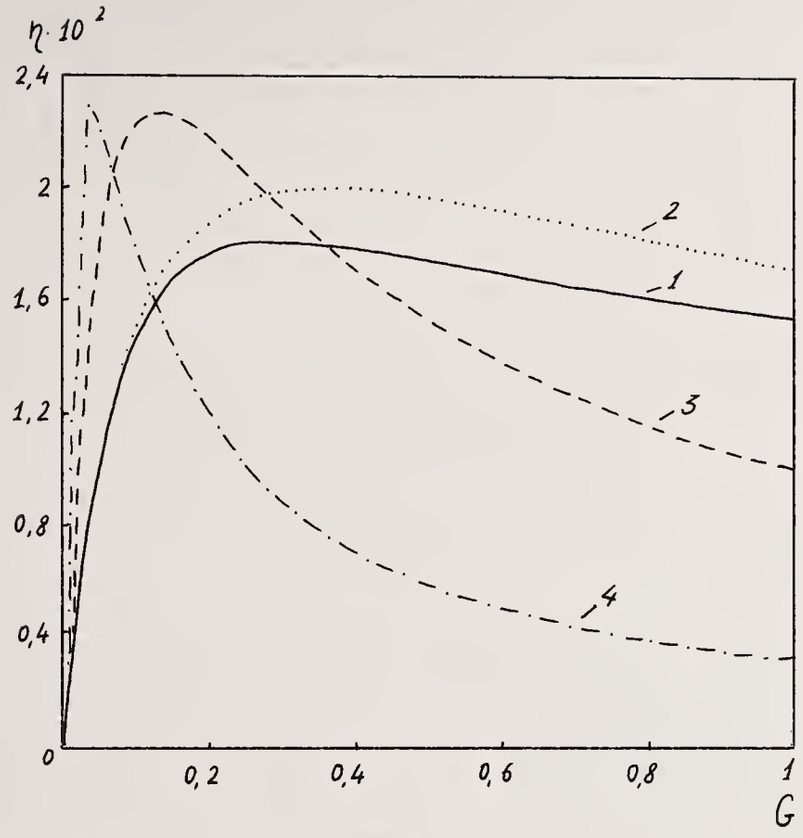

Fig.4. ETC for actuators of 19 - element AM with hexagonal array (b=0.45R, k_{31}=0.3) via relative stiffness G
1 - ρ=0; 2 - ρ=0.45R ; 3 - ρ=0.78R; 4 - ρ=0.9R

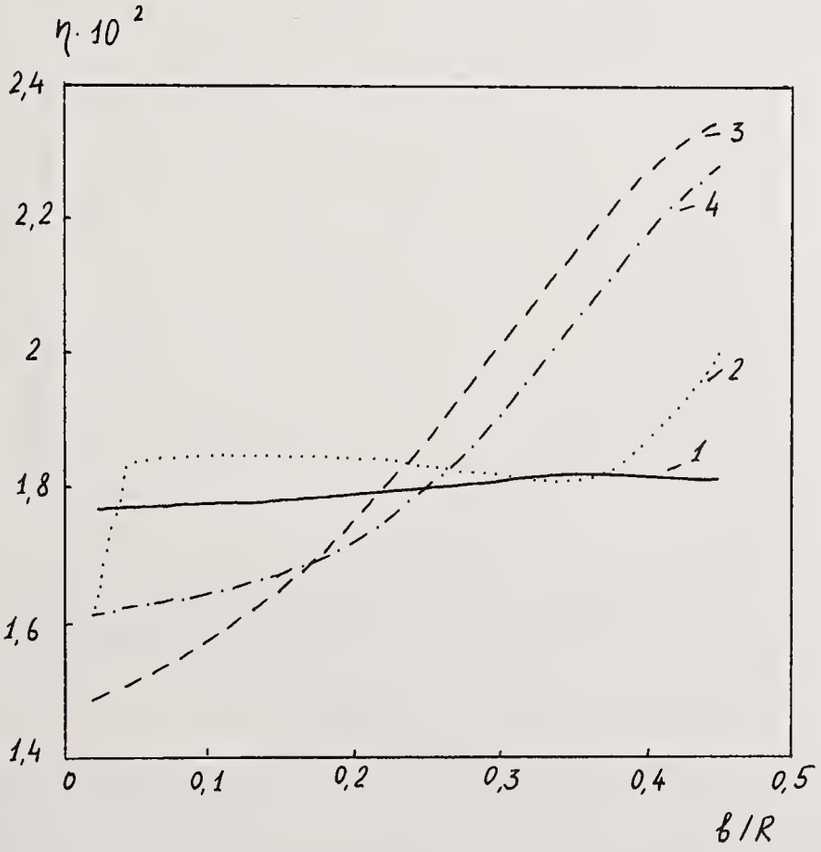

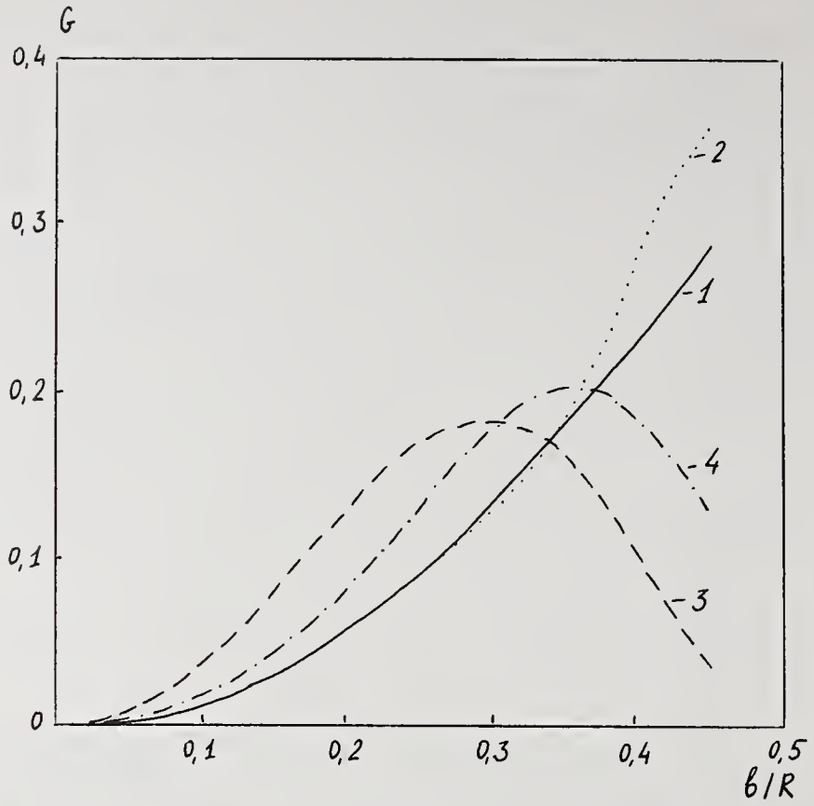

Fig.5. A) Maximum value of ETC via the distance betveen actuators of 19-element AM with hexagonal array (k_{31} =0.3)
B) Relative stiffness G corresponding to the maximum ETC via distance betveen the actuators of 19-element AM with hexagonal array (k_{31} =0.3)
1 - ρ=0; 2 - ρ=b; 3 - ρ=1.7b; 4 - ρ=2b

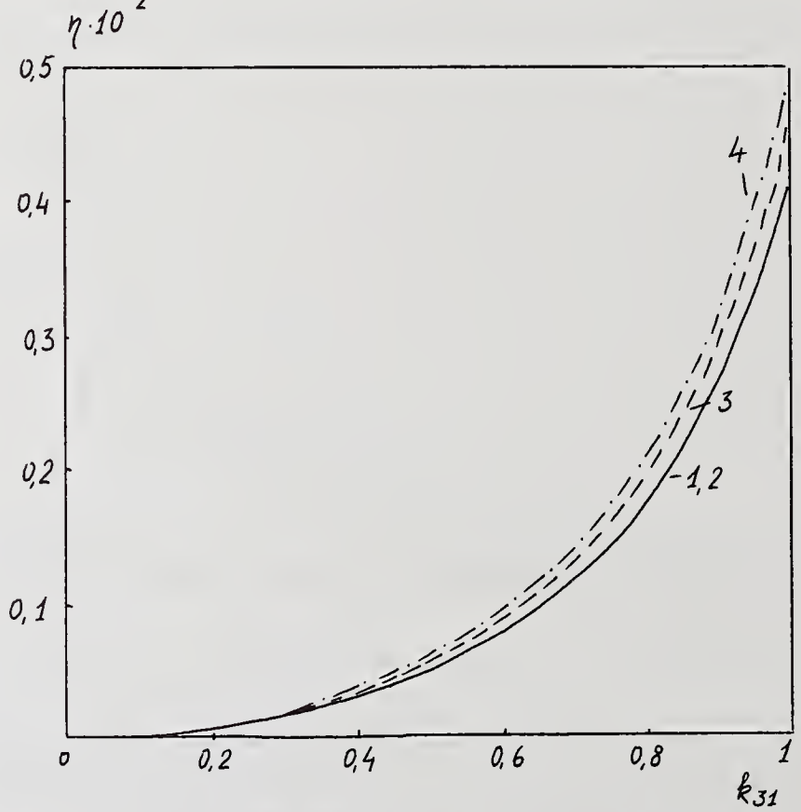

Fig.6. ETC via coefficient of piezomechanical coupling k_{31} for actuators of 19-element AM with hexagonal array (b=0.3R;G=0.2)
1 - ρ=0; 2 - ρ=0.3R; 3 - ρ=0.52R; 4 - ρ=0.6R

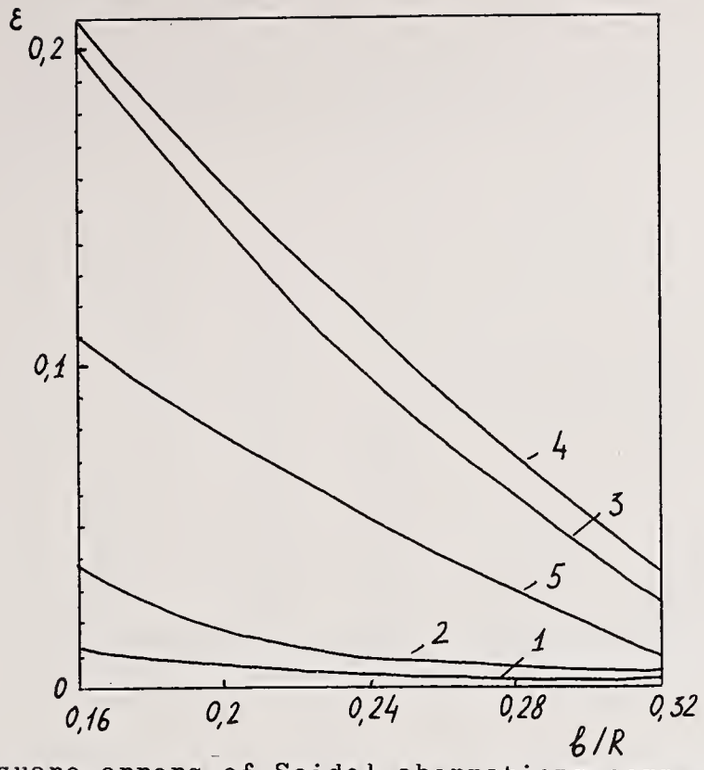

Fig.7. Meansquare errors of Seidel aberrations compensation by AM with hexagonal array of 37 actuators via distance betveen actuators (A=0.8R)
1 - defocus; 2 - spherical aberration; 3 - tilt;
4 - coma; 5 - astigmatism

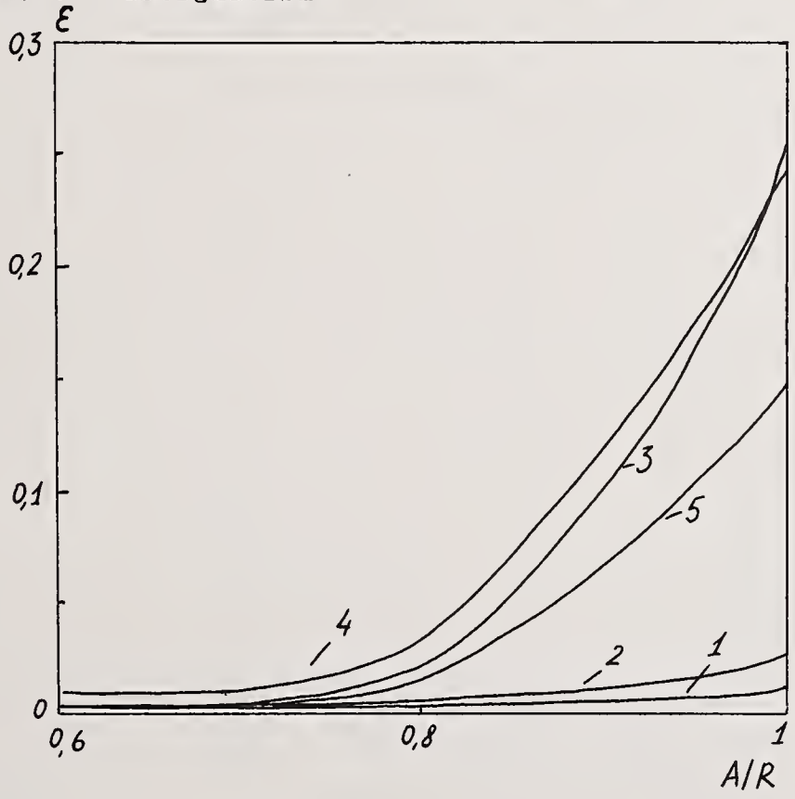

Fig.8. Meansquare errors of Seidel aberrations compensation by AM with hexagonal array of 37 actuators (b=0.32R) via radius of operating aperture
1 - defocus; 2 - spherical aberration; 3 - tilt;
4 - coma; 5 - astigmatism

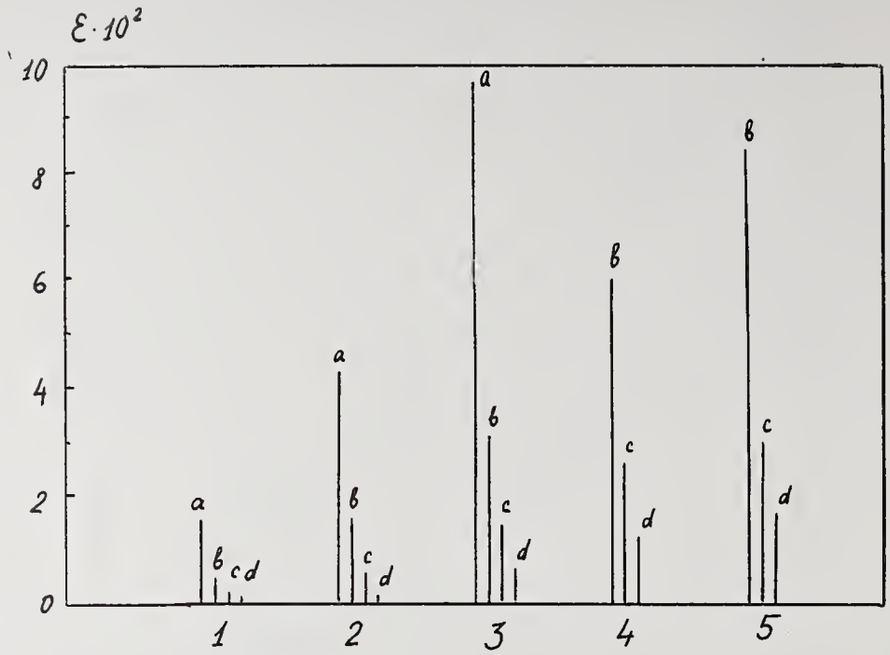

Fig.9. Meansquare errors of Seidel aberrations compensation by AM with hexagonal array of actuators via the number of actuators
a - N=7; b - N=19; c - N=37; d - N=61
1 - defocus; 2 - spherical aberration; 3 - tilt;
4 - coma; 5 - astigmatism

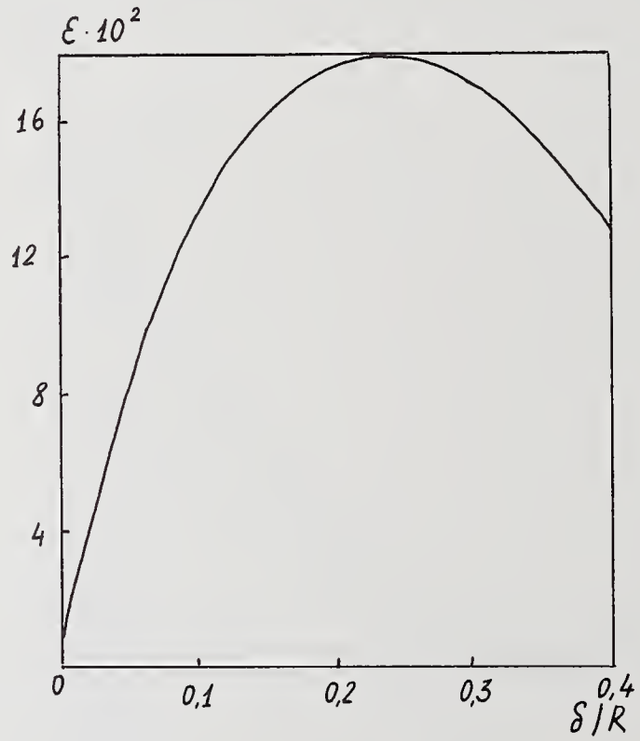

Fig.10. Meansquare errors of defocus compensation by AM with N=19, b=0.3R, A=0.6R, via shift of beam axis relatively to the mirror center

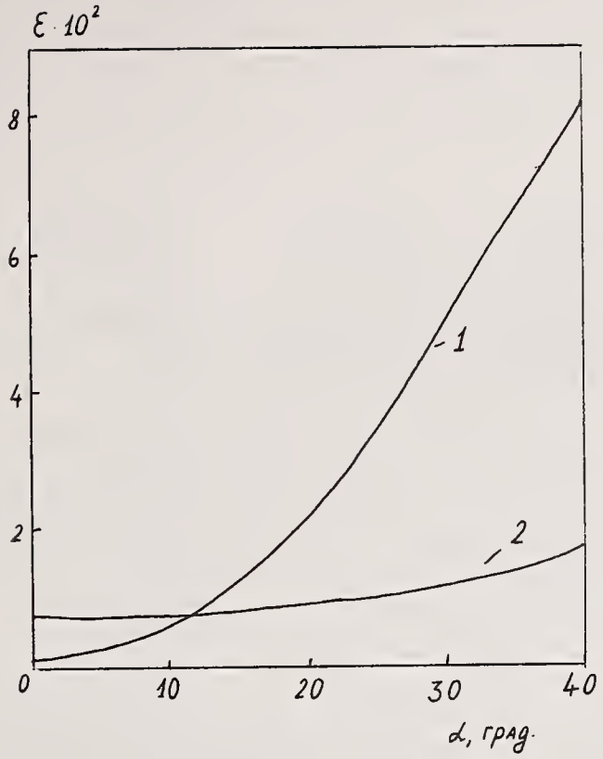

Fig.11. Meansquare errors of defocus (1) and astigmatism (2) compensation via AM tilt (N=19,b=0.48R,A=0.6R)

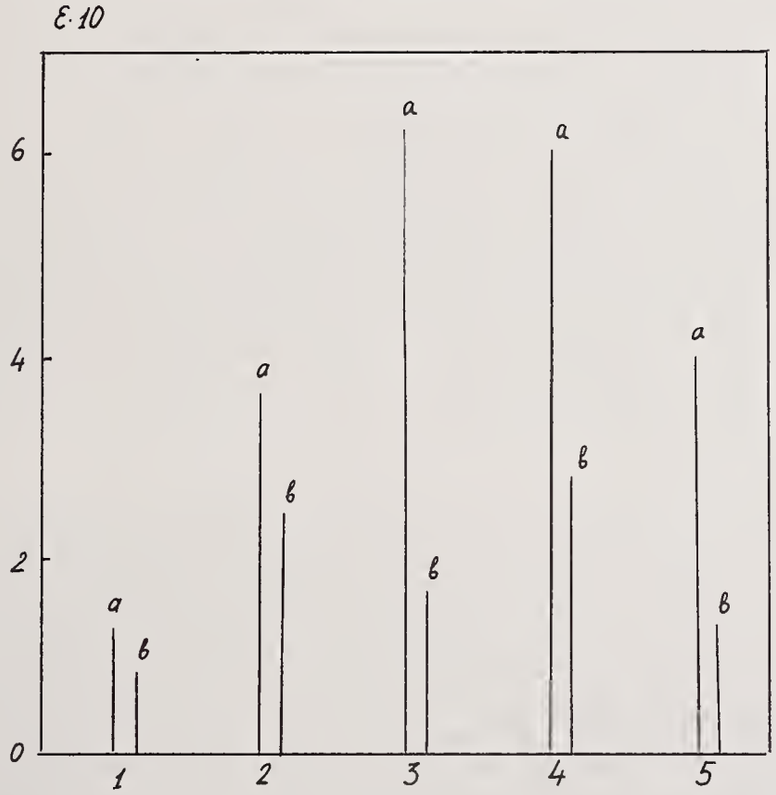

Fig.12. Errors of Seidel aberrations compensation by AM with hexagonal array of 19 actuators (b=0.42R) in case of optimal control (a) and in case of control in AOS with 19-channel Hartmann-type sensor (hexagonal array,b=0.26R)(b)
1 - defocus; 2 - spherical aberration; 3 - tilt;
4 - coma; 5 - astigmatism

Manuscript received
4-2-90

APPLICATION OF ULTRASONIC CAPILLARY EFFECT IN ELEMENTS OF POWER OPTICS COOLED BY MEANS OF A HEAT PIPE

V.V. Apollonov, S.A. Chetkin, V.N.Kharchenko, V.N. Motorin, A.M. Prokhorov

Institute of General Physics of the USSR Academy of Sciences, Vavilova 38, Moscow, 117942

INTRODUCTION

Development and creation of powerful technological lasers requires complex solution of problems of optics, quantum electronics and thermal physics. The achieving of stable in time energetic parameters of technological lasers with cooled elements of power (EPO) and adaptive (EAO) optics can be achieved only by a correct choice of their cooling modes, eliminating or compensating negative effects of heating EPO by laser radiation because of principal difference of reflectance of the mirror surface from I. The convective regime of EPO or EAO cooling is mainly used in laser technique and carried out by pumping the coolant through a penetrable disperse compact heat exchanger, on the work surface of which a thermally thin layer, separating radiation and the coolant liquid in heat changer, is made /1,2/. The intensity of heat transter and therefore, the degree of thermostatting of the reflecting surface of EPO are determined by a large number of design and technological factors not always reproducible in the EPO manufacturing. Nevertheless, for EPO, made on the basis of powder porous structures, the level of removing heat fluxes reach $2 \cdot 10^3$ wt/cm^2 under the thermal deformation of the mirror surface less than 1 μm, the effective heat transfer factor for a heating mirror surface equal to $\sim 10^5$ wt/m^2 . °C in this case /2/.

When solving the problems of thermostating of extended reflecting surfaces, the usage of convective intraporous cooling is not advisable since it requires high cooler consumption. The usage of heat pipes (HP) for thermostatting of extended optical surfaces is the most rational approach to creation of large-scale EPO. The choice of HP as a heat exchanger for EPO is followed from HP fuctional possibilities and advantages on a number of technical-and-economic indices. Among tham, first of all, large equivalent thermal conductivity of HP, amounting to $\sim 10^7$ wt/m . grad, sufficiently high efficiency of heat pick-up and, therefore, high degree of thermostatting of the heating mirror surface, carried out by means of heat flux transformation into the latent heat of phase transition. Moreover, EPO in this case has essentially lesser weight and overall dimensions of the whole cooling system, abscence of mobile parts (t.g., pumps) and, due to this, operats without vibration and noise; also the complete autonomy of EPO is reached in this case /3/.

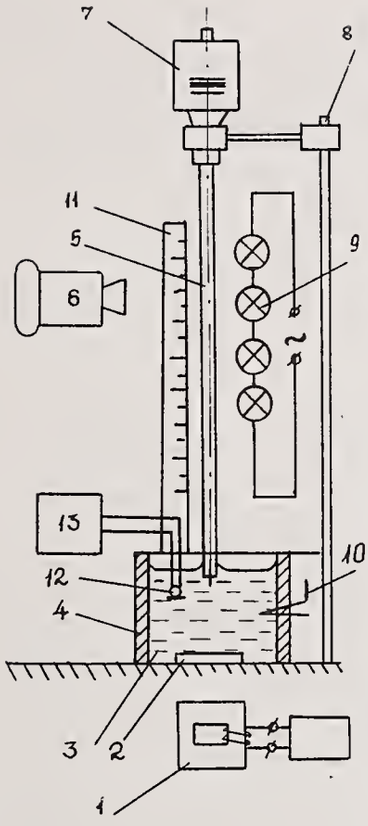

FIGURE 1. Design of an experimantal setup for investigating the ultrasonic capillar effect

However, the traditional approaches to creation of HP cannot completely satisfy the needs of high intensities laser optics in removing still larger specific heat fluxes from the reflecting surface of EPO. Largely, this because of the fact that for heat transferring devices, based on employing the HP methodology, the upper level of the removed heat flux is determined by the transport possibilities of capillary-porous structure of the HP wick. To remove the indicated limitation, the processes of the cooler transportation along the capillars of the HP wick shoud be substantially intensified. The well-known passive (not requiring the supply of energy) and active (with the supply of energy) methods are not able to completely eliminate the above limitations on the cooler transport in the HP wick. One of the promising and practically non-investigated, with respect to HP, methods - is the active way of intesifying the mass transfer in the HP wick, based on ultrasonic capillar effect by Konovalov (USCE) /4/. Using the process of liquid rise in an isolated capillar, exposed to ultrasound, one can solve the problem of intensifying the mass transfer in the HP wick, i.e. practically completely eliminate the transport limitations on capillary-porous structure and thus substantially raise specific heat loadings on the reflecting surfaces of EPO. Therefore, from the scientific point of view, the investigation of thermophysical characteristics of HP for EPO, in which USCE is emploied to intensify the heat mass transfer, is of interest.

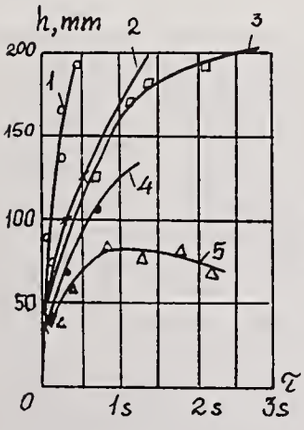

FIGURE 2A. Dependence of the height of water rise in a capillar on time (d= =1,2 mm; f=41 kHz; N=25 wt) for different values of clearance between the source's face and the capillar's cut:

1 - Δ =0; 2 - Δ =0.1 mm; 3 - Δ =0.2 mm; 4 - Δ=0.3 mm; 5 - Δ =0.5 mm.

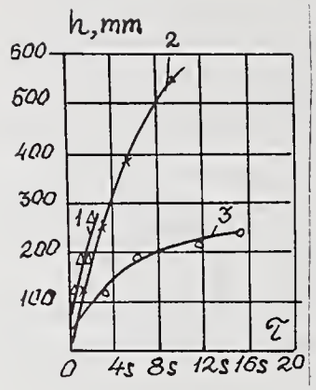

FIGURE 2B. The height of rise of transformer oil and ethyl alcohol in the capillar against time, for different values of the capillar's diameter and zero value of clearance between the radiator and the capillar's cut: 1 - 1.2 mm (ethyl alcohol); 2 - d=0.61 mm (oil); 3 - d=3 mm (oil).

THE PHYSICAL MODEL OF ULTRASONIC INTENSIFICATION OF HEAT MASS EXCHANGE IN HP

USCE, registered as invention in 1972, consists in raising heignt and velocity of liquid penetration into capillary channels under the action of ultrasound. Application of USCE will allow to raise the consumption of the cooler and thus to eliminate capillary limitations, imposed on mass transfer in the HP wick.

It is well known from the analysis of currently available work, that, the propagation of ultrasonic oscillation in liquids is accompanied by emergence of the so called secondary phenomena: sound pressure /5/, acoustic flows /6/, certain types of constant forces /7, 8/ affecting the element of the medium and its adjacent surfaces, and also cavitation /9/. Those mecanisms, however, can not explain the experimental results on USCE. With the purpose of finding out conditions, leading to the increase of capillary pressure under ultrasound, and developing a physical model of the process, a setup was created, involving: the system 6 of measurements and registration of velocity and height of the liquid in the capillar /Fig. 1/, a generator of ultrasonic oscillations (GUO), magnetostrictive transducer I and ultrasonic vibrator 2 placed in a bath with the liquid under investigation 3. Glass cylindrical capillars 5 fixed in the bath 4 at a given height using fine adjustment screw 7 and rod 8. For visual observation and taking photographs, the capillar was lighted with a lamp 9. The process was observed and photographed through a peephole using microscope. The temperature of the liquid was measured by a thermocouple 10 and the height of liquid in the capillar was determined using rule 11. The velocity of the liquid rise in the capillar under ultrasound was measured using contiguous photographing of its height. The experiments were carried out under following conditions: power of GUO was W=25 wt, inner diameters of the capillars d were from 0.2 mm to 3 mm. Water, alcohol and transformer oil were used as liquid.

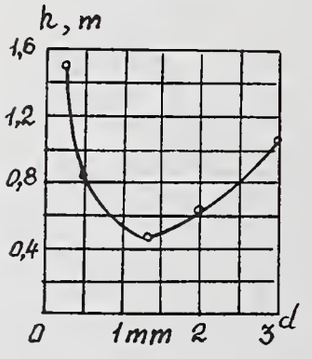

FIGURE 3A. The equilibrium height of rise of distilled water in the ultrasonic field against the capillar's diameter.

The ultrasonic effect on the capillar movement of the liquid was investigated at a frequency 41 kHz under acoustic power

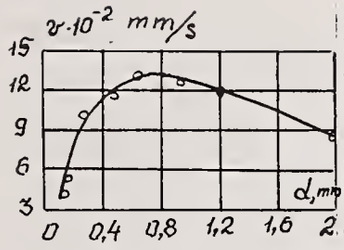

FIGURE 3B. The average velocity of water rise in the capillar under ultrasound against the capillar's diameter. Exposure time was 1 s.

12.5 wt, which corresponded to the intensity of ultrasonic field 1.6 . 10^4 wt/m^2.

The analysis of experimental data, showed in Figure 2A,B, discovers, that the height of the water rise in capillary channels of different diameters, with practically zero distance from the radiating surface of the magnetostricter to the capillar's cut, in case of reading the height of its rise from the height of the liquid rise in the capillar in the absence of ultrasound, increases many times and depends on the capillar's diameter. For example, in a capillar of diameter 3 mm under f=41 kHz the height of water's rise in the ultrasonic field exceeded the equilibrium one 110 times. The plot in figure 3A, shows that there exists an optimal size of the capillar's diameter dependent on the frequency of ultrasound with the velocity of rise of the liquid (water) is maximum. It should be noticed that the kind of liquid causes no substantial effect on the size of the optimal diameter of the capillar. If the capillar's diameter increases, the equilibrium height of the liquid's rise in the capillar decreases, together with the acoustic impedancem that is equal to the ratio of the amplitude of sound pressure P_m to the amplitude of volume velocity (V_m.S). In thiscase, mass forces begin to play larger role, since relatively large volume of liquid passes through the capillar. In the case of small diameter of the capillar (less than 1 mm), the equilibrium height of the liquid's rise in it is substantial and amounts to 10-50 mm. In thiscase, the impedance of the system is also large. However, sound-capillar pressure in this case decreases, since the resistance force, increases, due to increase of specific surface of contact of the liquid with the capillar's wall.

The observing of the liquid's behaviour over the ultrasonic radiator showed, that the area with developed acoustic cavitation emerges over the radiator's surface. The cavitation was observed at the same point of the surface of the GUO source. A white mobile cloud of cavitation bubbles emerged over that point. In the case of ultrasonic action at the transformer oil, the picture was some what different, i.e. cavitation was observed both in the center of the radiator and in its peripheral area. Because of viscosity of the transformer oil substantially exceeding the viscosity of water, and of substantially lower surface tension that the water's, the cavitational cloud is unstable and bubbles have larger dimensions

FIGURE 4. Photograph of cavitation picture near the capillar's face in water.

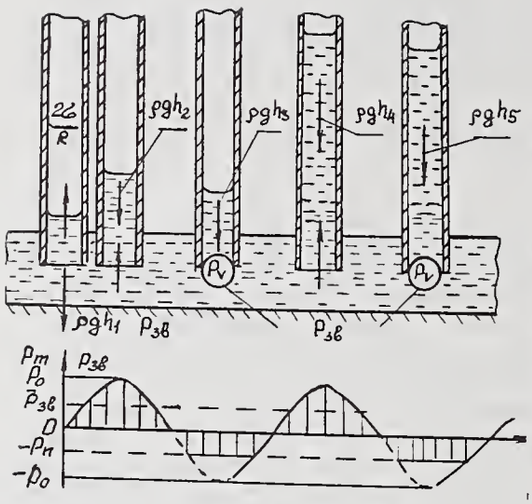

FIGURE 5. A physical model of ultrasonic capillar effect.

that in the water's case. When setting un the capillar into the cavitation cloud (Fig. 4), the maximum velocity of the capillar rise was observed. When setting up the capillar aside from the area with developed cavitation, the increase of velocity and height of capillary rise was insignificant. It should be noticed that cavitation at the surface of the GUO source progresses only under ultrasonic intensities exceeding the cavitation threshold. With the amplitude of ultrasonic pressure lower than the cavitation threshold ($P < 0.74 \cdot 10^5$ Pa), cavitation ceased and the water column lowed to the height of the equilibrium capillary rise in the abscence of ultrasound. When carrying out the experiment, it was noticed that the effect of cavitation exposes itself more distinctly in the case of water, saturated with gas, than in the case of using settled distilled water with a lowered proportion of dissolved gases. Attempt to treat the experimental results obtained, using the Konovalov methodology /10/, showed inconsistency of the physical model of USCE, considered in this work. Nevertheless, the analysis of the experimental results suggests that the rise of the liquid in the capillar under ultrasound occurs due to a periodical force. Sound sinusoidal pressure can not ensure the rise of the liquid in the capillar. The presence of pressure gradient along the capillar axis can emerge only in the case of asymmetrical, different from the sinusoidal for of ultrasound pressure (e.g., ultrasound with the pressure wave of the form showed in Figure 5 ensures the emergence of non-zero average pressure gradient along the capillar axis). Acoustic cavitation, for example, can ensure such transformation of harmonic ultrasonic wave. If the pressure in the liquid becomes lower than the threshold one for emergence of cavitation in the phase of rarefaction of the ultrasonic wave, a cavitation bubble emerges on the capillar's cut and closes it. In this case the colomn of liquid in the capillar experiences the action of surface tension force, the weight of the colomn of liquid and the pressure of saturated vapour of liquid inside the bubble P_v. This pressure is larger than the minimum pressure in the phase of rarefaction of the ultrasonic wave. Thus, during the action of the half-wave of rarefaction, the liquid flows from the carillar under gravitation and the difference of pressures $P_{atm} - P_v$. During the half-wave of com-

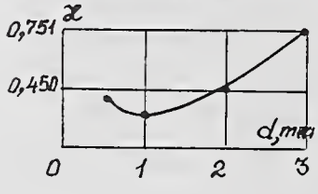

FIGURE 6. Water cavitation factor vs. the capillar's diameter for water temperature 20 °C.

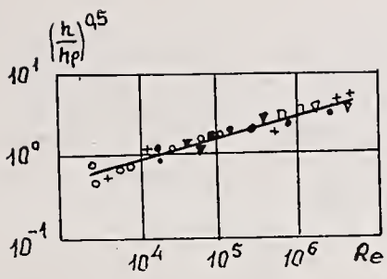

FIGURE 7. Relative height of water rise along a capillar vs. the acoustic Reynolds number; ● - data from /10/, water, f=23.5 kHz; + - data of the present paper, water, f=41 kHz; ▽ - data from /11/, water, f=40.4 kHz; □ - C_2H_5OH, f=40.4 kHz, from /10/; ■ - water, f=19.4 kHz, from /10/; ▼ - C_2H_5OH, f=19.4 kHz, from /10/.

pression the bubble collapses and the colomn of liquid experiences, apart from the above mentioned, the action of force of ultrasonic pressure sucking the liquid into the capillar. Hence, the acoustical cavitation is accompanied by distortion of the harmonic form of pressure oscillation in the ultrasonic wave and by emergence of some average in time force ensuring additional rise of the liquid in the capillar. In the case of capillars of sufficiently large diameters, a system of small cavitational bubbles emerges that shut off the pass section of the capillar. In such a situation the action of the system of cavitational bubbles will be equivalent to the above considered action of a separate bubble.

Kinetics of capillar movement of the liquid in the ultrasonic field is described, in accordance with the considered physical model, by the equation

$$h\frac{d^2h}{d\tau^2} + \left(\frac{dh}{d\tau}\right)^2 - \frac{2\sigma}{R\rho} + gh + \frac{8\mu}{R^2\rho}(h+l_o)\frac{dh}{d\tau} - \frac{P_{sound}\varkappa}{\rho} = 0 \qquad (1)$$

derived from the balance of forces, acting at the colomn of liquid of variable mass under following assumptions: 1. the flow of the liquid in the capillar is laminar and the Poiseuill's friction law holds: $f=64/Re$; the equilibrium height, if the liquid's rise in the capillar in the abscence of ultrasound, is determined according to the Juren formula.. In equation (1) the following notation is adopted: h - is the height of the liquid's rise in the capillar; σ - is the factor of surface tension of the liquid; R - is the capillar's radius; ρ - is the li-

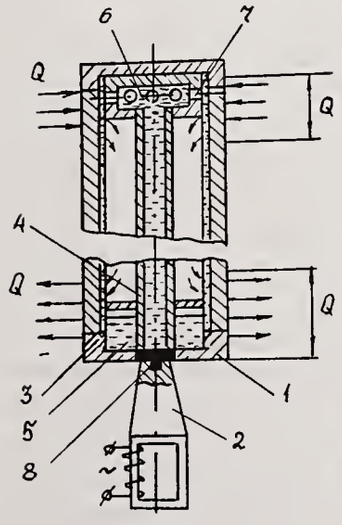

FIGURE 8. Schematic design of experimental HP with a source of ultrasonic oscillations: 1 - pressurized body; 2 - magneto-strictive radiator; 3 - capillapy-porous wick; 4 - pipe-artery; 5 - cooler in the condensation zone; 6 - upper cavity for gathering the cooler in the heating zone; 7 - opening for the cooler output; 8 - concentrator of ultrasonic magneto-stictive radiator

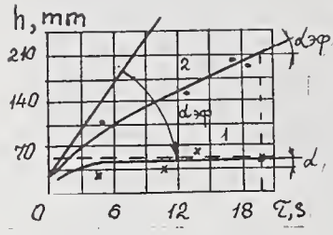

FIGURE 9. Experimentally obtained dependency of the height of water rise in a capillar of diameter 3 mm for determining σ_{ef}: 1 - without ultrasonic action; 2 - under ultrasound of power 1.5 kwt.

quid's density; μ - is its viscosity; h_{eq} - is the height of the liquid's rise along the capillar without ultrasound; P_{sound} - is the pressure in the field of ultrasonic wave; $\varkappa$ - is the factor of cavitation. To solve equation (1), let us use the following assumptions, i.e. omit the two first summands because of their small values and replace the variable value of ultrasonic pressure by its average value: $\overline{P}_{sound} = {}_0\int^T P_{sound} d\tau/T$; T is the period of oscillation; $P_{sound} = (2 P_{max} - \pi P_v)/2\pi$

$$-\frac{2\sigma}{\rho R} + gh + 8\mu(h+l_o)\frac{dh}{d\tau}/(R^2\rho) - \overline{P}_{sound}\varkappa/\rho = 0 \qquad (2)$$

Taking into account the adopted assumptions, the equation assumes the form:

$$V = \frac{dh}{d\tau} = \frac{R^2\rho}{8\mu(h+l_o)}\left(\frac{2\sigma}{\rho R} - gh + \frac{P_{sound}\varkappa}{\rho}\right) \qquad (3)$$

From equation (3) with V=0 the expression for determining the cavitation factor (Fig. 6) has form:

$$\varkappa = (\rho g h_{max} - 2\sigma/R)/\overline{P}_{sound} \qquad (4)$$

The developed theory allows to determine the height of the liquid's rise against time:

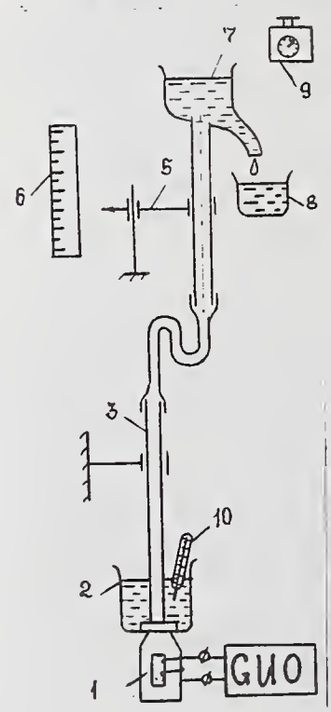

FIGURE 10. The design of a setup for reading consumption characteristics of an ultrasonic pump: 1 - magnetostrictive radiator; 2 - bath with water; 3 - steel capillar; 4 - compound glass capillar; 5 - attachement of the capillar; 6 - rule for measuring height; 7 - discharging funnel; 8 - measuring capasity; 9 - stop-watch; 10 - termometer.

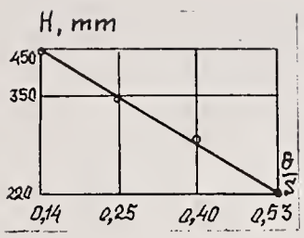

FIGURE 11A. Experimental dependence of consumption on the height of water in a capillar with T=22 °C, amplitude of GUO voltage U=80 V and angle of inclination of HP α=90 grad.

$$\tau = \frac{8\mu}{gR^2\rho}\left[(h_{max} + l_o)\ln\frac{h_{max}-h_o}{h_{max}-h} - h + h_o\right] \qquad (5)$$

which is a transcendental equation for determining the dependency $h = f(\tau)$.

The outcome of experimental study of USCE was a generalization of the experimental results in the form of the dependence $(h^*/h_{eq}) = f(Re_\omega)$, where $h^x = h - h_{eq}$ is the excess of the height of the liquid's rise in the capillar under ultrasonic action over the equilibrium height; $Re_\omega = 4\omega R^2/\nu$ - is the oscillatory Reynolds number, ν - is the kinematical viscosity of the liquid. The experimental results of different authors /10, 11/ are generaliwed by criterial equation /12/ (Fig. 7):

$$(h^*/h_{eq})^{0.5} = 0.092 \cdot Re^{0.27} \cdot (\tau^*)^{0.23} \qquad (6)$$

where τ^* - is dimensioneless time.

INVESTIGATION OF OPERATION OF A HEAT PIPE WITH A SOURCE OF ULTRASONIC OSCILLATIONS

The mechanism of ultrasonic influence on the processes of heat mass transfer in HP has not been studied ,though the received positive effect of such influence in other thermal devices is sufficiently large /13/. Here, a cylindrical HP, actuated in a vertical position with the evaporation zone located above, was investigated. The HP consisted of a sealed body (Fig. 8) in the internal space of which the face of a maghetostriction radiator of ultrasonic oscillations, capillary-porous wick, a transport artery-pipe were situated. The expression for determining the maximum heat flux, transported by HP in the condensation zone, as is well-know, has the form

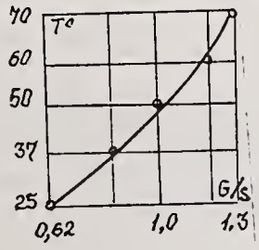

FIGURE 11B. Experimental dependence of water consumption on temperature T with voltage amplitude of U=80 V, angle of inclination 90 grad and height of a capillar pipe 220 mm.

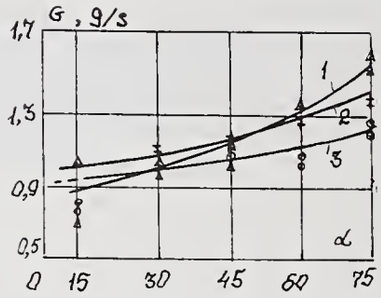

FIGURE 11C. Experimental dependence of water consumption through the artery on the angle of inclination of HP with voltage amplitude on GUO U=90 V.

$$Q_{max} = 2\rho^2 \cdot h_o b \delta g \cdot l_{max.sound} \, (\mu X K)^{-1} \qquad (7)$$

where X - is the length of the condensation zone, h_o - is the difference of enthalpies of vapour h_v and liquid h_l.

The ultrasonic influence reduces to increasing the maximum height of wick's absorption by the value of $\frac{l_{max.\ sound}}{l_{max.\ withaut\ sound}}$.

Let us asses the ultrasonic influence on thermal processes in the HP evaporation zone, assuming that only the surface tension factor changes in the ultrasonic field. As a rule, σ is the function of many variables and depends on a number of factors, that don't lend themselves to accurate analitical description. The assessment of change in the value of the surface tension factor in ultrasonic field was carried out here on the basis of the well-known formula, describing the velocity of liquid's rise in a capillar /14/:

$$\frac{dh}{d} = \frac{R^2 \rho}{8\mu h} \left(\frac{2\sigma \cos\theta}{\rho R} - gh\right) \qquad (8)$$

The analysis of expression (8) allows to obtain the assessment of alteration of the value of the surface tension factor in the form:

$$\frac{\sigma_{ef}}{\sigma} = \frac{R\rho g}{2} \cdot \frac{\tilde{K}-1}{\tilde{K}} \cdot \frac{h_{ef}}{\sigma} + \frac{h_{ef}}{h} \cdot \frac{1}{\tilde{K}} \qquad (9)$$

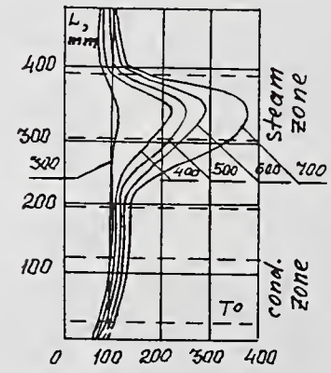

FIGURE 12. Distribution of water temperature along the HP axis in a stationary mode with different levels of heat loading.

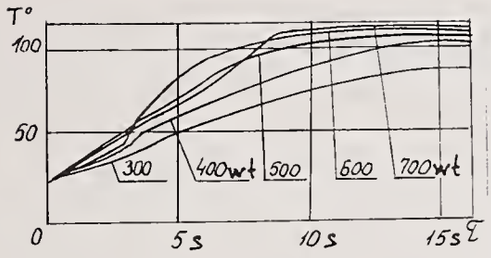

FIGURE 13. Temperature in the adiabatic zone of HP vs. time under different heater power.

The values h; h_{et}; K, entering expression (9) are obtained from the experimental data using the velocity of the liquid's rise in the capillar undes ultrasound (Fig. 9), allowing to determine the value of K from the measured values of h and h_{ef}. Thus, the analysis, carried out, showed, that the intensification of heat transfer in HP under ultrasonic action is related with intensification of mass transfer of the cooler along the feeding arteries of HP in the ultrasonic field. Ultimate possibilities of ultrasonic intensification of capillary mass transfer were determined in our experiments using a setup with a design, shown in Fig. 10. The employing in the setup of a compound capillar and mobile funnel allowed to measure consumption depending on the height of the artery's cut, its angle of inclination and water temperature. The frequency of ultrasonic radiation was fixed by dimensions of a concentrator of the ultrasonic radiator. The experiments were carried out using tap water settled during twenty-four hours.

The dependence of consumption of a capillary ultrasonic pump (CUP) on the height of the artery cut is chown in Fig. 11A, where the inverse dependence between the height of the liquid rise in the capillar and the consumption, provided by CUP, is observed. To determine the relationship between consumption and temperature, an electric heater was placed into a bath with water. The results of determining the efficiency of CUP operation against temperature are shown in Fig. 11, with the height of water in the bath amounting to 45 mm and the period of measurement equal to 50 s. Obviously, the consumption of water, ensured by CUP, increased with water temperature, since viscosity and surface tension decreased. Fig. 11B shows the dependence of water consumption through the capillar on the angle of inclination of its axis. Obviously, with the increase of the angle of inclination of the capillar, the water consumption through it under ultrasound increases since the projection of water gravity on the capillar axis decreases.

The investigation of processes of heat mass transfer was carried out on HP, operating in a vertical position, with a source of ultrasound. When investigating heat exchange the temperature difference on the walls of the evaporator and condenser

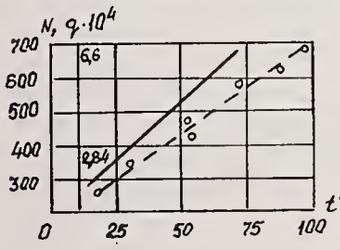

FIGURE 14. Specific radial heat power transmitted by HP operating with a source of ultrasonic oscillations vs. saturation temperature along the length of 300 mm: - calculations according formula /7/; --- experimental data for d=3 mm, T=25 °C.

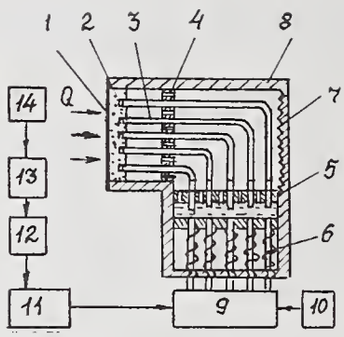

FIGURE 15. Schematical block-diagram of EPO based on HP with local control of heat exchange intensity along the reflecting surface on the basis of CUP, insuring correction of thermal deformations: 1 - reflecting surface; 2 - wick-base; 3 - capillary pipes of CUP; 5 - perphorated pipe boards, 6 - magnetostrictive radiators; 7 - channel (pin) wick of condensation zone; 8 - EPO body; 9 - commuting device, 10 - ultrasonic generator (USG) controlled on the volt tage amplitude of output signal; 11 - microprocessor; 12 - comparator; 13 - digital converter of transducer of thermal deformations; -14 - transducer of thermal deformations.

were determined according to the formulas: $\Delta T_{ev} = q_{ev} \cdot \delta/\lambda_w$; $\Delta T_{con.} = q_{con} \cdot \delta/\lambda_w$. The measurement of temperature of the HP body allowed to restore the distribution of vapour temperature along HP. Since the temperature distribution in HP was restored from measurements of the heat flow, the accuracy of such measurements was determined by the value of heat losses. For a given setup, the total heat losses amounted to 5 % of the nominal heat power, transmitted by HP.

Thus, the distribution of temperature of HP walls along the axis, in the stationary working mode, against the value of transmitted by HP heat power, are shown in Fig. 12. It follows from the given data that HP is activated under heat loadings exceeding 300 wt. The nature of temperature distribution in HP under heat loading 700 wt shows that in this case HP is still far from the limiting mode of operation that is characterised by the abscence of the temperature gradient along the condensation zone.

The described setup allowed to investigate dynamics of temperature changes in the adiabatic zone of HP with different powers of the heater. In this case the measurement error did not exceed 0.25 % (fig. 13).

To compare the experimental data with the results of calculations, Fig. 14 gives a generalizing dependence of specific heat power, transmitted by a radially water HP with a source of ultrasound, at length 330 mm. The comparison of theory and experimental data showed that CUP nearly to an order of magnitude intensified the capillary mass transfer, causing nearly to an order of magnitude the increase of the limiting heat flow, transmitted by HP. Moreover, HP with ultrasonic intensification of mass transfer possessed an operating ability in the vertical position, which the classical design of HP was not able to ensure.

THE ELEMENT OF POWER OPTICS OF A TECHNOLOGICAL LASER BASED ON HP WITH A SOURCE OF ULTRASONIC OSCILLATIONS

As is well-known, the main factor, restricting the value of the limiting heat flow, transmitted by HP, is the capillar pressure of the HP wick and the sound restriction on the vapour tract of HP. The power increase of technological lassers, the presence of local inhomogeneities in distribution of power in the cross-section of the laser beam determine the importance of the problem of creation of EPO in which a local control of heat exchange intensity along the reflecting surface is realized. The possibility of creation of such a thermo-controlled optical element, can be related with the usage of USCE. The principle scheme of the proposed and developed thermo-controlled EAO is shown in Fig, 15. The proposed design of EAO differs from the known designs in that the control by thermodeformations of the mirror surface is conducted by thermophysical methods. The developed design allowes to control the consumption of the cooler along the reflecting surface of EAO locally, in accordance with the value of local density of the heat flow. In addition in EAO, on the HP basis all constraints on capillary pressure of the wick are excluded, which increases its heat transmitting capasity. In this case the wick of the evaporation zone carries out the function of a uniform redistribution of the cooler along the surface of the EAO base, and the wick of the condensation zone serves to keep constant some excess of the cooler.

The carried out investigations of USCE, the testing of a model of HP with an ultrasound source corroborates the operating abilities and efficiency of EAO on the HP basis proposed here.

CONCLUSION

1. The physical model USCE is proposed and experimentally substantiated. A half-empirical quantitative treatement of USCE is proposed, consisting in emergence of ustrasonic cavitation of liquid near the capillar's cut.

2. An experimental HP with a source of ultrasound is developed and the limits of intensification of heat mass transfer if HP during the operation of USCE are determined.

3. A design of a thermoregulated EAO on the USCE basis is proposed.

REFERENCES

1. V.V. Apollonov, V.I. Borodin, I.V. Goncharenko, V.V. Ostanin, A.M. Prokhorov, V.Ju. Homich, E.V. Hristjan, S.A. Chetkin. Static and adaptive elements of power optics. // Izvestija of the USSR Acad. Sci., physical ser., 1984, vol. 48, no 8, p.1639-1643.

2. V.V. Apollonov, P.I. Bystrov, V.F. Goncharov et al. The prospects of using porous structures for cooling the elements of power optics. // Kvantovaja elektronika. - 1979, vol. 6, no 12, p. 2533-2545.

3. V.G. Voronin, A.B. Revjakin, V.Ja. Sasin, V.S. Tarasov. Lowtemperature heat pipes for flying vehicles. /Moscow, Mashinostroenie, 1976, 200p.

4. E.G. Konovalov. Ultrasonic capillar effect //Discoveries in the USSR. - Moscow, CNIIPI, 1973, p. 16-18.

5. O.K. Keller, G.S. Kratysh, G.D. Lubjanizky. Ultrasonic cleaning. /Leningrad, Mashinostroenie, 1977, 184p.

6. A.V. Kortnev, T.V. Makarova. Effect of ultrasonic oscillations on diffusion processes in liquid//In:Akustika i zvuk. - Kiev, Technika, 1966, p. 28-41.

7. C. Eckart. Vortices and stream caused by sound waves./ Phys. Rev. 1948, vol. 73, no 1, p.68-76.

8. I.N. Kanevski. Constant forces emerging in acoustic field// Akusticheskij jurnal, 1961, vol. 7, 1, p.3-17.

9. Ju.P. Rosin, V.S. Tichonova, M.N. Kostjuchek. On anomalously large pressures in a capillar in immediate vicinity of the source // Ukrainskij fizicheskij jurnal, 1975, vol. 20, no 2, p.214-219.

10. E.G. Konovalov, I.N. Germanovich. Ultrasonic capillar effect. Doklady of the USSR Acad. Sci., 1962, vol. 6, no 8, p.492-493.

11. V.I. Bulgakov. Experimental and theoretical study of processes of wood impregnation and painting in ultrasonic field. Thesis. Moscow, 1981, 232p.

12. G.N. Afanasjev, V.I. Bulgakov, A.N. Oblivin, A.K. Voskresenski. To the ultrasonic capillar effect // Nauchnye trudy of MLTI, 1981, vyp. 130, p.21-27.

13. V.G. Levich. Physical and chemical hydrodynamics. Moscow, Acad of Sci. of the USSR, 1952, 538p.

APPENDIX I

BOULDER DAMAGE SYMPOSIUM
November 1-3, 1989
List of attendees

Joseph Abate
Hampshire Instruments, Inc.
10 Carlson Road
P. O. Box 10159
Rochester, NY 14610

Mamoru Adachi
Adachi New Industrial Co., Ltd.
1-14-20 Itachibori Nishi-Ku
Osaka, 550
JAPAN
06 858-6203

Donnie Aminou
Rocky Mountain Instrument
1501 S. Sunset St.
Longmont, CO 80501
303 651-2211

Claude Amra
CNRS
ENSP de Marseille
Universitaire de St. Jerome
13013 Marseilles Cedex 13,
FRANCE
33 91288070

William L. Andre
US Army Strat. Def. Command
106 Wynn Dr.
P. O. Box 1500, CSSD-H-DT
Huntsville, AL 35807-3801
205 722-1666

Jonathan Arenberg
TRW
One Space Park, MS 01/1210
Redondo Beach, CA 90278
213 813-9551

Mark Babb
Montana Laser Optics
P. O. Box 4151
Bozeman, MT 59772
406 586-5100

Steve Bandettini
OCLI
2789 Northpoint Pk.
Santa Rosa, CA 95407-7397
707 525-7160

Steve Barnes
Oxford Inst. Ltd.
Eynsham, Oxford OX81TL,
ENGLAND
865 882 855 Ext. 321

Olivier Barnouin
Univ. of Illinois
214 Nuclear Engineering Lab
103 S. Goodwin Ave.
Urbana, IL 61801
217 333-1750

Philip Beck
Martin Marietta
P.O. Box 179, L8005
Denver, CO 80201
303 971-5075

Michael F. Becker
Univ. of Texas at Austin
ENS 143, ECE Dept.
Austin, TX 78712
512 471-3628

Denise Beeson
3-M Mountain View
420 N. Bearnard
Mountain View, CA 94043
415 969-5200

Raymond Bell
Lockheed
Mail Stop 9720/202
3251 Hanover Street
Palo Alto, CA 94304-1191
415 424-3396

Bernard Bendow
TRW
01/1280
One Space Park
Redondo Beach, CA 92647
213 813-9540

Harold Bennett
Naval Weapons Center
Michelson Labs.
Code 38101
China Lake, CA 93555
619 939-1440

Alain Bergeron
National Optics Inst.
369 Franquet St.
P. O. Box 9970
Sainte-Foy, Quebec G1V4C5
CANADA
418 657-7006

Jerry R. Bettis
Rocketdyne-Div Rockwell
M/S FA03
6633 Canoga Ave.
Canoga Park, CA 91303
818 700-6166

Robert Bieri
Lawrence Livermore Natl. Lab./MIT
P. O. Box 808, L-644
Livermore, CA 94550
415 423-0897

James D. Boyer
Los Alamos Nationl Lab.
P. O. Box 1663, MS J564
Los Alamos, NM 87545
505 667-9222

Robert K. Bratton
Litton Laser Systems
P. O. Box 547300
Orlando, FL 32854-7300
407 297-4522

Arthur Braundmeier
McDonnell-Douglas Elect.Sys.Co.
Bldg. 101, Mail Code 1066267
P. O. Box 516, Dept. Y440
St. Louis, MO 63166-0516
618 692-2359

Peter Braunlich
Washington State University
Department of Physics
Pullman, WA 99164-2814
509 332-3328

Ernie Braunschweig
R & D Associates
2600 Yale Boulevard, SE
Albuquerque, NM 87106
505 842-8911

Jerry Britten
Lawrence Livermore Nat'l. Lab.
P. O. Box 5508, L-367
Livermore, CA 94550
415 423-7653

Raymond Brusasco
Lawrence Livermore Nat'l. Lab.
P. O. Box 5508, L-490
Livermore, CA 94550
415 422-3111

Jack Campbell
Lawrence Livermore Nat'l. Lab.
P. O. Box 5508, L-490
Livermore, CA 94550
415 422-6497

Charles Carniglia
S Systems Corp.
P. O. Box 9316
Albuquerque, NM 87119
505 844-1064

Eduard Cartier
IBM
Watson Research Center
P. O. Box 48
Yorktown Heights, NY 10598
914 945-3339

Jack Chambers
II-VI Inc.
375 Saxonburg Blvd.
Saxonburg, PA 16056
412 352-4455

Lloyd L. Chase
Lawrence Livermore Nat'l. Lab.
P. O. Box 5508, L-490
Livermore, CA 94550
415 422-6151

Robert Chow
Lawrence Livermore Nar'l. Lab.
P. O. Box 808, L-791
Livermore, CA 94551
415 422-7615

Charles Cockrum
Rocky Mountain Instrument
1501 S Sunset St.
Longmont, CO 80501
303 651-2211

Daniel Cohn
MIT Lincoln Lab
167 Albany St.
Cambridge, MA 02139
617 253-5524

Lisa Connally
Wright Patterson AFB
WRDC/MLPJ
WPAFB, OH 45433-6533
513 255-1957

Michael Creighton
Perkin-Elmer Corp.
Mail Station 420
761 Main Ave.
Norwalk, CT 06859-0420
203 834-4511

John Daly
Litton Laser Systems
2707 S. Orange Blossom Tr.
Apopka, FL 32703
407 297-4457

Barbara Darnell
Spectral Systems
Ragged Hill Rd.
W. Brookfield, MA 01585
508 867-3321

Steven A. Davidson
MIT Lincoln Lab.
244 Wood St.
Lexington, MA 02173
617 981-3901

David Deacon
Deacon Research
900 Welch Rd., Suite 203
Palo Alto, CA 94304
415 326-1520

Donald Decker
Naval Weapons Center
Code 3816
China Lake, CA 93555
619 939-3247

Frank Demarco
Lawrence Livermore Nat'l. Lab.
P. O. Box 5508, L-491
Livermore, CA 94550
415 422-3022

John Detrio
Univ. of Dayton Res. Inst.
300 College Park Ave.
Dayton, OH 45469
513 229-3453

Randle Dewees
Naval Weapons Center
Code 3816
China Lake, CA 93555
619 939-3168

Manfred Dieckmann
Laser Zentrum Hannover e.V
Vahrenwalder Strasse 7
Welelfengarten 1
3000 Hannover 1,
WEST GERMANY
0511 762-4265

Jean Dijon
Commisiariat a l'Energie Atomique
D.LET1
CENG Ave des Martyrs
85X 38041
Grenoble, 38041
FRANCE
76884313

Terry Donovan
Naval Weapons Center
Code 3818
China Lake, CA 93555
619 446-2115

Fred Doss
Spectra-Physics Optics Corp.
1330 W. Middlefield Rd.
P. O. Box 7013
Mountain View, CA 94039-7013
415 961-2550

George Dugdale
Perkin-Elmer Corp
761 Main Ave.
Norwalk, CT 06859-0420
203 834-6271

Gary Edwards
Lawrence Livermore Nat'1. Lab.
P. O. Box 5508, L-486
Livermore, CA 94550
415 423-1921

Osama El-Bayoumi
U.S. Air Force
RADC/ESM
HAFB, MA 01731
617 377-3693

Phil Elizondo
Lockheed Research & Dev.
Dept. 97-20, Bldg. 202
3251 Hanover St.
Palo Alto, CA 94304
415 524-2315

David Emmony
Loughborough Univ. of Technology
Dept. of Physics
Loughborough, Leics LE11 3TV
UNITED KINGDOM
509 223306

Richard Eng
MIT Lincoln Laboratory
244 Wood Street
Lexington, MA 02173
617 981-3695

Gregory J. Exarhos
Battelle Northwest
Battelle Boulevard
P. O. Box 999, MS K2-44
Richland, WA 99352
509 375-2440

Bill Farmer
U.S.A. Strat. Def. Command
Attn: CSSD-H-D
P. O. Box 1500
Huntsville, AL 35807-3801
205 895-4780

George Ferguson
Lockheed Palo Alto Lab.
0/9720 B/202
3251 Hanover St.
Palo Alto, CA 94304
415 424-2319

Kim Ferris
Pacific Northwest Laboratory
P. O. Box 999
Richland, WA 99352
508 375-3754

Shari Powell Fisher
OCLI
Ridgeway
Hillend Industrial Park
Dun Fermline FIFE , KY11 SFR
UNITED KINGDON
0383 823-631

Herve Floch
Commissariat al'Energie
Centre d'Etudes de Limeil
BP27
Villeneuve St. Georg, 94190
FRANCE

Ronald Francis
Ball Aerospace
P. O. Box 1062
Boulder, CO 80303
303 939-5556

Jerome B. Franck
Naval Weapons Center
China Lake, CA 93555
619 939-3827

Alan Frank
Lawrence Livermore Nat'l. Lab.
P.O. Box 808, L-281
Livermore, CA 94550
415 422-7271

Mary Fuka
Univ. of New Mexico
800 Yale Blvd. NE
Albuquerque, NM 87131
505 277-2616

Yoshiyuki Fukui
Shin-etsu Quartz Prod Co
Shinjuku San-ei Bldg. 1-22-2
Shinjuku-ku, Tokyo
JAPAN
0429 44 9289

Andy Garay
US Army Strat. Def. Command
GBL PO
(CSSD-H-FB)
WSMR, NM 88002-1198
505 678-2383

Adolf Giesen
IFSW, Univ of Stuttgart
Pfaffenwaldring 43
7000 Stuttgart 80,
WEST GERMANY

Robert Goedert
US Army TACOM
AMSTA-RSC
Warren, MI 48397
313 574-5325

Johnny Grammer
Lockheed Missiles & Space
1111 Lockheed Way
0/51-50, B/586
Sunnyvale, CA 94089-3504
408 756-4491

Richard Grauslys
Kollsman
220 Daniel Webster H
M/S 2-B12-2
Merrimack, NH 03054-4809
603 595-6093

Arthur H. Guenther
Los Alamos National Lab.
P. O. Box 1663
Los Alamos, NM 87544
505 667-1331

Sandra R. Gyetvay
The Aerospace Corp.
P. O. Box 92957, M2/241
Los Angeles, CA 90009
213 336-8239

Yubong Hahn
Rocky Mountain Instrument Co
1501 S. Sunset
Longmont, CO 80501
303 651-2211

Christopher Hale
Optical Coating Lab. Inc
Ridgeway
Hillend Industrial Park
Fife, KY11 5FR UK
SCOTLAND
44 383 823631

Chuck Hamilton
Spectra Tech
2755 Northup Way
Bellevue, WA 98004
206 827-0460

Richard S. Hockett
Charles Evans & Associates
301 Chesapeake Dr.
Redwood City, CA 94063
415 369-4567

Lloyd Hodge
LMSC
14055 Palomino Way
Saratoga, CA 95070
408 742-6232

James Hoenigman
University of Dayton
Research Institute KL562
Dayton, OH 45469
513 229-3119

Robert Hoffman
Ctr. Night Vision & Electro-Optics
AMSEL-RD-NV-L
Rm 2, Bldg 317
Ft. Belvoir, VA 27060
703 664-1431

Samuel Holmes
Northrop Research & Tech Center
One Research Park
M/S 345/T20
Palos Verdes Peninsula, CA 90274
213 544-5314

Alan Hopkins
W. J. Shafer Assoc.
5100 Springfield Pik
Suite 511
Dayton, OH 45431
513 253-9572

Hamilton Hunter
Martin Marietta Energy Sys
P. O. Box 2008
Oak Ridge Natl. Lab.
Oak Ridge, TN 37831-6372
615 576-4295

Helmar Janee
Science Applications Int'l. Corp.
Pacifica Technology Division
11696 Sorrento Valley Rd., Ste A.
San Diego, CA 92121
619 453-2530

John Jewell
Naval Research Lab
Code 6505
4555 Overlook Ave., S.W.
Washington, DC 20375-5000
202-767-9325

Michael Jin
University of Rochester
250 E. River Rd.
Lab. for Laser Energetics
Rochester, NY 14623-1299
716 275-5101

Linda Johnson
Naval Weapons Center
Code 3818
China Lake, CA 93555
619 939-1422

L. John Jolin
Los Alamos National Lab.
MS J564
Los Alamos, NM 87545
505 667-7102

George Jones
Contraves Goerz Corp
610 Epsilon Dr.
Pittsburgh, PA 15238
412 967-7733

Mark A. Kahan
Optical Research Associates
945 Concord Street
Framingham, MA 01701
508 872-6001

Robert Keim
Eastman Kodak Co.
121 Lincoln Ave.
Rochester, NY 14653-8118
716 253-2375

Floyd Kinder
COMARCO
1201 N. China Lake Blvd.
Ridgecrest, CA

Margaret Kohin-Nitschelm
Litton/Itek Optical Sys
10 Maguire Rd.
Lexington, MA 02173
617 276-3332

Juergen Kolbe
Universitaet Hannover
Institut Fuer Quantenoptik
Welfengarten 1
D-3000 Hannover 1,
FEDERAL REPUBLIC OF GERMANY
049 511-762-3381

Mark Kozlowski
Lawrence Livermore Nat'l. Lab.
P. O. Box 5508, L-489
Livermore, CA 94550
415 422-2925

G. Edward Kuhl
W. J. Shafer Assoc.
5100 Springfield Pk.
Suite 511
Dayton, OH 45431
513 253-9572

Ramin Lalezari
PMS Electro-Optics
1855 South 57th Court
Boulder, CO 80301
303 443-7100

Huai-Chuan Lee
Hoya Optics, Inc.
3400 Edison Way
Fremont, CA 94538
415 490-1880

Olive Lee
Deacon Research
900 Welch Rd.
Suite 203
Palo Alto, CA 94304
415 326-1520

Charles Leung
XMR, Inc.
5403 Betsy Ross Dr.
Santa Clara, CA 95054
408 988-2426

Keith Lewis
Royal Signals & Radar Establishment
St. Andrews Rd.
Malvern, Worcs WR14 3PS
UNITED KINGDOM
44 684 895062

Matthew Magida
Perkin Elmer
100 Wooster Heights, MS848
Danbury, CT 06810
203 797-6355

Klaus Mann
Laser Laboratorium Grottingen eV.
Robert-Bosch-Breite 10
Grottingen, 3400
WEST GERMANY
0551 61067

C. Denton Marrs
Naval Weapons Center
Code 3817
China Lake, CA 93555
619 939-2470

Bryan Mason
Naval Weapons Center
Code 3817
China Lake, CA 93555
619 939-2470

John Gordon Mathew
Heriot-Watt University
Physics Dept.
Riccarton Campus
Edinburgh, Scotland EH14 4AS
UNITED KINGDOM
031 451-3069

Eckart Matthias
Freie Universitaet Berlin
Fachbereich Physik
Arnimallee 14
1000 Berlin 33
WEST GERMANY
FRG-30-8383340

Alasdair McInnes
Barr & Stroud Ltd.
Applied Physics Group
Anniesland
Glasgow, G13 1HZ
Scotland
UNITED KINGDOM
041 954 9601 x2527

Ted McMinn
McDonnell Douglas
P. O. Box 516, MC 1066267
St. Louis, MO 63166
314 234-4321

Kent Meeks
Sandia Nat'l Lab
P. O. Box 5800
Albuquerque, NM 87185
505 844-1040

John Midavaine
Eastman Kidak Co
D337
MS 38015
Rochester, NY 14653-8015
716 253-2462

Perry A. Miles
R & D Assoc
4640 Admiralty Way
Marina del Rey, CA 90295
213 822-1715

Kent Moncur
KMS Fusion
700 KMS Place
Ann Arbor, MI 48108
313 769-8500

Bryan Monosmith
NASA/Goddard
MS 723
Greenbelt, MD 20771
301 286-7017

Thomas Mooney
Barr Associates, Inc.
2 Lyberty Way
Westford, MA 01886
508 692-7513

Mark Moran
Naval Weapons Center
Code 3817
China Lake, CA 93555
619 939-3827

David Mordaunt
Hughes Aircraft Company
Bldg. E1/MSB129
P. O. Box 902
El Segundo, CA 90245
213 616-5422

Amber J. Morgan
Lawrence Livermore Nat'l. Lab.
P. O. Box 5508, L-249
Livermore, CA 94550
415 423-3277

Aspasia Sylvia Nasla
The Welding Institute
Abington Hall
Abington
Cambridge, CB16AL
ENGLAND
223 891162

Soe-Mie Nee
Naval Weapons Center
Code 38101
China Lake, CA 93555
619 939-1425

Brian Neff
Thermo Electron Technologies
9550 Distribution Av
San Diego, CA 92121
619 578-5885

Brian E. Newnam
Los Alamos National Lab.
MS-J564
Los Alamos, NM 87545
505 667-7979

Davis Nichols
Boeing Aerospace & Electronics
Mail Stop 8H-29
P. O. Box 3999
Seattle, WA 98124
206 773-8938

Hasegawa Niichiro
Shin-Etsu Quartz Product
22-2 Nishi-Shinjuku 1-Chome
Shinjuka
Tokyo,
JAPAN
03-348-1911

Hiroshi Noguchi
Daido Steel Co., Ltd.
2-30 Daido-Cho
Minami-Ku
Nagoya-City, Aichi-Ken 457
JAPAN
81 52-611-2511

Robert O'Connell
University of Missouri
Electrical & Computer Eng. Dept.
Columbia, MO 65211
314 552-8373

Elke Oertel
Laser Zentrum Hannover e.V.
Engelbosteler Damm 25
3000 Hannover 1
Hannover,
GERMANY
0511 762-3381

Albert Ogloza
Naval Weapons Center
Code 3816
China Lake, CA 93555
619 939-3247

Takayuki Okamoto
Okamoto Optics Co.
8-34 Hayamachi
Isogo-ku
Yokohama,
JAPAN
045 752 2233

Yoshiaki Okamoto
Okamoto Optics Co
8-34 Haramachi
Isogo-ku
Yokohama,
JAPAN
045 752-2233

Nora Osborne
Univ. of Dayton Res. Inst.
300 College Pk
KL 165
Dayton, OH 45469
513 229-4508

Frank Padilla
USASDC
P. O. Box 124
(CSSD-H-FB)
WSMR, NM 88002-1198
505 678-2441

Roger A. Paquin
Perkin Elmer
Electro-Optics Tech Div
100 Wooster Heights
Danbury, CT 06810
203 797-6130

Michael Pavia
Hampshire Instruments Inc.
10 Carlson Road
P. O. Box 10159
Rochester, NY 14610

Emile Pelletier
CNRS
ENSP de Marseille
Domaine Universitaire de StJerome
13397 Marseilles Cedex 13, 13013
FRANCE
91 28 83 28

G. Paul Perryman
Texas Instruments Inc.
8505 Forest Lane
P. O. Box 660246, MS 3122
Dallas, TX 75266
214 480-1157

Cathy Peterson
Hughes Santa Barbara Res. Cent.
M/S 54
75 Coromar Drive
Goleta, CA 93117
805 562-2913

Stefan Petzoldt
Freie Universitat Berlin
1000 Berlin 33
Arnimallee 14,
GERMANY

Robert Poirier
Corion Corp.
73 Jeffrey Ave.
Holliston, MA 01746
508 429-5065

Robert S. Polvani
NIST
Bldg 220, Rm A 107
Gaithersburg, MD 20899
301 975-3487

Bradley Pond
S Systems Corp.
P. O. Box 9316
Albuquerque, NM 87119
505 844-1064

James O. Porteus
Naval Weapons Center
Code 3817
China Lake, CA 93555
619 939-3827

Jack Price
US Naval Surface Warfare
10901 N. Hampshire Ave.
Code R41, White Oak Lab
Silver Spring, MD 20903
202 394-2272

Manfred Rahe
Laser Zentrum Hannover e.V.
3000 Hannover 1
Weckenstr. 19
Hannover,
FEDERAL REPUBLIC OF GERMANY
05 11 762-4265

Frank Rainer
Lawrence Livermore Nat'l. Lab.
P. O. Box 5508, L 490
Livermore, CA 94550
415 422-4376

Tilak Raj
Martin Marietta Energy Systems
P. O. Box 2003, MS7272
Oak Ridge, TN 37831-7272
615 574-4822

Juergen Reif
Freie Universitat Berlin
Fachbereich Physik
Arnimallee 14
1000 Berlin 33,
WEST GERMANY
49308387157

David Resendes
Physical Sciences, Inc.
Research Pk
P. O. Box 3100
Andover, MA 01810-7100
508 475-9030

Steven Risser
Battelle Pacific Northwest Lab
Box 999, K2-44
Richland, WA 99352
509 375-2323

Dan Rogers
Honeywell
3660 Technology Dr.
P. O. Box 1361 MM 65-2600
Minneapolis, MN 55440

Chris Rowan
EM Industries
5 Skyline Drive
Hawthorne, NY 10532
914 592-4660

Gary Saenz
Rockwell Int'l
Rocketdyne Div. FA03
6633 Canoga Ave
Canoga Park, CA 91303

Virgil Sanders
Los Alamos National Lab.
P. O. Box 1663, MS J564
Los Alamos, NM 87545
505 667-7398

Paul Schall
JAYCOR
2951 28th St., Suite 3075
Santa Monica, CA 90405
213 392-7229

Marion Scott
Los Alamos National Lab.
M/S E549
Los Alamos, NM 87545
505 667-7557

Robert W. Seibold
Hughes Aircraft Company
Mail Station E1/F150
P. O. Box 902
El Segundo, CA 90245
213 616-6183

Steven Seitel
Montana Laser Optics
P. O. Box 4151
Bozeman, MT 59772
406 586-5100

Robert Setchell
Sandia National Lab.
P. O. Box 5800
Kirtland AFB
Albuquerque, NM 87185
505 846-3156

Dennis Sigler
Burleigh Northwest Optical Inc.
Burleigh Park
Fishers, NY 14453
716 924-9355

Donald G. Simons
Naval Surface Warfare Center
White Oak
Silver Spring, MD 20903-5000
202 394-2272

George Sloan
U.S. Army Strat. Def.
106 Wynn Drive
Huntsville, AL 35807
205 895 3778

Jerry J. Smith
U.S. Dept. of Energy
ER-132
Washington, DC 20545
301 353-3426

Jim Snyder
Exotic Materials
2930 Bristol St.
Costa Mesa, CA 92626
714 545-9425

M.J. Soileau
University of Central Florida
Center for Research
in Electro-Optics & Lasers
12424 Research Parkway
Orlando, FL 32826
407 658-6834

Stephen Somerstein
Lockheed Missiles & Space
1111 Lockheed Way
Org. 51-50, B-586E
Sunnyvale, CA 94089-3504
408 742-7274

Michael C. Staggs
Lawrence Livermore Nat'l. Lab
P. O. Box 5508, L-489
Livermore, CA 94550
415 422-2925

James L. Stanford
Naval Weapons Center
Code 381
China Lake, CA 93555
619 939-1444

Molly Ann Stepko
Litton Airtron
200 E. Hanover Ave.
Morris Plains, NJ 07927
201 539-5500

Martin Stickley
BDM Intl, Inc.
1300 N. 17th St., Suite 950
Arlington, VA 22209
703 247-0370

Kenneth Sun
Rocketdyne, Div. Rockwell
6633 Canoga Ave.
Chatsworth, CA 91303
818 700-4953

Randall T. Swimm
Univ. of Southern Calif.
Center for Laser Studies
Los Angeles, CA 90089-1112

Chol Syn
Lawrence Livermore Nat'l Lab
P. O. Box 808, L-792
Livermore, CA 94550
415 423-8226

Paul Szczepanski
Airtron/Litton
200 East Hanover Avenue
Morris Plains, NJ 07950
201 539-5500

John R. Taylor
Lawrence Livermore Nat'l. Lab.
7000 E Ave.
P.O. Box 5508
Livermore, CA 94550
1415 423-4438

John S. Taylor
Lawrence Livermore Nat'l. Lab.
P. O. Box 808, L-792
Livermore, CA 94550
415 423-8227

Ian M. Thomas
Lawrence Livermore Nat'l. Lab.
P. O. Box 5508, L-483
Livermore, CA 94550
415 423-3896

Shizuo Udagawa
Canon Inc.
20-2 Kiyohaya Kogyodanchi
Utsunomiya-shi
Tochigi,
Japan
0286 67-5339

Walter Unites
Lawrence Livermore Nat'l. Lab.
P. O. Box 5508, L-474
Livermore, CA 94550
415 422-8381

George Valenta
Storage Tek
2270 S. 88th St.
Louisville, CO 80027

Marc Von Gunten
Spectra-Physics Optics Corp
Mail Stop 4-30
1330 W. Middlefield Rd.
Mountain View, CA 94039
415 961-2550 Ext. 3008

Ted Washburne
Lockheed Missiles & Space
1111 Lockheed Way
0/51-52 B/586E
Sunnyvale, CA 94089-3504
408 742-6651

Steve E. Watkins
Univ. of Missouri-Rolla
223 ERL
Rolla, MO 65401
314 341-4139

James Wells
Teledyne Brown Engineering
Mailstop 19
300 Sparkman Drive
Huntsville, AL 35816
205 726-1592

Patricia White
Battelle PNL
MSIN K3-59
P. O. Box 999
Richland, WA 99352
509 375-6876

Thomas Whittaker
US Army Tank-Automotive Comm
AMSTA-RSC
Warren, MI 48397-5000
313 574-5325

John G. Wilder
Lawrence Livermore Nat'l. Lab.
P. O. Box 5508, L-483
Livermore, CA 94550
415 423-3896

Ron Willey
Opto Mechanik Inc.
P. O. Box 361907
426 North Dr.
Melbourne, FL 32935
407 254-1212

Forrest Williams
S Systems Corp.
P. O. Box 9316
Albuquerque, NM 87119
505 844-1064

Richard Wirtenson
Lawrence Livermore Nat'l. Lab.
P. O. Box 808, L-398
Livermore, CA 94550
415 462-3798

C. Robert Wolfe
Lawrence Livermore Nat'l. Lab.
P. O. Box 5508, L-490
Livermore, CA 94550
415 422-3516

Frank J. Woodberry
Rocketdyne-Div Rockwell
M/S FA03
6633 Canoga Ave.
Canoga Park, CA 91303
818 700-4737

Kunio Yoshida
Osaka University
Institute of Laser Engineering
2-6 Yamada-oka
Suita Osaka, 565,
JAPAN
06 877-5111

Mark Youn
Rocky Mountain Instrument
1501 S. Sunset St.
Longmont, CO 80501
303 651-2211

Terry S. Zaccone
Lockheed Missiles & Space
1111 Lockheed Way
0/51-52, B586E
Sunnyvale, CA 94089-3504
408 742-6406

Vassilis Zarifis
Lockheed Research Labs.
0/97-20 B/202
3251 Hanover Street
Palo Alto, CA 94304-1191
415 354-5851

Chenzhi Zhang
Univ. of Texas at Austin
ETC 8-168
MS & E
Austin, TX 78712
471-4735

Richard Zoborowski
OCLI
Dept. 428-1
2789 Northpoint Pky
Santa Rosa, CA 95407-7397
707 525-7007

J. David Zook
Honeywell
10701 Lyndale Ave. S.
Bloomington, MN 55337
612 887-4383

Allen Zwan
General Dynamics
P. O. Box 85357
San Diego, CA 92138
619 547-4018

BL-114A
(5-90)

U.S. DEPARTMENT OF COMMERCE
NATIONAL INSTITUTE OF STANDARDS AND TECHNOLOGY

BIBLIOGRAPHIC DATA SHEET

1. PUBLICATION OR REPORT NUMBER
NIST/SP-801

2. PERFORMING ORGANIZATION REPORT NUMBER

3. PUBLICATION DATE
October 1990

4. TITLE AND SUBTITLE

Laser Induced Damage in Optical Materials: 1989

5. AUTHOR(S)
Harold E. Bennett (NWC), Lloyd L. Chase (LLNL), Arthur H. Guenther (LANL)
Brian E. Newnam (LANL), and M. J. Soileau (UCF)

6. PERFORMING ORGANIZATION (IF JOINT OR OTHER THAN NIST, SEE INSTRUCTIONS)
U.S. DEPARTMENT OF COMMERCE
NATIONAL INSTITUTE OF STANDARDS AND TECHNOLOGY
BOULDER, COLORADO 80303-3328

7. CONTRACT/GRANT NUMBER

8. TYPE OF REPORT AND PERIOD COVERED

9. SPONSORING ORGANIZATION NAME AND COMPLETE ADDRESS (STREET, CITY, STATE, ZIP)
National Institute of Standards and Technology (NIST)
American Society for Testing and Materials (ASTM)
International Society for Optical Engineering (SPIE)
Defense Advanced Research Project Agency (DARPA)
Department of Energy (DOE)

10. SUPPLEMENTARY NOTES

11. ABSTRACT (A 200-WORD OR LESS FACTUAL SUMMARY OF MOST SIGNIFICANT INFORMATION. IF DOCUMENT INCLUDES A SIGNIFICANT BIBLIOGRAPHY OR LITERATURE SURVEY, MENTION IT HERE.)

The Twenty-First Annual Symposium on Optical Materials for High-Power Lasers (Boulder Damage Symposium) was held at the National Institute of Standards and Technology in Boulder, Colorado, November 1-3, 1989. The Symposium was sponsored jointly by the National Institute of Standands and Technology, the American Society for Optical Engineering, the Defense Advanced Research Project Agency, and the Department of Energy. Approximately 200 scientists including representatives of the United Kingdom, France, Japan, Canada, and the Federal Republic of Germany, attended the Symposium. The Symposium was divided into sessions concerning Materials and Measurements, Mirrors and Surfaces, Thin Films, and, finally, Fundamental Mechanisms. As in previous years, the emphasis of the papers presented at the Symposium was directed toward new fromtiers and new developments. Particular emphasis was given to materials for high power apparatus. The wavelength range of the prime interest was from 10.6 μm to the uv region. Highlights included surface characterization, thin film substrate boundaries, and advances in fundamental laser-matter threshold interactions and mechanisms. The scalling of damage thresholds with pulse duration, focal area, and wavelength was discussed in detail. Harold E. Bennett of the Naval Weapons Center, Arthur H. Guenther of the Los Alamos National laboratory, Lloyd L. Chase of the Lawrence Livermore National Laboratory, Brian E. Newnam of the Los Alamos National Laboratory, and M. J. Soileau of the University of Central Florida were co-chairmen of the Symposium. The Twenty-Second Annual Symposium is scheduled for October 24-26, 1990, at the National Institute of Standards and Technology, Boulder, Colorado.

12. KEY WORDS (6 TO 12 ENTRIES; ALPHABETICAL ORDER; CAPITALIZE ONLY PROPER NAMES; AND SEPARATE KEY WORDS BY SEMICOLONS)

laser damage; laser interaction; optical components; optical fabrication; optical materials and properties; thin film coatings.

13. AVAILABILITY

[X] UNLIMITED

[ ] FOR OFFICIAL DISTRIBUTION. DO NOT RELEASE TO NATIONAL TECHNICAL INFORMATION SERVICE (NTIS).

[X] ORDER FROM SUPERINTENDENT OF DOCUMENTS, U.S. GOVERNMENT PRINTING OFFICE, WASHINGTON, DC 20402.

[ ] ORDER FROM NATIONAL TECHNICAL INFORMATION SERVICE (NTIS), SPRINGFIELD, VA 22161.

14. NUMBER OF PRINTED PAGES
670

15. PRICE

ELECTRONIC FORM

NIST Technical Publications

Periodical

Journal of Research of the National Institute of Standards and Technology—Reports NIST research and development in those disciplines of the physical and engineering sciences in which the Institute is active. These include physics, chemistry, engineering, mathematics, and computer sciences. Papers cover a broad range of subjects, with major emphasis on measurement methodology and the basic technology underlying standardization. Also included from time to time are survey articles on topics closely related to the Institute's technical and scientific programs. Issued six times a year.

Nonperiodicals

Monographs—Major contributions to the technical literature on various subjects related to the Institute's scientific and technical activities.

Handbooks—Recommended codes of engineering and industrial practice (including safety codes) developed in cooperation with interested industries, professional organizations, and regulatory bodies.

Special Publications—Include proceedings of conferences sponsored by NIST, NIST annual reports, and other special publications appropriate to this grouping such as wall charts, pocket cards, and bibliographies.

Applied Mathematics Series—Mathematical tables, manuals, and studies of special interest to physicists, engineers, chemists, biologists, mathematicians, computer programmers, and others engaged in scientific and technical work.

National Standard Reference Data Series—Provides quantitative data on the physical and chemical properties of materials, compiled from the world's literature and critically evaluated. Developed under a worldwide program coordinated by NIST under the authority of the National Standard Data Act (Public Law 90-396). NOTE: The Journal of Physical and Chemical Reference Data (JPCRD) is published quarterly for NIST by the American Chemical Society (ACS) and the American Institute of Physics (AIP). Subscriptions, reprints, and supplements are available from ACS, 1155 Sixteenth St., NW., Washington, DC 20056.

Building Science Series—Disseminates technical information developed at the Institute on building materials, components, systems, and whole structures. The series presents research results, test methods, and performance criteria related to the structural and environmental functions and the durability and safety characteristics of building elements and systems.

Technical Notes—Studies or reports which are complete in themselves but restrictive in their treatment of a subject. Analogous to monographs but not so comprehensive in scope or definitive in treatment of the subject area. Often serve as a vehicle for final reports of work performed at NIST under the sponsorship of other government agencies.

Voluntary Product Standards—Developed under procedures published by the Department of Commerce in Part 10, Title 15, of the Code of Federal Regulations. The standards establish nationally recognized requirements for products, and provide all concerned interests with a basis for common understanding of the characteristics of the products. NIST administers this program as a supplement to the activities of the private sector standardizing organizations.

Consumer Information Series—Practical information, based on NIST research and experience, covering areas of interest to the consumer. Easily understandable language and illustrations provide useful background knowledge for shopping in today's technological marketplace.

Order the **above** *NIST publications from: Superintendent of Documents, Government Printing Office, Washington, DC 20402.*

Order the **following** *NIST publications—FIPS and NISTIRs—from the National Technical Information Service, Springfield, VA 22161.*

Federal Information Processing Standards Publications (FIPS PUB)—Publications in this series collectively constitute the Federal Information Processing Standards Register. The Register serves as the official source of information in the Federal Government regarding standards issued by NIST pursuant to the Federal Property and Administrative Services Act of 1949 as amended, Public Law 89-306 (79 Stat. 1127), and as implemented by Executive Order 11717 (38 FR 12315, dated May 11, 1973) and Part 6 of Title 15 CFR (Code of Federal Regulations).

NIST Interagency Reports (NISTIR)—A special series of interim or final reports on work performed by NIST for outside sponsors (both government and non-government). In general, initial distribution is handled by the sponsor; public distribution is by the National Technical Information Service, Springfield, VA 22161, in paper copy or microfiche form.

U.S. DEPARTMENT OF COMMERCE
National Institute of Standards and Technology
(formerly National Bureau of Standards)
325 Broadway
Boulder, Colorado 80303-3328
